

**21ST INTERNATIONAL CONFERENCE
on Thermal Science
and Engineering of Serbia**

SimTerm.4E
PROCEEDINGS

2024

Faculty of Mechanical Engineering Niš, Serbia, October 22-25





The 21st International Conference on
Thermal Science and Engineering of Serbia

SimTerm2024

Niš, Serbia, October 22-25



University of Niš, Faculty of Mechanical Engineering in
Niš, Department of Thermal Engineering and
Society of Thermal Engineers of Serbia

ISBN 978-86-6055-192-6



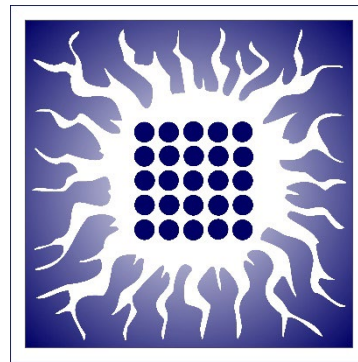
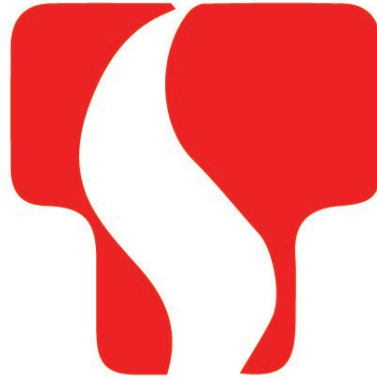
Publisher: Faculty of Mechanical Engineering in Niš
Niš, 2024



The 21st International Conference on
Thermal Science and Engineering of Serbia

SimTerm2024

Niš, Serbia, October 22-25



ENERGY

EFFICIENCY

ECONOMY

ECOLOGY



The 21st International Conference on
Thermal Science and Engineering of Serbia

SimTerm2024

Niš, Serbia, October 22-25



21st International Conference on Thermal Science and Engineering of Serbia

under the title:

ENERGY – ECOLOGY – EFFICIENCY – ECONOMY

organized by:

THE UNIVERSITY OF NIŠ,
FACULTY OF MECHANICAL ENGINEERING,
DEPARTMENT OF THERMAL ENGINEERING
AND
SOCIETY OF THERMAL ENGINEERS OF SERBIA

under the patronage of:

THE MINISTRY OF SCIENCE, TECHNOLOGICAL DEVELOPMENT AND INNOVATION OF
THE REPUBLIC OF SERBIA
THE MINISTRY OF ENVIRONMENTAL PROTECTION OF THE REPUBLIC OF SERBIA
THE MINISTRY OF MINING AND ENERGY OF THE REPUBLIC OF SERBIA

and supported by:

VINCA INSTITUTE OF NUCLEAR SCIENCES – NATIONAL INSTITUTE OF THE
REPUBLIC OF SERBIA



International Scientific Committee

President:

Dr Miodrag Mesarović, Academy of Engineering Sciences of Serbia

Members:

Dr Jordan Hristov, full professor,

University of Chemical Technology and Metallurgy, Department of Chemical Engineering, Sofia, Bulgaria

Dr Mikhail Shatrov, full professor

Automobile and Road Construction State Technical University, Moscow, Russia

Dr Zvonimir Guzović, full professor

University of Zagreb, Faculty of Mechanical Engineering and Naval Architecture, Zagreb, Croatia

Dr Igor Vušanović, full professor

University of Montenegro, The Faculty of Mechanical Engineering, Podgorica, Montenegro

Dr Anna Stoppato, associate professor

University of Padova, Department of Industrial Engineering, Padova, Italy

Dr Slavcho G. Slavtchev, associate member

Institute of Mechanics, Bulgarian Academy of Sciences, Sofia, Bulgaria

Dr Agis Papadoupoulos, full professor

Aristotle University Thessaloniki, Department of Mechanical Engineering, Thessaloniki, Greece

Dr Joseph N. Moore, research professor

University of Utah, Energy & Geoscience Institute, Salt Lake City, USA

Dr Konstantinos Papakostas, associate professor

Aristotle University Thessaloniki, Department of Mechanical Engineering, Thessaloniki, Greece

Dr Sophia Natalia Boemi, senior research

Aristotle University Thessaloniki, Department of Mechanical Engineering, Thessaloniki, Greece

Dr Iliya Iliyev, full professor

University of Ruse, Department of Thermotechnics, Hydraulic and Ecology, Ruse, Bulgaria

Dr Dušan Golubović, full professor

University of East Sarajevo, Faculty of Mechanical Engineering, Sarajevo, Republic of Srpska, BH

Dr Ljubica Kanevče, full professor

St. Kliment Ohridski University, Faculty of Technical Sciences, Bitola, North Macedonia

Dr Petar Gvero, full professor

University of Banja Luka, Faculty of Mechanical Engineering, Banja Luka, Republic of Srpska, BH

Dr Arpad Nyers, associate professor

University of Pecs, Faculty of Engineering and Information Technology, Pecs, Hungary

Dr Maria Ichim, scientific advisor

Institute for Bioengineering, Biotechnology and Environmental Protection, Bucharest, Romania

Dr Vesna Barišić, senior researcher

Sumitomo SHI FW, Espoo, Finland

Dr Dečan Ivanović, full professor

University of Montenegro, The Faculty of Mechanical Engineering, Podgorica, Montenegro

Dr Friedrich Dinkelacker, full professor

Leibniz University Hannover, Faculty of Electrical Engineering and Computer Science, Hannover, Germany

Dr Risto Filkoski, full professor

Ss. Cyril and Methodius University, Faculty of Mechanical Engineering, Skopje, North Macedonia

Dr Tetyana Morozyuk, full professor

Technical University Berlin, Institute for Energy Engineering, Berlin, Germany

Dr Zlatan Car, full professor

University of Rijeka, Faculty of Engineering, Rijeka, Croatia

Dr Darko Knežević, full professor

University of Banja Luka, Faculty of Mechanical Engineering, Republic of Srpska, Banja Luka, BH

Dr Gyula Gróf, full professor

Department of Energy Engineering Hungary, Budapest, Hungary



Dr Zdravko Milovanović, full professor

University of Banja Luka, Faculty of Mechanical Engineering, Banja Luka, Republic of Srpska, BH

Dr Breda Kegl, full professor

University of Maribor, Faculty of mechanical engineering, Maribor, Slovenia

Dr Vladimir G. Tuponogov, full professor

Ural Federal University named after the first President of Russia B. N. Yeltsin, Ekaterinburg, Russia

Dr Vladimir Mijakovski, full professor

St. Kliment Ohridski University, Faculty of Technical Sciences, Bitola, North Macedonia

Dr Violeta Rasheva, full professor

University of Food Technology Plovdiv, Department of Industrial Thermal Engineering, Plovdiv, Bulgaria

Dr Oleh Onysko, associate professor

Ivano-Frankivsk National Technical University of Oil and Gas, Ivano-Frankivsk, Ukraine

Dr Lubomir Dimitrov, full professor

Technical University of Sofia, Sofia, Bulgaria

Dr Birol Kilkis, full professor

Turkish Society of HVAC & Sanitary Engineers, Ankara, Turkiye

Dr Giannis Adamos, assistant professor

Department of Civil Engineering, Aristotle University of Thessaloniki, Greece

Dr Andrej Kitanovski, full professor

University of Ljubljana, Faculty Of Mechanical Engineering, Slovenia

Dr Milić Erić, associate research professor

University of Belgrade, Vinca Institute of Nuclear Sciences – National Institute of the Republic of Serbia, Belgrade, Serbia

Dr Zoran Marković, associate research professor

University of Belgrade, Vinca Institute of Nuclear Sciences – National Institute of the Republic of Serbia, Belgrade, Serbia



Program Committee

President:

Dr Mladen Stojiljković, full professor
University of Niš, Faculty of Mechanical Engineering, Niš, Serbia

Members:

Dr Predrag Stefanović, scientific advisor
President of the Society of Thermal Engineers of Serbia

Dr Milan Radovanović, full professor
University of Belgrade, Faculty of Mechanical Engineering, Belgrade, Serbia

Dr Simeon Oka, full professor
University of Belgrade, Vinča Institute of Nuclear Sciences, Belgrade, Serbia

Dr Miloš Banjac, full professor
University of Belgrade, Faculty of Mechanical Engineering, Belgrade, Serbia

Dr Dragoslava Stojiljković, full professor
University of Belgrade, Faculty of Mechanical Engineering, Belgrade, Serbia

Dr Dušan Gvozdenac, full professor
University of Novi Sad, Faculty of Technical Sciences, Novi Sad, Serbia

Dr Milun Babić, full professor
University of Kragujevac, Faculty of Engineering, Kragujevac, Serbia

Dr Vladan Karamarković, full professor
University of Kragujevac, Faculty of Mechanical and Civil Engineering, Kragujevac, Serbia

Dr Maja Todorović, full professor
University of Belgrade, Faculty of Mechanical Engineering, Belgrade, Serbia

Dr Dragoljub Živković, full professor
University of Niš, Faculty of Mechanical Engineering, Niš, Serbia

Dr Dragan Pantić, full professor
University of Niš, Faculty of Electronic Engineering, Niš, Serbia

Dr Velimir Strefanović, full professor
University of Niš, Faculty of Mechanical Engineering, Niš, Serbia

Dr Borislav Grubor, scientific advisor
University of Belgrade, Vinča Institute of Nuclear Sciences, Belgrade, Serbia

Dr Valentino Stojkovski, full professor
Ss. Cyril and Methodius University, Faculty of Mechanical Engineering, Skopje, North Macedonia

Dr Maja Đurović Petrović, full professor
University of Belgrade, Faculty of Mechanical Engineering, Belgrade, Serbia

Dr Mirjana Laković, full professor
University of Niš, Faculty of Mechanical Engineering, Niš, Serbia

Dr Mića Vukić, full professor
University of Niš, Faculty of Mechanical Engineering, Niš, Serbia

Dr Vukman Bakić, research professor
University of Belgrade, Vinča Institute of Nuclear Sciences, Belgrade, Serbia

Dr Dejan Ivezić, full professor
University of Belgrade, Faculty of Mining and Geology, Belgrade, Serbia

Dr Uroš Karadžić, associate professor
University of Montenegro, The Faculty of Mechanical Engineering, Podgorica, Montenegro

Dr Jelena Janevski, full professor
University of Niš, Faculty of Mechanical Engineering, Niš, Serbia

Dr Predrag Živković, full professor
University of Niš, Faculty of Mechanical Engineering, Niš, Serbia

Dr Predrag Rašković, full professor
University of Niš, Faculty of Technology, Leskovac, Serbia

Dr Miomir Raos, full professor
University of Niš, Faculty of Occupational Safety, Niš, Serbia



Dr Petar Stanojević, full professor
University of Belgrade, Faculty of Security Studies, Belgrade, Serbia
Dr Dejan Stojanović, director TOPS
Dr Branislava Lepotić Kovačević, UPES

Organizing Committee

President:

Dr Mirjana Laković, full professor
University of Niš, Faculty of Mechanical Engineering, Niš, Serbia

Members:

Dr Dejan Mitrović, full professor
University of Niš, Faculty of Mechanical Engineering, Niš, Serbia
Dr Mića Vukić, full professor
University of Niš, Faculty of Mechanical Engineering, Niš, Serbia
Dr Jelena Janevski, full professor
University of Niš, Faculty of Mechanical Engineering, Niš, Serbia
Dr Mirko Stojiljković, associate professor
University of Niš, Faculty of Mechanical Engineering, Niš, Serbia
Dr Marko Ignjatović, associate professor
University of Niš, Faculty of Mechanical Engineering, Niš, Serbia
Dr Branislav Stojanović, full professor
University of Niš, Faculty of Mechanical Engineering, Niš, Serbia
Dr Goran Vučković, associate professor
University of Niš, Faculty of Mechanical Engineering, Niš, Serbia
Dr Predrag Živković, full professor
University of Niš, Faculty of Mechanical Engineering, Niš, Serbia
Dr Miloš Tasić, assistant professor
University of Niš, Faculty of Mechanical Engineering, Niš, Serbia
Milica Jović, teaching assistant
University of Niš, Faculty of Mechanical Engineering, Niš, Serbia
Dr Saša Pavlović, assistant professor
University of Niš, Faculty of Mechanical Engineering, Niš, Serbia
Dr Marko Mančić, assistant professor
University of Niš, Faculty of Mechanical Engineering, Niš, Serbia
Dragana Dimitrijević Jovanović, research assistant
University of Niš, Faculty of Architecture and Civil Engineering, Niš, Serbia
Dr Ivan Pavlović, associate professor
University of Niš, Faculty of Mechanical Engineering, Niš, Serbia
Dr Jovan Škundrić, teaching assistant
University of Banja Luka, Faculty of Mechanical Engineering, Banja Luka, Republic of Srpska, BH

Danijela Stanisavljević, economist
University of Niš, Faculty of Mechanical Engineering, Niš, Serbia
Violeta Stamenković, legal adviser
University of Niš, Faculty of Mechanical Engineering, Niš, Serbia
Dr Milena Rajić, assistant professor
University of Niš, Faculty of Mechanical Engineering, Niš, Serbia
Milena Mančić, teaching assistant
University of Niš, Faculty of Occupational Safety, Niš, Serbia
Aleksandar Pantić, research assistant
University of Niš, Faculty of Electronic Engineering, Niš, Serbia
Dr Filip Stojkovski, Iskra Impuls
Branka Radovanović, teaching assistant
University of Niš, Faculty of Mechanical Engineering, Niš, Serbia



Vladan Jovanović, junior research assistant

University of Niš, Faculty of Mechanical Engineering, Niš, Serbia

Dr Milić Erić, associate research professor

University of Belgrade, Vinca Institute of Nuclear Sciences – National Institute of the Republic of Serbia, Belgrade, Serbia

Dr Zoran Marković, associate research professor

University of Belgrade, Vinca Institute of Nuclear Sciences – National Institute of the Republic of Serbia, Belgrade, Serbia

Dr Milica Mladenović, associate research professor

University of Belgrade, Vinca Institute of Nuclear Sciences – National Institute of the Republic of Serbia, Belgrade, Serbia

Dr Aleksandar Milićević, associate research professor

University of Belgrade, Vinca Institute of Nuclear Sciences – National Institute of the Republic of Serbia, Belgrade, Serbia

Sofija Stanojev, student

University of Niš, Faculty of Mechanical Engineering, Niš, Serbia

Mateja Polimac, student

University of Niš, Faculty of Mechanical Engineering, Niš, Serbia

Jana Tufanović, student

University of Niš, Faculty of Mechanical Engineering, Niš, Serbia

Honorary Committee

President:

Dr Goran Janevski, full professor

University of Niš, Faculty of Mechanical Engineering, Niš, Serbia

Members:

Dr Slobodan Laković, full professor

University of Niš, Faculty of Mechanical Engineering, Niš, Serbia

Dr Nenad Radojković, full professor

University of Niš, Faculty of Mechanical Engineering, Niš, Serbia

Dr Zoran Boričić, full professor

University of Niš, Faculty of Mechanical Engineering, Niš, Serbia



The 21st International Conference on
Thermal Science and Engineering of Serbia

SimTerm2024

Niš, Serbia, October 22-25



Disclaimer

The contents of the papers presented in this publication are the sole responsibility of their authors and can in no way be taken to reflect the views of the Organizer.

ENERGY

EFFICIENCY

ECONOMY

ECOLOGY

CONTENTS

I. PLENARY SESSION	7
Thermo-Hydraulic Drivers of the Global Climate System Miodrag Mesarović ^a	8 8
II. ENERGY SOURCES AND POTENTIALS	29
The Impact of CBAM and Variable Renewable Energy Integration on Energy Systems and Cross-Border Electricity Trade Boris Ćosić ^a , Neven Duić ^b	30 30
Drying the Hemp Flower in a Condensation Dryer Branka Radovanović ^a , Jelena Janevski ^b , Mića Vukić ^c , Saša Pavlović ^d , Dragana Dimitrijević Jovanović ^e	38 38
III. RENEWABLE ENERGY SOURCES	43
Assessment of Floating Solar Panels Potential for Electricity Generation in the Adriatic Sea Danka Kostadinović ^a , Milić Erić ^a , Zoran Marković ^a	44 44
Applications and Challenges of Digital Twins of Floating Wind Turbines Maria-Styliani Daraki ^a , Beatrice Mina ^b , Muhnad Almasoudi ^c , Barbara Charalambidi ^a , Marko Mančić ^d , Junlin Heng ^e , Charalampos Baniotopoulos ^e	53 53
Developing Solar Cavity Receivers to Improve Energy Governance Reyhaneh Loni ^a , Sasa Pavlovic ^b	60 61
Developing Renewable Energy Sources: Enhancing Energy Governance for a Sustainable Future Reyhaneh Loni ^a , Sasa Pavlovic ^b	67 67
IV. ENVIRONMENTAL PROTECTION AND DECARBONIZATION	76
Examining PAHs Presence in Novi Sad's Ambient Air: Sources and Assessment Maja Brborić ^a , Branka Nakomčić Smaragdakis ^a , Damir Šljivac ^b , Saša Pavlović ^c , Evangelos Bellos ^d	77 77
Improving Flow Homogeneity in the Chambers of the Electrostatic Precipitator of a 350 MW Unit and Reduction of Particulate Matter Emissions by Modifying the Turning and Damping Elements Milić D. Erić ^a , Zoran Marković ^b , Predrag Stefanović ^c , Aleksandar Milićević ^d Ivan Lazović ^e	84 84

Indicating Contribution of a Country to Global CO₂ Emission and Environmental Justice	95
Vojin Grković ^a	95
Optimisation of Electrostatic Precipitators in Pulverised Lignite-Fired Thermal Power Stations	103
Zoran Marković ^a , Milić Erić ^b , Aleksandar Milićević ^c , Ivan Lazović ^d , Predrag Stefanović ^e Ilija Stevanović ^f	103
Urban Resilience Planning to Climate Change Through Innovative Nexus Approach	113
Serena Caucci ^a , Giannis Adamos ^b , Tamara Rađenović ^c , Dejan Vasović ^d , Snežana Živković ^e	113
V. INNOVATIVE TECHNOLOGIES AND PLANTS IN ENERGY SCIENCE	118
Optimal System for Collecting Landfill Gas - Landfill Meglenci, Republic of North Macedonia	119
Blagoj Dimovski ^a , Vangelce Mitrevski ^b , Vladimir Mijakovski ^c , Cvete Dimitrieska ^d	119
Paddy Drying in Mixed-flow Tower-type Dryer	124
Filip Mojsovski ^a , Vladimir Mijakovski ^b	124
Determining the Reliability Function of the Thermal Power System in the Power Plant "Nikola Tesla, Block B2"	128
Ivan Popović ^a , Milan Đorđević ^b , Jasmina Skerlić ^c , Vladan S. Jovanović ^d , Snežana Kirin ^e	128
Experimental Investigation on the Effect of Water Based Nanofluids (Al₂O₃ And Mgo) Used as Htf in a Pcm Based Thermal Energy Storage System Integrated with Constant Heat Source	135
Krishna Reddy K ^a , Meenakshi Reddy R ^a , Sreenivasa Reddy B ^a , Madhava Reddy K ^a , Venkata Mohan Reddy Y ^a	135
Energy Efficiency of the Passive System for Extraction of Landfill Gas at the Landfill of Niš	147
Ljubica Stojković ^a , Ivan Mihajlović ^b , Dragoslav Pavlović ^c	147
Potential Methane Generation Capacity on the Landfill Gas Extraction Systems at the Landfill in Niš	153
Dragoslav Pavlović ^a , Ivan Mihajlović ^b , Ljubica Stojković ^c , Bojan Banković ^d , Gradimir Cvetanović ^e	153
Effect of Properties of Working Fluids on the Efficiency of a Low-Temperature Organic Rankine Cycle	159
Marija Živković ^a , Aleksandar Mijatović ^b , Dejan Ivezić ^c , Boban Pavlović ^d	159
Developing Solar Thermal Power Plant to Improve Energy Governance	166
Reyhaneh Loni ^a , Sasa Pavlović ^b	166

Natural Draught Cooling Tower Operation During Winter	173
Vladimir Mijakovski ^a , Monika Lutovska ^b , Filip Mojsovski ^c , Mile Spinovski ^a	173
 VI. ENERGY EFFICIENCY IN INDUSTRY, CIVIL ENGINEERING, COMMUNAL SYSTEMS, AND TRAFFIC	 179
Rational use of energy and waste heat at compressor plants in the wood processing industry of Serbia	180
Aleksandar Dedić ^a , Dušan Bajić ^b , Biljana Stojanović ^c , Srdjan Svrzić ^a , Matilda Lazić ^d , Duško Salemović ^d	180
Analytical Assessment of Cooling Degree-Days for Estimating Energy Consumption in Building Sector During Cooling Season in Belgrade	188
Branislav Petrović ^a , Milan Gojak ^b	188
Proposal of New Building 4E improvement	197
Darko Z. Ristanović ^a , Maja N. Todorović ^b	197
Air-conditioning Control Strategies for an Amphitheater for Different Occupancy Scenarios	204
Jovan Matić ^a , Nataša Nord ^b , Maja Todorović ^c , Milan Ristanović ^d	204
Application of Reinforced Learning in Intelligent Buildings	216
Matija Žuža ^a , Milan Ristanović ^b , Žarko Čojbašić ^c , Luka Filipović ^d	216
Usage Effect of the Selective Absorption Facade Instead an Insulation Layer and Influence on Energy Performance of the Family House	226
Nebojša Lukić ^a , Đorđe Radisavljević ^b , Aleksandar Nešović ^c , Novak Nikolić ^d , Novak Popović ^d	226
Impact Assessment of Energy Facilities on Geoecology	233
V.S. Davtyan ^a	233
Change in the Quality of Kolubara lignite Burned in the Thermal Power Plants "Nikola Tesla" Expressed in Terms of Emission Factor	239
Nikola Živković ^a , Vukman Bakić ^b , Marina Jovanović ^e , Sanja Vujnović ^d , Željko Đurović ^e , Dejan Cvetinović ^d	239
 VII. AUTOMATICS AND CONTROL OF PROCESSES, EQUIPMENT, AND PLANTS, FEMA	 249
Predicting Heat Demand of Residential Buildings with Lag and Time Variables	250
Mirko M. Stojiljković ^a , Marko G. Ignjatović ^b , Goran D. Vučković ^c , Vladan S. Jovanović ^d	250
Operational Optimization of Heating Systems with Air-Source Heat Pumps Based on Realistic Electricity Tariffs	257
Mirko M. Stojiljković ^a , Goran D. Vučković ^b , Marko G. Ignjatović ^c	257

Problems of Lead Screw Accuracy made by turning	263
Oleh Onysko ^a , Volodymyr Kopei ^b , Vitalii Panchuk ^c , Ivan Ivaniv ^d , Anatolii Verkalets ^e	263
VIII. FLOW, HEAT AND MASS TRANSFER, COMBUSTION	268
Theoretical thermodynamic analysis of the organic Rankine cycle	269
Evangelos Bellos ^a , Saša Pavlović ^b , Mića Vukić ^b , Branka Nakomčić-Smaragdakis ^c , Mirjana Laković ^b	269
Averaged Axisymmetric Flow Surfaces in Hydraulic Turbomachines	278
Jasmina Bogdanović Jovanović ^a , Živojin Stamenković ^b , Jelena Petrović ^c , Miloš Kocić ^d	278
Lignite combustion in Thermal power plant Kolubara A as a source of mercury pollution	288
Jovana Buha-Marković ^a , Ana Marinković ^b , Jasmina Savić ^c , Milić Erić ^d , Zoran Marković ^e , Aleksandar Milićević ^f , Mihajlo Gigov ^g	288
Analysis the Impact of Coal Mixing on Boiler Characteristics	295
Lidija Joleska Bureska ^a	295
Effect of Wall Heat Flux on Flow and Heat Transfer Characteristics in Coiled Corrugated Pipes	302
Milan Đorđević ^a , Marko Mančić ^b , Velimir Stefanović ^c , Mića Vukić ^d	302
Results of the Temperature Variation in Experimental Research of the Kolubara Lignite Drying Process in Fluidized Bed	309
Milić D. Erić ^a , Zoran Marković ^b , Danka Kostadinović ^c , Rastko Jovanović ^d , Ivan Lazović ^e and Mihajlo Gigov ^f	309
Heat Transfer Effects on the EMHD Flow of Ternary Hibrid Nanoluid in the Channel with Porous Medium	317
Milica Nikodijević Đorđević ^a , Jelena Petrović ^b , Miloš Kocić ^c , Živojin Stamenković ^d	317
Mixed Convective EMHD Flow of a Ternary Hybrid Nanofluid in a Vertical Channel with Porous Medium	326
Jelena Petrović ^a , Milica Nikodijević Đorđević ^b , Miloš Kocić ^c , Jasmina Bogdanović Jovanović ^d , Živojin Stamenković ^e	326
Optimizing Flue Gas Recirculation for Enhanced Efficiency in Biomass-Fired Boilers: A Comprehensive Study	336
Nenad Tomić ^a , Jovica Podunavac ^b , Mladen Tomić ^c , Aleksandar Anđelković ^d , Miroslav Kljajić ^e , Predrag Živković ^f	336
Determining Gas and Gas Mixture Viscosity Across Wide Temperature Ranges: Refinements and Predictive Models	342
Jovica Podunavac ^a , Nenad Tomić ^b , Mladen Tomić ^c , Aleksandar Anđelković ^d , Miroslav Kljajić ^e , Predrag Živković ^f	342

A Model of Two-Phase Flow in Pneumatic Transport of Powder Material	349
Saša Milanović ^a , Veljko Begović ^b , Miloš Jovanović ^c , Boban Nikolić ^d , Živan Spasić ^e , Petar Miljković ^f	349
Water Vapor Condensation from Combustion Products and its Usage Possibilities	358
Luka Marinović ^a , Dejan Mitrović ^b , Mirjana Laković ^c , Marko Ignjatović ^d	358
IX. MATHEMATICAL MODELING AND NUMERICAL SIMULATION	366
Influence of Building Shape on Wind Flow: CFD simulations	367
Danka Kostadinović ^a , Ivan Lazović ^a	367
Measurement elements and SCADA system operation in the remote heating system of the Faculty of Mechanical Engineering	375
Dejan Mitrović ^a , Marko Ignjatović ^a , Dušan Stojiljković ^a , Rajko Turudija ^a	375
Material Selection of Wave Energy Turbine Blade by using MCDM Solver	387
Dušan Petković ^a , Miloš Madić ^a	387
In-Depth Examination of Water Jet Formations and Patterns at Dam Outlets: Comparative Investigation Employing CFD Simulations and On-Site Drone Footage	396
Filip Stojkovski ^a , Robert Broz ^b , Sašo Belšak ^c , Valentino Stojkovski ^d	396
Measurement of water quality parameters using the spectrophotometry method	407
Radmila Koleva ^a , Darko Babunski ^a , Emil Zaev ^a , Atanasko Tuneski ^a , Magdalena Koleva ^a	407
Numerical Study on Thermal Energy Storage System Integrated Flat Plate Solar Collectors in Buildings	417
Saša Pavlović ^a , Evangelos Bellos ^b , Velimir Stefanović ^a , Marko Ilić ^a , Mića Vukić ^a , Branka Nakomčić-Smaragdakis ^c , C Tzivanidis ^b	417
Three-dimensional Numerical Investigation of Fluidized Bed Gasification in a Pilot Plant Gasifier: Fluid Flow	425
Nikola Četenović ^a , Dejan Cvetinović ^b , Djordje Čantrak ^c	425
Development of a Mathematical Model of a Drum Steam Boiler by Using the Automatic Control System – Second Step	434
Aleksandra Janković ^a , Milica Ivanović ^a	434
X. ENERGY MANAGEMENT	442
Life Cycle Impact Assessment - A Review of Tools for Sustainable Energy Management	443
Milena Rajić ^a , Zorana Stanković ^b , Peđa Milosavljević ^c	443
Thermal Comfort Models for Future Tourism using Heart Rate Variability	457
Miloš D. Milovančević ^a	457



Is There a Circular Economy Business Model That can be Easily Implemented? Ana Kitić ^a , Miloš Milovančević ^a	465 465
NOTES	471



I.Plenary session

Thermo-Hydraulic Drivers of the Global Climate System

Miodrag Mesarović^a

^a *Academy of Engineering Sciences of Serbia, Belgrade, RS, mmesarovic@mts.rs*

Abstract: A lot of effort is required from the humanity to preserve the global climate from changes that could make the living conditions on Earth unsustainable. Decarbonization of the energy sector is meant to give the key contribution by humans to keep the global temperature rise by the end of this century below levels determined by the Paris Agreement. Transition from fossil to renewable and other energy sources that do not emit greenhouse gases is an inevitable goal for the humanity to preserve natural carbon cycle from a risky imbalance. As the climate system on Earth is extremely complex, there is no possibility for climate change phenomena to be examined in a laboratory like the majority of the thermo-hydraulic phenomena is, the thermal engineers and scientists are left to depend only on historic records and mathematical simulations of an extremely large quantity of climate change drivers studied within several tens or hundreds of scientific disciplines. Still, many of the inter-relations or feedbacks among climate phenomena remain quite uncertain or entirely unknown, so that many of the climate change drivers need to be identified and explained to make humanity aware of all the risks to be prevented in fighting against climate change beyond repair. The paper lists the major known thermo-hydraulic and other drivers of the climate system and related open questions in the field of the thermal science as a pathway for further research and studies of thermal and hydraulic kind in the climate system.

Keywords: climate change, thermal science, solar radiation feedbacks, climate models.

1. Introduction

The climate system is an interactive system consisting of five major components: the atmosphere, the hydrosphere, the cryosphere, the land surface and the biosphere, forced or influenced by various external forcing mechanisms, the most important of which is the Sun. Many physical, chemical and biological interaction processes occur among the various components of the climate system on a wide range of space and time scales, making the climate system extremely complex. Any change, whether natural or anthropogenic, in the components of the climate system and their interactions, or in the external forcing, may result in climate variations. The following sections introduce various aspects of natural climate variations and the human influence on the climate system. Although the components of the climate system are very different in their composition, physical and chemical properties, structure and behaviour, they are all interrelated and linked by fluxes of mass, heat and momentum, the major laws of the thermal science. As the current climate science is mainly based on statistical averaging of historical and current data over space and time and mathematical presentations of the climate drivers, it is of utmost importance to better understand nature and mechanisms of these drivers.

The *atmosphere* is the most unstable and rapidly changing part of the system and is composed mainly of nitrogen (N₂, 78.1%), oxygen (O₂, 20.9%), and argon (Ar, 0.93%), which have only limited interaction with the incoming solar radiation and they do not interact with the infrared radiation emitted by the Earth [1]. However, there also are a number of trace gases, such as carbon dioxide (CO₂), methane (CH₄), nitrous oxide (N₂O) and ozone (O₃), which do absorb and emit infrared radiation. These so called greenhouse gases, with less than 0.1% by volume, play an essential role in the Earth's energy budget, as does also the water vapour (H₂O), which is also a natural greenhouse gas, whose volume mixing ratio is highly variable (typically in the order of 1%). Because these greenhouse gases (GHGs) absorb the infrared radiation emitted by the Earth and emit infrared radiation up- and downward, they tend to raise the temperature near the Earth's surface. Beside these gases, the atmosphere also contains solid and liquid particles (aerosols) and clouds, which interact with the incoming and outgoing radiation in a complex and spatially very variable manner. The most variable component of the atmosphere is water in its various phases such as vapour, cloud droplets, and ice crystals. Water vapour is the

strongest GHG and for these reasons and because the transition between the various phases absorb and release much energy, water vapour is central to the climate and its variability and change.

The *hydrosphere* is the component comprising all liquid surface and subterranean water, both fresh water, including rivers, lakes and aquifers, and saline water of the oceans and seas. Fresh water runoff from the land returning to the oceans in rivers influences the ocean's composition and circulation. The oceans cover approximately 70% of the Earth's surface and store and transport a large amount of energy as well as dissolve and store great quantities of CO₂. Their circulation, driven by the wind and by density contrasts caused by salinity and thermal gradients (the so-called thermohaline circulation), is much slower than the atmospheric circulation. Mainly due to the large thermal inertia of the oceans, they damp vast and strong temperature changes and function as a regulator of the Earth's climate and as a source of natural climate variability, in particular on the longer time-scales.

The *cryosphere*, including the ice sheets of Greenland and Antarctica, continental glaciers and snow fields, sea ice and permafrost, derives its importance to the climate system from its high reflectivity (albedo) for solar radiation, its low thermal conductivity, its large thermal inertia and, especially, its critical role in driving deep ocean water circulation. Because the ice sheets store a large amount of water, variations in their volume are a potential source of sea level variations.

Vegetation and soils at the *land surface* control how energy received from the Sun is returned to the atmosphere: some is returned as long-wave (infrared) radiation, heating the atmosphere as the land surface warms, and some serves to evaporate water, either in the soil or in the leaves of plants, bringing water back into the atmosphere. Because the evaporation of soil moisture requires energy, soil moisture has a strong influence on the surface temperature. The roughness of the land surface, determined by both topography and vegetation, influences the atmosphere dynamically as winds blow over the land's surface, [1].

The marine and terrestrial *biospheres* have a major impact on the atmosphere's composition. The biota influence the uptake and release of GHGs. Through the photosynthetic process, both marine and terrestrial plants (especially forests) store significant amounts of carbon from CO₂. Thus, the biosphere plays a central role in the carbon cycle, as well as in the budgets of many other gases, such as CH₄ and N₂O. Other biospheric emissions are the so-called volatile organic compounds (VOCs [1]) which may have important effects on atmospheric chemistry, on aerosol formation and therefore on climate.

Because the storage of carbon and the exchange of trace gases are influenced by climate, feedbacks between climate change and atmospheric concentrations of trace gases can occur. The atmosphere and the oceans are strongly coupled and exchange, among others, water vapour and heat through evaporation. This is part of the hydrological cycle and leads to condensation, cloud formation, precipitation and runoff, and supplies energy to weather systems. On the other hand, precipitation has an influence on ocean salinity, its distribution and the thermohaline circulation. Atmosphere and oceans also exchange CO₂, maintaining a balance by dissolving it in cold polar water which sinks into the deep ocean and by outgassing in relatively warm upwelling water near the equator. These are just a few examples from a virtually inexhaustible list of complex interactions some of which are poorly known or perhaps even unknown.

With this in mind, it is still a lot of research in the field of thermal and hydraulics sciences to be done in order to reduce some of numerous scientific uncertainties that feed skepticism on human influence on climate change ([2]) and thus delay global actions to reduce its impact on the risks of climate change beyond repair. The text which follows is an overview of the present knowledge of physical climate processes and feedbacks, both natural and anthropogenic (man induced) with an aim to indicate those shortcomings in science that could attract interest of researchers in the field of thermal and hydraulic sciences.

2. Drivers of the Climate Variation

2.1. Solar Radiation is the Main Driver of the Climate System

The ultimate source of energy that drives the climate system on Earth is radiation from the Sun. Each square metre of the Earth's spherical surface outside the atmosphere receives an average throughout the year of 342 Watts of solar radiation, ~ 30% of which is immediately reflected back into space by clouds, by the atmosphere, and by the Earth's surface, while the remaining 235 W/m² is partly absorbed by the atmosphere but most (168 W/m²) warms the Earth's surface (the land and the ocean) [3]. The Earth's surface returns that heat to the atmosphere, partly as infrared radiation, partly as sensible heat and as water vapour which releases its heat

when it condenses higher up in the atmosphere. This exchange of energy between surface and atmosphere maintains under present conditions a global mean temperature near the surface of 14°C, decreasing rapidly with height and reaching a mean temperature of -58°C at the top of the troposphere [4]. For a stable climate, a balance is required between incoming solar radiation and the outgoing radiation emitted by the climate system. Therefore the climate system itself must radiate on average 235 W/m² back into space. Shares of this energy balance can be seen in Figure 1, which shows on the left hand side what happens with the incoming solar radiation, and on the right hand side how the atmosphere emits the outgoing infrared radiation [3].

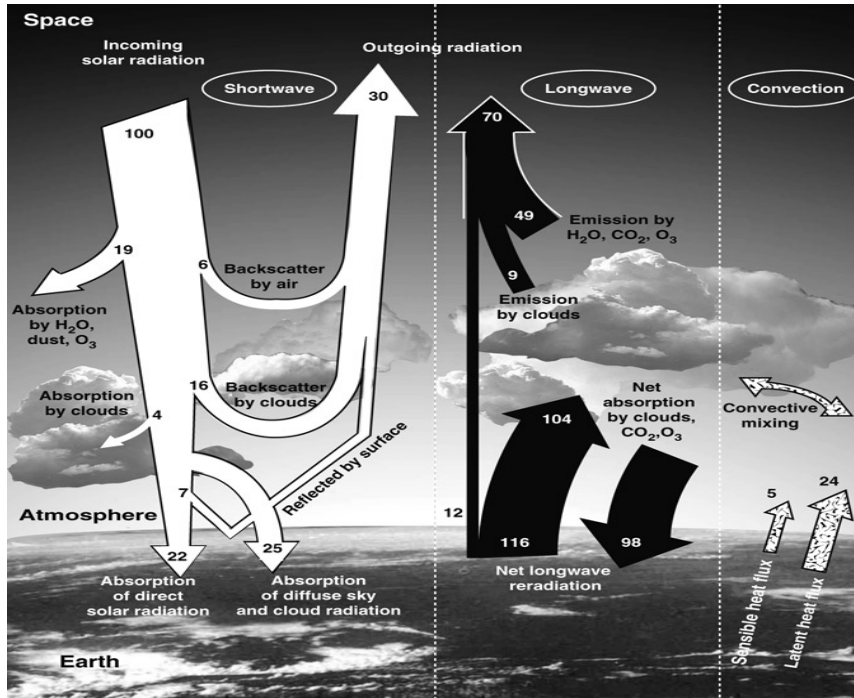


Figure 1: Shares of incoming and outgoing solar radiation

For the Earth to radiate 235 W/m², it should radiate at an effective emission temperature of -19°C which is 33°C lower than the average temperature of 14°C at the Earth’s surface [4]. To understand why this is so, one must take into account the radiative properties of the atmosphere in the infrared part of the spectrum. Long-term records of atmospheric gases, obtained from atmospheric measurements and from air bubbles trapped in glacial ice, show large increases in the major radiatively active gases (CO₂, CH₄, N₂O, and chlorofluorocarbons - CFCs) since the beginning of the industrial revolution 250 years ago. Human activities such as fossil fuel burning, industrial activities, animal husbandry, and fertilized and irrigated agriculture contribute to these increases. As concentrations of these gases rise, the atmosphere traps more of the longwave radiation emitted by Earth, enhancing the greenhouse effect and increasing Earth’s surface temperature as yearly averaged from 1850 shown on Figure 2 [5]

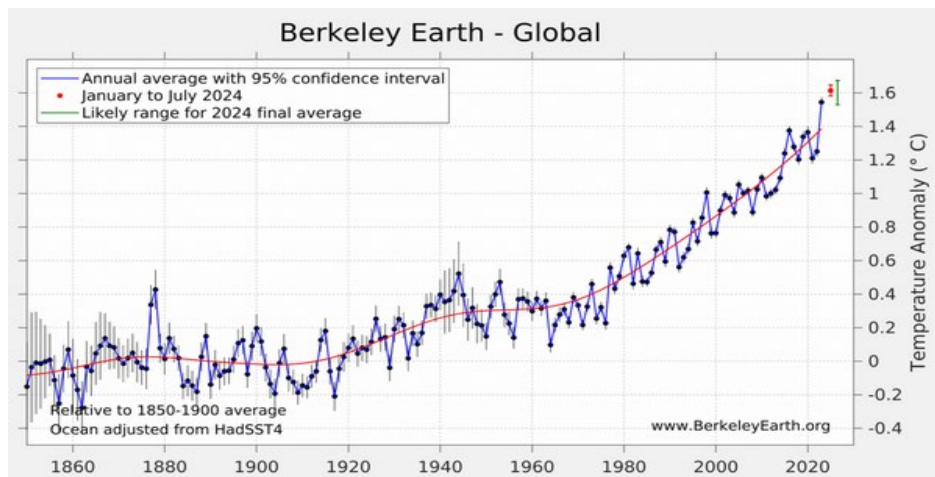


Figure 2: Annual average global surface air temperature anomaly

The above shown rise in global temperature is attributed to a small imbalance in the radiative flows, estimated to be only about 0.26% of the incoming radiation [6]. The Northern Hemisphere summer of 2023 and 2024 began a string of days and months where average global surface air temperatures broke their previous records by substantial margins. Notice that 2023 temperature was much higher than the overall trend (red line), while the red point represents 2024 temperature so far, and the green bar shows an estimated average for 2024 [5].

2.2. Natural and Antropogenic causes of climate change

Global temperature change is the result of many factors that act on different timescales. It can be helpful to break these causes down into those that are human-caused versus those that are natural, as well as those that are “forced” versus those that are “unforced.” Forced changes are imposed on the ocean-atmosphere system from some cause outside of the system, like a change in the amount of energy coming from the Sun or extra energy trapped by human emissions of greenhouse gasses like CO₂. However, global temperature can also spontaneously change without being forced to do so. Fittingly, these are referred to as “unforced” temperature changes. Unforced temperature changes come from natural ocean-atmosphere interactions that can rearrange the clouds, sea ice, and the distribution of heat, which results in global average surface air temperature change, Figure 3 [7].

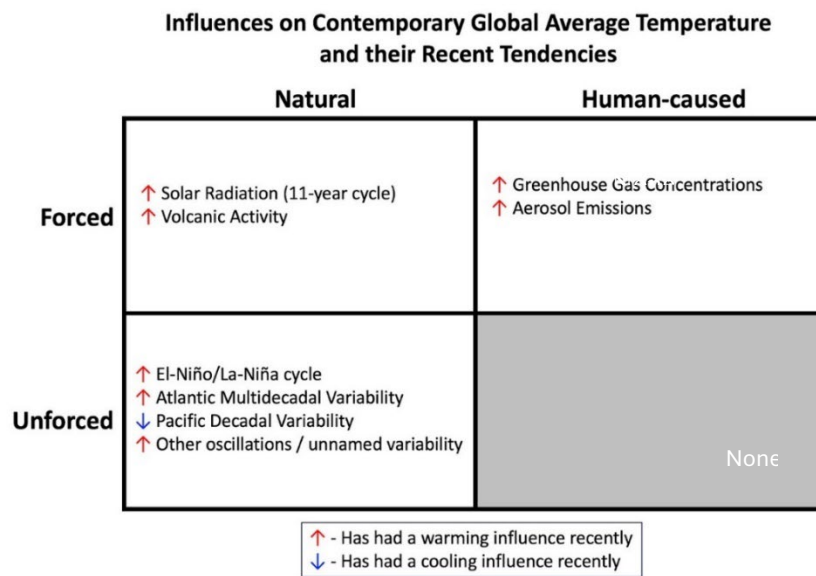


Figure 3: Natural and human causes of recent climate change

All these causes introduce temperature variability on different timescales, but the only cause currently pushing temperatures up on century timescales is the persistent increase in GHG concentrations from human activities like burning fossil fuels. Importantly, though, this upward push is relatively gradual and persistent from year to year, it cannot explain monthly or yearly lurches in temperature like the one currently seen. In order to explain the current spike, it is necessary to look at factors other than the relatively slow increase in GHG concentrations. It turns out that virtually all the other important short-term drivers of global temperature variability may be expected to cause an upward spike at the same time. The recent events, when 1.5°C over preindustrial was achieved, are short term changes in global temperature. They are likely temperature spikes brought about by rare causes, some of these have not yet determined. The Paris limit of 1.5°C refers to a long term average over decades and will be crossed some decades into the future. However the recent events do give us an insight of what a permanent 1.5°C will look like. It is important to note that there is a lag time between an increase in CO₂ and CH₄ in the atmosphere and an increase in temperature.

The amount of energy coming from the Sun follows an 11-year cycle. The last trough of activity bottomed out in 2020, and we are on our way to the next peak in 2024-2025—giving global temperatures a small boost. Also, the 2022 eruption of the Hunga Tonga volcano injected large amounts of water vapor (a greenhouse gas) into the upper atmosphere, where it can persist for several years and cause short-term warming, [8]. The spontaneous (unforced) El Niño/La Niña cycle in the Pacific Ocean has the most influence on global temperatures on timescales of months to years. During La Niña years, an unusual amount of heat is sequestered in the Pacific Ocean below the surface, while during El Niño years, that heat is released back to the surface,

where it temporarily elevates global temperatures before being radiated to space [9]. Atlantic Multidecadal Variability is also a spontaneous climate driver. Sea surface temperatures in the Atlantic ocean are subjected to an unforced variability, and currently are in their positive phase, pushing global temperatures up. There is a lot more unforced variability than just the named oscillations, as it appears that other components, like those related to Antarctic sea ice, may be acting to push global temperatures up as well.

2.3. Radiative Forcing and Heat Balance

Sun and outgoing heat by thermal radiation that escapes the Earth. The Earth constantly receives 342 watts/m² of energy by the Sun (that is the average, on the equator it's more, on the poles it's less). Of those 342 watts, a total of 235 watts are absorbed, 67 watts by the atmosphere, 168 by the surface, and 77+30 = 107 watts are reflected back into space, Figure 4a [10]. Compared to preindustrial times, GHGs maximally absorb an additional 2.43 watts/m², which acts as net anthropogenic forcing with all components taken into account Figure 4b [2].

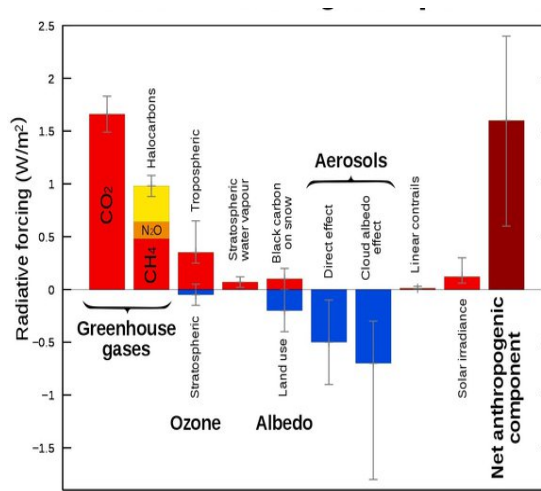
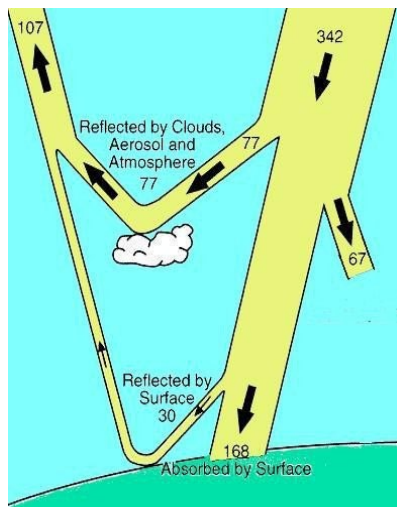


Figure 4: Heat balance (left) and radiative forcing components (right)

2.4. Calculating the Earth's Energy Budget

In general terms ([10]), the energy absorbed by the Earth can be written as:

$$E_i = (1 - a) \times \Omega / 4 \quad (1)$$

where 'a' is planetary albedo (0.31, this is the proportion of incoming radiation reflected to space and lost); 'Ω' is the solar constant (solar radiation reaching Earth, about 1367 W/m²). This is energy delivered at the top of the atmosphere. Ω is divided by 4 because the solar energy is spread over the surface of the planetary sphere assuming the same radius as the circle (area of circle/area of sphere of same radius = 0.25). Again in general terms, the energy emitted by the Earth can be written as:

$$E_o = \sigma \times T^4 \quad (2)$$

where $\sigma = 5.67 \cdot 10^{-8} \text{ J/m}^2\text{secK}^4$ and T is temperature in degrees Kelvin. The Earth's temperature reaches a balance (steady state) when the $E_i = E_o$. Under those conditions we can write an equation for planetary temperature:

$$T^4 = [(1 - a) \Omega] / 4 \sigma \quad (3)$$

The solution for equation 3 with measured solar flux [10] at the top of the atmosphere yields a value of 254°K (-19.2°C) for average planetary temperature. This estimate is close to observed conditions in the upper part of the troposphere, but of course is much below the average temperature at sea or ground level (about 14° C), which is the main surface of energy absorption and the place of most interest to humanity. Some factor is causing the climate to be recently nearly 42° C warmer than one can explain by calling on the Sun alone.

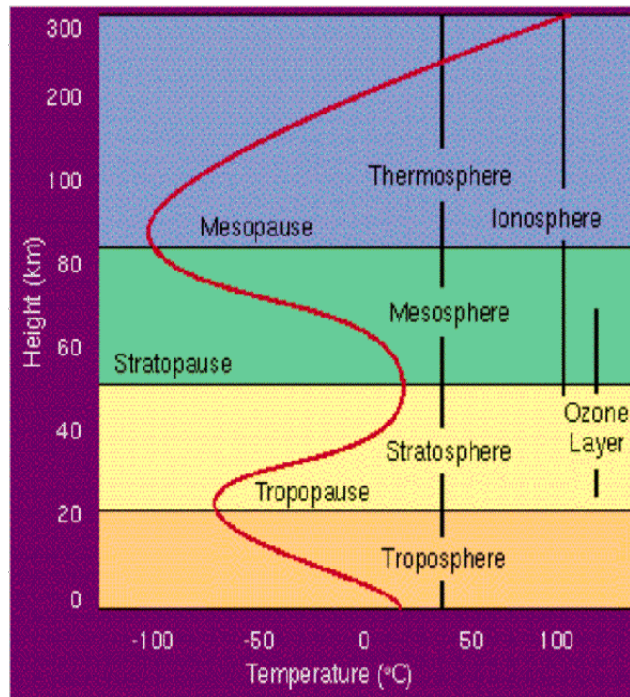


Figure 5: Upward variation of air temperature

There are claims that here is a lot of scientific malpractice at work to make the case that CO₂ and the radiation model is correct, [11]. Climate science violates Newton's laws of heating and cooling ($Q = m \times c \times \Delta T$) as it ignores specific heat 'c' mass 'm' and only focuses on radiation as if the atmosphere would be at 0°Kelvin and if not GHGs. The specific heat of air is greater than of CO₂ (1.012 J/g/°C vs 0.844 J/g/°C) and CO₂ adds no heat capacity to air. Air temperature changes during upward circulation (Figure 5) and when it becomes dry, air cools much faster than humid air which has nothing to do with radiation but with heat capacity. Vapor holds heat with the highest heat capacity of them all (4.1 J/g/°C, [11]). Climate science has convinced the ignorant public that 0.75 g of CO₂ (the amount in a cubic meter of air) at a specific heat of 0.844 J/g/°C is somehow heating the ocean. A cubic meter of air with CO₂ is holding a whopping (0.75×0.844) 0.633 J of energy per degree C. So, essentially, CO₂ is contributing of energy to the surface, and the reality is that CO₂ is cooling the atmosphere. The air would be better off with no CO₂, as the specific heat of air at 1.012 J/g/°C is higher. A cubic meter of air is 1.3 kg at a specific heat of 1012 J/kg/°C+0.75 g of CO₂ at a specific heat of 0.844 J/g/°C adds a whopping 0.633 J of energy to the system. Water has a specific heat of 4.1 J/g/°C. On a kilogram scale, that meter of air above water can not do squat to the 4100 J required to raise a kg of water by 1°C, and the 0.844 J of energy in CO₂ certainly can not have any effect [11]. With the continued rise of global temperature such events may become more frequent.

2.5. Predictions of Climate Change in the Future

Climate change refers to long-term shifts in temperatures and weather patterns. Such shifts can be natural, due to changes in the Sun's activity or large volcanic eruptions, but since the 1800s, human activities have been indicated as the main driver of climate change, primarily due to the burning of fossil fuels and generating GHG emissions that act like a blanket wrapped around the Earth, trapping the Sun's heat and raising temperatures. Scientists found that human GHG emissions are warming the world faster than at any time in at least the last two thousand years. The average temperature of the Earth's surface is now more than 1.2°C warmer than it was in the late 1800s (before the industrial revolution) and warmer than at any time in the last 100,000 years [12]. The last decade (2011-2020) was the warmest on record, and each of the last four decades has been warmer than any previous decade since 1850.

Anthropogenic and natural factors combined are currently pushing global temperatures in the upward direction, and as a result, the years 2023 and 2024 set a new annual record for global warming being the first to breach the +1.5°C level of warming above preindustrial levels. El Niño might cause further warming so that the year 2024 could be 0.2°C warmer than 2023, and reach +1.7°C [13]. The Figure 6 shows these hypothetical warming levels in the context of projections from climate models driven by long-term increases in GHG

concentrations (colors represent different amounts of emissions), but that simulate their own unforced variability. It can be seen that a hypothetical spike up to +1.7°C in 2024 would move temperatures from near the bottom of the envelope in 2021 to near the top in 2024, [14]. Figure 7 shows the same data superimposed on long-term projections by the end of this century based on the same climate models [15]. It shows that the temperature change from human emissions in 2024 would be around +1.35°C. So if 2024 did come in at +1.7°C, it could be that about 80% of that warming was due to human activity, and 20% was due to all the other factors [13].

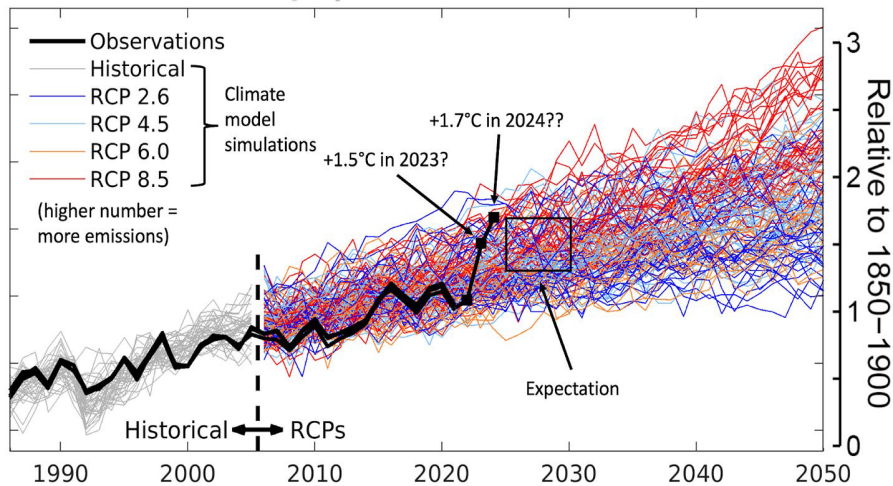


Figure 6: Global temperature rise by 2050 as predicted by climate models

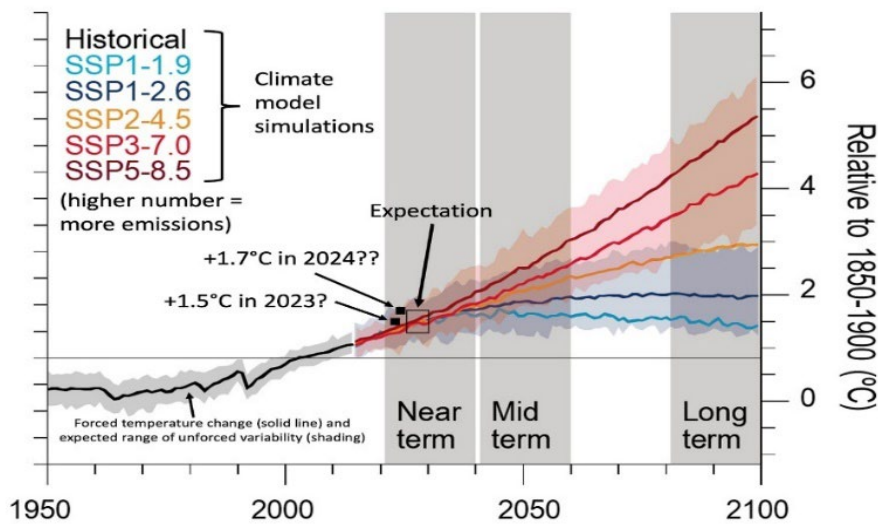


Figure 7: Global temperature rise by 2100 as predicted by climate models

The above figures also show that short-term spikes could not tell much about the long-term trajectory, and the trend would need to last for decades in order to have meaningful implications on long-term warming. Given the unusual coincidence of so many factors pushing in the warming direction at the same time, this fluctuation is not surprising.

3. Global Warming Models and Feed-backs

3.1. The Climate Models as Policy Tools

The climate changes are predicted by global warming models using the Earth's average temperature averaged over the whole planet, and over the whole year. Since climates are different at different places, describing a climate usually includes describing its changes are by the average values of various indicators over multiple years. The models describing climates are much more complicated than global warming models. The most complicated are models describing weather, which changes not only place-to-place and year-to-year, but

moment-to-moment and predictions of weather are based on current conditions in successively larger regions around the area whose weather is being predicted, so that predictions get less precise the farther into the future they go. None of these models predict all the variations in actual data since these data vary due to many other factors usually not included in the models.

Climate models include assumptions about human behavior, and future average global temperature depends on future human CO₂ emissions, so that detailed models include multiple predictions based on a range of future human actions. As the long term predictions of climate change are still in their infancy, they do not show the details of how changing the average global temperature will be low during the average winter or high during summer in specific regions of the Earth. The models are less able to predict weather variations, and even less able to predict effects on numbers or severities of hurricanes and tornadoes, and, it appears that weather in many different climate zones is getting more variable. However, one kind of climate change models solidly based in both thermodynamics and long term patterns, can represent well the water cycle that transports water from drier areas to wetter areas, and that increasing temperature will *on average* increase this transport.

Scientists expect most of the factors other than increasing GHG concentrations to reverse in the coming years, and the mainstream expectation could be that temperatures would fall back down into the middle of the projections in the 2nd half of this decade [16]. Even if temperatures return to the middle of their climate model projection envelope by the late 2020s, the expected temperatures like those in 2023 and 2024 could be common in the 2030s. Any drastic change in weather at the regional level associated with this level of global warming would be quite concerning when considering climate impacts over the coming decades.

Basic science is enough to let anyone know that temperatures will continue to rise, and that this will lead to huge impacts in all parts of the world, so it can already reliably predict the existence of the threat. The climate models can help policy makers to know what things will look like if certain actions to reduce GHG emissions are taken or not. The difference between the two should provide them basis for weighing up the various climate policies. Although they are now regularly confronted with evidence of climate change impacts: droughts, heatwaves, wildfires, floods and so on, accurate predictions provide them a peculiar sort of comfort: at least they have some idea of what the outcomes might look like.

Faced with the daunting threat of changing climate, one feels better to know what the future might look like. Bearing in mind an extreme complexity of the climate system, question is whether it is really possible to predict the future climate? There are certainly many people trying to use computer models of the climate system, and in recent years a lot of money is spent in making them ever more detailed. As models become more complex they look increasingly realistic, so it is tempting to believe the predictions will be good. In July this year, a summit was convened in Berlin to discuss Earth Virtualization Engines or “Eve” with the organisers calling for massive investment billions of euros to buy huge new computers. “Eve” will no doubt gain trust of governments and other funders, but is the rush to build bigger and bigger models the best use of resources to guide global response to climate change? [17].

Big computer models provide all kinds of detailed predictions, but the complexity of the systems they are dealing with gives a reason to question whether they actually do that, and even whether more advanced ones ever could do. The problem is to know how close to reality a model needs to make good predictions. A chaotic nature of the climate system means that small differences in the representation of a single item could have a very large impact on something quite distant and seemingly unrelated. Part of the problem is that, as the models become more and more complex, they often look increasingly realistic, so it is very tempting to believe that the predictions will be good.

Climate models are assessed on how well they simulate the past. But climate change is bringing world to a never-before experienced situation, so the past may not be an accurate guide. There is no doubt that the latest climate models are outstanding achievements of computer-based science, but they are not equivalent to reality [18]. They might not represent the real world with all the stunning complexity of Earth’s many interlocking systems, but they might be useful tools for scientific research. Being not meant for weather forecast, climate models are as good guesses in testing a theory against reality (known as “fit test models”) used to see if the theory can predict future events and to estimate if the situation is approximately like the theory is. Well-designed experiments could use models only to get information about the scope of effects different responses could have including the uncertainties and the range of plausible futures.

So, if the models can not give reliable, detailed climate predictions, policy makers should accept to deal with incomplete information. Instead of trying to make the responses just right for the climate of the future, they

should seek out resilient and flexible solutions, remedies that will be robust in a wide range of possible climate outcomes. Even though the uncertainties are large, the information is still a useful basis for making decisions. The risk is that investment in ultra-high resolution models could actively undermine a timely response to climate change.

3.2. Feedbacks in the Climate System

The Earth augments solar heating through a response to the Sun's energy. As the amount of water vapor in the atmosphere increases with temperature, warming the Earth adds water vapor to the atmosphere, and adding water vapor to the atmosphere magnifies that warming. Since the water vapor relationship to temperature is exponential (Figure 8, [19]), and under warmer conditions a modest increase in temperature can lead to a large increase in water vapor and associated greenhouse effect. The water vapor response is the primary cause of greenhouse warming on Earth, and it will magnify the warming by CO₂ and other gases. The water vapor effect might sound terminal for the planet Earth as it feeds the progressive warming. However, this warming is balanced by cloud formation, and increases albedo, thus reducing the solar energy that reaches the lower atmosphere and Earth's surface. This cloud effect provides negative feedback on planetary temperature. The formation of clouds depends on water vapor content in the atmosphere and the temperature change with the elevation. The role of clouds in balancing positive feedback from GHGs is complex and the response of cloudiness to changes in GHG concentrations is still not well understood [20]).

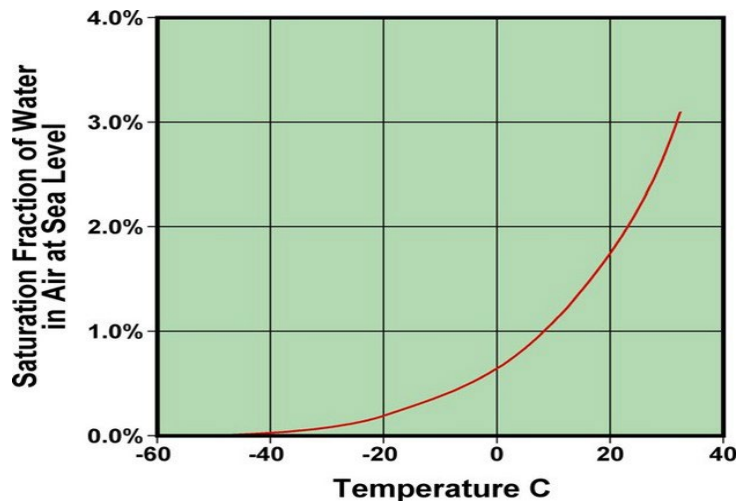


Figure 8: Vapor dew point vs air temperature at sea-level

As atmospheric composition responses to solar warming provide positive feedback on planetary temperature, other responses mitigate change and provide negative feedback. Negative responses could increase planetary reflectivity, so less solar energy is absorbed by Earth; or they might prevent significant changes in atmospheric composition. Dominance of climate/environmental processes by negative feedback would lead to homeostasis, a concept developed by James Lovelock [21]. How much stabilization the Earth's climate gets from negative feedbacks is, at least in part, revealed by the climate history of the past 2 million years during which the Ice Ages occurred and planetary temperature dropped (4–5°C). It is a fact that large climate changes occurred across the globe, and that atmospheric CO₂ concentrations co-varied with the temperature changes (Figure 5). Indeed, the CO₂ variations help to account for 50% fraction of the Ice Age temperature changes [22]. This is what we would expect from positive, rather than negative, feedback processes

One interesting idea ([23]) connects ocean circulation to atmospheric CO₂ content and planetary temperature, so that climate change alters circulation and then circulation can alter climate (a positive feedback). This idea takes us to the Southern Ocean surrounding Antarctica where deep ocean water upwells and returns to the surface circulation system. This deep water is cold, and it contains lots of dissolved carbon. This makes the deep ocean a repository for dissolved carbon. The result of carbon transfer to depth in the oceans is that water is carbon enriched, and when it rises to the surface it will give up a fraction of its carbon load to the atmosphere as it warms. How much CO₂ there is in the atmosphere depends, in part, on the balance of oceanic drawdown and release. With more upwelling, increased volumes of CO₂ could be released to the atmosphere and warming would be accelerated. This could account for the lock step pattern in atmospheric CO₂ and glaciations which we observe and the positive feedback that the climate record implies.

4. Challenging Secrets of the Climate System

4.1. Carbon Budget and How It Changed

In pre-industrial times there was around 120 Gt of carbon taken up by land plants every year and another 120 Gt released back into the air by respiration of plants and all living things that eat plants. There is another flow of about 0.8 Gt of carbon carried by rivers into the ocean and about 87 Gt of carbon was absorbed into the ocean. About 88 Gt of carbon was released back into the atmosphere out of the ocean (1 Gt more than absorbed) from respiration and simple release of dissolved CO₂. These numbers all balanced out evenly more or less and for ten thousand years the carbon stored in the atmosphere remained steady at around 590 Gt. (1 kg of carbon = 3.67 kg of CO₂). The volume of the atmosphere is estimated at $4.431 \cdot 10^{18} \text{ m}^3$. At current 420 ppmv, the atmosphere contains $420 \cdot 10^{-6} \times 4.431 \cdot 10^{18} = 1.86 \cdot 10^{15} \text{ m}^3 \text{ CO}_2$. Converted to GtC by a factor 12/24, this leads to $9.31 \cdot 10^{14} \text{ kg C} = 931 \text{ GtC}$, so that 1 ppmv of CO₂ corresponds to 2.22 GtC. (At atmospheric conditions, 1 kmol of gas has a volume of 24 m³, and 1 m³ of gas equals 1/24 kmol so that 1 m³ of CO₂ has a weight of 44/24 kg which corresponds to 12/24 kg carbon, [24]).

After the industrial revolution, the amount of carbon added to the atmosphere is rising every year. In the 1960's was added around 3 Gt of carbon per year and today we are adding around 9.6 Gt of carbon per year [25]. Since 1990, global CO₂ emissions have increased by more than 60%. Global CO₂ emissions from fossil fuels and industry totaled 37.15 billion metric tons (GtCO₂) in 2022. Emissions are projected to have risen 1.1 percent in 2023 to reach a record high of 37.55 GtCO₂. In addition we are cutting down the forests and clearing land for agriculture, roads and cities which adds another 1.2 Gt of carbon per year. Plants are able to use a bit more and now take up around 123 Gt of carbon [26]. The ocean is presently taking up around 3 Gt of carbon every year and if we immediately stop all emissions the oceans and plants would continue to remove around 5 or 6 Gt per year (declining each year as the CO₂ in the atmosphere reduced) and so in around 150 years the excess CO₂ in the atmosphere might be expected to return to 590 Gt (all things being equal). However the global ocean conveyor formed in the polar seas where cold water absorbs CO₂ before it sinks to the ocean floor and flows into Indian and North Pacific Oceans before returning the North Atlantic. The ocean conveyor takes around 1,000 years to complete one loop [26]. This means that the CO₂ absorbed today will eventually be returned to the atmosphere CO₂ emissions recycled back as the ocean conveyor completes its cycle.

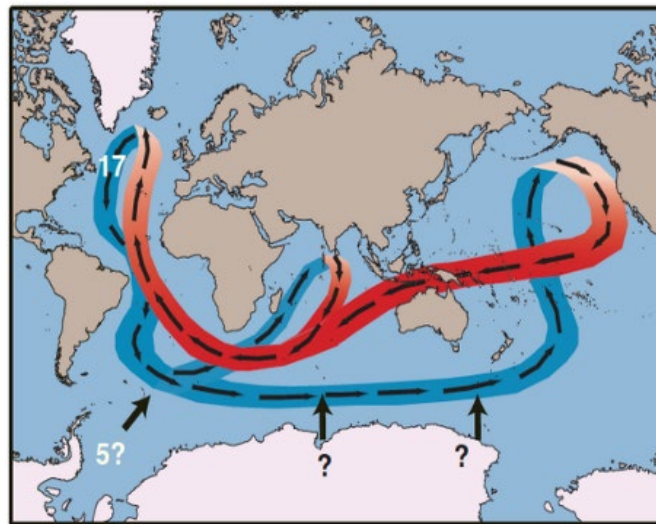


Figure 9: The ocean conveyor loop

4.2. Why the Earth is Not Cooling Now

Global warming and climate change have always had causes in regular changes of the energy received from the solar radiation due to changes of the Earth's position towards the Sun. According to Mlanković's ice ages theory, the changes of radiation the Earth's surface receives from the Sun changes due to cyclical changes of the shape of the Earth's orbit around the Sun (Figure 10a), as well as of the the tilt of Earth's axis (Figure 10b) and its precession (Figure 10c).

Milankovitch Cycle

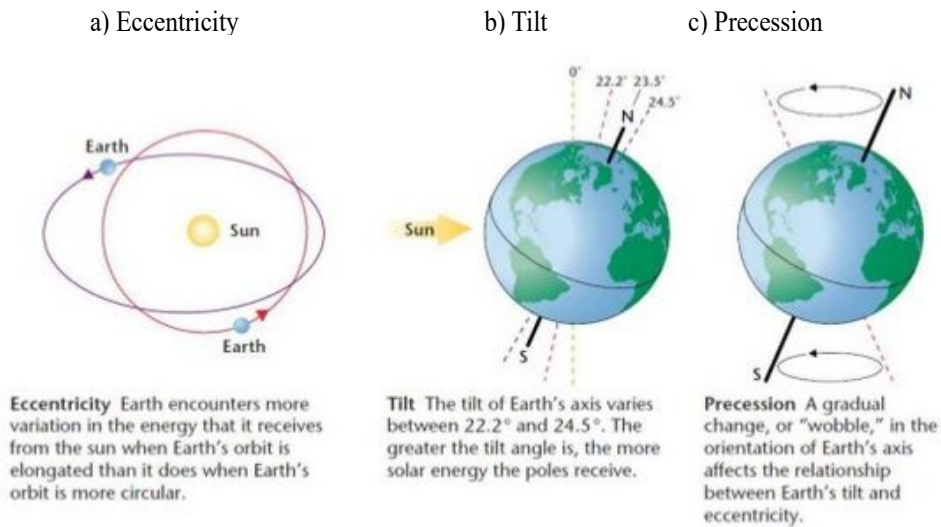


Figure 10: Milanković's cycles of the Earth's rotation;

The Earth encounters more variation the energy that it receives from the Sun when Eart's orbit is elongated than it does when the orbit is more circular. The tilt of the Earth's axis varies between 22.2° and 24.5°, so that the greater the tilt angle is, the more solar energy poles receive. Also, a gradual change (wobble) in thre orientation of Earth's axis affects relationship between Eart's tilt and excentricity of the Earth's orbit while rotating around the Sun.

According to Milanković's cycles theory, the Earth should still be cooling as it has been cooling slowly for over 6500 years [27]. Earth's axis has tilted it measurably away from the source of heat and it should be cooling. Earth's wobble has similarly been conducive to cooling. For over half a century, the current Solar cycle has diminished Earth-warming solar irradiance. However, the Earth warming has continued over the last 100 and more years due to human caused disturbance of the natural carbon cycle by burning fossil fuels, [28].

4.3. Heat Exchange Between Ocean and Atmosphere

The global climate system is also regulated by the energy balance in the oceans and the atmosphere. Global ocean circulation and atmospheric circulation are driven by forces that strive to even out differences in temperature between high and low latitudes. Heat exchange between ocean and atmosphere is an important factor in regional climate patterns. Conditions that influence this balance, such as changes in air and sea temperatures, or cloud and sea ice cover – will thus influence how the climate evolves. On a geological time scale, changes in the shape and location of continents can have strong effects on circulation and heat balance and thus also on global climate. However, given that the continents have been in approximately the same place for the past 500000 years, this is not a factor of any importance for ongoing climate change. On geological time scales, the concentrations of GHGs (especially CO₂) change through natural processes [29]. Volcanos emit CO₂ to the atmosphere. This release is balanced by processes that capture CO₂ in the seabed, and it can be demonstrated in several ways that the increase in atmospheric CO₂ levels since the industrial revolution has been caused by human activities.

The Earth traps most of its energy at the land-ocean surface, so that the atmosphere is heated from below, and the oceans are warmed from above. Much more heat is absorbed at low than at high latitudes because the Earth's surface gradually tilts away from the Sun as moving away from the equator. That tilting spreads the solar energy supply over progressively larger areas of ground or ocean surface, so that each square meter gets less and less heat poleward. At low latitudes the Earth's surface actually absorbs more energy that its upper atmosphere emits to space, while at high latitudes is reverse is true because the latitudinal temperature gradient in the upper troposphere is less than at the surface

5. Motion in the Climate System

5.1. Motion of Energy Within Climate System

The motion in the climate system is due to both vertical and horizontal energy gradients in the atmosphere and oceans. Because absorbing more energy than is lost at low latitudes, and the reverse closer to the poles, is not sustainable, there has to be a balancing so that temperatures stabilize across the planet, and this requires a transfer of heat from the equatorial region to higher latitudes. The transfer is done through large scale motions in the atmosphere and oceans. Motion (winds and currents) happen because solar heating and heat loss to space create pressure gradients so that wind and water move from high to low pressure conditions, [30].

5.2. Motion of the Air

Heating the bottom of the atmosphere, especially in the tropics, makes the air less dense so it becomes buoyant and rises which makes the atmosphere unstable and leads to air lifting to altitude, especially near the equator. Rising lower density air in the tropics forms the largest vertical motion in the atmosphere (the Hadley Cell) and the rising air from the tropics spreads poleward and loses heat to space by radiation. The cooling causes density to increase and the air sinks, most intensely at about 30° either side of the equator. The downward motion creates a region of higher air pressure at the Earth's surface that balances the area of the low pressure within the equatorial zone. The air pressure gradient along the surface will make the winds blow from mid to low latitude. A pressure gradient also develops poleward of 30 degrees so that winds are driven to higher latitudes as well. From the mid-latitude surface high pressure center, winds are directed north and south. Heating air along the equator lowers its density so that it rises and spreads to the higher latitude and cools by radiating energy to the outer space.

Winds are also generated by the rotation of the Earth. Unlike the northern and southern direction of the winds, there are westward and eastward winds. These winds affect ocean currents. Warm, tropical waters carry heat pole-ward along the east coast of continents; cold water from the poles is forced toward the equator along the west coast. Warm surface currents can carry heat well away from the tropics, bringing temperate climates to areas nearer the poles than the equator. Deeper currents are driven by a combination of Earth's rotation and temperature differences between the tropics and the poles. Cold, dense melted water from the icecaps flows underneath warmer surface waters towards the equator.

Figure 11 ([30]) presents the motion of the air at different latitudes. Figure 11a shows the atmospheric circulation once the Coriolis effect is incorporated with the vertical circulation cells, with produces the dominant surface winds. Figure 11b shows an equator to pole (meridional) view of the circulation cells in the atmosphere, which broadly divide the Earth into climate belts. The combination of wind and ocean currents redistributes heat and moisture across Earth's surface. Around 60% of the solar energy that reaches the earth is redistributed around the planet by atmospheric circulation and around 40% by ocean currents [30]. The flow of the winds is made trickier by the fact that the motion is happening over a rotating surface as the Earth spins to the east and the speed of that rotation at the surface is fastest at the equator and drops to zero at the poles. The winds blowing to lower latitude get left behind as they rotate eastward at a lower speed than the the speed of surface they are traveling over which increases towards the equator, and, due to the Coriolis Effect, the winds blowing to the equator turn towards the west. Winds blowing poleward of the high pressure center near 30 degrees latitude veer to the east as their eastward motion outstrips that of the surface they are flowing over. In this way a steady flow from west to east (the Westerlies) is created at about 45 degrees latitude [30].

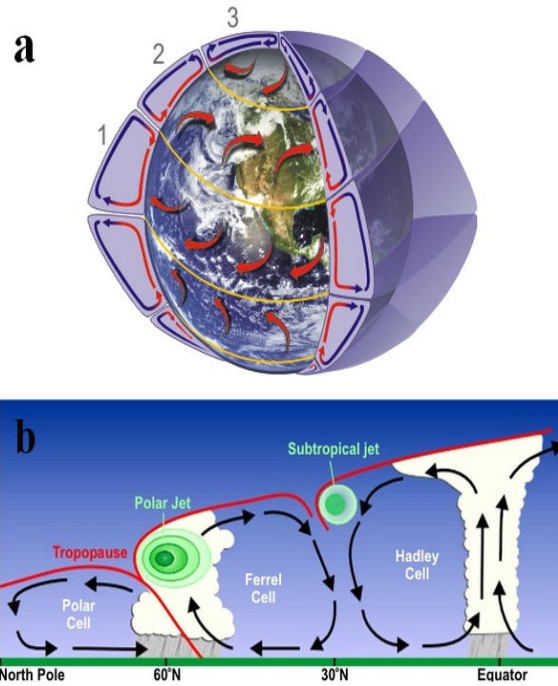


Figure 11: Atmospheric circulation along latitudes

Poleward of 60° N and 60° S, the winds generally blow westward and equatorward as the polar easterlies. In the northern polar regions, where water and land are interspersed, the polar easterlies give way in summer to variable winds. Combined, the vertical and horizontal movements of the winds serve to collect heat in tropical regions and transfer it poleward as one part of the planetary energy balancing act.

5.3. Polar Vortex

A circumpolar vortex, or simply polar vortex, is a large volume of cold air, rotating around both of Earth's polar regions, [31]. The term "vortex" refers to the counter-clockwise flow of air that helps keep the colder air near the Poles. The polar vortex always exists stable (Figure 12a) near the poles, but weakens in summer and strengthens in winter. During winter in the northern hemisphere, the polar vortex will expand, sending cold air southward with the jet stream (Figure 12b). Those light blue arrows are the "jet stream" - very fast high altitude winds that form at the boundary of the vortex and the warmer southern air. When they are fast, they generally result in the polar vortex remaining stable and cold air remains near the polar regions, but when very hot air from the tropics comes north, it slows down the jet stream. Although this allows hot air to push much further north, it also means that the cold air in the polar vortex pushes south, often reaching as far as the southeast and the air temperatures become record low. Now, these sorts of system are rare (once in about every 40 years [32]). Situations like these might become more frequent in warmer climate conditions faced by the current society.

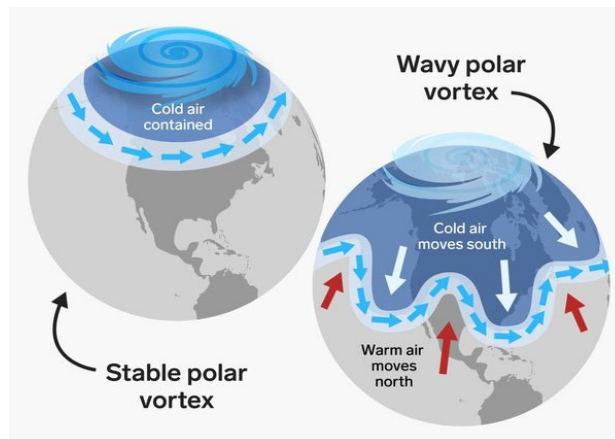


Figure 12. Stable (a) and wavy (b) polar vortex

5.4. Precipitation Patterns

Solar energy heats water to evaporate by consuming the heat of evaporation, rises up as steam and, when cooled down, it condenses by releasing the heat of condensation, thus forming clouds and water droplets fall as precipitation. At the same time as driving evaporation and precipitation patterns, sunlight is creating winds. As warm air moves upward, colder air from neighboring areas rush in to fill the void left behind. At the equator, the Earth receives greater exposure to the Sun's rays where both air and extensive bodies of water warm under the influence of the Sun. The warm air that rises in the tropics is wet. Sunlight causes water to evaporate from plants, soils, and bodies of water. Some of the cold, dry rising air flows to the poles, where it absorbs moisture creating the cold climates of the polar regions. Some of the air is drawn back toward the equator, and some is drawn toward the pole as part of a new air mass. At latitudes around 60° north and south, the air again rises, cools and releases precipitation.

Whereas most coastal regions experience high levels of precipitation, continental interiors are typically arid. Distant from large bodies of water, these areas lack sources of water to recharge moisture in the air. In addition, any air masses reaching them tend to have already discharged any moisture that they carried. Some rain shadows create extremely arid, desert-like conditions. With modest changes in winds, patterns of precipitation do not change much, but result in dry areas becoming drier (generally throughout the subtropics) and wet areas becoming wetter, especially in the mid- to high latitudes.

There is a direct influence of global warming on precipitation. Increased heating leads to greater evaporation and thus surface drying, thereby increasing the intensity and duration of drought. However, the water holding capacity of air increases by about 7% per 1°C warming, which leads to increased water vapor in the atmosphere [33]. The atmospheric and surface energy budget plays a critical role in the hydrological cycle, and also in the slower rate of change that occurs in total precipitation than total column water vapor, Figure 13.

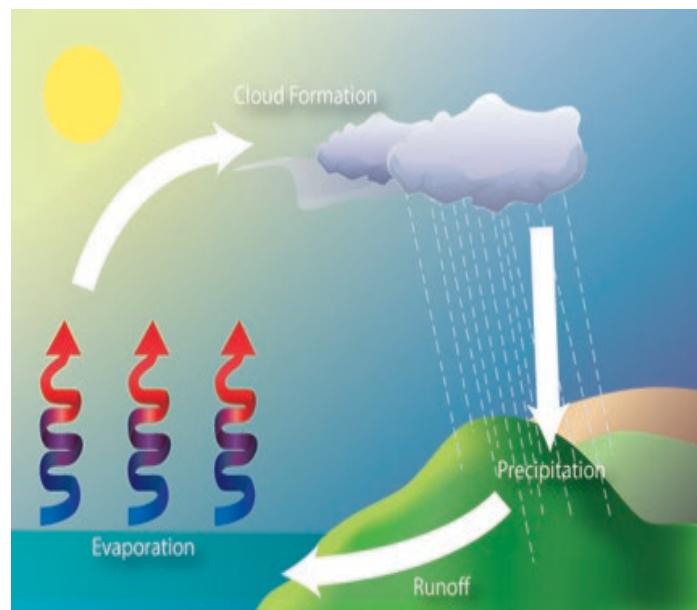


Figure 13: Precipitation cycles

Molecules are more closely packed together when are cold than when they are warm, which makes warm air and water less dense than cold air and water. This difference in relative density causes heat to rise. These water molecules rise to become part of the air; because the air is warm and less dense, there is sufficient room for water molecules within the air mass. But as the air gains altitude it cools, reducing density and space for water. The water molecules condense to form clouds and fall as precipitation.

In tropics and subtropics, precipitation patterns are dominated by shifts as the sea surface temperature change with El Niño [34]. Also, the volcanic eruption of Mount Pinatubo in 1991 ([35]) led to unprecedented drop in precipitation and runoff and to widespread drought, as precipitation shifted from land to oceans and evaporation faltered, providing lessons for a possible geoengineering. Most models simulate such a precipitation that occurs prematurely and too often, and with insufficient intensity, resulting in recycling that is too large and a lifetime of moisture in the atmosphere that is too short, which affects runoff and soil moisture.

5.5. Motion of the Sea Water

The winds blowing over the oceans move water by friction on the surface. As the water begins to move, the currents veer westwards if going to lower latitudes and easterwards if going poleward due to Coriolis Effect. Surface ocean currents are driven in circles called gyres [36]. The largest of these, the subtropical gyre, fills the middle of all oceans and rotates such that poleward flow is on the western side of the basin. Heat transfer from low to high latitudes is via the western boundary currents of the oceans (like the Gulf Stream in the North Atlantic, [30]). This is another part of the planetary energy balancing act. The Gulf Stream is what keeps Europe warm but it also puts the ice on Greenland building it up. The Gulf Stream is the part of this current system that goes from the Gulf of Mexico towards northern Europe. It is run by the heat of the Sun over the oceans and also driven by the electro-capacitive interaction with the Solar Wind. Stopping it requires the Sun to stop pushing it, which happened to a great extent in “The Little Ice Age”.

The ocean circulation is responsive to climate conditions [37]. The surface currents of the oceans operate in a relatively thin upper layer of the sea which is heated by the Sun. This heating is kept relatively close to the ocean surface because warming water makes it less dense and more resistant to sinking or mixing downwards. The result is a barrier, called the thermocline, which develops particularly at lower and mid-latitudes and that separates surface waters from the deep ocean. The boundary, marked by a rapid downward temperature drop, usually occurs within a few hundred meters of less of the surface. Below it, the greater mass of the oceans (down to an average depth of about 3800 m, [30]) is cold and isolated from the winds. Since the light surface water would be resistant to mixing downwards, the deep sea is in motion initiated where the oceanic water column breaks down and surface water sinks due to processes which raise its density. The primary cause of water column destabilization is extreme cooling over a large depth range combined with sea-ice formation. Making ice, leaves behind a brine which is quite salty and so quite dense and heads for the deep sea. .

The deep water masses develop at high latitudes, particularly in the Atlantic basin [38]. Deep waters born in the Atlantic spread to the other ocean basins using the circum-planetary highway that surrounds Antarctica. This seaway serves as the roundabout connecting all the oceans allowing deep Atlantic water to spread heat gradients as these drive wind and deep ocean flow. The winds provide upward draw on deep waters thanks to the Coriolis Effect. Along the eastern sides of ocean basins and around Antarctica winds blow such that Coriolis veering drives surface waters oceanward, and the result is a process called Upwelling which causes deeper water to rise and replace the water pulled away from the shore [39]. Interestingly, deep ocean circulation can also feedback into climate change to alter the way it develops. Figure 14 compares vertical circulation in the Atlantic ocean in the modern age (a) and modeled for the last ice age (b), as redrawn from Sigman *et al.* 2010 [40]. Centers for sinking surface water are located at either end of the Atlantic basin. The circulation in Antarctic ocean in the modern times (A) produces intermediate depth waters (SAMW, AAIW) which fill the mid-depths of the ocean; and bottom water (AABW) which fills the deep ocean southern basin. When sinking, surface waters in the North Atlantic (NADW) fill the deep northern basin. In Ice Age times (B), the equivalent of AABW likely was more dense than at present (colder, saltier) and more isolated from the atmosphere by sea-ice. It formed its own circulation cell more separated from that of the North Atlantic which was relatively less dense and so circulated at shallower depths [37]). The solar warming will lead to decreasing density and a return of water to the upper ocean circulation system. Deep water flow gives a third dimension to the ocean's response to the planetary temperature gradient. The cycle of surface and deep ocean circulation, is vital to the distribution of heat, chemicals and life in the oceans. It is sensitive to anything which will alter seawater densities in regions where sinking occurs ([41]), or any process which changes winds and ocean-atmosphere interaction in upwelling areas.

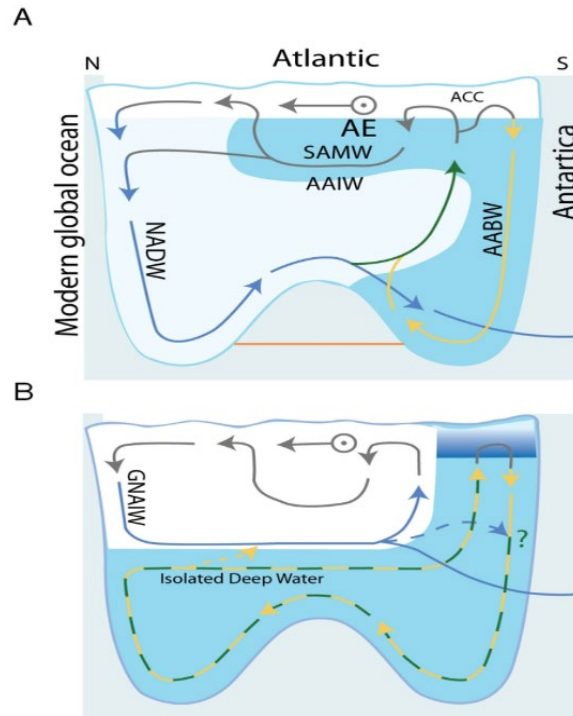


Figure 14: Vertical circulation in the Atlantic ocean in modern age (a) and modeled for the last ice age (b)

5.6. Ocean Currents

Ocean currents are driven by a combination of Earth's rotation and temperature differences between the tropics and poles. Ocean currents vary on depths in which they flow, with denser pole melted waters flowing beneath warmer surface waters towards the equator. Unlike the northern and southern direction of the winds described above, there are westward and eastward winds. Winds are also generated by the rotation of the Earth. These winds affect ocean currents. Warm, tropical waters carry heat pole-ward along the east coast of continents: cold water from the poles is forced toward the equator along the west coast. Warm surface currents can carry heat well away from the tropics, bringing temperate climates to areas nearer the poles than the equator Figure 15 presents the global oceanic circulation at these three depths [41].

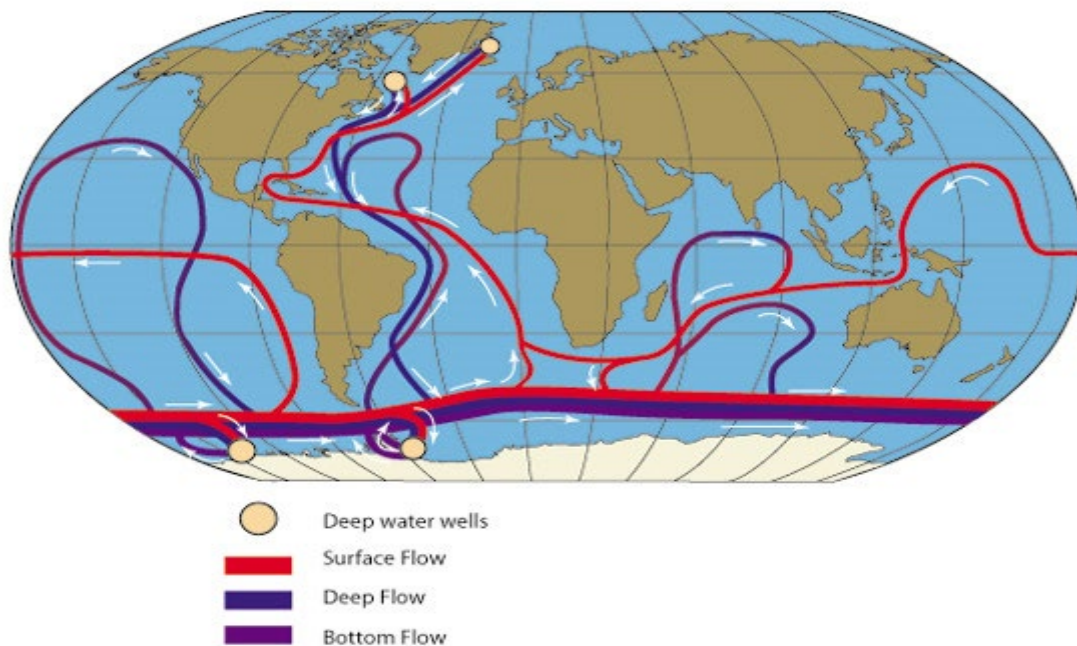


Figure 15: Global oceanic circulation

Deeper currents are driven by a combination of Earth's rotation and temperature differences between the tropics and the poles. Cold, dense melted water from the icecaps flows underneath warmer surface waters towards the equator. The combination of wind and ocean currents redistributes heat and moisture across Earth's surface. Around 60% of the solar energy that reaches the Earth is redistributed around the planet by atmospheric circulation and around 40% by ocean currents, [41].

Proximity to large bodies of water influences climate on a regional scale. Coastal areas experience less seasonal variation in their climates than do continental interiors. Winters are milder, summers cooler, and the temperature swing between daytime high and nighttime low is much less extensive. This is partly due to the high heat capacity of water, i.e. its ability to hold heat for very long periods of time (8 to 10 centuries, [26]) and to release that heat when the atmosphere cools, and partly due to redistribution of heat by ocean currents.

5.7. El Niño-Southern Oscillation (ENSO)

A simple model of the coupled Pacific Ocean and atmosphere, forced with orbital insolation variations, suggests that seasonal changes in insolation can produce systematic changes in ENSO behaviour [40]. This model simulates a progressive, somewhat irregular increase in both event frequency and amplitude due to the Bjerknes feedback mechanism ([42]) and ocean dynamical thermostat [43]. Snapshot experiments conducted with some coupled GCMs also reproduce an intensification of ENSO between the early Holocene and the present, although with some disagreement as to the magnitude of change. Both model results and data syntheses suggest that before the mid-Holocene, the tropical Pacific exhibited a more La Niña-like background state. In palaeoclimate simulations with GCMs, ENSO teleconnections robust in the modern system show signs of weakening under mid-Holocene orbital forcing [44].

Under normal conditions, warm water pools in the western Pacific, but during an El Niño event, the heat covers most of the tropical Pacific. During an El Niño event, the trade winds decrease, and the surface currents follow suit. Rather than pooling in the western Pacific, warm water covers much of the ocean surface in the tropics. This redistribution of heat leads to evaporation, condensation, and precipitation in the eastern Pacific and is responsible for atypical flooding in North America, South America, even Europe, and for drought conditions in Australia, Indonesia, and parts of Africa. Scientists are currently working to more reliably predict El Niño events, in hopes of ameliorating their negative impacts on human and non-human populations [45].

Temporal changes in climate at small scales tend to be predictable: seasons occur consistently from year to year. However, changes may occur when oceanic currents and movement of air masses are disrupted. The best-known example of this phenomenon is the El Niño-Southern Oscillation, a global climate phenomenon that emerges from variations in winds and sea surface temperatures over the tropical Pacific Ocean. [46]. Figure 16 shows how ocean and atmospheric circulation change during a Niño event.

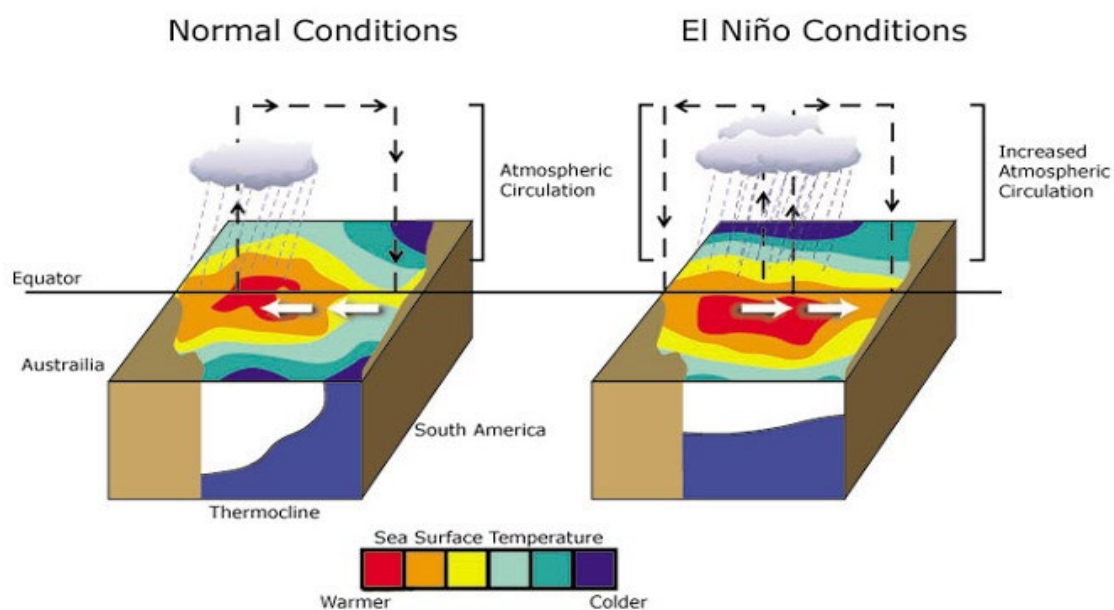


Figure 16: El Niño Southern Oscillations

5.8. Global Warming and Ocean Cooling

Humans are now facing the dominant effects of climate change, with about 98% of the globe much warmer than decades ago. It may seem quite unusual that, under these circumstances, the Atlantic ocean is cooling down during the global warming when global average temperatures of the oceans have increased rapidly since the 1970s (in line with the rapid increase in atmospheric temperatures) and continue to increase rapidly Figure 17 [47].

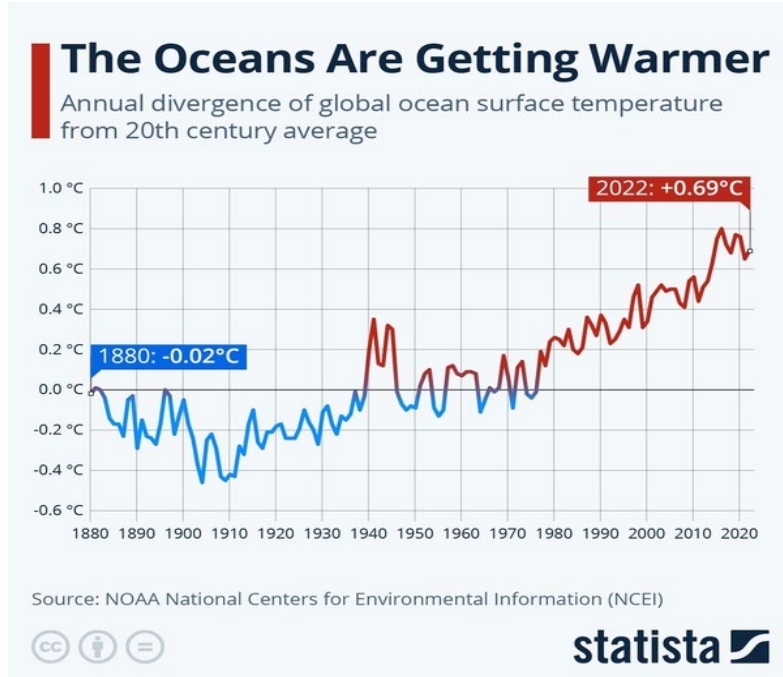


Figure 17: Annual divergence of global ocean surface temperature from 20th century average

Despite the fact that temperatures reached new highs in the Atlantic ocean, scientists found that the Ocean is cooling down, but they are not quite sure why, and the reason behind the cooling remains a mystery to them. There is also cooling in the eastern Pacific due to equatorial upwelling, and parts of Antarctica are also cooling, although there is warming overall. A few areas will cool from time to time, and natural changes continue, just as they have for billions of years. In case of Atlantic ocean, scientists are prone to believe that La Niña is replacing an El Niño and that That could be due to going from El Niño to La Niña the ocean surface cools [48]. Figure 18 ([49]) shows that a decline in Niños was from about 2000 to 2020 and they are becoming more active again. This year El Niño turned to La Niña in June.

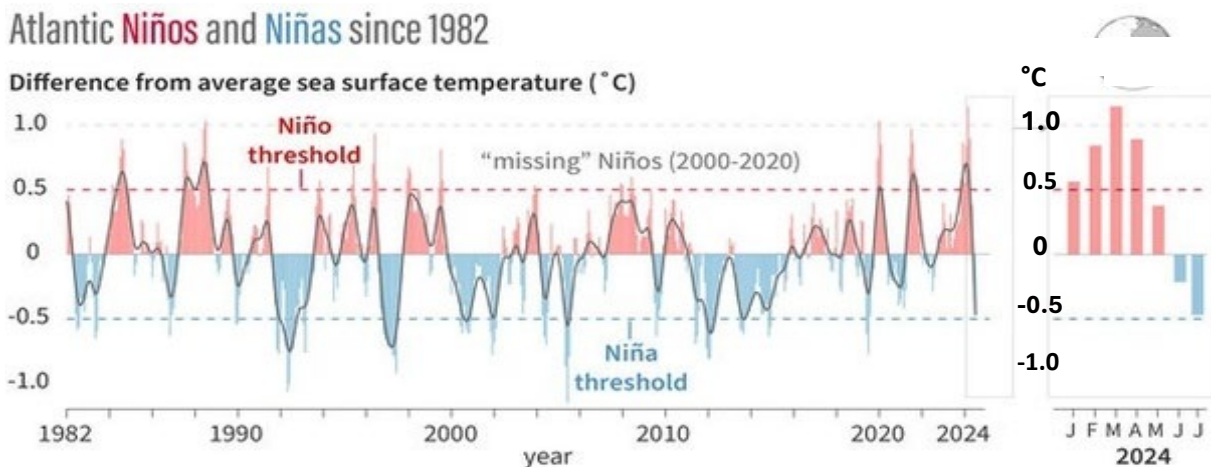


Figure 18: Atlantic Niños and Niñas since 1982 and during 7 months in 2024

The recent cooling in part of the Atlantic Ocean is not caused by anthropogenic climate change, although it is now the dominant force in climate change, and about 98% of the globe is warmer than 50 years ago. 2023 had

over a year of record high global ocean temperatures. but the eastern equatorial Atlantic has cooled rapidly during the last months. Scientists knew that the temperature rise in 2023 would be historic, but were surprised by how much. It just means that scientists can not understand yet all of the factors involved and that scientific models are incomplete because it is almost impossible to include everything with perfect precision.

Overall, ocean global average temperatures have increased rapidly since the 1970s (in line with the increase in atmospheric temperatures) and continue to increase rapidly, Figure 19 [50]. At early July 2024, temperatures are back to about where they were in 2023, a record year.

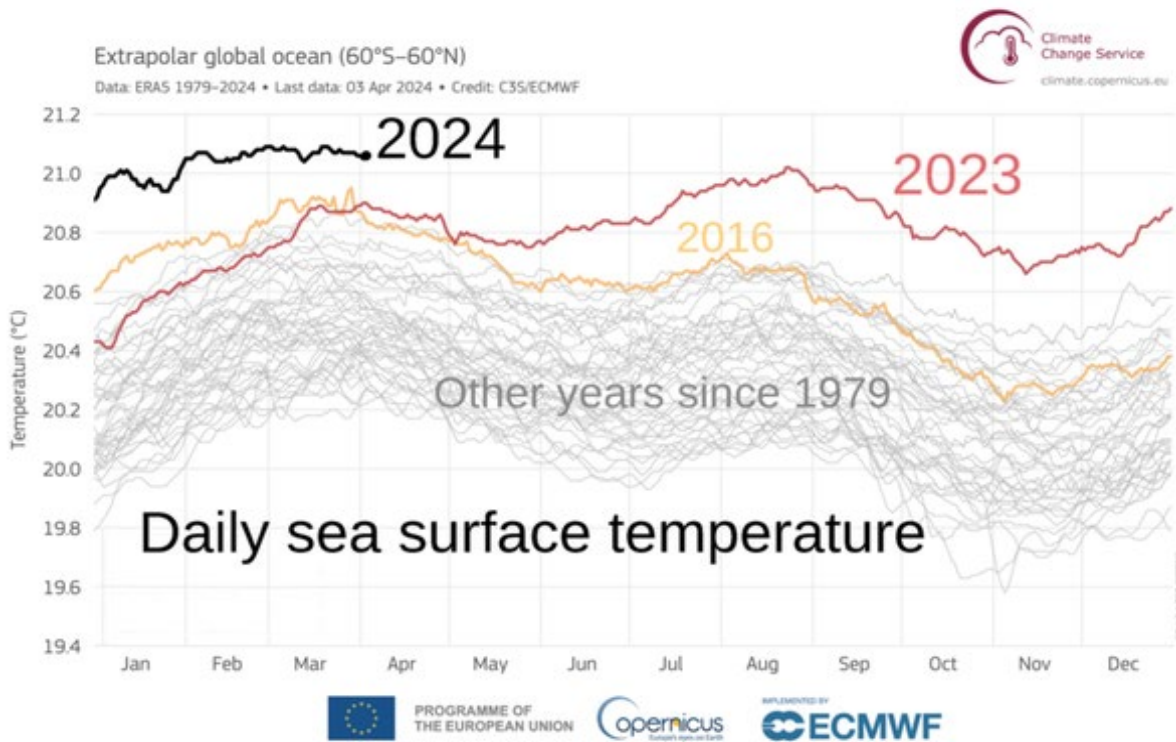


Figure 19: Daily sea surface temperatures since 1979

6. Conclusion

The global climate is a very complex system of systems, with literally millions of factors constantly interacting with each other. It is therefore practically impossible to have all of them modelled so precisely as to simulate the real situation irrespective of the size and power of supercomputers used. In addition to the number and complexity of the processes that need to be modeled, an insurmountable obstacle is represented by interactive positive feedback loops, some of which have not yet been studied nor observed at all. Even when models manage to simulate the known past of climate change with sufficient precision, neither supercomputers nor any other help can provide the ability for models to accurately simulate future climate [51].

On the other hand, to let society know precisely how to oppose unacceptable climate changes and to prepare for survival in the conditions of a changed climate, the models would have to provide precise information about the future climate conditions, which they have not demonstrated yet that can do. One of the reasons for this disadvantage may be methodological approach itself, which is dominated by statistical averaging every data in space and time instead of dynamic simulation of processes that constantly change by motion and interact with each other with a multitude of positive and negative feedback loops.

From a comprehensive review presented in this paper it could become evident to what extent the five components of the climate system interact with each other through all forms of movement and exchange their mass and energy, all being driven both by the energy received from the Sun and the portion of this energy prevented by the atmospheric greenhouse effect to escape into outer space. A closer look to what and how the processes within the climate system develop, it may become challenging for the thermal engineers to join the majority of active experts less aware of how helpful may be the thermal and hydraulic sciences in their efforts to better understand the nature of climate change and reduce risks from the new climate reality.

References

- [1] Baede A., The Climate System: an Overview, IPCC WG I Assessment Report, New York, 2000
- [2] Mesarović, M., Scientific Uncertainties Feed Skepticism on Climate Change, *Thermal Science*, Year 2015, Vol. 19, Suppl. 2, pp. S259-S278
- [3] The Balance of Power in the Earth-Sun System NASA, www.nasa.gov, Approached, Sept.1, 2024
- [4] Harte, J., Consider A Spherical Cow: A Course in Environmental Problem Solving, University Science Books, 2023, p 376
- [5] July 2024 Temperature Update - Berkeley Earth www.BerkeleyEarth.org, Approached September 1, 2024
- [6] F.S. Chapin, III et al., Principles of Terrestrial Ecosystem Ecology, 23 DOI 10.1007/978-1-4419-9504-9_2, © Springer Science+Business Media, LLC 2011
- [7] Global Temperatures are Spiking The Breakthrough Institute. Oct 23, 2023
- [8] Owen, R., Atmospheric effects of Hunga Tonga eruption lingered for years, *Eos*, 105, <https://doi.org/10.1029/2024EO240379>. Published on 22 August 2024.
- [9] El Niño–Southern Oscillation, Wikipedia Approached 30 August 2024
- [10] Harte, J., Consider A Spherical Cow: A Course in Environmental Problem Solving, University Science Books, 1988, p 283
- [11] Hill et al. Heat capacity, the ocean, and our weather, Section 4.2, Oceanography, University of California, Davis
- [12] <https://www.un.org/en/climatechange/what-is-climate-change>, Approached September 1, 2024
- [13] The Climate Report, The Liberal Patriot and The Breakthrough Institute, Berkeley, Oct 23, 2023
- [14] Hawkins, E., Warming Stripes, Climate Lab Book, May 14, 2024
- [15] Climate Change 2021: The Physical Science Basis. Contribution of WG I to the Sixth Assessment Report of the IPCC Chapter 4 Figure 4.2, IPCC New York 2021
- [16] Tollefson, J., Is it too late to keep global warming below 1.5 °C?, *Nature*, 21 Nov. 2023
- [17] Stainforth, D., The big idea: can we predict the climate of the future? *The Guardian*, 2 Oct. 2023
- [18] Cowtan, K et al, "Robust comparison of climate models with observations using blended land air and ocean sea surface temperatures", *Geophysical Research Letters*, vol. 42, pp. 6526-6534, 2015
- [19] Shiel, C.L et al, A Note on the Relationship between Temperature and Water Vapor in Quasi-Equilibrium and Climate States, Goddard Earth Sciences and Technology Center, University of Maryland, Baltimore Baltimore, February 7,2003
- [20] Dale, A., C. Fant, K. Strzepak, M. Lickley, and S. Solomon, Climate model uncertainty in impact assessments for agriculture: A multi-ensemble case study on maize in sub-Saharan Africa, *Earth's Future*, 5, (2017) 337–353, doi:10.1002/2017EF000539
- [21] Lovelock J. E, Geophysiology, the science of Gaia, *Reviews of Geophysics*, May 1989
- [22] <https://doi.org/10.1029/RG027i002p00215>, Approached August 22, 2024,
- [23] Hausfather, Z., Explainer: How the rise and fall of CO2 levels influenced the ice ages, *Carbon Brief*, 2 July 2020
- [24] Toggweiler J.R. & Key, R., Thermohaline Circulation Chapter in Ocean Circulation, In book: Encyclopedia of Atmospheric Sciences December 2003(pp.1549-555)
- [25] Rörsch, A. Et al, Global warming and the accumulation of carbon dioxide: A Critical Consideration of the Evidence, *Energy & Environment*, Vol. 16, No. 1, 2005
- [26] Tiseo, I., Annual global emissions of carbon dioxide 1940-2023, *Statista*, Jun 13, 2024
- [27] Sabine, C. L, et al, The Oceanic Sink for Anthropogenic CO2, *Science* 305(5682)2004, 367-371
- [28] Milankovitch (Orbital) Cycles and Their Role in Earth's Climate, NASA Science Editorial Team, Feb 27, 2020
- [29] Why Milankovitch (Orbital) Cycles Can't Explain Earth's Current Warming, NASA Science Editorial Team Feb 27, 2020
- [30] Mesarović, M., Global warming and other climate change phenomena on geological time scale, *Thermal Science*, Year 2019, Vol. 23, Suppl. 5, pp. S1435-S1455
- [31] Loubere, P. The Global Climate System. *Nature Education* 3(10) 2012:24
- [32] <https://www.weather.gov/safety/cold-polar-vortex>, Approached 02.10.2024
- [33] A Series of Rare Disturbances in the Stratosphere, NASA Earth Observatory, August 5, 2024
- [34] Trenberth, K.E., Changes in precipitation with climate change, Inter-Research, 2011, vol. 47, No.1-2, pp. 123-138
- [35] L'Heureux, M., What is the El Niño–Southern Oscillation (ENSO) in a nutshell? NOAA, Climate.gov, Published May 5, 2014
- [36] The Cataclysmic 1991 Eruption of Mount Pinatubo, Philippines, U.S. Geological Survey Fact Sheet 113-97
- [37] http://www.classzone.com/books/earth_science/terc/content/visualizations/es2401/es2401page01.cfm?chapter_no%7C%7C#eq%7C%7Cvisualization, Approached 26.Aug.2024
- [38] Rahmstorf, S., The thermohaline ocean circulation - a system with dangerous thresholds? *Climatic Change*, 2000. 46: p. 247-256
- [39] <http://svs.gsfc.nasa.gov/vis/a000000/a003600/a003658/> Approached 13.September 2024
- [40] http://www.classzone.com/books/earth_science/terc/content/visualizations/es2405/es2405page01.cfm?chapter_no%7C%7C#eq%7C%7Cvisualization Approached 26.Aug.2024

- [41] Clement, A. C, et al., Suppression of El Niño during the Mid-Holocene by changes in the Earth's orbit, Paleocenography and Paleoclimatology, 4 May 2010
- [42] Rahmstorf, S., Thermohaline Ocean Circulation. In: Encyclopedia of Quaternary Sciences, Edited by S. A. Elias. Elsevier, Amsterdam, 2006.
- [43] Bjerknes, J. Atmospheric teleconnections from the equatorial pacific. Journal of Physical Oceanography, 97(3), 163-172. Tellus, 18(4), 1969. pp. 820-829.
- [44] Clement A.C. et al., An Ocean Dynamical Thermostat, Journal of Climate, Volume 9,1996, pp.2190-2196
- [45] Otto-Bliesner, El Niño/La Niña and Sahel precipitation during the middle holocene, Geophysical Research Letters, 1999 - Wiley Online Library
- [46] L'Heureux, M. What is the El Niño–Southern Oscillation (ENSO) in a nutshell? NOAA, Climate.gov, Published May 5, 2014
- [47] https://en.wikipedia.org/wiki/El_Niño_Southern_Oscillation, Approached 24 August 2024
- [48] NOAA National Centers for Environmental Information, Washington, 2024
- [49] Wilson M., Scientists say the Atlantic ocean is cooling down and they don't know why, Spaces, August 21, 2024
- [50] Atlantic Niña on the verge of developing. Here's why we should pay attention, NOAA, www.Climate.gov, Approached September 3, 2024
- [51] Copernicus: May 2024, streak of global records for surface air and ocean temperatures continues <https://www.washingtonpost.com/climate-environment/2024/01/09/record-hot-year-2023-global-temperatures/> https://en.wikipedia.org/wiki/Sea_surface_temperature, Approached 28 Aug.2024
- [52] Z. Hausfather, H.F. Drake, T. Abbott, and G.A. Schmidt, Evaluating the Performance of Past Climate Model Projections, Geophysical Research Letters, vol. 47, 2020.



II. Energy sources and potentials

The Impact of CBAM and Variable Renewable Energy Integration on Energy Systems and Cross-Border Electricity Trade

Boris Ćosić^a, Neven Duić^b

^a *International Centre for Sustainable Development of Energy, Water and Environment Systems - SDEWES, Zagreb, HR, Boris@sdewes.org*

^b *University of Zagreb, Faculty of Mechanical Engineering and Naval Architecture, Zagreb, HR, Neven.Duic@fsb.unizg.hr*

Abstract: This paper explores the energy system planning for Croatia and Bosnia and Herzegovina (HR-BA zone) in response to the Carbon Border Adjustment Mechanism (CBAM) and the growing need for renewable energy integration between 2025 and 2035. Using the Dispa-SET unit commitment and dispatch model, three scenarios, NECP, LRES, and HRES, were developed to evaluate how different levels of Variable Renewable Energy Sources (VRES) integration and CO₂ pricing impact the region's energy system. In the NECP scenario, Bosnia and Herzegovina's electricity exports decrease from 3.39 TWh in 2025 to 1.29 TWh in 2035, driven by CBAM implementation and the rise in renewable energy use. The HRES scenario shows aggressive renewable energy deployment, resulting in 2.35 TWh of electricity export in 2035, but also reveals substantial curtailment issues, with a maximum hourly curtailment value reaching 3,926 MW and occurring over 4,114 hours during 2035. These findings underscore the difficulties of integrating large amounts of renewable energy without significant upgrades to grid infrastructure and storage solutions.

Keywords: CBAM, Dispa-SET, ETS, NECP, VRES.

1. Introduction

The global transition towards a low-carbon future is accelerating, primarily driven by the urgent need to mitigate climate change and reduce greenhouse gas emissions. The European Union (EU) has been at the forefront of this movement, introducing the Carbon Border Adjustment Mechanism (CBAM) [1] to prevent carbon leakage and ensure that imported products adhere to the same environmental standards as those produced within the EU [2] and [3]. CBAM specifically targets carbon-intensive sectors such as cement, aluminium, and electricity, which are essential for the energy transition [4].

The energy systems of Bosnia and Herzegovina (BA) and Croatia (HR), both part of the interconnected Western Balkans energy network, rely heavily on coal and natural gas. Both countries are under growing pressure to reduce their reliance on these fossil fuels and to increase the integration of Variable Renewable Energy Sources (VRES), such as wind and solar [5]. However, the intermittent nature of VRES introduces significant challenges in maintaining grid stability and avoiding curtailment, especially in interconnected power markets like those of the EU and the Energy Community [6] and [7]. Pumped Hydro Storage (PHS), heat and electric storage, and demand-side management have been identified as key solutions for enhancing the flexibility of power systems and supporting the integration of renewables. Flexible hydropower enables better management of VRES, helping to mitigate curtailment and balance supply and demand on the grid [8] and [9].

To evaluate the long-term impacts of CBAM and carbon pricing mechanisms, energy system models such as Dispa-SET are increasingly utilised. Dispa-SET is an open-source model designed for multi-zonal and multi-sector power dispatch optimisation, with applications across Europe and beyond [9] and [10]. The model provides insights into the operational and economic dynamics of power systems under various renewable energy integration and CO₂ pricing scenarios [11] and [12]. In Bosnia and Herzegovina, where lignite remains a dominant source of electricity, introducing CO₂ pricing under CBAM presents significant challenges. The country risks transitioning from being an electricity exporter to an importer, as carbon costs render lignite economically unviable [13].

In addition to technical challenges, the economic impacts of CBAM will be profound, particularly for non-EU countries exporting electricity to the EU. Studies have highlighted that cross-border electricity trade between Bosnia and Herzegovina and Croatia is highly sensitive to fluctuations in CO₂ prices and fossil fuel costs [14]. Under higher CBAM factors, countries without robust renewable energy portfolios or carbon pricing strategies may face significant economic pressures, making investments in renewable energy and grid infrastructure critical for maintaining competitiveness [15]. Moreover, understanding the role of sector coupling is essential for future energy transitions. Sector coupling involves integrating power, heating, and transportation systems to achieve greater flexibility and decarbonisation [16]. The concept has been explored in the context of European energy systems, demonstrating the potential to optimise energy use across sectors while reducing overall CO₂ emissions [9] and [17].

The scientific contribution of this paper lies in its comprehensive analysis of the impact of the Carbon Border Adjustment Mechanism (CBAM) and varying levels of Variable Renewable Energy Sources (VRES) integration on the energy systems of Croatia and Bosnia and Herzegovina from 2025 to 2035. By utilising the Dispa-SET model, this study uniquely integrates CO₂ pricing and renewable energy scenarios to simulate cross-border electricity flows, curtailment, and system flexibility. The novelty of the research stems from its application of the CBAM phase-in to a non-EU country (Bosnia and Herzegovina), providing valuable insights into how gradually rising carbon costs influence electricity trade and renewable energy utilisation. Additionally, the study highlights the importance of infrastructure upgrades, grid flexibility, and energy storage in mitigating the growing challenges of curtailment under high renewable energy penetration, offering critical policy and operational recommendations for energy transitions in interconnected regions.

2. Method

The Dispa-SET model, an open-source unit commitment and dispatch optimisation tool, is designed to simulate power systems across multiple zones and sectors. It is particularly effective for analysing power systems with a high share of variable renewable energy sources (VRES), such as wind and solar, alongside conventional power plants, energy storage solutions (e.g., pumped hydro and batteries), and cogeneration systems. The model utilises a Mixed-Integer Linear Programming (MILP) approach, implemented in Python and GAMS, to minimise total system costs. These costs include fuel consumption, plant start-up and shutdown operations, ramping, and load-shedding costs, all optimised within technical and regulatory constraints, such as generation capacities, transmission limits, and environmental policies. Dispa-SET can simulate operations on different time scales, from hourly dispatch to annual system planning, making it adaptable for both isolated power systems and large interconnected grids.

The main objective of the Dispa-SET model is to minimise total system costs by accounting for both operational and market-related expenses. The model operates under several constraints, such as limits on generation capacity, minimum up/down times for power plants, ramping limitations, and transmission capacities. Input data, such as detailed power plant characteristics, renewable energy generation profiles, and electricity demand, feed into the model, which then optimises generation across zones. Power plants are represented by parameters such as capacity, operational efficiency, ramp rates, and emissions, while transmission constraints ensure that electricity transfers between zones respect network limits and capacities. Moreover, the model incorporates existing power plant operations and the integration of new generation technologies, whether fossil-based or renewable, allowing for comprehensive analysis of the transition to a renewable-dominated system.

Dispa-SET is effective in simulating cross-border electricity flows, making it a valuable tool for assessing the economic and operational impacts of energy policies, such as carbon pricing. The model can simulate energy trading across zones with different carbon pricing schemes, offering valuable insights for policymakers focused on decarbonisation strategies. The model has been widely applied in various contexts, including evaluating renewable energy integration in the Western Balkans, assessing the operational flexibility required for systems with high shares of wind and solar energy [18] and [5], and exploring the water-energy nexus in African power pools [10]. Additionally, Dispa-SET has been used to assess strategic decisions in market-coupled zones, exploring how different energy policies and infrastructure investments impact cross-border electricity flows and system costs [13]. These applications demonstrate the model's flexibility in simulating regional and continental power systems under a wide range of policy and technical constraints.

3. Planning of the energy system in Croatia (HR) and Bosnia and Herzegovina (BA): The HR-BA zone

The reference energy system for Croatia and Bosnia and Herzegovina (HR-BA zone) serves as the foundation for this energy transition analysis. The system includes the existing generation mix in both countries, comprising fossil fuel power plants (coal, gas, and oil), hydropower, and Variable Renewable Energy Sources (VRES), such as wind and solar. Transmission interconnections between Croatia, Bosnia and Herzegovina, and their neighbouring countries are also considered. To accurately simulate operational conditions, power plant characteristics, such as capacity, efficiency, and ramp rates, are collected and integrated into the model. Renewable energy production profiles are derived from historical data, while electricity demand profiles remain constant throughout the analysis period, ensuring the reference system mirrors the actual operational structure of the HR-BA zone.

The data needed to design the reference energy system was obtained from multiple sources to ensure both accuracy and relevance. Key power plant characteristics, including capacities, efficiencies, and ramp rates, were obtained from various studies [5], [19], [20]. Electricity demand profiles were derived from historical consumption data and remained constant throughout the analysis period. Renewable energy production profiles were derived from historical weather data and generation records, ensuring that hourly variations in wind and solar output were adequately captured [21] and [22]. Transmission capacities and interconnections between Croatia, Bosnia and Herzegovina, and neighbouring countries were collected from reports published by the European Network of Transmission System Operators for Electricity (ENTSO-E), ensuring that cross-border flows and transmission limits accurately reflect real-world conditions [21].

Three energy transition scenarios were developed to assess the impact of different levels of VRES deployment and CO₂ pricing. These scenarios, designed explicitly for Bosnia and Herzegovina's potential alignment with the European Union's Emissions Trading System (EU ETS) by 2035, examine the combined effects of the Carbon Border Adjustment Mechanism (CBAM) and renewable energy integration on fossil fuel power plants and the broader energy market.

- **NECP Scenario:** This scenario aligns with the National Energy and Climate Plans (NECPs) of Bosnia and Herzegovina [23] and Croatia [24], projecting renewable energy capacities based on official targets for 2035. By 2035, Bosnia and Herzegovina aims to install 1,220 MW of wind power and 2,890 MW of solar photovoltaic (PV) capacity, while Croatia plans to install 1,980 MW of wind power and 1,825 MW of PV capacity. Other generation technologies remain unchanged compared to the reference scenario. This scenario serves as the baseline for comparing the effect of CBAM and VRES integration on the energy market in both countries.
- **LRES Scenario (Low Renewable Energy Source Integration):** In this scenario, Bosnia and Herzegovina adopts a more conservative approach to VRES deployment, with significantly lower installation rates for wind and PV plants compared to the NECP scenario. By 2035, wind capacity is expected to reach only 402 MW and PV capacity is projected to be 980 MW. Croatia maintains the same renewable energy targets as in the NECP scenario. This scenario evaluates the potential impacts of slower renewable energy integration on fossil fuel dependency and CO₂ pricing.
- **HRES Scenario (High Renewable Energy Source Integration):** This scenario envisions an accelerated deployment of renewable energy in Bosnia and Herzegovina, with wind capacity increasing to 2,440 MW and PV capacity reaching 3,825 MW by 2035. Croatia's renewable energy targets remain aligned with the NECP scenario. The HRES scenario assesses the impacts of a rapid shift towards renewable energy on system flexibility, cross-border electricity flows, and the responsiveness of the energy market to rising CO₂ prices.

These scenarios were analysed using the Dispa-SET model, which simulates electricity generation, demand, and cross-border electricity flows. This approach provides insights into the economic and operational effects of different energy transition pathways in the HR-BA zone. The results from each scenario support the evaluation of policy decisions aimed at optimising renewable energy integration, reducing CO₂ emissions, and enhancing energy security.

In the scenarios for Bosnia and Herzegovina, the Carbon Border Adjustment Mechanism (CBAM) was introduced gradually, aligning the country with EU carbon pricing. Bosnia and Herzegovina starts with no CO₂ pricing in 2025 (0%), with the CO₂ price gradually increasing from 2.5% in 2026 to 100% by 2035,

based on the CBAM phase-in factors. The hourly CO₂ price used in Croatia's EU ETS in 2022 is applied as a baseline, and Bosnia and Herzegovina's CO₂ price increases incrementally each year according to the CBAM schedule. This phased approach models the economic impact of Bosnia and Herzegovina's gradual integration into a carbon-regulated market, reflecting the transition towards full alignment with EU carbon policies by 2035.

4. Results

This section presents the results of the energy system analysis for Croatia (HR) and Bosnia and Herzegovina (BA) for the period 2025-2035. The analysis incorporates the Carbon Border Adjustment Mechanism (CBAM) and varying levels of CO₂ pricing across different scenarios. The results also take into account the levels of installed Variable Renewable Energy Sources (VRES), which have a significant impact on cross-border electricity flows, curtailment, and overall system flexibility. The key findings are illustrated in Figure 1 – Figure 4, highlighting electricity trade and curtailment dynamics between the two countries.

Figure 1 shows the electricity exchange between Bosnia and Herzegovina (BA) and Croatia (HR) from 2025 to 2035, with a focus on how CO₂ pricing under the CBAM phase-in and varying levels of renewable energy integration affect cross-border flows.

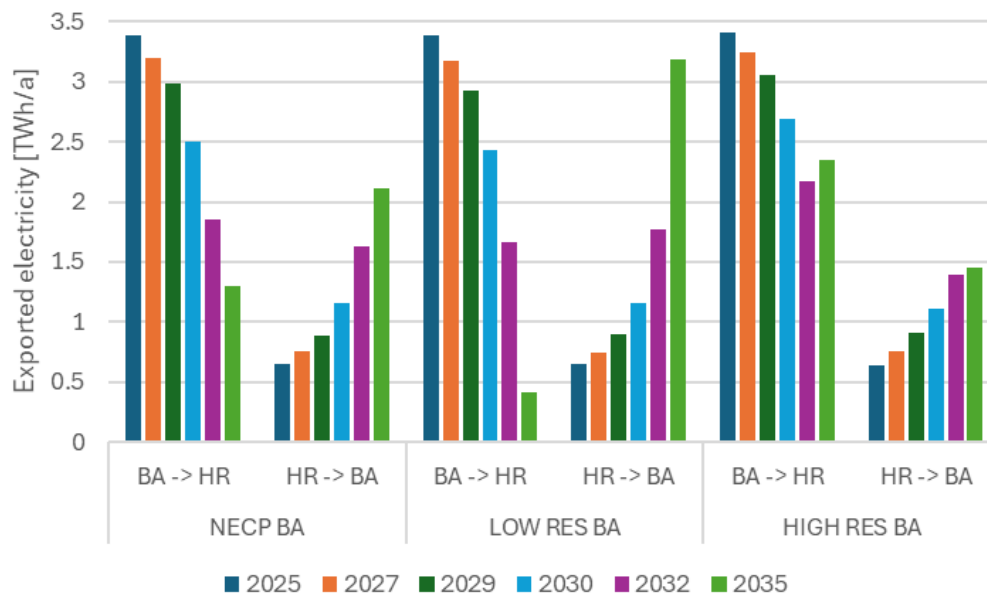


Figure 1. Electricity export per zone and scenario

In the NECP scenario, Bosnia and Herzegovina remains a net exporter of electricity to Croatia, starting with 3.39 TWh exported in 2025 and declining to 1.29 TWh by 2035. This decline is driven by higher CO₂ prices and increased renewable energy capacity in Bosnia (1,220 MW of wind and 2,890 MW of solar by 2035). Croatia, on the other hand, gradually increases its electricity exports to Bosnia, rising from 0.65 TWh in 2025 to 2.11 TWh in 2035, as higher CO₂ costs under the EU ETS make it more competitive.

In the LRES scenario, Bosnia and Herzegovina's slower renewable energy deployment (with only 402 MW of wind and 980 MW of solar by 2035) results in a more significant reduction in electricity exports, from 3.39 TWh in 2025 to just 0.41 TWh by 2035. The higher CO₂ price in Bosnia, due to the CBAM phase-in, reduces fossil fuel reliance, but also limits its ability to maintain high export levels. Conversely, Croatia becomes a more attractive source of low-carbon electricity, with its exports increasing to 3.19 TWh by 2035.

In the HRES scenario, Bosnia and Herzegovina undertakes aggressive renewable energy deployment (2,440 MW of wind and 3,825 MW of solar by 2035), enabling it to maintain higher exports to Croatia compared to the NECP scenario, ending at 2.35 TWh in 2035. However, Croatia's exports to Bosnia decrease after 2030 due to the increase in renewable capacity in Bosnia, reaching 1.46 TWh in 2035. This scenario demonstrates that high levels of renewable energy can mitigate the effects of rising CO₂ prices, especially under the CBAM regime.

Curtailment in these scenarios primarily affects the integration of wind and solar energy in Bosnia and Herzegovina. With increasing VRES capacity and rising CO₂ prices under the CBAM phase-in, Bosnia faces challenges in fully utilising its renewable energy potential, as surplus generation often exceeds grid capacity or local demand. Curtailment levels vary based on the scenario’s renewable deployment and system flexibility, with higher curtailment seen in scenarios with more aggressive renewable growth.

Figure 2 compares the curtailment duration in Bosnia and Herzegovina under the NECP scenario between 2025 and 2035. In 2025, curtailment is minimal, with the highest curtailment reaching 598 MW for just 1 hour, and no curtailment for 8,672 hours. However, as the renewable energy capacity increases and CO₂ prices rise, curtailment becomes more frequent and severe. By 2035, the maximum curtailment reaches 2,733 MW, with curtailment affecting 1,911 hours. This represents a significant increase in both frequency and magnitude compared to 2025, highlighting the growing challenge of integrating renewable energy as the system evolves.

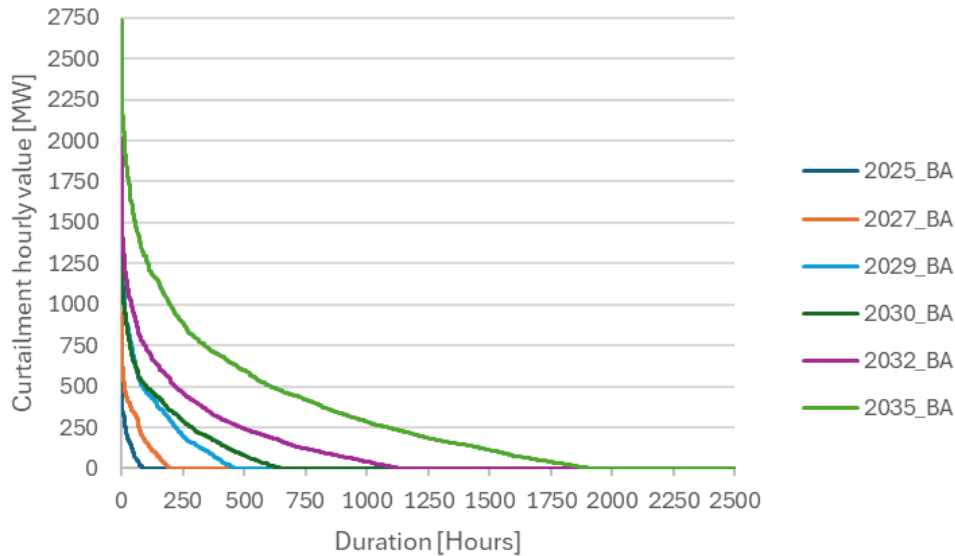


Figure 2. Curtailment duration curve for NECP scenario in zone BA

Figure 3 compares curtailment in Bosnia and Herzegovina under the LRES scenario between 2025 and 2035. In this scenario, slower renewable energy integration leads to lower curtailment throughout the period.

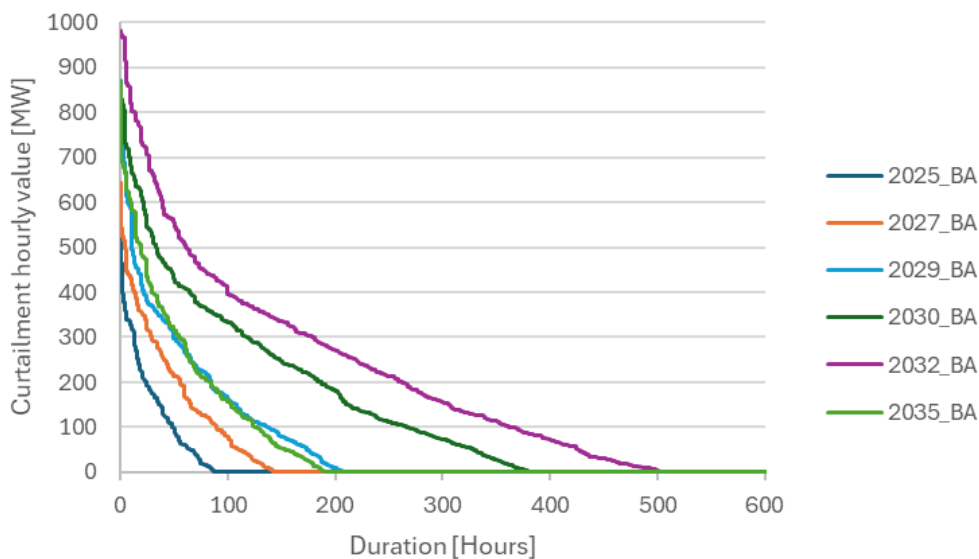


Figure 3. Curtailment duration curve for LRES scenario in zone BA

In 2025, curtailment is almost negligible, with the maximum curtailment of 598 MW occurring for only 1 hour, and no curtailment for 8,672 hours. By 2035, curtailment increases as renewable energy capacity grows, but

remains controlled compared to scenarios with faster renewable integration. The maximum curtailment in 2035 is 867 MW, occurring for 192 hours, with 8,568 hours experiencing no curtailment. The moderate increase in curtailment reflects the limited expansion of renewable energy in this scenario, allowing the system to manage renewable generation without overwhelming the grid.

Figure 4 compares curtailment in Bosnia and Herzegovina under the HRES scenario from 2025 to 2035. In this scenario, rapid and aggressive renewable energy deployment results in significantly higher curtailment levels by 2035.

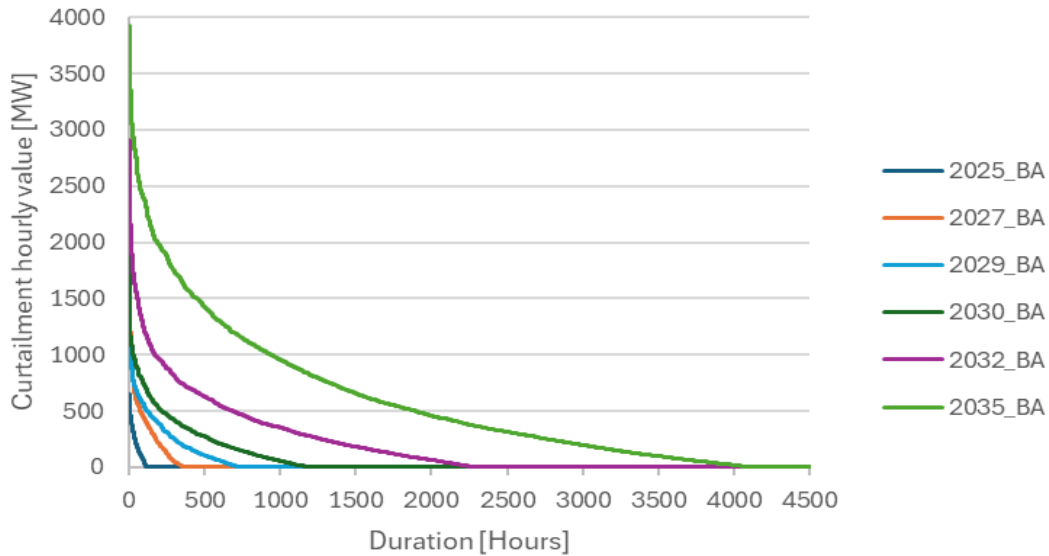


Figure 4. Curtailment duration curve for HRES scenario in zone BA

In 2025, curtailment is minimal, with a maximum curtailment of 646 MW occurring for 1 hour and no curtailment for 8,644 hours. However, as renewable capacity rapidly increases, curtailment becomes much more frequent and severe. By 2035, curtailment peaks at 3,926 MW, affecting 4,114 hours. This means that nearly half the year experiences curtailment, reflecting the difficulties of integrating large volumes of renewable energy without adequate investments in grid flexibility, storage, or demand-side management. The significant rise in curtailment highlights the challenge of fully utilising the renewable energy generated, leading to substantial energy wastage.

The results of these scenarios clearly show that the system's ability to manage surplus renewable energy diminishes as renewable capacity expands and CO₂ prices rise under the CBAM phase-in. By 2035, curtailment affects a substantial portion of the year, particularly in the HRES scenario, where more than 50% of the year faces curtailment. These findings underscore the urgent need for infrastructure upgrades, storage solutions, and demand-side management to fully utilise renewable energy and ensure grid reliability.

5. Conclusion

The analysis of the energy systems in Croatia and Bosnia and Herzegovina from 2025 to 2035 reveals significant differences in the impacts of renewable energy integration and CO₂ pricing across the three scenarios (NECP, LRES, and HRES). The results show that in the NECP scenario, Bosnia and Herzegovina remains a net exporter of electricity, with exports declining from 3.39 TWh in 2025 to 1.29 TWh in 2035, reflecting the increasing effect of rising CO₂ prices and renewable energy deployment (1,220 MW of wind and 2,890 MW of solar by 2035). In the LRES scenario, slower renewable integration results in minimal curtailment and lower export levels, with Bosnia's exports dropping from 3.39 TWh in 2025 to only 0.41 TWh by 2035. In the HRES scenario, aggressive renewable energy deployment (2,440 MW of wind and 3,825 MW of solar by 2035) leads to higher exports, reaching 2.35 TWh in 2035, but also results in substantial curtailment.

The curtailment analysis highlights the growing challenge of integrating large shares of renewable energy into the grid. In the NECP scenario, curtailment increases moderately, with a maximum curtailment of 2,733 MW occurring for 1,911 hours by 2035. In contrast, the HRES scenario sees curtailment peaking at 3,926 MW,

affecting 4,114 hours in 2035, indicating that nearly half of the year is impacted by curtailment. This underscores the need for enhanced grid flexibility, storage solutions, and demand-side management to effectively manage surplus renewable energy and fully utilise the benefits of renewable deployment. The findings emphasise that without these infrastructure upgrades, higher levels of renewable energy can lead to significant energy wastage, particularly under rising CO₂ prices.

References

- [1] The European Parliament and the Council of the European Union. Regulation (EU) 2023/956 of the European Parliament and of the Council of 10 May 2023 establishing a carbon border adjustment mechanism. Off J Eur Union 2023. <http://data.europa.eu/eli/reg/2023/956/oj> (accessed May 29, 2024).
- [2] Clora F, Yu W. GHG emissions, trade balance, and carbon leakage: Insights from modeling thirty-one European decarbonization pathways towards 2050. *Energy Econ* 2022;113. <https://doi.org/10.1016/j.eneco.2022.106240>.
- [3] Pan X, Liu S. The development, changes and responses of the European Union carbon border adjustment mechanism in the context of global energy transition. *World Dev Sustain* 2024;4:100148. <https://doi.org/10.1016/j.wds.2024.100148>.
- [4] Chen G. Impact of carbon border adjustment mechanism on China's manufacturing sector: A dynamic recursive CGE model based on an evolutionary game. *J Environ Manage* 2023;347:119029. <https://doi.org/10.1016/j.jenvman.2023.119029>.
- [5] Pavičević M, Quoilin S, Zucker A, Krajačić G, Pukšec T, Duić N. Applying the Dispa-SET Model to the Western Balkans Power System. *J Sustain Dev Energy, Water Environ Syst* 2020;8:184–212. <https://doi.org/10.13044/j.sdewes.d7.0273>.
- [6] Kara G, Tomasgard A, Farahmand H. Characterizing flexibility in power markets and systems. *Util Policy* 2022;75:101349. <https://doi.org/10.1016/j.jup.2022.101349>.
- [7] Impram S, Varbak Nese S, Oral B. Challenges of renewable energy penetration on power system flexibility: A survey. *Energy Strateg Rev* 2020;31:100539. <https://doi.org/10.1016/j.esr.2020.100539>.
- [8] Li J, Zhao Z, Xu D, Li P, Liu Y, Mahmud MA, et al. The potential assessment of pump hydro energy storage to reduce renewable curtailment and CO₂ emissions in Northwest China. *Renew Energy* 2023;212:82–96. <https://doi.org/10.1016/j.renene.2023.04.132>.
- [9] Pavičević M, Mangipinto A, Nijs W, Lombardi F, Kavvadias K, Jiménez Navarro JP, et al. The potential of sector coupling in future European energy systems: Soft linking between the Dispa-SET and JRC-EU-TIMES models. *Appl Energy* 2020;267:115100. <https://doi.org/10.1016/j.apenergy.2020.115100>.
- [10] Pavičević M, De Felice M, Busch S, Hidalgo González I, Quoilin S. Water-energy nexus in African power pools – The Dispa-SET Africa model. *Energy* 2021;228. <https://doi.org/10.1016/j.energy.2021.120623>.
- [11] Fernandez Vazquez CAA, Vansighen T, Fernandez Fuentes MH, Quoilin S. Energy transition implications for Bolivia. Long-term modelling with short-term assessment of future scenarios. *Renew Sustain Energy Rev* 2024;189:113946. <https://doi.org/10.1016/j.rser.2023.113946>.
- [12] Kihara M, Lubello P, Millot A, Akute M, Kilonzi J, Kitili M, et al. Mid- to long-term capacity planning for a reliable power system in Kenya. *Energy Strateg Rev* 2024;52:101312. <https://doi.org/10.1016/j.esr.2024.101312>.
- [13] Pfeifer A, Krajačić G, Haas R, Duić N. Consequences of different strategic decisions of market coupled zones on the development of energy systems based on coal and hydropower. *Energy* 2020;210. <https://doi.org/10.1016/j.energy.2020.118522>.
- [14] Ambec S, Yang Y. Climate policy with electricity trade. *Resour Energy Econ* 2024;76:101422. <https://doi.org/10.1016/j.reseneeco.2023.101422>.
- [15] Perdana S, Vielle M. Making the EU Carbon Border Adjustment Mechanism acceptable and climate friendly for least developed countries. *Energy Policy* 2022;170:113245. <https://doi.org/10.1016/j.enpol.2022.113245>.
- [16] Herc L, Feijoo F, Kodba A, Dorotić H, Stunjek G, Beljan D, et al. The management of an energy system in the realm of rapid energy transition and degasification as a consequence of energy crisis, examination in H2RES energy model. *Energy Convers Manag* 2024;315:118782. <https://doi.org/10.1016/j.enconman.2024.118782>.
- [17] Pastore LM, Groppi D, Feijoo F, Lo Basso G, Astiaso Garcia D, de Santoli L. Optimal decarbonisation pathways for the Italian energy system: Modelling a long-term energy transition to achieve zero emission by 2050. *Appl Energy* 2024;367:123358. <https://doi.org/10.1016/j.apenergy.2024.123358>.
- [18] Pavičević M, Kavvadias K, Pukšec T, Quoilin S. Comparison of different model formulations for modelling future power systems with high shares of renewables – The Dispa-SET Balkans model. *Appl Energy* 2019;252:113425. <https://doi.org/10.1016/j.apenergy.2019.113425>.
- [19] Dominković DF, Bačeković I, Čosić B, Krajačić G, Pukšec T, Duić N, et al. Zero carbon energy system of South East Europe in 2050. *Appl Energy* 2016;184:1517–28. <https://doi.org/10.1016/j.apenergy.2016.03.046>.
- [20] South East Europe Consultants - SEEC. Study on the Potential for Climate Change Combating in Power Generation in the Energy Community. 2011.
- [21] ENTSO-E. Data - ENTSO-E - European Network of Transmission System Operators for Electricity. *Transpar Platf* 2024. <https://www.entsoe.eu/data/> (accessed September 19, 2024).



- [22] Pfenninger S, Staffell I. Renewables.ninja. RenewablesNinja 2024. <https://www.renewables.ninja/> (accessed September 19, 2024).
- [23] Ministry of Foreign Trade and Economic Relations of Bosnia and Herzegovina. Integrated National Energy and Climate Plan for Bosnia and Herzegovina 2023:1–188. http://www.mvteo.gov.ba/data/Home/Dokumenti/Energetika/Nacrt_NECP_BiH_loc.pdf (accessed September 23, 2024).
- [24] Ministry of Economy and Sustainable Development. Integrated National Energy and Climate Plan for the Republic of Croatia 2023:1–240. <https://mingo.gov.hr/UserDocsImages/KLIMA/NECPdraftUpdateENGv1EC.pdf> (accessed September 23, 2024).

Drying the Hemp Flower in a Condensation Dryer

**Branka Radovanović^a, Jelena Janevski^b, Mića Vukić^c, Saša Pavlović^d,
Dragana Dimitrijević Jovanović^e**

^aUniversity of Niš, Faculty of Mechanical Engineering in Nis, RS, branka.radovanovic@masfak.ni.ac.rs

^bUniversity of Niš, Faculty of Mechanical Engineering in Niš, RS, jelena.janevski@masfak.ni.ac.rs

^cUniversity of Niš, Faculty of Mechanical Engineering in Niš, RS, mica.vukic@masfak.ni.ac.rs

^dUniversity of Niš, Faculty of Mechanical Engineering in Niš, RS, sasa.pavlovic@masfak.ni.ac.rs

^e University of Niš, Faculty of Civil Engineering and Architecture, RS, dragana.dimitrijevic@gaf.ni.ac.rs

Abstract: The drying process of hemp flowers is crucial for preserving the quality of cannabinoids, terpenes, aromas, and other valuable compounds. This study investigates the drying of hemp flowers using a condensation dryer, combined with a heat pump. This type of dryer allows for significant energy savings by retaining both the latent and sensible heat within the chamber. Although the drying process is somewhat slower than in conventional dryers, the quality of the drying is exceptional. The dryer operates at slightly lower temperatures, up to 60°C, making it ideal for delicate products such as hemp flowers, herbs, and chopped fruits and vegetables. The drying process plays a key role in the retention of aroma and in the overall quality of the products. Key drying parameters, including air temperature, humidity, and the amount of condensate collected, are continuously monitored. Results will provide detailed hourly insights into these parameters, along with an analysis of the drying regime, offering recommendations for optimizing the process to preserve product quality.

Keywords: Hemp flower, condensation dryer, drying parameters, air temperature and humidity change, condensate.

1. Introduction

Industrial hemp (*Cannabis sativa* L.) has a long history of cultivation across the globe, known primarily for its fiber used in textiles and construction materials. Hemp seeds are a valuable source of proteins and oils, with an ideal 3:1 ratio of omega-6 (linoleic acid) to omega-3 (alpha-linolenic acid) fatty acids, making them highly desirable for human nutrition. In recent years, however, growing attention has been directed toward the flowers (inflorescences) and leaves of the hemp plant due to their rich content of bioactive compounds with significant therapeutic and health benefits. Cannabidiol (CBD) has emerged as one of the most prominent compounds, known for its ability to relieve pain, reduce anxiety, and promote relaxation. Additionally, with low levels of psychoactive compounds such as tetrahydrocannabinol (THC), industrial hemp has gained traction in pharmaceutical, cosmetic, and even food applications. [1]

The hemp flower, in particular, is of significant interest due to its concentration of cannabinoids, terpenes, and other valuable secondary metabolites that contribute to its therapeutic effects. The flower is also highly aromatic, owing to the presence of a variety of terpenes, which play a crucial role in both the plant's aroma and its potential medicinal properties. However, preserving these delicate compounds during post-harvest processing, especially during drying, is a challenge. Effective drying of hemp flowers is essential not only to prevent microbial spoilage but also to retain the maximum amount of cannabinoids, terpenes, and aromatic compounds.

Nowadays, hemp is cultivated globally and utilized in a wide variety of industries, including food, dietary supplements, pharmaceuticals, body care products, fuel, paper, construction materials, and textiles. The plant boasts approximately 750 naturally occurring chemical compounds, which can be grouped into several distinct categories, each contributing to its diverse range of applications. [2]

Drying is the most common and fundamental technique for preserving herbs while retaining their bioactive compounds. Research indicates that the drying method and parameters significantly influence the chemical and biological activity of herbs, affecting the composition of their essential oils. Convection drying (CD), which uses hot air to remove moisture, is widely used, but newer methods like vacuum-microwave drying

(VMD) and combined approaches such as convectional pre-drying followed by vacuum–microwave finishing drying (CPD-VMFD) have been developed to improve drying efficiency. These alternative methods offer faster drying with better preservation of volatile compounds, though at a higher cost. [2]

The focus of this study is to explore the drying process of hemp flowers using a condensation dryer. This method allows for precise control of temperature and humidity, ensuring optimal conditions for retaining the quality of cannabinoids and terpenes. The study aims to analyze key drying parameters and offer recommendations for improving the drying process to maintain the integrity of hemp flower compounds.

In addition to the focus on drying methods, it is essential to consider the broader implications of optimizing the drying process for hemp flowers. The increasing popularity of hemp-derived products in wellness, beauty, and nutritional sectors highlights the need for high-quality dried hemp flowers that meet consumer demands. By improving drying techniques, we can ensure that the final products not only retain their therapeutic properties but also enhance their marketability. Furthermore, as regulations surrounding hemp cultivation and processing continue to evolve, implementing advanced drying methods that prioritize quality and efficiency will be crucial for producers looking to remain competitive. This study aims to contribute valuable insights into the optimization of the drying process, ultimately supporting the sustainable growth of the hemp industry while meeting the rising consumer interest in its health benefits.

2. Motiv

The motivation for this research is rooted in the increasing relevance of condensation dryers in drying delicate plant materials, such as hemp flowers. Condensation dryers offer significant advantages in terms of energy efficiency, moisture control, and preservation of product quality. One of the primary benefits is the ability to maintain a high quality of the final product, ensuring that important attributes such as color, flavor, aroma, and nutritional value are preserved throughout the drying process. This preservation is crucial for meeting consumer expectations and maintaining the integrity of the product.

In addition to quality preservation, condensation dryers are remarkably energy-efficient, with electricity consumption being 3 to 5 times lower compared to traditional drying methods. This not only reduces operational costs but also minimizes the environmental impact associated with high energy usage. Achieving very low moisture levels in the final products is another significant advantage, as it helps extend shelf life and prevents spoilage. The high degree of automation in condensation dryers enhances the overall efficiency of the drying process, allowing for precise control of humidity and temperature levels. This precision is vital for achieving consistent results and optimizing the drying conditions for sensitive materials like hemp flowers.

Furthermore, products dried using condensation dryers are maintained according to the HASAP standards regarding hygiene, ensuring that the end products are safe for consumption. By utilizing the heat generated during the drying process to warm the air, condensation dryers reduce the need for additional energy sources and lower emissions of harmful gases. This aspect aligns with global sustainability goals and highlights the importance of adopting innovative technologies in food processing and preservation. Given the rising demand for high-quality dried hemp products, this research aims to explore the potential of using condensation drying technology to optimize the drying process, reduce energy consumption, and improve the overall quality of the final product. This study serves as a step toward enhancing the drying techniques for hemp flowers, contributing to better post-harvest processing methods.

3. Materials And Methods

This research utilized the flowers of industrial hemp (*Cannabis sativa* L.). The company "Glarnisch building" DOO carried out the sowing of industrial hemp on May 13, 2024. The sowing was conducted on an area of 2560 square meters. A full bag (10 kg) of hemp seeds from the Helena variety was used for sowing. The seeds were purchased from the Institute for Agriculture and Horticulture "NS Seme," Novi Sad. The flowers were harvested at full maturity, packed in bags, and delivered to the faculty in Niš. The initial moisture content of the flowers before drying was 28%. The flowers were harvested with higher moisture, but several days elapsed from the time of harvesting to the start of the dryer operation. Since they were exposed to air, the flowers dried out somewhat. After harvesting, the flowers were separated from the stems and leaves and then chopped into equal parts to ensure uniform drying. The samples were then prepared for the drying process in a condensation dryer with a heat pump.

The condensation dryer was set to appropriate air temperature and humidity, and the parameters were adjusted according to regime 2, developed by the company Nigos Electronics, which manufactured the dryer at our request. This regime enabled effective drying of the flowers with a gradual increase in temperature, ensuring uniform reduction of moisture in the material. The maximum air temperature was set to 45°C, while the equilibrium moisture content (EMC) in the dryer was set to the final value in the product of 10.5%, according to literature recommendations. The hemp flowers were then placed on shelves inside the condensation dryer, ensuring they were evenly distributed to facilitate uniform drying. The shelves were spaced adequately, with every other shelf filled, to allow free airflow.

The total amount of hemp flowers was 5.3 kg, and this quantity was arranged on 10 shelves. Photographs below show the arrangement of flowers on the shelves within the dryer and the shelf layout, aimed at ensuring uniform drying. (Figure 1, Figure 2.). After that, the drying process commenced, and the drying parameters were continuously monitored throughout the entire process.

The drying of the hemp flowers lasted for 6 hours and 30 minutes, and the temperature and relative humidity of the air were measured and recorded every half hour.



Figure 1. Condensation dryer shelves



Figure 2. The method of placing hemp flower on the shelf

4. Results

The drying parameters were continuously monitored throughout the drying process, with measurements taken every half hour. The recorded parameters included air temperature and humidity, which are critical factors influencing the drying efficiency and quality of the final product.

The drying of the hemp flowers in this experiment lasted for a total of 7 hours. The results of the drying process, including the variations in air temperature and humidity over time, are summarized in the following table.

The data presented in the table provide a comprehensive overview of the environmental conditions maintained within the condensation dryer during the drying process. Monitoring these parameters is essential for ensuring that the drying occurs uniformly, preserving the quality of the hemp flowers and optimizing the efficiency of moisture removal.

The following figures show moisture content curves in relation to drying time and changes in moisture under the influence of different air temperatures (Figure 3., Figure 4.). Samples with an initial moisture content of about 28% were dried to a final moisture content of 10.5%. It is clearly visible from these curves that the moisture content continuously decreases with drying time.

Table 1. Drying Parameters

Time	Temperature (°C)	Air humidity (%)
8:30	21.5	22.8
9:00	26.5	20.7
9:30	27.9	21.2
10:00	28.9	19.4
10:30	29.8	18.2
11:00	30.8	16.7
11:30	31.5	15.2
12:00	32	14.4
12:30	32.4	13.3
13:00	32.8	12.4
13:30	33.3	11.5
14:00	33.3	9.8
14:30	33.3	8.8
15:00	33.8	8.1

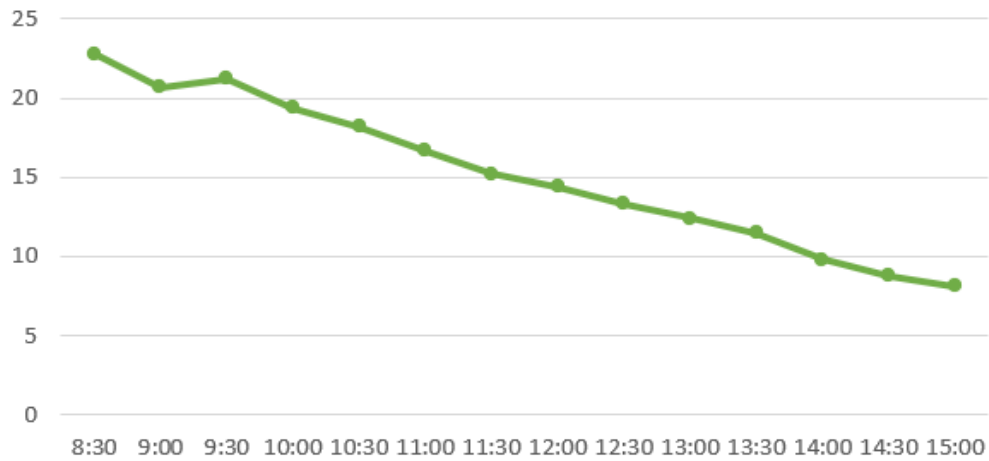


Figure 3. Moisture content curves in relation to drying time

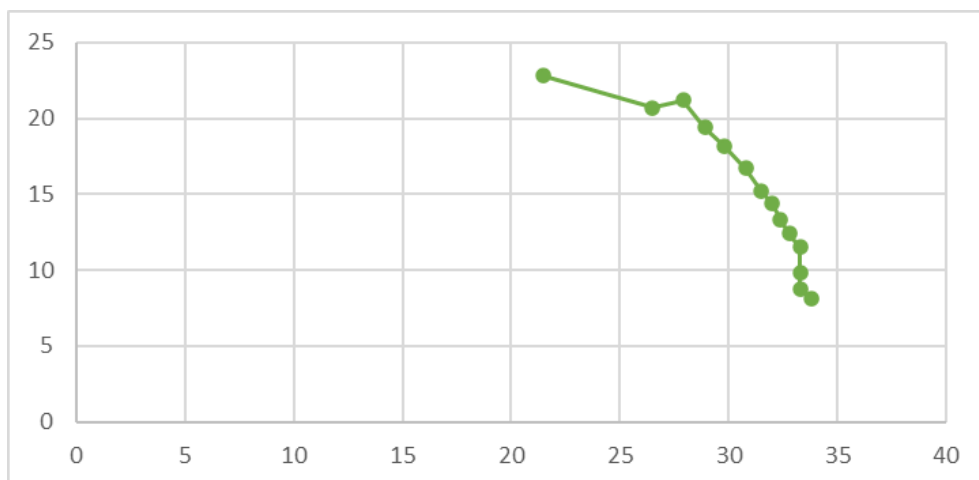


Figure 4. Changes in moisture under the influence of different air temperatures

5. Conclusion

This research focused on the drying process of industrial hemp flowers (*Cannabis sativa* L.) using a condensation dryer equipped with a heat pump. The study aimed to optimize the drying conditions to ensure the preservation of the flowers' quality while efficiently removing moisture. The parameters set for this experiment, including a maximum air temperature of 45°C and a target product moisture content of 10.5%, were crucial in achieving effective drying without compromising the integrity of the flowers.

Throughout the 6-hour and 30 minutes drying period, air temperature and humidity were monitored continuously, demonstrating the importance of precise control in the drying environment. The results indicated that maintaining optimal drying conditions contributes to uniform moisture removal, which is essential for producing high-quality dried hemp.

Moreover, the findings underline the advantages of using condensation dryers over traditional drying methods, particularly in terms of energy efficiency and the preservation of essential compounds. As the demand for hemp-based products continues to grow, refining the drying process becomes increasingly significant for both producers and consumers.

This work not only contributes to the understanding of hemp flower drying but also lays the groundwork for future research into optimizing drying techniques for various applications within the food and herbal industries.

Further studies could explore different drying regimes and their impact on the chemical composition and overall quality of the dried product, paving the way for innovative practices in hemp processing.

References

- [1] Chen C., Wongso I., Putnam D., Khir R., Pan Z., Effect of hot air and infrared drying on the retention of cannabidiol and terpenes in industrial hemp (*Cannabis sativa* L.), *Industrial Crops and Products*, 172 (2021), 114051
- [2] Kwasnica, A., Pachura, N., Masztalerz, K., Figiel, A., Zimmer, A., Kupeczynski, R., Wujcikowska, K., Carbonell-Barrachina, A. A., Szumny, A., & Rozanski, H., Volatile Composition and Sensory Properties as Quality Attributes of Fresh and Dried Hemp Flowers (*Cannabis sativa* L.), *Foods*, 9(8) (2020), 1118

Acknowledgements

This research was financially supported by the Ministry of Science, Technological Development and Innovation of the Republic of Serbia (Contract No. 451-03-65/2024-03; 451-03-66/2024-03/200095).



III. Renewable energy sources

Assessment of Floating Solar Panels Potential for Electricity Generation in the Adriatic Sea

Danka Kostadinović^a, Milić Erić^a, Zoran Marković^a

*^aUniversity of Belgrade, Vinča Institute of Nuclear Sciences-National Institute of the Republic of Serbia,
Department of Thermal Engineering and Energy, Belgrade, RS, dankak@vin.bg.ac.rs*

Abstract: Solar energy helps achieve several Sustainable Development Goals that have been proposed by the United Nations. Offshore solar energy deployment has not gained satisfactory attention when it comes to the Adriatic Sea. In this paper, the energy production, reduction of carbon dioxide emissions, and carbon credit of offshore solar power plant are estimated. The best location for a solar power plant in the Croatian part of the Adriatic Sea was selected considering solar potential, distance from shipping routes, proximity of existing onshore power grid, and visibility impact. The conceptual design of an offshore solar power plant was proposed. The obtained theoretical results show that offshore solar plant could annually produce 785 kWh of energy while avoiding 162 tons of carbon dioxide emissions. The floating solar panels could annually earn a carbon credit of 10,342 €. The findings of this research could serve policymakers for the creation of a future solar power generation policy and future pilot experimental investigations in Croatia.

Keywords: CO₂ emissions, Floating PV, Solar power plant, SDG, Solar energy.

1. Introduction

Solar energy helps achieve SDG 7 (Affordable and Clean Energy), SDG 13 (Climate Action), and SDG 9 (Industry, Innovation and Infrastructure). Solar energy is forecasted to be the leading renewable due to its potential to fulfill the global energy demand and the recent decline in the associated technology costs [1]. Offshore solar energy is an important element in reaching Europe's decarbonization objective. The energy produced from floating solar panels is one of the most promising and fastest-growing renewable energy. The growth trend of the cumulative global installed capacity of floating solar panels in MW is shown in Figure 1. Global floating solar panels deployment reached a cumulative global capacity of 3.8 GW in 2021. The solar panels market will continue to grow to help meet ambitious climate goals. The world's largest offshore solar plants are located in China, Japan, and the Republic of Korea [2]. In 2022, the largest floating solar plant with a capacity of 320 MW was installed in China. The floating solar panels can be installed in lakes, dams, ponds, rivers, seas and oceans. The components of a floating solar system are solar panels to harvest the solar energy, a floating buoyant structure to support, an anchoring and mooring system to position and help avoid excessive movement of the system, and electrical components for energy transformation and transportation. The floating solar systems help preserve land areas.

Compared to land-based solar panels, floating solar panels have higher efficiency due to the water-cooling effect, light reflection from the water, and less dust deposition [4], [5]. Furthermore, shading losses are minimized due to the open nature of sea surfaces. Floating solar panels reduce water evaporation and excessive algae growth [5], [6]. Problems with installing floating solar panels in offshore locations are saltwater corrosion and harsh wave and wind loads [7]. The studies showed that numerous benefits can be provided by the integration of floating solar plants with other RES technologies [8]. A combination of offshore wind and solar energy has proven to be an effective approach to mitigating the intermittency in energy supply.

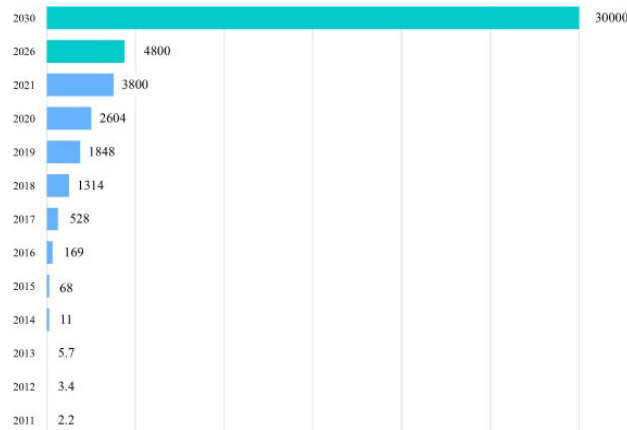


Figure 1. Growth trend of cumulative global installed capacity (MW) of floating solar systems [3]

In the Croatian part of the Adriatic Sea, there is not a single offshore renewable energy power plant. The Republic of Croatia is dependent on energy imports, while a large share of the primary energy consumption mix has oil (20.4%) and natural gas (9.6%). Hydropower plants with the largest share (47.5%) are the prevailing renewable sources of electricity [9]. Although the country has significant solar energy potential, only 1% of electricity comes from onsite solar power plants. In 2023, with 238.7 MW of added installed solar Croatia’s total installed solar capacity now stands at 462.5 MW. In 2024, solar power capacity reached 463 GW or 9%. Hydropower generation depends on the availability of water and is therefore highly affected by the impacts of climate change. Therefore, it is necessary to increase the deployment of other renewable sources in Croatia. The study [10] identified more than 290,00 km² of offshore area available for offshore wind and solar power plants. Although Croatia has significant offshore solar and wind energy potential, it needs a specific regulatory framework for these technologies and national strategic policies. The use of renewable energy in Croatia become an important issue as the country becomes increasingly dependent on fossil fuel imports. Previous studies investigated offshore wind energy exploitation in Croatia, while the exploitation of offshore solar energy isn’t explored. This paper aims to analyze potential energy production from solar power plant in the Croatian part of the Adriatic Sea. Furthermore, the contribution to a reduction of carbon dioxide emission and potential carbon credit were estimated.

2. Methodology

The methodology used to estimate the energy potential, reduced carbon dioxide emissions, and carbon credit of the solar power plant is presented in Figure 2. The best location of the solar power plant was selected considering solar resource potential and exclusion criteria. Moreover, the conceptual design of solar power is also presented along with the selection of commercial solar panels to be installed.

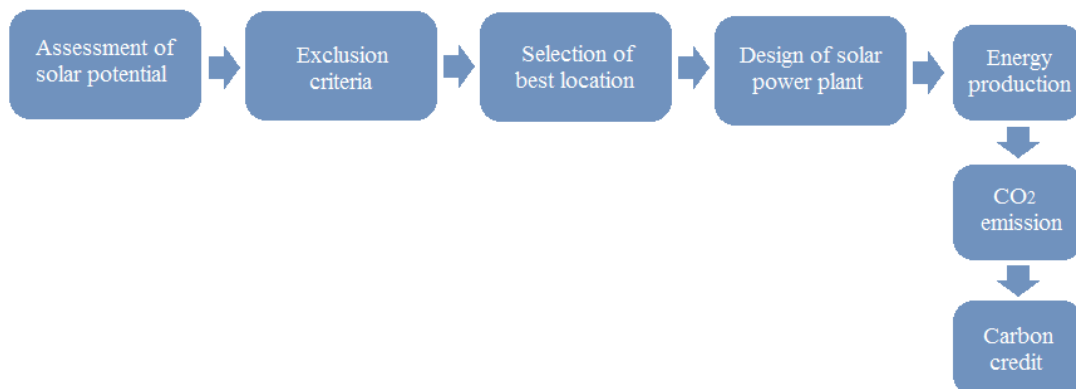


Figure 2. The workflow of this reserach

2.1. Solar Potential

The Republic of Croatia has a warm temperate Mediterranean climate (Csa), according to the Köppen-Geiger climate classification. Climate of northern and northeastern areas have a warm temperate humid climate (Cfa). The Adriatic coast enjoys a Mediterranean climate of hot, dry summers and cool, rainy winters. The Adriatic

Sea is a semi-enclosed sea bordered by the Republic of Croatia on the east. The area under investigation is the Exclusive Economic Zone (EEZ) of Croatia. The Croatian part of the sea occupies an area of 31,479 km², with the coastline 6,278 km long [11]. To identify the region with the highest solar resource potential i.e. global horizontal irradiation the Global Solar Atlas [12] was used. Croatia is a good candidate for the exploitation of solar energy due to its Mediterranean, continental, moderately warm climate. The intensity of solar radiation in Croatia is among the most important ones in Europe. The sunniest parts of Croatia, receive about 40% more solar energy than Central Europe and 60% more than Northern Europe [11]. Croatia is aiming for a solar power capacity of 0.77 GW by 2030 [13]. A map of global horizontal irradiation for Croatia is shown in Figure 3. Croatia has between 2000 and 2,700 hours of sunshine a year and it is characterized by high irradiation from 1,300 kWh/m² in northern Croatia to 1,850 kWh/m² in southern Croatia. Solar irradiation is highest in July with values ranging from 7.43 kWh/m² to 5.89 kWh/m², while December is the month with the lowest values for solar irradiation, ranging from 0.62 kWh/m² to 1.50 kWh/m² [14]. Possible annual electricity generation by 1 kW_p systems is from 975 kWh/kW in northern Croatia to 1,375 kWh/kW in southern Croatia [15]. Solar irradiation is the greatest on the open sea of the South Adriatic. An important aspect of using solar energy in Croatia is an increase in electricity consumption during summer months due to tourism. During the summer period, the global horizontal irradiation is up to five times higher compared to the winter months.

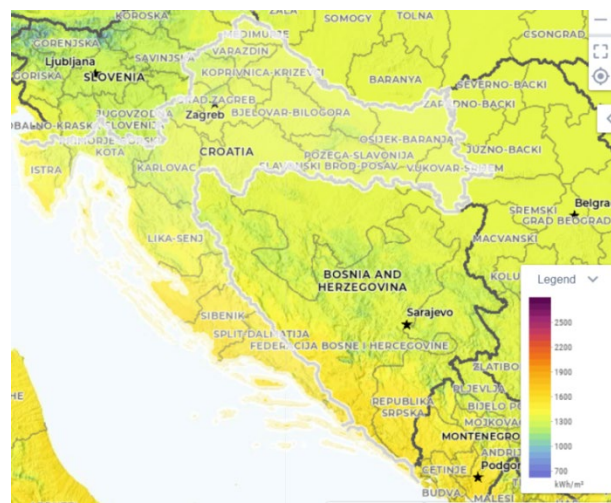


Figure 3. Global horizontal irradiation in Croatia [12]

2.2. Exclusion Criteria

Besides solar potential, the selection of an ideal location for a solar power plant should include several criteria such as shipping routes, environmental protected areas, military areas, distance from ports and airports, distance and capacity of existing electrical power grid, areas with high tectonic activity, etc. [16]. Two exclusion criteria were considered in this research:

- distance from shipping routes,
- proximity of onshore electrical power grid.

The offshore solar power plant should not be located near shipping routes. The buffer zone of 2 km from shipping routes was considered in this paper. The distance of offshore solar power plants to the onshore existing electrical grid determines the costs of cabling and other equipment. In the selection of an appropriate location for an offshore solar power plant, energy transmission needs to be considered. The distance from the electrical grid needs to be smallest to prevent high energy losses. Figure 4 shows a map of vessel density and electrical power grid in Croatia. The Adriatic Sea has high volumes of sea traffic. The currently available capacity can sustain small pilot projects. The onshore grid connection capacity needs to be significantly increased to support large-scale offshore projects. In the coastal part of Croatia, only the north-western region has additional grid connection capacity. There are three main lines of 110 kV cables on the coast: the first is laid along the main towns on the coast, the second one set down connecting islands of Krk, Cres, Mali Lošinj, and also Krk with Rab and Pag, and the third one laid along the islands of Brač, Hvar, Korčula, and Pelješac and further towards Dubrovnik [11].

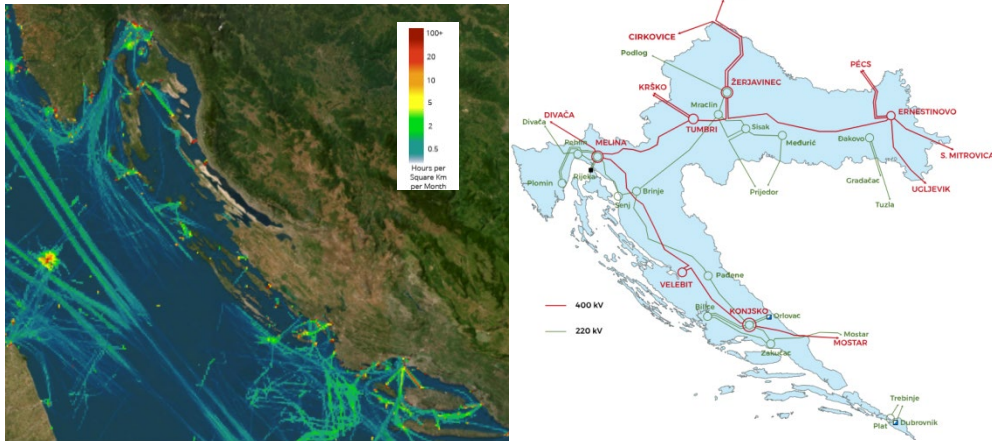


Figure 4. Ports and vessel density (left) [17], Croatian electrical power grid (right) [18]

2.3. Calculation of Energy Production and CO₂ Reduction

Croatia wants to cut its carbon dioxide emissions by 45% by 2030 and to abandon coal by 2033 [19]. Fossil carbon dioxide emissions in Croatia were above 17 million tons in 2022 [20]. To calculate the potential energy production of a solar power plant located in the selected location the following equation was used:

$$E = H \cdot A \cdot r \cdot PR \quad (1)$$

The data for monthly mean solar irradiation (H) were obtained from the PVGIS tool [21]. The open-source offshore solar data are not available, thus solar data for the onshore site closest to the selected location were used. The total solar panel area is $A=3689 \text{ m}^2$ and the solar panel yield is $r=0.18$ while performance ratio is $PR=0.75$. Besides producing energy from renewable source, one of the benefits of offshore solar power plant is the contribution to the reduction of carbon dioxide emissions. The annual carbon dioxide emission that could be reduced was calculated using the following equation:

$$CO_2 \text{ emissions} = E \cdot EF \quad (2)$$

The emission factor of $0.206 \text{ tCO}_2/\text{MWh}$ for the year 2023 was used according to [22]. Carbon credit that could be earned by the installation of solar power plant is calculated based on considering the carbon credit price of 63.96 €/t in the European market [23].

$$\text{Carbon credit} = CO_2 \text{ emissions} \cdot 63.96 \text{ €/t} \quad (3)$$

3. Results

3.1. Site Selection

Areas with high solar potential significantly influence the solar power plant efficiency and economic viability. Considering the solar potential, shipping routes, and the existing electrical grid, a location (43.60 lat., 15.88 long.) close to the towns of Šibenik and Primošten was selected for an offshore solar power plant as can be seen in Figure 5. The coast of Croatia has a large number of islands and high tourist activity during the summer period. Therefore, the visibility impact of solar power plant should be considered due to social acceptance. To avoid visual impact and ensure social acceptance the floating solar power plant is located 2 km from shore. The conceptual design of a solar power plant was proposed to calculate the occupied sea area.



Figure 5. Location for offshore solar power plant

3.2. Floater and Plant Design

The design of a floating platform for solar panels needs to minimize its footprint, influence the environment, and lower wave forces. For a conceptual design of solar power plants the patented flexible floating platform from the Norwegian company OceanSun [24] shown in Figure 6a) was selected. The composition of the OceanSun floating system is shown in Figure 6b). OceanSun's circular membrane uses buoyancy rings as floaters. The buoyancy rings are two airtight rings placed next to each other. This floating technology originated from the aquaculture industry. Membranes and mats are a type of floating technology that is generally made from rubber mats that act as a base for solar panel installation. The OceanSun platform can be used in rivers, lakes, and reservoirs, but also nearshore and offshore deployment. Logistics are significantly reduced compared to other floating solar systems. This type of platform was selected due to its ability to accommodate changes in the water level, and easy installation, and maintenance. This is a 1 mm thin flexible circular membrane with buoyancy rings made from HDPE with a 20-year lifetime in saltwater. The platform enables direct cooling of the solar panels (Figure 6c) increasing the power output by 10%, while CO₂ is reduced by 10% compared to other floating solutions [24].

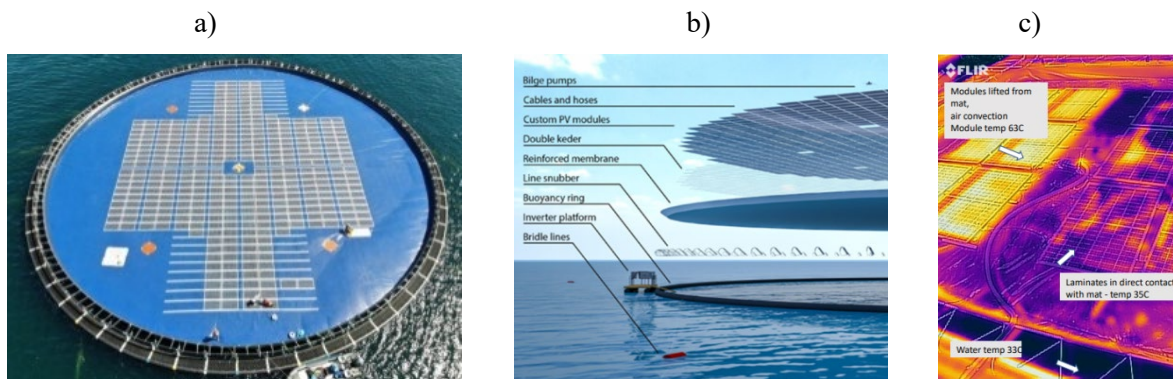


Figure 6. a) OceanSun platform, b) Elements of platform, c) Thermal image of platform [17]

The total weight of the platform is 55 tons including all panels, pumps, rings, and the membrane [24]. Several floating platforms could be placed in selected location with shared anchors and mooring system for larger power generation. This solution uses a minimum of materials to achieve the required buoyancy i.e. has a low Levelized Cost of Energy. Ocean Sun uses up to 65% less plastic, 90% less aluminum, and 50% less copper compared to other floating PV solutions [24]. The membrane allows the floating platform to move along with the waves, resulting in lower wave forces [25]. The hydro-elastic recyclable polymer floating membrane placed on a circular floater prevents waves from breaking and saltwater intrusion. Inverter stations could be placed on land or on barges next to the platform. The platform reduces water loss due to evaporation and mitigates underwater algae growth. OceanSun has operated several pilot and demonstration facilities in Europe and Asia. OceanAs Energy installed an innovative floating solar technology on the water reservoir of the Banja hydropower plants in Albania. This is the first floating PV project in Albania and the Western Balkan region. The plant with a total installed capacity of 500 kWp consists of four individual floating units, each unit has a

surface area of approximately 4,000 m² and is equipped with 1,536 solar panels [26]. During sunny days, this floating solar power plant generated 3,644 kWh/day [27].

To determine the energy production of the solar power plant, solar panels Sunmodule Plus SW 300 [28] were selected. Figure 7 shows the dimensions of the solar panel. Table 1 shows the characteristics of the selected solar panel and their performance under standard test conditions. The platform used in this research has a diameter of 75 m, where 2,200 solar panels are placed in horizontal position. This arrangement allows the walkway between the rows of the solar panels to enable cleaning and maintenance of the modules. Solar panel occupies 1.68 m² of area and has a power generation of 300 watts at peak hours. The occupied sea area of a floating platform is 4,071 m², while the total area of solar panels is 3,696 m².

Table 1. Technical specification of the solar panel

Maximum power	300 Wp
Open circuit voltage	40.0 V
Maximum power point voltage	32.6 V
Short circuit current	9.83 A
Maximum power point current	9.31 A
Module efficiency	18%
PV technology	Monocrystalline PERC
Operating temperature	-40 to +85 °C
Cells per module	60
Dimension	1675x1001x33 mm
Weight	18 kg

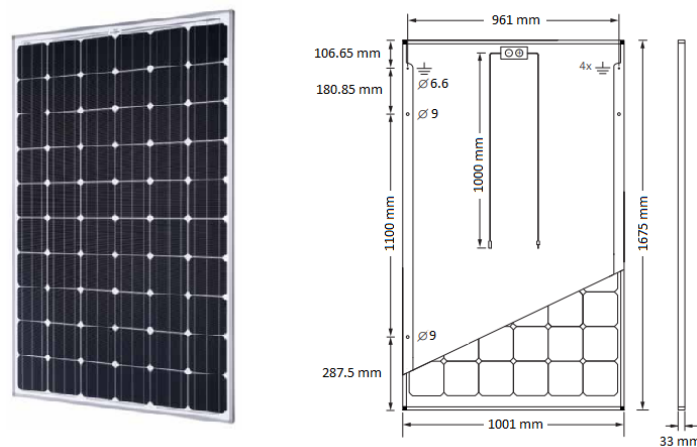


Figure 7. Solar panel Sunmodule Plus SW 300 [28]

3.3. Energy Production

The variation of monthly mean solar irradiation for selected location and estimated monthly energy production from offshore solar power plant are shown in Figure 8. The monthly mean solar irradiation is from 47 kWh/m² to 229 kWh/m². Solar radiation plays a key role in energy generation, which will be highest from May to August. The annual mean solar irradiation of the selected site is 132 kWh/m². The monthly mean energy production of solar power plant is from 31 kW to 152 kW. The annual mean energy production of solar power plant in selected location is 89 kW. The highest energy production could be obtained during the summer period (from June to August) while the lowest is during the winter period (from November to February). The high solar energy potential in the summer can help satisfy peak energy demand during the summer tourist season in Croatia. The obtained results show that offshore solar power plant could produce 785 MWh of energy

annually while 19,625 MWh of energy during the 25-years power plant lifetime. The construction of offshore solar power plants can reduce the need for electricity imports in Croatia.

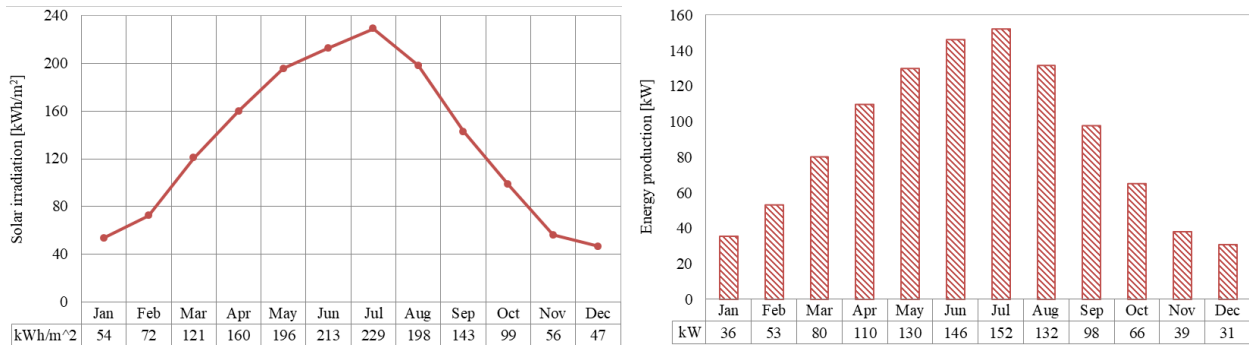


Figure 8. Mean solar irradiation (left), Mean energy production of offshore solar power plant (right)

3.4. CO₂ Reduction and Carbon Credit

Reduction of carbon dioxide emission and carbon credit for solar power plant is shown in Figure 9. Deployment of an offshore floating solar power plant in the selected location in the Adriatic Sea could annually reduce 162 tons of carbon dioxide emissions. The 10,342 € of carbon credit could be earned annually. Considering the 25-years lifetime of solar power plant, the total carbon dioxide emissions reduction is 4,050 tons and the potential carbon credit is 258,550 €. Croatia has not yet set a carbon dioxide removal (CDR) target. It should be emphasized that the price of carbon credit is expected to increase as well as carbon credit during the solar power plant lifetime.

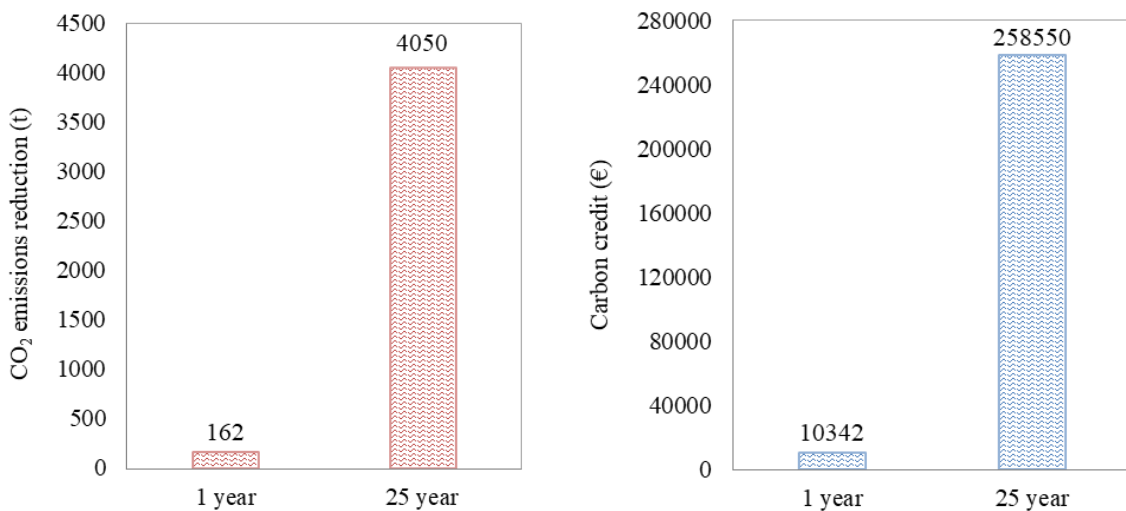


Figure 9. Reduction of carbon dioxide emissions (left), Carbon credit (right)

4. Conclusion

The land use limitation has raised interest in offshore solar energy worldwide. Croatia needs to decarbonize energy production and secure energy supply. Croatia has huge potential in using solar technology thanks to its geographical location and climate conditions. Therefore, this paper evaluates the energy production, reduction of carbon dioxide emissions, and carbon credit for an offshore solar power plant located in the Croatian part of the Adriatic Sea. The deployment of a solar power plant could annually produce 785 MWh of energy, avoid 162 tons of carbon dioxide emissions, and earn a carbon credit of 10,342 €. During the 25-years lifetime, solar power plant could produce 19,625 MWh of energy, reduce 4,050 tons of carbon dioxide emissions, and earn carbon credit of 258,550 €. Increasing offshore RES in Croatia can help the country achieve its decarbonization and climate goals as well as help the growth of the national economy. To harness this potential, Croatia will need to adopt various regulations in the field of offshore energy and increase the capacity of electricity grid. Future studies need to consider other exclusion criteria including environmental protected areas, water depth, fishing and military areas as well as the economic feasibility of offshore solar projects. Most studies from the

literature are based on analytical and simulation analysis. Experimental studies are needed to investigate the in-site efficiency of solar power plants in terms of energy generation and environmental impact.

Nomenclature

Latin symbols

- E – Energy production, in [MW].
 H – Solar radiation, in [kWh m⁻²].
 A – Total solar panel area, in [m²].
 r – Solar panel yield or efficiency, in [%].
 PR – Performance ratio.
 CO_2 – Carbon dioxide emissions, in [t].
 EF – Emission factor, in [kgCO₂ kWh⁻¹].

Acknowledgments

The research was funded by the Ministry of Education, Science and Technological Development of the Republic of Serbia (Contract No. 451-03-47/2023-01/ 200017). This article is based upon work from COST Action CA20109-Modular Energy Islands for Sustainability and Resilience (MODENERLANDS), supported by European Cooperation in Science and Technology.

References

- [1] Kabir, E., Kumar, P., Kumar, S., Adelodun, A.A., Kim K.H., Solar energy: potential and future prospects, *Renew Sustain Energy Rev*, 82(2018) pp. 894-900
- [2] IRENA (2020). *Fostering a blue economy: Offshore renewable energy*, International Renewable Energy Agency, Abu Dhabi, ISBN 978-92-9260-288-8
- [3] Silalahi, D.F., Blakers, A., *Global Atlas of Marine Floating Solar PV Potential*, *Solar*, 3(2020), 3, pp. 416-433
- [4] Amer, A. et al., *Floating Photovoltaics: Assessing the Potential, Advantages, and Challenges of Harnessing Solar Energy on Water Bodies*, *J. Ecol. Eng.*, 24(2023), 10, pp. 324-339
- [5] Ghosh, A., *A comprehensive review of water based PV: Flotovoltaics, under water, offshore & canal top*, *Ocean Eng.*, 281(2023), 115044
- [6] Wu, S., *Discussion on the development of offshore floating photovoltaic plants, emphasizing marine environmental protection*, *Front. Mar. Sci.*, 11(2024)
- [7] Al-Widyan, M., Khasawneh, M., Abu-Dalo, M., *Potential of Floating Photovoltaic Technology and Their Effects on Energy Output, Water Quality and Supply in Jordan*, *Energies*, 14(2021), 24, 8417
- [8] Claus, R., López, M., *Key issues in the design of floating photovoltaic structures for the marine environment*, *Renew. Sustain. Energy Rev.*, 164(2022), 112502
- [9] Eurostat-European statistics, <https://ec.europa.eu/eurostat>
- [10] Action plan for the uptake of offshore renewable energy sources in Croatia, 2023, <https://oie.hr/wp-content/uploads/2023/05/Action-Plan-for-the-uptake-of-Offshore-Renewable-5.pdf>
- [11] Racetin, I., Ostojić Škomrlj, N., Peko, M., Zrinjski, M., *Fuzzy Multi-Criteria Decision for Geoinformation System-Based Offshore Wind Farm Positioning in Croatia*, *Energies*, 16(2023), 13, 4886
- [12] *Global Solar Atlas*, <https://globalsolaratlas.info/map>
- [13] <https://www.statkraft.com/newsroom/news-and-stories/2023/country-series-sun-rising-for-croatia>
- [14] <https://renewablemarketwatch.com/news-analysis/388-croatia-solar-photovoltaic-pv-power-market-development-in-the-clean-energy-transformation-context-insights-political-climate-energy-strategy-forecast-renewable-market-watch>
- [15] Šljivac, D., Nakomec-Smaragdakis, B., Vukobratović, M., Topić, D., Cepić, Z., *Cost-benefit Comparison of On-grid Photovoltaic Systems In Pannonian Parts of Croatia and Serbia*, *Tehnicki vjesnik - Technical Gazette*, 21(2014), 5, pp. 1149-1157
- [16] Kurniawati, I., Beaumont, B., Varghese, R., Kostadinović, D., Sokol, I., Hemida, H., Alevras, P., Baniotopoulos, C., *Conceptual Design of a Floating Modular Energy Island for Energy Independency: A Case Study in Crete*, *Energies*, 16(2023), 16, 5921, <https://doi.org/10.3390/en16165921>
- [17] European Marine Observation and Data Network, <https://emodnet.ec.europa.eu/en>
- [18] <https://www.hops.hr/en/Home/Index>
- [19] <https://oie.hr/en/croatia-will-cut-co2-emissions-by-45-to-2030-and-abandon-coal-by-2033/>
- [20] <https://www.worldometers.info/co2-emissions/croatia-co2-emissions/>

- [21] PVGIS, European Communities, 2001-2021, https://re.jrc.ec.europa.eu/pvg_tools/en
- [22] <https://www.nowtricity.com/country/croatia>
- [23] <https://carboncredits.com/carbon-prices-today>
- [24] Ocean Sun, ESG Review, <https://oceansun.no/wp-content/uploads/2023/09/OS-ESG-Review.pdf>
- [25] Zhang, Y., Zhang, X., Chen, Y., Tian, X., Li, X., A frequency-domain hydroelastic analysis of a membrane-based offshore floating photovoltaic platform in regular waves, *Journal of Fluids and Structures*, 127 (2024), 5, 104125
- [26] <https://www.statkraft.com/newsroom/news-and-stories/2023/statkraft-completes-construction-of-first-rd-floating-solar-plant-in-albania>
- [27] Maraj, A., Kërtusha, X., Lushnjari, A., Energy performance evaluation for a floating photovoltaic system located on the reservoir of a hydro power plant under the mediterranean climate conditions during a sunny day and a cloudy-one, *Energy Conversion and Management: X*, 16 (2022), 100275
- [28] Sunmodule Plus SW 290-300, <https://www.altestore.com/static/datafiles/Others/sw-290-300-mono-solar-datasheet.pdf>

Applications and Challenges of Digital Twins of Floating Wind Turbines

**Maria-Styliani Daraki^a, Beatrice Mina^b, Muhnad Almasoudi^c, Barbara Charalambidi^a,
Marko Mančić^d, Junlin Heng^e, Charalampos Baniotopoulos^e**

^a School of Production Engineering and Management, Technical University of Crete, Chania, Greece, ISO 3166-2:GR, mdaraki1@tuc.gr, bcharalambidi@gmail.com

^b University School for Advanced Studies IUSS Pavia, Pavia, Italy, IT, beatrice.mina@iusspavia.it

^c School of Engineering, University of Birmingham, Birmingham, United Kingdom, GB, mx1538@student.bham.ac.uk

^d University of Nis, Faculty of Mechanical Engineering, Nis, Serbia, RS, marko.mancic@masfak.ni.ac.rs

^e Department of Civil Engineering, University of Birmingham, Birmingham B15 2TT, United Kingdom, GB, ccbano@gmail.com, h.junlin@bham.ac.uk

Abstract: A digital twin is a virtual model of a physical asset, like a wind turbine, synchronized with real-time data to provide insights into its performance, condition, and behavior. This technology has applications in environmental perception, condition assessment, predictive maintenance, anomaly detection, and optimizing the operational parameters of floating offshore wind turbines. This paper reviews the current state of research and practical applications of digital twins in this field. It explores the concept, focusing on the challenges posed by climate, system dynamics, and structural issues in wind turbines. Case studies include topics such as Fatigue Limit State, pitch blade control, drivetrain performance, power output, and structural strain. Technical challenges in implementing digital twins include issues related to data collection, transfer, communication, and standardization, as well as the robustness of models in accurately simulating physical behaviors. Solutions can be found through AI, IoT, advanced simulation tools, and improved monitoring techniques. Non-technical challenges, typical for emerging technologies, are mainly tied to human factors. However, the benefits and financial advantages of digital twin technology are expected to promote its widespread adoption in industrial applications.

Keywords: Digital twins, Fatigue, Floating offshore wind turbine, Wind energy.

1. Introduction

The development of digital twins technology provides an innovative approach to the monitoring and maintenance of offshore wind turbines, offering a flexible universal solution for performance prediction and improvement, design, monitoring, maintenance, life time predictions, stain and fatigue predictions etc. A digital twin is a virtual representation of a physical asset, such as a wind turbine, that is synchronised with real-time data, enabling a comprehensive understanding of its performance, condition, and behaviour [1], [2]. The offshore wind power has emerged as a critical component of the global transition to renewable energy, with ambitious targets for capacity expansion planned to be met by offshore wind in 2050 [3]. This is estimated to equal 450 GW worldwide [1]. While fixed-bottom offshore wind turbines have seen significant advancements in recent years, the deployment of floating offshore wind turbines (FOWTs) is poised to be a game-changer, unlocking previously in a deep-water wind resources [4]. The development of digital twins for floating offshore wind turbines is a relatively new and rapidly evolving field, with a growing body of research and industry applications emerging. One of the key challenges in creating digital twins for floating offshore wind turbines is the complex, dynamic nature of the offshore environment, which includes factors such as wind, waves, currents, and seabed conditions [5]. To address these challenges, researchers and industry players have developed advanced modelling techniques that combine computational fluid dynamics, structural dynamics, and other physics-based models to accurately represent the behaviour of the floating turbine system [6].

These digital representations can be leveraged for a variety of purposes, including environmental perception, response measurement, condition assessment, predictive maintenance, anomaly detection, and optimization of operational parameters [1]. By combining real-time data with physics-based models, digital twins can provide a more complete picture of the turbine's performance, allowing for proactive intervention and informed

decision-making [7]. Application of digital twins in offshore wind is the ability to create standalone, descriptive, and predictive models of the turbine and its operating environment [7]. Digital twins in the offshore wind industry offer the ability to simulate and test various scenarios before implementing them in the physical world [8]. This capability is particularly valuable in the context of reconfigurable manufacturing systems, where digital twins can be used to model and optimise the manufacturing process, ensuring that changes are thoroughly evaluated before implementation [8]. This allows for the modelling and optimization of the manufacturing process, ensuring that changes are thoroughly evaluated before implementation [9].

The goal of this work is to identify the challenges and opportunities associated with the development and application of digital twins for floating offshore wind turbines. The analysis and conclusions presented in the paper are based on the literature review. According to the literature review, digital twins provide many possibilities for academics, researchers and engineers, namely the estimation of aerodynamic loads [10], vibration analysis, anomaly detection and predictive maintenance [11] and prediction of power production [5].

2. The state of art of Digital Twins for floating wind turbines

Emerging technologies and challenges of Digital Twins in Wind Turbines are described in [1], where digital twins capabilities are ranked into categories from standalone to autonomous in five categories. In this review, the authors have identified the growing interest and need for digital twins, however in wind energy, digital twins are still in the early stage of implementation, with most of the applications focused on monitoring and diagnostics [1].

A digital twin typically consists of the following [12]:

- Physical System: This encompasses the actual wind turbine and its critical components, including the rotor, blades, shaft, generator, tower, and nacelle.
- Digital System: This system mirrors the physical system in a virtual environment, incorporating data storage, digital models, and mathematical modeling to simulate real-world behavior.
- Connection System: This system facilitates communication between the physical and digital twins, enabling data exchange through protocols like Modbus, OPC UA, MQTT, Ethernet/IP, and CANopen.
- Service System: This system leverages data from the DT to provide services like predictive maintenance, performance optimization, and fault diagnosis.

One more definition for the process of twinning in the Digital Twin (DT) approach is shown in Fig. 1, based on [13]. Essentially, data is collected from a specific physical asset (shown in orange) and used to update a related simulation model (or a simplified version of it, represented in green). The updated model is used to predict what might happen next, and those predictions help guide decisions to control the physical asset. The control system takes care of these actions automatically. This process of observing, updating, predicting, and acting keeps happening in real-time to adjust for any changes in the asset's behavior as time goes on.

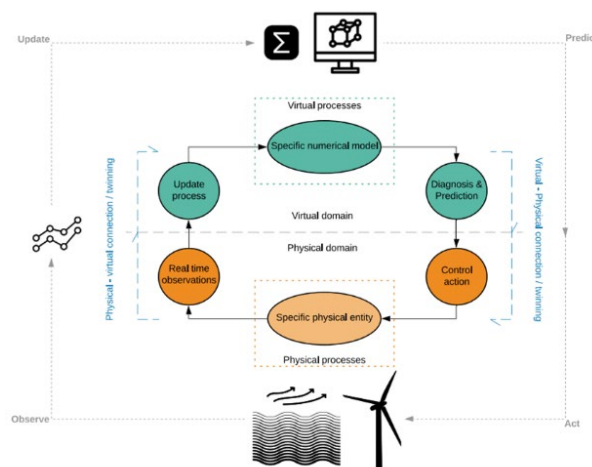


Figure 5. The process of twinning in the Digital Twin (DT) approach [13] (under CC BY 4.0).

Digital twin modelling was applied to predictive maintenance of gearboxes of offshore wind turbine drivetrains in [14], where complex dynamic behaviour of the drivetrain was analysed using multi degree of freedom

torsional model, an algorithm was proposed to estimate rotor-generator torque and its dynamics, and the goal was predicting the estimated lifetime of the gearbox [14]. Digital twin modelling was analyzed in [12] for monitoring and fault diagnostics. Digital twin application for predictive maintenance of drivetrains was also applied in [15], where anomaly diagnostics were determined.

The key challenges of development of digital twins for wind turbines are [1]:

- Standard related – there is a lack of standardised data formats and communication protocols which present difficulties for exchange of information, applied models and systems between different users.
- Data related – there is a lack of high quality data from different sources during the wind turbine lifecycle, followed by challenges of managing, storing and processing of this data [1], [12].
- Model-related – there is a challenge to develop high quality accurate and reliable models that can faithfully represent the physical and dynamic behavior of wind turbines, and finally,
- Industrial acceptance – there is a challenge of adopting new technologies, where demonstrations of benefits and financial benefits may play a key role.

The application of Digital Twin technology to improve the fatigue analysis of offshore wind turbine structures is presented in [13], where real-time observation data is integrated with simulation models, a DT may provide a more accurate and reliable assessment of the structural integrity of these critical assets. Despite real time data, uncertainty in predicting the fatigue life of OWT structures is stated by the authors [13] and is presented in the Figure 2.

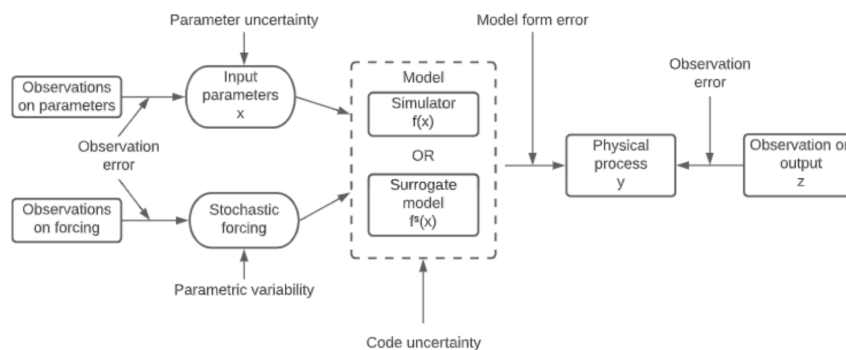


Figure 6. Sources of uncertainty relevant to the DT paradigm for some true physical process y , including those relevant to the observations z of the physical process, and those relevant to the model $f(x)$ (or it's surrogate $f^s(x)$) of the physical process [13] (under CC BY 4.0).

3. Digital twins of Floating Offshore Wind Turbines

The wind turbine operation and maintenance can be improved through developing a Digital Twin (DT). The most common abilities of a DT are to monitor, analyse, and forecast the performance of the wind turbines by giving a digital representation of the physical system. The DT supports preventive maintenance through early indications of probable problems. Consequently, this may lead to increased productivity, minimised downtime, and better security [16]. From their study, it was observed that the DTs of wind turbines can have different connectivity options, namely supervisory control and data acquisition (SCADA), wireless sensor networks (WSN), smart grids (SG), Internet of Things (IoT), and cloud-based systems. There are multiple purposes for these connecting protocols within the DT other than facilitating real-time monitoring and control over wind turbines. For instance, information collected via data acquisition or other sensors could be utilised to predict when maintenance should be done in a wind turbine in order to avoid serious breakdowns [17]. This combination makes DT more efficient when integrating such communication methods and can enhance performance, reduce maintenance costs, and increase reliability in terms of the turbine. In some cases, creating a Digital Twin (DT) system requires the integration of many different sensors, controls, and software parts that work together to emulate the behavior of the actual wind turbine.

Moreover, Moghadam and Nejad [15] have laid a foundation for establishing preventive maintenance in FWT drivetrain systems by monitoring component residual lifetime by using DT and employing a stochastic physics-based model to estimate the remaining useful life (RUL) of drivetrain components. The research from [1] suggests that wind farms' efficiency can be improved across their life cycle starting with design [18] and siting [19], through construction [20] and operations [21], finishing with maintenance [22] and decommissioning

[23], which are digitising. It is worth noting here that offshore wind farms are typically situated in remote hazardous environments where accessibility is challenging. Condition-based maintenance reduces the number of on-site maintenance tasks. Predictive maintenance helps prevent unscheduled equipment downtime as well as avoid catastrophic failures by reacting to small faults before they turn into big problems [22]. Therefore, the construction of a DT can provide an efficient solution. Regarding the infrastructures, the need for digital twins comes from the extreme loadings applied on energy-related infrastructure and the increased significance of fatigue effects. Digital twin technologies enable reliable models that could follow structures from their inception through their whole life cycles, making fatigue and degradation prediction more reliable and facilitating effective predictive maintenance schemes [24].

4. Identifying some problems related to weather, wind conditions on floating offshore wind turbines

According to [25] due to the harsh environment of the oceans, floating offshore wind turbines (FOWT) can be in danger especially if the wind speed increases more than the designed limit. As the authors mentioned, several issues can happen to the turbines such as mechanical temperature and physical temperature problems. In detail, mechanical problems can be described specifically in terms of potential high or low-temperature issues that result in failures in bearing. High temperature leads to a decrease in lubricant viscosity, fatigue, seals drying and cracking, and weakening retainer and cage. Low temperature causes raise the lubricant viscosity, skidding, and increasing torque. In addition, physical problems can be concluded in icing blades and moisture. Also, moisture can cause a reaction with metal parts that weaken and degrade mechanical elements. On the other hand, vibration is a critical issue that may stop or reduce the steady movement of the blades. The reasons behind this phenomenon are loading, flow of the sea water, wind speed, and rotation of the blades.

5. Potential digital twins' solutions for weather, wind conditions on floating offshore wind turbines

Digital twins can predict the issues before it happens and that can be through sensors and forecasting linked to the FOWT to insure the health and safety for this turbine [26]. In this work is detailed that the integration of the physical and digital engineering system is complicated, yet the applications of these combined technologies can prevent the failure of the turbine. According to [27], wind forecasting and wind data optimization can lead to prevent the collapse of offshore wind turbine (OWT) through Extreme Wind Period (EWP) that enable the turbines to shut down when the wind speed is more than 25 m/s and reoperate itself again when it becomes 20 m/s to achieve the best quality of the power optimization and to prevent any other issues.

Integrating more than one technology can lead to healthier wind turbines due to the multiple predictions of each possible problem. According to [28], three weather forecasting methods has been integrated; Markov Chains, gradient boosting, and hybrid progression/statistical method to use them as an input into the lifecycle of the wind turbine to enhance the performance of the energy production, availability, and revenue. In addition, it can predict the failure rate and the performance of the indicators. In [29] is investigated that Computational Fluid Dynamics (CFD) can be coupled with weather predictions, that can be based on Reynolds Averaged Navier Stokes (RANS) with mesoscale simulation to enhance the prediction of loads and energy output, the accuracy of the results of this coupled simulation compared with the open-source LiDAR that showed a relevant result. Many of the ideas can be applied in the floating offshore wind turbines, but the most important is the prediction of issue before it happens. That is what weather predictions and wind data optimization can do, preventing the mentioned problems above and many other problems that are not mentioned here, and that lead to extending the wind turbine health and safety.

6. Structural challenges of floating turbines and DT solutions

With respect to land-based wind turbines, floating offshore wind turbines (FOWT) undergo major loads and stability issues due to their interaction with the sea state. The aim, during the design stage, is to reduce platform motion in all the 6 degrees of freedom and in particular minimize pitch motion. Hence the natural frequencies of the platform oscillations need to be outside some critical regions corresponding to: the range of wave frequencies, the frequency at which the blade passes the tower and the third harmonic of such a frequency [25].

Another source of instability arises from the employment of the blade-pitch control techniques used for land-based turbines: when the wind speed is overrated, and thrust decreases, a negative damping develops, causing a large motion response [26], [27]. Hence control technique should be adapted to FOWT. Therefore, beyond the stability study in the designing phase, stability monitoring during the whole lifecycle of FOWTs has an important role in reducing and preventing failure risk.

Digital twin models come in handy for predicting the response of those structures, in terms of loads but also of power output, depending on the sea state. In [10] the implemented digital twin estimates the aerodynamic states and motions of the structure. It takes as input measured parameters like rotor speed, heave and pitch of the platform, and through a Kalman filter, which uses a linear wind turbine model (within WELIB toolkit), it predicts the desired states. Then those states are elaborated through a virtual sensing step to obtain the loads in the key points of the structure which give useful information to perform Operation and Maintenance (O&M) procedures.

Another implementation of digital twin technology is the prediction of the power output of wind turbines, this information indeed is crucial for the grid since the last one is susceptible to the variability and uncertainty of power supply. In [28] a physics-based output prediction model (P-bOPM) is developed for a 10 MW floating offshore wind turbine and is presented in the Figure 3. Within the physics-based model, instead of considering 6 degrees of freedom (dof) for the turbine motion, a reduced order model (ROM) that takes into account only 4 degrees of freedom (surge, heave, pitch, and yaw) is implemented. The ROM calculates in real time motion along the 4 dof of the floating body, receiving as input the marine environmental data and the blade pitch angle. Then the power output is calculated using the equation of the relative wind speed at the 4 dof and the real wind speed measured by an anemoscope. The ROM system is learned by Dynamic ROM Builder of ANSYS Twin Builder.

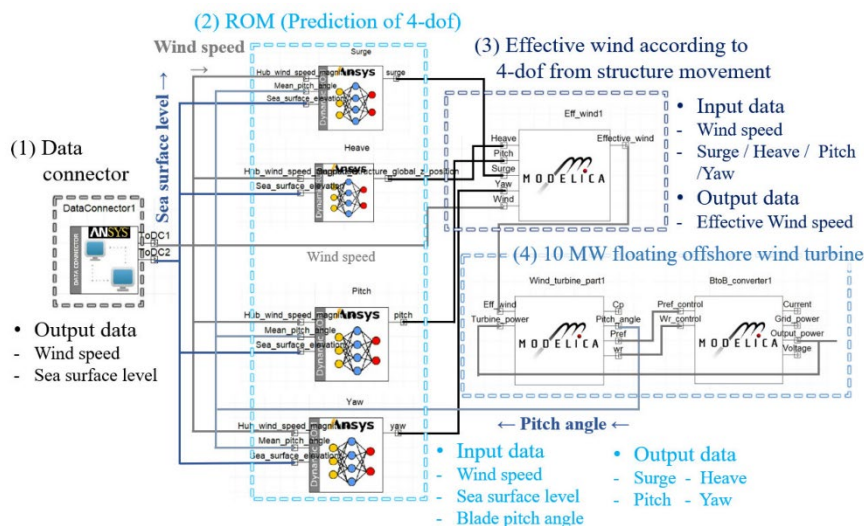


Figure 7. Configuration of the P-bOPM of a 10 MW FOWT model [28] (under open access Creative Common CC BY license).

Furthermore, essential components of FOWT are the mooring lines (MoLs); and their primary failure reasons are extreme loads and fatigue (both dependent on the axial tension). The usefulness of digital twins in this context can be two-fold [29]: on one hand they can predict the behaviour of a healthy mooring system and compare it with the actual one, and on the other they can forecast the real axial tension to enhance the MoLs' life span. The former kind of DT takes as inputs the instantaneous motion of the turbine and the sea state conditions, and outputs the healthy mooring lines axial tension, to be compared with the measured one. The latter instead, needs more input data: past and present motion, marine environment measurements and forecasted environmental conditions are required as well. To perform these analyses, Machine Learning algorithms are employed.

7. Real-scale applications and case study data review

Several sectors including manufacturing, healthcare, aviation, automotive transportation, infrastructure planning, and energy production have been using DTs in the recent past although they are not yet fully exploited and still face numerous challenges [30]. In particular, DTs are hardly used in wind power [31].

Among the others, there are findings in the literature that have implemented already real-scale applications and case studies. In the work of [13] is considered a further application of a DT paradigm to offshore wind turbine support structures for structural reliability under Fatigue Limit State (FLS) on bolted ring flange. In the research of [32], has been illustrated how a digital twin of the pitch angle controller was implemented on a TMS320F28379D Dual-Core Delfino™ Microcontroller device in Texas Instrument (TI). According to the hardware-in-loop (HIL) concept, a controller algorithm will be developed to diagnose the health condition of its behaviour on wind turbines. In the Figure 4, is described the design of the DT controller for the WT plant which has been done in two steps.

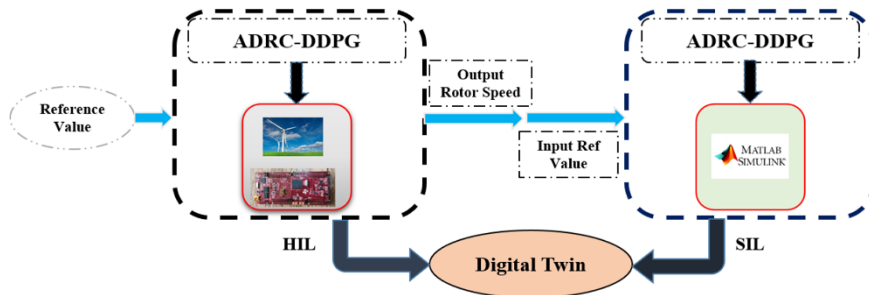


Figure 8. A proposed strategy for the combination of hardware-in-loop (HIL) and software-in-loop (SIL) testing [32] (under open access Creative Common CC BY license).

The paper of [15] uses a test case, which mainly proposes a residual life monitoring methodology for drivetrain components on floating offshore wind turbines. Specifically, in this work performance characteristics of the main shaft of the drivetrain system in DTU 10 MW wind turbine were simulated and tested for purposes of remaining useful life (RUL) estimation. Last but not least, in the terms of NorthWind industry project [1], two use cases are demonstrated of virtual reality. The first is referred to as onshore WT [5] and the second to offshore WT [7]. Based on [5] is visualized the DT of onshore WT and is detected in the Figure 5.



Figure 9. Descriptive digital twin with text and gauges showing active power of each turbine [5] (under CC BY 4.0).

Conclusions

The four main areas in which digital twins can be applied for the wind industry are condition monitoring, fault diagnosis, predictive maintenance, adaptive control and power output which can help it become an effective technology. Operators who are trying to monitor their wind turbine ID and other parts can create an accurate digital model of their systems and components, thus being able to carry out better asset management, detect problems, and diagnose the faults effectively and efficiently. The application of this technology is aimed at cutting down the cost of maintenance work, extending the life of wind turbines, and bringing up the efficiency level of wind turbines offshore through a monitoring system which provides real-time data and accurate information on the actual state of the system or subsystem. While there are still challenges for both

development and wider applications of digital twins, the research paper showed that progress is being made in this field and with it, the industry will gain tangible advantages.

A more rapid development of digital twins may be expected in the near future. Furthermore, with the development of data handling techniques and standardization progress, integration of data, simulation behavioural models to converge leading to a single digital twin system for floating wind turbines, which would represent almost a “turn key” solution for prediction of behaviour of wind turbines, helping decision makers and stakeholders strengthen the position of floating wind turbines to the market even further.

References

- [1] F. Stadtmann *et al.*, “Digital Twins in Wind Energy: Emerging Technologies and Industry-Informed Future Directions,” *IEEE Access*, vol. 11, pp. 110762–110795, 2023, doi: 10.1109/ACCESS.2023.3321320.
- [2] H. Van Der Valk, J. Hunker, M. Rabe, and B. Otto, “Digital Twins in Simulative Applications: A Taxonomy,” in *2020 Winter Simulation Conference (WSC)*, Orlando, FL, USA: IEEE, Dec. 2020, pp. 2695–2706. doi: 10.1109/WSC48552.2020.9384051.
- [3] G. Rinaldi, P. R. Thies, and L. Johannig, “Current Status and Future Trends in the Operation and Maintenance of Offshore Wind Turbines: A Review,” *Energies*, vol. 14, no. 9, p. 2484, Apr. 2021, doi: 10.3390/en14092484.
- [4] F. Li, L. Li, and Y. Peng, “Research on Digital Twin and Collaborative Cloud and Edge Computing Applied in Operations and Maintenance in Wind Turbines of Wind Power Farm,” in *Advances in Transdisciplinary Engineering*, D. Dobrotá and C. Cheng, Eds., IOS Press, 2021. doi: 10.3233/ATDE210263.
- [5] F. Stadtmann, A. Rasheed, and T. Rasmussen, “Standalone, Descriptive, and Predictive Digital Twin of an Onshore Wind Farm in Complex Terrain,” *J. Phys.: Conf. Ser.*, vol. 2626, no. 1, p. 012030, Oct. 2023, doi: 10.1088/1742-6596/2626/1/012030.
- [6] Jpt Staff, “Digital Twins Mature in the North Sea,” *Journal of Petroleum Technology*, vol. 71, no. 12, pp. 41–43, Dec. 2019, doi: 10.2118/1219-0041-JPT.
- [7] F. Stadtmann, H. A. G. Wassertheurer, and A. Rasheed, “Demonstration of a Standalone, Descriptive, and Predictive Digital Twin of a Floating Offshore Wind Turbine,” in *Volume 8: Ocean Renewable Energy*, Melbourne, Australia: American Society of Mechanical Engineers, Jun. 2023, p. V008T09A039. doi: 10.1115/OMAE2023-103112.
- [8] J. Kombaya Touckia, N. Hamani, and L. Kermad, “Digital twin framework for reconfigurable manufacturing systems (RMSs): design and simulation,” *Int J Adv Manuf Technol*, vol. 120, no. 7–8, pp. 5431–5450, Jun. 2022, doi: 10.1007/s00170-022-09118-y.
- [9] J. D. M. De Kooning, K. Stockman, J. De Maeyer, A. Jarquin-Laguna, and L. Vandevelde, “Digital Twins for Wind Energy Conversion Systems: A Literature Review of Potential Modelling Techniques Focused on Model Fidelity and Computational Load,” *Processes*, vol. 9, no. 12, p. 2224, Dec. 2021, doi: 10.3390/pr9122224.
- [10] E. Branlard, J. Jonkman, C. Brown, and J. Zhang, “A digital twin solution for floating offshore wind turbines validated using a full-scale prototype,” *Wind Energ. Sci.*, vol. 9, no. 1, pp. 1–24, Jan. 2024, doi: 10.5194/wes-9-1-2024.
- [11] O. O. Olatunji, P. A. Adedeji, N. Madushele, and T.-C. Jen, “Overview of Digital Twin Technology in Wind Turbine Fault Diagnosis and Condition Monitoring,” in *2021 IEEE 12th International Conference on Mechanical and Intelligent Manufacturing Technologies (ICMIMT)*, Cape Town, South Africa: IEEE, May 2021, pp. 201–207. doi: 10.1109/ICMIMT52186.2021.9476186.
- [12] M. Wadhvani, S. Deshmukh, and H. S. Dhiman, “Digital Twin Framework for Time to Failure Forecasting of Wind Turbine Gearbox: A Concept,” 2022, *arXiv*. doi: 10.48550/ARXIV.2205.03513.
- [13] F. K. Moghadam, G. F. D. S. Rebouças, and A. R. Nejad, “Digital twin modeling for predictive maintenance of gearboxes in floating offshore wind turbine drivetrains,” *Forsch Ingenieurwes*, vol. 85, no. 2, pp. 273–286, Jun. 2021, doi: 10.1007/s10010-021-00468-9.
- [14] F. K. Moghadam and A. R. Nejad, “Online condition monitoring of floating wind turbines drivetrain by means of digital twin,” *Mechanical Systems and Signal Processing*, vol. 162, p. 108087, Jan. 2022, doi: 10.1016/j.ymsp.2021.108087.
- [15] J. Jorgensen, M. Hodkiewicz, E. Cripps, and G. M. Hassan, “Requirements for the application of the Digital Twin Paradigm to offshore wind turbine structures for uncertain fatigue analysis,” *Computers in Industry*, vol. 145, p. 103806, Feb. 2023, doi: 10.1016/j.compind.2022.103806.
- [16] M. Mahmoud, C. Semeraro, M. A. Abdelkareem, and A. G. Olabi, “Designing and prototyping the architecture of a digital twin for wind turbine,” *International Journal of Thermofluids*, vol. 22, p. 100622, May 2024, doi: 10.1016/j.ijft.2024.100622.
- [17] U. Singh and M. Rizwan, “SCADA system dataset exploration and machine learning based forecast for wind turbines,” *Results in Engineering*, vol. 16, p. 100640, Dec. 2022, doi: 10.1016/j.rineng.2022.100640.
- [18] T. Ashuri, M. B. Zaaijer, J. R. R. A. Martins, and J. Zhang, “Multidisciplinary design optimization of large wind turbines—Technical, economic, and design challenges,” *Energy Conversion and Management*, vol. 123, pp. 56–70, Sep. 2016, doi: 10.1016/j.enconman.2016.06.004.

- [19] R. Velo, P. López, and F. Maseda, “Wind speed estimation using multilayer perceptron,” *Energy Conversion and Management*, vol. 81, pp. 1–9, May 2014, doi: 10.1016/j.enconman.2014.02.017.
- [20] M. Asgarpour, “Assembly, transportation, installation and commissioning of offshore wind farms,” in *Offshore Wind Farms*, Elsevier, 2016, pp. 527–541. doi: 10.1016/B978-0-08-100779-2.00017-9.
- [21] V. R. Padullaparthi, S. Nagarathinam, A. Vasam, V. Menon, and D. Sudarsanam, “FALCON- Farm Level CONTROL for wind turbines using multi-agent deep reinforcement learning,” *Renewable Energy*, vol. 181, pp. 445–456, Jan. 2022, doi: 10.1016/j.renene.2021.09.023.
- [22] A. N. Nichenametla, S. Nandipati, and A. L. Waghmare, “Optimizing life cycle cost of wind turbine blades using predictive analytics in effective maintenance planning,” in *2017 Annual Reliability and Maintainability Symposium (RAMS)*, Orlando, FL, USA: IEEE, 2017, pp. 1–6. doi: 10.1109/RAM.2017.7889682.
- [23] C. A. Irawan, G. Wall, and D. Jones, “An optimisation model for scheduling the decommissioning of an offshore wind farm,” *OR Spectrum*, vol. 41, no. 2, pp. 513–548, Jun. 2019, doi: 10.1007/s00291-019-00546-z.
- [24] G. E. Stavroulakis, B. G. Charalambidi, and P. Koutsianitis, “Review of Computational Mechanics, Optimization, and Machine Learning Tools for Digital Twins Applied to Infrastructures,” *Applied Sciences*, vol. 12, no. 23, p. 11997, Nov. 2022, doi: 10.3390/app122311997.
- [25] A. Haghshenas, A. Hasan, O. Osen, and E. T. Mikalsen, “Predictive digital twin for offshore wind farms,” *Energy Inform*, vol. 6, no. 1, p. 1, Jan. 2023, doi: 10.1186/s42162-023-00257-4.
- [26] B. Schleich, N. Anwer, L. Mathieu, and S. Wartzack, “Shaping the digital twin for design and production engineering,” *CIRP Annals*, vol. 66, no. 1, pp. 141–144, 2017, doi: 10.1016/j.cirp.2017.04.040.
- [27] N. A. Cutululis, N. K. Detlefsen, and P. E. Sørensen, “Offshore Wind Power Prediction in Critical Weather Conditions: 10th International Workshop on Large-Scale Integration of Wind Power into Power Systems as well as on Transmission Networks for Offshore Wind Farms,” *Proceedings*, 2011.
- [28] A. Kolios, M. Richmond, S. Koukoura, and B. Yeter, “Effect of weather forecast uncertainty on offshore wind farm availability assessment,” *Ocean Engineering*, vol. 285, p. 115265, Oct. 2023, doi: 10.1016/j.oceaneng.2023.115265.
- [29] A. Castorrini, S. Gentile, E. Geraldini, and A. Bonfiglioli, “Investigations on offshore wind turbine inflow modelling using numerical weather prediction coupled with local-scale computational fluid dynamics,” *Renewable and Sustainable Energy Reviews*, vol. 171, p. 113008, Jan. 2023, doi: 10.1016/j.rser.2022.113008.
- [30] E. C. Edwards, A. Holcombe, S. Brown, E. Ransley, M. Hann, and D. Greaves, “Evolution of floating offshore wind platforms: A review of at-sea devices,” *Renewable and Sustainable Energy Reviews*, vol. 183, p. 113416, Sep. 2023, doi: 10.1016/j.rser.2023.113416.
- [31] J. Jonkman, “Influence of Control on the Pitch Damping of a Floating Wind Turbine,” in *46th AIAA Aerospace Sciences Meeting and Exhibit*, Reno, Nevada: American Institute of Aeronautics and Astronautics, Jan. 2008. doi: 10.2514/6.2008-1306.
- [32] T. J. Larsen and T. D. Hanson, “A method to avoid negative damped low frequent tower vibrations for a floating, pitch controlled wind turbine,” *J. Phys.: Conf. Ser.*, vol. 75, p. 012073, Jul. 2007, doi: 10.1088/1742-6596/75/1/012073.
- [33] C. Kim *et al.*, “Design, Implementation, and Evaluation of an Output Prediction Model of the 10 MW Floating Offshore Wind Turbine for a Digital Twin,” *Energies*, vol. 15, no. 17, p. 6329, Aug. 2022, doi: 10.3390/en15176329.
- [34] J. Walker, A. Coraddu, M. Collu, and L. Oneto, “Digital twins of the mooring line tension for floating offshore wind turbines to improve monitoring, lifespan, and safety,” *J. Ocean Eng. Mar. Energy*, vol. 8, no. 1, pp. 1–16, Feb. 2022, doi: 10.1007/s40722-021-00213-y.
- [35] F. Tao and Q. Qi, “Make more digital twins,” *Nature*, vol. 573, no. 7775, pp. 490–491, Sep. 2019, doi: 10.1038/d41586-019-02849-1.
- [36] A. Ciuriuc, J. I. Rapha, R. Guanache, and J. L. Domínguez-García, “Digital tools for floating offshore wind turbines (FOWT): A state of the art,” *Energy Reports*, vol. 8, pp. 1207–1228, Nov. 2022, doi: 10.1016/j.egy.2021.12.034.
- [37] A. Parvareh, S. Abrazeh, S.-R. Mohseni, M. J. Zeitouni, M. Gheisarnejad, and M.-H. Khooban, “A Novel Deep Learning Backstepping Controller-Based Digital Twins Technology for Pitch Angle Control of Variable Speed Wind Turbine,” *Designs*, vol. 4, no. 2, p. 15, Jun. 2020, doi: 10.3390/designs4020015.

Developing Solar Cavity receivers to Improve Energy Governance

Reyhaneh Loni^a, Sasa Pavlovic^b

^a Faculty of Governance, University of Tehran, 14398-14151, Tehran, IR, rloni@ut.ac.ir

^b Faculty of Mechanical Engineering, University of Niš, Niš, RS, sasa.pavlovic@masfak.ni.ac.rs

Abstract: This paper explores the development of solar cavity receivers as a pivotal technology in enhancing energy governance. Solar cavity receivers, which harness concentrated solar power (CSP) to achieve high thermal efficiencies, present a promising solution to the challenges of sustainable energy production. By integrating advanced materials and innovative design principles, this research aims to optimize the performance of solar cavity receivers, thereby increasing their viability for large-scale energy applications. The study examines the implications of improved energy governance through the adoption of solar cavity receivers, focusing on their potential to reduce reliance on fossil fuels, lower greenhouse gas emissions, and promote energy equity. Furthermore, the paper discusses policy frameworks and governance strategies necessary to facilitate the widespread implementation of this technology. Ultimately, the findings underscore the importance of solar cavity receivers in the transition towards a more sustainable and resilient energy future.

Keywords: Solar Cavity Receivers, Concentrated Solar Power (CSP), Energy Governance, Sustainable Energy Production, Policy Frameworks.

1. Introduction

As the world grapples with the pressing challenges of climate change, energy security, and the need for sustainable development, the transition from fossil fuel-based energy systems to renewable energy sources has become imperative [1]. The energy sector is at a crossroads, where innovative technologies must be harnessed to meet the growing demand for clean, reliable, and affordable energy [2]. Among the various renewable energy technologies, solar energy has emerged as a frontrunner due to its vast potential and versatility [3]. Solar energy systems, particularly concentrated solar power (CSP), offer a promising pathway to harness the sun's abundant energy, converting it into usable thermal energy for electricity generation and other applications [4].

Solar cavity receivers represent a significant advancement in CSP technology, designed to capture and concentrate solar radiation effectively [5]. These receivers utilize a reflective cavity to focus sunlight onto a working fluid, achieving high thermal efficiencies that can surpass traditional solar thermal systems [6]. The ability to operate at elevated temperatures not only enhances energy conversion efficiency but also expands the range of applications for solar energy, making it suitable for industrial processes, heating, and electricity generation on a large scale. As such, solar cavity receivers are positioned as a pivotal technology in the quest for sustainable energy solutions [7].

This paper aims to explore the development and optimization of solar cavity receivers, emphasizing their role in enhancing energy governance. Energy governance encompasses the policies, regulations, and institutional frameworks that guide energy production, distribution, and consumption [8]. By integrating advanced materials and innovative design principles, this research seeks to improve the performance and viability of solar cavity receivers, thereby facilitating their adoption in diverse energy markets. The implications of this technology extend beyond mere efficiency gains; they also encompass broader societal benefits, including the potential to reduce reliance on fossil fuels, lower greenhouse gas emissions, and promote energy equity.

In addition to the technological advancements, this study will address the critical policy frameworks and governance strategies necessary to support the widespread implementation of solar cavity receivers [9]. Effective governance is essential to ensure that the benefits of solar energy are equitably distributed and that barriers to adoption are systematically addressed [10]. By examining the intersection of technology and governance, this paper aims to provide a comprehensive understanding of how solar cavity receivers can contribute to a more sustainable and resilient energy future. Ultimately, the findings of this research underscore

the importance of solar cavity receivers not only as a technological innovation but also as a vital component in the transition towards a cleaner, more sustainable energy landscape. By leveraging the potential of solar cavity receivers, we can pave the way for a future that prioritizes environmental sustainability, energy security, and social equity.

2. Solar Cavity Receivers

Solar cavity receivers are an innovative technology within the realm of concentrated solar power (CSP) systems, designed to efficiently capture and convert solar energy into usable thermal energy. Solar cavity receivers are specialized devices that utilize a reflective cavity to concentrate sunlight onto a working fluid. This technology is a key component of CSP systems, which generate electricity by converting solar energy into thermal energy. The receiver typically consists of a highly reflective inner surface that directs incoming solar radiation towards a focal point where the working fluid is heated. The design minimizes heat loss and maximizes the absorption of solar energy. Common working fluids include water, oil, or molten salts, which are heated to high temperatures. The heated fluid can then be used to produce steam that drives turbines for electricity generation or for direct heating applications.

Solar cavity receivers can operate at significantly higher temperatures compared to traditional solar thermal systems, enhancing their efficiency and expanding their range of applications. The design allows for a high concentration ratio, meaning that a large amount of solar energy can be focused onto a small area, resulting in higher temperatures and more efficient energy conversion. Also, the enclosed cavity design minimizes heat loss to the environment, allowing for better retention of thermal energy. By harnessing solar energy, these systems contribute to the diversification of energy sources, reducing dependence on fossil fuels and enhancing energy security. The use of solar cavity receivers significantly lowers greenhouse gas emissions compared to conventional energy generation methods, making them an essential technology in combating climate change. Solar cavity receivers can be deployed in various configurations, from small-scale installations to large solar power plants, making them adaptable to different energy needs and geographical locations.

While solar cavity receivers offer numerous advantages, there are challenges to their widespread adoption including the capital costs associated with the development and installation of solar cavity receiver systems can be high, which may deter investment. The advanced materials and engineering required for efficient operation necessitate specialized knowledge and expertise. Incorporating solar cavity receivers into existing energy infrastructures may require significant modifications and supportive policies.

Generally, solar cavity receiver harness concentrated solar power to achieve high thermal efficiencies, making them a promising solution to the challenges of sustainable energy production. Their ability to convert solar energy into thermal energy efficiently positions them as a critical technology in the transition towards renewable energy systems. As research and development continue to advance this technology, solar cavity receivers could play a pivotal role in achieving global sustainability goals, reducing environmental impacts, and promoting energy equity.

The optimization of solar cavity receivers through the integration of advanced materials and innovative design principles is crucial for enhancing their performance and increasing their viability for large-scale energy applications. The choice of materials used in solar cavity receivers significantly impacts their efficiency, durability, and overall performance. Materials such as ceramics, advanced composites, and specialized alloys are designed to withstand the high temperatures generated within the receiver. These materials maintain structural integrity and thermal performance, ensuring long-term operation. The use of advanced reflective coatings on the inner surfaces of the cavity enhances the concentration of solar energy. These coatings are engineered to maximize reflectivity while minimizing absorption losses, allowing more sunlight to be directed towards the working fluid. Incorporating materials that can store thermal energy, such as phase change materials (PCMs) or molten salts, allow for better energy management. This enables the system to provide a continuous energy supply even when sunlight is not available, enhancing reliability.

The shape and size of the cavity are optimized to maximize solar concentration and minimize heat loss. Designs that incorporate parabolic or cylindrical geometries can enhance the focusing of sunlight onto the working fluid. Innovative designs that improve heat transfer between the working fluid and the receiver surface can significantly enhance thermal efficiency. This may involve the use of enhanced heat exchangers or optimized flow patterns to ensure uniform heating. Developing modular solar cavity receiver systems allows for

scalability and flexibility in deployment. These systems can be easily expanded or adapted to meet varying energy demands, making them suitable for large-scale applications.

By maximizing solar energy capture and minimizing heat losses, optimized solar cavity receivers can achieve higher thermal efficiencies, making them more effective at converting sunlight into usable energy. The use of durable materials and robust designs ensures that solar cavity receivers can operate effectively over extended periods, reducing maintenance needs and downtime. Improved performance and efficiency can lead to lower operational costs and a more favorable return on investment, making solar cavity receivers more attractive for large-scale energy projects. Optimized designs can be scaled up to meet the energy demands of large facilities, such as solar power plants, industrial processes, and district heating systems. High-performance solar cavity receivers can be integrated into existing energy grids, providing a reliable source of renewable energy that complements other energy sources. As countries and regions strive to transition to renewable energy sources, the enhanced performance and reliability of solar cavity receivers position them as a key technology in achieving sustainability goals.

Generally, the integration of advanced materials and innovative design principles is essential for optimizing the performance of solar cavity receivers. These enhancements lead to increased thermal efficiency, reliability, and cost-effectiveness, making solar cavity receivers a viable solution for large-scale energy applications. As research and development continue to advance this technology, solar cavity receivers are poised to play a significant role in the global transition towards sustainable energy systems.

3. Enhancing Energy Governance with Solar Cavity Receivers

The exploration of solar cavity receivers as a pivotal technology in enhancing energy governance involves several key aspects, including their technological development, operational principles, benefits, challenges, and implications for energy policy and governance. The integration of solar cavity receivers into energy systems has profound implications for energy governance including policy development, regulatory frameworks, and stakeholder engagement. In this regards, policymakers must create supportive frameworks that encourage investment in solar technologies, including incentives, subsidies, and research funding. Establishing regulations that facilitate the deployment of solar cavity receivers while ensuring environmental protection and energy reliability is crucial. Also, engaging various stakeholders, including local communities, industry players, and government entities, is essential for successful implementation and acceptance of solar cavity receiver technologies.

The exploration of solar cavity receivers as a pivotal technology in enhancing energy governance highlights their potential to transform the energy landscape. By addressing the challenges and leveraging the benefits, solar cavity receivers can play a crucial role in achieving sustainable energy goals, reducing environmental impacts, and promoting energy equity. As research and development continue, the integration of this technology into energy governance frameworks will be vital for fostering a resilient and sustainable energy future.

In other words, the examination of the implications of improved energy governance through the adoption of solar cavity receivers reveals significant potential benefits in several key areas: reducing reliance on fossil fuels, lowering greenhouse gas emissions, and promoting energy equity. The adoption of solar cavity receivers can play a crucial role in decreasing dependence on fossil fuels, which are a major contributor to environmental degradation and climate change. Solar cavity receivers harness solar energy, a renewable resource that is abundant and widely available. By integrating this technology into energy systems, countries can diversify their energy portfolios and reduce their reliance on finite fossil fuel resources. Reducing dependence on imported fossil fuels enhances energy security for nations, making them less vulnerable to price fluctuations and geopolitical tensions associated with fossil fuel markets. This shift can lead to greater energy independence and stability. The implementation of solar cavity receivers can serve as a transitional pathway for regions heavily reliant on fossil fuels. By gradually integrating renewable technologies, these regions can move towards a more sustainable energy future while maintaining energy supply.

The environmental benefits of adopting solar cavity receivers are significant, particularly in terms of reducing greenhouse gas emissions. Solar cavity receivers produce energy without emitting greenhouse gases during operation. By replacing fossil fuel-based power generation with solar energy, significant reductions in carbon dioxide (CO₂) and other harmful emissions can be achieved. Lowering greenhouse gas emissions is critical in the fight against climate change. The widespread adoption of solar cavity receivers can contribute to national

and global efforts to meet climate targets, such as those outlined in the Paris Agreement. While the manufacturing and installation of solar cavity receivers do involve some emissions, these are generally much lower than the lifecycle emissions associated with fossil fuel extraction, processing, and combustion. As technology advances, the overall carbon footprint of solar technologies continues to decrease.

The integration of solar cavity receivers can also have profound implications for energy equity, ensuring that the benefits of renewable energy are accessible to all communities. Solar cavity receivers can be deployed in remote and underserved areas, providing access to clean and reliable energy where traditional energy infrastructure may be lacking. This can help bridge the energy access gap and improve the quality of life for marginalized communities. The development and deployment of solar cavity receiver technologies can create jobs in manufacturing, installation, and maintenance. These opportunities can be particularly beneficial in regions transitioning away from fossil fuel industries, providing new pathways for economic development. Effective energy governance involves engaging local communities in the decision-making process regarding energy projects. By involving communities in the planning and implementation of solar cavity receiver systems, energy equity can be promoted, ensuring that local needs and priorities are addressed.

The adoption of solar cavity receivers necessitates a reevaluation of energy governance frameworks to support the transition to renewable energy. Governments must create supportive policies that incentivize the adoption of solar cavity receivers, such as tax credits, grants, and feed-in tariffs. These policies can encourage investment and accelerate the deployment of renewable technologies. Establishing clear regulations that facilitate the integration of solar cavity receivers into existing energy systems is essential. This includes streamlining permitting processes and ensuring grid access for renewable energy sources. Effective energy governance requires collaboration among various stakeholders, including government agencies, private sector actors, and local communities. Building partnerships can enhance knowledge sharing, resource mobilization, and the successful implementation of solar cavity receiver projects. The examination of the implications of improved energy governance through the adoption of solar cavity receivers highlights their potential to significantly reduce reliance on fossil fuels, lower greenhouse gas emissions, and promote energy equity. By addressing these critical areas, solar cavity receivers can contribute to a more sustainable and resilient energy future, aligning with global efforts to combat climate change and ensure equitable access to clean energy for all. As such, the integration of this technology into energy governance frameworks is essential for realizing its full potential and achieving long-term sustainability goals.

4. Policy Frameworks and Governance Strategies

The broad adoption of solar cavity receivers requires robust policy frameworks and governance strategies to address various challenges and promote the growth of this technology. The critical components of these frameworks and strategies include:

1. Supportive Policy Frameworks

For effective implementation of solar cavity receivers, governments must establish policies that foster investment and deployment. Key components include:

- **Incentives and Subsidies:** Financial support mechanisms such as tax credits, grants, and subsidies can substantially decrease the initial costs of solar cavity receiver projects. These incentives enhance the attractiveness of the technology for investors and developers, accelerating its deployment.
- **Feed-in Tariffs and Power Purchase Agreements (PPAs):** The establishment of feed-in tariffs or long-term power purchase agreements can provide fixed prices for electricity generated by solar cavity receivers. This financial stability can encourage investment and ensure the economic viability of projects.
- **Research and Development Funding:** Allocating resources for research and development can stimulate innovation in solar cavity receiver technology, improving efficiency and reducing costs. Supporting partnerships between academia and industry can lead to advancements in materials, design, and integration.

2. Regulatory Frameworks

Developing clear regulatory frameworks is essential for effectively incorporating solar cavity receivers into existing energy systems. Important considerations include:

- **Streamlined Permitting Processes:** Simplifying the permitting process for solar cavity receiver installations can reduce bureaucratic hurdles and expedite project timelines. This may involve creating standardized guidelines and shortening approval periods.
- **Grid Access and Interconnection Standards:** Ensuring that solar cavity receivers have access to the energy grid is vital for their success. Regulatory frameworks should specify interconnection standards that enable the efficient integration of renewable energy sources into the grid.
- **Environmental and Safety Regulations:** While promoting solar cavity receivers, it is fundamental to adhere to environmental and safety standards. Regulations must ensure that installations do not negatively impact local ecosystems and that safety protocols are strictly followed during construction and operation.

3. Governance Strategies

Effective governance strategies are necessary to coordinate efforts among diverse stakeholders and ensure the successful deployment of solar cavity receivers. Key strategies include:

- **Stakeholder Engagement:** Engaging a wide range of stakeholders—including government agencies, industry representatives, local communities, and environmental organizations—is crucial for reaching consensus and addressing concerns. Collaborative decision-making can improve project acceptance and support.
- **Capacity Building and Education:** Providing training and educational resources to policymakers, industry professionals, and local communities can enhance understanding of solar cavity receiver technology and its benefits. Capacity-building initiatives empower stakeholders to participate actively in the transition to renewable energy.
- **Monitoring and Evaluation:** Implementing systems for monitoring and evaluating the performance of solar cavity receiver projects can yield valuable insights into their effectiveness and impact. This information can inform future policy adjustments and enhance governance strategies.

4. Long-Term Energy Planning

Integrating solar cavity receivers into long-term energy planning is vital for ensuring their sustainability and effectiveness. Key considerations include:

- **Integrated Resource Planning:** Energy planners should incorporate solar cavity receivers into a holistic energy strategy that includes various renewable sources, energy efficiency measures, and demand-side management. This integrated approach can optimize resource allocation and strengthen grid stability.
- **Climate Action Goals:** Aligning the deployment of solar cavity receivers with national and international climate action commitments can increase their relevance and urgency. Policies should reflect goals to reduce greenhouse gas emissions and promote a low-carbon economy.

5. International Cooperation

In light of the global nature of energy challenges, international cooperation is essential for facilitating the adoption of solar cavity receivers. Key aspects include:

- **Knowledge Sharing:** Countries can gain from sharing best practices, research findings, and lessons from successful solar cavity receiver projects. International forums and partnerships can facilitate this exchange of knowledge.
- **Technology Transfer:** Supporting technology transfer initiatives can assist developing nations in accessing solar cavity receiver technologies and expertise. This assistance can strengthen worldwide efforts to promote renewable energy and sustainable development.

Generally, the widespread implementation of solar cavity receivers requires comprehensive policy frameworks and governance strategies that address financial, regulatory, and operational challenges. By establishing supportive policies, clear regulations, and effective governance practices, governments can facilitate the adoption of solar cavity receivers, promoting the transition to renewable energy and achieving sustainability objectives. Prioritizing stakeholder engagement, investing in research and development, and fostering international cooperation will be crucial for unlocking the full potential of this promising technology.

5. Conclusion

In conclusion, the exploration of solar cavity receivers as a pivotal technology in enhancing energy governance highlights their significant potential in addressing the pressing challenges of sustainable energy production. This paper has demonstrated that solar cavity receivers, through their ability to harness concentrated solar power (CSP) with high thermal efficiencies, can play a crucial role in the transition towards a cleaner and more sustainable energy landscape. By optimizing their performance through advanced materials and innovative design principles, these receivers not only improve energy output but also contribute to the broader goals of reducing reliance on fossil fuels and lowering greenhouse gas emissions. The implications of adopting solar cavity receivers extend beyond technological advancements; they also encompass critical aspects of energy governance. By promoting energy equity and ensuring that the benefits of solar energy are accessible to diverse communities, solar cavity receivers can help create a more inclusive energy system. This is particularly important in the context of global efforts to combat climate change and achieve sustainable development goals.

Moreover, the discussion of necessary policy frameworks and governance strategies underscores the importance of a supportive regulatory environment for the successful implementation of solar cavity receivers. Policymakers must prioritize the development of incentives, funding mechanisms, and collaborative initiatives that facilitate the integration of this technology into existing energy systems. By addressing barriers to adoption and fostering innovation, we can accelerate the transition to renewable energy sources and enhance energy security. Ultimately, the findings of this research reinforce the critical role of solar cavity receivers in shaping a sustainable and resilient energy future. As we move forward, it is essential to continue investing in research, development, and policy initiatives that support the deployment of solar cavity receivers and other renewable technologies. By doing so, we can pave the way for a cleaner, more equitable, and sustainable energy landscape that meets the needs of current and future generations, ensuring a healthier planet for all.

Acknowledgment

The authors relied on OpenAI's ChatGPT solely for grammar checks and writing enhancements during the preparation of this work. Following its use, they meticulously reviewed and edited the content as necessary, assuming full responsibility for the final publication.

References

- [1] J. Zhang, Energy access challenge and the role of fossil fuels in meeting electricity demand: Promoting renewable energy capacity for sustainable development, *Geoscience Frontiers*, 15 (2024) 101873.
- [2] S. Kumar, K. Rathore, Renewable energy for sustainable development goal of clean and affordable energy, *International Journal of Materials Manufacturing and Sustainable Technologies*, 2 (2023) 1-15.
- [3] R. Loni, A. Kasaeian, E.A. Asli-Ardeh, B. Ghobadian, S. Gorjian, Experimental and numerical study on dish concentrator with cubical and cylindrical cavity receivers using thermal oil, *Energy*, 154 (2018) 168-181.
- [4] R. Loni, E.A. Asli-Ardeh, B. Ghobadian, E. Bellos, W.G. Le Roux, Numerical comparison of a solar dish concentrator with different cavity receivers and working fluids, *Journal of Cleaner Production*, 198 (2018) 1013-1030.
- [5] R. Loni, E.A. Asli-Ardeh, B. Ghobadian, A. Kasaeian, S. Gorjian, G. Najafi, E. Bellos, Research and review study of solar dish concentrators with different nanofluids and different shapes of cavity receiver: Experimental tests, *Renewable Energy*, 145 (2020) 783-804.
- [6] R. Loni, B. Ghobadian, A. Kasaeian, M. Akhlaghi, E. Bellos, G. Najafi, Sensitivity analysis of parabolic trough concentrator using rectangular cavity receiver, *Applied Thermal Engineering*, 169 (2020) 114948.
- [7] S. Pavlovic, R. Loni, E. Bellos, D. Vasiljević, G. Najafi, A. Kasaeian, Comparative study of spiral and conical cavity receivers for a solar dish collector, *Energy Conversion and Management*, 178 (2018) 111-122.
- [8] M. Bazilian, S. Nakhooda, T. Van de Graaf, Energy governance and poverty, *Energy Research & Social Science*, 1 (2014) 217-225.
- [9] T. Güneş, Solar energy, governance and CO₂ emissions, *Renewable Energy*, 184 (2022) 791-798.
- [10] N.K. Dubash, A. Florini, Mapping global energy governance, *Global policy*, 2 (2011) 6-18.

Developing Renewable Energy Sources: Enhancing Energy Governance for a Sustainable Future

Reyhaneh Loni^a, Sasa Pavlovic^b

^a Faculty of Governance, University of Tehran, 14398-14151, Tehran, IR, rloni@ut.ac.ir

^b Faculty of Mechanical Engineering, University of Niš, Niš, RS, sasa.pavlovic@masfak.ni.ac.rs

Abstract: This paper explores the integration of renewable energy sources (RES) into contemporary energy governance frameworks to enhance sustainability, security, and equity in energy systems. As global energy demands continue to rise and environmental concerns become increasingly pressing, RES such as solar, wind, hydro, and biomass offer transformative solutions to mitigate climate change and reduce reliance on fossil fuels. The study examines case studies from various regions implementing innovative governance models that facilitate the adoption of RES. It highlights key strategies, including policy reforms, stakeholder engagement, and technological advancements, that promote efficiency and transparency in energy management. Additionally, the paper discusses the challenges faced, such as regulatory barriers and the need for cross-sector collaboration. By proposing a holistic approach to governance that incorporates decentralized energy systems and community participation, this research underscores the potential of RES to not only address energy needs but also empower local communities and promote socio-economic resilience. The findings advocate for a shift in energy governance paradigms that prioritizes sustainability and inclusivity, thereby paving the way for a more sustainable energy future.

Keywords: Renewable energy sources (RES), Energy governance, Sustainability, Policy reforms, Decentralized energy systems.

1. Introduction

The intensifying global demand for energy, paired with the urgent need for environmental stewardship, has placed renewable energy sources (RES) at the center of contemporary energy discourse [1]. Traditional energy generation methods, primarily reliant on fossil fuels, are increasingly recognized for their profound environmental implications, including greenhouse gas emissions, air pollution, and climate change [2]. In light of these challenges, countries worldwide are turning to RES, such as solar, wind, hydroelectric, and biomass energy, as fundamental components of a more sustainable energy paradigm [3]. These technologies not only have the potential to significantly reduce carbon footprints but also offer opportunities for energy independence, security, and economic development in diverse socio-economic contexts.

One of the critical factors determining the successful integration of RES into energy systems is the governance framework that surrounds their implementation [4]. Energy governance encompasses the structures, policies, regulations, and stakeholder interactions that shape how energy resources are managed and utilized [5]. It plays a vital role in influencing the degree of adoption of RES and ensuring that energy systems are resilient, efficient, and equitable. However, traditional governance models often struggle to adapt to the dynamic nature of renewable energy technologies and the decentralization of energy production. Therefore, there is a pressing need for innovative governance approaches that can effectively support the transition to renewable energy while addressing the diverse challenges associated with this shift.

This paper seeks to explore the intersection of RES integration and contemporary energy governance frameworks by examining various innovative governance models employed across different regions [6]. Through detailed case studies, the research aims to identify key strategies that enhance sustainability, security, and equity in energy systems [7]. These strategies include policy reforms that promote favorable regulatory environments, stakeholder engagement that fosters collaboration among diverse actors, and technological advancements that improve the efficiency and transparency of energy management practices [8]. Furthermore, the study addresses the challenges that impede the integration of RES, such as regulatory barriers, economic constraints, and the complexity of cross-sector collaboration. By critically analyzing these obstacles, the research underscores the necessity of a coherent and inclusive governance approach that accommodates the

needs and capacities of all stakeholders involved, particularly local communities. At the heart of this paper is the proposition of a holistic governance approach that emphasizes the importance of decentralized energy systems and community participation [9]. By empowering local communities to actively engage in energy decision-making processes, it is possible to not only fulfill immediate energy needs but also create pathways for socio-economic resilience. Such empowerment enhances local ownership of energy resources, fosters innovation, and promotes equity in energy access, ensuring that the benefits of renewable energy transitions are equitably distributed.

This research advocates for a paradigm shift in energy governance that prioritizes sustainability and inclusivity. By embracing a more collaborative and adaptive governance framework, we can pave the way for a sustainable energy future that meets the challenges of the 21st century. This paper contributes to the ongoing discourse regarding the role of governance in shaping energy transitions and offers insights into fostering resilient and inclusive energy systems that leverage the full potential of renewable energy sources. Generally, the transition to renewable energy is not just a technical shift; it necessitates a comprehensive rethinking of how energy systems are governed. By integrating innovative governance practices with the deployment of RES, stakeholders can create a more sustainable, secure, and equitable energy future for all.

2. Renewable Energy

In recent years, global energy demands have been experiencing an upward trajectory, driven by factors such as population growth, urbanization, and economic development. According to the International Energy Agency (IEA), energy consumption is expected to rise significantly, particularly in emerging economies where industrialization and improvements in living standards lead to increased energy requirements. This surge in demand necessitates a reassessment of energy production and consumption patterns, particularly as traditional fossil fuel resources become strained and increasingly unsustainable. On the other hand, environmental concerns have escalated, particularly in the context of climate change. The burning of fossil fuels—such as coal, oil, and natural gas—leads to the release of greenhouse gases (GHGs), primarily carbon dioxide (CO₂), which significantly contribute to global warming. The effects of climate change are becoming more evident, manifesting in extreme weather events, rising sea levels, and widespread ecological disruption. As a result, there is an urgent need for systemic changes to energy systems to address these challenges.

Renewable energy sources, including solar, wind, hydro, and biomass, provide viable alternatives to fossil fuels and hold transformative potential for energy systems across the globe. In this regard, solar energy harnesses sunlight through photovoltaic panels or solar thermal systems to generate electricity. It is abundant and available in most regions of the world. Advancements in solar technology have significantly reduced costs, making solar installations more accessible for residential, commercial, and utility-scale applications. By replacing fossil fuel-generated electricity with solar power, countries can significantly lower their carbon footprints and enhance energy independence. Also, wind energy is produced by converting the kinetic energy of wind into electricity using turbines. Wind power has seen substantial growth globally due to its cost-effectiveness and scalability. Onshore and offshore wind farms can generate large amounts of clean energy. The proliferation of wind energy technologies not only helps reduce greenhouse gas emissions but also provides opportunities for job creation in manufacturing, installation, and maintenance sectors.

Another kind of RE is known as hydropower that generates electricity by harnessing the energy of flowing or falling water, typically using dams or run-of-river systems. It is one of the oldest and most established forms of renewable energy, providing a substantial portion of the world's electricity. Hydropower is particularly valuable for its ability to provide baseload power and support grid stability. However, careful consideration must be given to its environmental impacts on aquatic ecosystems and local communities. Biomass energy is another kind of RE that derived from organic materials, such as plant matter, agricultural waste, and animal manure. It can be converted into biofuels, biogas, and electricity. Biomass offers the potential for carbon neutrality, as the CO₂ released during combustion is offset by the CO₂ absorbed during the growth of the biomass. Additionally, the utilization of waste materials for energy contributes to waste reduction and resource efficiency.

The integration of RES into energy systems plays a pivotal role in mitigating climate change effects. By transitioning to renewable sources, countries can significantly cut their greenhouse gas emissions, thus helping to meet international climate targets such as those outlined in the Paris Agreement. Furthermore, adopting RES reduces reliance on fossil fuels, which are finite resources susceptible to market fluctuations and geopolitical

challenges. The shift towards renewables also fosters energy diversification, enhancing energy security by reducing dependency on imported fossil fuels. This is particularly important for energy-importing nations that seek to stabilize their energy supply and protect against price volatility. Generally, as global energy demands continue to rise and environmental concerns become more pressing, the adoption of renewable energy sources such as solar, wind, hydro, and biomass not only addresses the immediate needs for clean and sustainable energy but also contributes to long-term environmental resilience and economic stability. Emphasizing the transformative potential of RES can drive policy changes, investment in renewable technologies, and innovations that align with a sustainable future. The collective focus on transitioning to a low-carbon energy system calls for strategic governance, stakeholder collaboration, and continuous advancements in renewable energy deployment.

3. Integration of Renewable Energy and Energy Governance

The integration of renewable energy sources (RES) into contemporary energy governance frameworks represents a critical shift in the way energy systems are managed and deployed, addressing pressing global challenges such as climate change, energy access, and social equity. The primary goal of incorporating RES into energy governance is to foster sustainable energy practices. Renewable energy technologies, such as solar, wind, and geothermal, produce minimal greenhouse gas emissions compared to conventional fossil fuels. By integrating RES into governance frameworks, policymakers can promote policies that encourage the transition to a low-carbon economy. This involves establishing clear targets for renewable energy adoption, implementing incentives for clean energy investments, and creating supportive regulatory environments that facilitate innovative solutions, such as energy efficiency programs and demand-side management. On the other side, energy security is a fundamental aspect of governance that involves ensuring a reliable and stable energy supply. The diversification of energy sources through RES can significantly enhance this security. By reducing reliance on fossil fuels, countries can mitigate risks associated with price volatility and supply disruptions due to geopolitical tensions or natural disasters. Effective governance frameworks can facilitate this transition by developing robust infrastructure for renewable energy integration, such as smart grids that enhance grid resilience and flexibility. Additionally, these frameworks can incorporate measures for energy storage technologies, which are essential in managing the intermittent nature of renewable generation.

Equity is a crucial consideration when exploring the integration of RES into energy governance. Ensuring that all communities have fair access to renewable energy resources and the benefits they provide is critical for social justice. This involves addressing disparities in energy access, particularly for low-income and marginalized populations who may face barriers to adopting renewable technologies. Governance frameworks can play a key role in promoting equitable policies, such as community solar programs, that allow shared access to renewable energy. Furthermore, stakeholder engagement processes are essential to ensure that the perspectives and needs of diverse community members are considered in energy decision-making. Also, effective energy governance necessitates the involvement of various stakeholders, including government entities, private sector actors, civil society organizations, and local communities. Collaborative governance models can facilitate knowledge sharing, resource pooling, and joint problem-solving in the integration of RES. This exploration emphasizes creating platforms for dialogue and partnerships among stakeholders to align interests and foster co-creation of policies and initiatives that advance renewable energy integration. It should be mentioned that, the transition to renewable energy requires innovative regulatory frameworks that adapt to the evolving energy landscape. This includes revising existing laws and regulations to support new business models, such as decentralized energy systems, and enabling the participation of prosumers - consumers who also produce energy. Additionally, policymakers must address barriers to renewable energy deployment, such as permitting processes, grid interconnections, and financial access for projects, particularly in underserved areas. The paper may highlight case studies that illustrate successful regulatory innovations aimed at optimizing the integration of RES. Finally, the exploration of RES integration into energy governance includes an examination of technological advancements that can facilitate this process. Innovative technologies, such as battery storage, microgrids, and demand response systems, play a vital role in enhancing the reliability and efficiency of renewable energy systems. Governance frameworks must support research and development initiatives that drive technological innovation and promote the commercialization of advanced energy solutions. Generally, the exploration of integrating renewable energy sources into contemporary energy governance frameworks aims to create a multifaceted approach that enhances sustainability, ensures energy

security, and promotes equity. This holistic perspective is essential for developing resilient energy systems capable of meeting current and future energy needs while addressing environmental and social challenges.

4. Examining Case Studies of Innovative Governance Models

The examination of case studies from various regions that have successfully implemented innovative governance models provides valuable insights into best practices for promoting the adoption of renewable energy sources (RES). These models often incorporate unique approaches tailored to local contexts, regulatory environments, and resource availability. Below are a few notable examples:

•Germany's Energiewende (Energy Transition):

Germany has been at the forefront of renewable energy adoption through its Energiewende policy framework, which aims to shift the country towards a low-carbon economy. Key governance components include significant policy reforms, such as the Renewable Energy Sources Act (EEG), which established feed-in tariffs to guarantee fixed payments for renewable energy producers. The model emphasizes stakeholder engagement, involving local communities in the decision-making process and promoting citizen ownership of energy projects. This inclusive approach has facilitated widespread public support and investment in RES.

•Costa Rica's Renewable Energy Strategy:

Costa Rica has achieved remarkable success in integrating RES into its energy mix, achieving over 99% of its electricity generation from renewable sources, primarily hydropower, wind, and solar. The government has implemented innovative policies to promote public-private partnerships, attracting investments in renewable energy infrastructure. The collaboration between government agencies, private companies, and non-governmental organizations (NGOs) has been crucial in enhancing energy access and sustainability in rural areas.

•California's Clean Energy Policies:

California has adopted a comprehensive governance model that incorporates ambitious renewable energy targets and regulatory frameworks to support clean energy deployment. The state's policy reforms include the Renewable Portfolio Standard (RPS) which mandates utilities to procure a certain percentage of their energy from renewable sources. Moreover, California emphasizes technological advancements, such as incentives for energy storage systems and smart grid technologies, to enhance reliability and efficiency in energy management.

Several key strategies can be identified from these case studies that promote efficiency and transparency in energy management. Effective policy frameworks are essential for creating an enabling environment for RES adoption. This includes establishing clear goals and targets (e.g., renewable energy mandates), providing financial incentives (e.g., tax credits, subsidies), and harmonizing regulations to simplify the permitting process for renewable energy projects. Such policy reforms help attract investments and encourage private sector participation. Also, engaging a diverse range of stakeholders—including government agencies, businesses, local communities, and civil society—is crucial for building consensus around renewable energy initiatives. Transparent communication channels, public consultations, and participatory decision-making processes foster trust and ensure that the needs and concerns of all stakeholders are addressed. This engagement can also facilitate local ownership of renewable energy projects, leading to enhanced community support and buy-in. In this regard, investment in research and development (R&D) of renewable energy technologies is vital for improving efficiency and reducing costs. Governments can promote innovation through grants and funding for startups involved in renewable energy development. Additionally, harnessing data analytics, artificial intelligence, and smart grid technologies can enhance grid management, optimize energy distribution, and facilitate real-time monitoring of energy consumption.

Despite the successes associated with adopting innovative governance models for RES, There are several challenges persist. In this regards, regulatory frameworks may not always keep pace with emerging technologies and market dynamics, leading to uncertainties that can deter investment in renewable energy. Complex permitting processes, outdated grid interconnection standards, and lack of harmonization among regulations at different governmental levels can create obstacles for project development. Also, effective adoption of RES often requires collaboration between multiple sectors, including energy, transportation, and urban planning. However, achieving alignment among diverse stakeholders can be challenging due to differing priorities, funding mechanisms, and operational protocols. Promoting cross-sectoral integration requires

establishing platforms for dialogue and cooperation among government agencies, industry players, and local communities. Access to affordable financing remains a key barrier, particularly in developing countries where capital markets may be limited. Innovative financing mechanisms, such as green bonds, public-private partnerships, and community financing models, can help address these challenges. However, developing suitable financial products and attracting investments require concerted efforts from both public and private sectors. On the other side, public opposition to renewable energy projects (e.g., concerns about land use, visual impacts, and perceived risks) can hinder development efforts. Ensuring ongoing community engagement, effective communication about the benefits of RES, and addressing public concerns through transparent processes are essential for gaining social acceptance.

Generally, the exploration of case studies demonstrating innovative governance models for renewable energy adoption reveals a range of effective strategies, including policy reforms, stakeholder engagement, and technological advancements. However, it is crucial to recognize and address the multifaceted challenges that accompany this transition, such as regulatory barriers and the need for cross-sector collaboration. By sharing lessons learned and best practices, stakeholders can work together to create a more sustainable, efficient, and equitable energy future that harnesses the full potential of renewable energy sources.

5. Holistic Approach to Governance

A holistic approach to governance in the context of energy systems involves considering the interconnections between different elements of energy production, distribution, and consumption, as well as their social, economic, and environmental impacts. It recognizes that energy systems do not operate in isolation but are deeply intertwined with community needs, economic development, and environmental sustainability. This approach is critical in addressing the complexities of the energy transition and ensuring that it is inclusive and equitable.

Decentralized energy systems refer to energy generation and distribution methods that operate at a local or community level rather than relying solely on centralized power plants. These systems can include community solar projects, microgrids, and localized wind or biomass energy installations. Decentralization allows for energy production that is closer to the point of consumption, which offers several advantages. Such as, energy generated near consumption points minimizes losses that occur during long-distance transmission, enhancing overall system efficiency. Also, decentralized systems can enhance energy resilience by reducing vulnerability to large-scale system failures, making communities less reliant on a single energy source or grid infrastructure. In the other side, in the event of a natural disaster or grid outage, localized systems can continue to operate independently. Communities can take control of their energy needs through decentralized systems, allowing them to manage and participate in energy production and consumption, too. This can empower residents, foster local ownership, and create jobs related to the installation and maintenance of renewable energy technologies.

On the other hand, community participation is essential in designing and implementing energy governance frameworks that reflect local priorities and needs. Involving community members in the decision-making process can ensure that energy solutions are culturally appropriate, economically viable, and socially accepted. Key aspects of community participation include:

- Engagement in Planning:** Local communities should have a say in the planning and development of energy projects. This includes conducting public consultations, allowing residents to express their concerns, and considering the local knowledge and expertise that can inform project design.
- Building Capacity:** Education and capacity-building initiatives can empower communities to take an active role in energy management. Training programs can equip community members with the technical skills needed to operate and maintain renewable energy systems, fostering local employment opportunities.
- Creation of Community Energy Cooperatives:** Community energy cooperatives enable residents to collectively invest in, own, and manage renewable energy projects. These cooperatives often operate on the principle of shared benefits, allowing members to reap the rewards of their investments while strengthening community ties.

On the other side, by integrating decentralized renewable energy systems and fostering community participation, this holistic approach holds the potential to promote socio-economic resilience in several ways such as, the development, installation, and maintenance of renewable energy projects can create local jobs, reducing unemployment rates and stimulating economic activity within the community. Localized energy

production can reduce reliance on imported fossil fuels, providing communities with more control over their energy sources and prices. This independence can shield them from global energy market volatility and enhance local economic stability. Also, communities can leverage local RES to drive sustainable economic development by attracting clean-tech businesses and investments. Renewable energy projects can serve as anchor initiatives, stimulating growth in related sectors such as energy efficiency, sustainable agriculture, and green building. Access to affordable and reliable energy is essential for improving the quality of life in communities. By meeting local energy needs with renewable sources, communities can enhance their livelihoods, improve public services (such as healthcare and education), and create vibrant local economies.

Generally, proposing a holistic approach to governance that incorporates decentralized energy systems and community participation underscores the transformative potential of renewable energy sources (RES). This framework not only addresses immediate energy needs but also empowers local communities by providing them with control over energy resources, fostering economic development, and promoting socio-economic resilience. By embracing such inclusive governance models, societies can pave the way for a sustainable energy transition that benefits both people and the planet.

6. Sustainable Energy Future

Energy governance refers to the structures, processes, and regulations through which energy policies are formulated and implemented. These governance frameworks significantly influence how energy resources are allocated, how energy systems operate, and how stakeholders, including governments, businesses, and communities, interact within the energy landscape. Traditionally, energy governance paradigms have often focused on centralized decision-making, prioritizing economic growth, fossil fuel dependency, and large-scale infrastructure development. However, as global energy demands and environmental challenges evolve, there is a growing recognition of the need to rethink and transform these paradigms.

The shift towards sustainability in energy governance involves adopting principles that emphasize the long-term viability of energy systems. New governance frameworks must prioritize the reduction of emissions through the adoption of low-carbon energy sources, energy efficiency measures, and sustainable transportation options. Sustainable governance promotes responsible use of energy resources, encouraging practices such as energy conservation, recycling, and the use of renewable resources. Also, decision-making processes should include comprehensive assessments of the environmental impacts of energy technologies throughout their entire lifecycle, from production to disposal. Inclusivity refers to the involvement of diverse stakeholders in energy governance processes, ensuring that all voices are heard and considered. On the other side, key aspects of inclusive governance include:

- **Equitable Energy Access:** Effective governance frameworks should aim to provide equitable access to energy for all communities, particularly underserved and marginalized populations. This can help address energy poverty and ensure that everyone benefits from advancements in energy technology.
- **Stakeholder Engagement:** Continuous engagement with a broad range of stakeholders, including local communities, indigenous groups, civil society organizations, and the private sector, is essential. Collaborative governance models can facilitate dialogue and cooperation among these groups, leading to informed decision-making that reflects community needs and aspirations.
- **Participatory Processes:** Governance frameworks should incorporate participatory mechanisms that allow communities to actively participate in energy planning and decision-making. This can include public consultations, community-driven projects, and the establishment of energy cooperatives.

Shifting towards a governance paradigm that emphasizes sustainability and inclusivity can enhance the resilience of energy systems. Communities that are engaged in energy governance are better equipped to adapt to changes and challenges, such as climate impacts or shifts in energy technology. Emphasizing sustainability and inclusivity fosters innovation in clean energy technologies and practices. Collaborative governance encourages partnerships among public and private sectors, research institutions, and communities, leading to the development of innovative solutions to complex energy challenges. Also, sustainable and inclusive governance frameworks enable communities to take charge of their energy resources. By prioritizing local energy generation through renewables, communities can keep energy investments local, create jobs, and foster economic development while reducing energy costs. This shift in governance aligns with international sustainability objectives, such as the United Nations Sustainable Development Goals (SDGs). It supports the

transition to affordable, reliable, sustainable, and modern energy for all (SDG 7) and contributes to efforts to combat climate change (SDG 13). A focus on sustainability encourages holistic decision-making that considers the interdependencies between energy, water, land use, and social factors. This integrated approach leads to more comprehensive policies that create synergies across sectors and enhance overall community well-being.

While the findings advocating for this paradigm shift highlight the potential benefits, several challenges may arise. In this regards, institutions and stakeholders entrenched in traditional energy models may be resistant to adopting new governance structures and practices. Transforming energy governance to prioritize sustainability and inclusivity requires reconfiguring existing systems, which can be complex and resource-intensive. Achieving consensus among diverse stakeholders with different interests can be challenging. Effective facilitation and negotiation skills will be necessary to align priorities and expectations. Generally, advocating for a shift in energy governance paradigms that prioritizes sustainability and inclusivity presents a pathway toward a more sustainable energy future. This approach fosters resilience, innovation, empowerment, and alignment with global sustainability goals. However, to realize these benefits, stakeholders must actively engage in overcoming the challenges inherent in such a transformation, paving the way for energy systems that are not only effective but also equitable and just for all.

7. Suggested Polices

Policies collectively aim to create an enabling environment that promotes the widespread adoption of renewable energy sources while ensuring sustainability, security, and equity for all stakeholders involved. Implementing strategies can help realize the potential of RES to transform energy systems and empower local communities, paving the way for a more sustainable energy future. Some suggested policies that could facilitate the integration of renewable energy sources (RES) into contemporary energy governance frameworks, thereby enhancing sustainability, security, and equity in energy systems:

1. Incentive Programs for Renewable Energy Adoption

- **Tax Credits and Subsidies:** Implement financial incentives such as tax credits, rebates, or direct subsidies for individuals and businesses that invest in renewable energy technologies (e.g., solar panels, wind turbines).
- **Feed-in Tariffs (FiTs) and Power Purchase Agreements (PPAs):** Establish guaranteed pricing structures for energy producers that sell renewable energy back to the grid, encouraging more rapid adoption of RES.

2. Regulatory Reforms

- **Streamlined Permitting Processes:** Simplify and expedite the permitting process for renewable energy projects to reduce bureaucracy and enhance project timelines.
- **Grid Access Regulations:** Develop regulations that ensure fair and non-discriminatory access to the energy grid for small-scale and community-based renewable energy producers.

3. Stakeholder Engagement Frameworks

- **Community Energy Planning:** Create programs that actively involve local communities in the energy planning process, allowing them to identify their specific energy needs and priorities.
- **Multistakeholder Advisory Panels:** Establish advisory panels that include representatives from government, industry, academia, and civil society to provide input on renewable energy policies and governance models.

4. Energy Efficiency Standards and Codes

- **Building Codes:** Update building codes to incorporate standards for energy efficiency, promoting the use of renewable energy systems in new construction and major renovations.
- **Energy Use Benchmarking:** Mandate energy benchmarking for commercial and industrial buildings to encourage transparency in energy consumption and promote energy efficiency upgrades.

5. Cross-Sector Collaboration Initiatives

- **Interagency Coordination:** Facilitate collaboration between various government agencies, such as energy, environment, and transportation, to create cohesive policies that support renewable energy integration.

- **Public-Private Partnerships (PPPs):** Encourage partnerships between government entities and private companies to leverage resources and expertise in developing renewable energy projects.

6. Financial Mechanisms for RES Development

- **Green Bonds:** Promote the issuance of green bonds to raise capital for renewable energy projects, providing investors with a sustainable investment opportunity while funding necessary infrastructure.
- **Low-Interest Loans:** Offer low-interest loans or financing options for community-based renewable energy projects to mitigate the upfront costs for local entities.

7. Educational and Capacity-Building Programs

- **Training and Certification Programs:** Develop training programs to build local workforce capacity in the installation and maintenance of renewable energy technologies.
- **Public Awareness Campaigns:** Launch campaigns to educate the public about the benefits of renewable energy and energy conservation practices to encourage greater community involvement and support.

8. Monitoring and Evaluation Frameworks

- **Performance Metrics:** Establish clear metrics to assess the effectiveness of renewable energy policies and governance models, ensuring transparent reporting and accountability.
- **Feedback Mechanisms:** Implement systems for collecting feedback from stakeholders on the effectiveness of governance strategies, allowing for continual adaptation and improvement.

9. Decentralized Energy Systems Support

- **Microgrid and Community Solar Initiatives:** Support the development of microgrids and community solar projects that empower local communities to manage their energy resources effectively.
- **Utility Regulation Revisions:** Revise utility regulations to accommodate decentralized energy production and storage solutions, promoting local energy resilience.

10. Equity and Inclusion Policies

- **Equitable Access Programs:** Develop targeted programs to ensure low-income and marginalized communities have access to renewable energy opportunities and benefits, such as subsidies for solar installations or energy efficiency upgrades.
- **Just Transition Plans:** Create plans that outline how to transition workers from fossil fuel industries to jobs in renewable energy sectors, ensuring that socio-economic impacts are addressed equitably.

8. Conclusion

In conclusion, this paper demonstrates the critical role that renewable energy sources (RES) can play in reshaping contemporary energy governance frameworks to improve sustainability, security, and equity within energy systems. As the world confronts pressing environmental challenges and increasing energy demands, the integration of RES such as solar, wind, hydro, and biomass emerges as a viable solution to mitigate climate change and reduce dependence on fossil fuels. Through the exploration of diverse case studies, the research reveals innovative governance models that effectively facilitate the adoption of RES, emphasizing the importance of policy reforms, stakeholder engagement, and technological advancements in promoting efficiency and transparency in energy management. Moreover, the paper highlights the necessity of addressing regulatory barriers and fostering cross-sector collaboration to overcome existing challenges in the transition toward sustainable energy systems. By advocating for a holistic approach that incorporates decentralized energy systems and actively involves local communities, this research illustrates the potential of RES not only to meet energy needs but also to empower communities and bolster socio-economic resilience. Ultimately, the findings underscore the need to shift prevailing energy governance paradigms toward frameworks that prioritize sustainability and inclusivity. Such a transformation is essential for paving the way toward a more sustainable energy future, where equitable access to clean energy is not merely an aspiration but a reality for all communities. This calls for collective action from policymakers, industry stakeholders, and civil society to embrace innovative solutions and collaborative strategies, ensuring that the transition to renewable energy is inclusive, just, and beneficial for generations to come.

Nomenclature

The authors used OpenAI's ChatGPT exclusively for grammar checks and writing improvements while preparing this work. After utilizing this tool, they carefully reviewed and edited the content as needed, taking full responsibility for the final publication.

References

- [1] J. Caputo, Sustainable forest biomass: promoting renewable energy and forest stewardship, Citeseer2009.
- [2] K. Kaygusuz, Energy and environmental issues relating to greenhouse gas emissions for sustainable development in Turkey, *Renewable and Sustainable Energy Reviews*, 13 (2009) 253-270.
- [3] M.J.B. Kabeyi, O.A. Olanrewaju, Sustainable energy transition for renewable and low carbon grid electricity generation and supply, *Frontiers in Energy research*, 9 (2022) 743114.
- [4] N.K. Dubash, A. Florini, Mapping global energy governance, *Global policy*, 2 (2011) 6-18.
- [5] M. Bazilian, S. Nakhooda, T. Van de Graaf, Energy governance and poverty, *Energy Research & Social Science*, 1 (2014) 217-225.
- [6] T. Van de Graaf, J. Colgan, Global energy governance: a review and research agenda, *Palgrave Communications*, 2 (2016) 1-12.
- [7] F.Y. Fu, M. Alharthi, Z. Bhatti, L. Sun, F. Rasul, I. Hanif, W. Iqbal, The dynamic role of energy security, energy equity and environmental sustainability in the dilemma of emission reduction and economic growth, *Journal of Environmental Management*, 280 (2021) 111828.
- [8] S. Gustafsson, J. Ivner, J. Palm, Management and stakeholder participation in local strategic energy planning—Examples from Sweden, *Journal of cleaner production*, 98 (2015) 205-212.
- [9] A. Dunsire, Holistic governance, *Public Policy and Administration*, 5 (1990) 4-19.



IV.Environmental protection and decarbonization

Examining PAHs Presence in Novi Sad's Ambient Air: Sources and Assessment

*Maja Brborić^a, Branka Nakomčić Smaragdakis^a, Damir Šljivac^b, Saša Pavlović^c,
Evangelos Bellos^d*

^a *University of Novi Sad, Faculty of Technical Sciences, Department of Environmental Engineering and Occupational Safety and Health, Novi Sad, RS, majabrboric@uns.ac.rs, nakomcic@uns.ac.rs,*

^b *Faculty of Electrical Engineering, Computer Science and Information Technology, Osijek, HR, damir.sljivac@ferit.hr*

^c *University of Niš, Faculty of Mechanical Engineering University of Niš, Niš, RS, sasa.pavlovic@masfak.ni.ac.rs*

^d *Department of Mechanical Engineering, School of Engineering, University of West Attica, Athens, GR, bellose@uniwa.gr*

Abstract: Air pollution poses a significant global health risk, with severe consequences for respiratory and cardiovascular diseases, particularly among vulnerable populations facing heightened exposure. The respiratory system is particularly susceptible to pollutants, resulting in various adverse health effects. Ambient air monitoring for benzo(a)pyrene (B(a)P) was conducted at four sites in Novi Sad throughout 2020, representing diverse environmental conditions. Sampling and analytical methods adhered to standardized protocols. B(a)P concentrations exceeded prescribed limits at most sites, with combustion processes and traffic emissions identified as primary pollution sources. Principal component analysis highlighted the dominance of combustion-related pollution, particularly during winter. Hierarchical cluster analysis revealed distinct pollution patterns across sites, with areas less burdened by traffic and combustion showing lower B(a)P levels. The study underscores the urgent need to mitigate local pollution sources, especially combustion and traffic emissions, to safeguard public health. The findings provide crucial baseline data for future monitoring efforts and highlight the importance of addressing air pollution for sustainable development and climate change mitigation.

Keywords: PAHs, benzo(a)pyrene; air pollution; sources identifications, assessment

1. Introduction

Air pollution is recognized as a significant global health risk, with severe consequences for respiratory and cardiovascular diseases, particularly among vulnerable populations facing heightened exposure [1,2]. The respiratory system is particularly susceptible to pollutants, leading to various adverse health effects [3,4]. According to the World Health Organization (WHO), nearly seven million deaths are attributed to air pollution each year, with 99% of the world's population breathing air that exceeds WHO guideline limits [1]. Vulnerable populations, including children, the elderly, and individuals with pre-existing health conditions, are particularly susceptible to the adverse effects of air pollution [5]. The respiratory system serves as the primary entry point for airborne pollutants, leading to a range of health issues, including inflammation, oxidative stress, and decreased lung function [6,7]. Long-term exposure to polluted air is associated with the development of respiratory diseases such as asthma, chronic obstructive pulmonary disease (COPD), and lung cancer [8,9,10].

Polycyclic aromatic hydrocarbons (PAHs) are recognized as a group of persistent organic pollutants that are formed through the incomplete combustion of organic materials [11]. These contaminants are ubiquitous in urban environments and have been associated with significant adverse health effects, particularly concerning respiratory and cardiovascular diseases [12]. Among the PAHs, benzo(a)pyrene (BaP) is classified as a probable human carcinogen and is frequently monitored due to its toxicity and potential for bioaccumulation [13]. The presence of PAHs in the environment can arise from various sources, including vehicular emissions, industrial activities, and residential heating [14]. These pollutants can enter the air, water, and soil, subsequently accumulating in the environment and biota [12]. Understanding the distribution and behavior of PAHs in the environment is crucial for assessing their impact on human health and ecosystems.

Novi Sad, the second largest city in Serbia, is confronted with air quality challenges due to intense traffic, industrial activities, and residential heating [15,16]. The presence of PAHs in the ambient air of Novi Sad may have serious health implications for the local population. However, limited studies have been conducted to examine the presence and sources of PAHs in this city [17,18].

Numerous studies have been conducted globally to evaluate the presence of PAHs in different environmental media. For instance, a study in China reported that concentrations of BaP in urban air ranged from 0.3 to 15.7 ng/m³, with higher levels observed during winter months due to increased heating activities [19]. In Italy, research indicated that BaP concentrations in soil varied from 0.01 to 1.5 mg/kg, with elevated levels near industrial sites and roadways [20]. A study in Japan found that BaP concentrations in river sediments ranged from 0.01 to 1.2 mg/kg, with higher concentrations detected in urban areas [21].

The primary objective of this research is to assess the presence and concentrations of polycyclic aromatic hydrocarbons (PAHs), specifically benzo(a)pyrene (BaP), in the ambient air of Novi Sad. This study aims to identify the main sources of these pollutants and evaluate their potential health risks to the local population. By employing multivariate techniques, the research will provide insights into the potential sources and distribution of PAHs in environmental. Additionally, the study seeks to contribute to the understanding of the impact of PAHs on public health and inform strategies for effective air quality management and pollution mitigation in urban environments.

2. Materials and methods

2.1. Sampling sites

Twenty-four-hour measurements of benzo(a)pyrene (B(a)P) were conducted during 2020 at four sampling sites in Novi Sad, a highly industrialized and populated city in Serbia with approximately half a million inhabitants. The sampling points were selected to represent different environmental conditions, including monitoring sites classified by the 2008/50/EC Directive as urban and suburban, traffic and background stations (Figure 1) [22]. Air sampling for the determination of B(a)P concentrations was carried out at the following representative measuring points:

- MM11-Kač (MZ "Kač", Kralja Petra I, no. 2 and Elementary School "Đura Jakšić", Kralja Petra I, no. 9, Kač) ("suburban traffic")
- MM2-NS1 (JKP "Vodovod i kanalizacija", Jiričekova 2, Novi Sad) ("urban background")
- MM3-NS2 (Corner of Rumenačke and Bulevar Jaše Tomić, Novi Sad (PM10)) ("urban traffic")
- MM4-SK (Sremska Kamenica, SOS Children's Village "Dr. Milorad Pavlović", Sremska Kamenica 1-14, Novi Sad) ("suburban background")

The sampling was conducted over a one-year period in accordance with the standard SRPS EN 12341:2015 and processed by experts from the Center for Hygiene and Human Ecology of the Institute of Public Health of Vojvodina.

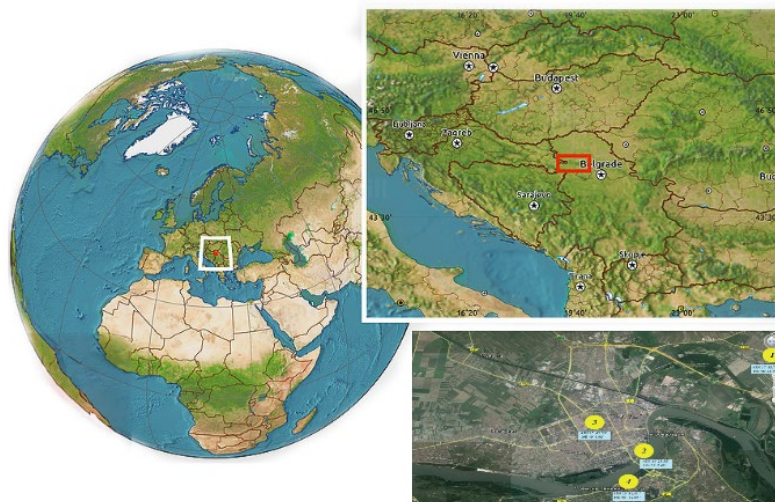


Figure 1. Measuring points for B(a)P sampling in the City of Novi Sad during 2020

2.2. Sampling and analytical methods

The concentration of benzo[a]pyrene (B[a]P) pollutants in the air was determined using a variety of air sampling equipment, including the Sven Leckel LVS3 and SEQ 47/50-RV models, provided by Comde-Derenda GmbH. The methodology adhered to the standards outlined in SRPS EN 12341:2015, Section 5.1, for air pollutant concentration determination, while SRPS EN 15549:2010 was utilized for specific concentration measurements of B[a]P. A gas chromatograph coupled with a mass spectrometer (GC/MS) served as the analytical instrument for quantifying these pollutants. This method ensured precise detection and quantification of B[a]P in atmospheric samples, offering reliable data for subsequent analyses.

2.3. Data Analyses

Data concerning B[a]P concentrations, collected from four monitoring sites over a one-year period, were subjected to basic statistical analysis. Descriptive statistics, including mean, median, standard deviation, standard error of the mean, and range (minimum and maximum values), were calculated to summarize the data set. The standard deviation provided insight into data variability, while the standard error indicated the reliability of the sample mean. For values falling below the detection limit, a surrogate value equal to half of this limit was assigned.

Advanced statistical analyses were conducted to discern patterns among the sampling sites and to infer possible emission sources. Hierarchical cluster analysis (HCA) and principal component analysis (PCA) were employed on the monthly average B[a]P data, utilizing Varimax rotation and Kaiser normalization to enhance interpretability. These analyses were performed using IBM SPSS Statistics 25 software. The application of PCA and HCA facilitated the visualization of data, revealing clusters of sites with similar pollution characteristics, which may indicate shared emission sources. The methodologies and results presented in this study provide a robust framework for identifying priority areas requiring further investigation, thereby informing effective decision-making and guiding remedial actions.

3. Results and discussion

During 2020, at the monitoring locations in the City of Novi (MM1-Kač, MM2-NS1, MM3-NS2, and MM4-SK), the average daily concentration of benzo(a)pyrene (B[a]P) in suspended PM10 particles was determined. The values ranged from 0.22 ng/m³ at site MM4 to 19.52 ng/m³ at site MM1. Monthly concentrations of B[a]P, depicted in Figure 1, varied from 0.49 ng/m³ at site MM4 to 7.993 ng/m³ at site MM1.

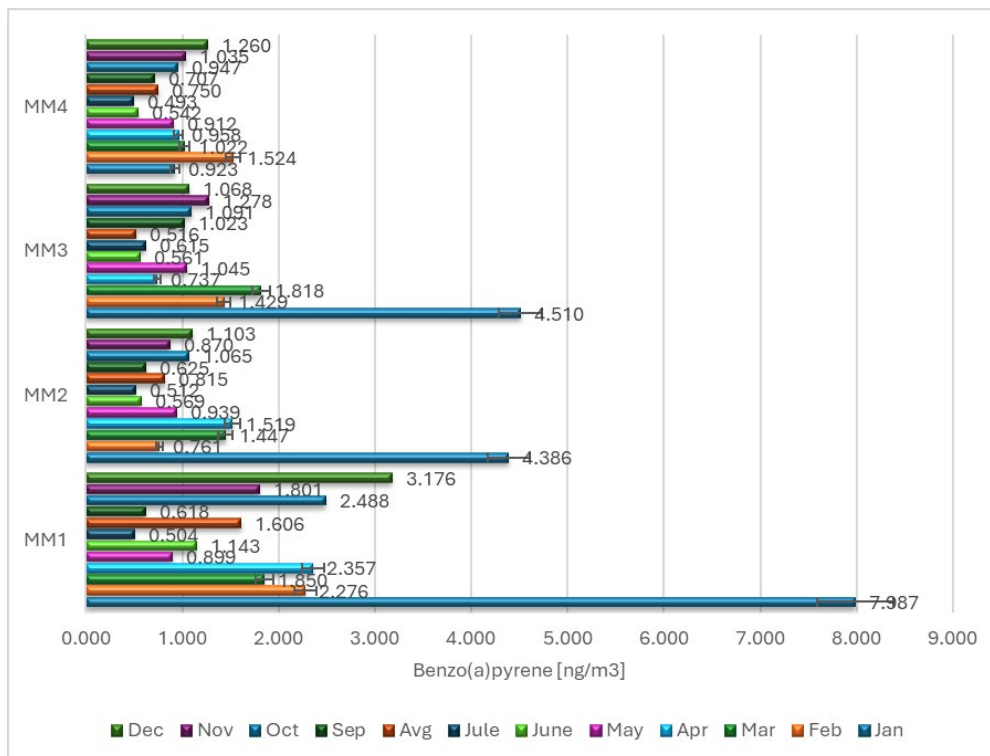


Figure 2. B(a)P air concentrations during 2020 in Novi Sad

The average monthly concentrations for MM1, MM2, and MM3 were found to be 2.23 ng/m³, 1.22 ng/m³, and 1.31 ng/m³, respectively. These values exceed the target annual level of 1 ng/m³ for total polycyclic aromatic hydrocarbons in the air, as stipulated by the relevant standards. At these measuring sites over the one-year period, the minimum daily concentration of polycyclic aromatic hydrocarbons, expressed as B[a]P on a monthly level, was below the detection limit of the analytical method employed (<0.5 ng/m³), while the maximum values recorded were 7.99 ng/m³, 4.39 ng/m³, and 4.51 ng/m³, respectively. The site MM4-SK was the only location where the prescribed average B[a]P concentration in the air (mean = 0.92 ng/m³) was not exceeded.

3.1. Identification of pollution sources

Principal Component Analysis (PCA) with Varimax rotation was employed to determine the quantitative contribution of various benzo(a)pyrene (BaP) sources, yielding highly robust results. Three principal components, accounting for 99.56% of the total variance, are depicted in Figure 3. The first principal component (PC1) explained approximately 40.85% of the variance, with significant loadings observed at site MM3, indicating contributions from **combustion processes**. The second principal component (PC2) accounted for about 38.64% of the variance, with high loadings at site MM1, suggesting **traffic emissions** resulting from the combustion of diesel and gasoline in motor vehicles. The third principal component (PC3) explained approximately 20.07% of the variance, with substantial loadings at site MM2, pointing to sources related to **industrial activities**. Site MM4 exhibited moderate loadings across all factors.

Given that Novi Sad, an urban region with substantial traffic and combustion processes, was included in the study, it can be confirmed that polycyclic aromatic hydrocarbons (PAHs) are produced from both pyrolytic and pyrolysis emission processes. The dominance of pollution sources is evident, particularly within the expected city zones. The presence of BaP, one of the most toxic PAHs, is pervasive throughout Novi Sad, which is concerning due to its carcinogenic, mutagenic, and teratogenic effects on the human population [23].

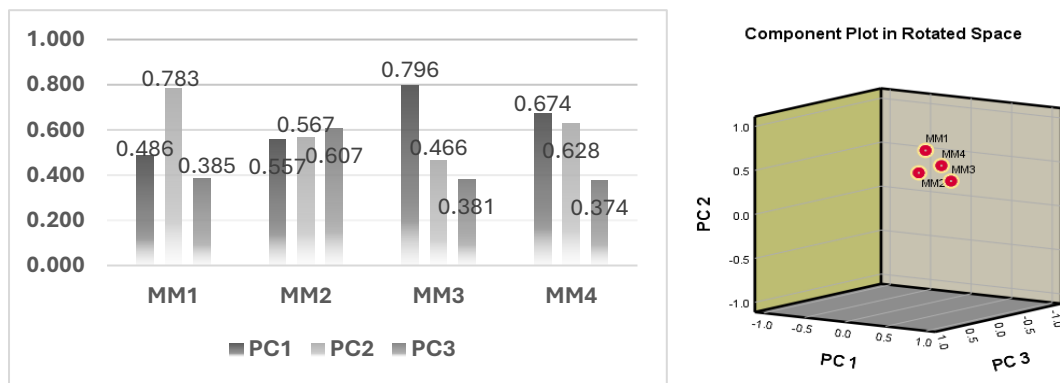


Figure 3. Principal component analysis after Varimax rotation for B(a)P

From a scientific standpoint, the results of the PCA highlight the complexity of BaP pollution in urban environments like Novi Sad. The identification of distinct sources of BaP, such as traffic emissions and biomass burning, underscores the need for targeted mitigation strategies. Traffic-related emissions are a significant contributor, suggesting that improvements in vehicle emissions standards and the promotion of public transportation could reduce BaP levels. Furthermore, the contribution from biomass burning suggests a need to address residential heating practices and promote cleaner alternatives. The findings highlight the critical importance of continuous monitoring and source apportionment studies to guide effective policy measures.

3.2. Identification of hot-spot

The results of the cluster analysis are graphically represented as a dendrogram, illustrating the grouping of sampling sites (Figure 4). The analysis identified two distinct clusters: the first cluster comprises sampling sites MM1, MM2, and MM3, while the second cluster consists solely of the MM4 site, distinguished by reduced concentrations of benzo(a)pyrene (BaP). The first group of locations is characterized by a significant presence of BaP in the ambient air, predominantly during the winter months, when combustion processes are most intense. This includes emissions from individual heating systems at MM1 and substantial contributions from the "NIS Gazprom Neft" Oil Refinery, its production facilities, oil and gas processing, transportation of

oil derivatives, and a nearby cogeneration system affecting MM2 and MM3. These factors collectively result in heightened BaP concentrations at these sites.

Conversely, MM4, located in Sremski Karlovci, is identified as less impacted by BaP emissions. This locality benefits from reduced traffic compared to the city center sites (MM2 and MM3) and fewer individual heating sources compared to MM1, making it a comparatively safer and less polluted area concerning BaP emissions. The findings of this cluster analysis provide valuable insights into the spatial distribution of air pollution sources and highlight the potential health risks associated with BaP exposure in urban environments.

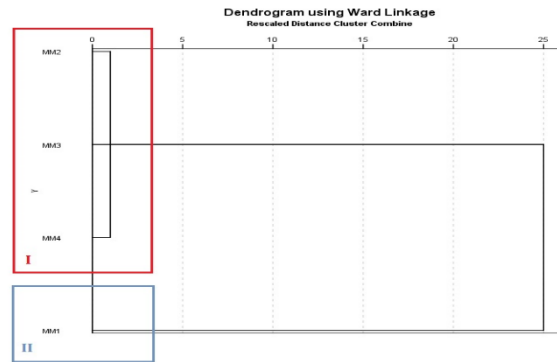


Figure 4. Dendrogram of monthly B(a)P air concentrations

Correlation relations between benzo(a)pyrene (BaP) concentrations at selected monitoring sites in Novi Sad were assessed using Pearson's correlation analysis.

Table 1: Pearson correlation coefficients for benzo(a)pyrene concentrations at selected monitoring sites in Novi Sad

Pearson Correlation				
	MM1	MM2	MM3	MM4
MM1	1	.948**	.901**	.957**
MM2	.948**	1	.938**	.959**
MM3	.901**	.938**	1	.964**
MM4	.957**	.959**	.964**	1

** . Correlation is significant at the 0.01 level (2-tailed).

The results revealed extremely high mutual correlations, indicating a strong connection in the distribution of BaP across the urban area. Such correlations suggest that the emission sources of BaP are likely similar or that the atmospheric conditions affecting its dispersion are consistent. For instance, elevated BaP levels are frequently associated with common sources such as traffic emissions and industrial activities (Ravindra et al., 2008). When correlation coefficients exceeding 0.90 are recorded, it implies that these locations may experience comparable pollution levels due to shared emission sources or similar meteorological conditions. Identifying these high correlations can help in targeting specific areas for interventions to reduce BaP exposure, thereby informing regulatory measures aimed at improving air quality and protecting public health.

4. Conclusion

This study provides a comprehensive assessment of the presence and sources of polycyclic aromatic hydrocarbons (PAHs), specifically benzo(a)pyrene (BaP), in the ambient air of Novi Sad. Through the application of advanced analytical techniques and statistical analyses, including Principal Component Analysis (PCA) and Hierarchical Cluster Analysis (HCA), the study identifies key emission sources contributing to air pollution in the region. The PCA revealed that combustion processes, traffic emissions, and industrial activities are the primary contributors to BaP concentrations, with site-specific variations observed. The cluster analysis delineated two distinct groups of sampling sites, highlighting the spatial distribution of pollution sources. The urban locations, particularly MM1, MM2, and MM3, exhibited elevated BaP levels, primarily due to industrial activities, vehicular emissions, and increased heating during winter. In contrast, the MM4 site in Sremski

Karlovci demonstrated lower BaP concentrations, underscoring the influence of reduced anthropogenic activities.

These findings emphasize the significant impact of urbanization and industrialization on air quality and the associated health risks posed by PAHs. The study underscores the need for targeted regulatory measures and pollution control strategies to mitigate BaP emissions and improve air quality in Novi Sad. Continuous monitoring and comprehensive assessment of PAH sources are crucial for informed decision-making and effective environmental management in urban areas.

Acknowledgements

This research has been supported by the Ministry of Science, Technological Development and Innovation (Contract No. 451-03-65/2024-03/200156), the Faculty of Technical Sciences, University of Novi Sad through project “Scientific and Artistic Research Work of Researchers in Teaching and Associate Positions at the Faculty of Technical Sciences, University of Novi Sad” (No. 01-3394/1), and by the Science Fund of the Republic of Serbia, grant number 6707, REMote WATER quality monitoRING anD IntelliGence – REWARDING.

References

- [1] World Health Organization. (2021). Air quality and health. Retrieved from WHO website.
- [2] Brook, R. D., Rajagopalan, S., Pope, A., et al., Particulate matter air pollution and cardiovascular disease: An update to the scientific statement from the American Heart Association, *Circulation*, 121 (2010), 21, pp. 2331-2378.
- [3] Pope, C. A., III, Burnett, R. T., Thun, M. J., et al., Lung cancer, cardiopulmonary mortality, and long-term exposure to fine particulate air pollution, *JAMA*, 287 (2009), 9, pp. 1132-1141.
- [4] Kelly, F. J., & Fussell, J. C., Air pollution and public health: Emerging hazards and improved understanding of risk, *Environmental Geochemistry and Health*, 37 (2015), 4, pp. 631-649.
- [5] Andersen, Z. J., Bonnelykke, K., Hvidberg, M., Jensen, S. S., Ketzel, M., Loft, S., et al., Long-term exposure to air pollution and asthma hospitalisations in older adults: A cohort study, *Thorax*, 67 (2012), pp. 6–11.
- [6] Gowers, A. M., Cullinan, P., Ayres, J. G., Anderson, H. R., Strachan, D. P., Holgate, S. T., et al., Does outdoor air pollution induce new cases of asthma? Biological plausibility and evidence; a review, *Respirology Carlton, Vic*, 17 (2012), pp. 887–898.
- [7] Wang, M., Aaron, C. P., Madrigano, J., Hoffman, E. A., Angelini, E., Yang, J., et al., Association between long-term exposure to ambient air pollution and change in quantitatively assessed emphysema and lung function, *JAMA*, 322 (2019), pp. 546–556.
- [8] Guarnieri, M., & Balmes, J. R., Outdoor air pollution and asthma, *Lancet*, 383 (2014), pp. 1581–1592.
- [9] Liu, S., Lim, Y. H., Pedersen, M., et al., Long-term air pollution and road traffic noise exposure and COPD: the Danish Nurse Cohort, *European Respiratory Journal*, 58 (2021a), 6, pp. 2004594.
- [10] Liu, S., Lim, Y. H., Pedersen, M., et al., Long-term exposure to ambient air pollution and road traffic noise and asthma incidence in adults: The Danish Nurse cohort, *Environmental International*, 152 (2021b), pp. 106464.
- [11] Samanta, S. K., Singh, O. V., & Jain, R. K., Polycyclic aromatic hydrocarbons: Environmental pollution and bioremediation, *Trends in Biotechnology*, 20 (2002), 6, pp. 243-248.
- [12] Abdel-Shafy, H. I., & Mansour, M. S., A review on polycyclic aromatic hydrocarbons: Source, environmental impact, effect on human health and remediation, *Egyptian Journal of Petroleum*, 25 (2016), 1, pp. 107-123.
- [13] IARC (International Agency for Research on Cancer), IARC Monographs on the Evaluation of Carcinogenic Risks to Humans: Volume 92. Some Non-heterocyclic Polycyclic Aromatic Hydrocarbons and Some Related Exposures, Lyon: IARC, 2010.
- [14] Ravindra, K., Sokhi, R., & Van Grieken, R., Atmospheric polycyclic aromatic hydrocarbons: Source attribution, emission factors and regulation, *Atmospheric Environment*, 42 (2008), 13, pp. 2895-2921.
- [15] Jovanović, M., Đurić, M., & Vuković, M., Air pollution in Novi Sad: Current state and future challenges, *Environmental Monitoring and Assessment*, 190 (2018), 2, pp. 1-14.
- [16] Šuša, T., Šešlija, S., & Stanković, M., Assessment of air quality in Novi Sad: A case study of PM10 and PM2.5, *Atmospheric Pollution Research*, 11 (2020), 1, pp. 1-10.
- [17] Marković, M., Savić, S., & Vuković, M., Polycyclic aromatic hydrocarbons in urban air: A case study from Novi Sad, Serbia, *Environmental Science and Pollution Research*, 26 (2019), 12, pp. 12156-12166.
- [18] Đurić, M., Jovanović, M., & Stanković, M., Analysis of air quality in Novi Sad: Focus on PAHs, *Journal of Environmental Management*, 287 (2021), pp. 112307.
- [19] Liu, Y., Tao, S., Dou, H., Zhang, T., Zhang, X. L., & Dawson, R., Exposure of traffic police to polycyclic aromatic hydrocarbons in Beijing, China, *Chemosphere*, 66 (2007), 10, pp. 1922-1928.

- [20] Malawska, M., & Wiłkomirski, B., An analysis of soil and plant (*Taraxacum officinale*) contamination with heavy metals and polycyclic aromatic hydrocarbons (PAHs) in the area of the railway junction Ława Główna, Poland, *Water, Air, and Soil Pollution*, 127 (2001), 1-4, pp. 339-349.
- [21] Ohlenbusch, G., Zwiener, C., Meckenstock, R. U., & Nitschke, L., Identification and quantification of polar naphthalene transformation products in contaminated groundwater of a former gas plant site by liquid chromatography-electrospray ionization tandem mass spectrometry, *Environmental Science & Technology*, 36 (2002), 20, pp. 4476-4482.
- [22] EC - European Council, 2008/50/EC Directive on ambient air quality and cleaner air for Europe, 2008.
- [23] Brborić, M., Vrana, V., Radonić, J., Vojinović Miloradov, M., & Turk Sekulić, M., Spatial distribution of PAHs in riverbed sediments of the Danube River in Serbia: Anthropogenic and natural sources, *Journal of the Serbian Chemical Society*, 84 (2019), 12, pp. 1439–1453.

Improving Flow Homogeneity in the Chambers of the Electrostatic Precipitator of a 350 MW Unit and Reduction of Particulate Matter Emissions by Modifying the Turning and Damping Elements

*Milić D. Erić^a, Zoran Marković^b, Predrag Stefanović^c, Aleksandar Milićević^d
Ivan Lazović^e*

^a*Vinca Institute of Nuclear Sciences – National Institute of the Republic of Serbia - University of Belgrade, RS, milic@vinca.rs*

^b*Vinca Institute of Nuclear Sciences – National Institute of the Republic of Serbia - University of Belgrade, RS, zoda_mark@vinca.rs*

^c*Vinca Institute of Nuclear Sciences – National Institute of the Republic of Serbia - University of Belgrade, RS, pstefan@vinca.rs*

^d*Vinca Institute of Nuclear Sciences – National Institute of the Republic of Serbia - University of Belgrade, RS, amilicevic@vinca.rs*

^e*Vinca Institute of Nuclear Sciences – National Institute of the Republic of Serbia - University of Belgrade, RS, ivan.lazovic@vinca.rs*

Abstract: In order to protect nature, legal regulations on environmental protection are becoming ever stricter. The increasing development of exhaust gas cleaning technologies has led to quick solutions and ever shorter deadlines for the reconstruction and modernization of electrostatic precipitators. This has led to problems in the operation of electrostatic precipitators over a long period of time after reconstruction and to a lower efficiency of the plants. This paper presents the optimization of flue gas flow in the electrostatic precipitator chambers of the 350 MW unit after reconstruction. During the overhaul of the thermal power plant, the distribution of air velocities in the cross-section of the chambers was investigated and the results were used to validate the numerical model. A new conceptual solution was proposed based on the results of several numerical simulations of the flue gas velocity distribution for different configurations of turning and damping elements. The particulate matter concentration was reduced from over 70 mg/Nm³ to a value below 35 mg/Nm³ after the modification and modernization.

Keywords: ESP chamber, Distribution of velocities, Cross-section, Homogeneity of the flow field.

1. Introduction

Electrostatic precipitation is one of the most practical methods for separating coal dust and ash particles from the flue gas stream in thermal power plant boilers. The separation of coal dust and ash particles significantly reduces the negative impact of these waste materials on the ecosystem and human health. Worldwide standards, which are also accepted in this country, require emission limit values (ELV) of less than 50mg/m³, in some European countries even less than 25mg/m³. As the limit values are expected to fall further in the near future, this is the right time to develop acceptable and promising technologies and to develop new energy-efficient technologies to reduce emissions of flue gases and other pollutants (sulphur oxides, nitrogen, ...) [1, 2]

To meet these requirements, it is necessary to simultaneously increase the active surface area of the electrodes, improve the distribution of the flue gases to achieve a uniform distribution profile of the flue gases and reduce the erosive effect of the dust particles, which together increase the volume and weight of the flue gases, or even use a high-frequency high-voltage (HF HV) supply [3] instead of a transformer and diode rectifier (T/R) set. The performance of an electrostatic precipitator is usually determined by the voltage-current (V-I) characteristic, which affects the precipitation efficiency of the electrostatic precipitator and is highly dependent on the calorific value of the coal, the ash content of the coal and the electrical resistance of the ash, which in turn depends on the alkali and sulphur content of the ash [4] by affecting the current when a reverse corona occurs.

As part of the capital overhaul of Unit 2 of the KOSTOLAC-B thermal power plant in 2012, the electrostatic precipitator plant was reconstructed and modernized with the primary aim of keeping the total particulate

matter (PM) concentration at the outlet of the plant below the emission limit value (ELV) of 50 mg/Nm³ (at standard conditions: dry flue gas at standard conditions and an oxygen content of 6%), which was prescribed by national (regulation in force at the time of reconstruction) and European regulations (EU Directive 2001/80/EC) [1, 5].

After completion of the guarantee tests, where the condition that the measured concentration is below the emission limit value is fulfilled, there was an increase in the particle concentration at the outlet of the electrostatic precipitator. The annual reports on periodic testing of emissions from unit B2 for 2015 and 2016 show that the output concentration of particulate matter was well above the permitted value of the ELV. In December 2015, a particulate matter concentration of 118 to 122 mg/Nm³ was measured [6]. Two tests were carried out in 2016: A particulate matter concentration of 110÷115 mg/Nm³ was measured in May and 132÷140 mg/Nm³ in December [7, 8].

TPP Kostolac has made great efforts to improve the operation of the electrostatic precipitator plant and significantly reduce concentrations. In November 2017, concentrations of 75÷79 mg/Nm³ were measured, in 2018 it was 74÷76 mg/Nm³ [9, 10]. In 2019, the concentrations measured were 69÷72 mg/Nm³ and in 2020 66÷70 mg/Nm³ [11-14].

Since the concentration of particulate matter could not be reduced below the emission limit value, the Joint Stock Company Joint Stock Company Elektroprivreda Srbije, Kostolac Thermal Power Plants Branch, conducted a public tender to carry out an analysis of the condition of the electrostatic precipitator, experimental tests of the air flow and a CFD analysis of the flue gas flow in the chambers, on the basis of which the homogeneity of the flow field can be determined and improved in order to increase the efficiency of the electrostatic precipitator.

2. Basic information and analysis of the condition of electrostatic precipitator

The reconstructed electrostatic precipitator consists of two units, each with a chamber divided into four mechanical dedusting zones, the first two of which (zones 1 and 2) are divided into two electrical fields fed by high frequency devices (20 kHz), while fields 3 and 4 are fed by transformer rectifier units of the traditional 50 Hz type. In total, there are 6 independent electric fields in the left chamber and 6 in the right chamber. The basic technical data of the electrostatic precipitator and the design parameters of the unit, boiler, fuel and flue gas at the inlet of the electrostatic precipitator are given below.

Table 1. Project Parameters of Boiler Operation, Quality of Coal and Flue Gas at the Inlet to the ESP TEKO B2

Parameter	Unit	Value
Nominal power of the unit	MW _e	348,5
Nominal steam production of the boiler	t/h	1000
Pressure of the superheated steam	bar	186
Temperature of the superheated steam	°C	540
Lower calorific value of the coal	kJ/kg	6590
Moisture content of the coal	%	44,10
Ash content of the coal	%	23,9
Sulfur content of the coal	%	1,17
Carbon content of the coal	%	20,0
Hydrogen content of the coal	%	1,87
Oxygen and nitrogen content of the coal	%	8,96
<i>Dry flue gas flow for an existing ESP:</i>		
<i>Average coal quality</i>	m ³ /h, suvi	1 442 392
<i>Poorer coal quality</i>		1 506 800
Flue gas temperature: normal/max/min	°C	180/200/150
Particulate matter concentration at the inlet to the ESP (0 °C, 1013 mbar, dry gas with O ₂ =6%): normal/max.	g/Nm ³	67,1/75,6
Particulate matter concentration at the exit of the reconstructed ESP (0 °C, 1013 mbar, dry gas with O ₂ =6%)	mg/Nm ³	≤50
Static pressure drop of the flue gas at the inlet/outlet of the ESP	mbar	≤2,5

The characteristic parameters of the electrostatic precipitator reconstructed in 2012 are: two chambers, 2*4 mechanical zones for ash separation, 12 independent electric fields (Figure 1), 24 separate hoppers for ash collection. The active height of the electric field is 15.5 m, and the active length of the electric field is 16 m

(four dedusting zones of 4 m each). The distance between the electrodes for the gas passage is 400 mm in zones 1 and 2 and 500 mm in zones 3 and 4. In zones 1 and 2 there are $2 \times 20 = 40$ passages for the gas, in zones 3 and 4 $2 \times 16 = 32$ passages. The total area of the collecting electrodes is 35.712 m². The cross-sectional area for the flue gas flow is $2 \times 248 = 496$ m². The maximum velocity of the flue gas in the electric field is 1.8 m, the minimum dwell time in the electric field zone is 9 s [14].

The flow of an incompressible fluid in chambers/channels with changing duct cross-sections (with diffusers and confusers) and in channels with bends and elbows was investigated both for single-phase flows (gas only) and for two-phase systems (gas with particles) and from the point of view of the uniformity of the velocity field behind the diffuser/confuser and the bends/elbows as well as from the point of view of the pressure drop in such ducts, both theoretically and experimentally.

In order to reduce the velocity of the flue gas flow from 17 m/s at the inlet to the diffuser (cross-section 3.5m*9m) to 1.5÷1.8 m/s, the designer of the new filter has created as uniform a velocity distribution as possible in the electrostatic precipitator chamber (cross-section 16.78m*16m) a short flat diffuser with a scattering angle of $2 \times 48^\circ = 96^\circ$ in the horizontal plane and scattering angles of 56° upwards and 54° downwards in the vertical plane of the diffuser.

In the front part of the diffuser there are two horizontal and five vertical turning plates and axially behind them, at a mutual longitudinal distance of 900 mm, three further walls made of perforated plates in the form of vertical plates with circular openings with a relatively large diameter of Ø85 mm. The turning plates divide the flow in the diffuser into smaller scattering angles. The turning plates divide the flow in the diffuser into smaller scattering angles.

To eliminate the vertical component of the flue gas velocities (towards the ceiling/floor of the chamber), there are seven turning plates in the upper half of the diffuser behind the second wall with a length of 155 mm (in the axial direction along the chamber axis) and an angle of -50° (in relation to the vertical), which divert part of the flue gas flow downwards. In the lower half of the diffuser, in front of the third wall, there are 7 turning plates with a length of 155 mm (in the axial direction along the chamber axis) and an angle of $+50^\circ$ (in relation to the vertical), which direct part of the flue gas flow upwards.

Due to their geometry and dimensions, these turning plates only partially eliminate the vertical component of the flue gas velocity (resulting in an uneven velocity profile across the height of the chamber) and significantly increase the intensity of the turbulence, which also has a negative impact on the efficiency of particle matter separation in the electrostatic precipitator. The lateral-horizontal component of the flue gas velocity at the diffuser outlet is not eliminated, resulting in an uneven velocity profile across the width of the chamber.

To equalize the distribution of velocities along the vertical and horizontal sides of the chamber, damping plates are placed in the confuser and turning vanes in the elbow at the outlet of the chamber to eliminate the uneven suction effect of the flue gas fan through the central outlet duct. According to the original documents, the designer did not provide for the installation of turning vanes in the elbow of the exhaust duct.

Between September 2018 and July 2019, the Vinca Institute conducted a study at the Kostolac B thermal power plant entitled "Analysis of the situation and possibilities for increasing the efficiency of the electrostatic precipitator in unit 2" (the first phase of research).

In this study, an analysis of the design values of the basic parameters of the electrostatic precipitator of unit B2 and a comparative analysis of the design and operating parameters of the electrostatic precipitators of thermal power plants on lignite with a capacity of 300÷350 MW in the joint-stock company Electric Power Company of Serbia and TPP Ugljevik were carried out. All electrical parameters in all electrical fields showed stable values during all tests and were in the upper range of the design values.

As part of the study, the velocity distribution in the cross-section of the electrostatic precipitator chamber the was measured. In this measuring section, seven velocities per height were measured in 14 gas passages in each chamber, resulting in a grid of 98 measuring points in total.

During the measurement of the velocity distribution in the cross-section of the electrostatic precipitator chamber, the boiler and unit B2 were not in operation. For this measurement, the flue gas and fresh air fans were switched on with the usual operating parameters for the operation of the plant, but in such a way that an average velocity of $\approx 1 \div 2$ m/s was achieved in the cross-section of the ESP chamber.

The results of the measurement of the velocity distribution in the cross-section of the left and right chambers of the ESP outside the first dedusting zone performed in 2018, indicate an unsatisfactory uniformity of the velocity field. The relative standard deviation of the measured velocities is over 50 % and should be reduced to less than 25 % by this work [15].

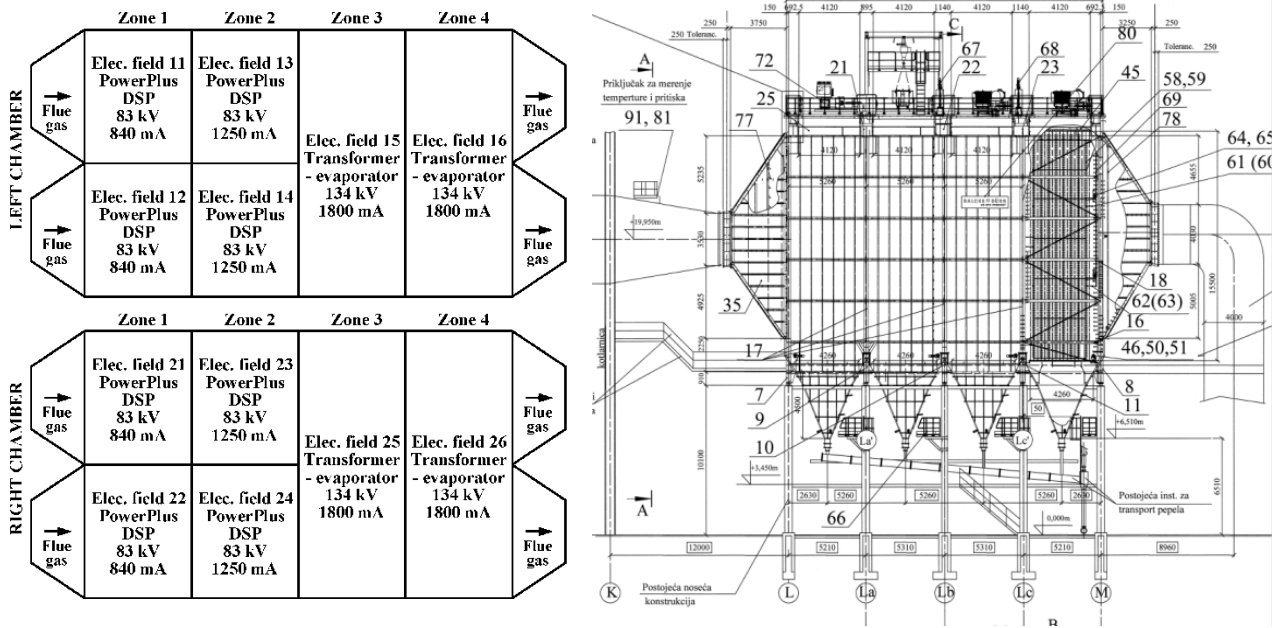


Figure 1. Arrangement of zones and electric fields in the electrostatic precipitator of unit B2

In order to achieve the required high dedusting performance and to increase the uniformity of the flue gas velocity profile in the cross-section of the electrostatic precipitator chambers, the first step was to analyse the existing condition of the inlet/outlet ducts, turning and damping elements in the electrostatic precipitator chambers (the second phase of research).

The turning elements in the chamber under the rotary air heater were reconstructed in 2005. Damage to these elements caused by the erosion of fly ash is regularly repaired as part of the annual repairs (Figure 2).

The condition of the turning and damping elements in the ESP diffuser is shown in Figure 3. In particular, the turning plates at the entrance of the diffuser and the first wall of the damping plates in the electrostatic precipitator diffuser (viewed in the direction of the flue gas flow) show considerable damage due to the erosion of the fly ash, which significantly impairs the flow pattern in the chamber, i.e. there is an uneven distribution of velocities in the cross-section of the electrostatic precipitator chambers.



Figure 2. The condition of the turning elements under the rotary air heater

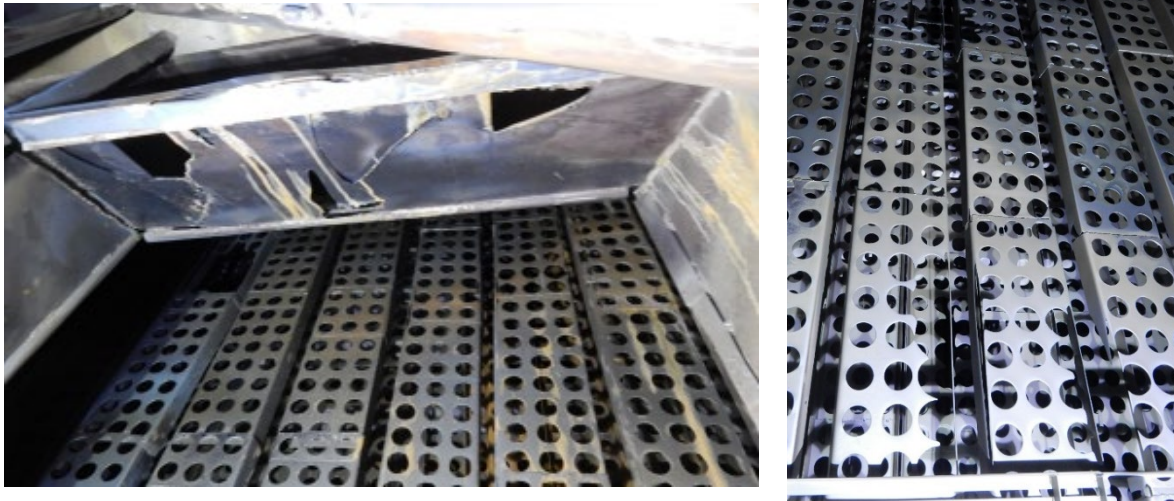


Figure 3. Damage to turning and perforated plates at the diffuser inlet

3. Results of the velocity profile measurements in the ducts upstream of the ESP chambers

The vertical measuring cross-section for measuring the velocity distribution in the cross-section of the flue gas duct in front of the electrostatic precipitator is located behind the wall of the boiler room and in front of the diffuser at the entrance to the electrostatic precipitator chamber. The 6.2 m x 4.95 m cross-section of each flue gas duct is divided into 36 equally sized areas in which the velocities are measured in the middle of each new area (the second phase of research).

Standard methods were used to measure the velocity profile in the flue gas ducts upstream of the electrostatic precipitator: The flue gas flow rate was determined according to the SRPS EN ISO 16911-1 and SRPS ISO 10780 standards, the content of O₂ and CO₂ in the flue gas according to SRPS ISO 12039, the content of CO in the flue gas according to SRPS EN 15058 and the content of H₂O in the flue gas according to SRPS EN 14790. Three tests were carried out for each flue gas duct.

Figure 4.a for Test 1 shows the corresponding 2D velocity distribution in the measurement section of the left flue gas duct upstream of the ESP. The results show that the velocity field in the measurement cross-section is shifted to the left. Figure 4.b for Test 3 shows the 2D velocity distribution in the measurement cross-section of the right flue gas duct upstream of the ESP. It can be seen that the velocity field in the measurement cross-section is shifted to the right. These shifts of the velocity fields to the outside of the flue gas ducts result from the asymmetrical flue gas outlets from the rotary air heater and hardly can be corrected by deflecting plates in the flue gas ducts at the entrance to the ESP chambers.

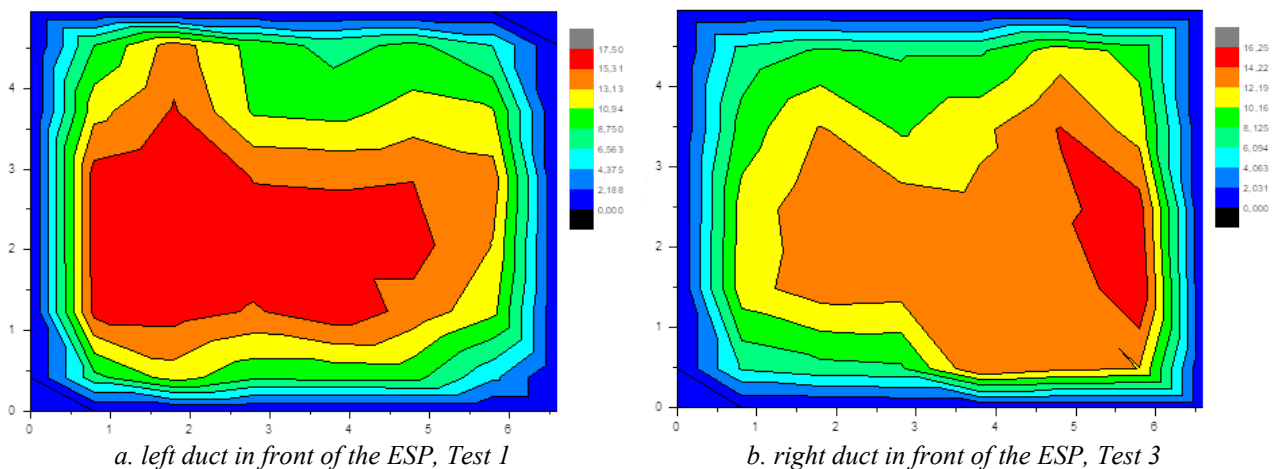


Figure 4. 2D distribution of velocities in the measuring section of the flue gas duct upstream of the ESP

The homogeneity of the flow field in the measured cross-section of the flue gas duct upstream of the ESP chamber was evaluated quantitatively using the following parameters: coefficient of variation CV, linear homogeneity coefficient $\gamma L1$, quadratic homogeneity coefficient $\gamma L2$, dimensionless coefficient of the amount of motion (Boussinesq coefficient Mk), dimensionless coefficient of kinetic energy (Coriolis coefficient Nk). According to the criterion of the coefficient of variation CV ($CV \leq 25\%$), which is the most stringent, the values were between 23.5% and 27.1%, which shows that the homogeneity of the velocities in the measurement section is satisfactory in the limit range. According to other criteria, the homogeneity of the current field is satisfactory [16].

4. CFD analysis of the flow in the chamber and in the ducts upstream and downstream of the ESP chamber

The model represents the complete geometry of the structure of an ESP chamber according to the technical documentation: with an inlet duct at the exit of the boiler room, a system of 5 vertical and 2 horizontal turning plates at the entrance to the diffuser, 3 walls with perforated plates in the diffuser, a chamber with 4 dedusting zones : in the first two zones with 2*20 gas passages forming separating electrodes at a distance of 400 mm, in the last two zones with 2*16 gas passages forming separating electrodes at a distance of 500 mm and with a central vertical space for the support beams of the roof, confuser with damping vertical plates and outlet duct.

The geometry of the flow chamber (inlet duct, EF chamber and outlet duct) is completely symmetrical with respect to the central vertical longitudinal plane, so that only one half of the vertical longitudinal plane was simulated by numerical simulation in order to reduce the required computer resources (memory and time). of the side wall, Figure 5 The coordinate origin lies in the plane of the measurement section (with the measurement openings behind the boiler chamber wall) of the inlet duct, i.e. in the vertical longitudinal plane, i.e. in the vertical longitudinal symmetry plane and in the middle of the duct height, with the x (+) axis oriented in the direction of the flue gas flow along the longitudinal chamber axis, the y (+) axis along the height and the axis along the width EF, Figure 5. The flue gas flow was calculated as isothermal (180°C) with initial conditions in the inlet duct according to nominal flow values and actual parameters according to measurements in the inlet duct (Chapter 3).

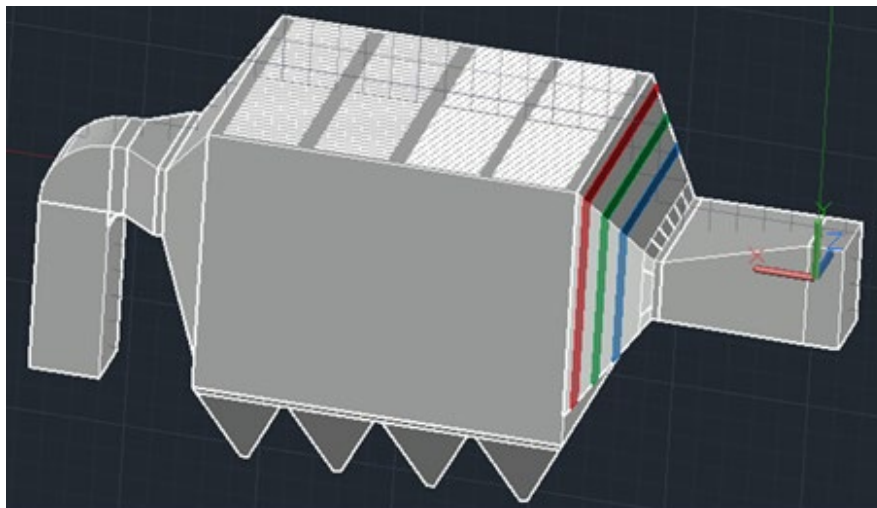


Figure 5. Model geometry for ESP

The CFD analysis of the incompressible fluid flow through the flue gas ducts upstream of the ESP, the ESP chamber and the flue gas duct downstream of the ESP of unit B2 was carried out using the ANSYS CFX 2020 R2 software package, which is based on the method of discretization of the three-dimensional flow domain with finite volume elements. The problem of single-phase isothermal steady-state turbulent 3D (three-dimensional) flow of an incompressible gas through the flow space of a closed contour is described by the time-averaged Navier-Stokes equations of Reynolds for the conservation of mass, momentum, energy, kinetic energy of turbulence and its dissipation. The discretization of the nonlinear partial transport differential equations using the first order Eulerian feedback scheme is performed for each of the variables for the steady state by establishing the equilibrium of the conventional flux, the diffusive flux and the source of the variables in the observed final volume. The field of variables computed in the nodes of the finite volume is applied using

the high-resolution differential scheme of Barth and Jespersion, and the shape function of the finite element is approximated to the integration points of the finite volume element. Two additional equations for the turbulent kinetic energy and the dissipation of the turbulent kinetic energy are used to close this system of equations in the form of the standard turbulence model $k-\epsilon$ extended for the 3D case. The calculation of the value of the velocity components was performed in a "non-shifted grid" so that the control volumes are identical for all transport equations. By applying the alternative discretization method of Rhie and Chow's continuity equation and introducing the term for the pressure redistribution, the coupling of the continuity equations and the amount of motion, i.e. the pressure field and the velocity field, was performed.

The formation and calculations of the numerical models of the flow through the channels and the ESP chamber were performed on a 64-bit computer configuration Intel® Xeon® CPU E3-1231 v3 4 Cores 8 Threads 8MB Intel® Smart Cache at 3.40 GHz with 32GB DDR3 RAM under the operating system Windows Server 2019 Essentials using the ANSYS CFX 2020 R2 software within the ANSYS Workbench 2020 R2 workspace with an ANSYS Academic Associate CFD license. The geometry of the numerical model was created using FreeCad 0.18, ANSYS SpaceClaim and ANSYS DesignModeler software for 3D modeling. A numerical finite volume mesh was created using the ANSYS Workbench 2020 R2 Mesh module. The definition of the properties of the fluid (flue gas), the boundary and initial conditions in the model, the properties of the numerical calculation (advective and interpolation schemes, shape functions, turbulence model, coupling model of pressure and velocity fields, convergence criteria), the calculation of the numerical model created and the presentation of the results obtained are carried out using ANSYS CFX 2020 R2 software [17-19].

The symmetry boundary condition of the model is that the velocity component perpendicular to the plane of symmetry must be zero. The conditions in the finite volumes located up to the wall - the boundary of the domain - are described in the so-called "wall functions", both for velocities and for scalar quantities, where the walls were considered to be ideally smooth. As a convergence criterion for the iterative solution of the differential equation system, it was adopted that the normalized sum of the residuals of all finite volumes in the flow space should be smaller than 10^{-4} above a certain size.

To verify the CFD model, the results of the measurement of the velocity distribution in the cross-section of the ESP chamber upstream of the first electric field with the air flow with the flue gas fan and fresh air fan switched on were used. The optimum geometry of the turning and damping elements in the ESP chamber and in the outlet duct was determined using an iterative procedure. A CFD analysis was carried out for each of the proposed solutions (the second phase of research).

The new version of the model with the existing turning plates at the beginning of the diffuser (2 horizontal and 5 vertical) includes the following conceptual solutions:

- a new solution with three perforated walls with new smaller rectangular openings, but at the same axial positions in the diffuser as in the original solution,
- a new solution with horizontal and vertical turning plates inserted between the perforated walls,
- a new arrangement of damping vertical plates in the diffuser,
- a system of turning vanes in the elbow at the exit of the ESP chamber, which was not exist in the original solution.

Figure 6 shows the flow lines (lines along the vector of the flue gas velocity) in the entire volume from the measuring plane in the inlet duct to the measuring plane in the duct at the outlet of the ESP in the right half of the chamber of EF unit B2. The color of the currents corresponds to the intensity of the velocity vector at this point according to the attached color scale in the picture on the left. A satisfactory velocity field was obtained: very uniform in the chamber ESP with velocities running in the direction of the longitudinal axis of the chamber and minimal flow outside the zones of influence of the electric field (ceiling zone, chamber floor zone, i.e. the funnel zone and the zone in the central vertical channel where they are carriers of the chamber roof). The proposed new horizontal/vertical plates in the diffuser completely eliminate the transverse component of the flue gas velocity generated by the existing turning plates at the beginning of the diffuser and the wall jets formed on the end faces of all three perforated walls until they enter the full cross-section of the chamber.

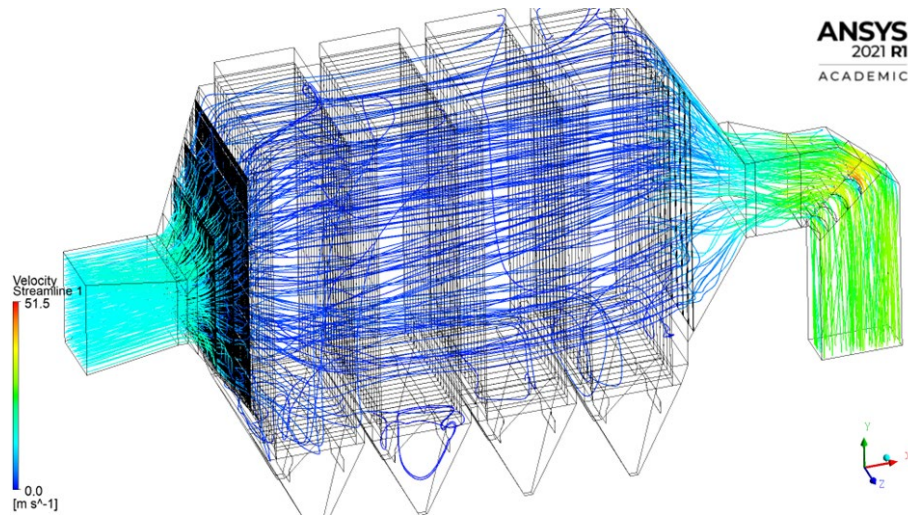


Figure 6. Intensity of the flue gas velocity (according to the corresponding color on the scale on the left) along the flow lines in the ducts upstream/downstream of the ESP and in the ESP chamber

A more detailed analysis of the flow in the chamber obtained by numerical simulation for this variant of the model was performed by showing the intensity field of the axial component of the velocities (in the x-direction along the axis of the chamber) in nine vertical and eight horizontal planes at different distances from the vertical and horizontal axial planes of the chamber. An example of the distribution of the axial component of the velocity in the vertical longitudinal plane at a distance of 3.28 m from the axis of the chamber is shown in Figure 7.

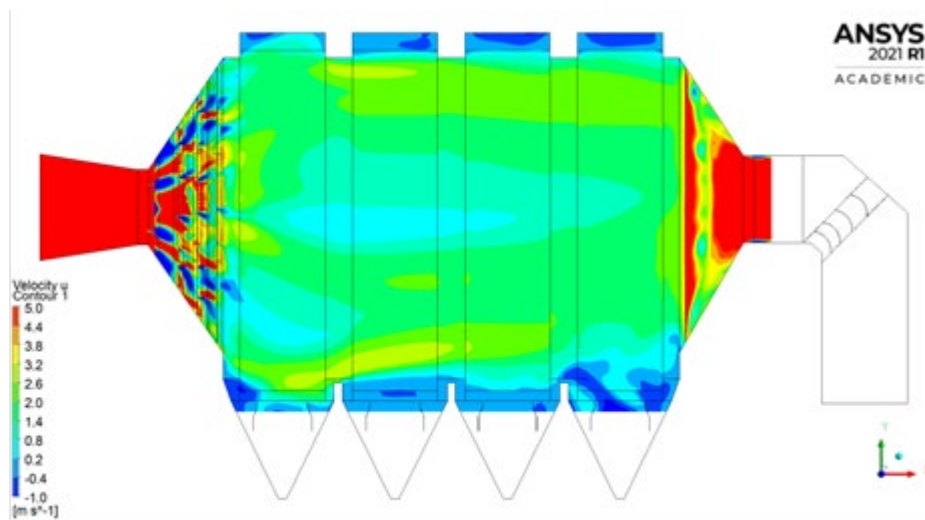


Figure 7. Distribution of the axial component of velocity in the vertical longitudinal plane at a distance of 3.28 m from the axis of the chamber

The flue gas flow at the height of the chamber is very uniform and parallel to the axis of the chamber, i.e. there is no pronounced flow towards the ceiling and from the ceiling or towards the funnels. It can be concluded that the conceptual solution of the geometry of the horizontal and vertical plates in the perforated walls 1, 2 and 3 completely eliminates the transverse component of the velocity at the outlet of the diffuser and in many ways helps to reduce the intensity of turbulence, all of which should contribute to improving the efficiency of the electrostatic precipitator.

An example of the distribution of the axial velocity component in the horizontal longitudinal plane, 2 m below the axis of the diffuser, is shown in Figure 8. The inlet duct and the diffuser are on the right-hand side, the confuser and the outlet duct on the left side of the figure. The results show that the defined geometry and arrangement of the turning/damping plates in the diffuser and confuser lead to a satisfactory uniformity of velocities across the width of the chamber at almost all height levels of the chamber.

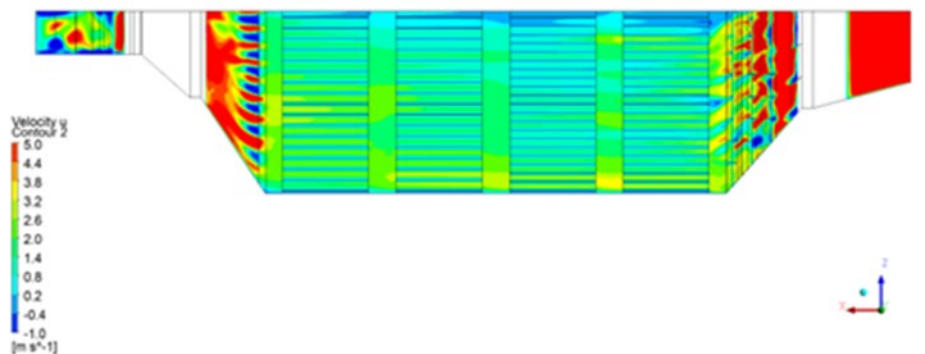


Figure 8. Distribution of the axial velocity component in the horizontal longitudinal plane, 2 m below the axis of the diffuser

The distribution of the intensity of the axial velocity in the diffuser and in the first part of the chamber is determined by the geometry of the five vertical turning plates at the beginning of the diffuser and the geometry of the perforated walls 1, 2 and 3 - and the system of vertical plates in these walls. In the second half of the chamber, the distribution of the axial velocity intensity over the cross-section of the chamber is mainly determined by the geometry/arrangement of the damping plates in the confusor. The results presented show that the defined geometry and arrangement of the turning/damping plates in the diffuser and confusor lead to a satisfactory uniformity of velocities across the width of the chamber at almost all height levels of the chamber.

The selected optimum geometry of the turning and damping elements was the basis for the creation of detailed documentation for the derived elements, according to which new elements were manufactured and installed in the electrostatic precipitator as part of the overhaul work.

The choice of the optimal solution was confirmed by the results of periodic measurements of particulate matter emissions at the outlet of the electrostatic precipitator in June and November 2021. In June, particulate matter concentrations of 31 to 38 mg/Nm³ were measured, and during the test, the electric field of the first zone in the chambers had problems with operation and could not work at 100% [20]. In November, particulate matter concentrations of 28 to 32 mg/Nm³ were measured after additional work was carried out to eliminate problems with the electrical fields in the first zone of the chambers [21].

6. Conclusions

After completion of the guarantee tests, where the condition that the measured concentration is below the emission limit value is fulfilled, there was an increase in the particle concentration at the outlet of the electrostatic precipitator. TPP Kostolac has made great efforts to improve the operation of the electrostatic precipitator plant and significantly reduce concentrations.

The increase in the efficiency of the electrostatic precipitator plant was carried out in two phases, i.e. in two large projects. In the first phase, an analysis of the design values of the basic parameters of the electrostatic precipitator of unit B2 and a comparative analysis of the design and operating parameters of the electrostatic precipitators of lignite-fired power plants were carried out. In addition, experimental investigations were carried out on the velocity distribution in the cross-section of the electrostatic precipitator chamber and in the vertical measurement cross-section in the cross-section of the flue gas duct upstream of the electrostatic precipitator. Based on these results, the homogeneity of the flow field in the measurement cross-sections was determined and these results were used to verify the CFD model.

In the second phase of the research, an analysis of the existing condition of the inlet and outlet ducts, the turning and damping elements in the electrostatic precipitator chambers was first carried out.

The optimum geometry of the turning and damping elements in the ESP chamber and in the exhaust duct was determined iteratively. The new version of the model with the existing turning plates at the beginning of the diffuser (2 horizontal and 5 vertical) includes the following conceptual solutions:

- a new solution with three perforated walls with new smaller rectangular openings, but at the same axial positions in the diffuser as in the original solution,
- a new solution with horizontal and vertical turning plates inserted between the perforated walls,
- a new arrangement of damping vertical plates in the diffuser,
- a system of turning vanes in the elbow at the exit of the ESP chamber, which was not exist in the original solution.

The CFD analysis of the incompressible fluid flow through the flue gas ducts upstream of the ESP, the ESP chamber and the flue gas duct downstream of the ESP of unit B2 was carried out using the ANSYS CFX 2020 R2 software package. A satisfactory velocity field was obtained: very uniform in the ESP chamber with velocities running in the direction of the longitudinal axis of the chamber and minimal flow outside the zones of influence of the electric field.

The proposed new horizontal/vertical plates in the diffuser completely eliminate the transverse component of the flue gas velocity generated by the existing turning plates at the beginning of the diffuser and the wall jets formed on the end faces of all three perforated walls until they enter the full cross-section of the chamber.

The choice of the optimal solution was confirmed by the results of periodic measurements of particulate matter emissions at the outlet of the electrostatic precipitator after the overhaul and installation of new elements. The particulate matter concentration measured at the outlet of the electrostatic precipitator is well below the emission limit values and is twice as high as the particulate matter concentration measured before the reconstruction.

Acknowledgements

The research was funded by the Ministry of Science, Technological Development and Innovation of the Republic of Serbia (Contract Annex: 451-03-66/2024-03/200017). The authors are very grateful for the support of this work by the Joint Stock Company Elektroprivreda Srbije.

References

- [1] Directive 2001/80/EC of the European Parliament and of the Council of 23 October 2001 on the limitation of emissions of certain pollutants into the air from large combustion plants.
- [2] REGULATION ON THE LIMIT VALUES FOR THE EMISSION OF POLLUTANTS INTO THE AIR FROM COMBUSTION PLANTS, "Official Gazette of the RS", No. 6/2016 and 67/2021.
- [3] High Frequency Power Supply for Electrostatic Precipitators in Thermal Power Plants, Slobodan Vukosavić, Electronics, Vol. 15, No. 1, June 2011, pp. 11-20.
- [4] Chandra A., Enhancement of Collection Efficiencies of Electrostatic Precipitators: Indian Experiments. In: Yan K. (eds) Electrostatic Precipitation. Springer, Berlin, Heidelberg, 2009, DOI: 10.1007/978-3-540-89251-9_4
- [5] REGULATION ON THE LIMIT VALUES FOR THE EMISSION OF POLLUTANTS INTO THE AIR, "Official Gazette of the RS", No. 71 of October 4, 2010.
- [6] Erić, M., Marković, Z., Periodic Measurement of Pollutant Emissions in the Air of Unit B2 of the Kostolac Power Plant in Kostolac, Technical Report NIV-LTE-593, Vinča Institute, December 2015, Belgrade-Vinča.
- [7] Erić, M., Marković, Z., Periodic Measurement of Pollutant Emissions in the Air of Unit B2 of the Kostolac Power Plant in Kostolac, Technical Report NIV-LTE-600, Vinča Institute, May 2016, Belgrade-Vinča.
- [8] Erić, M., Marković, Z., Periodic Measurement of Pollutant Emissions in the Air of Unit B2 of the Kostolac Power Plant in Kostolac, Technical Report NIV-LTE-611, Vinča Institute, December 2016, Belgrade-Vinča.
- [9] Erić, M., Marković, Z., Periodic Measurement of Pollutant Emissions in the Air of Units B1 and B2 of the Kostolac Power Plant in Kostolac, Technical Report NIV-LTE-622, Vinča Institute, November 2017, Belgrade-Vinča.
- [10] Erić, M., Marković, Z., Periodic Measurement of Pollutant Emissions in the Air of Units B1 and B2 of the Kostolac Power Plant in Kostolac, Technical Report NIV-LTE-632, Vinča Institute, May 2018, Belgrade-Vinča.
- [11] Erić, M., Marković, Z., Periodic Measurement of Pollutant Emissions in the Air of Units B1 and B2 of the Kostolac Power Plant in Kostolac, Technical Report NIV-LTE-649, Vinča Institute, June 2019, Belgrade-Vinča.
- [12] Erić, M., Marković, Z., Periodic Measurement of Pollutant Emissions in the Air of Units B1 and B2 of the Kostolac Power Plant in Kostolac, Technical Report NIV-LTE-655, Vinča Institute, December 2019, Belgrade-Vinča.

- [13] Erić, M., Marković, Z., Periodic Measurement of Pollutant Emissions in the Air of Units B1 and B2 of the Kostolac Power Plant in Kostolac, Technical Report NIV-LTE-662, Vinča Institute, July 2020, Belgrade-Vinča.
- [14] Erić, M., Marković, Z., Periodic Measurement of Pollutant Emissions in the Air of Units B1 and B2 of the Kostolac Power Plant in Kostolac, Technical Report NIV-LTE-669, Vinča Institute, January 2021, Belgrade-Vinča.
- [15] Stefanović, P., Erić, M., Marković, Z., Analysis of the situation and possibilities for increasing the efficiency of the electrostatic precipitator at unit 2, Version 1.0, Study, NIV-LTE-665, Vinča Institute, June 2019, Belgrade-Vinča. .
- [16] Stefanović, P., Marković, Z., Erić, M., CFD model and numerical analysis of the flow in the channels upstream and downstream of the electrostatic precipitator of unit B2 TPP Kostolac, Version 1.0, Technical Report NIV-LTE-665, Vinča Institute, September 2020, Belgrade-Vinča.
- [17][19] Marković, Z., Erić, M., Jovanović, R., Lazović, I., Numerical Simulation of the Gas Flow Through the Rectangular Channel With Perforated Plate, Thermal Science, Year 2023, Volume 27, Issue 3, pp 2241 – 2253.
- [18] Marković, Z., Erić, M., Stefanović, P., Jovanović, R., Lazović, I., Optimization of the Flue Gas Flow Controlling Devices of the Electrostatic Precipitator of Unit 4 In TPP "Nikola Tesla", Thermal Science, Year 2023, Volume 27, Issue 5, pp 3591 – 3606.
- [19] Marković, Z., Erić, M., Stefanović, P., Lazović, I., Milićević, A., Mančić M., Jovčevski, M., Jovanović, R., Investigation of velocity distribution in channels and chambers of the electrostatic precipitator at TPP Nikola Tesla Unit A1, Thermal Science, Year 2023, Volume 27, Issue 6, pp 4877 – 4892.
- [20] Erić, M., Marković, Z., Periodic-Control Measurement of Pollutant Emissions in the Air of Unit B2 of the Kostolac Power Plant in Kostolac, Technical Report NIV-LTE-677, Vinča Institute, June 2021, Belgrade-Vinča.
- [21] Erić, M., Marković, Z., Periodic Measurement of Pollutant Emissions in the Air of Unit B2 of the Kostolac Power Plant in Kostolac, Technical Report NIV-LTE-682, Vinča Institute, December 2021, Belgrade-Vinča.

Indicating Contribution of a Country to Global CO₂ Emission and Environmental Justice

Vojin Grković^a

^a*University in Novi Sad, Faculty of Technical Sciences, Novi Sad, RS vojingr@uns.ac.rs*

Abstract: The paper discusses the problem of objectively comparing different countries in terms of their carbon dioxide emissions, in the light of climate and environmental justice. Two traditional and three nontraditional indicators are included. The indicators were applied to a selected group of thirteen countries that includes part of the BRICS countries and the G7 countries. The ratio of the share of carbon dioxide emissions of a country in the global emission and the share of its population in the global population makes a basis for comparison different countries. For defining just relation among the countries regarding carbon dioxide emissions, it is necessary to identify the sinks of carbon dioxide and to include them into the definitions of the emission's indicators. A possible approach in that direction is presented in the paper. Further improvements in the definition of appropriate indicators for an objective comparison of different countries in terms of their carbon dioxide emissions are presented and exemplified.

Keywords: environmental justice, climate justice, carbon dioxide emission indicators

1. Introduction

Emissions of carbon dioxide in certain countries, that is, across their borders, are increasingly the subject of heated discussions at the international level. On the one hand, there are the wishes of developed countries from the G7 group to abolish coal subsidies [1]. On the other hand, underdeveloped and developing countries have a legitimate desire to increase their level of development as soon as possible and to reduce their lag behind developed countries. For them, an increase in the consumption of primary energy per capita is necessary for their development. The fastest and for them the simplest way to increase the consumption of primary energy per capita is directly related to the increase in the consumption of fossil fuels and, ultimately, to the increase their carbon dioxide emissions [2]. In this context, important questions of energy, environmental and climate justice have to be raised.

The tendency to impose strict carbon emissions obligations on developing countries with significantly different energy use patterns, which find it difficult to meet these obligations, or to meet them quickly enough, raises issues of both environmental and climate justice in the form of accountability (current vs. historical) and rights (whose needs are most urgent and who decides who can emit how much carbon dioxide) [3]. The principles of environmental justice set in this way actually follow from the concept of energy justice that Neville and Mulvaney (Newell and Mulvaney) presented in the literature [4].

Regardless of defining how much carbon dioxide a country can emit and who decides about it, it is necessary first to define an objective assessment of the contribution of each individual country to the total global emission.

2. Basic indicators

The simplest indicator of a country's carbon dioxide emissions is the ratio of its annual emissions to its population, expressed in tons per capita. It implies that every inhabitant of the world has the same rights and the same obligations regarding carbon dioxide emissions. In analytical form, this indicator is defined by equation (1), as:

$$\mu_{CO_2} = \frac{M_{CO_2_Em}}{P_{Ct}} \quad (1)$$

Here $M_{CO_2_Em}$ and P_{Ct} denote the total annual emission of carbon dioxide and the number of inhabitants of the observed country. A comparative view of carbon dioxide emissions per capita for some countries from the BRICS group and for the countries of the G7 group, according to data provided in the literature [5], is presented in Fig. 1.

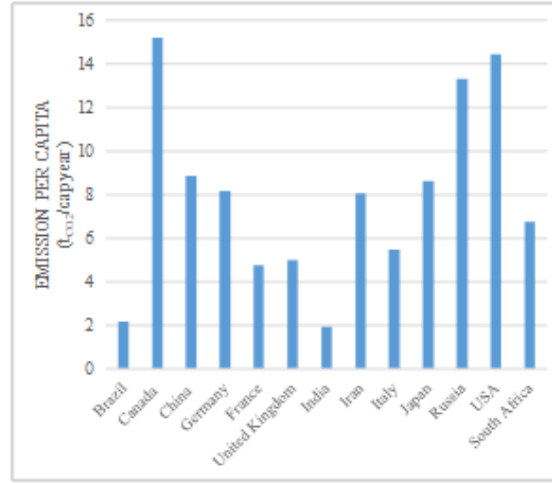


Figure 1. Carbon dioxide emissions per capita for selected group of countries, according to data from [5]

A slightly more complex indicator represents the ratio of the participation of an individual country in the total global emission of carbon dioxide and the participation of the population of that country in the global population. The indicator formulated in this way seems very suitable for assessing the contribution of an individual country to global emissions. It was, for example, used in the literature [6], as a starting point for considering the connection between possible political changes in the upcoming elections in five countries that are large emitters of carbon dioxide and possible changes in attitudes towards the proclaimed reduction of carbon dioxide emissions in those countries. In analytical form, this indicator is determined by equation (2).

$$\Lambda_{MP} = \frac{\frac{M_{CO_2}}{M_{GCO_2}}}{\frac{P_{Ct}}{P_G}} = \frac{\mu_{GeCO_2}}{\pi_{Gp}} \quad (2)$$

M_{CO_2} and P_{Ct} denote the carbon dioxide emission and the number of inhabitants of the observed country, respectively, while M_{GCO_2} and P_G denote the total global carbon dioxide emission and the global population. μ_{GeCO_2} and π_{Gp} indicate the participation of the observed country's emission in the global carbon dioxide emission and the participation of its population in the global population, respectively. The mutual distribution of the selected countries according to this indicator must be the same as in Figure 1, since the ratio of these two indicators is:

$$\frac{\Lambda_{MP}}{\mu_{CO_2}} = \frac{P_G}{M_{GCO_2}} = K_G \quad (3)$$

Where the K_G represents the global characteristic.

Equation (2) has some other important advantages. For example, we can form a two-dimensional coordinate system: "Country share in global population" – "country share in global carbon dioxide emissions", which is graphically represented in Fig. 2, according to [3]. We see that equation (2), defines the tangent of the angle which the position vector of each country from Fig. 2 overlaps with the axis: "population share in the world population". This kind of presentation further enables us to numerically indicate the countries that "transfer" a part of their emissions to other countries, that is, to the "global level". A country for which $\Lambda_{MP} > 1$ will have a greater share in global carbon dioxide emissions than its share in global population. For a country with $\Lambda_{MP} < 1$, it follows that its share in global carbon dioxide emissions will be less than its share in the global population. In other words, all countries above the red dotted line in Fig. 2 will have $\Lambda_{MP} > 1$, which we can interpret as those countries "spilling" part of their carbon dioxide emissions to other countries. On the other hand, all countries below that line will have $\Lambda_{MP} < 1$, which practically means that they will "receive" part of

the carbon dioxide emissions from other countries. The described approach also leads us to the conclusion that a country with the same numerical values of participation in global emissions and in the global population, i.e. with $A_{MP} = 1$, has zero "spillover" of its emissions to other countries and zero "reception" of emissions from other countries. The principle of dividing all countries in the world into countries that transfer their emissions to other countries and those that receive emissions from other countries, as well as neutral countries in this respect, looks very usable and very practical. However, we can put the question: is this approach in line with environmental and climate justice?

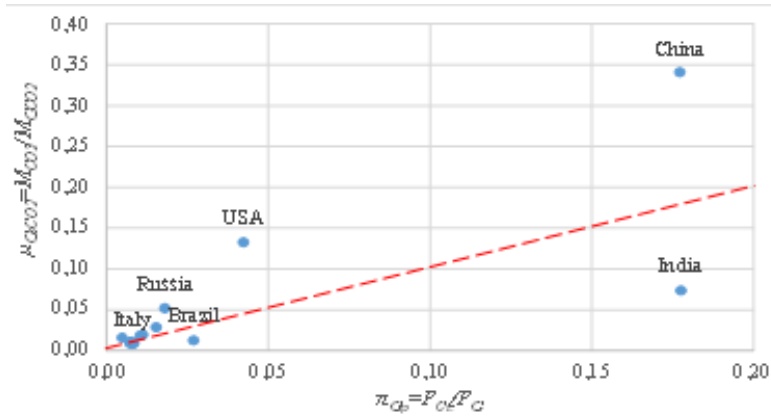


Figure 2. Considered countries in the diagram: "Share in global population - share in global carbon dioxide emissions", based on data from Refs. [5, 7]

3. A contribution to development of complex indicators

In principle, the entire carbon dioxide emission of a country does not have to be the basis for defining its participation in the global emission. Certain countries may have specific natural conditions that enable the absorption of part of their emissions and, therefore, a smaller contribution to global emissions. In other words, we can assume that every country, in addition to anthropogenic sources of carbon dioxide, also has natural sinks of carbon dioxide, whereby the capacity of these sinks, in principle, varies from country to country. An example of such a sink is a forest expanse in the country under consideration. In principle, for comparing the contribution of one country to the global emission, it is important to comprise and the effect of the carbon sinks in it.

3.1. Forests as carbon dioxide sinks

According to data published in the literature [8], in the period between 2001 and 2019, all the world's forests absorbed approximately twice as much carbon dioxide as they emitted, so we can consider them as a large and powerful "carbon sink". Long spanning research the results of which are published in [9], point out that the global forest carbon sink is equivalent to almost half of fossil-fuel emissions. However, not every forest absorbs the same amount of carbon dioxide. The differences between individual forests in terms of the amount of absorbed carbon dioxide per unit area of the land on which the forest is spread can be very large, which according to [8] essentially depends on how they are managed. According to data published by Moseman and others in [10], the most powerful forests in terms of absorptive capacity are able to absorb up to 100 times more carbon per hectare than the least powerful forests. In this regard, the preservation of existing forests has priority over the growth of new forests [10].

3.2. Complex indicators

The simplest way to introduce areas under forests into the procedure for estimating effective carbon dioxide emissions would be to reduce the emission of anthropogenic carbon dioxide of a country to the product of its population and its area under forests expressed in square kilometers. Thus, we arrive at the definition of "Relative carbon dioxide emissions" (in relation to population and area under forest) of a country ξ_{CO2Sf} , which is numerically determined by the following equation:

$$\xi_{CO2Sf} = \frac{M_{CO2}}{P_{Ci} \cdot S_f} = \frac{M_{CO2}}{P_{Ci} \cdot \sigma_{Sf} \cdot S_{uk}} \quad (4)$$

Here, S_f and S_{tik} denote the area occupied by forest in the considered country and the total area of that country, respectively. With σ_{Sf} , the afforestation of the country is indicated as the ratio of the area under forest to the total area of the country.

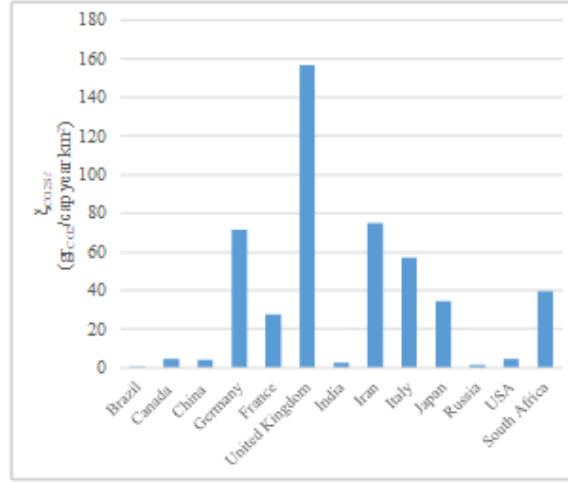


Figure 3. Relative carbon dioxide emissions for selected group of countries, according to data from [5, 7] and [11]

The contribution of each of the countries from the selected group to the global emission of carbon dioxide, calculated using equation (4), is shown in Fig. 3. This calculation is made under the assumption that all countries have forests with the same ability to absorb carbon dioxide and that they differ only in the area covered by their forests, which does not correspond to reality. We can see that the order of the considered countries is somewhat different compared to the order in Fig. 1, that is, when using equation (1). The dimension of the relative carbon dioxide emissions indicator is tons of carbon dioxide per inhabitant and square kilometer of the considered country's surface. However, even this indicator does not provide an answer to the question of how much a specific country "spills over" part of its anthropogenic carbon dioxide emissions to other countries, that is, to the global level.

When defining the forest's impact on the spillover part of anthropogenic carbon dioxide to other countries, it is necessary to take into account the absorptive capacity of the forest in the specific, or considered, country. Such considerations lead us to the specifically formulated indicator named "Carbon dioxide emission indicator" of a country. This indicator is defined as the ratio of the difference between emitted and absorbed carbon dioxide and the number of inhabitants of the observed country, or in analytical form with the following equation:

$$\mu_{CO2sf} = \frac{(M_{CO2_Em} - M_{CO2_Absf})}{P_{Ct}} = \frac{M_{CO2_Em}}{P_{Ct}} \cdot \left(1 - \frac{M_{CO2_Absf}}{M_{CO2_Em}}\right) = \mu_{CO2} \cdot (1 - \Theta) \quad (5)$$

Here M_{CO2_Em} (in t/a¹) indicates the amount of anthropogenic carbon dioxide emissions for one year in the observed country, M_{CO2_Abs} (in t/a) indicates the annual amount of anthropogenic carbon dioxide absorbed by forests in the same country for one year, P_{St} is the number of inhabitants of that country, μ_{SO2} is determined by equation (1), while Θ represents the ratio of annual amounts of absorbed and emitted carbon dioxide.

If we assume the general case that certain parts of the total forest area of a country have different absorption capacities of carbon dioxide, then the ratio of annual amounts of absorbed and emitted carbon dioxide Θ will be determined by the following equation:

$$\Theta = \frac{M_{CO2_Absf}}{M_{CO2_Em}} = \frac{\sum_{i=1}^n q_{fCO2i} \cdot S_{fi}}{M_{CO2_Em}} = \frac{\bar{q}_{fCO2} \cdot S_f}{M_{CO2_Em}} \quad (6)$$

Here q_{CO2i} (in t/km²a) and S_{fi} (in km²) denote the average amount of absorption power and the area of the i -th part of the total forest area S_f of the observed country, respectively. For a country with a sufficiently large area

¹ t/a – tons per annum

under forest and a relatively small emission of anthropogenic carbon dioxide, it can be $\Theta > 1$, which has, as a consequence, a negative numerical value of the indicator of carbon dioxide emission defined by equation (5). Such a country is a net absorber of carbon dioxide, in contrast to countries with a positive numerical value of this indicator, which are net emitters of carbon dioxide due to $\Theta < 1$. A country for which $\Theta = 1$ will be emission neutral, i.e. it will neither spillover nor receive carbon dioxide.

Determining the numerical value of the average forest absorption capacity factor for each individual country \bar{q}_{fCO_2} (in t/km²a) represents a special and very complex problem. To solve it, it is necessary to combine field measurements and satellite images. On the other hand, it can significantly contribute to the objective assessment of each country's emission in relation to the global emission and to the objective assessment of the spillover of anthropogenic carbon dioxide emissions to other countries, that is, to the global level. In final level, it contributes to the environmental justice in comparison carbon dioxide emissions among different countries.

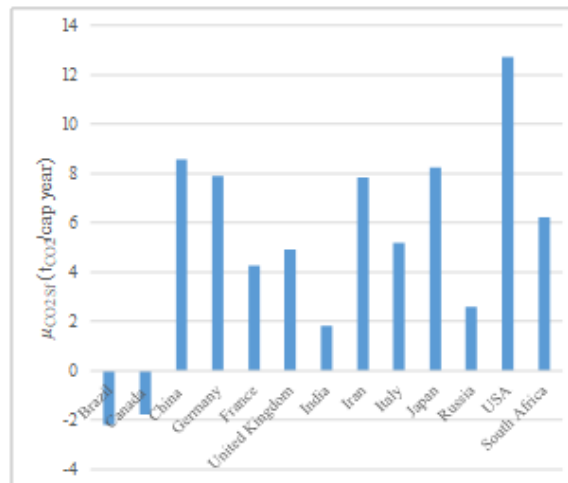


Figure 4. Carbon dioxide emission indicator for selected group of countries, according to data from [5, 7, 11]

The contribution of each country from the selected group to global carbon dioxide emissions, calculated using equation (5), is shown in Fig. 4, according to [3]. The calculations were made with the numerical value $\bar{q}_{fCO_2}=190$, which approximately corresponds to the average absorption capacity of forests at the global level, calculated according to the data published in the literature [8 and 11]. From Fig. 4, two groups of countries are clearly visible: 1) net emitters of carbon dioxide, for which $\mu_{CO_2sf} > 0$, i.e. $\Theta < 1$, and which can be large, medium and small net emitters, and 2) net absorbers of carbon dioxide for which is $\mu_{CO_2sf} < 0$, i.e. $\Theta > 1$. The introduction of the available forest area in the calculation of the contribution of individual countries to the total global emission of carbon dioxide significantly changes the mutual relationship of the countries from the selected group. Of the largest emitter countries from Figure 1, namely: Canada, Russia and the USA, according to this criterion the USA is still the largest emitter, Russia, together with India, is in the group of the smallest net emitters, while Canada, together with Brazil, is in the group of net absorbers carbon dioxide. This calculation is made under the assumption that all countries have forests with the same absorption capacity, approximately equal to the average carbon dioxide absorption capacity of all forests in the world, and that countries differ only in the area covered by their forests, which, of course, represents a significant approximation.

The next thing that can be done toward improving the assessment of each country's contribution to global emissions is to include the absorptive capacity of the flora found in the surface waters of each country. In this sense, in [3] is assumed that surface waters on land will also absorb part of the emitted carbon dioxide. This thinking leads to the concept of "Total carbon dioxide emission indicator", which is defined by the following equation:

$$\mu_{CO_2sf_{sw}} = \frac{(M_{CO_2_Em} - M_{CO_2_Absf} - M_{CO_2_Absw})}{P_{ct}} = \mu_{CO_2} \cdot (1 - \Theta - \Omega) \quad (7)$$

Here, $M_{CO_2_Absf}$ and $M_{CO_2_Absw}$ (in t/a) denote the annual amount of anthropogenic carbon dioxide absorbed by forests and aquatic flora for one year, respectively, μ_{SO_2} is determined by equation (1), while Ω represents the

ratio of water flora absorbed annually the amount of carbon dioxide and emitted carbon dioxide in the observed country. In the general case when certain parts of the total water surface of a country have different carbon dioxide absorption capacities, the ratio of annual amounts of absorbed and emitted carbon dioxide Ω will be determined by the following equation:

$$\Omega = \frac{M_{CO2_Absw}}{M_{CO2_Em}} = \frac{\sum_{j=1}^m q_{wCO2j} \cdot S_{wj}}{M_{CO2_Em}} = \frac{\bar{q}_{wCO2} \cdot S_w}{M_{CO2_Em}} \quad (8)$$

With q_{wCO2j} (in t/km²a) is denoted the mean amount of absorption power of the j -th part of the water surface, with S_{wj} (in km²) the surface of the j -th part of the total water surface, and with S_w the total surface under water in the observed country, respectively.

The average amount of the hydroflora's absorption power depends on the purity of the water and its temperature. For the purposes of the calculation example, in [3] is assumed numerical value of $\bar{q}_{wCO2} = 75$. The calculations performed in [3] point out almost the same distribution of considered countries as in Figure 4, with Canada now being the largest carbon dioxide absorber. It should be kept in mind that these calculations, as well as the calculations for the Fig. 4 were made with supposed numerical values of the mean absorptive capacity of forests and of surfaces under water.

Note also that equations (1), (5) and (7) have the same dimension: ton of carbon dioxide per inhabitant per year, equation (4) has the dimension: ton of carbon dioxide per inhabitant per year and square kilometer, while equation (2) is dimensionless.

In previous analyses, only continental surface waters were taken into account, but not the surface of seas and oceans, given that we consider these other surfaces as a common good that belongs to all countries.

4. Just energy transition and climate justice

Inclusion the absorptive capacity of forests in the evaluation of the carbon dioxide's effective emission represents an important issue of ecological and climate justice, but also an important issue of a just energy transition. Considering forests as sinks of carbon dioxide follows from the United Nations Framework Convention on Climate Change [12]. Since forests as carbon sinks reduce the effects of anthropogenic carbon dioxide emissions, for each specific country, it is necessary to take into account the area under forest, the maintenance of forests and the nature of forests in order to accurately define the absorption coefficient of those forests.

In the draft of the Strategy for development of energetics in Republic of Serbia [13], the reduction of the share of coal-fired power plants (lignite) in the total production of electricity is foreseen to about 50% in 2040, at the expense of increasing production from i-RES, for the purpose of reducing carbon dioxide emissions. This implies a corresponding reduction of employees in coal mines and thermal power plants, but also a reduction of the GDP in the areas of coal mines and thermal power plants. All this for the sake of reducing carbon dioxide emissions in Serbia.

The rough analysis carried out for the purpose of this paper shows that the current area covered by forests in Serbia, with the average absorption capacity of the world's forests (190 t/km²), in terms of reducing the effective emission of carbon dioxide, corresponds to the reduction of the possible production of thermal power plants Nikola Tesla A and B in 2019 [14], by 25%. This figure is already of great importance for the extension of coal and electricity production activities, because the eventual reduction in production would be only about half of the predicted figure from the Strategy for development of energetics in Republic of Serbia [13]. Of course, the figure of 190 t/km² is based on the estimated value of the absorption capacity of Serbian forests. This assumption must be proven by appropriate empirical research. However, it is not unreasonable to assume that these studies could also show even higher absorptive capacity of Serbian forests taken together with flora in the water surfaces, as well as with the agricultural flora.

Precise determination of the capacity of Serbian forests to absorb carbon dioxide is possible only within a complex scientific research project. That project should have two parts. In the first part, it should be realized the necessary recordings on the ground and, if the need dictates and the possibilities permit, satellite recordings. On the basis of these studies, the sectors of areas under the forest with similar carbon dioxide absorption capabilities should be determined, as well as the average absorption capabilities of each of the defined sectors.

In the second part of the scientific research project, it is necessary to create a specific mathematical model for calculating the possible and the most likely absorption of carbon dioxide emitted from various industrial emitters in Serbia. Here, in addition to the emission intensity of individual emitters and the absorption capacity of individual sectors of the forest area, their spatial distribution and movement of air masses with carbon dioxide should be taken into account. One of the results of such a project would be software for calculating carbon dioxide absorption in Serbian forests in real time.

If, through appropriate research can be achieved, on one hand the more precisely determination of the absorptive capacity of Serbian forests, as well as the possible achievement that could be obtained by better forest management, and on the other hand of possible increase in the area under forests in Serbia by 2040, that is, by 2050, the prospects for further production of electricity from coal in Serbia and, on that basis, the realization of a GDP are not at all without foundation. On the other hand, in order to install solar power plants and wind power plants in Serbia, the most probably even cutting of forests will be necessary.

5. Conclusions

From the point of view of ecological justice and the protection of existing forests, but also from the point of view of energy justice, it is very important that underdeveloped and developing countries are the owners of the land and forests on their territory. By protecting and domestically managing their forests, those countries can provide, for them, the most favorable energy from solid fossil fuels without increasing cross-border carbon dioxide emissions. This conclusion is in line with the view of Moseman and others that the enforcement of ownership rights of indigenous peoples and local communities over their forests is a proven strategy for protecting existing forests and increasing the total amount of carbon stored in them [10].

Indicating the share of carbon dioxide emissions from individual countries in the global emission aims to indicate which countries transfer part of their emissions to the global level, and which countries have emissions only within their borders. This is a very sensitive question and therefore the answer to it must be objective and scientifically based. This paper provides a contribution to the analysis of the problem of objective comparison of different countries in terms of their carbon dioxide emissions. Observing a country's carbon dioxide emissions in relation to its population and its area under forests could contribute to environmental and climate justice on the global level. In this light, we can look at the discussed possibilities of further improving the objectivity of comparing carbon dioxide emissions between different countries.

Finally, it is important to mention that above defined environmental indicators can be applied within the scope of expanding, in the literature [15] already presented, analysis of energy systems' energy transition and post-transition and in that respect for selection of the most competitive transition trajectory. Environmental indicators enable joint analysis of an energy system and the environment in the scope of the energy transition. Development of forestation can lead to better achievements in main energy transition goals: the country's sustainable development, as well as a carbon-free economy.

Disclaimer (Artificial intelligence)

Author hereby declares that no generative AI technologies such as large language models (*ChatGPT*, *COPILOT*, etc.) and text to image generators have been used during writing or editing this manuscript.

Competing interests

Author hereby declares that there have been no conflicting financial interests or personal relationships that could influence the creation of the presented work.

References

- [1] G7 Leaders' Communiqué, Elmau, 28 June 2022, available at: <https://www.governo.it/sites/governo.it/files/2022-06-28-abschlusserklaerung-eng-web-data.pdf>, (16.08.2022).
- [2] XIV BRICS Summit, available at: http://brics2022.mfa.gov.cn/eng/dtxw/202206/t20220624_10709295.html, (16.08.2022.).
- [3] Grković, V. 2024. "Contribution to Comparison Different Countries Regarding Carbon Dioxide Emissions". *Journal of Energy Research and Reviews* 16 (7):30-36. <https://doi.org/10.9734/jenrr/2024/v16i7360>.
- [4] Newell P., Mulvaney D., The political economy of the "just transition". *Geogr J.* 179, (2013),132–140. <https://doi.org/10.1111/geoj.12008>

- [5] https://en.wikipedia.org/wiki/List_of_countries_by_carbon_dioxide_emissions_per_capita (21.05.2024.)
- [6] Maltapaty S., Tollefson J., Wong C, Wild S. and Gaidn N., 2024: A Climate Super-Election Year, Nature, Vol. 627, 7 March 2024, pp. 22-25.
- [7] <https://www.worldometers.info/world-population/population-by-country/> (Population and Area, 21.05.2024.)
- [8] Harris N. and Gibbs D. Forests Absorb Twice as Much Carbon as They Emit Each Year, available at <https://www.wri.org/insights/forests-absorb-twice-much-carbon-they-emit-each-year> (Forest, 21.05.2024.)
- [9] Pan Y., Birdsey A. R., Phillips L. O., Houghton A. R., Fang J., Kauppi E. P., Keith H., Kurz A. W., Ito A., Lewis L. S., Nabuurs G-J., Shvidenko A., Hashimoto S., Lerink B., Schepaschenko D., Castanho A. & Murdiyarsa D., The enduring world forest carbon sink, Nature, Vol 631, 18 July 2024, pp. 563-569.
- [10] Moseman A., Harwey C. and Terrer C., How many new trees would we need to offset our carbon emissions?, MIT, (2024), available at: <https://climate.mit.edu/ask-mit/how-many-new-trees-would-we-need-offset-our-carbon-emissions>
- [11] Ritchie H. (2021) - Forest area, Published online at OurWorldInData.org. Retrieved from: <https://ourworldindata.org/forest-area> (Forest, 21.05.2024.)
- [12] United Nations Framework Convention on Climate Change, 1992, available at: <https://unfccc.int>
- [13] Strategy of the development of energetics of Republic of Serbia until 2040 year with projections until 2050-year, draft, (in Serbian), available at <https://www.mre.gov.rs/extfile/sr> (21.08.2024.)
- [14] Electro energy portfolio of EPS, 2019.
- [15] Grković V.: Transition and post transition: energy and technology, Society of engineers in Zrenjanin and City national library in Zrenjanin, Serbia, 2024 (in Serbian).

Optimisation of Electrostatic Precipitators in Pulverised Lignite-Fired Thermal Power Stations

*Zoran Marković^a, Milić Erić^b, Aleksandar Milićević^c, Ivan Lazović^d, Predrag Stefanović^e
Ilija Stevanović^f*

^a*Vinca Institute of Nuclear Sciences – National Institute of the Republic of Serbia - University of Belgrade, RS, zoda_mark@vinca.rs*

^b*Vinca Institute of Nuclear Sciences – National Institute of the Republic of Serbia - University of Belgrade, RS, milic@vinca.rs*

^c*Vinca Institute of Nuclear Sciences – National Institute of the Republic of Serbia - University of Belgrade, RS, amilicevic@vinca.rs*

^d*Vinca Institute of Nuclear Sciences – National Institute of the Republic of Serbia - University of Belgrade, RS, ivan.lazovic@vinca.rs*

^e*Vinca Institute of Nuclear Sciences – National Institute of the Republic of Serbia - University of Belgrade, RS, pstefan@vinca.rs*

^f*Electrical Engineering institute Nikola Tesla Joint Stock Company, Belgrade, RS, istevan@ieent.org*

Abstract: The energy transition while maintaining energy security and environmental protection is recognized by the Republic of Serbia and Joint Stock Company Elektroprivreda Srbije (EPS) as a priority in the implementation of the Green Agenda. From 2004, a detailed reconstruction and modernization of the electrostatic precipitators (ESP) of the 15 units of the thermal power plant (TPP) in the EPS system was carried out. The aim was to reduce particulate matter emissions from each unit below the limit value of 50 mg/Nm³. This resulted in a reduction of more than 90% in particulate matter. Over the past ten years, however, periodic measurements of particulate emissions have revealed a decline in the efficiency of many ESP systems, usually due to deterioration in coal quality. The plate-wire ESP achieves maximum dust removal efficiency by simultaneously generating the maximum spark voltage over a homogeneous velocity field of the flue gas between the plates. The consortium consisting of the Vinča Institute of Nuclear Sciences and the Nikola Tesla Electrotechnical Institute successfully diagnoses these new working conditions of the ESP based on the results of periodic measurements of particulate emissions, the results of measurements of flue gas velocity distribution in the ESP channels and chambers and the results of measurements of various electrical parameters of the ESP. Detailed analyses and numerical simulations are used to identify the existing limitations of ESP properties and to investigate suitable measures to improve ESP efficiency. This paper presents the results of the testing and optimization of the ESP of five thermal power units in the EPS system, which was carried out from 2020 onwards. The implementation of the measures proposed by the consortium, both the reconstruction of the mechanical turning and damping elements of the ESP and the installation of the proposed new power control elements, was carried out as part of the annual overhaul of these units. The effectiveness of the measures applied is demonstrated by the fact that the particulate emissions of each optimized ESP were reduced from over 60 mg/Nm³ to around 30 mg/Nm³.

Keywords: electrostatic precipitator, particulate emission, computational fluid dynamics simulations, on site measurements.

1. Introduction

Particulate matter emissions are one of the most serious environmental problems that pose a major health risk to people [1]. About 70% of electricity generation in the Republic of Serbia is based on the combustion of low-grade lignite from open pit mines in thermal power plants. Currently, the Republic of Serbia has neither the resources nor the potential to ensure a stable and independent electricity supply without relying on coal. Therefore, taking into account the national circumstances and interests of the Republic of Serbia and EPS, energy transition while maintaining energy security and environmental protection is recognised as a priority in the implementation of the Green Agenda [2]. From 2004, the refurbishment and modernisation of the electrostatic precipitators (ESP) in all 15 thermal power plant (TPP) units of the EPS system was completed with a total investment of around 97 million euros, reducing particulate matter emissions from these units to below the limit value of 50 mg/Nm³. As a result, particulate matter emissions were reduced by up to 90% (from

66,626 tonnes in 2003 to 6,344 tonnes in 2022). During operation, some of these plants have experienced increased particulate matter emissions compared to the permitted [3] emission limit value (ELV), which is due to the change in working conditions compared to the design conditions, as shown by the results of periodic and continuous measurements carried out in recent years. The most frequent causes of the deterioration in operating conditions are poorer coal quality compared to the design, erosion of turning vanes in the ducts upstream of the ESP and of distribution plates in the ESP [4], increased temperature and flow of the flue gases compared to the design values [5], obsolescence of the equipment, failures of the electrical fields of the high-voltage supply systems, etc. Many factors influence ESP dedusting performance, such as the flue gas velocity distribution and turbulence level [4, 6], the strength and distribution of the electrical field [7], the size, resistivity and charge of particles [8], electrode configurations inside an ESP [9], temperature and compositions of the gas [5], etc. The Matts-Öhnfeldt [8, 9] generalized form of the ordinary Deutsch-Anderson equation gives relation for the ESP collection efficiency η as the ratio of outlet C_{out} and inlet C_{in} dust concentration via the particle migration velocity, ω_k , the ESP collecting area, A , and the gas flow rate, Q :

$$\eta = \frac{C_{out}}{C_{in}} = e^{\left[-\left(\frac{\omega_k A}{Q} \right)^k \right]} \quad (4)$$

with the parameter k allowing to compensate for different particle size distribution of the incoming dust (of the values around 0.5 for coal-fired boilers, while $k = 1$ corresponds to a uniform particle size, thus to the original Deutsch equation). It could be shown that, if we take so called coefficient of variation (CV) as a measure of the uniformity of the cross sectional gas flow profile in ESP, defined as the ratio of the standard deviation to the mean [4, 10]:

$$CV = \frac{S_{dev}}{\bar{v}} = \frac{1}{\bar{v}} \sqrt{\frac{\sum_{i=1}^n (v_i - \bar{v})^2}{n-1}} \quad (5)$$

with \bar{v} being the average gas velocity in the ESP cross-section $\bar{v} = \frac{1}{n} \sum_{i=1}^n v_i$, for the case of relatively small velocity variation and not extremely high value of the collection efficiency, the maximum theoretical ESP collection efficiency results from perfectly uniform gas velocity [4]:

$$\eta \approx e^{\left[-\left(\omega_k (1-k(CV)^2)^{\frac{1}{k}} \frac{A}{Q} \right)^k \right]} \quad (6)$$

where Q [m³/s] is gas flow rate, ω_k [m/s] – particle migration velocity, A [m²] - the ESP collecting electrode area. The eq. (3) indicates that maximum theoretical ESP collection efficiency results from perfectly uniform gas velocity distribution over the ESP's chamber cross section ($CV = 0$).

The migration velocity ω represents the ability to collect particles within a certain ESP and depends on the particle size, the strength of the electric field and the viscosity of the flue gas [9]:

$$\omega = \frac{d_p \cdot E \cdot E_m}{4 \cdot \mu \cdot \pi} = \frac{q \cdot E}{3 \cdot \mu \cdot \pi \cdot d_p} \quad (7)$$

where d_p - is the particle diameter [μ m], q - charge of a particle [C], E_m - electric field strength [V/m] in charged particles, E - electric field strength [V/m] in the collected particles (normal field near the deposition electrodes, expected values 300-400 kV/m), μ - gas viscosity [Pa·s], $\pi = 3.14$. Therefore, the dust removal efficiency also depends on the intensity of the electric field in the ESP chamber. If presents the efficiency of dust removal as:

$$\eta = 1 - \frac{C_{out}}{C_{in}} = 1 - e^{\left(-a \frac{P}{Q} \right)} \quad (8)$$

where P/Q [$W/1000 \cdot m^3/h$] is the power density of the corona, then high dust removal efficiency could be obtained only for high values of the power density of the corona [11]. A high dust removal efficiency of an ESP is achieved by simultaneously establishing a homogeneous flue gas velocity field in the vertical sections of the ESP chamber, which flows through the optimally regulated electric field inside the ESP chamber [12]. The consortium, consisting of the Vinča Institute for Nuclear Sciences, the Institute of National Importance for the Republic of Serbia, the University of Belgrade and the Electrotechnical Institute Nikola Tesla AD Belgrade, has been successfully developed and applied new measurement equipment [13] and original methodology for diagnosing the working conditions of the ESP. The methodology consists of the following steps:

- a) inspection of the electrical and mechanical equipment of the ESP;
- b) on-site measurements (distribution of velocity, temperature and flue gas composition in the flue gas ducts, particulate matter emissions, distribution of air velocity in vertical cross-sections of the ESP chamber) and laboratory analyses of coal, fly ash and bottom ash;
- c) numerical CFD simulations of various geometric solutions of the structural elements of the ESP (channels, turning and guide vanes, distribution plates) in order to obtain the geometrical solution which enable the best flow homogeneity in the ESP chamber. The most commonly used parameters for assessing flow homogeneity were the dimensionless momentum M_k (Boussinesq coefficient) and energy correction coefficient N_k (Coriolis coefficient) [14]:

$$M_k = \frac{\int v^2 dA}{v_{avg}^2 A_{tot}} = \frac{1}{A_{tot}} \sum_{i=1}^n \left(\frac{v_i}{v_{avg}} \right)^2 \Delta A_i, \quad N_k = \frac{\int v^3 dA}{v_{avg}^3 A_{tot}} = \frac{1}{A_{tot}} \sum_{i=1}^n \left(\frac{v_i}{v_{avg}} \right)^3 \Delta A_i \quad (1)$$

where v_i [m/s] is a mean velocity through the elementary surface i of the cross-section of the ESP chamber, v_{avg} [m/s] – mean velocity in the cross-section, ΔA_i [m^2] – elementary surface i and n – number of elementary surfaces i in the cross-section of the ESP chamber. The values of M_k and N_k are equal to unity only under the uniform flow conditions. The further the flow deviates from uniformity, the greater these values become.

- d) numerical simulation of the structural and electrical parameters of ESP (gas flow rate, ratio of total length and height of ESP, gas residence time, specific surface area of the specific collection area (SCA), effective migration velocities ω_e , ESP efficiency, etc.) for the various ESP power supply solutions.

The results of the applied methodology enable detailed theoretical and numerical analyses with the aim of identifying the existing limitations and defining the measures to be taken in order to achieve a high efficiency of the analysed EF systems. The effectiveness of the proposed measures is reflected in the fact that, following their application to the ESP of unit A4 of the TPP TENT A4, ESP of unit B2 of the TPP TEKO B and ESPs of units A1 and A2 of the TPP TEKO A, particulate emissions have been reduced from over 60 mg/Nm^3 to around 30 mg/Nm^3 , which puts emissions well below the ELV.

2. Results and discussion

2.1. Unit A4 of TPP Nikola Tesla A

The TENT A4 350 MW power unit has two 4-stage, plate-type, dry ESPs, reconstructed and modernized during the capital overhaul made in 2007. The reconstructed ESP consists of two separate chambers with eight hoppers for dust collection. The flue gas duct is long and very complex with a wide-angled, asymmetrical diffuser and confuser (Fig.1). Chambers are electrically divided into four zones, equipped with four 50 Hz transformers of conventional type and with single-phase anti-parallel thyristor bridges. The effective length, width and height of each ESP casing are 17.6 m, 16.24 m and 17.7 m respectively. The total area of collecting electrodes (CEs) in one chamber is 23296 m^2 . Each of four electrical zones I-IV contains 40 CEs with 400 mm wide passages between neighboring CEs. A new control and power supply systems were installed, providing primary voltage of 400 V/50 Hz, primary current of 430 A, secondary voltage peak (without load) of 106 kV, average secondary current for the field of 1700 mA. The reconstructive interventions proposed by the INN Vinca – EI Nikola Tesla consortium are marked in red in Figures 1 and 2 and consists of installation of new set of turning vanes in the inlet elbow (I), new set of guide vanes in the difusser (II) and new set of turning vanes in the outlet elbow (III). The fourth proposed intervention was the replacement of two existing single-phase thyristor power supplies (1-T/R) in the first zone of the left and right ESP chambers with three-phase thyristor power supplies

(3-T/R) with increased secondary voltage and current values. The results of the numerical simulation for the ESP model with the newly proposed structural elements are shown in Figure 2. The newly established flow has one small dead zone in the center of the ESP chamber, but results in very acceptable homogeneity parameters in the front of each and behind the last electrical field.

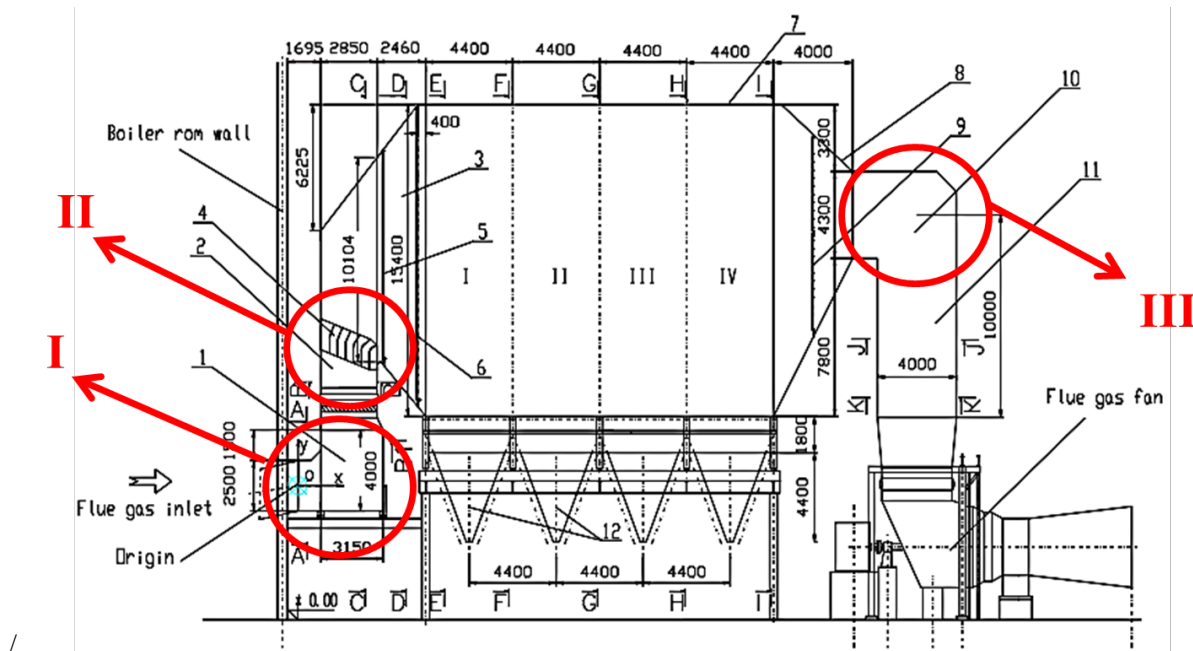


Figure 1. ESP of unit A4 of TPP TENT A – side view: 1 - inlet elbow, 2 - inlet channel, 3 - ESP diffuser, 4 - turning vanes, 5 - 1st perforated plate, 6 - 2nd - perforated plate, 7 - ESP casing, 8 - confusor, 9 - outlet screen, 10 - outlet elbow, 11 - outlet channel, 12 - hoppers, I - IV - electrical zones. Red marks for reconstructive intervention: I - new set of turning vanes in the inlet elbow, II - new set of guide vanes in the diffuser, III - new set of turning vanes in the outlet elbow

Applied measures resulted in reduction of PM concentration from 49.5 mg/m³ and 84.8 mg/m³ [15] to the level of 33.8 mg/m³ and 16.2 mg/m³ [16] for the left / right ESP chamber, considerably below the ELV.

2.2. Unit B2 of TPP Kostolac B

The TEKO B2 350 MW power unit has two 4-stage, plate-type, dry ESPs, reconstructed and modernized during the capital overhaul made in 2012.

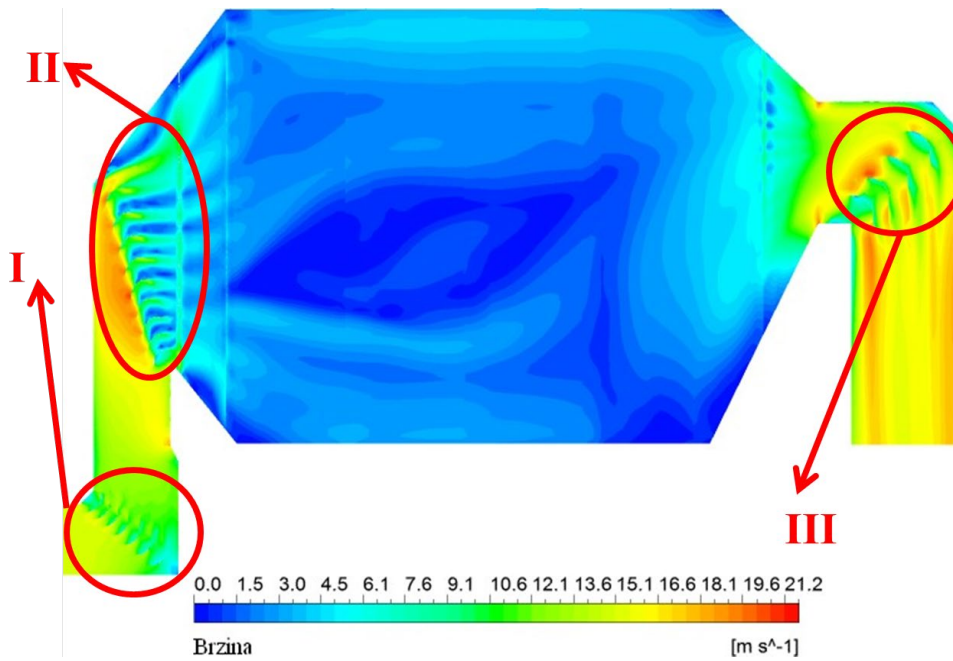


Figure 2. Model of ESP of unit A4 with new proposed set of turning vanes in the inlet elbow (I), new proposed set of guide vanes in the diffuser (II) and new proposed set of turning vanes in the outlet elbow (III), results of numerical simulation, distribution of x-component of the velocity, u [m/s]

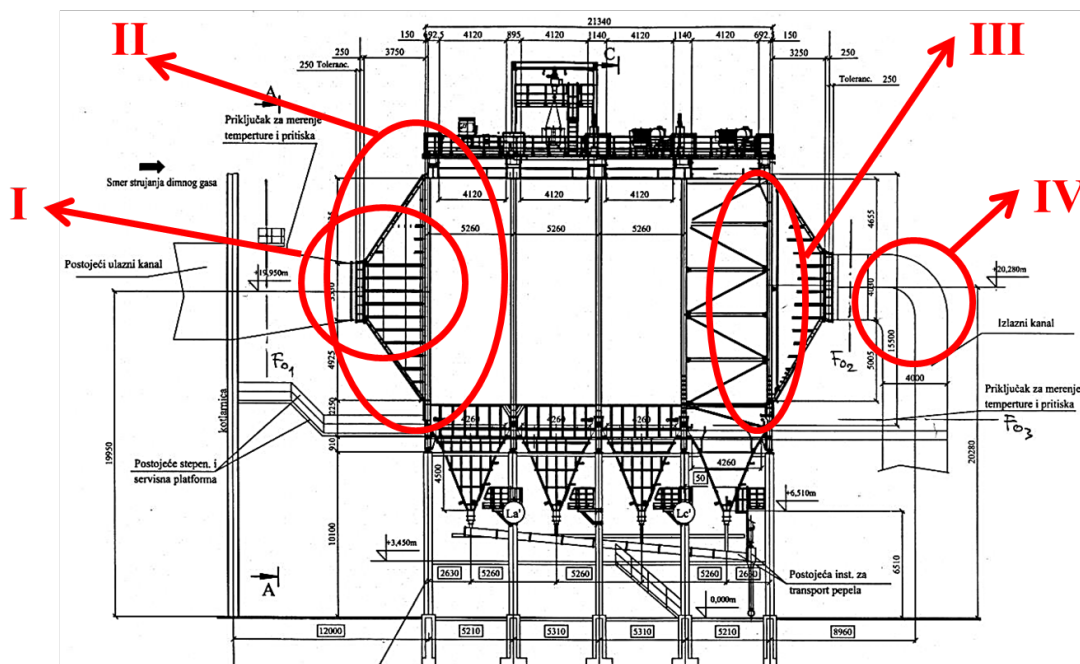


Figure 3. ESP of unit B2 TPP TEKOB – side view. Red marks for reconstructive intervention: I – new set of turning plates in the diffuser, II – new set of guide vanes in the diffuser, III – new distribution plate in the confusor, IV – new set of turning vanes in the outlet elbow

The reconstructed ESP consists of two units, each with a chamber divided into four mechanical dedusting zones (Fig.3), of which the first two (zones 1 and 2) are divided into two electric fields powered by high-frequency devices (20 kHz), and fields 3 and 4 are fed by transformer rectifier units of the conventional 50 Hz type. In total, there are 6 independent electric fields in the left and 6 in the right chamber. The effective length, width and height of each ESP casing are 21.34 m, 16.87 m and 15.5 m respectively. The total area of collecting electrodes (CEs) in one chamber is 35712 m². Each of electrical zones 1 and 2 contains 40 CEs with 400 mm wide passages between neighboring CEs and 32 CEs in the zones 3 and 4 with 500 mm wide passages between neighboring CEs. The reconstructive interventions proposed by the INN Vinca – EI Nikola Tesla consortium

are marked in red in Figures 3 and 4 and consists of installation of new set of turning plates in the diffuser (I), new set of guide vanes in the diffuser (II), new design of distribution plate in the conffusor (III) and new set of turning vanes in the outlet elbow (IV).

The flue gas parameters at the inlet of the ESP of unit B2 of TPP Kostolac B in the previous period were lower than the design values in the past period. The actual value of migration velocity ω_{ef} is 36% lower than design value. The area of the CE of about 48000÷58000 m² is required instead of the existing 35712 m² in order to obtain dedusting efficiency of $\eta = 99.93\%$. The existing geometry of the electrodes in the ESP chamber allows for much higher values for the secondary current and secondary voltage than the built-in power supply units can realise. The realised values of specific corona current and corona current density are at the lower limit of the recommended for power units of 300÷350 MW. Dedusting efficiency η can be increased by increasing the electrical parameters of the power supply (installation of new power supplies).

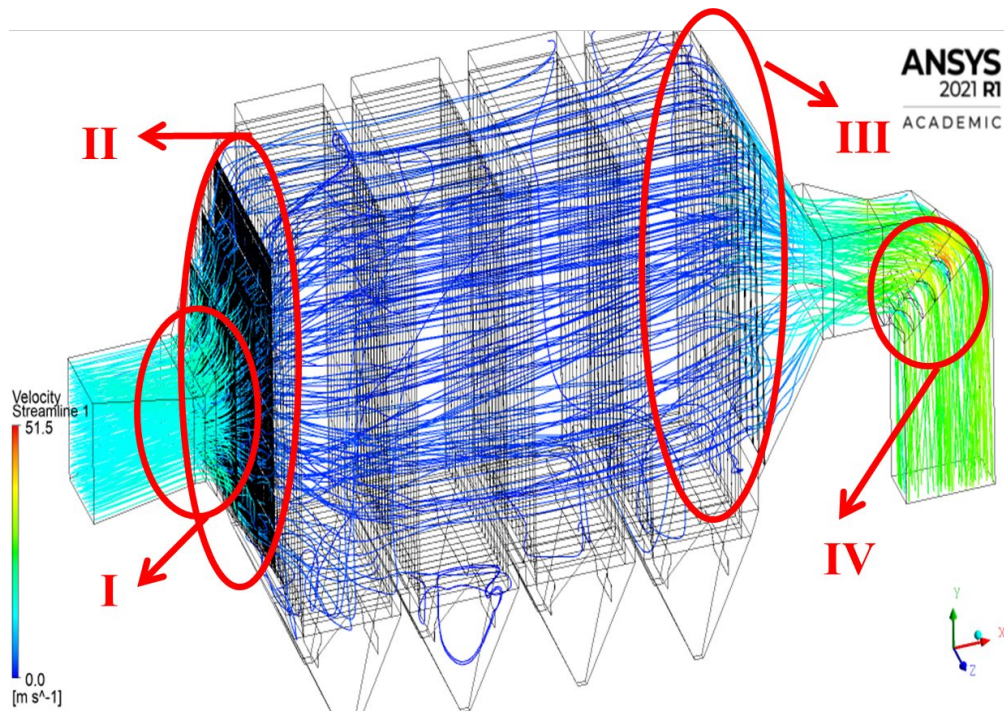


Figure 4. Model of ESP of unit TEKO B2 with new proposed set of turning plates in the diffuser (I), new proposed set of guide vanes in the diffuser (II), new design of distribution plate in the conffusor (III), new proposed set of turning vanes in the outlet elbow (IV), distribution of x-component of the velocity, u [m/s]

Applied measures resulted in good flow homogeneity in the ESP chambers (Fig. 4), with flow homogeneity parameters $M_k < 1.1$ and $N_k < 1.2$ in the cross-sections of the ESP chamber in the front of the first and behind the last electrical field. The good homogeneity of the flue gas flow was therefore reflected in the reduction of the average PM concentration in three consecutive tests of both ESP chambers from more than 70 mg/m³ [17] to 29.6 mg/m³ [18], which is well below the ELV.

2.3. Unit A1 of TPP Kostolac A

Each boiler of TEKO A1 110 MWe power unit has its own ESP plate-type, dry ESP, reconstructed and modernized during the capital overhaul made in 2005.

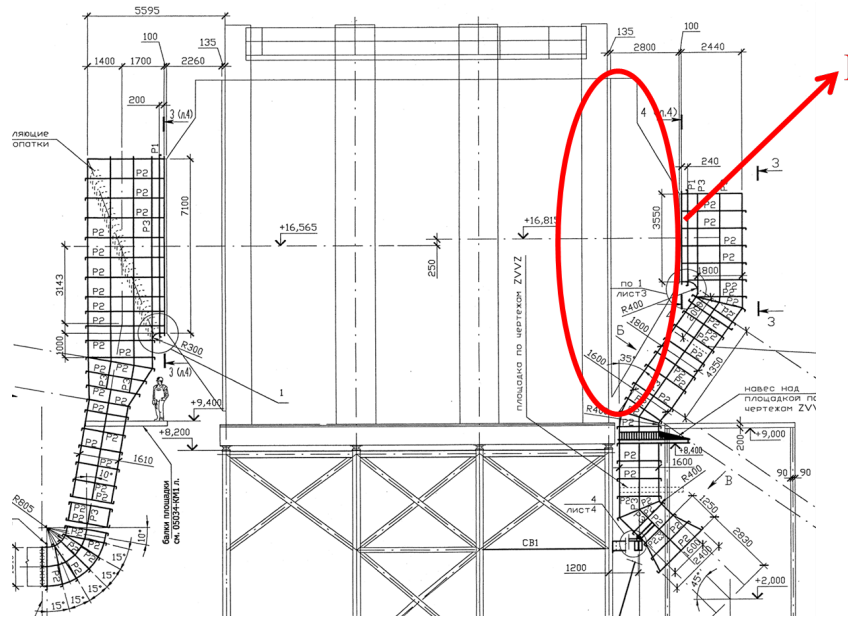


Figure 5. ESP of unit A1 TPP TEKO A – side view. Red marks for reconstructive intervention: I – new distribution plate in the confusor

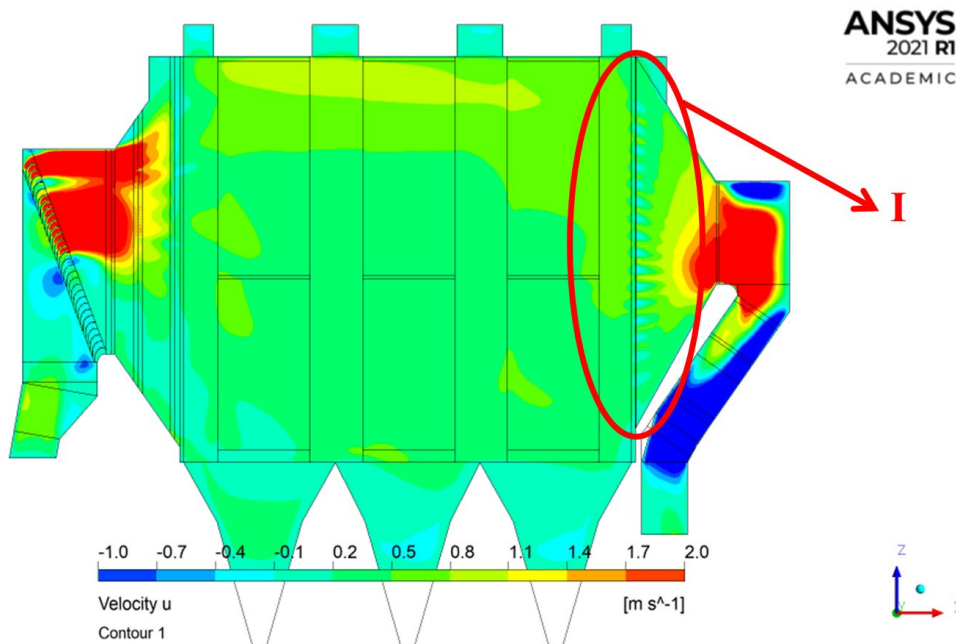


Figure 6. Model of ESP of unit TEKO A1 with new proposed design of distribution plate in the confusor (I), distribution of x-component of the velocity, u [m/s]

The flue gas duct is long and very complex with a wide-angled, asymmetrical diffuser and confusor (Fig.5) with a strong confusor suction effect. The reconstructed ESP consists of two units, each with a chamber divided into 3 mechanical dedusting zones, with 24 CEs with 500 mm wide passages between neighboring CEs. The effective length, width and height of each ESP casing are 15.56 m, 12.2 m and 13.5 m respectively. The total area of collecting electrodes (CEs) in one chamber is 35712 m². The reconstructive interventions proposed by the INN Vinca – EI Nikola Tesla consortium are marked in red in Figures 5 and 6 and consists of installation of new design of distribution plate in the confusor (I).

Maximum design value of the effective migration velocity $\omega_{ef} = 0.2456$ m/s. Minimum specific surface area of the CE is $SCA = 29.2$ m²/(m³/s). Maximum design values of the specific corona current of 0.593 mA/m².

The corona current values were below the design value of 1250 mA in all electrical zones, especially in zones 1 and 2. The temperature and oxygen content in the flue gas were above, while the flue gas flow was approximately equal to the design value and the PM concentration at the inlet of the ESP was below or close to the design value. During the annual overhaul of the ESP TEKO A1 in 2022, the single-phase thyristor-controlled (1-T/R) supplies of the first electrical fields were replaced by improved three-phase thyristor power supplies (3-T/R). Periodic emission measurements carried out after the modernisation showed that the corona current in the first zone had increased to 1035÷1135 mA, i.e. ~90% of the design value. In addition, the installation of a new distribution plate in the confusor significantly improved the flow homogeneity in the ESP chamber by elimination of confusor suction effect, which overall helped to increase the efficiency of the ESP above the design value of 99.923% and reduce particulate emissions from more than 75 mg/Nm³ to level of 27.8÷42.2 mg/Nm³.

2.4. Unit A2 of TPP Kostolac A

The ESP of unit TEKO A2 210 MWe has two 4-stage, plate-type, dry ESPs, reconstructed and modernized during the capital overhaul made in 2006. The flue gas duct is long and very complex with a wide-angled, asymmetrical diffuser and confusor (Fig.7) with a strong confusor suction effect. The reconstructed ESP consists of two units, each with a chamber divided into four mechanical dedusting zones, with 36 CEs with 400 mm wide passages between neighboring CEs. The effective length, width and height of each ESP casing are 17.28 m, 14.59 m and 15.23 m respectively. The total area of collecting electrodes (CEs) is 37897 m². The reconstructive interventions proposed by the INN Vinca – EI Nikola Tesla consortium are marked in red in Figures 7 and 8 and consists of installation of new set of turning plates in the diffuser (I), new design of distribution plate in the confusor (II) and new set of stop plates in the dust collecting hoppers (III).

Detailed analysis concluded that effective migration velocity $\omega_{ef} = 0.1229$ m/s was correctly assumed. Also, it was found that ESP has a high specific CE surface area of $SCA = 57.42$ m²/(m³/s) and low design flue gas velocity through the chamber of 1.5 m/s, a long length of the active electric fields of 17.28 m and long residence time in the zone of active electric fields of 11.5 s. Actual corona current were below the design value of 4100 mA/chamber. The temperature and oxygen content in the flue gas were above, while the flue gas flow was below or around the design value. PM concentration at the inlet to the ESP were around the design value. Low dedusting efficiency in previous period was the result of a combination of unfavourable electrical parameters and flue gas parameters, but after reconstruction proposed by the INN Vinca – EI Nikola Tesla consortium the flow field in the ESP chamber has improved significantly (Fig.8), eliminating confusor suction effect and dust reentrainment from hoppers, thus leading to a reduction in PM emissions.

3. Conclusion

A complex methodology was developed and successfully applied to define a technical solution for increasing the dedusting efficiency of ESP unit A4 of TPP Nikola Tesla A, unit B2 of TPP Kostolac B and units A1 and A2 of TPP Kostolac A. The methodology is based on complex on-site measurements of flue gas temperature, composition and velocity distribution in the ducts and chambers of the ESP, as well as on the analysis of the measured operating parameters of the ESP and the TPP unit, the properties of coal, fly ash and bottom ash determined in the laboratory, the results of numerical CFD analyses and the results of the calculation of the complex electrical parameters of the ESP.

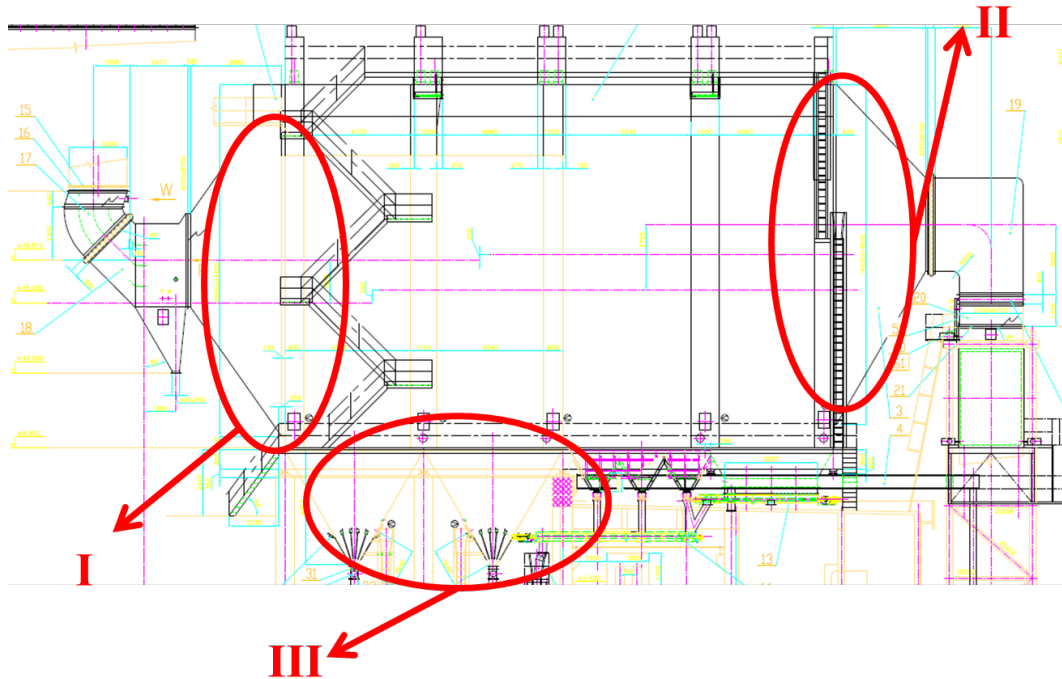


Figure 7. ESP of unit A2 TPP TEKO A – side view. Red marks for reconstructive intervention: I – new set of turning plates in the diffuser, II – new distribution plate in the confusor, III – new set of stop plates in the dust collecting hoppers

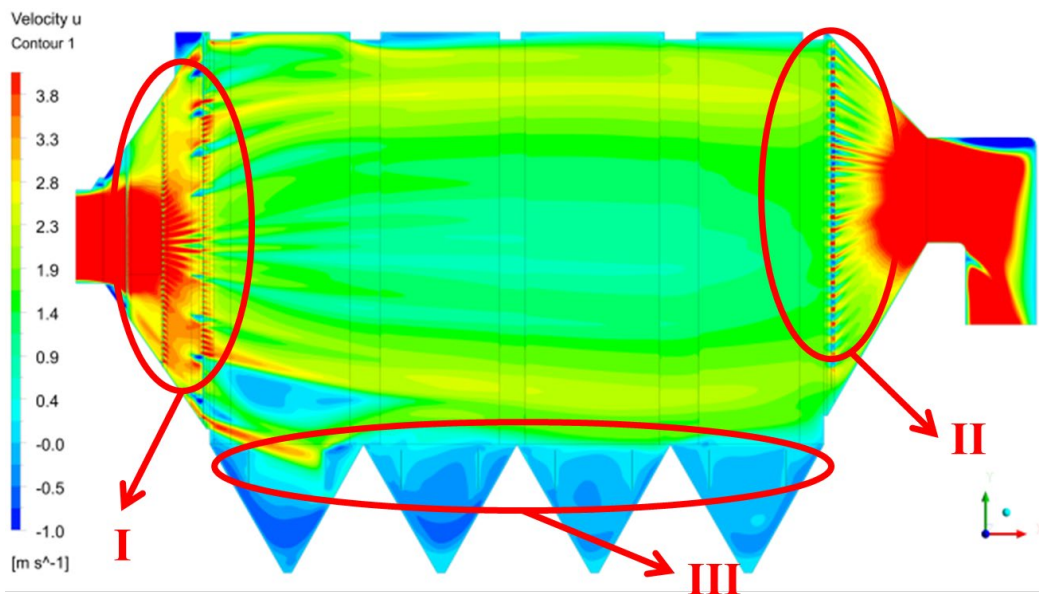


Figure 8. Model of ESP of unit TEKO A2 with new proposed set of turning plates in the diffuser (I), new proposed design of distribution plate in the confusor (II) and new proposed set of stop plates in the dust collecting hoppers (III), distribution of x-component of the velocity, u [m/s]

A mathematical algorithm was developed to calculate the parameters of the ESP and increase the efficiency of its operation. Special measuring devices were developed and successfully used to measure the air velocities in large vertical cross-sections of the ESP chamber. The need for regular, periodic measurements of particulate matter emissions is once again evident and proves to be a reliable source of information on the operating parameters of the ESP. Regular inspections and measurements of the velocity distribution in the ESP chamber during the periodic overhaul of the TPP unit and the ESP are necessary to determine mechanical elements that are damaged by erosion and need to be replaced in order to improve the flow homogeneity and thus the efficiency of the ESP.

Acknowledgements

The research was funded by the Ministry of Science, Technological Development and Innovation of the Republic of Serbia (Contract Annex: 451-03-66/2024-03/200017). The authors are very grateful for the support of this work by the Joint Stock Company Elektroprivreda Srbije.

References

- [1] Cliff I. Davidson , Robert F. Phalen & Paul A. Solomon, Airborne Particulate Matter and Human Health: A Review, *Aerosol Science and Technology*, 39:8, (2005), pp. 737-749, DOI: 10.1080/02786820500191348
- [2] EUROPEAN COMMISSION, Guidelines for the Implementation of the Green Agenda for the Western Balkans Accompanying the Communication from the Commission to the European Parliament, the Council, the European Economic and Social Committee and the Committee of the Regions An Economic and Investment Plan for the Western
- [3] Balkans, COM(2020) 641 final, pp. 1-22, https://www.mei.gov.rs/upload/documents/eu_dokumenta/2020/green_agenda_for_the_western_balkans_en.pdf
- [4] Directive 2001/80/EC of the European Parliament and of the Council of 23 October 2001 on the limitation of emissions of certain pollutants into the air from large combustion plants
- [5] A. Bäck, Relation Between Gas Velocity Profile and Apparent Migration Velocity in Electrostatic Precipitators, *International Journal of Plasma Environmental Science & Technology*, Vol.11, No.1, (2017), pp. 104-111
- [6] Bao-YuGuo, Ai-BingYu, JunGuo, Numerical modeling of electrostatic precipitation: Effect of Gas temperature, *Journal of Aerosol Science* 77 (2014), pp. 102–115
- [7] Munnannur A, et al., Development of Flow Uniformity Indices for Performance Evaluation of Aftertreatment Systems, *SAE Int.J.Engines*, 4 (1), (2011), pp. 1545 – 1555
- [8] Jaworek, A., et al., Two-stage vs. two-field electrostatic precipitator, *Journal of Electrostatics* 90, (2017), pp. 106–112
- [9] Arkadiusz Świerczok, Maria Jędrusik, The collection efficiency of ESP model - Comparison of experimental results and calculations using Deutsch model, *Journal of Electrostatics*, 91 (2018), pp. 41–47
- [10] Ning, Z., et al, Electrode configurations inside an electrostatic precipitator and their impact on collection efficiency and flow pattern, *Eur. Phys. J. D* 70: (2016), 126
- [11] Dazhou Zhao et al, Flow Field Simulation and Optimization Design of SCR of 660MW Power Unit Based on CFD Study, 2018 *IOP Conf. Ser.: Earth Environ. Sci.* 170 (2018), 042031
- [12] Ken Parker, Electrical Operation of Electrostatic Precipitators, Institute of Engineering and Technology, London (2007), p. 74, Figure 4.10
- [13] Marković Zoran J., Erić Milić D., Stefanović Predrag Lj., Jovanović Rastko D., Lazović Ivan M., Optimization of the flue gas flow controlling devices of the electrostatic precipitator of unit 4 in TPP "Nikola Tesla", *Thermal Science*, (2023), OnLine-First (00):24-24.
- [14] Lazović, Ivan; Marković, Zoran; Erić, Milić; Jovanović, Rastko; Tasić, Viša; "Transport trolleys for anemometers for testing the air velocity profile in the chambers of electrostatic precipitators of large emitters", Petty Patents, Intellectual Property Gazette 2022/11 (12/12), published 30.11.2022., Republic of Serbia, ISSN 2217-9143 (Online) Intellectual property office (in serbian)
- [15] Zhou, J., et al., Energy and momentum correction coefficients within contraction zone in open-channel combining flows, *Water Science and Engineering*, 14(4), (2021), pp. 337-344
- [16] Test report no. E-28/16/JPEPS/TENT-A 456, December 2016, Laboratory for work and environment protection, Mining Institute Belgrade (in serbian)
- [17] Test report no. E-05/20/JPEPS/TENT-A 456, February 2020, Laboratory for work and environment protection, Mining Institute Belgrade (in serbian)
- [18] Erić, M., Marković, Z., Periodic Measurement of Pollutant Emissions in the Air of Units B1 and B2 of the Kostolac Power Plant in Kostolac, Technical Report NIV-LTE-662, Vinča Institute, July 2020, Belgrade-Vinča (in serbian)
- [19] Erić, M., Marković, Z., Periodic Measurement of Pollutant Emissions in the Air of Unit B2 of the Kostolac Power Plant in Kostolac, Technical Report NIV-LTE-682, Vinča Institute, December 2021, Belgrade-Vinča (in serbian)

Urban Resilience Planning to Climate Change Through Innovative Nexus Approach

*Serena Caucci^a, Giannis Adamos^b, Tamara Rađenović^c, Dejan Vasović^d
Snežana Živković^e*

^a *United Nations University (UNU-FLORES), Dresden University of Technology (TUD), Dresden, DE,
caucci@unu.edu*

^b *Aristotle University of Thessaloniki, Department of Civil Engineering, Thessaloniki, GR,
adamos.giannis@gmail.com*

^c *University of Niš, Faculty of Occupational Safety, Niš, RS, tamara.radjenovic@zrnrfak.ni.ac.rs*

^d *University of Niš, Faculty of Occupational Safety, Niš, RS, dejan.vasovic@zrnrfak.ni.ac.rs*

^e *University of Niš, Faculty of Occupational Safety, Niš, RS, snezana.zivkovic@zrnrfak.ni.ac.rs*

Abstract: Addressing the need for enhanced urban resilience planning is pressing in response to the escalating impacts of climate change in many regions of the world, particularly in the wider Western Balkans region and Mediterranean areas. Rapid urbanization, and water extremes, coupled with unsustainable land use practices, exacerbate the vulnerability of cities to climate-related hazards such as heatwaves, floods, and wildfires. Recognizing the urgency of this challenge, this study adopts an innovative Nexus Approach to support the transition of municipalities and institutional policy frameworks into a solid system for resilient urban planning. By leveraging the strengths of GIS-based models and engaging multiple stakeholders in co-creation processes, the Nexus approach aims to develop robust strategies for enhancing urban and peri-urban resilience. Drawing on the principles of the Water-Energy-Food-Ecosystem (WEFE) Nexus, the study employs a multifaceted approach to address the complex challenges of urban resilience planning and integrates urban water management, energy systems, green infrastructure, and peri-urban agriculture into holistic planning frameworks. Through stakeholder engagement and capacity-building initiatives, it aims to co-create innovative solutions tailored to the specific needs of different regions. These endeavors are directed towards empowering decision-makers and communities to develop and implement effective strategies for climate resilience.

Keywords: Urban Resilience Planning, WEFE Nexus Approach, Climate Change.

1. Introduction

The escalating impacts of climate change present profound challenges for urban areas worldwide. This is particularly evident in regions such as the Western Balkans and Mediterranean areas, where rapid urbanization and unsustainable land use practices increase vulnerability to climate-related hazards. Cities face a range of threats, including heatwaves, floods, and wildfires, which are intensified by the interplay of urban growth and environmental degradation. To address these challenges, innovative and comprehensive planning approaches are required [1].

Urban planning faces several challenges in responding to extreme climatic events. Rapid urbanization often leads to increased impervious surfaces, exacerbating flood risks and heat island effects [2]. Traditional urban planning methods frequently lack the flexibility to adapt to the dynamic nature of climate change, resulting in insufficient preparedness for extreme weather events [3]. Furthermore, the fragmentation of urban governance structures can impede the effective implementation of resilience strategies, as responsibilities and resources are often dispersed across multiple agencies [4].

Moreover, the integration of natural resource management into urban planning is often inadequate. Effective management of natural resources is critical for enhancing urban resilience and adapting to climate change. Sustainable practices such as water reuse, energy-efficient infrastructure, and the preservation of green spaces can mitigate the adverse effects of extreme climatic events [5]. However, these practices are not always incorporated into urban planning due to institutional barriers, lack of technical expertise, and limited financial resources [6].

At the same time, natural resource management plays a vital role in urban development and adaptation to climate change. Effective management can enhance the sustainability and resilience of urban areas by promoting the efficient use of resources, reducing environmental impacts, and supporting ecosystem services [7]. Integrated water management, for example, can mitigate flood risks, ensure water availability during droughts, and support the health of urban ecosystems [8]. Incorporating green infrastructure into urban planning can also provide multiple benefits, including temperature regulation, stormwater management, and improved air quality [9]. Renewable energy sources, such as solar and wind power, can reduce greenhouse gas emissions and enhance energy security [10]. By adopting a holistic approach to resource management, cities can build resilient infrastructures capable of withstanding the impacts of climate change [11].

The integrated approach of the Water-Energy-Food-Ecosystem (WEFE) Nexus has the flexibility to integrate such domains of natural resource management into of urban management thus allowing for the creation of resilient urban environments under extreme climate events. By leveraging GIS-based models and engaging multiple stakeholders, the WEFE Nexus aims to develop strategies that enhance the capacity of municipalities and generate settings for improved policy frameworks to respond to and recover from climate-related impacts [8].

2. Methodology

2.1. Nexus Approach

The Nexus Approach central to WEFE Nexus focuses on the interconnectedness of water, energy, food, and ecosystems and their management in urban and peri-urban areas of Municipalities. This holistic perspective is critical in urban resilience planning as it ensures that interventions in one sector consider the impacts on others, thereby promoting sustainable development. The Nexus Approach facilitates integrated urban water management, energy efficiency, sustainable agriculture, and the enhancement of green infrastructure [12]. Below are the multiple approaches that are to be included in the Urban Resilience Planning to Climate Change for Municipalities.

2.2. GIS-Based Models

Geographic Information Systems (GIS) play a crucial role in the WEFE Nexus as provide detailed spatial analysis and visualization capabilities of urban and peri-urban resources. Thus, the GIS-based models enable the identification of areas most vulnerable to climate-related hazards and the simulation and analysis of different scenarios, including the assessment of the potential impacts of proposed interventions. These models support evidence-based decision-making and the development of targeted strategies for resilience [13].

2.3. Stakeholder Engagement and Co-creation of Solutions

Engaging stakeholders from diverse sectors and levels of governance is essential for the success of WEFE Nexus. The approach employs a co-creation process that involves municipalities, policymakers, community organizations, and experts in the fields of water management, energy systems, agriculture, and urban planning. This collaborative approach ensures that the developed strategies are context-specific, socially acceptable, and technically feasible [14].

2.4. Capacity Building Approaches

Capacity-building initiatives are integral to the Nexus approach, aiming to empower local authorities and communities to implement and sustain resilience strategies. Training programs, workshops, and knowledge-sharing platforms are designed to enhance the skills and knowledge of stakeholders, enabling them to effectively manage urban resilience initiatives [5], especially in urban planning design.

3. Results

3.1. Integration of Urban Water Management and Enhanced Energy Systems

The legacy of the WEFE Nexus is to successfully integrate urban water management into the broader urban resilience framework. By utilizing GIS-based models, the critical areas for water reuse and optimized water distribution networks were identified. This integration has enhanced the efficiency of water use in urban and peri-urban areas, reducing vulnerability to water scarcity and extreme weather events [7].

Additionally, the development and adoption of suggested energy-efficient practices tend to reduce the carbon footprint of urban areas and enhance energy security. The integration of energy systems with water and food management has created synergies that further enhance resilience [10].

3.2. Sustainable Peri-Urban Agriculture and Green Infrastructure

The WEF Nexus also extends to the interconnected peri-urban area neighboring the Municipalities. Here the concept of sustainable peri-urban agriculture which promotes the reuse of water and the implementation of agroecological practices becomes fundamental to circular economy management, and thus a more balanced natural resources use and management. This approach indeed supports food security, reduces urban heat islands, and enhances biodiversity. The peri-urban agriculture can play a significant role in building resilient urban ecosystems [15]. Additionally, the enhancement of green infrastructure is supported by the development of parks and green roofs or gardens which provide multiple benefits, including temperature regulation, stormwater management, and improved air quality. Green infrastructure also enhances the aesthetic and recreational value of urban areas, contributing to the well-being of residents [9].

3.3. Urban Planning Strategies for Integrated Resource Management and Preparedness for Climate-Related Emergencies

The WEF Nexus emphasizes urban planning strategies that integrate resource management to create sustainable infrastructures. One critical strategy is the development of multi-functional green spaces that serve as both recreational areas and flood control systems. These green infrastructures, such as bioswales and retention ponds, help manage stormwater while enhancing urban biodiversity and providing social benefits [2]. Additionally, the integration of smart water systems and renewable energy sources into urban planning reduces the delay in response to climate-related emergencies by ensuring resource availability and resilience.

To improve preparedness for climate-related emergencies instead, the WEF Nexus aims at identifying strategies for the development of integrated early warning systems for multi-risk assessment of natural hazards which should be integrated with GIS-based models approaches that could provide prompt data on potential hazards and forecasts, thus enabling a rapid response and mitigation measures from Municipalities. The WEF Nexus could also support the development of community-based emergency response plans that should include training and actions for local populations. This participatory approach ensures that communities are well-prepared to respond to emergencies such as floods, heatwaves, and wildfires [16].

Through the identification of climate disaster-prone areas within the Western Balkans and Mediterranean regions via integrated Nexus management and GIS-based models, the highly vulnerable hotspot areas prone to hazards such as floods, droughts, and landslides could be mapped and a priority interventions strategy promoted and resources for intervention allocated effectively. The identification of hotspots also facilitates targeted public awareness campaigns and the development of localized emergency response plans [17].

3.4. Drafting of Emergency Planning Through the Nexus Approach

Emergency planning under the WEF Nexus approach is conducted by ensuring that all aspects of resource management are considered. For urban and peri-urban areas, this involves the integration of water safety plans, energy security measures, and food supply continuity into emergency response strategies. For instance, in municipalities prone to landslides and flooding, plans that incorporate early warning systems, sustainable drainage systems, and community-led response initiatives could be developed. This holistic approach not only enhances immediate response capabilities but also builds long-term resilience by addressing underlying vulnerabilities [11]. This is especially true in municipalities where water and safety plans are of high relevance, such as those susceptible to landslides, flooding, and drought. These plans should include measures for water conservation, efficient water use, and pollution control. By addressing the Nexus of water management and urban planning, it is ensured that municipalities are better equipped to handle the dual challenges of water scarcity and increased pollution during climate-related emergencies [18].

4. Discussion

The WEF Nexus approach offers several advantages over traditional planning methods. By recognizing the interdependencies between water, energy, food, and ecosystems, the approach promotes a holistic understanding of urban resilience. This leads to more integrated and sustainable solutions that address multiple challenges simultaneously [12]. The use of GIS-based models enhances decision-making by providing detailed

spatial analysis and visualization capabilities. These models enable policymakers to identify vulnerable areas, assess the impacts of proposed interventions, and prioritize resources effectively. This evidence-based approach ensures that decisions are grounded in robust data and analysis [13]. WEF Nexus emphasizes stakeholder engagement and capacity building, which are critical for the success and sustainable implementation of resilience initiatives. By involving local communities and authorities in the planning process, this approach fosters a sense of ownership and empowerment. This participatory approach ensures that resilience strategies are socially acceptable and tailored to local needs [14].

The integration of green infrastructure, renewable energy, and sustainable agriculture into urban planning promotes long-term sustainability. These initiatives not only enhance resilience to climate-related hazards but also contribute to broader environmental and social benefits. By creating synergies between different sectors, the WEF Nexus approach supports the development of resilient, sustainable, and livable urban environments [2].

5. Conclusion

The WEF Nexus represents a comprehensive and innovative approach to urban resilience planning in the face of climate change. By adopting the Nexus Approach, leveraging GIS-based models, engaging stakeholders, and building local capacity, WEF Nexus allows for robust development of urban planning strategies under extreme climatic events towards more resilient urban and peri-urban areas. By emphasizing integrated resource management, early response planning, and community empowerment the WEF Nexus approach ensures that municipalities are well-equipped to mitigate and adapt to the impacts of climate change. Ultimately, this approach aims to build resilient, environmentally sustainable, and socially just urban environments capable of thriving in an era of climate uncertainty.

Acknowledgment

Part of this publication is based upon work from the COST Action <CA20138: Network on water-energy-food nexus for a low-carbon economy in Europe and beyond – NEXUSNET>, supported by COST (European Cooperation in Science and Technology).

References

- [1] IPCC. Climate Change 2021: The Physical Science Basis. Contribution of Working Group I to the Sixth Assessment Report of the Intergovernmental Panel on Climate Change. Cambridge University Press. 2021.
- [2] Gill, S. E., Handley, J. F., Ennos, A. R., & Pauleit, S. Adapting cities for climate change: The role of the green infrastructure. *Built Environment*, 2007, 33(1), 115-133.
- [3] Huq, N., Hugé, J., Boon, E., & Gain, A. K. (2015). Climate change impacts in agricultural communities in rural areas of coastal Bangladesh: A tale of many stories. *Sustainability*, 7(7), 8437-8460.
- [4] Anguelovski, I., Shi, L., Chu, E., Gallagher, D., Goh, K., Lamb, Z., ... & Teicher, H. Equity impacts of urban land use planning for climate adaptation: Critical perspectives from the global North and South. *Journal of Planning Education and Research*, 2016, 36(3), 333-348.
- [5] Brown, R. R., & Keath, N. Drawing on social theory for transitioning to sustainable urban water management: Turning the institutional super-tanker. *Australian Journal of Water Resources*, 2008, 12(2), 73-83.
- [6] Bai, X., Roberts, B., & Chen, J. Urban sustainability experiments in Asia: Patterns and pathways. *Environmental Science & Policy*, 2018, 84, 47-56.
- [7] Fletcher, T. D., Shuster, W., Hunt, W. F., Ashley, R., Butler, D., Arthur, S., ... & Mikkelsen, P. S. SUDS, LID, BMPs, WSUD and more – The evolution and application of terminology surrounding urban drainage. *Urban Water Journal*, 2015, 12(7), 525-542.
- [8] Hoff, H. Understanding the nexus. Background paper for the Bonn2011 Conference: The Water, Energy and Food Security Nexus. Stockholm Environment Institute. 2011.
- [9] Tzoulas, K., Korpela, K., Venn, S., Yli-Pelkonen, V., Kaźmierczak, A., Niemelä, J., & James, P. Promoting ecosystem and human health in urban areas using Green Infrastructure: A literature review. *Landscape and Urban Planning*, 2007, 81(3), 167-178.
- [10] Lund, H. Renewable energy strategies for sustainable development. *Energy*, 2007, 32(6), 912-919.
- [11] FAO. The water-energy-food nexus: A new approach in support of food security and sustainable agriculture. Food and Agriculture Organization of the United Nations. 2014.
- [12] Weitz, N., Nilsson, M., & Davis, M. A nexus approach to the post-2015 agenda: Formulating integrated water, energy, and food SDGs. *SAIS Review of International Affairs*, 2017, 35(2), 37-50.
- [13] Mills, G., Coutts, A., Harris, R., & White, C. Climate information for improved planning and management of urban environments: State of the art and future direction. *Climate Services*, 2010, 1(1), 1-6.



- [14]Reed, M. S., Graves, A., Dandy, N., Posthumus, H., Hubacek, K., Morris, J., ... & Stringer, L. C. Who's in and why? A typology of stakeholder analysis methods for natural resource management. *Journal of Environmental Management*, 2009, 90(5), 1933-1949.
- [15]Zasada, I. Multifunctional peri-urban agriculture—A review of societal demands and the provision of goods and services by farming. *Land Use Policy*, 2011, 28(4), 639-648.
- [16]UNISDR. Sendai Framework for Disaster Risk Reduction 2015-2030. United Nations Office for Disaster Risk Reduction. 2015.
- [17]De Sherbinin, A., Warner, K., & Ehrhart, C. Climate change and migration. International Organization for Migration (IOM). 2012.
- [18]WHO. Water safety planning for small community water supplies: Step-by-step risk management guidance for drinking-water supplies in small communities. World Health Organization. 2011.



V. Innovative technologies and plants in energy science

Optimal System for Collecting Landfill Gas - Landfill Meglenci, Republic of North Macedonia

Blagoj Dimovski^a, Vangelce Mitrevski^b, Vladimir Mijakovski^c, Cvete Dimitrieska^d

*^aFaculty of Technical Sciences, University „Kliment Ohridski”, Bitola, MK,
blagoj.dimovski@uklo.edu.mk*

*^bFaculty of Technical Sciences, University „Kliment Ohridski” Bitola, MK,
vangelce.mitrevski@uklo.edu.mk*

*^cFaculty of Technical Sciences, University „Kliment Ohridski” Bitola, MK,
vladimir.mijakovski@tfb.uklo.edu.mk*

*^dFaculty of Technical Sciences, University „Kliment Ohridski” Bitola, MK,
cvete.stefanovska@tfb.uklo.edu.mk*

Abstract: The energy strategy of Republic of North Macedonia until 2040, in addition to the use of classic renewable energy sources and high criteria for environmental protection, also foresees the use of landfill gas that is produced in the open landfills on its territory. In addition to the large number of wild illegal landfills, the only legal landfill in North Macedonia is landfill Drisla near Skopje. In the Meglenci regional landfill near TPP (Thermal power plant) Bitola, which is planned to serve the southwestern part of the country, the efficient collection of landfill gas, which would be used as energy, is of great importance. This paper presents an analysis based on results obtained from theoretical and experimental research, with the aim of choosing the optimal system for the collection and conversion of gas in the Meglenci landfill. In doing so, the latest relevant data on the quantity and quality of the organic fraction from the waste, the conditions in the landfill, climatic factors and other input data were used in order to obtain data on the yield of landfill gas. Technologies that are available and applicable for the specific landfill have been studied, based on the data obtained from the mathematical model and the techno-economic analysis. The "collection" of greenhouse gases, such as landfill gas, is a legal obligation within the framework of environmental protection, but the possibility of using it as an energy source contributes to the energy system at the local level.

Keywords: Landfill gas, Methane production model, Waste to energy systems, Optimal solution.

1. Introduction

The Republic of North Macedonia has a low level of development in the sector of waste management. In 2024, 54 non-standard landfills [1] and one standard landfill Drisla, located southeast of Skopje, [2] were determined. According to the EU Directive on landfills [3] and the Strategy for the development of energy in the Republic of North Macedonia until 2040 [4], it is planned to close non-standard landfills and open centralized regional landfills. Accordingly, an analysis was made for the establishment of an integrated self-sustaining system for waste management in the Southwestern region of Macedonia - Meglenci, which will fulfill the requirements related to the control of gases that cause the greenhouse effect (GHG - greenhouse gases), [5], [6]. Also, a system for the extraction and utilization of landfill gas as a source of energy was proposed, where an analysis was made for the expected production of methane and the extent of its utilization through the Afvalzorg model [7]. An analysis of the economic benefit related to the capacity of the landfill and the quality of the produced landfill gas is also given.

2. Regional landfill Meglenci

The landfill Meglenci is located in the southwestern part of the Republic of North Macedonia (Fig. 1 and 2) in the immediate vicinity of the lignite mine "Suvodol", which has been out of operation for some time due to the excavated lignite reserves according to the previous deposits. The lifetime of the landfill is divided into: phase A (8 years, surface area 17500 m², real capacity 185000 m³ waste) and phase B (16 years, surface area 25000 m², real capacity 395000 m³ waste) [3]. The annual delivery of waste to the landfill is 37 522 t/year.



Figure 1 and Figure 2. Location of the landfill Meglenci on a Google earth map

3. Landfill Gas Production and Utilization Assessment

Landfill gas is a greenhouse gas (GHG – Greenhouse Gas) which consists mainly of generated methane and carbon dioxide as a result of the anaerobic biodegradation of municipal solid waste (MSW) in landfills, primarily of organic origin. LFG (Landfill Gas) is usually composed of methane (CH₄) (about 50%), carbon dioxide (about CO₂) (45%) and other minor elements, such as nitrogen (N₂), hydrogen sulfide (H₂S) and non-methane organic compounds (NMOC) (about 5%) [8]. The greenhouse gas emissions increase the temperature of the atmosphere and poses a threat to the environment and human health. Methane emitted by landfills is among the most significant contributors to the greenhouse effect with at least 28 times more global warming potential than carbon dioxide and accounts for about 20% of the global greenhouse gas impact on the atmosphere [9]. The rate of increase of CH₄ in the previous few decades is from 1 to 2% per year, with a tendency to increase if appropriate measures are not taken [10].

The amount of LFG produced and collected from a certain amount of waste varies depending on the parameters (temperature, moisture, composition of waste, structure of waste, disposal, distribution, bulking of waste, other local conditions, *etc.*). With more recent research on a projected time period of waste collection lasting 40-80 years, the expected production of LFG would be 50-100 m³ per ton of waste [11].

To estimate the production and utilization of landfill gas, in previous researches [7], the single-phase model (Afvalzorg model) is usually used, which is upgraded and adjusted based on the characteristics of the landfill that is the subject of research [7]. Afvalzorg model is a first-order decay model based on the mathematical expressions of the IPCC (Intergovernmental Panel of Climate Change) and default parameters (DOC – degradable organic carbon, k – reaction rate constant...). The model is single-phase and during data processing it is assumed that organic matter decomposes at the same rate. This model is applied in the case where little or no detailed data on the composition of the waste is available [7]. The output diagrams of the Afvalzorg model, adjusted for the conditions of the landfill Meglenci, are presented in Figure 3 and Figure 4, where it is assumed that the peak of the produced and captured methane will be in 2055, after the closure of the landfill. Parameters corresponding to the climatic conditions in the region of the landfill Meglenci have been adopted, and also the percentage representations of the waste components in the Southwestern region of North Macedonia have been entered.

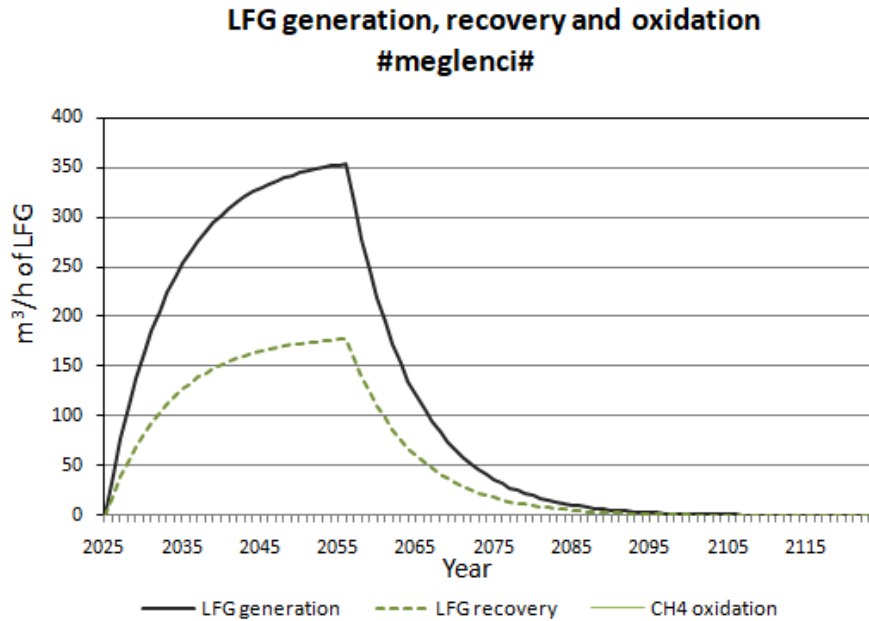


Figure 3: Afvalzorg model volume flow for landfill gas production and recovery (no oxidation)

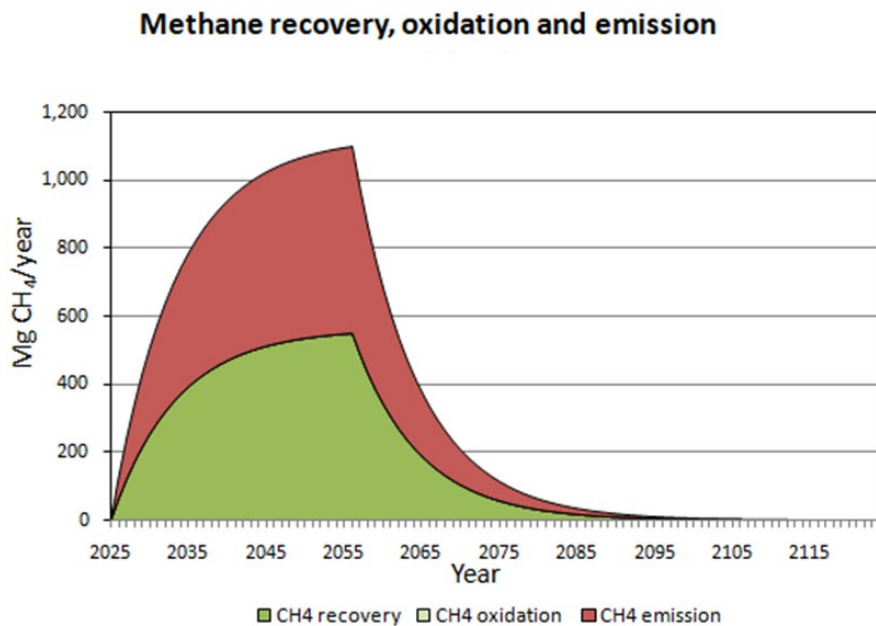


Figure 4: Afvalzorg model mass flow for methane emission and recovery (no oxidation)

During the researches, field measurements were also made at specific landfills for which an estimation was made for the production and extraction of landfill gas according to Afvalzorg's model, showing that the average actual extraction for the 14 LFG plants was only 39.6% of the extraction estimated in the model, [11].

4. Landfill gas utilization systems

LFG utilization plants typically consist of an extraction system and an exploitation system [11]. The simplest system is by capturing LFG through vertical gas pipes and using it for energy purposes. The gas engine-generator unit can produce electricity or represent a combined plant for obtaining heat and electricity.

When the use of LFG for energy purposes is not economically viable, the gas should be burned in a flare. Incineration is done for environmental reasons, in order to reduce methane emissions and their contribution to the greenhouse effect. Combustion also reduces unpleasant odors and the risk of fire and explosion.

Figure 5 shows the types of landfill gas utilization systems in the world by 2023 [12]. The largest part refers to plants for the production of electricity, direct use is made by burning and obtaining thermal energy in boilers, while RNG (Renewable natural gas) systems improve the quality of landfill gas to that of natural gas and it is transported in gas pipelines. RNG plants have the smallest application in the world, but have seen significant growth in recent years.

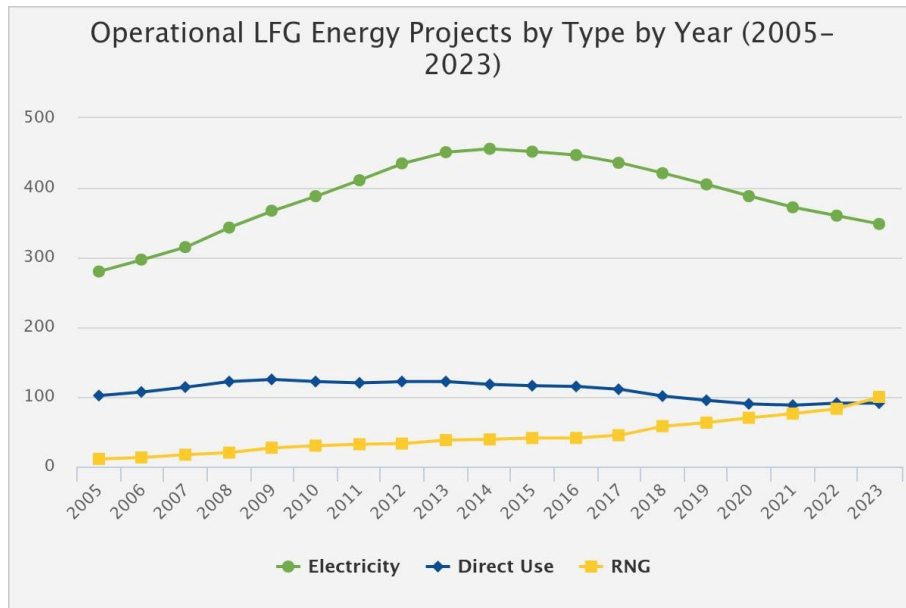


Figure 5: Statistics from the EPA (Environmental Protection Agency) on types of landfill gas systems

5. Economic analysis

To estimate the economic benefits of energy production from landfill gas, a mathematical model is used where investment, operational and maintenance costs are included. Indicators are also used that show specific investment costs related to equipment for capturing LFG of different quality, adjusting the system to implement the legislation, *etc.* In addition, with such research, the benefits resulting from the difference in the preferential tariffs and the costs of electricity production have been estimated, [13]. From Figure 6 it can be seen that the specific costs are lower in case of higher landfill gas quality and lower installed capacity of the power plant. The optimum of specific costs is located between an installed power of 0.2 MWe and 0.6 MWe [13]. Landfill gas quality is presented in three scenarios (10 MJ/m^3 , 13 MJ/m^3 , 18 MJ/m^3) depending on the quality and stage of waste decomposition.

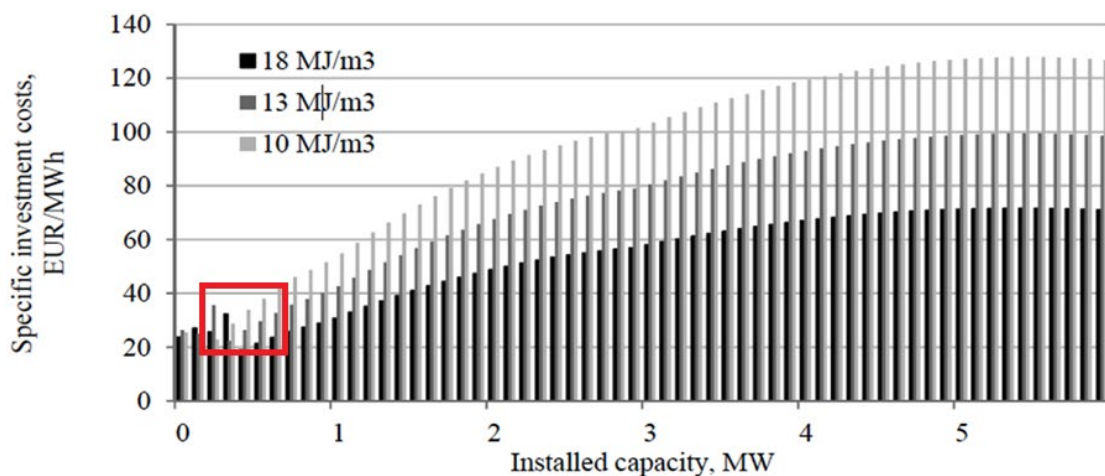


Figure 6: Specific investment costs for electricity generation from landfill gas

6. Solutions for utilization of landfill gas production in Meglenci

If we take into account the results of Figure 3, where in the period of 2035-2055 the landfill generates methane of about $120 \text{ m}^3/\text{h}$ and if we add the factor 0.396 that indicates the actual utilization of methane extraction, in eq. 1 is obtained:

$$C = Q \cdot LHV_{CH_4} \cdot R \quad (1)$$

where:

$C \approx 0.5 \text{ MW}$ is the capacity of the gas engine-generator unit;

$Q = 120 \text{ m}^3/\text{h}$ is the volume flow delivered by the landfill;

$LHV_{CH_4} = 37.074 \text{ MJ/m}^3$ is the lower heating power of methane;

$R = 0.396$ is the utilization factor of methane extraction.

According to the economic framework from 0.2 MWe to 0.6 MWe (Fig. 6), this capacity of the planned plant is justified. According to the obtained results, it can be concluded that the construction of a plant with a gas engine for obtaining electricity from landfill gas at the landfill Meglenci is realistic and justified in the operational period of 2035-2055.

7. Conclusion

The technologies for LFG utilization, the obtained results of the model for estimating the produced and absorbed methane in the landfill Meglenci, as well as the given optimal framework for the costs of the conceptual plant, provide the possibility of building a plant with a gas engine for obtaining electricity energy from landfill gas with an expected capacity of 0.5 MW. Also, the results provide an opportunity for further research related to improving the efficiency of the systems according to the specific conditions of the landfill Meglenci. In case of problems with integrating the plant into the electricity distribution network, an alternative option is to install a gas combustion system in order to prevent methane emissions into the atmosphere.

References

- [1] [https://app.gdi.mk/download/%D0%A1%D0%BF%D0%B8%D1%81%D0%BE%D0%BA%20%D0%BD%D0%B0%20%D0%BD%D0%B5%D1%81%D1%82%D0%B0%D0%BD%D0%B4%D0%B0%D1%80%D0%B4%D0%BD%D0%B8%20\(%D0%B4%D0%B8%D0%B2%D0%B8\)%20%D0%B4%D0%B5%D0%BF%D0%BE%D0%BD%D0%B8%D0%B8%20%D0%B2%D0%BE%20%D0%A0%D0%9C.pdf](https://app.gdi.mk/download/%D0%A1%D0%BF%D0%B8%D1%81%D0%BE%D0%BA%20%D0%BD%D0%B0%20%D0%BD%D0%B5%D1%81%D1%82%D0%B0%D0%BD%D0%B4%D0%B0%D1%80%D0%B4%D0%BD%D0%B8%20(%D0%B4%D0%B8%D0%B2%D0%B8)%20%D0%B4%D0%B5%D0%BF%D0%BE%D0%BD%D0%B8%D0%B8%20%D0%B2%D0%BE%20%D0%A0%D0%9C.pdf)
- [2] <https://drisla.mk/>
- [3] Environmental impact assessment study for the investment project "Establishment of an integrated and financially self-sustainable waste management system in the Pelagonian and Southwestern regions", Skopje, 2022;
- [4] Strategy for the development of energy in the Republic of North Macedonia until 2040, Skopje, 2019;
- [5] Kyoto Protocol to the United Nations Framework Convention on Climate Change, Kyoto, 2005;
- [6] Kostovski Z., „Potential for the utilization of solid municipal waste for the production of electricity in the Bitola region“, Master's thesis, University „Kliment Ohridski“ Bitola, Bitola, NMK, 2012;
- [7] <https://www.afvalzorg.com/landfill-gas/lfg-models>
- [8] Ahmed, S. I., Johari, A., Hashim, H., Mat, R., Lim, J. S., Ngadi, N., Ali, A. (2015). Optimal landfill gas utilization for renewable energy production. *Environ. Prog. Sustain. Energy*, 34, 289–296, DOI: 10.1002/ep.11964.
- [9] Li, S., Yoo, H. K., Macauley, M., Palmer, K., Shih, J.-S. (2015). Assessing the role of renewable energy policies in landfill gas to energy projects. *Energy Econ.*, 49, 687–697. DOI: 10.1016/j.eneco.2015.03.022.
- [10] Singh, C. K., Kumar, A., Roy, S. S. (2018). Quantitative analysis of the methane gas emissions from municipal solid waste in India. *Sci. Rep.*, 8, 2913. DOI: 10.1038/s41598-018-21326-9.
- [11] Terraza H., Willumsen H., „Guidance Note on Landfill Gas Capture and Utilization“, 2009;
- [12] <https://www.epa.gov/lmop/switch-renewable-natural-gas>
- [13] Dace E., Blumberga D., Kuplais G., Optimization of landfill gas use in municipal solid waste landfills in Latvia, International Scientific Conference “Environmental and Climate Technologies – CONECT 2014”, Riga, Latvia, October 14-16, 2014, pp. 293 – 299

Paddy Drying in Mixed-flow Tower-type Dryer

Filip Mojsovski^a, Vladimir Mijakovski^b

^a Faculty of Mechanical Engineering, Skopje, MK, filip.mojsovski@mf.edu.mk

^b Faculty of Technical Sciences, Bitola, MK, vladimir.mijakovski@tfb.uklo.edu.mk

Abstract: The purpose of this paper is to present the relevant data for paddy drying in mixed-flow dryer, obtained with conducted research on high-capacity dryer. An examination was carried out to reach the correct drying condition in industrial rough rice dryer. The attention was concentrated on main dryer element, the horizontal drying module. One drying module is composed of one or two drying rooms and one tempering section. By field tests, the heat flow amount and continuity were observed and evaluated in multi-thermal zoned drying process. The dryer is composed of five modules with double drying room and one tempering section, one module of three drying rooms without tempering section and four drying rooms in package as cooling section. Two thermal-zones drying system was exploited, with inlet air temperatures up to 44 °C, and with inlet air temperatures up to 40 °C. In the cooling section the air temperature was dictated by the grain outlet temperature up to 36 °C. Intermittent paddy tempering of up to two hours was accepted.

Keywords: Mixed-flow dryer, Intermittent process, Paddy.

1. Introduction

Rice is one of the most important food for humans and animals. World production in 2021 was more than 787.000.000 tonnes [1].

The rice varieties in North Macedonia are mostly from Italian origin. In 2023, rice was cultivated at 3.000 ha and production of about 18.000 tonnes was realized [2]. In the past times, maximum reached values were, area of 10.000 ha and 50.000 tonnes paddy crop. Rice is important component of national food reserves.

About 50 % of world paddy production is parboiled. Parboiled rice is more nutritious than white rice. Paddy parboiling is done in three steps: soaking, steaming and drying [3]. During the steaming, nutrients contained in the bran, diffuse in the mass of white rice. Parboiled rice is also dried in mixed-flow tower-type dryers.

Rice quality depends on rice variety, environmental conditions during the growing period, time and system of harvesting, postharvest treatment, storage practices and transport procedures [4].

The harvested rice kernel, known as paddy or rough rice, is enclosed by the hull. Paddy has the roughest hull surface of all cereals. About one-fifth of paddy weigh is hull. The losses for dehulling are up to 30 %. Paddy hull removed in the milling process is then stored in silos for the drying period, when it is used as a fuel.

Rice is harvested at moisture contents that are too high for safe storage. Therefore, paddy is exposed to drying process, ideally within 24 hours. To avoid the uneven drying, harvested paddy ought to be cleaned.

The final moisture content of dried paddy depends of intended use: for sale, for one year storage or for many years storage. Some paddy producers, waiting for better price on the market, store the grain up to 5 years, and only than dehull it and sell it as white rice. Visually, the staleness of white rice kernel cannot be discovered, but the quality is different.

The change of moisture content during the drying process is most often elaborated graphically, in the form of drying curves [5].

In mixed-flow tower-type dryer, paddy is introduced at the top of the dryer, then passes into the drying modules and finally into the cooling section. Grain is moving down by gravitation. Its falling is disturbed by the elements of internal module construction and by the air flow. Air is moving by ventilator effect. Its direction is formed by deflectors and regulation valves. At the bottom of the dryer horizontal unloading auger is located. Its duties are the regulation of the grain movement and the bringing out of the dried product. The dryer used in the research was designed as universal, for all cereals drying. Some corrections in the dryer construction

were made in order to obtain specific dryer for rice, to involve multi-thermal zoned drying, to enable the intended procedure for measurement and regulation.

Drying process is crucial for rice quality. Rice quality is estimated according to grain size, shape uniformity, translucency, milling yield, cooking characteristics, cleanliness and soundness.

In the actual mixed-flow dryer, the dried product, paddy, and the drying medium, atmosphere air, are in mutual movement which is combination of cocurrent-flow, cross-flow and countercurrent-flow. Such an action of the flow, provides very small variation in the rice moisture content.

The drying process is interrupted by inserting tempering section. A tempering section offers enough time for harmonization of dried product state. During the tempering period the grain is not exposed to hot air flow and thus the temperature and moisture gradients within the individual kernels are diminished before drying is resumed. Drying rice slowly, with intermittent tempering is a suitable drying method, because rice is highly sensitive to the amount and the intensity of received heat. That favors the application of mixed-flow dryer with discontinuous heat supply.

Paddy drying is thermal process of simultaneous heat and mass transfer. The process consists of two phases: 1. water pass in gas state and 2. water vapor is taken away from the dried product. The intensity of transport phenomena is under the influence of the characteristics of dried product, drying medium and dryer.

The structure of rice body is capillary-porous. The movement of evaporated water inside the grain is influenced by capillary forces, but at the kernel surface, the partial vapor pressure difference, between the water-vapor in the kernel and the surrounding air, is the driving force. The moisture movement in capillary-porous body is also influenced by diffusion and Earth gravitation. The problem of simultaneous heat and mass transfer from indeterminate and changeable space and mass, under the influence of outside state, capillary forces, diffusion, gravitation and location in the dryer is complicated.

The existing theory for simultaneous heat and mass transfer in capillary-porous body cannot offer solution for drying rate calculation under different drying conditions. It remains to search for the results with the use of field and laboratory tests.

Field tests can show the real situation, but their application is expensive because the mixed-flow tower-type dryer uses large quantities of dried product. In the case of incorrect drying, that mass of grain is lost. Therefore, theory of similarity can be used to carry out the research in laboratory conditions.

2. Equipment - Mixed-flow Tower-type Dryer

Before the realization of planned tests, the construction of the dryer was modified in order to enable zoned air flow, to uniform the air velocities at the drying module entrance, to make simultaneously stop of grain movement and hot air supply and to have access at all measuring points.

The hot air duct was divided in two hot air ducts. Deflectors were placed in the air ducts. The function of the centrifugal ventilators and the unloading auger was coordinated. Measuring platforms and sampling tubes were installed.

Mixed-flow tower-type dryers are high-capacity dryers. Exploited dryer is composed of filling module, 13 drying rooms, 5 tempering sections, 4 cooling modules, unloading auger, three centrifugal ventilators and two heat exchangers.

The dimensions of one drying room are: 3 m x 3 m x 1 m, Figure 1. The inner construction of the drying room provides mixed-flow. The tempering section is 0,5 m high. It is built as vertical duct without direct drying air supply. This is the first pause in grain heating. Its duration depends of drier construction. The second pause in grain heating is planned by the intermitting regime, and is controlled by unloading auger and heating supply.

The heat exchanger, composed of several heating coil sections assembled into a bank, uses hot water as heating medium. The heat demand for heat exchangers is provided by applying paddy hulls as fuel.

In total, the dryer reaches 26 m height.

On the one side, the dryer is connected with hot air duct and cold air duct, while at the opposite side the modules are equipped by regulatory valves. The hot air flow is divided in two hot air ducts. During the pass in the upper side of the dryer, since paddy is still cool and has relatively high moisture content, hot air temperature can be higher.

Dried material state, drying medium state and dryer function were continuously controlled by visual evaluation, measurements and test judging. The measurement program included: 1. grain moisture content and temperature, 2. air temperature, relative humidity and velocity, and 3. dryer zonal drying time and energy consumption. Measuring points were selected for initial, zonal and final state.

For paddy state control, the method of sampling in time and space was used. Measuring platforms and sampling instrument were added. Sampling tube, constructed as tube-in-tube device, enabled to take specimen from every module. The movement of the sampling probe is not easy, because it is obstructed by the paddy hull roughness. Grain specimens were examined in the laboratory, to verify the expected rice quality. Direct measurement, moisture content determination method, with device based on infra-red radiation was applied.

For drying medium state control, fixed and portable digital psychrometers and anemometers were used.

For dryer function control, the basic regime parameters were continuously checked and operation problems were immediately resolved. The air flow rate from centrifugal fans was controlled by measurement, conducted before the start of the drying process.

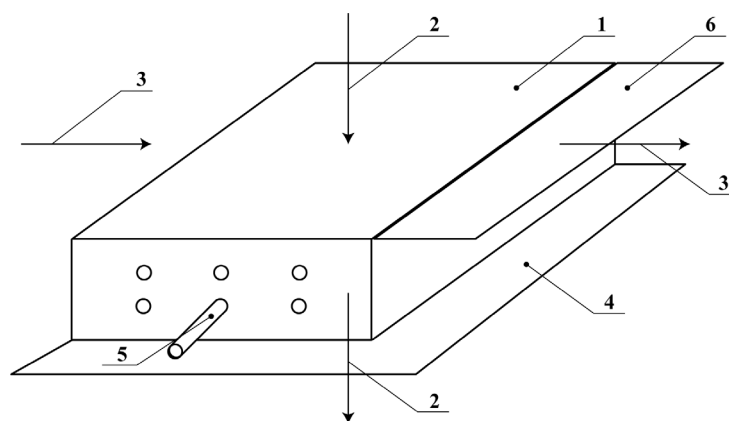


Figure 1. Drying room of mixed-flow tower-type dryer; 1-Module, 2-Paddy (in/out), 3-Air (in/out), 4-Platform, 5-Sampling tube, 6-Valve

3. Results and Comments

Reconstructed dryer showed good effects in practice. The installed five tempering sections were enough for satisfying the tempering process. With two hot air ducts, equipped by deflectors, the distribution of hot air at the entrance of the drying rooms was favorable. Added measuring platforms were functional.

Entered impurities with the paddy mass, weed seeds, soil, twigs and straw provoked same obstruction of needed grain flow. Registered quantity was only 1 % of the dried product mass, but in some modules, the tendency of impurities accumulation was observed and therefore grain cleaner was additionally connected to the filling module. For the drying medium, three zones system was selected as convenient. The temperature at the entrance of the first two modules, was up to 44 °C, at the entrance of the next eleven heating modules was up to 40 °C, and at the entrance of the next four cooling modules, was the same as the temperature of the atmosphere air.

The analysis of the drying medium state and estimation of the quantity of atmosphere air, required to remove the moisture from the dried product was based on psychrometry [6]. The maximum ability of moist air to absorb moisture from the dried rice was calculated with the help of the psychrometric chart, as a difference between its saturation moisture at wet-bulb temperature and its moisture content at dew-point.

According to the climatic curves and the psychrometric diagram, the range of atmosphere air temperatures, relative humidities and enthalpies, for the period of rice drying from September until October is: 2 - 30 °C, 35 - 80 % and 10 - 54 kJ/kg. The calculated amount of heating energy for the two extreme states of atmosphere air (2 °C, 80 %) and (30 °C, 35 %) is very different (39 kJ/kg and 11 kJ/kg). These data exactly determine the expected thermal zone in which the drying process will occur.

The process of heat transfer from the hot air to the dried product was interrupted by inserting tempering periods. The pauses of up to two hours, offered conditions for drying process which provided first class dried product.

When the harvest season is wet, the paddy moisture content, wet basis is between 18 % and 30 %, but during the normal, dry harvest season, the paddy moisture content, wet basis is 16 - 28 %. Variations of up to 8 % are registered in the moisture contents, wet basis of mature and least mature kernels.

Three rice varieties were used in the conducted research: Monticelli, Saint Andrew and RS 76. In the rice quality evaluation, the Laboratory for rice and seed quality control in Kočani, was included in the test program.

Paddy was entering in the filling module with moisture contents, wet basis 16 - 28 % and temperatures 12 - 22 °C. In the first two modules the moisture content, wet basis was 14 - 23 % and the temperature was 15 - 28 °C. In the third to thirteenth module the moisture content, wet basis was 11 - 15 % and the temperature was 24 - 36 °C. In the fourteenth to seventeenth module the moisture content, wet basis was 10 % and temperature was 14 °C. For long term storage, lower exit moisture content is needed. The paddy exit temperature of 35 °C was not surpassed. During the cooling process some moisture was also removed.

Dried paddy is hygroscopic material, therefore immediately after the exit of the unloading auger it must be stored in a space with controlled atmosphere.

For the control of centrifugal fans capacity, portable flow measuring duct was constructed. Measuring instruments were standard hand-held Pitot-tube in conjunction with a micromanometer and digital anemometer.

By measuring the generated heat, during combustion of paddy hull in calorimeter, heating value of 15 MJ/kg was obtained. This value is 20 % lower of beech wood heating value. The use of paddy hull as fuel has three advantages: 1. secondary product is consumed at the same location where it is produced, 2. the deposition of paddy hulls is solved, because in its composition it has more than 90 % silicon (something like pebbles at the beach), and it would be very harmful to mix its combustion products with field land, and 3. the burned paddy hull is important component of some cleaning powders.

4. Conclusion

As a result of the carried out research, performed on high-capacity mixed-flow dryer, suitable drying conditions were established in field-test procedure. The universal, for all types of cereals drying construction of the dryer, was modified before the start of the planned research and has shown good effects in practice.

Applied slow drying process, with intermittent heat supply provided quality dried product. The small quantity of broken kernels in the dehulling process was confirmation that they haven't internal stresses acquired in the drying process.

The measurements focused on thermal state of the drying medium and the dried product offered values for minimum and maximum required heat flow in the process.

The search for the results with the use of field and laboratory tests, proved to be an appropriate way in the approach for solving these types of problems in drying.

References

- [1] FAO (Food and Agriculture Organization of the United Nations), FAOSTAT Database, 2024
- [2] Statistical Yearbook of the Republic of N. Macedonia 2023, State Statistical Office, Skopje, Republic of N. Macedonia
- [3] Mojsovski, F., Dimitrovski, D., Thermal conditions for rice parboiling process realised with the use of renewable energy resource, *Journal of Environmental Protection and Ecology*, 16 (2015), 2, pp. 699 - 704
- [4] Brooker, D. B., Bakker-Arkema, F. W., Hall, C. W., *Drying and storage of grains and oilseeds*, Van Nostrand Reinhold, New York, 1992
- [5] Mojsovski, F., Dimitrovski, D., The effect of the heat flow amount and continuity on dried rice quality, *Mechanical Engineering-Scientific Journal*, 38 (2020), 1, pp. 89-92
- [6] Mojsovski, F., Analysis of humidity level in psychrometric thermal processes, Ph.D. thesis, „Ss. Cyril and Methodius” University, Faculty of Mechanical Engineering, Skopje, 2007

Determining the Reliability Function of the Thermal Power System in the Power Plant “Nikola Tesla, Block B2”

Ivan Popović^a, Milan Đorđević^b, Jasmina Skerlić^c, Vladan S. Jovanović^d, Snežana Kirin^e

^aFaculty of Technical Sciences, Kosovska Mitrovica, RS, ivan.popovic@pr.ac.rs

^bFaculty of Technical Sciences, Kosovska Mitrovica, RS, milan.djordjevic@pr.ac.rs

^cFaculty of Technical Sciences, Kosovska Mitrovica, RS, jasmina.skerlic@pr.ac.rs

^dFaculty of Mechanical Engineering, Niš, RS, vladan.jovanovic@masfak.ni.ac.rs

^eInnovation Centre of the Faculty of Mechanical Engineering, Belgrade, RS, skirin@mas.bg.sc.rs

Abstract: In the modern world, where a uninterrupted energy supply is required for proper functioning, thermal energy systems are key components of the infrastructure. Considering the complexity of these systems, it is essential to develop procedures that enable specific determination of the reliability function of thermal energy systems. Analysis of the reliability of the thermal energy system is crucial for maintaining the stability and efficiency of the system. In this paper, by applying the mathematical theory of reliability to the exploitation research data and using simple and complex two-parameter Weibull distribution, the theoretical reliability functions of the thermal power plant Nikola Tesla, Block B2 were determined. A significant advantage of such a study is the possibility of an early and thorough understanding of the logic and mechanisms of risky behavior in the system, as well as a more precise assessment of its functioning throughout the future exploitation.

Keywords: Thermal power system, Reliability, Weibull distribution.

1. Introduction

A reliable and uninterrupted supply of energy from thermal energy systems is crucial for social stability and economic development. In the last few years, with the ageing of infrastructure and increasingly severe climatic stresses, the reliability of energy systems has become a topic of wider importance around the world [1]. The thermal power system comprises a complex infrastructure and requires attentive planning and monitoring to ensure continuous energy delivery. In the event of a malfunction and stoppage during the operation of the thermal power system, the outcome is reflected in a direct outage of the power plant and disturbances in the power system. Resolving those delays requires quick and efficient detection of causes, as well as the application of appropriate measures to eliminate them. Therefore, reliability analysis becomes crucial in the identification of potential issues and risks that may lead to interruptions in electricity supply.

Term reliability means the probability of working without outages for a certain period of time and under certain environmental conditions, *i.e.* the probability that the production process of technical systems takes place without interruption and downtime by providing the required deadlines, production volumes, product range, and quality (criterion function) with planned normative materials, labour and costs for a specified time period and predetermined working conditions [2].

Ensuring the stable operation of the thermal energy system is a challenging task due to the complexity and numerous components that comprise the system. It is needed to conduct thorough and long-term research in order to understand the characteristics of these components. Accordingly, in this paper, the reliability of the thermal energy system in the thermal power plant Nikola Tesla, Block B2 (TENT-B2) for the period 2012-2023 was examined. Simple and complex two-parameter Weibull distributions were used for modelling the reliability of the thermal power system during the normal life period.

The thermal power system is represented as a set of three subsystems: a fossil fuel boiler, steam turbines and a three-phase alternator. Control limits were adopted in order to determine the transmission limits of the thermal power subsystems within the thermal scheme. The control limit that encloses the thermal power system does not encompass: systems for storage and delivery of fuel, systems for collecting and treating cooling water, the block transformer and the ash dump. [3]

2. Determining reliability functions using simple Weibull distribution

Reliability theory is grounded in probability theory and mathematical statistics and represents a process in which elements can be found in the working condition or at a standstill. If the system performs its intended function, reliability is defined positively. An initial assumption in reliability analysis is that failures of repairable systems are independent and occur randomly. That means that a failure in one component of the system will not directly cause a breakdown in another part. During the regular operation of the system, random failures occur sporadically, the frequency of which can be determined. Similarly, it is important to take into account that as the system ages, the failure rate increases, and this phenomenon continues throughout the system's lifetime. In other words, the reliability reduction is typical for systems that age, so with the passage of time, they fail more frequently.

The thermal energy system consists of a large number of components, which are often exposed to various influences that can affect their functionality and reliability. That is why it is necessary to continuously monitor the system's performance and identify potential failures in order to determine the regularity of the behaviour of these components. For the analysis and improvement of reliability, it is essential to consider the historical data of exploitation research. In order to determine the real indicators and characteristics of reliability, it was necessary to have all relevant data about the exploitation of the mentioned system. The key source of information relies on the annual downtime reports, which are in the legal possession of TENT-B2.

Exploitation data related to the normal life period of the system are crucial for reliability analysis. The system failure rate is considered relatively constant during that period. The interpretation of this data is very important for understanding system performance and forecasting inevitable failures. In the process of analysis, the selection of the right theoretical model of probability distribution is of significant importance. However, determining the mathematical form of distribution is often not straightforward, especially when relying on empirical data.

The characteristics and behaviour of all technical systems are by nature highly stochastic quantities and processes, which is one of the essential features of the concept of reliability. It means that all information related to the reliability of thermal power systems are random variables, subjected to specific laws of probability. Therefore, collected data can be processed only with the help of statistical mathematics [3]. To define the reliability of the aforementioned system, it is required to analyze the number of unplanned outages, which are shown in Tab. 1. Operating time intervals that include all data required for system analysis are defined on an annual basis, or 8760 working hours. These intervals are defined for the period from 2012 to 2023.

Table 1. Data on operational reliability of the system

Observation period				Reliability						
i	Tk_i	T_{i-1}	T_i	Nn_i	$\sum_{i=1}^{Nn_i}$	Nt_i	f_i	F_i	R_i	λ_i
[-]	[year]	[h]		[-]	[-]	[-]	[h ⁻¹]	[-]	[-]	[h ⁻¹]
1	2	3		4	5	6	7	8	9	10
1	2012	0-8760		15	15	114	0.12	0.12	0.88	0.1316
2	2013	8760-17520		7	22	107	0.05	0.17	0.83	0.0650
3	2014	17520-26280		8	30	99	0.06	0.23	0.77	0.0810
4	2015	26280-35040		9	39	90	0.07	0.30	0.70	0.1000
5	2016	35040-43800		10	49	80	0.08	0.38	0.62	0.1250
6	2017	43800-52560		13	62	67	0.10	0.48	0.52	0.1940
7	2018	52560-61320		14	76	53	0.11	0.59	0.41	0.2640
8	2019	61320-70080		7	83	46	0.05	0.64	0.36	0.1520
9	2020	70080-78840		5	88	41	0.04	0.68	0.32	0.1220
10	2021	78840-87600		9	97	32	0.07	0.75	0.25	0.2810
11	2022	87600-96360		15	112	15	0.12	0.87	0.13	1.000
12	2023	96360-105120		17	129	0	0.13	1.00	0	$+\infty$

Determining the distribution based on empirical data is not a simple task. Due to the complexity of this process, it is primarily recommended to enter the data into the probability paper for Weibull two-parameter distributions. The use of graphical methods and probability papers in order to find a class of distribution functions and their parameters, despite their relative simplicity, has a number of benefits that can meet requirements beyond the scope of engineering practice [4]. The graphical method of the Weibull distribution enables a visual presentation of data and helps to understand the behaviour of the system during exploitation.

The behaviour of thermal power systems in terms of reliability could be best approximated by the Weibull distribution, while using normal, lognormal and exponential distributions could lead to considerable disagreements [5]. The Weibull distribution, as well as its modified forms, can describe diverse forms for failure rate functions and is widely used in lifetime modeling within the scope of reliability engineering [6]. The reason for the very frequent practical application of the Weibull distribution stems from the fact that many forms of failure can be very well approximated by it. Also, the Weibull distribution can include decreasing, constant and increasing functions of failure intensity [7].

In this paper, by applying the graphical method and probability, an analysis of the collected data obtained during the exploitation of the thermal power system in TENT B-2 was carried out. Principles of constructing the probability plotting graph paper and empirical data entry have been described by many authors [8-9].

Based on operational reliability indicators of the thermal power plant system, the data shown in Table 1. can be entered as points in the Weibull probability paper in order to obtain the parameters η and β , as shown in (Fig. 1).

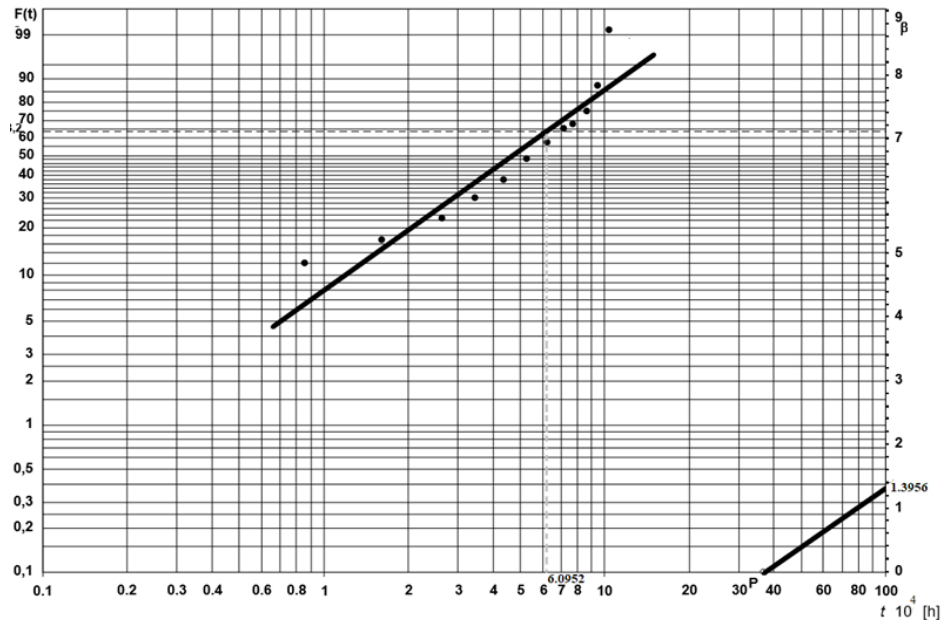


Figure 1. Weibull probability paper for simple Weibull distribution

The Weibull distribution parameters were obtained by drawing the best fitted straight lines through the plotted points,:

$$\eta = 6.0952, \beta = 1.3956$$

The listed functions are analytical expressions that represent distribution laws of the observed random variable [10]:

Reliability
$$R_{ts}(t) = \exp\left(\frac{-t^{1.3956}}{12.4601}\right) \quad (9)$$

Failure density
$$f_{ts}(t) = 0.112 \cdot t^{0.3956} \cdot \exp\left(\frac{-t^{1.3956}}{12.4601}\right) \quad (10)$$

Failure rate
$$\lambda_{ts}(t) \frac{f_t(t)}{R_t(t)} = 0.112 \cdot t^{0.3956} \quad (11)$$

3. Determining reliability functions using complex Weibull distribution

Based on the results of plotting the probability of failures and time plots and their respective cumulative failure percentages ($t_i, F(t_i)_{50\%}$) on the Weibull probability paper, it has been identified that two lines fit the indicated points better than one line.

For the case of the complex two-parameter Weibull distribution, the failure probability samples for the observed time interval were divided into two parts [11]. Following the separation of samples, the cumulative percentage of failures was calculated for each of the parts, and a chart was drawn based on applicable data. In this particular case, the first time interval includes 7 (Table 2), while the second includes 5 years (Table 3).

Table 2. Values of exploitation indicators - line I

i	Tk_i	Nn_i	$\sum_{i=1} Nn_i$	f_i	F_i
[-]	[year]	[-]	[-]	[h^{-1}]	[-]
1	2012	15	15	0.31	0.31
2	2013	7	22	0.14	0.45
3	2014	8	30	0.16	0.61
4	2015	9	39	0.18	0.79
5	2016	10	49	0.2	0.99

Table 3. Values of exploitation indicators - line II

i	Tk_i	Nn_i	$\sum_{i=1} Nn_i$	f_i	F_i
[-]	[year]	[-]	[-]	[h^{-1}]	[-]
1	2017	13	13	0.16	0.16
2	2018	14	27	0.17	0.33
3	2019	7	34	0.09	0.42
4	2020	5	39	0.06	0.48
5	2021	9	48	0.11	0.59
6	2022	15	63	0.19	0.78
7	2023	17	80	0.21	0.99

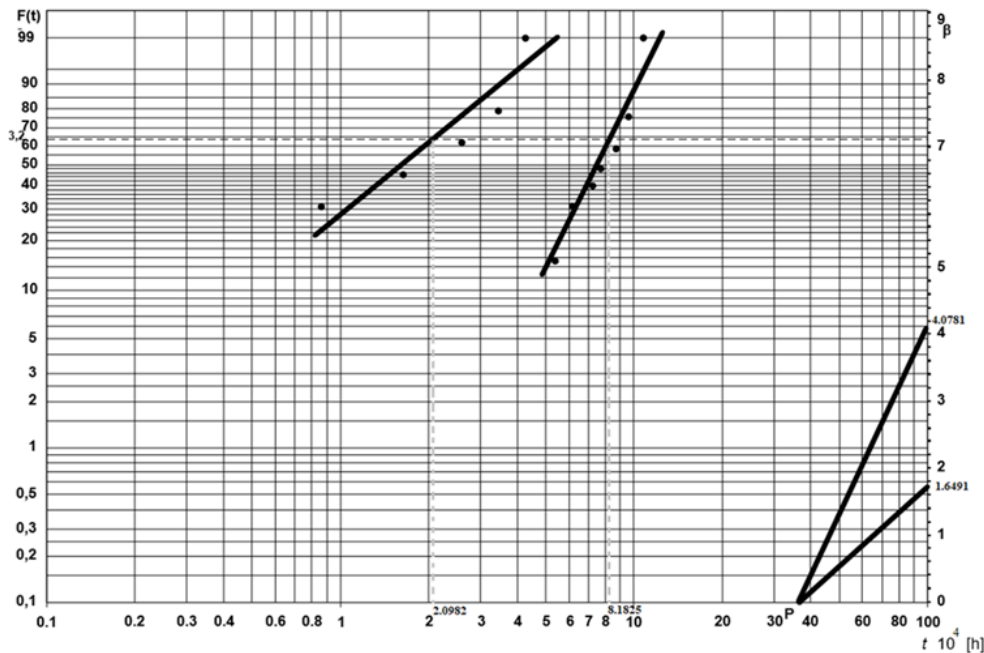


Figure 2. Weibull probability paper for complex Weibull distribution

By drawing the best possible straight lines through the plotted points (Fig. 2), the Weibull distribution parameters were obtained for both lines:

$$\eta_I = 2.0982, \beta_I = 1.6491$$

$$\eta_{II} = 8.1825, \beta_{II} = 4.0781$$

The parameters for the best fitted statistical data are estimated by the least-square method. Theoretical reliability functions for each interval are:

$$R_{II} = \exp\left(-7.462 \cdot 10^{-8} \cdot t^{1.6491}\right) \quad (12)$$

$$R_{II} = \exp\left(-9.220 \cdot 10^{-21} \cdot t^{4.0781}\right) \quad (13)$$

Analytical expressions for theoretical reliability functions which represent the distribution laws of the observed random variable for the complex two-parameter Weibull distribution are [12]:

Reliability

$$R_{tc}(t) = 0.38 \cdot \exp\left(-7.462 \cdot 10^{-8} \cdot t^{1.6491}\right) + 0.62 \cdot \exp\left(-9.220 \cdot 10^{-21} \cdot t^{4.0781}\right) \quad (14)$$

Failure density

$$f_{tc}(t) = 4.674 \cdot 10^{-4} \cdot t^{0.6491} \cdot \exp\left(-7.462 \cdot 10^{-8} \cdot t^{1.6491}\right) + 2.332 \cdot 10^{-16} \cdot t^{3.0781} \cdot \exp\left(-9.220 \cdot 10^{-21} \cdot t^{4.0781}\right) \quad (15)$$

Failure rate

$$\lambda_{tc}(t) = \frac{4.674 \cdot 10^{-4} \cdot t^{0.6491} \cdot \exp\left(-7.462 \cdot 10^{-8} \cdot t^{1.6491}\right) + 0.62 \cdot \exp\left(-9.220 \cdot 10^{-21} \cdot t^{4.0781}\right)}{0.38 \cdot \exp\left(-7.462 \cdot 10^{-8} \cdot t^{1.6491}\right) + 0.62 \cdot \exp\left(-9.220 \cdot 10^{-21} \cdot t^{4.0781}\right)} \quad (16)$$

Graphical comparisons between operational and obtained values for theoretical functions of reliability, failure density and failure rate of the thermal power system in TENT-B2 during the observation period were shown in figs 3-5.

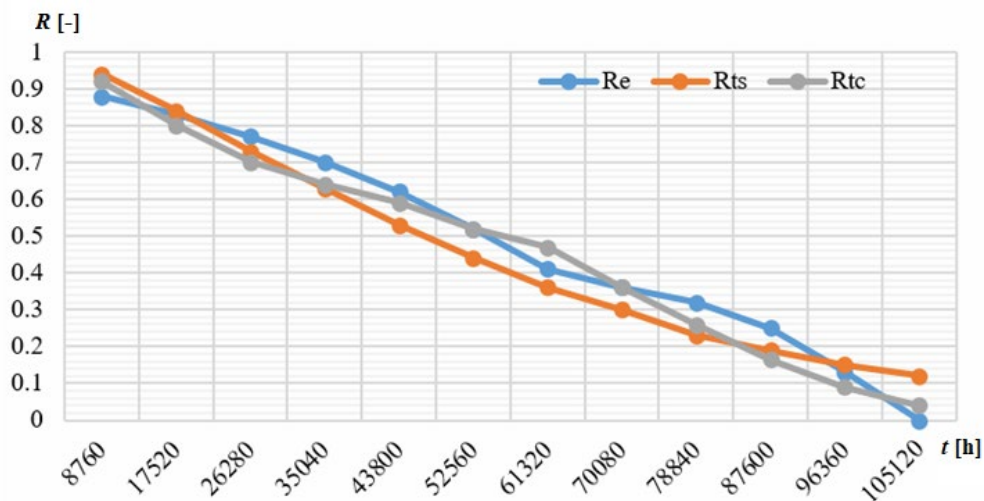


Figure 3. Exploitation and theoretical forms of the reliability functions

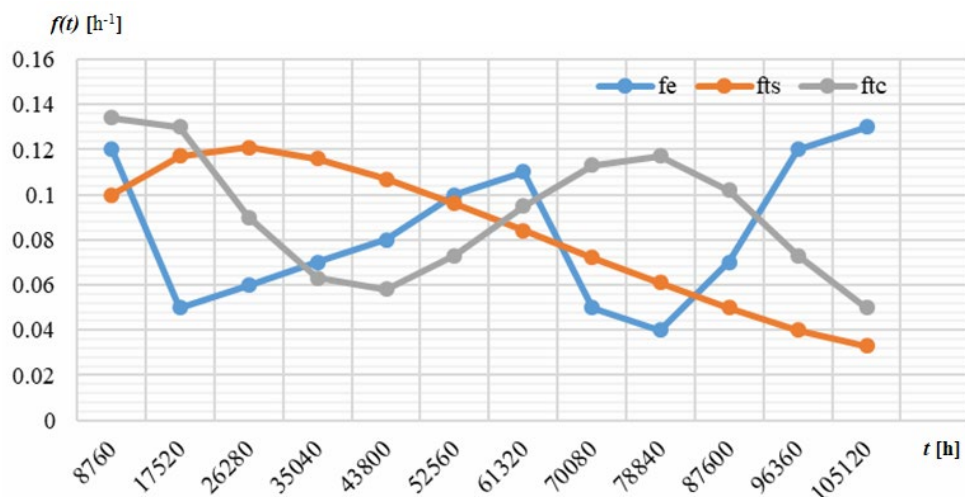


Figure 4. Exploitation and theoretical forms of the failure density functions

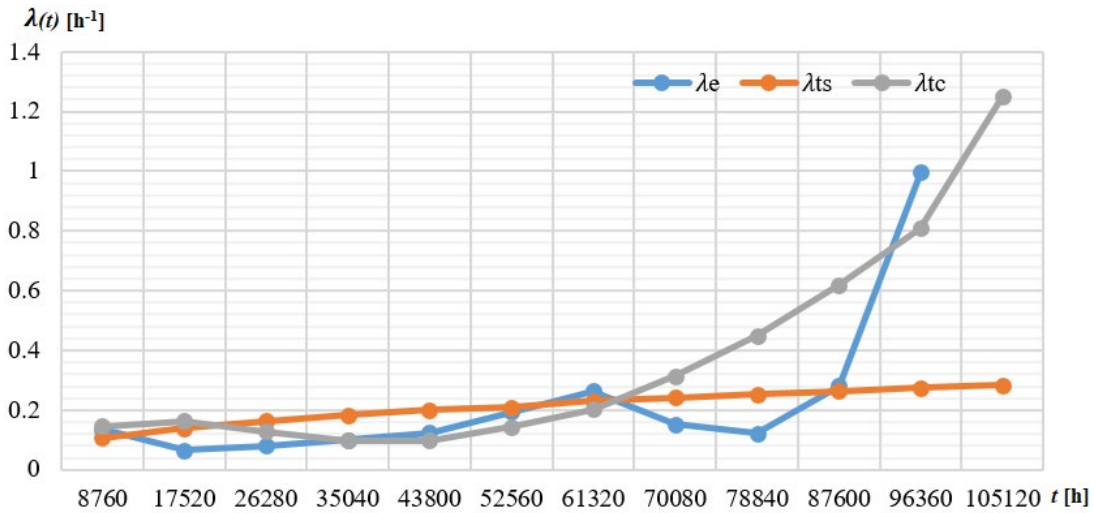


Figure 5. Exploitation and theoretical forms of the failure rate functions

4. Conclusion

The operational research of the thermal power system in the TENT-B2 and application of reliability theory resulted in presentation of theoretical laws of random variable distribution. The assessment of reliability, failure density and failure rates were implemented by the graphic method and probability paper, which enabled the analysis and interpretation of data in a visually clear manner. An initial hypothesis suggesting that the distribution of this random variable approaches the Weibull distribution is confirmed. The findings disclosed that the functions obtained by the simple and complex Weibull distributions failed to accurately reproduce the empirical data. Finally, a relatively good data match between empirical and theoretical failure rate functions was obtained by complex Weibull distribution. It is more accurate to use the complex rather than the simple Weibull distribution to estimate the distribution law of the failure rate during the useful life of this particular thermal power system.

Nomenclature

Latin symbols

F_i	Unreliability $\left(= \sum_{i=1}^n f_i \right)$, [-]
f_i	Failure density $\left(= N_{n_i} / \sum_{i=1}^n N_{n_i} \right)$, [h ⁻¹]
$F(t_i)_{50\%}$	Cumulative percentage of failures or Median rang, $(= (j - 0.3) / (n + 0.4))$, [%]
n	Total number of failures in the reported period, [-]
N_n	Total number of failures, [-]
$\sum_{i=1}^n N_{n_i}$	Cumulative sum of failures $\left(j = \sum_{i=1}^n N_{n_i} \right)$, [-]

N_t	Reverse cumulative sum of failures, [-]
R_i	Reliability, [-]
t	Time, [h]
T_k	Calendar time, [year]

Greek symbols

β	Shape parameter, [-]
η	Scale parameter, [-]
λ	Failure rate $(= N_{n_i} / N_{t_i})$, [h ⁻¹]

Subscripts

e	Exploitation
i	Number of operating intervals of the system
t	Theoretical

Acknowledgements

The authors would like to thank the Ministry of Science, Technological Development and Innovation of the Republic of Serbia for funding the scientific research work, contract no. 451-03-65/2024-03/200155, realized by the Faculty of Technical Sciences in Kosovska Mitrovica, University of Pristina.

References

- [1] Bao, M., Ding, Y., Yin, X., Shao, C., Definitions and Reliability Evaluation of Multi-state Systems Considering State Transition Process and its Application for Gas Systems, *Reliability Engineering and System Safety*, 207 (2021), pp. 107387
- [2] SRPS A. A2.005
- [3] Kalaba, D., *Thermal Power System Reliability*, (in Serbian), University of Priština, Faculty of Technical Sciences, Kosovska Mitrovica, 2011
- [4] Barlow, R., *Engineering Reliability*, SIAM, Philadelphia, 1998
- [5] Kalaba, D., Radaković, Z., Đorđević, M., Kirin, S., Determining the Theoretical Reliability Function of Thermal Power System Using Simple and Complex Weibull Distribution, *Thermal Science*, 18 (2014), pp. S229-S238
- [6] Jia, X., Reliability Analysis for Weibull Distribution With Homogeneous Heavily Censored Data Based on Bayesian and Least-Squares Methods, *Applied Mathematical Modelling*, 83 (2020), pp. 169-188
- [7] Ahmada, A., Ghazal, M., Exponentiated Additive Weibull Distribution, *Reliability Engineering and System Safety*, 193 (2020), pp. 106663
- [8] McCool, J., *Using the Weibull Distribution: Reliability, Modeling, and Inference*, John Wiley & Sons Inc., New Jersey, 2012
- [9] Milčić, D., *Reliability of Mechanical Systems* (in Serbian), Faculty of Mechanical Engineering, University of Nis, Nis, 2005
- [10] Murthy, P., Min, X., Renyan, J., *Weibull Models*, John Wiley & Sons Inc., New York, 2004
- [11] Milčić, D., Mijajlovi, M., *Reliability of Mechanical Systems – Collection of Solved Tasks* (in Serbian), Faculty of Mechanical Engineering, University of Nis, Nis, 2008
- [12] Nelson, W., Weibull Prediction of a Future Number of Failures, *Quality and Reliability Engineering*, 16 (2000) pp. 23-26

Experimental Investigation on the Effect of Water Based Nanofluids (Al₂O₃ And Mgo) Used as Htf in a Pcm Based Thermal Energy Storage System Integrated with Constant Heat Source

Krishna Reddy K^a, Meenakshi Reddy R^a, Sreenivasa Reddy B^a, Madhava Reddy K^a, Venkata Mohan Reddy Y^a

^aDept.of Mechanical Engg, G.Pulla Reddy Engineering College, Kurnool, A.P, India, kkreddy642014@gmail.com

Abstract: This research focuses on evaluating the thermal performance of a combined sensible and latent heat storage unit using a packed bed design integrated with a constant heat source. The Thermal Energy Storage (TES) system features a cylindrical, insulated storage tank filled with spherical capsules containing phase change materials (PCMs) — specifically, paraffin wax and stearic acid. PCMs offer significant benefits in thermal management by enabling isothermal operation and higher thermal storage capacity, contributing to a reduction in system size and cost. To enhance the thermal conductivity of the heat transfer fluid (HTF), nanoparticles are introduced into water, creating nanofluids that improve the efficiency of heat transfer. These water-based nanofluids facilitate heat transfer between the constant heat source and the storage tank, serving as a sensible heat storage medium. The study examines different HTF configurations, starting with water alone and extending to nanofluids with Al₂O₃ and MgO nanoparticles at three volume concentrations (0.2%, 0.5%, and 0.8%). Experiments were conducted at varied flow rates of 2, 4, and 6 liters per minute to analyze the effect of these parameters on heat transfer and PCM melting time. Performance parameters, including charging time, instantaneous stored heat, cumulative stored heat, and system efficiency, were evaluated for each HTF-PCM combination. Additionally, batch-wise discharging experiments were conducted to assess the system's heat recovery capability. The results offer insight into the comparative advantages of different HTF materials and configurations, highlighting the thermal performance enhancements achieved by using nanoparticle-enhanced HTFs.

Keywords: Paraffin wax, Stearic acid, Nanoparticles, Nanofluids, Charging, Discharging, Thermal Energy Storage System (TESS), Phase Change Material (PCM), Heat Transfer Fluid (HTF), Al₂O₃ Nanoparticles, MgO Nanoparticles, Sensible heat storage, Latent heat storage, System efficiency, Instantaneous stored heat, Cumulative stored heat.

1. Introduction

Karabulut et al. [1] conducted a numerical study on heat transfer and flow dynamics for cube and circular hollow models in channels under cross flow-impinging jet conditions, using water and a 2% CuO-water nanofluid as the working fluids. This approach provides valuable insights into optimizing TES systems for various applications, helping to identify the most effective combinations of PCM, flow rate, and capsule size for efficient thermal energy storage and release. [2]. Materials like solid particles, sand, and alumina are commonly used in sensible heat storage due to their capacity to store heat based on temperature changes. On the other hand, phase change materials (PCMs) like paraffin and stearic acid are suited for latent heat storage, where energy is stored during a solid-liquid phase transformation. [3]. In this context, various experimental and numerical investigations have been conducted to examine the thermal behavior of thermal energy storage systems (TESS) that incorporate both latent and sensible heat storage. These studies explore different heat transfer fluids (HTFs) to optimize energy transfer and storage performance within the system. Given their broad applicability and enhanced thermal properties, nanofluids—created by suspending nanoparticles in conventional fluids—have become a major focus of research [4]. Researchers have focused on the synthesis, characterization, and modeling of nanofluid systems, examining a range of thermo physical properties such as density, specific heat capacity, viscosity, and thermal conductivity. These properties are critical in determining how effectively nanofluids can transfer and store heat in applications like thermal energy storage systems (TESS) [5]. Several studies have explored the applications of heat transfer fluids (HTFs) in solar energy systems, including both experimental and numerical investigations of solar collectors. In this research, a

number of critical parameters have been identified to optimize system performance. These include enhancing the efficiency of solar collectors, determining the optimal volume fraction of nanoparticles in nanofluids, and assessing how particle size affects heat transfer efficiency [6]. Key characteristics of Al_2O_3 - H_2O nanofluids include increased thermal conductivity and heat capacity, which contribute to more efficient thermal energy exchange [7]. Godson et al. [8] conducted an extensive investigation into the heat transfer characteristics of nanofluids through both numerical and experimental studies. Their research examined a range of critical parameters that affect nanofluid performance, including heat transfer efficiency, thermo physical properties, and potential applications. Key factors studied included thermal conductivity, specific heat capacity, viscosity, and density, all of which significantly influence how well nanofluids transfer and dissipate heat. Qinbo He et al. [9] conducted studies on alumina (Al_2O_3) particles, focusing on their thermo physical properties, which are crucial in determining their effectiveness as components in heat transfer fluids. The research highlighted key properties such as density, specific heat capacity, viscosity, and thermal conductivity, all of which significantly impact the temperature control and thermal efficiency of systems using alumina-based nanofluids. Ryan Anderson et al. [10] demonstrated that Al_2O_3 (alumina) aqueous nanofluids exhibit significantly enhanced thermal conductivity, making them highly effective for a variety of thermal applications. The improved thermal conductivity of Al_2O_3 -based nanofluids allows for faster and more efficient heat transfer, which is advantageous in applications such as cooling systems, solar thermal energy storage, and industrial heat exchangers. Wu Shuying et al. [11] investigated TiO_2 (titanium dioxide) nanoparticles and highlighted their critical thermal properties, particularly chemical compatibility and strong physical interactions with base fluids. These properties make TiO_2 -based nanofluids highly suitable as heat transfer fluids for solar energy applications, particularly in domestic solar heating systems. S. Harikrishnan et al. [12] conducted experimental validation studies on CuO -oleic acid-based nanofluids, presenting them as a novel type of phase change material (PCM) for thermal energy storage, particularly in cooling systems. The study explored these nanofluids as solid-liquid composite materials, showcasing their potential for efficient thermal management. S.M.S. Murshed et al. [13] conducted an investigation into the enhanced thermal conductivity of TiO_2 (titanium dioxide) nanofluids, emphasizing the role of nanofluids in significantly improving heat transfer capabilities. Their experimental findings underscore the importance of nanofluids as efficient thermal conductors in various applications, especially where heat dissipation and transfer are critical. Mahbubul et al. [14] conducted a study examining the effects of sonication time on the properties of nanofluids, specifically using an ultrasonic homogenizer to vary the sonication duration from 0 to 180 minutes. Their findings revealed that longer sonication times led to improved particle dispersion within the fluid, which is crucial for enhancing the overall stability and performance of nanofluids. Senthilraja et al. [15] conducted an experimental study focused on the thermal conductivity and heat transfer characteristics of copper oxide (CuO) nanofluids, comparing their performance with both water and alumina (Al_2O_3) nanofluids, as well as hybrid nanofluids composed of Al_2O_3 and CuO suspended in water. Hemanth Kumar Gupta et al. [16] conducted an experimental investigation into the performance of Al_2O_3 (alumina) water nanofluids, specifically examining how varying flow rates affect the efficiency of conventional solar collectors. Their study demonstrated that Al_2O_3 nanofluids can significantly enhance thermal efficiency, showing improvements of over 8% compared to pure water. Michael Joseph Stalin Prakasam et al. [17] conducted a detailed investigation into the performance of a solar flat plate collector using Al_2O_3 /water nanofluid as the working fluid. Their study focused on a low volume concentration of 0.01% Al_2O_3 nanoparticles, while also varying the flow rates from 1 to 3 liters per minute. Chandra Prakash et al. [18] highlighted the capabilities of Al_2O_3 (alumina) nanofluids in enhancing the performance of conventional solar thermal energy storage (TES) systems. Their research demonstrated that these nanofluids could effectively generate hot water for domestic applications, showcasing their practical utility in everyday settings. The present work emphasizes the use of nano mixed base fluids at mass flow rates of 2 liters per minute, 4 liters per minute, and 6 liters per minute to investigate the enhancement of heat transfer and assess their impact on the performance of phase change material (PCM) based thermal energy storage systems (TESS). By utilizing these nano mixed fluids, the study aims to explore how the incorporation of nanoparticles can optimize the thermal performance of PCMs, which are critical for effective energy storage and management.

2. Experimental Setup and Procedures

2.1 Experimental Setup

The experimental TES setup, as represented in Figure 1, combines efficient design and strategic material choices for optimal thermal storage. The photograph of the experimental construction is presented in Figure 2. This cylindrical, stainless steel tank with a 57-liter capacity and specifications of 535 mm in height and a 370 mm diameter is well-suited to household use for 5-6 people. The division into two chambers encourages thermal stratification, which improves heat layering, while the 30 mm thick glass wool insulation minimizes heat loss. Containing 90 mild steel spherical capsules of 70 mm inner diameter and 2 mm wall thickness, the tank uses paraffin wax as the PCM. This PCM choice is particularly advantageous, given paraffin's high latent heat of fusion (213 kJ/kg) and a melting point of 61°C, a suitable range for domestic hot water needs. The use of wire mesh helps secure the capsules in a uniform arrangement, aiding stability and efficient packing. The dual approach of using both water and nanofluids as HTFs and SHS materials further enhances the system's performance. While water offers reliable thermal mass, nanofluids improve thermal conductivity, accelerating PCM heating and expediting heat release. This setup is designed for responsive and efficient energy storage, ensuring faster performance and more effective thermal management for domestic applications. Figure 3 shows the arrangement of linked PCM capsules filled in the tank. Table 1 represents the thermo physical properties of PCM.

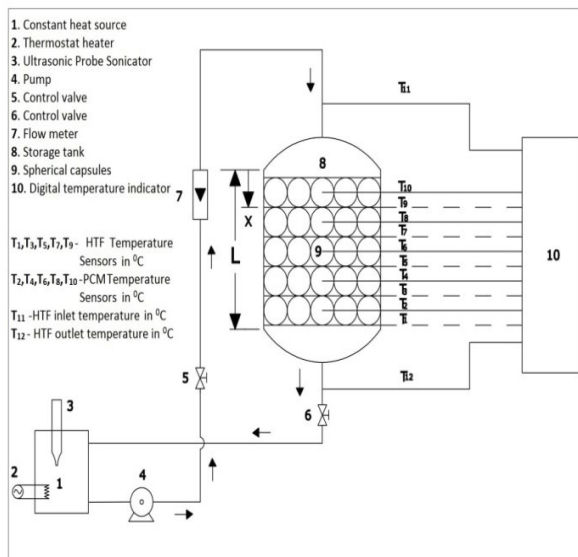


Figure 1 Experimental setup's Schematic



Figure 2 Photograph of experiment



Figure 3 Arrangement of PCM capsules in the TES tank

Table1. PCM properties - Thermo-physical

Phase change material	Temperature of Melting [°C]	Latent heat of fusion [kJ/kg]	Density [kg/m ³]		Specific heat [J/kg°C]		Thermal conductivity [W/m°C]	
			Solid	Liquid	Solid	Liquid	Solid	Liquid
* Type-II Paraffin wax	61	213	861	778	1850	2384	0.4	0.15
** (Grade-TGV-MP) Stearic acid	57	198.91	960	840	1600	2300	0.3	0.172

Suppliers: *CPCL, Chennai. ** TGV SRAAC Limited, Kurnool, AP.

2.2 Preparation of nanofluids

Using different concentrations of nanoparticles (0.2%, 0.5%, and 0.8%) in water enhances the thermal conductivity of the HTF, which can improve heat transfer efficiency in the TES system. The selected sonication time of 180 minutes helps break up any nanoparticle agglomerates, ensuring a stable and uniform dispersion in the fluid. This approach maximizes the effective surface area of the nanoparticles, improving thermal conductivity and stability within the HTF. [14]. This two-step approach using an ultrasonic probe sonicator (figure 4) followed by magnetic stirring (figure 5) ensures optimal nanoparticle dispersion. Sonication helps break up any initial agglomerations of nanoparticles, especially as they approach the target 180-minute period. The subsequent magnetic stirring maintains even distribution and prevents re-agglomeration, allowing the nanofluid to retain enhanced thermal conductivity properties for more effective heat transfer. Table 2 shows the thermo physical properties often characterized for nanoparticles and nanofluids. Specific details about the SEM (Scanning Electron Microscope) images in Figures 6 and 7.

Table2. Nanoparticles and Nanofluids - Thermo-physical properties

Property	Nanoparticles		Al ₂ O ₃ Nanofluid			MgO Nanofluid		
	Al ₂ O ₃	MgO	0.2 vol%	0.5 vol%	0.8 vol%	0.2 vol%	0.5 vol%	0.8 vol%
Density	3970 kg/m ³	3580 kg/m ³	1594	2485	3376	1516	2290	3064
Thermal conductivity	30 W/m°C	60 W/m°C	1.013	2.1934	6.0885	1.0284	2.286	6.8224
Specific heat	0.955kJ/kg°C	1.03kJ/kg°C	2.5735	1.6038	1.146	2.6922	1.7177	1.2356
Avg particle size	30-50 nm	30-50 nm	---	---	---	---	---	---

Suppliers: PNPL, Kachwach, Mahagama, Jharkhand.



Figure 4 Ultrasonic probe sonicator



Figure 5 Magnetic stirrer

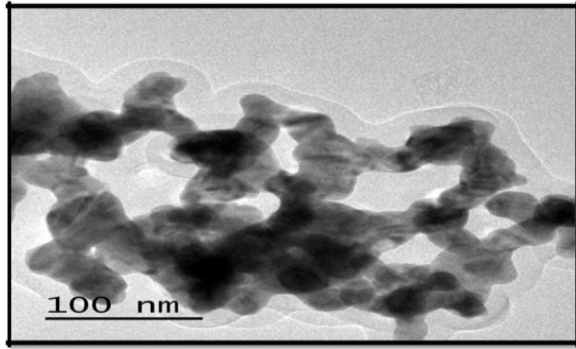


Figure 6 Crystal orientations of Al_2O_3 nanoparticles for SEM analysis

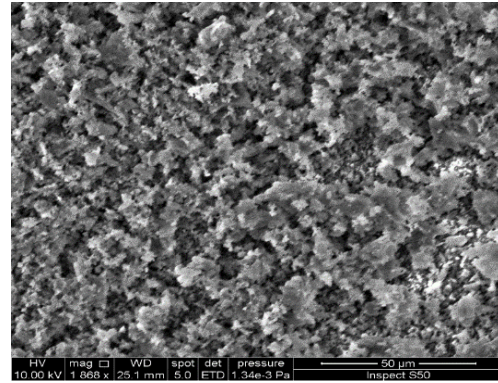


Figure 7 Magnified view of MgO nanoparticles for SEM analysis

2.3 Procedure of the Experiment

2.3.1 Charging Process

This charging process, repeated with different nanofluids, allows for detailed performance analysis of the TES system. The initial sensible heating of the PCM to its melting point, followed by latent heat storage during melting, and finally, the sensible heat storage in the liquid phase, all contribute to a comprehensive understanding of how each HTF enhances heat transfer. The use of nanofluids like Al_2O_3 , and MgO can significantly influence the charging time and efficiency due to their higher thermal conductivity compared to water. Recording temperatures every 5 minutes provides a precise profile of the thermal dynamics within the TES tank, crucial for assessing the performance impact of each nanofluid on both heat storage rate and efficiency.

2.3.2 Discharging Process

The batch-wise method allows for full extraction of thermal energy from the TES tank. By removing hot water in specific quantities (20 liters per batch), efficiently manage the discharge process while monitoring temperature changes. Collected hot water is stored in an insulated drum to minimize heat loss during the monitoring period. This is crucial for obtaining accurate temperature readings and ensures that the hot water remains effective for its intended use. Continuous monitoring of the withdrawn hot water's temperature allows for the assessment of the heat extraction efficiency and helps in calculating the average temperature across multiple batches. This average can indicate the effectiveness of the TES system in delivering hot water. Keeping the inlet flow to the tank constant at 2.0 l/min ensures a consistent supply of cold water, which is important for maintaining the thermal dynamics within the TES system. This consistency allows for more reliable data collection during discharge. Allowing a retention period of 20 minutes between batches helps stabilize the thermal conditions within the tank. This period allows for thermal stratification to develop, ensuring that the hottest water is extracted first while maintaining a steady temperature gradient. Continuing the discharge process until the outlet temperature reaches $45^\circ C$ provides a clear endpoint for the experimental phase. This threshold can help in assessing the performance of the TES system in meeting the desired hot water supply temperature.

3. Results and discussion

3.1 Experiments for Charging

3.1.1 History of Temperatures

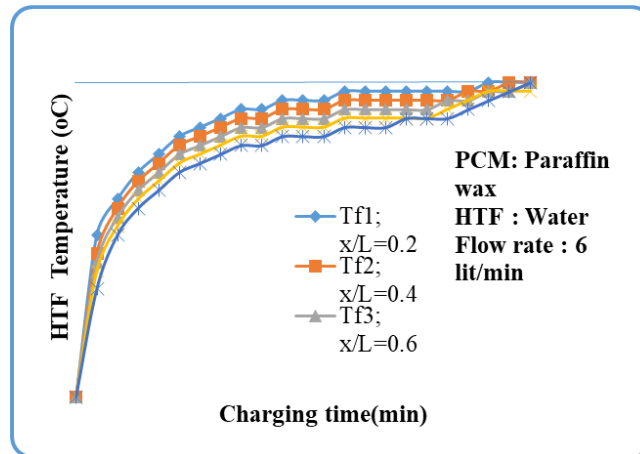


Figure 8 Variations in PCM temperatures during charging process and rate of flow of 6.0 l/min for water as HTF

Figure 8 illustrates, measuring PCM temperatures at five different axial segments ($x/L = 0.2, 0.4, 0.6, 0.8,$ and 1.0), clearly understand that heat is distributed throughout the tank during charging. This segmentation is crucial for identifying thermal gradients and efficiency in heat transfer. The gradual increase in PCM temperature along the axial direction indicates effective heat transfer from the hot HTF (water) to the PCM. This progression suggests that the design facilitates proper thermal conduction and convection. The observation that the uppermost layers of PCM have higher temperatures at any given time aligns with expected thermal stratification effects. This is likely due to the proximity of these layers to the HTF inlet and the natural tendency of warmer fluids to rise. The slow increase in PCM temperature during the initial charging stages reflects the sensible heat absorption before reaching the melting point. This is essential for preparing the PCM for the phase change. The PCM's temperature remaining unchanged during the melting process confirms that latent heat is being absorbed without a temperature increase, a hallmark of effective thermal energy storage systems. After phase change, the sudden rise in temperature during the liquid PCM heating phase indicates that the system is now storing additional energy as sensible heat. This rapid temperature change highlights the efficiency of the TES system in utilizing the latent heat stored during phase change. The total charging time of 110 minutes at a flow rate of 6 l/min for the PCM to reach 70°C indicates a well-defined operational period for the system. This information is critical for evaluating system performance and optimizing charging protocols.

3.1.2 HTF's flow rate effect

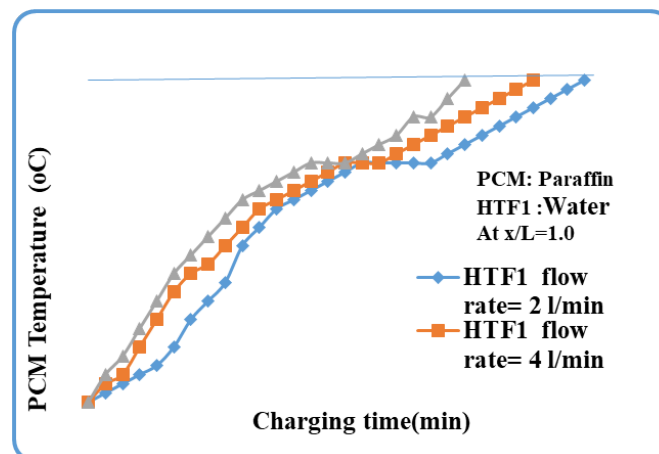


Figure 9 HTF's flow rate effect on the time required for the process of charging (at $x/L=1.0$)

Figure 9 indicates the total charging times of 145 min for 2.0 l/min, 130 min for 4.0 l/min, and 110 min for 6.0 l/min highlight the impact of flow rates on system performance. As flow rates increase, the time required for charging decreases. The observed reductions in charging time of 10.34% from 2.0 l/min to 4.0 l/min and 24.13% from 2.0 l/min to 6.0 l/min indicate a clear advantage of higher flow rates.

3.1.3 Effect of Nanoparticles volume concentration

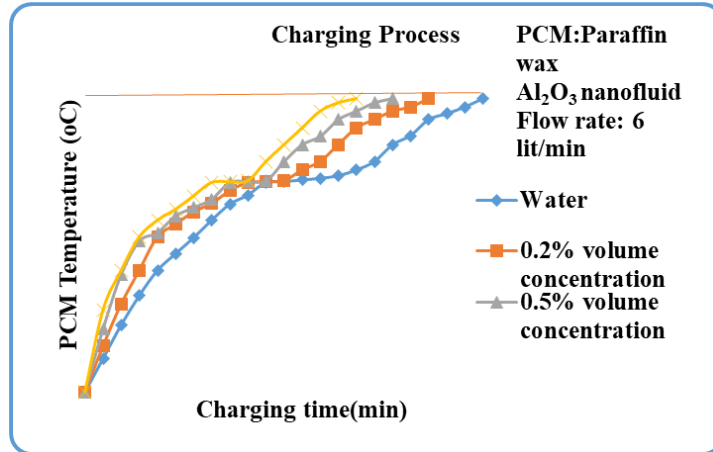


Figure 10 Variations in PCM temperatures during charging period for 0.2% volume concentration of Al_2O_3 nanofluid as HTF and rate of flow of 6.0 l/min

Figure 10 indicates, the initial increase in PCM temperature indicates effective heat transfer from the 0.2% volume concentration Al_2O_3 nanofluid at a flow rate of 6 l/min. This aligns with expectations, as higher thermal conductivity of nanofluids enhances the heat transfer capabilities compared to water. The PCM maintaining a constant temperature during the melting phase further confirms efficient energy storage, as latent heat is absorbed without increasing temperature. This characteristic is essential for the effectiveness of a TES system. After the melting phase, the PCM's temperature rising rapidly in the liquid state indicates that energy is now being stored as sensible heat. This behaviour illustrates the transition from latent heat storage to sensible heat storage once the PCM has melted. The observation that the topmost segments of the PCM attain the phase change temperature faster and complete the phase change earlier is consistent with thermal stratification principles. These segments are likely receiving direct exposure to the HTF and thus heat up more quickly. The total charging times of 110 min for water, 95 min for 0.2 vol. %, 85 min for 0.5 vol. %, and 75 min for 0.8 vol. % highlight the improved efficiency as the concentration of Al_2O_3 nanofluid increases. The results suggest that higher concentrations of nanoparticles enhance heat transfer capabilities. The reductions in charging time of 10.52% from 0.2% to 0.5% and 21.05% from 0.2% to 0.8% indicate that increased nanoparticles concentration can significantly improve thermal energy transfer rates.

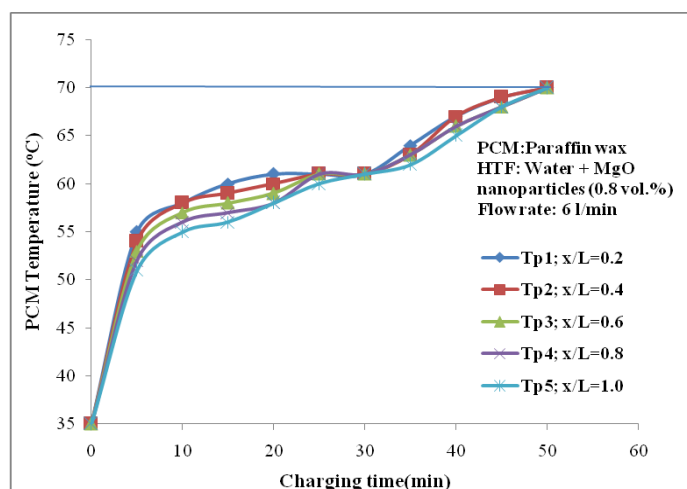


Figure 11 Variation of PCM temperatures during process of charging for 0.8 vol. % MgO nanofluid as HTF and flow rate of 6 l/min

Figure 11 represents the gradual increase in PCM temperature at the initial charging period suggests effective heat transfer from the MgO nanofluid to the PCM. This is indicative of the improved thermal properties of the nanofluid, which can enhance heat transfer rates compared to conventional HTFs. The total charging time of 50 minutes for the PCM when using 0.8% MgO nanofluid at a flow rate of 6 l/min suggests a very efficient charging process. This relatively short time indicates that the MgO nanofluid significantly enhances the heat transfer characteristics, leading to quicker charging.

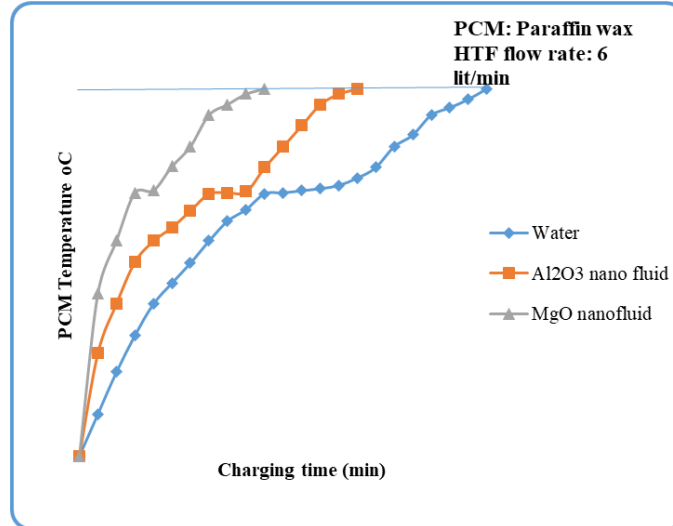


Figure 12 Variation of PCM temperatures during charging period for 0.8 vol. % of nanoparticles and paraffin as PCM, flow rate of 6 l/min

Figure 12 indicates that the initial slow rise in PCM temperatures indicates that the system is efficiently absorbing heat from the HTF, whether it's water, Al₂O₃ nanofluid, and MgO nanofluid. The observed charging times of 110 min for water, 75 min for Al₂O₃ nanofluid and 50 min for MgO nanofluid showcase a remarkable decrease in time with the use of nanofluids. The charging time reductions of 31.81% for Al₂O₃ nanofluid and 54.54% for MgO nanofluid compared to water demonstrate the substantial benefits of using nanofluids in thermal energy storage systems. The greater reduction in charging time indicates an even more significant enhancement in heat transfer properties, suggesting that MgO nanofluid is particularly advantageous for applications requiring rapid heat accumulation.

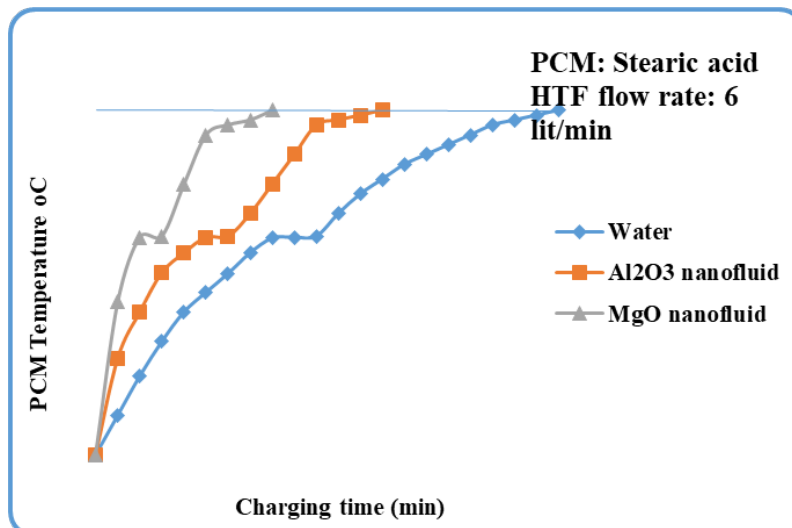


Figure 13 Variations of PCM temperatures during charging process for 0.8 vol. % of nanoparticles and stearic acid as PCM, flow rate of 6 l/min

Figure 13 illustrates the charging process of PCM, showing how the temperature increases gradually at the initial stage, remains constant during the phase transition, and then rises sharply during the heating of the liquid PCM. The observed charging times of 110 min for water, 65 min for Al₂O₃ nanofluid and 40 min for MgO nanofluid showcase a remarkable decrease in time with the use of nanofluids. The charging time reductions of

40.90% for Al₂O₃ nanofluid and 63.63% for MgO nanofluid compared to water demonstrate the substantial benefits of using nanofluids in thermal energy storage systems.

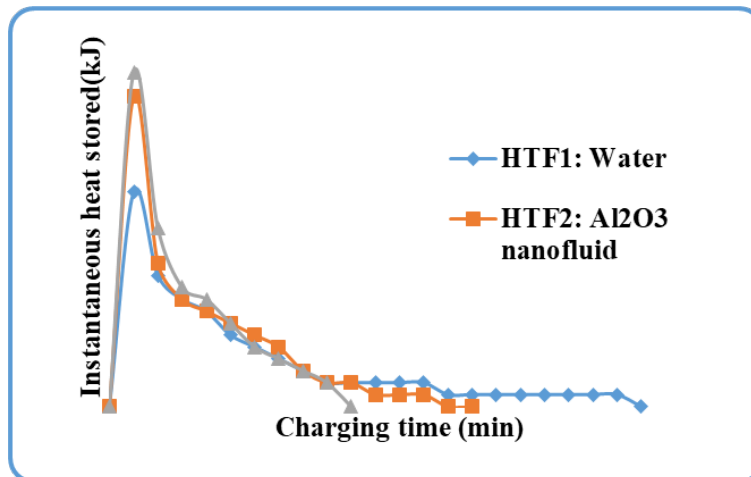


Figure 14 Variation of Instantaneous heat stored in the charging process for various HTFs -Varying heat source

Figure 14 illustrates the instantaneous rate of accumulated heat in the thermal energy storage (TES) tank during the charging process at a flow rate of 6.0 l/min, using water, Al₂O₃ nanofluid, and MgO nanofluid as heat transfer fluids (HTFs). The graph is based on the real-time temperatures of the HTF at both the inlet and outlet. There is a high rate of heat accumulation in the PCM, indicating effective heat transfer when there is a significant temperature difference between the HTF and the TES tank. As the charging process progresses, the rate of heat storage decreases. This decline is attributed to the diminishing temperature difference between the HTF and the PCM, leading to reduced heat transfer efficiency. As the PCM begins to melt, the amount of stored heat stabilizes. During this phase, the temperature remains relatively constant, indicating that the heat energy is being utilized for the phase change rather than increasing the temperature of the PCM.

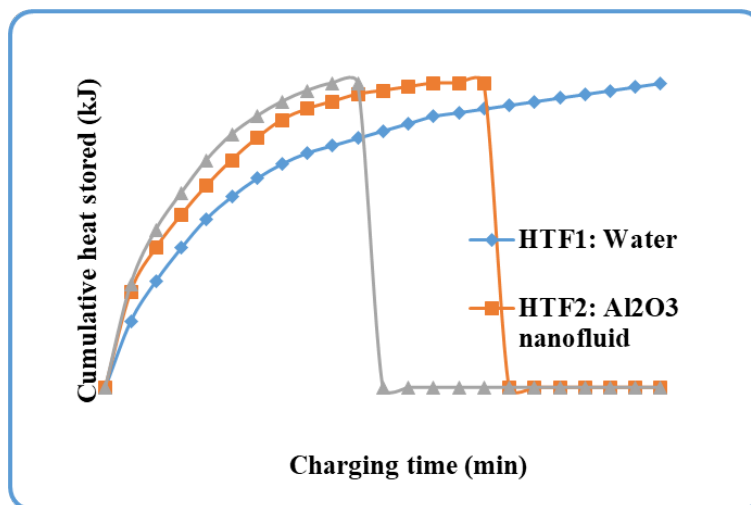


Figure 15 Variation of Cumulative stored heat for total system at charging period for various HTFs -Varying heat source

Figure 15 illustrates the cumulative stored heat in the thermal energy storage (TES) tank during the charging process at a flow rate of 6.0 l/min, comparing water, Al₂O₃ nanofluid, and MgO nanofluid as heat transfer fluids (HTFs). The cumulative heat stored is significantly greater when using 0.8 vol. % of either Al₂O₃ or MgO nanofluid compared to water. This increase in stored heat can be attributed to the superior heat transfer capabilities of nanofluids, which enhance the thermal performance of the system. When the PCM temperature reaches 70°C, the total amount of cumulative stored heat in the system is recorded at 10,400 kJ. This value reflects the effective energy storage capacity achieved through the use of nanofluids.

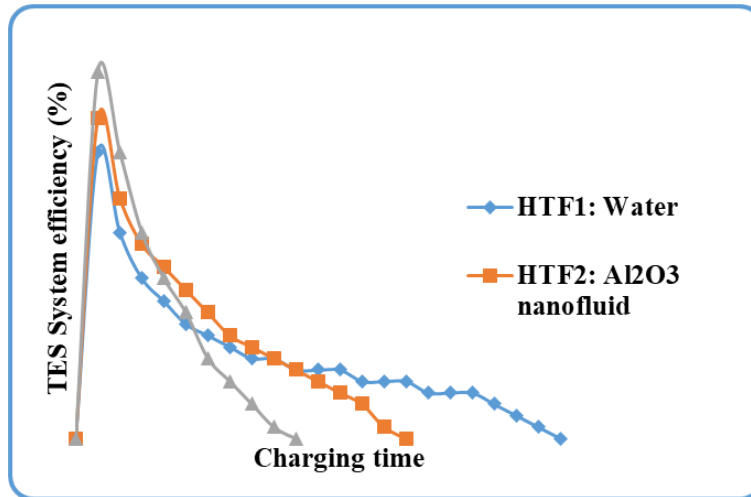


Figure 16 Variation of TES System efficiency during charging process for different HTFs

Figure 16 illustrates the system efficiency of the storage tank during the charging process at a flow rate of 6.0 l/min, comparing different heat transfer fluids (HTFs). The efficiency is calculated based on the ratio of the energy stored in the tank to the thermal energy harvested from solar radiation. As charging progresses, system efficiency decreases. This trend is particularly evident during the phase transition of the PCM and subsequently during the sensible heating of the liquid PCM. The drop in efficiency can be attributed to the diminishing temperature difference between the HTF and the PCM as the PCM approaches its melting temperature. The TES system efficiency increases of 10.81% for Al₂O₃ nanofluid and 27.02% for MgO nanofluid compared to water demonstrate the substantial benefits of using nanofluids in thermal energy storage systems.

3.2 Discharging experiments

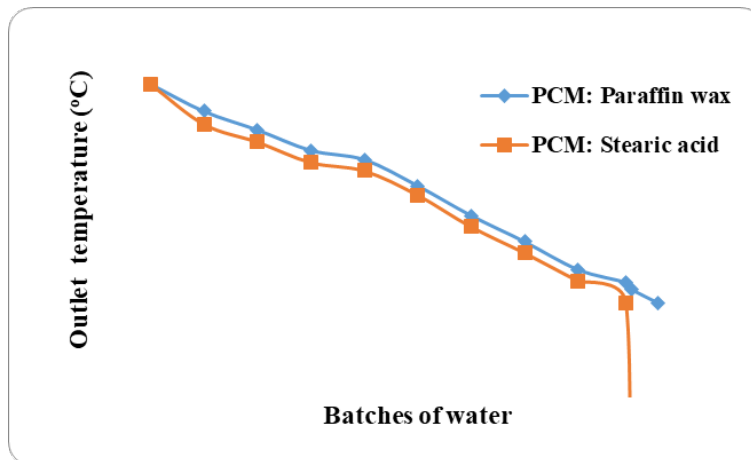


Figure 17 Batches of withdrawn water vs. Outlet temperature of water

Figure 17 result indicates that paraffin wax, as the PCM, enables a slightly higher quantity (210 litres) of hot water extraction compared to stearic acid (198 litres). The higher thermal storage capacity of paraffin wax likely accounts for this difference, allowing it to sustain a higher temperature over a greater volume. This makes it more effective for applications requiring a consistent supply of hot water over time.

4. Conclusions

This research provides valuable insights into optimizing PCM melting times by adjusting the HTF flow rates and nanoparticles concentrations. The use of Al₂O₃ and MgO nanofluids enhances heat transfer, with MgO showing the most substantial effect in reducing melting time.

Using water as the HTF with increasing flow rates of 2.0, 4.0, and 6.0 l/min significantly reduces the total charging time from 145 minutes to 130 minutes and finally to 110 minutes. This decrease illustrates the effectiveness of higher flow rates in improving heat transfer, as they allow more rapid temperature increase

and energy storage in the PCM. This insight is valuable for optimizing TES systems where water serves as the primary HTF.

The results indeed highlight that higher HTF flow rates lead to a noticeable reduction in charging time, specifically by 10.34% when increased from 2.0 to 4.0 l/min, and by 24.13% from 2.0 to 6.0 l/min. This efficiency boost makes higher flow rates advantageous, as they facilitate quicker thermal energy transfer to the PCM, thereby improving the overall performance of the TES system.

Using Al₂O₃ nanofluid with different volume fractions as HTF effectively decreases the total charging time, 95 minutes for 0.2%, 85 minutes for 0.5%, and 75 minutes for 0.8%. This trend underscores that higher concentrations of Al₂O₃ nanoparticles enhance heat transfer properties, reducing the time required to fully charge the TES system. This efficiency gain makes higher nanoparticles concentrations a practical approach to improving TES performance.

The results clearly illustrate that increasing the volume concentration of Al₂O₃ nanofluid leads to significant improvements in charging efficiency. The 10.52% reduction in charging time when increasing from 0.2% to 0.5% and the 21.05% reduction when increasing from 0.2% to 0.8% demonstrate that higher nanoparticles concentrations facilitate better thermal conductivity and heat transfer.

When compared in relation with the existing HTF, water, there is significant rate of simplification in the charging period, in case of flow rate of 6 l/min and 0.8% volumetric based percentages of nanoparticles, around 31.81 % for Al₂O₃ nanofluid and 54.54% for MgO nanofluid.

The cumulative stored heat of 10,400 kJ at a PCM temperature of 70°C indicates a significant amount of energy storage achieved by the system. This value is critical for understanding the system's capacity to supply heat when needed; reflecting its efficiency in thermal energy storage applications.

The observed efficiency improvements of 10.81% for Al₂O₃ nanofluid and a remarkable 27.02% for MgO nanofluid at a 0.8% volume concentration compared to water as HTF highlight the significant benefits of using nanofluids. Nanofluid of MgO has given a remarkable state in melting time reduction due to higher thermal conductivity, Brownian motion, low density, agglomeration and micro convection.

The faster performance of MgO nanofluid as HTF makes it a suitable choice for various domestic applications, including water heating, clothes drying, and cooking. Its enhanced heat transfer capabilities can lead to quicker heating times and greater energy efficiency, providing significant benefits for household energy management. This insight could encourage broader adoption of nanofluids in domestic heating systems.

The collection of 210 liters of hot water with paraffin wax as PCM, compared to 198 liters with stearic acid, indicates that paraffin wax has a higher thermal storage capacity in this application.

4.1 The present study limitation

In nanofluids, increasing the volume concentration of nanoparticles beyond 1% results in a decrease in the specific heat capacity of the heat transfer fluid (HTF). Therefore, to optimize heat transfer efficiency while maintaining the desired thermal properties, the selected nanoparticles volume concentrations are 0.2%, 0.5%, and 0.8%. This careful selection allows for effective enhancement of heat transfer without compromising the HTF's performance, making it suitable for various thermal applications.

References

- [1] Karabulut, K., Heat Transfer Increment Study Taking into Consideration Fin Lengths for CuO-Water Nanofluid in Cross Flow-Impinging Jet Flow Channels, *Thermal Science*, 27 (2023), 6A, pp. 4345-4360.
- [2] R. Meenakshi Reddy, N Nallusamy, AB Prasad, K. Hemachandra Reddy, Thermal energy storage system using phase change materials: constant heat source, *Thermal science*, 16(2012), pp.1097-1104.
- [3] M.S. Mohammad, Al- Azawii, Carter Theade, Megan Danczyk, Erick Johnson, Experimental study on the cyclic behavior of thermal energy storage in an air alumina packed bed, *Journal of Energy Storage*,18(2018), pp. 239-249.
- [4] A.A. Minea, M.G. Moldoveanu, Studies on Al₂O₃, CuO, and TiO₂ water based nano fluids, A comparative approach in laminar and turbulent flow," *Journal of Engineering Thermo physics*, 28(2017), pp.1-11.
- [5] Y. Li, J. Zhou, S. Tung, E. Schneider, S. Xi, A review on development of nano fluid preparation and characterization, *Power Technology*,196(2009), pp.89-101.
- [6] Omid Mahian, Ali Kianifar, A.K. Soteris Ioan Pop, Samchai Wongwises, A review of the applications of nano fluids in solar energy, *International Journal of Heat and Mass Transfer*, 57(2013), pp.582-594.

- [7] M. Abdollahzadeh, M. Esmailpour, Enhancement of phase change material (PCM) based latent heat storage system with nano fluid and wavy surface,” *International Journal of Heat and Mass Transfer*, 80(2015), pp. 376-385.
- [8] L. Godson, B. Raja, D.M. Lal, S. Wongwises, Enhancement of heat transfer using nano fluids – an overview,” *Renewable Sustainable Energy Review*, 14(2010), pp. 629-641.
- [9] Qinbo He, Shuangfeng Wang, Mingwei Tong, Yudong Liu, Experimental study on thermo physical properties of nanofluids as phase change material (PCM) in low temperature cool storage, *Energy Conversion and Management*, 64(2012), pp.199-205.
- [10] Ryan Anderson, Samira Shiri, Hitesh Bindra, F.M. Jeffrey, Experimental Results and Modeling of Energy Storage and Recovery in a Packed Bed of Alumina Particles, *Applied Energy*, 119(2014), pp. 521-529.
- [11] Wu. Shuying, Dongsheng Zhu, Xinfang Li, Hua Li, Junxi Lei. Thermal energy storage behavior of Al₂O₃ – H₂O nano fluids, *Thermochimica Acta*, 483(2009), pp.73-77.
- [12] S. Hari Krishnan, S. Magesh, S.Kalaiselvam, Preparation and thermal energy storage behavior of stearic acid – TiO₂ nano fluids as a phase change material for solar heating systems, *Thermochimica Acta*, 565(2013), pp.137-145.
- [13] S.M.S. Mushed, K.C. Leong, C. Yang, Enhanced thermal conductivity of TiO₂ – water based nano fluids,” *International Journal of Thermal Sciences*, 44(2005), pp.367-373.
- [14] Mahbulul, I.M., et al., Experimental investigation on effect of ultrasonication duration on colloidal dispersion and thermo physical properties of alumina-water nanofluid, *International Journal of Heat and Mass Transfer*, 88(2015), pp. 73–81
- [15] Senthilraja, S., Vijayakumar, K., & Gangadevi, R. , A Comparative Study on Thermal Conductivity of Al₂O₃/WATER, CuO/WATER and Al₂O₃-CuO/Water Nanofluids, *Digest Journal of Nanomaterials and Bio structures*, 10(4) (2015), pp. 1449-1458.
- [16] Hemanth Kumar Gupta, et al., Investigations for the effect of Al₂O₃-H₂O nanofluid flow rate on the efficiency of direct absorption solar collector, *Case Studies in Thermal Engineering*, 5 (2015), pp. 70-78.
- [17] Michael Joseph Stalin Prakasam., et al., An Experimental Study of the mass flow rates effect on Flat Plate Solar Water Heater Performance using Al₂O₃/Water nanofluid, *Thermal Science*, 21 (2017), 2, pp. S379-S388.

Energy Efficiency of the Passive System for Extraction of Landfill Gas at the Landfill of Niš

Ljubica Stojković^a, Ivan Mihajlović^b, Dragoslav Pavlović^c

^aPublic Utility Company "Mediana", Niš, RS, ljubica.stojkovic@jcpmediana.rs

^bPublic Utility Company "Mediana", Niš, RS, ivan.mihajlovic@jcpmediana.rs

^cElectricity Company, Niš, RS, dragoslav.pavlovic@odt.rs

Abstract: LANDFILL gas (LFG), which mainly includes methane, is a greenhouse gas collected by extraction systems, released into the air, or directly used to generate electricity. The paper measured the temperature of landfill gas (LFG) on biothorns, at the landfill in Niš, and investigated the possibility of utilizing the potential of landfill gas before its closure. Infrared thermographic method (IF) of radiation was used to test the QUANTITY of methane on the passive system. The paper concludes that heat and gases are released that cannot be further used for the production of electricity in thermal power plants. Analyzing the results, no thermal irregularities in the immediate environment were observed, and the conclusion is reached that the passive GASA degassing system has no impact on the environment.

Keywords: Landfill gas, BioThorn, gasification, electricity

1. Introduction

Disposal of municipal waste, for the city of Niš, is carried out at the unsanitary city landfill, which occupies an area of 35.4 hectares of land, with a total volume of 128571 m³/god. shown in Figure 1 [1].

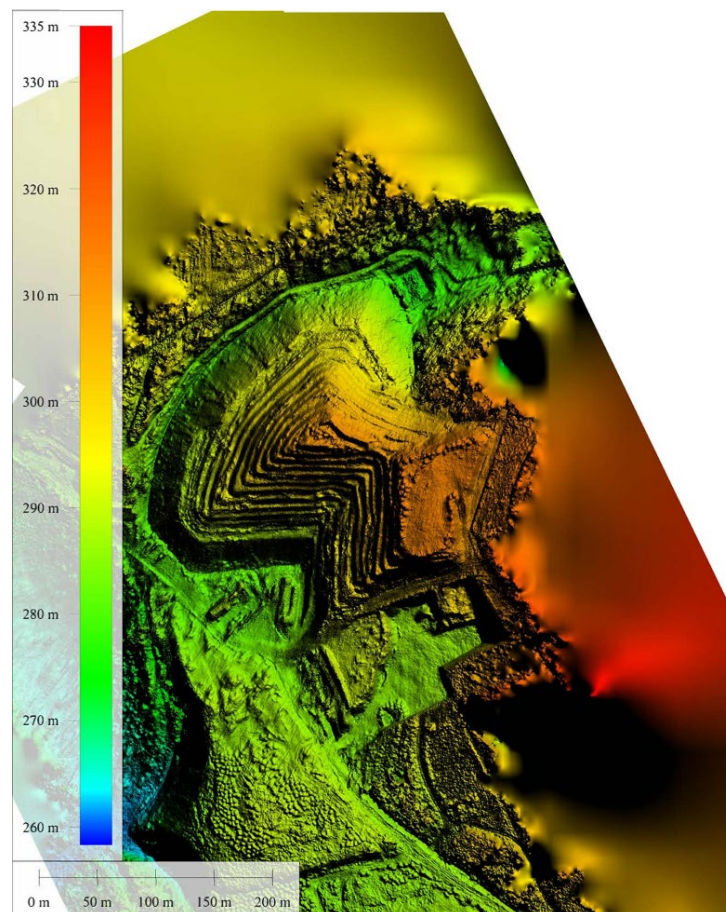


Figure 1 3D model of the S4 field complex of the Nish

The amount of waste collected and disposed of at the landfill, on a daily basis, amounts to 411,644.2 kg/day or 150,250,145 kg/year. annually. The average density of waste is 0.7 - 0.9 t/m³ [2]. Within the landfill, four segments from (S1 to S4) were formed, which contain cassette disposal of waste, compaction and covering with inert material (soil). Landfill gases (LFG) are produced by the decomposition of organic waste and the collection of effluents. The consumption of oxygen leads to anaerobic fermentation, as a result of which GASES, without an adequate selection of purification systems, represent a significant source of pollution, but also a significant source of methane [3]. During gasification, heat and gases are released that can be used in thermal power plants to generate electricity [4]. For the degassing of landfill gas (LFG), a passive system was built, consisting of individually placed biothorns, which are present in all segments of the landfill [5]. The layout of the placement of biothorns, on the active field S4, is shown in Figure 2 [6].

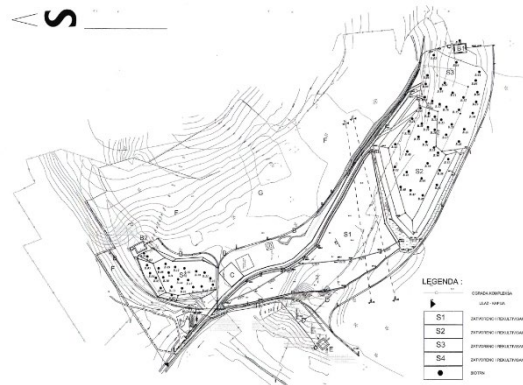


Figure 2 Schedule of placement of biothorns on the

On the tops of biothorns, burners can be placed to burn gases. In this way, it is easier to extract gas from the beginning of its production, and the gas can be collected before closing and covering the landfill. The study of the magnetic field of the flow of an incompressible electroconductive fluid is of significant scientific and research interest in the possible technical and technological applications of the obtained results of thermographic methods. Processes in which heat transfer takes place require the study of the influence of external magnetic fields on thermal-physical processes in the magnetohydrodynamic generator (MHD) dynamic and temperature heat source/transmitter and thermal radiation, where the electrical conductivity of the fluid is constant [7].

2. Material and methods

To measure the temperature of the LFG, the infrared thermographic method (IF) is used. The advantages of the method are the time interval and high mobility of the sensors, the possibility of data storage and analysis, as well as their comparison. A thermographic camera (IR) is used to determine the rate of temperature change before and after irradiation, on the surface of the biothorn. The sensor beam of the IR camera measures the temperature of several areas and thus draws an image. It is remote, a safe distance from the site. The incident radiant heat of fire can also be detected with high sensitivity [8]. An IR camera FLIP T335, shown in Figure 3, was used to measure LFG.



Figure 3 Equipment for measuring the temperature of landfill gas - thermal imaging camera FLIP T335

Setting the boundary conditions is important for determining the min. and max. measurement temperatures, and the process itself is performed by a software package [9]. The model at the Niš landfill represents a convergence of the strategy and the model (Dfe/EMS/SD) that takes into account the thermal power of the gas depending on the method of purification [10].

2.1. Experimental measurements and ANSYS FLUENT simulation

For the degassing of the Niš landfill, individual well-type technical facilities (biothorns) were installed. Biotrn consists of a degassing pipe and a protective grate. The efficiency of the system depends on the pressure of the gas formed in the landfill of the working body and the cooling of the gas, which represents the heat exchange of the upper surface of the working body by radiation and convection to the environment [11]. The upper part of the foundation is a concreted protective grid and a plastic perforated pipe (PVC) (degassing pipe). Gas degassing is done through holes with a diameter of 15 mm (about 200 holes per long meter). The length of the pipe depends on the height of the layer of waste and inert material. Due to the drainage of landfill gas, the space between the protective grid and the pipe is filled with coarse-grained gravel. The protective grid is installed before the waste is filled. A protective knee at a 90° angle was made on the upper part of the biotrn for gas escape and protection from atmospheric precipitation. Biotrns are placed around the perimeter and inside the landfill, in a checkerboard arrangement with an assumed radius of action of 25 m. The diameters of biothorns are in the interval 0.5-1.0 m, and their depth is 50-90% of the depth of the waste. Parameters when testing one biotrine: Location: B.05 Date and time: 7/7/2021, time 2:30 p.m., reference temperature: 20°C, atmospheric temperature 35°C, external optional temperature 52°C, distance of 1m, inclined 1, emissivity: 0.95, relative humidity: 35%, no precipitation, wind direction Z, air flow speed: 2.0±0.6m/s, weather clear. The temperature field of biothorn B5 is shown in Figure 4 [12].

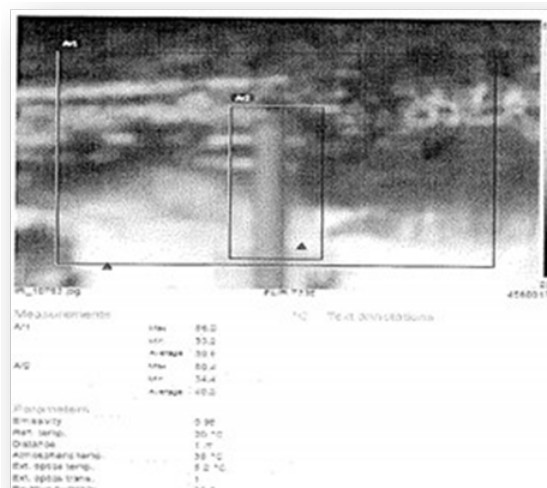


Figure 4 Thermal imaging of biothorn B5

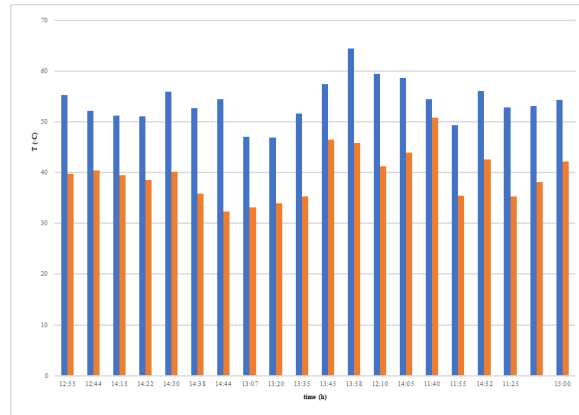
Useful mechanical work per kilogram of waste is equal to:

$$Q = T_b - T_g [kwh / kg] \quad (17)$$

3. Results and discussion

The obtained results were analyzed through diagrams of speed and temperature changes and given diagrams of integral and differential characteristics of the boundary layers. Heat expansion [14] takes place in the horizontal and vertical direction, in the direction from higher to lower gas concentration, within the body of the landfill ($T_b > T_g$) [15]. Gas production within the landfill is dependent on atmospheric pressure, which creates areas of higher pressure within which gas movement is restricted by the final layer. The permeability of the final layer describes the movement of gas. Dry soil is very permeable, while clay has higher humidity and is significantly less permeable [16]. Gas tends to move towards more permeable areas. The final layer is usually formed from less permeable materials, such as clay. Therefore, the gas has a greater possibility to move in horizontal planes than up and through the final layer. If there is no final layer, the generated gas will move uncontrollably outside the body of the landfill, because it is lighter and its concentration in the atmosphere is lower than inside the body of the landfill itself. Due to the difference in pressures, there is a convection of gas

that moves towards areas of lower pressure. The temperature of the gas inside the landfill increases the pressure compared to the atmospheric pressure ($P > P_a$). Also, the gas will move in the direction of least resistance. The measurement results show the highest gas temperature, on biotorns, under serial numbers 12, 13, 22, while the highest gas temperature by convention is on biotorns no. 11, 12, 17. Analysis gas saturations, in the temperature field S4 of the Nish landfill, are shown in graphic 1.



Graph 1. Analysis of gas saturation, in the temperature field S4 of the Niš landfill

If the temperature values of the landfill gas and the biotorne, from Graph.1, are entered into expression (1), the mechanical work of the working body (biotorne) per kilogram of waste, shown in table 1, is obtained.

Table 1. Useful mechanical work of the working body (Biotrna) in the temperature field S4 of the Niš landfill

Biotrn	Q (kWh/kg)
B1	53.851.27
B2	40.649.02
B3	40.649.02
B4	43.775.87
B5	54.893.55
B6	58.715.25
B7	77.128.91
B8	48.292.43
B9	45.165.58
B10	56.978.12
B11	38.217.03
B12	64.621.52
B13	63.231.81
B14	51.419.28
B15	46.902.72
B16	48.639.86
B17	70.875.22
B18	61.147.25
B20	52.114.13
B21	42.038.73
B22	9,727,971
B23	51.419.28
B24	43.775.87
B25	40.649.02

4. Conclusion

Based on the above, the following can be concluded:

- From the aspect of environmental protection, the constructed passive system for the extraction of landfill gas has no negative impact on the environment
- The paper discusses the thermal imaging method for determining the amount of useful mechanical work for the production of electricity.
- The existing passive system for landfill gas extraction has no potential for energy utilization and electricity production.
- Thermovision research can further be used to monitor the flow and pressure of gas, which reacts with oxygen, due to improper disposal of waste, remains in the body of the landfill and leads to the occurrence of explosions and air pollution.
- Thermovision testing is widely used in determining the energy efficiency of steam power plants and magnetohydrodynamic generator (MHD) applications.
- Concluding remarks and recommendations are given for the future development of integral gas management, whose potential can be used to obtain electricity in thermal power plants.

Nomenclature

Latin symbols

L – Characteristic linear dimension, in [m].

Re – Reynolds number.

Superscripts

t – Time interval.

0 – Environment

Q - useful mechanical work [13]

T_b – temperature of the biotrine

T_g – gas temperature

References

- [1] Boričić AZ Laković MS, Jovanović MM, (2024) New method for calculating heat transfer in unsteady MHD mixed boundary / layers with radiative and generation heat over a cylinder, Thermal science: Year 2023, Vol. 27, No. 6A, pp. 4417-4429
- [2] Milošević L., Mihajlović E., Đorđević A., Radosavljević Jasmina (2015) General principles and characteristics of the formation and occurrence of fire at sanitary landfills, Safety Engineering, vol. 5, no. 2, p. 91-95, University of Nis, Faculty of Occupational Safety, Serbia
- [3] Radosavljević, J., Ristic, J. (2012). Landfills and municipal waste disposal Faculty of Occupational Safety, Niš ISBN - 978-86-6093-010-3
- [4] Krstić, D. & Sokolović, D., (2020), Methods and results of electromagnetic radiation research in the environment, University of Niš, Faculty of Occupational Safety, Niš, 2021, ISBN 978-86-6093-092-9
- [5] Glišović, S., (2017) Sustainable design and the environment: Faculty of Occupational Safety, Niš, ISBN - 978-86-6093-075-2
- [6] Raos M., (2020) Thermodynamics with thermotechnics, University of Niš, Faculty of Occupational Safety, Niš, 2020
- [7] Pavlović, T., Mirjanić, D., Milosavljević, D. (2018). Electric power industry, in Serbia and the Republic of Srpska. Academy of sciences and arts of the Republic of Srpska, Banja Luka
- [8] Radosavljević, J., Đorđević, A. (2013). Landfills and municipal waste disposal Faculty of Occupational Safety, Niš ISBN - 978-86-6093-010-3, pp. 1-123
- [9] Radosavljević, J., Vukadinović A., MUNICIPAL WASTE MANAGEMENT, University of Niš, Faculty of Occupational Safety, 2024, pp.108-124
- [10] Stojković, Lj., (2022), Plasma gasification technology, Protection in practice, Journal of occupational safety, fire protection, occupational medicine and ecology, University of Niš, Faculty of Occupational Safety, no. 340, p. 50 - 53, December 2022

- [11] Stojković Lj., Pavlović D., Mihajlović I., Study of waste of treatment energy efficiency, Serbia - Niš, Oct. 18-21, pp. 529-533
- [12] Stojković, Lj., and Pavlović D. (2022, November 16). Thermal energy for sterilization of hazardous waste (Online). University of Niš, Faculty of Mechanical Engineering VOL. 1, NO 3, 2022, PP. 80 – 86. Received: November 16, 2022 / Accepted December 29, 2022. Original scientific paper *
- [13] Stojković, Lj., Pavlović, D., Mihajlović I., (2022) Energy efficiency treatment of waste in the city of Niš. 19th international conference "Man and working Environment" - OESEM, pp 225-229 Occupational and Environmental Safety Engineering & Management (OESEM), www.znrfak.ni.ac.rs/oesem2022
- [14] KARLJIĆ, N. STANOJEVIĆ, M., RADIĆ, D., JOVOVIĆ, A., OBRADOVIĆ, M., TODORVIĆ, D., (2017) IMPACT OF LOW-RANK COAL FLY ASH PERMEABILITY FACTOR ON CONDITIONS OF PNEUMATIC TRANSPORT , Jubilee, 30th International Process Industry Congress, Process Engineering Society at SMEITS, June 1 and 2
- [15] Model of organizing transfer stations in the regional municipal waste management system: Master's thesis Stojković, Ljubica, Master's thesis, Publishing and production - Niš : [Lj. Stojković], 2014, Language – Serbian COBISS.SR-ID – 46199055
- [16] Gauss, Bureau of Geodesy (2023), Elaborate photogrammetric measurement - monitoring - Sector "S4"
- [17] Hidrozavod dtd, (2021) Main project of rehabilitation, closure and recultivation of segment S4, LANDFILL "BUBANJ" in Niš
- [18] Report on landfill gas testing, (2021) Vatrogas, Novi sad
- [19] Institut Vatrogas, (2021) Thermal imaging examination of landfill gas, Novi Sad

Potential Methane Generation Capacity on the Landfill Gas Extraction Systems at the Landfill in Niš

*Dragoslav Pavlović^a, Ivan Mihajlović^b, Ljubica Stojković^c, Bojan Banković^d,
Gradimir Cvetanović^e*

^aElectricity Company, Niš, RS, dragoslav.pavlovic@odt.rs

^bPublic Utility Company "Mediana", Niš, RS, jkpmediana@jcpmediana

^cPublic Utility Company "Mediana" Niš, RS, ljubica.stojkovic@jcpmediana.rs

^dFaculty of Electronic Engineering, University of Niš, RS, bojan.bankovic@elfak.ni.ac.rs

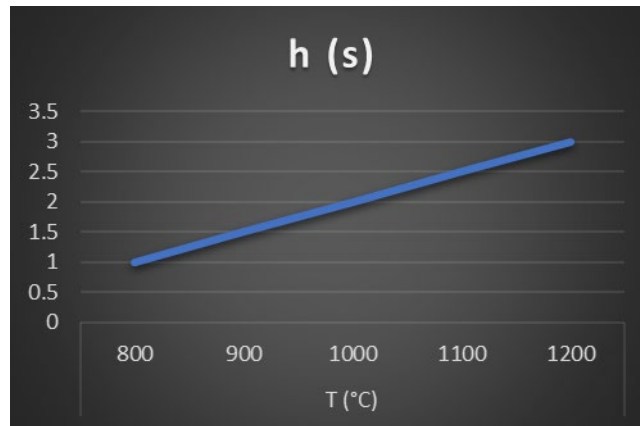
^eUniversity of Niš, Faculty of Technology, University of Niš, RS, gradimir.cvetanovic@gmail.com

Abstract: Systems for the production of electricity require the previous collection of gas from the organic matter of municipal waste. Collection of landfill gas is done by a degassing system. In the case of the Niš landfill, this system was partially built by installing biothorns for the evacuation of landfill gas into the air. The paper presents the results of testing landfill gases, which include: determination of the volume fraction of methane (CH₄), carbon dioxide (CO₂), hydrogen sulfide (H₂S), carbon monoxide (CO) and hydrogen (H₂). Measurements were made at the control points at the exit from the biothorn, at the closed and rehabilitated fields S 2 and S 3, simulated results at the control point of the pilot project of the active system, at the exit from the horizontal and vertical drain, at the active field S4, Niš landfill. Measurements were performed using the electrochemical method, with a GEM TM 2000 Plus gas analyzer, once a month. The LandGEM emission model was used to estimate the energy potential of methane. The paper concluded that the most energy-efficient method for waste disposal is the use of an active degassing system. Using an active landfill gas extraction system, a 1MW power plant can be built.

Keywords: Methane, gas extraction systems, gasification, electricity

1. Introduction

Requirements regarding economic and thermodynamic performance of plant and system components, in terms of conversion, distribution and consumption of different types of energy are continuously studied. The basis for the study of energy systems are conservation of mass and the First Principle of Thermodynamics. [1]. The disposal of municipal waste produces landfill gas (LFG), which mainly includes methane, a greenhouse gas, therefore its management is very important. [2]. The carbon footprint is used as an indicator of greenhouse gases at the landfill. Carbon footprint emissions are generally expressed as CO₂ equivalents quantify the main sources of emissions and represent (CO₂e), which consists of the emission of fuel components: carbon monoxide (CO), hydrogen (H₂), various hydrocarbons - methane (CH₄), and non-combustible components of water (H₂O), nitrogen (N₂), carbon dioxide (CO₂) [3]. The legal obligation to collect and burn landfill gas obligates the burning of gas for energy purposes with the creation of economic profit. Systems for obtaining energy require preliminary gas collection. A passive landfill gas extraction system was installed at the Niš landfill, built from horizontally perforated pipes (biothorns). During the research, an active extraction system was also used, which collects gas instead of the system, using one vertical pipe in the well (probe). The gas is further evacuated towards the power generation station through interconnected systems of horizontal pipes (main gas collectors), placed above the landfill cover layer. The gas is extracted, compressed, dried and directed to the gas engine via the compressor plant. For safety reasons, it is recommended to install a high-temperature torch. The torch must be insulated, which increases its efficiency. Gas combustion is achieved at a temperature of 1200°C for at least 3 seconds. The pressure change in the condenser significantly affects the economy of the generator operation. Bearing in mind that a change in condensation pressure of 1kPa leads to a change in the degree of utilization of 1% [4]. The pressure change in the condenser occurs due to the temperature change per unit volume of the condenser. The following graphic shows the dynamic analysis of the system for saturation temperature [5].



Graph 1. Dynamic analysis of the system for saturation temperature

2. Methodology

The method of analysis, synthesis and optimization REPRESENT a great role in the reliability of energy systems. The method of the Second Law of Thermodynamics is one of these methods [6]. The emission software model LandGEM, developed by the American Environmental Protection Agency (EPA) [<https://www.epa.gov/landfills/municipal-solid-waste-landfills>] was used to estimate the amount of landfill gas at the Bubanj landfill in Niš.]. The first edition of the software was created in 1991. and is based on the first-order decay rate equation. The model determines the amount of gas during landfill operation and several years after closure. It gives higher values, because it does not take into account the different content of organic matter, but the total amount of waste (the part is inert). The basic model used by the software requires constant amounts of disposed waste (IPCC Tier 1 model).

2.1. Calculation for calculating the amount of methane produced

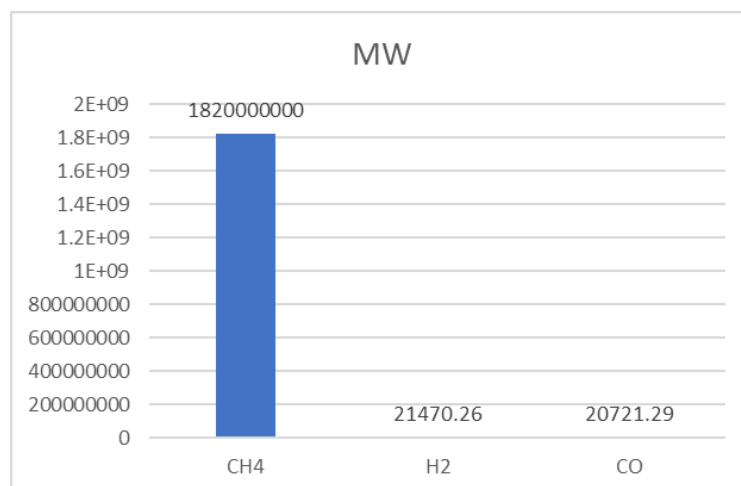
The annual amount of methane produced can be determined according to the equation [7]:

$$QCH_4 = \sum \sum kLo(Mi \& 10)e^{-kti} \quad (1)$$

3. Results and discussion

3.1. Passive system for landfill gas degassing

Measurements of temperature and atmospheric pressure of biogas were made by inserting a probe with a sensor into the biethorn at a depth of 2m for 3 minutes. Atmospheric conditions during the measurement were; outside temperature 32°C, relative humidity 45%, wind speed 3km/h, atmospheric pressure $p = 1005$ mbar, visibility good, no precipitation. If values for heat capacity (Lo) are entered into equation (1). the potential value for energy use shown in graph 2 is obtained..



Graph 2. Potential for energy utilization of methane on biethorns for 2023.

3.2. Simulation of an active biogas degassing system

Landfill gas degassing (Figure 1b).



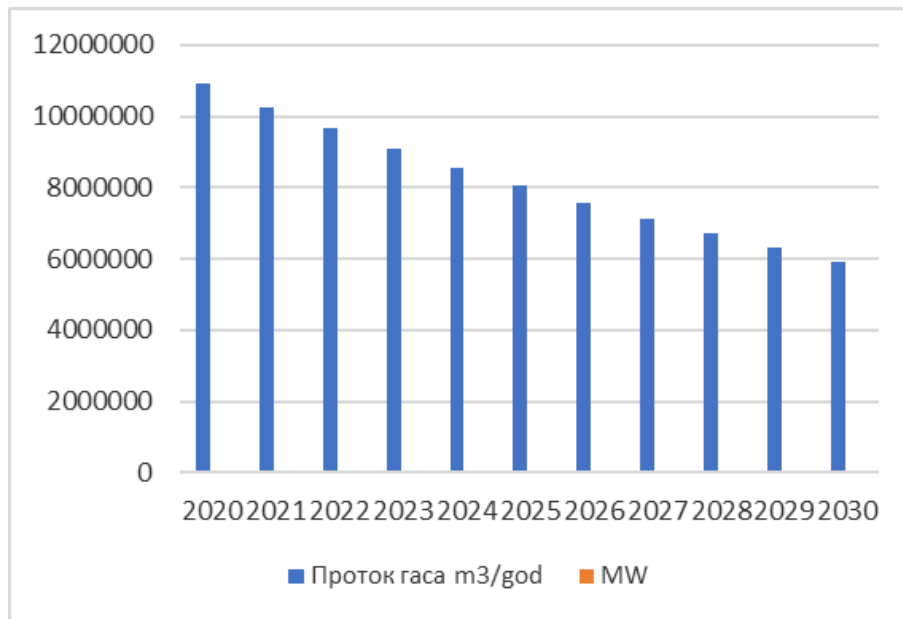
a) Layout of the biogas degassing probe



b) View of the horizontal connection of biogas degassing pipes

Figura 1. Landfill gas degassing

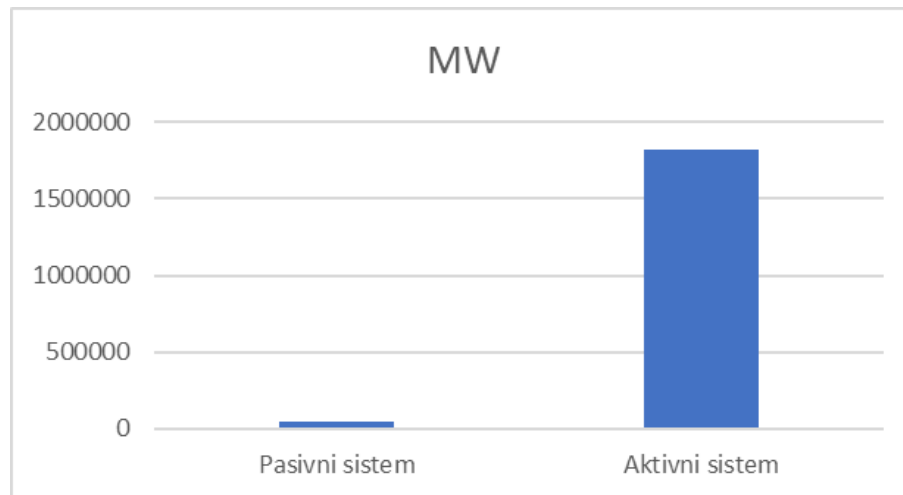
Estimated quantities of landfill gas range between 2000-4000 tons per year for the period between 2020 - 2030 year. A desulphurization system and an active carbon system are provided for gas purification to pure methane, as natural gas. The model assumes that the mean proportion of methane in landfill gas is 50%, varying from 30-70%, during the year. Valorization of LFG, for energy utilization by years, is shown in (graph 3).



Graph 3 Valorization of LFG, for energy utilization by years

The landfill does not have a sealing lining at the base of the landfill, which leads to heat losses and lateral leakage of landfill gas into the surrounding soil. In contrast to the passive system, the produced biogas has a significant carbon dioxide content (25-45%), which reduces the thermal power due to the volume it occupies. Its purification (hydrogen sulfide is emitted) reduces the volume of the produced gas, but increases its thermal power [9]. Gas flow and temperature ie. the calorific value of landfill gas varies seasonally. The largest production of landfill gas is achieved after the rehabilitation of the landfill, after 2017, and amounts to 298.78 m³/h. Ten years after the closure of the landfill, the amount of gas decreases by 30%, and after 20 years by more than 50%. Combined with an average methane content of 50%, it is expected that the utilization of

electricity as well as boilers with a fluidized bed [10] should not be more than 1.75-2.15 kWh/ m³. On average, from segment S4 of this landfill, in the next 10 years from the closing of the cassette and the construction of the plant for obtaining energy from waste, a total of 168,473,905 kWh of electricity can be valorized in ideal conditions of exploitation [11]. Taking into account the efficiency of the active landfill gas collection system, the amount of electricity produced is 151626514 kWh. In accordance with the REGULATION ON FEE FOR INCENTIVES OF PREFERRED ELECTRICITY PRODUCERS ("Official Gazette of RS", No. 50/2024) Fee for privileged producers of electricity - Fee for renewable energy sources. It is calculated as the product of the total energy used and the price of 0.801 din/kWh. Fee for the improvement of energy efficiency - calculated as the product of the total energy used and the price 0.015 din/kWh. Revenues from electricity for the period at the annual level amount to RSD 12,372,723.5 or €10,556,931. Gas temperature and flow rate have a great influence on the energy efficiency of the system for obtaining electricity [12]. The electric power obtained from active and passive systems for 2023 is shown in graphic 4.



Graph 4. Electric power of the active and passive system for 2023

For the power generation process, the gas is purified through a steam generator (HRSG) and the heat recovery is used to generate steam that is sent to steam turbine for the production of electricity in one process cycle. The cooled gas is then cleaned, it is compressed and used as fuel in a combustion gas turbine that drives an electric generator. Shut down compressed and used as fuel in a combustion gas turbine that drives an electric generator. The the exhaust gases are then passed through a second HRSG to pre-produce additional steam and clean the gas before it is emitted to the atmosphere. [13].

4. Conclusion:

Based on the above, the following is reached:

- Landfill gas (LFG) is produced by the decomposition of the organic part of solid waste [14].
- LFG is a greenhouse gas, the recommendations are to release it into the air, or to collect it for energy production.
- Landfill gas extraction systems can be:

Passive and active

- Advantages of an active landfill gas extraction system:
 - The technology is considered Best Available Technique (BAT).
 - The degree of efficiency of the passive system is 0.55%, while the degree of efficiency of the active system is 0.90%
 - Direct contact with disposed waste increases gas efficiency
 - Gas temperature directly depends on the amount of oxygen in the waste [15]
 - Active gas extraction system, electricity production equivalent to approximately 1MW [16,17]
 - Analysis of landfill gas, the required amount of air for complete combustion, thermal power of fuel, quantity and composition of combustion products and combustion temperature [18].

Nomenclature

Latin symbols

QCH ₄	–	annual amount of methane produced, amount of methane (m ³ /year),
I	–	increment (1 year)
J	–	increment
n	–	initial year of waste disposal
k	–	rate of methane generation (yr ⁻¹)
Lo	–	potential methane production capacity (m ³ /t)

Superscripts

M _i	–	mass of waste deposited in that year (t),
e	–	speed of heat transfer of the working body [8].

References

- [1] Laković., M., Živković., P., Rašković.P., (2005) Method of exergy analysis in process integration of nitric acid production plant, Facta universitatis – series: Mechanical Engineering, vol.3, no.1 , pp. 109 – 116, Niš
- [2] Tozlu.,A, Özahi, E., Abuşoğlu.,A., (2016) Waste to energy technologies for municipal solid waste management in Gaziantep, Renewable and Sustainable Energy Reviews, Renewable and Sustainable Energy Reviews, Volume 54, Pages 809-815
- [3] Jović, M.; Laković., M., (2018) Carbon footprint method – a case study for thermal power plants in the Republic of Serbia, University of Nis, Faculty of Mechanical Engineering, Niš, SERBIA
- [4] Živković., P., Laković., M. Rašković., P. (2004) Exergetic analysis method for process integration, Facta universitatis – series: Mechanical Engineering, Volume 2, no.1, Pages 135-140, Niš, Serbia
- [5] Laković, M. Stefanović., S., V., P, Stojiljković M., Živković, D., PM, (2010) Daily pressure change in the condenser of a re-cooled steam block for an average summer day, Termotehnika, vol. 36, no.1, pp.93-102, University of Niš, Faculty of Mechanical Engineering, Niš, Serbia
- [6] Jovčevski, M., Laković., M., Stojković., F., Ivanović., M., (2022) Mathematical and CDF Methods for reduction of thermal pollution caused by thermal power plant Mechanical Engineering – Scientific Journal, vol . 40, no. 2, pp. 99-104
- [7] Laković., M., Jović.M., (2015), Boilers for fuel combustion in a fluidized bed, Boilers for fuel combustion in a fluidized bed, Technology - Mechanical Engineering 64
- [8] Laković., M.Banjac MJ, Bogdanović - Jovanović, Jović., M., Milovanović, Z., (2018) Risk of thermal pollution of the Danube passing through Serbia due to thermal power plants, Thermal science, Vol. 22, suppl. 5, pp. S1323 – S1336
- [9] Stojković, Lj. (2022), Journal of occupational safety, fire protection, occupational medicine and ecology, Protection; No. 340, University of Niš, Faculty of Occupational Safety, pp. 50-53, ISSN 1451-1142, COBISS.SR-ID 41827340
- [10] Živković., Lj., Raos, M., (2003), Termostrojenja collection of tasks, University of Niš
- [11] Lambić., M., (2007), Energy, University of Novi Sad, Technical Faculty "Mihajlo Pupin", Zrenjanin
- [12] Radosavljević, J., Ristic, J. (2012). Landfills and municipal waste disposal Faculty of Occupational Safety, Niš ISBN - 978-86-6093-010-3
- [13] Mitić, D., Stanković., M., Protić., M., (2009) Biomass for thermal energy, University of Niš, Faculty of Occupational Safety, Niš
- [14] Mitić., D., Energy, University of Niš, Niš, 2008
- [15] Pavlović, MT, Mirjarić., D.Lj., Milosavljević., DD, (2018) Electric power in Serbia and the Republic of Serbia, Academy of Science and Arts of the Republic of Srpska, Banja Luka
- [16] Mitić, D., (2001) Stoichiometric calculations in combustion processes, University of Niš
- [17] Chapters
- [18] Radosavljević, J., Đorđević, A. (2013). Landfills and municipal waste disposal Faculty of Occupational Safety, Niš ISBN - 978-86-6093-010-3, pp. 1-123
- [19] Radosavljević, J., Vukadinović A., MUNICIPAL WASTE MANAGEMENT, University of Niš, Faculty of Occupational Safety, 2024, pp.108-124

- [20] Pavlovic S., Evangelos B. b, M. Grozdanovic, V. Stefanovic d, M. Vukic, M. Lakovic-Paunovic f, C. Tzivanidis, Dynamic analysis of a solar dish concentrating collector coupled to an organic Rankine cycle with reheating, The 20th International Conference on thermal science and Engineering of Serbia, SimTerm2022, Niš, Serbia, Oct.18-21.2022, pp.529-533
- [21] Stojković, Lj., (2022), Plasma gasification technology, Protection in practice, Journal of occupational safety, fire protection, occupational medicine and ecology, University of Niš, Faculty of Occupational Safety, no. 340, p. 50 - 53, December 2022
- [22] Stojković Lj., Pavlović D., Mihajlović I., Study of waste of treatment energy efficiency, Serbia - Niš, Oct. 18-21, pp. 529-533
- [23] Stojković Lj., Pavlović D., Mihajlović I., Study of waste of treatment energy efficiency, Serbia - Niš, Oct. 18-21, pp. 529-533
- [24] Model of organizing transfer stations in the regional municipal waste management system: Master's thesis
- [25] Stojković, Ljubica, Master's thesis, Publishing and production - Niš : [Lj. Stojković], 2014, Language – Serbian COBISS.SR-ID – 46199055
- [26] Gauss, Bureau of Geodesy (2023), Elaborate photogrammetric measurement - monitoring - Sector "S4"
- [27] Hidrozavod dtd, (2021) Main project of rehabilitation, closure and recultivation of segment S4, LANDFILL "BUBANJ" in Niš
- [28] GEOPUT d.o.o., Public utility company "Mediana" Niš, (2018) Utilization of landfill gas for Bubanj landfill in Niš, Belgrade, www.geoput.com
- [29] Institut Vatrogas, (2021) Thermal imaging examination of landfill

Effect of Properties of Working Fluids on the Efficiency of a Low-Temperature Organic Rankine Cycle

Marija Živković^a, Aleksandar Mijatović^b, Dejan Ivezić^c, Boban Pavlović^d

^aUniversity of Belgrade, Faculty of Mining and Geology, Belgrade, RS, marija.zivkovic@rgf.bg.ac.rs

^bUniversity of Belgrade, Faculty of Mining and Geology, Belgrade, 688,

aleksandar.mijatovic@rgf.bg.ac.rs

^cUniversity of Belgrade, Faculty of Mining and Geology, Belgrade, RS, dejan.ivezic@rgf.bg.ac.rs

^dUniversity of Belgrade, Faculty of Mining and Geology, Belgrade, RS, boban.pavlovic@rgf.bg.ac.rs

Abstract: Decarbonization of all segments of energy systems, both on the supply and demand side, is one of the main goals of the energy transition. Electricity supply in the future will largely rely on generation from intermittent energy sources: wind and solar. Locally available, non-utilized alternative low-temperature energy sources as hydro-geothermal wells, and abundant oil and gas wells, have the potential to provide continual energy production over the year. Electricity generation from these energy sources is carried out with working fluids with low evaporation temperatures. Commonly used fluids are categorized into several groups based on their chemical composition, which determines their thermophysical properties. In this paper the effect of chemical composition of six fluids from three groups on thermophysical properties was analyzed. The effect of fluids' properties on the efficiency of ORC is analyzed for the case of a typical range of temperatures of hydro-geothermal and abundant oil and gas wells in Serbia, which may be used as heat sources for electricity generation.

Keywords: Properties, Working fluids, Efficiency, ORC, Low temperature

1. Introduction

The transition to low or carbon-neutral energy systems implies the utilization of renewable and alternative energy sources across all segments of energy systems, both on the supply and demand sides [1]. Electricity generation is identified as a critical factor and a major contributor to the reduction of GHG emissions [2]. In addition, green electricity is a prerequisite for the decarbonization of final energy consumption [3] through the use of heat pumps, the introduction of electric vehicles, and the production of green hydrogen.

It is known that electricity can be generated from any renewable energy source. Scenarios describing future energy systems indicate high utilization and significant contributions from intermittent energy sources such as wind and solar [4]. However, the contribution of all renewable and alternative energy sources is expected, including low-temperature energy sources.

Low temperature heat sources can be utilized by Organic Rankine Cycle (ORC), which operates at lower pressures and temperatures [5]. Working fluids that can be used in performing ORC firstly need to have ability to evaporate at low temperatures and additionally to meet other requirements: an appropriate slope of the vapor saturation line in the T-s diagram, critical temperature and pressure, normal boiling temperature, global warming potential, and safety level [6].

Substances that may be used as working fluids are commonly categorized into several groups based on their chemical compositions. The main groups of fluids are hydrocarbons, halogenated hydrocarbons, and siloxanes. This paper aims to examine the effect of working fluid properties on efficiency of ORC that utilize low-temperature heat sources, such as geothermal sources, heat from abandoned oil and gas wells, or waste heat from industry.

2. Working fluids for Organic Rankine Cycle

Technologies for electricity generation for utilizing low or medium-grade heat energy are based on the Kalina cycle, Organic Rankine cycle (ORC), and supercritical Brayton cycle with carbon dioxide. ORC is preferred due to its simplicity, low maintenance, and component availability [7]. The basic Organic Rankine Cycle is

similar to the conventional steam Rankine cycle, and it is usually performed with organic fluid derived from carbon chemistry.

Working fluids used in ORCs are classified into three main categories based on the slope of the vapor saturation line in the T-S diagram, which is determined by the saturated properties of the fluids. Fluids are categorized as wet, isentropic, or dry (Figure 1) [8], based on the process of the isentropic expansion of the dry steam. If the process of expansion ends at two phase zone, the fluid is classified as wet. If the isentropic expansion closely follows the saturation curve, the fluid is classified as isentropic. If the expansion ends in the superheated vapor zone, the fluid is classified as dry.

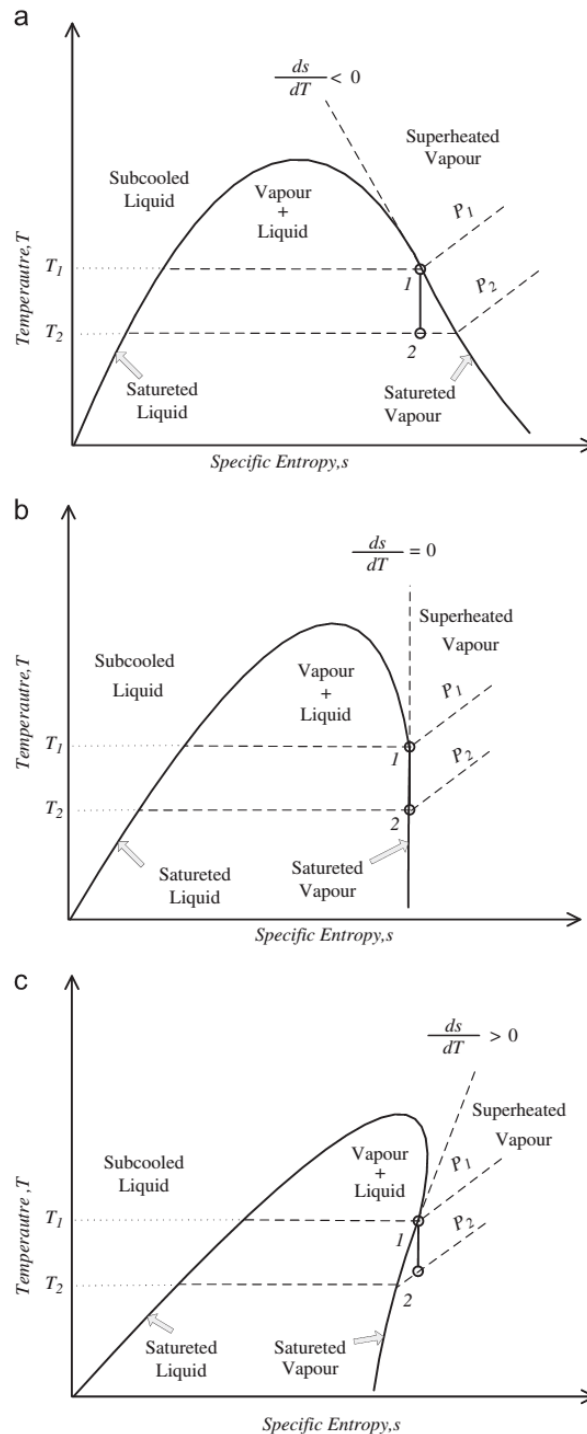


Figure 1. Classification of working fluids: a) wet, b) isentropic, c) dry [8]

The behavior of fluids during phase change has been the subject of many studies. It has been shown that the complexity of the molecular structure influences fluid behavior. Fluids with simple molecular structures are

commonly wet fluids, while fluids with higher complexity tend to act as dry fluids. Intermediate fluids behave as isentropic fluids [9].

Additionally, dry fluids are high molecular mass organic fluids, wet fluids are low molecular mass organic fluids, and isentropic fluids have medium molecular mass [10].

Liu et al. [11], concluded that the presence of hydrogen bond in the molecules of some organic working fluids is a probable cause of some fluids behaving as wet fluids. This is due to their larger vaporizing enthalpies, which are inappropriate for application in ORC systems [10].

The performance, i.e. the efficiency of the ORC, is dependent on the thermo-physical characteristics of the working fluids, which are also influenced by chemical composition and the structure of the molecule.

The practice shows that the commonly used working fluids are halogenated hydrocarbons, pentane, cyclopentane, n-heptane, hexane, hexamethyldisiloxane (MM), octomethyloxane (MDM) [12]. The performance of pentane, n-heptane, and hexane suggests that these fuels may contribute to greater efficiencies due to the high latent heat of vaporization. Working fluids with excellent thermal stability and low vapor pressure, such as hexamethyldisiloxane (MM) and octamethylisodimethylsiloxane (MDM), have been shown to increase Rankine cycle efficiency [12].

3. Methods and materials


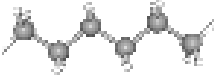
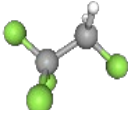
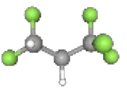
Given that the slope of vapor saturation curve and thermophysical properties of working fluids depend on the chemical composition, for the evaluation and analyses of working fluids properties on efficiency of ORC, six working fluids were selected, two from each group:

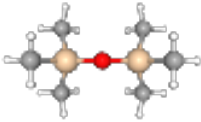
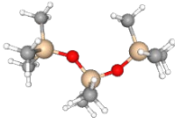
1. Hydrocarbons: n-pentane and n-hexane,
2. Halogenated hydrocarbons: R134a and R245fa,
3. Siloxanes: MM and MDM.

The first group of fluids includes more inert straight chain hydrocarbons (n-pentane and n-hexane), which lack the possibility of additional interactions between molecules. The second group includes hydrocarbons in which terminal H atoms are substituted by F atoms, so their polarity is significantly increased, as well as the possibility of additional dipole-dipole interactions. The third group of selected fluids consists of inactive siloxanes containing the main Si-O chain of different lengths of an inorganic chain with side hydrocarbon groups. These siloxanes are characterized by their bulkier molecules, which also influence their thermophysical properties.

Main data about the selected fluids are provided in Table 1.

Table 1. Basic data of selected working fluids [13, 14]

Working fluid	Name	Formula	Structural formula	Molar mass kg/kmol	Acentric factor	Critical point temperature K
n-pentane	n-pentane	C ₅ H ₁₂		72.148	0.25103	469.7
n-hexane	n-hexane	C ₆ H ₁₄		86.175	0.3003	507.82
R134a	1,1,1,2-Tetrafluoroethane	C ₂ F ₄ H ₂		102.032	0.32684	374.21
R245 fa	1,1,1,3,3-Pentafluoropropane	C ₃ F ₅ H ₃		134.047	0.3776	427.01

MM	Hexamethyltri siloxane	$C_6H_{18}OSi_2$		162.377	0.418	518.75
MDM	Octamethyltri siloxane	$C_8H_{24}O_2Si_3$		236.532	0.52806	564.09

Within the specified group, the increase of molar mass is followed with the increase of critical temperature and acentric factor [15]. The acentric factor describes deviations in thermodynamic properties of fluids containing non spherical molecules from their spherical counterparts. It is also a measure of the non-sphericity of molecules. Among examined fluids the highest value of acentric factor is MDM whose molecule has the most complex structure, while the lowest value has n-pentane.

Figure 2 presents T-s diagrams for each working fluid. Based on the slope of vapor saturation curve it can be concluded that each of them is suitable to operate in the ORC with the dry steam. Fluids with the highest molar mass and acentric factor (MM and MDM) act as exceptionally dry fluids.

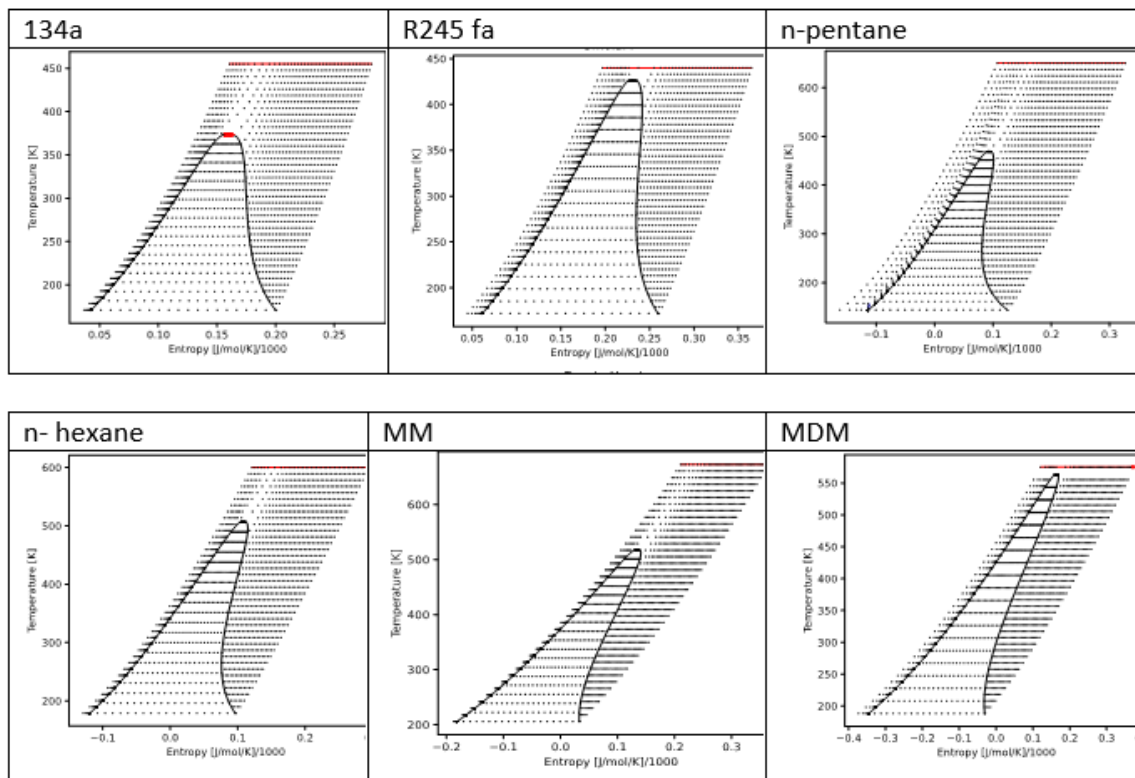


Figure 2. T-s diagrams for the selected fluids [13]

The effect of working fluids properties on the efficiency of ORC was analyzed for the case of dry steam cycle (Figure 3). This cycle is preferred over the superheated steam cycle due to the absence of superheating and required heat exchangers [13]. The highest temperature in the cycle was set to 70°C - temperature of evaporation, while the lowest temperature was 15°C - temperature of condensation. These temperatures were selected based on data from available low temperature heat sources in Serbia [16, 17]. The shapes of T-s diagrams presented at Figure 2 indicate that all selected fluids are suitable for the dry steam ORC in the given range of temperature.

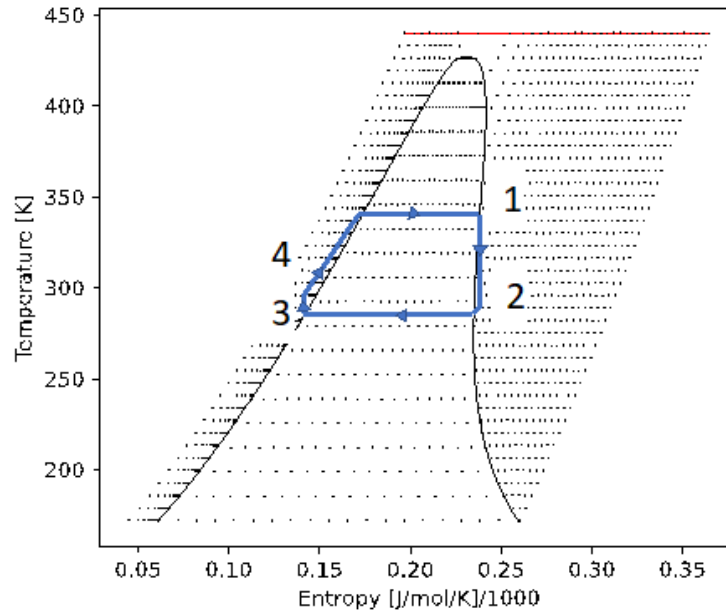


Figure 3. Rankine Cycle with dry steam

Efficiency of the ORC is determined by:

$$\eta = 1 - \frac{|h_3 - h_2|}{h_1 - h_4} \quad (1)$$

To calculate the thermodynamic properties for each state of the cycle, CoolProp software [13] was used to obtain values of properties for the selected fluids from, all from the same source.

4. Results and discussion

Results for efficiencies of the dry steam ORC for each of examined fluids are presented in Table 2.

Table 2. Basic data of selected working fluids

Fluid	Efficiency	Heat of evaporation at 70°C, kJ/kg
n-pentane	0.1381	328.0
n-hexane	0.1383	334.3
R134a	0.1320	124.6
R245fa	0.1346	161.9
MM	0.1291	208.1
MDM	0.1270	186.8

The results show that the efficiency of the cycle is dependent on the properties of the selected working fluid. The highest efficiency is achieved with n-hexane (0.1383), which is approximately 9% higher compared to the lowest efficiency, obtained with MDM (0.1270).

The highest efficiency is observed with hydrocarbons as working fluids and the lowest with siloxanes. Within the examined group the higher efficiency is attributed to fluids with a higher heat of phase change at the temperature of evaporation (Table 2).

Figure 4 illustrates the relationship between efficiency and the acentric factor. In most cases, a higher efficiency corresponds with a lower acentric factor.

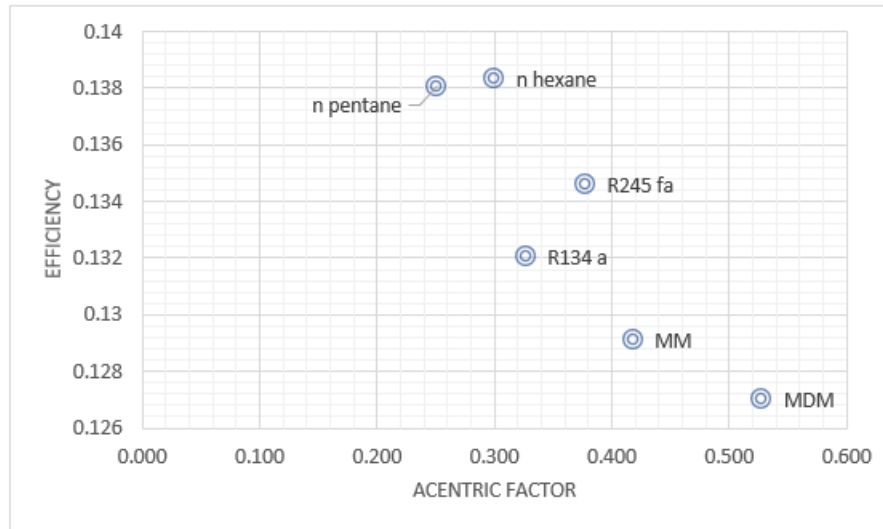


Figure 4. Relation between acentric factor and efficiency

Further analysis of the results shows that the highest temperature at the exit of the turbine was achieved for MDM as the working fluid, while the lowest was observed with R 134a. This was the only case when expansion in the turbine ended in the zone of the wet vapor. No significant relationships between efficiency and other fluid properties were observed.

The highest efficiencies are attributed to fluids with isentropic slope of the vapor saturation curve, such as n-pentane and n-hexane. In these cases, the expansion process in the turbine closely follows the vapor saturation curve.

5. Conclusion

Low temperature energy sources can be utilized for electricity generation by implementing Organic Rankine Cycle. However, the efficiency of such cycles is relatively low, since the difference between the temperature of the heat source and heat sink is small.

For the dry steam ORC effect of properties of six working fluids is analyzed. It is shown that chemical composition affects thermophysical properties of the fluid, including the shape of vapor saturation curve.

The efficiency of the cycle depends on the properties of the working fluid, such as its composition and structure. In the analyzed cases the highest efficiency was achieved with hydrocarbons which have near isentropic slope of the saturation curve in the observed temperature interval between the heat sink and the heat source.

The lowest efficiency was obtained with siloxanes as working fluids, which acts as exceptionally dry fluids and have the biggest values of acentric factors among examined fluids. It can be concluded that the problem is complex, with intervening influential parameters that are not easy to identify.

The potential application of ORC must be carefully evaluated, as changes in the working fluid can significantly affect efficiency, which certainly should not be neglected, particularly in low-efficiency cycles.

Acknowledgements

The research was supported by funds provided by the Ministry of Science, Technological Development, and Innovation under Contracts No. 451-03-65/2024-03/200126 and 451-03-66/2024-03/200126.

References

- [1] Lamnatou, C., Cristofari, C., Chemisana, D., Renewable energy sources as a catalyst for energy transition: Technological innovations and an example of the energy transition in France, *Renewable Energy* 221 (2024), 119600
- [2] Távora Maia, R.G., Garcia, K.C., What they say, what they do and how they do it: An evaluation of the energy transition and GHG emissions of electricity companies, *Energy Policy* 174 (2023), 113462

- [3] Georg Thomaßen, G., Kavvadias, K., Jiménez Navarro, J.P., The decarbonisation of the EU heating sector through electrification: A parametric analysis, *Energy Policy* 148 (2021), Part A, 111929
- [4] Lotfipour, A., Mohtavipour, S.S., A multi-criteria decision-making model to determine the optimal share of variable renewable energy sources in a wholesale electricity market, *Sustainable Energy, Grids and Networks* 39 (2024), 101408
- [5] Karimi, S., Safavi, A., Bahram, S., Optimizing electricity generation through the utilization of wasted heat from process streams in a LURGI methanol plant, *Heliyon* 10 (2024), e30982
- [6] Vivian, J., Manente, G., Lazzaretto, A., A general framework to select working fluid and configuration of ORCs for low-to-medium temperature heat sources, *Applied Energy* 156 (2015), pp. 727-746
- [7] Chitgar, N., Hemmati, A., Sadrzadeh, M., A comparative performance analysis, working fluid selection, and machine learning optimization of ORC systems driven by geothermal energy, *Energy Conversion and Management* 286 (2023), 117072
- [8] Bao, J., Zhao, L., A review of working fluid and expander selections for organic Rankine cycle, *Renewable and Sustainable Energy Reviews* 24 (2013), pp. 325-342
- [9] Herath, H.M.D.P., Wijewardane, M.A., Ranasinghe, R.A.C.P., Jayasekera, J.G.A.S., Working fluid selection of Organic Rankine Cycles, *Energy Reports* 6 (2020), pp. 680-686
- [10] Babatunde, A.F., Sunday, O.O., A Review of Working Fluids for Organic Rankine Cycle (ORC) Applications, *IOP Conf. Series: Materials Science and Engineering* 413 (2018), 012019
- [11] Liu, B., Chien, K., Wang, C., Effect of working fluids on organic Rankine cycle for waste heat recovery, *Energy* 29 (2004), pp. 1207-1217
- [12] Chowdhury, A.S., Ehsan, M.M., A Critical Overview of Working Fluids in Organic Rankine, Supercritical Rankine, and Supercritical Brayton Cycles Under Various Heat Grade Sources, *International Journal of Thermofluids* 20 (2023), 100426
- [13] CoolProp Team, CoolProp Version 6.4.0. (2024), <http://www.coolprop.org>.
- [14] PubChem., Compound ID, (2024), <https://pubchem.ncbi.nlm.nih.gov/compound/24705#section=3D-Conformer>
- [15] Matuszewska, D., Kuta, M., Gorski, J., A thermodynamic assessment of working fluids in ORC systems, *EPJ Web of Conferences* 213 (2019), 02057
- [16] Ilić, M., Živković, M., Danilović, D., Crnogorac, M., Karović Maričić, V., Tomić, L., Određivanje teorijskog termičkog potencijala napuštenih naftnih i gasnih bušotina, *Tehnika – Rudarstvo, Geologija i Matalurgija* 74 (2023), 6, pp. 667-672 (In Serbian)
- [17] Soleša, M., Đajić, N., Parađanin, L.J., Proizvodnja i korišćenje geotermalne energije, Rudarsko-geološki fakultet, Beograd, 1995 (In Serbian)

Developing Solar Thermal Power Plant to Improve Energy Governance

Reyhaneh Loni^a, Sasa Pavlovic^b

^a Faculty of Governance, University of Tehran, 14398-14151, Tehran, IR, rloni@ut.ac.ir

^b Faculty of Mechanical Engineering, University of Niš, Niš, RS, sasa.pavlovic@masfak.ni.ac.rs

Abstract: This paper explores the development of solar thermal power plants as a viable solution to enhance energy governance in the context of sustainable energy systems. With the increasing global demand for clean and renewable energy sources, solar thermal technology has emerged as a promising alternative that can significantly contribute to reducing greenhouse gas emissions while ensuring energy security. The paper outlines the potential benefits of solar thermal power plants, including their ability to provide base load power, their scalability, and their compatibility with existing energy infrastructure. Additionally, it examines the critical role of effective energy governance in facilitating the successful implementation and operation of solar thermal projects. This includes the establishment of clear regulatory frameworks, stakeholder engagement, and the promotion of public-private partnerships. The paper presented best practices and key challenges encountered in the development of solar thermal power plants, emphasizing the importance of integrated planning and comprehensive policy approaches. Ultimately, this research aims to contribute to the discourse on energy governance by providing insights into how solar thermal power can be leveraged to foster sustainable energy transitions and enhance energy governance frameworks.

Keywords: Solar thermal power, Energy governance, Renewable energy, Greenhouse gas emissions, Sustainable energy systems.

1. Introduction

The urgent need for clean and renewable energy solutions has never been more pressing, as the world grapples with the dual challenges of climate change and energy security [1]. As global populations continue to rise and industrial activities increase, the demand for energy is projected to escalate significantly [2]. In this context, transitioning from fossil fuels to sustainable energy sources is critical for reducing greenhouse gas emissions and mitigating the impact of climate change [3]. Among the various renewable energy technologies available, solar thermal power has emerged as a promising alternative that offers not only environmental benefits but also strategic advantages for energy governance [4].

Solar thermal power plants capture and convert sunlight into thermal energy, which can be used to generate electricity or provide heating [5]. This technology stands out due to its capability to deliver baseload power—energy that is consistently available regardless of weather conditions—making it compatible with existing energy infrastructure and able to support grid stability [6]. Furthermore, solar thermal systems are scalable, allowing for flexibility in meeting the diverse energy needs of different regions, from small-scale facilities to large, utility-scale plants [7]. However, the successful development and operation of solar thermal power plants hinge on the effectiveness of energy governance [8]. Establishing clear regulatory frameworks is essential to provide certainty for investors and operators.

Moreover, stakeholder engagement is crucial for aligning interests and building public support for renewable energy initiatives. Public-private partnerships play a pivotal role in leveraging resources, expertise, and innovation necessary for advancing solar thermal projects [9].

This paper seeks to explore these dynamics by examining the development of solar thermal power plants as a viable solution to enhance energy governance within sustainable energy systems. This study aims to contribute to the discourse on energy governance by offering insights into how solar thermal power can not only foster sustainable energy transitions but also strengthen governance frameworks that are critical for the future of energy systems worldwide. Ultimately, this research underscores the importance of an integrated approach to

energy planning, policy-making, and governance in harnessing the full potential of solar thermal power in pursuit of a sustainable energy future.

2. Solar Thermal Power Plant

Clean energy refers to forms of energy that have little or no negative impact on the environment. Renewable energy sources, such as wind, solar, hydroelectric, and geothermal, are replenished naturally and are considered sustainable in that their use does not deplete finite resources. The shift towards these sources is driven by policy changes, technological advancements, and increasing awareness of climate challenges. Solar thermal technology captures sunlight and converts it into heat, which can then be used to generate electricity or provide direct heating. Different systems, such as concentrating solar power (CSP) plants and flat-plate collectors, exemplify this technology. Across the globe, there is a growing recognition of the environmental impacts of fossil fuels, particularly in terms of greenhouse gas emissions that contribute to climate change. As populations expand and economies develop, the demand for energy is projected to rise. This trend necessitates exploring new energy solutions that are sustainable and environmentally friendly. Solar thermal technology has gained attention as a viable solution to meet energy demands. This is largely due to its ability to provide substantial energy generation while minimizing environmental impacts compared to traditional fossil fuel sources.

One of the primary advantages of solar thermal technology is its potential to significantly reduce greenhouse gas emissions. Unlike fossil fuels, solar energy is clean—when it is produced, it does not emit carbon dioxide or other harmful pollutants that contribute to climate change. As nations aim to fulfill international climate commitments like the Paris Agreement, adopting solar thermal technology can play a crucial role in transitioning away from carbon-intensive energy sources and lowering overall emissions. On the other hand, energy security refers to the reliable availability of energy resources at an affordable price. Ensuring energy security involves reducing dependency on imported fuels, diversifying energy sources, and enhancing resilience against disruptions. Solar thermal technology contributes to energy security in several ways. First, by harnessing abundant sunlight, countries can reduce their reliance on imported fossil fuels, which are subject to market volatility and geopolitical tensions. Secondly, solar thermal plants can provide stable and consistent power supply (base load power) that enhances the overall reliability of the energy grid. In these days, a significant trend is observed in the energy sector, emphasizing the growing global shift toward clean and renewable resources due to rising energy demands and environmental concerns. Solar thermal technology is highlighted as a viable and effective alternative that not only helps reduce greenhouse gas emissions but also contributes to national and global energy security.

The potential benefits of solar thermal power plants, focusing on the three aspects mentioned: their ability to provide base load power, their scalability, and their compatibility with existing energy infrastructure. Solar thermal power plants can provide base load power positions them as a reliable energy source capable of supporting grid stability. Scalability allows to be tailored to meet diverse energy needs in various locations, enhancing their effectiveness. Also, the solar thermal power plants have enough compatibility with existing energy infrastructure facilitates integration into current systems, supporting a smoother transition to renewable energy. Together, these attributes make solar thermal power a compelling option for addressing the challenges of modern energy demands and environmental sustainability.

Unlike photovoltaic (PV) solar systems, which only produce electricity during sunny conditions, solar thermal power plants can generate heat and electricity consistently. This is achieved by storing thermal energy for use even when the sun is not shining. Many solar thermal facilities use thermal energy storage systems, such as molten salt, which can hold heat generated during the day and release it during the night or during periods of high demand. This ability allows them to act as base load providers, contributing stability to the energy supply. By providing reliable and controllable power output, solar thermal plants help balance supply and demand on the electrical grid. This reduces the reliance on fossil fuel plants to meet base load requirements and diminishes the risks associated with fluctuations in power supply.

Another benefit of the solar power plants is scalability. Scalability refers to the capability of a system to grow and adapt in size or capacity according to demand. This flexibility is crucial for meeting varying energy needs across different regions and contexts. Solar thermal power plants can be designed in a modular fashion, meaning they can be built in smaller units or larger complexes, depending on the energy requirements of a specific location. This allows for efficient scaling up or down as needed, addressing local energy demands without overinvesting in infrastructure. Solar thermal technology can be implemented in various settings—

from small-scale community systems to large utility-scale plants. This adaptability makes it suitable for both rural areas lacking access to centralized power and urban settings where energy consumption may be higher.

Compatibility with existing energy infrastructure is another benefit of the solar thermal power plants. Solar thermal power plants can be connected to existing energy grids, making it easier for them to contribute to the energy supply without requiring extensive modifications to the current infrastructure. This is particularly important for regions looking to transition to renewable energy sources while maximizing their existing investments in energy generation. Many solar thermal plants can work in conjunction with other energy sources, such as natural gas or biomass. This hybrid approach can enhance reliability and reduce emissions by allowing the plant to use conventional fuel sources when solar energy is insufficient, thereby ensuring continuous power supply. In regions where solar thermal plants are installed, they can often utilize existing transmission lines and energy storage systems, facilitating a more integrated and efficient energy system. This compatibility also implies that investment in solar thermal does not necessitate the complete overhaul of existing energy infrastructure, which can be cost-prohibitive.

Generally, the development of solar thermal power plants can significantly benefit from best practices that include effective stakeholder engagement, innovative financing, optimized technologies, robust regulations, and infrastructure investments. However, challenges such as high costs, technical issues, regulatory hurdles, land use conflicts, and energy storage concerns must be addressed. Emphasizing integrated planning and comprehensive policy approaches is crucial; these strategies help align projects with broader energy objectives, promote sustainability, and improve project viability, ultimately leading to more successful solar thermal initiatives.

3. Energy Governance

Energy governance is a multifaceted concept that involves the coordination of policies, institutions, and stakeholder engagement to ensure that energy systems are managed effectively and equitably. It plays a critical role in shaping how energy resources are developed and utilized, guiding the transition to more sustainable energy systems while balancing economic, social, and environmental considerations. Through effective energy governance, countries and organizations can work toward achieving energy security, sustainability, and social welfare. Effective energy governance is crucial for the successful implementation and operation of solar thermal projects. Establishing clear regulatory frameworks creates a stable environment for investment, while stakeholder engagement ensures that diverse perspectives are considered and local communities are involved in the decision-making process. Promoting public-private partnerships can facilitate resource mobilization, risk sharing, and innovation, ultimately leading to more successful and sustainable solar thermal initiatives. Together, these elements of governance help create a conducive atmosphere that supports the growth of renewable energy technologies, contributing to broader sustainability goals and energy transitions.

The critical role of effective energy governance in the context of solar thermal projects, emphasizing the components: the establishment of clear regulatory frameworks, stakeholder engagement, and the promotion of public-private partnerships. As mentioned establishment of clear regulatory frameworks is a critical role of effective energy governance in the context of solar thermal projects. A regulatory framework encompasses laws, guidelines, and policies that govern the development and operation of energy projects. Clear regulations provide certainty and stability for investors and developers, which is essential for attracting financing and resources to solar thermal projects. Consistency and predictability in regulatory frameworks are crucial for long-term planning. Sudden changes in regulations can deter investment and disrupt project implementation, while stable policies foster confidence among stakeholders. In this regard, regulatory frameworks must include streamlined permitting processes that define the step-by-step requirements for project approval. This can reduce the time and costs associated with project initiation. Also, regulations should outline performance standards for technology efficiency, emissions, and safety, ensuring that solar thermal plants operate within environmental and operational guidelines that protect public interests. Effective governance includes policies that facilitate the integration of renewable energy onto the grid, such as rules for access to transmission networks and grid management practices that prioritize renewable sources, too.

Stakeholder engagement is known as another critical role of effective energy governance in the context of solar thermal projects. Stakeholders include all individuals and groups who have an interest or investment in the solar thermal project. This can encompass government agencies, local communities, environmental groups, investors, and utility companies. Public forums, consultations, and informational sessions can inform

community members about the potential impacts and benefits of solar thermal projects, ensuring that their voices are heard in the governance process. Engaging stakeholders early in the project development process can help build trust and reduce opposition. Effective communication about the benefits and impacts of solar thermal projects is essential to gain local support. By involving a wide range of stakeholders, project developers can incorporate diverse perspectives and concerns into project planning. This may lead to better decision-making and outcomes that are aligned with community needs and environmental considerations. Proactive engagement can identify potential conflicts and help resolve issues before they escalate. Meaningful dialogue can lead to compromises that benefit all parties involved.

Finally, Promotion of Public-Private Partnerships (PPPs) is another critical role of effective energy governance in the context of solar thermal projects. Public-private partnerships are collaborative agreements between public sector entities (like government agencies) and private sector companies (like energy developers). These partnerships leverage the strengths and resources of both sectors to achieve shared goals. Many successful solar thermal projects worldwide have been achieved through partnerships between governments and private entities. By aligning incentives and responsibilities, these partnerships can lead to the successful deployment of solar thermal technology. PPPs can facilitate access to funding and investment that might not be available through public funding alone. Private investors often bring capital and expertise that can enhance project viability. By pooling resources and sharing responsibilities, risks associated with the development, operation, and maintenance of solar thermal projects can be distributed between public and private partners, improving project resilience. Private companies may introduce innovative technologies and management practices that enhance project performance and cost-effectiveness.

4. Good Energy Governance with Developing Solar Thermal Power Plant

Developing good energy governance through the establishment of solar thermal power plants involves creating a robust framework that supports effective decision-making, transparency, accountability, and stakeholder engagement. In other words, developing good energy governance with solar thermal power plants requires a multifaceted approach that prioritizes policy alignment, stakeholder engagement, transparency, and accountability. By implementing these strategies, stakeholders can create an enabling environment that supports the successful development and operation of solar thermal projects while promoting sustainable energy practices. Ultimately, good governance will enhance the effectiveness of solar thermal initiatives, contributing to a more sustainable and resilient energy future.

There are several strategies to achieve good energy governance in this context including:

1. Establishing Comprehensive Policy Frameworks

- **Clear Regulatory Guidelines:** Develop comprehensive policies and regulations specifically designed for solar thermal technologies. This includes permitting processes, safety standards, and environmental regulations that facilitate project development while protecting public interests.
- **Incentive Structures:** Implement financial incentives, such as tax credits, grants, or feed-in tariffs, to encourage investment in solar thermal projects. These incentives can lower barriers to entry and stimulate private sector participation.

2. Enhancing Stakeholder Engagement

- **Community Involvement:** Engage local communities in the planning and decision-making processes for solar thermal projects. This ensures that local concerns and needs are addressed, fostering public support and acceptance.
- **Multi-Stakeholder Platforms:** Create forums that bring together government agencies, private sector players, non-governmental organizations, and community representatives to discuss challenges, share best practices, and collaborate on solutions.

3. Promoting Transparency and Accountability

- **Transparent Processes:** Implement measures to ensure transparency in the approval processes for solar thermal projects, including public access to information regarding project plans, impacts, and financial aspects.

- **Performance Reporting:** Establish metrics to regularly assess the performance of solar thermal power plants, and require periodic reporting to stakeholders. This can include environmental impact assessments, energy output data, and economic benefits.

4. Investing in Capacity Building and Education

- **Training Programs:** Develop training initiatives for policymakers, energy managers, and local communities to enhance knowledge about solar thermal technologies, governance practices, and renewable energy systems.
- **Public Awareness Campaigns:** Run campaigns to inform the public about the benefits of solar thermal energy and the importance of governance in energy transitions, fostering broader support for renewable energy initiatives.

5. Facilitating Public-Private Partnerships (PPPs)

- **Encourage Collaboration:** Foster partnerships between government entities and private companies to share resources, expertise, and risk. These collaborations can facilitate the financing, development, and management of solar thermal projects.
- **Innovative Financing Models:** Explore financing mechanisms such as green bonds or crowdfunding to attract diverse funding sources for solar thermal initiatives, ensuring that investments align with governance objectives.

6. Implementing Integrated Planning

- **Consistency with Energy Policy:** Ensure that solar thermal development aligns with broader national or regional energy policies, including goals for renewable energy targets, carbon emissions reduction, and energy security.
- **Holistic Energy Planning:** Integrate solar thermal initiatives into regional and local energy plans, considering factors such as resource availability, infrastructure needs, and potential impacts on existing energy systems.

7. Monitoring and Evaluation

- **Effectiveness Assessment:** Develop a framework for monitoring and evaluating the impact of solar thermal power plants on energy governance, including social, economic, and environmental outcomes.
- **Adjusting Policies Based on Data:** Utilize data gathered through monitoring to inform policy adjustments, improve project implementation, and enhance the overall governance framework.

8. Aligning with Global Standards and Initiatives

- **International Collaboration:** Engage with international organizations and frameworks that promote good governance in energy sectors, such as the International Renewable Energy Agency (IRENA) or adherence to the Sustainable Development Goals (SDGs).
- **Best Practices:** Learn from other countries and regions that have successfully integrated solar thermal power into their energy systems, adopting best practices that contribute to effective governance.

Generally, the contributing to the discourse on energy governance by providing insights into the role of solar thermal power is crucial for fostering sustainable energy transitions. By showcasing how solar thermal technology can be effectively utilized within energy governance frameworks, stakeholders can enhance their understanding of renewable energy's potential and integrate it into broader sustainability goals. This not only supports the shift toward cleaner energy systems but also helps create resilient, equitable, and effective energy governance structures that can better adapt to the challenges of the future.

5. Recommended Practices

There are some recommended policies to support the development of solar thermal power plants, enhance energy governance, and promote sustainable energy systems:

1. Regulatory Frameworks

- **Streamlined Permitting Processes:** Implement regulations that establish clear and efficient permitting processes for solar thermal projects, reducing bureaucratic hurdles and expediting approvals while ensuring environmental protections.

- **Standardization of Technical Guidelines:** Develop standardized codes and technical guidelines for the design, construction, and operation of solar thermal power plants to enhance safety, reliability, and integration with existing infrastructure.

2. Incentive Programs

- **Financial Incentives:** Create financial support programs, such as tax credits, grants, or subsidies, to lower the upfront costs for solar thermal projects, making them more accessible for developers and investors.
- **Feed-in Tariffs or Power Purchase Agreements (PPAs):** Establish long-term feed-in tariffs or PPAs to provide guaranteed pricing for energy generated by solar thermal plants, encouraging investment and ensuring predictable revenue streams.

3. Stakeholder Engagement Policies

- **Public Consultation Processes:** Mandate public consultation requirements for solar thermal projects to ensure community input and address potential concerns, boosting local support and social acceptance.
- **Multi-Stakeholder Partnerships:** Promote the formation of collaborative partnerships between government, industry, and civil society to foster dialogue, share best practices, and enhance governance in solar thermal project implementation.

4. Investment in Research and Development

- **Funding for Innovation:** Increase government funding and support for research and development of advanced solar thermal technologies, including energy storage solutions and improved efficiency systems.
- **Technology Transfer Initiatives:** Facilitate technology transfer programs that allow emerging economies to access advanced solar thermal technologies and expertise, promoting global cooperation in renewable energy development.

5. Integrated Energy Planning

- **Comprehensive Energy Policies:** Develop integrated energy policies that consider solar thermal energy contributions within broader energy systems, balancing renewable energy sources with energy storage, demand-side management, and conventional energy generation.
- **Long-Term Energy Roadmaps:** Create long-term energy roadmaps that set forth clear targets for the deployment of solar thermal energy, ensuring alignment with national energy security and climate goals.

6. Monitoring and Evaluation Frameworks

- **Performance Monitoring Systems:** Implement comprehensive monitoring and reporting systems for solar thermal projects to evaluate their performance, energy output, environmental impacts, and alignment with policy objectives.
- **Benchmarking and Best Practices:** Establish benchmarking metrics to assess solar thermal projects against best practices and facilitate continuous improvement and knowledge sharing among stakeholders.

7. Education and Capacity Building

- **Training Programs for Workforce Development:** Establish training programs aimed at developing skills in solar thermal technologies for engineers, technicians, and project managers, ensuring a skilled workforce to support industry growth.
- **Public Awareness Campaigns:** Launch educational initiatives to inform the public and key stakeholders about the benefits and opportunities of solar thermal power, enhancing understanding and support for renewable energy policies.

8. Aligning with International Standards

- **Global Standards Adoption:** Adopt international standards and best practices related to solar thermal energy development and governance, ensuring that local policies are consistent with global frameworks for sustainable development.

- Participation in International Initiatives: Encourage participation in global partnerships and initiatives focused on renewable energy development to share knowledge, resources, and strategies for effective governance and implementation.

By implementing these recommended policies, governments and stakeholders can create a conducive environment for the development of solar thermal power plants. These policies will not only facilitate the successful integration of solar thermal energy into existing energy systems but will also enhance energy governance, transparency, and public trust—ultimately contributing to a sustainable energy transition and addressing climate change challenges.

6. Conclusion

This paper underscores the critical role that solar thermal power plants can play in enhancing energy governance within sustainable energy systems. As global demand for clean and renewable energy rises, solar thermal technology presents a viable solution that not only addresses the urgency of reducing greenhouse gas emissions but also strengthens energy security through its capability to provide base load power and scalability. The integration of effective energy governance practices is essential for the successful implementation and operation of solar thermal projects. This includes the establishment of transparent regulatory frameworks, active stakeholder engagement, and the encouragement of public-private partnerships that align diverse interests. The findings highlight that there are significant prospects associated with solar thermal power. This research contributes to the broader discourse on energy governance, suggesting that solar thermal power not only offers a pathway towards sustainable energy transitions but also reinforces the governance structures needed to support such advancements. Ultimately, embracing solar thermal technology can assist countries in achieving their energy and climate goals, facilitating a more sustainable and resilient energy future.

Acknowledgment

In preparing this work, the authors utilized OpenAI's ChatGPT solely for grammar checks and writing enhancements. After employing this tool, they thoroughly reviewed and edited the content as necessary, assuming full responsibility for the publication's content.

References

- [1] B.K. Sovacool, The best of both worlds: Environmental federalism and the need for federal action on renewable energy and climate change, *Stan. Envtl. LJ*, 27 (2008) 397.
- [2] J.P. Dorian, H.T. Franssen, D.R. Simbeck, Global challenges in energy, *Energy policy*, 34 (2006) 1984-1991.
- [3] M.J.B. Kabeyi, O.A. Olanrewaju, Sustainable energy transition for renewable and low carbon grid electricity generation and supply, *Frontiers in Energy research*, 9 (2022) 743114.
- [4] R. Loni, E.A. Asli-Areh, B. Ghobadian, A. Kasaeian, S. Gorjian, G. Najafi, E. Bellos, Research and review study of solar dish concentrators with different nanofluids and different shapes of cavity receiver: Experimental tests, *Renewable Energy*, 145 (2020) 783-804.
- [5] R. Loni, E.A. Asli-Ardeh, B. Ghobadian, E. Bellos, W.G. Le Roux, Numerical comparison of a solar dish concentrator with different cavity receivers and working fluids, *Journal of Cleaner Production*, 198 (2018) 1013-1030.
- [6] R. Loni, A. Kasaeian, E.A. Asli-Ardeh, B. Ghobadian, S. Gorjian, Experimental and numerical study on dish concentrator with cubical and cylindrical cavity receivers using thermal oil, *Energy*, 154 (2018) 168-181.
- [7] R. Loni, B. Ghobadian, A. Kasaeian, M. Akhlaghi, E. Bellos, G. Najafi, Sensitivity analysis of parabolic trough concentrator using rectangular cavity receiver, *Applied Thermal Engineering*, 169 (2020) 114948.
- [8] T. Güneş, Solar energy, governance and CO₂ emissions, *Renewable Energy*, 184 (2022) 791-798.
- [9] T. Van de Graaf, J. Colgan, Global energy governance: a review and research agenda, *Palgrave Communications*, 2 (2016) 1-12.

Natural Draught Cooling Tower Operation During Winter

Vladimir Mijakovski^a, Monika Lutovska^b, Filip Mojsovski^c, Mile Spirovski^a

*^aFaculty of Technical Sciences, University "St. Kliment Ohridski", Bitola, MK,
vladimir.mijakovski@tfb.uklo.edu.mk*

*^bFaculty of Technical Sciences, University „Mother Teresa”, Skopje, MK,
monika.lutovska@unt.edu.mk*

*^cFaculty of Mechanical Engineering, University "Ss. Cyril and Methodius", Skopje, MK,
filip.mojsovski@mf.edu.mk*

*^aFaculty of Technical Sciences, University "St. Kliment Ohridski", Bitola, MK,
mile.spirovski@tfb.uklo.edu.mk*

Abstract: Operation of natural draught cooling towers and its ability to cool water is solely dependent on ambient air parameters (temperature and humidity). During winter period, at low temperatures of external air, circulation of air through the natural draught cooling tower causes greater cooling of the water and appearance of ice on places where air enters into the tower. In such case, with proper operation of the system cooling tower – pump station, and by reducing water's cooling range, temperature of the cold water ought to be maintained at sufficiently high temperature level in order to avoid freezing of the water in the tower and appearance of ice at air entering surfaces.

Keywords: Natural draught, Cooling tower, Winter.

1. Introduction

Thermo power plant (TPP) "Bitola" is the largest coal-fired power plant in North Macedonia that has been operating for more than 40 years. Historically, coal plants have retired at an average lifetime of 46 years globally, [1], but in many cases they can operate for 50–60 years or longer, [2]. In the case of TPP "Bitola", this means that the power plant is already on the end of its operational life. The Strategy for energy development of North Macedonia until 2040"[3] foresees revitalization or deactivation of TPP "Bitola" in the following years, depending on the considered scenario. A particularly radical transition from conventional energy sources to abandoning lignite through the application of new policies is foreseen in the green scenario. However, the lack of investment in this sector, especially in the basic electricity production facilities, gives us the right to expect that this power plant will continue to operate in the near future. Furthermore, in the same context, the construction of district heating system for the city of Bitola is well underway where the power plant is considered as a primary heat source.

Gathered experience from its operation represents valuable basis for further analysis in order to improve its efficiency, especially efficiency of the cold end. This article is based upon the previously developed climatic curve [4], (dependence of temperature and relative humidity of the air), and its influence on the operation of the cooling tower in winter periods.

Air entering areas are the most 'sensitive' surfaces in regards to winter operation of the natural draught cooling tower. Especially this is a case when the cooling tower is of counterflow type.

Temperature regulation of water in winter conditions is performed through three installed technical systems for antifreeze protection. The procedure of regulation is defined according to heat demand of the corresponding plant's block and values from the climatic curve.

Regulation of water temperature in all three systems is done by varying of the water flow. According to defined procedure, application of all three systems reduces the danger of ice appearance for different working modes of the turbine and for different climatic curve values. Control of the systems is individual and their usage is simultaneous or, at least two of them must operate simultaneously.

Under normal working conditions of the cooling tower, the water runs through the water distribution system onto the tower's fill and the protective ring and orbital pipeline are not in operation. Under these conditions, the temperature of water in the basin and at cooling tower's fill exit is equal.

The operating modes and calculations presented in this article refer to design operating values for the power plant before modernization in 2012. Following most recent (in 2022) refurbishment and restoration of the cooling tower of block 2 comprised of complete replacement of asbestos-cement fill and piping system with plastic fill and pipes, together with appropriate valves and fittings, new calculations and proposals for more efficient winter operation of cooling tower in block 2 must be performed followed by newly determined climatic curve for the corresponding period.

2. Normal winter operation of the cooling tower

Different values of climatic curve, for which the temperature of water leaving the cooling tower are determined, are shown on Table 1. These values are calculated for three operating modes in winter conditions.

Table 1. Climatic curve parameters used for determination of exiting water temperature in winter conditions

t_{a1} , °C	-3,0	1,0	5,0	10,0	15,0
φ_{a1} , %	35,0	50,0	35,0	50,0	50,0
t_{wb} , °C	-6,0	-2,0	0,0	5,4	9,5

Values from the climatic curve on Table 1 are used as a basis for calculation of the water temperature leaving the tower. Input parameters and the results from this calculation, determination of t_{w2} for 100% heat load and 100% water flow, are presented on Table 2 for winter operating mode I, whereas 100% heat load corresponds to 225 MW of turbine output and 100% water flow equals 30000 m³/h (nominal working parameters for thermo power plant's cold end).

Table 2. Input parameters and calculation results from the determination of water temperature leaving the tower during winter operating mode I

$t_{a1} = 5,0$	°C	dry-bulb air temperature entering the cooling tower
$\varphi_{a1} = 35,0$	%	relative humidity of air entering the cooling tower
$t_{wb} = 0,0$	°C	wet-bulb temperature of air entering the cooling tower
$x_{a1} = 0,002$	kg/kg	humidity ratio of air entering the cooling tower
$t_{w1} = 28,8$	°C	temperature of water entering the cooling tower
$p_{at} = 94152$	Pa	barometric pressure of ambient air
$g_{w1} = 6632$	kg/m ² h	specific mass flow of water entering the cooling tower
$g_a = 3603$	kg/m ² h	specific mass flow of air in the tower
$\sigma_V = 3531$	kg/m ³ h	volume coefficient of evaporation
$t_{a2} = 11,3$	°C	dry-bulb air temperature exiting the cooling tower
$\varphi_{a2} = 91,4$	%	relative humidity of air exiting the cooling tower
$x_{a2} = 0,008$	kg/kg	humidity ratio of air exiting the cooling tower
$t_{w2} = 17,2$	°C	temperature of water exiting the cooling tower

Input data from the climatic curve and results from calculation of exiting water temperature, t_{w2} , for 100% heat load and 80% water flow through the tower – winter operating mode II, are shown on Table 3.

Table 3. Input data and results from calculation of water temperature leaving the tower during winter operating mode II

$t_{a1} = 5,0$	°C
$\varphi_{a1} = 35,0$	%
$t_{wb} = 0,0$	°C
$x_{a1} = 0,002$	kg/kg
$t_{w1} = 29,6$	°C
$p_{at} = 94152$	Pa

$g_{w1} = 6632$	$\text{kg/m}^2\text{h}$
$g_a = 3603$	$\text{kg/m}^2\text{h}$
$\sigma_v = 3531$	$\text{kg/m}^3\text{h}$
$t_{a2} = 12,9$	$^{\circ}\text{C}$
$\varphi_{a2} = 97,2$	$\%$
$X_{a2} = 0,009$	kg/kg
$t_{w2} = 15,2$	$^{\circ}\text{C}$

Input data from the climatic curve on Table 1 and the results from calculation of exiting water temperature, t_{w2} , for 50% heat load and 100% water flow through the tower – winter operating mode III, are shown on Table 4.

Table 4. Input parameters and resulting value for water temperature, t_{w2} , determination during winter operating mode III

$t_{a1} = 5,0$	$^{\circ}\text{C}$
$\varphi_{a1} = 35,0$	$\%$
$t_{wb} = 0,0$	$^{\circ}\text{C}$
$x_{a1} = 0,002$	kg/kg
$t_{w1} = 17,6$	$^{\circ}\text{C}$
$p_{at} = 94152$	Pa
$g_{w1} = 6632$	$\text{kg/m}^2\text{h}$
$g_a = 11938$	$\text{kg/m}^2\text{h}$
$\sigma_v = 3531$	$\text{kg/m}^3\text{h}$
$t_{a2} = 5,04$	$^{\circ}\text{C}$
$\varphi_{a2} = 83,9$	$\%$
$x_{a2} = 0,005$	kg/kg
$t_{w2} = 13,0$	$^{\circ}\text{C}$

Values of water temperature leaving the tower depending on the climatic curve values and for three different winter operating modes: mode I – 100% heat load and 100% water flow through tower; mode II: 100% heat load and 80% water flow and mode III: 50% heat load and 100% water flow through the tower, are presented on Table 5.

Table 5. Values of water temperature leaving the tower depending on values from the climatic curve

$t_{wb}, ^{\circ}\text{C}$		-6,0	-2,0	0,0	5,4	9,5
	Mode I	14,4	16,2	17,2	19,6	21,4
$t_{w2}, ^{\circ}\text{C}$	Mode II	12,0	14,2	15,2	18,1	20,3
	Mode III	8,9	11,6	13,0	16,6	19,3

The dependence between the water temperature leaving the tower, t_{w2} , and climatic curve for all three winter operating modes of the cooling tower is shown on Fig.1.

It is obvious from the diagram that for the conditions of nominal water flow and nominal heat load, that is winter operating mode I, there is no possibility of water freezing in the cooling tower's basin and at tower fill's exit until extremely low air temperatures occur.

Since there are different values for water gradient between central and external sections of the cooling tower's fill, temperatures of water in the basin lower than $4,5^{\circ}\text{C}$ poses danger for water freezing, [5], [6], [7]. Decreasing of water flow running through the tower significantly increases the possibility of local ice occurrence inside cooling tower's fill (Fig. 1).

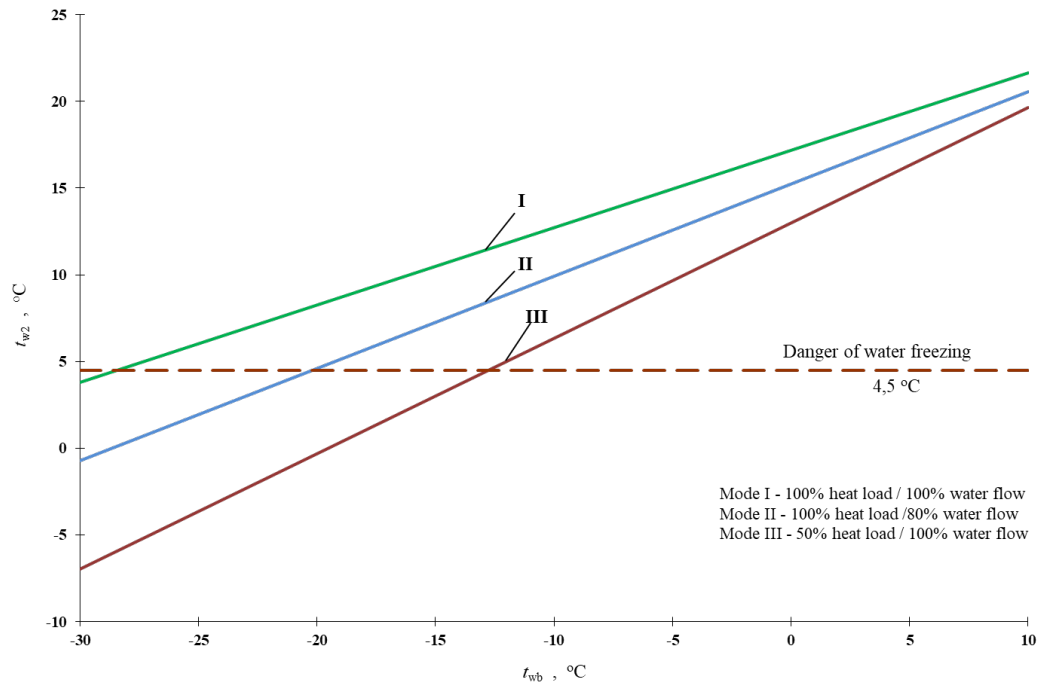


Fig. 1. Dependence of cooling water temperature exiting the tower and wet-bulb temperature of air entering the tower

3. Antifreeze systems (protection from water freezing)

There are three available systems for effective protection of water freezing for this type of cooling tower:

System 1 – Water circulation through sequined pipeline

Usage of this system implies partial or total water flow redirection from the condenser straight to the cooling tower's basin. During the start - up of the system, in winter operating conditions, the complete circulation of the water is done through the sequined pipeline (pipeline directed into cooling tower's basin), and this operational mode is kept on until the water temperature is raised to a degree that would enable anti-freezing protection for the cooling tower's fill. Fill sections are engaged gradually, depending on the block's requirements.

For a certain air temperature, if a larger quantity of water is transported through the orbital pipeline, temperature of water in the basin rises, while temperature of water at fill's exit drops. This decline in water temperature is a result of a water flow decrease, further resulting in decrease of the heat extraction capability of the cooling tower. Under stationary operating conditions it is possible to regulate water temperature by orbital pipeline even at lower external air temperatures.

System 2 – Protective pipeline ring against freezing

Efficient protection from freezing, in natural draught cooling towers is achieved by orbital pipeline and protective ring and eventually, by installing a system for zone distribution of cooling water through the tower.

Protective ring is installed in the inner side of the cooling tower under its fill. The pipeline of the protective ring has orifices on the bottom side that enables formation of water curtain at air entrance into the tower.

Essence of this solution is that at any wet-bulb temperature of the air, increase in water flow through the protective ring results in increase of water temperature in the basin. Protective ring is designed to enable 20% of total water flow through the tower. Its function is to pre-heat the air entering the tower and by doing so, to prevent the occurrence of ice in the external sections of the fill. Water curtain on the top side of the air entrance has higher density and causes change in the direction of air flow towards lower parts of the air entrance. External sections of the entrance and of cooling tower's fill remain protected from direct influence of entering cold air.

Increase in water flow quantity through the circulation pipeline, increases the water temperature in the protective ring and in the basin causing decrease in water temperature in the fill. During extremely low air

temperatures and operating mode with lower than designed power output of the turbine, the valve on the circulation pipeline opens and enables the level of water in the vertical square-shaped pipeline to decrease below the level of water distributing system pipeline. By doing so, the whole water flow is transported through the protective ring and it does not affect the fill.

System 3 – Distribution of cooling water by zones (zonal distribution)

When the external temperature is extremely low, zonal distribution of cooling water is used as an additional protection against freezing. The essence of this solution is to divert the water flow of hot water from the central to the outer parts of the fill while the central part remains dry.

4. Operating modes for antifreeze protection

Cooling towers of TPP „Bitola” can implement four operating modes in order to protect its fill from freezing. They are used depending on the values from the climatic curve and the heat load of the appropriate block.

Operating mode I – Nominal operation of the cooling tower with 100% water flow. Protective ring is not in function. Circulation pipeline is in function, if the temperature of water in the basin is to be kept at optimal values, while keeping the turbine at most economical - design parameters.

Operating mode II – Operation with protective ring, aimed at protecting the external parts of the fill at air entrance in the cooling tower. Operation of the protective ring is foreseen to maintain certain water temperature in the tower’s basin.

Operating mode III – Protective ring is in full operation and zone distribution of water is also applied. Circulation pipeline is also in operation, but not with full capacity.

Operating mode IV – Total quantity of water is transported through the circulation pipeline and protective ring. Areas of cooling tower’s different operating modes, depending on the climatic curve values and heat load are presented on Fig. 2.

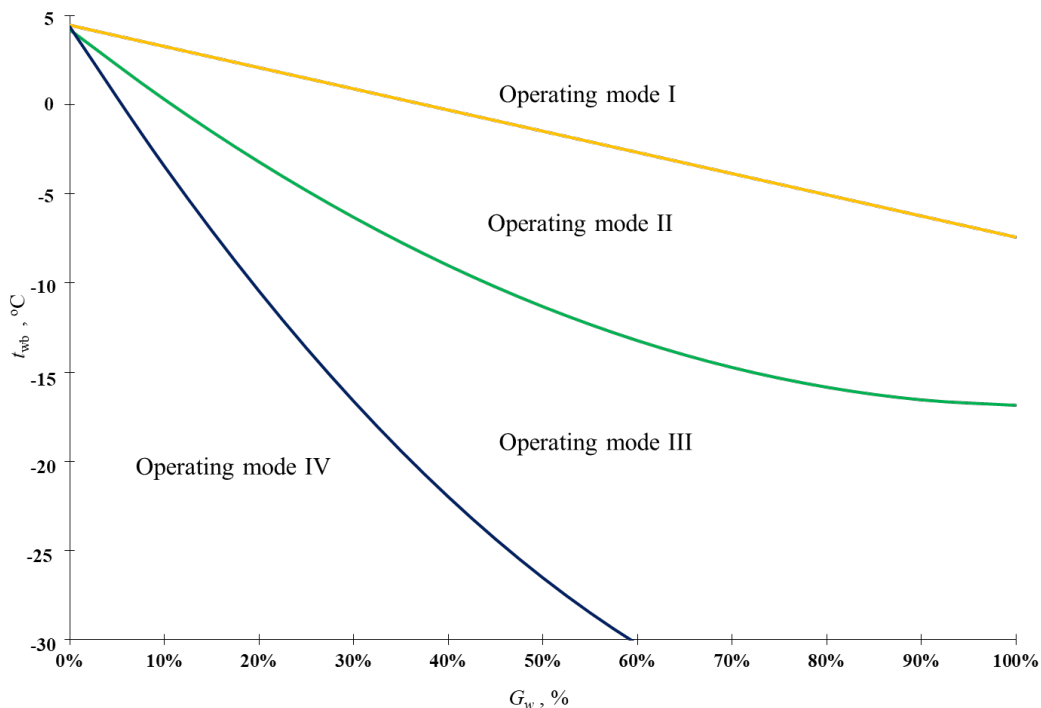


Fig. 2. Operating modes for antifreeze protection of the cooling tower

5. Conclusion

During winter, air circulation through the natural draught cooling tower can induce greater cooling of the water and appearance of ice at air entering areas, [8], [9]. Three systems for protection from freezing are used for natural draught cooling towers.

Determination of cooling water temperature at tower's exit – t_{w2} depending on climatic curve values and for three winter operating modes are presented in this article.

The diagram developed from this calculation shows that under nominal water flow and nominal heat load, operating mode I, there is no possibility for freezing of the water in the basin and at cooling tower fill's exit, as long as extremely low external air temperatures occur. By reducing the water flow, the danger for freezing of water in the tower is increasing.

6. References

- [1] Global Energy Monitor, Global Coal Plant Tracker, July 2018, <https://endcoal.org/global-coal-plant-tracker/> (2018)
- [2] Mills, A. D., Wiser, R. H. & Seel, J. Power Plant Retirements: Trends and Possible Drivers (No. LBNL-2001083). (Lawrence Berkeley National Lab (LBNL), Berkeley, CA (United States), 2017).
- [3] The strategy for energy development of the Republic of North Macedonia until 2040, MANU Skopje, 2019.
- [4] Mijakovski V., Popovski K., "Influence of climatic curve values on the operating regime of the turbine at TPP "Bitola", *International conference Power plants 2010*, Vrnjačka Banja, Srbija, 2010
- [5] Operating cooling towers in freezing weather, Marley cooling technologies, Kansas City, 1997.
- [6] Cooling towers fundamentals, second edition, SPX cooling technologies, Kansas City, 2009.
- [7] *2024 ASHRAE Handbook - HVAC Systems and Equipment*, chapter 40. Cooling towers, American Society of Heating, Refrigerating and Air-Conditioning Engineers, Atlanta, 2024
- [8] Andrejevski B., Mojsovski A., Dimitrov K., *Vlijanje na temperaturata na oladenata voda vo ladinata kula na snagata na turbinata i potrošuvackata na jaglen*, Institut za termotehnika i termoenergetika, Mašinski fakultet-Skopje, 1986.
- [9] Mijakovski V., Mijakovski I., *Influence of the Climatic curve on Cooling Tower Evaporation at Thermo Power Plant "Bitola"-Macedonia*, Conference of RTU 2007, Power and Electrical Engineering-International Conference, Riga, Latvia.



VI. Energy efficiency in industry, civil engineering, communal systems, and traffic

Rational use of energy and waste heat at compressor plants in the wood processing industry of Serbia

*Aleksandar Dedić^a, Dušan Bajić^b, Biljana Stojanović^c, Srdjan Svrzić^a, Matilda Lazić^d,
Duško Salemović^d*

^{a)} *University of Belgrade, Faculty of Forestry, Belgrade, RS, aleksandar.dedic@sfb.bg.ac.rs*

^{b)} *Šzr Bravura PR Boban Bajić, Čačak, RS, ca.bravura@gmail.com*

^{d)} *AD IMLEK, Padinska Skela, RS, biljana.stojanovic@imlek.rs*

^{c)} *High Technical School of Applied Sciences, Zrenjanin, RS, duskosalemovic@gmail.com*

Abstract: Obtaining pressurized air represents a significant expenditure of energy for every branch of industry, and today it is simply unthinkable to exist industrial plants without the production, distribution and use of pressurized air. This is particularly representative in the wood processing industry where it has been shown that there is a low awareness of the savings that can be made with the produced air under pressure, starting from its proper use to the use of waste heat through recovery. Bearing the above in mind, research was carried out in companies of the wood industry in Serbia in order to analyze the economics of obtaining and adequate use of pressurized air. Also, solutions were suggested for the recovery of waste heat in screw and reciprocating compressor plants, which are most present in the wood processing industry, as shown by the survey. The conclusions were drawn in the form of guidelines for the rational use of pressurized air, which can bring significant savings in energy consumption and increase efficiency and productivity in work.

Keywords: compressors, energy savings, heat recovery, wood industry.

1. Introduction

Pneumatic plants are widely used in many branches of industry. They are also present to a large extent in the wood industry, so today it is unthinkable existence even a micro-enterprise without having at least one compressor with a tank and the use of pressurized air. The application of pressurized air in the wood industry involves various purposes, such as [2]:

- the main movement of machines (pneumatic tools, presses, staplers, etc.)
- auxiliary movements of machine tools (drills, grinders, canting, etc.)
- cleaning workplaces and surfaces from waste (sawdust)
- painting and varnishing (pneumatic guns for applying varnish)
- creation of overpressure in the painting cabins
- pneumatic transport

As the production of pressurized air is a significant consumer of energy, the idea was to conduct research on the state and use of pneumatic systems in the wood processing industry on the territory of Serbia [3]. This research involved a detailed analysis of pneumatic systems from the aspects of: energy efficiency, its proper use, maintenance, etc. In order to obtain reliable data on the actual state of pneumatic equipment and gain insight into the proper exploitation and maintenance of pneumatic systems, a survey was compiled in the form of a questionnaire, which will later be processed and analyzed. Participants in the survey were asked to give their answers as conscientiously and honestly as possible, so that the importance of the survey would make sense. The goal of this research is to assess how much attention companies actually pay to pneumatic equipment: choosing its quality, proper maintenance and economical use; as well as the utilization of the waste heat generated by the compressors. Also, the research will show: the age of the pneumatic equipment, the types of compressors used and whether the capacities of the tanks used are commensurate with the needs.

2. Research results with analysis

The following participated in the research: micro, small, medium, and in the smallest percentage 7.69% large companies. The classification was made according to the literature of internet sources [8], supported by the law on accounting [6].

In the sample on which the research was conducted, according to the mentioned classification of companies, the largest percentage share includes micro-enterprises with even more than 80%, which according to [9] depicts the state of the timber industry in Serbia. This confirms that the sample of the 15 mentioned company was representative.

The analysis of the research results was carried out for the questions from the questionnaire, the survey and the necessary conclusions were drawn.

The results of the age of the equipment are shown in table 1. It was surprising that more than 69% of the companies were dominated by newer equipment up to 5 to 10 years old. If we take into account that according to European research, according to [5], the lifespan of compressors with engine power from 10 to 110 kW is about 13 years, it can be concluded that pneumatic equipment in the territory of Serbia in wood processing companies has not worn out, and that relatively regularly changes in accordance with the average recommended period of use.

About 23% of respondents stated that their equipment is between 10-15 years old. So those companies should replace the equipment to prevent unwanted downtime in production, or pay more attention to maintenance.

Table 1: Age of pneumatic equipment in companies [1]

Age of equipment	Percentage
Under 5 years	7.69 %
From 5 to 10 years	69.24 %
From 10 to 15	23.07 %

Certainly, the presence of new equipment is desirable from the point of view of greater reliability in operation, i.e. less probability of failure. On the other hand, the use of modern equipment under pressure implies a higher level of automation, etc. specificities that require greater training of the personnel who service the equipment during exploitation and, if necessary, carry out its periodic servicing.

The next question was about the type of compressor or plant used. The research results indicate that 38.46% of companies use only reciprocating compressors and 23.07% of companies have screw compressors, while 38.46% have both types. It is interesting that the companies that participated in the research do not use other types of compressors, such as: diaphragm compressors, turbo compressors, Ruts compressors, etc. All this points to the fact that these compressors are slowly going out of use, at least when they are in question in wood industry companies. This especially applies to membrane compressors, which have a larger capacity, so they are not needed in the micro-enterprises that dominate in Serbia.

The fact that reciprocating compressors are more present in the companies that participated in the research. Their purchase price is lower than screw-type ones of the same capacity, they are simpler and cheaper to maintain, and this is probably a decisive factor for slightly smaller companies in these areas.

The range of power values that would be generated at the maximum operating pressure of the compressor would be, which is impressive. If we adopt, according to [4], that 80% of this power is generated as heat due to increased pressure, including the present losses in heat transfer in order to bring it to the user, we obtain significant values of (17.6÷134.4) kW

If the cooling of the compressor is air, which is mostly present in older reciprocating compressors of smaller capacities, the recommendation for using that waste heat would be heating the rooms near the location of the compressor. When it comes to cooling the compressor through: water, oil or some other cooling agent, adaptation and the introduction of additional heat exchangers and a secondary circuit that would bring the generated heat to the place of application, along with the present transmission losses, is required. Of course, this heat would be constantly generated and recuperated because the need for compressor operation in the company is non-stop. Therefore, it would ideally serve for consumers who work all year round, such as: painting and varnishing rooms, dryers, etc.

The next question related to the possibility of separating parts of the system (executive bodies) from the central system (installation) if they are not currently working via valves. It was concluded that 76.92% of users have the ability to separate parts of the system from the central system. This is a very satisfactory percentage and is a pleasant surprise. It speaks of the awareness of our colleagues that by installing only

one valve, i.e. with insignificant costs, they achieve significant savings because potential air leakage and pressure drop in the pneumatic installation are eliminated.

The causes of pressure drop and loss of air flow in a pneumatic system are covered in the following question. The purpose was to see if the maintenance service is realistically looking at the causes of problems with the functioning of the pneumatic installation. The biggest problem of air loss in the pneumatic system is air leakage from the installation. Even up to 77% of respondents confirmed that statement. The results are shown in Figure 1.

For the maintenance survey (Figure 2), users were asked for precise and honest answers, for procedures they regularly perform. However, the analysis, to a negative surprise, says that companies absolutely do not attach so much importance to the maintenance of pneumatic equipment.

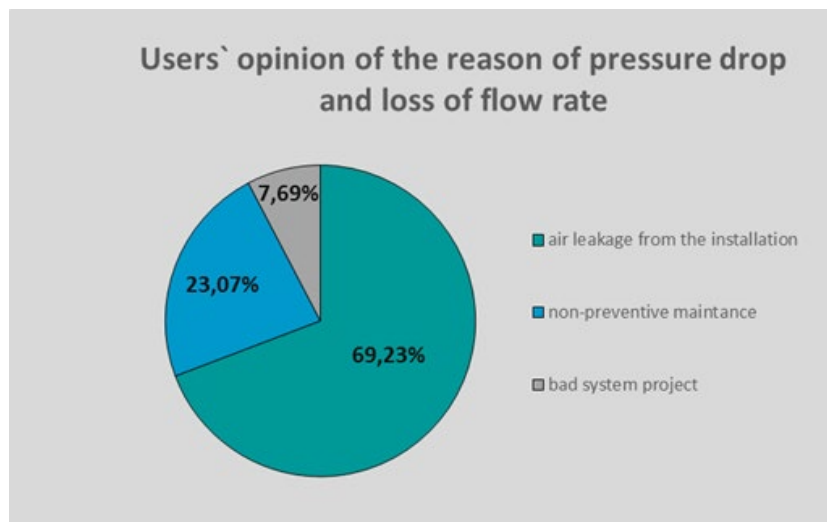


Figure 1: Losses in the pneumatic system

Unfortunately, some users pointed out that the pneumatic equipment is serviced and inspected only when it breaks down and stops working.

Regular maintenance of the pressurized air system ensures the stable development of production without unforeseen interruptions and the achievement of the set goals in the management of pressurized air, the most important of which are the continuous operation of the system and adequate supply of the end user with pressurized air. It is best to follow the manufacturer's recommendations because different systems and components have different maintenance intervals and types.

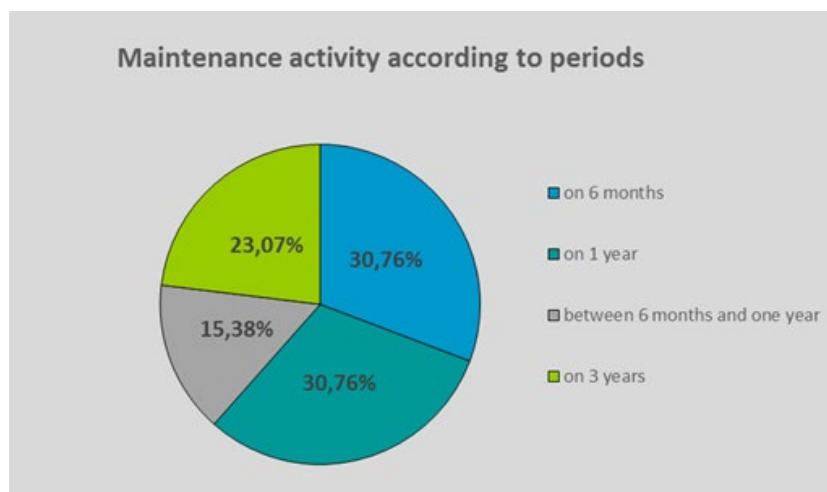


Figure 2: Periodicity of pneumatic equipment maintenance

The last question from the survey asked companies to answer whether they evaluate the efficiency of the system.

From the diagram in Figure 3, it can be seen that even 77% of the surveyed companies engaged in wood processing do not evaluate the efficiency of the system, i.e. measurement and monitoring of system performance.

Merely measuring the performance of the system will not improve energy efficiency, but it would be the first step in improving energy efficiency for two basic reasons:

- Measuring air and energy consumption is essential for determining whether changes in maintenance practices or investments in equipment are cost-justified or not.
- By monitoring the performance, negative changes are observed, as well as changes in the quantity and quality of the use of pressurized air.

As already mentioned in the introduction, the three basic parameters that are monitored are: air flow, air pressure and electricity consumption. An ultrasonic gun helps to facilitate the measurement, to help detect the location of the leak.

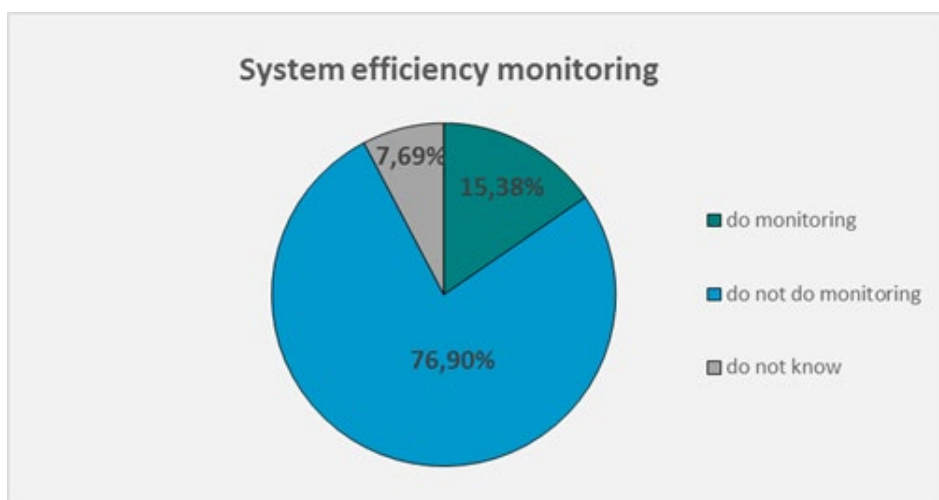


Figure 3: Evaluation of system efficiency by the company

3. Recovery of waste heat

In theory, any amount of heat that can be recovered from an industrial refrigeration system offers the possibility of improving the system's efficiency ([10], [11], [12]). Practically, the amount of recovered heat must be large enough to justify the investment in the main equipment, as well as any additional operating cost (e.g. maintenance) or complexity of the installation requires additional utilization of waste heat [7].

Locations within the industrial cooling system where it is possible to take waste heat, which is suitable for recovery, are:

- oil cooling (oil cooling with fluid in screw compressors);
- cooling of cylinder heads (piston compressors);
- high pressure gas flow:
- reciprocating compressors,
- screw compressors;
- low pressure of gas flow (minimum capabilities).

Modern screw compressors use oil for lubrication, regulated actuation and rotor sealing to maintain volumetric efficiency during the compression process. The consequence of using oil in these machines is that when the oil passes through the compressor, it absorbs part of the "heat of compression" from the cooling fluid. That is why the oil at the outlet of the compressor will be at a temperature approximately equal to the temperature of the cooling fluid on the thrust. Excluding various versions of liquid injection oil cooling, maintaining proper compressor operation requires oil cooling after compression to limit oil temperature rise. With thermo-syphon oil cooling and oil cooling with water (or glycol), heat exchangers are located in the compressor units, which cool the oil from the pressure temperature to an acceptable temperature at the compressor inlet (e.g. 54°C). Therefore, the heat removed by cooling the oil is a potential source of heat recovery.

Reciprocating compressors operating at moderate or high compression ratios require a supply of water, glycol or coolant to cool the cylinder heads. The fluid used to cool the heads (water or glycol) is another potential source of heat suitable for recuperation.

Heat recovery from the refrigerant leaving the compressor under pressure is the next obvious possibility in industrial refrigeration systems. The quality of the heat, which is available for recovery, will depend on the type of compressor (piston or screw), the operating pressures on the suction and discharge of the compressor and the load. With screw compressors, the heat quality will also vary depending on whether the oil is cooled internally (e.g. by coolant injection) or externally. By their very nature, compressors equipped with an oil cooling system by injecting a cooling fluid have lower pressure temperatures, and therefore a lower quality or energy level of heat available for recovery. Machines with coolant injection have a higher mass flow of steam under pressure, so the amount of heat that can be recovered is usually higher than in units with thermo-siphon or external oil cooling. Let's see how much heat can be recovered and what is the quality of the heat available to us from these sources. Figure 4 shows the savings in heating costs due to heat recovery for different primary fuel prices and water flow rates. The recovered heat could replace the operation of a boiler with an efficiency of 80% that would normally be used to provide heating needs.

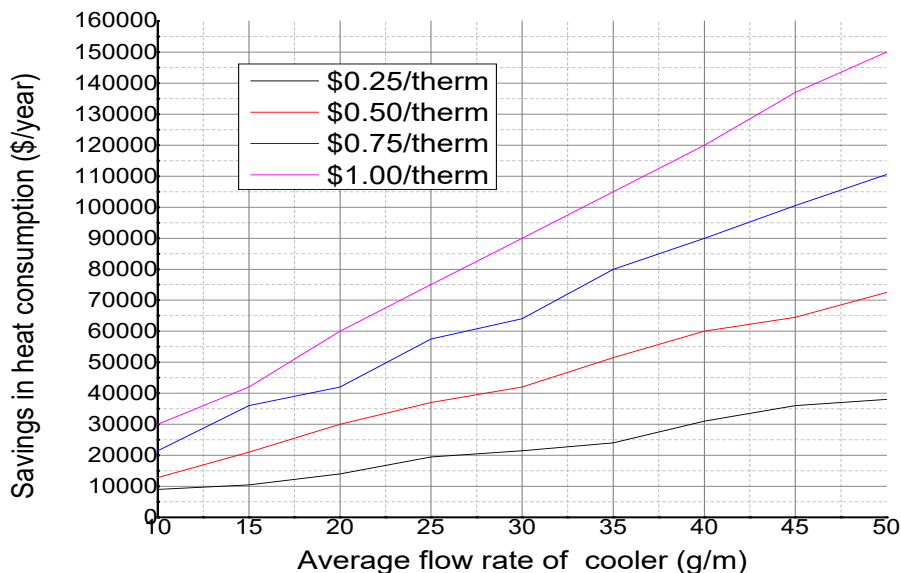


Figure 4: Annual savings in energy costs for heating at a temperature of 30°C waste water [4]

3.1. Heat recovery at oil-free compressor

1) within an air-cooled

Oil Free VSD Air Compressor with Heat Recovery as an option is the only Oil Free Air Cooled Compressor on the market today with Heat Recovery as an option.

This eliminates the need for an external cooling water system i.e. cooling water pumps, Blast Coolers, pipe work, etc. associated with water-cooled compressors. In the new Ingersoll Rand E Series Compressor, the heat exchangers, pump and controls are all within the compressor enclosure and you get usable water temperatures of up to 80°C (Figure 5).

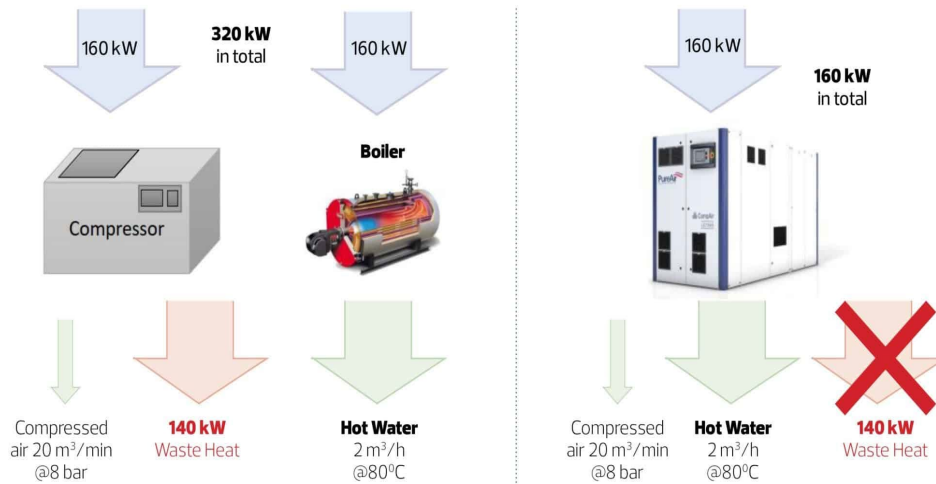


Figure 5: Oil-free compressor: a) within a water-cooled, b) within an air-cooled [16]

Thousands of savings are achievable each year as not only does the Heat Recovery element reduce energy bills, the E-Series has the lowest specific power of any Oil Free, VSD, Rotary Screw Compressor (between 75kw & 160kw) in the market today – thereby, amplifying the ability to reduce operating costs. The potential energy savings can mean a return of investment in just two to three years.

2) within a water-cooled

With water-cooled oil-free compressors, the Heat Recovery Solution requires the installation of a control unit between the compressor and the customers’ cooling and heating circuit. The compressor operates independently from the customers’ process.

3.2 Oil-lubricated compressors

Considerable savings can be achieved with oil-lubricated compressors. In fact, of the 100 percent of the electrical energy consumed, some 94 percent is converted to heat, that can be put to good use after it has been recovered (Figure 6).

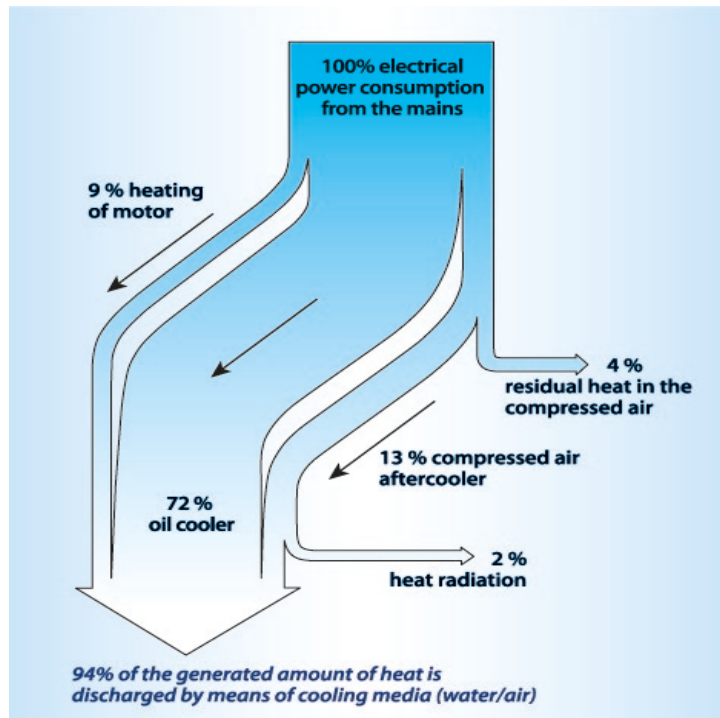


Figure 6: Exegetic diagram of utility of invested electric energy [14]

There are two ways of cooling oil-lubricated compressors:

1) *Thermo-siphon cooling*, the most modern solution for oil cooling in screw compressor aggregates [13]. In thermo-siphon oil cooling, saturated liquid coolant is used as a coolant in the coolant-oil heat exchanger, which is integrated into the compressor unit. The coolant liquid in the heat exchanger is at a lower temperature and therefore absorbs heat from the hotter oil and evaporates. The refrigerant vapor is then led to the condenser(s) where it condenses again, allowing it to be further used to cool the oil or meet the cooling needs of the cooling system. Thermo-siphon oil coolers are flooded evaporators with gravity circulation.

Thanks to its working principle, thermosiphon oil cooling requires a minimum amount of energy for heat exchange – only additional energy is needed to drive the condenser fans and pumps. Thermo-siphon oil cooling is particularly effective when properly constructed; however, it is also a technology that has not been satisfactory in exploitation in many plants. Improperly dimensioned thermosiphon receiver, equalization lines, return or distribution lines can individually or together cause numerous problems in installations. In addition, systems with thermos-siphon oil cooling are not particularly suitable for expansions. When problems arise in thermos-siphon systems (which happens quite often), solving and eliminating them is difficult and frustrating.

2) *Water (or glycol) oil cooling in heat exchangers* is a less commonly applied cooling technology [15]. In this method, water or a glycol solution is used as a secondary cooling fluid that receives the heat of the oil. In this case, the glycol is passed through an oil cooler, receiving heat from the oil, and then cooled, i.e. giving up heat, in a closed-type liquid cooler, which is located outside. This heat can be recovered and used to meet the relatively moderate heating needs of the plant. Typically, oil cooling heat exchangers accept hot oil from the screw compressor separator at a temperature close to the pressure steam temperature, which is in the range of 71°C to 85°C, and cool it to the temperature at which it is returned to the compressor, which most often it is 54°C. With oil in this operating temperature range we clearly have a heat source of acceptable quality (temperature). Now the question is, "What amount of oil cooling heat is available to us?" The amount of heat that can be used from the oil cooler depends on several factors, including: - compressor size (capacity); - suction pressure; - thrust pressure and - degree of partial load.

4. Conclusion

After a detailed analysis of the survey, one gets the impression that the participants in the survey answered most of the questions credibly. From all that has been stated so far, it can be concluded that pneumatic equipment on the territory of Serbia in wood processing companies:

- 1) has a wide range of uses, and is mostly used in the implementation of: main and auxiliary movement of machines, painting and varnishing;
- 2) it has not worn out, and that it is changed relatively regularly in accordance with the average recommended period of use (as many as 70% of companies own equipment between 5 and 10 years old);
- 3) it mostly uses reciprocating compressors (around 70%), while in addition to them only screw compressors are present, the use of which is gradually increasing;
- 4) generates a considerable amount of heat in the process of air compression in the compressor, which should be adequately utilized through recuperation;
- 5) it has insufficient automation of the plant, which is mainly reduced to on-off regulation of the operation of the compressor coupled to the tank; while manual and mechanical (68%) dominate the distributor activation methods;
- 6) the majority have the ability to separate parts of the system from the central system (77% of users)

What is still definitely a problem:

- that the presence of leakage is not considered, and there is no awareness of what losses are involved through the increased consumption of electricity to compensate for the losses;
- non-preventive maintenance and a small number of workers servicing pneumatic equipment (over 60% of respondents claim that there is no need to spend resources on maintenance in the service center for their equipment, but they maintain their equipment independently)

With the increase in the price of fuel used for heating, there are greater opportunities to economically recover heat from industrial cooling systems. Classical approaches to heat recovery focus on heat recovery from the steam stream at the thrust of a high-pressure compressor (superheated steam cooler). Another possibility, which should not be overlooked, is the recovery of heat from the oil coolers of screw compressor aggregates. The advantages of this solution include:

- the possibility of heat recovery from the oil cooler, both with low and high pressure compressors;
- recovery of relatively high-quality waste heat is enabled;
- the result of an oil cooling approach that is less prone to problems compared to thermosiphon oil cooling;
- the use of a fluid that receives sensible heat and a pump allows greater control over oil cooling (removes the influence of "mother nature" from the classic thermosiphon circuit);
- it is easier to adapt to the addition of new compressors when expanding the plant compared to systems with thermos-syphon cooling;
- great possibilities for modification of compressors with oil cooling by injection of cooling fluid liquid;
- makes the cooling of the oil independent of the pressures in the system, which enables easier commissioning; and
- enables the use of plate heat exchangers without fear of pressure drop on the coolant side.

Although the advantages are attractive, other factors must be considered when applying this method of heat recovery. First, each compressor unit must be equipped (or modified) with a suitable oil cooler. Second, the heating needs should match the cooling heat of the oil. If there is a mismatch between heating needs and supplied heat, additional infrastructure is needed to accommodate this mismatch. Finally, the economy of heat recovery from the oil cooler needs to be evaluated on a case-by-case basis.

Acknowledgments

The work was carried out within the project of the Ministry of Science, Technological Development and Innovation of the Republic of Serbia, number: 451-03-65/2024-03/ 200169 dated on 05.02.2024.

5. References

- [1] Bajic D.: Analysis of the state and use of pneumatic plants in the wood industry of Serbia, Graduation thesis, Faculty of Forestry, University of Belgrade, 2022. (in Serbian)
- [2] Dedic A. : Fundamentals of mechanical engineering with examples of solved tasks - part 1, Faculty of Forestry, University of Belgrade, 2009.
- [3] Dedić A., Bajić D., Svrzić S., Dedić L.: Analiza stanja i korišćenja pneumatskih postrojenja u nekim preduzećima drvne industrije Srbije, Glasnik Šumarskog fakulteta, 129, p. 7-16, Faculty of Forestry, University of Belgrade, 2024.
- [4] Reindl D.T., Jekel T. B.: Heat recovery in industrial cooling, KGH, 38(2), p. 63-68, 2009.
- [5] Seslija D., Lagod B.: State of pneumatic systems in Serbian industry - from the aspect of energy efficiency, Center for Automation and Mechatronics, Novi Sad, 80pp, 2006.
- [6] <https://www.paragraf.rs/propisi/zakon-o-racunovodstvu-2020.html>
- [7] <http://ba.chinamfilter.com/info/what-are-the-routines-for-air-compressorenerg-36164210.html>
- [8] <https://www.companywall.rs/>
- [9] http://www.europeanprogres.org/dokumenti/48_186782_akcioni-plan-podrske-drvnoj-industrii-srbije.pdf
- [10] <https://joairsolutions.com/products/energy-recovery-scrubber>
- [11] https://www.gea.com/en/binaries/hrt-industrial-heat-recovery_tcm11-67581.pdf
- [12] <https://hal.science/hal-03838890/document>
- [13] <https://www.airbestpractices.com/technology/air-compressors/air-compressor-heat-recovery>
- [14] <https://america.sullair.com/en/products/eesr-air-compressor-heat-recovery-system>
- [15] <https://www.compressedairchallenge.org/data/sites/1/media/library/factsheets/factsheet10.pdf>
- [16] <https://oneillcompressedair.com/products/heat-recovery/>

Analytical Assessment of Cooling Degree-Days for Estimating Energy Consumption in Building Sector During Cooling Season in Belgrade

Branislav Petrovic^a, Milan Gojak^b

^a *University of Belgrade Faculty of Mechanical Engineering, Belgrade, RS bpetrovic@mas.bg.ac.rs*

^b *University of Belgrade Faculty of Mechanical Engineering, Belgrade, RS mgojak@mas.bg.ac.rs*

Abstract: Although the degree-day method for heating is classified as a single-parameter method, as it only accounts for daily changes in outdoor air temperature to estimate the heating demand of a building due to climatic influences, it has proven to be highly reliable over decades of practice and is now widely regarded as a standard method for determining heating requirements. However, due to evident climate changes and rising outdoor air temperatures, treating the heating degree days as a prescribed constant value for the specified location, leads to significantly inaccurate results, as demonstrated in this paper through an analysis of data from the Republic Hydrometeorological Service. Meanwhile, the use of the cooling degree days method to determine cooling demand has proven to be highly unreliable. This is because the method does not account for solar radiation, which, during the summer months, is as significant a factor as outdoor air temperature. To address this issue, while preserving the core concept of the method the heat load to be removed from a cooled space is proportional to the difference between the average daily outdoor air temperature and the base indoor temperature, a considerably lower base indoor temperature can be used in place of the internal design (reference) temperature. This paper presents the corrected method, along with international experiences and best practices, and includes data from the Republic Hydrometeorological Service. Additionally, cooling degree days for Belgrade have been calculated and presented, providing more accurate and reliable cooling demand forecasts.

Keywords: Cooling degree-days; Average daily outside temperature; Annual energy consumption; Climate change

1. Introduction

Climate change is ongoing and will likely continue in the coming decades. Globally, an increase in average air temperature during both summer and winter months has been observed. In Serbia's building sector, heating and cooling currently account for about 45% of total energy consumption according to official data [1]. The forecasted climate changes will significantly alter this balance. Specifically, higher temperatures are expected to reduce energy demand for heating during the winter period and increase energy consumption for cooling during the summer months.

Computer simulations are continuously being improved to provide support in assessing energy consumption in the building sector. However, in addition to complex simulations, simpler and well-established tools, such as the degree-day method and the bin method, are also used [2]. Cooling degree days (*CDD*) and heating degree days (*HDD*) are often used as climate indicators to assess heating and cooling needs. This stationary, single-parameter method allows for the evaluation of a building's energy performance and is based on current or averaged differences between the reference indoor air temperature and the daily mean outdoor air temperature.

Therefore, the degree-day method is relevant when the thermophysical properties of building structures can be considered constant. This method assumes no heat accumulation in building structures during the analyzed period. Using the degree-day concept, it is possible to estimate monthly or annual heating and cooling requirements of buildings at various locations.

The average heating degree day value currently used in the "*Regulation on Energy Efficiency of Buildings*" [3] for Belgrade is $HDD = 2520$ [3, 4, 5]. This value was obtained using meteorological data from the period 1925 to 1968. Since the "*Regulation on the Methodology for Calculating the Number of Degree Days for Heating and Cooling*" [6] prescribes the determination of degree days over the last 25 years, the study [7] found that the heating degree day value for Belgrade during this heating period is $HDD = 2179.7$.

The newly obtained value is 13.5% lower than the value currently used in the "Regulation on Energy Efficiency of Buildings." In Table 1, θ_h [°C] represents the average temperature of the heating season, and Z is the number of days in the heating season.

Table 1. Comparison of currently used heating degree day values with newly obtained results from study [7]

Belgrade model 12/19			
Period	$HDD_{average}$	Z [day]	θ_h [°C]
1925-1968.	2520	175	4,6
1998-2022.	2179,7	152	4,66

The currently applicable "Regulation on Energy Efficiency of Buildings" [3] only takes into account the annual heating energy demand. Due to the intensifying climate changes during the summer period, which lead to increased energy consumption for cooling, the aim of this paper is to determine the number of cooling degree days, which will be used to calculate the annual cooling energy demand, $Q_{c,nd}$ [kWh/month].

2. Methodology for calculating cooling degree days

The methodology according to ASHRAE guidelines [2] is widely accepted for calculating the number of cooling degree days (CDD), using the following equation:

$$CDD_{annual} = \sum_{j=1}^N cc \cdot (\theta_{average,i} - \theta_b) \quad (1)$$

where N represents the number of days in the year (365 or 366), $\theta_{average,i}$ [°C] denotes the daily average outdoor air temperature, and θ_b [°C] is the base (reference) temperature for cooling. If the daily average outdoor air temperature is higher than the base temperature, cc equals 1; otherwise, cc equals 0.

The base temperature refers to the outdoor air temperature at which no additional heating or cooling is needed, meaning it is the temperature within the range of comfortable conditions for the occupant, without the need for mechanical heating or cooling systems. During the summer period, when the average daily outdoor temperature exceeds the base temperature, cooling systems need to be activated to maintain comfortable indoor conditions. Determining the base temperature requires a detailed consideration of specific factors, such as: thermal characteristics of the construction, internal heat sources, heat gains through the thermal envelope of the building, and the desired indoor air temperature [9,10]. Therefore, the base temperature should be individually determined based on the specific case for accurate energy consumption estimation.

Many countries use 18.3°C as the base temperature for calculating cooling degree days [9]. However, the base temperatures used for calculating CDD vary across different countries, for example: 18.3°C in the United States and Saudi Arabia, 15.5°C in the United Kingdom, and 15.0°C in Germany.

In study [8], the calculation of cooling degree days for Belgrade was carried out for the reference period from 1971 to 2000, based on a base temperature of 18.3°C. According to this study, the obtained value for cooling degree days is $CDD = 432$.

On the other hand, in Serbia, the methodology for calculating degree days was prescribed in 2021 by the "Regulation on the Methodology for Calculating Degree Days for Heating and Cooling" [6]. According to this methodology, the daily, monthly, and annual number of cooling degree days is calculated using expressions (2-5) as follows:

$$CDD_{daily} = \begin{cases} (\theta_{average,i} - \theta_{in}) & \text{if } \theta_{average,i} \geq 24^\circ\text{C} \\ 0 & \text{if } \theta_{average,i} < 24^\circ\text{C} \end{cases} \quad (2)$$

$$CDD_{monthly} = \sum_{i=1}^z CDD_{daily} \quad (3)$$

$$CDD_{annual} = \sum_{j=1}^{12} CDD_{monthly} \quad (4)$$

$$CDD_{\text{average}} = \frac{\sum_{i=1}^z CDD_{\text{annual},i}}{25} \quad (5)$$

According to the Regulation [6], the number of cooling degree days for a calendar year is determined using the 24/21 model. In the model name, the number 21 represents the indoor reference air temperature θ_{in} [°C], while the number 24 represents the base temperature, which is the average daily outdoor air temperature at which the cooling system begins to operate. Additionally, the average number of cooling degree days (CDD_{average}) refers to the arithmetic mean of the number of cooling degree days over the past 25 years. If this value is not available, data from a shorter period can be used, but not less than 15 years.

To determine CDD according to the specified expressions, it is necessary to have data on the average daily outdoor air temperatures at a given location. As shown in equation (6), there are three different methods for calculating the average daily outdoor air temperature. This value can be obtained as the arithmetic mean of the maximum and minimum daily outdoor air temperatures, using measured air temperatures at three intervals: 7, 14, and 21 hours local time, or using average daily outdoor air temperatures measured every hour.

$$\theta_{\text{average},i} = \begin{cases} \frac{\theta_{\text{max},i} + \theta_{\text{min},i}}{2} \\ \frac{\theta_{7,i} + \theta_{14,i} + 2 \cdot \theta_{21,i}}{4} \\ \frac{\sum_{k=1}^{24} \theta_{\text{sr},k}}{24} \end{cases} \quad (6)$$

3. Results

In accordance with the prescribed Regulation [6], the average number of cooling degree days for Belgrade (CDD_{average}) is determined as the arithmetic mean of the number of cooling degree days over the past 25 years, i.e., for the period from 1998 to 2022. The data on average daily outdoor air temperatures were obtained based on climatological measurements and observations at measuring stations at three intervals: 7, 14, and 21 hours local time. These values were provided by the Republic Hydrometeorological Institute of Serbia (RHMZ) - from the automatic meteorological station at the Vračar Observatory, Belgrade (44°48' N, 20°28' E, 132 m above sea level).

For the period from 1998 to 2022, the average annual number of cooling degree days for the calendar year and the average annual number of cooling degree days for the cooling period (from May 15 to September 15) are presented in Tables 2 and 3. Additionally, the table shows the number of days during the cooling period (Z), the average temperature during that period (θ_c), as well as the differences in the number of cooling degree days for each year compared to the average value over the observed interval. These differences are presented as absolute and relative deviations.

Table 2. The number of annual cooling degree days for the calendar year in Belgrade, determined by the 24/21 model

Model 24/21					
Year	Z	θ_c	$CDD_{24/21}$	$\Delta CDD_{24/21}$	$\Delta CDD_{\tau 24/21}$
–	day	°C	°C-day	°C-day	%
1998.	49	26,96	291,8	5,0	1,76
1999.	24	26,1	122	-164,8	-57,46
2000.	55	27,19	340,5	53,7	18,74
2001.	34	26,42	184,4	-102,4	-35,70
2002.	36	26,54	199,4	-87,4	-30,47
2003.	60	26,6	335,7	48,9	17,06
2004.	25	26,54	138,4	-148,4	-51,74
2005.	24	26,14	123,4	-163,4	-56,97

2006.	42	26,6	235,2	-51,6	-17,98
2007.	56	27,39	357,7	70,9	24,74
2008.	52	26,9	307	20,2	7,06
2009.	47	26,21	245,1	-41,7	-14,53
2010.	44	26,7	251	-35,8	-12,47
2011.	51	27,12	312,2	25,4	8,87
2012.	79	27,42	507,5	220,7	76,97
2013.	51	27,09	310,5	23,7	8,28
2014.	29	25,82	139,8	-147,0	-51,25
2015.	65	27,66	432,7	145,9	50,89
2016.	45	25,99	224,4	-62,4	-21,75
2017.	59	28,02	414,3	127,5	44,47
2018.	59	25,91	289,5	2,7	0,95
2019.	65	26,83	378,8	92,0	32,09
2020.	52	26,09	264,7	-22,1	-7,69
2021.	55	28	387,5	100,7	35,13
2022.	64	26,9	375,6	88,8	30,98

Table 3. The number of annual cooling degree days for the cooling season in Belgrade, determined by the 24/20 model

Model 24/21					
Cooling season	Z	θ_c	$CDD_{24/21}$	$\Delta CDD_{24/21}$	$\Delta CDDr_{24/21}$
–	day	°C	°C-dan	°C-dan	%
1998.	49	26,96	291,8	13,4	4,82
1999.	23	26,1	117,2	-161,2	-57,90
2000.	53	27,3	334	55,6	19,97
2001.	34	26,42	184,4	-94,0	-33,76
2002.	36	26,54	199,4	-79,0	-28,37
2003.	50	26,85	292,5	14,1	5,07
2004.	25	26,54	138,4	-140,0	-50,29
2005.	24	26,14	123,4	-155,0	-55,67
2006.	42	26,6	235,2	-43,2	-15,51
2007.	53	27,55	347,4	69,0	24,79
2008.	52	26,9	307	28,6	10,28
2009.	46	26,17	242	-36,4	-13,07
2010.	44	26,7	251	-27,4	-9,84
2011.	48	27,23	299,8	21,4	7,69
2012.	71	27,7	476	197,6	70,98
2013.	44	27,46	284	5,6	2,01
2014.	29	25,82	139,8	-138,6	-49,78
2015.	59	27,78	400	121,6	43,68
2016.	43	26,07	218,1	-60,3	-21,66
2017.	58	28,06	409,4	131,0	47,06
2018.	57	25,96	282,8	4,4	1,58
2019.	65	26,83	378,8	100,4	36,07
2020.	49	26,17	253,3	-25,1	-9,01

2021.	54	28,1	382,7	104,3	37,47
2022.	63	26,9	371,4	93,0	33,41

Taking into account the observed period over 25 years, Table 4 shows the average number of cooling degree days, the number of days during the cooling period, and the average temperatures for the cooling season for both the calendar year and the entire cooling season.

Table 4. Presentation of the obtained results

1998. – 2022.			
	$CDD_{\text{average model 24/21}}$	Z [day]	θ_c [°C]
Calendar year	286,8	49	26,77
Cooling season	278,4	47	26,83

Figures 1 and 2 graphically present the number of cooling degree days determined by the 24/21 model, for the entire calendar year and the cooling season, compared to the average number of cooling degree days from Table 4. The smallest relative deviation of the number of cooling degree days from the average value over 25 years for the cooling season is 0.95% (cooling season 2018), while for the calendar year it is 1.58% (2018).

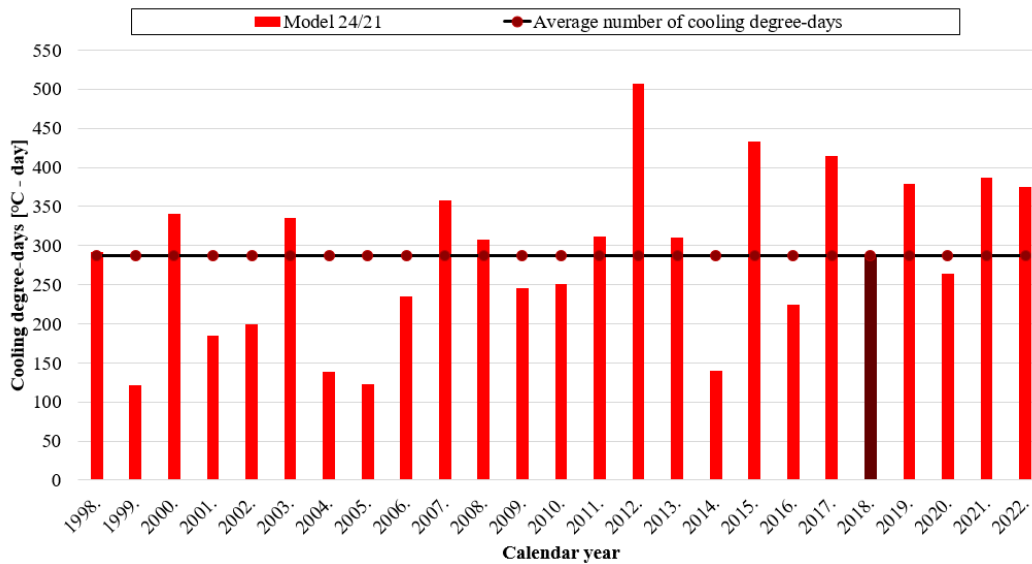


Figure 1: Graphical representation of the annual number of cooling degree days for the period from 1998 to 2022, determined by the 24/20 model, compared to the overall average number of cooling degree days for calendar year

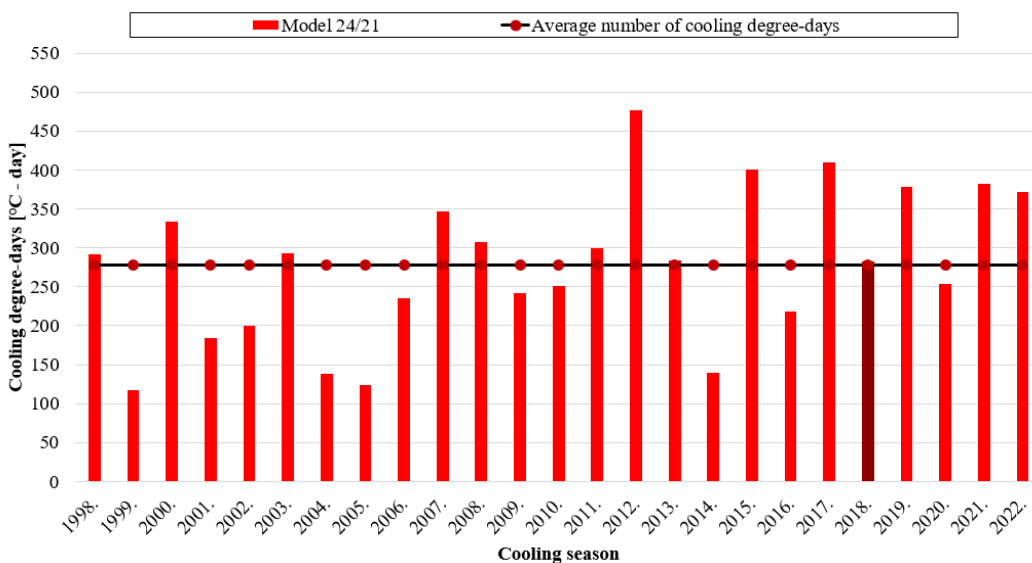


Figure 2: Graphical representation of the annual number of cooling degree days for the period from 1998 to 2022, determined by the 24/20 model, compared to the overall average number of cooling degree days for cooling season

Based on the data shown in Tables 2 and 3, diagrams have been created to illustrate the variation in the average number of cooling degree days throughout the calendar year (Figure 3) and during the cooling season (Figure 4) over the past 25 years.

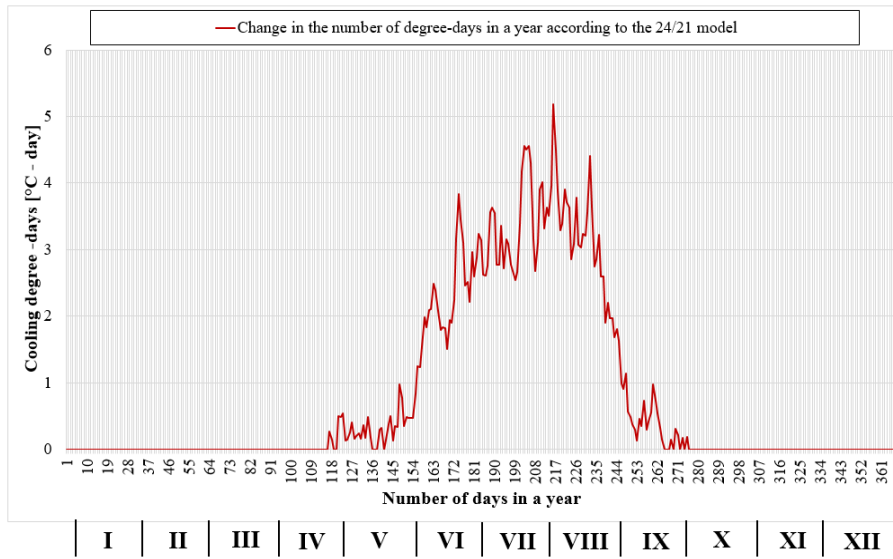


Figure 3. Diagram showing the change in cooling degree days during the calendar year from 1998 to 2022.

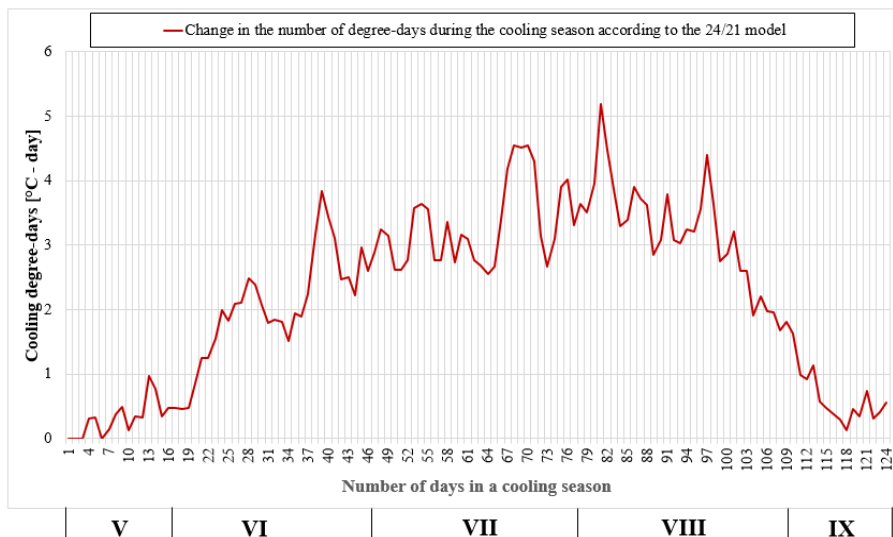


Figure 4: Diagram showing the change in cooling degree days during the cooling season from 1998 to 2022.

The number of cooling degree days (CDD_{annual}) can also be expressed graphically as a function of the number of days during the cooling period (Z), according to the following equation:

$$CDD_{\text{annual}} = \underbrace{Z(\theta_b - \theta_{\text{in}})}_{A_1} + \underbrace{\sum_{n=1}^Z (\theta_{\text{average},i} - \theta_b)}_{A_2} \quad (7)$$

By applying equation (7), the number of cooling degree days is determined as the sum of area A_1 , which corresponds to the first term of the equation, and area A_2 , which corresponds to the second term. The graphs allow for the determination of the number of days in the cooling period (Z) obtained from the intersection of the average monthly air temperature profile curve and the cooling isotherm boundary curve.

Figure 5 graphically presents the daily cooling degree day profile for an exceptionally warm cooling season (2012), while Figure 6 provides a graphical representation for an exceptionally cold cooling season (1999) during the observed period.

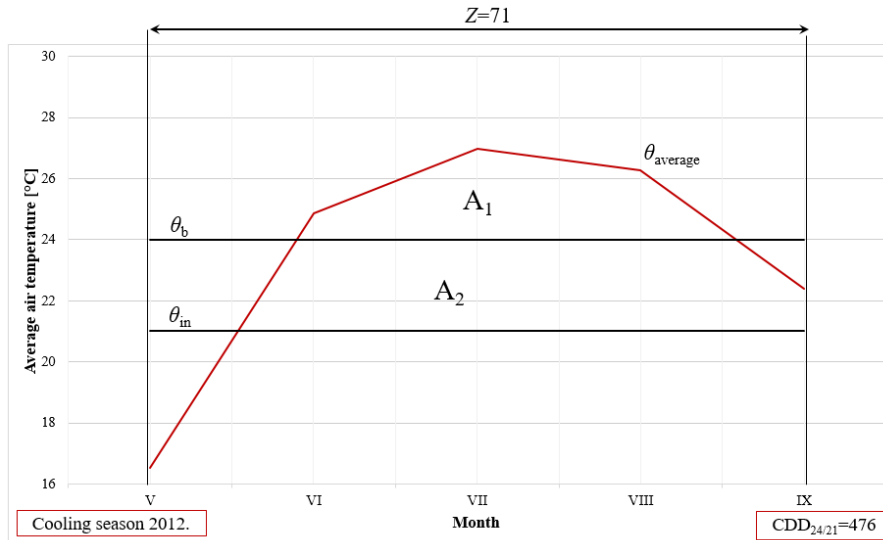


Figure 5. Graphical representation of cooling degree days for Belgrade during the exceptionally warm cooling season (2012) over the observed 25 years, based on average monthly outdoor air temperatures

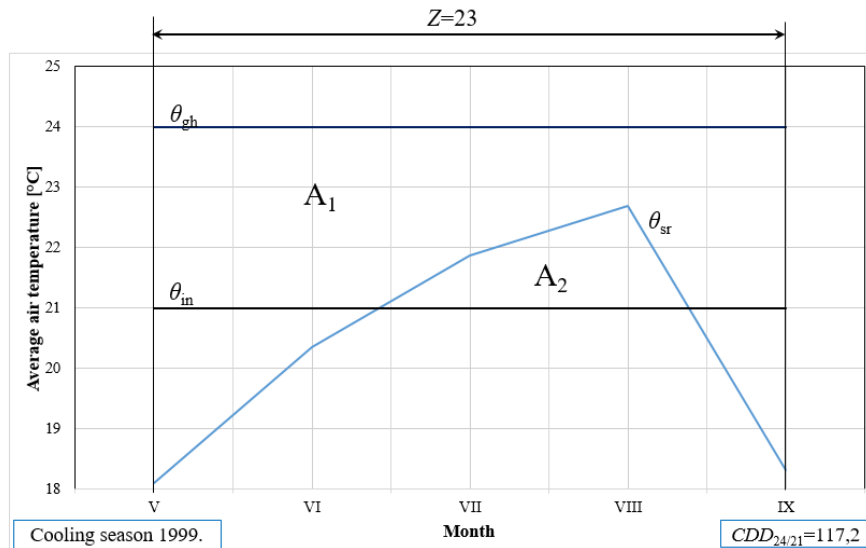


Figure 6. Graphical representation of cooling degree days for Belgrade during the exceptionally cold cooling season (1999) over the observed 25 years, based on average monthly outdoor air temperatures

In addition, the number of cooling degree days can also be graphically represented using average daily outdoor air temperatures. Figure 7 shows the exceptionally warm cooling season (2012), while Figure 8 illustrates the exceptionally cold cooling season (1999) over the observed period. During the exceptionally warm cooling season, the lowest average daily temperature (May 17) was 11.4°C, while the highest (August 6) was 32.6°C. In contrast, during the exceptionally cold cooling season, the lowest average daily temperature (June 22) was 11.1°C, and the highest (August 10) was 30.5°C.

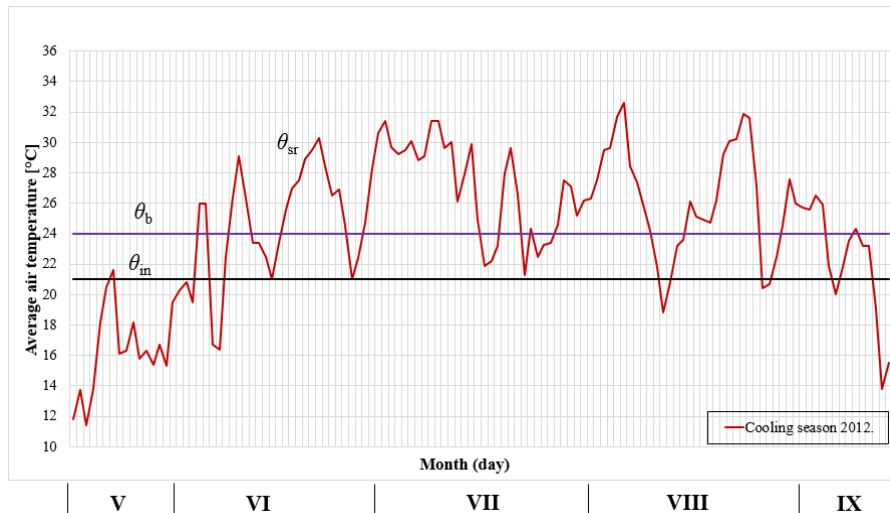


Figure 7. Graphical representation of cooling degree days for Belgrade during the exceptionally warm cooling season (2012) over the observed 25 years, based on average daily outdoor air temperatures

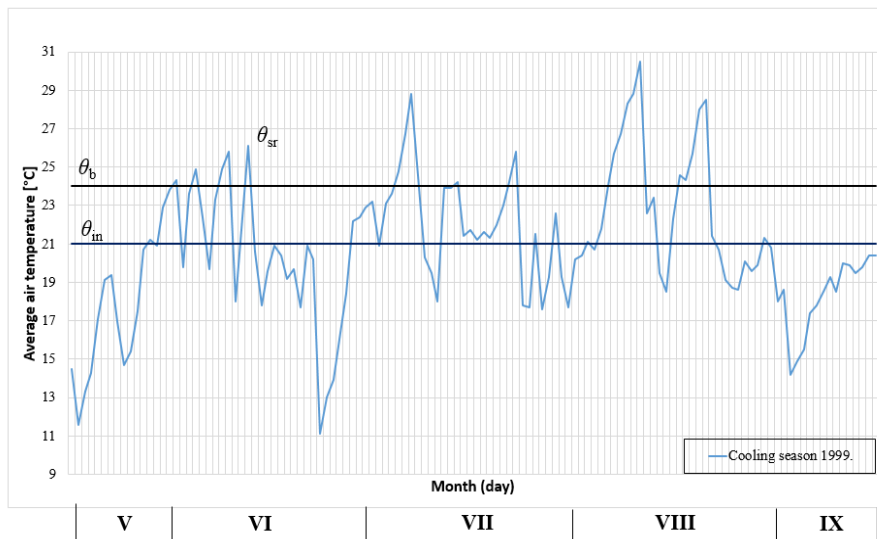


Figure 8. Graphical representation of cooling degree days for Belgrade during the exceptionally cold cooling season (1999) over the observed 25 years, based on average daily outdoor air temperatures

4. Conclusion

Cooling degree days (*CDD*) is an important climatic parameter used to estimate energy consumption in buildings during the summer period. This method represents the cumulative difference between the outdoor air temperature and a reference (base) temperature over a specified time period. The base temperature is crucial in determining *CDD* and represents the temperature at which cooling systems are not needed to maintain the desired indoor air temperature. Using a base temperature of 24°C, as established by the "Methodology for Calculating Degree Days for Heating and Cooling," the average cooling degree days values obtained are $CDD=286.8$ (for the calendar year) and $CDD=278.4$ (for the cooling season). In contrast to the proposed regulation that specifies a base temperature of 24°C, many countries use a base temperature of 18.3°C for calculations. Based on a base temperature of 18.3°C, the study [8] calculated the cooling degree days for Belgrade for the reference period (1971–2000), yielding a value of $CDD=432$.

The significant differences in the average cooling degree days values, considering base temperatures of 24°C and 18.3°C, highlight the importance of carefully selecting the base temperature. Further research should focus on accurately defining the base temperature to obtain more precise estimates of cooling degree days, which is essential for determining the required cooling energy.

Acknowledgements

The results shown here are the result of research supported by the Ministry of Science, Technological Development and Innovation of the Republic of Serbia under Contract 451-03-65/2024-03/200105 dated 05.02.2024.

References

- [1] Jankovic, A., Podrascanin, Z., Djurdjevic, V. Future climate change impacts on residential heating and cooling degree days in Serbia, *Idojaras Quarterly Journal of the Hungarian Meteorological Service*, 123 (2019), 3, pp. 351-370.
- [2] *** National Renewable Energy Action Plan of the Republic of Serbia Ministry of Energy, Development and Environmental Protection, Belgrade, 2013.
- [3] Handbook – Fundamentals (SI). American Society of Heating, Refrigerating and Air-Conditioning Engineers, ASHRAE, Atlanta, 2005.
- [4] *** Pravilnik o energetskej efikasnosti zgrada ("Sl. glasnik RS", br. 61/2011), 2011.
- [5] Todorovic, B. Stepen-dan kao podatak za određivanje potrebne količine toplote za grejanje u našoj zemlji, *Međunarodni sajam o KGH – Interklima '73*, Zagreb, Hrvatska, June, 1973.
- [6] Todorovic, B. Projektovanje postrojenja za centralno grejanje, *Mašinski fakultet Univerziteta u Beogradu*, Beograd, 1996.
- [7] *** Pravilnik o metodologiji za proračun broja stepen dana grejanja i broja stepen dana hlađenja („Službeni glasnik RS”, broj 96/21 od 8.10.2021. godine).
- [8] Petrović, B., Banjac, M. Analysis of the Climate Data for Belgrade from 1998 to 2022 for Building Energy Performance Simulation Using the Heating Degree Days Method, *KGH – Klimatizacija, grejanje, hlađenje*, 53 (2023), 2, pp. 29-35.
- [9] Bhatnagar, M., Mathur, J., Garg, V., Determining base temperature for heating and cooling degree-days for India, *Journal of Building Engineering*, 18 (2018), pp. 270-280.
- [10] Salem, H., Khanafer, K., Alshammari, M., Sedaghat, A., Mahdi, S., Cooling Degree Days for Quick Energy Consumption Estimation in the GCC Countries, *Sustainability*, 14 (2022), 21, pp. 1-7.

Proposal of New Building 4E improvement

Darko Z. Ristanović^a, Maja N. Todorović^b

^a *Energynet D.O.O., Novi Sad, RS, dristanovic@energynet.rs*

^b *University of Belgrade, Faculty of Mechanical Engineering, Belgrade, RS, mtodorovic@mas.bg.ac.rs*

Abstract: Based on numerous analyzes, expertise and energy audits of buildings in the last decade, as well as on the basis of data published by the line ministries responsible for the field of construction and energy sectors, it is evident that the gross final energy consumption in the Building sector in Republic of Serbia is growing. The new and amended EU directives, as well as the legislative framework, imply, in addition to reducing the primary energy used in buildings, the implementation of efficient technical systems that include renewable energy sources (hereinafter referred to as RES), have a minimized impact on the environment (Zero Emission Buildings), as well as positive economic indicators. For these reasons, especially when it comes to newly designed buildings, it is necessary to implement improvements in terms of the 4Es: Energy, Efficiency, Ecology and Economy. The paper gives a proposal of bulding 4E improvement, based on the analisys of different energy sources and technical systems in a newly designed residential building located in Belgrade. Four scenarios with different energy sources, as well as internal installations in the building, which include a heating system and domestic hot water preparation, were analyzed. Energy source types, which are compared are as follows: district heating system that generates heat from fossil fuels, biomass, natural gas and air to water heat pumps, with the calculation of primary energy, CO₂ emission and the exploitation cost for each scenario. The results obtained after the conducted analysis indicate the optimal solution.

Keywords: building energy class, energy source type, primary energy, buildings technical systems, CO₂ emission, operating energy cost.

1. Introduction

The way we manage energy has a direct impact on our environment and quality of life. That is why it is important not only to reduce energy consumption, but also to ensure that it is used in the most efficient way possible. Other benefits of improving the energy efficiency of buildings are reflected in the reduction of harmful environmental impacts, as well as the financial benefits that can be achieved by improving the energy efficiency of buildings.

Raising awareness of the importance of energy efficiency can be challenging. One of the most effective ways to achieve this is by demonstrating the concrete economic benefits that come with investing in energy-efficient systems and technologies, which is actually the primary goal of the Energy Performance of Buldings Directive (hereinafter referred to as EPBD). What are the different types of energy that affect the cost of heating and cooling? What types of energy sources, such as natural gas, electricity, pellets or other renewables, provide the greatest savings and efficiency as well as minimal environmental impact? What types of technical systemsin building should be applied depending on the energy source? These questions will be analysed in the paper, in order to provide a clear insight into the 4E benefits of different energy sources and their role in improving the energy efficiency of buildings.

2. Model of a newly designed Residential Building

A newly designed residential building in Belgrade [6] was adopted as a building model for the purposes of the 4E improvement analysis. According to the position on the plot, the object is free-standing, with basement, ground and 3 floors, with total number of 10 apartments. The building is designed in the spirit of modern architecture. The base of the object is rectangular. The volume of the object is in the form of a cuboid. The basement and part of the ground floor are excluded from the volume of the building and left as an open-covered space on pillars at the level of the natural terrain. The last floor is designed as an attic. The roof is on two slopes, shaped like two opposing single-pitched roofs.

The total heated area of the residential space in the building is 444.80 m², shown in table 1.

Table 1. Summary of the heated area in the modle building [6]

Apartment No.	Ground floor	1.Floor	2. Floor	Attic
S1	48.20 m ²			
S2	53.50 m ²			
S3		48.20 m ²		
S4		34,50 m ²		
S5		51.10 m ²		
S6			48.20 m ²	
S7			34.50 m ²	
S8			49.80 m ²	
S9				47.50 m ²
S10				29.30 m ²
Total	101.70 m ²	133.80 m ²	132.50 m ²	76.80 m ²
	444.80 m ²			

The building project documentation has been prepared in accordance with the Law on Planning and Construction and the by-laws that regulate in more detail the procedure for the issuing of Energy Performance Certificates (hereinafter referred to as EPC) for buildings, as well as the procedure for issuing construction and use permits.

The Energy Efficiency Elaborate [1] is part of the project documentation and proves that all the required conditions have been met in terms of insulation of the thermal envelope of the building and achieving the energy class.

Table 2 present U values for the elements of the thermal envelope of the building.

Table 2. Summary of the U values for the elements of the thermal envelope of the building

Building element	Mark	U [W/(m ² K)]	U _{max} [W/(m ² K)]	Satisfies YES / NO
Exterior walls	FW1	0,27	0,30	YES
Pitched roof over the heated space	RO	0,10	0,15	YES
Interfloor structure above the open passage	IS1	0,19	0,20	YES
	IS2	0,19	0,20	YES
Construction in contact with the ground	IS3	0,27	0,30	YES
	IS4	0,28	0,30	YES
Exterior Window	W1	1,38	1,50	YES
Balcony doors	BD	1,37	1,50	YES
Front door	FD	1,43	1,60	YES

The energy class of a building is an indicator of the energy performance of a building. It is expressed over the relative value of the annual final energy consumption for heating [%], and represents the percentage ratio of the specific annual heat required for heating to the maximum allowed for a residential building with more than one apartment.

The results obtained by the calculation within the Energy Efficiency Elaborate show that the newly designed building belongs to the energy class "C", where the value of the specific required energy for heating on annual basis is 42 kWh/m²a, and the relative value is 70%, which is shown in Figure 1.

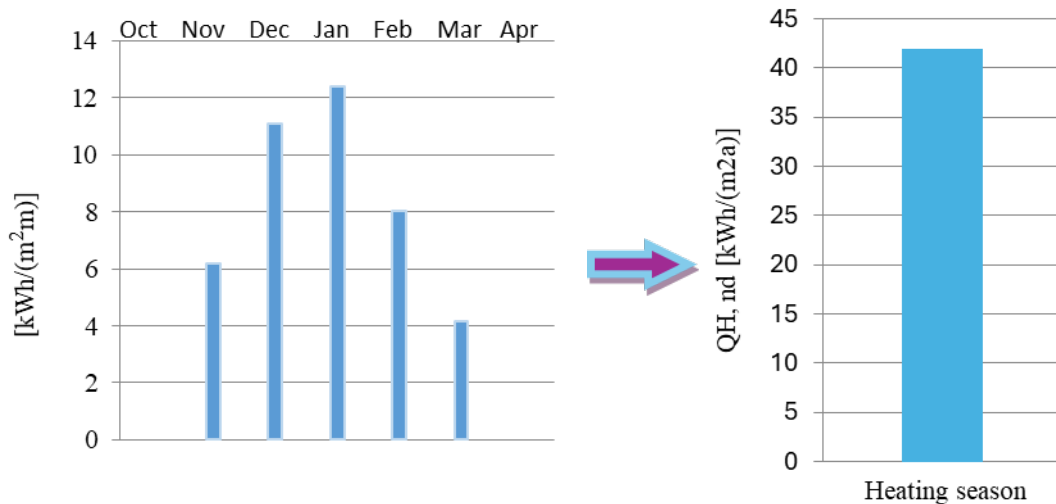


Figure 1. Heat energy required for heating - by month (left) and for the entire heating season (right)

3. Heating and domestic hot water installation and energy sources

The design of the building envisages a central heating system with radiators as heating elements in a hot water temperature regime of 80/60°C, and as a heat source used is the heat exchanger in the heat substation connected to the primary circulation circuit for the delivery of heat from the district heating system (hereinafter referred to as DHS) of the Public Utility Company "Beogradske Elektrane". The preparation of domestic hot water (hereinafter referred to as DHW) is carried out by local storage tanks, which use electric heaters. The above-mentioned case is a common practice in the design of residential buildings in Belgrade and is treated as a basic case in this paper.

From the point of view of primary energy use, system efficiency, environmental impact and energy costs, the following cases are considered in this paper:

1. DHS + local preparation of DHW (basic case);
2. Natural gas as energy carrier for heating and central preparation of DHW;
3. Wood pellets as energy carrier for heating and central preparation of DHW;
4. Air to water heat pump (hereinafter referred to as HP) for heating and local preparation of DHW;
5. Air to water heat pump (HP) for heating and central preparation of DHW.

In the cases with the HP, heating elements are fan coils in a hot water temperature regime of 45/35°C. When calculating the primary energy of a central heating system with a heat pump, it must be taken into account that the heat pump is shouldn't be sized for the design external conditions, as it would then be oversized for most of the heating period and the operating point would not be in the optimal range. For this reason, it is necessary to divide the total heat load of the heating system into base and peak. The base heat load will be covered by an air-to-water heat pump in which the heat source is the outside air. The peak part load will be covered by the supplementary system, i.e. the electric heater. The calculation of the annual primary energy of such a system is done in the following way:

$$E_{prim} = x_B \cdot Q_H \cdot \frac{f_p}{COP} + x_P \cdot Q_H \cdot f_p \quad (1)$$

where:

E_{prim} [kWh] - primary energy for heating,

Q_H [kWh] - delivered heat,

f_p [-] - conversion factor for electricity,

x_B [-] - Base load share,

x_P [-] - Peak load share.

The proportions of base x_B and peak load x_P are determined on the basis of a load diagram (figure 2) that is a function of the length of the heating season [3]. It can be seen that the outside temperature for less than 5% of

the time in the season falls below the limit value of -5°C . Also, the number of days with an outdoor temperature below zero is quite small and amounts to about 40 days, which represents approximately 20% of the duration of the heating season. In order to get a better overview of the operation of the heat pump during the entire heating season, it is necessary to observe the frequency of the outside air temperature values.

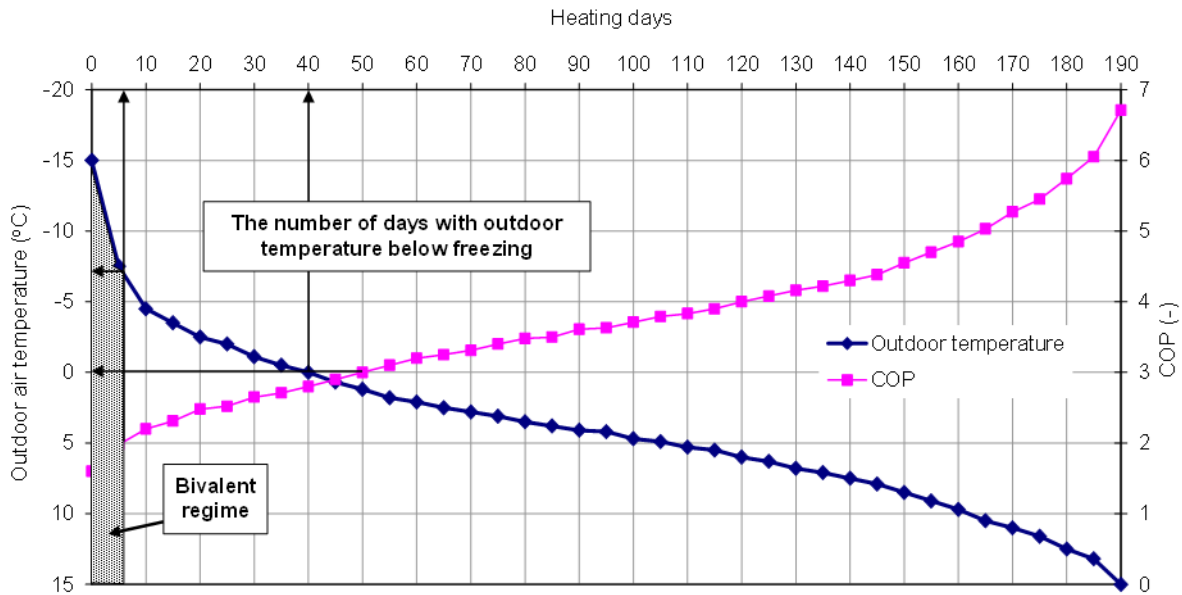


Figure 2. The relationship between the temperature frequency curve and the COP value [4]

It can be seen that the outside temperature for only 8 days in the season drops below the limit value of -7°C , which represents less than 5% of the duration of the heating season. Also, the number of days with an outside temperature below zero is quite small, when the heat pump operates in a mode with unfavorable COP values (lower than 3). On the other hand, an additional heat source should cover less than 10% of the total energy consumption. Therefore, for the purposes of further calculation, the values of the base load $x_B = 90\%$ and the peak $x_P = 10\%$ were used.

The monthly COP values of a heat pump that uses ambient air as a heat source and refrigerant R410a are taken from the literature [5] and used to calculate the primary energy for each month, both for the heating system and when DHW is prepared centrally. The heat pump is used both for heating the building and for heating the domestic hot water in case 5, without additional increase in capacity. A heat pump is primarily focused on maintaining the desired indoor temperature. As long as the water temperature in the central water tank is at the desired value, the system does not switch to DHW heating

The system switches to DHW heating when it is detected that the level of DHW temperature in the tank is below a certain minimum, the control system automatically switches the operation of the heat pump from space heating to domestic hot water heating. Switching the system from space heating mode to domestic hot water heating mode will not affect the temperature in the building and the desired comfort, due to thermal inertia of the building.

Table 3 Monthly COP values of the air to water heat pump for Belgrade weather conditions

	Oct	Nov	Dec	Jan	Feb	Mar	Apr
COP	5,26	3,91	3,2	2,93	3,18	4,03	4,83

4. A comparative analysis of the results obtained

4.1 Analysis of the primary energy needs

Based on the calculations conducted for 5 different cases, one can see that each of the proposed models leads to significant reductions in primary energy (Figure 3). The highest decrease in primary energy occurs with pellet heating compared to the base case, due to the low value of the conversion factor for biomass (pellets). It can also be seen how much influence the method of preparing sanitary hot water has. The very transition from

electro-boilers to other forms of heating has led to a noticeable reduction in primary energy. By switching to a heat pump and using electric boilers to prepare the DHW, we can say that we are reversing the positive impact of the heat pump application on the overall reduction of primary energy, so that this system ultimately has a higher primary energy consumption compared to all other improvement measures. The central preparation of the DHW in combination with the heat pump provides an optimal way to prepare hot water, with minimal energy consumption.

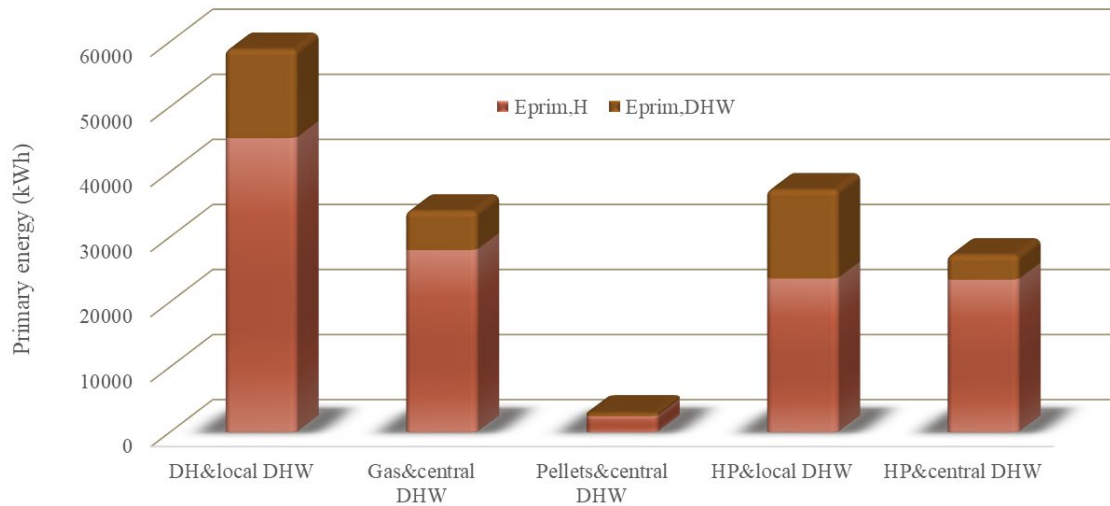


Figure 3. Annual values of primary energy for different cases

4.2 Analysis of the CO₂ emission

A diagram of the annual carbon dioxide emission is shown in Figure 4. From an environmental point of view, the most important thing is to reduce CO₂ emissions. The largest reduction in CO₂ emissions occurs with pellet heating. Pellets are biomass and are considered a renewable energy source. When pellets are burned, CO₂ is emitted, but this CO₂ is considered neutral because trees absorb carbon dioxide from the atmosphere as they grow. Because of this, the overall "carbon footprint" of pellets is smaller than in the other cases.

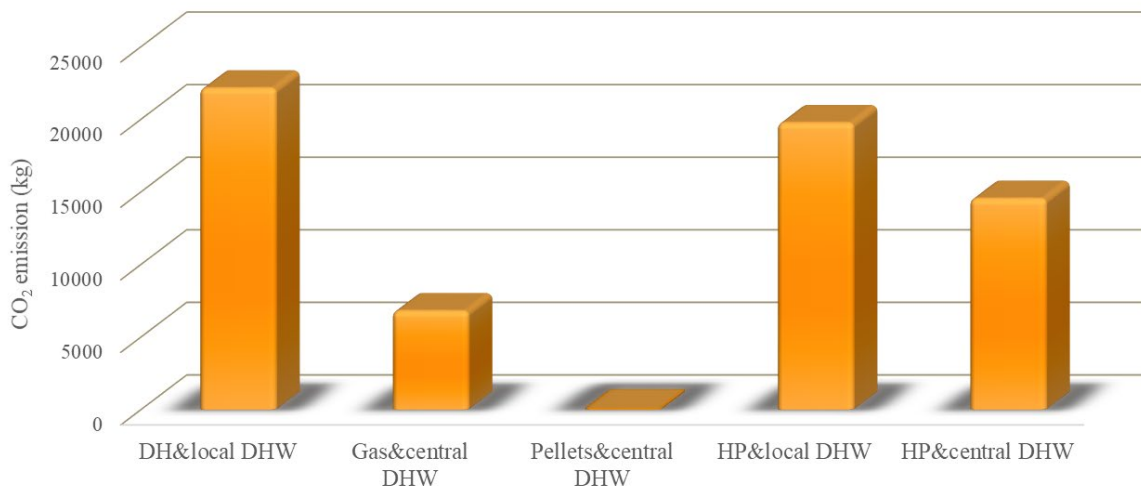


Figure 4. Annual CO₂ emission

The process of burning pellets releases particles (PM₁₀, PM_{2.5}) and other pollutants such as nitrogen oxides (NO_x) and carbon monoxide (CO). Although pellets are more efficient at burning compared to firewood, they still produce a certain amount of smoke. In urban areas, where the ventilation of buildings is limited and where buildings are closely positioned against each other, smoke can be a problem, especially if used in large quantities during the winter. The combustion of pellets produces ash, which must be regularly removed and disposed.

Proper ash disposal can be problematic due to limited waste storage space. Pellet heating requires storage space. Also, as there is a need for the consumption of domestic hot water throughout the year, the preparation outside the heating season would have to be watered using electric water heaters, which would lead to an increase in total primary energy and CO₂ emissions.

Heat pumps have extremely high efficiency, compared to pellet boilers and the pellet itself as an energy source which has lower energy efficiency due to losses in the combustion process, heat pumps can significantly reduce operating costs and energy consumption. There is no local air pollution, no direct emissions of harmful gases or particulate matter. Unlike pellet systems, which require regular refueling, ash cleaning, and boiler maintenance, heat pumps are virtually automated and require very little maintenance. This significantly reduces the effort and time that users have to invest in maintaining the system. Heat pumps enable precise temperature control inside buildings, providing a stable and comfortable indoor climate throughout the year. Heat pumps can be used not only for heating during the winter, but also for cooling during the summer, they can also heat domestic hot water outside the heating season, so there is no need to install electric water heaters, making them a multifunctional system that can meet the needs of users all year round.

4.3 Analysis of the energy cost

A comparative analysis of operating costs was carried out by comparing the costs of a district heating system and the application of a heat pump. Figure 5 shows the monthly bills for heating and domestic hot water with the base case compared to case 5.

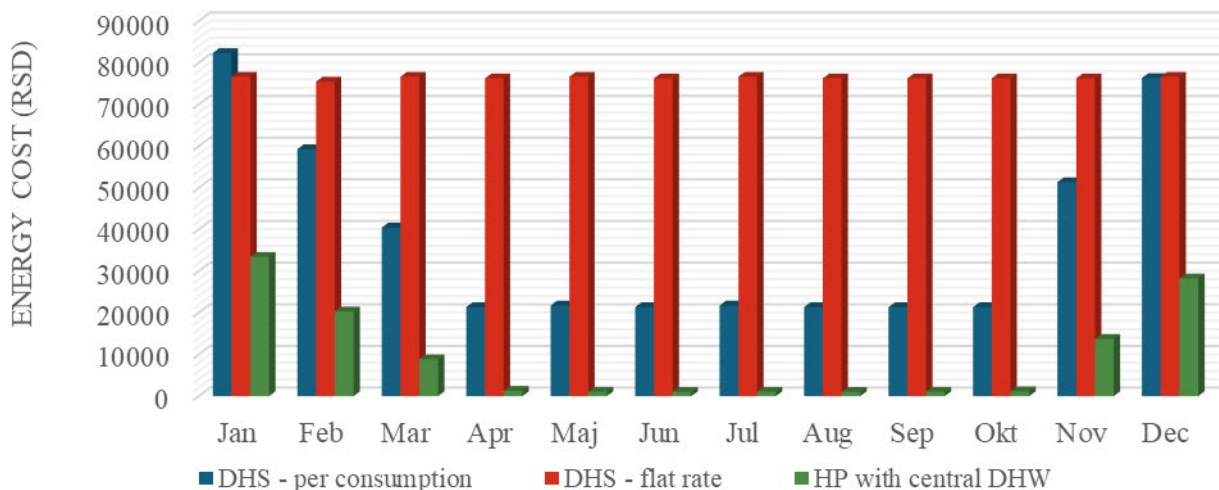


Figure 5. Monthly energy cost

For the calculation of the annual cost of heating when district heating is applied, it is characteristic that there is a difference between charging per consumption and a flat rate payment. Flat rate charging implies that there is a fixed price of heating per square meter of living space when the same monthly fee is allocated throughout the year without the impact of energy consumption on the bill. This type of charging usually has a lot of disadvantages and the tendency is to completely switch to billing by consumption in the future, with certain conditions met. An unfavorable trend in flat rate billing is that consumers can consume energy irrationally because they are not motivated to "save" energy since they receive the same fee every month.

The transition from a flat rate to a charge based on energy consumption would also create an even larger gap between old and new buildings, because modern buildings have better thermal insulation and therefore would have lower heating bills per consumption.

The annual energy supplied for the entire building was also used for billing per consumption. Price data were taken from the price list of PUC "Beogradske elektrane"[7]. When it comes to billing per consumption, there is a fixed and a variable part. The fixed part is charged mainly per square meter of living space throughout the year and is intended for the costs of materials, services, labor, maintenance, depreciation, etc., while the variable part is charged depending on the energy consumed and includes the costs of energy products, current maintenance, own consumption of thermal energy.

In order to show the costs for the preparation of sanitary hot water, which in the observed case is prepared using electric water heaters, it was necessary to show the consumption of electricity throughout the year. It is also necessary to calculate the electricity consumed to drive the heat pump. Data on the price of electricity are available on the official website of the Electric Power Company of Serbia [8]. It is assumed that 1/3 of the time the system works at a lower tariff and 2/3 at a higher tariff.

The use of a heat pump would lead to significant reductions in exploitation compared to district heating, so that the bills for the observed building would be up to 90% lower compared to district heating with a flat rate payment system and 75% compared to district heating with a charge per consumption.

Lower energy consumption and stable costs throughout the year make this system the best choice for users who want to reduce their operating costs and at the same time have high energy efficiency.

5. Conclusion

The analysis presented in the paper showed that a flat rate charge for district heating can lead to irrational use of energy and higher costs compared to charging per consumption. Also, systems that use electric water heaters to prepare DHW are particularly sensitive to tariff zones, where entering a "red" tariff zone can significantly increase costs, making them a less desirable choice.

Taking all this into account, the adoption of a system with a heat pump and central preparation of DHW is recommended as the best option for improving the energy performance of the building and optimizing operating costs in the future.

Energy certification of buildings and the deployment of renewable energy sources are key steps towards achieving a sustainable future. These processes not only contribute to the reduction of energy consumption and operating costs, but also significantly reduce the negative impact on the environment. The introduction of energy efficiency measures and the use of renewable energy sources, such as heat pumps and solar energy, lays the foundations for the construction of energy-sustainable and environmentally friendly buildings that will ensure a better quality of life for future generations.

References

- [1] The Regulation on Energy Efficiency of Buildings, Official Gazette of the Republic of Serbia, No. 61/2011.
- [2] Standard SRPS EN ISO 13790:2010 – Energy performance of buildings – Calculation of energy use for space heating and cooling, 2010.
- [3] Weather data for Typical Meteorology Year for Belgrade, (n.d.).
http://www.eere.energy.gov/buildings/energyplus/weather_data.cfm
- [4] Maja N. Todorovic, Miloš J. Banjac, Tamara S. Bajc and Milan R. Ristanovic: Achieving Savings by Implementation of Efficient Hybrid Heating Systems, Thermal Science, 2019, Vol. 23, Suppl. 5, pp. S1683-S1693
- [5] Todorović M., Grujički, B.: Application of Air to Water Heat Pump in Serbian Climate Conditions, Proceedings of the 17th International symposium on Thermal science and engineering of Serbia, Sokobanja 2015, Serbia, ISBN 978-86-6055-077-6
- [6] ZIA Zoran Ivković Arhitektura d.o.o., Design for the construction of the residential building in Radislava Boškovića street, Belgrade
- [7] Public Utility Company "Beogradske Elektrane" - Price list for heating energy, available on <http://www.beoelektrane.rs/cenovnik/>
- [8] Public Company EPS - Decision on the Regulated Price of Electricity for Guaranteed Supply, Official Gazette of the Republic of Serbia, No. 84/14, 109/15, 105/16, 99/18, 158/20 and 141/22, 2023.

Air-conditioning Control Strategies for an Amphitheater for Different Occupancy Scenarios

Jovan Matić^a, Nataša Nord^b, Maja Todorović^c, Milan Ristanović^d

^a*University of Belgrade – Faculty of Mechanical Engineering, Belgrade, RS, 1017-2022@studenti.mas.bg.ac.rs*

^b*Norwegian University of Science and Technology, Trondheim, NO, natasa.nord@ntnu.no*

^c*University of Belgrade – Faculty of Mechanical Engineering, Belgrade, RS, mtodorovic@mas.bg.ac.rs*

^d*University of Belgrade – Faculty of Mechanical Engineering, Belgrade, RS, mristanovic@mas.bg.ac.rs*

Abstract: This work focuses on the ventilation control strategies employed in Amphitheater A at the Faculty of Mechanical Engineering, University of Belgrade, Serbia with a particular emphasis on occupancy-based control. Given the amphitheater's high occupancy capacity of up to 500 people and variable usage patterns, designing an efficient ventilation system is essential for maintaining optimal indoor air quality and minimizing energy use. The study explored the implementation of Constant Air Volume (CAV) and Variable Air Volume (VAV) systems, with ventilation controlled by mean indoor air temperature and CO₂ concentration. Various occupancy scenarios were simulated using the IDA ICE software to assess how each control strategy maintains indoor air quality under different conditions. The simulation results revealed significant differences in the performance of the CAV and VAV system. The VAV system, particularly when controlled by temperature allowed for precise adjustments of ventilation rates based on real-time usage, reducing energy use during periods of lower occupancy. In contrast, the CAV system, while maintaining constant airflow, showed higher energy use, due to its inability to adjust dynamically to change in occupancy levels. Overall, this paper provides valuable insights into the benefits of demand-controlled ventilation based on occupancy in large spaces.

Keywords: Ventilation Control, Occupancy, Constant Air Volume (CAV), Variable Air Volume (VAV), Energy Efficiency

1. Introduction

This paper aimed to provide a comprehensive analysis for ventilation control strategies and their impact on indoor air quality and thermal comfort in Amphitheater A at the Faculty of Mechanical Engineering, University of Belgrade. The simulations were conducted using IDA ICE 5.0, a software developed by EQUA, which offers advanced capabilities for evaluating the energy performance of buildings [1]. Given the amphitheater's large capacity and varying occupancy rates, maintaining optimal indoor air quality and thermal comfort presents a significant challenge, especially during periods of high usage.

The study focused on the implementation of Constant Air Volume (CAV) and Variable Air Volume (VAV) systems [2], which are commonly used in large public spaces to manage ventilation. Both systems were tested under different control strategies, specifically based on CO₂ levels and mean air temperature. The CO₂ level and the mean air temperature measured in the exhaust duct were used as a signal for these control strategies and they played a critical role in ensuring that air quality and overall comfort of occupants remained within acceptable limits while minimizing energy use.

Integrated Dynamic Analysis of Indoor Climate and Energy (IDA ICE) is a program for study of the indoor climate of individual zones within a building, as well as energy use for the entire building. IDA Indoor Climate and Energy is an extension of the general IDA Simulation Environment. This means that the advanced user can, in principle, simulate any system whatsoever with the aid of the general functionality in the IDA environment.

Through a series of detailed simulations, the study evaluated the indoor air quality and the overall energy performance of the ventilation systems in Amphitheater A. Various occupancy scenarios were considered to mimic the real-life usage patterns of the amphitheater, ranging from partial to full capacity. The results of the study provide valuable insights into how these systems can be optimized to balance energy efficiency with

occupant comfort, offering practical recommendations for improving ventilation strategies in similar large-scale spaces.

2. Methodology

The methodology involved building a detailed model in the simulation software, followed by running simulations to identify which ventilation strategy provided the best results in terms of energy efficiency and thermal comfort for the occupants. In all strategies, the regulation of air temperature was achieved by the cooler supply airflow.

2.1 Data collection

Different information about the Amphitheater A were collected to provide resource for the simulation using IDA ICE software. simulate. The amphitheater was modeled based on precise geometric details and it was designed as a single thermal zone. Internal structures adjacent to the neighboring rooms and external walls exposed to the environment were assigned distinct heat transfer coefficients.

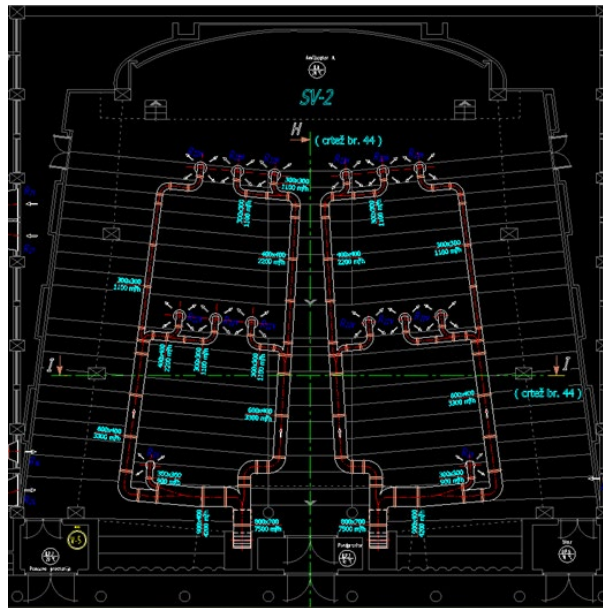


Figure 1. The CAD drawing

The building geometry of the amphitheater as shown in Figure 1. was modeled. The dimensions of the amphitheater were extracted from a vector file, which provided precise geometric data. This file contained detailed information about the layout and structural elements of the space, enabling accurate modeling. These extracted dimensions offer a comprehensive understanding of the amphitheater, ensuring that the simulation faithfully represents the physical characteristics of Amphitheater A. This accuracy allows for more reliable assessments of ventilation strategies and their impact on indoor air quality and energy performance. The placement of anemostats, as shown in Figure 1, was not specified in the software due to the irrelevance of their exact position, as they are automatically added.

To simulate the building construction, the heat transfer properties, U-values, were defined for different surfaces. For instance, for external walls a U-value of 1.45 W/m²K was set, for internal walls and doors 1.3 W/m²K was set, and the for the single-pane glazing windows a U-value of 5.8 W/m²K was set. Although thermal bridges are acknowledged, they were considered insignificant for the heat load calculations and are disregarded in the model. The thermal load was calibrated with the previous design calculation shown in Table 1. These calculations were essential for determining the heat gains and losses within the amphitheater but are outside the scope of this study, which focuses specifically on the ventilation control strategies and their impact on indoor air quality and energy efficiency. The total heat load, the sum of all previously calculated loads, are presented in Table 1. [3]

To simulate an air handling unit (AHU) the following information were used. Figure 2 shows the simulated AHU. The AHU consists of a heat recovery wheel, a mixing box, a heating coil, a cooling coil, and supply and exhaust fans. This configuration allows a 5 K temperature rise where, with variable water flow enabling the

air to reach the setpoint of 16° C. Considering a 1 K temperature rise in the ducts, representing losses, the supply air temperature is set at 17° C. The mixing box maintains a constant fresh air-to-exhaust air ratio of approximately 80%, and its effects on energy use will not be addressed in this paper. The rotary heat exchanger operates at an efficiency of 0.85.

Table 10. The total heat load calculation

Total heat load													
time [h]	8	9	10	11	12	13	14	15	16	17	18	19	20
QOccupancy	35000	35000	35000	35000	35000	35000	35000	35000	35000	35000	35000	35000	35000
QLights	352.224	2054.64	2142.696	2201.4	2260.104	2318.808	2377.512	2406.864	2465.568	2494.92	2524.272	2553.624	2582.976
QRooms	4784	4784	4784	4784	4784	4784	4784	4784	4784	4784	4784	4784	4784
Qequipment	0	0	0	0	0	0	0	0	0	0	0	0	0
Qwalls	3534	3361	3384	3578	3936	4389	4987	5659	6414	7108	7709	8176	8430
Qwindows	218	799	1343	1743	2142	2396	2505	2542	2505	2324	1997	1525	1053
QSolar radiation	2480	2107	1809	1925	2347	2807	3153	3307	3194	2889	2355	1783	1403
sumQ	46368.224	48105.64	48462.696	49231.4	50469.104	51694.808	52806.512	53698.864	54362.568	54599.92	54369.272	53821.624	53252.976

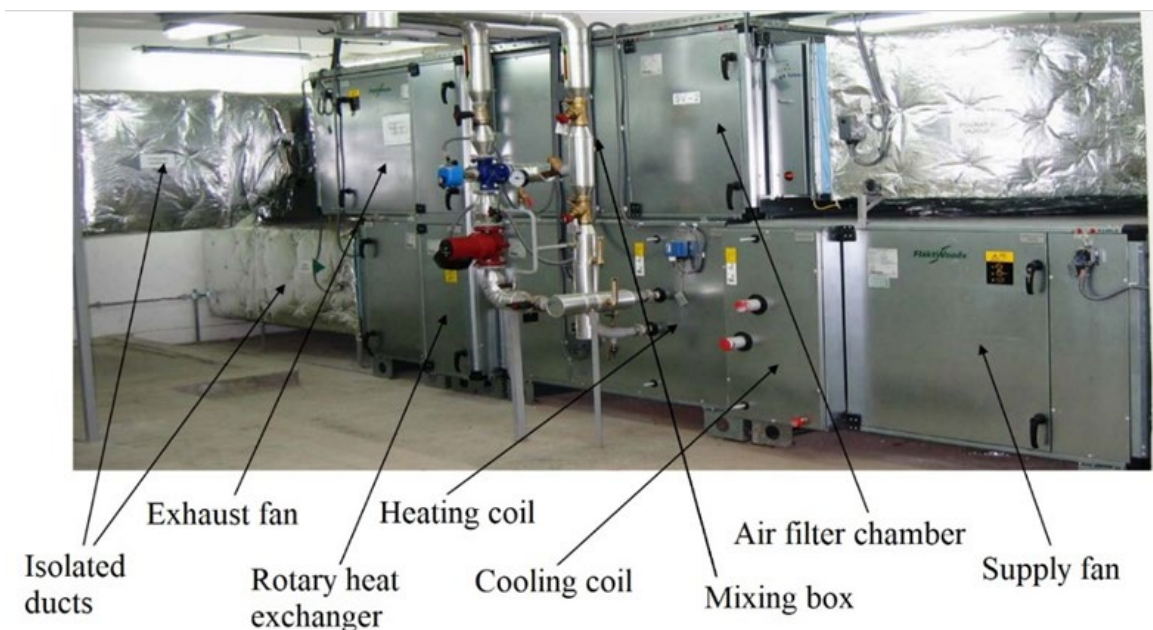


Figure 2. The air handling unit

2.2 Simulation model

In Figure 3, some areas of the zone envelope are shown in white, representing internal structures, while the darker shades indicate external walls and the rooftop.

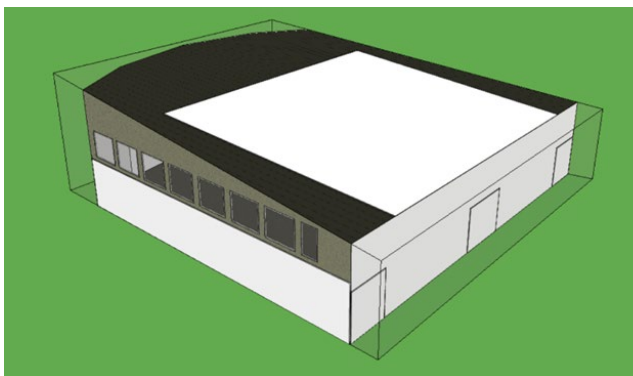


Figure 3. Model of the Amphitheater A



Figure 4. Google maps view on the zone

Figure 4 illustrates the orientation of the building and the amphitheater, which is also incorporated into the IDA ICE simulation software.

Another important aspect of the control algorithm for the model is the collection of setpoint for the ventilation and the limits for the regulating signals:

- Temperature:
 - Min Setpoint for heating controller = 20° C
 - Max Setpoint for cooling controller = 26° C
- Mech. supply air flow
 - Min Minimum flow at VAV. Recommended minimum airflow. = 3 L/sm²
 - Max Maximum flow at VAV. Recommended maximum airflow. = 8 L/sm²
- Mech. return air flow
 - Min Minimum flow at VAV. Recommended minimum airflow. = 3 L/sm²
 - Max Maximum flow at VAV. Recommended maximum airflow. = 8 L/sm²
- Level of carbondioxide
 - Min Level of CO₂ below which maximum VAV flow is kept. Only for VAV with CO₂ controlling. = 400 ppm (vol)
 - Max Level of CO₂ above which maximum VAV flow is kept. Only for VAV with CO₂ controlling. = 1100 ppm (vol)

Setpoints for the model were set accordingly to the calculations. The temperature setpoint refers to the value of the mean air temperature, which will be the parameter regulated during the simulations. The ventilation system is balanced, meaning that the supply and return airflows must be equal. For variable air volume (VAV) ventilation, the minimum airflow volume should be at least 30% of the maximum airflow to ensure that conditioned air effectively reaches the occupants. If the airflow is too slow, it could result in dead zones where fresh air does not circulate properly. The upper airflow limit is set to match the supply airflow used in the CAV ventilation system. The CO₂ level has a maximum limit of 1100 ppm, the threshold where people may start to feel drowsy, while the minimum is set at the ambient level of 400 ppm.

2.3 Scenarios

Occupancy changes are the most unpredictable parameter that must be observed and monitored to ensure that air temperature, indoor air quality, and overall occupant comfort are maintained. Different scenarios were selected to reflect real-life situations that may occur.

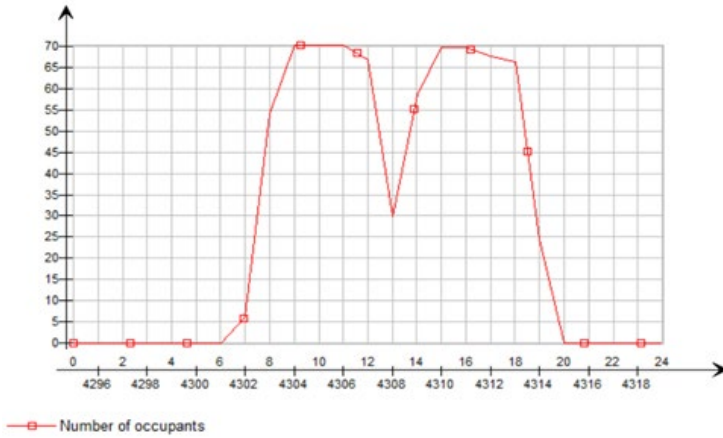
The reference scenario represents the validation of the model. The CAV system is designed for the maximum occupancy of 500 people and the airflow is calculated using the equation:

$$\dot{V} = \frac{Q_{max}}{c_p \rho \Delta t} = \frac{55600}{1010 * 1.2 * 9} = 5 \frac{m^3}{s} \quad (1)$$

This airflow rate also serves as the upper limit for the VAV systems. Maximum occupancy is present in the zone from 08:00 to 19:00 on a warm summer day (June 28th was selected as a representative day, as it exhibits similar temperature variations to the summer project day).

The reference scenario is unlikely to happen, but the following two scenarios represent real-life situations that will occur.

The first scenario models a typical day of lectures, starting on the hour from 08:00 to 19:00, with 15-minute breaks before each class and a longer break from 12:45 to 14:00. The schedule shown on the Figure 5. a) has smoothing applied, so it doesn't have emphasized peaks that would occur because of the frequent breaks.



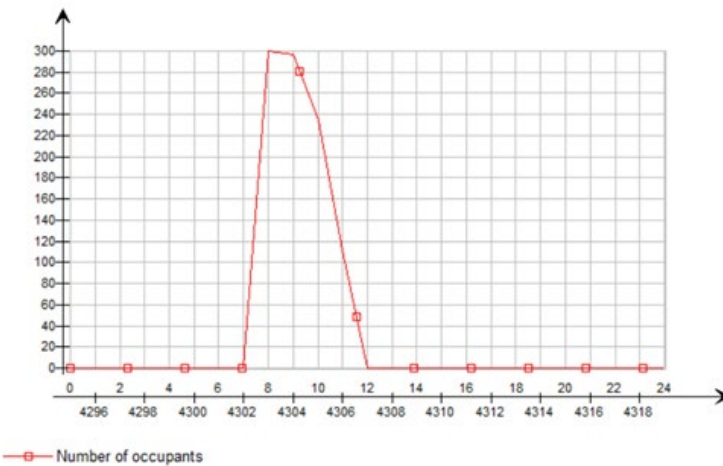
a) Schedule



b) A lecture in the amphitheater

Figure 11. Occupancy during a lecture

The second scenario simulates students taking an exam. The occupancy trend is shown in Figure 6.



a) Schedule



b) An exam in the amphitheater

Figure 6. Occupancy during an exam

Naturally, not all 300 students present at the start of the exam will stay for the entire duration; after 2 hours and 30 minutes about 50% remain, and the rest gradually leave in the following one and a half hours.

3. Results and discussion

The energy balance results for the reference scenario using the CAV model are presented in Figure 7. A constant ventilation flow of $5 \text{ m}^3/\text{s}$ ($18000 \text{ m}^3/\text{h}$ or $8 \text{ L}/\text{sm}^2$) was set for the 625 m^2 floor area and the total volume of the zone around 4500 m^3 . The energy balance of the zone shows that the heat load around 17:00 is approximately 58 kW , while the calculated value is 54.6 kW (see Table 1.), resulting in a 6% error.

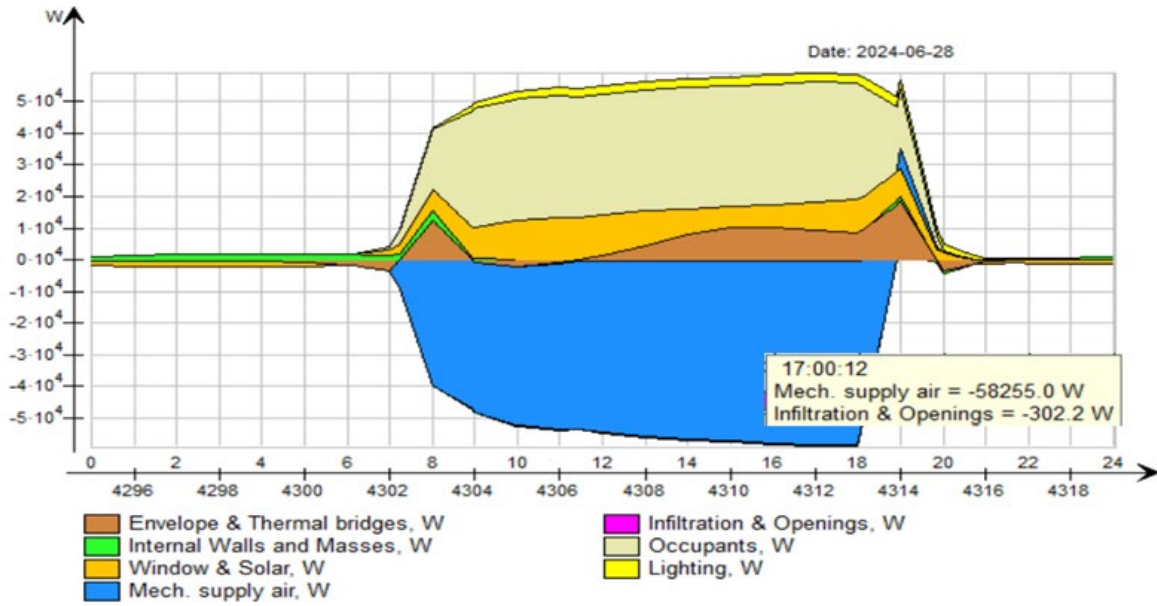


Figure 7. Validation of the model

Based on the desired temperature of 26°C, the mean air temperature remains (Figure 8.) close to this target but does not achieve a perfect match throughout the simulation. Slight fluctuations can be observed.

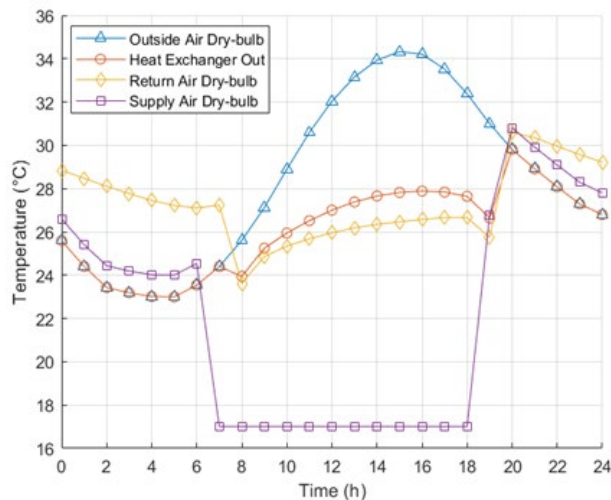


Figure 8. Air temperature for CAV system

A notable dip, or negative peak, in the return air temperature occurs when the ventilation system is activated one hour prior to the start of the occupancy schedule. This early activation helps precondition the space but also contributes to temporary deviations from the setpoint temperature, especially during the initial phase before occupants enter the zone. The constant rise in temperature is caused by the increase in outdoor temperature throughout the day. This is because the CAV system maintains a constant airflow, preventing it from adjusting the cooling rate as needed to compensate for the rising external heat. As a result, the system is unable to adequately control the temperature in the zone beyond that point.

The VAV with temperature control (Figure 9. a) clearly shows that the mean air temperature can be kept at a constant 26°C as it represents the setpoint value, but not all the time.

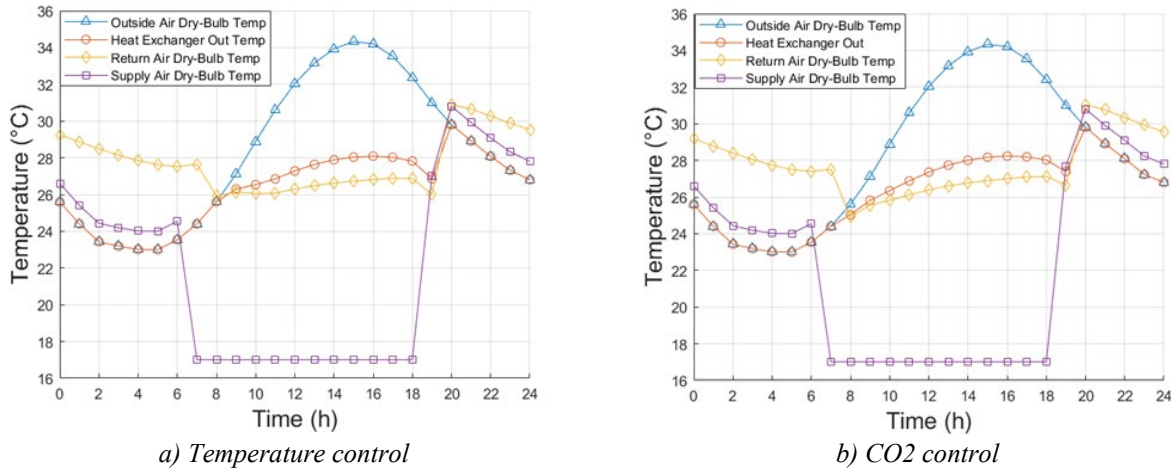


Figure 9. Air temperatures for VAV systems

The setpoint of 26°C is reached around 12.00h, but temperature regulation becomes ineffective afterward because the maximum airflow is reached, so nothing can help in lowering down the air temperature in the zone. In the interval before 12.00h the changing air flow keeps the air temperature at a setpoint value. For the VAV system with CO₂ control (Figure 9. b), it operates similarly to a proportional (P) regulator, where the airflow to the zone is directly proportional to the CO₂ concentration. As the CO₂ level in the zone approaches a steady state, the airflow stabilizes and maintains a constant value, ensuring that indoor air quality is kept within acceptable limits while adjusting ventilation based on real-time occupancy and CO₂ levels (Figure 11.).

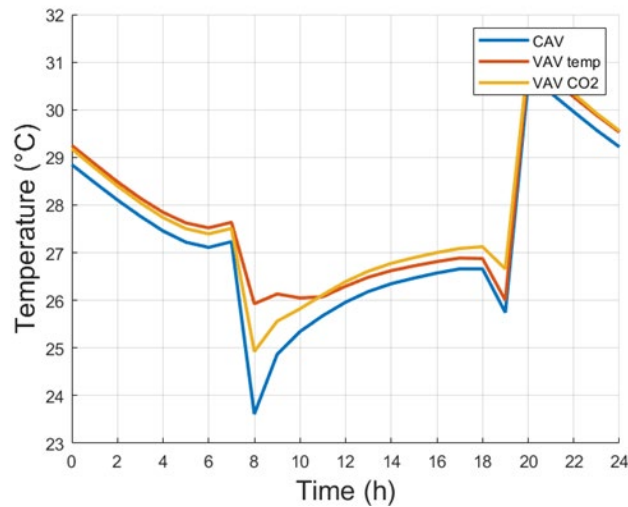


Figure 10.. Comparison of all mean air temperatures for ventilation systems

Comparison of all mean air temperatures for all three ventilation systems is given in the Figure 10. It can be noticed that there isn't very big difference in performance, especially after 12.00h, when the heat loads are bigger than the maximum calculated load in the Table 1.

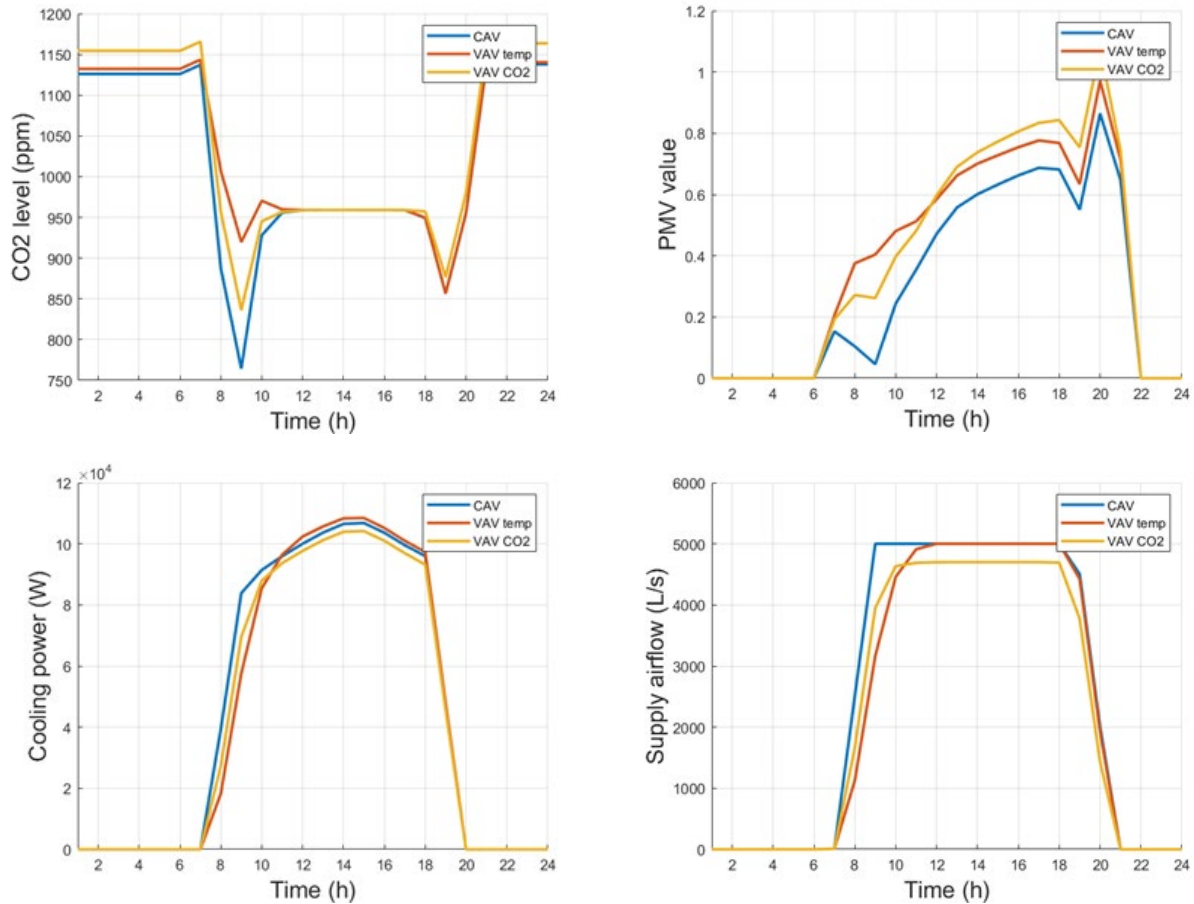


Figure 11. Comparison of additional characteristics for the reference scenario across all types of ventilation systems

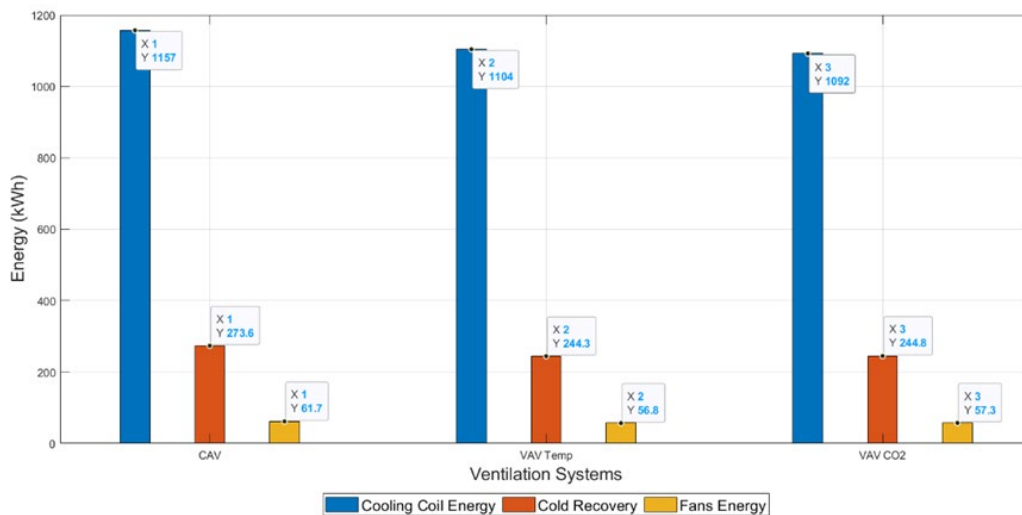


Figure 12. Energy usage for reference scenario

It can be observed in Figure 11. that all characteristics and indices are quite similar, owing to the predictable occupancy schedule and the ventilation system suitable for the reference model. All energy use values are illustrated in Figure 12, and there are no significant differences in energy use among the systems.

3.1 Lectures - scenario

As described in subsection 2.3, "Scenarios," the scenario for the all-day lectures is simulated. Figure 13. clearly illustrates significant differences among the three cases. The CAV system delivers excessive airflow to the zone, resulting in an air temperature around 23°C, which is undesirable, especially during the summer months. The PMV value diagram (Figure 14. b)) indicates that, while people in the room generally feel comfortable, some may feel slightly cooler, which is unwanted, especially in the summer months.

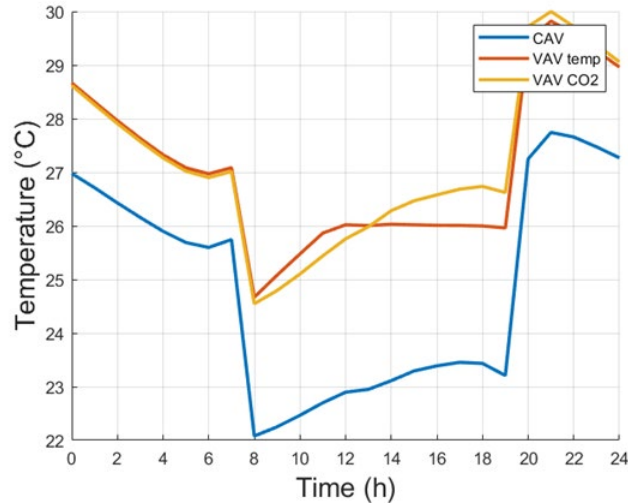


Figure 13. Comparison of mean air temperatures for lectures scenario

In contrast, the VAV system with temperature control effectively pre-cools the air and maintains it at a constant setpoint value. While the VAV system with CO₂ control performs better than the CAV, yet worse than previous VAV system, it in terms of managing air quality, it does not consistently achieve the desired temperature setpoint. Instead, it supplies air in accordance with the CO₂ levels, as depicted in Figure 14 a).

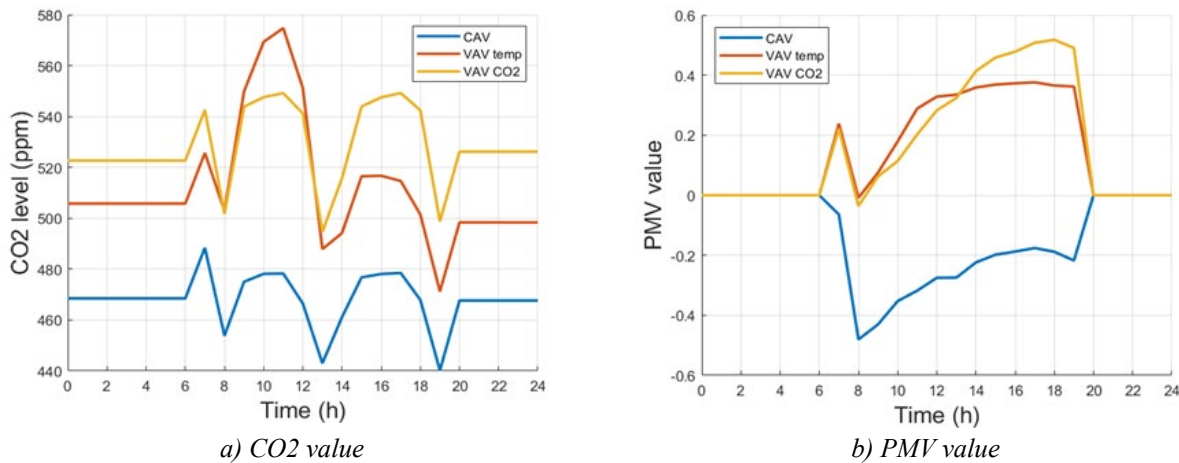


Figure 14. Indices for the lectures scenario

The comparison in the energy usage is huge as shown in Figure 16. About 40% reduction in cooling coil energy is going to make a lot of saving, and the fans are working with 50% less energy. However, when examining the previous diagrams—especially those related to occupant comfort and indoor air quality—it becomes evident that the VAV systems outperform CAV. They deliver comparable results in maintaining comfort and air quality while using considerably less energy, highlighting the advantages of implementing VAV systems in such settings where the occupancy is variable, and even if it is unpredictable.

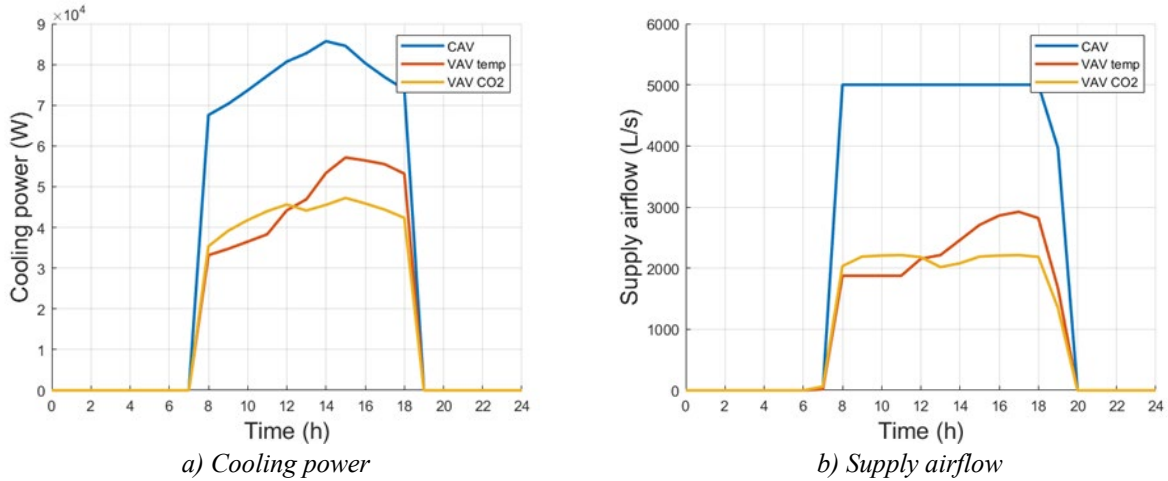


Figure 15. Air flow and cooling power for lectures scenario

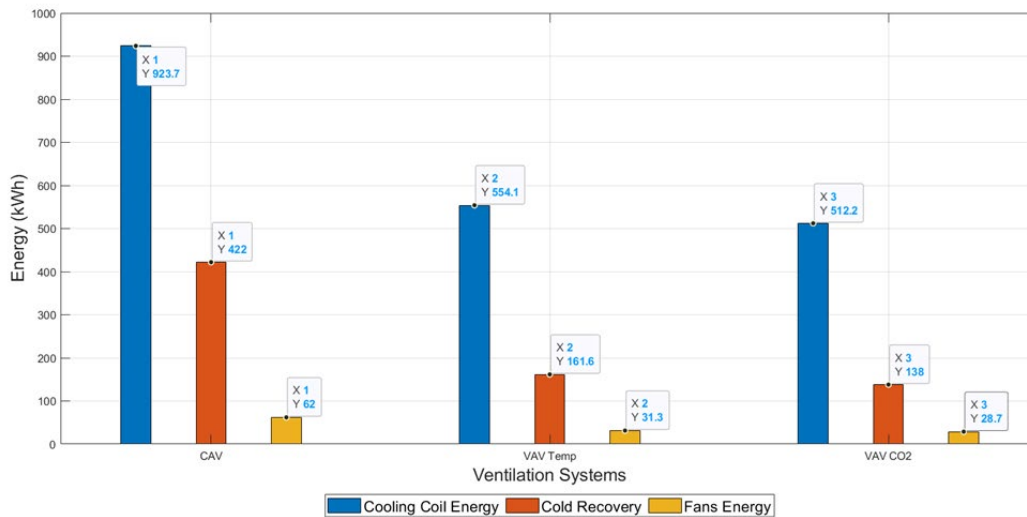


Figure 16. Energy usage for lectures scenario

3.2 Exam – scenario

In the case of shorter-lasting and variable occupancy such as when students are taking an exam, the results are the following:

In this scenario, similar to the previous one, the air temperature (Figure 17.) for both VAV systems hovers around the setpoint value of 26°C. The CO₂ generated by the occupants, along with the heat load they produce, has a comparable impact on the airflow supplied to the zone, which explains why both systems effectively maintain the temperature close to the desired level. The key difference lies in how each system achieves this: the VAV system with CO₂ control indirectly regulates the temperature by adjusting airflow based on CO₂ levels, while the VAV system with temperature control directly manages the temperature to keep it stable.

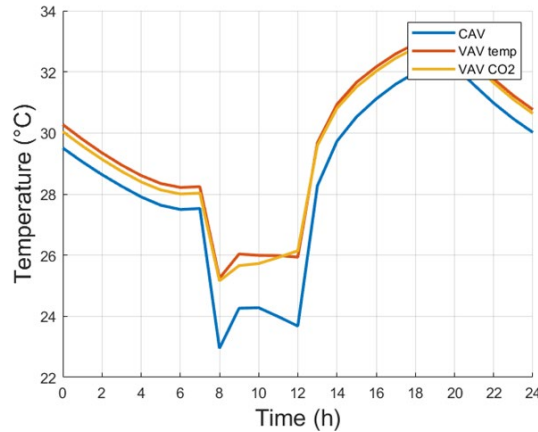


Figure 17. Comparison of mean air temperatures for exam scenario

Referring to Figure 18. b), the CAV model gives the impression of ideal comfort indices, while both VAV systems maintain values around +0.4, which is still well within acceptable comfort levels.

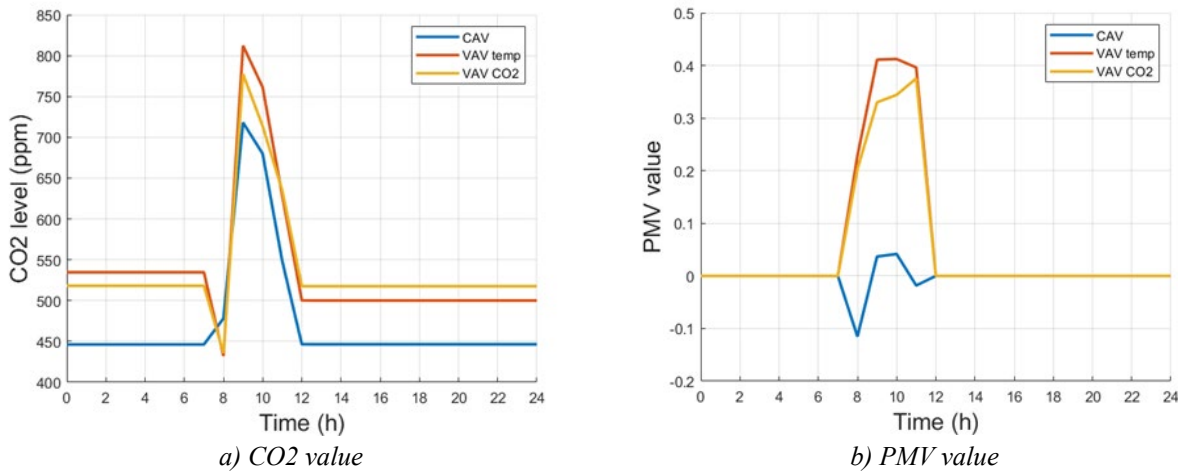


Figure 18. Indices for the exam scenario

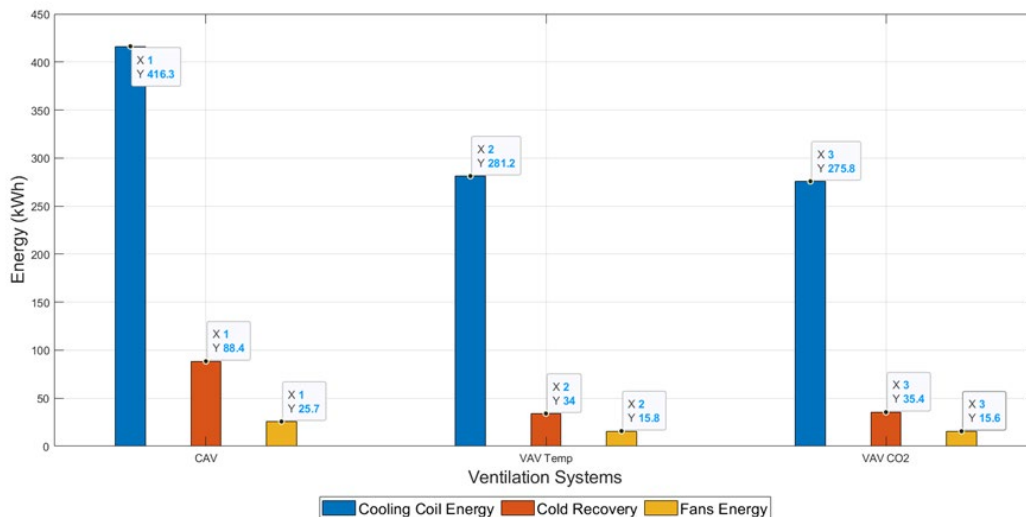


Figure 19. Energy usage for exam scenario

Although the CAV system produces better comfort, this comes at a significant energy cost. The cooling coil energy use increases by approximately 50%, and the energy demanded by the fans rises by about 65%, as

shown in Figure 19. This highlights the trade-off between slightly improved comfort and much higher energy usage.

4. Conclusion

The aim of this study was to demonstrate the benefits of implementing a Variable Air Volume (VAV) ventilation system in large spaces like an amphitheater, where maintaining good indoor air quality is crucial for students. Optimal air quality can help them feel more alert and focused during lectures or when taking exams, while also minimizing costs and reducing the environmental impact by using less energy. This balance between comfort and efficiency highlights the importance of sustainable ventilation strategies in educational settings.

In the reference scenario, the absence of significant differences in energy use indicated that each ventilation system performed comparably under the specified conditions. This finding emphasized the importance of understanding how different systems could achieve similar performance levels, especially in environments with predictable usage patterns. Although this scenario was unlikely to occur in real life, it served to validate the reliability of the simulated model and demonstrated that Constant Air Volume (CAV) ventilation could also be valuable in managing predictable heat loads, but also when properly dimensioned for the specific scenario.

In the first scenario, which simulated professors delivering lectures throughout the day, high energy use occurred when using the Constant Air Volume (CAV) system, as it was dimensioned for the maximum occupancy of 500 people, while only a fraction of that capacity was present. The system's inability to adjust airflow to lower occupancy levels led to unnecessary energy usage, making it inefficient in such cases. The Variable Air Volume (VAV) system with temperature control delivered better results in terms of comfort compared to the VAV system with CO₂ control, although it consumed slightly more energy. The fluctuating occupancy levels caused CO₂ concentrations to vary, effectively simulating a real-life scenario. In this situation, the CAV system was not recommended due to its inefficiency. However, if the CAV system had to be used, implementing a manual ON-OFF control strategy could have helped save energy while still maintaining acceptable performance.

The conclusion for the exam scenario was straightforward: Variable Air Volume (VAV) systems were essential for achieving energy efficiency while delivering desirable results, such as high comfort levels and satisfactory indoor air quality. The outcomes of both VAV systems were quite similar, largely due to their shared working mechanisms for regulating air temperature when occupancy was the primary variable. However, in cases where other loads—such as equipment or lighting—contributed to heat without generating CO₂ (unlike humans), the two systems produced different results. In such situations, a VAV system that controlled both temperature and CO₂ would have been most suitable. The operating principle was that temperature was the primary parameter to be maintained at the setpoint, but if CO₂ levels exceeded predefined limits (with only the upper limit considered), the ventilation rates adjusted accordingly to ensure optimal conditions.

Acknowledgements

The results shown here are the result of research supported by the Ministry of Science, Technological Development and Innovation of the RS under the Agreement on financing the scientific research work of teaching staff at accredited higher education institutions in 2024, no. 451-03-65/2024-03/200105 of February 5, 2024.

References

- [1] EQUA Simulation AB. User Manual. 4.3. Available at: <https://www.equaonline.com/iceuser/pdf/ICE45eng.pdf>. IDA Indoor Climate and Energy, 2013.
- [2] Pacific Northwest National Laboratory. Variable Air Volume (VAV) Systems Operations and Maintenance. url: <https://www.pnnl.gov/projects/om-best-practices/variable-air-volume-systems>
- [3] Matić, J., Ventilation Control Strategies for an Amphitheater with reflection on the Passive House Standard, Master thesis, Belgrade University, Belgrade, Serbia, 2024
- [4] B. Živković at all: „Main Mechanical Project for the Reconstruction of HVAC Installations at the Faculty of Mechanical Engineering in Belgrade”, Belgrade 2003

Application of Reinforced Learning in Intelligent Buildings

Matija Žuža^a, Milan Ristanović^b, Žarko Čojbašić^c, Luka Filipović^d

^aUniversity of Belgrade – Faculty of Mechanical Engineering, Belgrade, RS, zuza.matija@gmail.com

^bUniversity of Belgrade – Faculty of Mechanical Engineering, Belgrade, RS, mtodorovic@mas.bg.ac.rs

^cUniversity of Niš – Faculty of Mechanical Engineering, Niš, RS, zcojba@ni.ac.rs

^dUniversity of Belgrade – Faculty of Mechanical Engineering, Belgrade, RS, lfilipovic@mas.bg.ac.rs

Abstract: This paper aims to present the fundamental mathematical framework necessary for understanding reinforcement learning (RL) and provides an overview of RL algorithms, focusing on their application in Heating, Ventilation, and Air Conditioning (HVAC) systems. Specifically, the paper addresses the use of RL in Building Energy Management Systems (BEMS) to tackle the issue of high CO₂ emissions resulting from HVAC operation, with RL proposed as a potential solution for reducing emissions by enhancing energy efficiency while maintaining occupant comfort. Additionally, the paper highlights the key advantages and limitations of RL when applied in intelligent buildings. The review bridges theoretical concepts and findings from the literature to identify appropriate algorithms for various problems and highlight research gaps. Furthermore, the future research direction of meta-RL is discussed, which trains agents on diverse tasks, offering strong generalization capabilities, making RL algorithms more adaptable to real-world conditions.

Keywords: Reinforcement learning, HVAC, Intelligent Building, BEMS.

1. Introduction

The Heating, Ventilation, and Air Conditioning (HVAC) system plays a crucial role in maintaining a comfortable and safe indoor environment in residential, commercial, and industrial buildings by regulating temperature, air quality, and domestic hot water. In 2022, HVAC systems represented around 16.4% of global energy consumption, with most of this energy sourced from fossil fuels like coal, oil, and natural gas. As a result, these systems are responsible for 14% of the world's operational CO₂ emissions, a significant contributor to global warming.

This heightened awareness of HVAC systems impact on carbon emissions has gained importance with international efforts to combat climate change. The Paris Agreement, established during the 2015 United Nations climate conference, emphasized reducing carbon emissions, prompting many countries to develop building energy regulations. In response, several nations are adopting stringent energy efficiency standards that require the implementation of advanced digital controllers based on MPC and RL algorithms. These modern systems are designed to optimize HVAC performance, reducing energy usage while maintaining occupant comfort.

2. Brief introduction to reinforcement learning

Reinforcement learning (RL) is unsupervised method of machine learning. Key components of reinforcement learning are **agent** and **environment**, see figure 1, where the agent is responsible for taking actions that changes state of the environment. Agent in state s_t in the environment is taking action a_t . When agent took action a_t he changed state of environment, resulting in next state s_{t+1} and gets reward r_{t+1} .

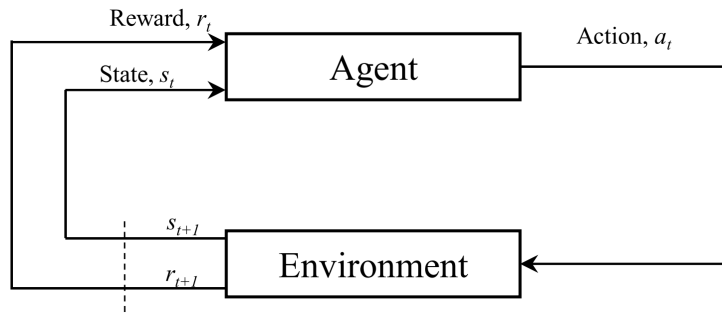


Figure 1. Schematic of Markov Decision Process (MDP)

3. Modeling of environment with RL

Markov decision process (MDP) is the framework for modeling environment with RL. MDP is a tuple $\langle \mathcal{S}, \mathcal{A}, \mathcal{R}, \mathcal{T}, \mathcal{P}, \Omega, \mathcal{O} \rangle$, where:

- \mathcal{S} is a set of states ($s \in \mathcal{S}$),
- \mathcal{A} is a set of actions ($a \in \mathcal{A}$),
- \mathcal{R} is a set of rewards ($r \in \mathcal{R}$),
- \mathcal{T} is a set of time epochs
- \mathcal{P} is **dynamic**/transition model, it represents the probability that agent change state from $s \rightarrow s'$, and getting a reward after he take an action a in every epoch e , which satisfies Markov property (1).

$$\mathcal{P}(s', r | s, a, e) = \mathbb{P}(S_{t+1} = s', R_{t+1} = r | S_t = s, A_t = a, T = e), \quad \forall s', s, a, r \quad (1)$$

- Ω is a set of observations
- \mathcal{O} is probability distribution of getting observation o after taking action a and visiting state s' (2):

$$\mathcal{O}(o | s', a) = \mathbb{P}(O_{t+1} = o | S_{t+1} = s, A_{t+1} = a). \quad (2)$$

3.1 State \mathcal{S}

State is representing current state of the environment, giving enough amount of data used for making decisions. In HVAC systems, states can be divided in two categories:

- **Endogenous** elements, like room temperature, energy consumption, air quality in the term of concentration of CO₂, relative humidity, and actuators can take actions to change the those states like fan speed and airflow rate, system mode (heating, cooling, ventilation), ventilation levels.
- **Exogenous** elements, like outside temperature, energy prices, using schedule (if occupancy in a building or room changes in a way that is not predictable or controlled by the HVAC system), weather conditions (wind speed, solar radiation, precipitation), *etc.*

This division of states allows us to clearly distinguish between the states that can be directly controlled (endogenous states), and those that are beyond influence of agent actions (exogenous states), thereby enabling more precise and efficient optimization of HVAC systems. The HVAC system can control indoor temperature by adjusting its heating or cooling output. This is a key endogenous parameter that the system regulates to maintain occupant comfort. The speed of the HVAC system's fans or the rate of air circulation is a controllable parameter. Adjusting fan speed influences energy consumption and temperature regulation inside the building. The level of fresh air ventilation is often controllable by the HVAC system, affecting both indoor air quality and energy efficiency. The system can adjust this parameter based on current needs, such as when indoor CO₂ levels are high. Variable energy tariffs or real-time electricity prices are typically beyond the control of the system but have a significant impact on how the HVAC system operates, especially if energy cost optimization is part of the goal. Beyond temperature, other weather-related factors like wind speed, solar radiation, and precipitation can affect building thermal dynamics but are not directly controllable by the system.

3.2 Actions \mathcal{A}

Action space in MDP is a set of decisions through which controller can influence the environment. In HVAC systems complexity appears in diversity of components that HVAC system contains, where each one of them has different control mechanisms. Those components are:

- condenser – crucial component in refrigeration cycle of chillers and heat pumps,
- the Source component, such as boilers, chillers, and heat pumps, which creates the heating or cooling medium.
- Air Handling Units – AHUs
- Terminal components, like VAV boxes, fan coils, radiators, which offers localised temperature control.

Action space gives as overview of elements that we control, to obtain thermal comfort.

3.3 Rewards \mathcal{R}

Reward in HVAC systems is defined as weighted sum of following terms:

$$R_t = \alpha R_{comfort_t} + \beta R_{CO_2_t} + \lambda R_{energy_t} + \delta R_{cost_t} + \sigma R_{other_t}, \quad (3)$$

Where it is important to mention that product $\lambda\delta = 0$, which means that negative reward R_{energy_t} and R_{cost_t} can exclusively be derived by one of them. Either from energy consumption (measured in kWh) or the cost of energy consumption (measured in \$/€).

Positive rewards $R_{comfort_t}$ and $R_{CO_2_t}$, are gained if thermal comfort and optimal level of CO2 is obtained. And R_{other_t} specifies other rewards in HVAC systems, *e.g.* indoor relative humidity comfort or the management of the battery state-of-charge, particularly in PV systems (photovoltaic systems), it encourages charging the battery during off-peak hours when electricity prices are lower [7,8].

3.4 Probabilities \mathcal{P} and \mathcal{O}

Those probabilities are essential in defining the MDP. They determine type of environments for our MDP problem, and it is derived as follows:

- partially observable Markov decision processes (POMDP),
- standard stationary Markov decision processes (SSMDP),
- standard non-stationary Markov decision processes (SNSMDP).

POMDP is the situation where the sensors are noisy or where certain aspects of environment are hidden from agent. When environment is not observable problem can be modeled through the definition of Ω and \mathcal{O} while in case of observable environment, which is modeled with equations (4) and (5):

$$\Omega = \mathcal{S}, \quad (4)$$

$$\mathcal{O}(s'|s, a) = \begin{cases} 1, & \text{if } s' = s \\ 0, & \text{otherwise} \end{cases} \quad (5)$$

Standard categories can be defined.

3.5 Environment problem

The main issue in implementing RL algorithms in intelligent buildings is the problem of the environment. The problem appears in lack of implementation of RL algorithms in real buildings. Main cause of the lack of implementation in real buildings is the disturbance of occupants comfort during the training procees, which can be etrimely long. The solution is to use simulations, with tools like EnergyPlus, TRNSYS, Dymola, *etc.*, see figure 2.

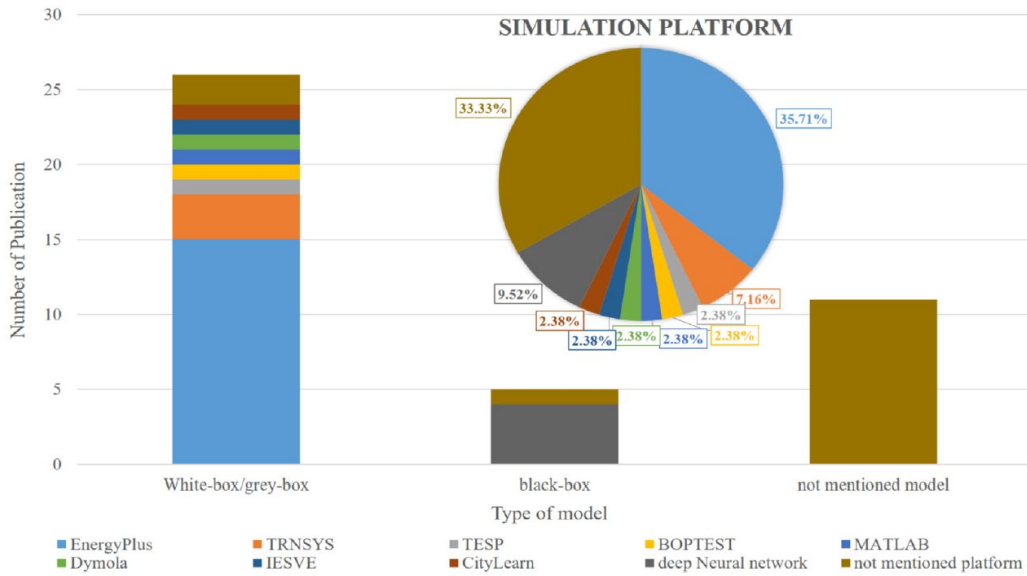


Figure 2. Setup of the simulation platform utilized for training the RL controller.

4. Classification of reinforcement learning algorithms

In each time stamp $t \in \mathbb{N}$ the agent interacts with the environment (building) receiving a state $S_t \in \mathcal{S}$ consisting of endogenous and exogenous HVAC factors, and selects action $A_t \in \mathcal{A}$ accordingly. In the next time step $t + 1$ and as a result of its action A_t , a scalar reward $R_{t+1} \in \mathcal{R}$ is given to the agent that has entered a new state S_{t+1} until the agent reaches the terminal state.

At every time stamp, the agent interacts with the environment according to a function-based policy, which is defined as follows:

Definition 4.1[9] A policy π is a distribution over actions given states,

$$\pi(a|s) = \mathbb{P}(A_t = a | S_t = s), \quad (6)$$

Where the goal is to maximize the **return**, which is defined as:

Definition 4.2[9] The return G_t is a total discounted reward form time-step t .

$$G_t = R_{t+1} + \gamma R_{t+2} + \gamma^2 R_{t+3} = \sum_{k=0}^{\infty} \gamma^k R_{t+k+1} \quad (7)$$

Where $\gamma \in [0,1]$ is discount and represents the present value of future rewards.

In the contest of HVAC control problem, a γ close to 0 is typically used when the goal is to achieve optimal occupant comfort with minimal energy consumption at each timestep. In contrast, a γ close to 1 allows for occasional comfort violations or even excessive energy consumption during some time-steps, in order to achieve long-term energy savings as a final result at the end of the day, month, or year (depending on the episode length).

Categorization of RL algorithms can be show in the terms of model of the environment. According to that algorithms are divided into two categories:

- model-based algorithms
- model-free algorithms

In model-based algorithms, the dynamic of the world (\mathcal{P}) is known. On the other hand, model-free algorithms does not need to know the real-world dynamics \mathcal{P} , and instead approximate the optimal policy trough trail-and-error experiences gathered from the real interaction with the environment in less cases, or with simulations.

Despite previous division, another can be made. The algorithm's strategies for formulating the optimal decision-making policy can be segmented into three principal approaches:

- value-based
- policy-based

– actor-critic

4.1 Value Based

This methodology is applicable in finite action space. The key concept in this approach is the estimation of state-action value function according to a specific policy. The definition of value function for the policy π is as follows:

Definition 4.1.1 [9] The state value function $v_\pi(s)$ of an MDP is the expected return starting from state s , and then following policy π .

$$v_\pi(s) = \mathbb{E}_\pi[G_t | S_t = s] \quad (8)$$

Definition 4.1.2 [9] The state-action value function $q_\pi(s, a)$ of an MDP is the expected return starting from state s , taking action a , and then following policy π .

$$q_\pi(s, a) = \mathbb{E}_\pi[G_t | S_t = s, A_t = a] \quad (9)$$

The Bellman equation for v_π and q_π states that each value has its own fundamental recursive relationship [9].

$$v_\pi(s) = \sum_{a \in \mathcal{A}} \pi(s|a) \sum_{s', r} \mathcal{P}(s', r|s, a) [r + \gamma v_\pi(s')] \quad (10)$$

$$q_\pi(s, a) = \sum_{s', r} \mathcal{P}(s', r|s, a) [r + \gamma v_\pi(s')] \quad (11)$$

$$v_\pi(s) = \sum_{a \in \mathcal{A}} \pi(s|a) q_\pi(s, a) \quad (12)$$

According to the definition, the optimal policy π^* is the policy that maximizes value function or action-value function. Having that in mind, the optimal state-value function and optimal action-value function can be defined.

Definition 4.1.3 [9] The optimal state-value function $v_\pi(s)$ is the maximum value function over all policies.

$$v_*(s) = \max_{\pi} v_\pi(s) \quad (13)$$

Definition 4.1.4 [9] The optimal action-value function $q_\pi(s, a)$ is the maximum action-value function over all policies.

$$q_*(s, a) = \max_{\pi} q_\pi(s, a) \quad (14)$$

According to the equations (10), (11), (13), (14) Bellman optimality equations can be defined as:

$$v_*(s) = \max_{a \in \mathcal{A}} \sum_{s', r} \mathcal{P}(s', r|s, a) [r + \gamma v_*(s')] \quad (15)$$

$$q_*(s, a) = \sum_{s', r} \mathcal{P}(s', r|s, a) [r + \gamma \max_{a' \in \mathcal{A}} q_*(s', a')] \quad (16)$$

It is not requisite for optimal policy to be singular. Rather, a general formulation for any optimal policy, denoted as π_* can be stated as follows:

$$\pi_*: \mathcal{S} \times \mathcal{A} \rightarrow [0,1], (s, a) \rightarrow \pi_*(s, a) = 0 \text{ if } a \notin \Sigma(s) \quad (17)$$

$$\Sigma(s) = \arg \max_{a \in \mathcal{A}} \sum_{s', r} \mathcal{P}(s', r|s, a) [r + \gamma v_*(s')] = \arg \max_{a \in \mathcal{A}} q_*(s, a) \quad (18)$$

The key elements for devising an optimal policy are v_* and q_* .

All value-based RL algorithms employs the framework of generalized policy iteration (GPI) to ascertain v_* (or q_*) and π_* . This technique intertwines two key processes, (1) the policy improvement, where the policy is iteratively refined based on the current value/action-value function:

$$\pi'(s) = \arg \max_a q_\pi(s, a) \forall s \Rightarrow v_\pi(s) \leq q_\pi(s, \pi'(s)) \forall s \Rightarrow v_\pi(s) \leq v_{\pi'}(s) \forall s \Rightarrow \pi \leq \pi' \quad (19)$$

And (2) the policy evaluation, where the approximated value/action-value function incrementally aligns with its true value, whether wholly (in dynamic programming case) or in part (Monte-Carlo and TD(0)), for the

designated policy. Upon convergence of these evaluation and improvement phases, both the value/action-value function and the policy are deemed optimal.

In a value-based RL framework, the approximation methods for v_* (or q_*) can be classified into three primary categories, each with its unique frequency of updates in GPI. These three categories are:

- Dynamic programming,
- Monte Carlo methods,
- Temporal-difference (TD) learning.

Dynamic programming approach is limited due to necessity of having the model of the environment which is usually not the case. Dynamic programming algorithm is shown in Algorithm 1. Within dynamic programming two algorithms are essential:

- Value iteration,
- Policy iteration.

Algorithm 1 Value iteration

- 1: **Parameter:** a small threshold $\theta > 0$
 - 2: **Initialize:** $v(s) \forall s \in \mathcal{S}^+$ arbitrarily except $V(\text{terminal}) = 0$
 - 3: **repeat**
 - 4: $\Delta \leftarrow 0$
 - 5: **for** each $s \in \mathcal{S}$ **do**
 - 6: $v \leftarrow V(s)$
 - 7: $V(s) \leftarrow \max_a \sum_{s',r} \mathcal{P}(s', r|s, a)[r + \gamma V(s')]$
 - 8: $\Delta \leftarrow \max(\Delta, |v - V(s)|)$
 - 9: **end for**
 - 10: **until** $\Delta < \theta$
 - 11: **Output:** deterministic policy π such that:

$$\pi(s) = \arg \max_a \sum_{s',r} \mathcal{P}(s', r|s, a)[r + \gamma V(s')]$$
-

Monte Carlo MC is model-free algorithm; it prioritizes the approximation of action-value function Q over the state-value function V during policy evaluation. The policy evaluation does not entail rigorous approximation of Q like dynamic programming does for V . For policy improvement, an ε -greedy strategy is employed to ensure comprehensive exploration of states throughout environmental interaction. One of the important algorithms, GLIE Monte-Carlo Control (GLIE MC) (Algorithm 2) samples episodes and updates the visitation count $N(s_t, a_t)$ for each state–action pair and adjusts the action-value function Q based on the incremental returns G_t ; it then progressively refines the policy using an ε -greedy approach that becomes less exploratory as the number of encounters increases. As more episodes are processed, the estimated Q converges to the optimal action-value function Q_* under the optimal policy π_* .

Various components of HVAC system leads to huge state and action spaces, which represent a challenge for storing action-value for every state in conventional lookup table. Also, ensuring that policy explores every state sufficient number of times require large number of episodes. To address this problem, function approximations can be employed. Types of function approximations are linear approximators, which are rarely used, and nonlinear approximators like neural networks (NN). NN is trying to estimate action-value function for each state-action pair, denoted as $\hat{Q}(s, a; w)$, where NN is parametrized by w . Those weights are adjusted via stochastic gradient descent (SGA) to minimize a designed loss function L :

$$L(w) = \mathbb{E}_\pi \left[\left(G_t - \hat{Q}(s, a; w) \right)^2 \right] \quad (20)$$

$$\Delta w = \frac{1}{2} \alpha \nabla_w L(w) = \alpha \left(G_t - \hat{Q}(s, a; w) \right) \nabla_w \hat{Q}(s, a; w) \quad (21)$$

Algorithm 2 GLIE MC

- 1: Sample k^{th} episode using $\pi: \{s_1, a_1, r_2, \dots, s_T\} \sim \pi$
- 2: **Initialize:** $v(s) \forall s \in \mathcal{S}^+$ arbitrarily except $V(\text{terminal}) = 0$
- 3: **for** each $s \in \mathcal{S}$ **do**
- 4: $N(s_t, a_t) \leftarrow N(s_t, a_t) + 1$
- 5: $Q(s_t, a_t) \leftarrow Q(s_t, a_t) + \frac{1}{N(s_t, a_t)} (G_t - Q(s_t, a_t))$
- 6: **end for**
- 7: Improve policy based on new action-value function:

$$\varepsilon \leftarrow \frac{1}{k}$$

$$\pi \leftarrow \text{greedy}(Q)$$

Temporal-difference, TD(0) is a model free algorithm. Similar to Monte Carlo methods, it focuses on approximating the action-value function Q , and it uses ε – greedy tactic for policy improvement. TD methods does not wait until the end of the episode to adjust the policy, this approach operates on a one-step basis for evaluation and improvement. Temporal difference methods use $r + \gamma Q(s', a')$ as a target, opposite to G_t in MC methods. Two most popular algorithms are:

- State, action, reward, next state, next action (SARSA),
- Q-learning.

SARSA is on-policy algorithm, which means that the agent is choosing next action a' according to the same exploration-exploitation tradeoff the agent is using (e.g. ε -greedy), the policy is improving gradually as agent explores the environment, which benefits with safe learning and simplicity as well as easy implementation, but convergence is slow and it is policy-dependent.

Q-learning is off-policy algorithm, which means that the agent is choosing next action a' according to the some other policy, called behavioral policy μ . In Q-Learning, the algorithm updates the Q-value based on the best possible action at the next state even if the agent did not take that action. It is exploration independent, which implies that Q-learning is less sensitive to exploration-exploitation tradeoff. One disadvantage of this algorithm is exploration challenge, improper exploration strategies can lead to suboptimal results, and the other is instability with function approximation. Ref. [2] employs a DQN algorithm to regulate chilled water temperature setpoints, aiming to minimize energy consumption while preserving thermal comfort in a single zone. Consequently, this approach exhibited improved performance in energy efficiency and control efficacy, surpassing rule-based control and traditional RL, and closely matching the performance of MPC.

Algorithm 3 SARSA

- 1: **Initialize:** $Q(s, a), \forall s \in \mathcal{S}, a \in \mathcal{A}$ arbitrarily, and $Q(\text{terminal- state}, \cdot) = 0$
- 2: **for** each episode **do**
- 3: Initialize s
- 4: Chose a from s using policy derived from Q (e.g., ε - greedy)
- 5: **repeat** for each step of episode
- 6: Take action a , observe r, s'
- 7: Chose a' from s' using policy derived form Q (e.g., ε - greedy)
- 8: $Q(s, a) \leftarrow Q(s, a) + \alpha (r + \gamma Q(s', a') - Q(s, a))$
- 9: $s \leftarrow s'; a \leftarrow a';$
- 10: **until** s is terminal
- 11: **end for**

4.2 Policy Based

In this methodology, policy is optimized directly to ensure reward improvement and training stability, it bypasses the need of value-function estimation. In this approach policy is parametrized with parameter θ , and generally is a NN with weights θ . Here the objective is to train neural policy π_θ , with data gathered from environment, where parameter θ is update through stochastic gradient ascent (SGA) to find the maximum of objective function J :

$$J(\theta) = \sum_s d^{\pi_\theta}(s) \sum_a \pi_\theta(s, a) r_s^a \quad (22)$$

$$\Delta\theta = \alpha \nabla_\theta J(\theta) = \alpha \nabla_\theta \log \pi_\theta(s_t, a_t) v_t \quad (23)$$

Where d^{π_θ} is stationary distribution of Markov chain for π_θ , and v_t is G_t for episodic cases or r_t for step updates.

Algorithm 4 REINFORCE

- 1: **Initialize:** policy parameters θ arbitrarily
 - 2: **for** each episode $\{s_1, a_1, r_2, \dots, s_{T-1}, a_{T-1}, r_T\} \sim \pi_\theta$ **do**
 - 3: **for** $t = 1$ to $T - 1$ **do**
 - 4: $\theta \leftarrow \theta + \alpha \nabla_\theta \log \pi_\theta(s_t, a_t) G_t$
 - 5: **end for**
 - 6: **end for**
 - 7: **return** θ
-

4.3 Actor-Critic

The Actor-Critic method is a popular reinforcement learning (RL) algorithm that combines elements of both policy-based and value-based approaches. In the context of HVAC systems, this method can be used to optimize the control of heating, ventilation, and air conditioning by learning both how to act (through a policy) and how to evaluate those actions (through a value function). It is particularly useful for complex, continuous control problems like HVAC, where there may be many states and actions, and efficient exploration is required. This method consists of two components:

- Actor: actor decides what action to take in a given state. It is responsible for the policy $\pi(s, a)$, which maps states to the probability distribution over actions. In continuous environments, the policy can directly output the action (such as adjusting the temperature setpoint or fan speed in HVAC systems).
- Critic: The critic estimates the value of the state (or state-action pair) by evaluating how good it is to be in a particular state, following the current policy. This is done through a value function $V(s)$ or an action-value function $Q(s, a)$. The critic provides feedback to the actor on how good its actions are and helps guide policy updates.

The actor uses the critic's feedback to improve the policy over time, and the critic evaluates the policy to ensure it improves based on the rewards received from the environment.

Actor-Critic directly parametrizes policy, employing the approximate gradient theorem (24)

$$\nabla_\theta J(\theta) = \mathbb{E}_{\pi_\theta} [\nabla_\theta \log \pi_\theta(s, a) \hat{Q}(s, a; w)] \quad (24)$$

This strategy seeks the optimal policy by training the neural policy, π_θ , and the critic network $\hat{Q}(\cdot, \cdot, w)$ using data collected by the interaction with the environment. Parameter optimization are implemented in two phases:

- Parameters θ are fine-tuned with SGA to increase objective function J ,
- Parameters w are tuned via SGD to decrease loss function L .

$$\Delta\theta = \alpha \nabla_\theta \log \pi_\theta(s, a) \hat{Q}(s, a; w) \quad (25)$$

$$\Delta w = \alpha \left(r + \gamma \hat{Q}(s', a'; w) - \hat{Q}(s, a; w) \right) \nabla_w \hat{Q}(s, a; w) \quad (26)$$

4.4 Overview of implemented algorithms

Figure 3 show that the current trend in literature is the adoption of value-based approaches. The most popular algorithm is DQN, which implies of the need for algorithms that can deal with large or continuous state spaces. Actor-Critic algorithm are also widely used, due to need to control continuous state/action spaces. The leading algorithms in this method are deep deterministic policy gradient (DDPG) and soft actor critic (SAC). The policy-based algorithm are not in use in current literature. It is important to note that model-free algorithms are widely in use (87.75%) in contrast to model-based algorithms (12.25%). This is due to large state/action spaces, and exogenous state parameters that model environment.

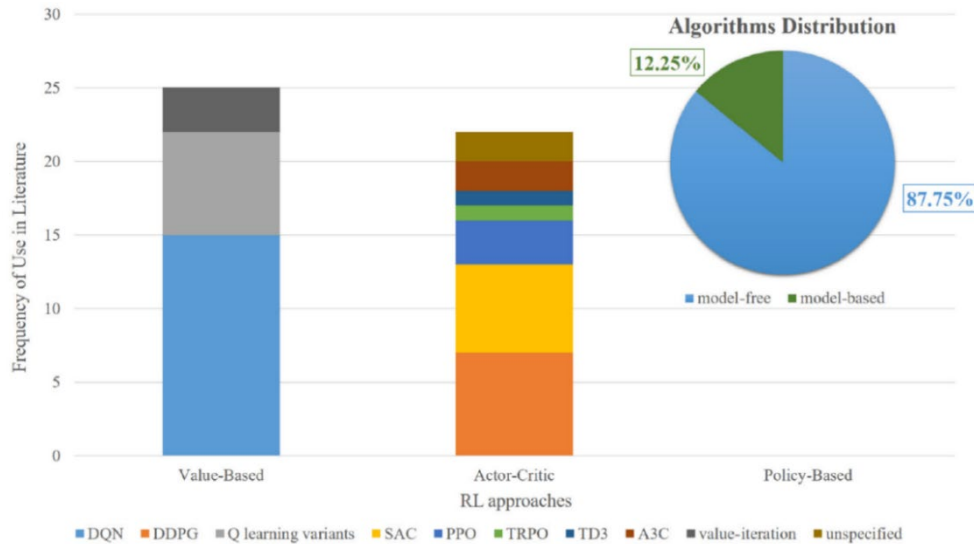


Figure 3. Usage of algorithm in current literature for HVAC control.

5. Conclusion

This paper shows basic concepts of reinforcement learning and presents the key challenges on the way of implementing RL algorithms to the real world problems. It gives a brief overview of current algorithm implementation in HVAC systems. Incorporating RL controllers into HVAC systems has proven to significantly enhance energy efficiency and cost reduction, outperforming traditional control methods. Particularly, RL controllers exhibit a reduction in energy usage by 27%–30% compared to rule-based controllers, while still maintaining optimal thermal comfort levels [2]. They also offer considerable cost savings, up to 39.6% over standard controllers, while preserving thermal comfort [3]. Alongside heating energy savings ranging from 5%–12%, with the added benefit of improved interior climate control [4]. Additionally, these controllers achieve 8% energy savings relative to rule-based algorithms, ensuring comfort for both indoor environments and domestic hot water [5]. Furthermore, RL controllers are effective in reducing electricity costs and peak energy demands by 23% in comparison to manually designed rule-based systems, without compromising on thermal comfort [6]. Theoretically, agents trained with (DQN, QPG, SAC, etc.) algorithms may not perform well during real deployment due to the change in the environment model to SNSMDP. The only solution to fix the disturbance in the agent's performance is to undergo periodic extensive retraining, which is computationally expensive. In future works, the focus should be on addressing the high computational cost associated with retraining the RL agent before it is deployed in an actual building for HVAC system control, which is modeled as an SNSMDP. In this context, the use of a meta-RL technique is proposed. This approach has been theoretically proven to facilitate rapid adaptation to the disturbances generated by the nature of SNSMDP during real-world deployment. Meta-RL can improve adaptability and reduce the computational cost associated with retraining. Future research should focus on applying Meta-RL to HVAC system control.

Acknowledgements

The results shown here are the result of research supported by the Ministry of Science, Technological Development and Innovation of the RS under the Agreement on financing the scientific research work of teaching staff at accredited higher education institutions in 2024, no. 451-03-65/2024-03/200105 of February 5, 2024.

References

- [1] K. He, Q. Fu, Y. Lu, Y. Wang, J. Luo, H. Wu, J. Chen, Predictive control optimization of chiller plants based on deep reinforcement learning, *J. Build. Eng.* (ISSN: 2352-7102) 76 (2023) 107158
- [2] Z. Zou, X. Yu, S. Ergan, Towards optimal control of air handling units using deep reinforcement learning and recurrent neural network, *Build. Environ.* 168 (2020) 106535.
- [3] S. Touzani, A.K. Prakash, Z. Wang, S. Agarwal, M. Pritoni, M. Kiran, R. Brown, J. Granderson, Controlling distributed energy resources via deep reinforcement learning for load flexibility and energy efficiency, *Appl. Energy* 304 (2021) 117733.
- [4] S. Brandi, M.S. Piscitelli, M. Martellacci, A. Capozzoli, Deep reinforcement learning to optimise indoor temperature control and heating energy consumption in buildings, *Energy Build.* 224 (2020) 110225.
- [5] P. Lissa, C. Deane, M. Schukat, F. Seri, M. Keane, E. Barrett, Deep reinforcement learning for home energy management system control, *Energy AI* 3 (2021) 100043.
- [6] G. Pinto, D. Deltetto, A. Capozzoli, Data-driven district energy management with surrogate models and deep reinforcement learning, *Appl. Energy* 304 (2021) 117642.
- [7] S. Touzani, A.K. Prakash, Z. Wang, S. Agarwal, M. Pritoni, M. Kiran, R. Brown, J. Granderson, Controlling distributed energy resources via deep reinforcement learning for load flexibility and energy efficiency, *Appl. Energy* 304 (2021) 117733.
- [8] L. Yu, W. Xie, D. Xie, Y. Zou, D. Zhang, Z. Sun, L. Zhang, Y. Zhang, T. Jiang, Deep reinforcement learning for smart home energy management, *IEEE Internet Things J.* 7 (4) (2020) 2751–2762, <http://dx.doi.org/10.1109/JIOT.2019.2957289>.
- [9] D. Silver. Lecture 2: Markov decision processes. UCL. Retrieved from www0.cs.ucl.ac.uk/staff/d.silver/web/Teaching/files/MDP.pdf, 2015.

Usage Effect of the Selective Absorption Façade Instead an Insulation Layer and Influence on Energy Performance of the Family House

*Nebojša Lukić^a, Đorđe Radisavljević^b, Aleksandar Nešović^c, Novak Nikolić^d,
Novak Popović^d*

^aUniversity of Kragujevac, Faculty of Engineering, Kragujevac, RS, lukic@kg.ac.rs

^bUniversity of Kragujevac, Faculty of Engineering, Kragujevac, RS, djordje.ara@gmail.com

^cUniversity of Kragujevac, Faculty of Engineering, Kragujevac, RS, aca.nesovic@gmail.com

^dUniversity of Kragujevac, Faculty of Engineering, Kragujevac, RS, novak.nikolic@kg.ac.rs

^dUniversity of Kragujevac, Faculty of Engineering, Kragujevac, RS, novakpopovickg4@gmail.com

Abstract: In this paper the usage influence of the selective absorption façade instead an insulation layer on heating energy consumption of the family house is simulated. Using EnergyPlus software on the model of existing family house the defined influence has been analyzed. On selected exterior walls (especially southern) the insulation layers were removed and replaced with the selective absorption façade. This procedure resulted in the increased radiation gains as well as increased convection losses. Sixteen simulation scenarios were carried out. Results of these simulations were shown that a lack of insulation layer on southern façade can be compensated by application of the selective absorption surface.

Keywords: Energy consumption, Selective façade, Residential house.

1. Introduction

Decades ago the residential buildings in Europe are very important consumers of the final energy. This share constantly moves around 30% (according current data for EU 28%, [1]). Due to its geographical position and climatic conditions the biggest part of this final energy is spent on heating demands of the residential building spaces in cold months, which amounts 60-70% (for EU this share is 64.4%, [2]). Therefore, it is not needed to emphasize an importance of the energy saving measures in heating sector. Regarding transmission heat energy losses of the residential buildings, the thermal characteristics of the outer walls, windows and doors as well as applied insulation have the most important influence on heating energy consumption. With increasing of insulation layer the building heating losses by conduction and convection are certainly reduced but also possibilities to use heating gains of the winter solar radiation on vertical outer walls. The question arises whether it is possible to reduce heating losses by decreasing insulation layer or even removing this layer especially from south outer wall. Using a simple dynamical model of the building it was shown that under defined weather conditions the heating energy savings can be achieved by removing insulation layer from south outer wall of the residential house, [3]. This effect was weakly expressed due to the stripped façade retains a high thermal emittance (long-wave infrared radiation).

Among other improvements, development of the solar collector systems has brought a new technology of the selective surfaces with high solar absorptance and low thermal emittance. A thin absorber coating in the solar collector is protected from the whether influence and damage by a glass cover. Similar case can be found at passive solar systems especially contemporary design of Trombe wall, where the selective surfaces are applied, [4]. However, such selective coatings can be applied on outer walls of the residential and other buildings. In [5] for defined simulation cases the heating energy saving of 17% is achieved by using the mineral particles coating on outer thermal insulation. In [6] the thermal solar façade with transparent insulation and selective absorbers. Thermal insulation with high reflectance selective coating achieved better heating energy savings than classic one without selective coating, [7]. Façade with high solar reflectance can be used to reduce energy consumption for cooling in summer months, [8]. Selective coatings can be applied on inner walls in order to save heating energy, [9]. In [10] the measured energy consumption data of the residential building with a selective façade is compared with simulation one. After simulation model adjustment the simulations of well and poorly insulated object are carried out. Results show that more significant energy savings are achieved in the case of poorly insulated object. Changed characteristics of the façade absorptance (a) and emittance (ϵ)

during summer and winter period can be realized by its special surface configuration in the form of the grooved cavities, which absorbs winter solar radiation well, as opposed to summer when the building needs cooling process, [11]. Of course, depending on the climatic conditions, the effect of applying the selective façade will not be the same. Due to an intense convection on outer walls under harsher winter conditions, the selective façade will achieve better results in winter environment of higher temperature and solar radiation [12].

Obviously that change of the absorptance and emittance of the outer and inner walls leads to additional heating and cooling energy saving. On the other hand the insulation layer reduces energy losses as well as energy gains of the solar radiation. The question arises as to what effects removing the insulation layers from certain exterior walls at the same time as the application of a selective façade would have on the heating energy consumption of the residential building? Using EnergyPlus software the simulation model of the real (existing) residential house will point on some answers.

2. Simulation model

Simulation model – the existing residential house is modeled by software GoogleSketchUp. House consists of three levels: basement, ground level and first floor. It is placed on sloping ground, relatively protected from the wind influence. The modeled appearance of the house is shown in figures 1 and 2.

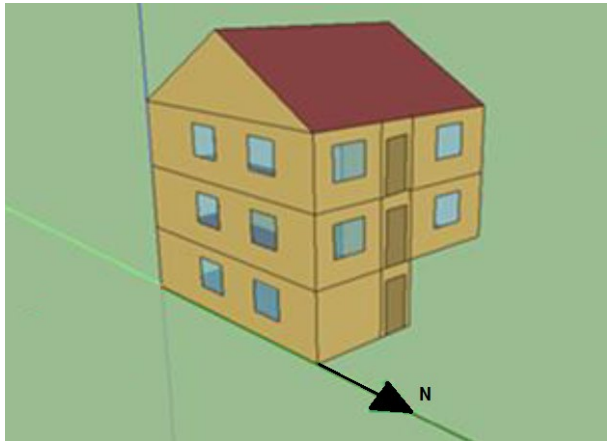


Figure 12 Perspective of the northern and eastern façade

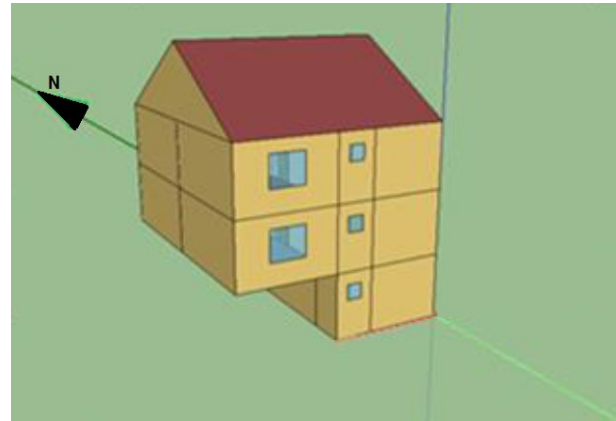


Figure 13 Perspective of the southern and western façade

The interior of the house consists of 13 rooms with a total heating area of 215 m² (basement - 85 m², ground level - 85 m², first floor - 85 m²). The layout of the rooms is shown in figures 3 and 4. Layout of the rooms in first floor is identical the ground level one. Simulated house is heated by electrical heaters.

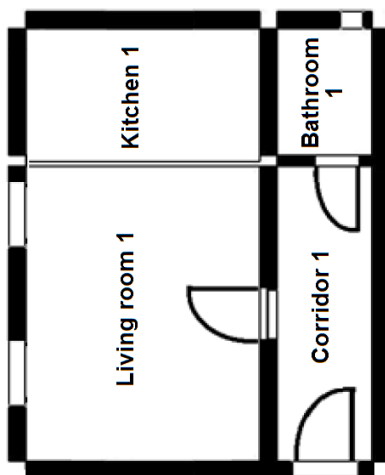


Figure 3. Basement cross section

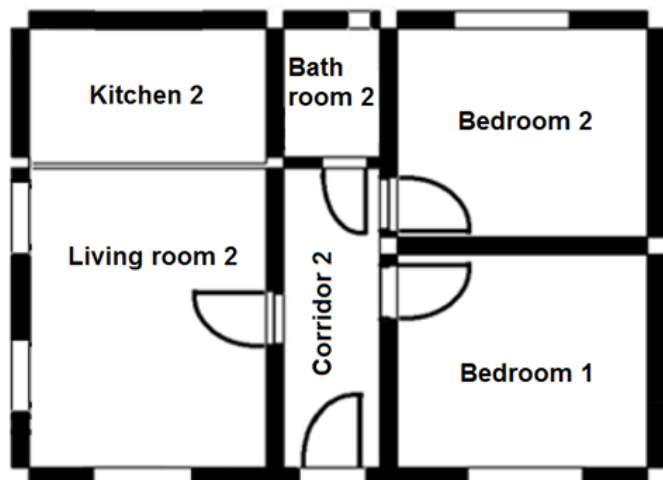


Figure 4. Ground lever cross section

Weather data is taken from the EnergyPlus database for city of Kragujevac (latitude 44.02°N, longitude 20.92°E, mean altitude 209 m). Characteristics of the house envelope applied materials are shown in Table 1.

The element structure of the house envelope is shown in Table 2. It is received according to real data (existing object).

Table 1. Applied materials characteristics of the considered residential house

Material	Density [kg/m ³]	Thickness [m]	Specific heat [J/kgK]	Thermal conductivity [W/mK]
Lime mortar	1600	0.015	1050	0.81
Cement screed	2100	0.04	1050	1.4
PVC foil	1460	0.00015	1100	0.19
Mineral wool	50	0.05/0.15	840	0.04
Styrodur	33	0.05-0.15	1260	0.03
Ceramic tiles	1700	0.015	920	0.87
Parquet floor	700	0.02	1670	0.21
Tile	1900	0.01	880	0.99
Brick block	1200	0.19	920	0.52
Reinforced concrete	2400	0.04	960	2.04
Gravel	1700	0.2	840	0.81
Concrete	1800	0.15	960	0.93
Interfloor filling	1200	0.16	920	0.6
Pine wood	550	0.035	2090	0.14
Polystyrene	15	0.05-0.15	1260	0.041
Gypsum boards	800	0.012	1090	0.19

In formed outer walls the insulation layer (polystyrene) is placed outside (before lime mortar). Adopted overall heat transfer coefficient of windows is 1.5 W/m²K. Air infiltration and ventilation are adopted as air changes per hour (kitchens – 1.5 h⁻¹, bathrooms – 1.25 h⁻¹, corridors – 0.75 h⁻¹, living and bedrooms – 0.5 h⁻¹). For standard façade the absorptance and emittance are adopted as $a=\varepsilon=0.7$, for solar radiation and $a=\varepsilon=0.9$, for long-wave infrared radiation. In the case of selective façade the adopted coefficients are $a=\varepsilon=0.95$, for solar radiation and $a=\varepsilon=0.2$, for long-wave infrared radiation.

Table 2. Envelope structure of the considered residential house

Building construction	Elements	Thickness [m]
Outer wall	Lime mortar	0.015
	Polystyrene	0.05-0.15
	Brick block	0.19
	Lime mortar	0.015
Inner wall	Lime mortar	0.015
	Brick block	0.19
	Lime mortar	0.015
Ground floor (parquet)	Gravel	0.2
	Concrete	0.15
	PVC foil	0.00015
	Styrodur	0.05-0.15
	Cement screed	0.04
	Parquet	0.02
Ground floor (tiles)	Gravel	0.2
	Concrete	0.15
	PVC foil	0.00015
	Styrodur	0.05-0.15

	Cement screed	0.04
	Ceramic tiles	0.015
Door	Pine wood	0.035
Roof	Tile	0.01
	Air gap	
	Mineral wool	0.05-0.15
	Gypsum boards	0.012
Interfloor (to attic)	Reinforced concrete	0.04
	Interfloor filling	0.16
	Lime mortar	0.015
Outer wall (tiles)	Lime mortar	0.015
	Polystyrene	0.05-0.15
	Brick block	0.19
	Ceramic tiles	0.015
Inner wall (tiles)	Lime mortar	0.015
	Brick block	0.19
	Ceramic tiles	0.015
Interfloor (tiles)	Ceramic tiles	0.015
	Cement screed	0.04
	Reinforced concrete	0.04
	Interfloor filling	0.16
	Lime mortar	0.015
Interfloor (parquet)	Parquet	0.02
	Cement screed	0.04
	Reinforced concrete	0.04
	Interfloor filling	0.16
	Lime mortar	0.015

3. Simulation scenarios

The main goal of carried out simulations was to compare the heating energy consumption of non-insulated and insulated object with standard façade with selective façade one. In the case of object with selective façade in some simulation scenarios the certain insulation layers are removed retaining selective surface to outside. All carried out scenarios are defined in Table 3.

Table 3. Simulation scenarios and the applied insulation thickness

Scenario mark	Roof insulation [cm]	Floor insulation [cm]	South wall insulation [cm]	East wall insulation [cm]	West wall insulation [cm]	Nort wall insulation [cm]
0.1	0	0	0	0	0	0
0.2	5	5	5	5	5	5
0.3	10	10	10	10	10	10
0.4	15	15	15	15	15	15
1.1	0	0	0	0	0	0
1.2	5	5	5	5	5	5
1.3	10	10	10	10	10	10
1.4	15	15	15	15	15	15
2	5	5	0	5	5	5
3	10	10	0	10	10	10
4	15	15	0	15	15	15
5	5	5	5	10	10	10
6	10	10	5	15	15	15

7	15	15	0	0	0	10
8	5	5	0	0	10	10
9	10	10	0	10	0	10

Scenarios with first number 0 refer to house with standard façade while scenarios with first number 1 to 9 refer to house with selective façade. Scenarios from 2 to 9 indicate to removing or reducing the insulation layer from certain walls (especially southern).

4. Results and discussion

After carried out simulations the heating energy consumption for all scenarios could be analyzed. Energy consumption of the non-insulated and insulated object for scenarios 0 and 1 is shown in Table 4.

Table 4. Heating energy consumption of the residential house in case of the variable insulation thickness and façade absorption characteristic

Simulation scenario	Energy consumption per heating season [kWh]	Energy consumption per heating area [kWh/m ² a]	Energy saving scenario 1 vs. scenario 0 [%]
0.1 (0 cm)	33365	155.2	
0.2 (5 cm)	22602	105.1	
0.3 (10 cm)	19770	92.0	
0.4 (15 cm)	18444	85.8	
1.1 (0 cm)	21043	97.9	36.9
1.2 (5 cm)	17531	81.5	22.4
1.3 (10 cm)	16434	76.4	16.9
1.4 (15 cm)	15892	73.9	13.8

Data of first four rows in Table 4 (standard object without selective façade) shows that the heating energy consumption decreases with insulation layer increasing but relatively less towards high insulation thickness (ventilation losses becomes dominant in relation to transmission one). In the case of the object with selective façade (four remained rows) trend is similar except that the decrease of energy consumption is less expressed with increasing of the insulation thickness. The last column in Table 4 shows the percentage energy consumption saving of the object with selective façade vs. standard object with corresponding insulation layer (from 0 to 15 cm). The most pronounced relative saving is observed at the non-insulated object, while the object with maximal insulation layer (15 cm) is on opposite side. That would be logical since an insulation prevents heat energy losses as well as outside gains (increased solar absorption).

Simulated heat energy consumption of the object with selective façade in the case of the complete (scenarios 2, 3 and 4) and incomplete (scenarios 5-9) insulated outside walls is shown in Table 5. As well the relative energy saving of defined scenarios vs. standard object (third column) and object with selective façade (fourth column) is shown.

Table 5. Heating energy consumption of the residential house in case of the selective façade, variable insulation thickness and lack of the certain insulation layer according to defined simulation scenario

Simulation scenario	Energy consumption per heating season [kWh]	Energy saving vs. corresponding scenario 0 [%]	Energy saving vs. corresponding scenario 1 [%]
2	17470	22.7	0.3
3	16425	16.9	0.1
4	15916	13.7	-0.2
5	16493	16.6	-0.4
6	15988	13.3	-0.6
7	18708	5.4	-13.8
8	17496	11.5	-6.5
9	17638	10.8	-7.3

From table 5 can be seen that the object with selective façade and lack (or reduction) of the certain insulation layer (on southern wall mostly) shows constantly less energy consumption relative to standard object with

corresponding insulation layer (third column). The most pronounced energy saving is observed at the poorly insulated object with selective façade (5 cm) and removed insulation layer from southern wall. (Scenario 2 – 22.7 %). In the other hand, least pronounced energy saving is observed at the well-insulated object with selective façade (15 cm) and removed three insulation layers from southern, eastern and western walls (Scenario 7 – 5.4 %). However, removing certain insulation layers from outside walls compared to completely insulated object with selective façade (fourth column) does not give a positive result. In the cases of scenarios 2-6 the effect of the increased solar gains is practically canceled out by effect of the increased heat losses from the non-insulated southern wall, so the energy saving are zero. In the cases when the insulation layers are removed from two or three outside walls, the increased energy consumption is observed (Scenarios 7-9).

It is interesting to analyze energy consumption savings of the certain scenarios monthly, during heating season (October-April). Relative heating energy savings of the object with selective façade vs. standard one with corresponding insulation level is shown in Figure 5. The smaller the layer of insulation up to the non-insulated object, the greater the relative energy savings. These savings are the most pronounced for months with enlarged solar radiation (October, April, March and November).

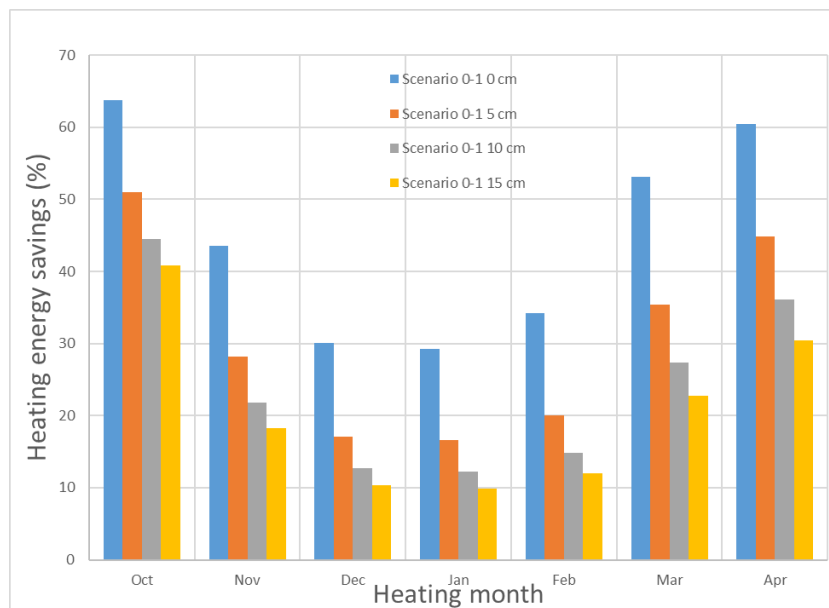


Figure 5. Monthly relative heating energy saving of the residential house with selective façade vs. classical envelope house for different insulation levels

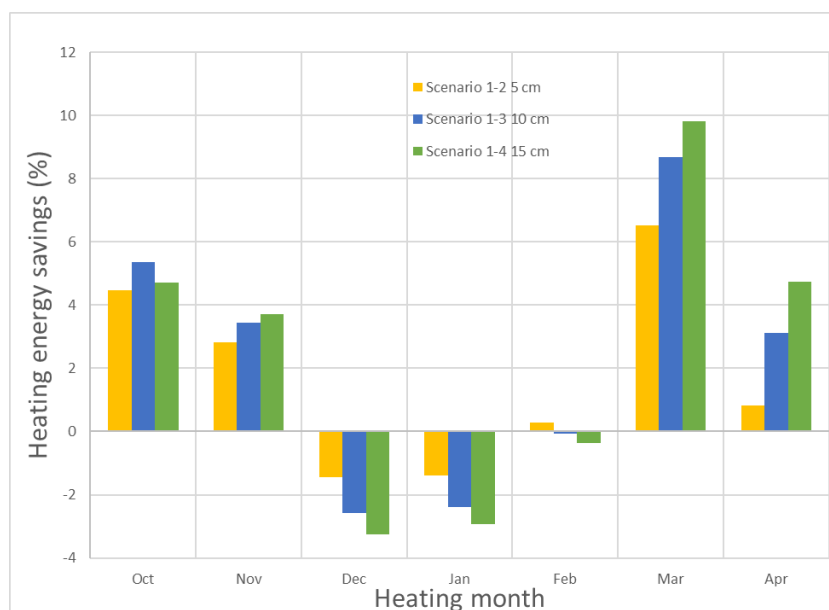


Figure 6. Monthly relative heating energy saving of the residential house with selective façade with lack of the south wall insulation layer vs. fully insulated selective façade for different insulation levels

Relative heating energy savings of the object with selective façade and removed insulation layer from southern wall (Scenarios 2-4) vs. complete insulated one with corresponding insulation level is shown in Figure 6. Although the energy saving for heating season is approximately zero (Table 5), for months with the least solar radiation (December, January) it is negative. In addition to the application of a selective facade, the idea of applying a variable insulation thickness (something opposite to intumescent materials) is imposed to increase energy saving.

5. Conclusion

Selective surfaces and coatings are widely used in the production of solar collectors. They are also applied in passive solar systems (Trombe wall). The application of selective building façade can contribute to a significant reduction of heating energy transmission losses in the winter period. More pronounced positive effects of selective facade application can be observed at latitudes and heating months with significant solar insolation. On the example of the residential house, depending on the climatic conditions, the energy savings of the selective facade compared to the classic one, with the same level of insulation, amount from 13.8 to 36.9%. As the thickness of the insulation increases, the positive effects of applying a selective facade decrease. Selective façade can be combines with the removing or reducing of an insulation layer, especially on southern outside wall. Simulation results have shown that in climatic condition characteristic of our latitudes the mentioned measure can lead to the similar heating energy consumption as in a completely insulated object with selective façade. Those relations are very sensitive to solar radiation amounts, so the energy saving effects are more pronounced in the warmer winter months then colder one with reduced solar radiation (December and January).

Acknowledgments

This investigation is a part of project TR33015 of the Technological Development of the Republic of Serbia. We would like to thank the Ministry of Education, Science and Technological Development of the Republic of Serbia for their financial support during this investigation.

References

- [1] www.odyssee-mure.eu (accessed on May 2024)
- [2] <https://ec.europa.eu/statistics-explained> (accessed on May 2024)
- [3] Bojić, M., Lukić, N., Numerical evaluation of solar-energy use through passive heating of weekend houses in Yugoslavia, *Renewable Energy*, 20/2 (2000), pp. 207-222
- [4] Szyszka, J., From Direct Solar Gain to Trombe Wall: An Overview on Past, Present and Future Developments, *Energies*, 15 (2022), 8956
- [5] Azemati, A. A., Hadavand, B. S., Hosseini, H., Tajarrood, A. S., Thermal modeling of mineral insulator in paints for energy saving, *Energy and Buildings*, 56 (2013), pp. 109-114
- [6] Čekon, A., Čurpek, J., A transparent insulation façade enhanced with a selective absorber: A cooling energy load and validated building energy performance prediction model, *Energy and Buildings*, 183 (2019), pp. 266-282
- [7] Guan, T. H., Wu, C. Q., Liu, H. M., Shen, Y., Xu, Y. B., Influence of Reflective Insulation Coating on Heat Transfer Characteristics of Composite Thermal Insulation Wall, *Applied Mechanics and Materials*, 633-634 (2014), 909-912
- [8] Cozza, E. S., Alloisio, M., Comite, A., Tanna, G. D., Vicini, S., NIR-reflecting properties of new paints for energy-efficient buildings, *Solar Energy*, 116 (2015), pp. 108-116
- [9] Simpson, A., Fitton, R., Rattigan, I. G., Marshall, A., Parr, G., Swan, W., Thermal performance of thermal paint and surface coatings in buildings in heating dominated climates, *Energy and Buildings*, 197 (2019), pp. 196-213
- [10] Prager, C., Köhl, M., Heck, M., Herkel, S., The influence of the IR reflection of painted facades on the energy balance of a building, *Energy and Buildings*, 38(12) (2006), pp. 1369-1379
- [11] Naraghi, M. H., Harant, A., Configuration of Building Façade Surface for Seasonal Selectiveness of Solar Irradiation-Absorption and Reflection, *Journal of Solar Energy Engineering*, 135(1) (2012), pp. 1-9
- [12] Lukić, N., Nešović, A., Nikolić, N., Širde, A., Volkova, A., Latosov, E., Energy performance of the Serbian and Estonian family house with a selective absorption facade, *IRMES 2019*, IOP Publishing, IOP Conf. Series: Materials Science and Engineering 659 (2019) 012047

Impact Assessment of Energy Facilities on Geoecology

V.S. Davtyan ^a

^aRussian-Armenian University, 0051, Armenia, vahe.davtian@gmail.com

Abstract: The article is devoted to the problems of the impact of energy facilities on geoecology. The main criteria for the impact of the operation of energy facilities on the environment are identified. Separate sectors of the energy sector (nuclear, thermal, hydro- and alternative energy) are singled out for a separate determination of the level of influence of different energy facilities on the geoecological situation. The main geoecological problems of energy development of Armenia are considered. A geoecological assessment of the key energy facilities in Armenia is given.

Keywords: geoecology, energy, facilities, assessment, pollution, ecosystem.

1. Introduction

In the modern world, energy is the basis for the development of basic industries that determine the progress of social production. In all industrialized countries, the pace of development of the energy industry outpaced the development dynamic of other industries.

At the same time, energy is one of the sources of adverse effects on the environment and humans. It affects the atmosphere (oxygen consumption, emissions of gases, moisture and particulate matter), the hydrosphere (water consumption, creation of artificial reservoirs, discharges of polluted and heated waters, liquid waste) and the lithosphere (consumption of fossil fuels, landscape change, emissions of toxic substances).

The main forms of energy impact on the environment are:

- air pollution: thermal effect, emission of gases and dust into the atmosphere;
- pollution of the hydrosphere: thermal pollution of water bodies, emissions of pollutants;
- pollution of the lithosphere during the transportation of energy carriers and waste disposal, in the production of energy;
- pollution of the environment by radioactive and toxic wastes;
- changes in the hydrological regime of rivers by hydroelectric power plants (HPPs) and, as a result, pollution in the territory of the watercourse;
- creation of electromagnetic fields around power lines [1].

Figure 1 shows a diagram of greenhouse gas emissions from various sectors of the world economy. As you can see, generating facilities operating on traditional energy sources contribute about 70% of the global anthropogenic greenhouse gas emissions to the atmosphere, pollute land and water with combustion products and wastewater.

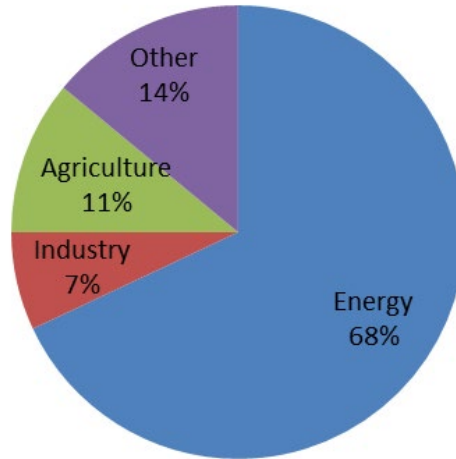


Fig. 1. Greenhouse gas emissions from various sectors of the world economy

2. Methods

The research methodology is based on an integrated approach, including the study of international practice of impact assessment of energy on geoecology. The study uses a structural-functional method, as well as a comparative analysis method in order to identify the features of the geoecological influence of energy facilities. By comparing the different kind of electricity production, the study reveals the basic problems of geoecology security. Methods of statistical and systemic analysis are also used in the research.

3. Results

From the point of view of the impact of energy facilities on the geosphere, several groups of the most important interactions can be distinguished:

- water consumption and water use, causing a change in the natural material balance of the aquatic environment (transfer of salts, nutrients, etc.);
- deposition on the surface of solid emissions of products of combustion of organic fuels from the atmosphere, causing a change in the properties of water, its color, albedo, etc.;
- fallout on the surface in the form of solid particles and liquid solutions of atmospheric emissions products, including: acids and acid residues, metals and their compounds, carcinogens;
- emissions directly onto the surface of land and water of the products of burning solid fuels (ash, slag), as well as products of blowdown, cleaning of heating surfaces (soot, ash, etc.);
- emissions of liquid and solid fuels onto the surface of water and land during transportation, processing, reloading;
- releases of solid and liquid radioactive waste, characterized by the conditions of their distribution in the hydro- and lithosphere;
- heat emissions, the consequences of which may be: a constant local increase in temperature in the reservoir; temporary rise in temperature; changes in freezing conditions, winter hydrological regime; change in the distribution of precipitation, evaporation, fog;
- creation of reservoirs in river valleys or using the natural relief of the surface, as well as the creation of artificial cooling ponds, which causes: changes in the qualitative and quantitative composition of river flows, changes in the hydrology of the water basin; increased pressure on the bottom, penetration of moisture into crustal faults and changes in seismicity; changes in fishing conditions, development of plankton and aquatic vegetation; microclimate change; changing the conditions of recreation, sports activities, balneological and other environmental factors;
- landscape changes during the construction of heterogeneous energy facilities, consumption of lithosphere resources, including: deforestation; withdrawal from agricultural circulation of arable land, meadows; interaction of coasts with reservoirs;
- the impact of emissions, removals and changes in the nature of the interaction of water basins with land on the structure and properties of the continental shelves. Impurity pollution can collectively affect the natural circulation and material balances of certain substances between the hydro-, litho- and

atmosphere. Common to all energy sources (both traditional and non-traditional) is the problem of thermal emissions [2].

All of these interactions are interconnected, and each of them cannot be considered separately. In addition, the mechanism of interaction in each of the groups is based on heterogeneous physical and physico-chemical processes and phenomena.

On a spatial basis, the sources of technogenesis are divided into point (wells, barns), linear (pipelines, water conduits) and areal (deposits). Most of the geo-ecological risks in the field of oil and gas production are generated by emergency situations: the flowing of wells, the formation of griffins, leakage of pollutants from tanks, pipeline ruptures, etc. should be highlighted. As noted by I.A. Karlovich, geochemical changes in soils begin at the stage of drilling a well, and pollutants (e.g., nitrates, lead, and zinc) are found in the soil within a radius of 2 km from the drilling site. In the process of drilling, the main risks are caused by cuttings and settling pits for flushing fluid, which include such chemical components as thinners, heat stabilizers, emulsifiers, weighting agents, etc. [3]. In all cycles and production and technological stages of drilling for oil, gas and condensate, land is allocated for wells, waste storage, for the construction of oil and gas pipelines, which inevitably leads to soil and vegetation pollution [4].

Now, let's briefly consider the features of the impact of main energy facilities on geoecology.

4. Discussion

4.1. Thermal power plants (TPP)

TPPs are characterized by high radiation and toxic pollution of the environment. Traditionally, thermal power plants operate on fossil fuels - coal and fuel oil. When fuel is burned at TPPs, combustion products are formed, which contain many substances that pollute the atmosphere. These include, for example, fly ash, sulfuric and sulfurous anhydride, nitrogen oxide, vanadium compounds, coke, sodium salts, soot particles, etc. When switching from solid to gas fuel, the cost of electricity generated increases significantly, but there is no ash when using liquefied gas.

Also polluting the environment is the waste water from TPPs, which contain petroleum products. At the same time, at stations where liquid fuel is used, the volumes of industrial water discharges are somewhat higher. The negative impact of thermal power plants is exacerbated by the fact that their operation must be ensured by the constant production of fuel, which is accompanied by additional negative impacts on the environment. Such impacts include, for example, pollution of the air basin, water and land, consumption of land and water resources, etc. [5].

Depending on the initial composition of the fuel, combustion products emitted into the atmosphere contain nitrogen oxides (NO_x), carbon oxides (CO_x), sulfur oxides (SO_x), hydrocarbons, water vapor and other substances in solid, liquid and gaseous states, which are the main environmental pollutants. Pollution of the atmosphere with fine solid particles of ash is mainly associated with the use of coal as a fuel, which is pre-ground in special mills. However, with the proper organization of the combustion process and the use of modern filters with an efficiency factor (COP) of 95...99%, their number can be reduced to the required minimum. When burning liquid fuel (fuel oil), sulfur and nitrogen oxides, gaseous and solid products of incomplete combustion of fuel, and vanadium compounds enter the atmosphere with emissions. When natural gas is burned, nitrogen oxides also enter the atmosphere, but they are formed significantly less than when fuel oil is burned. This is due not only to the properties of the fuel itself, but also to the peculiarities of the combustion processes.

Obviously, today natural gas is the cleanest type of energy fuel. Improving the design of TPP equipment, as well as compliance with its operation standards, can significantly reduce the amount of oil products entering wastewater, and the use of traps and settling tanks practically eliminates their entry into the external environment [1].

4.2. Nuclear power plants (NPP)

The impact of NPPs on the environment, taking into account the technology of construction and operation, is much less than other technological facilities. However, radiation in the event of an accident is one of the dangerous factors for the environment, human life and health. In this case, emissions are equated to those arising from the testing of nuclear weapons. For the operation of nuclear facilities, uranium ore is mined, from

which radioactive uranium is obtained by enrichment. Reactors produce plutonium, which is the most toxic man-made substance in existence. Processing, transportation and disposal of waste from NPPs require careful precautions and safety measures.

The impact of an NPP on the environment begins from the moment of construction, continues during operation and even after its completion. On the territory of the location of the station for the generation of electricity and beyond, various negative influences may occur. These include, for example, the withdrawal of a land plot for the construction and arrangement of sanitary zones, the destruction of vegetation due to construction, air pollution if blasting is necessary, the resettlement of local residents to other territories, harm to populations of local animals, the chemical impact of NPPs, etc.

One of the most significant polluting factors is the thermal impact of NPPs which occurs during the operation of cooling towers, cooling systems and spray pools. They affect the microclimate, the state of waters, the life of flora and fauna within a radius of several kilometers from the object. The efficiency of NPPs is about 33...35%, the rest of the heat (65...67%) is released into the atmosphere. Under normal operating conditions, radiation contamination and the effect of ionizing radiation are minimized and do not exceed the permissible natural background. The catastrophic impact of NPPs on the environment and people can occur in case of accidents and leaks [6].

In accordance with the IAEA “Nuclear Safety Rules for Nuclear Power Plants”, the designs of all systems and components of NPPs that affect nuclear safety must contain a detailed analysis of all possible failures of constituent elements, highlighting dangerous failures and assessing their consequences. Taking into account the distribution of emissions during accidents, sanitary protection zones are established at NPPs. All other types of NPP effects on the hydro- and lithosphere that are not related to radioactivity (the effect of the water supply system, inlet and outlet channels, filters), do not qualitatively differ from similar effects of TPP.

The main heat release from NPPs to the environment, as well as at TPPs, occurs in the condensers of steam turbine plants. However, the specific heat release into the cooling water at NPPs is greater than at TPPs, due to the higher specific steam consumption. This determines significant specific costs of cooling water. In connection with the foregoing, most new NPPs provide for the installation of cooling towers in which heat is removed directly to the atmosphere. The cooling water then enters the pre-cooler. This reservoir of separate use is designed to provide a closed water supply system for nuclear power plants.

The most difficult environmental problem in the operation of NPPs is the disposal of large-tonnage radioactive waste generated during the dismantling of equipment elements that are radioactive at the end of their service life or for other reasons, as well as spent nuclear fuel. Several disposal options are envisaged: placement of all radioactively contaminated elements in mine workings; burial of only the most contaminated by induced radioactivity with the reuse of the rest for their intended purpose; periodic decontamination of equipment on site with the disposal of concentrated waste and washouts. A nuclear power plant differs from any industrial facility at which an accident may occur with the release of harmful substances into the environment; in the case of an accident at a nuclear power plant, radioactive elements can enter the environment, which are the result of the life of a NPP and pose a serious danger to the environment and the population. The sufficiency of protecting the environment and the population is achieved when dose loads and concentrations of harmful substances in the media do not exceed the limiting, critical values defined in the rules and regulations for nuclear energy [7].

The impact of an NPP must be controlled at every stage of plant design and operation. Special comprehensive measures are designed to predict and prevent accidental emissions and their development, and to minimize the consequences. One of the factors of environmental protection from the impact of NPPs is the rationing of indicators, i.e. establishing acceptable values for a particular risk, and following them. Modern NPPs are built with high levels of security and safety [1].

4.3. Hydropower plants (HPP)

The main advantages of HPPs are the low cost of generated electricity, quick payback (the cost is about 4 times lower, and the payback is 3-4 times faster than at TPPs), high maneuverability, which is very important during periods of peak loads, the possibility of energy accumulation. However, the construction and operation of HPPs lead to many geocological problems.

A huge geocological problem of HPPs is the construction of reservoirs, which affect climate change in nearby areas and are natural accumulators of pollution. Reservoirs, necessary to ensure the uniform operation of HPPs,

cause climate change in adjacent areas at distances of up to hundreds of kilometers, and are natural accumulators of pollution. Also, the construction of dams leads to flooding of nearby areas. Dams impede fish migration upstream, resulting in the impoverishment of river ecosystems [8].

To solve this problem, some countries create artificial reservoirs for fish. The most significant factors influencing local conditions are: changes in the landscape, groundwater levels, reshaping of banks, as well as changes in other natural conditions (soil, flora and fauna) in the areas of both the reservoir and the lower basin of the HPP.

The change in the hydrogeological regime of rivers during the construction of HPP is characterized by a change in the redistribution of runoff; level regime and its dependence on winds; current regimes, wave, thermal, and ice regimes. The flow rates can decrease by dozens of times, and completely stagnant zones appear in some zones of the reservoir. In shallow parts, sharp fluctuations in water temperature are observed depending on changes in air temperature.

More promising is the construction of HPPs on mountain rivers. This is due to the higher hydropower potential of mountain rivers compared to lowland rivers. During the construction of reservoirs in mountainous areas, large areas of fertile land are not withdrawn from land use [1].

4.5. Alternative energy

Solar modules cause dimming over the area, which leads to a change in the soil cover. Also, solar stations cause heating of the surrounding air, which leads to a change in the heat balance. The very production of solar modules with the manufacture of monocrystalline or semi-crystalline silicon cells is a rather dirty production.

The most significant aspect of the impact of wind energy on the environment is noise pollution. The removal of these stations from settlements and recreation areas solves the problem of the noise effect for people [8]. However, noise affects the surrounding fauna, including marine life, since wind farms are often installed in marine areas. Wind farms can influence the migration of birds and fish.

Geothermal power plants have the main impact on the natural environment during the development of the field, the construction of steam pipelines and station buildings. The potential impact of such stations may be soil subsidence. Thus, the underlying layers cease to support the upper layers of the soil, and there is a decrease in the flow rates of thermal springs and geysers. Another aspect of the influence of these stations is the pollution of surface and ground waters in case of release of concentrates during well drilling. In this case, waterlogging of the soil or salinization may occur, depending on the climate.

Hydrocarbon fuels are not burned at such stations, so emissions from such sources have a different chemical composition. Gas impurities consist mainly of carbon dioxide and contain small amounts of methane, hydrogen, nitrogen, ammonia and hydrogen sulfide. The most harmful is hydrogen sulfide [9].

Bioenergy plants are fairly clean technologies, but direct combustion of wood produces large amounts of particulate matter, organic compounds, carbon monoxide and other gases. Compared to wood, biogas is a cleaner fuel, producing no harmful gases or particles. At the same time, precautions are necessary in the production and consumption of both biogas and synthesis gas, since methane is explosive. Therefore, during its storage, transportation, use, monitoring should be carried out to detect and eliminate leaks [1].

4.6. The impact of energy on the geocology of Armenia

The energy system of the Republic of Armenia has a significant impact on geocology - the environment and population, social and ecological subsystems. Such an impact occurs as a result of the construction and operation of elements of the economic subsystem, namely, from NPPs, TPPs, HPPs.

As a result of the construction of the Sevan-Hrazdan HPP cascade, water intake from Lake Sevan turned out to be excessive. The ecosystem of Lake Sevan, the only major source of fresh water in the country, was disturbed [10]. The fall in the lake level, together with an increase in wastewater emissions, adversely affected the biochemical turnover of substances, led to a disruption in the normal functioning of ecosystems, which ultimately led to the process of eutrophication - an increase in the accumulation of organic substances in water. The biota of the ecosystem has qualitatively changed - from salmon to cyprinids.

This problem also affected the social subsystem - many rural residents who were engaged in fishing lost their source of income. Recently, the repair of the Arpa-Sevan hydrotechnical tunnel was completed, through which water is transferred from the Arpa River to Sevan. As a result, the water level in the lake began to rise again.

This caused great harm to the environment. Now it is necessary to rationally use this resource and maximize energy production from these power plants by investing in their modernization. Recently, there has been an increase in the construction of HPPs and, in particular, small HPPs. Such stations have a much smaller impact on the environment compared to others.

The largest emissions from the energy system of Armenia are observed at TPPs. The operation of TPPs has a negative impact on both the environmental and social subsystems. Reducing the negative impact from these sources can be addressed by modernizing TPPs, while at the same time increasing their energy efficiency. The recent modernization and construction of new power units at the Yerevan and Hrazdan TPPs have made it possible to significantly reduce emissions into the environment. In addition, the new power plant will consume 2-2.3 times less fuel (natural gas) to generate 1 kWh of electricity than other power plants in the country.

In addition to electricity, NPPs produce highly radioactive, medium radioactive and slightly radioactive waste, which is also very toxic. They need to be buried in a safe place for a very long time. For many countries this problem is still not solved, but for Armenia with such a small territory it is especially relevant [1].

Now radioactive waste is stored in special canisters in a dry storage facility on the territory of the NPP. The amount of waste is 30 tons per year. Radioactive waste should be sent to Russia for disposal, but for this it is necessary to ensure their removal by rail. As we know, the road is closed due to the blockade, and it is forbidden to transport such waste by air. Building a burial ground in the country is also very difficult due to the resistance of the local population and the difficulty of finding a suitable area.

5. Conclusion

Thus, the impact of energy facilities on the geo-ecological situation is quite high, which dictates the need to develop new environmentally-centric methods and approaches to the energy development of both individual countries and regions as well as the world. The negative impact of energy on the environment significantly affects the pace of sustainable development, creating various risks and threats to security of society and ecological system.

Armenia with its main sources of electricity generation (TPP, NPP, HPP, alternative), is also exposed to these risks and threats due to the low level of environmental responsibility in the basis of the national energy policy. Therefore, consistent diversification of the energy system of Armenia, aimed at its convergent development (harmonization of conventional and alternative energy) is a strategic challenge.

Acknowledgement

The work was supported by the Science Committee of Republic of Armenia, in the frames of the research project № 21T-2H107.

References

- [1] Methods and technologies for assessing the impact of energy on the geoecology of the region, L.V. Massel et al., NPUA, Yerevan, 2019, 252 p.
- [2] Vardanyan A.H., Yeghiazaryan G.M., Ayzazyan G.Y., Vardanyan A.A., Biomass Energy, Yerevan, 2017, 120 p.
- [3] Karlovich I.A., Geoecology, Academic project: Alma-Mater, Moscow, 2005, 512 p. (in Russ.)
- [4] Davtyan V.S., On seismic risks of shale extraction in Armenia, Crisis management and technologies, N2 (2021), pp. 55-62.
- [5] Malyarenko V. A., Introduction to the engineering ecology of energy, SAGA Publishing House, 2008, 185 p. (in Russ.)
- [6] Osipov V.I., Geoecology is an interdisciplinary science about the environmental problems of the geospheres, Geoecology, No. 1 (1993), pp. 4-18 (in Russ.).
- [7] Safety of Nuclear Power Plants: Commissioning and Operation: IAEA Safety Standards Safety of Nuclear Power Plants: Commissioning and Operation for protecting people and the environment. Specific Safety Requirements No. SSR-2/2, International Atomic Energy Agency, Vienna, 2011.
- [8] Pierpont N., Wind Turbine Syndrome, NM: King Printing, Lowell, Mass, Santa Fe, 2009, 292 p.
- [9] Energy infrastructure of the central ecological zone: impact on the natural environment and ways to reduce it, B.G. Saneev, I.Yu. Ivanova, E.P. Maysyuk, T.F. Tuguzovai et al., Geography and natural resources, No. 5 (2016), pp. 45-48 (in Russ.).
- [10] Integral assessment of the ecological state of Lake Sevan, Danielyan K. et al, 2011, Yerevan, 100 p.

Change in the Quality of Kolubara lignite Burned in the Thermal Power Plants "Nikola Tesla" Expressed in Terms of Emission Factor

*Nikola Živković^a, Vukman Bakić^b, Marina Jovanović^c, Sanja Vujnović^d, Željko Đurović^e,
Dejan Cvetinović^d*

^aVinča Institute of Nuclear Sciences – National Institute of the Republic of Serbia - University of Belgrade, RS, nikolaz@vin.bg.ac.rs

^bVinča Institute of Nuclear Sciences – National Institute of the Republic of Serbia - University of Belgrade, RS, bakicv@vin.bg.ac.rs

^cVinča Institute of Nuclear Sciences – National Institute of the Republic of Serbia - University of Belgrade, RS, marinaj@vin.bg.ac.rs

^dUniversity of Belgrade, School of Electrical Engineering, 11120 Belgrade, Republic of Serbia, svujnovic@etf.bg.ac.rs

^eUniversity of Belgrade, School of Electrical Engineering, Belgrade, RS, zdjurovic@etf.bg.ac.rs

^fVinča Institute of Nuclear Sciences – National Institute of the Republic of Serbia - University of Belgrade, RS, deki@vin.bg.ac.rs

Abstract: The paper presents experimental investigation, calculations and analyzes of emission factors of low-quality domestic lignite from the Kolubara Basin, which is used for the operation of the Thermal Power Plant "Nikola Tesla". The studied lignite samples presented in this paper and their mutual comparison cover seven years of operation in the period 2012-2018. Standard analytical methods were used to determine the emission factor of lignite, including ultimate analysis, proximity analysis and determination of lower heating value. Based on the experimental results obtained, correlated dependencies of the emission factor of lignite were determined for the specified years and a comparison was made. From 2020, J.S.C. "Elektroprivreda Srbije", the operator of TPP "Nikola Tesla", imports coal of better quality, mixes it with Kolubara lignite and uses the mixture for firing the units of power plant B. A comparison was made between the lignite from Kolubara, which was offered for a long period of time, and the mixture with imported coal from last year. The change in the quality of domestic lignite, expressed as an emission factor, over time was presented together with the analysis of the change in the emission factor found for the coal blends used in recent years..

Keywords: Laboratory Analysis, Ultimate Analysis, Proximate Analysis, Carbon Emission Factor, Kolubara Lignite, Coal Blends.

1. Introduction

The methodology has been proposed at the international level (2006 IPCC Guidelines for National Greenhouse Gas Inventories. In order to harmonise the inventory of GHG emissions, some refinements has been made – 2019 Refinement to the 2006 IPCC Guidelines for National Greenhouse Gas Inventories) [1-3]. Adopting for simplification, as already stated, predefined values for the net calorific value and the carbon emission factor (CEF) for fossil fuels, according to [2, 3], the proposed default value for the emission factor for lignite is 27.6 tC/TJ, and for the net calorific value for lignite is 11.9 TJ/Gg. However, the use of these default values leads to an error in the calculation of the GHG emissions inventory. For this reason, the international methodology [1-3] recommends the use of more accurate data. In the case of lignite from open-pit mines of the Republic of Serbia used for operation of utility boilers of TPP of the Joint Stock Company Electric Power Company of Serbia (EPS), the CEF and low temperature values deviate significantly from the recommended default values. The CEF values change over time, so it is necessary to determine them experimentally on a regular basis. Emission of Greenhouse Gasses in EPS for the Period from 1990 – 2008, has been presented in our internal publication [4], including complete data on emissions of pollutants from thermal energy plants within EPS for the specified period, as well as the methodology for calculating emissions and emission factors of used coals (mainly lignites). The calculation of the CEF for fuels for the production of electricity and thermal energy in the Republic of Serbia and the comparison with the IPCC standard values and other experimentally determined CEF values for lignite has been already presented in our previous work [5-13]. An alternative experimental

methodology [4-6], has been described in detail, it was adopted and applied to determine the carbon emission characteristics of Serbian and Balkan lignites. The methodology has been established in the Laboratory for Thermal Engineering and Energy, VINČA Institute of Nuclear Sciences. The CEF is determined according to experimental measurements and calculations and the dependencies are established. It is found that the values of the emission factor are inversely proportional to the lower heating value, i.e. as the heating value increases, the value of the emission factor decreases and converges towards a certain value. Our group has a long time history investigating quality of the coals (lignites) used on TPPs in The Republic of Serbia and in the region (Bosnia and Herzegovina, Macedonia, Montenegro, Greece, Turkey etc.). The first publication was the internal one in which we presented methodology in order to calculate CEF factor based on experimental results and emission of greenhouse gasses from the utility boilers from Joint Stock Company Electric Power Company of Serbia, for the period 1990-2008, [4]. In 2011 and 2012 Evaluation of Kolubara Lignite Carbon Emission Characteristics has been presented, in Serbian [5] and in English [6]. The quality of Kostolac Lignite Carbon Emission Characteristics has been examined in 2017, [7]. Lignite from Montenegro (Pljevlja) and from Bosnia and Herzegovina (Lignite from Bogutovo selo) has been examined [9, 10] respectively. Carbon emission factor of Balkan lignites, including lignites from Serbia, Bosnia and Herzegovina, Montenegro, Turkey and Greece were investigated and mutually compared [11]. Variability of lignite from Kostolac basin for certain year period has been presented [12].

2. Laboratory methodology

In this work, samples mainly from the open-pit mine Kolubara for the the operation of Thermal Power Plant utility boilers "Nikola Tesla" were tested in the laboratory used. Kolubara lignite samples from 2015, 2017 and 2018 were tested in the laboratory, while the results of the 2012 test samples are presented and analyzed in our previous works [5, 6]. The laboratory testing of the samples from 2015 – 2018, were carried out, and also for samples with imported better quality coal from 2023, which represent a mixture of Kolubara lignite and imported coal. A total of 10 samples from 2015, 6 samples from 2017 and 7 samples from 2018 year, 4 samples of mixture from 2023 and 3 samples of imported better quality coal from 2023 were tested. As already stated in our previous works [5-7 and 9-12], sample preparation and laboratory analysis were performed at the Laboratory for Thermal Engineering and Energy of the "Vinca" Institute of Nuclear Sciences, National Institute of the Republic of Serbia, University of Belgrade, Department for fuel characterisation. Sample preparation was carried out prior to laboratory measurements in accordance with the standard ISO 5069-2: 1993. For the experimental laboratory tests, the samples were considered on an "as received", "as determined" and "on dry" basis. Proximate analysis, ultimate analysis and determination of calorific value were performed in accordance with ASTM D7582, ASTM D5373 (Standard Test Methods for Determination of Carbon, Hydrogen and Nitrogen in Analysis Samples of Coal and Coke), ASTM D3176 (Standard Practise for Ultimate Analysis of Coal and Coke) and the standard ISO 1928: 2009, respectively. For experimental laboratory tests, LECO CHN628 ultimate analyzer, LECO CHN628 module S, for Sulfur content determination, Thermogravimetric analyzer LECO TGA 701 for proximate analysis and IKA C200 calorimeter has been used.

3. Experimental results

Experimental tests were performed for 10 Kolubara samples (year 2015), 6 samples (2017) and 7 samples (2018 year), 4 mixture samples (2023 year) and 3 samples of imported coal (2023 year), on an "as determined" basis, and the contents for the other two bases ("as received" and "dry") were calculated from the first one. The contents of the Kolubara samples on an "as received" basis for years 2015, 2017 and 2018 are shown in the tables. 1., 2. and 3. respectively. Results of the experimental analysis for mixture samples are presented in table 4., and the results for the imported coal are presented in table 5. Results from previous test for Kolubara lignite for 2012 year were taken out from our previous work [5, 6]. Correlations were made on the basis of the results obtained: total Carbon content and combustible content, total hydrogen content and combustible matter content, total Carbon content and lower heating value, Lower heating value and combustible matter content and correlation between CEF and lower heating value. Based on correlations given, a comparison has been made for different years and different coal compositions and different type of coal.

As previously stated experimental investigation of the samples from 2015, 2017, 2018 and 2023 years were performed in laboratory environment. Experimental tests were performed on 27 samples, on an as determined basis. The other bases, as received and dry, were calculated from the first one. The contents of the samples on

an “as received” basis, for the years 2015, 2017, 2018 and 2023 are presented in the Tables. 1., 2., 3. and 4, respectively.

Table 1. Table 1. The results of experimental test of lignite samples used for operation of TPP “Nikola Tesla”. (Kolubara open-pit mine), “as received” basis, sampling year 2015

Sample N ^o	Proximate analysis					Ultimate analysis				
	W	A	C _{fix}	Comb.	H _d	C	H	S _{tot.}	S _g	N + O
	[%]	[%]	[%]	[%]	[kJ/kg]	[%]	[%]	[%]	[%]	[%]
1	47.96	13.52	15.54	38.52	8447	25.09	2.16	-	-	11.27
2	47.86	13.89	15.24	38.25	8385	24.61	2.16	-	-	11.48
3	48.20	17.83	13.57	33.97	6920	21.89	2.29	0.35	0.10	9.68
4	47.13	17.91	13.30	34.96	7315	22.57	2.32	0.35	0.15	9.93
5	47.81	18.07	13.79	34.12	7135	22.18	2.27	0.28	0.14	9.54
6	47.49	18.42	13.48	34.09	7137	22.24	2.28	0.29	0.13	9.43
7	44.74	15.62	15.52	39.64	8866	26.43	2.19	0.34	0.14	10.87
8	50.97	18.26	7.72	30.77	6199	19.91	1.88	0.38	0.16	8.82
9	47.12	16.71	14.85	36.17	7842	23.85	2.08	0.41	0.15	10.08
10	45.69	22.56	12.50	31.75	6617	20.56	1.86	0.45	0.21	9.12

Table 3. The results of experimental test of lignite samples used for operation of TPP “Nikola Tesla”. (Kolubara open-pit mine), “as received” basis, sampling year 2018

Sample N ^o	Proximate analysis					Ultimate analysis				
	W	A	C _{fix}	Comb.	H _d	C	H	S _{tot.}	S _g	N + O
	[%]	[%]	[%]	[%]	[kJ/kg]	[%]	[%]	[%]	[%]	[%]
1	46.52	20.12	12.40	33.36	7177	21.63	1.98	-	-	9.76
2	47.70	17.92	13.60	34.38	7352	22.41	1.86	0.35	0.09	10.03
3	46.10	18.17	13.92	35.73	7532	23.50	1.99	0.35	0.12	10.11
4	45.70	21.90	12.69	32.40	7297	21.42	1.94	0.39	0.16	8.87
5	48.70	20.32	11.84	30.98	6382	20.33	1.95	0.49	0.22	8.48
6	48.10	18.97	12.79	32.93	7020	21.36	1.97	0.46	0.20	9.40
7	47.40	20.50	12.40	32.10	6706	20.99	1.97	0.43	0.19	8.96

Table 4. The results of experimental test of lignite samples used for operation of TPP “Nikola Tesla”. (mixture of domestic lignite and imported better quality coal), “as received” basis, sampling year 2023

Sample N ^o	Proximate analysis					Ultimate analysis				
	W	A	C _{fix}	Comb.	H _d	C	H	S _{tot.}	S _g	N + O
	[%]	[%]	[%]	[%]	[kJ/kg]	[%]	[%]	[%]	[%]	[%]
1	39.90	23.00	14.22	37.10	8131	24.53	2.12	0.49	0.42	10.04
2	39.84	19.44	15.72	40.72	9526	27.89	2.30	0.67	0.21	10.32
3	42.46	19.68	15.01	37.86	8312	24.24	2.15	0.36	0.09	11.37
4	50.33	15.84	12.95	33.83	7354	21.89	1.93	0.44	0.27	9.75

Table 5. The results of experimental test of samples of imported better quality coal, “as received” basis, sampling year 2023

Sample N ^o	Proximate analysis					Ultimate analysis				
	W	A	C _{fix}	Comb.	H _d	C	H	S _{tot.}	S _g	N + O
	[%]	[%]	[%]	[%]	[kJ/kg]	[%]	[%]	[%]	[%]	[%]
1	40.74	4.24	24.39	55.02	13242	37.60	2.83	0.19	0.09	14.51
2	39.69	2.81	27.35	57.50	14789	40.24	2.88	0.37	0.09	14.29

Sample N ^o	Proximate analysis					Ultimate analysis				
	W	A	C _{fix}	Comb.	H _d	C	H	S _{tot.}	S _g	N + O
	[%]	[%]	[%]	[%]	[kJ/kg]	[%]	[%]	[%]	[%]	[%]
3	44.87	5.10	22.71	50.03	12214	34.01	2.56	0.15	0.04	13.41

4. Calculations and comparison

According to the data presented in the tables based on experimental tests and the calculations, linear dependences of the total Carbon content and combustible matter content has been calculated and presented, for each specified year:

$$2012: \quad C = 0.7785 \cdot \text{Combustible} - 4.6405 \quad (1)$$

$$2015: \quad C = 0.651 \cdot \text{Combustible} - 0.018 \quad (2)$$

$$2017: \quad C = 0.651 \cdot \text{Combustible} - 0.089 \quad (3)$$

$$2018: \quad C = 0.652 \cdot \text{Combustible} - 0.053 \quad (4)$$

$$2023: \quad C = 0.660 \cdot \text{Combustible} - 0.087 \quad (5)$$

The experimental data of Carbon content on Combustible matter content are presented on diagram on Figure 1. Linear analytical correlations are presented by eq. (1-5), and graphically on diagram Figure 2., for the specified years and mutual comparison.

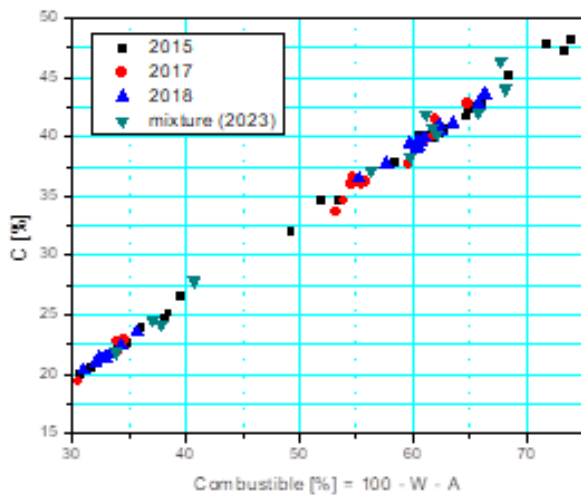


Figure 1. Total Carbon content as a function of combustibles content, for the samples of lignite, for 2015 – 2023 years, experimental data

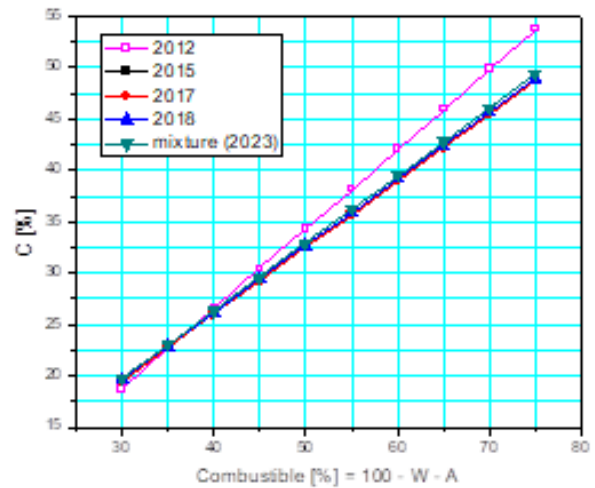


Figure 2. Total Carbon content as a function of combustibles content, for the samples of lignite, for 2012 – 2023 years, analytical data

According to the data presented in the tables based on experimental tests and the calculations, linear dependences of the total Hydrogen content and combustible matter content has been calculated and presented, for each specified year:

$$2012: \quad H = 0.0594 \cdot \text{Combustible} \quad (6)$$

$$2015: \quad H = 0.059 \cdot \text{Combustible} + 0.067 \quad (7)$$

$$2017: \quad H = 0.060 \cdot \text{Combustible} + 0.016 \quad (8)$$

$$2018: \quad H = 0.057 \cdot \text{Combustible} + 0.069 \quad (9)$$

$$2023: \quad H = 0.056 \cdot \text{Combustible} + 0.00004 \quad (10)$$

The experimental data of Hydrogen content on Combustible matter content are presented on diagram on Figure 3. Linear analytical correlations are presented by eq. (6-10), and graphically on diagram Figure 4., for the specified years.

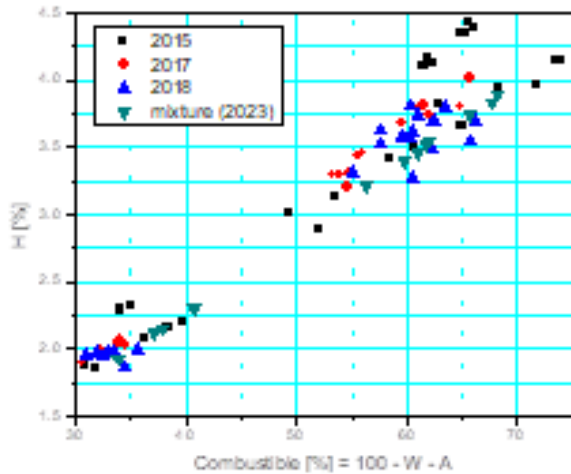


Figure 3. Total Hydrogen content as a function of combustibles content, for the samples of lignite, for 2015 – 2023 years, experimental data

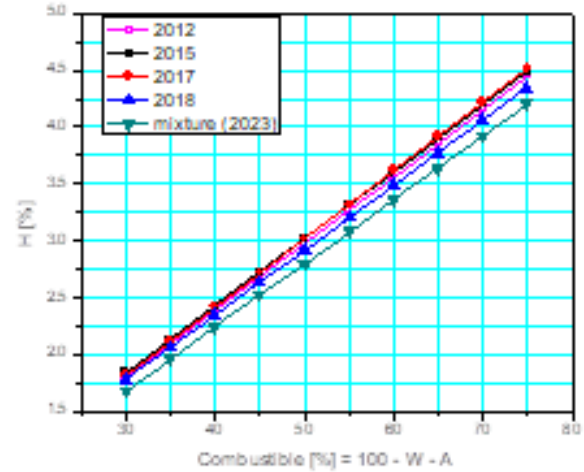


Figure 4. Total Hydrogen content as a function of combustibles content, for the samples of lignite, for 2012 – 2023 years, analytical data

The diagram in Figure 5 shows the experimental results of the total carbon content (%) as a function of the low heating value. The linear correlations for the years 2012 - 2023 are presented by dependencies, eq. (11-15), while the linear analytical correlations are presented together on the diagram on Figure 6. Based on the diagrams, a slight change in the dependency with the years is noticeable, which is especially clearly in the diagram in Figure 6, since the linear dependencies are almost superimposed over each other.

$$2012: \quad C = 2.3718 \cdot H_d + 4.2637 \quad (11)$$

$$2015: \quad C = 2.309 \cdot H_d + 5.639 \quad (12)$$

$$2017: \quad C = 2.288 \cdot H_d + 5.571 \quad (13)$$

$$2018: \quad C = 2.280 \cdot H_d + 5.535 \quad (14)$$

$$2023: \quad C = 2.279 \cdot H_d + 5.653 \quad (15)$$

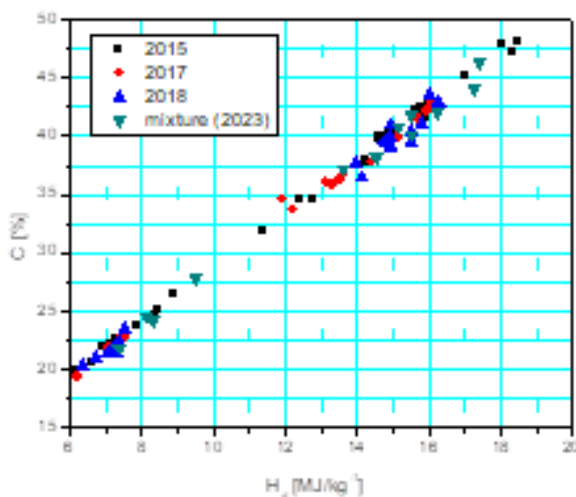


Figure 5. Total carbon content as a function of low heating value, for the samples of lignite, for 2015 – 2023 years, experimental data

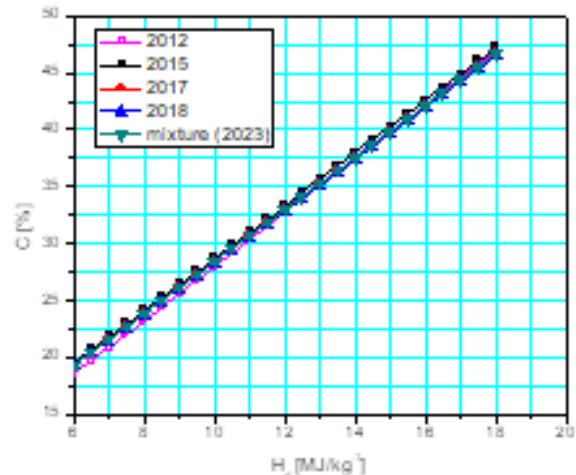


Figure 6. Total carbon content as a function of low heating value, for the samples of lignite, for 2012 – 2023 years, analytical data

The essential dependence is the dependence of the Carbon Emission Factor on the lower heating value, obtained based on the following formula, eq (16):

$$CEF = 10 \frac{C}{H_d} \quad (16)$$

Including formulas eq.(11-15) in eq. (16), we get the following dependencies, eq. (17-21):

$$2012: \quad CEF = 23.718 + \frac{42.637}{H_d} \quad (17)$$

$$2015: \quad CEF = 23.09 + \frac{56.39}{H_d} \quad (18)$$

$$2017: \quad CEF = 22.88 + \frac{55.71}{H_d} \quad (19)$$

$$2018: \quad CEF = 22.80 + \frac{53.35}{H_d} \quad (20)$$

$$2023: \quad CEF = 22.79 + \frac{56.53}{H_d} \quad (21)$$

Based on experimental measurements (Tables 1-4) and calculations eq. (16-21), the diagrams in Figures 7-9 show the dependence of *CEF* on the lower heating value. The diagram in Figure 7 presents the dependences of *CEF* on H_d for the years 2015-2023, obtained by experimental research. The diagrams in Figures 8 and 9 presents analytical dependencies for the years 2012-2023. Based on the analytical dependencies eq. (16-21) and from diagrams 8 and 9, one can notice and conclude:

- The deviations of the value of the emission factor by year are small, and for some years negligible,
- Based on the results of the emission factor taken over from our previous work [5, 6], for 2012 year and their comparison with other years (2015 - 2023), the *CEF* factor of lignite used for the operation of TPP "Nikola Tesla" had the lowest values, especially in the part up to 10 MJ/kg, which indicates that higher quality lignite was used then and less CO₂ was emitted compared to later years,
- Based on certain experimental measurements and calculations, the emission factor of lignite used in 2015 year has the highest value,
- Lignites from other years are found in terms of quality between these two cases.

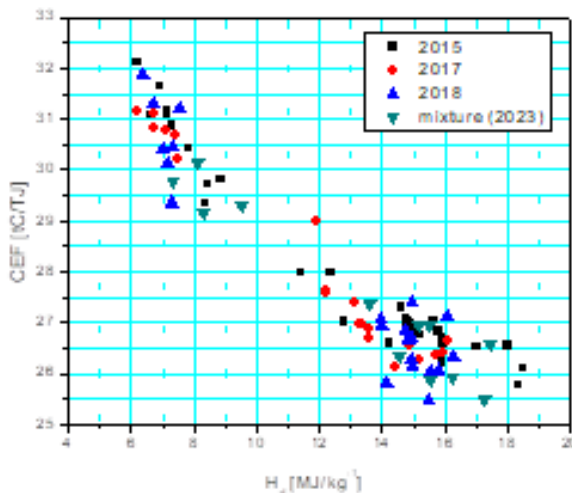


Figure 7. *CEF* as a function of low heating value, for the samples of lignite, for 2015 – 2023 years, experimental data

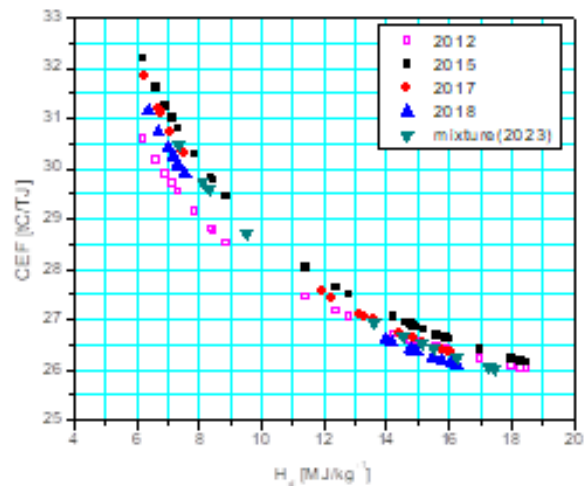


Figure 8. *CEF* as a function of low heating value, for the samples of lignite, for 2012 – 2023 years, analytical data

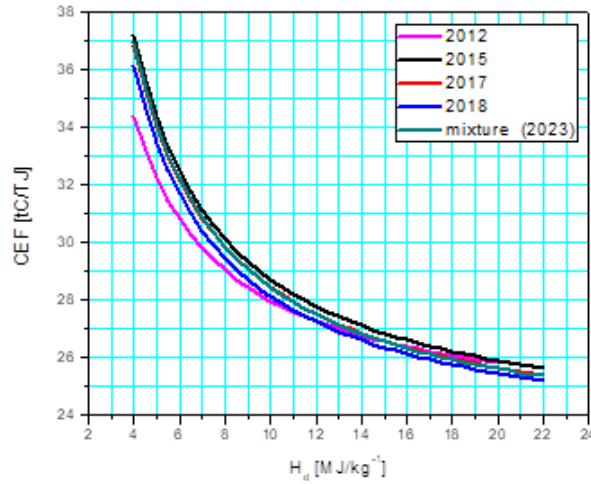


Figure 9. CEF as a function of low heating value, for the samples of lignite, for 2012 – 2023 years, analytical data

The deviation of the CEF value from the standard prescribed values recommended by the IPCC for lignite and for “as received” sample ($6 \leq H_d \leq 10$ MJ/kg) is of great importance. Therefore, it is necessary to carry out a detailed review of the stated deviations based on the diagram presented in Figure 9. Enlarged part of the diagram, Figure 10, shows the deviation of the CEF value for lower heating values of $H_d = 6$ MJ/kg and $H_d = 8$ MJ/kg, for the coal samples 2012 – 2023, with emphasis on values for 2012 and 2015 years (year with highest and lowest CEF values of the samples tested). These values are also presented in Table 6.

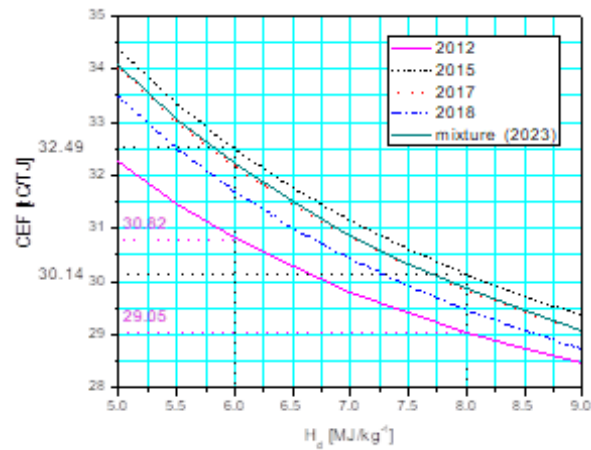


Figure 10. Deviation of CEF values as a function of lower heating values $H_d = 6$ MJ/kg and $H_d = 8$ MJ/kg, for the samples, for 2012 – 2023 years

Table 6. CEF values for the coal samples, years 2012 – 2023, for lower heating values, $H_d = 6$ MJ/kg and $H_d = 8$ MJ/kg.

Year	CEF tC/TJ ($H_d = 6$ MJ/kg)	CEF tC/TJ ($H_d = 8$ MJ/kg)
2012	30.82	29.05
2015	32.49	30.14
2017	32.17	29.84
2018	31.69	29.47
2023	32.31	29.86

The diagram in Figure 10 presents enlarged portion of diagram (Figure 9.) for the range of lower heating values $6 \leq H_d \leq 8$ MJ/kg, showing the differences in the CEF value of lignites and mixture for each of the years. For $H_d = 6$ MJ/kg and $H_d = 8$ MJ/kg the CEF values for each year are presented in Table 6 and also for the years 2012 and 2015 on diagram in Figure 10. For the coal samples from year 2012, for $H_d = 8$ MJ/kg, the CEF value 29.05 tC/TJ has been registered, while for $H_d = 6$ MJ/kg the CEF value is 30.82 tC/TJ. As in the previous case, for the coal samples from year 2015, for the value of $H_d = 8$ MJ/kg, the CEF value is 30.14 tC/TJ, while for

$H_d = 6$ MJ/kg the CEF value is 32.49 tC/TJ. It can be seen from the previous that the deviation of the CEF factor is higher than 2 tC/TJ for a particular lower heating value. The largest deviation was registered for the samples from 2023 and 2015, 2.35 tC/TJ, while the smallest deviation is 1.77 tC/TJ for the samples from 2012 year. It is evident that CEF values are certainly higher than the prescribed one (27.6 tC/TJ), recommended according to the IPCC, Table 6.

The diagram in Figure 11 shows the dependence of the lower heating value on the content of combustible matter in the samples for the years 2015 - 2023. The diagram shows slight deviations of the linear dependences by year. This is in agreement with the diagrams representing the dependence of CEF by years (diagrams in Figures 8 and 9).

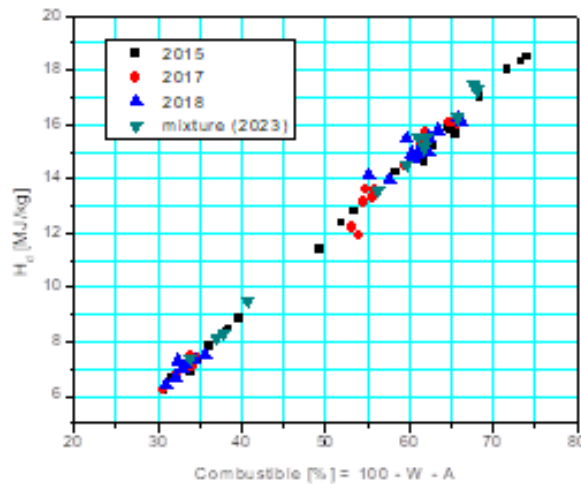


Figure 11. Lower heating value values as a function combustible matter content, for the samples, for 2015 – 2023 years

The diagram in Figure 12 shows the dependence of the CEF value on the lower heating value for imported better quality coal (Table 5). Considering that the content of Carbon (34 – 40 %) and Hydrogen (2.5 - 2.9 %) in the samples on the “as received” basis is significantly higher than that of Kolubara lignite. It is logical and evident that the Lower heating value (LHV) of that coal (over 10 MJ/kg, per “as received” basis) is also higher than Kolubara basin lignite, so this paper did not intend to compare the lignites used for operation of TPP "Nikola Tesla", nor with the mixture of these coals with the Kolubara lignites, but to indicate their differences by showing the emission characteristics. As an example, for the sample, “as received” basis, the lower heating value of better quality coal is from 10 MJ/kg, to over 26 MJ/kg, depending on the sample basis, in contrast to Kolubara lignite, where the lower heating value is in the range of about 7 - 19 MJ/kg.

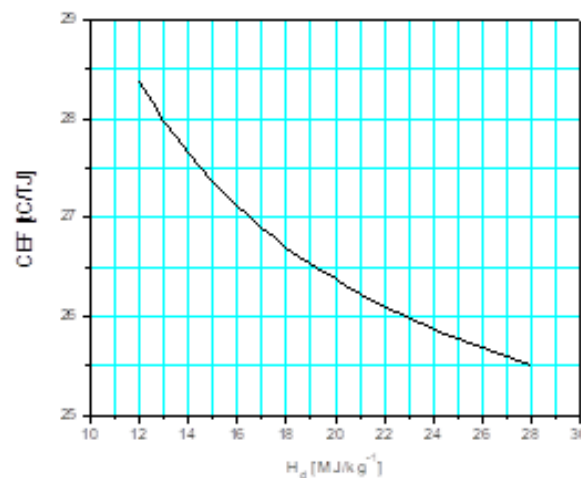


Figure 12. CEF as a function of low heating value, for the imported better quality coal, 2023 year, analytical data

5. Conclusion

This paper presents a methodology that represents a combination of experimental research and calculations in order to determine the emission characteristics of lignite and coal which is used for the operation of TPP within the Joint Stock Company Electric Power Company of Serbia. The results of experimental investigations of lignite used for the operation of TPP "Nikola Tesla", which are mainly lignite from the open-pit mine Kolubara, are given. Samples from 2015 (10 samples), 2017 (6 samples), 2018 (7 samples) and 2023 (4 samples) of a mixture of lignite from the open-pit mine of Kolubara and imported better quality coal from import were used for experimental research. Also, for the investigation, Kolubara lignite from 2012 (30 samples), were used in this paper, which were presented in our previous work. Based on the presented experimental research and calculations, the following conclusions can be drawn:

- The deviations of CEF factor values by years are not negligible, although at first glance they appear so. The fact leading to higher amounts of emitted CO₂, causing higher penalties for exceeded emissions,
- Deviations of the CEF factor for the lower heating values $H_d = 6$ MJ/kg and $H_d = 8$ MJ/kg, by years, are significant in absolute value,
- Based on the results of CEF taken over from our previous works [5, 6], for 2012 year and their comparison with other years (2015 - 2023), the emission factor of lignite used for the operation of TPP "Nikola Tesla " had the lowest values, indicating that year was used lignite of higher quality compared to later years,
- Based on certain experimental measurements and calculations, the emission factor of lignite used in 2015 year has the highest value,
- Lignite from other years are found in terms of quality between these two cases,
- The paper highlights the necessity for periodic sampling of coal, in order to determine the exact values of emission characteristics, instead of using pre-defined values by IPCC,
- Using the methodology described for experimental determination of CEF, it is possible to determine the emissions from particular energy sources and total CO₂ emissions on the country level.

Nomenclature

A – ash content, [%]

C – carbon content, [%]

CEF – carbon emission factor, [tC/TJ]

Combustible – combustibles content, [%]

H – hydrogen content, [%]

H_d – lower heating value, net calorific value, at constant pressure, [kJ/kg] [MJ/kg]

N + O – nitrogen + oxygen content, [%]

S – sulfur content, [%]

W – moisture content, [%]

Subscripts

d – lower heating value
(lower calorific value)

fix – fixed

g – combustible,

tot – total

Acronyms

TPP – thermal power plant,

IPCC – intergovernmental panel on climate change

Acknowledgment

This work was financially supported by the Ministry of Science, Technological Development and Innovation of the Republic of Serbia under contract number: 451-03-65/2024-03/200103 and Science Fund of the Republic of Serbia, 1375/2023, NO_x Reduction Based Thermal Power Plant Optimization – NOXTROT.

References

- [1] ***, United Nations Framework Convention on Climate Change, <https://unfccc.int>,
- [2] ***, 2006 IPCC Guidelines for National Greenhouse Gas Inventories, <https://www.ipcc-nggip.iges.or.jp/public/2006gl/index.html>, 2006

- [3] ***, 2019 Refinement to the 2006 IPCC Guidelines for National Greenhouse Gas Inventories, <https://www.ipcc.ch/report/2019-refinement-to-the-2006-ipcc-guidelines-for-national-greenhouse-gas-inventories/>, 2019
- [4] Stefanović, P., *et al.*, Emission of Greenhouse Gasses in Public Enterprise Electric Power Industry of Serbia in the Period from 1990 – 2008, NIV-LTE-422 rev.2.0., February, Vinča, Belgrade, Serbian, 2010
- [5] Stefanović, P., *et al.*, Emission Factor of Kolubara Basin Lignite (in Serbian), *Termotehnika*, 37 (2011), 2, pp. 241-251
- [6] Stefanović, P. Lj., *et al.*, Evaluation of Kolubara Lignite Carbon Emission Characteristics, *Thermal Science*, 16 (2012), 3, pp. 805-816
- [7] Spasojević V. D., *et al.*, Evaluation of Kostolac Lignite Carbon Emission Characteristics, *Proceedings*, 18th Symposium on Thermal Science and Engineering of Serbia, Simterm, 2017, Sokobanja, Serbia, pp. 803-809,
- [8] Zoran Marković, Milić Erić, Dejan Cvetinović, Vuk Spasojević, Predrag Škobalj, Predrag Stefanović, "Determination of Specific Carbon Dioxide Emission Factor From Thermal Power Plants Nikola Tesla A and B", Full Papers Proceeding of International Conference "Power Plants 2014", 28-31.October 2014, Zlatibor Serbia, ISBN 978-86-7877-024-1, pp. 854 – 863,
- [9] Stefanović, P. Lj., *et al.*: Pljevlja Lignite Carbon Emission Characteristics, *Thermal Science*, 23 (2019), 5, pp. S1523-S1531,
- [10] Stefanović, P. Lj., *et al.*: Evaluation of Carbon Emission Factor for Lignite Bogutovo Selo, Ugljevik, VII Regional Conference IEEP '19, INDUSTRIAL ENERGY AND ENVIRONMENTAL PROTECTION IN SOUTH EASTERN EUROPEAN COUNTRIES, June 19-22, 2019, pp. 159-168, Congress Center Romania, Zlatibor, Serbia,
- [11] Dejan Cvetinović, Nikola Živković, Aleksandar Erić, Nada Milutinović, Vukman Bakić, "Carbon Emission Factor of Balkan Lignites", 5th South East European Conference on Sustainable Development of Energy, Water and Environment Systems, 5th SEE SDEWES Conference, <https://www.vlore2022.sdewes.org/>, 22.5.2022. – 26.05.2022, Vlore, Albania, SEE2022.0145, ISSN–2706-3682 (digital proceedings),
- [12] Živković, N. V., *et al.*: Variability of Carbon Emission Factors from Lignite of the Kostolac Basin in Time, *THERMAL SCIENCE: Year 2023*, Vol. 27, No. 6B, pp. 4911-4917, <https://doi.org/10.2298/TSCI230727243Z>,
- [13] Mirković-Gorgievski, M. D., *et al.*, Gravimetric and Instrumental Methods Comparison for Experimental Determination of Carbonate Carbon Content in Solid Mineral Fuels, *Thermal Science*, 26 (2022), 1A, pp. 319-328,



VII. Automatics and control of processes, equipment, and plants, FEMA

Predicting Heat Demand of Residential Buildings with Lag and Time Variables

Mirko M. Stojiljković^a, Marko G. Ignjatović^b, Goran D. Vučković^c, Vladan S. Jovanović^d

^aUniversity of Niš, Faculty of Mechanical Engineering in Niš, Niš, RS, mirko.stojiljkovic@masfak.ni.ac.rs

^bUniversity of Niš, Faculty of Mechanical Engineering in Niš, Niš, RS, marko.ignjatovic@masfak.ni.ac.rs

^cUniversity of Niš, Faculty of Mechanical Engineering in Niš, Niš, RS, goran.vuckovic@masfak.ni.ac.rs

^dUniversity of Niš, Faculty of Mechanical Engineering in Niš, Niš, RS, vladan.jovanovic@masfak.ni.ac.rs

Abstract: Building heat demand depends on various parameters: the properties of the materials, geometry, climate conditions, occupancy patterns, usage habits, etc. Short-term forecasts of the heat demand can be based on different subsets of these parameters, depending on the application and available data. Recently, black-box models that apply machine learning methods became widely used to predict the heat demand. This paper is a part of a broader research effort and investigates the time-series prediction properties of a simple model based on the Random Forest regression that uses only lag and time-related variables as inputs. The time resolution is one hour. The lag variables are the heat demand one hour before, 24 hours before, and 25 hours before the time of prediction. The time-related variables are the hour of day, day of week, and month. The model has the coefficient of determination of over 0.99, root-mean-square error 38.2 kWh, and mean absolute error 19.1 kWh. The most important predictor is the 24-hours lag. Large errors occur mainly early in the morning and late in the evening, when the heat demand changes have high values and the setpoint temperatures are being modified.

Keywords: building simulation, multi-story apartment building, random forest, time-series forecasting.

1. Introduction

Modern and smart design and operation of energy-efficient buildings, that have complex energy supply systems, require accurate forecasts of the building energy performance. Traditionally, this is achieved with building simulations, which are built around knowledge-based models. Recently, the models based on knowledge and physical laws are often replaced or supplemented with data-driven or surrogate models, which are rely on machine learning algorithms.

Data-driven models are often desirable because they can be very precise and do not require full detailed information on the variables that the building heating demand depends on the properties of the materials, geometry, climate conditions, occupancy patterns, usage habits, etc. Gathering such information is often time- or resource-consuming. These models can perform sufficiently well with different subsets of the aforementioned parameters, depending on the application and available data. In addition, they can also be faster and more accurate [1].

However, sufficiently precise surrogate models require input data of appropriate quantity and quality. The inputs are usually obtained either with real measured data [2] or synthetic data obtained with building simulations [3].

Surrogate models can be applied in the design phase [4], in the case of building retrofit analysis [5], or for the operation of building energy systems [2]. They can be used to predict either annual, monthly, daily, hourly, or sub-hourly energy consumption data. A particularly important category of machine learning models applied to the heating and cooling demand are the models that predict time series data.

Li et al. [3] applied several supervised machine learning models to create building meta-models that are supposed to replace computationally expensive building simulation models and predict time series. They used hourly data obtained with EnergyPlus [6] simulations of an office building. The input variables were heating and cooling demand lags, physical properties of the building elements, climate data, hour, and day type. The most important features for the prediction of the heating energy consumption appeared to be the day type and

the first lag of the outdoor dry-bulb temperature, while for the cooling energy consumption, the outdoor dry-bulb temperature and solar heat gain coefficient were the most significant.

Liang et al. [7] applied the K-Nearest Neighbors method for surrogate modeling buildings in the pre-design stage, as well as predicting the heating and cooling load of retail, hotel, and office buildings. They used input variables related to the building geometry, indoor temperature, occupancy, lightning, and equipment.

Zhang et al. [8] presented an approach for day-ahead prediction of the cooling load of an office building by reorganizing historical data based on daily time and weather similarity and then applying machine learning models such as Linear Regression, Random Forest, Support Vector Regression, and Gaussian Process Regression.

Chou and Ngo [9] proposed a hybrid model for day-ahead forecasts of time-series data from smart grids, based on weekly sliding window. They combined a seasonal autoregressive integrated moving average model (SARIMA) with support vector regression (SVR) and used metaheuristic optimization firefly algorithm (FA) to tune the hyper-parameters. The combination of SVR and FA was applied to overcome the limitations of the linear nature of SARIMA. They analyzed the results obtained with the following inputs: the energy consumption lags, day type (weekday or weekend), hour of the day, and outdoor temperature. The conclusion is that the scenario with the first three features yields the best results. Ikeda and Nagai [10] presented a different hybrid of machine learning and metaheuristic optimization. They optimized operation of a complex building energy system by applying deep neural networks on cooling towers and connected components, and metaheuristics to the rest of the system.

In addition to energy demand, machine learning models have been used to predict the electricity production of a photovoltaic system [11, 12], solar irradiation [13], temperature [14], etc.

This paper examines the predictive performance of a time-series model that forecasts hourly heating demand of a group of multi-story residential buildings. The model uses Random Forest method [15] for regression. The forecast horizon is one-step ahead. This part of a broader research is focused on the model that uses only time-related and heating-demand-lag variables, and attempts to analyze the performance in the cases when the weather-related data is not collected, as well as the data on building geometry, physical properties, occupancy and other relevant patterns, etc.

The buildings have the total floor area of 27000 m². Their behavior is simulated with EnergyPlus to obtain synthetic data for model training and testing. The buildings are divided into 524 thermal zones. The time step of the simulation outputs is one hour.

Prediction of the heating demand of these buildings is of interest for the district heating plant that provides the heat to them.

2. Methodology

As mentioned above, this paper presents the model that predicts the heating demand of a group of residential buildings. The demand is forecast in a time-series manner, one hour ahead. The prediction model is based on Random Forest (RF) regression method. RF is chosen because of its wide range of applicability, relatively fast and computationally non-intensive training procedure, and small number of hyperparameters.

The analyzed period is eight years (from 2014 to 2021). The first six years (from 2014 to 2019) are used to train the model and the last two years (2020 and 2021) remained for testing.

The performance indicators of the regression model are:

- Coefficient of determination (R^2)
- Root mean square error (RMSE)
- Mean absolute error (MAE)

The coefficient of determination, defined in Eq. (1), is dimensionless and shows the ratio of the variance of the predicted variable (in this case the heating demand) explained by the independent variables in the model:

$$R^2 = 1 - \frac{\sum_{i=1}^n (y_i - \hat{y}_i)^2}{\sum_{i=1}^n (y_i - \bar{y})^2} \quad (1)$$

where n is the number of samples, y_i is a true value of the predicted variable for the sample point i , which is obtained with the building simulation in this case, \hat{y}_i is the predicted value, their difference $y_i - \hat{y}_i$ is the error of prediction, and \bar{y} is the arithmetic mean of all true values, as shown in Eq. (2):

$$\bar{y} = \frac{1}{n} \sum_{i=1}^n y_i \quad (2)$$

RMSE, defined in Eq. (3), corresponds to the quadratic error and has the same unit as the predicted variable, i.e. kWh in this case:

$$\text{RMSE} = \sqrt{\frac{1}{n} \sum_{i=1}^n (y_i - \hat{y}_i)^2} \quad (3)$$

MAE, defined in Eq. (4), is also expressed in kWh and shows the absolute error:

$$\text{MAE} = \frac{1}{n} \sum_{i=1}^n |y_i - \hat{y}_i| \quad (4)$$

The model contains only two kinds of variables: (1) time and (2) lag variables. Selection of the lag variables that should be included in the model is performed based on the values of the Pearson correlation coefficient. Figure 1 illustrates these values for the lag variables up to the 100th shift.

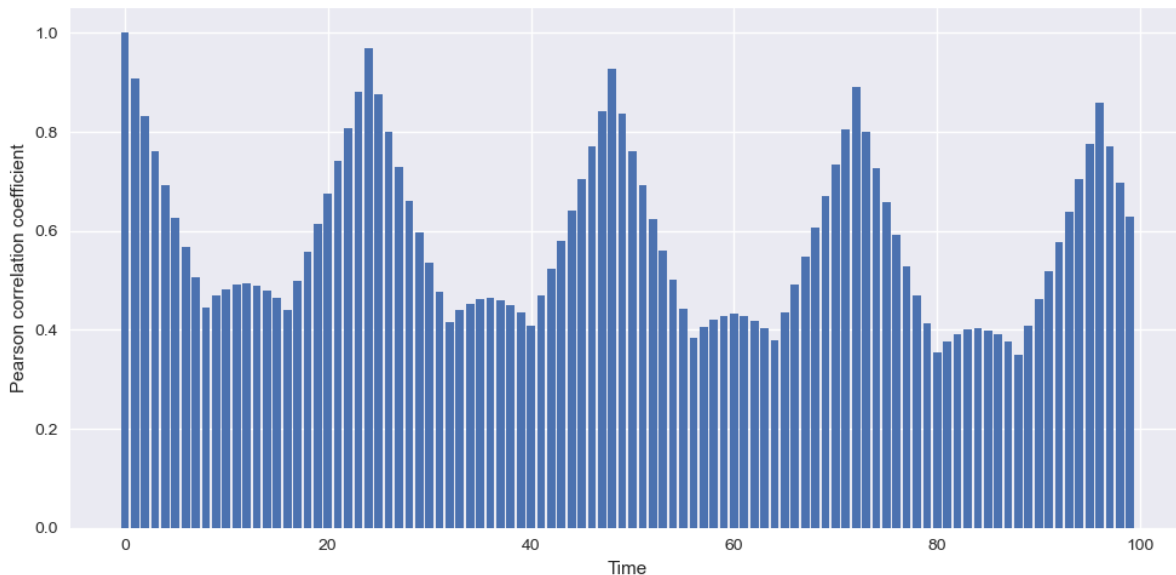


Figure 1. Pearson correlation coefficients for the heating demand and its lags

In addition to the expected drop after the first lag, the correlation coefficient increases again as the time approaches 24 h and again for 48 h, 72 h, and so on. This raises an assumption that the 24th lag gives more information than most of the earlier lags. For that reason, this lag is included in the list of input variables. Since the first lag is naturally involved in the prediction, it seemed as an interesting idea to include the 25th lag as well, so that some relations between the values of the heating demand that occurred 24 and 25 hours in the past can be learned and applied to the demand value from the past hour.

Another interesting detail is noticed for the autocorrelation between the heating demand and its first lag. The Pearson correlation coefficient is very close to one for all the hours of the day except for the morning and evening hours. These are the hours when the changes in the heating demand are usually very large. Figure 2 shows this pattern.

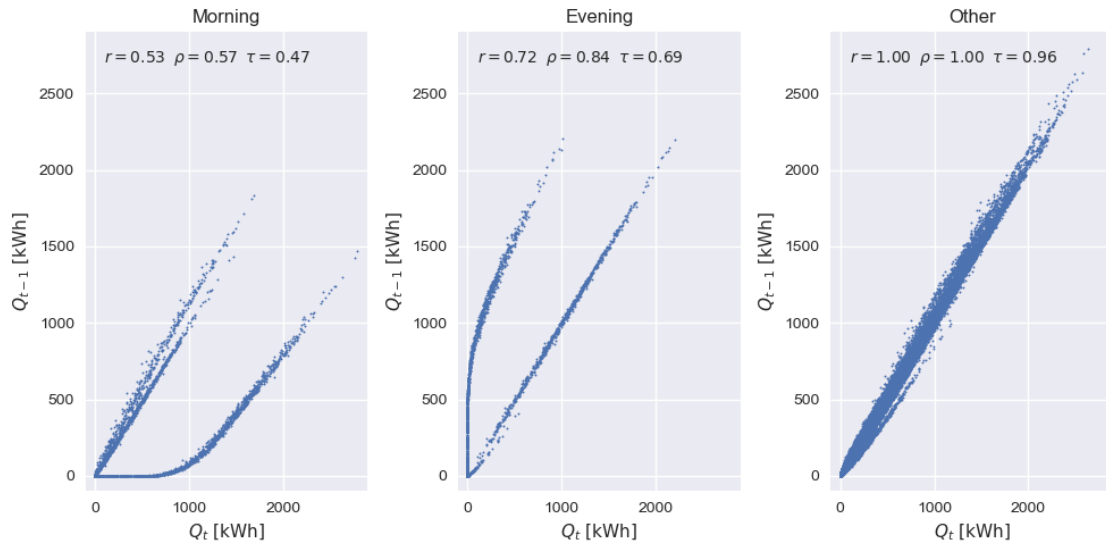


Figure 2. Autocorrelation according to the time of day

Finally, eight features are selected:

- Time variables: hour of day, day of week, day of month, month, and year.
- Lag variables: the heating demand one, 24, and 25 hours before the time of prediction.

The hyperparameters of RF model are defined based on experience and include:

- Number of decision trees: 200,
- Quality of the split: Friedman Mean Squared Error
- Minimal sample size needed to split an internal node: 20
- Number of considered features during the search for the best split: 6

RF model is implemented in Python programming language using Scikit-learn library [16].

3. Results and discussion

The performance of the model is evaluated using the indicators defined in Eqs. (1), (3), and (4). Table 1 illustrates the obtained values of these indicators for training and test data. The values of the coefficient of determination are very high. The values of RMSE and MAE are satisfying, bearing in mind that the maximal simulated value of the heating demand is 2179 kWh.

Table 1. Predictive performance of the model

Indicator	Training data	Test data
Coefficient of determination (R^2)	> 0.99	> 0.99
Root mean square error (RMSE)	30.41 kWh	38.24 kWh
Mean absolute error (MAE)	13.44 kWh	19.08 kWh

Figure 3. shows high correlation between the simulated and corresponding predicted values of the heating demand, which also indicates good overall performance of the model.

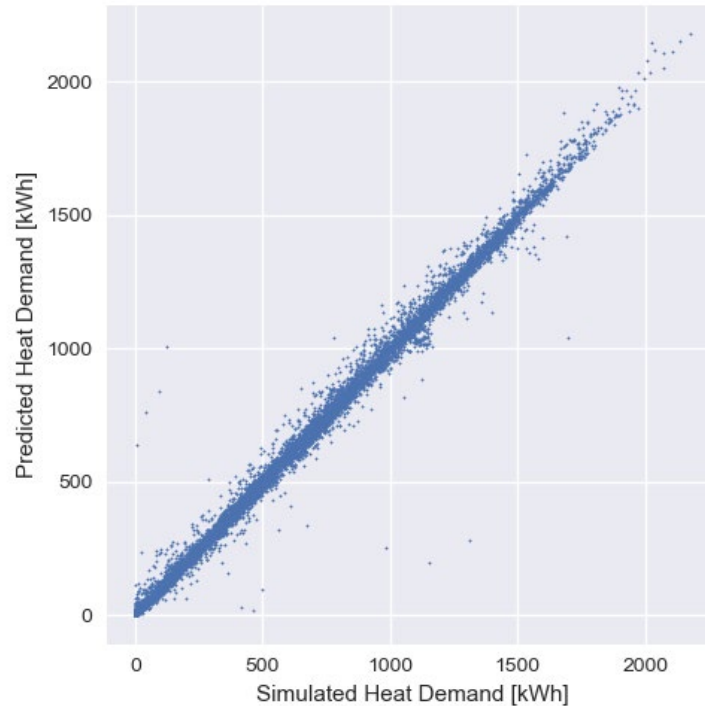


Figure 3. Correlation between simulated and predicted values

However, the maximal absolute error on the test set is 1028.65 kWh, which is too high. Moreover, there are some samples with very high errors. There are 185 sample points in the test set with errors above 100 kWh. The histogram on the left-hand side shown that the most such errors, i.e. 38 of them, have a value between 1000 and 1250 kWh. Most of these data points, 151 of them, are related to the morning hours (between 05:00 and 07:00) and evening hours (between 21:00 and 22:00), which coincide with the significant demand rises and drops that follow the setpoint temperature change.

Figure 5. illustrates feature importance calculated by RF model. The most important feature is the heat demand that occurred 24 h before the prediction time, followed by 1 h and 25 h lags, and the hour of the day. This corresponds to the correlation coefficients from Figure 1.

4. Conclusions

This paper presents a case of time-series, one hour ahead prediction of the heating demand of a group of residential buildings. The hourly demand data is obtained from detailed building simulations, using EnergyPlus software. The machine learning model is based on Random Forest regressor with 200 decision trees and has only time and lag variables as the inputs.

It appears that the 24th lag variable is highly correlated to the predicted heating demand, and it is the variable with the highest feature importance. In general, the heat demand lag variables have much higher importance compared to the time variables.

The performance indicators, the coefficient of determination, root mean squared error, and mean absolute error, suggest good overall prediction performance, but there is a number of samples that are poorly predicted. These samples are mostly related to the early morning and late evening hours and correspond to high demand changes and setpoint temperature shifts.

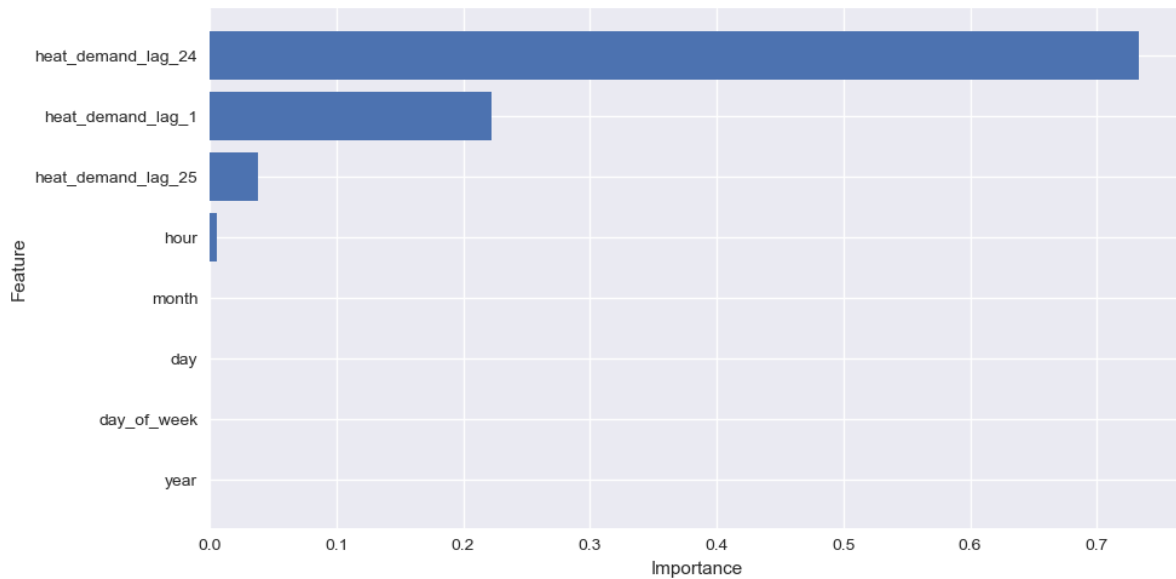


Figure 5. Feature importance

Acknowledgments

This research was supported by the Science Fund of the Republic of Serbia, Grant No. 23-SSF-PRISMA-206, Explainable AI-assisted operations in district heating systems - XAI4HEAT.

References

- [1] Soheil Fathi, Ravi Srinivasan, Andriel Fenner, Sahand Fathi, Machine learning applications in urban building energy performance forecasting: A systematic review, *Renewable and Sustainable Energy Reviews* 133 (2020) 110287, <https://doi.org/10.1016/j.rser.2020.110287>
- [2] Haoan Sha, Majd Moujahed, Dahai Qi, Machine learning-based cooling load prediction and optimal control for mechanical ventilative cooling in high-rise buildings, *Energy & Buildings* 242 (2021) 110980, <https://doi.org/10.1016/j.enbuild.2021.110980>
- [3] Guangchen Li, Wei Tian, Hu Zhang, Xing Fu, A novel method of creating machine learning-based time series meta-models for building energy analysis, *Energy & Buildings* 281 (2023) 112752, <https://doi.org/10.1016/j.enbuild.2022.112752>
- [4] Flavian Emmanuel Sapnken, Mohammad M. Hamed, Božidar Soldo, Jean Gaston Tamba, Modeling energy-efficient building loads using machine-learning algorithms for the design phase, *Energy & Buildings* 283 (2023) 112807, <https://doi.org/10.1016/j.enbuild.2023.112807>
- [5] Mirko M. Stojiljković, Goran D. Vučković, Marko G. Ignjatović, Classification of retrofit measures for residential buildings according to the global cost, *Thermal Science* 25 (2021), No. 4 Part A, pp: 2677-2689, <https://doi.org/10.2298/TSCI200825306S>
- [6] EnergyPlus, Energy Simulation Software, Available at: <https://energyplus.net/>, [accessed 01-Sep-2024].
- [7] Yumin Liang, Yiqun Pan, Xiaolei Yuan, Wenqi Jia, Zhizhong Huang, Surrogate modeling for long-term and high-resolution prediction of building thermal load with a metric-optimized KNN algorithm, *Energy and Built Environment* 4 (2023) 709–724, <https://doi.org/10.1016/j.enbenv.2022.06.008>
- [8] Xu Zhang, Yongjun Sun, Dian-ce Gao, Wenke Zou, Jianping Fu, Xiaowen Ma, Similarity-based grouping method for evaluation and optimization of dataset structure in machine-learning based short-term building cooling load prediction without measurable occupancy information, *Applied Energy* 327 (2022) 120144, <https://doi.org/10.1016/j.apenergy.2022.120144>
- [9] Jui-Sheng Chou, Ngoc-Tri Ngo, Time series analytics using sliding window metaheuristic optimization-based machine learning system for identifying building energy consumption pattern, *Applied Energy* 177 (2016) 751–770, <http://dx.doi.org/10.1016/j.apenergy.2016.05.074>
- [10] Shintaro Ikeda, Tatsuo Nagai, A novel optimization method combining metaheuristics and machine learning for daily optimal operations in building energy and storage systems, *Applied Energy* 289 (2021) 116716, <https://doi.org/10.1016/j.apenergy.2021.116716>
- [11] Gianni Di Giovanni, Marianna Rotilio, Letizia Giusti, Muhammad Ehtsham, Exploiting building information modeling and machine learning for optimizing rooftop photovoltaic systems, *Energy & Buildings* 313 (2024) 114250, <https://doi.org/10.1016/j.enbuild.2024.114250>

- [12] Marina M. Milićević, Budimirka R. Marinović, Machine learning methods in forecasting solar photovoltaic energy production, *Thermal Science* 28 (2024), No. 1, Part B, pp: 479-488, <https://doi.org/10.2298/TSCI230402150M>
- [13] Omer Dagistanli, Hasan Erbay, Hasim Ahmet Yurttakal, Hakan Kor, Solar irradiation forecast by deep learning architectures, *Thermal Science* (26) 2022, No. 4, Part A, pp: 2895-2906, <https://doi.org/10.2298/TSCI2204895D>
- [14] Ihsan Tugal, Fatih Sevgin, Analysis and forecasting of temperature using time series forecasting methods a case study of Mus, *Thermal Science* (27) 2023, No 4, Part B, pp: 3081-3088, <https://doi.org/10.2298/TSCI2304081T>
- [15] Leo Breiman, Random Forests, *Machine Learning*, 45 (2001), pp. 5-32, <https://doi.org/10.1023/A:1010933404324>
- [16] Pedregosa, F., Varoquaux, G., Gramfort, A., Michel, V., Thirion, B., Grisel, O., Blondel, M., Prettenhofer, P., Weiss, R., Dubourg, V., Vanderplas, J., Passos, A., Cournapeau, D., Brucher, M., Perrot, M., Duchesnay, E., Scikit-learn: Machine Learning in Python, *Journal of Machine Learning Research* 12 (2011), pp. 2825-2830

Operational Optimization of Heating Systems with Air-Source Heat Pumps Based on Realistic Electricity Tariffs

Mirko M. Stojiljković^a, Goran D. Vučković^b, Marko G. Ignjatović^c

^aUniversity of Niš, Faculty of Mechanical Engineering in Niš, Niš, RS, mirko.stojiljkovic@masfak.ni.ac.rs

^bUniversity of Niš, Faculty of Mechanical Engineering in Niš, Niš, RS, goran.vuckovic@masfak.ni.ac.rs

^cUniversity of Niš, Faculty of Mechanical Engineering in Niš, Niš, RS, marko.ignjatovic@masfak.ni.ac.rs

Abstract: Heat pumps are among the crucial technologies for increasing renewable energy utilization in the building sector. One of the main factors for adopting heat pumps is their economic attractiveness, which depends on several factors. Air-source heat pumps are especially challenging in this regard because their performance relates significantly to the outdoor conditions. Optimization of operational regimes can lead to lower running costs of heating systems with heat pumps. However, most research efforts in this area are based on relatively simple pricing rules. This paper presents an attempt to perform operation optimization of a heating systems based on a realistic electricity pricing policy, applicable to the households in Serbia. The approach uses the results of detailed building simulations and existing rules for charging electricity as the inputs. It applies mixed integer linear programming to obtain the operation regimes that minimize the operational cost of a heating system over one year. The paper shows the comparison of the obtained results and the results drawn from simplified electricity pricing rules. Finally, it discusses the importance, applicability, and limitations of the presented approach.

Keywords: heat pump, mixed integer linear programming, operational optimization, residential building.

1. Introduction

Heat pumps are a very important technology for adopting renewable energy sources for heating and cooling of buildings [1]. Economic attractiveness is one of the main factors for adopting heat pumps. Cost optimization of design and operation is a tool that improves the economy of the heat pumps and might motivate their adoption. Optimization of operation regimes is important for achieving satisfactory economic results:

- In the planning stage, as a part of integrated design and operation optimization,
- During the operation period, to reduce the running costs.

Pesola [2] demonstrated the importance of operation optimization for the integration of decentralized heat pumps with the existing centralized district heating systems and reduction of the operation cost. Li et al. [3] used the non-dominated sorting genetic algorithm II for multiobjective optimization of the system that combines a photovoltaic heat pump and thermal storage. Aguilera et al. [4] combined mixed integer linear programming (MILP) with demand forecasting to reduce the costs of large-scale heat pumps with thermal storage. Krützfeldt et al. [5] also used MILP for combined design and operation optimization of a heat pump system for a residential building.

However, in most cases, the authors treat electricity (and other) prices as predefined model inputs. In practice, electricity prices might depend on the consumption, and as such, cannot be the inputs to the optimization models.

This paper considers one such case. It uses MILP to find the cost-optimal operation regime of a household heating system with air-source heat pump (ASHP) and district heating network connection. The optimization results are applied to analyze the difference between the operation regimes that correspond to the realistic and simplified prices.

2. Methodology

This paper aims to optimize the operation of a heating system of a residential building. The heating system consists of ASHP and a district heating networks connection. The optimization problem is adjusted to consider realistic Serbian electricity pricing for households.

The tariff system is defined in a progressive manner that motivates electricity savings, which might be problematic in terms of choosing heat pumps over alternative technologies such as gas boilers. There are three pricing zones:

- Green zone, with the lowest price of electricity, available until the total monthly consumption exceeds 350 kWh, for the period of 30 days,
- Blue zone, available from the moment the monthly consumption reaches the threshold of 350 kWh, until it exceeds 1600 kWh, for the period of 30 days,
- Red zone, with the highest price of electricity, valid after the monthly consumption exceeds 1600 kWh, for the period of 30 days.

If the accounting period is different than 30 days, the thresholds are adjusted proportionally.

In addition, the pricing model also includes taxes and incentives.

There are two kinds of tariffs applicable to households:

- Unique tariff, with the same electricity price throughout the day,
- Dual tariff, with the day-time electricity price (valid for 16 hours per day) being four times larger than the night-time price (valid for the remaining eight hours per day).

The pricing rules described — in particular the existence of the green, blue, and red zone — show that the price of electricity in each moment depends on the amount of electricity already consumed. Since the electricity amount must be a decision variable, the prices cannot be inputs.

The optimal operation parameters, which define how much heat is obtained from the heat pump and district heating system at each time step, are determined by formulating and solving MILP problem. The time step used is 1 h and the optimization horizon is one year.

The objective function to minimize is the total annual operational cost of electricity and district heating, expressed in Serbian Dinars (RSD), as defined in Eq. (1):

$$\min \sum_{i=1}^m \left(C_{e,\text{fix}}^i + C_{t,\text{fix}}^i + \sum_{j=1}^n c_{e,G}^j W_{e,G}^j + c_{e,B}^j W_{e,B}^j + c_{e,R}^j W_{e,R}^j + c_t^j Q_t^j \right) \quad (1)$$

where:

- i and j are the indices of a month and hour, respectively;
- m and n are the number of months considered and the number of hours in an observed month, respectively;
- $C_{e,\text{fix}}^i$ and $C_{t,\text{fix}}^i$ are the fixed monthly costs of electricity and district heating, respectively, in RSD; these quantities are the inputs into the optimization problem and affect only the value of the objective function, but not the optimal values of the decision variables;
- $c_{e,G}^j$, $c_{e,B}^j$, and $c_{e,R}^j$ are the prices of the electricity in the hour j , for the blue, green, and red zone, respectively; the prices are expressed in RSD/kWh and might depend only on the time of day, i.e. on j , so they are the inputs to the optimization problem;
- $W_{e,G}^j$, $W_{e,B}^j$, and $W_{e,R}^j$ are the non-negative continuous decision variables that represent the amounts of electricity consumed during the hour j , for the blue, green, and red zone, respectively, expressed in kWh;
- c_t^j is the price of the district heat in the hour j , expressed in RSD/kWh, which is an input to the optimization problem;
- Q_t^j is the non-negative continuous decision variable that represents the amount of heat taken from the district heating system during the hour j , expressed in kWh.

In addition to the afore-mentioned decision variables, the model also uses:

- $Q_{t,\text{HP}}^j$, which is the non-negative continuous decision variable that represents the amount of heat produced by the heat pump during the hour j , expressed in kWh;
- δ_G^j , δ_B^j , and δ_R^j , which are auxiliary binary decision variables that indicate whether the electricity is consumed in the blue, green, and red zone, respectively, during the hour j .

The model has a number of constraints. For brevity, they are omitted from this paper. The main categories of the constraints are:

- Constraints that bound the decision variables, i.e. grid electricity, district heat, and heat pump output amounts,
- Constraints that ensure the satisfaction of electricity and heat demand for each hour,
- Constraints related to the electricity pricing rules

The binary decision variables and constraints related to the electricity pricing make the model considerably more complex and harder to formulate and solve. This might lead to an outstanding increase in the computational time and resources needed to solve it.

This model covers a relatively simple energy supply system of a building that contains the connections to the electrical grid and district heating system, as well as ASHP. The model is applicable to all kinds of electrical heat pumps with a wide practical application. ASHP is chosen for the demonstration of the model because its coefficient of performance (COP) and capacity vary significantly with the environment conditions.

The model can be further extended to support:

- Cooling applications,
- Semi-continuous decision variables, as used in [6, 7],
- Other components such as heat and cool storage, boilers, or cogeneration, as described in [6, 7],
- Solar thermal and photovoltaic systems,
- Consideration of additional objectives, i.e. multiobjective optimization.

Furthermore, this model in its simplest variant can be decomposed over time into a series of smaller monthly models, which might result in the significant reduction of computational time required to obtain the optimal solution.

The model is implemented in the Python programming language by the first author of the paper. It uses the Gurobi Optimizer [8] as MILP backend.

3. Results and discussion

The described operation optimization approach is applied to a case of a single-family residential building with the heated floor area of 150 m². The demand is obtained with the EnergyPlus software [9], using the weather data provided as a typical meteorological year for the City of Niš, Serbia. ASHP properties are taken from manufacturer data and account for the dependence of the capacity and COP on the outdoor and indoor conditions. The optimization procedure is applied for the entire heating season, i.e. from October to April, which makes a total of 5088 hourly time steps.

The results are obtained considering three tariff scenarios:

- Existing unique tariff,
- Existing dual tariff,
- Hypothetical simple tariff that uses always the same price, equal to the blue-zone price.

It is worth mentioning that the simple tariff does not have the zones, which means that the model is simpler, and the price of electricity is a constant and input to the optimization problem.

The results obtained for operation optimization in three scenarios clearly show that, for the current prices, ASHP is preferable over the district heating supply, except when the electricity is consumed in the red pricing zone. Figure 1 shows this conclusion.

Consequently, in both unique and dual tariff cases, the part of the heating demand covered by ASHP is constrained with the threshold value of the red zone. In other words, ASHP and all other electricity consumers are about to use at most 1600 kWh (in a month with 30 days). The rest of the heating demand is covered from the district heating system. In the case of the simple tariff, the price of the electricity is always the same and the entire demand can be satisfied with ASHP, if its capacity is sufficient. Figure 2 shows the demand coverage by ASHP and district heating system.

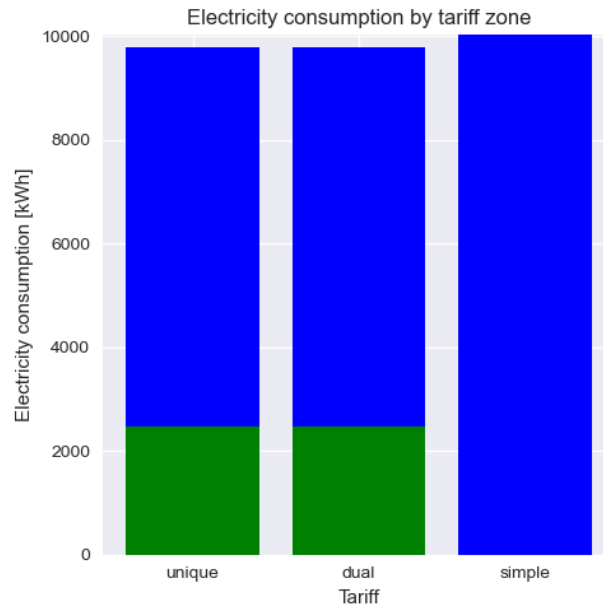


Figure 1. Electricity consumption in different tariff zones

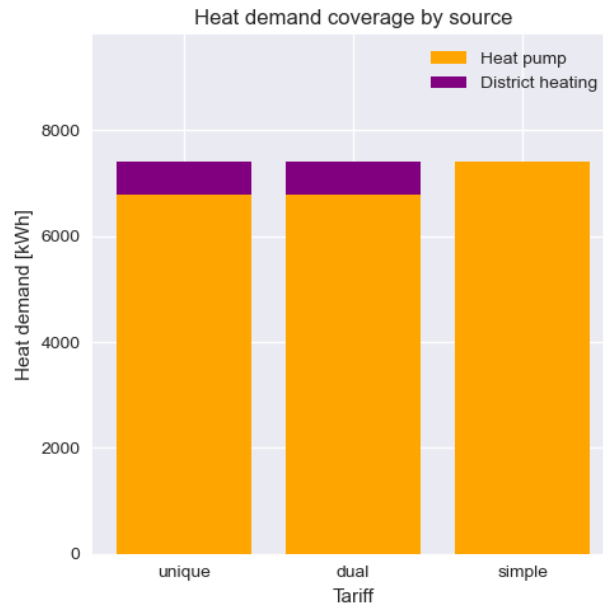


Figure 2. Heat demand covered by the heat pump and district heating system

The above consideration raises a very serious question whether and to what extent the existing electricity pricing rules obstruct a wider acceptance of heat pumps.

Figure 3 shows the histogram with the distribution of the heat demand coverage by source for various outdoor temperature values. An interesting observation is that the heat demand that corresponds to the outdoor temperatures above 0°C is provided entirely by ASHP, due to larger COP values.

Another important conclusion that cannot be seen from the figures is that the heat generated during nights comes from the heat pumps completely due to low prices of electricity.

Figure 4 compares the values of the objective function for all three scenarios. The operational cost of the system is the highest for the unique tariff, mostly because it does not benefit from the low night prices. The case of simple tariff underestimates the cost by over 30% just by neglecting the red zone prices.

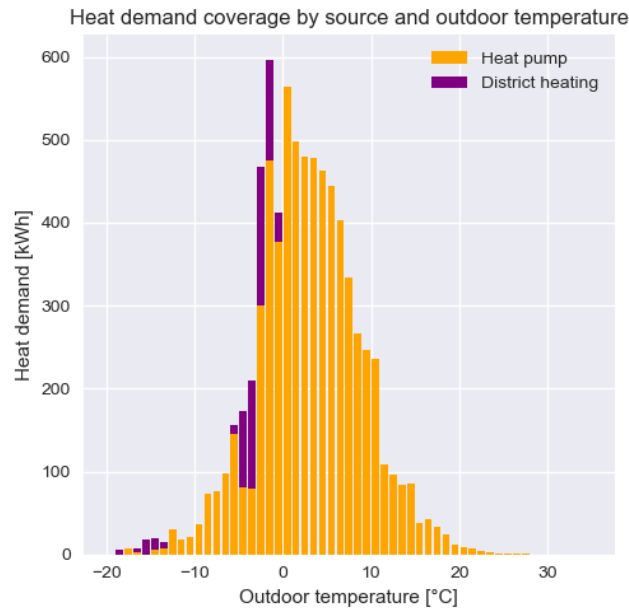


Figure 3. The distribution of the heat demand coverage by source for various outdoor temperature values

4. Conclusions

This paper presents operational optimization of a building heating system with a heat pump and district heating network connection. The most important aspect of the paper is using realistic electricity pricing rules that apply for Serbian households, which make the optimization problem more complex and computationally intensive. The cases with real prices are compared to a simplified case with a fixed price. It is concluded that the differences in the value of the objective function and the variables that define the operation regime can be significant.

It is necessary to underline that the obtained values of the objective function and operation parameters are highly dependent on the electricity and heat demand, properties of the components, and the prices.

The presented model covers a relatively simple energy system but can be extended to include other components and applications, more complex representation of decision variables, and multiobjective optimization.

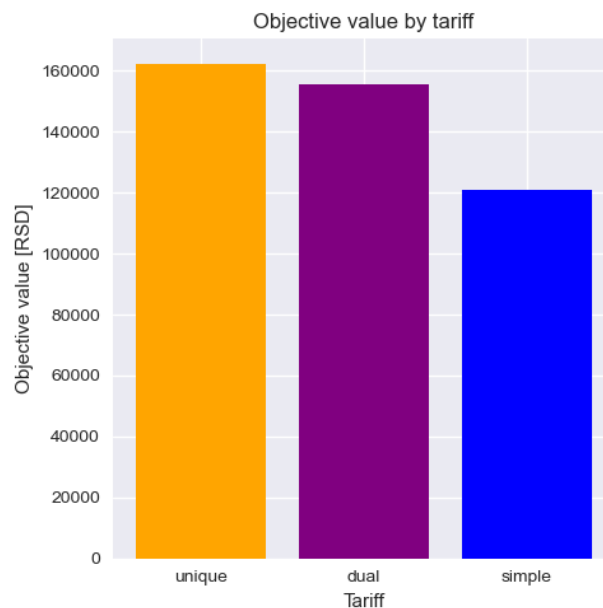


Figure 4. The values of the objective function for different tariffs

The main reasons that can justify the application of such an approach are:

- VII. Automatics and control of processes, equipment, and plants, FEMA

- Operational regimes and objective values might differ significantly with realistic compared to simplified pricing.
- More accurate results of optimization problems can provide a better insight into the potential for cost reduction.
- More accurate results might also have the benefit of better understanding of desirable operation regimes.

However, detailed and accurate approaches might require more complex and computationally intensive mathematical models, which can be an obstacle to wider adoption of such an approach.

Finally, a very important limitation of this approach is that it is very complicated to be implemented directly. It requires the electricity and heating demand predictions until the end of the observed month, as well as all the parameters that impact the performance of heat pumps significantly. However, it might be possible to incorporate the obtained results into a machine learning models and extract rules to predict desirable operation of energy supply systems. This can be a guideline for future work.

Acknowledgment

This research was financially supported by the Ministry of Science, Technological Development, and Innovation of the Republic of Serbia (Contract No. 451-451-03-65/2024-03).

References

- [1] Philip Adebayo, Charaka Beragama Jathunge, Amirhossein Darbandi, Nicholas Fry, Roman Shor, Abdulmajeed Mohamad, Carsten Wemhöner, Aggrey Mwesigye, Development, modeling, and optimization of ground source heat pump systems for cold climates: A comprehensive review, *Energy & Buildings* 320 (2024) 114646, <https://doi.org/10.1016/j.enbuild.2024.114646>
- [2] Aki Pesola, Cost-optimization model to design and operate hybrid heating systems – Case study of district heating system with decentralized heat pumps in Finland, *Energy* 281 (2023) 128241, <https://doi.org/10.1016/j.energy.2023.128241>
- [3] Benjia Li, Zhongbing Liu, Yue Zheng, Huahui Xie, Ling Zhang, Economy and energy flexibility optimization of the photovoltaic heat pump, system with thermal energy storage, *Journal of Energy Storage* 100 (2024) 113526, <https://doi.org/10.1016/j.est.2024.113526>
- [4] José Joaquín Aguilera, Roger Padullés, Wiebke Meesenburg, Wiebke Brix Markussen, Benjamin Zühlsdorf, Brian Elmegaard, Operation optimization in large-scale heat pump systems: A scheduling framework integrating digital twin modelling, demand forecasting, and MILP, *Applied Energy* 376 (2024) 124259, <https://doi.org/10.1016/j.apenergy.2024.124259>
- [5] Hannah Krützfeldt, Christian Vering, Philipp Mehrfeld, Dirk Müller, MILP design optimization of heat pump systems in German residential buildings, *Energy & Buildings* 249 (2021) 111204, <https://doi.org/10.1016/j.enbuild.2021.111204>
- [6] Mirko M. Stojiljković, Marko G. Ignjatović, Goran D. Vučković, Greenhouse gases emission assessment in residential sector through buildings simulations and operation optimization, *Energy* 92 (2015), Part 3, pp. 420-434, <https://doi.org/10.1016/j.energy.2015.05.021>
- [7] Mirko M. Stojiljković, Bi-level multi-objective fuzzy design optimization of energy supply systems aided by problem-specific heuristics, *Energy* 137 (2017), pp. 1231-1251, <https://doi.org/10.1016/j.energy.2017.06.037>
- [8] Gurobi Optimization, LLC, Gurobi Optimizer Reference Manual, 2024, <https://www.gurobi.com>, [accessed 01-Sep-2024]
- [9] EnergyPlus, Energy Simulation Software, Available at: <https://energyplus.net/>, [accessed 01-Sep-2024].

Problems of Lead Screw Accuracy made by turning

Oleh Onysko^a, Volodymyr Kopei^b, Vitalii Panchuk^c, Ivan Ivaniv^d, Anatolii Verkalets^e

^a*National Technical University of Oil and Gas, Ivano-Frankivsk, Ukraine 482, onysko.oleg@gmail.com*

^b*National Technical University of Oil and Gas, Ivano-Frankivsk, Ukraine 482, VKopey@gmail.com*

^c*National Technical University of Oil and Gas, Ivano-Frankivsk, Ukraine 482, v_panch@ukr.net*

^d*National Technical University of Oil and Gas, Ivano-Frankivsk, Ukraine 482*

^e*National Technical University of Oil and Gas, Ivano-Frankivsk, Ukraine 482, anatolii.verkalets-a13124@nung.edu.ua*

Abstract. The accuracy of closing and opening of gate valves or taps, and accordingly the efficiency of energy saving, largely depends on the accuracy of the lead screw. Lead screws are mostly made using lathes. The accuracy of the thread of the lead screw is primarily the accuracy of the thread profile. Basically, the shape and profile of the screw must meet the standards of the trapezoidal thread and, accordingly, with the Archimedean form. However, based on the real conditions of the turning process, the shape of the thread will have a convoluted character, which functionally depends on the accuracy of the setting of the needle relative to the part. Taking this approach into account, it is possible to effectively apply the calculation algorithm, which provides for the maximum possible accuracy of the actual production of a lead screw with a trapezoidal or triangular profile.

Keywords: turning process, manufacturing of machine, thread accuracy.

1. Introduction

The production of lead screws for power needs (taps and gate valves), as well as for drives for machine tools and mechanical jacks, is usually carried out on lathes. To increase the accuracy of strength and stability in conditions of aggressive environments, special materials are used for the production of lead screws, their special thermal treatment processing, and sometimes, in addition to turning operations, they also use thread grinding. However, additional grinding operations reduce the production of lead screws performance. Replacing the grinding process with only turning operations can, of course, significantly speed up the production of lead screws manufacturing. However, there is a problem of accuracy, because cutters for turning thread-part made from hard and strong materials require different geometric parameters in their working part than usual tools, which actually reduce accuracy. To prove the possibility of using such cutters with changed geometric parameters, the shape of the helical surfaces obtained in the turning process should be analysed.

2. Literature Review

According to standards [1,2], lead screws for energy shut-off fittings, and especially for machine tools, are produced with a given trapezoidal profile, which is regulated by a profile angle of 30° [1] or 29° [2] (fig.1). It is clear from the standard that the axial profile of the side surfaces of the threads is a straight line.

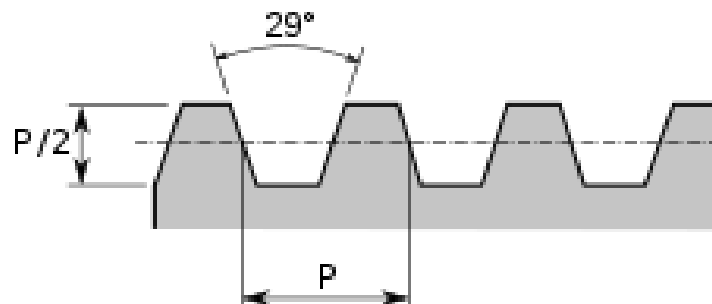


Figure 1. Lead screw profile schema ANSI/ACME. P - thread pitch.

The standard [2] regulates the accuracy of the semi-profile angle as a function of the number of thread threads per 1 inch length. Therefore, the tolerance for the semi-profile angle of 29° is in the range from 47' to 12'.

TABLE 8 TOLERANCES ON 14.5 deg FLANK ANGLE FOR EXTERNAL AND INTERNAL PRODUCT THREADS

Threads/in.	14.5 deg Variation	
	deg	min
16	0	47
14	0	44
12	0	41
10	0	39
8	0	35
6	0	30
5	0	27
4	0	25
3	0	22
2.5	0	20
2	0	18
1.5	0	16
1.33	0	15
1	0	12

Figure 2. The accuracy tolerances of the angle of the half-profile of the thread according to the ASME standard

Today, the most productive method of thread screw manufacturing is whirling process. It is obvious that with an increase in the strength and hardness of a screw with a trapezoidal profile, as well as an improvement in the accuracy of the threaded profile, its service life will increase [3] (Fig. 3).

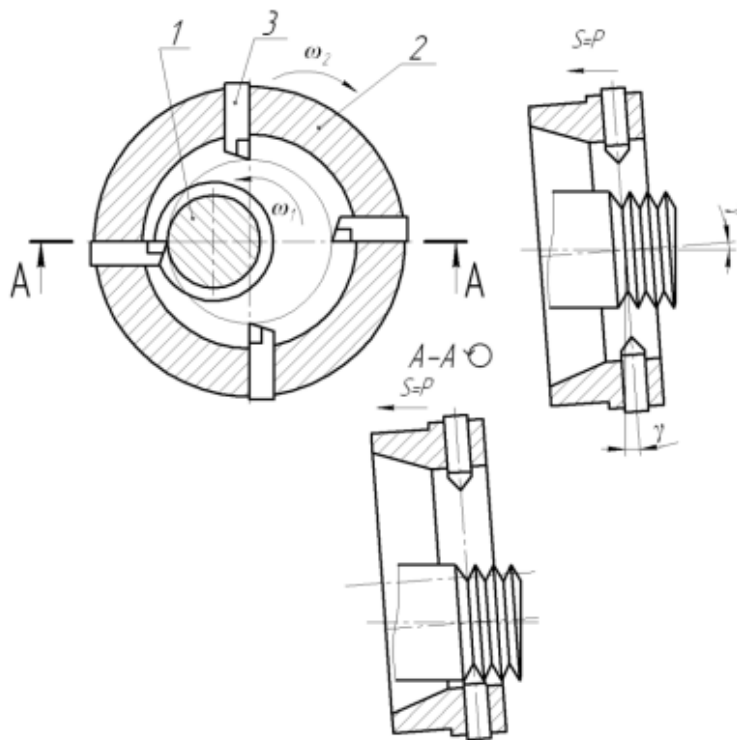


Figure 3. Schema of whirling process: 1-workpiece, 2- whirling head *вихрова головка*, 3-cutting tool.

This method consists in the fact that during the rotation of the processed workpiece and the parallel movement of the cutter head along its axis with a certain step in one rotation of the workpiece, the resulting movement is carried out along a helical line. The axis of the cutter head is shifted parallel to the axis of the processed workpiece by the special amount, so the cutting process is intermittent.

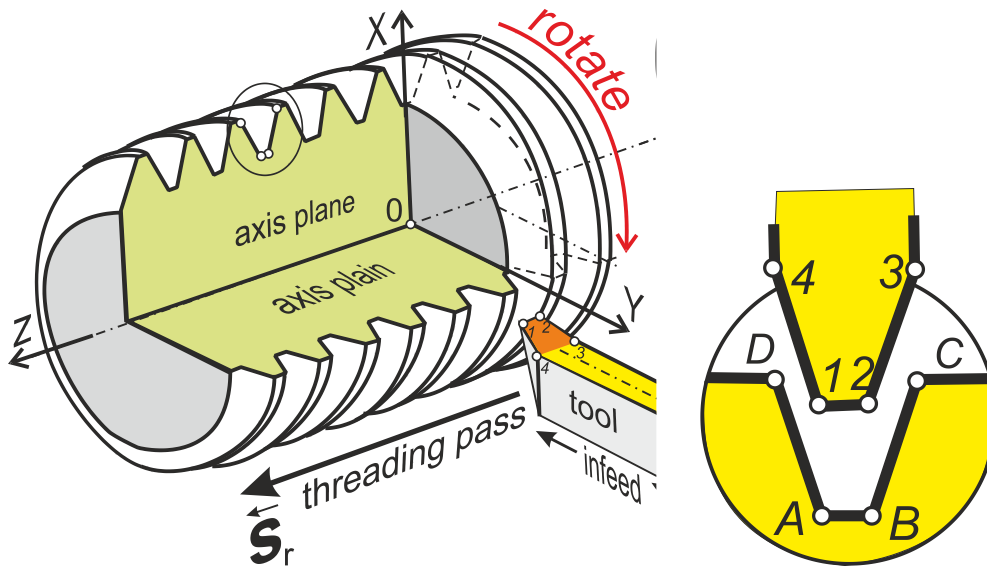


Figure 6. Shema of the turning of screw by using cutter with non-zero rake angle.

In the study, the rake angle is equal to 12° , according to recommendations for turning threads from stainless steel. In the figure, the front surface of the cutter is shown in orange to emphasize its inclination relative to the yellow main plane. (Fig. 6, 7).

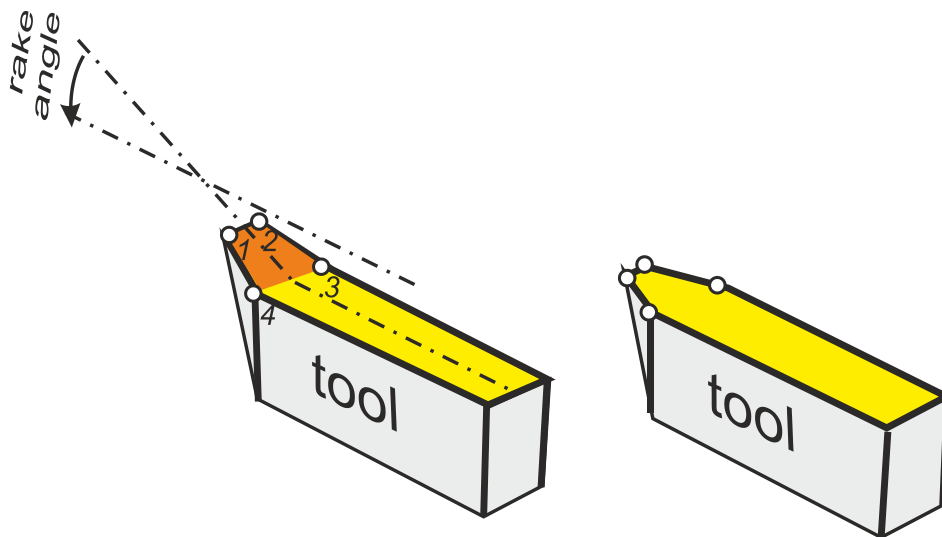


Figure 7. Shema of the turning-tool used for screw -making by using cutter non-zero (left) and zero rake angle (right).

Non-zero values of the rake angle are recommended for turning difficult-to-machine materials with an ultimate strength of more than 1200 MPA.

The following expressions are the theoretical basis of the method of calculating of the convoluted screw axial profile (Fig. 6) [7]:

$$Z(x) = tg(\alpha)x \frac{\sin \tau}{\sin \gamma} - \frac{Pt}{2\pi} \quad (1)$$

Where:

$$\tau = \gamma - \arcsin\left(\frac{d_{\min or}}{2x} \sin \gamma\right) \quad (2)$$

α - half-profile of cutting edge. (the same as thread half profile).

4. Conclusion

The axial profile of the lead screw obtained by turning and whirling are:

- -curve,
- asymmetric,
- largely depends on the location of the cutters relative to the part and the value of their rake angle.

References

- [1] ISO Metric Trapezoidal Screw Thread; Nominal Dimensions. Standard DIN 103-4 1977-04
- [2] Standard:ASME-B1-5-1988-Acme-Screw-Threads <https://ru.scribd.com/document/253785811/ASME-B1-5-1988-Acme-Screw-Threads>. (Last 10.11.2024)
- [3] Andriy Diachun, Vasyl Vasylykiv, Oleg Korol, Volodymyr Myhailiuk, Ivan Golovaty, Andriy Kuras. Investigation of geometrical parameters in screw surfaces whirling process. Scientific Journal of the Ternopil National Technical University, Vol. 1(101), 2021, P. 68-78.
- [4] Lexiang Wang, Yan He, Chao Liu, Yulin Wang, Yufeng Li, Shilong Wang, Yan Wang. Analytical modeling of temperature distribution in lead-screw whirling milling considering the transient un-deformed chip geometry. *International Journal of Mechanical Sciences*, Vol. 157–158, 2019, P. 619-632. <https://doi.org/10.1016/j.ijmecsci.2020.105419> [Get rights and content](#)
- [5] Vasile Merticaru, Gheorghe Nagiț, Oana Dodun, Eugen Merticaru, Eugen Merticaru, Eugen Merticaru, Eugen Merticaru. Influence of Machining Conditions on Micro-Geometric Accuracy Elements of Complex Helical Surfaces Generated by Thread Whirling. *Micromachines* 2022, 13(9), 1520; <https://doi.org/10.3390/mi13091520>
- [6] Onysko, O., Kopei, V., Onysko, O., Kopei, V., Kusyj, Y., Kornuta, O., Schuliar, I. (2023). Turning of NC10 Threads for Drill Pipes: Theoretical Study of the Designed Profile. In: Ivanov, V., Trojanowska, J., Pavlenko, I., Rauch, E., Pitel, J. (eds) *Advances in Design, Simulation and Manufacturing VI. DSMIE 2023. Lecture Notes in Mechanical Engineering*. Springer, Cham. P. 356-366. doi:10.1007/978-3-031-32767-4_34
- [7] Oleh Onysko, Iuliia Medvid, Vitalii Panchuk, Vesna Rodic, Cristian Barz. (2021). Geometric Modeling of Lathe Cutters for Turning High-Precision Stainless Steel Tapered Threads. In: Vitalii Ivanov et al. (Eds). *Advances in Design, Simulation and Manufacturing: Proceedings of the 4-th International Conference on Design, Simulation and Manufacturing: The Innovations Exchange, DSME-2021*. / DSME 2021, LNME, P. 472–480. doi: 10.1007/978-3-030-77719-7_47



VIII. Flow, heat and mass transfer, combustion

Theoretical thermodynamic analysis of the organic Rankine cycle

*Evangelos Bellos^a, Saša Pavlović^b, Mića Vukić^b, Branka Nakomčić-Smaragdakis^c,
Mirjana Laković^b*

^a *Department of Mechanical Engineering, School of Engineering, University of West Attica, Athens, GR,
bellose@uniwa.gr*

^b *Faculty of Mechanical Engineering, University in Niš, Niš, RS*

^c *Faculty of Technical Sciences, University of Novi Sad, Novi Sad, RS*

Abstract: The present work is a theoretical investigation of the organic Rankine cycle (ORC). A simplified cycle is studied aiming to determine the ORC thermodynamic efficiency in an analytical and simplistic way. Reasonable assumptions have been made and the methodology is based on an analysis of the cycle depiction in the temperature – specific entropy diagram. An analytical solution for the ORC efficiency was developed using the low cycle temperature, the high cycle temperature, the superheating degree, the liquid and vapor-specific heat capacities and the fluid latent heat at the high-temperature level. The reported mean deviation of the suggested analytical model compared to the detailed thermodynamic one was found at 5.03% which is an acceptable value. Moreover, analytical approximations for the efficiency with regression models were created for three different working fluids names n-pentane, toluene and R600. The present approach can be extended to extra working fluids and operating conditions and the present work consists of the first step for the establishment of this methodology.

Keywords: Theoretical cycle, Thermodynamic cycle, Organic Rankine Cycle, Thermal efficiency, Power cycle

1. Introduction

The organic Rankine cycle (ORC) is an established technology for the efficient exploitation of low-grade energy sources like solar [1], geothermal [2] biomass and waste heat [3]. They can also be used for complex systems such as thermal Carnot batteries [4] and trigeneration units [5]. The modeling of ORC is based on the development of analytical thermodynamic models based on energy and mass balances that use thermodynamic properties from libraries and tools [6] [7], something that is reliable, but it creates difficulties when the ORC has to be studied further. Specifically, in dynamic simulation and optimization procedures, there is a need to develop simpler models for the ORC analysis that present simplicity, and they lead to reduced complexity in the simulation and generally reduced computational time.

In the literature, there are some studies that have examined the ORC in detail aiming to develop analytical approaches for its performance. Li [8] and Li et al. [9] performed two studies about the trapezoidal approach for estimating the performance of the ORC. This idea was further expanded by Wang et al. [10] who separated the ORC into three smaller cycles; trilateral, Carnot and Brayton cycles. The same research team performed another work with the trapezoidal design [11] and both studies ([10] [11]) emphasized the working fluid investigation. The separation of the ORC into three cycles was also studied by Scangolatto et al. [12] and they gave emphasis on the detailed modeling of the subcomponents. Moreover, another literature study worked with the entropy generation principle for analyzing the ORC [13].

In this direction, the investigation suggests a new idea regarding ORC modeling by using the proper assumptions. This idea has been based on the previous literature review, and mainly in Ref. [10], but it has some different points aiming to increase the accuracy and to be presented as a simpler one. Therefore, this work has added value to the existing literature. Moreover, the present work shows how the suggested efficiency equation can be used for the ORC analysis and some regression equations are developed to simplify further the ORC performance.

2. Material and methods

2.1 The suggested theoretical cycle modeling

2.1.1 Cycle description

The organic Rankine cycle is modeled in a simplistic way as depicted in Figure 1. The heat input is separated into three parts (1→2), (2→3) and (3→4). The heat input of (1→2) is the preheating, which is an approximately isobaric process, as well as the (3→4) which is the superheating. The evaporation (2→3) is performed under the constant high-temperature level (TH). The heat rejection is conducted in the process of (5→6), (6→7) and (7→1). The temperature is not constant in the process (5→6), while in the others is constant. The work production is the area instant the space 1-2-3-4-5-6-7-1.

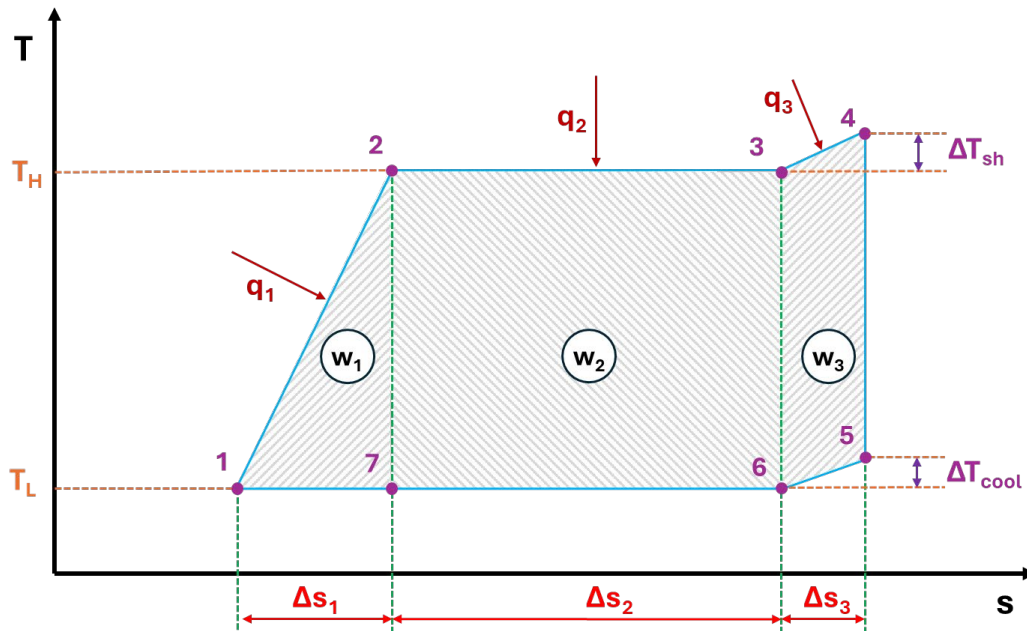


Figure 1. Thermodynamic cycle depiction in temperature (T) – specific entropy (s) diagram

2.1.2 Suggested cycle modeling

The following equations present the mathematical modeling for simulating the ORC cycle efficiency in an analytical way.

The specific work production (w) is calculated as below:

$$w = w_1 + w_2 + w_3 \quad (1)$$

The specific work (w_1) of the space (1-2-7-1) is calculated as:

$$w_1 = \frac{1}{2} \cdot \Delta s_1 \cdot (T_H - T_L) \quad (2)$$

The specific work (w_2) of the space (2-3-6-7-2) is calculated as:

$$w_2 = \Delta s_2 \cdot (T_H - T_L) \quad (3)$$

The specific work (w_3) of the space (3-4-5-6-3) is calculated as:

$$w_3 = \Delta s_3 \cdot (T_H - T_L) + \frac{1}{2} \cdot \Delta s_3 \cdot \Delta T_{sh} - \frac{1}{2} \cdot \Delta s_3 \cdot \Delta T_{cool} \quad (4)$$

The specific heat input (q) is calculated as below:

$$q = q_1 + q_2 + q_3 \quad (5)$$

The specific heat input in the process (1→2) is calculated as:

$$q_1 = \int_{s_1}^{s_2} T(s) \cdot ds = \int_{s_1}^{s_2} \left[T_L + \frac{s - s_1}{s_2 - s_1} \cdot (T_H - T_L) \right] \cdot ds = \frac{1}{2} \cdot \Delta s_1 \cdot (T_L + T_H) \quad (6)$$

The specific heat input in the process (2→3) can be calculated as:

$$q_2 = \Delta s_2 \cdot T_H \quad (7)$$

The specific heat input in the process (3→4) can be calculated as:

$$q_3 = \int_{s_3}^{s_4} T(s) \cdot ds = \int_{s_3}^{s_4} \left[T_H + \frac{s - s_3}{s_4 - s_3} \cdot \Delta T_{sh} \right] \cdot ds = \frac{1}{2} \cdot \Delta s_3 \cdot \left(T_H + \frac{\Delta T_{sh}}{2} \right) \quad (8)$$

The specific entropy generation in the process (1→2) is calculated as below:

$$\Delta s_1 = c_{p,l} \cdot \ln \left(\frac{T_H}{T_L} \right) \quad (9)$$

Practically, this process is approximately the sum of an isentropic compression and of an isobaric liquid heat input. Thus, the previous formula is a very good approximation.

The specific entropy generation in the process (2→3) is calculated as below:

$$\Delta s_1 = \frac{r_H}{T_H} \quad (10)$$

The latent heat of the high-temperature [$r_H = r(T_H)$] is used in the previous formula.

The specific entropy generation in the process (3→4) is calculated as below:

$$\Delta s_3 = c_{p,v} \cdot \ln \left(\frac{T_H + \Delta T_{sh}}{T_H} \right) = c_{p,v} \cdot \ln \left(1 + \frac{\Delta T_{sh}}{T_H} \right) \approx c_{p,v} \cdot \frac{\Delta T_{sh}}{T_H} \quad (11)$$

Practically, this process is approximately an isobaric gas heat input. Thus, the previous formula is a very good approximation. Moreover, the ratio $\left(\frac{\Delta T_{sh}}{T_H} \right)$ is relatively low, thus the previous approximation can be done (with Taylor series utilization).

The mean specific heat capacity of the liquid [$c_{p,l} = c_{p,l}(T_m)$] and mean specific heat capacity of the vapor [$c_{p,v} = c_{p,v}(T_m)$] can be estimated in the mean temperature:

$$T_m = \frac{T_L + T_H}{2} \quad (12)$$

Regarding the temperature difference between the state points (5) and (6), this has to be estimated by using the superheating degree, the low and the high-temperatures. The specific entropy variation in the process (3→4) and (5→6) are the same as absolute value. Assuming that these processes are approximately isobaric, it can be said:

$$\Delta s_3 = c_{p,v} \cdot \ln \left(1 + \frac{\Delta T_{sh}}{T_H} \right) = c_{p,v} \cdot \ln \left(1 + \frac{\Delta T_{cool}}{T_L} \right) \quad (13)$$

Therefore, by assuming the same specific heat capacities, it is concluded:

$$\Delta T_{cool} = \frac{T_L}{T_H} \cdot \Delta T_{sh} \quad (14)$$

The net specific work production can be written as below, after combining the reported equations:

$$w = \left[\frac{1}{2} \cdot c_{p,l} \cdot T_H \cdot \ln \left[\frac{T_H}{T_L} \right] + r_H + c_{p,v} \cdot \Delta T_{sh} + \frac{1}{2} \cdot c_{p,v} \cdot T_H \cdot \left(\frac{\Delta T_{sh}}{T_H} \right)^2 \right] \cdot \left[1 - \frac{T_L}{T_H} \right] \quad (15)$$

The specific heat input can be written as below, after combining the reported equations:

$$q = c_{p,l} \cdot \left(\frac{T_L + T_H}{2} \right) \cdot \ln \left[\frac{T_H}{T_L} \right] + r_H + c_{p,v} \cdot \Delta T_{sh} + \frac{1}{2} \cdot c_{p,v} \cdot T_H \cdot \left(\frac{\Delta T_{sh}}{T_H} \right)^2 \quad (16)$$

The theoretical ORC efficiency ($\eta_{model,ORC}$) can be written as:

$$\eta_{th,ORC} = \frac{\frac{1}{2} \cdot c_{p,l} \cdot T_H \cdot \ln \left[\frac{T_H}{T_L} \right] + r_H + c_{p,v} \cdot \Delta T_{sh} + \frac{1}{2} \cdot c_{p,v} \cdot T_H \cdot \left(\frac{\Delta T_{sh}}{T_H} \right)^2}{c_{p,l} \cdot \left(\frac{T_L + T_H}{2} \right) \cdot \ln \left[\frac{T_H}{T_L} \right] + r_H + c_{p,v} \cdot \Delta T_{sh} + \frac{1}{2} \cdot c_{p,v} \cdot T_H \cdot \left(\frac{\Delta T_{sh}}{T_H} \right)^2} \cdot \left[1 - \frac{T_L}{T_H} \right] \quad (17)$$

The thermal efficiency of the “similar” Carnot cycle is given as below, assuming as high temperature the (T_H) and avoiding the use of superheating which is generally low.

$$\eta_{\text{carnot}} = 1 - \frac{T_L}{T_H} \quad (18)$$

Therefore, it can be written:

$$\eta_{\text{model,ORC}} = \frac{\frac{1}{2} \cdot c_{p,l} \cdot T_H \cdot \ln \left[\frac{T_H}{T_L} \right] + r_H + c_{p,v} \cdot \Delta T_{\text{sh}} + \frac{1}{2} \cdot c_{p,v} \cdot T_H \cdot \left(\frac{\Delta T_{\text{sh}}}{T_H} \right)^2}{c_{p,l} \cdot \left(\frac{T_L + T_H}{2} \right) \cdot \ln \left[\frac{T_H}{T_L} \right] + r_H + c_{p,v} \cdot \Delta T_{\text{sh}} + \frac{1}{2} \cdot c_{p,v} \cdot T_H \cdot \left(\frac{\Delta T_{\text{sh}}}{T_H} \right)^2} \cdot \eta_{\text{carnot}} \quad (19)$$

or

$$\eta_{\text{th,ORC}} = f \cdot \eta_{\text{carnot}} \quad (20)$$

The factor (f) shows how the theoretical ORC is close to the respective Carnot cycle, and it is defined as:

$$f = \frac{\frac{1}{2} \cdot c_{p,l} \cdot T_H \cdot \ln \left[\frac{T_H}{T_L} \right] + r_H + c_{p,v} \cdot \Delta T_{\text{sh}} + \frac{1}{2} \cdot c_{p,v} \cdot T_H \cdot \left(\frac{\Delta T_{\text{sh}}}{T_H} \right)^2}{c_{p,l} \cdot \left(\frac{T_L + T_H}{2} \right) \cdot \ln \left[\frac{T_H}{T_L} \right] + r_H + c_{p,v} \cdot \Delta T_{\text{sh}} + \frac{1}{2} \cdot c_{p,v} \cdot T_H \cdot \left(\frac{\Delta T_{\text{sh}}}{T_H} \right)^2} \quad (21)$$

2.1.3 Classical thermodynamic modeling

This subsection includes the main expressions for the typical thermodynamic modeling for the ORC. This modeling is used in the present work to compare the suggested modeling of section 2.1.2 with the typical one. The ORC depiction is given in Figure 2, and it is the simplest possible illustration of this power cycle.

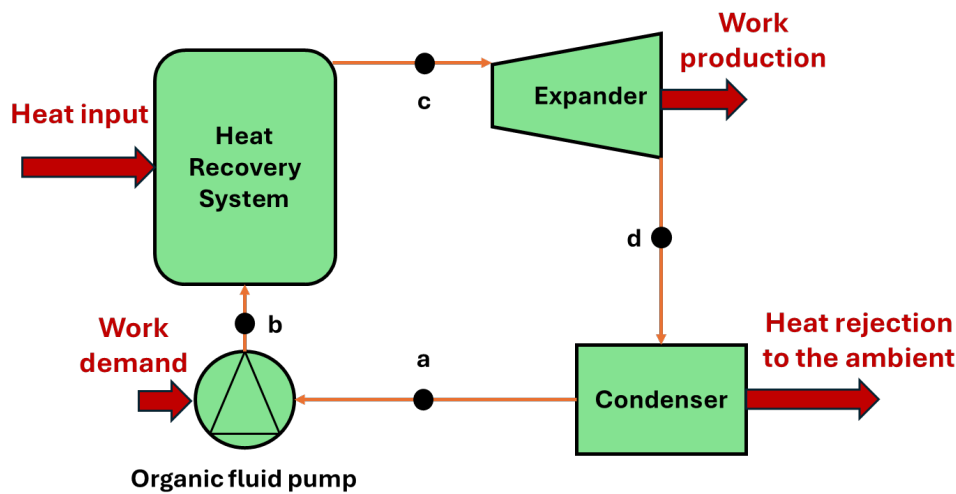


Figure 2. Depiction of the thermodynamic ORC configuration

The specific heat input in the unit is calculated as:

$$q_{\text{in}} = h_c - h_b \quad (22)$$

The heat rejection to the environment is given as:

$$q_{\text{out}} = h_d - h_a \quad (23)$$

The work production in the expander device is given as:

$$w_{\text{exp}} = h_c - h_d \quad (24)$$

The work demand in the organic fluid pump is given as:

$$w_{\text{pump}} = h_b - h_a \quad (25)$$

The net work production of the cycle is given as:

$$w_{\text{net}} = w_{\text{exp}} - w_{\text{pump}} \quad (26)$$

The ORC thermal efficiency is given as:

$$\eta_{\text{real,ORC}} = \frac{W_{\text{net}}}{Q_{\text{in}}} \quad (27)$$

The previous formula regards the ORC efficiency that is calculated with the traditional thermodynamic models.

2.2 Followed methodology

In this work, the analytical approach of section 2.1.2 is compared with the analytical thermodynamic approach of section 2.1.3. The main analysis is conducted with n-pentane as a working fluid, while extra analysis is conducted for toluene and R600. Different combinations of low temperature, high temperature and superheating degree are investigated. All the examined scenarios concern subcritical operation. The thermodynamic properties are retrieved by the libraries of Engineering Equation Solver [14]; a tool that is used for the thermodynamic analysis with the modeling of section 2.1.3.

3. Results and discussion

Figure 3 depicts the thermodynamic efficiency of the ORC with the analytical model and with the thermodynamic analysis which is called real efficiency with n-pentane as working fluid. Also, the respective Carnot cycle efficiency is depicted in this figure. The deviation between the model and the real value is generally low with a mean value around 5.03%. Therefore, it is clear that the suggested analytical model is accurate enough. Also, the deviation is generally constant for the studied high temperatures the fact which shows good behavior of the model under different operating conditions.

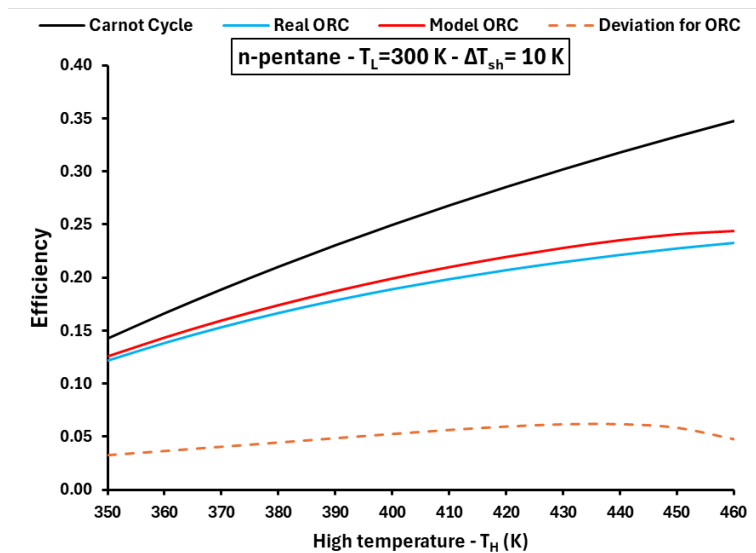


Figure 3. Efficiency cycle for n-pentane with low cycle temperature at 300 K, 10 K superheating degree and variable high cycle temperatures

The next stage is the presentation of an example for the application of the present methodology. Figures 4 and 5 show the variation of the (f) factor for different operating conditions with n-pentane as the working medium. This factor is the ratio of the ORC efficiency to the respective Carnot cycle efficiency. In Figure 4, the (f) is given for low temperature at 300 K, while in Figure 5 for superheating at 10 K. It can be concluded from these figures that the rise of the high temperature decreases the value of (f). Moreover, the increase of the superheating degree in the expander inlet leads to higher values for the ratio (f). The rise of the lower temperature increases the values of (f) in low high temperatures, but after T_H=445 K, the reverse result is obtained. Generally, in low high temperatures, the (f) is close to 90%, while in higher high temperatures is closer to 70%. This interesting result indicates that the ORC is the most appropriate cycle in applications with relatively low-temperature heat sources.

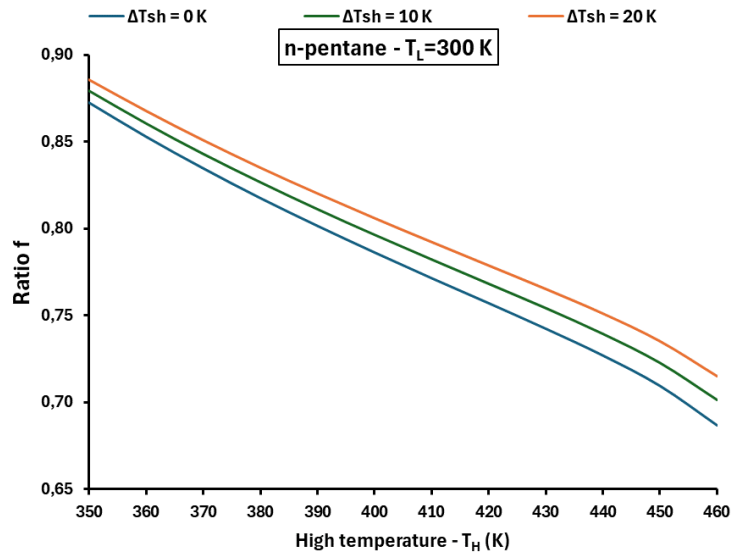


Figure 4. Ratio (f) for *n*-pentane with low cycle temperature at 300 K, 0-10-20 K superheating degrees and variable high cycle temperatures

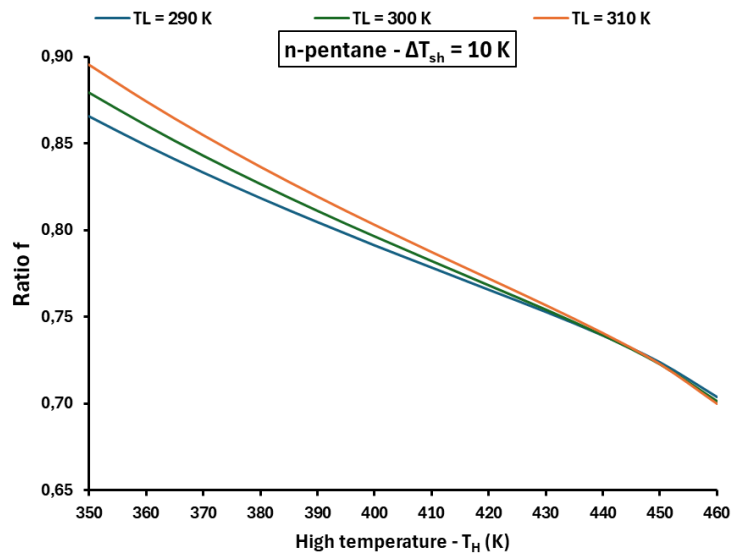


Figure 5. Ratio (f) for *n*-pentane with low cycle temperatures at 290-300-310 K, 10 K superheating degree and variable high cycle temperatures

Moreover, the development of some linear regression equations regarding the factor (f) is something very interesting. The following approximation equations were developed for three working fluids.

A) *n*-pentane (0.50% mean deviation and $R^2=99.09\%$)

$$f = 1.2401 - 0.001554 \cdot T_H + 0.000566 \cdot T_L + 0.001012 \cdot \Delta T_{sh} \quad (28)$$

Applicability for: $350 \text{ K} \leq T_H \leq 460 \text{ K}$, $290 \text{ K} \leq T_L \leq 310 \text{ K}$, $0 \text{ K} \leq \Delta T_{sh} \leq 20 \text{ K}$

B) Toluene (0.40% mean deviation and $R^2=98.60\%$)

$$f = 1.0821 - 0.001024 \cdot T_H + 0.000605 \cdot T_L + 0.000496 \cdot \Delta T_{sh} \quad (29)$$

Applicability for: $350 \text{ K} \leq T_H \leq 460 \text{ K}$, $290 \text{ K} \leq T_L \leq 310 \text{ K}$, $0 \text{ K} \leq \Delta T_{sh} \leq 20 \text{ K}$

C) R600 (0.67% mean deviation and $R^2=98.46\%$)

$$f = 1.4362 - 0.002312 \cdot T_H + 0.00077 \cdot T_L + 0.00121 \cdot \Delta T_{sh} \quad (30)$$

Applicability for: $350 \text{ K} \leq T_H \leq 420 \text{ K}$, $290 \text{ K} \leq T_L \leq 310 \text{ K}$, $0 \text{ K} \leq \Delta T_{sh} \leq 20 \text{ K}$

Figures 6, 7 and 8 show the results regarding the accuracy of the model for the (f) compared to the real analytical model values for n-pentane, toluene and R600 respectively. It is clear that the suggested formulas have high accuracy, and they can easily be applied to thermodynamic calculations.

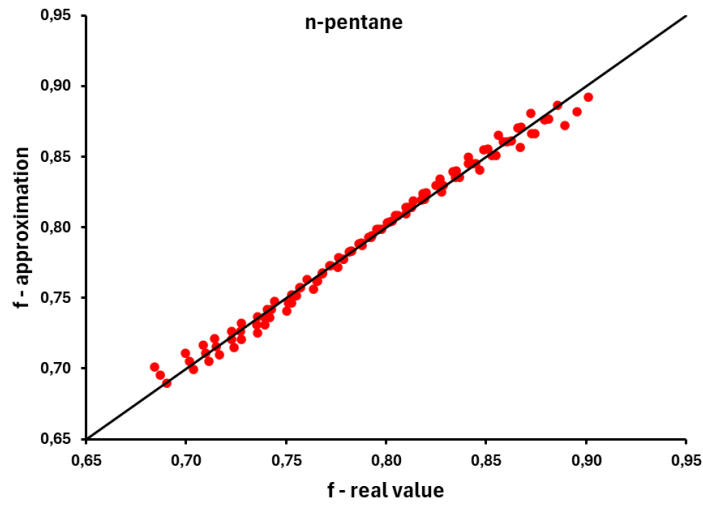


Figure 6. Comparison of the approximation model for the (f) ratio for n-pentane as working medium

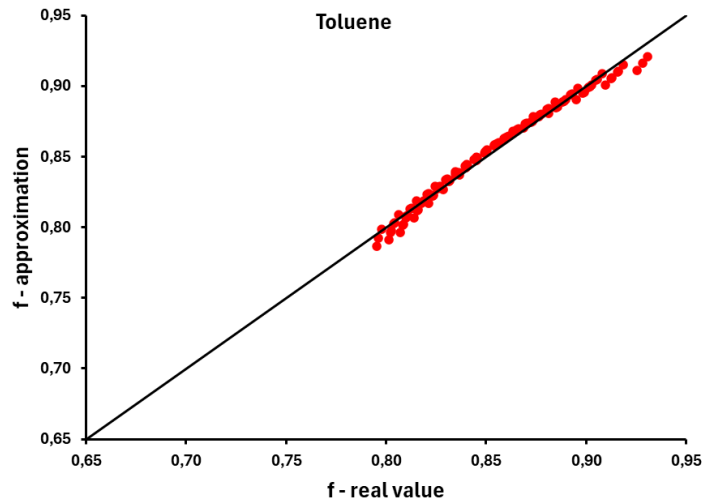


Figure 7. Comparison of the approximation model for the (f) ratio for Toluene as working medium

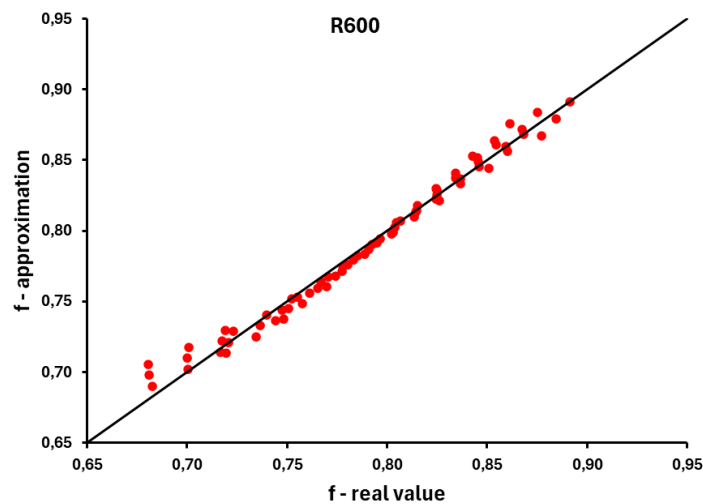


Figure 8. Comparison of the approximation model for the (f) ratio for R600 as working medium

4. Conclusions

The present work suggests an analytical model regarding the thermal efficiency calculation of a basic ORC. This model needs the low cycle and the high cycle temperatures, the superheating degree, the specific heat capacities of the fluid in liquid and vapor phases, as well as the latent heat in the high-temperature level. This model is able to determine the efficiency of the cycle with a 5% accuracy compared to the traditional thermodynamic models. Moreover, this model can be used for quick simulations regarding ORCs, for example, in dynamic simulations and in optimization procedures.

Furthermore, in the present work, extra studies were conducted by exploiting the developed model. Specifically, the (f) factor, which is the ratio of the ORC to the respective Carnot cycle was calculated for different operating conditions with n-pentane. Also, linear approximation equations were developed for the (f) for n-pentane, toluene and R600. The results of this investigation can be used for the analysis of systems that include ORC aiming to simplify the calculations and to decrease the computational time. Also, in the future, the present model can be extended to other ORC architectures and to other working fluids.

Nomenclature

$c_{p,l}$	Specific heat capacity of the liquid, kJ/kgK
$c_{p,v}$	Specific heat capacity of the vapor, kJ/kgK
f	Factor for ORC efficiency ratio
h	Specific enthalpy, kJ/kg
q	Specific heat, kJ/kg
q_{in}	Specific heat input in the heat recovery system, kJ/kg
q_{out}	Specific heat rejection in the condenser, kJ/kg
T	Temperature, K
T_H	High cycle temperature, K
T_L	Low cycle temperature, K
T_m	Mean temperature, K
s	Specific entropy, kJ/kgK
w	Specific work, kJ/kg
w_{net}	Net specific work production, kJ/kg
w_{pump}	Specific work demand by the pump, kJ/kg
w_{exp}	Specific work production by the expander, kJ/kg

Greek Symbols

Δs	Specific entropy variation, kJ/kgK
ΔT_{sh}	Superheating degree in the expander inlet, K
ΔT_{cool}	Superheating degree in the expander outlet, K
η_{carnot}	Carnot cycle efficiency
$\eta_{model,ORC}$	ORC efficiency with the suggested model
$\eta_{real,ORC}$	ORC efficiency with the traditional thermodynamic analysis

Abbreviation

ORC Organic Rankine Cycle

References

- [1] Loni R, Mahian O, Markides CN, Bellos E, le Roux WG, Kasaeian A, et al. A review of solar-driven organic Rankine cycles: Recent challenges and future outlook. *Renewable and Sustainable Energy Reviews* 2021;150:111410. <https://doi.org/10.1016/j.rser.2021.111410>.
- [2] Loni R, Mahian O, Najafi G, Sahin AZ, Rajae F, Kasaeian A, et al. A critical review of power generation using geothermal-driven organic Rankine cycle. *Thermal Science and Engineering Progress* 2021;25:101028. <https://doi.org/10.1016/j.tsep.2021.101028>.
- [3] Loni R, Najafi G, Bellos E, Rajae F, Said Z, Mazlan M. A review of industrial waste heat recovery system for power generation with Organic Rankine Cycle: Recent challenges and future outlook. *Journal of Cleaner Production* 2021;287:125070. <https://doi.org/10.1016/j.jclepro.2020.125070>.
- [4] Huang B, Fang Y, Miao Z, Xu J. Thermodynamic analysis and optimization of the TI-PTES based on ORC/OFC with zeotropic mixture working fluids. *Journal of Energy Storage* 2024;100:113669. <https://doi.org/10.1016/j.est.2024.113669>.
- [5] Bellos E, Pavlovic S, Stefanovic V, Tzivanidis C, Nakomcic-Smaradgakis BB. Parametric analysis and yearly performance of a trigeneration system driven by solar-dish collectors. *International Journal of Energy Research* 2019;43:1534–46. <https://doi.org/10.1002/er.4380>.

- [6] Welcome to CoolProp — CoolProp 6.6.0 documentation n.d. <http://www.coolprop.org/> (accessed September 27, 2024).
- [7] REFPROP. NIST 2013.
- [8] Li X. A trapezoidal cycle with theoretical model based on organic Rankine cycle. *International Journal of Energy Research* 2016;40:1624–37. <https://doi.org/10.1002/er.3528>.
- [9] Li X, Wang J, Wu X. Shift-characteristics and bounds of thermal performance of organic Rankine cycle based on trapezoidal model. *Sci China Technol Sci* 2018;61:1802–13. <https://doi.org/10.1007/s11431-018-9331-9>.
- [10] Wang Y, Zhao J, Chen G, Deng S, An Q, Luo C, et al. A new understanding on thermal efficiency of organic Rankine cycle: Cycle separation based on working fluids properties. *Energy Conversion and Management* 2018;157:169–75. <https://doi.org/10.1016/j.enconman.2017.11.079>.
- [11] Chen G, An Q, Wang Y, Zhao J, Chang N, Alvi J. Performance prediction and working fluids selection for organic Rankine cycle under reduced temperature. *Applied Thermal Engineering* 2019;153:95–103. <https://doi.org/10.1016/j.applthermaleng.2019.02.011>.
- [12] Scagnolatto G, Cabezas-Gómez L, Bigonha Tibiriçá C. Analytical model for thermal efficiency of organic Rankine cycles, considering superheating, heat recovery, pump and expander efficiencies. *Energy Conversion and Management* 2021;246:114628. <https://doi.org/10.1016/j.enconman.2021.114628>.
- [13] Li M, Zhao B. Analytical thermal efficiency of medium-low temperature organic Rankine cycles derived from entropy-generation analysis. *Energy* 2016;106:121–30. <https://doi.org/10.1016/j.energy.2016.03.054>.
- [14] EES: Engineering Equation Solver | F-Chart Software: Engineering Software n.d. <https://fchartsoftware.com/ees/> (accessed September 26, 2024).

Averaged Axisymmetric Flow Surfaces in Hydraulic Turbomachines

Jasmina Bogdanović Jovanović^a, Živojin Stamenković^b, Jelena Petrović^c, Miloš Kocić^d

^a Faculty of Mechanical Engineering, Niš, RS, jasmina.bogdanovic.jovanovic@masfak.ni.ac.rs

^b Faculty of Mechanical Engineering, Niš, RS, zivojin.stamenkovic@masfak.ni.ac.rs

^c Faculty of Mechanical Engineering, Niš, RS, jelena.petrovic@masfak.ni.ac.rs

^d Faculty of Mechanical Engineering, Niš, RS, milos.kocic@masfak.ni.ac.rs

Abstract: Hydraulic turbomachines represent a group of turbomachines that operate with incompressible fluid, mostly water. They have a huge application in different hydraulic systems, such as water supply, irrigation, in cooling systems, hydraulic transport, as part of technological procedures in the industry etc. The optimal design of the hydraulic turbomachine is crucial for its optimal operation, i.e. work with maximum efficiency. In the process of turbomachine designing one of the basic assumptions is that fluid flow passing the impeller is axisymmetric, and on that bases the elementary stages of the impeller are determined. This paper presents the procedure for determining the averaged axisymmetric flow surfaces based on the results obtained using numerical simulations of flow in the impeller. Numerical simulations are used to verify and correct results of flow velocity in impeller domain, enabling the correction of the impeller geometry in accordance with the obtained results of the numerical analysis. According to the obtained results, the correction of specific works of elementary stages can be calculated in order to compare with the assumption made in the previous iteration.

Keywords: hydraulic turbomachines, averaged flow surface, numerical simulations.

1. Introduction

Ever since the design of the first turbomachines, the design process has relied heavily on previous experience. Due to the complex geometry of flow domain and the impossibility of explicitly calculating the flow parameters in it, this task is complex and requires some assumptions to be made. The assumptions may be more or less correct, which must be confirmed in the turbomachine testing phase. The entire process of designing a turbomachine is a long and demanding job, and each correction requires the creation of a new prototype whose working parameters must be checked on the test stand. Therefore, any correction that can be made before experimental testing of the prototype greatly reduces design time and cost.

The main designing element is certainly impeller, which is the main intermediary in the transformation of energy, and it is designed with special attention.

In the designing process the basic assumptions are that fluid flow is stationary and that the fluid flow is axisymmetric, and the theory is the theory refers to an impeller with an infinite number of infinitely thin blades [1-3]. Also, fluid flow in the impeller is continual, while flow energy increases in the non-turbine impellers and decreases in turbine impellers [4, 5]. Impeller calculation usually involves defining a certain number of elementary stages (min 5) which usually have equal specific work. There are also studies showing that in some cases it is shown that it is better to have different values of the specific work of elementary stages [6].

Different methodologies for optimization of turbomachinery impellers have been for turbomachines designing purpose [7].

The procedure of averaging the flow velocities according to the circular coordinate enables us to reduce the flow in the impeller to the flow in a fictitious impeller with an infinite number of thin blades that achieve the same flow deflection [8-10].

Numerical simulation of flow in hydraulic turbomachines are valuable tool which allows us to obtain all flow parameters in the flow domain. In this way, relatively quickly, we obtained all the values of the flow parameters of impeller and determine the averaged flow surfaces. Obtaining flow parameters in the flow domain and operating parameters of the turbomachine using CFD software and methodology that has shown good results in practice [11-14].

With the help of CFD techniques, the flow parameters obtained in the impeller of the hydraulic turbomachine can be used to recalculate the averaged flow surfaces [9, 10]. Meridian streamlines are calculated using the integral continuity equation for previously averaged flow parameters [8]. The presented methodology is used to obtain the fictive impeller with infinite number of infinitely thin blades, what allows to compare meridian streamlines with assumed ones.

2. Averaging of flow parameters

Here we will consider the curvilinear orthogonal coordinate system which suits better the fluid flow inside the impeller. The coordinate surfaces are: $q_3 = \text{const.}$ - meridian planes (planes passing through the axis of the rotating impeller), $q_2 = \text{const.}$ - axisymmetric surfaces approximate to averaged flow surfaces and $q_1 = \text{const.}$ - axisymmetric surfaces perpendicular to $q_3 = \text{const.}$ and $q_2 = \text{const.}$, shown in Fig.1 [8]. It is the right (positive) coordinate system and the direction of circumferential coordinate $q_3(\vec{e}_3^o)$ did not need to follow the direction of the impeller rotation.

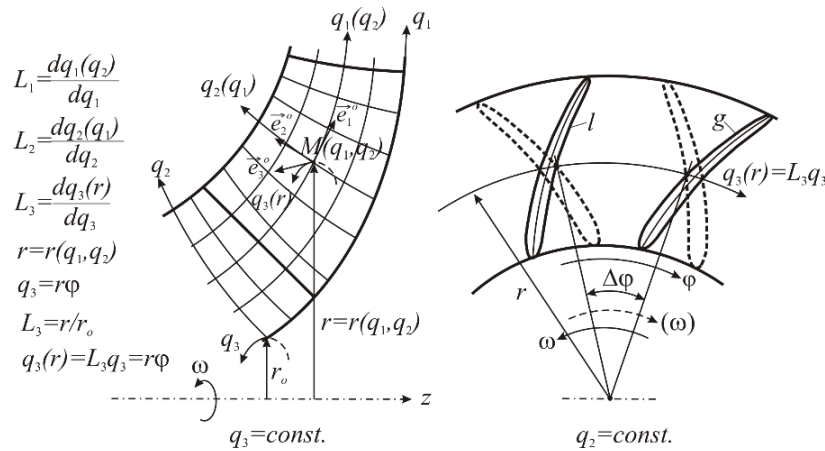


Figure 1. Curvilinear orthogonal coordinate system applied for centrifugal hydraulic turbomachine

Figure 1 shows the cross-section of a centrifugal pump, where dashed line defines pump blades for impeller rotation in the clockwise direction. Lamé's coefficients are function of curvilinear coordinates, $L_1(q_1, q_2)$, $L_2(q_1, q_2)$ and $L_3 = r/r_o$, where $r = r(q_1, q_2)$ is a radial distance from the origin of the cylindrical coordinate system (r, φ, z) [8]. For turbomachinery it is commonly used the cylindrical coordinate system (r, φ, z) : $q_1 = z$, $q_2 = r$ i $q_3 = r_o\varphi$ ($L_1 = 1$, $L_2 = 1$, $L_3 = r/r_o$), where r_o is the radial distance in inlet cross-section of the turbomachine.

Averaging of flow parameters according to circular coordinate is a method that implies the use of the following mathematical expression for averaging a scalar function $f(q_1, q_2, q_3)$:

$$\tilde{f}(q_1, q_2) = \frac{1}{\Delta q_3} \int_{q_{3a}(q_1, q_2)}^{q_{3b}(q_1, q_2)} f(q_1, q_2, q_3) \cdot dq_3, \quad (1)$$

where $\Delta q_3 = \Delta q_3(q_1, q_2) = q_{3b}(q_1, q_2) - q_{3a}(q_1, q_2)$ and a and b are two next blade surfaces in the blade passage.

Scalar flow parameters, such as pressure $p(q_1, q_2, q_3)$ and flow velocity components $w_j(q_1, q_2, q_3)$ and $c_j(q_1, q_2, q_3)$ ($j = 1, 2, 3$) can be averaged according to circumferential coordinate $q_3 = r_o\varphi$, using equation (1).

In Fig.1 circumferential coordinate line $q_3 = L_3q_3 = r\varphi$ passes through the point $M(q_1, q_2)$ in meridian cross-section of pump impeller and equation (1) can be written:

$$\tilde{f}(q_1, q_2) = \frac{1}{\Delta q_3} \int_{q_{3a}(r)}^{q_{3b}(r)} f[q_1, q_2, q_3(r)] \cdot dq_3(r) = \frac{1}{\Delta\varphi(r)} \int_{\varphi_a(r)}^{\varphi_b(r)} f[q_1, q_2, \varphi(r)] \cdot d\varphi(r), \quad (2)$$

where: $r = r(q_1, q_2)$, $\Delta q_3(r) = r\varphi(r)$, $\Delta\varphi(r) = \varphi_b(r) - \varphi_a(r)$.

Velocities in the impeller satisfy the equation:

$$\vec{c} = \vec{w} + \vec{u} = \vec{w} + [\vec{\omega}, \vec{r}], \quad (3)$$

where \vec{c} is absolute, \vec{w} is relative velocity and \vec{u} is circumferential velocity.

Formula (2) leads to the following equation:

$$\text{rot} \vec{c} = \text{rot} \vec{w} + 2\vec{\omega}, \quad \text{i. e.} \quad \text{rot} \vec{w} = \text{rot} \vec{c} - 2\vec{\omega}. \quad (4)$$

For $\vec{e}_3^o = -\vec{u}^o$, there is: $u = -\omega \cdot r < 0$, $c_3 = -c_u < 0$, $w_3 = c_3 + \omega \cdot r = -c_u + \omega \cdot r > 0$.

For $\vec{e}_3^o = \vec{u}^o$, there is: $u = \omega \cdot r > 0$, $c_3 = c_u > 0$, $w_3 = c_3 - \omega \cdot r = c_u - \omega \cdot r < 0$.

Index a becomes l and b becomes g for $\vec{e} = -\vec{u}$, while $a=g$ and $b=l$ for $\vec{e} = \vec{u}$.

Averaging of scalar values $f(q_1, q_2, q_3)$ is obtained according to its function distribution over a circular arc and scalar values $\bar{p}(q_1, q_2)$, $\bar{w}_j(q_1, q_2)$, $\bar{c}_j(q_1, q_2)$, $j=1,2,3$ can be determined using numerically obtained distribution of these values over circular arcs in the blade passage. Since numerical simulations give us numerous data for those values, equation (2) can be calculated using the trapezoid rule with good accuracy.

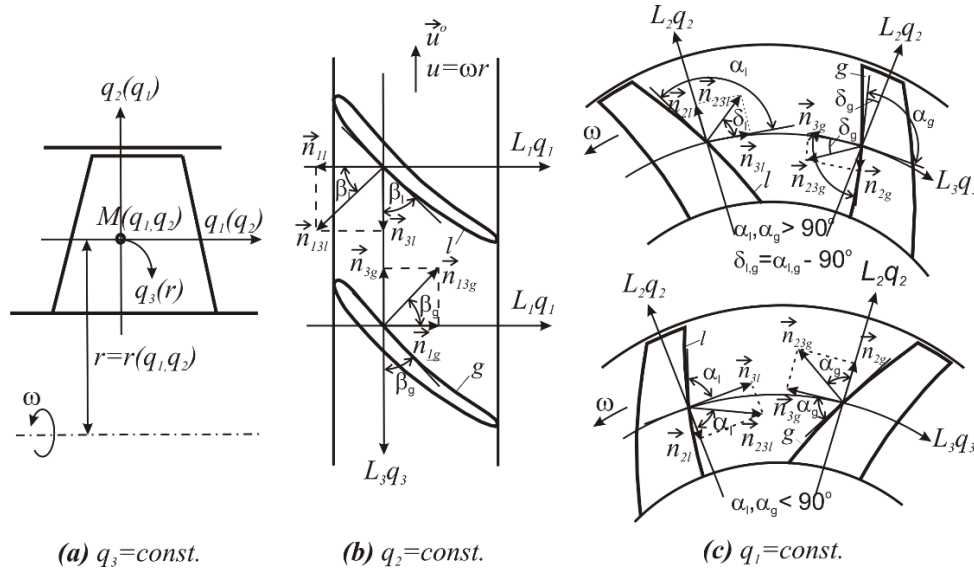


Figure 2. Impeller of axial flow turbopump, where $\vec{e}_3^o = -\vec{u}^o$ ($a=l, b=g$)

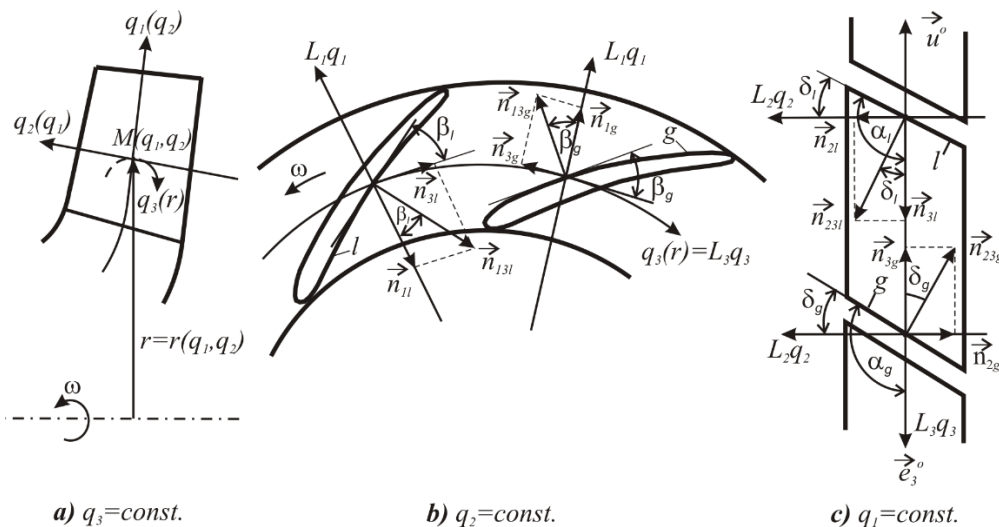


Figure 3. Impeller of centrifugal turbopump, where $\vec{e}_3^o = -\vec{u}^o$ ($a=l, b=g$)

Using equation (2) there are following expressions derived:

$$\left(\frac{\square \partial f}{\partial q_3} \right) = \frac{1}{\Delta q_3} \Delta f \quad \text{where } \Delta f = f_b(q_1, q_2) - f_a(q_1, q_2) \quad (5)$$

and

$$\left(\frac{\square \partial f}{\partial q_{1,2}} \right) = \frac{1}{\Delta q_3} \frac{\partial (\Delta q_3 \tilde{f})}{\partial q_{1,2}} - \frac{1}{\Delta q_3} \Delta \left(f \frac{\partial q_3}{\partial q_{1,2}} \right), \quad (6)$$

$$\text{where } \Delta \left(f \frac{\partial q_3}{\partial q_{1,2}} \right) = \left(f \frac{\partial q_3}{\partial q_{1,2}} \right)_b - \left(f \frac{\partial q_3}{\partial q_{1,2}} \right)_a$$

For the case $\vec{e}_3^o = -\vec{u}^o$, when $a=l$ and $b=g$ the following expressions can be made:

$$\left(\frac{dq_3}{dq_1} \right)_{a,b} = \frac{L_1}{L_3} \text{ctg} \beta_{a,b} = -\frac{L_1}{L_3} \left(\frac{n_1}{n_3} \right)_{a,b} \quad \text{and} \quad \left(\frac{dq_3}{dq_2} \right)_{a,b} = \frac{L_2}{L_3} \text{ctg} \alpha_{a,b} = -\frac{L_2}{L_3} \left(\frac{n_2}{n_3} \right)_{a,b}, \quad (7)$$

Where: $L_1 = L_1(q_1, q_2)$, $L_2 = L_2(q_1, q_2)$ and $L_3 = r(q_1, q_2) / r_o$ are Lamé's coefficients.

According to equation (7) equation (6) becomes:

$$\left(\frac{\square \partial f}{\partial q_{1,2}} \right) = \frac{1}{\Delta q_3} \frac{\partial (\Delta q_3 \tilde{f})}{\partial q_{1,2}} + \frac{1}{\Delta q_3} \frac{L_{1,2}}{L_3} \Delta \left(f \frac{n_{1,2}}{n_3} \right), \quad (8)$$

$$\text{where for point } M(q_1, q_2), \quad \Delta \left(f \frac{n_{1,2}}{n_3} \right) = \left(f \frac{n_{1,2}}{n_3} \right)_b - \left(f \frac{n_{1,2}}{n_3} \right)_a.$$

Furthermore, formulas for $\text{grad} f(q_1, q_2, q_3)$, $\text{div} \vec{v}(q_1, q_2, q_3)$ and $\text{rot} \vec{v}(q_1, q_2, q_3)$ are obtained:

$$\left. \begin{aligned} \square \text{grad} f &= \frac{1}{\Delta q_3} \text{grad} (\Delta q_3 \tilde{f}) + \frac{1}{L_3 \Delta q_3} \Delta \left(f \frac{\vec{n}}{n_3} \right) = \text{grad} \tilde{f} + \frac{1}{L_3 \Delta q_3} \Delta \left(f' \frac{\vec{n}}{n_3} \right) \\ \square \text{div} \vec{v} &= \frac{1}{\Delta q_3} \text{div} (\Delta q_3 \tilde{\vec{v}}) + \frac{1}{L_3 \Delta q_3} \Delta \left(\frac{\vec{n}}{n_3}, \vec{v} \right) = \text{div} \tilde{\vec{v}} + \frac{1}{L_3 \Delta q_3} \Delta \left(\frac{\vec{n}}{n_3}, \vec{v}' \right) \\ \square \text{rot} \vec{v} &= \frac{1}{\Delta q_3} \text{rot} (\Delta q_3 \tilde{\vec{v}}) + \frac{1}{L_3 \Delta q_3} \Delta \left[\frac{\vec{n}}{n_3}, \vec{v} \right] = \text{rot} \tilde{\vec{v}} + \frac{1}{L_3 \Delta q_3} \Delta \left[\frac{\vec{n}}{n_3}, \vec{v}' \right] \end{aligned} \right\} \quad (9)$$

Considering turbulent flow in turbomachinery, scalar and vector values can be defined as:

$$f' = f - \tilde{f} \quad \text{and} \quad \vec{v}' = \vec{v} - \tilde{\vec{v}}, \quad (10)$$

and equations (9) become:

$$\overline{\text{grad} f'} = \square \text{grad} f' = \frac{1}{L_3 \Delta q_3} \Delta \left(f', \frac{\vec{n}}{n_3} \right), \quad \overline{\text{div} \vec{v}'} = \square \text{div} \vec{v}' = \frac{1}{L_3 \Delta q_3} \Delta \left(\frac{\vec{n}}{n_3}, \vec{v}' \right), \quad \overline{\text{rot} \vec{v}'} = \square \text{rot} \vec{v}' = \frac{1}{L_3 \Delta q_3} \Delta \left[\frac{\vec{n}}{n_3}, \vec{v}' \right]. \quad (11)$$

In the flow domain without blades, equations (11) are equal to zero.

3. Averaging of flow equations

As previously described, the flow in turbomachines is assumed to be axisymmetric and stationary. Since the flow is extremely turbulent, kinematic characteristics of time averaged turbulent flow are in a good agreement with the calculation obtained for inviscid fluids.

Continuity equation for incompressible fluids is:

$$\text{div} \vec{w} = 0. \quad (12)$$

Using equation (9), continuity equation becomes:

$$\operatorname{div}(\Delta q_3 \cdot \tilde{w}) + \frac{1}{L_3} \Delta \left(\frac{\tilde{n}}{n_3}, \tilde{w} \right) = 0. \quad (13)$$

Since blade surfaces are perpendicular to the flow surfaces, the first term is equal to zero, then equation (13) becomes:

$$\frac{\partial}{\partial q_1} (L_2 L_3 \Delta q_3 \tilde{w}_1) + \frac{\partial}{\partial q_2} (L_3 L_1 \Delta q_3 \tilde{w}_2) = 0. \quad (14)$$

Previous equation can be transformed, by multiplying to $2\pi / \tau$, where $\tau = 2\pi / z_1$:

$$\frac{\partial}{\partial q_1} (2\pi r_o k L_2 L_3 \tilde{w}_1) = - \frac{\partial}{\partial q_2} (2\pi r_o k L_3 L_1 \tilde{w}_2), \quad (15)$$

and
$$\frac{\partial \tilde{\psi}_m}{\partial q_1} = -2\pi r_o k L_3 L_1 \tilde{w}_2 \quad \text{and} \quad \frac{\partial \tilde{\psi}_m}{\partial q_2} = 2\pi r_o k L_2 L_3 \tilde{w}_1, \quad (16)$$

where k – blockage factor, which is the coefficient of flow reduction due to the thickness of the blades.

The flow equation for inviscid fluid, if the gravitational influence is neglected, can be define as:

$$[\tilde{w}, \operatorname{rot} \tilde{c}] = \operatorname{grad} E \quad (17)$$

where: $\operatorname{rot} \tilde{c} = \operatorname{rot} \tilde{w} - 2\tilde{\omega}$ and E is the Bernoulli's integral for relative fluid flow,

$$E = \frac{p}{\rho} + \frac{w^2}{2} - \frac{(r\omega)^2}{2}, \quad E = E(q_1, q_2, q_3). \quad (18)$$

Equation (18) for turbulent flow becomes:

$$[\tilde{w}, \operatorname{rot} \tilde{c}] + [\tilde{w}', (\operatorname{rot} \tilde{c})'] = \operatorname{grad} E. \quad (19)$$

Using equation (9) the previous formula can be written:

$$[\tilde{w}, \operatorname{rot} \tilde{c}] + \tilde{F}^{(1)} + \tilde{F}^{(2)} + \tilde{F}^{(3)} = \operatorname{grad} \tilde{E}, \quad (20)$$

where;

$$\tilde{F}^{(1)} = \left[\tilde{w}, \frac{1}{L_3 \Delta q_3} \Delta \left[\frac{\tilde{n}}{n_3}, \tilde{w}' \right] \right], \quad \tilde{F}^{(2)} = - \frac{1}{L_3 \Delta q_3} \Delta \left(E', \frac{\tilde{n}}{n_3} \right), \quad \tilde{F}^{(3)} = [\tilde{w}', \operatorname{rot} \tilde{w}'] \quad \text{and} \quad \tilde{E} = \frac{\tilde{p}}{\rho} + \frac{\tilde{w}^2}{2} - \frac{\omega^2 r^2}{2}.$$

4. Using numerical simulation results

CFD software, such as ANSYS CFX, can be used to obtain numerical results of fluid flow passing through the hydraulic turbomachine, and as a result all flow parameters (pressure, velocity, etc) in the whole geometric domain can be calculated. This this allows us to use the obtained numerical data for averaging these values by circular coordinate.

For symmetrical impeller, it is enough to observe only one blade passage, whether it is a space between two blades, or we consider one blade and half of blade passages on both sides of the blade (Figure 4).

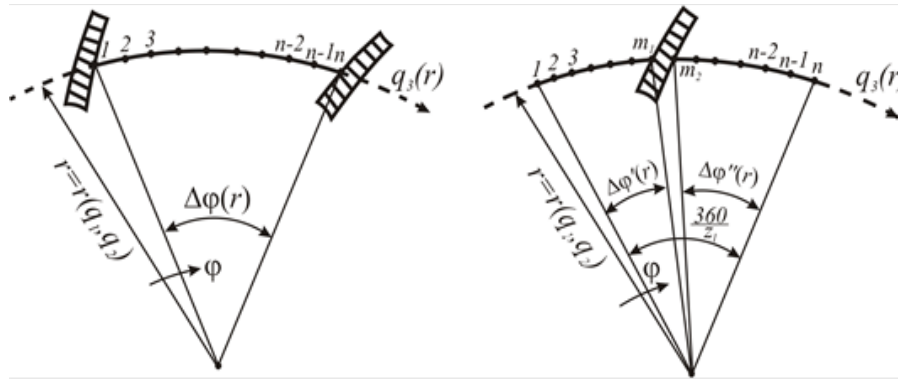


Figure 4. Averaging over circular coordinate q_3 (between and around the blade)

As shown in Figure 4, points 1, 2, 3, 4, ..., n are discrete densely distributed points on the circular arc in the blade passage, which passes through the point $M(q_1, q_2)$ in the meridian plane, which corresponds to radius vector $r = r(q_1, q_2)$. Denoting by $f_1, f_2, f_3, \dots, f_n$ the scalar quantities f numerically obtained on the circular arc, using the trapezoidal integration rule, equation (2) becomes:

$$\tilde{f}(q_1, q_2) = \frac{1}{\Delta\varphi} \left(\frac{1}{2} \sum_{j=2}^n (f_j + f_{j-1}) (\varphi_j - \varphi_{j-1}) \right) \quad (21)$$

where $\Delta\varphi(r) = \varphi_n - \varphi_1$ and $r = r(q_1, q_2)$, $\varphi_j = \varphi_j(r)$, $f_j = f_j(r)$, $j = 1, 2, 3, \dots, n$.

When Ansys CFX is used, due to the symmetry of the impeller geometry, the flow domain can be only one blade with half of blade passage on both sides of the blade. In that case, the angle of circular coordinate is $360^\circ/z_l$ (z_l – number of blades), and the equation for averaging flow parameters is:

$$\tilde{f}(q_1, q_2) = \frac{1}{\Delta\varphi'(r)} \int_{\varphi_1(r)}^{\varphi_{m_1}(r)} f(q_1, q_2, \varphi(r)) d\varphi(r) + \frac{1}{\Delta\varphi''(r)} \int_{\varphi_{m_2}(r)}^{\varphi_n(r)} f(q_1, q_2, \varphi(r)) d\varphi(r) \quad (22)$$

where $\Delta\varphi'(r) = \varphi_{m_1}(r) - \varphi_1(r)$ and $\Delta\varphi''(r) = \varphi_n(r) - \varphi_{m_2}(r)$ (Fig.2).

Using trapezoidal integration rule, previous equation becomes:

$$\tilde{f}(q_1, q_2) = \frac{1}{\Delta\varphi'(r)} \left(\frac{1}{2} \sum_{j=2}^{m_1} (f_j + f_{j-1}) (\varphi_j - \varphi_{j-1}) \right) + \frac{1}{\Delta\varphi''(r)} \left(\frac{1}{2} \sum_{j=m_2+1}^n (f_j + f_{j-1}) (\varphi_j - \varphi_{j-1}) \right) \quad (23)$$

where $r = r(q_1, q_2)$, $\varphi_j = \varphi_j(r)$, $f_j = f_j(r)$, $j = 1, 2, 3, \dots, m_1, m_2, \dots, n$.

4.1. Obtaining meridian streamlines of averaged flow and calculation of the flow rate

For obtaining meridian streamlines of averaged flow using integral continuity equation, it is necessary to calculate averaged flow velocities $\tilde{w}_1 = \tilde{w}_1(q_1, q_2)$ and $\tilde{w}_2 = \tilde{w}_2(q_1, q_2)$ in point $M(q_1, q_2)$ (Figure 5).

For known components of averaged meridian velocities $\tilde{w}_1 = \tilde{w}_1(q_1, q_2)$ and $\tilde{w}_2 = \tilde{w}_2(q_1, q_2)$, and known function of the coefficient of flow reduction due to the thickness of the blades, so called blockage factor $k(q_1, q_2)$, the meridian streamlines $\tilde{\psi}_m(q_1, q_2) = const.$ can be determined using equation (16). Meridian streamlines represent traces of the cross-section in the meridian plane.

In Figure 5 (a, b) the cylindrical coordinate system is shown, where $q_1=z$, $q_2=r$, $q_3=r_o\varphi$, $\tilde{w}_1 = \tilde{w}_z$, $\tilde{w}_2 = \tilde{w}_r$. Assuming form meridian flow on the inner part of the impeller disk $\tilde{\psi}_m(q_1, q_2) = 0$, the meridian flow on the outer part of the disk is $\tilde{\psi}_m(q_1, q_2) = Q$. Figure 5.c shows the curvilinear orthogonal coordinate system, where $q_2 = const.$ corresponds to an axisymmetric flow surface, while coordinate $q_1(q_2)$ corresponds to meridian streamline of the averaged fluid flow.

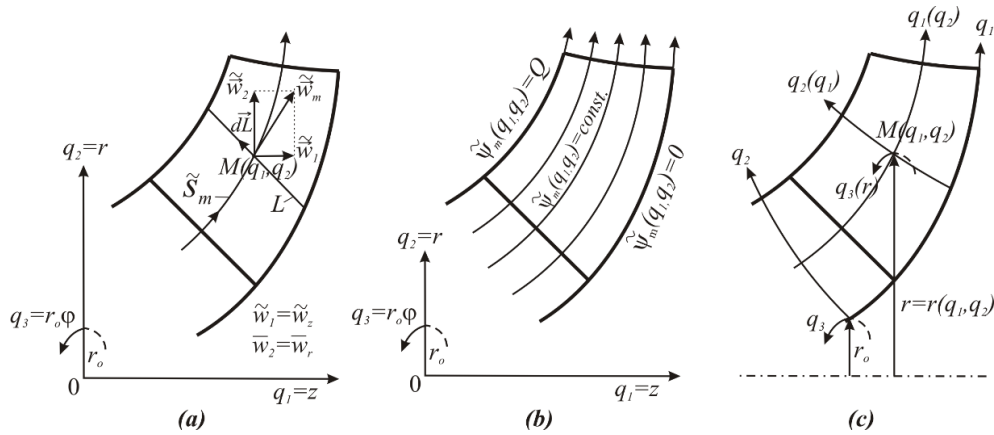


Figure 5. Meridian streamline in centrifugal turbopump

Equation (16) gives an expression for the volume flow rate through the axisymmetric flow surface of the meridian trace dL :

$$dQ = 2\pi k r_o (L_2 L_3 \tilde{w}_1 dq_2 - L_3 L_1 \tilde{w}_2 dq_1), \quad (24)$$

where $k = \Delta\phi / \tau = \Delta q_3 / \tau r_o = k(q_1, q_2)$, i.e. $\Delta q_3 = k \tau r_o = 2\pi k r_o$.

Velocity components \tilde{w}_1 and \tilde{w}_2 in cylindric coordinate system and integral formulas for flow rate distribution on the flow surfaces $L_1, L_2, L_3, \dots, L_{10}$ (Figure 6), lead to the following equation:

$$dQ = 2\pi k r (\tilde{w}_z dr - \tilde{w}_r dz), \quad (25)$$

where $k = \Delta\phi / \tau = k(z, r)$.

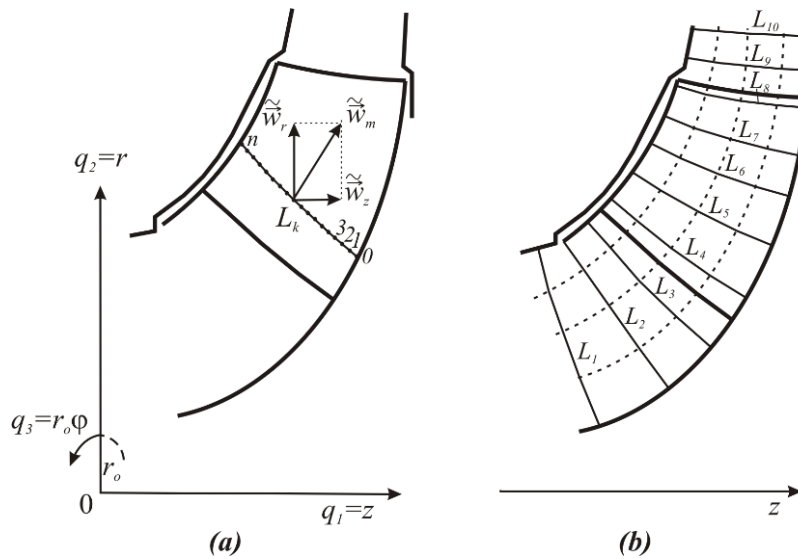


Figure 6. Meridian traces of flow cross-section L_k

The previous equation can be written:

$$Q_j^{(L_k)} = 2\pi \int_{r(L_{k,0})}^{r(L_{k,j})} k r \tilde{w}_z \cdot dr + \left(-2\pi \int_{z(L_{k,0})}^{z(L_{k,j})} k r \tilde{w}_r \cdot dz \right), \quad j = 1, 2, \dots, n, \quad (26)$$

for the chosen points $L_{k,j}$ ($j=0, 1, 2, \dots, n$) in meridian surface, defined by coordinates $z(L_{k,j})=z_{k,j}$ and $r(L_{k,j})=r_{k,j}$, the following functions are defined:

$$f_j = (kr\tilde{w}_z)_{L_{k,j}} = f(z_j, r_j) = k(z_j, r_j) \cdot r(z_j, r_j) \cdot \tilde{w}_z(z_j, r_j), \quad j=1,2,\dots,n \quad (27)$$

$$F_j = (kr\tilde{w}_r)_{L_{k,j}} = F(z_j, r_j) = k(z_j, r_j) \cdot r(z_j, r_j) \cdot \tilde{w}_r(z_j, r_j), \quad j=1,2,\dots,n$$

Using trapezoid rule volume flow rate can be calculated:

$$Q_j^{(L_k)} = \pi \sum_{i=1}^j (f_i + f_{i-1})(r_i - r_{i-1}) + \pi \left(-\sum_{i=1}^j (F_i + F_{i-1})(z_i - z_{i-1}) \right), \quad j=1,2,\dots,n. \quad (28)$$

4.2. Calculation of torque, power and specific work of the turbomachine impeller

The meridian trace of the flow cross-section at the impeller inlet (1-1) is L_1 , and the meridian trace of the flow cross-section at the impeller outlet (2-2) is shown with line L_2 (Figure 7), for pump and turbine impeller.

The torque of the turbopump impeller can be calculated using equation:

$$M_k^{(P)} = \int_{A_2} \rho r \omega \tilde{c}_u(\tilde{c}_m, d\vec{A}) - \int_{A_1} \rho r \omega \tilde{c}_u(\tilde{c}_m, d\vec{A}), \quad (29)$$

where A_1 and A_2 are control cross-sections of axisymmetric flow surface on the inlet (A_1) and outlet (A_2).

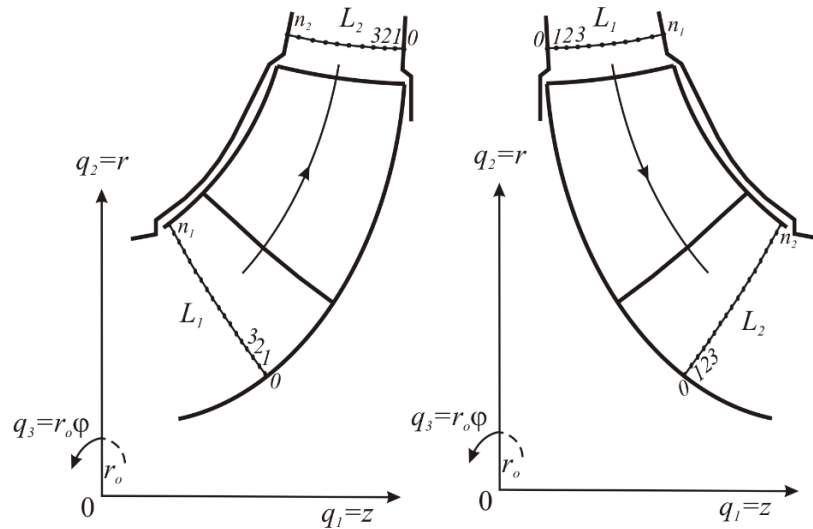


Figure 7. Meridian traces of flow surfaces L_k (turbopump left and turbine right)

Previous equation can be also written:

$$M_k^{(P)} = M_k(2) - M_k(1), \quad (30)$$

where,

$$\left. \begin{aligned} M_k(2) &= 2\pi\rho \int_{L_2} r^2 \tilde{c}_u \tilde{c}_z dr - 2\pi\rho \int_{L_2} r^2 \tilde{c}_u \tilde{c}_r dz, \quad (L_2 = L_2(z, r)) \\ M_k(1) &= 2\pi\rho \int_{L_1} r^2 \tilde{c}_u \tilde{c}_z dr - 2\pi\rho \int_{L_1} r^2 \tilde{c}_u \tilde{c}_r dz, \quad (L_1 = L_1(z, r)) \end{aligned} \right\} \quad (31)$$

Calculation points on the meridian traces of control sections L_1 and L_2 can be denoted by:

$$L_{1,j} = L_{1,j}(z_{1,j}, r_{1,j}), \quad j=0,1,2,\dots,n_1 \quad \text{and} \quad L_{2,j} = L_{2,j}(z_{2,j}, r_{2,j}), \quad j=0,1,2,\dots,n_2. \quad (32)$$

Defining the following functions:

$$z_j^{(1)} = z_{1,j}, \quad r_j^{(1)} = r_{1,j} \quad (j=0,1,2,\dots,n_1) \quad \text{and} \quad z_j^{(2)} = z_{2,j}, \quad r_j^{(2)} = r_{2,j} \quad (j=0,1,2,\dots,n_2),$$

$$g_j^{(1)} = r^2 \tilde{c}_u \tilde{c}_z = g_j^{(1)}(z_j^{(1)}, r_j^{(1)}), \quad G_j^{(1)} = r^2 \tilde{c}_u \tilde{c}_r = G_j^{(1)}(z_j^{(1)}, r_j^{(1)}) \quad (j=0,1,2,\dots,n_1),$$

$$g_j^{(2)} = r^2 \tilde{c}_u \tilde{c}_z = g_j^{(2)}(z_j^{(2)}, r_j^{(2)}), \quad G_j^{(2)} = r^2 \tilde{c}_u \tilde{c}_r = G_j^{(2)}(z_j^{(2)}, r_j^{(2)}) \quad (j=0,1,2,\dots,n_2),$$

And the trapezoidal integration rule, equation (30) becomes:

$$\left. \begin{aligned} M_k(2) &= \pi\rho \sum_{j=1}^{n_2} (g_j^{(2)} + g_{j-1}^{(2)})(r_j^{(2)} - r_{j-1}^{(2)}) - \pi\rho \sum_{j=1}^{n_2} (G_j^{(2)} + G_{j-1}^{(2)})(z_j^{(2)} - z_{j-1}^{(2)}), \\ M_k(1) &= \pi\rho \sum_{j=1}^{n_1} (g_j^{(1)} + g_{j-1}^{(1)})(r_j^{(1)} - r_{j-1}^{(1)}) - \pi\rho \sum_{j=1}^{n_1} (G_j^{(1)} + G_{j-1}^{(1)})(z_j^{(1)} - z_{j-1}^{(1)}) \end{aligned} \right\} \quad (33)$$

The torque of the turbine impeller can be calculated using equation:

$$M_k^{(T)} = M_k(1) - M_k(2). \quad (34)$$

Power of the pump ($P_k^{(P)}$) and power of the turbine ($P_k^{(T)}$) can be determined:

$$P_k^{(P)} = \omega_p M_k^{(P)} \quad \text{and} \quad P_k^{(T)} = \omega_T M_k^{(T)}. \quad (35)$$

Specific work of the pump impeller and turbine impeller are:

$$Y_k^{(P)} = \frac{P_k^{(P)}}{\dot{m}} = \frac{\omega_p M_k^{(P)}}{\rho Q} \quad \text{and} \quad Y_k^{(T)} = \frac{P_k^{(T)}}{\dot{m}} = \frac{\omega_T M_k^{(T)}}{\rho Q}. \quad (36)$$

Conclusion

In this paper the procedure of averaging axisymmetric flow surfaces in hydraulic turbomachines is presented. Averaging the operating parameters of hydraulic turbomachines obtained by numerical simulations are used for determining the averaged flow surfaces and determining the meridian streamlines, flow rate, specific work, torque and power of the turbomachine impeller.

The procedure shown in the paper is simple and uses the numerical method of the trapezoidal integration rule.

This procedure of averaging flow surface, using numerical simulations and mathematical calculation lead to obtain useful information about the hydraulic turbomachine, allowing the designers to compare those results with assumptions made in the first stage of designing the hydraulic turbomachine impeller.

According to the distribution of the calculated operating parameters (for example specific works of elementary stages) the correction of the geometry of the impeller can be performed before making and testing the prototype of the turbomachine. The presented procedure greatly reduces designing time and costs.

Nomenclature

Latin symbols

\vec{c}	– absolute velocity [m/s].
\vec{w}	– relative velocity [m/s].
\vec{u}	– circumferential velocity [m/s].
c_u	– circumferential component of absolute velocity [m/s].
c_m	– meridian component of absolute velocity [m/s].
P	– pressure [Pa].
k	– blockage factor.
Q	– volume flow rate [m ³ /s].
\dot{m}	– mass flow rate [kg/s].

Greek symbols

Ψ	– stream function.
τ	– angular blade pitch.
Ω	– angular velocity [rad/s].

Subscripts

a, b	– surfaces of the two next blades
------	-----------------------------------

- z_l – number of blades
 M_k – torque of the impeller [Nm]

 P_k – power of the impeller [W]
 Y_k – specific work of impeller [J/kg]
 L_i – Lamé's coefficients, $i=1,2,3$
 g – pressure side of the blade
 l – suction side of the blade

Acknowledgments

This research was financially supported by the Ministry of Science, Technological Development and Innovation of the Republic of Serbia (Contract No.451-451-03-65/2024-03).

References

- [1] Obradović, N., Basics of Turbomachinery, Gradjevinska knjiga, Belgrade, Serbia (in Serbian), 1973
- [2] Ristić, B., Pumps and Fans, Naučna knjiga, Belgrade, Serbia (in Serbian), 1987
- [3] Krsmanović, Lj., Gajić A., Turbomachinery - theoretical basics, University of Belgrade, Faculty of Mechanical Engineering Belgrade, Belgrade, Serbia (in Serbian), 2005
- [4] Babić, M., Stojković, S., Basics of Turbomachinery: operating principles and mathematical modeling, Naučna knjiga, Belgrade, Serbia (in Serbian), 1990
- [5] Voronjec, K., Obradović, N., Fluid Mechanics, Gradjevinska knjiga, Belgrade, Serbia (in Serbian), 1973
- [6] Bogdanović-Jovanović, J., Bogdanović, B., Božić, I., Design of small bulb turbines with unequal specific work distribution of the runner's elementary stages, Facta Universitatis, series: Mechanical Engineering, 12(2014), 1, pp. 73-84
- [7] An, Z., Zhounian, L., Peng, W., Linlin, C., Dazhuan, W., 2015, Multi-objective optimization of a low specific speed centrifugal pump using an evolutionary algorithm, Engineering Optimization, 48(7), pp. 1251-1274.
- [8] Bogdanović-Jovanović, J., Determination of Averaged Axisymmetric flow in hydraulic turbomachinery runner, PhD Thesis, University of Niš, Faculty of Mechanical Engineering, Serbia, 2014
- [9] Bogdanović-Jovanović, J., Bogdanović, B., Milenković, D., Determination of Averaged axisymmetric flow surfaces according to results obtained by numerical simulation of flow in turbomachinery, Thermal Science, 16(2012), 2, pp. 647-662.
- [10] Bogdanović-Jovanović, J., Milenković, D., Stamenković, Ž., Spasić, Ž., Determination of averaged axisymmetric flow surfaces and meridian streamlines in centrifugal pump using numerical simulation results, Facta Universitatis, series: Mechanical Engineering, 15(2017), 3, pp.479-493.
- [11] Van den Braembussche, R., Turbomachinery component design by means of cfd, Task Quarterly, 6(2002), 1, pp. 39-61.
- [12] Pinto, R. N., Afzal, A., D'Souza, L. V., Ansari, Z., M. D. Mohammed Samee, Computational Fluid Dynamics in Turbomachinery: A Review of State of the Art, Arch Computat Methods Eng, DOI 10.1007/s11831-016-9175-2
- [13] Dornberger, R., Stoll, P., Büche, D., Multidisciplinary turbomachinery blade design optimization, AIAA-2000-0838, 2000, p.8
- [14] Shah, S.R., Jain, S.V., Patel, R.N., Lakhera, V.J., CFD for centrifugal pumps: a review of the state-of-art, Procedia Engineering, 51(2013), pp. 715 – 720

Lignite combustion in Thermal power plant Kolubara A as a source of mercury pollution

Jovana Buha-Marković^a, Ana Marinković^b, Jasmina Savić^c, Milić Erić^d, Zoran Marković^e, Aleksandar Milićević^f, Mihajlo Gigov^g

^a*Vinca Institute of Nuclear Sciences – National Institute of the Republic of Serbia - University of Belgrade, RS, jbuha@vinca.rs*

^b*Vinca Institute of Nuclear Sciences – National Institute of the Republic of Serbia - University of Belgrade, RS, aradojevic@vinca.rs*

^c*Vinca Institute of Nuclear Sciences – National Institute of the Republic of Serbia - University of Belgrade, RS, jasnas@vinca.rs*

^d*Vinca Institute of Nuclear Sciences – National Institute of the Republic of Serbia - University of Belgrade, RS, milic@vinca.rs*

^e*Vinca Institute of Nuclear Sciences – National Institute of the Republic of Serbia - University of Belgrade, RS, zoda_mark@vinca.rs*

^f*Vinca Institute of Nuclear Sciences – National Institute of the Republic of Serbia - University of Belgrade, RS, amilicevic@vinca.rs*

^g*AMG Chemtech Solutions, Belgrade, RS, mihajlo.gigov@amgchemtech.rs*

Abstract: Coal combustion is a major contributor to environmental pollution, releasing various harmful pollutants, including mercury, which poses significant risks to soil and water quality through atmospheric deposition. For this reason, some countries have established regulatory limits on mercury emissions from coal combustion, requiring the use of advanced pollution control technologies to capture and effectively reduce mercury emission. In this study, the mercury content in coal, coal ash samples and flue gas from the Kolubara A thermal power plant is determined. The results show that the mercury concentration in coal was 0.73 mg/kg, whereas the concentrations in fly ash and bottom ash were 0.02 mg/kg and 0.03 mg/kg, respectively. The mercury concentrations in coal and coal byproducts were in accordance with existing literature. In addition, the overall mercury content in flue gas was 38.73 µg/Nm³, falling within the permissible emission limit for thermal waste treatment in Serbia. The calculated mercury emission factor was below the lower limit specified in the Air Pollutant Emission Inventory Guideline of the European Monitoring and Evaluation of Air Pollutants (EMEP/EEA). These findings provide useful data for long-term environmental monitoring and regulation of mercury emission from coal combustion in Serbia.

Keywords: coal, coal ash, mercury, emission, direct mercury analyzerIntroduction

In many countries coal is considered as the primary source of energy, but also one of the major anthropogenic sources of environmental pollution [1]. The rise of renewable energy and international climate agreements are pushing many countries to reduce coal dependency, leading to economic shifts in coal-producing regions. Lignite is one of Serbia's most abundant energy resources. With significant reserves concentrated in the Kolubara and Kostolac basins, lignite plays a crucial role in the country's energy sector, primarily as a fuel for electricity generation in thermal power plants (TPPs) where these plants provide around 60% of Serbia's electricity [2].

Coal combustion generates wastes such as fly ash, bottom ash and flue gas [3]. The pollution of water, air, and soil by some trace elements contained in the ashes and/or flue gases produced during coal combustion drew attention since most of them are extremely dangerous and carcinogenic [4]. Trace elements (TEs) found in coal, such as mercury, arsenic, selenium, lead, cadmium and chromium are recognized to pose serious environmental and public health risks [5]. These element concentrations in combustion byproducts are dependent on operating conditions, coal and combustor type [6]. Among mentioned trace elements, mercury is one of the most significant environmental pollutants and one of the top 10 chemicals of major public health concern designed by the World Health Organization (WHO) [7], causing concern due to its severe toxicity to human health, long-range transport, persistence, and bioaccumulation in the environment [8]. Mercury transformation during coal combustion can be divided into homogeneous (without fly ash) and heterogeneous

(with fly ash) reaction, which are influenced by the coal types, flue gas components, flue gas temperature, combustion atmosphere, coal ash properties, etc [9]. Mercury emitted from coal combustion can be present in various forms, such as elemental mercury (Hg^0), gaseous oxidized mercury (Hg^{2+}), and particulate mercury (Hg^p) [9]. Then, Hg^{2+} and Hg^p can combine with organic molecules to form methyl mercury (MeHg), which is the most toxic form of mercury. The results indicated that Hg was the predominant in flue gas with more than 90% [10].

Today's coal-fired power plants use selective catalytic reduction (SCR), electrostatic precipitators (ESPs), and flue gas desulfurization (FGD) to manage NO_x, particulates, and SO_x[11]. Dust removal equipment, such as the ESP which is used in TPP Kolubara A, can efficiently reduce the concentration of Hg^p from flue gas.

Coal combustion emits around 475 tons of mercury into the atmosphere globally each year, according to the most recent air emissions inventory. In comparison, other fossil fuels contribute with 10 tons. Figure 1 shows mercury emissions from coal combustion in some countries [12].

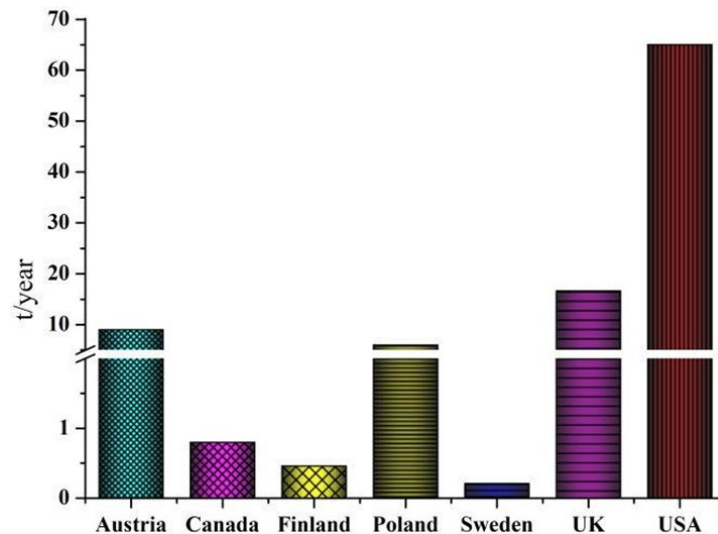


Figure 1. Mercury emissions from coal combustion in the UK, Austria, Canada, Finland, Sweden, Poland and the USA.

Furthermore, the large increase in worldwide anthropogenic mercury emissions demonstrates the critical need for effective solutions to reduce coal use and regulate mercury emissions. This understanding is essential for accurate mercury emission estimations and the development of effective mercury removal technologies, particularly during coal combustion for power generation. Addressing these challenges is important for protecting human health and the environment in the face of the ongoing utilization of coal. Given the public health and ecological risks associated with mercury in coal, the aim of this work is to determine mercury content and its distribution in coal, as well as in flue gas and coal byproducts.

1. Materials and Methods

1.1. Collection and storage of coal, fly and bottom ash

Lignite originated from the Kolubara basin and fly ash from the electrostatic precipitator, as well as bottom ash were sampled in TPP Kolubara A (44° 28' 49" N, 20° 17' 37" E). The total installed capacity of the TPP Kolubara A block is 245 MW [13], with rates of lignite consumption of 350 t/h and ash production of 64 t/h. Three lignite from three regimes samples were collected and mixed. Sampling and sample preparation was done according to standard methods. Fly ash was sampled from an electrostatic precipitator, and its temperature was around 160°C. The sampling of fly and bottom ashes was carried out in each of the three operational regimes (different air and fuel flow, and maximal boiler power) separately. The ashes from each of the regimes were combined according to the standard method [14]. Before analysis, ash samples were homogenized [14] and stored in a glass container [15] at a dark place under the temperature below 15°C.

1.2. Sampling of flue gas from TPP Kolubara A

Flue gas was extracted representatively from a chimney over a certain period of time with a controlled flow and a known volume according to the standard method [16]. Flue gas flows and parameters are shown in Table 1. Sampling was performed by the isokinetic sampling system. Dust in the sampled gas stream is collected on

a quartz filter Munktell with an efficiency of more than 99,9%, whereafter the gas passed through a series of absorbers, which contains absorbed solution (2%w/w KMnO₄/10 %w/w H₂SO₄). At the end of the sampling period the filter, the absorption solution and the rinsing solution are collected in the glass container and stored at room temperature.

Table 1. Flue gas parameters and flows for TPPs under working conditions (f_w), under standard conditions and dry flue gas (f_{st}), and under standard conditions for dried flue gas and oxygen content of 6% (f_R)

TPP Kolubara A	
Temperature of flue gas (°C)	197.9
Oxygen content in flue gas (%)	10.70
Volume ratio of moisture in flue gas (%)	16.73
Mean velocity of flue gas (m/s)	10.19
f_w (m ³ /h)	524003
f_{st} (Nm ³ /h)	250614
f_R (Nm ³ /h)	172099

1.3. Proximate and ultimate analysis of lignite and coal ash samples

The proximate and ultimate analyses of lignite from TPP Kolubara, fly and bottom ash samples were done. The proximate analysis was done by LECO TGA 701 using the standard test method [17]. The high heating value of coal was determined by an IKA C200 calorimeter while low heating values was calculated according to standard method [18]. The ultimate analysis was done by a LECO CHN 628 Series with a Sulfur add-on module using the standard test methods [19,20]. The calculation for oxygen content was outlined in [21].

1.4. Mercury analysis of flue gas and coal, fly ash and bottom ash on Direct Mercury Analyzer- DMA1 evo

Samples of coal, fly and bottom ash were analysed on DMA1 evo directly.

After sampling flue gas, two bottles of absorption solution, were prepared for analysis. A previously prepared 10% solution of hydroxyammonium chloride is slowly added to the bottles containing the absorption solution until the solutions turn discolored. Then, aliquots of these absorption solutions, aliquots of rinsing solution and filters were directly analysed on Direct Mercury Analyzer- DMA1 evo.

1.5. Mercury emission factor (MEF)

Mercury emission factor (mg/GJ) represents mercury emission from flue gas per unit of low heating value of coal. It is calculated using the following equations:

$$\text{MEF} = m/GQ(1)$$

$$m = VC(2)$$

where, m (mg/h) is the emission of mercury from flue gas; G (ton/h) is coal consumption; Q (kJ/kg) is the low heating value (LHV) of feed coal; V (Nm³/h) is the flow rate of flue gas; C (μg/Nm³) is mercury content in flue gas.

2. Results and Discussion

Coal can be characterized by its physical and chemical properties, and the quality of coal is evaluated by proximate, ultimate analysis and upper heating value. A complete proximate analysis of coal determines: total (analytical moisture and total moisture), ash content, combustible substances, volatile substances, fixed carbon content (C_{fix}), upper and lower heating values. The ultimate analysis includes determining the total carbon, hydrogen, nitrogen, and oxygen content, as well as the total, bound, and combustible sulfur content. Foreign authors first classified domestic coals based on volatile substances (V), carbon (C), hydrogen (H) and oxygen (O). Furthermore, it can be seen that lignites have lower carbon values but higher volatile values [22]. Lignite used as a feed fuel in TPP Kolubara A was examined and the results of its proximate and ultimate analysis are presented in Table 2A. When these results are compared to literature data [23,24] lignite from TPP Kolubara A is regarded as low grade coal due to its high ash content and low C_{fix} value. Furthermore, examined lignite can be categorized as medium-sulfur coal since its sulfur level ranges between 1% and 3% [25].

Table 2A. Proximate analysis and ultimate analysis of coal from TPP Kolubara

		Coal
Proximate analysis	Total moisture*	47.43
	Inherent moisture**	3.39
	Ash	% 33.73
	Total sulfur	1.52
	Cfix	25.97
	Volatile	40.31
Heating value	Upper	MJ/kg 17.8
	Lower	16.9
Ultimate analysis	Total carbon	44.33
	Hydrogen	3.90
	Comb. sulfur	% 0.80
	Nitrogen	0.75
	Oxygen	16.50

*as-received; **as determined; all other data are given on a dry basis

The proximate analysis results for fly ash indicate a low combustible content (Table 2B), suggesting almost complete coal combustion in TPP Kolubara A. As indicated in Table 2B, bottom ash has substantially lower ash content than fly ash, which is expected given its high proportion of unburned carbon [26].

Table 2B. Proximate analysis of bottom and fly ash from TPP Kolubara

	Bottom ash	Fly ash
Inherent moisture**	2.39	0.04
Ash	65.80	99.70
Combustible	34.20	0.30
Total sulfur	0.94	0.73
Comb. sulfur	0.35	0.02

**as determined; all other data are given on a dry basis

The measured mercury concentration in lignite is 0.73 mg/kg, while literature data for mercury content found in different types of coals goes to 10.5 mg/kg (Figure 2). There is limited data on mercury concentrations in Serbian coals and their corresponding fly and bottom ashes. However, as illustrated in Figure 2, the findings from this study align closely with mercury concentrations found in Indian, Polish, and Russian coals utilized in different power plants, whereas the levels are significantly lower than those reported for certain Chinese coals.

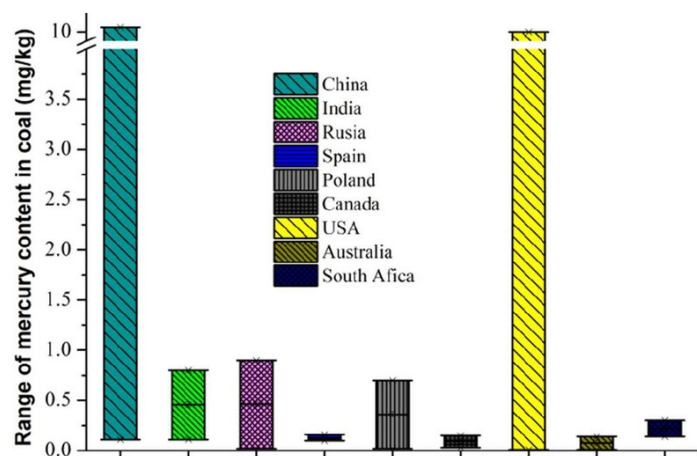


Figure 2. Range of mercury content in coals from different countries [9,10,27-29]

The mercury content in bottom ash is 0.03 mg/kg, whereas fly ash has 0.02 mg/kg. Mercury content in fly and bottom ashes can vary significantly depending on the type of coal and combustion conditions. Understanding these dynamics is crucial for assessing the environmental impact of coal combustion and developing effective remediation strategies. Figure 3 shows that the mercury contents in the fly ash and bottom ash studied in this study are similar to the literature.

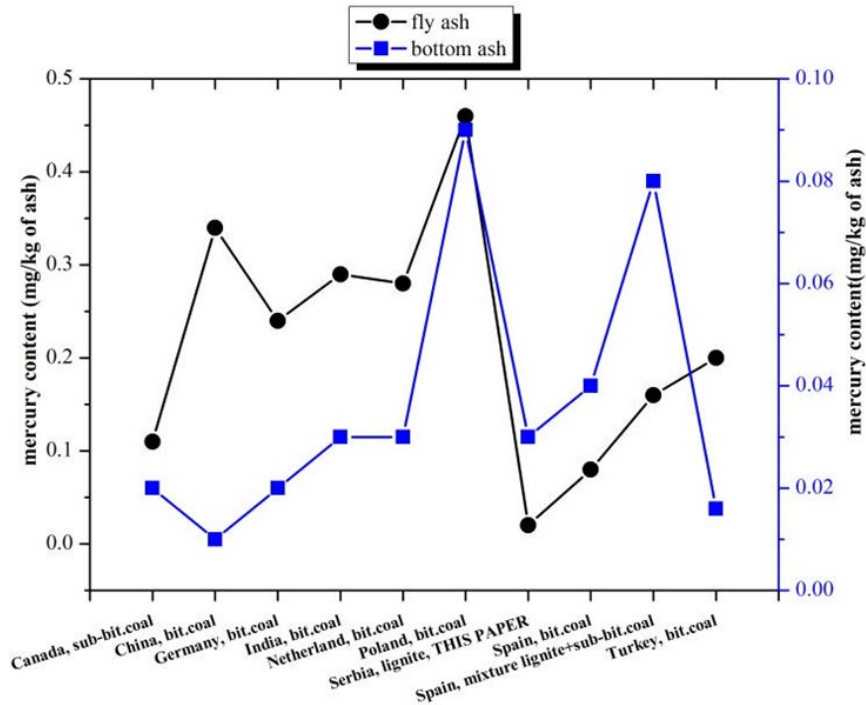


Figure 3. Mercury content in fly and bottom ashes from different countries [9,10,27-31] and determined in this paper

Mercury in coal is highly related to sulfur content in most coals, with pyritic mercury being the most common form, although organic- and sulfide-bound mercury (mainly pyritic mercury) are the predominant species in low-sulfur coals. Although higher mercury concentration is expected for fly ashes than bottom ashes [32], in our instance, the higher mercury concentration in bottom ash is most likely related to its higher sulfur content (Table 2B).

Total mercury emission in flue gas from TPP Kolubara A was 12.72 $\mu\text{g}/\text{m}^3$ (Table 2), or 38.73 $\mu\text{g}/\text{Nm}^3$ under standard conditions for dried flue gas and oxygen content of 6%. Mercury emissions in this paper are significantly higher than those in Poland but substantially lower than those in India (Table 3).

Table 3. Literature data for the distribution of mercury in flue gas and particulate phase associated with flue gas

Coal Type, thermal power plant capacity	Literature	Flue gas with particulate associated with flue gas ($\mu\text{g}/\text{m}^3$)
Bituminous coal, India, TPP 220MW	[29]	22.72
Mixture of lignite and sub-bituminous coal, Spain, TPP 350MW	[10]	20.5
Bituminous coal, Poland, TPP 113MW	[28]	2.49
Bituminous coal, Poland, TPP 160MW	[28]	1.88
Bituminous coal, Poland, TPP 560MW	[28]	1.51
Total mercury content in flue gas	THIS PAPER	12.72

Legislation regarding mercury emission is established in some countries, but mercury maximum limit values are applicable to different industries or processes. In Serbia, the limit value for Hg emission is 0.05 mg/Nm³, but that limit value is applicable to the thermal treatment of waste, while Austria has a value for mercury emission that is applicable exclusively to coal-fired power stations. The measured mercury concentration in flue gas from TPP Kolubara A is below all limit values for mercury emission given in Table 4.

Table 4. National guidelines and legislation regarding mercury emission

Country	Limit value for Hg* (mg/Nm ³)	Applicable to
Australia	3	Any industry or process
Austria	0.05	Coal-fired power stations
Canada	1	New or recently modified utility boilers
Netherland	0.20	Any industry or process
Serbia	0.05	Thermal treatment of waste

*mercury limit value is given under standard conditions for dried flue gas and oxygen content of 6%

The calculated Mercury Emission Factor value is 1.12 mg/GJ, which is significantly lower than the lower limit value given in the EMEP guidebook [33], for medium size non-residential sources, coal fuels and capacity from 1MW to 50 MW.

3. Conclusion

This study provides a comprehensive analysis of mercury content in coal and coal byproducts in TPP Kolubara A, which is crucial given its major influence on environmental contamination. The mercury content found in the lignite aligns closely with contents reported in coals from India, Poland, and Russia, while being significantly lower than those found in certain Chinese coals. The investigation into the mercury concentrations in fly and bottom ash indicates that the observed values are consistent with existing literature, emphasizing the influence of coal type and combustion conditions on mercury distribution in ash byproducts. These findings underscore the importance of understanding the dynamics of mercury emissions in relation to combustion technologies, which is essential for evaluating the environmental impacts of coal-fired power generation. Total mercury emissions from TPP Kolubara A were measured at 38.73 µg/Nm³, adhering to the existing legislative limits for mercury emissions in Serbia. The calculated Mercury Emission Factor of 1.12 mg/GJ is below the lower limit set in the EMEP guidebook for medium-sized non-residential sources. This indicates that the facility is operating within acceptable limits and suggests the potential for effective mercury management strategies in coal combustion processes. Overall, this research contributes valuable data to the limited knowledge surrounding mercury content in Serbian coals and their byproducts, highlighting the need for continued monitoring and the development of stringent regulatory frameworks to mitigate the environmental impacts of coal combustion.

Acknowledgments

This work was supported by the Ministry of Science, Technological Development and Innovation of the Republic of Serbia; grant number 451-03-66/2024-03/200017.

References

- [1] Finkelman, R. B., Orem, W., Castranova, V., Tatu, C. A., Belkin, H. E., Zheng, B., Lerch, H. E., Maharaj, S. V., Bates, A. L., Health impacts of coal and coal use: possible solutions, *International Journal of Coal Geology*, 50 (2002), pp. 425-443
- [2] Serbian Ministry of Mining and Energy, Annual Report on Energy Production, 2021
- [3] Kursun Unver, I., Terzi, M., Distribution of trace elements in coal and coal fly ash and their recovery with mineral processing practices: a review, *Journal of Mining and Environment*, 9 (2018), pp. 641-655
- [4] Das, S., Heavy metals and hydrocarbons: Adverse effects and mechanism of toxicity, 2014
- [5] Vejehati, F., Xu, Z., Gupta, R., Trace elements in coal: Associations with coal and minerals and their behavior during coal utilization – A review, *Fuel*, 89 (2010), pp. 904-911

- [6] Querol, X., Fernández-Turiel, J., López-Soler, A., Trace elements in coal and their behaviour during combustion in a large power station, *Fuel*, 74 (1995), pp. 331-343
- [7] Organization, W.H., Chemicals: Compendium of WHO and other UN guidance on health and environment, 2021
- [8] Wang, S., Zhang, L., Wang, L., Wu, Q., Wang, F., Hao, J., A review of atmospheric mercury emissions, pollution and control in China, *Frontiers of Environmental Science & Engineering*, 8 (2014), pp. 631- 649
- [9] Zhao, S., Pudasainee, D., Duan, Y., Gupta, R., Liu, M., Lu, J., A review on mercury in coal combustion process: Content and occurrence forms in coal, transformation, sampling methods, emission and control technologies, *Progress in Energy and Combustion Science*, 73 (2019), pp. 26-64
- [10] Otero-Rey, J. R., López-Vilariño, J. M., Moreda-Piñeiro, J., Alonso-Rodríguez, E., Muniategui- Lorenzo, S., López-Mahía, P., Prada-Rodríguez, D., As, Hg, and Se flue gas sampling in a coal-fired power plant and their fate during coal combustion, *Environmental Science and Technology*, 37 (2003), pp. 5262-5267
- [11] pp. 5262-5267
- [12] Liu, S., Chen, J., Cao, Y., Yang, H., Chen, C., Jia, W., Distribution of mercury in the combustion products from coal-fired power plants in Guizhou, southwest China, *Journal of the Air & Waste Management Association*, 69 (2019), pp. 234-245
- [13] Sloss Lesley, S. I., Trace element emissions, 2020,
- [14] Krgović, R. M., Mobilizacija i biodostupnost makro i mikro elemenata iz pepela Termoelektrane “Kolubara“, PhD, Univerzitet u Beogradu, Hemijski fakultet, Beograd, 2015 ASTM D346-90, Standard practice for collection and preparation of coke samples for laboratory analysis, ASTM International, 1998, West Conshohocken, PA
- [15] Lacorte, S., Bono-Blay, F., Cortina-Puig, M., Sample homogenization, Academic Press, Oxford, 2012
- [16] SRPS ISO 13211, S. I., Air Quality - Stationary source emissions - Manual method of determination of the concentration of total mercury, 2009, Belgrade, Serbia
- [17] ASTM D7582-12, Standard test methods for proximate analysis of coal and coke by macro thermogravimetric analysis, ASTM International , 2012, West Conshohocken, PA
- [18] SRPS ISO 1928, S. I., Coal and coke — Determination of gross calorific value, Institution, 2022, Belgrade, Serbia
- [19] ASTM D5373-14, Standard test methods for determination of carbon, hydrogen and nitrogen in analysis samples of coal and carbon in analysis samples of coal and coke, ASTM International, 2014, West Conshohocken, PA
- [20] ASTM D5016-08, Standard test method for total sulfur in coal and coke combustion residues using a high-temperature tube furnace combustion method with infrared absorption, ASTM International, 2008, West Conshohocken, PA
- [21] ASTM D3176-09, Standard practice for ultimate analysis of coal and coke, ASTM International, 2009, West Conshohocken, PA
- [22] Oleg, P., Petrologija kaustobilita, Beopres, Beograd, 1992
- [23] Chakravarty, S., Mohanty, A., Banerjee, A., Tripathy, R., Mandal, G. K., Basariya, M. R., Sharma, M., Composition, mineral matter characteristics and ash fusion behavior of some Indian coals, *Fuel*, 150 (2015), pp. 96-101
- [24] Czajka, K. M., Proximate analysis of coal by micro-TG method, *Journal of Analytical and Applied Pyrolysis*, 133 (2018), pp. 82-90
- [25] Chou, C.-L., Sulfur in coals: A review of geochemistry and origins, *International Journal of Coal Geology*, 100 (2012), pp. 1-13
- [26] Iordanidis, A., Asvesta, A., Kapageridis, I., Vasileiadou, A., Koios, K., Oikonomidis, S., Kantiranis, N., A Comprehensive Analytical Characterization of Greek Lignite Bottom Ash Samples, *Thermal Science*, 25 (2020), pp. 299-299
- [27] Chen, G., Sun, Y., Wang, Q., Yan, B., Cheng, Z., Ma, W., Partitioning of trace elements in coal combustion products: A comparative study of different applications in China, *Fuel*, 240 (2019), pp. 31- 39
- [28] Tolvanen, M., Mass balance determination for trace elements at coal-, peat- and bark-fired power plants, PhD, University of Helsinki, Helsinki, Finland, 2004
- [29] Reddy, M. S., Basha, S., Joshi, H. V., Jha, B., Evaluation of the emission characteristics of trace metals from coal and fuel oil fired power plants and their fate during combustion, *Journal of Hazardous Materials*, 123 (2005), pp. 242-249
- [30] Meij, R., Vredendregt, L. H., te Winkel, H., The fate and behavior of mercury in coal-fired power plants, *Journal of the Air & Waste Management Association*, 52 (2002), pp. 912-917
- [31] Bulut, Y., Karayigit, A., Hower, J., Sakulpitakphon, T., Characterization of Feed Coal, Fly Ash and Bottom Ash from the Soma Power Plant, Manisa, Turkey, 2002
- [32] Goodarzi, F., Characteristics and composition of fly ash from Canadian coal-fired power plants, *Fuel*, 85 (2006), pp. 1418-1427
- [33] European monitoring and evaluation programme. Available online: <http://www.emep.int/> (accessed on access date 2020/04/02).

Analysis the Impact of Coal Mixing on Boiler Characteristics

Lidija Joleska Bureska^a

^a*AD ESM, TPP Bitola, Republic of Macedonia, lidija.j.bureska@elem.com.mkb*

Abstract: Due of the depletion of the mines that were basis for the design and construction of the Thermal Power Plants in Macedonia, the necessary quantities of coal have to be supplied from other mines. The issue is further complicated by the fact that the current mines are providing coal with higher mineral matter content and lower calorific values towards the end of their operation, resulting in a lower quality compared to the originally intended specifications. Utilizing such coal in boilers has a number of disadvantages, such as lower efficiency, limited power, higher load on the fuel supply and preparation system, as well as slag and ash removal systems, an increased frequency of failures, and so on. To increase the quality of coal the existing one should be mixed with coal of a higher quality. This paper analyzes the selection of coal for blending, coal characteristics, and boiler operation with a few types of coal. Through analyzing calculation results, ash composition, and fusion temperatures, it is evident that the choice of coal for mixing should not solely focus on increasing calorific value but should consider a broader range of characteristics for a comprehensive analysis.

Keywords: Coal, Mixing, Boiler, Ash, Slagging

1. Introduction

Over the time, the best lignite was depleted from our coal mines. Now there currently exists only poor coal (low quality) available for exploitation in our mines. We have to keep using that coal because this type of energy is still required. Utilizing these coals requires overcoming the difficulties related to operating with variable and poor quality coal. For the seamless operation of thermal power plants (regarding fuel) it is essential to supply a sufficient amount of coal with the required quality. From the perspective of the mines, it makes sense to exploit the areas of the mine where the coal is lower quality because doing increases resource utilization, prolongs the mine's life time, etc.

However, from the perspective of the thermal power plant, the acceptance of low quality coal is always met with resentment because its combustion necessitates a higher fuel oil consumption to support the burning, lowers the thermal power plant's output, increases maintenance issues and costs, etc. Mixing coals of lower quality with coals of higher quality and homogenization are the methods to prevent the problems mentioned above and achieve satisfactory coal quality. Homogenization is a procedure for equalizing the quality of the coal delivered to the thermal power plant, refers to coal sourced from a single mine. The homogenization, it would be increased the amount of coal whose exploitation is justified, to reduce the costs of transport, the costs of burning coal, conveyance and ash deposition, as well as enhance environmental protection systems against contamination—particularly during combustion phases [1].

Combining lower quality coal with higher quality coal involves mixing coal from different mines to improve its overall quality. This process aims to increase the calorific value of coal, improve combustion, and reduce harmful elements such as sulfur and nitrogen for environmental benefits [1]. The paper discusses specific factors that should be taken into account when mixing coal which directly or indirectly affect the performance of the boiler. Furthermore, the calculation and analysis of efficiency for different types of coal used in the combustion process of the boiler model are given. Coal types A, B, and C belong to the same mine, while types D, E, and F are obtained by mixing coal from different mines. In the table 2 are presents the ultimate and proximate analyses of these coals.

Coal blending is a process that aims to produce a fuel with characteristics closely matched to the fuel designed in the boiler. This fuel allows the boiler and its auxiliary equipment, such as fuel supply systems, slag and ash removal systems, air supply systems, and gas removal systems, to achieve maximum efficiency.

2. Characteristics of coal that should be taken into account in coal mixing and that affect the combustion

Coal mixing should create a coal mixture that meets design coal characteristics such as heat value, moisture, ash content, coal grindability (HGI), etc. In addition, it should check the micro petrographic composition of coal, chemical analysis of ash, temperatures of deformation, softening, hemispherization and flow, discriminant indexes of ash, comprehensive index, etc. or in other words the affinity of coal for slagging.

The calorific value of coal is an important indicator in determining its quality. When coal has a lower-than-designed calorific value, it can result in unstable and incomplete combustion, which may turn off the flame within the furnace and make it difficult to achieve the required temperature. On the other hand, burning coal with a calorific value higher than designed can lead to overheating of heating surfaces, higher temperatures within the gas tract, and potential shutdown of the boiler for protection if temperature regulation along the water-steam tract is not possible. Such issues can significantly impact the normal operation of boilers.

Coal moisture is to some extent compatible with volatile matter. A small amount of moisture can have a positive impact on the overall combustion process. From a combustion kinetics perspective, moisture vapor at high temperatures has a catalytic effect on combustion, accelerating the burning of coal dust coke and enhancing flame emissions. Furthermore, during the breakdown of moisture vapor, hydrogen and hydroxide compounds are produced, which contribute to more efficient heat transfer within the flame.

However, too high a moisture content in coal can negatively affect the combustion process. When the moisture content is too high, the necessary heat for ignition substantially increases, leading to excessive heat consumption for evaporating excess water in the coal. Consequently, this reduces the temperature of hot gases which adversely impacts the ignition process.

Increased moisture content in the coal causes increased fuel consumption to achieve the required input heat in the furnace [2]. Especially mills' capacity is particularly sensitive to moisture in coal [3].

The ash content of coal does not produce heat during burning. Instead, energy is used to heat the ash. When there is more ash content in the coal, the amount of heat produced is reduced. In these conditions, the ignition process of coal is more difficult and may lead to a delay in ignition. The furnace temperature and the burning rate of the coal also drop, and the amount of combustible matters in the fly ash rises significantly.

As the ash content increases, the surrounding ash prevents the carbon particles from interacting with oxygen, resulting in incomplete combustion. As the ash concentration increases, so does the fly ash concentration, resulting in increased abrasion on the convection heating surfaces. Physical heat losses due to fly ash and slag also increase, resulting in decreased boiler efficiency [4].

Volatile matters have a significant impact on the combustion process. They are separated at low temperatures (150 to 180°C) in the brown coals [5]. During combustion, coke particles warm up quickly, allowing them to ignite and burn. The more volatile matters in the coal, the easier it is to ignite and the faster it burns. In other words, coal with a large amount of volatile matters ignites more quickly, but coal with a low percentage of volatile matters has a significantly higher ignition temperature, making it much more difficult to ignite. In this case, it will take longer to reach the ignition point, which reduces combustion stability. In addition, the center of combustion rises higher, reducing heat in the furnace while increasing heat absorbed by the convective heating surfaces. The temperature of the flue gas is then increased increasing the flue gas loss. Coal with a low volatile matters content should be finely milled.

When the coal particles are too large, they remain in the furnace for a very short time, so the coke does not have time to burn. In this case, the slag's carbon concentration rises, increasing heat loss due to the slag's physical heat. When the coal particles are too small, they pass easily through the furnace, do not make good contact with oxygen, and are carried out with flue gas, resulting in increased heat losses due to the fly ash. In order to prevent the above situations, the coal grinding fineness must be adjusted according to: coal quality and grindability, the flow of secondary air, the type of combustion in the furnace, etc. The grindability of coal is determined by the Hard Growth Index, HGI. The coal with a higher HGI, is easier to grind and vice versa. When grinding harder coal, mill capacity drops [6].

Coal affinity for slagging is an important factor to take into account while blending coals, because slagging affects combustion, heat transfer, boiler efficiency, etc. The coal ultimate analysis, ash concentration, ash melting temperature, and the mineral composition in the ash can all be used to evaluate the coal's tendency for

slagging. By calculating the discriminant index [7], which includes the base-acid ratio, silicon ratio, silica-alumina ratio, iron-calcium ratio, and comprehensive index, the slagging characteristics of coals can be anticipated. The following expressions specify each relationship [8]:

$$\text{Base-Acid ratio, } B/A = (\text{Fe}_2\text{O}_3 + \text{CaO} + \text{MgO} + \text{Na}_2\text{O} + \text{K}_2\text{O}) / (\text{SiO}_2 + \text{Al}_2\text{O}_3 + \text{TiO}_2) \quad (18)$$

$$\text{Silicon ratio, } G = 100 \text{ SiO}_2 / (\text{SiO}_2 + \text{Fe}_2\text{O}_3 + \text{CaO} + \text{MgO}), \quad (19)$$

$$\text{Silica-Alumina ratio} = \text{SiO}_2 / \text{Al}_2\text{O}_3 \quad (20)$$

$$\text{Iron-Calcium ratio} = \text{Fe}_2\text{O}_3 / \text{CaO} \quad (21)$$

$$\text{Comprehensive index, } R = 5,415 - 0,002ST + 1,237B/A - 0,019G + 0,282\text{SiO}_2/\text{Al}_2\text{O}_3 \quad (22)$$

In the table 1 are shown the limits values of the discriminant indexes for slagging. The composition and properties of the minerals, determine the bituminous coal's and lignite's slagging characteristics [9]. For the same coal, results based on discriminant indexes may sometimes show results that are completely at disagreement with each other and have little precision. The slagging characteristics of coal can be precisely predicted by determining fusion temperatures [8].

Table 1. The limits values of discriminant indexes for slagging [9]

Index	Tendency of slagging		
	slight	medium	severity
B/A	<0,206	0,206-0,4	>0,4
G	>78,8	78,2-66,1	<0,66
SiO ₂ / Al ₂ O ₃	<1,87	1,87-2,65	>2,65
Fe ₂ O ₃ /CaO	Out of 0,3-3	0,3-3	Near 1
R	<1,5	1,5-2,5	>2,5

In same literature [10], one can also find the parameter of AFT (Ash Fusion Temperature) next to the other relevant indicators for slagging. The ash fusion temperature serves as an indicator of ash agglomeration and deposition resulting from combustion, and it can be calculated using a specific formulation:

$$\text{AFT} = (4DT + HT) / 5 \quad (6)$$

where DT and HT are ash temperatures for deformation start and hemispheric temperature respectively. If the calculated AFT values fall within the range of 1052 to 1232 °C, that is indicator for high potential for slagging. Conversely, if the values are below 1052 °C, there is a high probability of significant slagging occurring [14,15].

3. Analysis and discussion of research results

The boiler type P65, which was designed for burning lignite coal in a flight, was the subject of the study. According to the literature, the boiler furnace is octagonal-shaped, and the fuel is fed by six fan mills [13]. The calculation for determining boiler efficiency, heat losses, required amount of fuel, etc. was performed in accordance with European Standard EN 12952, Part 15. Six types of coal were used, with characteristics given in Table 2.

Table 2. Coal specifications

Coal Specification	Unit	Coal					
		Type A	Type B	Type C	Type D	Type E	Type F
Water, W	[%]	39,12	37,8	37,2	42,61	44,56	42,99
Ash, A	[%]	32,70	34,28	32,99	23,47	21,61	28,03
Carbon, C	[%]	16,39	16,73	17,72	22,2	22,07	18,3
Hydrogen, H	[%]	1,47	1,57	1,67	2,02	1,95	1,71
Sulphur, S	[%]	0,84	0,67	0,9	1,09	0,72	1,04
Oxygen, O	[%]	9,19	8,7	9,65	8,71	9,03	7,8
Nitrogen, N	[%]	0,30	0,25	0,31	0,49	0,47	0,42
Law Heat Value, LHV	[KJ/kg]	5856	5534	6006	7465	7225	5974

Tables 3 and 4 show the fusion temperature and chemical analysis of the ash for the respective coals.

Table 3. Summary of the formatting rules

Ash from coal	Deformation Temperature (DT) [°C]	Softening Temperature (ST) [°C]	Hemisphere Temperature (HT) [°C]	Flow Temperature (FT) [°C]
Typ A	1246	1366	1379	1398
Typ B	1278	1368	1382	1394
Typ C	1370	1438	1458	1472
Typ D	900	995	1220	1270
Typ E	900	995	1230	1220
Typ F	890	985	1220	1355

Table 4. Ash analysis of the relevant types of coal

Ash from coal	SiO ₂ [%]	Al ₂ O ₃ [%]	TiO ₂ [%]	Fe ₂ O ₃ [%]	K ₂ O [%]	CaO [%]	MgO [%]	Na ₂ O [%]
Typ A	57,25	20,15	0,73	6,49	2,86	2,89	1,60	1,13
Typ B	55,52	20,88	0,83	5,99	2,78	2,90	1,77	1,48
Typ C	55,07	24,43	0,82	7,24	2,73	2,80	1,92	0,89
Typ D	50,51	24,09	0,82	7,61	1,30	6,26	3,54	0,10
Typ E	53,33	25,12	0,77	6,75	1,34	6,15	2,22	0,11
Typ F	52,93	30,49	0,8	6,37	1,61	3,55	2,31	0,11

A computer calculation was performed in order to compare the operation of the boiler with above mentioned types of coal (Fig. 1). The input data included ultimate and proximate coal analysis, design values for flow, pressure, and temperature of feed water, temperature of heating surfaces, etc. It is assumed that the boiler will operate with a maximum steam production of 700t/h with design parameters [13]. The calculation was made according to the European standard EN 12952, part 15, applying case 4, where the flow of slag and fly ash is determined from the ash balance and with the estimated degree of ash separation in the furnace [14].

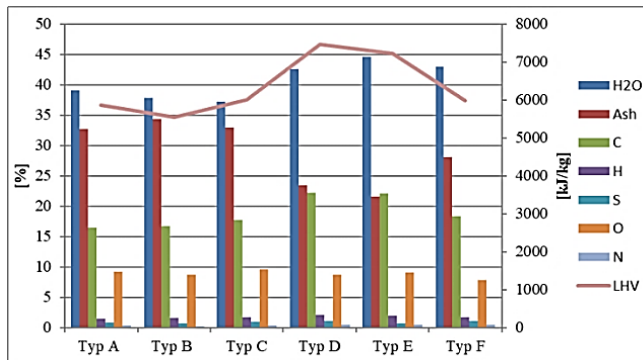


Figure 1. The coal's characteristics type A, B, C, D, E, F

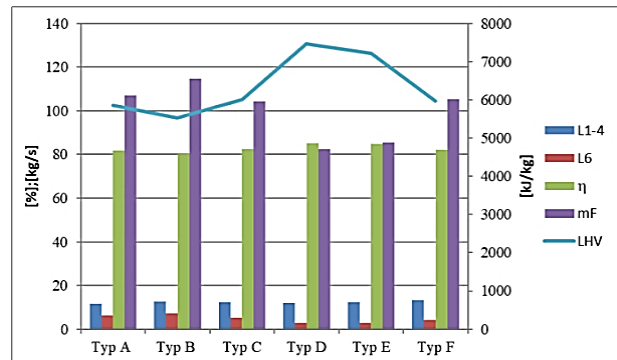


Figure 2. The calculation's results

It is evident from the characteristics of the analyzed types of coal (Fig. 1) that all types have a relatively high ash content (23,61 to 34,28%), which is higher than the fuel designed (max 20%), for the boiler taken as a model. This is certainly reflected in the boiler efficiency through increased losses (L6) due to the unburned in slag and ash (Fig.2). Naturally, a higher ash content is reflected in the coal's reduce calorific value. Due to the reduced calorific value of coal, more fuel is required, resulting in an increase in (mF) fuel consumption (Fig. 2). The amount of fuel needed to supply the boiler for its maximum capacity while burning coal types A, B, C, and F is 107 kg/s; 114,9 kg/s; 104,5 kg/s; 105,3 kg/s respectively and is greater than the mills' capacity (100 kg/s) [13]. This indicates that it is not possible boiler to operate with maximum capacity when burning coals of these types. Calculations show that types of coal D and E enable the boiler to operate at its maximum capacity with fuel consumption of 82,6 and 85,4 kg/s and efficiency at 85,1% and 84,8%, respectively. In the calculation is assumed that the sealing of the gas-air and coal tract, is within the range of acceptable values.

According to the chemical analysis of the ash (Fig. 3), the ash from coal types D and E contains more than twice of CaO as that of other types of coal. Also, types C, D, E, and F coal ash contain an Al₂O₃ more than 20% compared to types A and B.

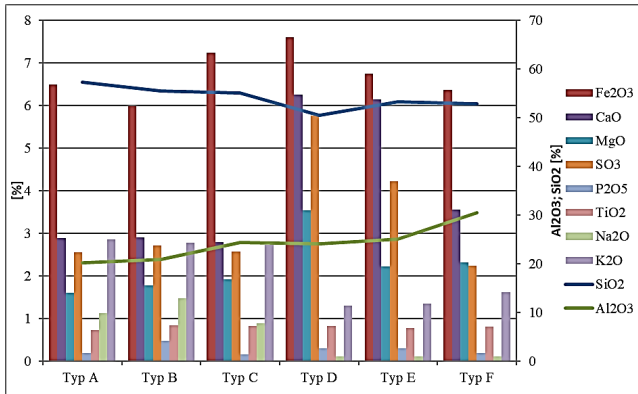


Figure 3. Chemical analysis of the ash of coal types A, B, C, D, E, and F

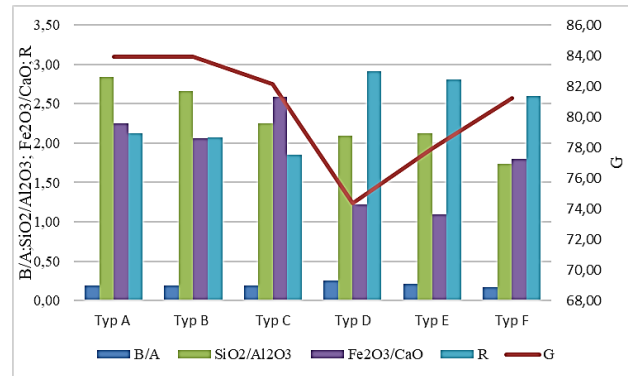
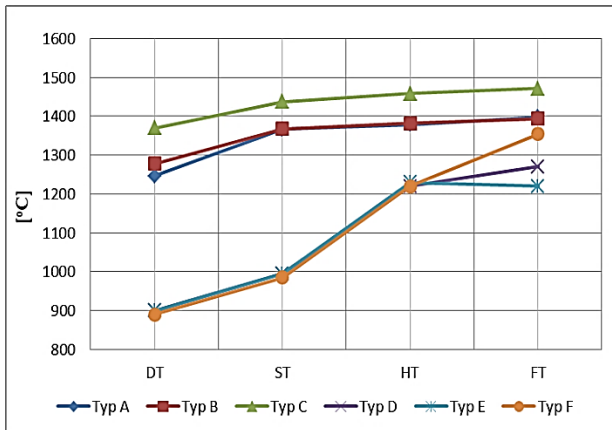


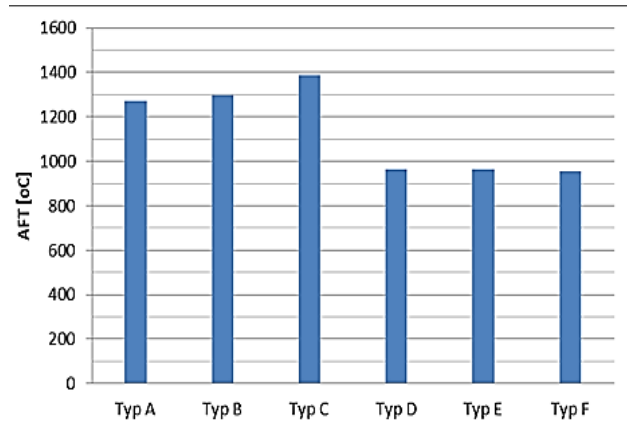
Figure 4. Discriminant indexes for slagging for coal types A, B, C, D, E, F

The discriminant indexes for slagging B/A, G, SiO₂/Al₂O₃, Fe₂O₃/CaO, and the comprehensive index R are calculated using these ash oxide values [8]. Figure 4 shows that the B/A, G, and SiO₂/Al₂O₃ index values for D and E-type coal ash are in the range corresponding to coals with medium tendency of slagging, while the Fe₂O₃/CaO index values and the total R index indicated coal with severity slagging tendency. For other types of coal A, B, C and F, only the Fe₂O₃/CaO index and the comprehensive index R show that have a medium tendency to slagging, while the other indexes show a slight tendency.

Analysis of the ash fusion temperatures is needed since, as I already indicated, the indexes sometimes give a different interpretation. The diagram (Fig. 5) shows typical ash temperatures for the considered coal types, including deformation temperature (DT), softening temperature (ST), hemispheric temperature (HT), and flow temperature (FT) and calculated AFT (Ash Fusion Temperature).



a)



b)

Figure 5. Characteristic ash temperature (a) and calculated ash fusion temperature (AFT) for coal types (b)

The fusion temperatures of the ash from coal types D, E, and F overlap at several locations on the diagram (Fig. 5a), but they are lower than the corresponding temperatures for ash from coal types A, B, and C. The temperature for the beginning of deformation (DT) of ash in coal types D, E, and F is lower by more than 300°C, while the hemisphere temperature (HT) is lower by less than 200°C. Namely, coal types D and E have lower flow temperatures (1270 and 1220°C), coal types A, B, and F have higher and with close values (1398, 1394, and 1355°C respectively), and coal type C has the highest flow temperature 1472°C. Based on the calculated values of ash fusion temperature (AFT) for various types of coal (as shown in Figure 5b), significant differences can be observed between coal types A, B, and C compared to coal types D, E, and F. Specifically, the AFT values for types A, B, and C are 1272°C, 1298.8°C, and 1387.6°C, respectively, while for types D, E, and F, they are 964°C, 966°C, and 956°C, respectively. Based on these values, it can be inferred that coal

types A, B, and C exhibit moderate potential for slagging, whereas types D, E, and F demonstrate a serious propensity for slagging.

The consequences of poor coal selection are shown in fig.6. Due to the slagging, Unit 3 at the TPP Bitola was non-operational for over three months in 2023 year.



Figure 6. Slagging in the boiler furnace

4. Conclusions

Based on the calculations of the boiler with different types of coal it can be concluded that only with coal types D and E boiler may reach maximum production with design parameters and efficiency of 85,1% and 84,8% respectively. Additionally, other types of coal make it hard to attain maximum output since they require more fuel than the mills' capacity. On the other hand, considering the values of the discriminant indexes and the ash fusion temperatures, the operation of the boiler with coal types D and E can be troublesome. Namely, the values of the indexes B/A, G, and $\text{SiO}_2/\text{Al}_2\text{O}_3$ for ash from coal types D and E are in the range of coals with a medium slagging tendency, but the values of the index $\text{Fe}_2\text{O}_3/\text{CaO}$ and the comprehensive index R indicate coal with a severity tendency of slagging.

Furthermore, the ash fusion temperatures of coal types D, E, and F are notably lower by approximately 200 to 300 °C compared to types A, B, and C, suggesting a probability of slagging during combustion of these coal types. This observation is supported by the calculated AFT values of 964°C, 966°C, and 956°C for types D, E, and F, respectively, placing them within the category of coals with a significant potential for slagging.

It can be summarize that when burning D and E types of coal due to their high calorific value, the boiler's maximum production would be achieved, but there would be a risk of the boiler furnace slagging due to the ash's slagging characteristics.

While selecting coal for mixing with existing coal, it is essential to consider not only the required calorific value, but also other coal and ash characteristics. Specifically, it is necessary to carry out the following tasks: analyzing the properties of the coal to be mixed, calculating the initial coal ratio for mixing, conducting test burns of the theoretically obtained optimal coal ratio, monitoring parameters during test combustion, collecting data beginning with the coal preparation system (grinding, humidity, air mixture temperature, etc.), temperature distribution to furnace heights, temperatures in recirculation ducts, temperatures of heat surfaces, temperature of the flue gas at the boiler's exit, amount of ash and slag and analysis, as well as data collecting and analysis. According to the results at the end have to prepare conclusion for coal selection, rate and methodology in order to achieve a homogeneous mix.

References

- [1] D.Ignjatovic, D Knezevic, B.Kolonja, N.Lilic, R.Stankovic,: Management with coal quality, Belgrade 2007.
- [2] R.R.Leonard: The role of coal characteristics in boiler operation, 27th Annual Steam Power Plant Operation Conference, University of Wisconsin, November 6-7, 1978.
- [3] Lidija Joleska Bureska: Choice of coal for mixing with existing for improving the performance of energetic boilers, International Conference Power Plants 2023, November 8-10, 2023, Zlatibor.

- [4] L.J.Bureska: Influence of the coal quality on the boiler efficiency and opportunity for improvement, GREDIT 2016, Skopje 31.03-01.04.2016, University Cyril and Methodius, Technical Campus.
- [5] Petrovski J. Ilija: Steam boilers, 2004r.
- [6] R.R.Leonard: The role of coal characteristics in boiler operation, 27th Annual Steam Power Plant Operation Conference, University of Wisconsin, November 6-7, 1978.
- [7] B.T.Rhodes: An empirical study of the relation of chemical properties to ash fusion temperature. J. Eng. Power 97(3) (1975) 393-403.
- [8] L.Guo, et al., Comparison of bituminous and lignite during combustion: Combustion performance, coking and slagging characteristics, Journal of the Energy Institute (2018).
- [9] M.Grigore, R.Sakurov, D.French, et al., Mineral matter in coals and their reaction during coking. Int. J. Coal Geol. 76(4)(2008) 301-308.
- [10] Singer J.G., 1981. Combustion Fossil Power Systems, 3rd ed., Combustion Engineering, Windsor, USA. pp. 67-95.
- [11] McLennan A.R., Bryant G.W., Stanmore B.R. and Wall T.F., 2000. Ash formation mechanisms during combustion in reducing conditions. Energy & Fuels 14(1), 150-159.
- [12] Dunnu G., Maier, J., and Scheffknecht G., 2010. Ash fusibility and compositional data of solid recovered fuels. Fuel 89(7), 1534-1540
- [13] S.Pecakov: Local instruction for exploitation steam boiler Pp-700-13,8-545 (P65)
- [14] European Standard EN 12952-15:2003

Effect of Wall Heat Flux on Flow and Heat Transfer Characteristics in Coiled Corrugated Pipes

Milan Đorđević^a, Marko Mančić^b, Velimir Stefanović^c, Mića Vukić^d

^a Faculty of Technical Sciences, Kosovska Mitrovica, RS, milan.djordjevic@pr.ac.rs

^b Faculty of Mechanical Engineering, Niš, RS, marko.mancic@masfak.ni.ac.rs

^c Faculty of Mechanical Engineering, Niš, RS, veljas@masfak.ni.ac.rs

^d Faculty of Mechanical Engineering, Niš, RS, micav@masfak.ni.ac.rs

Abstract: The objective of this paper was to study the influence of high-intensity asymmetric heat flux at the wall on pressure drop and heat transfer in the Archimedean spiral coil made of transversely corrugated tube that was exposed to radiant heating and is supposed to represent heat absorber of parabolic dish solar concentrator. The working fluids were water and a mixture of propylene glycol and water (90% and 10% by volume, respectively). An increase in the heat flux density at the pipe wall affects the increase in the pressure drop and peripherally averaged Nu number in the considered geometry in all flow regimes. The effect is most noticeable in the laminar region and monotonically decreases with increasing Reynolds number and curvature ratio. The intensification of heat transfer is less compared to the increase in pressure drop with increasing heat load at the wall. Quantitative comparison of the obtained data with results in the literature is lacking due to significant differences between the considered geometries and experimental conditions.

Keywords: Corrugated spiral coil, Heat flux density, Pressure drop, Heat transfer.

1. Introduction

Spiral pipes or spiral coils were introduced in 19th century and have been widely used in various thermal engineering applications, such as heat exchangers, electronic cooling, chemical reactors, etc. They have better heat transfer performance and compactness in comparison with commonly used straight tube exchangers, which results in occupying less space. The transport phenomena occurring in the spiral tubes are more complicated than those in straight tubes. Secondary flows observed in the flow patterns, induced by centrifugal force, significantly affect the flow field and heat transfer.

Even though the interest in spiral coiled systems is on the rise, there are still very few published articles on spiral coil tubes. They are less popular compared to helical tubes, which have attracted major attention in the study of coiled tubes for heat transfer. Most of the studies of thermal-hydraulic processes in the coils have been dedicated to the helical coils. Much less work has been reported for the hydrodynamics of flow and heat transfer in spiral coils. There is very little information and correlations on the Nusselt number, and in the absence of appropriate correlations, traditional approach is to use correlations developed for circular or helical tubes with an average curvature.

The property of continuously varying curvature along the length makes spiral coil flows never hydrodynamically and thermally fully developed, unlike the helical coil flows. The velocity profile and dimensionless temperature profiles are changing along the flow direction, as well as the friction factor and Nusselt number. The use of the friction factor in correlations is inappropriate, since the magnitude of the pressure drop per unit length is variable along the axial coordinate of the spiral and increases with the curvature ratio.

The presence of the superimposed secondary convection in the curved channel flow suppresses axial propagation of the initial turbulent fluctuations, so that the curvature stabilizes the flow while the transition from the laminar to the turbulent flow is delayed. The spiral coil flow is characterized by two critical Reynolds numbers [1, 2], the first one when the turbulence has set only in the outer turns with lowest curvature ratio, and the second one, when the inertia forces, even in the innermost turns with highest curvature ratio, are sufficient to overcome the damping effect of the secondary flow. In a spiral coil completely filled with laminar flow slow increase of Reynolds number causes the appearance of the turbulent flow zone at the outer end at

the approach of the first critical Reynolds number. Further increase of Reynolds number extends turbulent flow zone toward the inner end of the coil until it completely fills the coil with turbulent flow at the second critical Reynolds number. Moreover, there is a possibility of existence of mixed flow inside the spiral coil, where some length of the coil being in the laminar flow and some other length in the turbulent flow. Consequently, the phenomena of the forward and the reverse laminar-turbulent transition can occur in the spiral coil.

On the contrary, the transversal corrugations act as turbulence promoters, since the turbulence level is increased by a separation and reattachment mechanism. The corrugations act as roughness elements and disturb the existing laminar sublayer. There is the similarity of flow phenomena between heated straight pipes and unheated curved pipes, the techniques developed in treating the flow problem in the latter can be applied to study the flow development in the former. Morton [3] found that the flow in a heated straight pipe is similar to that in a curved pipe. For a heated pipe the secondary flow is created by the buoyancy force inside the thermal boundary layer. Heated pipes also develop vortices that result from the combination of the radial-directional and the downward motions of the fluid particles which are induced by the displacement of the boundary layer and develop along the pipe. A favorable pressure gradient is generated on the bottom wall of the pipe, while an unfavorable pressure gradient is induced on the top wall.

Another interesting character of the flow in heated pipes, revealed by Mori *et al.* [4], is that the secondary flow generated by heating can suppress the turbulence level when the inlet turbulence level is high and can enhance it when its level is low at the inlet. On the other hand, the curvature of the wall stabilizes the flow by delaying the transition to the turbulent flow.

The substantial features of each of these effects (curvature, corrugated wall and heating) are enhanced heat and mass transfer coefficients due to the cross-sectional mixing of fluid elements, as well as increased frictional losses. Natural convection and variable material properties play important roles in the heat transfer and fluid flow in a heated pipe. Frequently the prediction of the heat transfer by forced convection alone, without considering the secondary flow induced by buoyancy force, could cause significant errors, especially for laminar flow cases.

It is important to distinguish between the vortex flow within the main flow (in the minimum cross section of the corrugated pipe), which is characterized by the existence of Dean vortex cells, and the recirculation flow inside the corrugations, which is a consequence of the sudden expansion of the flow channel. Although both of these secondary flows are recirculating and vortexing, they differ fundamentally in terms of the mechanisms that cause them and their localization. The vorticity vectors of the secondary flow in the basic section of the tube and the vorticity vectors of the secondary flow inside the corrugations are mutually perpendicular.

Several experimental [5-12] and numerical [13-25] studies have been published that examined the flow and heat transfer phenomena in the smooth and hydraulically rough spiral pipes. Most of these papers investigated laminar flow conditions, while those that investigated turbulent flow conditions are less frequent in literature compared to the previous ones.

The literature review reveals that there is a lack of research related to the flow and heat transfer in transversely corrugated straight tubes characterized by a high value of relative roughness and spiral tube coils with transverse corrugations. Existing studies are generally limited to considering the results for relatively narrow ranges of geometric and flow parameters. Moreover, almost all take into account two common thermal boundary conditions - constant wall temperature and constant heat flux, which is significantly different from the high-intensity asymmetric flux considered in this research.

2. Experiment

The objective of this paper was to experimentally study the distribution of the convective heat transfer in a spirally coiled corrugated tube exposed to radiant heating that is characteristic of parabolic dish solar concentrators. Investigation of the influence of hydraulic, physical and thermal conditions, as well as the geometry of the spirally coiled corrugated heat absorber, on the local intensity of heat transfer and pressure drop was conducted using modern experimental methods.

The Archimedean spiral, with a pitch slightly larger than the maximal outside diameter of the corrugated coiling tube, was selected out of different types of spirals in order to achieve the most favorable ratio of active surface area and the total volume of the heat absorber in the parabolic dish receiver. The geometric

characteristics and experimental configurations of the transversely corrugated straight pipe and the transversely corrugated Archimedean spiral coil are shown in Figures 1 and 2, respectively, while Table 1 shows geometric parameters of the tested configuration.



Figure 1 Profile of transverse corrugated pipe made of stainless steel AISI 304 [26]

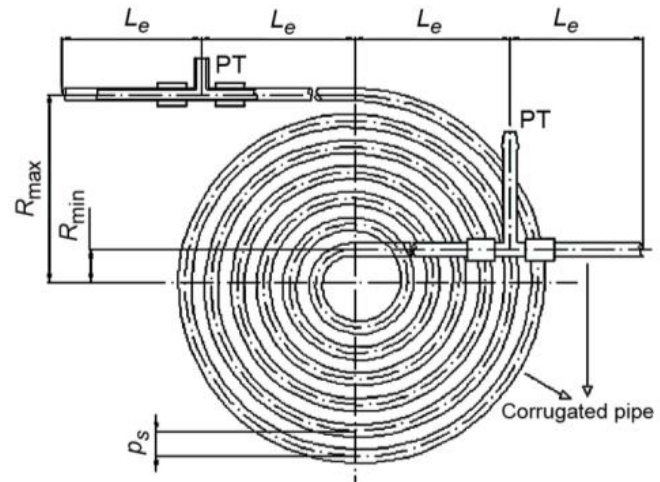


Figure 2 Geometry and configuration of transversely corrugated Archimedean spiral coil

In order to simulate the real working conditions of the heat absorber, an experimental installation was constructed. The installation consists of a spirally coiled corrugated tube of heat absorber with an accompanying flow loop and a radiant heating system. The schematic diagram of the hydraulic system is shown in Figure 2. The entire experimental apparatus enables variations of the following operating parameters: 1) intensity of the incident radiant heat flux; 2) flow rate and flow direction of the working fluid, and 3) angle of inclination of the spiral heat exchanger in relation to the horizontal plane.

Table 1. Geometric parameters of the tested configuration

Transversely corrugated straight pipe				Transversely corrugated Archimedean spiral coil			
d	9.3	mm	minimum internal diameter	R_{min}	25	mm	minimum radius of the coil
d_0	11.7	mm	maximum internal diameter	R_{max}	202	mm	maximum radius of the coil
d_{max}	12.2	mm	maximum external diameter	n	13	-	number of coil turns
s	0.25	mm	wall thickness	L	9.324	m	length of the coil
e	1.2	mm	corrugation depth	L_e	0.5	mm	length of entrance section
p_c	4.2	mm	corrugation pitch	p_s	13.6	mm	spiral coil pitch

The incident heat flux upon the tube external surface varies both in the circumferential and axial direction. It was obtained by the radiant heating system, which is specifically designed for the purposes of this experimental research. Detailed analyses of the radiant heat flux produced by the quartz heating system and radiant absorption characteristics of the corrugated curved tubes could be found in our previous papers [27, 28].

3. Results

3.1. Non-isothermal pressure drop

The previous considerations [2] refer to the hydrodynamic characteristics of the flow in the in spirally coiled corrugated pipes under isothermal conditions. There are few studies in the literature that consider the influence of non-isothermal conditions on the pressure drop in curved pipes, as well as in pipes characterized by high values of relative roughness.

The influence of heat flux at the wall on the pressure drop in the spirally coiled corrugated pipe is shown in Figure 3. The dependence of the pressure drop ratio for diabatic and adiabatic conditions on the Re_{ave} number ($Re_{ave}=(Re_{inlet}+Re_{outlet})/2$) and the total absorbed radiation heat flux averaged over the exposed surface of the absorber is shown.

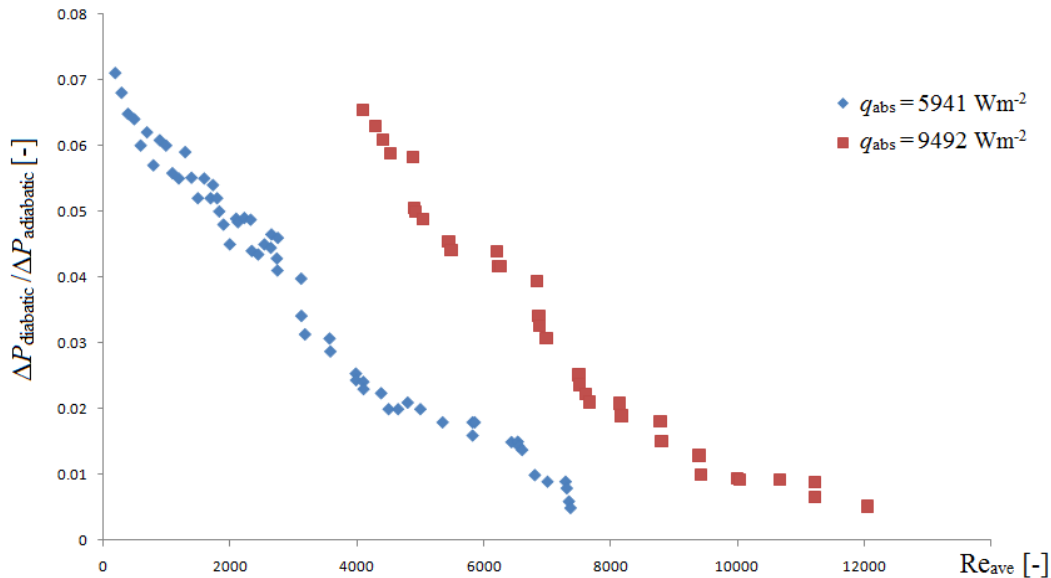


Figure 3. The effect of heat flux at the wall on the pressure drop in the spirally coiled corrugated pipe

Heat transfer causes the increase of the pressure drop in the considered flow geometry in all flow regimes. It could be noted that the largest increase occurs in the laminar region for the smallest values of the Re number. The ratio $\Delta P_{\text{diabatic}}/\Delta P_{\text{adiabatic}}$ decreases monotonically with increasing Re number for the same values of the heat flux density on the pipe wall. As the heat flux density on the wall increases, the pressure drop also increases.

The pressure drop increases due to the influence of the secondary flow caused by the buoyancy force, which changes the velocity field and thus affects the shear stress on the pipe wall. The effect of the buoyancy force contributes to the intensification of the secondary flow in relation to isothermal flow conditions in curved pipe, when the secondary flow is only under the influence of the centrifugal force. By intensifying the secondary flow, its kinetic energy also increases, which results in an increase in friction losses.

Heat transfer affects the friction factor, which increases with the amount of added heat, especially in the laminar region. The increase is due to buoyancy induced secondary flow that alters the velocity profile, which influences the shear stress at the pipe wall.

With the increase in the value of the heat flux density at the wall, the naturally convective flow becomes more intense, which causes additional resistance to the axial fluid flow. Consequently, with the increase in the heat flux density, the friction coefficient, i.e. the pressure drop, also increases. By exceeding a certain value of Re number, which is correlated with heat flux density at the wall, the flow becomes completely under the influence of the centrifugal force and it can be considered that there is no difference between the pressure drop for isothermal and non-isothermal conditions.

These findings are qualitatively in agreement with results in the literature [29, 30], but a quantitative comparison is lacking due to significant differences between the flow channel geometries and considered experimental conditions.

3.2. Effect of wall heat flux on heat transfer

The influence of the intensity of the heat flux density at the outer wall of the tube on the heat transfer, i.e. the value of Nu number, is very difficult to estimate for the given experimental conditions. The reason is very small differences in the experimental values of peripherally averaged Nu numbers, which are within the uncertainty limits of the experimentally determined Nu numbers (up to 3.85% [11]). The peripherally averaged Nu number increases with increasing the heat flux density at the wall, approximately 3% at the beginning of the test range ($Re \approx 200$) and approximately 1% at the end of the laminar range ($Re \approx 1,300$). Based on the experimental data, it is not possible to determine any influence of the intensity of the heat flux density at the wall on the Nu number in the transitional and turbulent region. The reason for this is not only the obvious reduction of the influence of heat flux density on heat transfer with increasing Re number, but also the inherent oscillation of the experimentally determined Nu numbers with flow intensification. There are few studies in the literature that have considered this aspect, and the results are rather speculative.

The influence of operating conditions outside the experimental range was additionally investigated by numerical simulations [31] in order to assess the influence of the intensity of the radiation heat flux density on the Nu number. The values of Nu number were compared for two different operating conditions, where the distributions of the heat flux density of incident thermal radiation on the outer wall of the absorber are proportional to each other. The first case corresponds to experimental conditions when the average value of absorbed radiation heat flux per exposed absorber surface is $9,492 \text{ Wm}^{-2}$, while the second case corresponds to conditions when the average value of absorbed radiation heat flux per exposed absorber surface is 6.36 times higher, i.e. when the mean value of the heat flux density of incident thermal radiation in the plane of the absorber is approximately $100,000 \text{ Wm}^{-2}$.

In order to evaluate the influence of wall heat flux density, the ratio of the peripherally averaged Nu numbers at higher and lower radiation heat flux density Nu_{II}/Nu_I was formed. Its dependance on the Re number and curve ratio δ are shown in Figures 4 and 5. Two curvature ratio values were chosen to make the data comparable: $\delta=0.033$ (5th coil turn) and $\delta=0.102$ (12th coil turn).

The results shown in Figure 4 represent the increase in the peripherally averaged Nu number for a mixture of propylene glycol and water (90% and 10% by volume, respectively) in laminar and transitional flow regimes, while Figure 5 shows the corresponding results for water in the turbulent region.

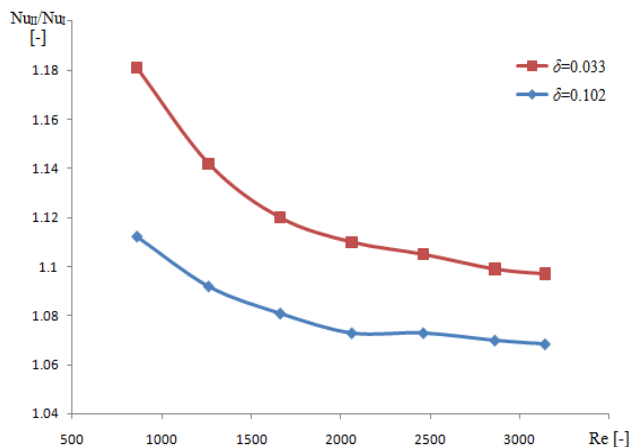


Figure 4. The influence of wall heat flux density on the peripherally averaged Nu number - laminar and transitional flow regimes

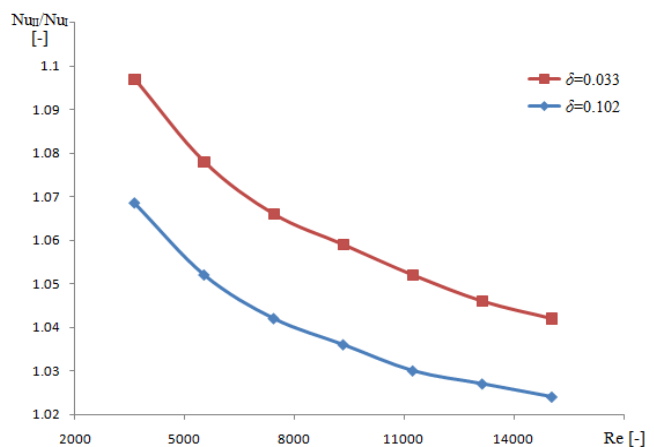


Figure 5. The influence of wall heat flux density on the peripherally averaged Nu number - turbulent flow regime

An increase in the intensity of the heat flux density at the wall affects the increase of the peripherally averaged Nu number in the considered geometry in all flow regimes. It was observed that the influence is greatest in the laminar region for the smallest values of Re number and curvature ratio δ . The Nu_{II}/Nu_I ratio monotonically decreases with increasing Re number.

The increase in the peripherally averaged Nu number is a consequence of the influence of the secondary flow caused by the effect of the buoyancy force, i.e. the intensification of the natural convective circulation and the change in the viscosity of the fluid within the boundary layer with the increase in the temperature gradient near the wall. The large heat flux at the wall increases temperature of fluid in the near wall region and significantly decreases the viscosity of fluid along the axial direction. The change in viscosity causes redevelopment of the hydrodynamic and thermal boundary layer, resulting in the formation of the region where the local heat transfer coefficient increases.

The effect of the secondary flow caused by the buoyancy force generally weakens with increasing Re number and curvature ratio δ . Increasing the curvature ratio δ affects the complex superposition of the secondary flows because the centrifugal force dampens the influence of the buoyancy force. On the other hand, by increasing the Re number and the curvature ratio δ , that is, the De number, the vortex flow inside the corrugations intensifies, which additionally suppresses the natural convective circulation.

4. Conclusion

Heat transfer affects the pressure drop increase in the considered geometry in all flow regimes. The influence is the most pronounced in the laminar region and ratio $\Delta P_{\text{diabatic}} / \Delta P_{\text{adiabatic}}$ decreases monotonically with increasing Re number for the same heat flux density at the pipe wall.

As the heat flux density at the wall increases, so does the pressure drop. For a certain value of the heat flux density at the wall, the value of the Re number can be determined, beyond which the secondary flow is completely under the influence of the centrifugal force and when there is almost no difference between pressure drop for isothermal and non-isothermal conditions.

An increase in the heat flux density at pipe wall affects the increase in the peripherally averaged Nu number in the considered geometry in all flow regimes. The influence is the most noticeable in the laminar region for the smallest values of Re number and curvature ratio δ and monotonically decreases with increasing Re number. The effect of the buoyancy force becomes negligible compared to the effect of the centrifugal force in the considered flow geometry even in the laminar flow regime for higher values of the Re number.

These observations are qualitatively in agreement with results in the literature, but a quantitative comparison is lacking due to significant differences between the considered geometries and experimental conditions.

It can be concluded that with the increase in the heat load at the wall of the considered flow channel geometry, both the pressure drop and the heat transfer increase, but the intensification of the heat transfer is less compared to the increase in the pressure drop.

Acknowledgements

The authors would like to thank the Ministry of Science, Technological Development and Innovation of the Republic of Serbia for funding the scientific research work, contract no. 451-03-65/2024-03/200155, realized by the Faculty of Technical Sciences in Kosovska Mitrovica, University of Pristina.

References

- [1] Ali, S., Seshadri, C., Pressure Drop in Archimedean Spiral Tubes, *Industrial and Engineering Chemistry Process Design and Development*, 10 (1971), 3, pp. 328-332
- [2] Djordjević, M., Stefanović, V., Mančić, M., Pressure Drop and Stability of Flow in Archimedean Spiral Tube with Transverse Corrugations, *Thermal Science*, 20 (2016), 2, pp. 579-591
- [3] Morton, B. R., Laminar Convection in Uniformly Heated Horizontal Pipes at Low Rayleigh Numbers, *Quarterly Journal of Mechanics and Applied Mathematics*, 12 (1959), 4, pp. 410-420
- [4] Mori, Y., *et al.*, Forced Convective Heat Transfer in Uniformly Heated Horizontal Tubes, *International Journal of Heat and Mass Transfer*, 9 (1965), 5, pp. 453-463
- [5] Naphon, P., Wongwises, S., An Experimental Study on the In-tube Convective Heat Transfer Coefficients in a Spiral Coil Heat Exchanger, *International Communications in Heat and Mass Transfer*, 29 (2002), 6, pp. 797-809
- [6] Naphon, P., Suwagrai, J., Effect of Curvature Ratios on the Heat Transfer and Flow Developments in the Horizontal Spirally Coiled Tubes, *International Journal of Heat and Mass Transfer*, 50 (2007), 3, pp. 444-451
- [7] Rajavel, R., Saravanan, K., Heat Transfer Studies on Spiral Plate Heat Exchanger, *Thermal Science*, 12 (2008), 3, pp. 85-90
- [8] Khan, M. K., *et al.*, Experimental Investigation on Diabatic Flow of R-134a through Spiral Capillary Tube, *International Journal of Refrigeration*, 32 (2009), 2, pp. 261-271
- [9] Balakrishnan, R *et al.*, Heat Transfer Correlation for a Refrigerant Mixture in a Vertical Helical Coil Evaporator, *Thermal Science*, 13 (2009), 4, pp. 197-206
- [10] Naphon, P., Study on the Heat Transfer and Flow Characteristics in a Spiral-Coil Tube, *International Communications in Heat and Mass Transfer*, 38 (2011), 1, pp. 69-74
- [11] Djordjević, M., Stefanović, V., Vukić, M., Mančić, M., Experimental Investigation of the Convective Heat Transfer in a Spirally Coiled Corrugated Tube with Radiant Heating, *FACTA UNIVERSITATIS Series: Mechanical Engineering*, 15 (2017), 3, pp. 495-506
- [12] Đorđević, M., Mančić, M., Stefanović, V., Vukić, M., Experimental Characterization of Heat Transfer in Coiled Corrugated Tubes, *Proceedings, 20th Conference on Thermal Science and Engineering of Serbia - SimTerm2022*, Niš, Serbia, October 18-21, 2022, pp. 407-416
- [13] Nakayama, A., *et al.*, Conjugate Numerical Model for Cooling a Fluid Flowing through a Spiral Coil Immersed in a Chilled Water Container, *Numerical Heat Transfer, Part A*, 37 (2000), 2, pp. 155-165

- [14] Bowman, A., Park, H., CFD Study on Laminar Flow Pressure Drop and Heat Transfer Characteristics in Toroidal and Spiral Coil System, *Proceedings, ASME 2004 International Mechanical Engineering Congress and Exposition*, Anaheim, Cal., USA, 2004
- [15] Naphon, P., Study on the Heat Transfer and Flow Characteristics in a Spiral-Coil Tube, *International Communications in Heat and Mass Transfer*, 38 (2011), 1, pp. 69-74
- [16] Sasmito, A. P., *et al.*, Numerical Evaluation of Laminar Heat Transfer Enhancement in Nanofluid Flow in Coiled Square Tubes, *Nanoscale Research Letters*, 6 (2011), 1, pp. 376-385
- [17] Kurnia, J. C., *et al.*, Numerical Investigation of Laminar Heat Transfer Performance of Various Cooling Channel Designs, *Applied Thermal Engineering*, 31 (2011), 6, pp. 1293-1304
- [18] Sasmito, A. P., *et al.*, Numerical Analysis of Laminar Heat Transfer Performance of In-plane Spiral Ducts with Various Cross-Sections at Fixed Cross-Section Area, *International Journal of Heat and Mass Transfer*, 55 (2012), 21, pp. 5882-5890
- [19] Kurnia, J. C., *et al.*, Laminar Convective Heat Transfer for In-Plane Spiral Coils of Non-Circular Cross-Sections Ducts: A computational fluid dynamics study, *Thermal Science*, 16 (2012), 1, pp. 107-116
- [20] Yoo, G., *et al.*, Fluid Flow and Heat Transfer of Spiral Coiled Tube: Effect of Reynolds Number and Curvature Ratio, *Journal of Central South University*, 19 (2012), 2, pp. 471-476
- [21] Altac, Z., Altun, O., Hydrodynamically and Thermally Developing Laminar Flow in Spiral Coil Tubes, *International Journal of Thermal Sciences*, 77 (2014), pp. 96-107
- [22] Djordjević, M., Stefanović, V., Vukić, M., Mančić, M., Numerical Investigation On the Convective Heat Transfer in a Spiral Coil with Radiant Heating, *Thermal Science*, 20 (2016), Suppl. 5, pp. S1215-S1226
- [23] Jia-dong, J., *et al.*, Numerical Investigation of Flow and Heat Transfer Performances of Horizontal Spiral-Coil Pipes, *Journal of Hydrodynamic*, 28 (2016), 4, pp. 576-584
- [24] Doshmanziari, F. I., *et al.*, Experimental and Numerical Study of Turbulent Fluid Flow and Heat Transfer of Al₂O₃/Water Nanofluid in a Spiral-Coil Tube, *Heat Transfer Engineering*, 38 (2017), 6, pp. 611-626
- [25] Naphon, P., *et al.*, Numerical Study on the Nanofluid Flows and Temperature Behaviors in the Spirally Coiled Tubes with Helical Ribs, *Case Studies in Thermal Engineering*, 27 (2021), 101204
- [26] ***, Pliable Corrugated Stainless Steel Resistant to Corrosion CSST Tubes for Plumbing, Heating Systems and Thermal Solar Plants, Eurotis S.l.r., Italy, <http://www.eurotis.it>.
- [27] Đorđević, M., Stefanović, V., Pavlović, S., Mančić, M., 2015, Numerical Analyses of the Radiant Heat Flux Produced by Quartz Heating System, *Proceedings, 3rd International Conference Mechanical Engineering in XXI Century*, Niš, Serbia, September 17-18, 2015, pp. 75-80
- [28] Đorđević, M., Stefanović, V., Kalaba, D., Mančić, M., Katinić, M., Radiant Absorption Characteristics of Corrugated Curved Tubes, *Thermal Science*, 21 (2017), pp. 2897-2906
- [29] Nunner W., Wärmeübergang und Druckabfall in rauhen Röhren (Heat transfer and pressure drop in rough tubes), Ph.D. thesis, *University Hannover*, Hannover, Germany, 1956
- [30] Tam, L., Ghajar, A. J., Effect of Inlet Geometry and Heating on Fully Developed Friction Factor in the Transition Region of a Horizontal Tube, *Experimental Thermal Fluid Science*, 15 (1997), pp. 52-64
- [31] Đorđević, M., Mančić, M., Stefanović, V., Numerical Investigation of the Convective Heat Transfer in Spirally Coiled Corrugated Pipes, *Proceedings, 19th Conference on Thermal Science and Engineering of Serbia - SimTerm 2019*, Sokobanja, Serbia, October 22–25, 2019, pp. 592-600

Results of the Temperature Variation in Experimental Research of the Kolubara Lignite Drying Process in Fluidized Bed

Milić D. Erić, Zoran Marković^b, Danka Kostadinović^c, Rastko Jovanović^d, Ivan Lazović^e and Mihajlo Gigov^f

^a*Vinca Institute of Nuclear Sciences – National Institute of the Republic of Serbia - University of Belgrade, RS, milic@vinca.rs*

^b*Vinca Institute of Nuclear Sciences – National Institute of the Republic of Serbia - University of Belgrade, RS, zoda_mark@vinca.rs*

^c*Vinca Institute of Nuclear Sciences – National Institute of the Republic of Serbia - University of Belgrade, RS, dankak@vinca.rs*

^d*Vinca Institute of Nuclear Sciences – National Institute of the Republic of Serbia - University of Belgrade, RS, virrast@vinca.rs*

^e*Vinca Institute of Nuclear Sciences – National Institute of the Republic of Serbia - University of Belgrade, RS, ivan.lazovic@vinca.rs*

^f*AMG Chemtech Solutions, Belgrade, RS, mihajlo.gigov@amgchemtech.rs*

Abstract: Of all the fossil fuels in the world, the largest coal reserves are the most evenly distributed, and their mass exploitation ensures a stable and relatively low price on the international market, but coal contributes significantly to total greenhouse gas emissions. Reducing carbon dioxide emissions by increasing the energy efficiency of converting fossil fuels, especially coal, into electricity is known as Clean Coal Technologies. Particular attention is paid to low-grade coals with high moisture content, including lignite, which has significant reserves worldwide. Against this background, intensive efforts are being carried out to increase the energy efficiency of electricity generation from low-grade coal with high moisture content in the thermal plant by developing and introducing the process of pre-drying using the thermal energy available in the thermal plant. The drying process was investigated under fluidized bed conditions. Experimental investigations of the drying process in the fluidized bed were carried out at two different fluidization velocities and three different air temperatures measured at the front of the sample. The experimental results obtained and the influence of the above parameter values show that the drying rate of the sample increases with increasing temperature, while the drying time of the sample decreases.

Keywords: Convective drying, Temperature, Lignite, Moisture, Fluidized bed.

1. Introduction

Lignite from the Kolubara and Kostolac open-pit mines will remain the most important source of energy in Serbian power plants in the future, mainly because it is the most abundant and cheapest fossil fuel and lignite from Kolubara is the most commonly used coal in the Republic of Serbia. Kolubara lignite is the most commonly used coal in the Republic of Serbia. It is a low-quality coal with a moisture content between 45 and 52%, which reduces the friability of the coal and has a negative impact on the quality of grinding and pneumatic transportation of pulverized coal. A lower moisture content in the coal leads to a higher efficiency of the power plant, a lower need for ash disposal and lower pollutant emissions [1].

It is well known that conventional convective evaporative drying involves complex transport phenomena consisting of three successive processes. The first is the movement of moisture (in liquid phase) in solids, which occurs from the moist interior to the gas-solid interface (internal pores, particle surface, etc.). This process is slower for larger solids and/or materials with low moisture content. The second process is evaporation, which is facilitated by heat (energy) that is either supplied from the outside or extracted from the solid and used to convert liquid to vapor. The last process is the movement of the vapor into the surrounding gas by diffusion and convection. The slowest of these processes determines the overall drying rate ([4-5] etc.).

Prediction of falling-rate drying kinetics by theory alone is very difficult. Thus, accurate small-scale experiments are required instead. It is possible to estimate drying rates under different conditions by applying concepts such as the "characteristic drying curve" or the "drying coefficient".

At the Vinca Institute of Nuclear Sciences, Laboratory for Thermal Engineering and Energy, a series of experiments were carried out in the field of convective drying. After the first step, drying in a packed bed, the research was continued with drying in a fluidized bed, which has a much wider range of applications.

Drying in a fluidized bed allows intensive contact of the gas required to achieve the fluidization state (heated air, flue gases or steam) with the particles of the material to be dried, whereby the gas flow must be sufficient to achieve the fluidization state (overcoming the weight of the particles and transferring the particles to the suspended state).

2. Experimental work

The experimental studies on the convective drying process in the fluidized bed of Kolubara lignite had the following objectives:

- determination of the drying kinetics curve of Kolubara lignite,
- analyse the drying process and the influence of the drying agent (hot air),
- determination of the influence of the parameters of the drying agent (temperature),
- determination of the influence of the particle size of the material,
- validation of the mathematical model.

The decrease in moisture content of the Kolubara lignite samples was determined by measuring the air mass flow balance at the dryer inlet and the dryer outlet. The following measured parameters were used for the calculations described above: Volume flow rate at the inlet, temperature and relative humidity of the air at the inlet and outlet of the experimental apparatus.

The drying experiments with Kolubara lignite samples in the fluidized bed were carried out using the Sherwood Tornado M501 fluidized bed dryer with a 5-litre sample container, Figure 1.

The basic elements of the device are: a fan, an air heater, a thermocouple for temperature measurement, a glass container with a plastic housing, a probe for measuring humidity and temperature and a control unit. The control unit is used to regulate the air flow and the air temperature upstream of the sample and to set the test duration. It can be used as a stand-alone device or connected to a computer using the Fluid Bed Drier Controller software. The software enables the test sequence to be controlled, the data to be monitored and all relevant measurement parameters to be recorded. The following parameters were recorded at the output of the test device: fan load, air temperature upstream of the sample and air temperature and relative humidity at the probe location.

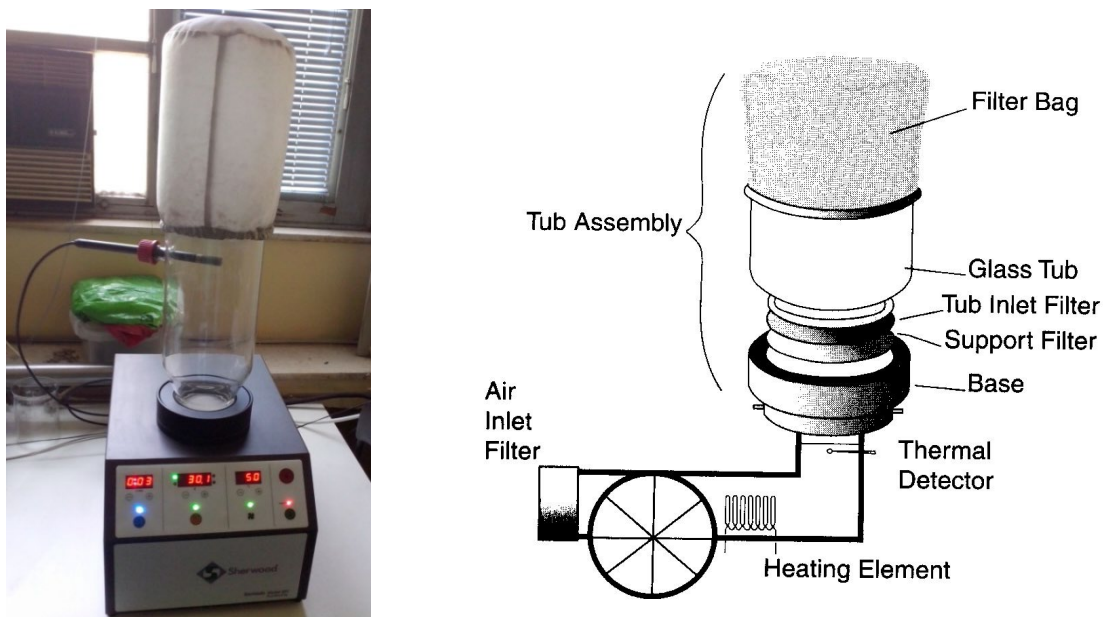


Figure 1. Sherwood Tornado M501 dryer [6]

The experimental apparatus was upgraded with additional equipment for measuring the air flow, Figure 2. The orifice plate with suction tube is installed at the device inlet and complies with the standards SRPS EN ISO

5167-1: 2012 and SRPS EN ISO 5167-2: 2012 "Measurement of fluid flow by means of pressure differential devices inserted in circular cross-section conduits running full", Part 1: "General Principles and Requirements" and Part 2: "Orifice plates".



Figure 2. Dryer Sherwood Tornado M501 with built-in orifice plate [1]

The measuring accuracy of the orifice plate was checked as follows. The accuracy measurement of the volume flow with the orifice plate method was carried out simultaneously with the measurement of the volume flow with a hot-wire anemometer. The probe for measuring the flow rate with a head with an inner diameter of 7 mm was placed on the stand. Due to the small inner diameter of the inlet nozzle of 55 mm, the measurements were carried out with the orifice plate in the center of the cross-section, in accordance with the SRPS ISO 10780: 2010 standard "Measurement of velocity and volume flow rate of gas streams in ducts". Control measurements were carried out at the flow inlet of the device using a hot-wire anemometer. The results obtained were in good agreement. The results of the volume flow rate measurements with orifice and anemometer differed by less than 5 % at five different fan loads: 20 %, 40 %, 60 %, 80 % and 100 %.

The duration of the drying process had to be determined experimentally, as the drying of the coal to a moisture content of zero is very different for the two following methods:

- use of the air mass flow scale at the inlet and outlet of the dryer,
- measuring the mass of the coal sample on the scale immediately before and after the drying process.

The greatest agreement between the results obtained with these two methods was achieved when the sample was dried from the initial moisture content to the equilibrium moisture content of the sample. It was assumed that the experiment was successful if the difference in the amount of moisture removed from the sample by the two methods was less than 2%.

3. The basic properties of the coal sample

For the drying process in the fluidized bed test, the most commonly used domestic lignite from the Kolubara opencast mine (referred to in the following text as Kolubara lignite) was selected, which has a relatively low calorific value and a very high moisture content..

The samples of Kolubara lignite were collected in the bunkers of units A1, A2 and B1 of the Nikola Tesla thermal power plant in Obrenovac [7-10]. The basic properties of the collected coal samples are listed in Table 1. The collected coal samples were ground to a fine grain size suitable for the drying process.

The moisture content of the samples was determined in the laboratory immediately after opening each sample container before the experiments were conducted with the selected coal particle size (grain size). The coal sample was dried in a Binder ED-53 drying oven at 105°C. The mass of the coal sample was measured before

and after the drying process in the drying oven on the Mettler AE200-S analytical balance with a working range of 0-205 g and an accuracy of 0.0001 g. Both instruments were calibrated regularly. Both devices were calibrated regularly. Both devices were calibrated regularly. Both devices were calibrated regularly.

Table 1. Basic characteristics of Kolubara lignite samples - raw coal parameter [1]

Unit	Carbon [%]	Hydrogen [%]	Oxygen [%]	Nitrogen [%]	Sulfur [%]	Ash [%]	Moisture [%]	LCV [kJ/kg]
A1	25.90 - 27.17	2.17 - 2.19	10.86 - 11.32	0.31 - 0.33	0.34 - 0.38	10.29 - 13.15	47.24 - 48.34	8776 - 9343
A2	19.40 - 22.78	1.75 - 1.99	8.54 - 9.74	0.27 - 0.30	0.27 - 0.30	17.02 - 18.37	47.87 - 51.39	7635 - 6167
A2II	20.89 - 23.37	1.86 - 2.01	9.38 - 9.72	0.28 - 0.30	0.30 - 0.35	15.06 - 17.38	49.19 - 49.91	6789 - 7203
B1	23.86	2.08	9.31	0.81	0.14	13.86	49.94	7861

4. Results of the experimental research

The drying process in the fluidized bed of Kolubara lignite samples was investigated for three different coal samples with mean particle diameters: 1.5 mm, 2.57 mm and 3.95 mm and three different air temperatures before the sample: 60°C, 90°C and 120°C. The minimum fluidization velocity was determined for all three sample sizes and all three air temperatures upstream of the sample. The determined values of the velocity parameter were in the following range: 0.63 m/s - 1.60 m/s, Table 2. This parameter is of utmost importance for the correct selection of the air flow size and for determining the required blower load for the drying process in the fluidized bed.

Table 2. Minimum fluidization velocity $v_{G,mf}$ for different air temperatures [1]

Air temperature $T_{G,in} = 60^\circ\text{C}$		
$d_s = 1,50 \text{ mm}$	$d_s = 2,57 \text{ mm}$	$d_s = 3,95 \text{ mm}$
$v_{G,mf} = 0,63 - 0,73 \text{ m/s}$	$v_{G,mf} = 0,99 - 1,13 \text{ m/s}$	$v_{G,mf} = 1,32 - 1,50 \text{ m/s}$
Air temperature $T_{G,in} = 90^\circ\text{C}$		
$d_s = 1,50 \text{ mm}$	$d_s = 2,57 \text{ mm}$	$d_s = 3,95 \text{ mm}$
$v_{G,mf} = 0,63 - 0,74 \text{ m/s}$	$v_{G,mf} = 1,01 - 1,16 \text{ m/s}$	$v_{G,mf} = 1,36 - 1,55 \text{ m/s}$
Air temperature $T_{G,in} = 120^\circ\text{C}$		
$d_s = 1,50 \text{ mm}$	$d_s = 2,57 \text{ mm}$	$d_s = 3,95 \text{ mm}$
$v_{G,mf} = 0,63 - 0,75 \text{ m/s}$	$v_{G,mf} = 1,03 - 1,19 \text{ m/s}$	$v_{G,mf} = 1,40 - 1,60 \text{ m/s}$

The results of the experimental investigation of the drying process of Kolubara lignite in the fluidized bed for different temperatures upstream of the sample, for the same sample masses and the three different sample particle sizes are shown in Figures 4-9, which show the drying curves of the tested sample. The results for coal drying in a fluidized bed at a fluidization rate slightly above the minimum are shown in Figures 4 to 6. For more intensive fluidization, where the air velocity in front of the sample is increased by about 50 %, the test results are shown in Figures 7 to 9.

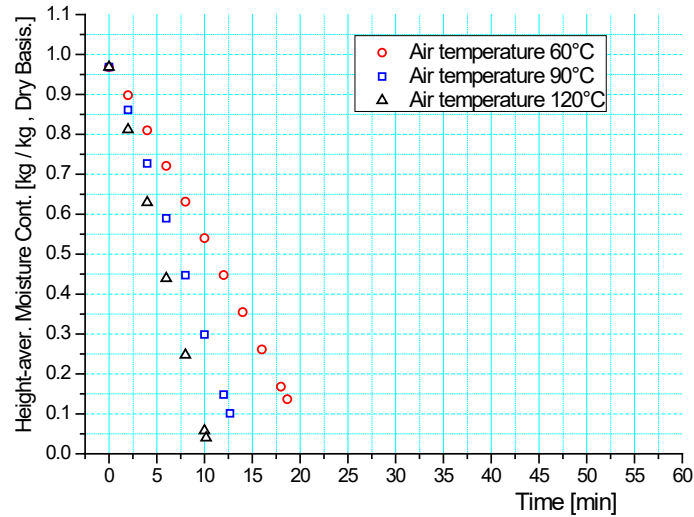


Figure 4. Experimentally determined kinetics of lignite drying in the fluidized bed;

$T_{G,in,30} = 60^{\circ}\text{C}$, $T_{G,in,31} = 90^{\circ}\text{C}$, $T_{G,in,32} = 120^{\circ}\text{C}$, $v_{G,in} = 1.3 \text{ m/s}$; $d_S = 1.50 \text{ mm}$, $m_{S0} = 210\text{g}$, $X_0 = 0.969$, $Y_0 = 0.007$

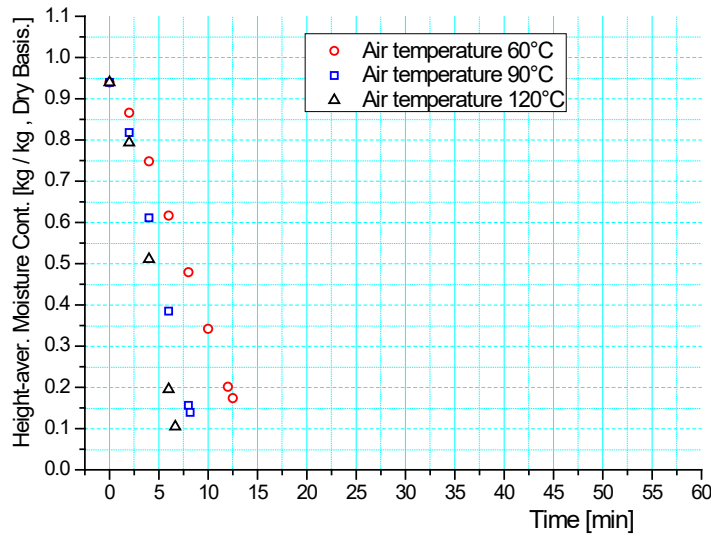


Figure 5. Experimentally determined kinetics of lignite drying in the fluidized bed;

$T_{G,in,42} = 60^{\circ}\text{C}$, $T_{G,in,43} = 90^{\circ}\text{C}$, $T_{G,in,44} = 120^{\circ}\text{C}$, $v_{G,in} = 2.0 \text{ m/s}$ $d_S = 2.57 \text{ mm}$, $m_{S0} = 210\text{g}$, $X_0 = 0.939$, $Y_0 = 0.009$

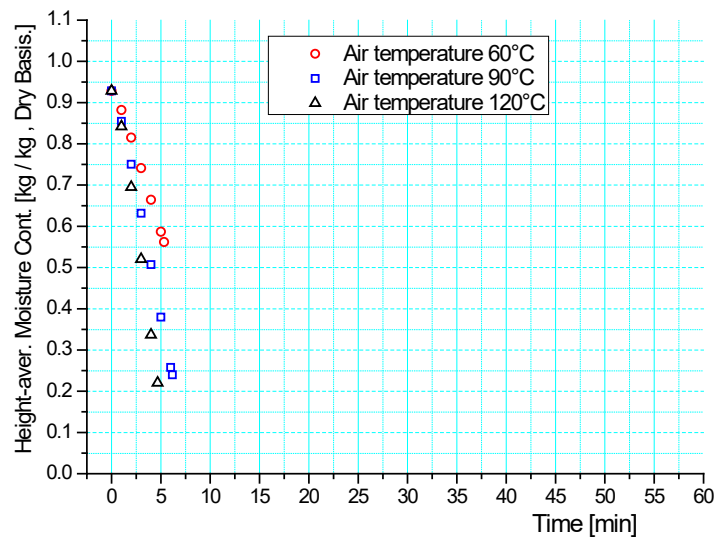


Figure 6. Experimentally determined kinetics of lignite drying in the fluidized bed;

$T_{G,in,53} = 60^{\circ}\text{C}$, $T_{G,in,52} = 90^{\circ}\text{C}$, $T_{G,in,54} = 120^{\circ}\text{C}$, $v_{G,in} = 2.1 \text{ m/s}$ $d_S = 3.95 \text{ mm}$, $m_{S0} = 210\text{g}$, $X_0 = 80.928$, $Y_0 = 0.008$

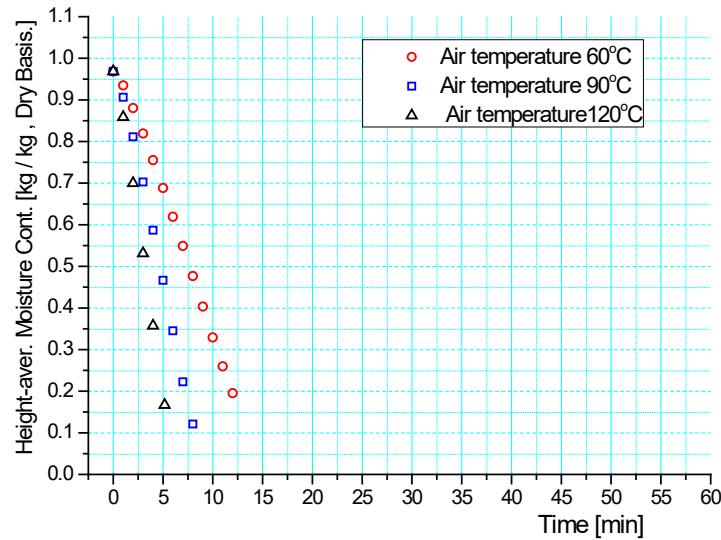


Figure 7. Experimentally determined kinetics of lignite drying in the fluidized bed;
 $T_{G,in,33} = 60^{\circ}\text{C}$, $T_{G,in,34} = 90^{\circ}\text{C}$, $T_{G,in,35} = 120^{\circ}\text{C}$, $v_{G,in} = 1.9 \text{ m/s}$ $d_S = 1.50 \text{ mm}$, $m_{S0} = 210\text{g}$, $X_0 = 0.969$, $Y_0 = 0.007$

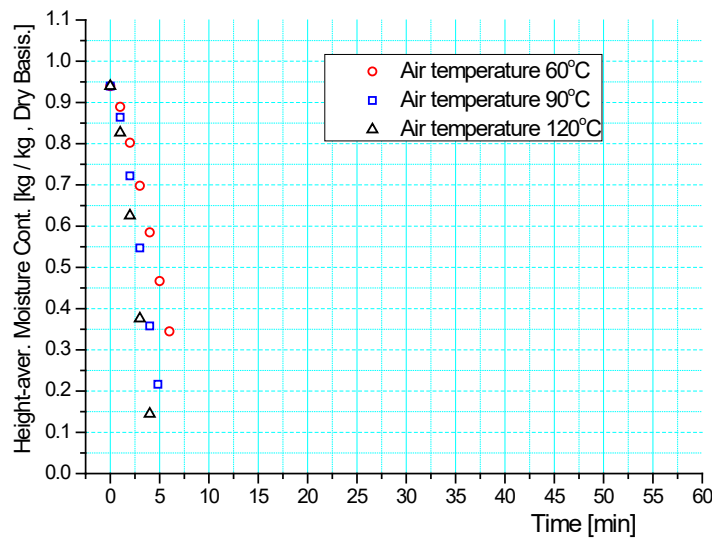


Figure 8. Experimentally determined kinetics of lignite drying in the fluidized bed;
 $T_{G,in,45} = 60^{\circ}\text{C}$, $T_{G,in,46} = 90^{\circ}\text{C}$, $T_{G,in,47} = 120^{\circ}\text{C}$, $v_{G,in} = 2.9 \text{ m/s}$ $d_S = 2.57 \text{ mm}$, $m_{S0} = 210\text{g}$, $X_0 = 0.939$, $Y_0 = 0.009$

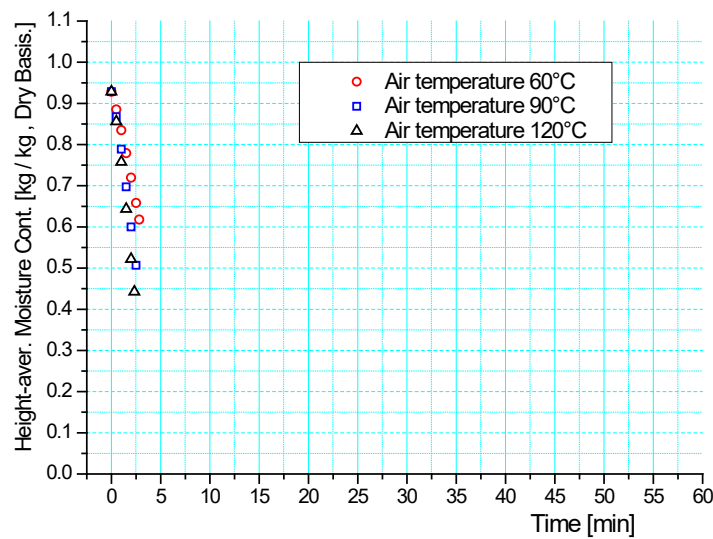


Figure 9. Experimentally determined kinetics of lignite drying in the fluidized bed;
 $T_{G,in,56} = 60^{\circ}\text{C}$, $T_{G,in,57} = 90^{\circ}\text{C}$, $T_{G,in,55} = 120^{\circ}\text{C}$, $v_{G,in} = 3.1 \text{ m/s}$ $d_S = 3.95 \text{ mm}$, $m_{S0} = 210\text{g}$, $X_0 = 0.928$, $Y_0 = 0.008$

6. Conclusions

The tests were carried out with the Sherwood 501 fluidized bed dryer for drying granular and powdered materials with air in a packed and fluidized bed, which is additionally equipped with devices for measuring the air flow rate, temperature and relative humidity at the inlet of the device, supplemented by automatic control and data logging. All measuring devices are calibrated in approved, accredited laboratories, where the accuracy of each measured parameter is determined. The control measurement of the air flow was carried out by parallel measurement with a standard orifice and a glow wire anemometer at the inlet of the device. In this way, all relevant parameters required to determine the change in average moisture content in the material during the drying tests were measured as accurately as possible.

The measurement and calculation of the change in absolute moisture of the material during the drying process based on the balance of the air mass flow at the inlet and outlet of the device was verified by direct measurement of the mass of the sample on a digital scale before and after each test.

It is obvious that the drying process is faster with smaller pieces of coal, as the resistance inside the particle is lower and the specific surface area of the material is larger, which leads to a more intensive transfer of moisture from the surface of the material to the ambient air. The influence of the particle size on the drying kinetics is not clearly recognisable in the Kolubara lignite fractions used in the tests. The reason for the minor influence of particle size on the drying process is to be found in the small fractions of lignite particles, which differ relatively little in size and whose mean equivalent diameters are as follows: 1.50 mm, 2.57 mm and 3.95 mm, which is due to the unequal particle size in the sample for the same fraction as well as their clearly irregular, mostly needle-like shape, so that one dimension of the particle is significantly larger than the other two. In addition, a smaller number of particles were fragmented during the drying process.

On the other hand, drying is faster at a higher temperature of the heated air, as the difference between the partial pressure of the water vapor (moisture) on the surface of the material and the partial pressure of the water vapor in the ambient air (humidity) is greater.

The influence of the temperature of the heated air can be observed well for all coal granulates for drying in the fluidized bed for both tested flows, i.e. the material dries much faster at a higher temperature of the heated air.

Looking at the drying kinetics curves of Kolubara lignite for three different air temperatures (60 °C, 90 °C and 120 °C), a similar character of the change in moisture content in the material can be observed, i.e. how the drying process of the coal is significantly faster with increasing air temperature.

The experiments were carried out up to a predefined moisture content of the material (on a dry basis) of about 0.2. Of course, coal can be dried to a final moisture content below this value, up to the equilibrium value of the moisture content, which depends on the parameters of the air used to dry the material. Drying the coal for longer to reach the equilibrium moisture content makes little sense from the point of view of the profitability of the entire process, including post-combustion. After the drying process, the coal is mixed with hot flue gases and ground in mills, where it dries further. It is then fed into the boiler in an air mixture with flue gases and water vapour at a temperature of 150 °C to 200 °C via the burners, where it losing an additional few percent of its moisture content.

Nomenclature

Latin symbols

- d – Mean particle diameter, in [mm].
 m – Sample mass, in [g].
 T – Temperature, in [°C].
 X Sample height-average moisture content, in [kg/kg, dry basis].
 Y Air height-average moisture content, in [kg/kg, dry basis].
 v – velocity [ms^{-1}].

Subscripts

- 0 – Initial.
 G – Gas (air).
 in – Inlet, in the front of.
 S Solid.

Acknowledgments

The research was funded by the Ministry of Science, Technological Development and Innovation of the Republic of Serbia (Contract Annex: 451-03-66/2024-03/200017). The authors are very grateful for the support of this work by the Joint Stock Company Elektroprivreda Srbije.

References

- [1] Milić Erić, DRYING PROCESSES OF LIGNITES WITH HIGHMOISTURE CONTENT IN PACKED AND FLUIDIZED BED, Doctoral Dissertation, University of Belgrade, Mechanical Faculty, Belgrade, 2016
- [2] van Meel, D.A., Adiabatic convection batch drying with recirculation of air, *Chemical Engineering Science*, 9(1958), pp. 36-44
- [3] Tsotsas, E., Measurement and modeling of intraparticle drying kinetics: A review, *Proceedings of the 8th International drying symposium (IDS '92)*, Montreal, 1992, pp. 17-41
- [4] Luikov, A.V., *Drying theory*, 1st ed., Energiya, Moscow, 1968 (in Russian)
- [5] Milojević, D., Stefanović, M., Convective drying of thin and deep beds of grain, *Chemical Engineering Communication*, 13 (1982), pp. 261-269
- [6] The Laboratory Fluid Bed Drier, Sherwood Scientific Limited, 1 The Paddocks Cherry Hinton Road, Cambridge, Issue 2, ECN 412, August 2006.
- [7] Erić M., Stefanović P., Marković Z., Dragan Živić, Željko Ilić, Reduction of Particulate Matter Emission by the Modernization of the Electrostatic Precipitators at Unit B1 of the TPP Kostolac B, *Proceedings of 17th Symposium on Thermal Science and Engineering of Serbia*, Sokobanja, Serbia, October 20–23, 2015, pp. 569 – 576, ISBN 978-86-6055-076-9
- [8] Stefanović P., Erić M., Marković Z., Particulate Emission Guarantee Test B of the Upgraded ESP at Unit B1 of TPP "Nikola Tesla", Technical report NIV LTE 548, Version 2.0, Institute of Nuclear Sciences "Vinča", Vinča, March 2014.
- [9] Erić M., Stefanović P., Marković Z., Periodic measurement of pollutants emissions in air at units A1, A2 and A3 of TPP "Nikola Tesla", Technical report NIV LTE 559, Institute of Nuclear Sciences "Vinča", Vinča, December 2014.
- [10] Erić M., Stefanović P., Marković Z., Periodic measurement of pollutants emissions in air at unit A2 of TPP "Nikola Tesla", second series of measurements, Technical report NIV LTE 560, Institute of Nuclear Sciences "Vinča", Vinča, December 2014.

Heat Transfer Effects on the EMHD Flow of Ternary Hibrid Nanoluid in the Channel with Porous Medium

Milica Nikodijević Đorđević^a, Jelena Petrović^b, Miloš Kocić^c, Živojin Stamenković^d

^aFaculty of Occupational Safety, Niš, RS, milica.nikodijevic@zrnfak.ni.ac.rs,

^bFaculty of Mechanical Engineering, Niš, RS, jelena.nikodijevic.petrovic@masfak.ni.ac.rs

^cFaculty of Mechanical Engineering, Niš, RS, milos.kocic@masfak.ni.ac.rs

^dFaculty of Mecanical Engineering, Niš, RS, zivojin.stamenkovic@masfak.ni.ac.rs

Abstract: EMHD flow and heat transfer of a ternary hybrid nanofluid is considered in this paper. The base fluid is blood with three types of nanoparticles suspended in it. Fluid flows in a horizontal channel with walls on different temperatures and its filled with porous medium. A homogeneous magnetic field acts perpendicular to the walls of the channel and a homogeneous electric field acts perpendicular to the direction of the magnetic field. The problem is considered in the induction-free approximation. The nanofluid velocity and temperature distributions, shear stresses and Nusselt numbers on the channel walls were determined. Some of the obtained results are presented graphically and tabularly.

Keywords: EMHD, Ternary hybrid nanofluid, Porous medium, Heat transport, Horizontal channel

1. Introduction

Convective heat transfer has significant applications in many industrial processes, as well as in biomedicine. That's why research is always present, the goal of which is to improve that process, and it is realized in different ways with more or less success. One way to realize these ideas is to improve the thermal conductivity of the working fluid. Since metals have a much higher thermal conductivity than fluids, the idea arose many years ago that the dispersion of metal particles in the fluid improves its thermal conductivity. However, only with the advancement of technology, Choi [1] was able to realize this idea, by dispersing nanometer-sized metal particles in a fluid and thus improving its conductivity and called this mixture a nanofluid. Since then, a large number of researchers have been dedicated to these fluids and their applications. Initially, one type of nanoparticles was dispersed in the fluid and these fluids are known as nanofluids (NF). It was later shown that better characteristics can be achieved by sputtering two types of nanoparticles and these fluids are known as chirid nanofluids (HNF). In recent years, fluids in which three types of nanoparticles are dispersed, which are known as three hydride nanofluids (THNF), have been investigated.

Many researchers indicate that heat transport of nanofluids in a porous medium in a magnetic environment is a relatively new area of research. A minimal number of fluid and nanofluid flow and heat transfer studies are cited here that sufficiently demonstrate how wide their distribution is. Lima et al. [2] investigated the magnetohydrodynamic (MHD) flow and heat transfer of two immiscible fluids in an inclined channel. They considered the effects of buoyancy, moving plates, layer porosity, tilted magnetic field, Joule and viscous dissipation, and heat generation/absorption. Raju and Satish [3] investigated the effect of slip on the electromagnetic hydrodynamic (EMHD) flow and heat transfer of two immiscible fluids in a horizontal channel including Hall currents. Nagavalli et al. [4] investigated the MHD flow of two immiscible, electrically conductive, incompressible fluids in a horizontal channel whose walls are horizontal plates. The canal walls are permeable. Hall currents are also taken into consideration. Unsteady MHD flow and heat transfer in a porous medium between two horizontal impermeable plates were investigated by Nikodijević et al. [5]. The applied magnetic field is inclined relative to the plates in the direction of the flow. Yadav et al. [6] investigated the effects of magnetic field and thermal radiation on entropy generation of immiscible micropolar and Newtonian fluids in a horizontal rectangular channel of a porous medium.

Manjeet and Sharma [7] investigated the MHD flow and heat transfer of an immiscible Newtonian and nanofluid (H₂O-Ag) in a horizontal channel with permeable walls. Umavathi and Oztop [8] performed a numerical simulation of EMHD flow and heat transfer of nanofluids in a vertical channel. The temperatures of

the channel walls are constant, but different. EMHD flow and heat transfer of immiscible Newtonian and nanofluids in horizontal and vertical channels of porous media, respectively, were investigated by Petrović et al. [9, 10]. The channel walls were maintained at constant, but different temperatures. Devi et al. [11] investigated the effect of different nanoparticles on unsteady MHD flow and heat transfer of two immiscible Newtonian and nanofluids in an inclined channel of porous medium and permeable walls. Petrović et al. [12] investigated the EMHD flow and heat transfer of Casson nanofluid Fe_3O_4 -blood in a porous medium between two horizontal plates that are at constant but different temperatures. A study on NF including the most commonly used nanoparticles (NPs), improving thermal conductivity, improving stability, their impact on health and the environment, their application in biomedicine, etc. was presented by Hamad et al. [13].

Atay et al. [14] experimentally investigated the thermal characteristics of an aluminum microchannel cooler with rectangular sections, and NF TiO_2 -water, Al_2O_3 -ode and HNF Al_2O_3/TiO_2 -water were used as coolants. Algehne et al. [15] investigated the flow and heat transfer of THNF ($TiO_2+MgO+CoFe_2O_4/EG$) along a horizontal stretchable plate for industrial and biomedical applications. MHD flow of Williamson THNF with thermal radiation in a porous medium over a horizontal stretchable plate was investigated by Riaz et al. [16]. The effect of thermal radiation and magnetic dipole on the MHD flow of water-based NF, HNF and THNF on a stretching sheet was investigated by Nasir et al. [17]. MHD flow and heat transfer of a water-based THNF along a vertical stretching plate with thermal radiation, viscous dissipation, and ioconvection were investigated by Revathi et al. [18]. Raza et al. [19] investigated the effects of NP size and shape on the MHD flow and heat transfer of a THNF ($Cu-Al_2O_3-TiO_2/H_2O$) between two rotating permeable parallel plates.

By reviewing the available research, the authors of this paper are convinced that the simultaneous effects of magnetic field, electric field, shear, Joule and Darcy dissipation on the flow of THNF, whose base fluid is blood, have not been sufficiently investigated. Therefore, in this work, EMHD flow and mixed convection of THNF($Al_2O_3MgO+ TiO_2/blood$) in a porous medium in a horizontal channel between two parallel stationary plates are investigated. The author's expectations are that this research will be applied later in biomedicine.

2. Mathematical formulation

In this paper, the flow of THNF in a porous medium whose permeability is K_0 is considered, and it is located in a channel between two horizontal plates that are at an interzonal distance h . The plates are impermeable, and their temperatures are constant and amount to T_{w1} on the top and T_{w2} on the bottom. The applied external magnetic field is homogeneous perpendicular to the plate, and its induction is B . The applied external electric field is homogeneous, of strength E and is perpendicular to the longitudinal vertical plane of the channel. The physical configuration of the described problem with the selected coordinate system is shown in Figure 1.

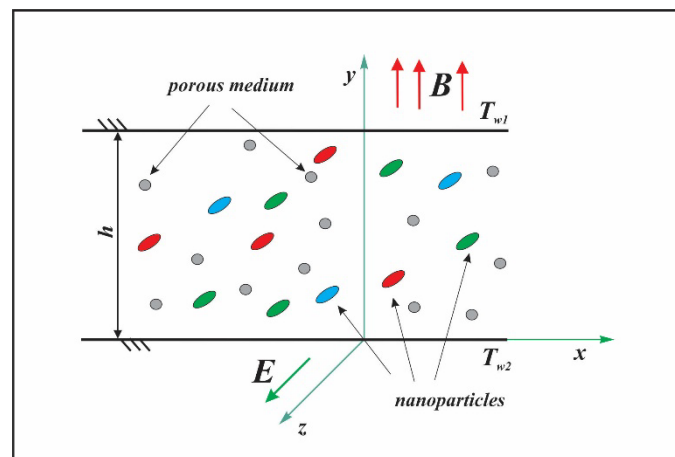


Figure 1

It is considered that the flow is stationary, laminar and fully developed, and the pressure gradient in the flow direction $\partial p/\partial X$ is constant. The problem is considered in the e-induction approximation, i.e. when the influence of the induced magnetic field can be neglected. The mathematical model of the described problem is described by the following equations and boundary conditions [7, 11]

$$-\frac{\partial p}{\partial X} + \mu \frac{\partial^2 U}{\partial Y^2} - \frac{\mu}{K_0} U - B\sigma(E + BU) = 0, \quad (1)$$

$$k \frac{d^2 T}{dY^2} + \mu \left(\frac{\partial U}{\partial Y} \right)^2 + \frac{\mu}{K_0} U^2 + \sigma(E + BU)^2 = 0, \quad (2)$$

$$(U, T)(0) = (0, T_{w_2}), (U, T)(h) = (0, T_{w_1}), \quad (3)$$

in which the usual symbols were used, namely: X, Y – Descartes' coordinates, p, U, T – pressure, flow rate, temperature of THNF, respectively and μ , δ and k – physical properties of THNF, i.e. coefficient of dynamic viscosity, coefficient electrical conductivity and thermal conductivity coefficient, respectively.

It is assumed that the physical properties of THNF are invariable and the following known relations are used for them [15]:

$$\begin{aligned} \mu &= \frac{\mu_f}{m}, m = [(1 - \Phi_1)(1 - \Phi_2)(1 - \Phi_3)]^{2.5}; \\ k &= \varphi_2 k_f, \varphi_2 = N(\Phi_3, k_3, k_f, \varphi_1), \varphi_1 = N(\Phi_2, k_2, k_f, \varphi_0), \\ \varphi_0 &= N(\Phi_1, k_1, k_f, 1), N(\Phi, S, R, M) = \frac{(1 + 2\Phi)S + 2(1 - \Phi)RM}{(1 - \Phi)S + (2 + \Phi)RM}; \\ \sigma &= \varphi_4 \sigma_f, \varphi_4 = N(\Phi_3, \sigma_3, \sigma_f, \varphi_3), \varphi_3 = N(\Phi_2, \sigma_2, \sigma_f, \varphi_0^*), \varphi_0^* = N(\Phi_1, \sigma_1, \sigma_f, 1). \end{aligned} \quad (4)$$

In the last relations, indices 1, 2 and 3 in the properties and volume fraction ϕ of nanoparticles refer to the material properties and volume fractions of nanoparticles 1 and 3.

For further analysis of the problem described here, it is convenient to introduce the following dimensionless quantities:

$$y = \frac{Y}{h}, u = \frac{U}{U_0}, \theta = \frac{T - T_{w_2}}{T_{w_1} - T_{w_2}} \quad (5)$$

in which U_0 is the characteristic velocity given by the relation:

$$U_0 = \frac{Ph^2}{\mu_f}, \quad (6)$$

where the label is introduced:

$$P = -\frac{\partial p}{\partial X} = const. \quad (7)$$

Using the introduced dimensionless quantities (5), equations (1), (2) and boundary conditions (3) are simply transformed to the following dimensionless equations and boundary conditions

$$\frac{d^2 u}{dy^2} - \omega^2 u = A, \quad (8)$$

$$\frac{d^2 \theta}{dy^2} = -\frac{Br}{m\varphi_2} \left[\left(\frac{du}{dy} \right)^2 + \omega^2 u^2 + Cu + D \right], \quad (9)$$

$$(u, \theta)(0) = (0, 0), (u, \theta)1 = (0, 1). \quad (10)$$

In the last equations and boundary conditions, for the sake of brevity, the following symbols were used:

$$\Lambda = \frac{h^2}{K_0}, Ha = Bh \sqrt{\frac{\sigma_f}{\mu_f}}, K = \frac{E}{BU_0}, \omega^2 = \Lambda + m\varphi_4 Ha^2, \quad (11)$$

$$A = m(K\varphi_4 Ha^2 - 1), C = 2m\varphi_4 Ha^2 K, D = \frac{1}{2}CK, Br = \frac{\mu_f}{k_f} \frac{U_0}{T_{w_1} - T_{w_2}}$$

where: Λ -porosity factor, Ha -Hartmann's number, K -factor of electrical load, Br - Brinkman's number.

3. Solution

For further analysis of the problem described here, equations (8) and (9) with boundary conditions (10) should be solved. These equations can be solved analytically using a known mathematical method for solving linear differential equations. First, equation (8) is solved and then using that solution, which represents the distribution of the dimensionless flow velocity THNF, the solution of equation (9), i.e. the distribution of the dimensionless temperature of this fluid, is also determined.

The solution of equation (8) is given by the relation:

$$u(y) = C_1 \exp(\omega y) + C_2 \exp(-\omega y) + F, \quad (12)$$

in which C_1 and C_2 are integration constants and the introduced notation is:

$$F = -\frac{A}{\omega^2}. \quad (13)$$

Using the boundary conditions (10) for the dimensionless velocity, it is obtained that the integration constants are given by the relations:

$$C_1 = E_1 [\exp(-\omega) - 1], C_2 = [1 - \exp(\omega)]. \quad (14)$$

where the label is used:

$$E_1 = \frac{F}{\exp(\omega) - \exp(-\omega)}. \quad (15)$$

By substituting relation (12) in equation (9) and solving that equation, it is obtained that its solution is given by the relation

$$\theta(y) = -\frac{Br}{m\varphi_2} [F_1 \exp(2\omega y) + F_2 \exp(-2\omega y) + R_1 \exp(\omega y) + R_2 \exp(-\omega y) + R_3 y^2 + C_3 y + C_4], \quad (16)$$

in which C_3 and C_4 are integration constants, and the symbols used are:

$$F_1 = \frac{1}{2}C_1^2, F_2 = \frac{1}{2}C_2^2, R_1 = RC_1, R_2 = RC_2, \quad (17)$$

$$R = \frac{1}{\omega^2}(C + 2\omega^2 F), R_3 = \frac{1}{2}(D + CF + \omega^2 F^2).$$

Using the boundary conditions (10) for the dimensionless temperature, it is obtained that the integration constants are given by the relations:

$$C_4 = -F_1 - F_2 - R_1 - R_2, \quad (18)$$

$$C_3 = -\frac{m\varphi_2}{Br} C_4 - R_3 - F_1 \exp(2\omega) - F_2 \exp(-2\omega) - R_1 \exp(\omega) - R_2 \exp(-\omega).$$

Thus, relations (12) and (16) represent, respectively, the distributions of dimensionless velocity and dimensionless temperature THNF in the observed channel.

The dimensionless shear stresses on the left and right channel walls are given, respectively, by the relations:

$$\tau_1 = \frac{\mu}{\mu_f} \left(\frac{du}{dy} \right)_{y=0} = \frac{\omega}{m} (C_1 - C_2), \quad (19)$$

$$\tau_2 = \frac{\mu}{\mu_f} \left(\frac{du}{dy} \right)_{y=1} = \frac{\omega}{m} [C_1 \exp(\omega) - C_2 \exp(-\omega)]. \quad (20)$$

The Nusselt numbers on the upper and lower channel walls, respectively, are represented by the relations:

$$N_{u_1} = \frac{k}{k_f} \left(\frac{d\theta}{dy} \right)_{y=0} = -\frac{Br}{m} [2\omega(F_1 - F_2) + \omega(R_1 - R_2) + C_3] \quad (21)$$

$$N_{u_2} = \frac{k}{k_f} \left(\frac{d\theta}{dy} \right)_{y=1} = -\frac{Br}{m} \{ 2\omega [F_1 \exp(2\omega) - F_2 \exp(-2\omega)] + \omega [R_1 \exp(\omega) - R_2 \exp(-\omega)] + 2R_3 + C_3 \} \quad (22)$$

4. Analysis of results

The results of dimensionless velocity and dimensionless temperature THNF, as well as dimensionless shear stresses and Nusselt numbers on channel walls, determined in the previous chapter, depend on the introduced physical factors that are significant for flow and heat transfer in the problem considered here. Therefore, they have generality because they refer to any THNF, not just one specific one, as well as to channels of different porosities that are in the environment of different magnetic and electric fields. They can be used for any THNF as well as for cases of different porosity of the channel medium and different magnetic and electric fields.

In this chapter, the flow and heat transfer of THNF whose base fluid is blood and nanoparticles are aluminum oxide (Al₂O₃), magnesium oxide (MgO) and titanium dioxide (TiO₂) are considered. The physical properties of the blood and nanoparticle materials used here are given in Table 1.

Part of the results obtained here for the distributions of dimensionless velocity and dimensionless temperature are given in the following figures, for several values of the introduced physical factors, in the form of graphs. Part of the results for dimensionless vertical shears on channel walls and Nusselt numbers on them are given in Table 1.

Table 1. Physical properties

Supstance properties	blood	Al ₂ O ₃	TiO ₂	MgO
$\rho(kg / m^3)$	997.1	3970	4250	3560
$c_p(J / (kgK))$	4179	765,	686.2	955
$K(W / (Km))$	0.613	40	8.9538	45
$\sigma(S / m)$	5.5×10^{-6}	35×10^6	2.6×10^6	5.392×10^{-7}
$\mu(Pas)$	0.001	-	-	-

Here the results are given for the values of the parameters Br=0.3, Ha=, K= -1, $\Lambda=$, $\phi_1= \phi_2= \phi_3=0.01$ and the value of the parameter whose influence is analyzed is changed.

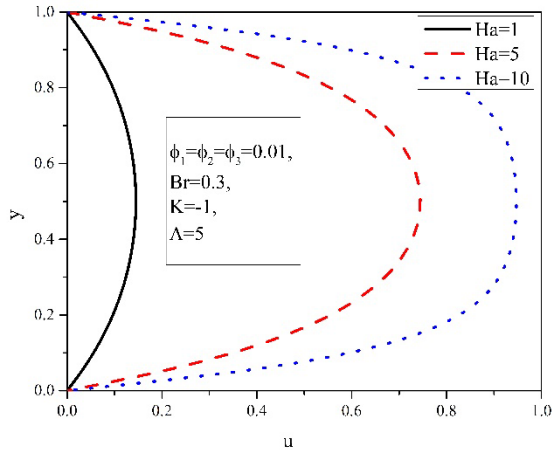


Fig. 2 Velocity distributions for different Ha values

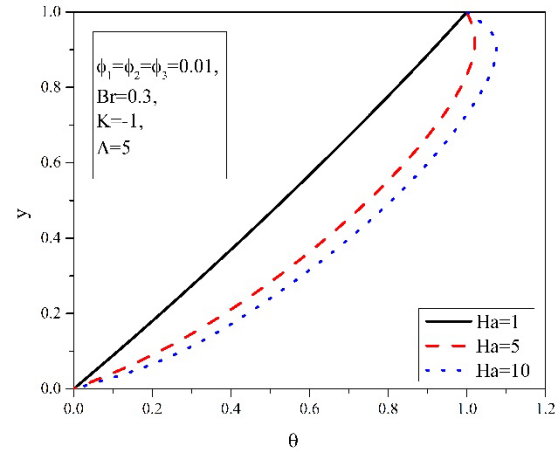


Fig. 3 Temperature distributions for different Ha values

Fig. 2 and Fig. 3 show distributions of speed and temperature of THNF in the channel for different values of the Ha number, respectively. Fig. 2 shows that an increase in the value of Hartmann's number increases the speed of fluid flow in the channel. The reason for this increase in speed is the increase in the intensity of the Lorentz force, which, in this case, is the driving force. The velocity distributions are symmetrical with respect to the horizontal plane of the middle of the channel. Fig. 3 shows that an increase in the value of the Ha number leads to an increase in the temperature of the fluid in the channel. This particle is physically explained by the increase in Joule's heat. For values of $Ha=1$, heat transfer is mainly by conduction. For the values of $Ha=5$ and $Ha=10$, the heat transfer is from the fluid to the upper channel wall.

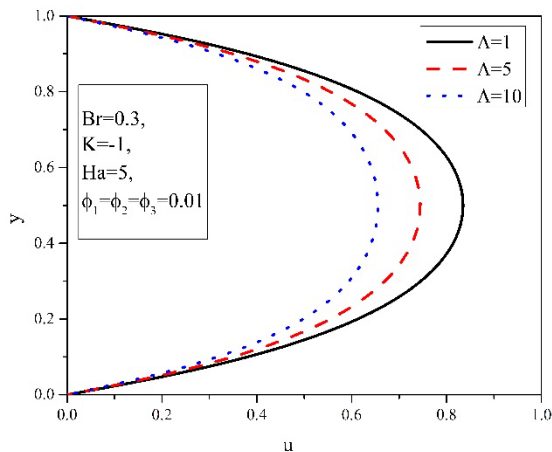


Fig. 4 Velocity distributions for different Λ values

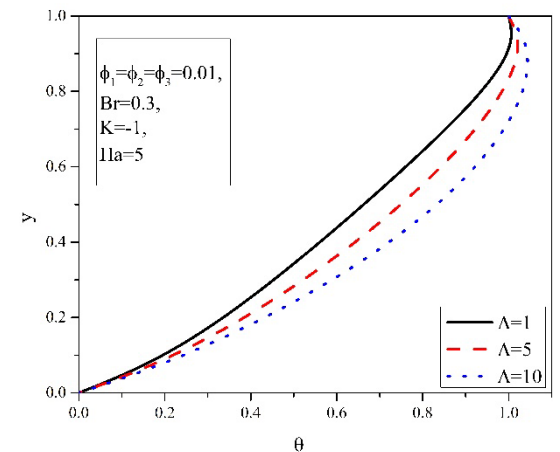


Fig. 5 Temperature distributions for different Λ values

In fig. 4 and 5 graphs of the distribution of fluid velocity and temperature in the channel for different values of the porosity factor (Λ), respectively, are given. It can be seen from Fig. 4 that higher values of Λ correspond to lower fluid flow speeds in the channel. The reason for this decrease in speed is the increase in the intensity of the Darcy force, which is the force of resistance to fluid flow. And in this case, the graphs of the speed distribution are symmetrical. Fig.5 shows that an increase in the value of Λ leads to an increase of temperature in the channel. This conclusion is physically explained by the increase in Darcy dissipation. For all three values of Λ , heat transport is from the fluid to the upper channel wall.

Distributions of fluid speed and temperature in the channel for different values of the external electrical load (K) are graphically presented in Fig. 6 and Fig. 7, respectively.

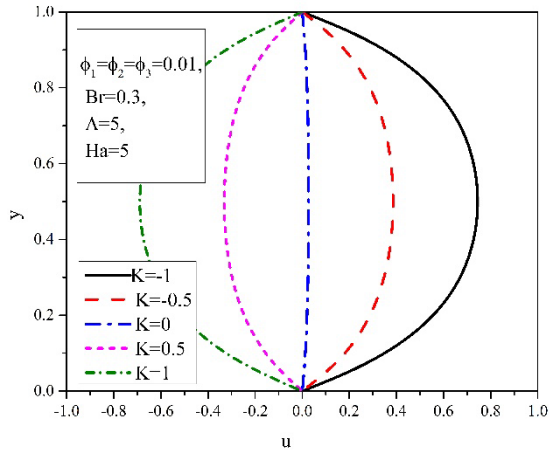


Fig. 6 Velocity distributions for different K values

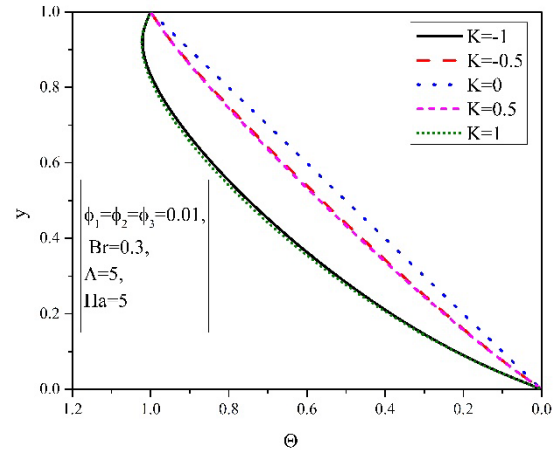


Fig. 7 Temperature distributions for different K values

Fig. 6 shows that larger values of $|K|$ higher velocities correspond, while changing the sign of the factor K changes the direction of fluid flow. This conclusion is physically explained by the fact that for $K < 0$ it is the Lorentz driving force, and for $K > 0$ it is the force of resistance to fluid flow and that its intensity is higher for higher values of $|K|$. Fig. 7 shows that larger values of $|K|$ correspond to higher fluid temperatures in the channel. This is physically explained by Joule heat transfer. For $K = 0$ heat transfer is mainly by conduction.

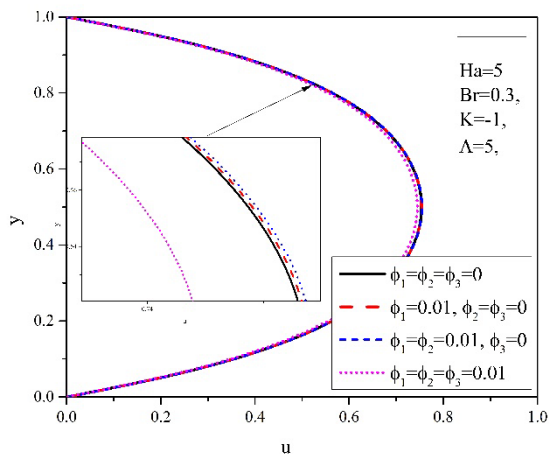


Fig. 8 Velocity distributions for different ϕ values

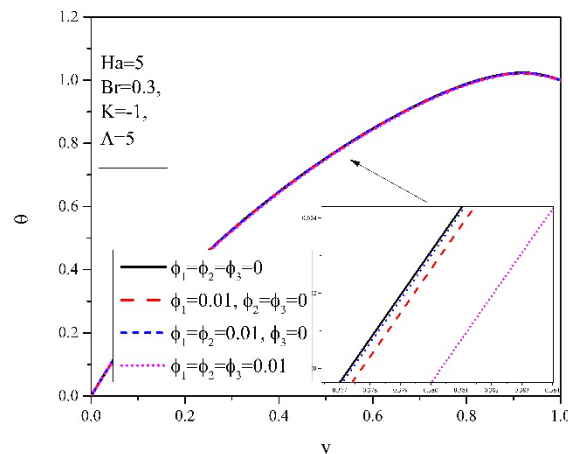


Fig. 9 Temperature distributions for different ϕ values

For base fluid (blood) ($\phi_1 = \phi_2 = \phi_3 = 0$), NF ($\phi_1 = 0.01, \phi_2 = \phi_3 = 0$), HNF ($\phi_1 = \phi_2 = 0.01, \phi_3 = 0$) and THNF ($\phi_1 = \phi_2 = \phi_3 = 0.01$) graphs of distribution of velocity and temperature of the fluid in the channel are presented in fig. 8 and Fig. 9, respectively. It can be seen, from Fig. 9, that the speed is the lowest when THNF is flowing in the channel. This can be physically explained by the fact that the fluid is denser, has a higher coefficient of dynamic viscosity, and then the force of resistance to the flow due to viscosity is more intense. From fig. 10, it can be seen that the temperature is the lowest when the THNF flows, which can be explained by the improved thermal conductivity.

Table 2 gives the values of shear stress and Nusselt numbers on channel walls for different values of the introduced influential physical parameters. From this table, it can be seen that higher values of the Ha number correspond to higher values of shear stress on the channel walls and higher values of Nusselt swarm on the bottom wall of the channel. On the upper wall of the channel for $Ha = 1$ is $Nu_2 > 0$, which means that heat transport is from the wall to the fluid. For the values of $Ha = 5$ and $Ha = 10$, $Nu_2 < 0$ and is greater than the absolute value for a greater value of Ha , which means that heat transport is greater for a greater value of Ha swarm.

Higher values of $|K|$ correspond to higher values of the shear stress on the channel walls and higher values of the Nu_1 number. On the upper wall of the channel, the value of the Nu_2 number is the highest for $K = 0$.

Table 2. Values of shear stresses and Nusselt numbers

	τ_1	τ_2	Nu_1	Nu_2
Ha=1	0.03415	-0.032	1.24266	0.930317
Ha=5	4.974293	-4.97429	2.951512	-0.77853
Ha=10	10.45318	-10.4532	4.810593	-2.6361
K=-1	4.974293	-4.97429	2.951512	-0.7853
K=-0.5	2.578781	-2.57878	1.555005	0.617974
K=0	0.183269	-0.18327	1.089503	1.083476
K=0.5	-2.21224	2.212243	1.555005	0.617974
K=1	-4.60775	4.607754	2.951512	-0.77853
$\Lambda = 1$	5.331527	-5.33153	2.724674	-0.5517
$\Lambda = 5$	4.974293	-4.97429	2.951512	-0.77853
$\Lambda = 10$	4.611617	-4.61162	3.177669	-1.00469
$\phi_1 = \phi_2 = \phi_3 = 0$	4.974293	-4.97429	2.951512	-0.77853
$\phi_1 = 0.01 \phi_2 = \phi_3 = 0$	4.835459	-4.83546	2.838311	-0.77991
$\phi_1 = \phi_3 = 0 \phi_2 = 0.01$	4.835459	-4.83546	2.834873	-0.78335
$\phi_1 = \phi_2 = \phi_3 = 0.01$	4.974293	-4.97429	2.951512	-0.77853

Higher values of the factor Λ correspond to smaller values of the shear stress on the channel walls, higher values of the Nu_1 number and higher absolute values of the Nu_2 number. For the values of Λ given here, on the upper wall of the channel is heat transport from the fluid to the wall.

5. Conclusion

In this paper, the electromagnetic hydrodynamic flow and heat transfer of a ternary hybrid nanofluid in a horizontal channel saturated with a porous medium is considered. Analytical distributions of velocity and temperature in the channel and shear stresses and Nusselt numbers on the channel walls were determined. Part of the obtained results for the case of the ternary hybrid nanofluid ($Al_2O_3+MgO+TiO_2$ /blood) is given in the form of graphs and tables. Based on the analysis of the obtained results, appropriate conclusions were drawn. It was concluded that an increase in the value of Hartmann's number leads to an acceleration of the fluid flow in the channel and to an increase in its temperature. Increasing the value of the factor Λ ie. the decrease in the permeability of the porous medium slows down the fluid flow in the channel and causes an increase in its temperature. Larger absolute values of the external electrical load factor lead to an acceleration of the flow and an increase in the temperature of the fluid in the channel. Changing the sign of the factor K leads to a change in the direction of fluid flow. Flow is slowest when in the THNF channel compared to flow when in the HNF, NF or base fluid channel.

Acknowledgements

This research was financially supported by the Ministry of Education, Science and Technological Development of the Republic of Serbia.

References

- [1] CHOI S.U.S. (1995) Enhancing thermal conductivity of fluids with nanoparticles, *Developments and Applications of Non-Newtonian Flows*, MD vol. 231 and FED vol. 66 ASME, pp. 95-105.
- [2] LIMA J. A., ASSAD G. E. and PAVIA H. S. (2016) *A simple approach to analyze the fully developed two-phase magnetoconvection type flows in inclined parallel-plate channels*, *Latin American Applied Research*, 46(3), pp. 93-98, doi:10.52292/jaar.2016.333
- [3] T.Linga Raju and P. Satish (2023), Slip regime MHD 2-liquid plasma heat transfer flow with Hall currents between parallel plates, *Int. J. Of Applied Mechanics and Engineering*, vol. 28, No. 3, pp. 65-85, doi:10.59441/ijame/172898
- [4] Nagavali, M., Linga Raju, T., Kameswaran, P. K.(2022). Two-Layered Flow of Ionized Gases ithin a Channel of Parallel Permeable Plates Under an Applied Magnetic Field with the Hall Efect. In: Rushi Kumar, B., Pannusamy, S., Giri, D., Thuraisingham, B., Clifton, C.W., Carminati, B.(eds) *Mathematics Computing*.

- ICMC2022. Springer Proceedings in Mathematics and Statistics, vol. 41, Singapore, doi: 10.1007/978_981_19_9307_7_43.
- [5] Milica Nikodijević, Živojin Stamenković, Jelena Petrović, Miloš Kocić, (2020), Unsteady Fluid Flow and Heat Transfer Through a Porous Medium in a Inclined Magnetic Field, Transactions of Famena, Vol. 44(4), pp. 31-46, doi:10.21278/TOF.444014420
- [6] Aaiza Gul, Ilyas Khan and Sharidan Shafie (2018), Radiation and Heat generation effects in magnetohydrodynamic mixed convection flow of nanofluids, Thermal Science, Vol. 22, No. 1A, pp. 51-62, doi:10.2298/TSCI150730049G
- [7] Manjet and Mukesh Kumar Sharma (2020), MHD flo and heat Convection in a channel filled with two immiscible newtonian and nanofluid fluids, JP Journal of Heat and Mass Transfer, Volume 21, Numer 1, Pages 1-21, doi: 0.17654/HM021010001
- [8] J.C.Umavathi and Hakan F.Oztop (2021), Investigation of MHD and applied electric field effects in a conduit cramed with nanofluids, International Communications in Heat and Mass Transfer, Vol. 121:105097, doi:10.1016/j.icheatmasstransfer.2020.105097
- [9] PETROVIĆ J.D., STAMENKOVIĆ Ž., BOGDANOVIĆ JOVANOVIĆ J., NIKODIJEVIĆ M., KOCIĆ M., NIKODIJEVIĆ D. (2022) *Electro-Magneto Convection Immiscible Pure Fluid and Nanofluid*, Transactions of FAMENA 46(3):13-28, doi:10.21278/TOF.463036021
- [10] Jelena D. Petrović, Živojin Stamenković, Miloš Kocić, Milica Nikodijević, Jasmina Bogdanović Jovanović, Dragiša D. Nikodijević (2022), Magnetohydrodynamic flow and mixed convection of a viscous fluid and a nanofluid a porous medium in a vertical channel, Thermal Science Volume 27, Issue 2 Part B, pp. 1453-1463, doi:10.2298/TSCI220903188P
- [11] M.Padma Devi, Kamal Goyal, S. Srinivas, B. Satyanarayana (2024), Effects of different nanoparticles on the two immiscible liquids flow in an inclined channel with Joule heating and viscous dissipation, Gulf Journal of Mathematics Vol. 16, Issue 2, 278-290, doi:10.56947/gjam.V16i2.1815
- [12] Petrović D. Jelena, Nikodijević Đorđević Milica, Kocić Miloš, (2023), Electromagnetic hydrodynamic flow and heat transfer of a Casson nanofluid Fe_3O_4 -blood in a porous medium, Thermal Science Volume 27, Issue 6 Part A, pp. 4461-4472, doi:10.2298/TSCI230516169P
- [13] Eyad M. Hamad, Aseel Khaffaf, Omar Yasin, Ziad Au El-Rub, Samer Al-Gharabli, ael Al-Kouz and Ali J. Chamkha (2021), Revie of Nanofluids and Their iomedical Applications, Journal of Nanofluids, Vol. 10, pp. 63-66, doi: 10.1166/jon.2021.1806
- [14] Mohammad Ataei, Farhad Sadegh Moghanlou, Saeed Noorzadeh, Mohammad Vajdi and Mehdi Shahedi, (2020), Heat transfer and flo characteristics of hrid Al_2O_3/TiO_2 -water nanofluid in a minichannel heat sink, Heat and Mass Transfer Volume 6, issue 9, pp. 2757-2767, doi: 10.100/s00231-020-02896-9
- [15] Ebrahim A. Algehyne, Haiffa F. Alrihieli, Muhammad Bilal, Anwar Saeed and Wajaree Weera (2022), Numerical Approach toward Ternary Hybrid Nanofluid Flow Using Variable Diffusion and Non-Fouriers Concept, ACS Omega 7 (33), 29380-29390, doi:10.1021/acsomega.2c03634
- [16] Saman Riaz, Muhammad F.Afzaal, Zhan Wang, Ahmed Jan and Umer Farooq (2023), Numerical heat transfer of non-similar ternary hybrid nanofluid flow over lineary stretching surface, Numerical Heat Transfer, Part A: Applications, doi:10.1080/10407782.2023.2251093
- [17] Saleem Nasir, Sehson Sirisubtawee, Pongpol Junthar, Adallah S Berrouk, Safyan Mukhtar, Taza Gul (2022), Heat transport study of ternary hyrid nanofluid flow under magnetic dipole together with nonlinear thermal radiation, Applied Nanoscience 12(2), doi:10.1007/s13204-022-02583-7
- [18] Gadamsetty Revathi, Isac Lare Animasaum, Venkata Surbahmanyam Sajja, Macherla Jayachandra Babu, Naresh Boora and Shakravarthula S. K. Raju (2022), Significance of adding titanium dioxide nanoparticles to an existing distilled water conveying aluminium oxide and zinc oxide nanoparticles: Scrutinizstion of chemical reactive ternary hyrid nanofluid due to bicconvection on a convectively heated surface, Nonlinear Engineering 11; 21-251, doi: 10.1515/nleng-2022-0031
- [19] Qadeer Raza, Xiaodong Wang, Hussein A. H. Muhammed, Bagh Ali, Mohamed R. Ali, Ahmed S. Hendy (2024), Numerically analyzed of ternary hybrid nanofluids fflow of heat and mass transfer subject to various shapes and size factors in two-dimensional rotatting porous channel, Case Studies in Thermal Engineering 56, 104235, doi: 10.1016/j.csite.2024.104235

Mixed Convective EMHD Flow of a Ternary Hybrid Nanofluid in a Vertical Channel with Porous Medium

Jelena Petrović^a, Milica Nikodijević Đorđević^b, Miloš Kocić^c, Jasmina Bogdanović Jovanović^d, Živojin Stamenković^e

^aFaculty of Mechanical Engineering, Niš, RS, jelena.nikodijevic.petrovic@masfak.ni.ac.rs

^bFaculty of Occupational Safety, Niš, RS, milica.nikodijevic@znrjak.ni.ac.rs,

^cFaculty of Mechanical Engineering, Niš, RS, milos.kocic@masfak.ni.ac.rs

^dFaculty of Mechanical Engineering, Niš, RS, jasmina.bogdanovic.jovanovic@masfak.ni.ac.rs

^eFaculty of Mechanical Engineering, Niš, RS, zivojin.stamenkovic@masfak.ni.ac.rs

Abstract: This paper considers the mixed convective EMHD flow of a ternary hybrid nanofluid in a vertical channel. There is a homogeneous porous medium in the channel whose walls are on different temperatures. A homogeneous magnetic field acts perpendicular to the channel walls and a homogeneous electric field acts perpendicular to the direction of the fluid flow. The base fluid is blood and nanoparticles of three types of materials are suspended in it. The induced magnetic field is neglected. Velocity and temperature distributions were analytically determined and presented in the form of graphs. The shear stresses and Nusselt numbers on the channel walls are calculated and tabulated.

Keywords: EMHD, Ternary hybrid nanofluid, Vertical channel, Porous medium, Nusselt number.

1. Introduction

Convective heat transport is present in many industrial processes, energy, medicine, etc. Because of his wide presence, his research has become an important topic for researchers of various specialties. A large number of researchers are dedicated to improving heat transport by increasing heat transfer surfaces, vibration of these surfaces, use of microchannels, etc. The low thermal conductivity of classical fluids compared to metals has been observed, and research is being carried out in order to increase it.

Choi [1] suggested improving the thermal conductivity of fluids by suspending nanometer-sized metal particles and called these fluids nanofluids. Today, a lot of researchers are dedicated to nanofluids and hybrid nanofluids. Attention is drawn to the fact that nanofluid heat transport in a magnetic environment is a relatively new research area. The minimal number of studies mentioned in this introduction sufficiently shows how wide their range is.

In the paper by Lima et al. [2], EMHD flow and heat transfer of two immiscible fluids in a channel between two inclined parallel plates were investigated. The effects of layer porosity, buoyancy, Joule and viscous heating, moving plates, tilted magnetic field and heat generation/absorption are included. Raju and Satish [3] investigated the influence of slip factor on EMHD flow and heat transfer of two immiscible plasma fluids in a horizontal channel between two parallel plates with Hall currents. Nikodijevic et al. [4] investigated unsteady magnetohydrodynamic flow and heat transfer in a horizontal channel between parallel plates. The medium in the channel is porous, and the applied magnetic field is inclined relative to the direction of the primary current. The influence of magnetic field and thermal radiation on entropy generation of immiscible micropolar and Newtonian fluid in a horizontal rectangular channel of porous medium was investigated by Yadav et al. [5]. Gul et al. [6] investigated the effects of radiation and heat generation in unsteady MHD mixed convective flow of nanofluids in a vertical channel. The influence of the size of nanoparticles on speed and temperature was analyzed in particular. Das et al. [7] investigated the MHD fully developed mixed convective flow of a nanofluid in a vertical channel. An induced magnetic field is included. Umavathi and Sheremet [8] investigated the mixed convection in a vertical channel where in its middle part there is a Newtonian fluid, and in the end parts, where the media are porous, there are nanofluids. Double-diffusion and forced convective flow of nanofluids in a vertical channel with Robin boundary conditions on the channel walls was investigated by Umavathi and Chamkha [9]. Umavathi and Oztop [10] presented a numerical simulation for the analysis of the influence of electric and magnetic fields on the flow and heat transfer of nanofluids in a vertical channel.

Petrovic et al. [11, 12] investigated EMHD flow and heat transfer of immiscible viscous and nanofluids in horizontal and vertical channels, respectively, whose media are porous. The channel walls are impermeable and are at constant but different temperatures. EMHD flow and heat transfer of Casson nanofluid Fe_3O_4 - blood in a horizontal channel of a porous medium with isothermal and impermeable walls was investigated by Petrovic et al. [13]. The influence of different nanoparticles on unsteady MHD flow and heat transfer of immiscible viscous and nanofluids in an inclined channel of porous media and permeable walls was investigated by Devi et al. [14]. The influence of the nanoparticle shape factor on the oscillatory MHD flow of two immiscible nanofluids in a horizontal channel of a porous medium with thermal radiation and sliding velocity and temperature on the channel walls was investigated by Devi et al. [15].

Xu and Sun [16] investigated the fully developed convective flow of a generalized hybrid nanofluid in a vertical microchannel. Chamkha et al. [17] investigated the MHD flow and heat transfer of a hybrid nanofluid in a vertical microchannel. Chamkha et al. [18] investigated the MHD flow and heat transfer of a hybrid nanofluid in a rotating system between two parallel plates that are permeable and stretchable under the influence of thermal radiation. Sudharani et al. [19] investigated the flow and heat transfer of a hybrid/tri-hybrid nanofluid over a moving plate. The influence of slip and radiation is included. It is shown that the rate of heat transfer in three hybrid nanofluids is higher than in hybrid nanofluids. Ebrahim [20] investigated the natural convective flow of three hybrid nanofluids along a horizontal stretchable sheet in a porous medium with radiation and chemical reaction. The main goal of this research is to examine the flow characteristics of this fluid for industrial and biomedical applications. Riaz et al. [21] investigated the MHD flow of non-Newtonian Williamson three hybrid nanofluids in a porous medium over a horizontal stretchable plate with thermal radiation.

By reviewing the existing research, it becomes clear that the simultaneous effects of magnetic field, electric field, viscous, Joule's and Darcy's dissipation on the convective flow of three hybrid nanofluids have not been sufficiently investigated. This especially applies to tri-hybrid nanofluids whose base fluid is blood. Therefore, in this work, the EMHD convective flow of tri-hybrid nanofluid $Al_2O_3+MgO+TiO_2$ /blood in a vertical channel whose medium is porous is investigated. Application of the results of this research is expected in many fields, especially in medicine.

2. Mathematical formulation

The problem investigated here is the mixed convective flow of three hybrid nanofluids in a channel between two parallel vertical walls (see Figure 1). The medium in the channel is porous, and its permeability is μ . The walls of the channel are at a mutual distance h , are impermeable and are at constant temperatures on both the right and left sides, respectively. The applied magnetic field of induction B is perpendicular to the walls of the channel, and the applied electric field of strength E is perpendicular to the longitudinal plane of the channel perpendicular to its walls. The pressure gradient in the flow direction is constant, and the flow is laminar, stationary and fully developed.

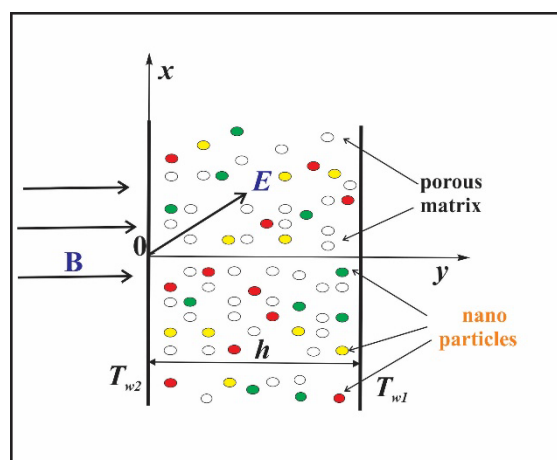


Fig.1 Physical model

The described problem is mathematically formulated by the momentum equation, energy equation and boundary conditions, respectively [8, 12]:

$$-\frac{dp}{dx} + \mu \frac{d^2U}{dZ^2} - \frac{\mu}{K_0}U - B\sigma(E + Bu) + g(\rho\beta)(T - T_{w2}) = 0, \quad (23)$$

$$k \frac{d^2T}{dY^2} + \mu \left(\frac{dU}{dY} \right)^2 + \frac{\mu}{K_0}U^2 + \sigma(E + Bu)^2 = 0, \quad (2)$$

$$(u, T)(0) = (0, T_{w2}), (U, T)(h) = (0, T_{w1}), \quad (3)$$

where the labels are used: X, Y – Cartesian coordinates, g – gravitational acceleration, p, T, u – pressure, velocity, temperatures of the three hybrid nanofluids, respectively, and $\rho, \beta, \mu, k, \sigma$ – the properties of the three hybrid nanofluids are density, coefficient of thermal expansion, coefficient of dynamic viscosity, coefficient of thermal conductivity and electrical conductivity, respectively.

The physical properties of three hybrid nanofluids are given by relations [19]:

$$\begin{aligned} \rho &= \omega_2 \rho_f, \omega_2 = (1 - \phi_3)\omega_1 + \phi_3 \frac{\rho_3}{\rho_f}, \\ \omega_1 &= (1 - \phi_2)\omega_0 + \phi_2 \frac{\rho_2}{\rho_f}, \omega_0 = 1 - \phi_1 + \phi_1 \frac{\rho_1}{\rho_f}, \\ \mu &= \frac{\mu_f}{m}, m = (1 - \phi_1)^{2.5}(1 - \phi_2)^{2.5}(1 - \phi_3)^{2.5}, k = \varphi_2 k_f, \varphi_2 = N(\phi_3, k_3, k_f, \varphi_1), \\ \varphi_1 &= N(\phi_2, k_2, k_f, \varphi_0), \varphi_0 = N(\phi_1, k_1, k_f, 1), N(\phi, S, R, M) = \frac{(1 + 2\phi)S + 2(1 - \phi)RM}{(1 - \phi)S + (2 + \phi)RM}, \\ \sigma &= \varphi_4 \sigma_f, \varphi_4 = N(\phi_3, \sigma_3, \sigma_f, \varphi_3), \varphi_3 = N(\phi_2, \sigma_2, \sigma_f, \varphi_0^*), \varphi_0^* = N(\phi_1, \sigma_1, \sigma_f, 1) \\ (\rho\beta) &= \varphi_6 (\rho\beta)_f, \varphi_6 = L(\phi_3, \sigma_3, 3), \varphi_6 = L(\phi_2, \sigma_2^*, 2), \varphi_5^* = L(\phi_1, 1, 1), \\ L(\phi, M, i) &= (1 - \phi)M + \phi \frac{(\rho\beta)_i}{(\rho\beta)_f}, (\rho c_p) = \Psi_2 (\rho c_p)_f, \Psi_2 = D(\phi_3, \Psi_1, 3), \Psi_1 = D(\phi_2, \Psi_0, 2), \\ \Psi_0 &= D(\phi_1, 1, 1), D(\phi, M, i) = (1 - \phi)M + \phi \frac{(\rho c_p)_i}{(\rho c_p)_f}. \end{aligned} \quad (4)$$

where the indices 1, 2 and 3 refer to the material properties and volume fractions of nanoparticles 1, 2 and 3 and the index f refers to the properties of the base fluid.

Introducing further dimensionless transformations:

$$y^* = \frac{Y}{h}, u = \frac{U}{U_0}, \theta = \frac{T - T_{w2}}{T_{w1} - T_{w2}},$$

and the volume fractions ϕ in which there is characteristic velocity U_0 and using relations (3) of equations (1), (2) and boundary conditions (3) are, respectively, transformed to:

$$\frac{d^2u}{dy^2} - \omega^2 u + aM\Theta = R_1, \quad (5)$$

$$\frac{d^2\theta}{dy^2} + \frac{Br}{m\varphi_2} \left[\left(\frac{du}{dy} \right)^2 + \omega^2 u^2 + 2Ru + R_2 \right] = 0, \quad (6)$$

$$(u, \theta)(0) = (0, 0), (u, \theta)(1) = (0, 1). \quad (7)$$

where tags are used:

$$\Lambda = \frac{h^2}{K_0}, Ha = Bh \sqrt{\frac{\sigma_f}{\mu_f}}, K = \frac{E}{BU_0}, M = g \frac{(\rho\beta)_f h(Tw_1 - Tw_2)^2}{\mu_f U_0},$$

$$P = -\frac{\partial p}{\partial X} \frac{h^2}{U_0 \mu_f}, \omega^2 = \Lambda + m\phi_4 Ha^2, a = m\phi_6, R = m\phi_4 K Ha^2, \quad (8)$$

$$R_1 = R - mP, Pr = \frac{\mu_f c_{pf}}{k_f}, Ec = \frac{U_0^2}{c_{pf}(Tw_1 - Tw_2)},$$

$$Br = Pr Ec, R_2 = RK,$$

where are: Λ – porosity factor, Ha – Hartmann number, K – electric load factor, Pr – Prandtl number, Ec – Eckert number, Br – Brinkman number.

3. Solution method

Equations (5) and (6) are non-linear, simultaneous differential equations and it is not possible to analytically find their exact solution. That is why their approximate solution will be analytically determined here, and the perturbation method will be used for that. To that end, the approximate solution can be presented in the form:

$$(u, \theta)(y) = (u_0, \theta_0)(y) + Br(u_1, \theta_1)(y), \quad (9)$$

where the Brinkman number is used as the perturbation parameter.

Using relation (9) and the perturbation method from equations (5), (6) and zero-order boundary conditions:

$$\frac{d^2 u_0}{dy^2} - \omega^2 u_0 + aM\theta_0 = R_1, \quad (10)$$

$$\frac{d^2 \theta_0}{dy^2} = 0, \quad (11)$$

$$(u_0, \theta_0)(0) = (0, 0), (u_0, \theta_0)(1) = (0, 1), \quad (12)$$

and equations and boundary conditions of the first order:

$$\frac{d^2 u_1}{dy^2} - \omega^2 u_1 + aM\theta_1 = 0, \quad (13)$$

$$\frac{d^2 \theta_1}{dy^2} + \frac{1}{m\phi_2} \left[\left(\frac{du_0}{dy} \right)^2 + \omega u_0^2 + 2Ru_0 + R_2 \right] = 0, \quad (14)$$

$$(u_1, \theta_1)(0) = (0, 0), (u_1, \theta_1)(1) = (0, 0). \quad (15)$$

The solution of equations (10) and (11) with boundary conditions (12) is:

$$u_0(y) = D_1 \exp(\omega y) + D_2 \exp(-\omega y) + \frac{aM}{\omega^2} y - \frac{R_1}{\omega^2}, \quad (16)$$

$$\theta_0(y) = y. \quad (17)$$

The solution of equations (13) and (14) with boundary conditions (15) is:

$$D_1 = \frac{R_1 [1 - \exp(-\omega)] - aM}{\omega^2 [\exp(\omega) - \exp(-\omega)]}, D_2 = \frac{R_1}{\omega^2} - D_1. \quad (18)$$

The solution of equations (13) and (14) with boundary conditions (15) is:

$$u_1(y) = D_3 \exp(\omega y) + D_4 \exp(-\omega y) + R_{10} \exp(2\omega y) + R_{11} \exp(-2\omega y) +$$

$$y(R_{12} + R_{13}y) \exp(\omega y) + y(R_{14} + R_{15}y) \exp(-\omega y) +$$

$$R_{16}y^4 + R_{17}y^3 + R_{18}y^2 + R_{19}y + R_{20} \quad (19)$$

$$\theta_1(y) = -\frac{1}{m\varphi_2} \left[\frac{1}{2} D_1^2 \exp(2\omega y) + \frac{1}{2} D_2^2 \exp(-2\omega y) + (R_3 + R_4 y) \exp(\omega y) + (R_5 + R_6 y) \exp(-\omega y) + R_7 y^4 + R_8 y^3 + R_9 y^2 + C_3 y + C_4 \right], \quad (20)$$

where tags are used:

$$\begin{aligned} R_3 &= \frac{2D_1}{\omega^2} (R - R_1 - \frac{aM}{\omega}), R_4 = \frac{2MaD_1}{\omega^2}, R_5 = \frac{2D_2}{\omega^2} (R - R_1 + \frac{aM}{\omega}), \\ R_6 &= \frac{2MaD_2}{\omega^2}, R_7 = \frac{a^2 M^2}{12\omega^2}, R_8 = \frac{aM}{3\omega^2} (R - R_1), \\ R_9 &= \frac{1}{2} \left(\frac{a^2 M^2}{\omega^4} + \frac{R^2}{\omega^2} - \frac{2RR_1}{\omega^2} + R_2 \right), S = \frac{aM}{m\varphi_2}, \\ R_{10} &= \frac{SD_1^2}{6\omega^2}, R_{11} = \frac{SD_2^2}{6\omega^2}, R_{12} = S \frac{2\omega R_3 - R_4}{4\omega^2}, \\ R_{13} &= \frac{SR_4}{4\omega}, R_{14} = -S \frac{2\omega R_5 + R_6}{4\omega^2}, R_{15} = -S \frac{R_6}{4\omega}, \\ R_{16} &= -S \frac{R_7}{\omega^2}, R_{17} = -S \frac{R_8}{\omega^2}, R_{18} = -S \frac{12R_7 + \omega^2 R_9}{\omega^4}, \\ R_{19} &= -S \frac{6R_8 + \omega^2 C_3}{\omega^4}, R_{20} = -S \frac{24R_7 + 2\omega^2 R_9 + \omega^4 C_4}{\omega^6}, \end{aligned}$$

$$\begin{aligned} R_{21} &= -R_{10} - R_{11} - R_{20}, R_{22} = -R_{10} \exp(2\omega) - \\ &R_{11} \exp(-2\omega) - (R_{12} + R_{13}) \exp(\omega) - (R_{14} + R_{15}) \exp(-\omega) \\ &- R_{16} - R_{17} - R_{18} - R_{19} - R_{20}, \\ C_3 &= \frac{1}{2} (D_1^2 + D_2^2) + R_3 + R_5 - \frac{1}{2} D_1^2 \exp(2\omega) \\ &- \frac{1}{2} D_2^2 \exp(-2\omega) - (R_3 + R_4) \exp(\omega) - \\ &(R_5 + R_6) \exp(-\omega) - R_7 - R_8 - R_9, \\ C_4 &= -\frac{1}{2} (D_1^2 + D_2^2) - R_3 - R_5, \\ D_3 &= \frac{R_{22} - R_{21} \exp(-\omega)}{\exp(\omega) - \exp(-\omega)}, D_4 = R_{21} - D_3. \end{aligned} \quad (21)$$

Thus, the velocity and temperature distributions of three hybrid nanofluids in the problem considered here are determined.

The dimensionless shear stresses on the left and right channel walls are given, respectively, by the relations:

$$\begin{aligned} \tau_1 &= \frac{\mu}{\mu_f} \left(\frac{du}{dy} \right)_{y=0}, \\ \tau_2 &= \frac{\mu}{\mu_f} \left(\frac{du}{dy} \right)_{y=1}, \end{aligned} \quad (22)$$

and the Nusselt numbers on these walls, respectively, are:

$$\begin{aligned} Nu_1 &= \frac{k}{k_f} \left(\frac{d\theta}{dy} \right)_{y=0}, \\ Nu_2 &= \frac{k}{k_f} \left(\frac{d\theta}{dy} \right)_{y=1}. \end{aligned} \quad (23)$$

4. Results and analysis

In the previous chapter, the distributions of velocity, temperature, shear stress and Nusselt numbers on the channel walls were determined as a function of the parameters important for this considered problem. Among

the influential parameters is the parameter M , which can be changed, and it also depends on the characteristic speed. In the available literature, this speed is defined in different ways, and here it is further defined in the form [8] $U_o = \nu_f / h$, where ν_f is the coefficient of kinematic viscosity of the base fluid. For the characteristic speed defined in this way, the parameter M becomes the Brinkmann number.

Used values of physical properties for blood and nanoparticle materials are given in Table 1 [7,21].

Table 1. Physical properties

Supstance properties	blood	Al ₂ O ₃	TiO ₂	MgO
$\rho (kg / m^3)$	997.1	3970	4250	3560
$c_p (J / (kgK))$	4179	765,	686.2	955
$K (W / (Km))$	0.613	40	8.9538	45
$\sigma (S / m)$	5.5×10^{-6}	35×10^6	2.6×10^6	5.392×10^{-7}
$\mu (Pas)$	0.001	-	-	-
$\beta [K^{-1}]$	0.18×10^{-5}	0.85×10^{-5}	0.90×10^{-5}	1.13×10^{-5}

The distributions of speed, temperature, shear stress and Nusselt numbers given analytically in the previous chapter depend on the type of base fluid and the type of nanoparticle material. In this section, a part of the obtained results is given for the case when the base fluid is blood, and the nanoparticles are made of aluminum oxide, magnesium oxide, and titanium dioxide. Velocity and temperature plots are given as graphs, and shear stresses and Nusselt numbers are tabulated.

Figures 2 and 3 show the graphs of the velocity distribution and temperature distribution of THNF in the channel for different values of the Ha number and the constant values of the other factors are given in these figures, respectively. It can be seen from Figure 2 that an increase in the value of the Ha number leads to an acceleration of the fluid flow in the channel and to an increase in the shear stress on the channel walls. The cause of this phenomenon is the increase in the intensity of the Lorentz force with an increase in the Ha number, which here, given the negative value of the external electrical load factor, represents the driving force. The velocity distributions are symmetrical in relation to the longitudinal axis of the channel. It can be seen from Figure 3 that an increase in the Ha number, for constant values of other factors, causes an increase in the temperature in the channel. The reason for the increase in the temperature of the fluid in the channel is the increase in Joule's heat with the increase in the Ha number.

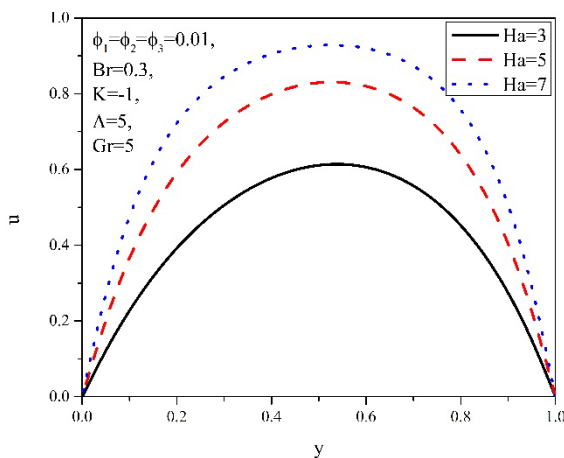


Fig. 2 Velocity distributions for different Ha values

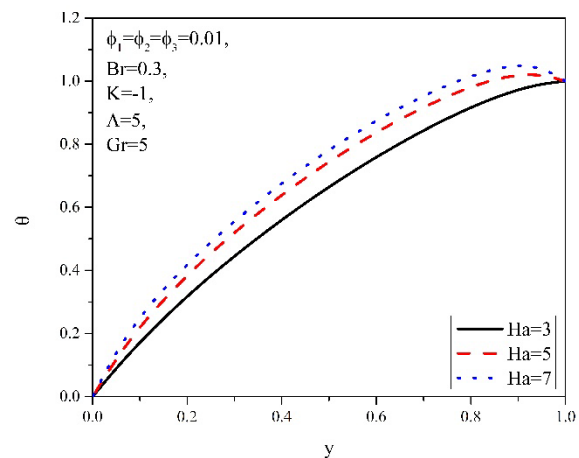


Fig. 3 Temperature distributions for different Ha values

Distributions of velocity and temperature of THNF in the channel for different values of the porosity factor, and constant values of the other factors are shown in Figures 4 and 5, respectively. It can be seen from Figure 4 that the growth of the porosity factor causes the flow in the channel to slow down. The cause of this decrease in the speed of the fluid flow is the increase in the intensity of the Darcy force with the growth of Λ , which represents the force of resistance to the flow of the fluid. As the factor Λ increases, the shear stresses on the channel walls decrease. In this case too, the speed distributions are symmetrical. It can be seen from Figure 5 that the temperature of the fluid in the channel increases with the increase in the value of Λ . The reason for this increase in temperature is the growth of Darcy dissipation with the increase of the factor Λ .

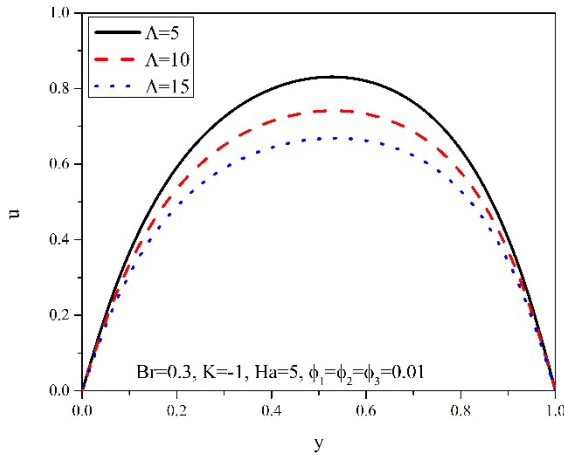


Fig. 4 Velocity distributions for different Λ values

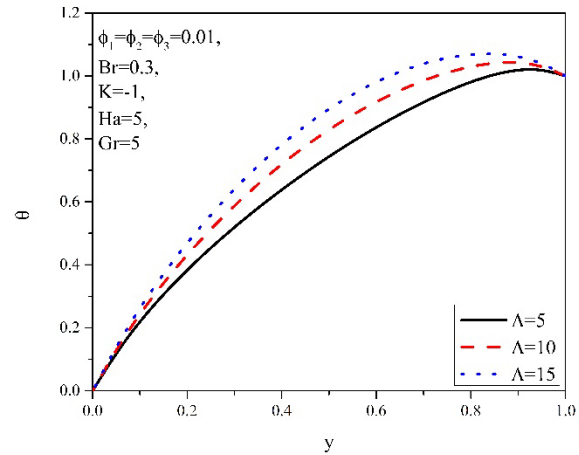


Fig. 5 Temperature distributions for different Λ values

Figures 6 and 7 show graphs of the distribution of speed and temperature for different values of the external electrical load factor K , and for constant values of the other factors given in these figures, respectively. It can be seen from Figure 6 that for $K=0$, the fluid flow velocity is of low intensity. For larger absolute values of K , the flow velocities are higher, and changing the sign of the factor K changes the direction of the flow velocity. The reason for this is the change in the direction of the external electric field. It can be seen from Figure 7 that the growth $|K|$ causes an increase in the temperature of the fluid in the channel. The cause of this temperature increase is the increase of Joule's heat with $|K|$ growth. For $K=0$, the heat transfer in the channel is mainly by conduction.

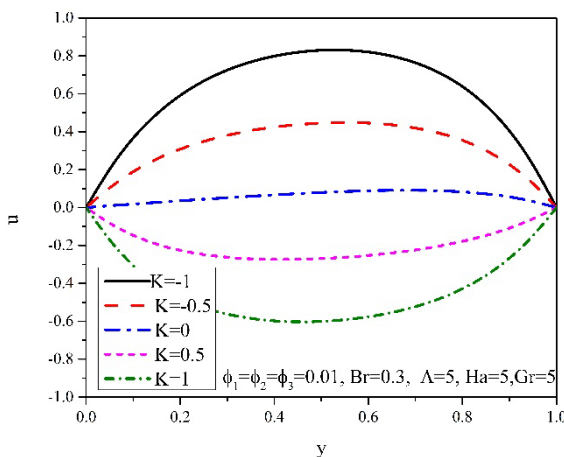


Fig. 6 Velocity distributions for different K values

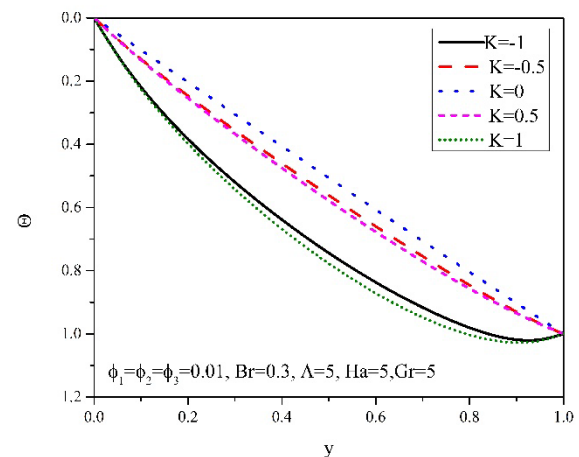


Fig. 7 Temperature distributions for different K values

Distributions of fluid velocity and temperature in the channel for different values of other factors are shown in Figures 8 and 9, respectively. It can be seen from Figure 8 that higher values of the Gr number correspond to faster fluid flows in the channel and lower shear stresses on the channel walls. The speed distribution graphs are symmetrical. The cause of this increase in flow speed is the growth of buoyancy force with increasing Gr number. As the Gr number increases, the temperature of the fluid in the channel increases, as can be seen from Figure 9. Heat transport is from the fluid to the right wall of the channel for the temperature distributions

shown. This increase in the temperature of the fluid in the channel occurs because higher values of the Gr number correspond to higher speeds, and then higher amounts of Joule heat.

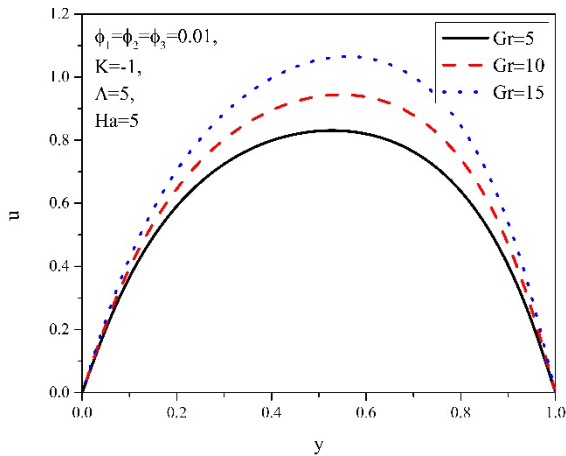


Fig. 8 Velocity distributions for different Gr values

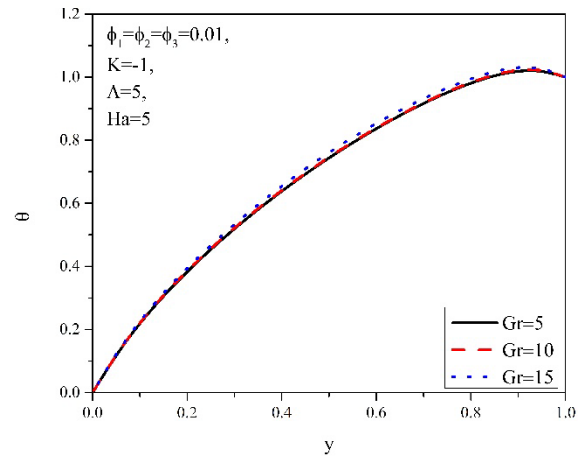


Fig. 9 Temperature distributions for different Gr values

From Figure 10, it can be seen that the flow rate is the highest for HNF, then NF, then classic fluid, and the lowest for THNF. For physical interpretation, viscous and Lorentz force relations are used. In NF, the Lorentz force is dominant in relation to the viscosity force and leads to an increase in speed in relation to the speed of a classic fluid. With HNF, the Lorentz force is even more dominant and leads to an increase in speed compared to the speed of NF. Finally, with THNF, the viscosity force is dominant compared to the Lorentz force and the velocity is the lowest. Figure 11 shows that the temperature is the highest for THNF, followed by NF and HNF, and the lowest for the classic fluid. This was brought about by the relations of viscous dissipation and Joule's heat in the flow of these fluids.

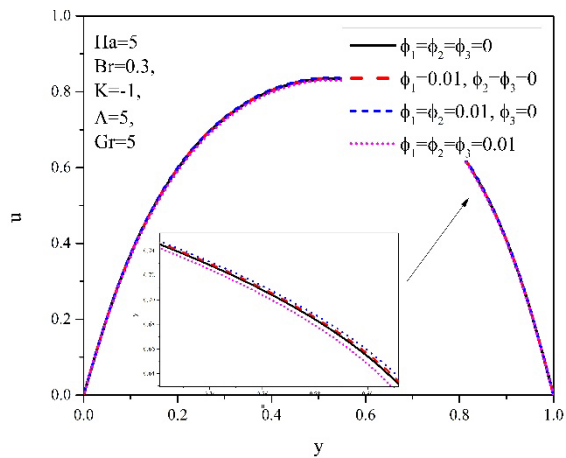


Fig. 10 Velocity distributions for different ϕ values

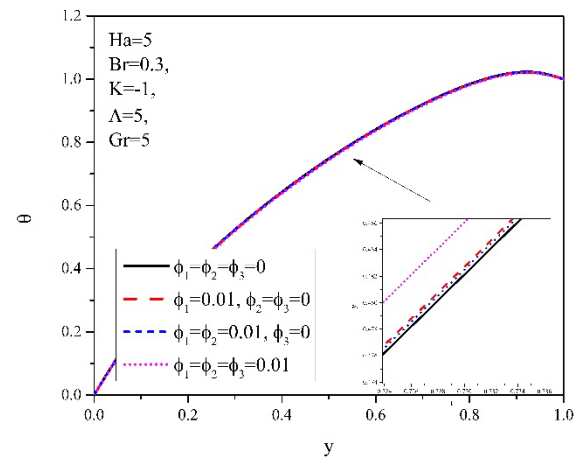


Fig. 11 Temperature distributions for different ϕ values

Table 2. Values of shear stresses and Nusselt numbers

	τ_1	τ_2	Nu_1	Nu_2
Ha=3	2.912266	-3.67165	2.081837	-0.50583
Ha=5	5.126765	-5.77732	2.952918	-1.34026
Ha=7	7.289024	-7.83983	3.733612	-2.01989
K=-1	5.126765	-5.77732	2.952918	-1.34026
K=-0.5	2.628182	-3.27957	1.563802	0.31941
K=0	0.200269	-0.85248	1.105691	1.048071
K=0.5	-2.15697	1.503931	1.578585	0.845726
K=1	-4.44355	3.789676	2.982485	-0.28762
$\Lambda = 5$	5.126765	-5.77732	2.952918	-1.34026

$\Lambda=10$	4.770315	-5.39505	3.179914	-1.45368
$\Lambda=15$	4.474055	-5.07584	3.360976	-1.55508
$\phi_1 = \phi_2 = \phi_3 = 0$	4.82886	-5.41528	2.760032	-1.26556
$\phi_1=0.01 \phi_2 = \phi_3 = 0$	4.964588	-5.56803	2.838747	-1.30024
$\phi_1 = \phi_2=0.01 \phi_3 = 0$	4.966532	-5.57311	2.835411	-1.30651
$\phi_1 = \phi_2=0 \phi_3 = 0.01$	4.849357	-5.46303	2.794903	-1.26539
$Gr=5$	5.126765	-5.77732	2.952918	-1.34026
$Gr=10$	5.447907	-6.75043	2.992951	-1.96475
$Gr=15$	5.787437	-7.74802	3.068626	-2.65818

Table 2 gives values of shear stresses on channel walls and local values of Nusselt number on walls for parameter values $\phi_1 = \phi_2 = \phi_3 = 0.01, Br = 0.3, Pr = 5, Ec = 2, K = -1, \Lambda = 5, Gr = 5$ (except when they change). From this table it can be seen that higher values of Ha and Gr numbers correspond to higher values of shear stresses and higher values of Nusselt number on both walls of the channel, while higher values of the porosity factor correspond to lower values of shear stress and higher values of Nusselt numbers on both walls. Higher values of $|K|$ correspond to higher values τ_1, τ_2 and Nu_1 .

5. Conclusion

EMHD flow and THNF heat transport in a vertical channel filled with a porous medium are discussed in the paper. The channel walls are two parallel vertical plates with constant but different temperatures. Using the perturbation method, analytical distributions of fluid velocity and temperature, shear stresses and local Nusselt numbers on the walls were determined. Part of the obtained results for $Al_2O_3+MgO+TiO_2/blood$ is given in the form of graphs for velocity and temperature distributions and in the form of tables for shear stresses and Nusselt numbers on the channel walls.

Based on the analysis of the results appropriate conclusions were drawn. It was concluded that the growth of the Hartmann number accelerates the fluid flow increases the temperature of the fluid, increases the shear stresses and Nusselt numbers on the channel walls. The growth of the porosity factor slows down the flow, increases the temperature of the fluid, reduces the stresses and increases the Nusselt numbers on the walls. Increasing K accelerates the flow and can change its direction depending on the direction of the electric field. Higher values of K correspond to higher temperatures. The influence of the Grashof number is qualitatively the same as the influence of the Hartmann number. For THNF, the speed is the lowest and the temperatures are the highest compared to these values for HNF, NF and base fluid (blood).

Acknowledgements

This research was financially supported by the Ministry of Education, Science and Technological Development of the Republic of Serbia.

References

- [1] CHOI S.U.S. (1995) Enhancing thermal conductivity of fluids with nanoparticles, *Developments and Applications of Non-Newtonian Flows*, MD vol. 231 and FED vol. 66 ASME, pp. 95-105.
- [2] LIMA J. A., ASSAD G. E. and PAVIA H. S. (2016) *A simple approach to analyze the fully developed two-phase magnetoconvection type flows in inclined parallel-plate channels*, *Latin American Applied Research*, 46(3), pp. 93-98, doi:10.52292/jaar.2016.333
- [3] T.Linga Raju and P. Satish (2023), Slip regime MHD 2-liquid plasma heat transfer flow with Hall currents between parallel plates, *Int. J. Of Applied Mechanics and Engineering*, vol. 28, No. 3, pp. 65-85, doi:10.59441/ijame/172898
- [4] Milica Nikodijević, Živojin Stamenković, Jelena Petrović, Miloš Kocić, (2020), Unsteady Fluid Flow and Heat Transfer Through a Porous Medium in a Inclined Magnetic Field, *Transactions of Famena*, Vol. 44(4), pp. 31-46, doi:10.21278/TOF.444014420
- [5] YADAV P.K., KUMAR A., EL_SAPA S. AND CHAMKHA A.J. (2022) Impact of thermal radiation and oriented magnetic field on the flow of two immiscible fluids through porous media with different porosity, *Waves in Random and Complex Media*, doi:10.1080/17455030.2022.2118897

- [6] [Aaiza Gul, Ilyas Khan and Sharidan Shafie (2018), Radiation and Heat generation effects in magnetohydrodynamic mixed convection flow of nanofluids, *Thermal Science*, Vol. 22, No. 1A, pp. 51-62, doi:10.2298/TSCI150730049G
- [7] S. Das, R. N. Jana, O. D. Makinde (2015), Mixed convective magnetohydrodynamic flow in a vertical channel filled with with nanofluid, *Engineering Science and Technology, an International Journal* doi: 10.1016/j.jestch.2014.12.009
- [8] UMAVATHI J.C., SHEREMET M.A. (2020) Heat transfer of viscous fluid in a vertical channel sandwiched between nanofluid porous zones, *Journal of Thermal Analysis and Calorimetry* 144(4), doi:10.1007/S10973-020-09664-1
- [9] J.C. Umavathi and Ali J. Chamkha(2021) , Thermo-Solutal convection of a Nanofluid Utilizing Fourier's-Type Compass Conditions, *Journal of Nanofluids* 9, No. 4, pp. 362-374, doi:10.1166/jon.2020.1759
- [10] [J.C.Umavathi and Hakan F.Oztop (2021), Investigation of MHD and applied electric field effects in a conduit cramed with nanofluids, *International Communications in Heat and Mass Transfer*, Vol. 121:105097, doi:10.1016/j.icheatmasstransfer.2020.105097
- [11] PETROVIĆ J.D., STAMENKOVIĆ Ž., BOGDANOVIĆ JOVANOVIĆ J., NIKODIJEVIĆ M., KOCIĆ M., NIKODIJEVIĆ D. (2022) *Electro-Magneto Convection Immiscible Pure Fluid and Nanofluid*, *Transactions of FAMENA* 46(3):13-28, doi:10.21278/TOF.463036021
- [12] Jelena D. Petrović, Živojin Stamenković, Miloš Kocić, Milica Nikodijević, Jasmina Bogdanović Jovanović, Dragiša D. Nikodijević (2022), Magnetohydrodynamic flow and mixed convection of a viscous fluid and a nanofluid a porous medium in a vertical channel, *Thermal Science* Volume 27, Issue 2 Part B, pp. 1453-1463, doi:10.2298/TSCI220903188P
- [13] Petrović D. Jelena, Nikodijević Đorđević Milica, Kocić Miloš, (2023), Electromagnetic hydrodynamic flow and heat transfer of a Casson nanofluid Fe_3O_4 -blood in a porous medium, *Thermal Science* Volume 27, Issue 6 Part A, pp. 4461-4472, doi:10.2298/TSCI230516169P
- [14] M.Padma Devi, Kamal Goyal, S. Srinivas, B. Satyanarayana (2024), Effects of different nanoparticles on the two immiscible liquids flow in an inclined channel with Joule heating and viscous dissipation, *Gulf Journal of Mathematics* Vol. 16, Issue 2, 278-290, doi:10.56947/gjam.V16i2.1815
- [15] Radma Devi Medisetty, Srinivas Suripeddi, Satyanarayana Badeti, Vajraveln Kuppalapalle (2024), Pulsatile MHD flow of two immiscible nanofluids through a porous channel with slip effects, *Int. J. Of Applied Mechanics and Engineering*, vol. 29, No. 1, pp. 105-129, doi:10.59441/ijame/175745
- [16] Hang Xu and Qiang Sun, (2019), Generalized Hybrid Nanofluid with the Application of Fully Developed Mixed Convection Flow in a Vertical Microchannel, *Communications in theoretical Physics*, Vol. 71, No. 8, 903-911, doi:10.1088/0253-6102/71/8/903
- [17] Ali J. Chamkha, A.S. Dogonchi and D.D. Ganji, (2019), Magneto-hydrodynamic flow and heat transfer of a hybrid nanofluid in a rotating system among two surfaces in the presence of thermal radiation and Joule heating, *AIP Advances* 9, 025103, doi:10.1063/1.5086247
- [18] M.V.V.N.L.Sudharami, D.G. Prakasha, K.Ganesh Kumar and Ali J.Chamkha (2023), Computational assessment of hybrid and try hibrid nanofluid influenced by slip flow and linear radiation, *Eur. Phys. J. Plus* 138, 257, doi:10.1140/epjp/S13360-023-03852-2
- [19] Ebrahim A. Algehyne, Haiffa F. Alriheli, Muhammad Bilal, Anwar Saeed and Wajaree Weera (2022), Numerical Approach toward Ternary Hybrid Nanofluid Flow Using Variable Diffusion and Non-Fouriers Concept, *ACS Omega* 7 (33), 29380-29390, doi:10.1021/acsomega.2c03634
- [20] Saman Riaz, Muhammad F.Afzaal, Zhan Wang, Ahmed Jan and Umer Farooq (2023), Numerical heat transfer of non-similar ternary hybrid nanofluid flow over lineary stretching surface, *Numerical Heat Transfer, Part A: Applications*, doi:10.1080/10407782.2023.2251093
- [21] A. Manigandan, Panyam Vankata Satya Narayana, (2024), Impact of variable fluid characteristics on MHD hybrid nanofluid (MgO+ZnO/H₂O) flow over an exponentially elongated sheet with non uniform heat generation, *Case Studies in Thermal Engineering* 55 (2024) 104077, doi:10.1016/j.csite.2024.104077

Optimizing Flue Gas Recirculation for Enhanced Efficiency in Biomass-Fired Boilers: A Comprehensive Study

*Nenad Tomić^a, Jovica Podunavac^b, Mladen Tomić^c, Aleksandar Anđelković^d,
Miroslav Kljajić^e, Predrag Živković^f*

^a Faculty of Technical Sciences, University of Novi Sad, RS, jovica.podunavac@gmail.com

^b Faculty of Technical Sciences, University of Novi Sad, RS, nenadtomich@yahoo.com

^c Faculty of Technical Sciences, University of Novi Sad, RS, mladen.tomic@uns.ac.rs

^d Faculty of Technical Sciences, University of Novi Sad, RS, aleksa@uns.ac.rs

^e Faculty of Technical Sciences, University of Novi Sad, RS kljajicm@uns.ac.rs

^f Faculty of Mechanical engineering, University of Niš, RS, predrag.zivkovic@masfak.ni.ac.rs

Abstract As sustainable energy practices become more popular, biomass-fired boilers are becoming a choice over traditional fossil fuel models due to their eco-friendly nature. Despite their environmental advantages, biomass boilers still emit pollutants like particulate matter (PM), sulfur dioxide (SO₂), nitrogen oxides (NO_x), and carbon monoxide (CO), posing environmental concerns. To mitigate these emissions, modern biomass-fired boilers often incorporate Flue Gas Recirculation (FGR). This research focuses on a 14 MW biomass-fired boiler operating with a 20% FGR rate, examining three scenarios: two with varying FGR levels and one without FGR. The analysis reveals a connection between emission reduction via FGR and boiler efficiency maintenance. Additionally, it suggests optimizing FGR levels to boost boiler efficiency. The study presents a comprehensive approach to effectively implement FGR in biomass-fired boilers while ensuring acceptable efficiency levels. NO_x emissions were analyzed using combustion simulation software and the Zeldovich method to estimate thermal NO_x production.

Keywords: Gas Mixture, Real Gases, Temperature-Dependent, Viscosity.

1. Introduction

Steam boilers play a vital role in diverse industries, providing steam for various applications such as power generation, heating, and industrial processes. With a growing emphasis on sustainability, biomass steam boilers have emerged as an eco-friendly alternative to conventional fossil fuel boilers. These biomass boilers have gained attention due to their potential to reduce greenhouse gas emissions and their use of cost-effective biofuels [1]. However, burning biomass in these boilers leads to flue gases containing pollutants such as particulate matter (PM), sulphur dioxide (SO₂), nitrogen oxides (NO_x), and carbon monoxide (CO), raising environmental and health concerns [2,3]. To address these emissions, techniques like flue gas recirculation (FGR) have gained traction.

FGR involves reintroducing a portion of flue gas into the combustion chamber to moderate the combustion temperature. It has emerged as a viable strategy to improve combustion efficiency and reduce the release of CO, PM, and NO_x, ensuring compliance with emission standards [3]. The implementation of FGR depends on factors like boiler design, fuel characteristics, and emission regulations.

Essentially, FGR has become a widespread method to concurrently reduce emissions and enhance the combustion efficiency of biomass steam boilers [3,4]. This study focuses on the operational performance of a 14 MW steam boiler designed to generate saturated steam at a pressure of 13 barg, utilizing agricultural residue straw as its primary fuel source. The boiler incorporates a flue gas recirculation system operating at a 20% recirculation rate, functioning at 80% of its maximum capacity, corresponding to 12.57 barg.

This research aims to evaluate the efficiency and NO_x emissions of the 14 MW steam boiler under varying parameters, specifically focusing on FGR and its impact on combustion efficiency and pollutant emissions. To achieve this, comprehensive data from process and temperature sensors were utilized. These sensors measured temperatures at critical points within the boiler system, including the steam generator furnace exit, downstream of water heater-economizer 4, and the terminal point of the flue gas channel. Oxygen concentration measurements determined excess air ratios, while temperature readings post-bag filter, feed water, and

downstream of economizer 4 were analyzed. The study meticulously calculated both the boiler's efficiency and NO_x emissions for each scenario. Intriguingly, the findings revealed a distinct pattern where the absence of FGR resulted in the highest efficiency but also the highest NO_x emissions, consistent with modeling predictions and calculations

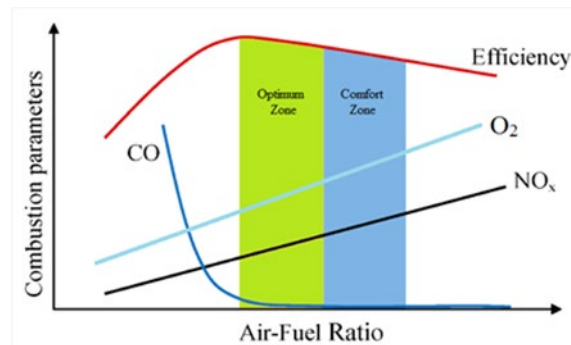


Figure 1 Influence of combustion parameters on efficiency and pollutant emission

The subsequent Results and Discussion section explored the influence of flue gas extraction points on NO_x production. It was found that this parameter had limited significance, with both Gaseq and Zeldovich methods indicating increased emissions with decreasing FGR rates. However, the Zeldovich method provided a more realistic representation of NO_x emissions compared to Gaseq's thermal equilibrium results. The study recommended an optimal FGR rate of around 10% to balance boiler efficiency and NO_x emissions, aiming for an emission level of approximately 300 mg/MJ, considering that most NO_x emissions originate from thermal NO_x.

Acknowledging that empirical data could significantly enhance the credibility of the conclusions drawn, the study emphasized the importance of empirical insights and experimental validation in refining the precision and applicability of the research outcomes. In summary, this study sheds light on the complex relationship between heat transfer, combustion efficiency, and pollutant emissions in a biomass-fired steam boiler. The systematic approach toward thermal design, performance analysis, and evaluating FGR's impact on NO_x emissions provides valuable insights for advancing biomass combustion technology.

2. Thermal Design and Performance Analysis of a Biomass Steam Boiler

Biomass undergoes combustion on a moving grate within the steam boiler system. The released flue gases transfer their heat to screens positioned in the furnace. Following this, the flue gases exit the furnace through an opening in the rear screen and enter an inclined downward flue gas duct. Within this duct, screen tubes aid in the transfer of heat. After passing through this duct, the flue gases make a 180° turn and ascend through a duct containing an evaporator and an economizer (ECO 4) for heat exchange. Subsequently, the flue gases alter their direction, descending to transfer heat to economizers ECO 3, ECO 2, and ECO 1 before leaving the flue gas duct and entering the cyclone and filter sections. A fraction of the flue gas is redirected back to the furnace for recirculation.

The technical specifications of the steam boiler are as follows:

- Boiler thermal power: 14 MW (producing saturated steam);
- Water/steam parameters:
 - Working pressure: 14 bar;
 - Feedwater temperature: 105°C;
 - Saturated steam temperature: 195°C;
- Flue gas temperature at boiler outlet: 170°C;
- Fuel type: Corn straw:
 - Lower Heating Value (LHV): 16 MJ/kg;
 - Designed moisture content: 15%;
 - Ash content on dry mass: < 8%;
 - Designed fuel ash melting point: < 750°C;
 - Designed fuel nitrogen content: < 0.3%;
 - Designed fuel chlorine content: < 0.3%;
 - Designed fuel sulfur content: < 0.1%.

The thermal design of the steam boiler was based on the specific characteristics of corn straw, forming the foundation for all calculations. Procedures outlined in authoritative literature regarding steam boiler thermal design [5-7] were meticulously followed throughout the process. These foundational texts provided a plethora of equations and methodologies crucial for understanding convective and radiant heat transfer coefficients essential to the boiler's operation. These coefficients are vital for understanding the complex heat exchange dynamics between the heated flue gases and the water/steam inside the boiler. Accurately determining these coefficients is crucial as they form the basis for optimizing the boiler's efficiency.

In pursuit of precision, comparative analyses were conducted between criteria equations governing convective and radiant heat transfer, revealing discrepancies below 10%. Notably, this margin remained consistent across both convective and radiant heat transfer fluxes [5-8]. This convergence of results underscores the accuracy of these methodologies, suggesting their interchangeability in steam boiler thermal design. However, it's important to acknowledge that the choice of methodology may depend on the specific characteristics of the steam boiler and its operating parameters. Therefore, seeking guidance from experienced experts in the field is prudent to judiciously select the optimal thermal design methodology for the given steam boiler.

Integral to the calculations is determining the air excess ratio, a step of utmost importance. In line with established literature guidelines, the excess air ratio for the presented scenario was determined as 1.2 within the furnace and 1.25 at the exit. Similarly, the excess air ratio downstream of water heater economizer 4 was calculated as 1.345 and used for subsequent calculations. Likewise, additional computations were carried out to determine the excess air ratios post-evaporator, economizer 3, and economizer 1. Assuming a consistent growth rate, the computed excess air ratios were 1.2975 post-evaporator, 1.3925 after economizer 3, and 1.4875 following economizer 1 at the exit. Adhering to authoritative recommendations, an incremental increase of 0.2 was applied post cyclone and filter, resulting in an excess air ratio of 1.6875.

The culmination of comprehensive analysis and diligent energy balance computations led to the determination of the flame adiabatic temperature, which remained constant at 1324°C. Notably, there was a significant congruence with the temperature at the exit of the combustion chamber, aligning seamlessly with previous literature findings. Further calculations yielded a temperature of 366.3°C following economizer 4, while the exit temperature from the flue gas channel was measured at 181.5°C.

These temperatures were calculated for each unit in the steam boiler, ensuring that the heat transfer energy balance between the heat exchanger and flue gases was within +/-1%:

for the flue gases

$$\dot{Q} = \dot{b} \cdot (I'' - I'), \quad (1)$$

for the heat exchanger:

$$\dot{Q} = k \cdot F \cdot \Delta\theta, \quad (2)$$

and in case of water heaters also the comparison with water side was considered:

$$\dot{Q} = \dot{m}_w \cdot c_w \cdot \Delta t_w. \quad (3)$$

The comparison with provided data is presented in the following Fig. 1 and Fig.2. The average RMS between the calculated and the obtained data was found to be 33°C. The water feed temperature adopted according to the available data was 105.3°C and the temperature at the Economizer 4 outlet was 191.5°C.

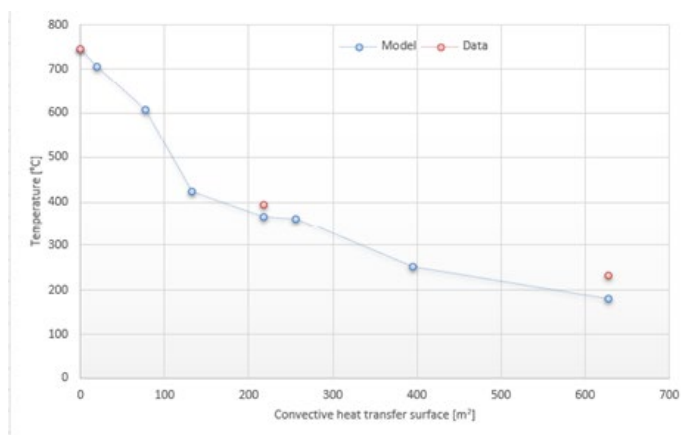


Figure 2. Comparison of temperature measurements and modelled temperatures

The calculated water temperature at the economizer outlet (evaporator inlet) was 193.6°C of steam with quality of 0.4%. The difference occurs because in the moment for which the data were presented the water drum was filled to the required level, so the water flow was larger and valued 18.6 t/h. This gives the total heat power of the economizer line 1 to 4 of 1911 kW, compared to the calculated 1990 kW, which gives the total difference of 4%.

3. Impact of Flue Gas Recirculation on Boiler Performance

The Flue Gas Recirculation (FGR) technique reintroduces a portion of the flue gas back into the combustion process. This action reduces the flame temperature and oxygen concentration, subsequently decreasing the formation of nitrogen oxides (NO_x) and other pollutants. However, while this method curtails emissions, it can also diminish combustion efficiency by contaminating the combustion air and reducing oxygen levels.

In accordance with the aforementioned methodology, calculations were conducted for power and efficiency considering FGR from the filters and at the boiler outlet, alongside a scenario without FGR. This analysis factored in the influence of reduced combustion efficiency without FGR. Table 1 illustrates the comparative results.

Utilizing the methodology outlined earlier, the results were juxtaposed between cases with and without FGR. As depicted in Table 1, the FGR scenario exhibited lower power output and efficiency, aligning with expectations. Remarkably, the power output difference was marginal, standing at only 1.5%. In contrast, the efficiency disparity exceeded 4%. Detailed temperatures from the combustion chamber and the outlet are provided in Table 2.

Table 1. Thermal power in [kW] and the efficiency of steam boiler in [%] for different scenarios

Location	FGR - (20%)	FGR - (10%)	Without FGR
Furnace	5670	6313	6946
Exh. manif.	660	470	605
Flue gas ch.	968	866	755
Evaporator	1625	1363	1146
Ecco 4	442	370	323
Turn chmb.	42	31	28
Ecco 3	977	844	750
Ecco 1-2	572	402	289
Net power	10996	10923	10842
Eff.	84.4%	86.6%	89.2%

4. NO_x Formation Analysis

The concentration of "thermal NO_x" hinges on the nitrogen and oxygen molar ratios and the combustion temperature. Combustion occurring well below 1,300°C results in notably reduced levels of thermal NO_x. To assess NO_x emissions, a two-pronged method was employed.

Initially, the Gaseq software was utilized, employing the Lagrange Method of Undetermined Multipliers. This facilitated the calculation of average temperatures within the combustion chamber [9,10]. Gaseq's approach, rooted in minimizing the Gibbs free energy of the system, enabled investigation into the composition at specific temperatures and pressures, crucially informing the thermal conditions governing combustion. This software provided insights into the equilibrium state/composition for main species (N₂, H₂O, O₂, CO₂), subsequently deriving NO_x thermal equilibrium at the chamber's average temperature.

Utilizing the Zeldovich mechanism at the combustion region, an estimation of NO_x concentration in the products becomes feasible. Simplifying this approach allows for deriving the rate of NO production [11,12,13,14]:

$$\frac{d[NO]}{dt} \approx 2 \cdot k_{f,1} \cdot [O] \cdot [N_2], \quad (4)$$

where the concentrations are in [mol·cm⁻³], T is the temperature in K, [O] is the concentration of atomic oxygen. Further, the formation of free oxygen atoms could be obtained as following [14]:

$$[O] = 3.97 \cdot 10^5 \cdot T^{-0.5} \cdot [O_2]^{0.5} \exp\left(\frac{-31090}{T}\right), \quad (5)$$

where the concentrations are in [mol·cm⁻³]. An alternative method to presented in the eq. (11) is presented by the following expression [14]:

$$[O] = 36.64 \cdot 10^5 \cdot T^{0.5} \cdot [O_2]^{0.5} \exp\left(\frac{-27123}{T}\right), \quad (6)$$

which generally leads to a bit higher partial O-atom concentration.

The methodology for determination of coefficients $k_{f,1}$ was chosen according to comparison between results of measurements presented in the [15] and coefficients presented in the paper [16]:

$$k_{f,1} = 1.473 \cdot 10^{13} \cdot \exp\left(\frac{-315000}{R_u T}\right), \quad (7)$$

and eq. (6).

The NO_x obtained by the model gives the production rate is in the range from 800, 21, and 18 mg_{NO_x} per MJ for 0, 10 and 20% of FGR respectively which is generally the same order of magnitude with IPCC specific emission factors [17,18]. On the other hand, method presented on the basis of Gaseq software gave the concentrations order of magnitude higher than expected.

Table 2. Adiabatic temperatures of the flame and flue gas temperature at the exit and NO_x production rate [17]

Exp no.	FGR (20%)	FGR (10%)	Without FGR
Adiab. temp. of the flame	1324	1501	1698
Flue gas temp. - chamber exit	745	746	736
Aver. flue gas temp. comb. cham.	1002	1071	1137
Flue gas temp. at the exit	182.0	166	170.0
NO _x prod. rate [kmol·m ⁻³ ·s ⁻¹]; Gaseq	5.32e-6	9.64e-6	16.1e-6
NO _x prod. rate [kmol·m ⁻³ ·s ⁻¹]; Model	1.86e-7	1.23e-7	4.9e-6

5. Conclusions

This study extensively investigated the thermal design and performance analysis of a steam boiler using corn straw biomass as fuel. The intricate dynamics of heat transfer within the boiler system were meticulously assessed, considering the unique characteristics of the fuel and operational parameters. Adopted thermal design methods, drawn from authoritative literature, facilitated the determination of essential convective and radiant heat transfer coefficients critical for enhancing boiler efficiency. Comparative analyses validated the interchangeability of criteria and radiant heat transfer coefficients in steam boiler thermal design.

Key technical details of the steam boiler were presented, encompassing critical parameters like thermal power, water/steam conditions, flue gas properties, and fuel composition, serving as the groundwork for subsequent analyses.

The investigation deeply explored the impact of Flue Gas Recirculation (FGR) on boiler performance. While FGR showed potential in reducing nitrogen oxide (NO_x) emissions, it was observed to possibly decrease combustion efficiency due to diluted combustion air and reduced oxygen levels. Calculations under different scenarios revealed a marginal decrease in power output (1.5%) and a more significant decline in efficiency (over 4%) with FGR implementation.

A comprehensive examination of NO_x formation employed both Gaseq software and the Zeldovich extended method. The Zeldovich method demonstrated higher accuracy and alignment with anticipated values, in contrast to Gaseq's consistently high emission predictions. A suggested NO_x emission target of approximately

300 mg/MJ was proposed, recommending a maximum FGR rate of around 10% to achieve this goal. The study emphasized the importance of empirical data for model validation, enhancing the reliability and practicality of the drawn conclusions.

In summary, this study highlighted the intricate relationships among heat transfer, combustion efficiency, and pollutant emissions in a biomass-fired steam boiler. The systematic approach to thermal design, performance analysis, and the assessment of FGR's impact on NO_x emissions provided comprehensive insights into the boiler's behavior, offering avenues for further enhancements in biomass combustion technology.

References

- [1] ***, Transparency Market Research, Biomass Boiler Market, <https://www.transparencymarketresearch.com/industrial-biomass-boiler-market.html>
- [2] Monks, P. *et al.*, The Potential Air Quality Impacts from Biomass Combustion, Department for Environment, Food and Rural Affairs; Scottish Government; Welsh Government; and Department of the Environment in Northern Ireland, UK, 2017.
- [3] Polonini, L. F., Petrocelli, D., Lezzi, A. M., The Effect of Flue Gas Recirculation on CO, PM and NO_x Emissions in Pellet Stove Combustion, *Energies*, 16 (2023), 2, pp. 1-16
- [4] Caposciutti P., *et al.*, An Experimental Investigation on the Effect of Exhaust Gas Recirculation in a Small-Scale Fixed Bed Biomass Boiler, *Chemical Engineering Transactions*, 92 (2022), pp. 397-402
- [5] LJ. Brkić, T. Živković, Termički proračun parnih kotlova. Mašinski fakultet Beograd. Beograd, Yugoslavia, 1987.
- [6] Bogner, M., Termotehničar, AGM, Beograd, Yugoslavia, 2004.
- [7] Đurić, V., Farmakoski, V., Parni kotlovi -deo I., Naučna Knjiga, Beograd, Yugoslavia, 1958.
- [8] Radojković, N., Ilić, G., Vukić, M., Stojanović, I., Živković, P., Termodinamika II. 2nd ed., Mašinski fakultet Niš, Niš, Serbia, 2007
- [9] Chris, M., Gaseq, <http://www.gaseq.co.uk/>, accessed on: April 25, 2023.
- [10] Tomić, M., *et al.*, The pollutant emissions assessment from personal vehicles in the republic of Serbia, Proceedings, 1st International conference on advances in science and technology – COAST 2022, Herceg Novi, Montenegro, 2022, pp. 248 – 254
- [11] Lalić, B., Poljak, A., Radica, G., Mišura, A., Low-Speed Marine Diesel Engine Modeling for NO_x Prediction in Exhaust Gases, *Energies*, 14 (2021) 15, pp. 4442
- [12] Wang, Y., Liu, J., Wang, L., Zaiguo, F.U., Weng, P., Thermal Calculations and NO_x Emission Analysis of a Micro Gas Turbine System Without a Recuperator, *Thermal Science*, 26 (2022) 5A, pp. 3817-3829
- [13] Weisser, G.A., Modelling of Combustion and Nitric Oxide Formation for Medium-Speed DI Diesel Engines: A Comparative Evaluation of Zero and Three-Dimensional Approaches, Ph. D. thesis, ETH Swiss Federal Institute of Technology, Zürich, Switzerland, 2001
- [14] ***, <https://www.afs.enea.it/project/neptunius/docs/fluent/html/th/node420.htm#Missaghi90>
- [15] Celtek, M.S., Pınarbasi, A., Investigations on Performance and Emission Characteristics of An Industrial Low Swirl Burner While Burning Natural Gas, Methane, Hydrogen-Enriched Natural Gas and Hydrogen as Fuels, *International Journal of Hydrogen Energy*, 43 (2018) 2, pp. 1194-1207
- [16] Parra, C.A.F., Heat Transfer Investigations in a Modern Diesel Engine, Ph.D. thesis, University of Bath Department of Mechanical Engineering, Bath, UK, 2008
- [17] Bhatt, A. *et al.*, Emission factors of industrial boilers burning biomass-derived fuels, *Journal of the Air & Waste Management Association*, 73 (2023) 4, pp. 241-257
- [18] ***, Netherlands Environmental Assessment Agency/Milieu en Natuur Plan Bureau, https://www.rivm.nl/bibliotheek/digitaaldepot/BOLK_I_biomass_Final.pdf

Determining Gas and Gas Mixture Viscosity Across Wide Temperature Ranges: Refinements and Predictive Models

*Jovica Podunavac^a, Nenad Tomić^b, Mladen Tomić^c, Aleksandar Anđelković^d,
Miroslav Kljajić^e, Predrag Živković^f*

^a Faculty of Technical Sciences, University of Novi Sad, RS, jovica.podunavac@gmail.com

^b Faculty of Technical Sciences, University of Novi Sad, RS, nenadtomic@yahoo.com

^c Faculty of Technical Sciences, University of Novi Sad, RS, mladen.tomic@uns.ac.rs

^d Faculty of Technical Sciences, University of Novi Sad, RS, aleksa@uns.ac.rs

^e Faculty of Technical Sciences, University of Novi Sad, RS, kljajicm@uns.ac.rs

^f Faculty of Mechanical engineering, University of Niš, RS, predrag.zivkovic@masfak.ni.ac.rs

Abstract This study delves into refining the ideal gas viscosity equation by introducing amendments that account for temperature variations and critical temperature ratios across diverse ideal gases. The investigation involves comparing the adjusted formula with empirical data obtained from various gases under extreme conditions, including ultra-critical temperatures and near-critical points like for water and carbon dioxide. The primary objective is to enhance the equation's accuracy and applicability. The research proposes novel modifications integrating a temperature-dependent dumping coefficient and a redefined temperature exponent. These adjustments aim to capture gas behavior across a wider spectrum of temperatures, pressures, and gas compositions. Building upon foundational works in gas dynamics and molecular theory, this study bridges the gap between theoretical formulations and empirical observations. To validate these modifications, empirical data from gases under diverse conditions, including ultra-critical temperatures and mixtures, were utilized. Notably, the study's focus extends to analyzing gases under extreme conditions, highlighting the formula's improved predictive capability, and assessing its performance against complex gas mixtures using software-generated data. The findings reveal that these proposed adjustments significantly enhance the equation's alignment with real-world observations. Specifically, the analysis showcases improved predictive accuracy, especially in extreme gas conditions, and promising results when evaluating complex gas mixtures. These modifications offer a more comprehensive framework for estimating viscosity across a broad range of gas types and conditions, thereby enhancing the predictive power of the ideal gas viscosity equation.

Keywords: Gas Mixture, Real Gases, Temperature-Dependent, Viscosity.

1 Introduction

Viscosity, a fundamental property governing the resistance of fluids to flow, holds paramount importance across of scientific and industrial domains. From facilitating efficient energy conversion processes in power generation to optimizing fluid dynamics in chemical engineering applications, understanding and accurately predicting viscosity is crucial for ensuring optimal performance and reliability. However, conventional viscosity equations, particularly those applicable to ideal gases, often encounter limitations when confronted with real-world complexities, necessitating refinements to enhance their predictive capabilities and broaden their applicability across diverse operating conditions. The theoretical foundation for estimating viscosity in ideal gas states is deeply rooted in the pioneering contributions of Chapman, who laid the groundwork in their work [1]. Bird's influential advancements further propelled the understanding of gas behavior and viscosity calculations [2].

Despite the efficacy of the ideal gas viscosity equation as a foundational tool, its practical applicability encounters inherent limitations, particularly in scenarios involving real-world complexities. Gases operating under extreme conditions or within intricate mixtures present challenges beyond the predictive capacity of conventional equations. Addressing these limitations requires a nuanced approach, prompting an in-depth exploration aimed at refining the ideal gas viscosity equation.

Precise characterization of fluid flows is essential and requires accurate estimations of bulk viscosity, particularly evident in systems like Rankine cycle power systems utilizing steam and those employing non-

aqueous working fluids. The latter proves advantageous in scenarios involving non-fossil fuel heat sources. Noteworthy studies, conducted by researchers focus on organic Rankine cycles, examining their efficiency and performance [3-7]. These investigations contribute to a comprehensive understanding of fluid flow behaviors in various applications, spanning traditional power systems to eco-friendly energy sources.

This study embarks on proposing innovative modifications to the existing equation to better account for variations in temperature and critical temperature ratios across diverse ideal gases. These proposed amendments seek to introduce a temperature-dependent coefficient and redefine the temperature exponent, intending to capture the intricacies of gas behavior over a broader spectrum of temperatures, pressures, and compositions.

The objective of this research is twofold: firstly, to bridge the theoretical and empirical gap between molecular-level interactions and macroscopic observations within gases, and secondly, to enhance the equation's accuracy and applicability in diverse real-world scenarios. By reconciling theoretical formulations with empirical data, this study aims to develop more precise viscosity equations, aligning them more closely with observed behaviors and intricate molecular dynamics within gases.

To validate the efficacy of these proposed modifications, data obtained from various gases under extreme conditions, including those operating at ultra-critical temperatures and near-critical points such as water and carbon dioxide, will be meticulously analyzed. Moreover, the assessment will extend to include complex gas mixtures, utilizing software-generated data to evaluate the versatility and predictive power of the modified equation.

The ultimate aspiration of this research lies in cultivating an enhanced ideal gas viscosity equation that can robustly estimate viscosity across a wide range of gas types and conditions, thereby refining predictive models and enabling more accurate estimations of viscosity in intricate real-world scenarios.

2 Fundamentals of Viscosity in Ideal Gases

Viscosity in ideal gases, as envisioned by kinetic and molecular theory, is intricately tied to the dynamic behavior of gas molecules. This theory posits that viscosity emerges from the complex interplay of various molecular properties. Central to this understanding are factors such as the average speed of gas molecules, the density of the gas, and the mean free path—the average distance traveled by a molecule between collisions.

The average molecular speed within a gas directly influences its viscosity. Higher speeds lead to increased molecular collisions and, consequently, greater resistance to flow. Density also plays a pivotal role, affecting the frequency of molecule-to-molecule interactions. Higher densities result in more frequent collisions, impacting the overall viscosity of the gas.

Additionally, the mean free path, representing the average distance traveled by molecules between collisions, is crucial. Shorter mean free paths imply more frequent collisions, increasing resistance to flow. At the molecular level, properties like the kinetic diameter of molecules and their individual masses further influence viscosity. Larger molecules or those with greater mass might exhibit different collision behaviors, impacting the overall viscosity of the gas.

Temperature stands as a critical parameter in this framework. Its influence on viscosity is multifaceted, altering molecular speeds and collision frequencies. Typically, as temperature increases, molecular speeds rise, potentially reducing viscosity due to heightened molecular motion.

The intricate relationship between these molecular properties and their effects on the macroscopic behavior of gases forms the foundation of understanding viscosity in ideal gases. Refining viscosity equations involves reconciling these molecular-level interactions with macroscopic observations, aiming to create more accurate models that encapsulate the behavior of gases across a broad spectrum of conditions

The relationship is commonly expressed through the kinetic theory equation for viscosity, which in its simplest form for an ideal gas can be represented as:

$$\mu = \frac{1}{3} \cdot \rho \cdot \bar{w} \cdot \bar{l}, \quad (1)$$

where:

- μ is the viscosity of the gas [Pa·s],
- ρ is the density of the gas [kg·m⁻³],

- \bar{w} is the average molecular speed [m/s],
- \bar{l} is the mean free path [m].

This equation highlights the fundamental factors contributing to gas viscosity as per the kinetic theory. The viscosity (μ) is directly proportional to the density (ρ) and the mean free path (\bar{l}), while it is also related to the average molecular speed (\bar{w}) of the gas molecules, or according to the kinetic and molecular theory in different form [7]:

$$\mu = \frac{2}{3} \cdot \frac{\sqrt{m_c \cdot k \cdot T}}{\pi^{1.5} \cdot d^2}, \quad (2)$$

where:

- m_c is the mass of the molecule [kg],
- k is the Boltzmann constant,
- d is the kinetic diameter of the molecule [m],
- T is the absolute temperature [K].

which can be written taking all the constants on one side as:

$$\mu = C \cdot \sqrt{T}. \quad (3)$$

Upon examining ideal gases operating significantly distant from their critical temperatures, notable disparities emerge between empirical measurements and theoretical predictions, as presented in the Fig 1. on the example of hydrogen.

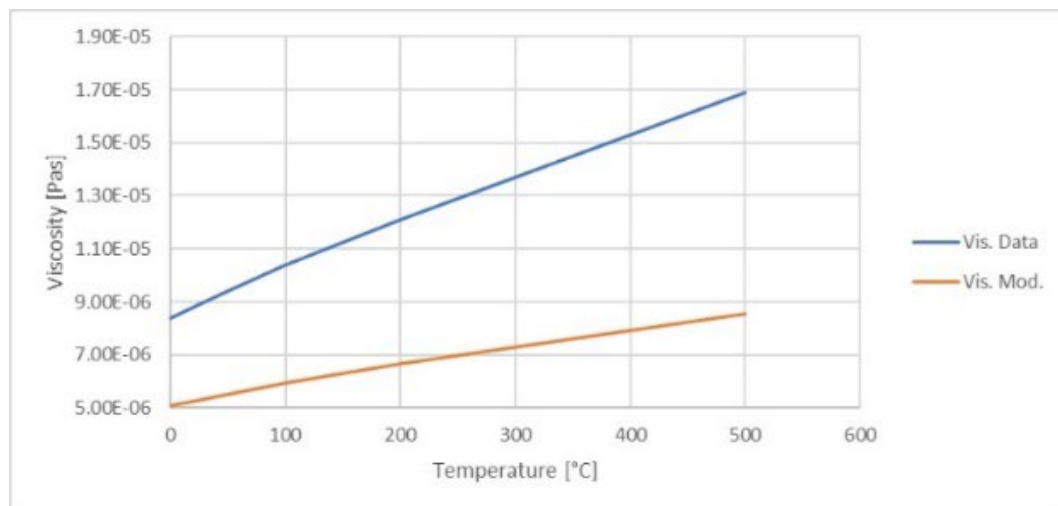


Figure 1 Comparison between modeled values and actual data for hydrogen

3 Temperature-Dependent Deviations and Model Refinements

The discrepancy between the ideal gas viscosity predicted by the kinetic theory and real-world data often necessitates adjustments to the temperature exponent in the viscosity equation [8,9]. Empirical observations reveal that a modification, typically involving a temperature exponent ranging between 0.50 to 0.7, is required to align theoretical predictions more closely with experimental results.

This adjustment acknowledges that the standard kinetic theory-based viscosity equation, which assumes a temperature exponent of 0.5, might not sufficiently encapsulate the intricate temperature dependence observed in real gas behavior. The need for a higher temperature exponent suggests that molecular interactions and collision dynamics within gases, especially under varying temperatures, might deviate from the simplistic assumptions inherent in the classical kinetic theory formulations. Thus, modifying the temperature exponent serves as a means to bridge the gap between theoretical predictions and observed real-world data, refining the equation to better represent the complexities of gas behavior across a broader temperature range. The empirical evidence strongly advocates for an adjustment in the temperature exponent to 0.583 to better harmonize theoretical predictions with experimental data under these conditions, as illustrated with Fig. 2 and recalculated viscosity of hydrogen.

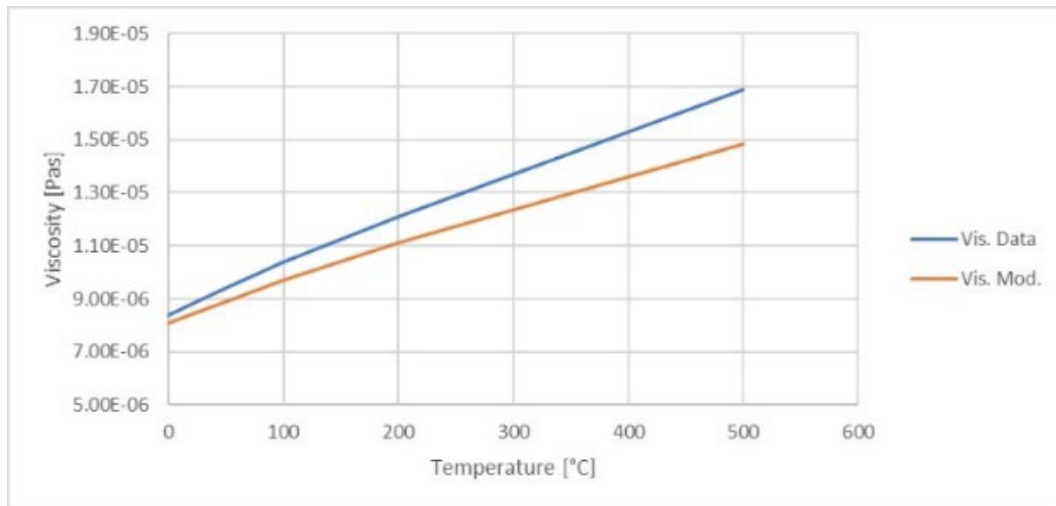


Figure 2 Comparison between modeled values with adjusted exponent and actual data for hydrogen

The comprehensive analysis conducted across a diverse array of ideal gases and mixtures has showed trends in viscosity behavior. Comparative assessments involving literature data and results generated through professional software across gases including methane, hydrogen, nitrogen, oxygen, flue gases, methane-air mixtures, and carbon dioxide have unveiled pivotal insights into viscosity variations relative to temperature ratios concerning critical temperatures.

The analysis highlights a critical divergence from conventional kinetic theory assumptions, particularly for temperature ratios lower than 5 as illustrated in Fig. 3.

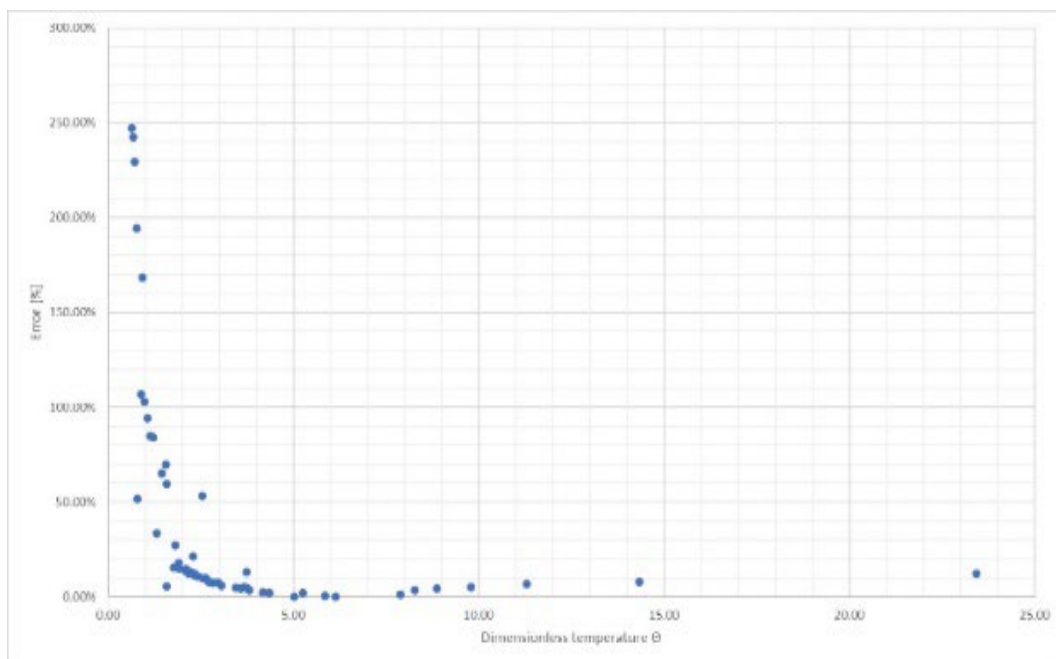


Figure 3 Deviation as a function of dimensionless temperature

Moreover, the observed equivalence between mass and kinetic diameter, when compared against mol-averaged values within these mixtures, implies a coherent behavior in viscosity calculations. This alignment between mixed gases and averaged properties suggests a potential avenue for simplification in modeling gas mixtures, showcasing the viability of using averaged values to achieve accurate viscosity predictions:

$$\mu = \frac{2}{3} \cdot \frac{\sqrt{m_{cm} \cdot k}}{\pi^{1.5} \cdot d_m^2} \cdot T^{0.583}, \quad (4)$$

where for the mixtures of n components:

$$m_{cm} = \sum_{i=1}^n r_i \cdot m_{ci},$$

$$d_m = \sum_{i=1}^n r_i \cdot d_i,$$
(5)

where r_i represents the molar/volume share of the i -th component in ideal gas. The results for some ideal gases mixtures gases are presented in Fig. 4 and 5.

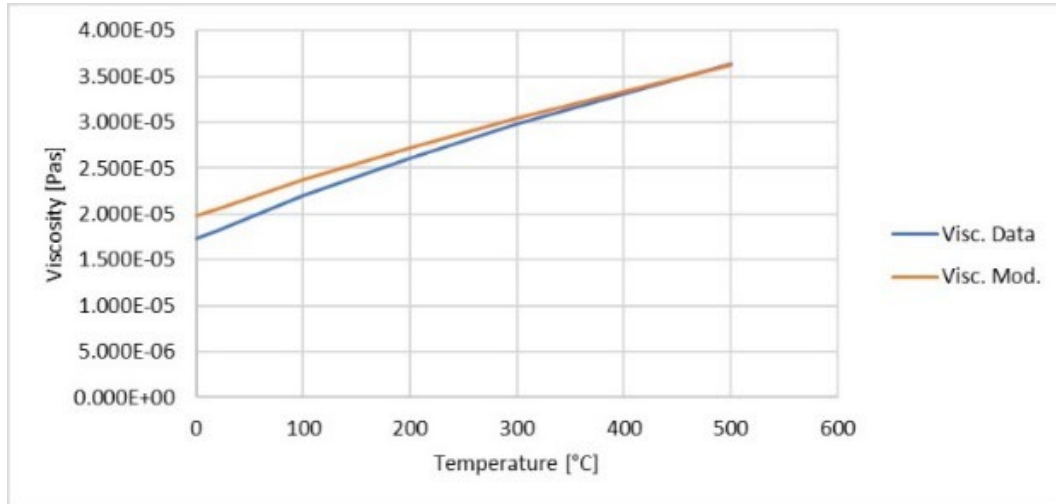


Figure 4 Comparison between modeled values with adjusted exponent and actual data for mixture – air

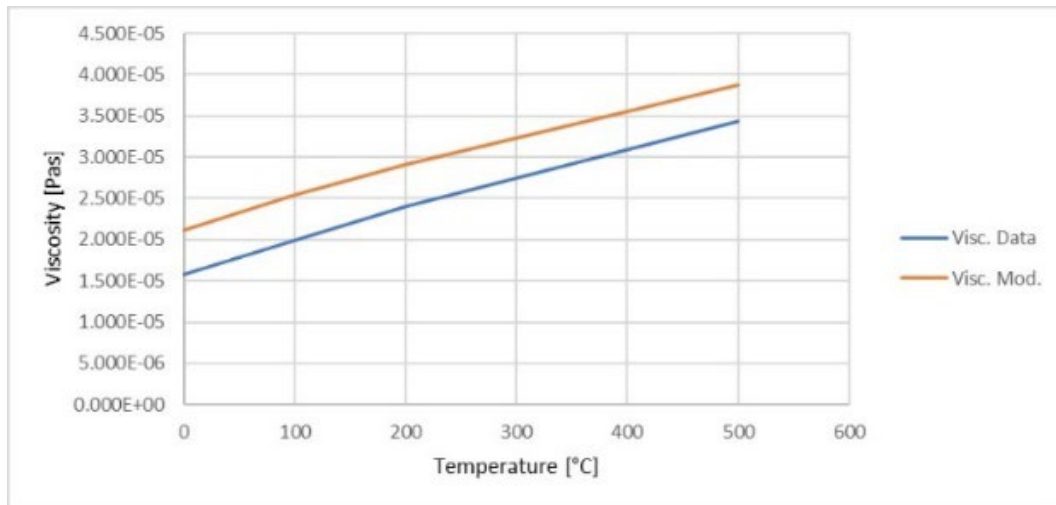


Figure 5 Comparison between modeled values with adjusted exponent and actual data for mixture – flue gases

The comparisons for ultracritical gasses show good agreement, while for gases close to critical point for ratio under 4 are significant differences with error less than 11% and average error under 7%., while for the gasses as carbon dioxide the difference was significant. Also, for critical temperature ratio over 20 the error starts rising again.

Expanding the applicability of the gas viscosity determination equation to near-critical regions, as well as to make an additional correction, a corrective coefficient has been introduced, accounting for the proximity to the critical temperature as a factor influencing viscosity. The correction factor is equal to:

$$\beta = -1.1018 \cdot 10^{-41.01655} \cdot \frac{\Theta^{1.83565}}{1.0223128 + \Theta^{1.83565}},$$
(6)

where $\Theta = \frac{T}{T_c}$, where the T_c represents a critical temperature, thus

$$\mu = \beta \cdot \frac{2}{3} \cdot \frac{\sqrt{m_{ce} \cdot k}}{\pi^{1.5} \cdot d_e^2} \cdot T^{0.583}. \quad (7)$$

The critical temperature of a mixture refers to the highest temperature at which the liquid and gas phases of the mixture can coexist in equilibrium. It's a characteristic property of the mixture and is influenced by the individual critical temperatures of its components as well as their proportions. To estimate the critical temperature of this mixture, one can use a simple mixing rule like the arithmetic average:

$$T_{cm} = \sum_{i=1}^n r_i \cdot T_{ci}. \quad (8)$$

The results show good agreement between predicted viscosity of gases and gas mixtures for temperatures ratio of 2.0., but for most gases which are considered ideal even closer to ratio of 1.5. The general correlation between model and literature values is presented in the Fig.6.

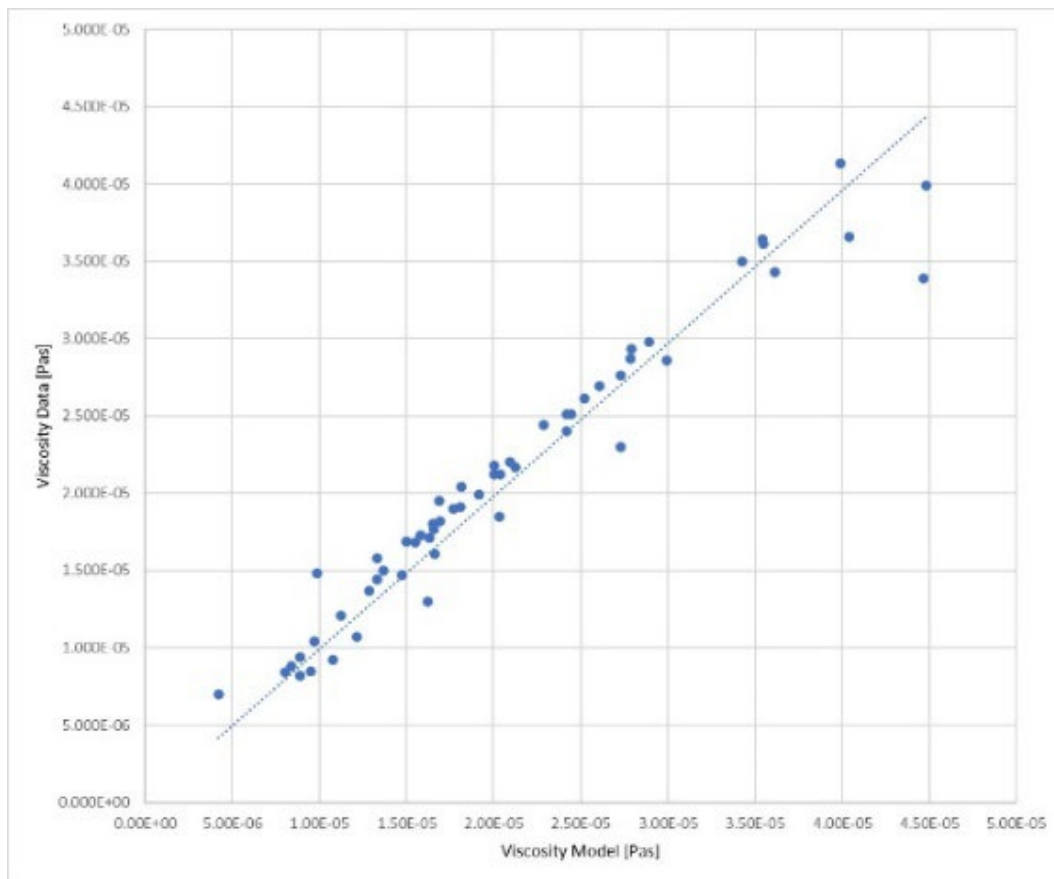


Figure 6 Correlation between modeled values and actual data

4 Conclusion

A simple method has been developed for calculating the viscosity of a mixture of gases. The development relies on additive contributions of molecule masses and its volume fraction momentum fraction as the primary compositional variable. A single global empirical constant is used in this model, which can be easily applied to near critical regions of fluids. The only data required by this equation to calculate viscosity for a known composition mixture are the molecular weights and critical temperatures of the pure components at the given temperature and pressure. For most binary gas mixtures, this equation performs at least as well as the best available method using comparable data.

Collectively, these findings underscore the imperative for refined adjustments in viscosity equations to accommodate diverse temperature dependencies, particularly in gases operating at elevated temperature ratios. Additionally, the implications of equivalences observed in mixed gases and averaged properties highlight the potential for streamlined modeling approaches in complex gas mixtures. This research significantly contributes

to advancing our understanding of viscosity estimations across a wide spectrum of gases and mixtures under diverse conditions, paving the way for enhanced predictive models in fluid dynamics and engineering applications.

References

- [1] S. Chapma, T. G. Cowling, *Mathematical Theory of Non-uniform Gases*, Cambridge university press, Cambridge, UK, 1991
- [2] G. A. Bird, *Molecular Gas Dynamics and the Direct Simulation of Gas Flows*, Clarendon, Oxford, UK, 1994
- [3] M. S. Cramer, Numerical estimates for the bulk viscosity of ideal gases, *Physics of Fluid*, 24 (2012), pp. 066102
- [4] B. T. Liu, K. H. Chien, and C. C. Wang, Impact of working fluids on the organic Rankine cycle for waste heat recovery, *Energy*, 29 (2004), pp. 1207-1217
- [5] D. Wei, X. Lu, Z. Lu, and J. Gu, Analysis and optimization of the performance of the organic Rankine cycle (ORC) for waste heat recovery, *Energy Convers. Manage.*, 48 (2007), pp. 1113-1119
- [6] B. Saleh, G. Koglbauer, M. Wendland, and J. Fischer, Working fluids suitable for low-temperature organic Rankine cycles, *Energy*, 32 (2007), pp. 1210-1221
- [7] A. Shuster, S. Karellas, and R. Aumann, Potential efficiency optimization in supercritical organic Rankine cycles, *Energy*, 35 (2010), pp. 1033
- [8] N. Radojković, G. Ilić, M. Vukić, I. Stojanović, P. Živković, *Termodinamika II*, 2nd ed., *Mašinski fakultet Niš*, Niš, Niš, Serbia, 2007.
- [9] ***, <https://www.engineeringtoolbox.com/> (as accessed on 01.11.2024)
- [10] M. Tomić, M. Vukić, P. Živković, B. Milutinović, *Zbirka zadataka iz termodinamike sa osnovama prenosa toplote*, *Fakultet tehničkih nauka Novi Sad*, Novi Sad, Serbia, 2021

A Model of Two-Phase Flow in Pneumatic Transport of Powder Material

Saša Milanović^a, Veljko Begović^b, Miloš Jovanović^c, Boban Nikolić^d, Živan Spasić^e, Petar Miljković^f

^a Faculty of Mechanical Engineering, Niš, RS, sasa.milanovic@masfak.ni.ac.rs

^b Faculty of Mechanical Engineering, Niš, RS, veljko.begovic@masfak.ni.ac.rs

^c Faculty of Mechanical Engineering, Niš, RS, milos.jovanovic@masfak.ni.ac.rs

^d Faculty Mechanical Engineering, Niš, RS, boban.nikolic@masfak.ni.ac.rs

^e Faculty Mechanical Engineering, Niš, RS, zivan.spasic@masfak.ni.ac.rs

^f Faculty Mechanical Engineering, Niš, RS, petar.miljkovic@masfak.ni.ac.rs

Abstract: The paper presents a numerical simulation of two-phase turbulent flow in straight horizontal channels with a square cross-section, with the dimensions of 200x200 mm and the length of $80D_h$. The flow of solid particles of quartz, flour and ash using air was chosen for the two-phase flow simulation. During the modelling of the flow, the transported particles were observed as spherical. The turbulence was modelled using a full Reynolds stress model, while the complete model was used to examine turbulent stresses and turbulent temperature fluxes. The same initial flow conditions and a single uniform grid were employed in all numerical experiments. The fineness of the numerical grid was tested during the simulation, and the paper shows the results of the numerical grid of the highest resolution beyond which the fineness did not affect the obtained results. The paper also presents the change in the velocity of the transported material by air in the cross-section and along the channel.

Keywords: Computer Simulation, Pneumatic Transport, Solid Particles, Channel, Two Phase Flow.

1. Introduction

Pneumatic transport is the transport of loose, granular or powder material mainly by using the flow of air or some other gas. This transport is made possible by the fact that aerodynamic forces are exerted on solid particles by the air flow, and when such forces become sufficiently strong at certain air velocities they can lift and move the transported material particles. Pneumatic transport is characterized by a chaotic motion of particles of material full of collisions, however, the motion still possesses a basic component of velocity along the channel that is lower than the velocity of the transporting air.

There are numerous examples of two-phase flows of the air-solid type in channels with a non-circular cross-section in engineering. The most common instances are found in systems of pneumatic transport of granular and powder material, air conditioning and ventilation systems, process and energy systems, etc. Two-phase flows comprise a multitude of flow phenomena that stem from interactions between the gas and the solid phase. These flows play a very important role in the whole mechanism of matter, impulse and heat transport in a channel and its surroundings. High intensity impulse transfer in the channel yields high gradients of transversal velocities in the cross-sectional plane.

Besides the main flow along the channel, in horizontal channels with a square cross-section secondary flows are also induced in the cross-sectional plane of the channel during a developed turbulent flow. A secondary flow known as secondary flow of the first kind occurs due to centrifugal forces in both laminar and turbulent flow in channels of arbitrary cross-sections. In straight channels with a square cross-section, and only in the completely developed turbulent flow mode, a secondary flow known as secondary flow of the second kind is induced in the cross-section of the channel. Secondary flows are a result of transversal gradients of primary shear stresses, and they produce increased shear stresses, significantly affecting the intensity of heat transfer from the fluid to the wall of the channel and vice versa. Gas-particle multiphase flow, which may include a solid or liquid particle, is a significant phenomenon in natural and industrial engineering. The interaction between the particles and the gas is difficult to establish because of the diversity and complexity of problems involved. Numerical simulation is a powerful tool for examining the characteristics of gas-particle multiphase

flow thanks to the development of computers. Three models, namely, Euler-Euler two-fluid model (TFM), Euler-Lagrange discrete particle model (DPM), and Lagrange-Lagrange pseudo-particle model, are widely used in these numerical simulations.

The inability of TFM to trace the path of individual particles was the main reason behind the development of Euler-Lagrange DPM. The soft-sphere model or discrete element model (DEM) is a granular dynamics simulation technique proposed by Cundall and Strack [1] and first presented in the open literature. Subsequently, a two-dimensional (2D) soft-sphere approach was applied to gas-fluidized beds [2]. On the other hand, the hard-sphere approach assumes that the interactions between particles are pair-wise additive and instantaneous. Campbell and Brennen [3] first studied granular systems using hard-sphere discrete particle simulation (DPM). Tanaka et al. [4] introduced DSMC (Direct Simulation Monte Carlo) to calculate particle collisions in gas–solid flows. Numerical simulations were performed for a dispersed gas–solid flow in a vertical channel [5] and fluidized beds using the DSMC method. This method is suitable for large-scale simulations. Paper [6] presented a modified model for the prediction of the erosion rate in pipe flows, on the basis of the simulation of fluid fluctuating velocities using the Discrete Random Walk model. Pneumatic conveying of spherical particles in a horizontal channel with a rectangular cross-section was numerically simulated and presented in [7].

This paper employs a full Reynolds stress model of turbulence, which implies that each of the components of turbulent stress is calculated from its own transport differential equation. These equations are modelled and not exact [8]. The modelled equations were obtained by keeping the correlation of the second order in its original form, while the members that contain correlations of the higher order were modelled using the gradient method.

2. Physical model

Turbulence is the most important factor and the cause of all the difficulties in the processes of matter, momentum and heat transport. It is a non-stationary, non-linear, irreversible, stochastic and three-dimensional phenomenon [9,10]. For a fully developed turbulent flow, in the case of a stationary and incompressible current, the transport equation of the vorticity component perpendicular to the cross-sectional plane Ω_1 [11], has the following form:

$$\underbrace{U_2 \frac{\partial \Omega_1}{\partial x_2} + U_3 \frac{\partial \Omega_1}{\partial x_3}}_{A_1} = \underbrace{\frac{\partial^2}{\partial x_2 \partial x_3} (u_3 u_3 - u_2 u_2)}_{A_4} - \underbrace{\left(\frac{\partial^2}{\partial x_3^2} - \frac{\partial^2}{\partial x_2^2} \right) u_2 u_3}_{A_5} + \nu \underbrace{\left(\frac{\partial^2 \Omega_2}{\partial x_2^2} + \frac{\partial^2 \Omega_1}{\partial x_3^2} \right)}_{A_6} \quad (24)$$

This implies that the difference between the turbulent members A_4 and A_5 , which are of the same order of magnitude as the convective member A_1 , stems directly from the mechanism generating secondary flow, that is, secondary flow is a consequence of the transverse gradients of the primary shear stresses in the region of the channel vertices. Thus it is necessary to model all Reynolds stresses as accurately as possible to provide a realistic simulation of secondary flow of the second kind in a straight channel with a square cross-section during a developed turbulent flow.

Two-phase flows are characterized by numerous interconnected complex phenomena that occur due to the mutual influence between the phases. While modelling such flows, one has to use a combined approach to solve the flow field. The Euler approach (the concept of continuum) is adopted to solve the gas flow, while the Lagrange approach (the concept of tracking the particle trajectories) is applied in solving the solid phase. An iterative task-solving procedure yields the interphase interaction of the gas and the solid phase.

On the one hand, the mathematical model of the gas phase is defined under the following assumptions: the flow is stationary, three-dimensional, incompressible, isothermal and chemically inert. On the other, the mathematical model of the solid phase is defined under the following assumptions: particles are of various dimensions, particles do not change their mass while travelling through the channel, particles have a constant temperature through the channel, the influence of particle collisions is neglected, particles lose a certain level of impulse upon hitting the channel walls and internal obstacles, particles move stochastically.

3. Mathematical model of the gas phase

The mathematical model is created for a three-dimensionally fully developed turbulent flow in a straight horizontal channel with a square cross-section. The turbulent flow is assumed to be stationary and incompressible, while the channel walls have a constant temperature. With the volumetric forces of gravity neglected, the general equation of conservation of impulse, matter and energy for the gas phase correlates to the equation of field conservation for a single-phase flow, with the addition of the interphase member, thus obtaining the following form [8,11]:

$$\frac{\partial}{\partial t}(\rho\Phi) + U_j \frac{\partial}{\partial x_j}(\rho\Phi) - \frac{\partial}{\partial x_j} \left(\Gamma_\Phi \frac{\partial \Phi}{\partial x_j} \right) = S_\Phi + S_\Phi^{IF} \quad (25)$$

Based on the adopted assumptions of the physical model, the averaged equations of conservation of matter, impulse and heat have the following forms:

- the continuity equation:

$$\frac{\partial U_j}{\partial x_j} = 0 \quad (26)$$

- the equation of motion:

$$U_j \frac{\partial U_i}{\partial x_j} - \frac{\partial}{\partial x_j} \left(\nu \frac{\partial U_i}{\partial x_j} \right) = -\frac{1}{\rho} \frac{\partial P}{\partial x_j} - \frac{\partial \overline{u_i u_j}}{\partial x_j} + S_{U_i}^{IF} \quad (27)$$

- the energy equation:

$$U_j \frac{\partial T}{\partial x_j} - \frac{\partial}{\partial x_j} \left(a \frac{\partial T}{\partial x_j} \right) = -\frac{\partial \theta u_j}{\partial x_j} \quad (28)$$

3.1 Model of Reynolds stresses

The starting point of the stress model of turbulence is a transport equation that defines the dynamic of Reynolds stresses [11]. The stress model of turbulence presumes the simultaneous solution of the transport equation of Reynolds stresses and the motion equation in the Reynolds averaged form. The exact form can only deal with particular components of the transport equation for Reynolds stresses, with the rest of the components being merely correlations to be modelled in the function of the available dependently variable values [11,12]. These values are as follows: averaged velocity, tensor of turbulent stresses, and velocity of dissipation of turbulent kinetic energy.

By modelling the components in the transport equation that defines the dynamics of Reynolds stresses, one can obtain the closed form of the transport equation for Reynolds stresses:

$$U_k \frac{\partial \overline{u_i u_j}}{\partial x_k} = \frac{\partial}{\partial x_k} \left(C'_g \frac{k}{\varepsilon} \overline{u_k u_n} \frac{\partial \overline{u_i u_j}}{\partial x_n} \right) + P_{ij} + \Phi_{ij,1} + \Phi_{ij,2} + \Phi_{ij,z} - \frac{2}{3} \delta_{ij} \varepsilon \quad (29)$$

The stress model for Reynolds stresses (6) is closed by an additional transport differential equation for the dissipation of turbulent kinetic energy ε :

$$U_k \frac{\partial \varepsilon}{\partial x_k} = \frac{\partial}{\partial x_k} \left(C_\varepsilon \frac{k}{\varepsilon} \overline{u_k u_j} \frac{\partial \varepsilon}{\partial x_j} \right) + \frac{\varepsilon}{k} (C_{\varepsilon 1} P - C_{\varepsilon 2} \varepsilon) \quad (30)$$

where the members in equations (6) and (7) are determined by modelling [13].

3.2 Model of turbulent temperature fluxes

Modelling the components in the transport equation for turbulent temperature fluxes leads to the following transport equation:

$$U_k \frac{\partial \overline{\theta u_i}}{\partial x_k} = \frac{\partial}{\partial x_k} \left(C_\theta \frac{k}{\varepsilon} u_k u_j \frac{\partial \overline{\theta u_i}}{\partial x_j} \right) + P_{\theta i} + \Phi_{\theta i} + \Phi_{\theta i, z} + \varepsilon_{\theta i} \quad (31)$$

where the members in equation (8) are determined by modelling [13].

4. Mathematical model of the solid phase

In the vast majority of technical processes, the presence of particles in flows produces aerodynamic resistances that condition the change in the momentum of both phases. The mathematical model of the solid phase is based on the Lagrange concept of task solution, and it gives a more realistic picture of the particle motion in the air. The position of particles is determined by solving the equation of motion:

$$\frac{dx_p}{dt} = \tilde{U}_p \quad (32)$$

The current velocity vector of solid particles \tilde{U}_p is determined from the equation of the solid phase impulse:

$$m_p \frac{d\tilde{U}_p}{dt} = \mathfrak{R}_p (U - \tilde{U}_p) + m_p b g - V_p \nabla P \quad (33)$$

where \mathfrak{R}_p is the function of the resistance of a solid particle and it is determined using the expression:

$$\mathfrak{R}_p = 0,5 \rho A_p C_D |U - \tilde{U}_p| \quad (34)$$

where C_D is the coefficient of resistance for spherical particles and Reynolds number $Re < 10^5$ [13].

When considering two-phase turbulent flows of the gas-solid particles type, the basic problem lies in the treatment of the mutual exchange of momentum, energy and mass between the phases, bearing in mind that the particles travel from one vortex to another. The presence of disperse phase during the modelling of the two-phase turbulent flow causes the occurrence of additional sources of momentum, energy and mass in the gas phase equations. The interphase components of interaction are determined on the basis of the division of the flow field into numerical cells, which are each taken as a control volume.

The mathematical model of the continual phase draws upon the models developed for a pure fluid – air, along with the correction caused by the presence of solids. When a particle flows through a numerical cell, the interphase interactions of changing the impulse, energy or mass occur. This means that if a particle moves with a speed larger than its surroundings, the particle slows down because of the interactions of phases, while the velocity of the gas phase in the surroundings of the solid particle increases. Interactions between phases are defined by interphase components, which are added in the equation of motion of the gas phase. The interphase components of interactions describe the changes in the momentum of the transported material particles, that is, the change in the momentum of the gas phase due to the presence of solid particles. The interphase component of the interaction in equation (4) represents the force of resistance to the motion of the particle in the air flow. It is assumed that the forces perpendicular to the trajectory of particles are balanced. This means that the interaction between the phases is given by the intensity of forces acting in the direction of particle motion, and the interphase component of the interaction is determined by integrating equations of particle motion:

$$m_p \frac{d\tilde{U}_p}{dt} = S_{U_i}^{IF} \quad (1)$$

Equation (12) is integrated for each numerical cell, taking into account the Lagrange time step so as to integrate each numerical cell.

5. Numerical model

When considering two-phase flows the basic problem comes from the change in the momentum, energy and mass of particles as they pass through a certain segment of the flow field. A change in the momentum of

particles while they are passing through the observed numerical control volume is considered the source or sink of the momentum of the gas phase. In this case, the mathematical model of the gas phase is set for the single-phase flow with the correction related to the presence of particles.

To solve the problem, a two-phase air-solid particle turbulent flow is observed in a straight channel with a square cross-section, and with the side dimensions of 200x200 mm. A channel of $80D_h$ in length, which amounts to 18 m, is taken to form a fully developed turbulent flow. The non-uniform numerical grid is chosen, causing the numerical cells to be of various sizes. The central numerical cells have larger surfaces, while the cells closer to the channel walls and vertices have smaller surfaces. The mass flow of solid particles through the cross-section of the channel is taken as a partial flow in the numerical cells, proportional to the surface of the cells. The partial flows differ due to the fact that the numerical cells are of different surfaces. In such a case, a balanced distribution of transported particles is present along the entire cross-section. In the simulation, the influence of the fineness of the numerical grid was examined for three different numerical grids (30x30x180, 35x35x180, and 40x40x180). The paper presents the results of the highest resolution of the numerical grid above which the fineness of the grid did not affect the obtained results, with the number of cells in the $x^1 \equiv x$, $x^2 \equiv y$, and $x^3 \equiv z$ directions being 40x40x180, respectively.

To solve the problem, the following particles were transported: quartz particles of 0.5 mm in diameter and 2500 kg/m³ in density, ash particles of 0.14 mm in diameter and 1800 kg/m³ in density, and flour particles of 0.20 mm in diameter and 1410 kg/m³ in density. The same initial particle velocity at the entrance to the channel of 2.8 m/s was adopted, matching the flying velocity of quartz particles. Besides defining the initial velocities of the transported particles, it was necessary to define the velocity of air at the entrance, which amounted to 12÷22 m/s for transporting quartz particles, 12÷20 m/s for ash particles, and approximately 20 m/s for flour particles [14]. To solve the problem, the adopted air velocity at the entrance was 22 m/s, with the pressure of 1 bar and 1,2 kg/m³ in density for all three models of two-phase flow.

The isothermal, stationary and three-dimensional flow of the transporting air was observed to simulate the two-phase turbulent flow, assuming that the mass and the temperature of the solid particles, which move stochastically along the channel, did not change during the transport process. In addition, the influence of mutual collisions of particles and collisions of particles with the walls were neglected.

The solution of the mathematical model was performed in the iterative manner until the solution convergence of 0.1% was reached. The iterative procedure comprised four successively repeated steps. In the first iterative step only the airflow field was considered, and the gas phase conservation equations were calculated as if the dispersed phase was absent. The integration conservation equation of the gas phase was carried out as if the existence of particles did not influence the gas phase flow field. The presence of the dispersed phase caused the appearance of additional terms in the gas phase momentum equation, as the sink term and the source term in the solid phase, due to the interaction between the gas and the solid phase. In the second iterative step the computed gas phase flow field was “frozen” with respect to time, and the forces by which the gas phase flow field acted on solid particles was calculated. Thus, the trajectories of solid particles were computed in the “frozen” gas phase flow field. On the basis of the obtained trajectories of the particles, it was possible to determine the interphase interaction sink term in the momentum equation of the gas phase and the source term in the solid phase momentum equation. In the next, third iterative step the gas phase flow field was again calculated but this time taking into account the interphase interaction sink term obtained on the basis of the calculated trajectories of the solid phase, which was temporarily “frozen”. The second and third iterative steps were repeated until the desired solution convergence criteria of 0.1% was achieved.

6. Results and discussion

For the sake of a comparison between the results of single-phase and two-phase flow, the numerical simulations of single-phase gas flow and two-phase flow were carried out for the same boundary conditions of the gas phase flow but for several different solid particles dispersed in the gas flow, with the mesh density kept unaltered. The dominant parameters that influence the secondary flow of the second kind are turbulent shear stresses in the channel cross-section, and they were chosen as the parameters for the two-phase flow comparison with different solid particles [13].

When the Reynolds equations are averaged in time, correlations of fluctuation parts of different physical quantities occur, and they are modelled in the function of the available dependently variable values: averaged velocity, tensor of turbulent stresses and velocity of dissipation of turbulent kinetic energies, which define the

mathematical model. The Reynolds stress model assumes that each component of Reynolds stress is determined from its own modelled differential equation. The mathematical model observes the motion of the spherical particles of the recommended values with equivalent diameters and densities. Since the chosen numerical grid is not uniform, the total mass flow given at the entrance fits the partial mass flows in the cells proportionally to the size of the cells. For the central numerical cells, where the sizes are larger, the flows are also larger, while the partial flows of the cells in the vicinity of the walls are lower, proportionally to the size of the cells.

The formation of the secondary flow of the second kind in a straight channel with a square cross-section during the fully developed turbulent flow causes the occurrence of the gradients of Reynolds stresses. The turbulent tangential stresses in the transversal plane of the channel are the dominant parameters that influence the secondary flow of the second kind. These members exert the effect of turbulent stresses on the production and destruction of turbulent vorticity.

Two-phase flows are generally characterized by numerous mutually related phenomena, as the consequences of multicomponentness of a mixture. The transported material particles move because of the action of the resistance reaction force. Besides said force that acts in the direction of the particle motion, the particles are also subjected to the forces perpendicular to the direction of their movement. If the vertical forces are not balanced, the disturbance of the particle motion may occur, and it can cause the precipitation and even the discontinuation of the transport. Here it is assumed that the vertical forces are balanced, which prevents the disturbance of the particle motion. The numerical simulations yielded a reliable stress model of turbulence and adequate interphase members of interaction in the two-phase flow systems.

Figures 1b, 2b and 3b show the distribution of particles (partial mass flow) at the entrance to the channel, while figures 1a, 2a and 3a show the particle trajectories. It can be seen that particles fill the entire cross-section of the channel from its entrance to its exit, which is how their transport is achieved. Figures 1c, 2c and 3c show the change in the velocity of particles in the cross-section, in the middle of the channel, from which one can observe that the velocity of central particles is greater than the velocity of particles closer to the walls and vertices of the channel. Figures 1d, 2d and 3d show the change in the velocity of particles along the channel as follows: the blue curve for central particles and the red curve for particles closer to the channel wall.

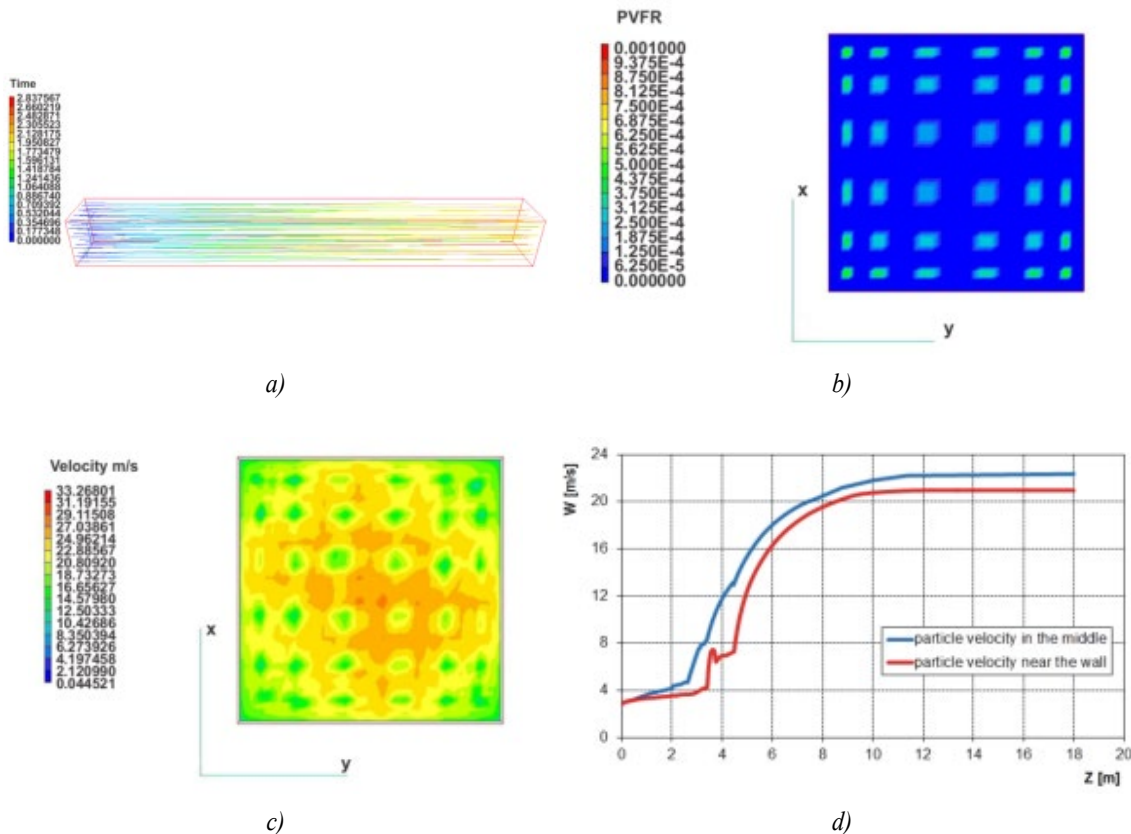


Figure 1. Motion of quartz particles

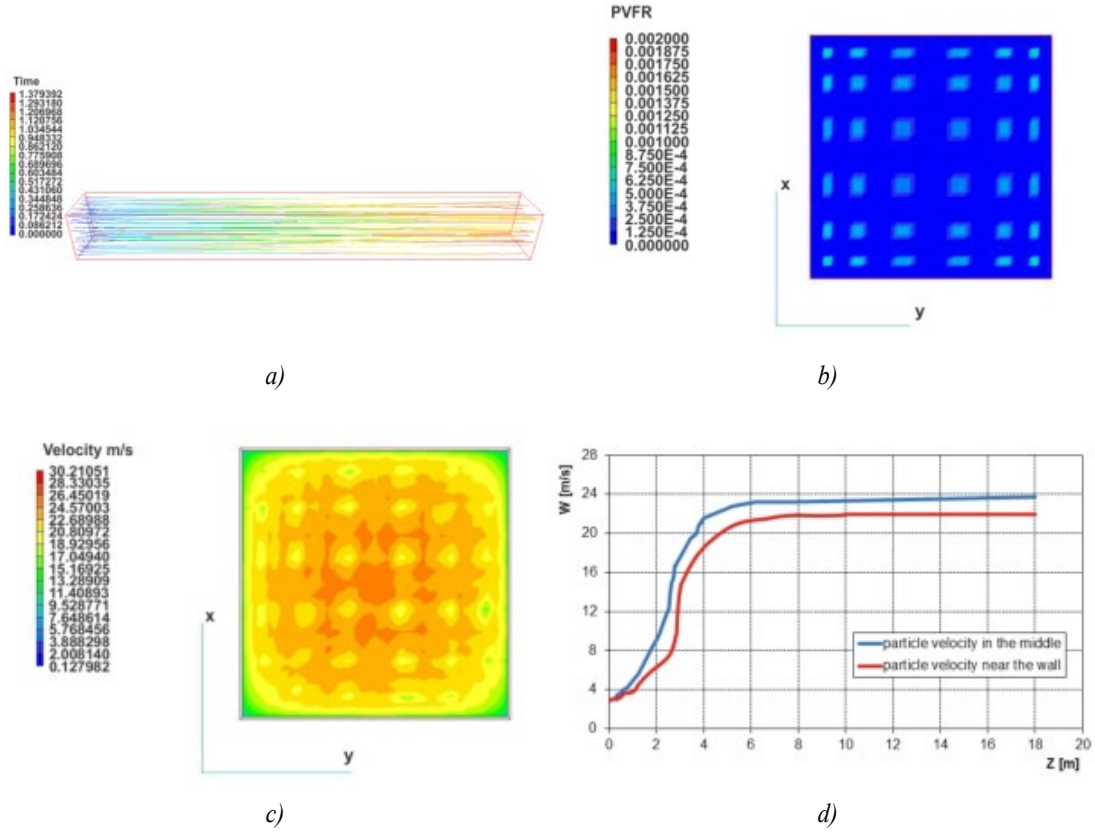


Figure 2. Motion of ash particles

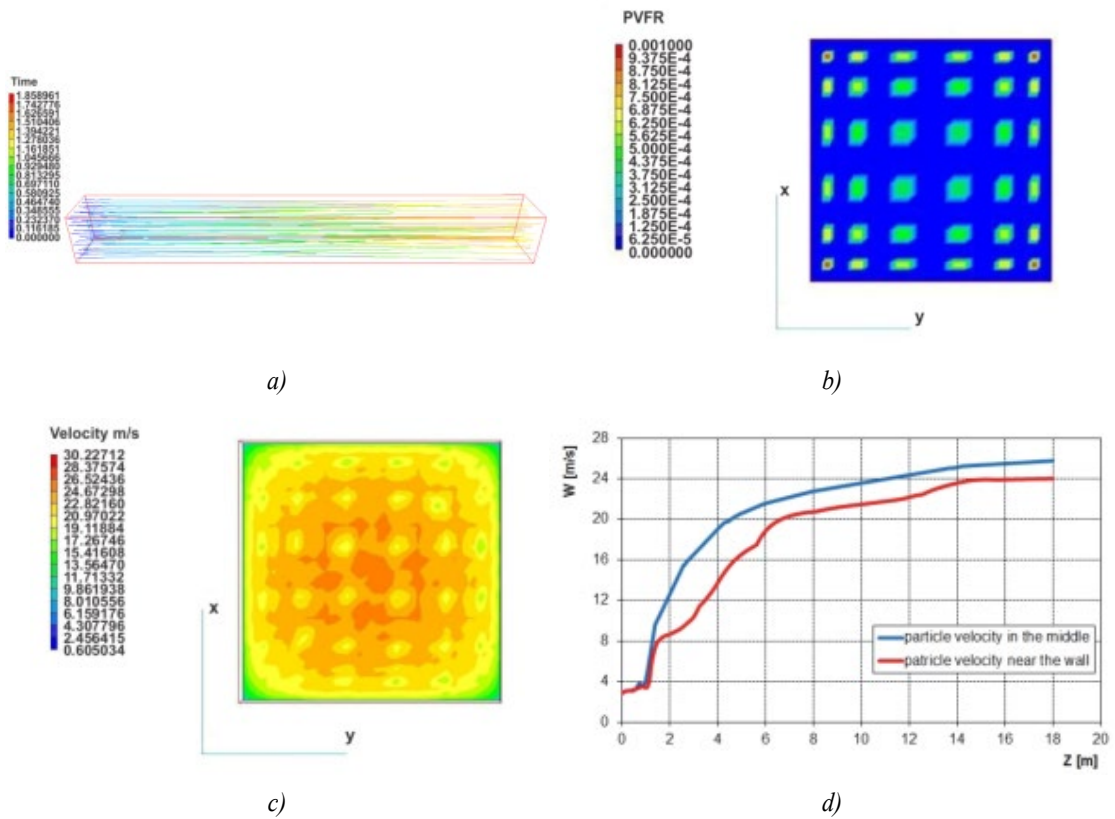


Figure 3. Motion of flour particles

7. Conclusions

The paper considered a fully developed turbulent flow in straight channels with a square cross-section, with the isolated effect of the secondary flow of the second kind. Numerical simulations of transport processes, matter and momentum during the turbulent two-phase flow were conducted using the PHOENICS 3.3.1 software package, which is based on the control volume method. The same initial flow conditions were used for all numerical experiments. A correction of the stress model of turbulence was performed taking into account the effect of damping-promoting interactions of the gas and the solid phase. The two-phase flow was solved using the full Reynolds stress model of turbulence, while the complete model was employed for turbulent stresses and turbulent temperature fluxes. The conducted numerical simulations yielded the distribution of the velocities of transported particles, showing that no precipitation occurred in the channel and proving that the desired transport could be realized.

Nomenclature

Latin symbols

A	– cross-section surface, [m ²]
a	– heat diffusion coefficient, $a = \lambda / \rho c_p$
b	– buoyancy force coefficient
c_p	– specific heat, [Jkg ⁻¹ K ⁻¹]
g	– solid particles diameter, [m]
k	– kinetic turbulence energy, [m ² s ⁻²]
m	– particle mass, [kg]
P	– averaged pressure, [Nm ⁻²]
∇P	– continuous phase pressure gradient
\tilde{p}	– current pressure, [Nm ⁻²]
Re	– Reynolds number,
S	– source term,
T	– averaged temperature, [K]
t	– time step, [s]
U	– averaged velocity, [ms ⁻¹]
\tilde{U}	– current velocity vector, [ms ⁻¹]
$\overline{u_i u_j}$	– components of turbulent stresses,
V	– particle volume, [m ³].

Greek symbols

Γ	– transport, diffusion parameter coefficient
ε	– dissipations of turbulent kinetic energy, [m ² s ⁻³]
η	– flow of number of particles per one cell, [s ⁻¹]
$\overline{\theta u_j}$	– turbulent temperature flux, [kgKm ⁻² s ⁻¹]
λ	– heat transfer coefficient, [Wm ⁻¹ K ⁻¹]
ν	– kinematic viscosity, [m ² s ⁻¹]
ρ	– density, [kgm ⁻³]
Φ	– gas phase universal parameter,
Ω	– vorticity, [s ⁻¹].

Superscripts

i, j, k	– vector component,
n	– end of time step,
p	– particle,
$\vec{x}, \vec{y}, \vec{z}$	– position vector,
0	– beginning of time step

Subscripts

IF	– interphase term of gas and solid phase interaction.
------	---

Acknowledgements

This research was financially supported by the Ministry of Science, Technological Development and Innovation of the Republic of Serbia (Contract No. 451-03-65/2024-03).

References

- [1] Cundall, P.A., Strack, O.D.L., A discrete numerical model for granular assemblies, *Géotechnique*, 29 (1979), 1, pp. 47–65
- [2] Tsuji, Y., Kawaguchi, T., Tanaka, T., Discrete particle simulation of two-dimensional fluidized bed, *Powder Technology*, 77 (1993), 1, pp. 79–87
- [3] Campbell, C.S., Brennen, C.E., Computer simulations of granular shear flows, *Journal of Fluid Mechanics*, 151, (1985), pp. 167–188
- [4] Tanaka, T., Yonemura, S., Kiribayashi, K., Tsuji, Y., Cluster formation and particle-induced instability in gas–solid flows predicted by the DSMC method, *International Journal of JSME*, 39 (1996), 2, pp. 239–245
- [5] Fuzhen, C., Hongfu, Q., Han, Z., Weiran G., Coupled SDPH-FVM method for gas-particle multiphase flow: Methodology, *International Journal for Numerical Methods in Engineering*, 109 (2017), 1, pp.73-101
- [6] Jafari, M., Mansoori, Z., Saffar Avval, M., Ahmadi, G., Ebadi, A., Modelling and numerical investigation of erosion rate for turbulent two-phase gas-solid flow in horizontal pipes, *Powder technology*, 267 (2014), pp. 362–370
- [7] Lain, S., Study of turbulent two-phase gas-solid flow in horizontal channels, *Indian Journal of Chemical Technology*, 20 (2013), 2, pp. 128-136
- [8] Mathematical models of turbulent transport processes, (in Serbian), Collection of papers dedicated to the Academician Muhamed Riđanović, Academy of Sciences and Arts of Bosnia and Herzegovina, Sarajevo, 1984.
- [9] Hinze, J.O., *Turbulence*, McGraw-Hill, New York, 1959
- [10] Bird B.R, Steward E.W., Lightfoot N.E., *Transport Phenomena*, Now York, 2001
- [11] Stevanović Ž., Numerical aspects of turbulent impulse and heat transfer, (in Serbian), Faculty of Mechanical Engineering, University of Niš, Niš 2008
- [12] Sijerčić M., Mathematical modelling of complex turbulent transport processes (in Serbian), Yugoslav Society of Thermal Engineers – Edition: Scientific research achievements, Belgrade 1998.
- [13] Milanović S., Research into the turbulent two-phase flow in straight channels with a non-circular cross-section during the pneumatic transport of granular materials, PhD Thesis, Faculty of Mechanical Engineering, University of Niš, Niš, 2014
- [14] Bogdanović B., Milanović S., Bogdanović-Jovanović J., *Flying Pneumatic Transport* (in Serbian), Faculty of Mechanical Engineering, University of Nis, Nis, 2009

Water Vapor Condensation from Combustion Products and its Usage Possibilities

Luka Marinović^a, Dejan Mitrović^b, Mirjana Laković^c, Marko Ignjatović^d

^aFaculty of Mechanical Engineering, University of Niš, Niš, RS, l.marinoviclmm@gmail.com

^bFaculty of Mechanical Engineering, University of Niš, Niš, RS, dejan.mitrovic@masfak.ni.ac.rs

^cFaculty of Mechanical Engineering, University of Niš, Niš, RS, mirjana.lakovic@masfak.ni.ac.rs

^dFaculty of Mechanical Engineering, University of Niš, Niš, RS, marko.ignjatovic@masfak.ni.ac.rs

Abstract: Moisture condensation from combustion products must appear in the fuel gasses stream of every boiler plant, in some period of operation. Discharging this condensate into environment leads to additional heat loss. Although this amount of heat compared to the total capacity of boiler house is not significant, it is not negligible. At the beginning, this paper deals with causes and sources of water vapor in the combustion products. Then possibilities of usage of formed condensate in the district heating system for improving energy efficiency and decreasing carbon dioxide emission on an example of system in District heating plant "Krivi Vir" in Niš, is presented. After that, some vital factors which have influence on efficiency of considered system are pointed, as well as possibilities for application.

Keywords: carbon dioxide emission reduction, district heating system, fuel saving, water vapor condensation from combustion products;

1. Introduction

Every energy plant which uses fossil fuel as a source of energy contains a boiler as a unit for transformation of fuel energy into heat energy. Because of cold surfaces of chimney, water vapor condensation from combustion products is unavoidable, especially during the system start. The condensate is very acidic, but it contains some heat energy which can be used (regenerated). The subject of this paper is condensation of water vapor from combustion products in the fuel gasses stream and possibilities of its usage in order to increase the energy efficiency and decrease carbon dioxide emission of the district heating system boiler house, through the presentation of the case of district heating plant (DHP) "Krivi Vir" in Niš.

2. Water vapor in combustion products

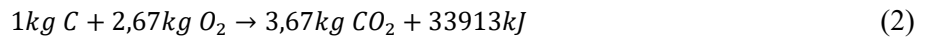
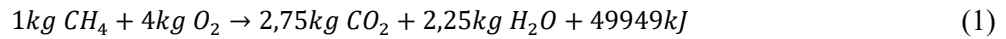
Under total combustion conditions in general, combustion products consist of CO_2 , N_2 , H_2O , O_2 , SO_2 , and solid unburnt residue - ash, whose quantity can be determined by analytical formulas obtained from stoichiometric equations.[1] Water vapor generated in the combustion process is of particular interest for this paper. Its quantity depends on the fuel type (moisture of fuel and amount of newly created water vapor as a combustion product from certain components) and, to a lesser degree, on air humidity.

2.1. Humidity from fuel

Depending on the type of fuel, water appears in the form of gross moisture or hygroscopic moisture, to a greater or lesser extent. In the solid fuel as biomass and lignite content of moisture is up to 50%. [1,2,3] In such cases water vapor harms combustion process, since latent heat of evaporation, which is not negligible, is lost. Because of that wet fuel must be dried. In the case of quality solid fuel, like biomass and lignite, the content of moisture is less than 10%[1,2,3]. Liquid and gaseous fuels don't contain moisture, or its amount is negligible. Consequently, in the case of their use, water vapor in the combustion products is result of combustion of particular fuel component.

2.2. Water vapor from combustion process

During combustion of certain fuel components, water vapor is formed. Depending on the type of fuel, the amount of water vapor can vary. Stoichiometric equations which describe combustion of some component of fuel define amount of formed water vapor: [1,2,3]:



By carbon combustion water vapor is not generated, while during methane combustion water vapor is the main combustion product, besides carbon-dioxide.

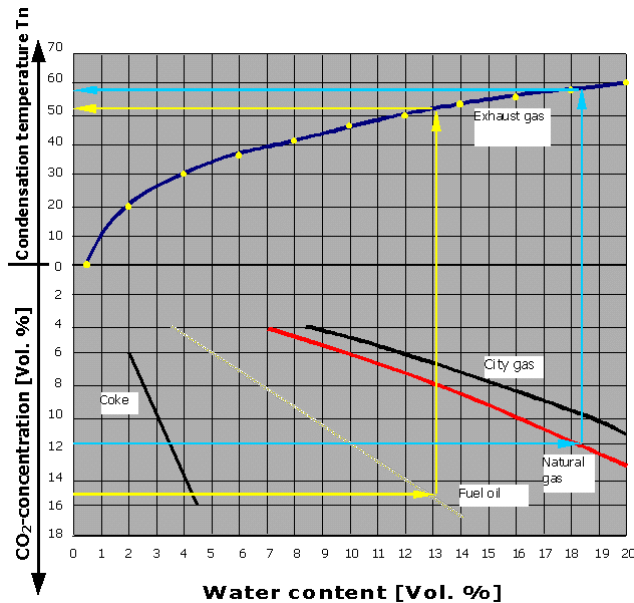


Figure 1. Diagram of dependence of dew point and percentage of water vapor on the share of carbon dioxide in combustion products according to standard DIN 4705 [8]

In case of highquality solid fuels as coke (black line in Figure 1), there is only a few percent of moisture in the products, while during combustion of 1 kg of natural gas, composed mostly of methane, about 2,25 kg water vapor is obtained with moisture up to 20% (Figure 1). It can be concluded that during combustion of fuel based on hydrocarbons, like liquid and gas fuel, amount of water vapor is significant, as well as amount of heat (latent and sensible) which is lost by that.

2.3. The heat in the water vapor of flue gases

The heat loss due to flue gases is a vital loss of boiler plant. The heat lost with water vapor is included in it. The heat lost with water vapor consists of latent heat (condensation) and physically sensible heat [4]. This heat can be used by installation of economizer, as well as by condensate recovery in chimney. The second way is especially important for this paper. In the case of gas, temperature is below than dew point temperature (T_n in the upper part of the Figure 1), for the defined absolute moisture of the combustion products (lower part in the Figure 1) condensation of the water vapor appears on the temperature which depends on the type of fuel. The condensation in chimney of the boiler plant has to appear during the operation start and on walls of chimney, because of cold surfaces. Dew point in case of natural gas, for usual combustion conditions is around 56-58°C. In the case of combustion of lignite, coke, fuel oil and other fuel with lot of impurities, this temperature is significantly lower. Since the temperature of condensate of the natural gas is higher, and condensate has physical and chemical properties suitable for further use, it can be used as feed water of district heating plants boilers with minimal chemical treatment. In this way its heat can be used, because the feed water, used from water supplier or onsite, sometimes is up to 40°C colder than condensate.

3. Condensate properties

The condensate of flue gases is acidic while softened water, where carbon dioxide from gases are dissolved, with pH value in the range between 2 and 6 [8], and in case of natural gas pH value is in the range between 2 and 7 [4,5,6]. It can not be used and also it must not be discharged into the public sewage system because of its aggressiveness. In order to increase pH value to value which can be discharged into the public sewage system it is necessary to pass through the bed of calcium carbonate (or, rarely, magnesium carbonate). In this way it is neutralized. Equation of neutralization is [6]:



As it can be seen, during acidic neutralization dissolution of Ca^{2+} occurs and its hardness increases. Since that condensate is very soft, this hardness increase is negligible. Neutralized condensate from the combustion products is practically clean and suitable for application as feed water of district heating system. Condensate from the combustion products of other fuels (first of all solid and liquid: coal, heavy fuel oil, biomass) have to be detailly treated because of other admixtures which are contained before injected in the water tract of the boiler. This kind of plant is carried out in Sweden, in the town Karlskoga. It is a plant for electric energy, heat energy and technological steam production. Fluidized bed combustion boiler is installed, and different types of waste can be used as fuel. Fuel gases and condensate are treated in the special plant with lot of treatment processes. [7] In this paper, the new system for collection and usage of condensate from the chimney for feed water in the district heating plant (DHP) "Krivi Vir" in Niš will be shown.

4. District heating plant "Krivi Vir" in Niš

District heating plant "Krivi Vir" is the biggest heat source for the district heating system in Niš. Capacity of the district heating plant is 128 MW. Natural gas, the composition of which is given in the Table 1, is used as primary fuel, while fuel oil is the alternative.

Table 1. The usual percentage composition of natural gas, used in DHP "Krivi Vir" in Niš [6]

Component	N_2	CO_2	CH_4	H_2S	C_2H_6	C_3H_8	C_4H_{10}	C_5H_{12}
Volume percentage [%]	0,99	0,47	96,18	0,01	1,62	0,51	0,18	0,04

The boiler house of this DHP has three boilers with capacity of 35 MW, 35 MW and 58 MW. Each boiler has its own chimney. Boilers with 35W capacities have metal chimneys inside of DHP, while third has brick-metal chimney outside.[5] New system for draining condensate is installed in this DHP in 2020 with its possible usage as feed water of the system because of the network losses. Except condensate, well water and water from the city water supply can be used for feeding the system because of water loss in the heating network. Starting from the heating season 2020/21 only well water and condensate are practically used. [9,10] A simplified schematic of this system is shown in Figure 2.

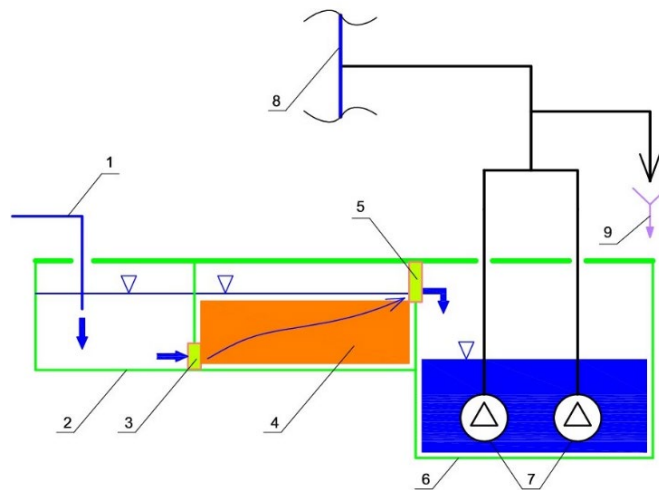


Figure 2. Principle scheme of the system for removal, treatment and use of condensate [6]

Condensate from all chimneys (1) comes into the slow channel (gross impurity settler) (2). After settling of coarse impurities, before passing through the pool with calcite bed (calcium carbonate) (4), it flows through filter for gross impurity (that were not settled) (3). After neutralization in calcium-carbonate, it passes through one more filter for mechanical impurity and enters the collection tank for treated and neutralized water (6). It can be sent by pumps (7) to expansion vessel (8), or to sewage system (9). [5]

4.1. Quality of treated condensate

Condensate treated in this way has lower value of pH (6-7) than needed value for boiler water (9,8+/-0,2) [9]. However, it is added in heat network, where it is mixed with water from the system. Condensate obtained in

this way is not a problem, since the amount of condensate is small compared to system water flow which is about 2500 and due to the fact the other parts of system are not sensitive to acidity as is the boiler. Since considerable feed of the system is by using condensate, water in the system would become acidic during time, which results as unallowed mode of operation. In order to prevent this situation, there is a plant for chemical treatment of the water: removing iron from return water and adjusting pH value of water (figure 3).



Figure 3. Device for removing iron and adjusting the pH value of returning water in DHP "Krivi Vir" in Niš

Condensate has greater hardness after passing through calcite bed than before. However, since condensate in the moment of its occurrence until contact with calcite bad has low hardness, increasing of hardness is not of great importance. In certain periods condensate has higher hardness than maximal prescribed value, but sometimes is below upper limit. Consequently, it never causes any problem. Hardness of water in district heating network and in boilers is always below upper limit (0,5 °dH – German degrees of hardness) [9].

5. Analysis of fuel saving and carbon dioxide emission reduction by using new system in "Krivi Vir" in Niš

Moisture from fuel gases condensates on the temperature between 56 – 57 °C, and contains certain heat, since return water from the city is often lower temperature, and water used as feed water is well water with adopted temperature of 10 °C. In this chapter savings in natural gas consumption will be described. Of course, condensate generation is not enough to completely replace use of well water at all, but certain part of feed can be done by condensate. The readings of the parameters of the condensate which goes into the system are mostly mornings when the condensate formation is at its peak. Data from internal records of DHP "Krivi Vir" are used [9]. Values were measured in the morning. Cooling of condensate in the collecting basin is neglected. This principle is possible for reviewing system usage, especially taking into consideration that the biggest amount occurs in mornings and immediately is injected into system. This methodology is acceptable for this paper, because the largest amount of condensate is produced in the mornings and it is in few minutes pumped in heating network, so that it does not have time to cool down. The amount obtained during the rest of a day has minor importance than at starting system.

5.1. The methodology for calculation of natural gas savings

Let assume condensate temperature in collection tank to be t_c , wall water temperature to be t_b , and temperature to which it is necessary to warm up supplementary water to be t , in which case $t_b < t_c < t$. Absolute saving of energy for warming water quantity is:

$$\Delta Q = \rho \cdot V \cdot c_{pw} \cdot (t_c - t_b) \quad (4)$$

Absolute saving of fuel ΔV_g is calculated according to lower heating value and boiler plant efficiency η :

$$\Delta V_g = \frac{\Delta Q}{\eta \cdot H_d} \quad (5)$$

Relative saving is calculated as:

$$\delta V_g = \frac{\Delta V_g}{\Delta V_g + V_g} \cdot 100\% \quad (6)$$

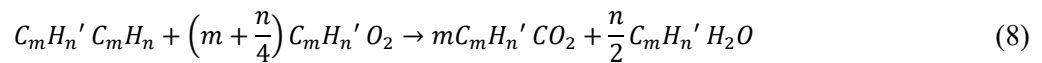
The medium daily temperature is calculated according to expression: [9,11]:

$$t_{sr} = \frac{t_7 + t_{14} + 2 \cdot t_{21}}{4} \quad (7)$$

Values in numerator of the fraction in expression (7) are temperatures measured at 7, 14 and 21 hour. In the way described before, by using data on a daily and monthly basis about fuel saving, next dimensions are determined: absolute heat saving by using condensate, and absolute and relative savings of the natural gas by using of condensate on annual and monthly basis for heating season 2022/23.

5.2. The methodology for calculating the reduction of carbon dioxide emissions

Carbon dioxide in natural gas combustion products comes from hydrocarbons and from fuel. The stoichiometric equations of the combustion of hydrocarbons in natural gas can be represented, per volume unit in general form:



where $C_m H_n'$ is volume ratio of each component. These stoichiometric equation have to be used for each hydrocarbon component in fuel. As can be seen, the amount of released carbon dioxide, from hydrocarbons, per volume unit of fuel is defined by first term on the right side in (8). Amount of carbon dioxide obtained by each component is then:

$$M_{C_m H_n} = m \cdot C_m H_n' \cdot \rho_{CO_2} \quad (9)$$

where:

$M_{C_m H_n}$ is amount of carbon dioxide from each hydrocarbon in [kg/m^3 of fuel], and

$\rho_{CO_2} = 1,96 kg/m_N^3$ is density of carbon dioxide in normal conditions.

The mass of emitted carbon dioxide per volume unit of fuel (specific amount of carbon-dioxide) is obtained by summing the emitted amounts of each hydrocarbon component, and carbon dioxide from fuel:

$$M = \sum_i M_{C_m H_n}^i + CO_2' \cdot \rho_{CO_2} \quad (10)$$

where CO_2' is volume ratio of carbon-dioxide in fuel.

The total amount of emitted CO_2 for burned volume of fuel V_g is then:

$$M_{CO_2} = M \cdot V_g \quad (11)$$

The absolute CO_2 emission reduction (unemitted amount of CO_2) by using presented system can be calculated according to (5) and (11) as:

$$\Delta M_{CO_2} = M \cdot \Delta V_g = M \cdot \frac{\Delta Q}{\eta \cdot H_d} \quad (12)$$

And relative CO_2 emission reduction is similarly to relative fuel savings:

$$\delta M_{CO_2} = \frac{\Delta M_{CO_2}}{\Delta M_{CO_2} + M_{CO_2}} \cdot 100\% = \frac{\Delta V_g}{\Delta V_g + V_g} \cdot 100\% = \delta V_g \quad (13)$$

5.3. Results

According to described methodologies and data from considered DHP from November 2022 to the last day of heating season in April 2023 fuel and energy saving is defined. Data about condensate production for October was not registered, because of a small number of heating days and small amount of condensate. Heating season 2022/23. is considered then without data about fuel consumption in October, too. Based on data from DHP plant efficiency is 91% that is, 0,91 [9]. Lower heating value of fuel is $34384 kJ/m_N^3$ [6]. Taking into consideration that efficiency is defined with devices, it can be concluded that without devices efficiency would be smaller. It is assumed efficiency of 90,9% without device, because it is difficult to calculate exactly without this device. Data of fuel savings calculation are shown in the Table 2.

Absolute monthly savings are calculated by summing daily savings. Relative savings of natural gas in every month (and entire heating season) were calculated by using data of natural gas consumption during the whole

month and absolute saving for the whole month (or entire heating season). Natural gas saving for the heating season 2022/23. is about 17247,26 m_N^3 , i.e. 0.146 %.

Table 2. Results of fuel saving calculation in DHP “Krivi Vir” in Niš for heating season 2022/23

Month	t_{sr} [°C]	t_c [°C]	V [m^3]	ΔQ [kWh]	ΔV_g [m_N^3]	δV_g [%]
November	9,77	39,12	820	27639,55	3183,561	0,202
December	6,18	37,49	882	28089,6	3235,398	0,151
January	5,29	39,37	877	29841,95	3437,236	0,146
February	4,1	34,11	552	15747,1	1813,773	0,071
March	9,28	40,2	792	27597,29	3178,693	0,173
April	10,14	37,25	665	20824,53	2398,598	0,172
Heating season 2022/23	7,46	37,92	$\Sigma=4588$	$\Sigma=149740,024$	17247,26	0,146

The amount of carbon dioxide emitted by burning volume unit of natural gas usually used in DHP “Krivi Vir” in Niš is presented in Table 3. The values of absolute and relative unemitted amounts of carbon dioxide are shown in Table 4.

Table 3. Amount of emitted carbon dioxide per volume unit of fuel for each component and total amount of carbon dioxide per volume unit of fuel

	CO_2	CH_4	C_2H_6	C_3H_8	C_4H_{10}	C_5H_{12}	M_{CO_2}
m	/	1	2	3	4	5	
Volume ratio	0,0047	0,962	0,016	0,005	0,002	0,0004	
M [kg/m_N^3]	0,009	1,885	0,064	0,03	0,014	0,004	2,006

Table 4. Absolute and relative reduction of emission by using considered device for heating season 2022/23

Month	November	December	January	February	March	April	Heating season 2022/23
ΔM_{CO_2} [kg]	6385,791	6489,769	6894,629	3638,182	6376,027	4811,26	34595,659
δM_{CO_2} [%]	0,202	0,151	0,146	0,071	0,173	0,172	0,146

Absolute carbon-dioxide emission reduction, by using new system in heating season 2022/23. is 34595,659kg. As can be seen, relative carbon-dioxide reduction is identical to relative fuel saving.

5.4. Discussion

From the expression (5) can be seen that absolute fuel savings and carbon dioxide emission reduction is in the direct dependency with absolute saved heat and in indirect dependency with boiler plant efficiency and fuel lower heating value. Based on that it can be concluded that this type of system is more efficient in case of less efficient plants. Diagrams of dependance between fuel savings and efficiency is given in the Figure 4a. Also, diagram of dependance between absolute emission reduction is given in the Figure 4b. These diagrams are nonlinear functions. However, nonlinearity can be neglected in the range of efficiency usual for gas fired plants, as can be seen in Figure 4.

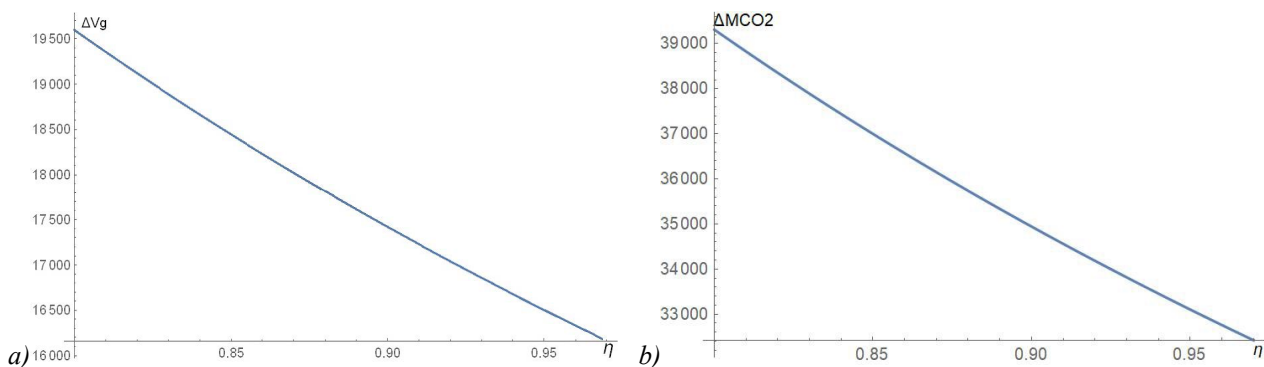


Figure 4. Dependance absolute fuel savings a) and absolute CO_2 emission reduction b) on boiler plant efficiency for efficiency values 0,8 to 0,97, for $H_d = 34384$ kJ/m_N^3 and $\Delta Q = 149740,024$ kWh

Values of ΔV_g and ΔM_{CO_2} for some values of efficiency are given in the Table 5.

Table 5. Values of absolute fuel savings and absolute emission reduction according to efficiency for same values of ΔQ and as in Figure 4

Efficiency η	0,8	0,85	0,9	0,95
ΔV_g [m^3]	19597	18444,3	17419,6	16502,8
ΔM_{CO_2} [kg]	39311,6	36999,3	34943,7	33104,6

Absolute condensate generation is in direct dependance with fuel consumption which is the highest at the biggest boiler output. However, it is in opposite dependency to fuel gasses temperature which is the lowest in warm weather, because of less boiler output. Since factors influence on condensate generation in different ways, it is necessary to establish mathematical function between condensate generation and mentioned parameters, and then search for maximum of the function, which is possible in the real conditions of boiler operation. It exceeds the scope of this paper.

However, based on data from Table 1 the biggest condensate production is in the warmer months. If linear method of the least squares is applied to data in Table 1, one can notice that with increasing of medium outside temperature production of condensate is increasing too, as well as savings. This approximation, since it is calculated only for 6 values, and because of neglecting other influential dimensions, is not near to real dependence which is difficult to determine, but for the purpose of this paper can show dependence saving on DHP external conditions, as in Figure 5.

Also linear method of the least squares can be implemented on carbon dioxide emission reduction as it is shown in Figure 6. The slope in this case is identical with slope of fuel savings approximation. The linear determination coefficient (r^2) for absolute parameters is 0,053 and for relative parameters is 0,733.

Collecting tank in analyzed plant is not isolated. If the tank were isolated, the savings would be much greater. Condensate temperature in collecting tank in that case is much higher than values in Table 1, and saving is more significant than now. Due to increased fuel savings, then carbon emission is also reduced. It can be solved with negligible financial costs according to befits.

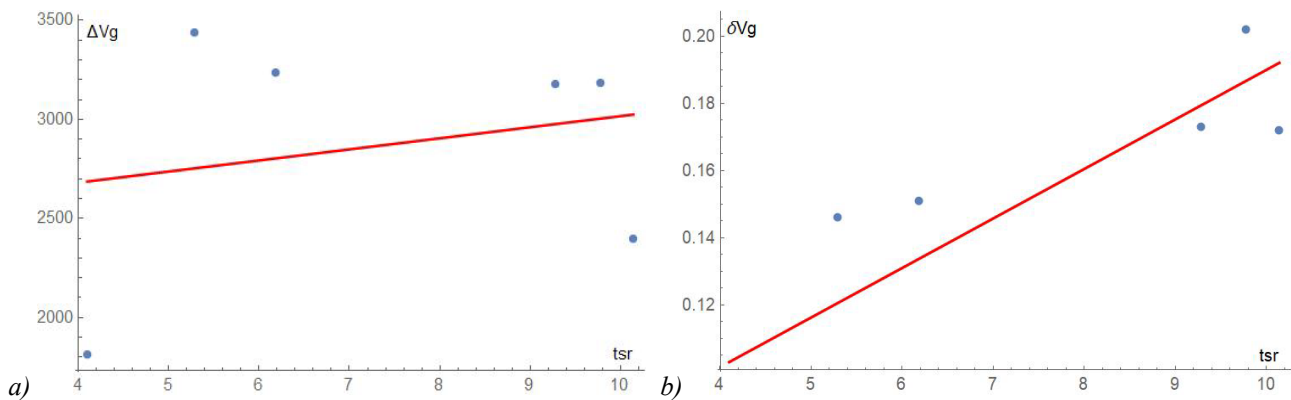


Figure 5. Dependence of savings on outside temperature according to data from the Table 1, by application of linear method of the least squares: a) absolute savings, b) relative savings

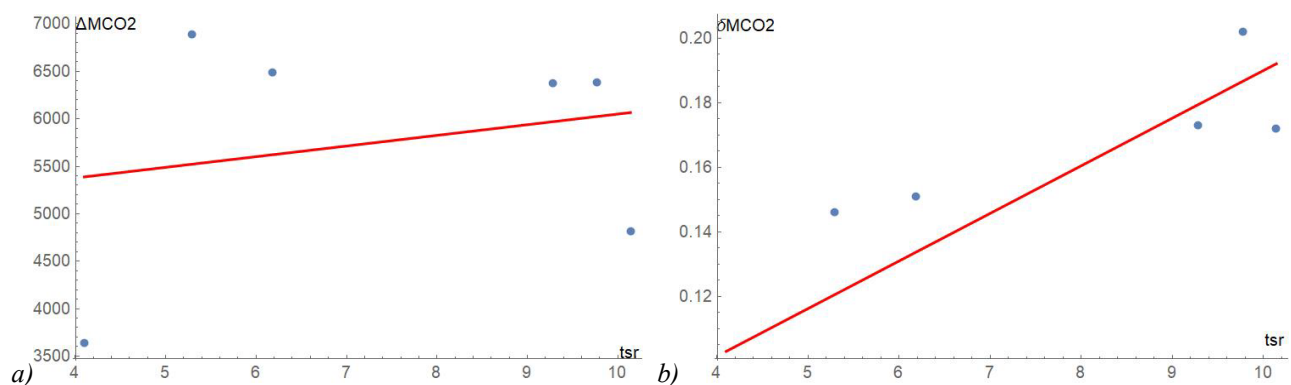


Figure 6. Dependence of CO_2 emission reduction on outside temperature according to data from the Table 1, by application of linear method of the least squares: a) absolute emission reduction, b) relative emission reduction

6. Conclusion

This concept of removal, treatment and use of condensate from fuel gases of gas fired heating plants is a simple and cheap way for efficiency increase. Fuel saving and emission reduction is significant according to financial costs of this device. Because of very low investment costs, it is very useful, especially for old and ineffective plants in case of unfavorable financial situation. A concept like this could be used in the case of other, dirtier fuels. However, in the case of these fuels, percentage of water vapor in combustion products is lower and condensate which is created requires serious chemical treatment. Hence, this way of using condensate does not pay off fast as in case of using natural gas. Since the winters are, on average, becoming more warm and that external temperature is much higher than in previous years, this type of auxiliary systems has greater importance in the future of district heating systems, because under these external conditions a larger amount of condensate is produced.

Acknowledgements

The authors wish to thank Company "Gradska toplana Niš" from Niš for the provided data.

This research was financially supported by the Ministry of Science, Technological Development and Innovation of the Republic of Serbia (Contract No. 451-451-03-66/2024-03).

References

- [1] Radovanović M, Propellant Materials – 1st Volume, Fuels (in Serbian), Faculty of Mechanical Engineering, Belgrade, 1986
- [2] Bogner M, Termotehničar Vol. 1: Handbook for Thermotechnics, Thermoenergetics and Process technics (in Serbian), Interklima Grafika, Vrnjačka banja; SMEITS, Belgrad, 2004
- [3] Stojanović B., Janevski J, Practicum in Steam Boilers (in Serbian), Faculty of Mechanical Engineering, Niš, 2009
- [4] Noor I, Martin A, Dahl O, Water recovery from Flue Gas Condensate in Municipal Solid Waste Fired Cogeneration Plants using Membrane Distillation, Chemical engineering journal, 399 (2020), <https://doi.org/10.1016/j.cej.2020.125707>
- [5] Kremzer R., Švarc B., (2001) The Technique of Using the Upper Heat Value of Gaseous Fuels (in Serbian), *Proceedings, International Congress KGH*, 32, (2001), 1, pp. 20-26
- [6] Ivanović Z, Project of system for drain, purification, neutralization and evacuation of condensate from chimney in Heating plant "Krivi Vir" in Niš, Jastrebac dimnjaci, Smederevo, 2019
- [7] Tepler M., Wood J., Buzzell P., Flue Gas Condensate and Energy Recovery, The Mcilvaine Company, Karlskoga, Sweden, http://www.mcilvainecompany.com/decision_tree/subscriber/articles/flue_gas_condensate_and_energy_recovery.pdf (accessed June 3, 2024)
- [8] www.eduvinet.de (accessed May 30, 2024)
- [9] Internal data from heating plant "Gradska toplana Niš"
- [10] <https://nitoplana.rs/>, (accessed on May 15, 2024)
- [11] Bogner M, Vujović Lj, District Heating (I) (in Serbian), KGH Journal, 9 (1980), 1, pp. 73-78



IX. Mathematical modeling and numerical simulation

Influence of Building Shape on Wind Flow: CFD simulations

Danka Kostadinović^a, Ivan Lazović^a

*^aUniversity of Belgrade, Vinča Institute of Nuclear Sciences-National Institute of the Republic of Serbia,
Department of Thermal Engineering and Energy, Belgrade, ISO 3166-1:RS, dankak@vin.bg.ac.rs*

Abstract: Buildings significantly affect the wind flow pattern over an urban area, leading to regions with an accelerated wind flow. The change in wind flow influences pollutant dispersion, urban microclimate, formation of fog and haze, urban heat island, comfort of pedestrians, and wind-created noise. It is important to include the simulation of wind flow around buildings in the early architectural design stage. The paper investigates the effect of different shapes of buildings on the wind flow pattern using Computational Fluid Dynamics (CFD) simulation. Results have been represented through pressure, velocity, and turbulence kinetic energy contours for five different cases. The ANSYS software was employed to solve the flow governing equations. The standard k- ϵ turbulent model was used for turbulence modeling while the Semi-Implicit Method for Pressure Linked Equation (SIMPLE) algorithm was applied as a solver for governing equations. This study clearly illustrates that different building shapes generate different wind flow patterns.

Keywords: ANSYS, Building, CFD, Turbulence, Velocity, Wind.

1. Introduction

Urbanization is one of the major driving forces behind the expansion of cities and the increase in built density. The wind flow around buildings in an urban area is an important consideration in the design of building layouts, natural ventilation design, air pollutant dispersion, and pedestrian comfort [1], [2]. The roughness of the ground surface affects the flow of air immediately above the terrain. In the atmospheric boundary layer, the wind speed changes from zero near the ground due to the no-slip condition to some constant value at a certain distance from the ground where surface friction has a negligible effect on wind speed. Within the boundary layer, the wind is turbulent with sudden changes in direction and speed due to the earth surface itself such as roughness, and friction. The wind speed increases with the distance from the ground, so high-rise buildings are exposed to stronger wind. The boundary-layer flow of the atmosphere affects the urban climate, urban heat island, and formation of fog and haze [3]. Wind flow around buildings is dependent on building density [4], while the arrangement and height of buildings affect urban ventilation [5], [6].

There is a large number of high-rise buildings constructed in developed countries. Taller and taller structures are being designed which have a significant effect on the surrounding wind pattern. Buildings change not only the direction of the wind but also change its speed. In the cities, the wind speed is reduced by 25-30%. Buildings produce air pollution in the form of exhaust from heating systems (fossil fuel boilers), kitchens, and smoking. Surrounding of buildings also experience air pollution from traffic. The wind flow around the buildings influences on dispersion of pollutants and the exposure of people to air pollution near the buildings. The distribution of pressure on the building and structural load is related to the wind flow around them. Strong winds can cause damage to buildings, therefore to prevent structural failures it is necessary to determine the wind load on buildings. The wind flow near a building affects the surface movement of rain as well as the performance of heating, cooling, and ventilating systems.

The change in wind speed at the pedestrian level influences on comfort of people near the building. Classification of wind speed and human body feeling, based on [7] is given in Table 1. At pedestrian level, a wind of 10 m/s is considered to be intolerable and disagreeable, while wind of 5 m/s is considered to be annoying [8]. Wind speed ranging from 1 m/s to 5 m/s is the most comfortable for humans. Pedestrian comfort needs to be considered during building design and city planning. Improving the structure of urban areas can improve the wind flow and environmental conditions. Consequently, the architect and planner need to predict the wind flow near buildings, and related aspects of its performance. The wind flow around buildings can be investigated from field experiments, in wind tunnel tests under strictly controlled conditions, and simulations based on Computational Fluid Dynamics (CFD). Field experiments give more realistic parameters, however

the testing period time-consuming, and require a lot of material resources and labor. Wind tunnel experiments are complex, time-consuming, and very expensive. Instead, CFD simulations are used. CFD models avoid the impacts of walls in wind tunnels, and allow simulations of objects with real scale dimensions and quick change of geometrical design and boundary conditions to analyze the influence of an individual parameter. The CFD simulations of wind flow in urban areas can be classified into three categories: full-scale models, mesoscale models, and individual buildings. The building configurations can be categorized into building complexes, street canyons, and isolated buildings. Previous review studies related to wind flow assessment have been published focused on the velocity measurement techniques [9], wind flow in street canyon [10], air quality and pollutant dispersion [11], [12], while study [13] reviewed wind tunnel and CFD techniques. Wind flow patterns around isolated buildings are crucial for a deep understanding of wind flow patterns around complex building layouts. Characteristics of wind flow around buildings with different shapes predicted by CFD simulation are discussed in this paper. This research is based on the following questions: What is the change in pattern of wind, pressure, and turbulence kinetic energy with the change of building's shape? The Ansys software was used to simulate the flow of wind around a building. This study highlights the role of urban physics characteristics on wind flow.

2. Methodology

Using CFD simulations, the impact of buildings on wind flow is examined. The process to obtain wind patterns may be divided into five main steps: model geometry, model meshing, setup boundary conditions, solution, and results.

2.1. Computational Domain and Mesh

Previous studies revealed that 2-D simulation encountered inaccurate prediction of wind pressure on the building [14], thus 3-D models were used in the present study. A three-dimensional rectangular computational domain with relevant distances, shown in Figure 1, is considered for modeling wind flow around the building. The dimensions of the computational domain were selected based on the study [15]. To ensure the full development of turbulent flow the computational domain was set as $5H$ upstream and $15H$ downstream, where H is the building height. The length of the domain behind the building is greater than the length from the inlet to the building due to reestablishing a uniform flow of airflow behind the building. From the top of the building to the upper boundary of the domain, the distance should be sufficient to prevent the occurrence of artificially induced acceleration in this zone. The computational geometry in the software is modeled at scale 1:1. Each building is regarded as rigid or non-deformable.

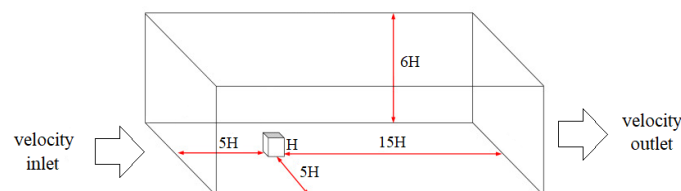


Figure 1. Computational domain with relevant distances

Simulation and result accuracy depend upon mesh quality. A finer mesh will yield more accurate results as it divides the volume around the model into smaller volumes, however, it increases the computing time. The meshing of the CFD domain and building model is presented in Figure 2. A structural tetrahedral grid was used for meshing. The finer mesh was used around the building to capture more details of the flow parameters near the envelopes of the building. Since the computational time required for the simulation larger elements were applied to the domain far from the building. It was considered that convergence is ensuring if the residual fell below the generally applied criteria of dropping to 10^{-4} . It was also necessary to create names for all external surfaces on which the boundary conditions would be later defined. For surfaces that have the same name, the same boundary conditions are set.

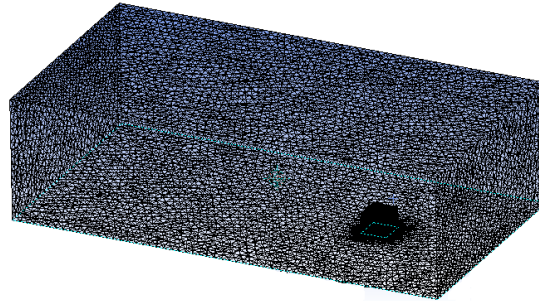


Figure 2. Grid used for three-dimensional representation of the cubic low-rise building

2.2. Governing equations

The Ansys Student Version 18.1 software [16], which is based on the finite volume method, was used to numerically solve the following partial differential equations: equation of continuity and momentum equations (Reynolds averaged Navier-Stokes - RANS) equation.

$$\frac{\partial \bar{v}_i}{\partial x_i} = 0 \quad (1)$$

$$\rho \left(\frac{\partial \bar{v}_i}{\partial t} + \bar{v}_j \frac{\partial \bar{v}_i}{\partial x_j} \right) = \rho \bar{F}_i - \frac{\partial \bar{p}}{\partial x_i} + \frac{\partial}{\partial x_j} \left(\eta \frac{\partial \bar{v}_i}{\partial x_j} - \rho \overline{v_i' v_j'} \right) \quad (2)$$

Previous studies examined the application of different turbulence models for the simulation of wind flow [17], [18]. It is noticeable that the k-ε model [19], also known as the Launder Spalding model, is the most commonly used engineering model for turbulence flow. The standard K-ε turbulence model was used in this research to address the simulation of wind flow. In this model, it is considered that the flow is completely turbulent, and the effect of molecular viscosity is negligible. Two supplementary transport equations are needed for the turbulence kinetic energy and its dissipation.

$$\left(\frac{\partial k}{\partial t} + \bar{v}_j \frac{\partial k}{\partial x_j} \right) = P - \rho \varepsilon + \frac{\partial}{\partial x_j} \left(\left(\eta + \frac{\eta_t}{\sigma_k} \right) \frac{\partial k}{\partial x_j} \right) \quad (3)$$

$$\rho \left(\frac{\partial \varepsilon}{\partial t} + \bar{v}_j \frac{\partial \varepsilon}{\partial x_j} \right) = \frac{\partial}{\partial x_j} \left(\left(\eta + \frac{\eta_t}{\sigma_\varepsilon} \right) \frac{\partial \varepsilon}{\partial x_j} \right) + C_{\varepsilon 1} \frac{\varepsilon}{k} P - \rho C_{\varepsilon 2} \frac{\varepsilon^2}{k} \quad (4)$$

The term of the connection of Reynolds stress and gradient of the mean field represents the production of turbulent energy.

$$P = -\rho \overline{v_i' v_j'} \frac{\partial \bar{v}_i}{\partial x_j} \quad (5)$$

Several empirically determined constants appear in the equations which have the following values when performing numerical simulations of wind flow:

$$C_\eta = 0.09 \quad C_{\varepsilon 1} = 1.44 \quad C_{\varepsilon 2} = 1.92 \quad \sigma_k = 1 \quad \sigma_\varepsilon = 1.3 \quad (6)$$

Pressure-velocity coupling is taken care of by the SIMPLE algorithm.

2.3. Boundary conditions

Boundary conditions that simulate the actual flow are necessary for the real physical demonstration of the airflow. The following types of boundary conditions were used:

- wind speed on the upstream side of the building at the domain inlet,
- pressure equal to atmospheric on the outlet downstream side,
- boundary condition on the wall.

At the inlet to the domain, a constant wind speed was set along the height. The wind speed wasn't the same in every case study. A wind direction is orthogonal to the observed domain. A pressure equal to atmospheric is set at the outlet of the domain. At all the sides of the building, the nonslip wall conditions were applied. The air temperature at the inlet and outlet of the domain is 26 °C, while the intensity of turbulence is 5%. The

solution is initialized with the values of the input boundary conditions. The no-slip wall condition is used for the building and ground surface.

3. Results

Wind flow around the cube, high-rise, L-shaped, and cylindrical building with an orientation normal to the incident wind flow was simulated. The pressure contours around buildings in a horizontal plane are shown in Figure 3. The horizontal plane is positioned at half of the building's height. The first case that was considered is the flow of wind with a speed of 5 m/s around an isolated cube building with dimensions of 10x10x10 m. The height of the L-shaped building is 15 m while the wind speed is 10 m/s. The isolated high-rise building has dimensions of 30x30x80 m and wind speed of 25 m/s. The cylindrical building has a diameter of 50 m and a height of 40 m while the wind speed is 10 m/s. In all observed cases, the positive pressure is on the upstream side of the building as a result of the wind hitting the windward side. A stagnation point with the highest pressure is at approximately two-thirds of the building height. The negative pressure is attained on the top face, lateral sides, and leeward sides due to flow separation. The pressure on the leeward sides is lower than the pressure on the leeward side, except in the case of high-rise building. Pressure increases from the edges to the center on the windward side, while on the leeward side, pressure decreases from top to bottom. In the case of L shape building, two stagnation points can be observed on the upstream side of the building. The underpressure zone on the downstream side of the building is much larger than in the other cases. Around the high-rise building, the concern of the wind flow is greater, as is the height of the building, so the overpressure zone on the windward as well as the underpressure on the leeward sides of the building are larger. The L-shaped and high-rise buildings have a larger zone of negative pressure on the leeward side than the cube and cylindrical buildings. In the case of cylindrical building positive pressure on the leeward side is obtained. Underpressure zones exist only on the lateral sides.

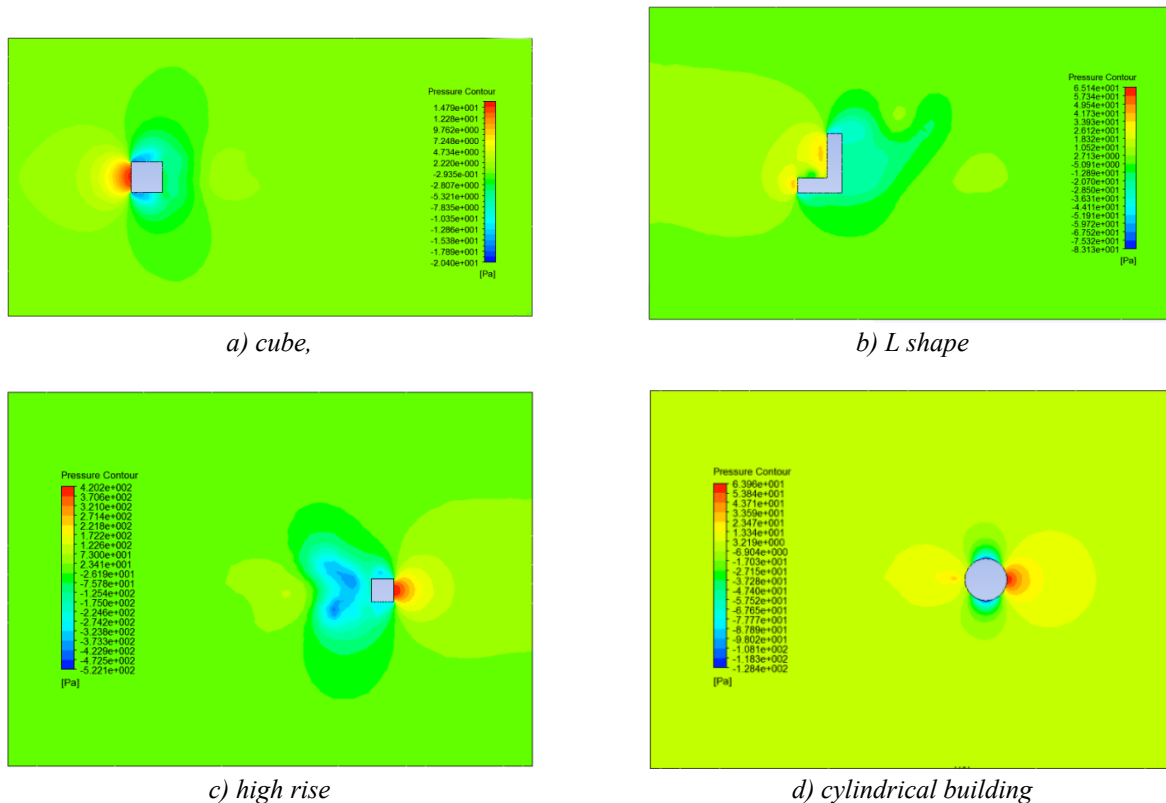


Figure 3. Pressure contours around a) cube, b) L shape, c) high rise, d) cylindrical building

The velocity contours around buildings in a horizontal plane are shown in Figure 4. Generally, the flow separation occurs at the lateral sides of the buildings where maximum wind velocity can be noticed (red area in Figure 4). In all observed cases, the zones of increased wind speed can be observed on the lateral sides of buildings. There is a large velocity gradient in these positions and underpressure zones. The velocity gradient is lowest in the case of cylindrical building. The velocity contours in the horizontal plane clearly show the

existence of a turbulent zone on the leeward side. The overall flow patterns show more substantial disturbance on the leeward side than on the windward side. The wind reaches the undisturbed field far away from the building. The wider building disturbs a longer and wider region on the windward and leeward side of the building. The non-symmetrical L shape of the building causes the non-symmetrical distribution of velocity contours around the building in the horizontal plane. For an L-shaped building with the larger wide, the wind flow deflecting towards the lateral sides travels a longer distance towards the flow detachment at the windward side of the building. Therefore, frictional effects exist over a longer distance and dissipate higher amounts of kinetic energy of the wind resulting in lower wind velocity around the lateral sides. The wider L-shaped building causes the formation of a longer recirculation region on the downstream side of the building. In the case of cylindrical building, the wind flow is least disturbed.

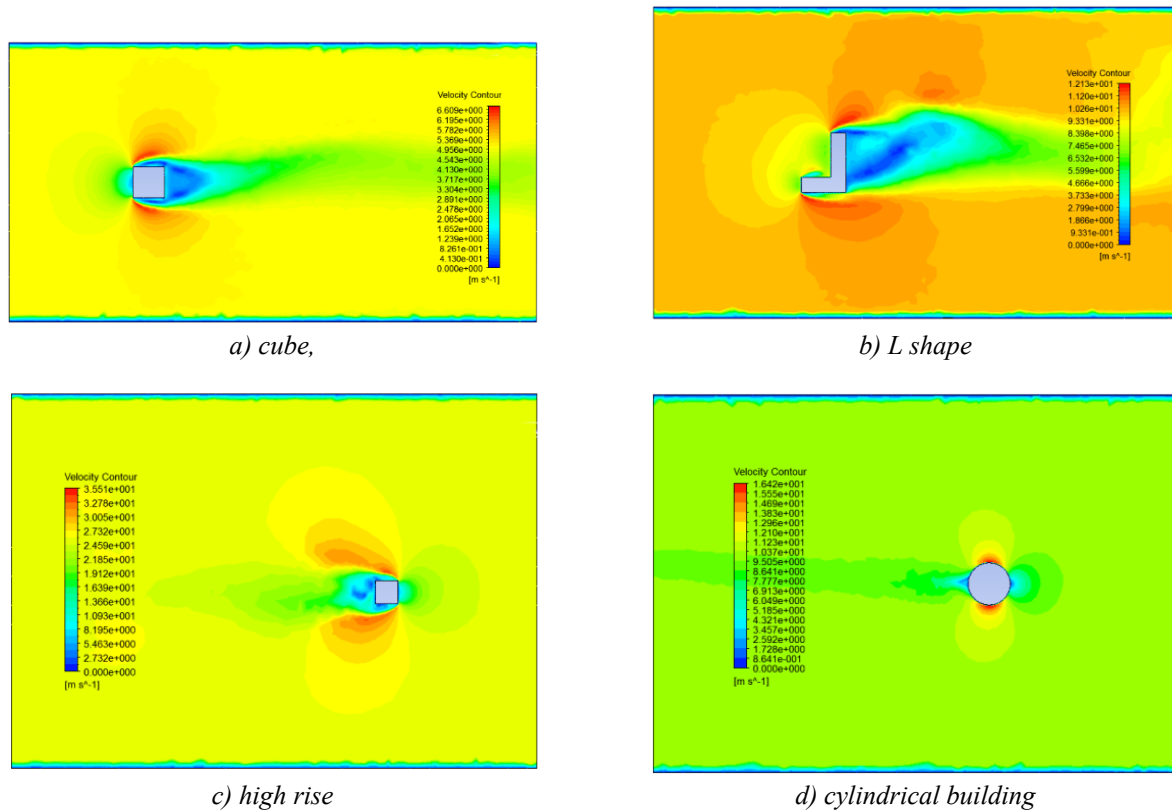


Figure 4. Velocity contours in horizontal plane around a) cube, b) L shape, c) high rise, d) cylindrical building

The velocity contours around buildings in the vertical plane are shown in Figure 5. The vertical plane is positioned at half of the domain width. The wind velocity around the upwind edges and the lateral sides of the building increases with increasing building height. The wind velocity is highest at the upwind edges on the windward face of the high-rise building. Figure 4 and Figure 5 clearly show that at the top of the buildings and their lateral sides wind flow is detached from the surface and flow separation takes place. The separation bubbles are formed in these places characterized by reverse flows, low-velocity distributions, and high turbulence intensities. This is caused by the air suction due to low-pressure zones on the roof and lateral sides of the building. The detached flow might reattach to the surfaces of the building depending on the upstream surface roughness that determines the turbulence intensity of the incidence flow as well as top and lateral aspect ratios. The downwash flow over the windward façade of the building causes a reverse flow. The reversed flow undercuts the incident wind flow and causes it to be detached from the street level creating a standing vortex near the ground surface upstream of the windward face of the building. This roll-like vortex induces the formation of additional vortices that are smaller in size and are eventually connected to the primary vortex around the lateral sides of the building. This vortex is then stretched around the lateral sides and is extended downwind the building creating a so-called horseshoe-shape vortex [21] (blue region in Figure 4 and Figure 5). The lateral wind flows together with the flow over the top of the building causing the formation of 3D vortices on the leeward side of the building.

The high-rise building's windward façade can direct the high-speed wind at higher elevations down the building's windward façade toward the street level, which is called the downwash effect. The high-rise building creates two longer counter-rotating vortices, thus a longer recirculation region downstream of the building can be noticed. Beyond the buildings, the reattached flow requires some distance to recover the features of incidence wind flow and release all perturbations. This so-called wake region is characterized by velocity deficits, higher turbulence intensities, and smaller-scale eddies compared to the eddies on the windward side. From the L-shape and high-rise building case, it can be seen that the length of wake region on the leeward side of the building increases with an increase in the building's height and length. In the case of cylindrical building with rounded edges, there is no reverse flow zone on the leeward side of the building. The wind flow is less disturbed thus this shape of the building is the most effective in terms of reducing wind loads.

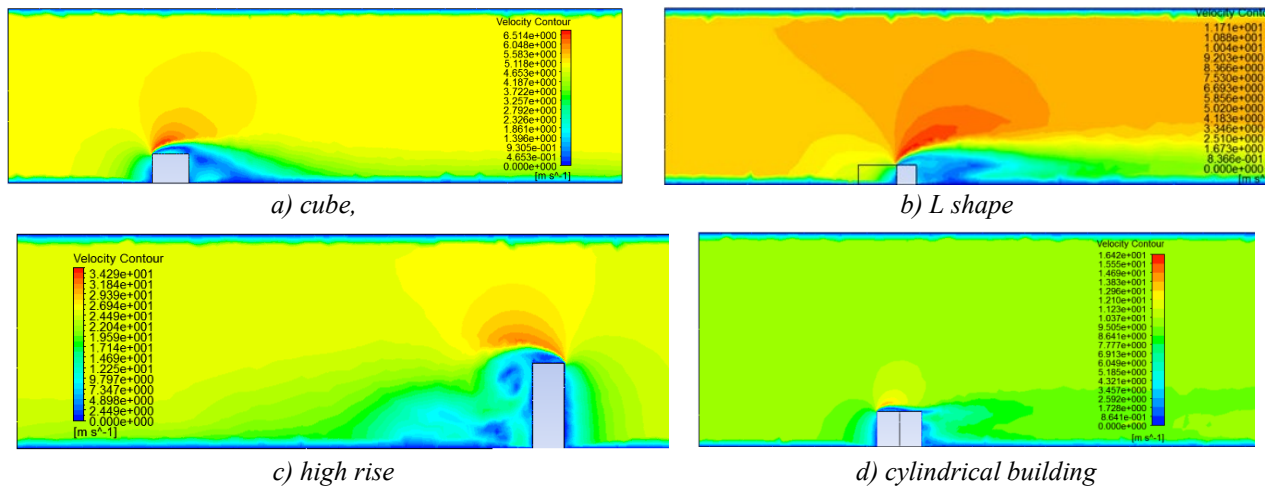


Figure 5. Velocity contours in vertical plane around a) cube, b) L shape, c) high rise, d) cylindrical building

The distribution of turbulence kinetic energy around buildings in the vertical plane is shown in Figure 6. As the height of the building increases, the turbulence kinetic energy also increases. The greatest kinetic energy is above the top face of the building and on the leeward side. The maximum turbulence kinetic energy can be observed near the top of the building while turbulent kinetic energy is lowest in the inflow state. The turbulent kinetic energy increases when wind reaches behind a building due to strong perturbations and a garter velocity gradient. Mean kinetic energy is converted to turbulent kinetic energy due to the formation of eddies that are rotating faster or slower compared to eddies in the mean flow. The kinetic energy is transferred from large to smaller eddies, then to even smaller ones, and so on. On the leeward side, with increased distance from the building, the turbulence kinetic energy decreases, due to dissipation. The turbulence dissipation rate is the velocity at which the mechanical energy of an isotropic small-scale vortex transforms into thermal energy, which greatly influences the diffusion process [22]. With an increase in height, the turbulence dissipation rates vary. The turbulence kinetic energy on the leeward side of the high-rise building is higher compared to other cases, due to the contribution of lateral velocity fluctuation caused by eddies shedding.

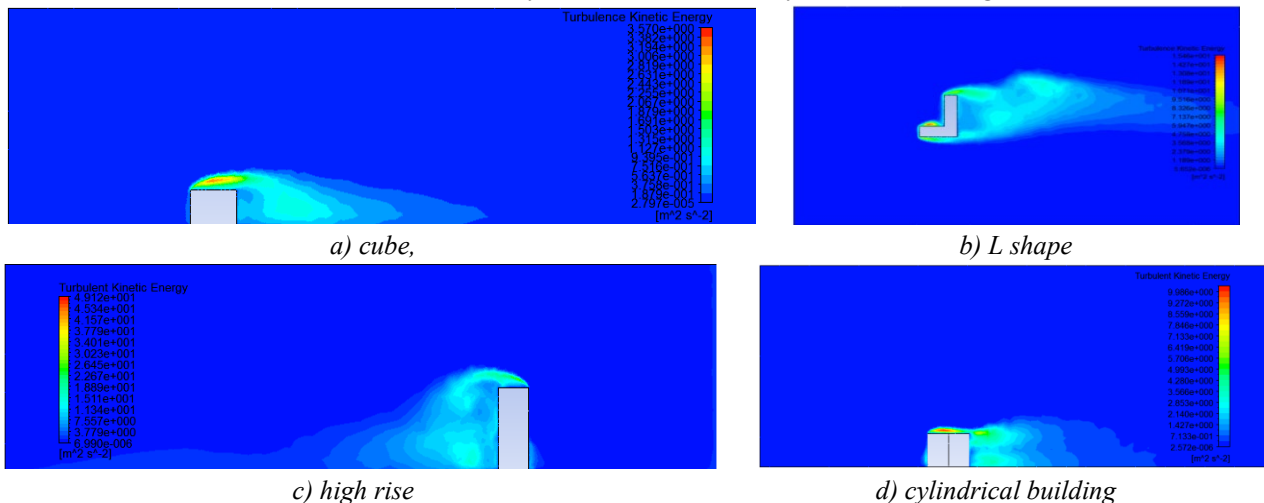


Figure 6. Distribution of turbulence kinetic energy around a) cube, b) L shape, c) high rise, d) cylindrical building

4. Conclusion

It is important to include simulations of wind flow in building design and modern city planning. In this paper, numerical simulations based on Computational Fluid Dynamics (CFD) are performed to study the effect of buildings with different shapes on wind pressure distribution, wind velocity distribution, and distribution of turbulence kinetic energy. The ANSYS Fluent software was used for simulations of wind flow around the isolated cube, high-rise, L-shaped, and cylindrical building. The 3D RANS equations were solved in combination with the standard k- ϵ model for turbulence modeling while the SIMPLE algorithm was used for pressure-velocity coupling. Analysis of the physics of buildings in terms of shape and height shows a significant correlation with wind flow changes. This is a sign of the direct impact of city physics on wind speed. Different building shape and heights has significant effects on the urban microclimate. Building with a round shape is very effective in withstanding wind stresses, while with the increase in building height, and edges wind flow becomes more disturbed. The results of numerical simulations need to be validated with experimental data from wind tunnel tests. Additional research is needed to study the influence of wind speed which varies with heights of the inlet domain as well as wind direction and wind speed on air temperature in dense built urban areas. Furthermore, the effect of roof slopes on wind flow should be explored.

Nomenclature

Latin symbols

- \bar{u}_i, \bar{v}_j – Time-averaged velocity components, [m s⁻¹].
 \bar{F}_i – External forces, [kg m s⁻²].
 \bar{p} – Time-averaged air pressure, in [bar].
 u_i', v_j' – Fluctuating part of velocity components, [m s⁻¹].
 k – Turbulence kinetic energy, [m² s⁻²].
 t – Time, [s].
 $C_{\epsilon 1}$ – Empirical constants.
 $C_{\epsilon 2}$ – Empirical constants.

Greek symbols

- ρ – Air density, in [kg m⁻³].
 η – Dynamic viscosity, [kg m⁻¹s⁻¹].
 ϵ – Turbulent dissipation rate, [m² s³].
 η_t – Turbulent viscosity, [m² s].
 σ_k – Empirical constants.
 σ_ϵ – Empirical constants.

Acknowledgments

The research was funded by the Ministry of Education, Science and Technological Development of the Republic of Serbia (Contract No. 451-03-47/2023-01/200017).

References

- [1] Zheng, S., Wang, Y., Zhai, Z., Xue, Y., Duanmu, L., Characteristics of wind flow around a target building with different surrounding building layers predicted by CFD simulation, *Building and Environment*, 201 (2021), 107962
- [2] Liu, S., Pan, W., Zhao, X., Zhang, H., Cheng, X., Long, Z., Chen, Q., Influence of surrounding buildings on wind flow around a building predicted by CFD simulations, *Building and Environment*, 140 (2018), pp. 1-10
- [3] Rajagopalan, P., Lim, K.C., Jamei, E., Urban heat island and wind flow characteristics of a tropical city, *Solar Energy*, 107 (2014), pp.159-170

- [4] Buccolieri, R., Sandberg, M., Sabatino, S.D., City breathability and its link to pollutant concentration distribution within urban-like geometries, *Atmospheric Environment*, 44 (2010), 15, pp. 1894-1903
- [5] Hang, J., Li, Y., Sandberg, M., Buccolieri, R., Di Sabatino, S., The influence of building height variability on pollutant dispersion and pedestrian ventilation in idealized high-rise urban areas, *Building Environment*, 56 (2012), pp. 346-360
- [6] Chang, C-H., Meroney, R.N., Concentration and flow distributions in urban street canyons: wind tunnel and computational data, *Journal of Wind Engineering and Industrial Aerodynamics*, 91 (2003), 9, pp. 1141-1154
- [7] Wen, X., Employment of CFD Simulation on Outdoor Wind Environment for Residential Project Planning and Construction, *Science and Technology Innovation Herald*, 2010, pp. 113-114
- [8] Hunt, J., Fundamental studies of wind flow near buildings, *Models and Systems in Architecture and Building*, LUBFS Conference Proceedings No.2, Published by Construction Press Ltd. (1975), Lunesdale House, Hornby, Lancaster, LA2 8NB
- [9] Cao, X., Liu, J., Jiang, N., Chen, Q., Particle image velocimetry measurement of indoor airflow field: A review of the technologies and applications, *Energy and Buildings*, 69 (2014), pp. 367-380
- [10] Jonas Allegrini, J., Viktor Dorer, V., Carmeliet, J., Wind tunnel measurements of buoyant flows in street canyons, *Building and Environment*, 59 (2013), pp. 315-326
- [11] Wang, Y., Zhong, K., He, J., Xu, J., Kang Y., Impacts of wind flow across street-side building gaps on traffic pollutant dispersion at pedestrian level with different block heights, *Building and Environment*, 246 (2023), 110972
- [12] Wu, M., Zhang, G., Wang, L., Liu, X., Wu, Y., Influencing Factors on Airflow and Pollutant Dispersion around Buildings under the Combined Effect of Wind and Buoyancy-A Review, *Int. J. Environ. Res. Public Health*, 19 (2022), 19, 12895
- [13] Blocken B., Stathopoulos, T., van Beeck, J.P.A.J., Pedestrian-level wind conditions around buildings: review of wind-tunnel and cfd techniques and their accuracy for wind comfort assessment, *Building and Environment*, 100 (2016), pp. 50-81
- [14] Oliveira, P.J., Younis, B. A., On the prediction of turbulent flows around full-scale buildings, *Journal of Wind Engineering and Industrial Aerodynamics*, 86 (2000), 2-3, pp. 203-220
- [15] Revuz, J., Hargreaves, D.M., Owen, J.S., On the domain size for the steady-state CFD modelling of a tall building, *Wind and Structures*, 15 (2012), 4, pp. 313-329
- [16] Ansys®, Fluent, ANSYS, Inc.
- [17] Blocken, J. Carmeliet, T. Stathopoulos: CFD Evaluation of Wind Speed Conditions in Passages Between Parallel Buildings-Effect of Wall Function Roughness Modifications for the Atmospheric Boundary Layer Flow, *Journal of Wind Engineering and Industrial Aerodynamics*, 95 (2007), 9-11, pp. 941-962
- [18] B. Blocken, T. Stathopoulos, J. Carmeliet: CFD Simulation of the Atmospheric Boundary Layer: Wall Function Problems, *Atmospheric Environment*, 41 (2007), 2, pp. 238-252
- [19] T. H. Shih, W. W. Liou, A. Shabbir, Z. Yang, J. Zhu: A New k-ε Eddy-Viscosity Model for High Reynolds Number Turbulent Flows-Model Development and Validation, *Computers and Fluids*, 24 (1995), 3, pp. 227-238
- [20] Meroney, R., Rafailidis, S., Paageau, M., Dispersion in Idealized Urban Street Canyons, *Air Pollution Modeling and its Application*, XI, 21, NATO, 1996
- [21] Pourteimouri, P., Campmans, G.H.P., Wijnberg, K.M., Hulscher, S.J.M.H., A Numerical Study on the Impact of Building Dimensions on Airflow Patterns and Bed Morphology around Buildings at the Beach, *J. Mar. Sci. Eng.*, 10 (2022), 1, 13
- [22] Dongpeng, G., Numerical and Wind Tunnel Simulation Studies of the Flow Field and Pollutant Diffusion around a Building under Neutral and Stable Atmospheric Stratifications, *Journal of Applied Meteorology and Climatology*, 58 (2019), 11, pp. 2405-2420

Measurement elements and SCADA system operation in the remote heating system of the Faculty of Mechanical Engineering

Dejan Mitrović^a, Marko Ignjatović^a, Dušan Stojiljković^a, Rajko Turudija^a

^aUniversity of Niš, Faculty of Mechanical Engineering in Niš, Niš, RS, dejan.mitrovic@masfak.ni.ac.rs

Abstract: The enormous amounts of energy consumed today for the production of thermal energy intended for households, on the one hand, and the reserves of all types of fuels available worldwide, on the other hand, require that a more rational consumption should be implemented among all consumers. One of the many enhancements to heating systems that aims to improve overall efficiency is the concentration of thermal energy output for a greater number of users, which produces a far better result. This has led to the implementation of a centralized supply of thermal energy for multiple buildings and facilities, residential blocks, and entire urban areas. This method of producing and transmitting thermal energy for heating purposes is called district heating. The thermal energy, produced centrally, is transferred via pipelines to substations, and then through heat exchangers and secondary networks to end-users. Due to the fact that energy consumption constitutes a significant part of the budgets of individual and collective users and requires compliance with the European Union directives on increasing efficiency in all spheres of energy transformation, there is a need for optimized production and consumption of thermal energy. Optimization involves adequate supervision of relevant parameters of the heating process, including production (boiler room), distribution (pipelines), transfer (substations), and consumption (end-user). Supervision entails the ability to command and monitor the operation and parameters of the process. To achieve this goal, the supervisory system must collect and display important process data to detect possible problems or causes of inefficiency in the process itself, thereby alerting the operator. The main goal of the supervisory system is to enable the operator to control and command a highly automated process. Therefore, supervision involves a series of tasks aimed at controlling the process and monitoring its parameters. The Supervisory Control and Data Acquisition (SCADA) system has wide application in district heating systems for monitoring, control, and data acquisition.

Keywords: SCADA system, remote heating system, measurement element

1. Introduction

SCADA (Supervisory Control And Data Acquisition) is a system used for automating general processes, collecting data from sensors and instruments located at remote stations, and transmitting and displaying this data at a central station for monitoring or control purposes. The collected data is typically observed on one or more SCADA computers at the central (main) station. In reality, a SCADA system can monitor and control up to hundreds of thousands of input and output values. Common analog signals monitored (or controlled) by the SCADA system include levels, temperatures, pressures, flow rates, and motor speeds in frequency regulation. Typical digital signals for monitoring (control) include level switches, pressure switches, motor status, and relays. As the name suggests, it does not have complete control over the system but is more focused on supervision and monitoring. As such, it is a software package positioned at the top of the hardware it relates to, mainly via PLC (Programmable Logic Controller) or other commercial hardware modules. SCADA systems have made significant advancements in functionality and performance over the years [1,2]. The term SCADA typically refers to the central system that monitors and controls the entire heat distribution system even over long distances (up to substations). Most of the control of a substation is actually automated by the PLC. The main control functions are almost always forbidden to the controller in the station. For example, the PLC may control the flow of heating water through part of the process, but the SCADA system can allow the operator to change the set flow value and can record and display any alarm conditions, such as loss of pressure or high temperature [3].

Data collection starts at the PLC level and involves reading measurements and statuses. Then, the necessary data is sent to the SCADA system, where it is translated and formatted so that the operator in the control room can make appropriate decisions based on them, which may be necessary to adjust or override normal PLC

controls. Data can also be stored in a history, often supported by a database, for trend display and other analytical actions.

1.1. Work Technology of Substations

Heat energy is distributed to substations in buildings through primary piping and transferred to the secondary system indirectly through heat exchangers water-water. The transferred heat energy is distributed to consumers through secondary piping within the building itself, as well as to neighboring buildings. To achieve the required parameters of the secondary fluid, the substation is equipped with appropriate equipment: a digital controller with corresponding sensors, a calorimeter, a shut-off valve, dirt traps, control valves, pressure regulators, and a differential pressure regulator. The pressure regulator brings the fluid pressure to the desired value. In the heat exchanger, heat exchange with the secondary fluid occurs indirectly – the heat exchange is not accomplished by mixing fluids from these two systems, but by circulating the cooler fluid (secondary system) around the pipes through which the warmer fluid (primary system) flows. The desired flow rate is achieved by a transient electromotor control valve located on the return branch of the primary system. A differential pressure regulator that runs without additional energy provides the range of nominal differential pressure needed for the control valve to operate. By measuring the flow and the temperature difference of the primary fluid at the supply and return line of the exchanger, the computational unit determines the transferred amount of heat energy. The cooled fluid of the primary system passes through a dirt trap and returns through the heating network to the plant. The temperature of the fluid in the primary system is controlled according to a given sliding diagram in the plant, and additional regulation of the desired temperature of the secondary fluid is achieved by "flow change" in the primary part of the substation through the action of the regulator on the executive organ. The desired temperature of the secondary fluid is a function of the outside temperature, time of day, and day of the week, and is set as a program for the regulator. The pump operating mode is also programmed. The digital controller is equipped with sensors for measuring the outside temperature, supply and return temperatures, pressure of the primary and secondary fluids, room temperature, and fluid flow in the primary system. All controllers are connected to a personal computer in the dispatch center via cable or GPRS network, where data acquisition and monitoring of the heating system operation are performed. The controllers in the substations operate automatically in a programmatically defined mode. Change of controller operating mode, individual control parameters, and remote commands can be executed from the dispatch center. This establishes a system of remote monitoring and control of the entire heating system, with the operation of the heat exchange stations fully automated. Substations contribute significantly to the success of district heating and have evolved over time from installations made in accordance with standards to technologically advanced products that represent a link with the consumer. Low maintenance costs, standardization, and system optimization have outweighed previously detailed project solutions and on-site installations. The configuration of modern substations and equipment selection should enable the following:

- Remote monitoring of parameters,
- Remote control and management,
- Local regulation,
- Measurement of heat energy consumption,
- Reporting of alarm conditions,
- Ability to manage the technical system.

These requirements can be met by applying the following principles:

a) Selection of modern solutions and equipment:

- Plate heat exchangers,
- Integrated "combo" and control valves,
- Ultrasonic heat meters,
- Application of "PLC" controllers,
- Frequency regulation of rotation speed,
- Application of SCADA software.

b) Connecting to a unified network:

- Optical cable,
- Wireless Ethernet.

The equipment of the heat substation consists of a mechanical (thermos-technical) part and an electro-energetic part.

The thermos-technical installation contains all the necessary elements for the operation of the substation: a heat exchanger (in the case of indirect connection of consumers), a pressure regulator and a flow control valve (in the case of direct connection of consumers), an electromotor control valve or combination valve, an ultrasonic flow sensor (integral part of the heat meter), a dirt trap and sedimentation tank, a circulation pump, an expansion vessel or pressure maintenance device, a safety valve, and sensors for measuring water pressure and temperature.

The electro-energetic part includes:

- *Power equipment:* Fuses, contactors with overcurrent protection, switches, and pump operation indication,
- *Measurement and control equipment:* Microprocessor controller, acquisition module, heat energy meter computing unit, and transmitter power supply (sensors),
- *Communication equipment:* Dual communication module, communication converter, GPRS modem.

The microprocessor controller enables the regulation of heat energy delivery, i.e. limiting the maximum water flow through the primary part of the substation (via the control valve), changing the supply water temperature in the secondary part depending on the outside air temperature according to the sliding diagram, and changing the heating mode. Requirements related to the control unit are primarily determined by the function of the given building. Additionally, there may be functions that are desirable from the perspective of the district heating provider, but they must be justified both technically and financially. In any case, the control unit and control valve must comply with the technical requirements of the heat energy provider, and standard control units intended for use in district heating usually meet these requirements. The minimum functions necessary to achieve quality heat energy delivery are as follows:

- Control of the supply water temperature in the secondary heating system as a function of the outside temperature,
- Possible adjustment of the regulation curve for the supply water temperature to adapt to the building's requirements,
- For non-residential buildings, the ability to program heat energy delivery based on the number of hours and days of the week,
- The control unit must be user-friendly and easy to program.

The control unit will contain at least the following elements:

- One controller with a control curve,
- At least 2 analog inputs for sensors, typically with a resistance of 0 to 25 k Ω for PT1000 type sensors,
- At least 1 analog output, typically 0–10 V; other variations relate to increase/decrease type regulation,
- It should have a calendar and a time channel,
- At least one digital output (for pump control); there should be the possibility of adjusting the temperature for device activation (set value) and the time interval for activation.

All other functions are usually additional, for example:

- Control of the supply water temperature curve for the secondary supply line, depending on the reference indoor temperature; 1, 2, 3, 4, or more sensors,
- Control of the supply water temperature curve for the secondary supply line, depending on the time of day (reducing the set temperature at night, morning heating),
- Automatic adjustment of the control curve depending on indoor reference temperatures,
- Automatic humidification due to changes in outside temperature,
- Pump control; operation with one or parallel inline pumps,
- Automatic switching to a parallel pump if the first pump is not operating,
- Frost protection,
- Summer operation function with automatic pump activation for a very short period each day,
- Pump shutdown in case of building overheating,
- Alarm functions for pumps, temperatures, sensors, etc.,
- Communication with the main program containing data, usually via RS232 or RS485,

- M-BUS communication of heat meters, sub-controllers, electric meters, water meters, etc.,
- Flow limitation.

1.2 The microprocessor controller

The microprocessor controller features a functional keypad and a graphical LCD screen, enabling users to view current values of all measured parameters in the system, set setpoints, and manually control electric drives. Information is organized into 2 groups of screens.

The first group comprises INFO screens displaying system operation information (measured and set values, input and output statuses, alarms, etc.). The content and layout of INFO screens depend on the selected application, allowing users to define their own INFO screens when creating their programs.

The second group consists of standard MENU screens, which remain consistent and display or allow setting of setpoints, input and output statuses, date and time, communication parameters with connected devices, active application, user interface language, etc. To prevent unauthorized access, the controller is equipped with 2 levels of passwords (user - for changing setpoints and manual control, and system - for changing the active application and user interface language).

Set parameters are permanently stored in the controller's internal memory, ensuring their retention in case of power loss. The built-in real-time clock enables the execution of time-based programs (heating reduction, operation within specified time intervals, operation in time sequences, time-based setpoint changes, etc.).

The MBUS master communication port allows direct connection to up to 4 devices with built-in MBUS slave communication ports (heat energy meters, circulation pumps, or similar smart devices).

By utilizing one of the available communication interfaces (RS232 or RS485), the microprocessor controller can be connected to a remote monitoring and control system. Built-in standard protocols facilitate integration of the controller into SCADA systems of leading global manufacturers and ensure full compatibility with standard software development tools.

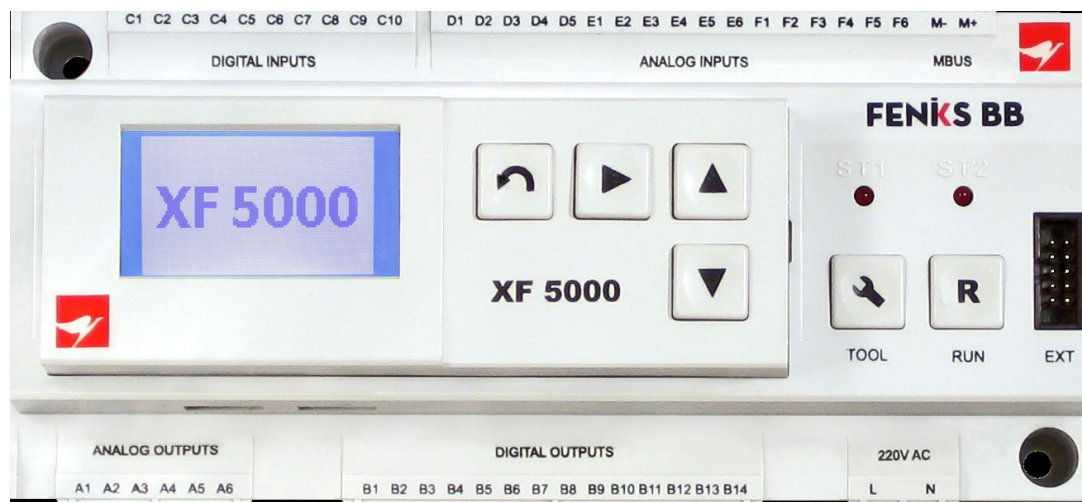


Figure 1. FX 5000 Appearance

1.3 The communication network

Communication of the central system (i.e. computers and microprocessor units) is based on the standard RS 485 communication interface, allowing direct connection of multiple stations at various distances. The connection is direct, two-wire, and of the "bus" type. The RS 485 connection on the PC is provided by converting the standard RS 232 port. An internal PC card is used for this conversion. The connection to the local controller should already be provided on a standard 9-pin connector on the device's housing.

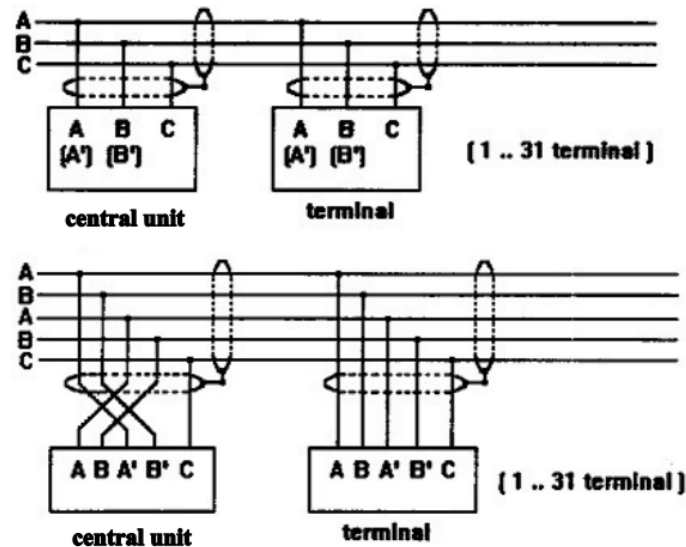


Figure 2. RS 485 interface connection

The RS 485 interface connection consists of two active conductors, labeled as A and B on the transmitter side, i.e., A' and B' on the receiver side, and a common ground. Depending on the requirements and application, a two-wire or four-wire network connection can be used, as shown in the previous pictures. The signal status is defined by the voltage difference between the A and B lines, or A' and B' lines, making it highly immune to electrical interference. The C (C') line is the network ground for equalizing the potential of the individual device grounds. Standard signal cables should be used for communication.

2. Regulation Systems

Depending on the location where regulation is implemented, there are central, group, local (district), and individual regulation systems [4].

- Central regulation is performed in the heating plant according to the change in heat load for most consumers when the heat load in the area is uniform.
- Group regulation is conducted in central substations for groups of similar consumers, ensuring the necessary flow and temperature of the heat carrier.
- Local regulation is provided in-house substations (at the consumer's connection point) for additional correction of heat carrier parameters, taking local conditions into account.
- Individual regulation is carried out directly at the heat transfer exchanger (on radiators) and complements other forms of regulation. It requires the use of many individual regulators, which increases initial investments.

When using water as the heat carrier, the following methods of central regulation can be used:

- Qualitative regulation, which consists of regulating the released heat by changing the temperature of the heat carrier at the supply line to the heating device, while maintaining a constant quantity (flow) of the heat carrier supplied to the regulated plant.
- Quantitative regulation, which involves regulating the released heat by changing the flow of the heat carrier at a constant temperature at the supply line to the regulated plant.
- Qualitative-quantitative regulation, which consists of regulating the heat release by simultaneously changing the flow and temperature of the heat carrier.
- Interrupted regulation is achieved by switching off the system, i.e., periodic interruptions in releasing the heat carrier into the network. Central interrupted regulation is only possible in networks with similar loads. For dissimilar loads, interrupted regulation is used for local regulation.

The heat load of many consumers in modern district heating systems is neither homogeneous in terms of heat consumption nor in terms of heat carrier parameters. To ensure high-quality heat supply, combined regulation should be applied, which should be a rational combination of three levels of regulation - central group or district (local), and individual. This ensures the best balance between heat release and actual consumer needs.

Effective regulation can only be achieved through appropriate automatic regulation systems, not manually, as was the case in the early development of centralized heat supply.

2.1 Automation of district heating systems

The most efficient way to regulate heat release in centralized heat supply systems with diverse thermal loads is a combination of central qualitative regulation with group or local quantitative regulation. The choice of the basic impulse for local regulation depends on the type and operating mode of the plant. Selecting an impulse for regulating heating loads is a complex task because temperatures in individual rooms of heated buildings can vary significantly and depend not only on the amount of heat supplied to the building but also on the characteristics of the building's heating system, conditions of use of individual rooms, heat gains from people, insolation, infiltration, as well as the arrangement of individual rooms in the building according to cardinal directions and wind roses. Therefore, to fully satisfy the thermal load, it is necessary to provide supplementary local regulation of individual rooms or zones in each building, exposed to different influences such as insolation, wind, heat distribution methods, and other conditions, alongside group or local regulation.

The parameters of interest are:

- Outdoor temperature,
- Primary supply temperature,
- Primary return temperature,
- Primary supply pressure,
- Primary return pressure,
- Secondary supply temperature,
- Secondary return temperature,
- Secondary side pressure,
- Current flow rate,
- Heat delivered.

States of interest include:

- Percentage of opening of the control valve,
- Pump operation indication,
- Pressure indication in the expansion vessel,
- Service intervention indication.

The SCADA solution for substations includes:

- Display of measurements and states in the substation,
- Adjustment of regulation parameters,
- Trend diagram of relevant measurements,
- Option to choose manual or automatic operation mode of the substation,
- In manual mode - control of valve and pumps,
- Display of alarm states,
- System transparency - most relevant data on one screen,
- Improved user awareness,
- Alarm lists, events, graphs – current and archived,
- Excel reports; Excel workbook dynamically linked to the SCADA system database,
- Simple and secure management - switching on/off pumps and opening/closing control valves,
- When managing the substation, the command and the user who issued it are registered,
- Optical network,
- Possibility of system expansion in the future.

Features of the considered SCADA system are:

- Universal system for visualization, monitoring, and control,
- Interface in Serbian language,
- Windows and/or Linux platform,
- Easy integration into existing IT environments,
- Client/server architecture,

- Object-oriented datapoint model,
- Unlimited number of datapoints,
- Direct drivers and OPC,
- Online design and engineering,
- Internet/intranet integration,
- WAP, SMS, email, fax, or voice messages.

On Figures 3 to 5, schemes of all measurements that are part of the SCADA system of the District Heating System MF Niš are shown, while in tables 1-3, technical specifications of all measuring devices installed are displayed.

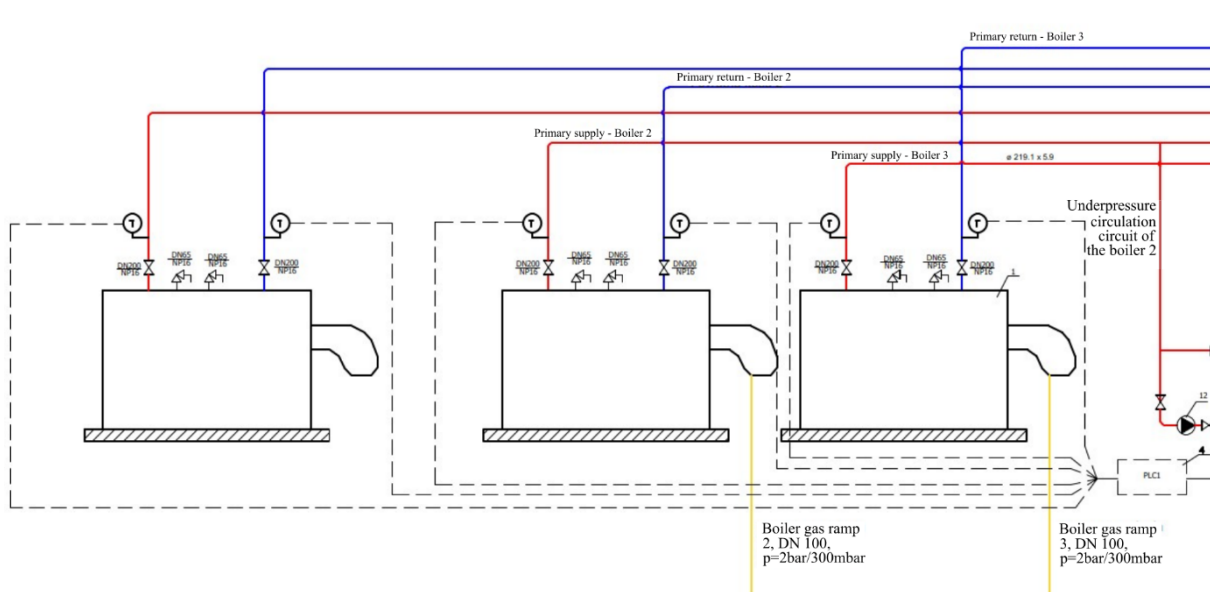


Figure 3. Diagram of measurements in the boiler circuit of the District Heating System

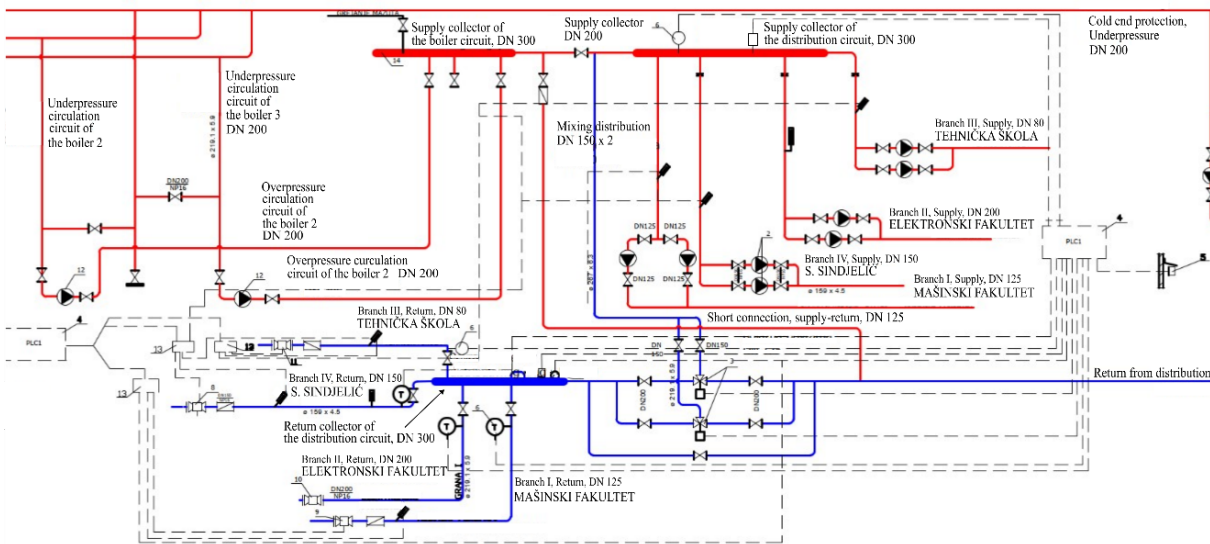


Figure 4. Diagram of measurements in the distribution circuit of the District Heating System

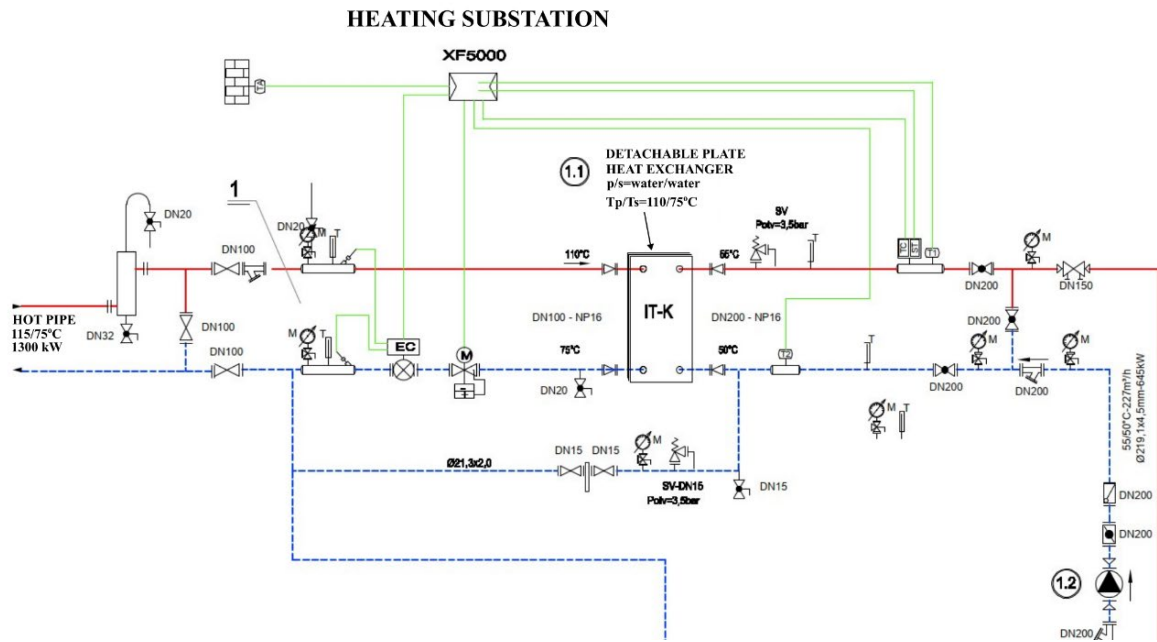


Figure 5. Diagram of measurements in the circuit of a typical consumer connected to the District Heating System

In tables 1 to 3, a list of applied sensors with their characteristics is shown.

Table 1. Characteristics of sensors in the boiler circuit of the District Heating System

Sensor	Description	Type, manufacturer	Min	Max	Unit	Signal type
Temperature sensor	Outdoor air temperature	STS-1, NTC	-40	+60	oC	AI, 0-10VDC
Temperature sensor	Initial temperature of water in boiler 3	Pt100	+30	+150	oC	AI, 4-20mA
Temperature sensor	Return temperature of boiler 3	Pt100	+30	+150	oC	AI, 4-20mA
Temperature sensor	Initial temperature of water in boiler 2	Pt100	+30	+150	oC	AI, 4-20mA
Temperature sensor	Return temperature of boiler 2	Pt100	+30	+150	oC	AI, 4-20mA
Temperature sensor	Initial temperature of water in boiler 1	Pt100	+30	+150	oC	AI, 4-20mA
Temperature sensor	Return temperature of boiler 1	Pt100	+30	+150	oC	AI, 4-20mA

The following statuses are displayed:

- Burner operation status (for each boiler)
- Indication of primary fuel: natural gas / fuel oil (for each boiler)
- Boiler pump operation status (for each boiler)
- Set temperature for boiler cold end protection (process parameter)

Table 2. Characteristics of sensors in the distribution circuit of the District Heating System

Sensor/device	Description	Type, manufacturer	Min	Max	Unit	Signal type	Accuracy
Heat energy meter	Ultrasonic	Depends on the consumer					
Temperature sensor	Primary supply water temperature	Pt100					
Temperature sensor	Return temperature of primary supply water	Pt100					
Pressure sensor	Pressure of primary supply water	WIKA	0	16	Bar	AI, 4-20mA	<1% mernog opsega
Pressure sensor	Pressure of primary return water	WIKA	0	16	Bar	AI, 4-20mA	<1%
Temperature sensor	Secondary supply water temperature	CTS-1/Pt Pt1000	-50	+200	oC		
Temperature sensor	Secondary return water temperature	CTS-1/Pt Pt1000	-50	+200	oC		
Pressure sensor	Pressure of secondary return water	WIKA	0	6	Bar	AI, 4-20mA	<1%
Temperature sensor	Outdoor air temperature	STS/Pt, Pt100	-35	+50	oC		

The following statuses/sizes are also displayed:

Circulation pump operation status for the secondary network (for each pump)

Circulation pump operation status (manual / automatic)

Failure of the circulation pump bimetallic strip (for each pump)

Electromotor control valve operation status (opening/closing)

Control valve position status (fully open - 100% / fully closed - 0%)

Set temperature of the secondary supply water (process parameter)

Water flow to the consumer (parameter from ultrasonic heat energy meter)

Current power of the heat substation (parameter from ultrasonic heat energy meter)

Cumulative heat energy delivered (parameter from ultrasonic heat energy meter)

Table 3. Characteristics of sensors in the circuit of a typical consumer in the District Heating System

Sensor/device	Description	Type, manufacturer	Min	Max	Unit	Signal type	Accuracy
Heat energy meter	Ultrasonic	Depends on the consumer					
Temperature sensor	Primary supply water temperature from the meter	Pt100					
Temperature sensor	Return temperature of primary supply water from the meter	Pt100					
Pressure sensor	Pressure of primary supply water	WIKA	0	16	Bar	AI, 4-20mA	<1%
Pressure sensor	Pressure of primary return water	WIKA	0	16	Bar	AI, 4-20mA	<1%
Temperature sensor	Temperature of the secondary supply water	CTS-1/Pt Pt1000	-50	+200	°C		
Temperature sensor	Temperature of the secondary return water	CTS-1/Pt Pt1000	-50	+200	°C		
Pressure sensor	Pressure of the secondary return water	WIKA	0	6	Bar	AI, 4-20mA	<1%
Temperature sensor	Outdoor air temperature	STS/Pt, Pt100	-35	+50	°C		

The following statuses/sizes are also displayed:

- Secondary network circulation pump operation status (for each pump)
 - Circulation pump operation status (manual/automatic)
 - Failure of the circulation pump bimetallic strip (for each pump)
 - Electromotor control valve operation status (opening/closing)
 - Control valve position status (fully open - 100%/fully closed - 0%)
 - Set temperature of secondary supply water (process parameter)
 - Water flow to the consumer (parameter from ultrasonic heat energy meter)
 - Current power of the heat substation (parameter from ultrasonic heat energy meter)
 - Cumulative heat energy delivered (parameter from ultrasonic heat energy meter)
-

By implementing these modern solutions, the following objectives are achieved:

- Savings of delivered or produced thermal energy (automatic regulation of secondary water temperature based on changes in outdoor air temperature and limitation of maximum flow rate of each heat substation).
- Ensuring quality heat supply (remote management of heat substations from a single location - balancing and even distribution of thermal energy).
- Reduction of district heating system operation costs (automatic control and monitoring of operation, functional parameters, and equipment conditions enable planned preventive maintenance, reduced number of failures, longer lifespan, and lower maintenance costs).
- Increase in the availability of the district heating system (continuous automated monitoring and reporting (statuses, warnings, and alarms) in the dispatch center reduce intervention and downtime).
- Facilitating better payment rates and rational consumption (introduction of a system for individual measurement, registration, and calculation of delivered and consumed thermal energy for each consumer).
- Optimization of investments and preservation of investment value (application and transfer of technology and knowledge - end-user training - provision of technical support and spare parts (10-20 years)).

3. Characteristics of the heat substation

The measurement was conducted in a residential building, block 12, in the residential area "Stevan Sindelic" in Niš. The building is connected to the district heating system. The distribution of hot water is provided from the boiler room located within the Faculty of Mechanical Engineering building in Niš. A central heating system with hot water 90/70 °C and forced circulation is adopted for heating the building. The system is a two-pipe system with bottom water distribution. Steel radiators of the "Jugoterm" type are adopted for heating elements. All radiators are equipped with radiator valves and radiator thermostatic valves with thermostats. Thermostatic heads and heat meters are installed in one reference apartment (apartment number 2), and only heat meters are installed in the other two reference apartments. Hot water supply is provided from the substation, which consists of a mechanical (thermotechnical) part and an electro-energetic part.

The thermotechnical installation consists of:

- Heat exchanger $Q = 600$ kW,
- Adjustable flow regulator with integrated electromotor control valve (combination valve), KV-050/32 "Feniks BB" Niš
- Ultrasonic flow meter, which is an integral part of the heat energy meter,
- Circulation pumps,
- Sensors for measuring water temperature in the secondary part of the installation (supply and return water)
- Sensors for measuring outdoor air temperature.

The electro-energetic part contains a microprocessor regulator, a computing unit of the heat energy meter, a module for dual communication, as well as accompanying electrical equipment housed in the electrical cabinet: circuit breakers, contactors with overcurrent protection, switches, etc.

Connecting the heat substation to the distribution network of the district heating system is achieved via a plate heat exchanger. The heat substation performs qualitative-quantitative regulation of thermal energy delivery to consumers. Qualitative regulation is achieved by changing the water temperature in the primary water return of the district heating network depending on changes in outdoor air temperature, directly at the heat source (boiler room).

Quantitative regulation is achieved by local flow regulation in the heat substation. The task of the automation is to regulate the room temperature indirectly through the regulation of water temperature in the supply water of the secondary circuit. This function is performed by a microprocessor regulator (4-point regulation has replaced 2-point regulation), acting on the electromotor combination valve. The installed regulator XF5000 has replaced the existing MR5007/Q, both products of FeniksBB from Niš.

The central regulator in the boiler room is connected via GPRS to the regulator in the heat substation, which performs local regulation, thus ensuring data transmission in both directions: from the system to the operator and vice versa.

A system overview and remote parameter modification are enabled. Additionally, the central control system operator has insight into the statuses of all electrical drives and the ability to issue unconditional commands to all electrical drives (switching on, off, opening and closing valves).

4. Presentation of the CENUS program application

The ultimate goal of the district heating system is to achieve the desired temperature in heated rooms, as defined by the project conditions (target temperature = 20°C). This is achieved by regulating the temperature of the distribution water in the secondary network, changing the set values of system parameters via a sliding diagram. When defining the sliding diagram, consideration must also be given to the accumulation of thermal energy in the building itself. For this reason, instead of the classical fixed regime (90/40°C secondary supply water for external conditions of -15/12°C), remote control enables more frequent changes in the regime, with significantly lower values of the sliding diagram temperature.

Figure 6 shows a comparative diagram of the change in the temperature of the primary water in the secondary network *tost* (measured secondary supply water temperature) and *trac* (calculated secondary supply water temperature), the outside air temperature (*ts*), and the inside air temperature (*tu*) over time, after the implementation of the SCADA system and with the old type of controller (left) and the new type of controller (right) [5].

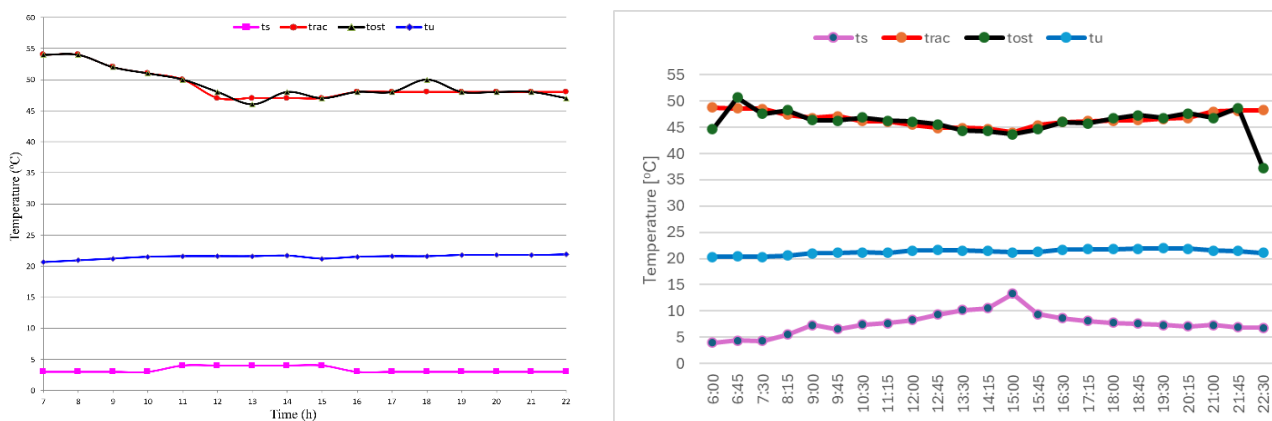


Figure 6. Diagram of temperature change with the SCADA system (*tost* - measured secondary supply water temperature, *trac* - calculated secondary supply water temperature, *tu* - indoor temperature, *ts* - outdoor temperature)

The diagram of temperature change before the implementation of the SCADA system is shown in Figure 7.

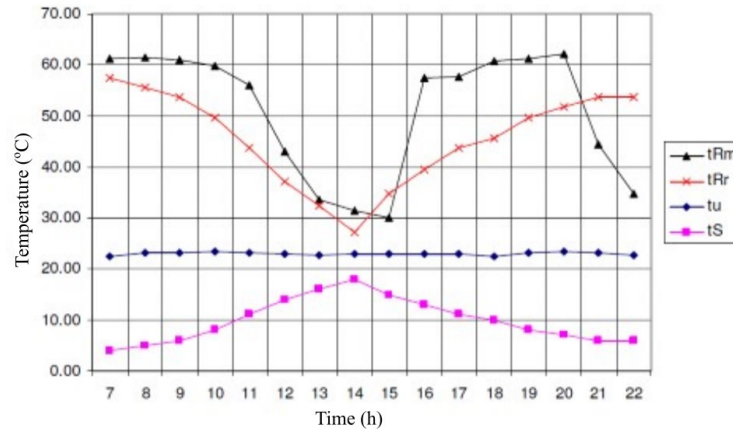


Figure 7. Diagram of temperature change without the SCADA system. tRm - measured temperature of the supply water in the secondary circuit, tRr - calculated temperature of the supply water in the secondary circuit, t_u - indoor temperature, t_s - outdoor temperature

From the diagram, it can be observed that the air temperature in the reference room was slightly higher than projected, but it was well regulated throughout the day primarily by the temperature of the supply water. The temperature of the supply water in the secondary circuit closely followed the trend of the calculated temperature values with the implementation of the SCADA system, mainly through changes in the sliding diagram (to a value of 60/40°C). In the case without remote monitoring and control, the temperature of the supply water in the secondary circuit was at a higher temperature level (averaging around +10°C), which represents an opportunity for savings and increased system efficiency.

5. Conclusion

Based on all measurements and the presented characteristic changes, the following conclusions can be drawn:

- The temperature of the supply water in the secondary circuit should follow the trend of calculated temperature values.
- The sliding curve of the supply water temperature in the secondary circuit should be adjusted to the characteristics of the facility, i.e., its thermal storage capacity, and should accommodate changes during the heating day.
- Changes in the sliding curve during the heating day are only possible through remote control, and such operation mode offers the potential for significant energy savings. Of course, provided that user comfort (indoor temperature) is not compromised, as evident from Figure 6.

Acknowledgements

This research was supported by the Science Fund of the Republic of Serbia, Grant No. 23-SSF-PRISMA-206, Explainable AI-assisted operations in district heating systems - XAI4HEAT.

References

- [1] G. Cvetkov, M. Marašević, R. Karamarković. "Continual monitoring of heat sources operation in PUC "Toplana" Kraljevo in order to improve energy efficiency", Proceedings of the 39th International Congress on HVAC, Belgrade, Serbia, 2008,
- [2] Peter Dannenbring. "Modern Substations – Design and Installation", Proceedings of the 36th International Congress on HVAC, Belgrade, Serbia, 2005,
- [3] D. Bailey and E. Wright, "Practical SCADA for Industry", Elsevier, 2003,
- [4] Branislav Stojanovic, Jelena Janevski, Dejan Mitrovic, Marko Ignjatovic, Mirko Stojiljkovic, "Heating Substation Work Regulation", Proceedings of the 13th Symposium on Thermal Science and Engineering of Serbia and Montenegro, Sokobanja, Serbia, 2007,
- [5] Feniks BB, "CENUS 3000 - User manual" (in Serbian), 2007.

Material Selection of Wave Energy Turbine Blade by using MCDM Solver

Dušan Petković^a, Miloš Madić^a

^aFaculty of Mechanical Engineering University of Niš, Niš, RS, dusan.petkovic@masfak.ni.ac.rs

Abstract: Selection of materials is a complex and multi-criteria decision making problem, which requires a lot of knowledge and experience. Selection process is influenced by few factors such as thermal, mechanical, electrical, chemical, physical and technological properties as well as their price and availability. This paper considers material selection problems of wave energy extraction turbine blade by using MCDM approach. Due to help decision makers in solving this complex task, a decision support system named MCDM Solver. MCDM Solver was used in decision-making process to rank materials for the turbine blade with respect to several criteria. Based on the results the best ranked materials are Carbon fiber reinforced polymer, titanium alloys and Glass fiber reinforced polymer.

Keywords: Material selection, Wave energy extraction turbine blade, Multi-criteria decision making, MCDM Solver, Decision support system.

1. Introduction

Engineering design is significantly depended on objectives of performance, cost and environmental sensitivity, which are often limited by materials. To optimize product design, it is necessary to select the materials which best meet the needs of the design, maximizing its performance and minimizing its cost.

Material selection is the process of choosing the best material for a particular design. In mechanical design, this process enters at every stage of the design process. In the total design model material selection is rated as one of the fundamental parameters along with market investigation, product design specification, component design, design analysis, manufacture and assembly [1].

The objectives and criteria in the material selection process are often in conflicts which involves certain trade-offs amongst decisive factors. Therefore, only with a systematic and structured mathematical approach the best alternative for a specific engineering product can be selected [2]. The material selection problems with multiple non-commensurable and conflicting criteria can be efficiently solved using multi-criteria decision making (MCDM) methods. The MCDM methods have the capabilities to generate decision rules while considering relative significance of considered criteria upon which the complete ranking of alternatives is determined [3-4].

Decision support system (DSS) is a special class of information system oriented to the decision-making process and aims to support, mainly business decision-doing processes [5]. DSS is a symbiosis of information systems, application of functional knowledge and ongoing decision-making process [6]. Their main goal, as the goal of other information systems, is to improve the efficiency and effectiveness of an organization.

This paper is focused on the application of developed DSS named MCDM Solver for material selection of wave energy extraction turbine blade. A real time case study was solved by using MCDM Solver with obtained complete rankings.

2. Wave energy

The energy from ocean waves is the most conspicuous form of ocean energy, possibly because of the wave destructive effects. The waves are produced by wind action and are therefore an indirect form of solar energy. The wave energy absorption is a hydrodynamic process in which relatively complex diffraction and radiation wave phenomena take place [7].

The utilization of wave energy involves a chain of energy conversion processes. Each of the processes is characterized by its efficiency and constraints which must be controlled. Particularly relevant is the hydrodynamic process of wave energy absorption.

The main disadvantage of wave power, as with the wind from which it originates, is its (largely random) variability in several time-scales: from wave to wave, with sea state, and from month to month (although patterns of seasonal variation can be recognized). The assessment of the wave energy resource is a basic prerequisite for the strategic planning of its utilization and for the design of wave energy devices.

2.1. Oscillating water column (OWC)

The oscillating water column (OWC) wave energy harnessing method is considered as one of the best techniques of converting wave energy into electricity. These devices stand on the sea bottom (Figure 1) or fixed to a rocky cliff.

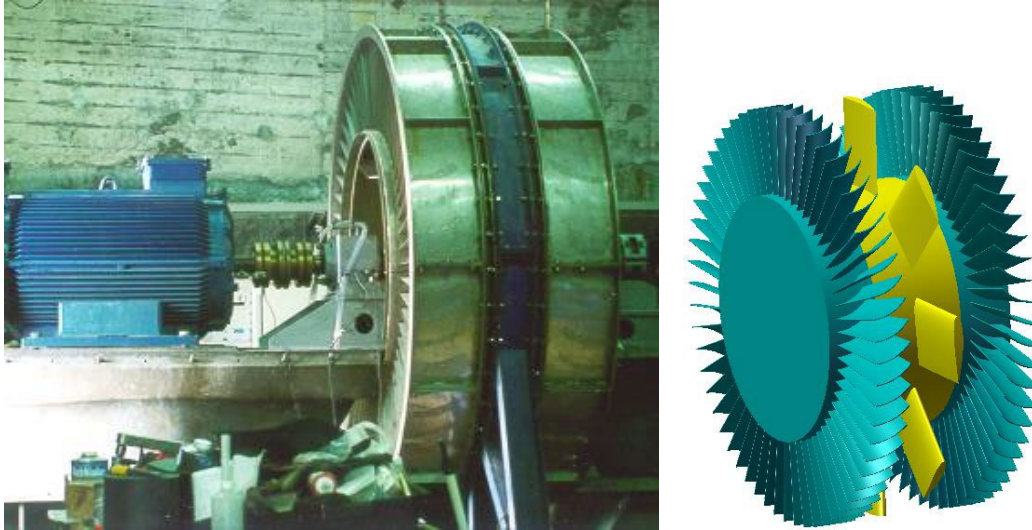


Figure 1. Back view of the 400 kW OWC plant on the island of Pico, Azores, Portugal, 1999 [7]

It is an economically viable design due to its simple geometrical construction, and is also strong enough to withstand against the waves with different heights, periods and directions. The design (Figure 2) consists of an OWC chamber and a circular duct, which reciprocally moves the air from and into the chamber during the process of wave approach and retreat. A self-rectifying turbine mounted inside the duct is designed to turn in one direction only although the airflow moves bi-directionally [8]. A matching generator is coupled to the turbine to produce electricity.

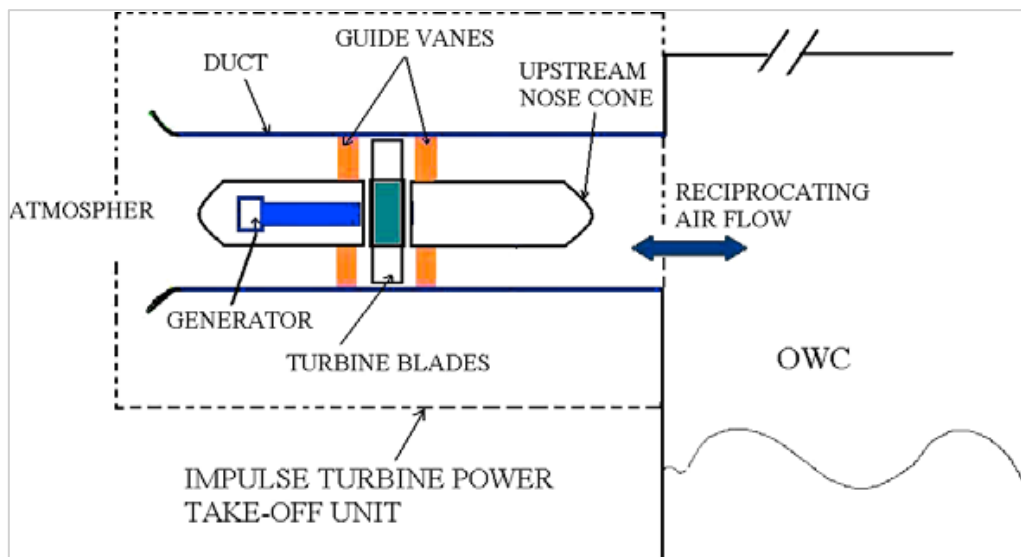


Figure 2. Impulse turbine power take-off unit with OWC [9]

The turbine's blade is designed to convert the pneumatic energy of air produced by the OWC to mechanical shaft power. This will be transmitted to a generator to produce electricity.

3. MCDM Solver

MCDM Solver is an “on-line” DSS which was developed within the doctoral dissertation of Dušan Petković [10]. The developed DSS is located on the “Virtuode” Company web site (<https://virtuodeportalapp.azurewebsites.net/WebTools/Home>) and it is available to everyone who registers by creating an account (Figure 3). This DSS offers the possibility of working with maximization, minimization and target criteria [11].

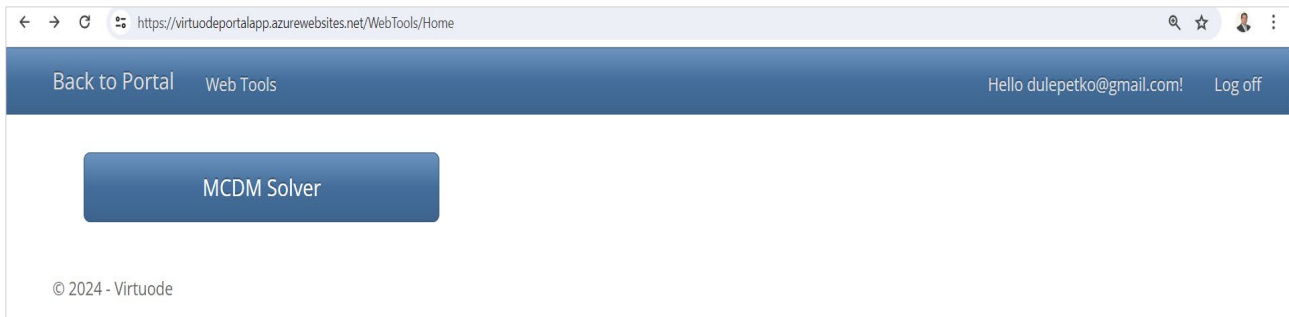


Figure 3. MCDM Solver – initial layout

The input data for MCDM Solver:

- Initial matrix of decision-making with target value of criteria (Step 1);
- η - Confidence level of decision maker in significance of the selected criteria (where $\eta=1$ corresponds to 100% confidence level, while $\eta=0$ corresponds to a confidence level of 0);
- Pairwise significance evaluation of the selected criteria.

Based on the input data, MCDM Solver can determine the values of the criteria weights (Step 2) and ranking alternatives (Step 3) with the corresponding values by means of Extended TOPSIS [12], Comprehensive VIKOR [13] and Comprehensive WASPAS [10, 14] methods.

Developed DSS architecture is flexible and easy to upgrade, so it enables the inclusion of new models that will come in future. MCDM Solver has a user-friendly interface, which enables a simple and efficient way of entering the necessary data which not strictly related to material selection process [15]. Its use simplifies the solution of the MCDM problems because it does not require expert knowledge from the decision making theory from the user.

4. Turbine blade material selection

4.1. General requirements

A material selection process begins by considering the material requirements which are needed for a specific application. Therefore it is necessary to select criteria that can be used to select the most suitable turbine blade material. Mechanically speaking, a blade is considered as a tie rod loaded in tension due to the centrifugal load. The latter could easily be translated to a tensile force equivalent F , so the blade must support the axial tensile load F . The blade height, h , is specified once the turbine diameter and the hub-to-tip ratio have been chosen. The cross sectional area (A_b) is fixed by the optimum aerodynamic design [16]. Here, maximizing performance means minimizing the mass while still carrying the load F safely. In other words, the blade must be as light as possible to reduce stress r . This is known to be highly concentrated at the blade root and proportional to material density (q_b) multiplied by the square of specific (tip) blade speed [9].

4.2. Materials screening

Thakker et al [9] was carried out selection of candidates for turbine blade materials based on criteria such as: strength, specific weight, corrosion resistance, ease of manufacture and availability. Strength is maximum tolerance of loads before failure. The component should be designed to perform its function without failure. When the stress level caused by the load, e.g., centripetal force, reaches the ultimate stress (tensile strength) the material fails. The yield stress (lower than tensile strength), which is the starting point of plastic deformations (yield point) is another measure of strength. Specific weight (density) is important because centripetal force is proportional to the specific weight. Also, the material should have a good corrosion resistance to perform in a severe environment such as that of sea salt atmosphere. Additionally, it is important

that the material can be processed by the most common methods such as by forging, casting, machining and welding. Finally, the material should be readily available.

Taking into account before mentioned criteria the best materials for manufacturing the turbine blades are:

1. Titanium alloys;
2. Nickel alloys;
3. Aluminum alloys;
4. GFRP (Glass fiber reinforced polymer);
5. Stainless steel alloys;
6. Copper alloys;
7. Silicon nitrides;
8. CFRP (Carbon fiber reinforced polymer).

4.3. Materials ranking

Material selection process should be finalized by using the MCDM approach for selected materials ranking. For this purpose MCDM Solver has been used. Criteria for ranking the materials were:

- *Stiffness* (rigidity): Minimum deformation (strain) under a given load; the blade should be designed to bear the aerodynamic transverse load. The modulus E, in effect, denotes stiffness or rigidity for any kind of applied load, i.e., tension, compression or shear.
- *Elongation at break* (ductility): This is an index measure of the material ability for plastic deformation in tension. It is defined as the amount of plastic or permanent deformation determined after fracture by realigning and fitting together the broken end of the specimen.
- *Fatigue strength*: The majority of engineering failures are caused by fatigue, which is defined as the tendency of the material to fracture by means of progressive brittle cracking under repeating alternating or cyclic stresses of intensity considerably below the normal strength. Although the fracture is of brittle type, it may take some time to propagate, depending on both the intensity and frequency of the stress cycles. Nevertheless, there is very little, if any, warning before failure if the crack is not noticed.
- *Cost of manufacture* (economic): The raw cost of the material and the cost of processing/manufacturing should be minimized. Though the material (blade) manufacturing cost could not be established a priori, the raw cost would be a strong indication for selecting an economic blade material.
- Initial decision matrix with selected materials properties and expected cost is shown in Table 1.

Table 1. Initial decision matrix for materials ranking

No.	Material	Stiffness E/ ρ (MJ/kg)	Elongation at break (%)	Expected cost (£/kg)	Fatigue strength (MPa)
1	Titanium alloys	24	10	30	630
2	Nickel alloys	24	30	7	230
3	Aluminum alloys	28	14	1	140
4	GFRP	13	3	9	600
5	Silicon nitrides	92	0.5	45	200
6	Copper alloys	16	40	4	160
7	Stainless steel	26	25	5	240
8	CFRP	73	2	45	500
	Target value	92	40	1	630

5. Results and discussion

Two scenarios are presented to test *MCDM Solver* and analyze sensitivity of the results to the change in weight of criteria.

Scenario 1: significance of the criteria (criteria weights) is evaluated by the authors of this paper by means of *MCDM Solver* (Figure 4) which has MDL (modified digital logic) as background [10]. The authors of this

article mean that *fatigue strength* is the most significant criterion, followed by *stiffness*, *expected cost* and *elongation at break*, respectively.

Scenario 2: criteria weights are taken from previous study (0.250 0.125 0.250 0.375) [9], where the most significant criterion is also *fatigue strength* and the least significant is *elongation at break*, while *stiffness* and *expected cost* are considered equally significant.

Calculate weights
✕

$\eta = 1$
 $\eta \in [0.0 - 1.0]$

Stiffness E/ ? (MJ/kg) > ▾

Stiffness E/ ? (MJ/kg) > ▾

Stiffness E/ ? (MJ/kg) < ▾

Elongation at break (%) < ▾

Elongation at break (%) < ▾

Expected cost (£/kg) < ▾

Elongation at break (%) > ▾

Expected cost (£/kg) > ▾

Fatigue strength (MPa) < ▾

Expected cost (£/kg) < ▾

Fatigue strength (MPa) < ▾

Calculate

	Stiffness E/ ? (MJ/kg)	Elongation at break (%)	Expected cost (£/kg)	Fatigue strength (MPa)
Weights	0.29167	0.12500	0.20833	0.37500

Confirm

Figure 4. Pairwise significance evaluation of the criteria by MCDM Solver

5.1. Scenario 1

Ranking results for Scenario 1 are shown in Figure 5 and also given in Table 2.

Back to Portal		Web Tools		Hello dulepetko@gmail.com! Log off		
		TOPSIS	WASPAS	VIKOR		
Titanium alloys		2	2	2		
Nickel alloys		6	6	5		
Aluminium alloys		8	3	8		
GFRP		3	4	3		
Silicon nitrides		4	8	6		
Copper alloys		7	7	7		
Stainless steel		5	5	4		
CFRP		1	1	1		
<div style="background-color: #0056b3; color: white; padding: 2px 5px; border-radius: 5px; display: inline-block;">Export</div>						
	Stiffness E/ ? (MJ/kg)	Elongation at break (%)	Expected cost (£/kg)	Fatigue strength (MPa)	C	TOPSIS
Titanium alloys	24	10	38.0	630	0.56097	2
Nickel alloys	24	30	9.0	230	0.35392	6
Aluminium alloys	28	14	1.5	140	0.32772	8
GFRP	13	3	11.0	600	0.55290	3
Silicon nitrides	92	0.5	56.0	200	0.42037	4
Copper alloys	16	40	5.0	160	0.33756	7
Stainless steel	26	25	6.0	240	0.36714	5
CFRP	73	2	57.0	500	0.56737	1
Targets	92	40	1.5	630		
Weights	0.29167	0.12500	0.20833	0.37500		

Figure 5. Ranking result – Scenario 1

Based on the results, rank of the first three ideal solutions/alternatives is: CFRP, titanium alloys and GFRP respectively. In the above order of the ideal solutions, CFRP is without any doubt the best alternative while titanium alloys and GFRP is the second and third promising candidates respectively.

Table 2. Ranking results - Scenario 1

No.	Material	TOPSIS		WASPAS		VIKOR	
		C(i)	Rank	Q(i)	Rank	P(i)	Rank
1	Titanium alloys	0.561	2	0.325	2	0.243	2
2	Nickel alloys	0.354	6	0.388	6	0.773	5
3	Aluminum alloys	0.328	8	0.351	3	1.000	8
4	GFRP	0.553	3	0.297	4	0.250	3
5	Silicon nitrides	0.420	4	0.306	8	0.807	6
6	Copper alloys	0.338	7	0.348	7	0.851	7
7	Stainless steel	0.367	5	0.408	5	0.739	4
8	CFRP	0.567	1	0.324	1	0.150	1

5.2. Scenario 2

Ranking results for Scenario 2 are given in Table 3 and shown in Figure 6 too.

Table 3. Ranking results – Scenario 2

No.	Material	TOPSIS		WASPAS		VIKOR	
		C(i)	Rank	Q(i)	Rank	P(i)	Rank
1	Titanium alloys	0.574	2	0.375	2	0.112	2
2	Nickel alloys	0.397	5	0.320	6	0.712	5
3	Aluminum alloys	0.373	7	0.412	1	0.942	8
4	GFRP	0.593	1	0.350	4	0.074	1
5	Silicon nitrides	0.372	8	0.265	8	0.903	7
6	Copper alloys	0.381	6	0.312	7	0.801	6
7	Stainless steel	0.412	4	0.346	5	0.680	4
8	CFRP	0.527	3	0.374	3	0.327	3

As could be seen, the ranking of materials for turbine blade is obtained as: GFRP-Titanium alloys-CFRP.

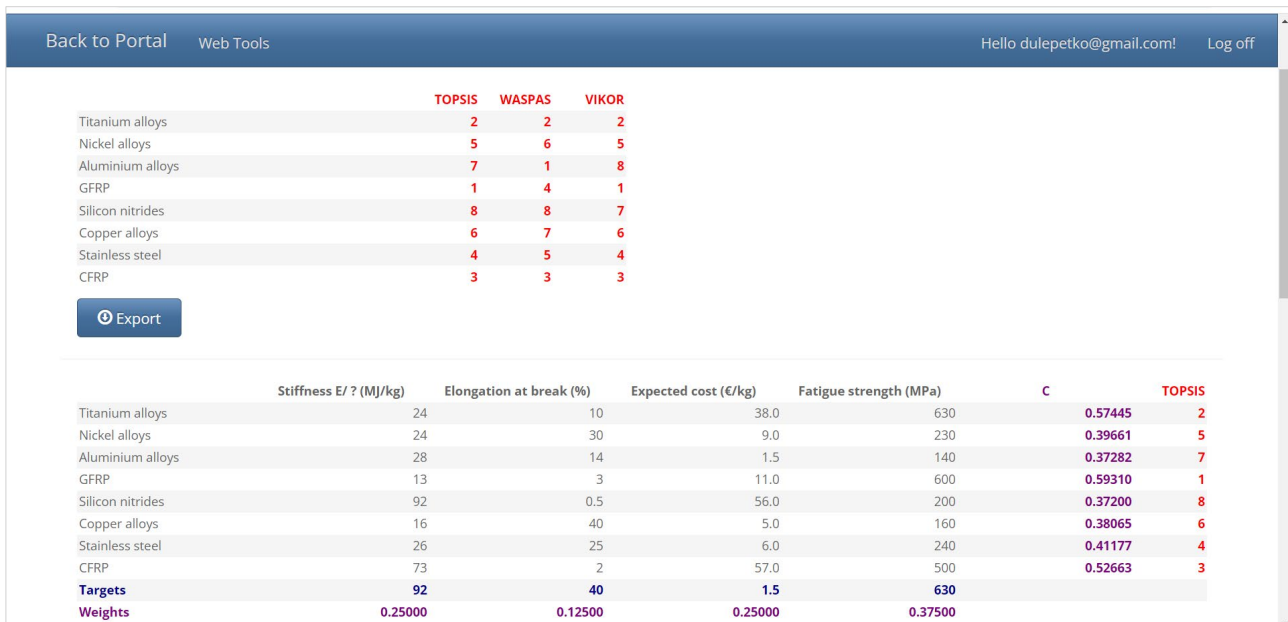


Figure 6. Ranking result – Scenario 2

In other words, GFRP is observed to be the most appropriate for this application, but not without doubt since WASPAS method ranked it as the fourth preferable one. Titanium alloys have the stable second preference while CFRP has also stable the third preference.

5.3. Comparison of results

The afore-stated material selection MCDM problem was solved by past researchers [9] using TOPSIS method. In this section the comparison of the obtained complete rankings is presented. It has to be noted that past researches while applying TOPSIS methods have used a little different criteria weights, which may affects significantly final rankings.

The results show difference between the first and third ranked material. Namely, previous authors' research gives GFRP as the most appropriate material while CFRP is third-ranked material. This paper is turned out that CFRP is best ranked material and titanium alloys second ranked material without any doubt while GFRP is third-ranked. In both scenarios titanium alloys are second-ranked material. This is due to the increase in stiffness weight where CFRP is superior and the decrease in expected cost weight where they are equal. Moreover in both scenarios it can be seen that the ranking parameters are very close and do not single out any material as absolutely superior. In this regard, all three materials should be considered as potential for making turbine blades, with the final decision being influenced by some limiting or new criterion, such as impossible purchase, difficulty in manufacturing, etc.

The different sensitivity of the methods in relation to the weighting coefficients of the criteria is also evident, which is a consequence of the mathematical procedure that is in the background of the methods. The highest sensitivity is observed with the WASPAS method for the first-ranked material, while the matching of the ranks for the other materials is the highest (total of 6), Figure 7.

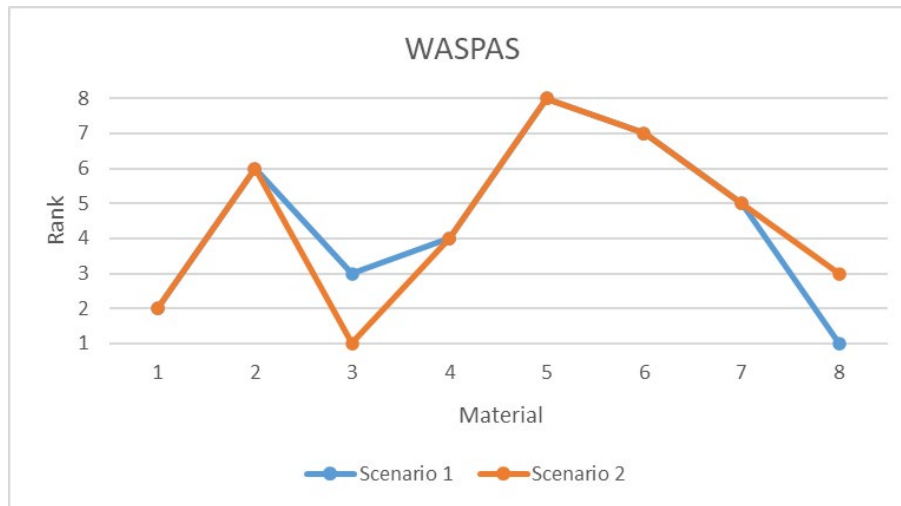


Figure 7. Ranking results by WASPAS method

In Figure 8 can observed the highest deviation/sensitivity with the TOPSIS method, where the match is only for the second-ranked material, which is otherwise absolutely stable.

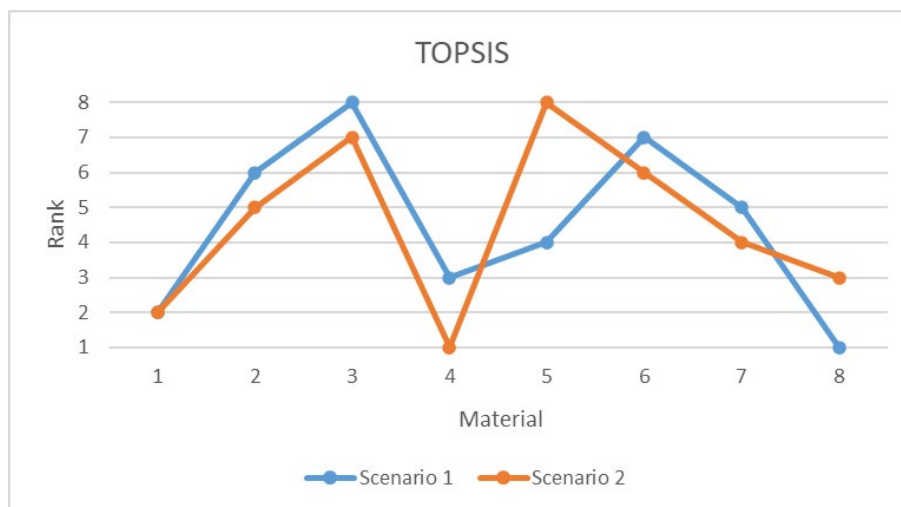


Figure 8. Ranking results by TOPSIS method

Additionally, VIKOR method gives matching of 50% but not for the first and third ranked material (Figure 9).

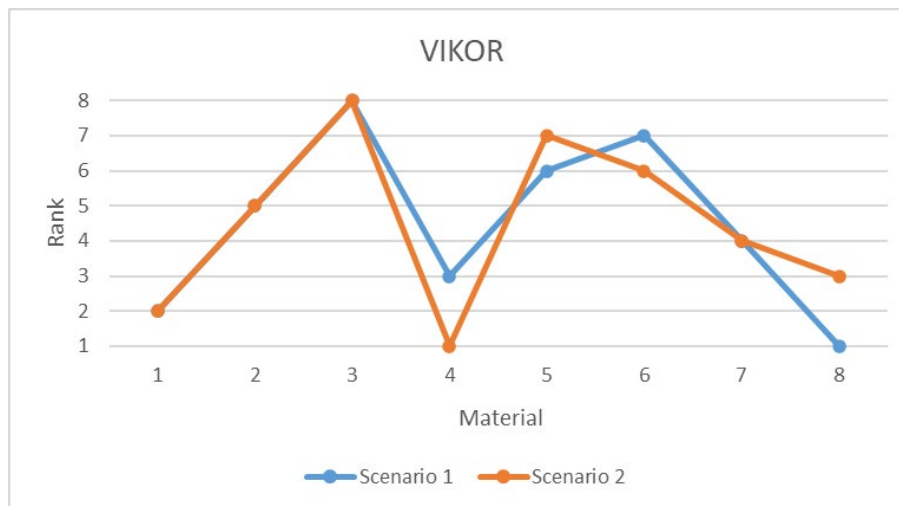


Figure 9. Ranking results by VIKOR method

6. Conclusion

In this paper MCDM Solver is proposed for material selection of wave energy extraction turbine blade. The detail procedure of MCDM use was demonstrated while solving the material selection problem in two scenarios. The conclusions can be as follows:

- MCDM Solver has been used directly for choosing a turbine blade component material and can also be extended to cover other machines such as fans and pumps.
- Without any doubt, it can be claimed that the best ranked materials are GFRP, Titanium alloys and CFRP.
- The obtained ranking results have good correlation with those derived by the past researchers using different criterion weights. In both scenarios, it is observed that the first three top-ranked materials exactly match with those derived by the past researchers.
- TOPSIS method is most sensitive for criteria weight change
- Computational procedure is relatively simple and can be easily traced by decision maker.
- Solving different MCDM problems by using MCDM Solver doesn't require the use of specialized software packages since the method can be easily implemented.

Acknowledgements

This research was financially supported by the Ministry of Science, Technological Development and Innovation of the Republic of Serbia (Contract No. 451-03-65/2024-03).

References

- [1] Charles JA, Crane FAA, Furness JAE. Selection and use of engineering materials, 3rd ed. Oxford, UK: Butterworth-Heinemann; 1997
- [2] Petković D., Madić M., Radenković G., Manić M., Trajanović M., Decision Support System for Selection of the Most Suitable Biomedical Material, *Proceedings, ICIST 2015*, Kopaonik, March 8-10, 2015, pp. 27-31
- [3] Chatterjee P., Chakraborty S., Material selection using preferential ranking methods, *Materials and Design*, Vol. 35 (2012), pp. 384-393
- [4] Petković D., Madić M., Radenković G., Gear material selection using WASPAS method, *Proceedings, SMAT 2014*, Craiova, Romania, October 23-25, 2014 pp. 45-48
- [5] Petković D., Madić M., Radenković G., Živković P., An example of MCDM Solver application for material selection problems, *Proceedings, DEMI 2019*, Banja Luka, May 24-25, 2019, pp.
- [6] Čupić M., Tummala R., Suknović M., Odlučivanje - formalni pristup, Fakultet organizacionih nauka, Beograd, 2001
- [7] Falcão A.F.O., Modelling of Wave Energy Conversion, Instituto Superior Técnico, Universidade de Lisboa, 2014
- [8] Falcão A.F.O., First-generation wave power plants: current status and R&D requirements, *J Off-Shore Mech Arctic Eng*, Vol. 126 (2004), pp. 384-388.

- [9] Thakker A., Jarvis J., Buggy M., Sahed A., A novel approach to materials selection strategy case study: Wave energy extraction impulse turbine blade, *Materials and Design* Vol. 29 (2008), pp. 1973–1980
- [10] Petković D., Selection of biomaterials - Multi-criteria decision analysis and development of decision support system, PhD dissertation, University of Niš, Faculty of Mechanical Engineering, Niš, 2017
- [11] Petković D., Madić M., Radenković G., Knee Prosthesis Biomaterial Selection by Using MCDM Solver, *Advanced Technologies & Materials*, Vol. 46 (2) (2021), pp. 37-41
- [12] Petković D., Madić M., Non-conventional machining processes selection using MCDM Solver, *Innovative Mechanical Engineering*, Vol. 1, No. 2 (2022), pp. 48 - 57
- [13] Jahan A., Bahraminasab M., Edwards K.L., A target-based normalization technique for materials selection, *Materials and Design*, Vol. 35 (2012), pp. 647-654
- [14] Jahan A., Mustapha F., Ismail M.Y., Sapuan S.M., Bahraminasab M., A comprehensive VIKOR method for material selection, *Materials and Design*, Vol. 32 (2011), pp. 1215-1221
- [15] Petković D., Madić M., Radenković G., Ranking of Biomedical Materials by Using Comprehensive WASPAS Method, *Proceedings, MASING 2015*, Faculty of Mechanical Engineering Niš, September 17-18, 2015, pp. 339-344
- [16] Setoguchi T, Santhakumar S, Maeda H, Takao M, Kaneko K., A review of impulse turbine for wave energy conversion, *J Renew Energy*, Vol. 23 (2001), pp. 261–292

In-Depth Examination of Water Jet Formations and Patterns at Dam Outlets: Comparative Investigation Employing CFD Simulations and On-Site Drone Footage

Filip Stojkovski^a, Robert Broz^b, Sašo Belšak^c, Valentino Stojkovski^d

^a *Iskra Impuls Kranj, Engineering Division Maribor, Maribor, SI, filip.stojkovski@iskraimpuls.si*

^b *Iskra Impuls Kranj, Engineering Division Maribor, Maribor, SI, robert.broz@iskraimpuls.si*

^c *Iskra Impuls Kranj, Engineering Division Maribor, Maribor, SI, saso.belsak@iskraimpuls.si*

^d *“Ss. Cyril and Methodius” University in Skopje, Faculty of Mechanical Engineering Skopje, MK, valentino.stojkovski@mf.edu.mk*

Abstract: This scientific paper presents a comprehensive study on the Computational Fluid Dynamics (CFD) modeling of water jet formations at dam bottom outlets, with a focus in the comparative analysis of CFD results against actual drone footage captured on-site. The research commences with the development of a detailed CFD models, encompassing the geometric and hydraulic characteristics of the dam bottom outlet structure. Special attention is given to incorporating boundary conditions and numerical schemes that accurately simulate the water jet formation process. Computational simulations are conducted for a range of operational scenarios i.e. bottom outlet gate openings. To validate the CFD results and prove their applicability, a field campaign is carried out, involving the use of camera equipped drone and one stationary camera, to capture real-time footage of water jet formations at dam bottom outlet. The drone footage provides invaluable visual data that allows a direct comparison between the CFD predictions and actual on-site observations. The comparative analysis involves a quantitative assessment of key parameters, such as jet velocities, trajectories, flow patterns etc. Discrepancies between the CFD predictions and real-world observations are analyzed to identify potential areas for model refinement and future improvement. The results of this research contribute to a better understanding of the hydraulic behavior of dam bottom outlets. By leveraging advanced CFD modeling and real-world drone footage, this study provides a holistic approach to studying water jet formations at dam outlets, bridging the gap between numerical simulations and empirical observations in a complex hydraulic environment.

Keywords: Computational Fluid Dynamics (CFD), Water Jet Formations, Comparative Analysis, Dam Bottom Outlet, Hydraulic Modeling, Volume of Fluid (VOF), Multiphase Flow.

1. Introduction

Dams are vital infrastructural components that serve a multiple purposes, such as water supply, flood control, irrigation and hydroelectric power generation. Ensuring the safe and efficient operation of dams is of paramount importance, as their failure can have catastrophic consequences. One critical aspect of dam operation is the controlled release of water through bottom outlet, a process that involves the formation of high-velocity and long-spanned water jets. These jets are responsible for discharging water from the reservoir and can exert considerable forces on the outlet hydraulic steel structure.

Traditional engineering approaches have relied on empirical correlations and simplified analytical models to estimate jet characteristics and discharge ratios. While these methods have been valuable in practice, they often lack the precision needed to account for the complex flow phenomena that occur in dam bottom outlets, such as spraying, water-air mixtures etc. A certain time ago model tests were also conducted for this type of hydraulic infrastructures, but today they are more and more abandoned, as the prices for doing such a laboratory (scaled model) research are very high.

Recent advancements in Computational Fluid Dynamics (CFD) have provided engineers and researchers with powerful tools to simulate and analyze fluid flow and its complex flow phenomena. CFD offers the capability to model the fluid flow behavior with a high degree of fidelity, making it an ideal choice for studying the flow patterns associated with water jet formations in dam outlets. However, the successful application of CFD in this context requires rigorous validation against real-world observations, which is the primary objective of this paper.

The motivation for this research arises from the need to bridge the gap between theoretical simulations and practical field data. By combining state-of-the-art CFD modeling with actual drone footage captured at dam site, we aim to enhance our understanding of water jet formations and validate the accuracy of numerical predictions. Such validation is critical for the broader adoption of CFD in dam engineering and the development of reliable guidelines for outlets design, maintenance and safety.

This paper is structured to provide a comprehensive investigation into the hydraulic behavior of dam bottom outlets, with a specific focus on water jet formations. In addition to the abstract's outlined methodology, the subsequent sections will delve into the details of the CFD model setup, field data acquisition, and the comparative analysis of results. The findings of this study will not only contribute to the scientific understanding of water jet formations, but also serve as a practical resource for hydro engineers seeking to improve their understandings of the subject, for future hydro-mechanical equipment development.

2. Case Study Description

Dams and hydropower facilities in the Balkan region, particularly in the former Yugoslavian countries, are approaching a phase where the consideration of reconstruction is imperative. This is done with the aim of extending their operational lifespan and enhancing their performance. Specifically, the reconstruction of hydraulic gates on the dam bottom outlets is a task that lacks standardized guidelines and is primarily reliant on the practical experience accumulated by engineers over the years of working with such equipment. To assess the scope of refurbishment required for a hydraulic gate, it is essential to undertake analytical and numerical calculations, to anticipate on-site conditions, expected loads, hydrodynamic forces, discharge rates and outflow conditions and other relevant factors [11, 12].

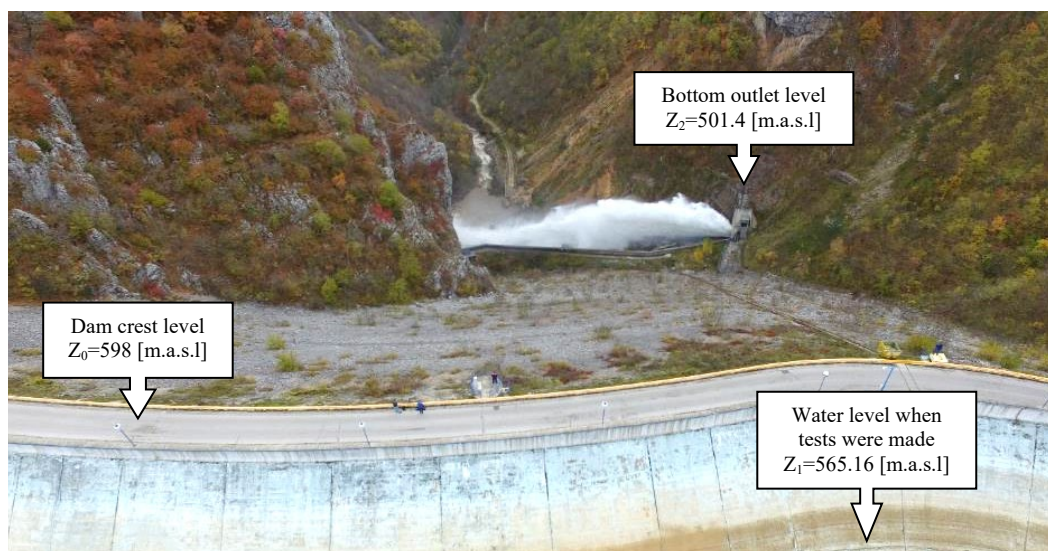


Figure 1. View on the dam crest and bottom outlet configuration.

Back in the 60's, a fixed-wheel vertical bonneted gate was installed at the outlet section of the dams' bottom outlet tunnel. The gate's dimensions, including gate body height, span and depth are 4.3x3.3x0.75 [m], respectively. The gate lip at the lower seal is profiled and has a 45 [°] slope angle. To operate the gate, a hydraulic cylinder is mounted on the top of the gate casing cover, connected directly without the use of lifting rods. The gate can be lifted to a maximum height of 4.2 [m], while the net clearance height for the bottom outlet is $Z_0=4$ [m], creating a net cross-sectional area of 4×1.9 [m] i.e. $A_0=7.6$ [m²]. The bottom outlet has an inclination slope of approximately +8 [°], resulting in an outflow resembling projectile motion in the form of a jet. The concrete channel where the jet is formed is with side slopes of +7 [°], which start immediately after the gate body [11].

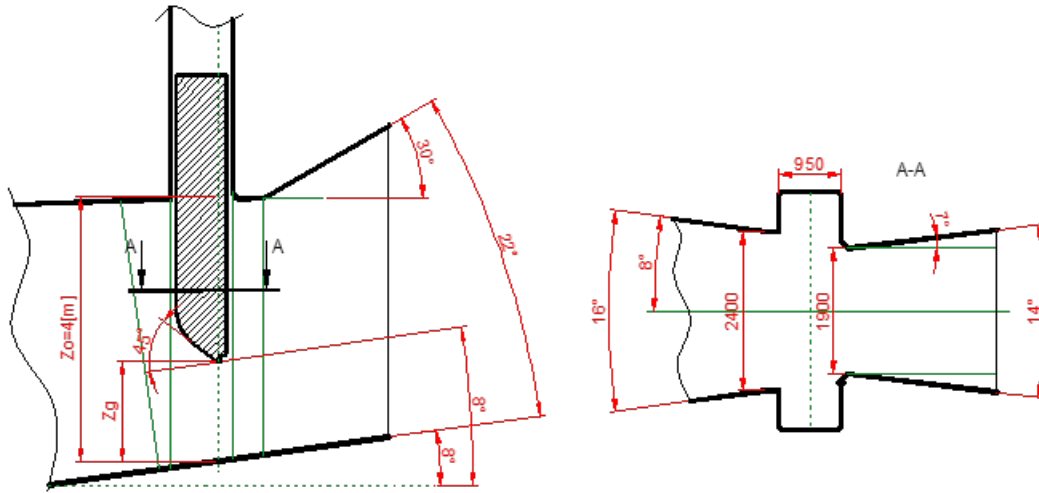


Figure 2. Bottom outlet gate section dimensions.

The outlet terrain slope was taken from the geodetic measurements available. Having that data, primarily a theoretical calculations were made to see the expected jet length and size. Using the simple kinematic theory of projectile motion, the water was taken as massless object without air resistance. For the given conditions, the following model was used:

$$y = x \cdot \tan \theta - \frac{g \cdot x^2}{2 \cdot v_0^2} \cdot (1 + \tan^2 \theta) \quad (1)$$

where x is the terrain length coordinates, v_0 is the water velocity under the gate, θ is the angle of the bottom outlet inclination slope and g is the gravitational acceleration. The theoretical velocity under the gate is calculated according the Torricelli formula as [1, 2]:

$$v_0 = \sqrt{2 \cdot g \cdot (H - C_c \cdot Z_g)} \quad (2)$$

where H is the water column in the reservoir, C_c is the contraction coefficient of the gate lip, where acc. to [1] for 45 [°] gate lip $C_c \approx 0.75$, and Z_g is the gate opening height. From this relations, the following chart was obtained. Having these conditions in-mind, the computational domain was created, using the terrain data, but simplified, and the length of the theoretical jet.

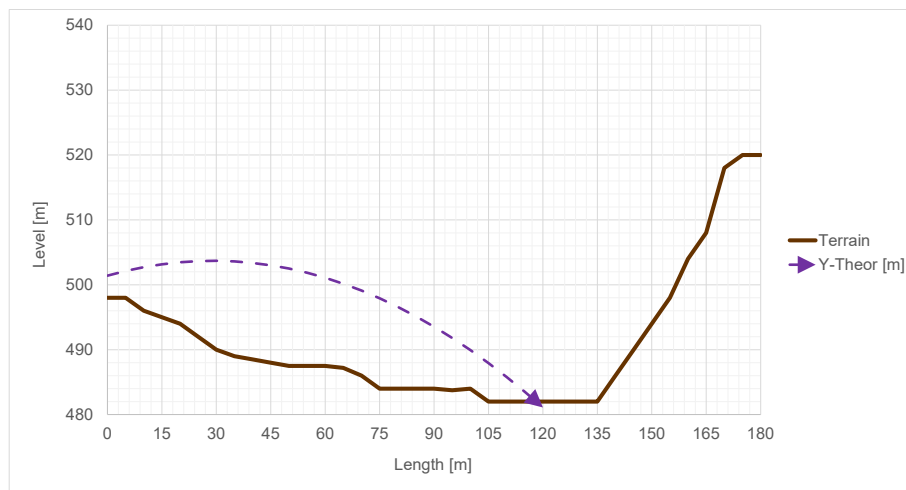


Figure 3. Terrain configuration and theoretical jet length calculated for gate opening of 50 [%].

3. Numerical Modeling

Numerical simulations were conducted using a true-scale model of the dam's bottom outlet. The simulations were carried out using the Ansys Fluent software. To accurately capture the narrow spaces between the gate and the bonnet, a Watertight meshing technique with Polyhedral mesh was employed when creating the

numerical mesh in Fluent Mesher. The outflow region was modeled to replicate the actual on-site conditions. Additionally, a partial representation of the steel liner in the bottom outlet was included in the model to reduce the size of the numerical domain.

3.1. Multiphase Flow Modeling Approach

In order to analyze the water jets formations behind the gate, it is necessary to employ multiphase flow modeling, as the flow in this region is characterized by the creation and dispersion of water jets into the surrounding air [9]. In multiphase flow, a “phase” is defined as a distinct category of material with specific characteristics in response to the flow and the potential field in which it exists. In this context, two phases were considered: air and water. Multiphase flow refers to the simultaneous flow of multiple phases, making it a two-phase flow scenario.

Because the two phases are interpenetrating between each other, the Euler-Euler Volume of Fluid (VOF) approach in multiphase modeling was used. This approach involves tracking the interface between two immiscible fluids, such as water and ambient air, on a fixed Eulerian mesh. In the VOF model, a single set of momentum equations is shared by both fluids, and the volume fraction of each fluid in each computational cell is continuously tracked throughout the domain. This methodology is well-suited for predicting phenomena like jet breakup, liquid motion after a dam break, free surface flows and tracking of liquid-gas interfaces, whether in steady or transient scenarios [4].

The VOF formulation is based on the principle that multiple fluids do not mix with each other [4]. When introducing an additional phase into the model, a new variable is introduced, which represents the volume fraction of that phase within each computational cell. These variables and properties are shared among all the phases and represent volume-averaged values, provided that the volume fraction of each phase is known at every location. Consequently, the variables and properties within a cell can either exclusively represent one of the phases or represent a combination of the phases, depending on the volume fraction values. To track the interface between the phases, a continuity equation for the volume fraction of one of the phases is solved:

$$\frac{1}{\rho_q} \left[\frac{\partial}{\partial t} (\alpha_q \rho_q) + \nabla \cdot (\alpha_q \rho_q \vec{v}_q) \right] = S_{\alpha_q} + \sum_{p=1}^n (\dot{m}_{pq} - \dot{m}_{qp}) \quad (3)$$

where \dot{m}_{qp} is the mass transfer from phase q to phase p , and \dot{m}_{pq} denotes the reverse transfer. In this specific scenario, right-hand side of this equation is not relevant because there is no mass transfer mechanism present. So, the volume fraction inside a cell of the mesh is computed for the secondary phase (the driving phase - water) starting as:

$$\sum_{q=1}^n \alpha_q = 1 \quad (4)$$

When α_q falls within the range of 0 to 1, it signifies the presence of an interface between the phases. An implicit scheme was employed to concurrently solve the phase continuity equation alongside iterations involving momentum and pressure. In a two-phase system designated as phases 1 and 2, where the second phase serves as the driving phase, the density and viscosity in each cell were computed as follows:

$$\rho = \alpha_2 \rho_2 + (1 - \alpha_2) \rho_1 ; \mu = \alpha_2 \mu_2 + (1 - \alpha_2) \mu_1 \quad (5)$$

The calculation method for all other physical properties remains consistent. A unified momentum equation is resolved across the entire domain, and the resultant velocity field is applied to all the phases. The expressions for the continuity and momentum equations governing the mixture of phases are as follows:

$$\frac{\partial}{\partial t} (\rho \vec{v}) + \nabla \cdot (\rho \vec{v}) = S \quad (6)$$

$$\frac{\partial}{\partial t} (\rho \vec{v}) + \nabla \cdot (\rho \vec{v} \vec{v}) = -\nabla p + \nabla \cdot [\mu (\nabla \vec{v} + \nabla \vec{v}^T)] + \rho \vec{g} + \vec{T}_\sigma$$

which are dependent from the volume fractions of the phases thorough the density and viscosity from Eq.5. Based on the local value of α_q , the appropriate properties and variables are assigned to each control volume within the domain.

The modeling approach employed for the fractional interface is referred to as “Sharp”, specifically between water and air. It is calculated using the “Compressive Interface” capturing scheme, which is well-suited for “Steady-State Implicit” solutions employing the “Implicit Body Force” formulation. In this analysis, the Energy equation was omitted because heat transfer and the physical properties of the surrounding air, such as compressibility, are considered insignificant. Although the surface tension between the phases is exceptionally small, it is present from physical standpoint, and for the modeling purposes, it was set at 0.072 [N/m] as a continuum surface force between air and water.

3.2. Computational Domain and Boundary Conditions

Figure 4 provides an illustration of the computational domain along with its boundary conditions. This domain encompasses several components: a section of the steel liner originating from the bottom outlet, a reducer, the gate body enclosed in the bonnet, the outlet terrain slope, and the surrounding ambient volume. The operating pressure was set to atmospheric pressure of $p_{atm} = 101325$ [Pa], and the gravity was applied vertically with $g_z = -9.81$ [m/s²].

At the inlet, the total pressure was defined based on the water level in the reservoir, which corresponds to the water level when the footage was made, i.e $H_W = 63.76$ [m] or $p_{inlet} = 624311$ [Pa]. At the inlet in front of the gate, the secondary (driving) phase was imposed as 100 [%] water presence. The outlet sections are represented with the pressure outlet boundary conditions. On the top of the domain was given a static pressure outlet with 0 [Pa] intensity, with imposed primary phase (air) of 100 [%]. On the left, right and front side of the outlet domain, the pressure outlet boundary condition was imposed, with enabled Open-Channel condition, giving a negligible small free surface water level of 1 [m], to address that it represents an outflow of the secondary phase (water). As it was mentioned, the numerical mesh was developed as Polyhedral mesh. The models is consisted of cca. 600.000 cells.

The chosen turbulence model was Standard $k-\epsilon$. The Coupled solver was enabled, coupled with the Volume Fractions. Additionally, Pseudo-Transient mode was initiated to adress the Navier-Stokes equations. Even though the simulations were set-up as Steady State, the Pseudo-Transient mode introduces a “fictional” time step to enhance convergence when dealing with volume fractions between phases. The ultimate outcome of the case still represents a Steady-State solution. Convergence of the residuals was achieved, reaching a value of 10^{-5} .

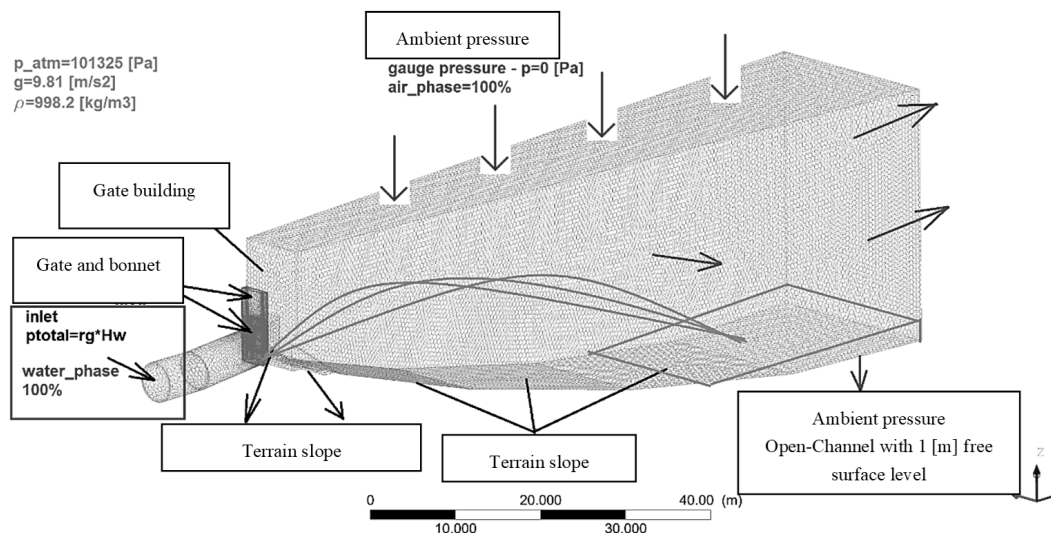


Figure 4. Computational Domain and Boundary Conditions.

4. Simulation Results

In this section, the outcome of the simulations is presented. Previous analysis [11] were conducted to estimate the hydrodynamic forces on the gate, by measuring the lifting pressures and comparing them with the numerical simulations, where matched results were obtained. This was a part of a reconstruction project that our company had to make 2 years ago, in order to develop a quality analysis of the scope of works, loads and all the phenomena occurring on-site, via numerical simulations. Within this chapter, we delve into the analysis

of water jet formations behind the gate and compare them with drone footage captured during on-site tests. Unfortunately, the footage only covers up to 50 [%] of the gate’s opening, so our results are limited to this range of gate positions. Based on this comparisons, we found a strong agreement between the CFD results and the footage.

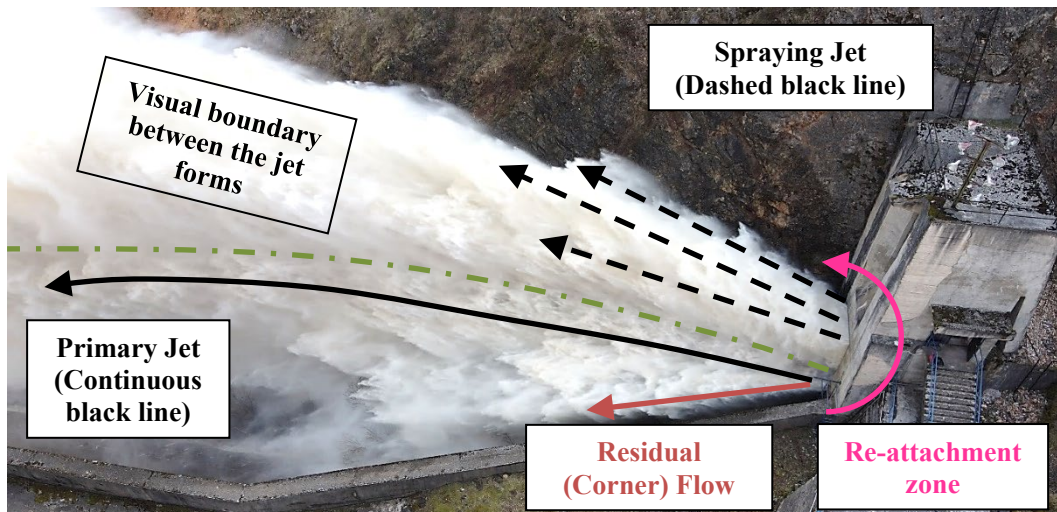


Figure 5. Description of primary jet and spray jet flow patterns.

Evaluating a pure water jet can be challenging since the actual outflow represents a mixture of water and air phases, characterized by spraying of non-interpenetrating phases, shown as water dispersion into the surrounding environment. As the gate opens, high pressure of water is converted into a flow, in a form of a water jet. The water flow profile “expands” in the opened chamber just behind the gate, forming two visual jet configurations: Primary jet (this pattern is in the lower zone) and Spraying jet (expanded flow pattern mixed with air, attached on the ceiling of the chamber – upper zone).

From the video footages it can be seen that the primary jet flow pattern has higher velocity than the spraying jet, and it is representing the simplified kinematic pattern of water flow. The spraying jet is formed in a complex manner. The expanded water which attaches on the top of the chamber ceiling, firstly it slows down, than it recirculates. One part of it, travels forward with decreased velocity at the beginning, reattaches on the primary jet and then travel together. The other detaches from the ceiling, recirculates and sticks on the primary jet, forming a top corner flow pattern, and they travel together too. These phenomena were detected in several simulations which are described further in this chapter.

The following figures depicts sequential snapshots of the gate opening from 0 to 50 [%] offering a comparison with drone footage images taken under identical operating conditions. Overlapping of the simulation results and the actual footage was made to see the jet formation and following phenomena which occur.

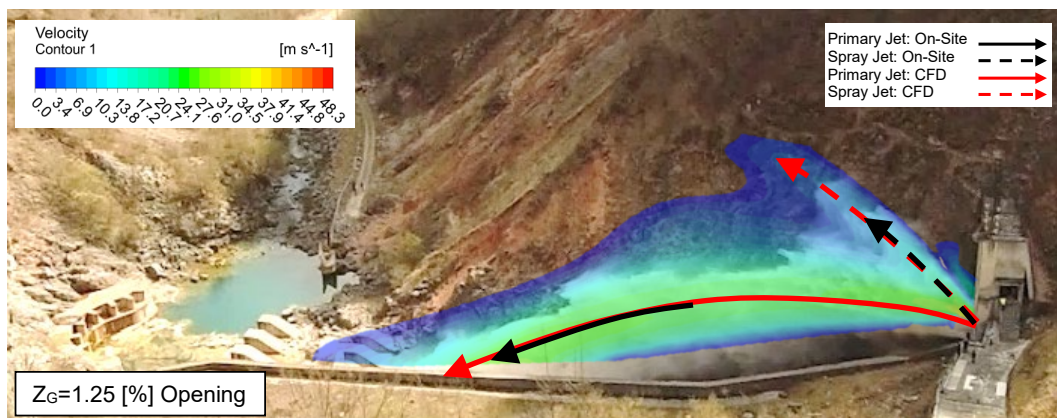


Figure 6. Gate opening at 1.25 [%] – Start.

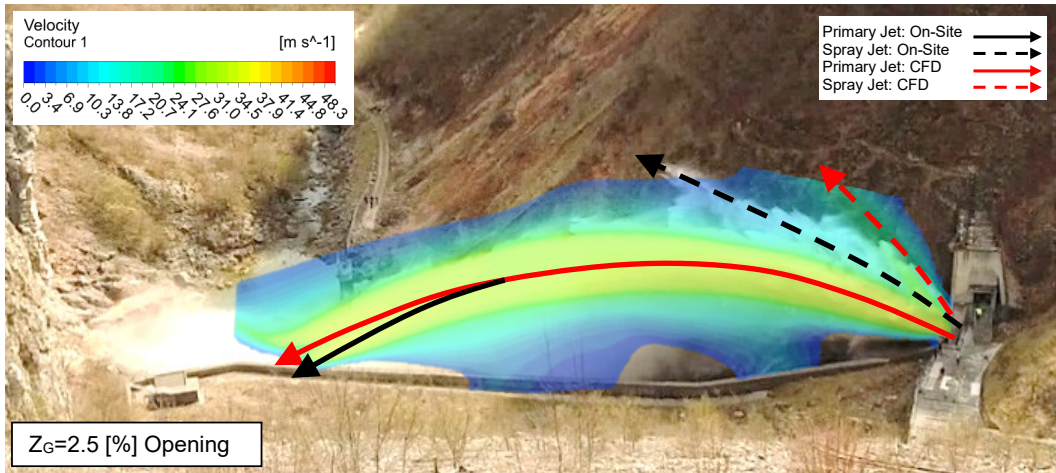


Figure 7. Gate opening at 2.5 [%].

Figures 6 and 7 reveal that, under these specific partial operating conditions, the water jet formations obtained through CFD align closely with the real-world on-site conditions. On figure 7 for gate opening of 1.25 [%] it can be seen the two characteristic flow patterns described earlier. The computed primary jet and the spraying jet perfectly matches the on-site conditions. Compared with the flow on figure 7 for 2.5 [%] a slight discrepancy is obtained in the spraying jet pattern between the on-site and numerically obtained results. The discrepancies between those two is considered to originate from the “tightness” of the modeled computational domain, especially by height, to capture the spraying patterns more precisely. The computed primary jet pattern overlaps perfectly with the on-site conditions, by length and by its “parabola” height.

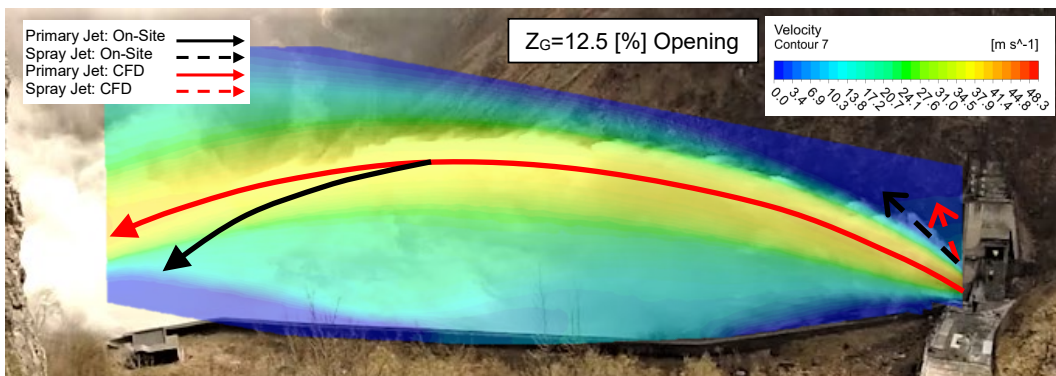


Figure 8. Gate opening at 12.5 [%].

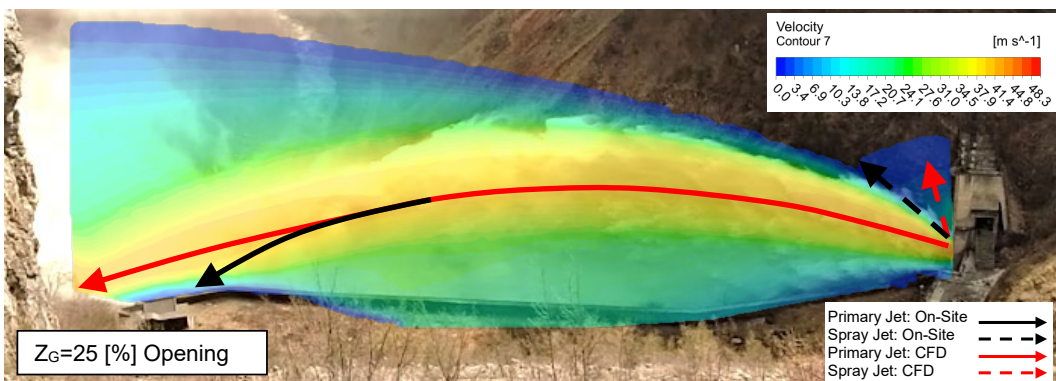


Figure 9. Gate opening at 25 [%].

On figure 8 for gate opening of 12.5 [%], it can be seen that the spray jet is present on-site with decreased intensity, and also in the computed results, which shows a good prediction, with slight discrepancy in the slope. One discrepancy is obtained between the computed results and the on-site conditions, in the primary jet length. Same as the previous scenario, here on figure 9 it can be seen similar discrepancies for 25 [%] of gate opening.

On figure 10 for gate opening of 50 [%], it can be seen that the length discrepancy of the computed primary jet with the actual on-site footage is shortened, which shows that the overall jet behavior and form is highly dependent from the gate opening. For smaller openings than 50 [%], the water jet is characterized with increased height and length, but without any intensity, as the gate interferes the flow substantially. When the gate is opened at 50 [%], the jet is more “firm”, almost fully formed and it is characterized by almost fixed length and height, with less other phenomena occurring, like sprays and etc.

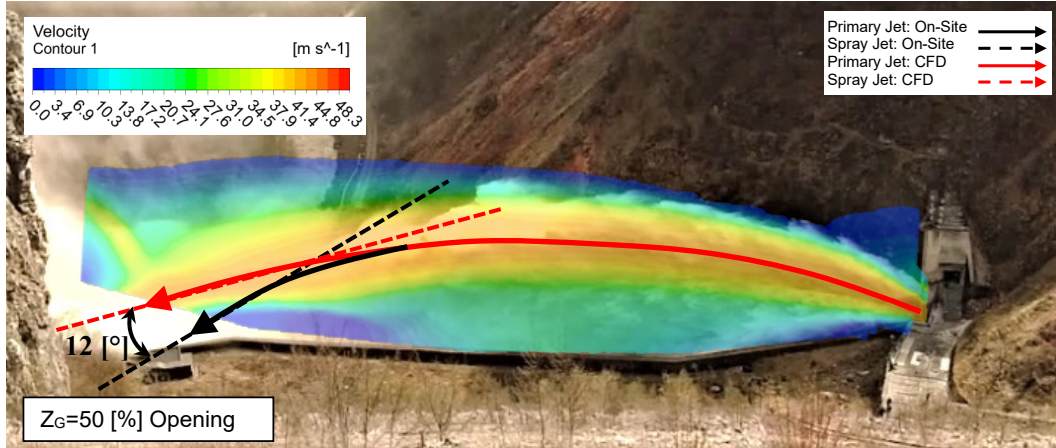


Figure 10. Gate opening at 50 [%].

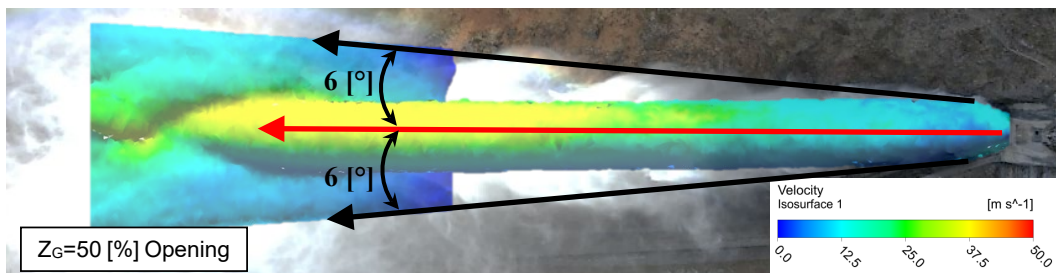


Figure 11. Gate opening at 50 [%] – Top view.

Other discrepancy noticed is shown on figure 11 where the top view shows the on-site jet expands, and the computed one is rather straight. By measuring the tangency of the angles where the primary jet is on-site shortened than the calculated one, we can see a discrepancy of cca. 12 [°]. On the top view, measuring the discrepancies in the jet spreading, we can see a discrepancy of cca. $2 \times 6 [°] = 12 [°]$, which is same as the length shortening angle. This indicates that the jet spreading in real-world conditions results in jet shortening by length. Possible solution to outcome this situation can be in the geometric modeling of the computational domain, which shows that increasing the width of the domain might lead to jet spreading.

On figure 13 the jet cross sections are shown. As the surface under the gate is rectangular, when it's opened, on-site cross sections of the jet are expected to be similar to rectangular shape, shown in figure 12. The simulated jet has rounded circular shape. Possible solution to outcome this situation can be in the boundary conditions applied on the sides of the domain, which are adopted as pressure boundaries. Perhaps symmetry or wall boundary conditions would lead to a better prediction of the jet cross section, jet spread, and with that, the jet length.



Figure 12. Visual on-site jet cross section.

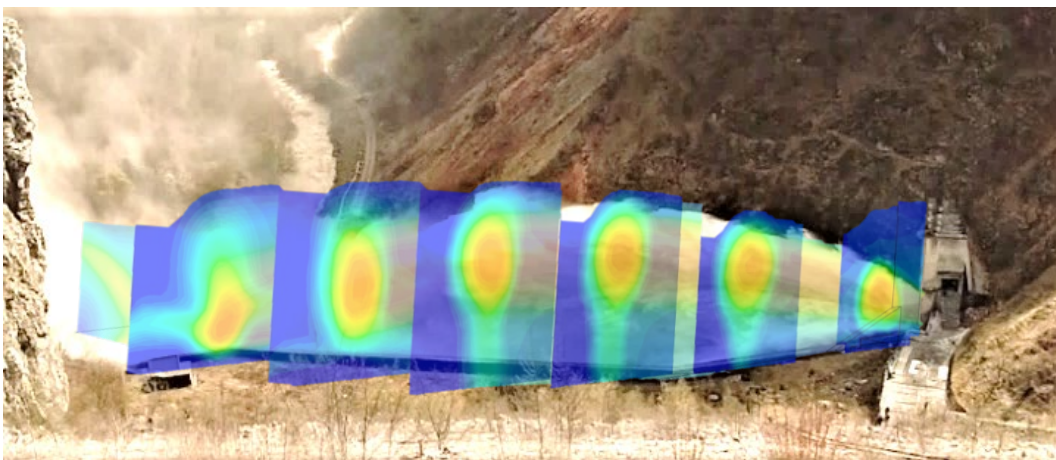


Figure 13. Jet cross section profiles for gate opening of 50 [%].

As it is shown, the on-site conditions shows that the jet spreads and shrinks, compared with the CFD results, an orthogonal projection of the CFD results was made and plotted against the theoretical calculated jet length. It can be seen on the chart on figure 14 that the CFD calculated jet length is shorter and milder than the theoretical jet assumed as pure projectile movement, for cca. 25-30 [m] difference. This shows that despite of the discrepancies obtained from the numerical simulations, still the CFD solution is far closer to the on-site flow conditions than the theoretical approach.

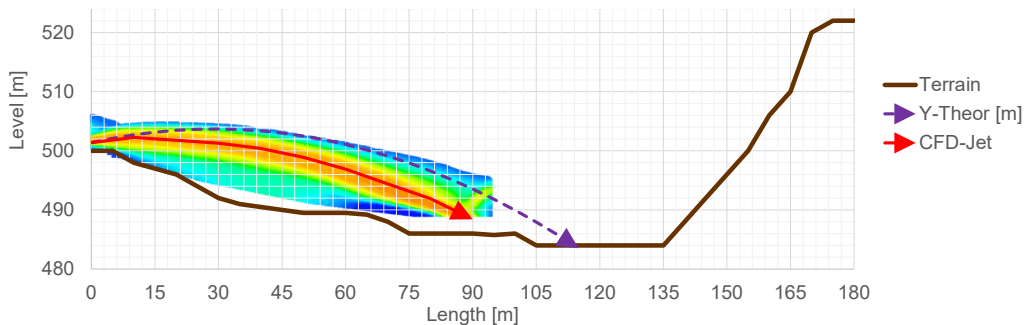


Figure 14. Comparison between CFD results and theoretical jet length for 50 [%] gate opening.

One step further was made to ensure that the results are in good correspondence with the on-site conditions, with comparing the discharge rates from the CFD analysis with an available old data from model tests for the bottom outlet. The results show good overlapping and satisfactory precision, shown on figure 15. The calculated jet forms and patterns shows that they do not influence on the discharge rate as a parameter, for the given conditions, and also on the hydrodynamic forces on the gate, as previously measured [11].

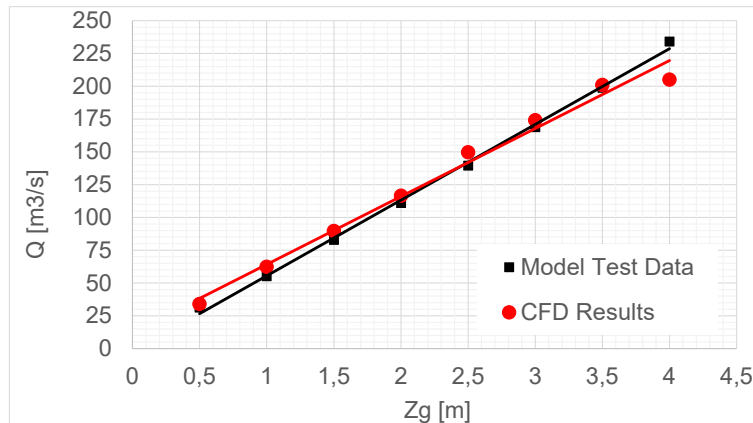


Figure 15. Compared discharge rates with available data from old Model Tests.

5. Conclusions

In this paper, a comprehensive study was carried out on the modelling approach of jet formations at dam bottom outlets, and comparisons of the obtained results with on-site footages. Primarily, the case study was explained, by defining the geometric parameters of the bottom outlet gate and channel, with the terrain slopes and configuration and the estimated theoretical jet length, on which basis the computational domain can be developed.

Second, the numerical approach was defined, by developing a multiphase volume of fluid methodology to capture the wanted effects. By defining the computational domain, the boundary conditions were explained and the solver used to obtain the needed results.

The simulated scenarios are compared with on-site drone footages to see similarities and the discrepancies between the real-world jet formation conditions, and the CFD results. For partial gate openings below 10 [%], the computed results show great match with real-world conditions on-site, by comparing the main outflow jet by length and height, and by comparing the following phenomena which occur, such as the jet sprays. For gate opening from 10 to 25 [%], jet spraying phenomena doesn't occur on-site, and so on the computed results. The main discrepancies here are in the jet length.

For gate opening of 50 [%] which is the maximal opening captured with footages, it can be seen that the computed trajectory of the main jet follows the on-site formed jet, with a discrepancy in the length. Approximately, the angle between the tangencies of the jet length was measured cca. 12 [°]. The top view of the jet shows that real-world jet spreads for about $2 \times 6 [°] = 12 [°]$ compared with the computed one, which indicates that the jet spreading leads to jet shortening. This shows that some model improvements can be made to overcome this discrepancies and to get closer to the on-site conditions. Another comparison was made for the CFD results and the theoretical jet length, where it is shown that the CFD results give closer prediction of the jet length than the theoretical one, plus several jet phenomena were captured like sprays etc. which analytically cannot be obtained.

The discharge rates obtained with the CFD analysis were compared with old model test data of the bottom outlet, where good precision was obtained, showing that despite of the jet form discrepancies, the results are precise.

In summary, this study has provided valuable insights into the modeling of jet formations at dam bottom outlets, highlighting areas of alignment with on-site conditions and opportunities for model enhancements. These findings contribute to our understanding of flow dynamics in such critical engineering structures and offer potential avenues for improved design and performance evaluation in the future.

References

- [1] Naudascher E. Hydrodynamic Forces, University of Karlsruhe, Germany, 1991.
- [2] Erbisti P.C.F. Design of Hydraulic Gates, 2nd edition. CRC Publishers, 2014.
- [3] Fluent 6.3 User's Guide.
- [4] Brennen C. Fundamentals of Multiphase Flows. CALTECH, 2005.

- [5] Badas M. et al. May a Standard VOF Numerical Simulation Adequately Complete Spillway Laboratory Measurements in an Operational Context? The Case of Sa Stria Dam, *Water* 2020, 12, 1606; doi:10.3390/w12061606, 2020.
- [6] Denner F. Compressive VOF method with skewness correction to capture sharp interfaces on arbitrary meshes, *Journal of Physics* 279, doi: 10.1016/j.jcp.2014.09.002, pp. 127 – 144, 2014
- [7] Hui D. Numerical study of advection schemes for interface-capturing using gradient smoothing method. *Numerical Heat Transfer Fundamentals* 73(4), doi: 10.1080/10407790.2018.1462005, pp. 242 – 261, 2018.
- [8] Viti N. Numerical simulations of Hydraulic Jumps. Part 2: Recent Results and future work. *Water* 2019, 11, 28; doi:10.3390/w11010028, 2019.
- [9] Awad M.M. Two-Phase Flow, doi:10.5772/76201.
- [10] Muralha A. Assessment of CFD solvers and turbulent models for Water Free Jets in Spillways, *Fluids*, 5, 104; doi:10.3390/fluids5030104, 2020.
- [11] Stojkovski F. et al., Multiphase Flow Modeling to Predict Hydrodynamic Forces and Outflow Conditions of a Dam Bottom Outlet Regulation Gate. 20th International Symposium of Thermal Engineering, Niš, Serbia, 2022, pp. 361 – 371.
- [12] Stojkovski F. et al. Reconstruction Steps to Improve Performance of s Dam Bottom Outlet Regulation Gate. XXXVII International Symposium of Energetics, 21st – 24th June, Zlatibor, Serbia, 2022
- [13] Stojkovski F. et al. Challenges in the Design and Construction of a Large Scale Hydro-Mechanical Equipment. XXXVth International Symposium of Energetics, Zlatibor, Serbia, 2020, pp. 305 – 311
- [14] DIN19704. Hydraulic Steel Structures, 2004.

Measurement of water quality parameters using the spectrophotometry method

Radmila Koleva^a, Darko Babunski^a, Emil Zaev^a, Atanasko Tuneski^a, Magdalena Koleva^a

*^aSs. Cyril and Methodius University in Skopje - Faculty of Mechanical Engineering, Skopje, MK,
radmila.koleva@mf.edu.mk*

Abstract: Having quality drinking water is a leading factor in maintaining public health, environment protection, and the promotion of sustainable development in industrial and agricultural needs. Measurement and analysis of chemical parameters in drinking water are crucial for ensuring the safety and quality of water for public health. This research was conducted using the spectrophotometry method including a UV-VIS DR 6000 HACH Lange spectrophotometer with a wavelength range of 190 to 1100 nm and a high-speed temperature thermostat HT 200 S. Chemical parameters that are measured in this research are chlorides, nitrates, nitrites, potassium, phosphates, and ammonium. All of them are measured on a different wavelength. Samples were taken from three measuring points, all of which are used as drinking water sources and irrigation in the nearby villages. One measuring point is a thermal spring and the other two springs from the foot of a mountain. The water from all three water sources is considerable drinking water. One sample is taken from Vardar River and its water is considered as non-drinking. The results of all measured parameters will be represented through a table and bar graphic chart.

Keywords: water quality parameters, water quality analysis, drinking water, spectrophotometry, DR6000.

1. Introduction

Water quality is a crucial aspect of the well-being of both ecosystems and human populations. It is important to accurately measure and monitor water quality parameters to understand the health of aquatic systems and ensure safe drinking water [1].

There are traditional analytical methods for water quality monitoring that can be expensive, time-consuming, and require specialized laboratory conditions and equipment, making the measurement inconvenient and unsuitable. In contrast, ultraviolet/visual spectrometry (UV/Vis) offers significant benefits due to its accessibility and affordability. This makes UV/Vis a more practical option for water quality monitoring [2]. According to the needs and water properties, there are also available UV, Vis, or UV-Vis measurement technology. UV-Vis spectroscopy works by measuring how pollutant molecules in water absorb light at specific wavelengths, causing electron transitions from the ground state to an excited state and reducing transmitted light. This method relies on the Lambert-Beer law, which establishes a strong correlation between the absorption spectrum and the concentration of the substance, allowing for the detection of water pollutants [3]. Usually, UV-Vis is the most popular technique since it offers a wider area of wavelength. Also, UV-Vis spectrometry is suitable for multi-parameter monitoring, classifying water quality, and setting up quality alarms [4]. In [5] is represented by the usage of UV-Vis spectrophotometry for detecting possible pollution while producing NaCl because it also can detect metal ions, organic pollutants, chemical oxygen demand (COD), and many other parameters. Measurement of total sulfate (SO₄) and nitrate (NO₃) is done by using the UV-Vis spectrophotometry method [6]. Despite the water parameters, the UV-Vis spectrophotometry method can be applied in the determination of bacteria in the water samples, for example, cyanobacteria and hexavalent chromium which is very poisonous and can cause severe illness. According to [7], despite the measurement, the results from the UV-Vis are used to determine the water quality index (WQI) using artificial neural networks (ANN). Paper [8] aims to simplify the monitoring of the water used in agriculture by combining UV-Vis spectrometry using ANN with (convolution neural networks) CNN and partial least squares (PLS) to calculate water parameters.

The measured parameters in this paper are chloride, nitrate, calcium, nitrite, ammonium, phosphate, and COD and BOD. In this paper, measurements are done on water samples from two springs (currently used as drinking water), one thermal water spring (currently used as drinking water as well), and one river.

2. Measuring parameters

The purpose of this paper was to do water quality (WQ) measurements using spectrophotometry equipment. The samples that were collected were mostly from springs from the southern part of Macedonia, mainly in the Gevgelija region and the foot of Kozuf Mountain. Samples are taken from three different spring points, Smrdliiva Voda (mountain spring), Konsko (mountain spring), Negorski Banji (thermal spring), and Vardar River. The water from all three springs is used as drinking water by the citizens of the country and the tourists. The test samples are taken directly from the spring where people often fill bottles of water and use it as drinking water. To ensure the water quality level (WQL), chlorides, nitrite, nitrate, calcium, phosphate, and ammonium have been taken into consideration for measuring the WQ.

2.1. Chlorides in the water

In drinking water, chloride levels are significant because they can affect water quality, taste, and corrosivity. The taste threshold for chloride (sodium, magnesium, and calcium salts) in the water is in the range of 200 up to 300 mg/L. Above that, the water taste is affected by getting a salty taste [9]. High levels of chloride, especially when combined with high levels of sulfate, can cause corrosion in plumbing systems like copper, lead, and iron. This corrosion can damage pipes and appliances and increase metal levels in the water, posing a health risk. While chloride itself is not toxic and is an essential nutrient, very high levels may signal pollution or contamination from industrial waste or agricultural runoff, which could introduce other harmful substances into the water supply [10]. Low chloride levels typically indicate good water quality, suggesting the absence of pollution from sources like industrial waste or agricultural runoff. This is common in freshwater and spring water with minimal contamination. Water with low chloride levels is less likely to taste salty, does not contribute to corrosion in plumbing, and is generally preferred by consumers for drinking and cooking.

2.2. Nitrate and nitrite in the water

According to the EU Drinking Water Directive (202/2184), there are parametric limits for nitrite and nitrate in drinking water. World Health Organization (WHO) guidelines value for nitrate is a maximum of 3 mg/L for drinking water, but the best-measured value for the nitrite is 0.50 mg/L for drinking water and 0.10 mg/L for water after chemical treatment. The same directive, the EU Drinking Water Directive (202/2184), provides information about the nitrate in the water which is 50 mg/L according to the WHO guidelines for the drinking water [11]. High nitrate levels often result from agricultural runoff, industrial discharges, and fertilizers. These sources introduce excessive amounts of nitrates into the water supply, indicating potential contamination and poor water quality. In terms of health risks, increased levels of nitrates in drinking water can pose serious health risks, especially to infants and pregnant women. One significant risk is methemoglobinemia where nitrates interfere with the blood's capacity to carry oxygen. For adults, long-term exposure to high levels of nitrates is associated with an increased risk of certain cancers and other health problems. A lower number of nitrates in drinking water represents the so-called ecological balance. Lower nitrate levels indicate a well-balanced ecosystem and minimal contamination from human activities. It indicates that water treatment processes effectively manage pollution and maintain water quality. For health safety reasons, drinking water with low nitrate levels is generally considered safe for all populations, including vulnerable groups such as infants and pregnant women. Minimizes the risk of methemoglobinemia and other nitrate-related health problems. [12][13]. Nitrites themselves are relatively harmless, but they can be rapidly transformed into nitrate, which is a concern because of the problems that can arise from human exposure above the above nitrate levels.

2.3. Potassium (calcium) in the water

Potassium is an essential nutrient that plays a key role in a variety of body functions, such as heart regulation, fluid balance, and nerve and muscle communication. In the context of drinking water, potassium levels are generally low and usually not a major concern for water quality or health. However, understanding the implications of high and low potassium levels in drinking water may be important in specific contexts. High levels of calcium in drinking water are relatively rare. When present, they may indicate contamination from natural sources, agricultural runoff (especially from fertilizers), or industrial processes. Low levels of calcium in drinking water are common and generally considered safe. Calcium intake from water is typically a small component of total daily intake, with the majority coming from foods such as fruits, vegetables, meat, and dairy products. There are no direct health risks associated with low potassium levels in drinking water. The average concentration of potassium in drinking water is approximately 10 mg/L, and normal concentration is considered 2.5 mg/L. A large concentration in drinking water is considered 3000 mg. Springs usually have a

lower concentration of potassium in mg/L which is proved according to the measurement in Table 1 and the measurements represented in [14].

2.4. Phosphate in the water

Normally, naturally occurring phosphate levels in drinking water are low. Low levels may not pose a direct health risk, but phosphates are essential nutrients for plant growth. Thus, if water with low phosphate levels is used for irrigation, it may not provide enough nutrients for optimal plant growth. High levels of phosphates in water can indicate contamination from sources such as fertilizers, sewage, or detergents. While phosphates themselves are not typically harmful to humans in small amounts, their presence at elevated levels can lead to eutrophication in water bodies. Eutrophication can cause excessive growth of algae and other aquatic plants, depleting oxygen in the water and harming aquatic life. In drinking water, excessive levels of phosphates can cause problems in the water treatment process, and although not directly harmful, they can indicate the presence of other contaminants that can be harmful [15].

2.5. Ammonium in the water

Ammonia and its ionized form, ammonium, are naturally occurring organic compounds produced during the decomposition of proteins, manure, urine, and other nitrogen-containing substances. Ammonia gas is commonly found in areas with large numbers of confined animals, chickens, or birds, and it causes a sharp odor associated with soiled diapers. Some drinking water treatment processes add small amounts of ammonia, typically less than 0.4 mg/l (ppm), to enhance chlorine's disinfecting ability. Ammonia is rarely present in unpolluted surface or well water, but contaminated water with sewage, animal waste, or fertilizer runoff may have elevated levels. The US Environmental Protection Agency (USEPA) has not set a maximum contaminant level (MCL) for ammonia in drinking water. Environmental limits for ammonia in US surface water range from 0.25 to 32.5 mg/l (ppm). The National Academy of Science recommends, and many European countries have adopted, a drinking water standard of 0.5 mg/l (ppm) [16].

This paper together with [17] indicates and opens a path to using the measurements for developing a machine-learning model that can predict the existence of some bacteria in the water.

3. Measurement process – Hardware

In this paper, UV-Vis spectrophotometry has been used to analyze the water samples. Besides the spectrophotometer, the thermostat for solution digestion has been used. A high-speed thermostat has been used because some of the reagents needed the solution to be digested before it is inserted in the spectrophotometer. Hardware equipment used for this research are HACH Lange DR 6000 spectrophotometer and High-speed temperature thermostat HT 200 S. Spectrophotometry as a method, quantifies the light absorption of a chemical substance by analyzing the intensity of light passing through a sample solution. It operates on the principle that each compound absorbs or transmits light within specific wavelength ranges, enabling the measurement of known chemical substances. Spectrophotometry in theory is based on Beer-Lambert Law [18], where equation 1 states that the absorption (A) of light by a substance in solution is directly proportional to its concentration (c) and the length of the light path (l) through the solution, provided the wavelength of the light and the molar absorptivity (ϵ) of the substance are constant.

$$A = \epsilon \cdot l \cdot c \quad (2)$$

Figure 1 represents the UV-VIS HACH Lange DR 6000 spectrophotometer while Figure 2 represents the HT 200 S high-speed temperature thermostat, laboratory equipment used for measurement of the mentioned parameters.



Figure 14. HACH Lange DR 6000 spectrophotometer



Figure 15. HT 200 S high-speed thermostat

The measuring process was divided into five steps, taking a strictly defined amount of sample according to the requirements based on the measured parameter, putting the amount of the sample into the suitable LCK reagent, shaking the mixture in the LCK reagent, and if the measuring parameter and the reagent requires, it must be put into the high-speed thermostat so the reagent could be warmed in order the chemical to reach with the water sample. Then the LCK cuvette is put into the spectrophotometer. The measuring procedure is represented in Figures 4 to 9, and Figure 3 represents the measurement setup.



Figure 16. Measuring equipment with HACH Lange DR 6000 and HT 200 S

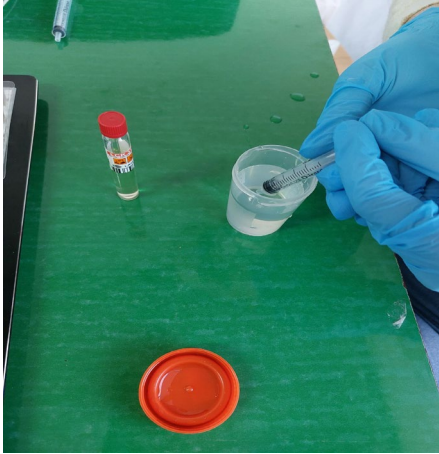


Figure 17. Taking a specific amount of sample



Figure 18. Putting the specific amount of sample into the LCK cuvette

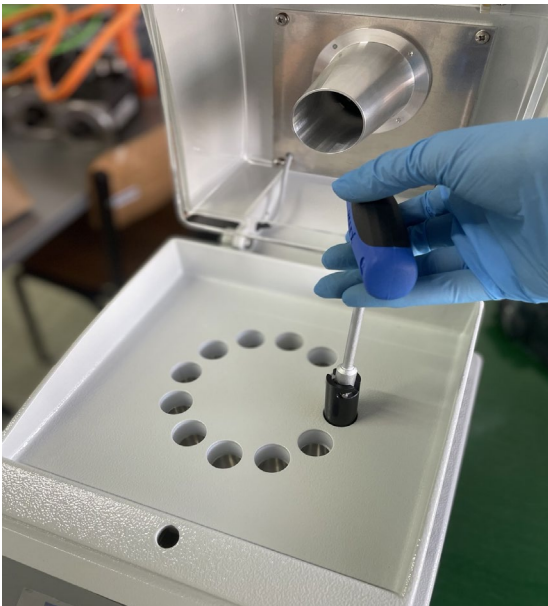


Figure 19. Preparing the high-speed HT 200 S thermometer

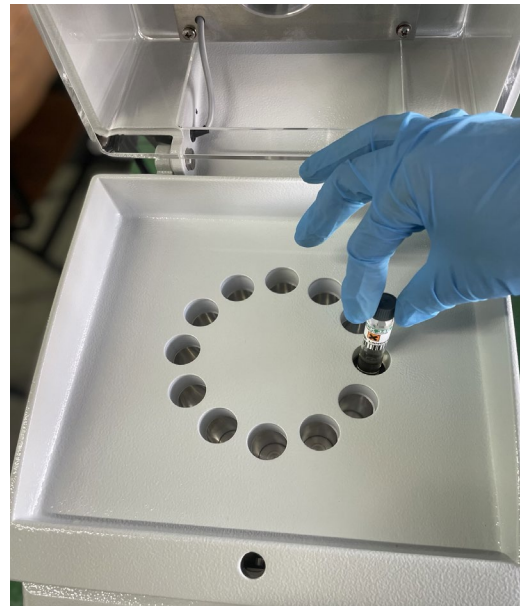


Figure 20. Putting the LCK cuvette inside the HT 200 S so the mixture can be warmed



Figure 21. Putting LCK cuvette into the HACH Lange DR 6000 spectrophotometer



Figure 22. Closing the lid, so the spectrophotometer can start measurement

4. Results and discussion

As represented above in this paper, chloride, nitrate, calcium, nitrite, ammonium, and phosphate were measured parameters to analyze the WQ from the spring that is used by the people living in the region as drinking water.

Measured results are represented in Table 1. It indicates that each measuring reagent has a specific measuring range. Based on the data, all parameters except for nitrites fall within the proposed range, and nitrites are the only parameters that are outside the proposed range.

Table 1. Measured water quality parameters

No.	Measuring parameter	Symbol	Reagent name	Smrdliiva Voda (spring)	Konsko (spring)	Negorski Banji (thermal spring)	Vardar	Measured value	Measuring range
1	Chloride	Cl	LCK 311	3.47	3.30	1.11	1.27	mg/L	1-1000 mg/L
2	Nitrate	NO ₃ ⁻ (-N)	LCK 339	0.070	0.269	0.098	1.51	mg/L	0.23-13.50 mg/L
3	Calcium/ Potassium	K ⁺	LCK 328	11.4	10.8	19.2	11.5	mg/L	8-50 mg/L
4	Nitrite	NO ₂	LCK 541	-0.004	-0.004	-0.004	-0.004	mg/L	0.0015-0.03 mg/L
5	Ammonium	NH ₄	LCK 304	0.007	0.076	0.084	0.131	mg/L	0.015-2.0 mg/L
6	Phosphate	PO ₄	LCK 349	0.264	0.002	0.9	0.084	mg/L	0.05-1.50 mg/L

According to the results represented in Table 1, Figures 10 to 15 will represent the comparison between all four measuring points by the measuring parameters one by one.

Figure 10 represents the comparison between all four measuring points by the measuring parameter chloride. The lower concentration of chloride in all four water samples indicated that in the water, there were no discharges from the agricultural runoffs or any industrial waste. Also, the high concentration in Smrdliiva Voda spring and Konsko spring is expected due to the corrosion presence on the pipes. The pipe corrosion is visible to the naked eye. The water in Smrdliiva Voda also contains a lot of iron. Thermal spring Negorski Banji has a lot less concentration of chloride which also means that there is no corrosion on the supply pipeline which can be also seen with the naked eye. Measured values for all four measuring points are in the permitted area that is safe for human health when consuming this type of water.

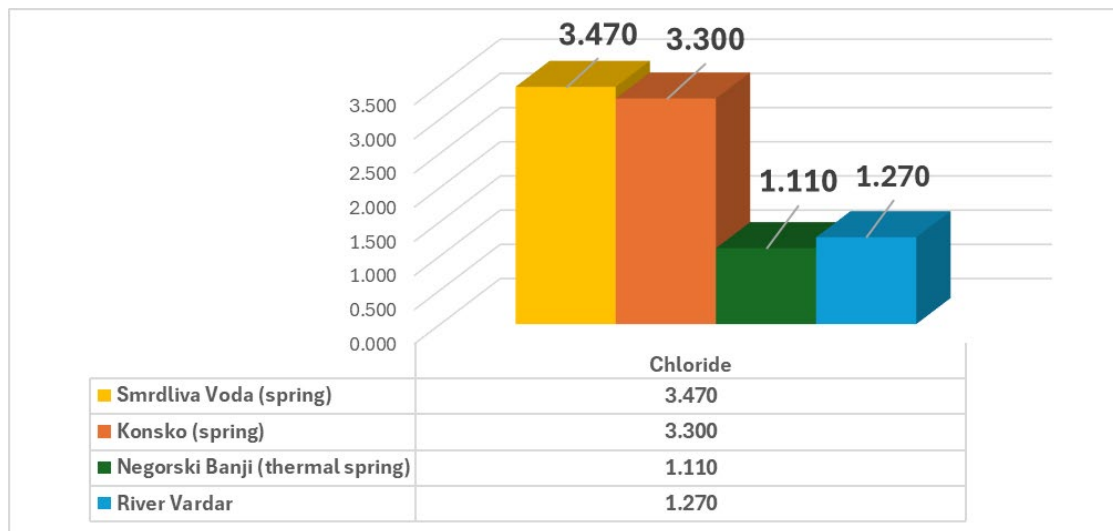


Figure 23. Comparison between the measuring points (springs and river) for chloride presence

Figure 11 represents the comparison between all four measuring points by the measuring parameter nitrate. According to the WHO directives, the maximum level of drinking water must not exceed 0.5 mg/L. The represented results show that the water from the Smrdliwa Voda spring, Konsko spring, and Negorski Banji thermal spring have nitrate levels smaller than the maximum defined, 0.5 mg/L which indicates that from the nitrate point of view, it is safe water to be drunk. Also, the low level of nitrates indicates that there are now agricultural runoffs in the spring or any other waste discharge. According to the value of nitrate in River Vardar, could be concluded that that water is not suitable for drinking but also the small amount of nitrate indicates that there are no agriculture runoffs or any industry discharges with heavy metals.

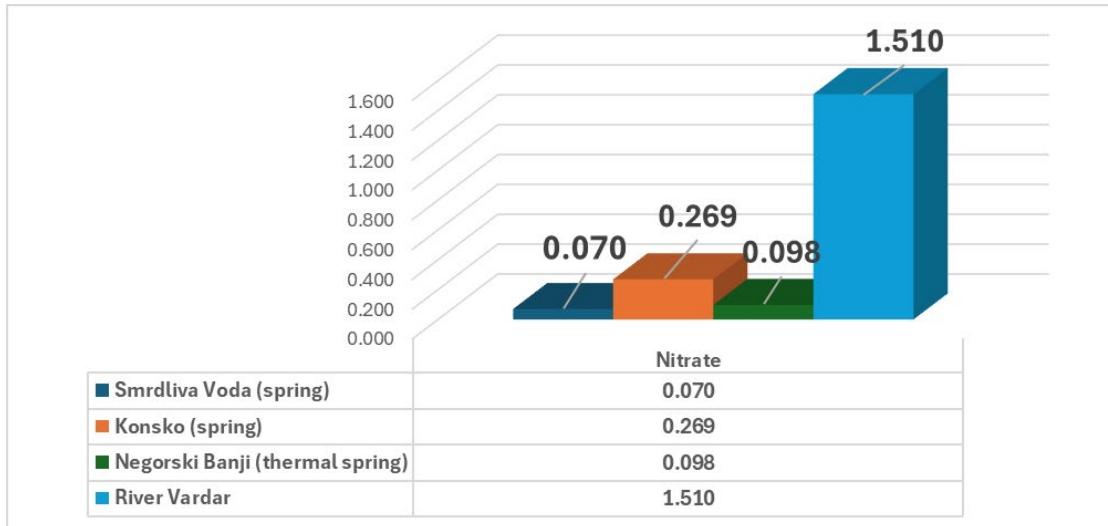


Figure 24. Comparison between the measuring points (springs and river) for nitrate presence

Figure 12 represents the nitrite level in all four measuring points. The results are negative and all the same. That could indicate that the reagent LCK 541 is damaged and cannot mix up with the water sample. However, according to the nitrate results it is expected the results for the nitrite to be similar to those of the nitrate.

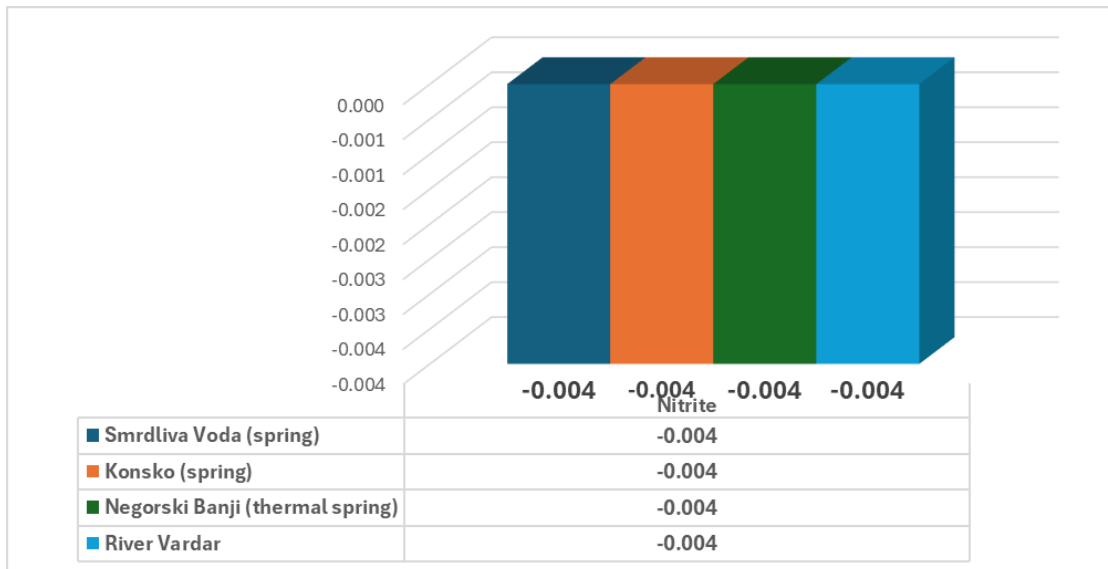


Figure 25. Comparison between the measuring points (springs and river) for nitrite presence

Figure 13 represents the comparison between all four measuring points by the measuring parameter potassium/calcium. According to the measured and represented results in Table 1, the potassium level in Smrdliwa Voda, and Konsko as a mountain spring is near the average potassium level of 10 mg/L. However, in Negorski Banji as a thermal spring, the potassium concentration is greater since that water contains a larger amount of minerals. But still, the potassium level is not extremely high. The potassium level in the human body could be calculated according to the table presented in [19]. The potassium levels in the water are not high enough to cause worrisome effects.

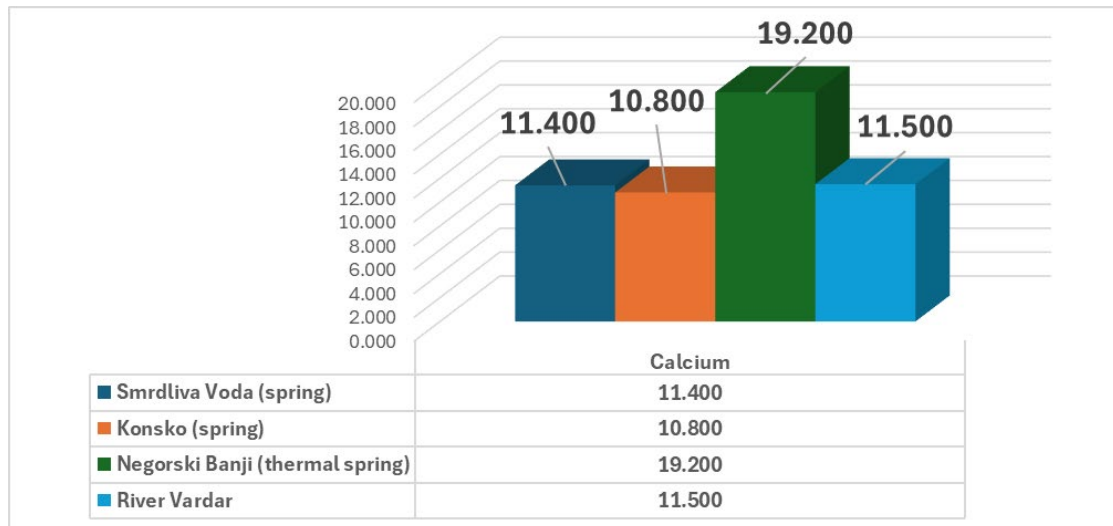


Figure 26. Comparison between the measuring points (springs and river) for potassium/calcium presence

Figure 14 represents the comparison between all four measuring points by the measuring parameter ammonium. According to the results, it is evident that Smrdliva Voda Spring, Kopsko Spring, and Negorski Banji thermal spring are non-polluted water sources and that they are safe for drinking water. According to the WHO, the minimal level of pollution in drinking water is 0.25 mg/L, even Vardar River has a lower level of the minimum permitted level of pollution.

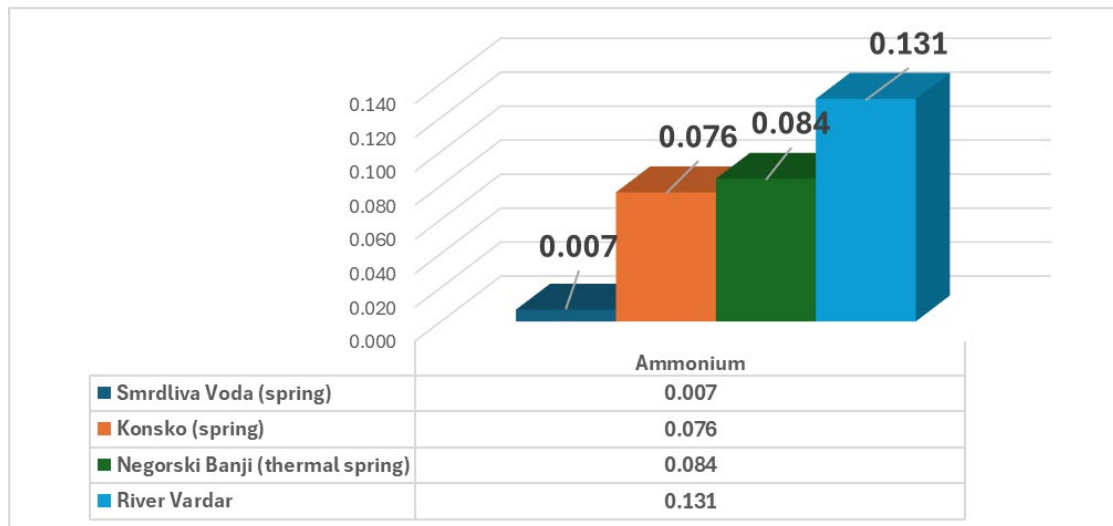


Figure 27. Comparison between the measuring points (springs and river) for ammonium presence

Figure 15 represents the comparison between all four measuring points by the measuring parameter phosphate. The phosphate presence in the water does not harm human health but it stimulates plant growth. According to the measured results, the phosphate level in Negorski Banji thermal spring and in Smrdliva Voda spring, is the highest, meaning lush vegetation. That is proved when the situation on-site is checked.

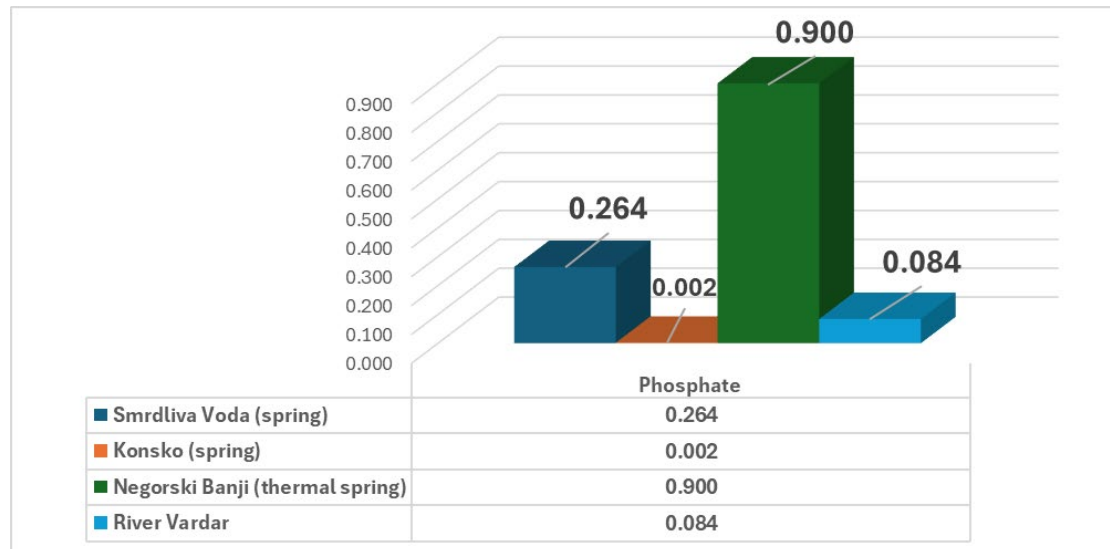


Figure 28. Comparison between the measuring points (springs and river) for phosphate presence

5. Conclusion

In this paper, water quality measurement with UV-VIS spectrophotometer HACH Lange DR 6000 and high-speed temperature thermostat HT 200 S is done. Measured parameters are chlorides, nitrates, nitrites, potassium, phosphates, and ammonium. During the sample-taking, measuring, and analyzing process, four measuring points were taken into consideration, Smrdлива Voda spring, Konsko spring, Negorski Banji thermal spring, and Vardar River. All the water points, except the Vardar River are considered as drinking water and people use them daily. According to the measured parameters, the results, and the analysis, the water from all four measuring points does not contain any waste discharges or agricultural runoff. According to the minimum and maximum values for each measured parameter separately announced by the WHO, neither of the parameters doesn't exceeds the proposed range.

References

- [1] G. V. Korshin, M. Sgroi, and H. Ratnaweera, "Spectroscopic surrogates for real time monitoring of water quality in wastewater treatment and water reuse," *Curr Opin Environ Sci Health*, vol. 2, pp. 12–19, Apr. 2018, doi: 10.1016/j.coesh.2017.11.003.
- [2] A. Radzevičius, M. Dapkienė, N. Sabienė, and J. Dzięcioł, "A Rapid UV/Vis Spectrophotometric Method for the Water Quality Monitoring at On-Farm Root Vegetable Pack Houses," *Applied Sciences*, vol. 10, no. 24, p. 9072, Dec. 2020, doi: 10.3390/app10249072.
- [3] Y. Guo, C. Liu, R. Ye, and Q. Duan, "Advances on Water Quality Detection by UV-Vis Spectroscopy," *Applied Sciences*, vol. 10, no. 19, p. 6874, Sep. 2020, doi: 10.3390/app10196874.
- [4] HOU Di-bo, ZHANG Jian, CHEN Lin, HUANG Ping-jie, and ZHANG Guang-xin, "Water Quality Analysis by UV-Vis Spectroscopy: A Review of Methodology and Application," *SPECTROSCOPY AND SPECTRAL ANALYSIS*, vol. 33, no. 07, pp. 1839–1844, 2013.
- [5] X. Tang, A. Tong, F. Zhang, W. Wang, S. Zhou, and S. Liu, "Concentration Determination of Pollutants in Water Using Ultraviolet Spectrophotometry and Partial Least Squares Method," in *2018 IEEE International Conference on Smart Cloud (SmartCloud)*, IEEE, Sep. 2018, pp. 181–189. doi: 10.1109/SmartCloud.2018.00038.
- [6] A. Mammeri *et al.*, "Assessment of Surface Water Quality Using Water Quality Index and Discriminant Analysis Method," *Water (Basel)*, vol. 15, no. 4, p. 680, Feb. 2023, doi: 10.3390/w15040680.
- [7] E. M. Alves *et al.*, "Use of ultraviolet-visible spectrophotometry associated with artificial neural networks as an alternative for determining the water quality index," *Environ Monit Assess*, vol. 190, no. 6, p. 319, Jun. 2018, doi: 10.1007/s10661-018-6702-7.
- [8] H. Zhang, L. Zhang, S. Wang, and L. Zhang, "Online water quality monitoring based on UV-Vis spectrometry and artificial neural networks in a river confluence near Sheffield-on-Loddon," *Environ Monit Assess*, vol. 194, no. 9, p. 630, Sep. 2022, doi: 10.1007/s10661-022-10118-4.
- [9] World Health Organization, "Chloride in Drinking-water - Background document for development WHO Guidelines for Drinking-water Quality," in *Guidelines for drinking-water quality*, 2nd ed., vol. 2, Geneva, 1996.

- [10] Y. Hong, Z. Zhu, W. Liao, Z. Yan, C. Feng, and D. Xu, “Freshwater Water-Quality Criteria for Chloride and Guidance for the Revision of the Water-Quality Standard in China,” *Int J Environ Res Public Health*, vol. 20, no. 4, p. 2875, Feb. 2023, doi: 10.3390/ijerph20042875.
- [11] Health Service Executive (HSE) and Environmental Protection Agency (EPA), “JOINT POSITION PAPER Nitrate & Nitrite in Drinking Water 2023,” 2023.
- [12] R. Picetti *et al.*, “Nitrate and nitrite contamination in drinking water and cancer risk: A systematic review with meta-analysis,” *Environ Res*, vol. 210, p. 112988, Jul. 2022, doi: 10.1016/j.envres.2022.112988.
- [13] M. Ward *et al.*, “Drinking Water Nitrate and Human Health: An Updated Review,” *Int J Environ Res Public Health*, vol. 15, no. 7, p. 1557, Jul. 2018, doi: 10.3390/ijerph15071557.
- [14] S. Morr, E. Cuartas, B. Alwattar, and J. M. Lane, “How Much Calcium is in your Drinking Water? A Survey of Calcium Concentrations in Bottled and Tap Water and Their Significance for Medical Treatment and Drug Administration,” *HSS J*, vol. 2, no. 2, pp. 130–135, Sep. 2006, doi: 10.1007/s11420-006-9000-9.
- [15] A. O. Fadiran, S. C. Dlamini, and A. Mavuso, “A comparative study of the phosphate levels in some surface and ground water bodies of Swaziland,” *Bull Chem Soc Ethiop*, vol. 22, no. 2, Jul. 2008, doi: 10.4314/bcse.v22i2.61286.
- [16] O. D. of H. S. E. T. S. Department of Human Services, “HEALTH EFFECTS INFORMATION -Ammonia,” 2000.
- [17] R. Koleva, E. ZaeV, D. Babunski, G. Rath, and D. Ninevski, “IoT System for Real-Time Water Quality Measurement and Data Visualization,” in *2023 12th Mediterranean Conference on Embedded Computing (MECO)*, IEEE, Jun. 2023, pp. 1–4. doi: 10.1109/MECO58584.2023.10155050.
- [18] I. Oshina and J. Spigulis, “Beer–Lambert law for optical tissue diagnostics: current state of the art and the main limitations,” *J Biomed Opt*, vol. 26, no. 10, Oct. 2021, doi: 10.1117/1.JBO.26.10.100901.
- [19] World Health Organization, “Potassium in drinking-water,” 2009.

Numerical Study on Thermal Energy Storage System Integrated Flat Plate Solar Collectors in Buildings

Saša Pavlović^a, Evangelos Bellos^b, Velimir Stefanović^a, Marko Ilić^a, Mića Vukić^a, Branka Nakomčić-Smaragdakis^c, C Tzivanidis^b

^a Faculty of Mechanical Engineering, Department of Thermal Engineering, Thermoenergetics and Process Engineering, University in Niš, Niš, RS

^b Thermal Department, School of Mechanical Engineering, National Technical University of Athens, GR

^c Faculty of Technical Sciences, University of Novi Sad, RS

Abstract The use of renewable energy sources for electricity is one of the most promising techniques in order to face environmental problems and high CO₂ emissions. However, the power production from photovoltaics and wind energy is not stable and this fact creates issues between the production profile and the demand profile. Therefore, an effective storage technique is needed, except for the idea of batteries. The objective of the present investigation is the investigation of a novel pumped thermal energy storage system. This system uses the volatile electricity from renewables in order to feed a heat pump that produces heating at a medium temperatures level (e.g. 150°C) and stores it in a latent storage unit. The stored thermal energy can be used later in an organic Rankine cycle for power production when there is the proper demand. The novelty of this work is the incorporation of flat plate collectors for assisting the heat pump in order to increase the overall performance of the examined storage system. According to the results, the ambient source system leads to maximum power to power ratio of 38.5% and this value is lower than the respective values of the solar-assisted system. The maximum system efficiency was found for storage tank temperature at 220°C and evaporator temperature at 30°C, and in this case, the system energy efficiency is 19.1%, while the system exergy efficiency is 19.7%. For the typical case of ($T_{st}=150^{\circ}\text{C}$ and $T_{\text{evap}}=70^{\circ}\text{C}$) the solar-assisted system presents a 61.1% power to power ratio which is 58.7% higher than the ambient source case.

Keywords: Solar energy, Flat plate collector, latent storage, volatile electricity, renewables

1. Introduction

The use of renewable energy sources for electricity production becomes more and more famous in the last year because it is an effective way to face the numerous environmental problems of our society [1-3]. The use of photovoltaics and wind energy are common ways to produce electricity from clean energy at a reasonable cost [4]. However, there is a problem with the need for a storage system for overcoming the deviations between the production and the demand profiles. Therefore a lot of research has been performed in the last years in order to determine the proper ways which can lead to suitable and viable storage of electricity. The recent research has been focused on alternative techniques and not on the usual choice of batteries which is associated with some disadvantages as the reduced life [5].

An interesting idea for the storage of volatile electricity from renewables is the use of pumped thermal energy storage. In this idea, the produced electricity from the renewables that cannot be used directly in the grid feeds a heat pump (HP) in order to produce heating in a high temperature (e.g. at 150°C) by absorbing heat by the ambient heat sink. This produced heating is stored with a sensible or latent storage tank and it will be used later when there is demand for electricity. More specifically, this stored heat can be used in a thermodynamic cycle, usually an organic Rankine cycle (ORC) for producing electricity when there is demand. In this direction, there are literature studies that have studied this idea. Frate et al. [6] studied this idea and they found power to power ratio of 55% after a detailed investigation. They found that the use of cyclopentane on both thermodynamic cycles is a proper choice when there are regenerators in the cycles. Roskosch et al. [7] studied the idea of HP-ORC and calculated the power to power ratio to be ranged from 37% to 56%.

Moreover, another choice is to feed the heat pump with a heat source in order to insert heat in the heat pump at a higher temperature. Solar energy or geothermal energy can be used in order to feed the heat pump and so finally the power to power efficiency can be increased. The use of a geothermal heat sink for feeding the heat

Table 1. Inputs parameters in the present investigation

Parameter	Symbol	Value
Electricity input in the HP	$P_{el,in}$	20 kW
Isentropic efficiency of the turbine	$\eta_{is,tur}$	80%
Isentropic efficiency of the compressor	$\eta_{is,com}$	80%
Pump isentropic efficiency	$\eta_{is,p}$	80%
Electromechanical efficiency in the ORC generator	η_{mg}	97%
Compressor motor efficiency	$\eta_{mot,com}$	97%
Pump motor efficiency	$\eta_{mot,p}$	97%
Storage tank efficiency	η_{st}	95%
HP evaporator temperature	T_{evap}	[20 °C - 80°C]
Melting temperature of the storing material	T_{st}	[120 °C - 220°C]
Temperature difference in the heat exchange	ΔT_{min}	5°C
Temperature in the ORC's condenser	T_{reject}	30°C
Ambient temperature level	T_{am}	25°C
Solar irradiation level	G_T	800 W/m ²

2.2 Basic mathematical formulation

The collector solar thermal efficiency (η_{col}) is given as below [13]:

$$\eta_{col} = \frac{Q_u}{Q_{sol}} = 0.77 - 3.75 \cdot \frac{T_{f,in} - T_{am}}{G_T} - 0.015 \cdot \frac{(T_{f,in} - T_{am})^2}{G_T} \quad (1)$$

The solar irradiation on the solar field (Q_{sol}) is found by the product of the collecting area (A_{col}) and of the solar irradiation (G_T):

$$Q_{sol} = A_{col} \cdot G_T \quad (2)$$

The useful heat product is calculated as:

$$Q_u = m_{col} \cdot c_p \cdot (T_{f,out} - T_{f,in}) \quad (3)$$

The fluid input temperature in the collector ($T_{f,in}$), the fluid outlet temperature ($T_{f,out}$), the ambient temperature (T_{am}), the solar irradiation (G_T), the mass flow rate on the collector (m_{col}) and the specific heat capacity (c_p) are used in the previous equations.

The HP coefficient of performance (COP) is defined as below:

$$COP = \frac{Q_{cond}}{P_{el,in}} \quad (4)$$

The latent storage tank efficiency of the storage system (η_{st}) is given as below:

$$\eta_{st} = \frac{Q_{hrs}}{Q_{st}} \quad (5)$$

The ORC electrical efficiency of the ORC is defined as below:

$$\eta_{orc} = \frac{P_{el,out}}{Q_{hrs}} \quad (6)$$

The system energy efficiency ($\eta_{en,sys}$) is calculated as below:

$$\eta_{en,sys} = \frac{P_{el,out}}{P_{el,in} + Q_{sol}} \quad (7)$$

The system exergy efficiency ($\eta_{ex,sys}$) is calculated as below by using the Petela model for the solar irradiation exergy factor [14]:

$$\eta_{ex,sys} = \frac{P_{el,out}}{P_{el,in} + Q_{in} \cdot \left[1 - \frac{4}{3} \cdot \frac{T_0}{T_{sun}} + \frac{1}{3} \cdot \left(\frac{T_0}{T_{sun}} \right)^4 \right]} \quad (8)$$

The sun temperature is selected at $T_{sun}=5770$ K and the reference temperature at $T_0=298.15$ K. Moreover, figure 1 can be used for the definition of the various heat and power rates.

3. Results and discussion

The first step in the results section is the investigation of the heat pump performance and of the ORC efficiency. Figure 2 shows that higher storage temperature leads to higher ORC efficiency and also to lower COP in the heat pump. The higher evaporator temperature leads to higher COP in the heat. These are reasonable results and in accordance with the thermodynamics and the behavior of the equivalent Carnot cycle in the same conditions (both work and refrigeration Carnot cycles respectively). The next step is the investigation of the ambient source system which is the reference one. Figure 3 shows that the electricity production is maximized for the storage tank temperature at 150°C and in this case, the power production is 7.7 kW and the respective power to power ratio is 38.5% . So, it is obvious that there is a need for optimizing the storage tank temperature level in the ambient source system.

The next step is the investigation of the system that is assisted by the flat plate collectors. The results are given in figures 4 to 7. Figure 4 illustrates the power to power ratio for different combinations of the evaporator temperature and the storage temperature. It is obvious that a higher evaporating temperature increases the power to power ratio, while a higher storage temperature has a negative impact on this parameter. However, after the limit of 200°C , the reduction is not so intense. Moreover, a critical issue is that in all the cases, there is an enhancement compared to the case of the ambient source heat pump. Figure 5 depicts the demanded collecting area for the operation of the solar-assisted HP-ORC system. It can be said that higher power to power efficiency is associated with a higher collecting area; a reasonable result because the higher performance requires higher heat inputs in the evaporator. So, it can be said that it is not possible to design a system of maximum power to power efficiency because in this case there is a need for a huge collecting area. More specifically, in the cases of maximum power to power ratio at 90.7% , the demanded collecting area is 320 m² ($T_{st}=120^\circ\text{C}$ and $T_{evap}=80^\circ\text{C}$).

Figures 6 and 7 depict the energy and the exergy efficiencies of the examined system. Both figures show that higher storage temperature leads to higher system efficiency and lower evaporator temperature leads to higher system efficiency (both energetic and exergetic). The curves of these figures have similar trends and it is an interesting result. The maximum system efficiency was found for storage tank temperature at 220°C and evaporator temperature at 30°C , and in this case, the system energy efficiency is 19.1% , while the system exergy efficiency is 19.7% .

The previous analysis indicates that the solar-assisted system is more efficient than the ambient source system. For the case of $T_{st}=150^\circ\text{C}$ which maximizes the efficiency of the ambient source system, the power to power ratio of it is 38.5% . On the other hand, for this storage temperature and for a typical evaporator temperature of 70°C for FPC, the power to power ratio is 61.1% , which means a 58.7% increase with the FPC assistance. In this case, the collecting area that is demanded is 129 m² which is a reasonable value.

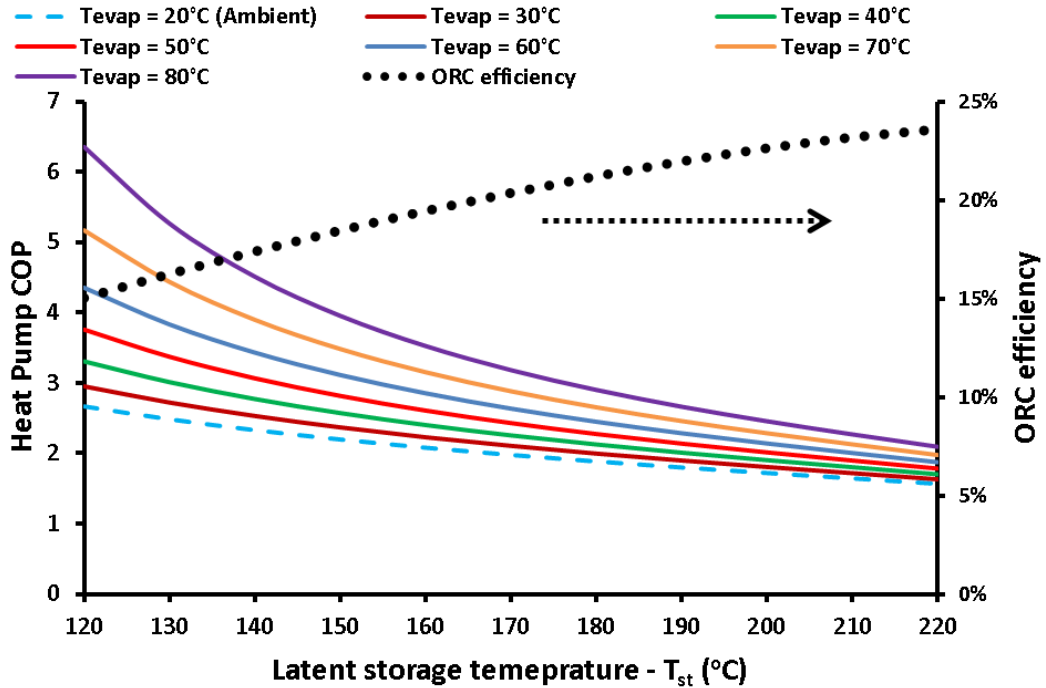


Figure 2. Performance of the heat pump and of the ORC for different values of the evaporator temperature and the storage temperature

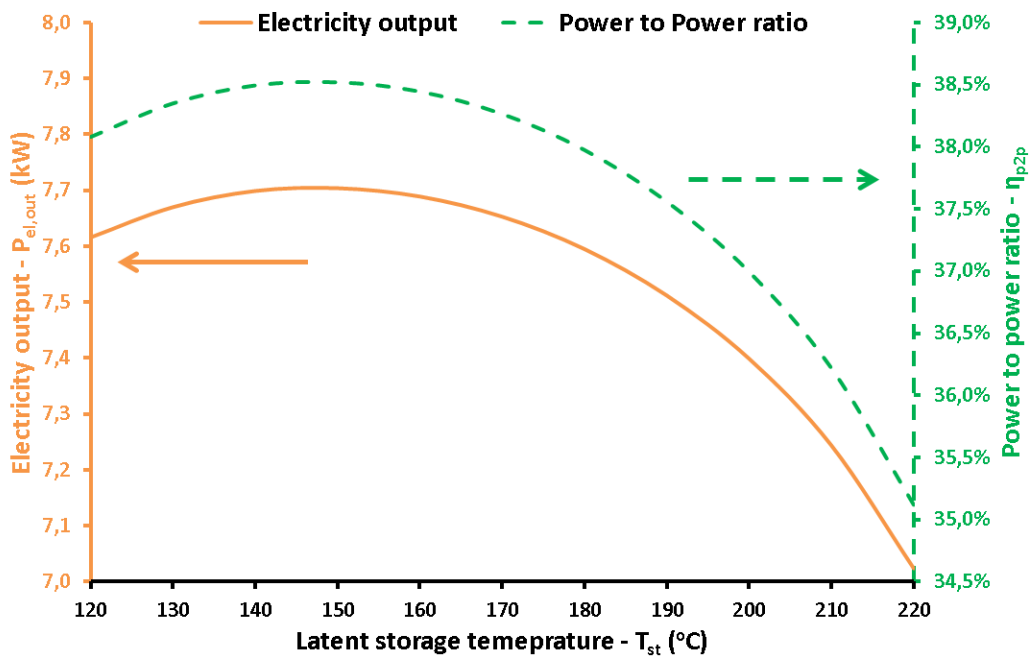


Figure 3. Performance of the ambient source HP-ORC system

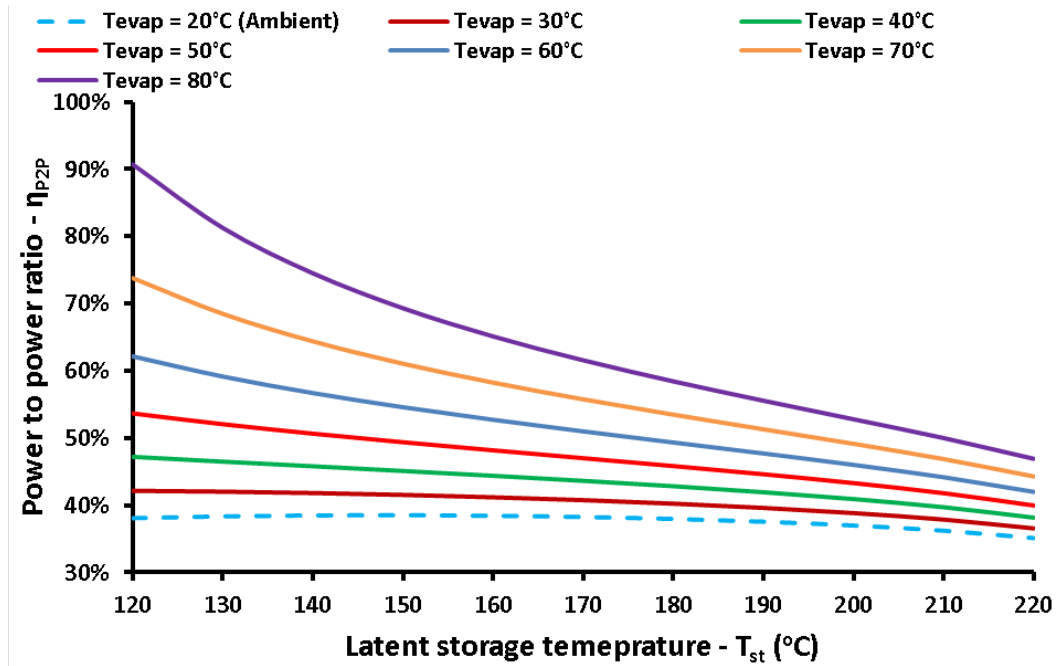


Figure 4. Power to power efficiency for different values of the evaporator temperature and the storage temperature

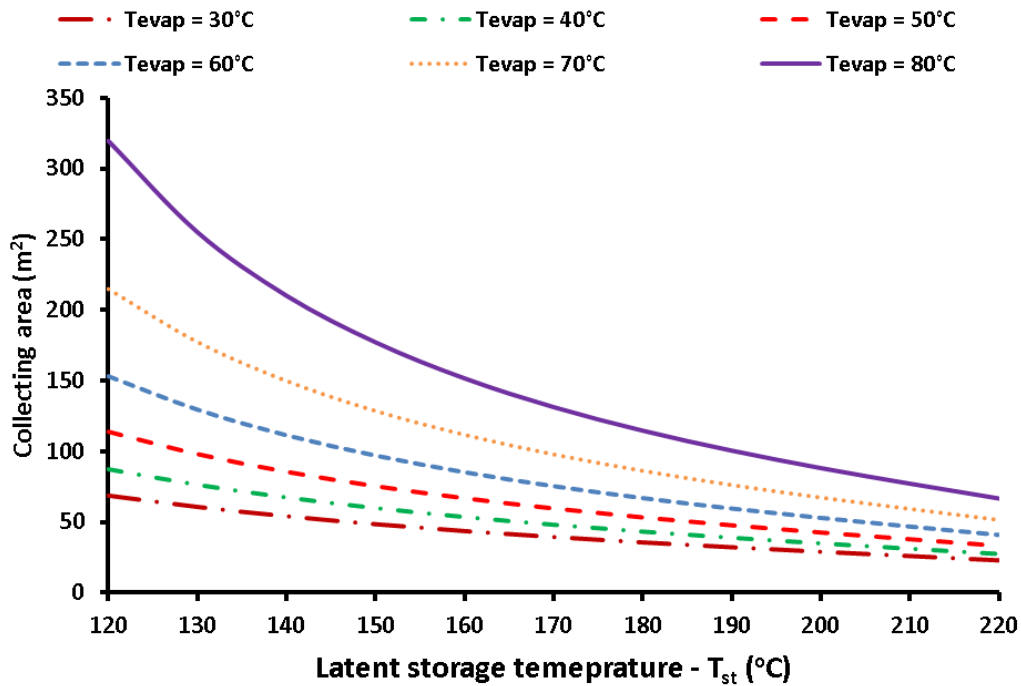


Figure 5. Demanded collecting area for different values of the evaporator temperature and the storage temperature

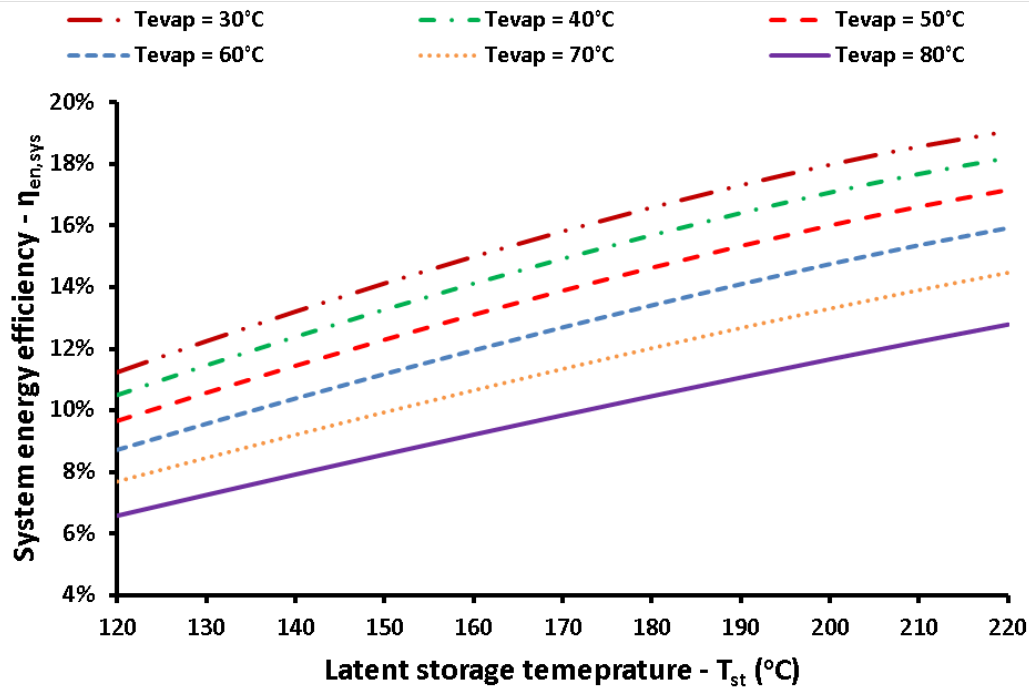


Figure 6. System energy efficiency for different values of the evaporator temperature and the storage temperature

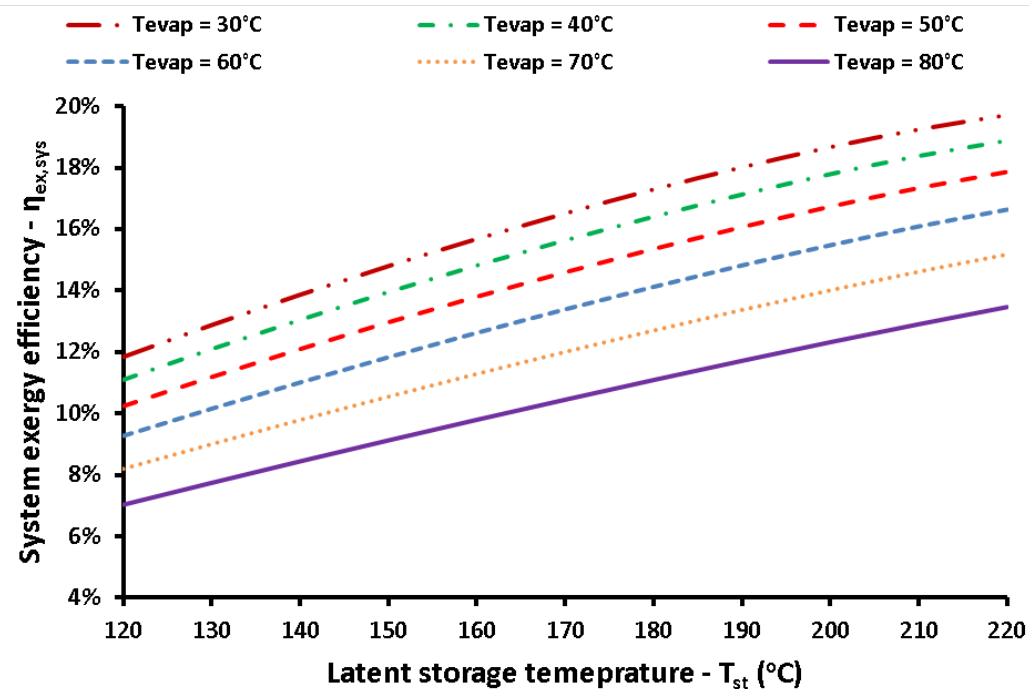


Figure 7. System exergy efficiency for different values of the evaporator temperature and the storage temperature

4. Conclusions

The objective of the present study is the investigation of a pumped thermal energy storage latent system that uses flat plate collectors in order to feed a heat pump – ORC configuration. The analysis is parametric with a developed model in Engineering Equation Solver. The most important conclusions of this work are given below:

- The higher storage temperature leads to higher ORC efficiency and also to lower COP in the heat pump. The higher evaporator temperature leads to higher COP in the heat.
- In the ambient source system, the electricity production is maximized for the storage tank at 150°C and in this case, the power production is 7.7 kW.
- It is found that higher power to power efficiency is associated with higher collecting area; a reasonable result because the higher performance requires higher heat inputs in the evaporator.
- The maximum system efficiency found for storage tank temperature at 220°C and evaporator temperature at 30°C, and in this case, the system energy efficiency is 19.1%, while the system exergy efficiency is 19.7%.
- For the typical case of ($T_{st}=150^{\circ}\text{C}$ and $T_{evap}=70^{\circ}\text{C}$) the solar-assisted system presents a 61.1% power to power ratio which is 58.7% higher than the ambient source case of 38.5% and the demanded collecting area for this case is 129 m².

In the future, there is a need for dynamic analysis of an HP-ORC system coupled to FPC in order to examine the daily enhancement by the use of the solar collectors. Also, the dual system can be studied by the use of both ambient and solar as heat sinks, especially for days with low solar potential.

Acknowledgement

"This research was financially supported by the Ministry of Education, Science and Technological Development of the Republic of Serbia (Contract No. 451- 03-9/2021-14/200109)"

References

- [1] S. Pavlovic, E. Bellos, W.G. Le Roux, V. Stefanovic, C. Tzivanidis, Experimental investigation and parametric analysis of a solar thermal dish collector with spiral absorber, *Applied Thermal Engineering* 2017;121:126-135
- [2] Y. Fang, Y. Wei, Climate change adaptation on the Qinghai–Tibetan Plateau: The importance of solar energy utilization for rural household, *Renewable and Sustainable Energy Reviews* 2013;18:508-518
- [3] V.P. Stefanovic, S.R. Pavlovic, E. Bellos, C. Tzivanidis, A detailed parametric analysis of a solar dish collector, *Sustainable Energy Technologies and Assessments* 2018;25:99-110
- [4] M.J. Khan, A.K. Yadav, L. Mathew, Techno economic feasibility analysis of different combinations of PV-Wind-Diesel-Battery hybrid system for telecommunication applications in different cities of Punjab, India, *Renewable and Sustainable Energy Reviews* 2017;76:577-607
- [5] V. Barbosa, T. Nogueira, E. Carati, C. Felgueiras, Supercapacitor in battery charges of photovoltaic panel: analysis of the technical feasibility, *Energy Procedia* 2018;153:0-85
- [6] G.F. Frate, L. Ferrari, U. Desideri, Multi-criteria investigation of a pumped thermal electricity storage (PTES) system with thermal integration and sensible heat storage, *Energy Conversion and Management* 2020;208:112530
- [7] D. Roskosch, V. Venzik, B. Atakan, Potential analysis of pumped heat electricity storages regarding thermodynamic efficiency, *Renewable Energy* 2020;147(3):2865-2873
- [8] D. Scharrer, B. Eppinger, P. Schmitt, J. Zenk, P. Bazan, J. Karl, S. Will, M. Pruckner, R. German, Life Cycle Assessment of a Reversible Heat Pump–Organic Rankine Cycle–Heat Storage System with Geothermal Heat Supply, *Energies* 2020; 13:3253
- [9] S. Sonsaree, S. Jajitsawat, T. Asaoka, H. Aguirre, K. Tanaka, Organic Rankine Cycle Power Generation from Industrial Waste Heat Recovery Integrated with Solar Hot Water System by using Vapor Compression Heat Pump as Heating Booster in Thailand, 2016 International Conference on Cogeneration, Small Power Plants and District Energy (ICUE 2016) BITEC, Bang-Na, Thailand, 14-16 September 2016
- [10] S. Henchoz, F. Buchter, D. Favrat, M. Morandin, M. Mercangöz, Thermoeconomic analysis of a solar enhanced energy storage concept based on thermodynamic cycles, *Energy* 2012;45(1):358-365
- [11] B. Eppinger, L. Zigan, J. Karl, S. Will, Pumped thermal energy storage with heat pump-ORC-systems: Comparison of latent and sensible thermal storages for various fluids, *Applied Energy* 2020;280:115940
- [12] F-Chart Software, Engineering Equation Solver (EES), 2015. Available at: (<http://www.fchart.com/ees>)
- [13] Technical Guidelines, Technical Chamber of Greece, TOTEE 20701-1/2017, 1st Edition, Athens, 2017
- [14] R. Petela, Exergy of undiluted thermal radiation, *Solar Energy* 2003;74(6):469-488

Three-dimensional Numerical Investigation of Fluidized Bed Gasification in a Pilot Plant Gasifier: Fluid Flow

Nikola Četenović^a, Dejan Cvetinović^b, Djordje Čantrak^c

^a *Vinča Institute of Nuclear Sciences, National Institute of the Republic of Serbia, University of Belgrade, Laboratory for Thermal Engineering and Energy, Belgrade, RS, nikola.cetenovic@vin.bg.ac.rs*

^b *Vinča Institute of Nuclear Sciences, National Institute of the Republic of Serbia, University of Belgrade, Laboratory for Thermal Engineering and Energy, Belgrade, RS, deki@vin.bg.ac.rs*

^c *Faculty of Mechanical Engineering, University of Belgrade, Belgrade, RS, djcantrak@mas.bg.ac.rs*

Abstract: Fluidized bed combustion offers key advantages such as high efficiency, environmental friendliness, fuel flexibility, and load adaptability, making it suitable for various applications such as power generation, biomass gasification, and petrochemical processing. This study presents a numerical investigation of the gasification processes in a pilot-scale fluidized bed gasifier using a 3D computational model. The model simulates the complex turbulent multiphase flow within the real gasifier geometry of the pilot plant and focuses on the interactions between air and sand, as well as the temperature distribution. Initial numerical results show good agreement of fluid flow structure with experimental data. Future work will include combustion modeling, with the numerical results to be validated by experiments in the pilot plant. After model validation, the model will be used for similarity analysis to optimize the process parameters.

Keywords: Fluidized bed, 3D Mathematical modeling, Multiphase flow, Turbulence, Gasifier.

1. Introduction

Fluidized bed combustion (FBC) offers several technical advantages, such as high thermal efficiency, enhanced environmental performance due to reduced emissions of pollutants, the capacity to utilize low-grade fuels, and increased operational flexibility. This flexibility allows for adjustments in both, the fuel type and combustion load, making it adaptable to variable operating conditions. FBC technology finds applications across various industrial sectors, including heat and power generation, drying processes, biomass gasification, and in petrochemical industries such as oil refineries. Given these diverse applications, an in-depth investigation of the gasification processes is of significant interest, particularly from a thermodynamic and kinetic perspective.

Following the energy crisis of the 1970s, intensive research began on new fuel combustion technologies. This primarily relates to the fluidized bed method, which, in many aspects, proved superior to previous combustion technologies in boilers. The first boiler designs utilizing this technology operated on the principle of a bubbling fluidized bed, where particles of inert material move intensely, but the bed itself remains stationary.

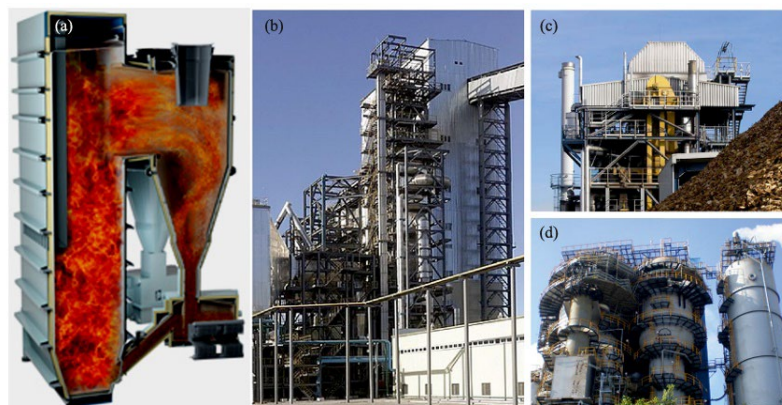


Figure 1. Variety of the fluidized bed applications in industrial sectors:
a) Circulating fluidized bed boiler, b) Dryer, c) Wood gasification plant, d) Oil processing plant [2]

Later, the circulating fluidized bed was introduced, where the inert material is rapidly fluidized and moves vertically upward through the reactor, after which it is separated in a cyclone and returned to the bottom of the combustion chamber. [1]

The inert material (such as sand or limestone) serves as the medium in which fuel combustion occurs, with the material fluidized by air. This creates highly favorable conditions for combustion. The mixture of air and inert material exhibits fluid-like behavior. Fuel can be injected either on the surface of the bed or beneath it. Above the bed, there is a free space where the combustion of fine and volatile fuel components continues. Particles that do not burn during their first pass through the combustion chamber can be recirculated for further combustion, which is characteristic of the circulating fluidized bed. The primary advantage of fluidized bed combustion is the intense mixing of particles, allowing combustion to occur throughout the entire space occupied by the inert material. This method is characterized by a high thermal capacity of the bed and excellent heat transfer to the fuel particles, enabling the rapid ignition of various, including low-quality, fuels. An important feature is that different types of fuel can be burned simultaneously or alternately in fluidized bed boilers. Another key benefit of these boilers is the reduced amount of harmful emissions in flue gases, such as SO₂, NO_x, CO, and chlorine compounds. The combustion temperature typically ranges between 800-900 °C. [3, 4, 5, 6, 7]

Combustion in a circulating fluidized bed occurs at higher fluidization velocities. In one or more cyclones, the solid material, composed of sand and unburned fuel, is separated and returned to the combustion chamber. Sand particles move significantly slower than the gas, causing them to return to the bed in clusters. There is intense interphase heat transfer and a high combustion rate. Mixing occurs equally in both the vertical and transverse directions, resulting in a uniform temperature throughout the combustion chamber. The recirculation of solid materials allows for easy adjustment of power output across a wide range. The following diagram schematically illustrates a combustion chamber using a circulating fluidized bed.

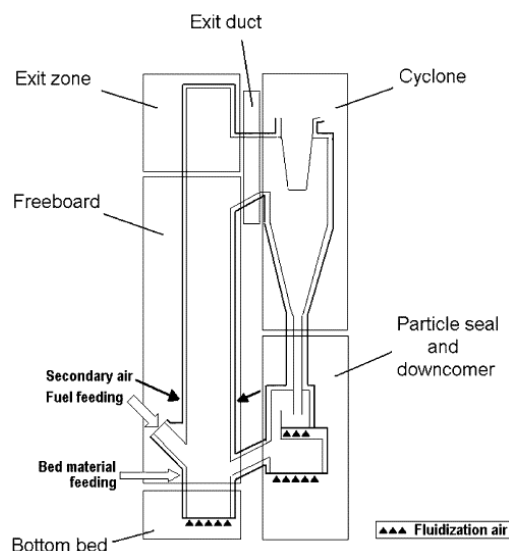


Figure 2. Schematic representation of a combustion chamber with a circulating fluidized bed [8]

This research focuses on presenting numerical results derived from a 3D computational model of a pilot-scale fluidized bed gasifier. The mathematical modeling undertaken here involves simulating the turbulent, multiphase flow behavior within the actual geometry of the gasifier, accounting for complex interactions between the gas (air) and solid phases (sand), as well as the resulting temperature distribution throughout the system. The model incorporates advanced turbulence and multiphase interaction schemes, essential for capturing the heterogeneous flow dynamics that occur in the fluidized bed environment [9].

Preliminary flow simulations indicate a strong correlation between the predicted and observed gasifier performance, validating the suitability of the developed model. The next research phase will extend this work to include detailed combustion modeling, which will enable the prediction of chemical reactions and heat release within the bed. Upon completion, the numerical outcomes will be rigorously compared with experimental data obtained from tests conducted in a pilot plant, to further refine and validate the model. This will provide a comprehensive understanding of both fluid dynamics and thermochemical behavior within fluidized bed systems.

2. Geometry model

The fluidization problem observed from a numerical perspective in this work has its experimental setup, based on which the geometry of the combustion chamber was formed. The model was created in Catia® and later implemented in Ansys® for forming the numerical mesh. The focus in creating the geometry was on designing the combustion chamber, while other system components were not of interest, as the goal was to observe the fluidization process through numerical simulations.

The vertical cylinder, as the main part of the combustion chamber where the burning process occurs, has a height of 2 m and a diameter of 0.76 m. It is followed by a chamber with a height of 0.66 m, from which 31 pipes with a diameter of 63.5 mm exit. In this group of pipes, the flue gas travels in the opposite direction to the original airflow and performs heat exchange with water. The height of the inert layer of sand is 0.76 m. At the bottom of the combustion chamber, there are 30 pipes representing burners, through which air enters. They are arranged concentrically in three radii: 54 mm, 152 mm, and 250 mm. The burner diameter is 19 mm, and the total length is 0.44 m. On the side of the cylinder, there is a fuel feeder, but it did not play a significant role as combustion was not tested. Its length is 0.65 m, and its diameter is 90 mm. Figure 3 shows a schematic of the entire experimental setup [10], while Figure 4 shows the geometric model of the combustion chamber used in the simulations.

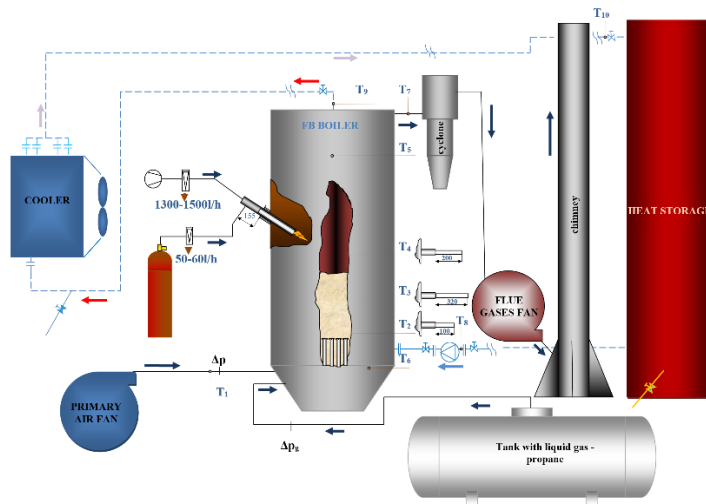


Figure 3. Schematic representation of an experimental setup

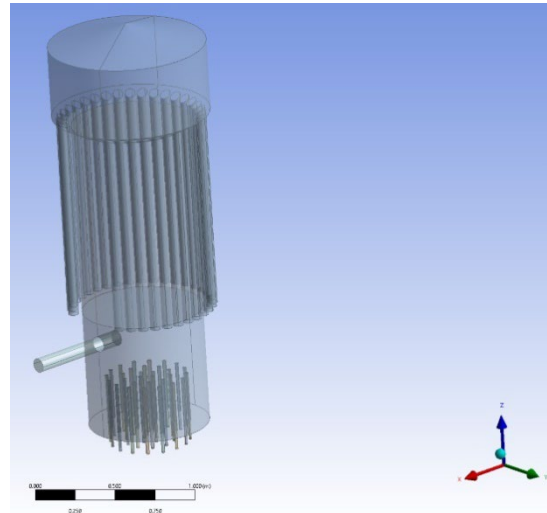


Figure 4. The real geometry model

3. Mathematical modeling

The mesh used contained 508394 elements due to the limitations of Ansys Student® [11, 12] software. In areas of interest, the mesh had a higher number of elements to capture specific phenomena. The numerical method applied for discretization was the finite volume method.

Since the problem involves multicomponent and multiphase flow, appropriate mathematical models must be used in Fluent® to accurately represent the fluidized bed. For this reason, the Eulerian Multiphase model was employed. Initially, based on the conservation laws of mass, momentum, and energy, the continuity equation, momentum equation, and energy equation will be presented. These equations will be modified from their standard form due to the presence of multiphase flow, already shown in [13, 14, 15].

$$\frac{\partial}{\partial t} (\alpha_q \rho_q) + \nabla \cdot (\alpha_q \rho_q \vec{U}) = \dot{m}_{pq} - \dot{m}_{qp} \quad (1)$$

The previous equation represents the continuity equation for the case of two-phase flow, where α_q denotes the volume fraction of the phase, which can be labeled with g or s in the subscript, depending on whether it refers to gas or solid. The mass flux \dot{m}_{pq} represents the mass transfer from one phase to another, while \dot{m}_{qp} represents the mass transfer occurring in the opposite direction.

$$\frac{\partial}{\partial t} (\alpha_q \rho_q \vec{U}) + \nabla \cdot (\alpha_q \rho_q \vec{U} \vec{U}) = -\alpha_q \nabla p + \nabla \cdot \vec{\tau}_q + \alpha_q \rho_q \vec{g} + \vec{R}_{pq} + \dot{m}_{pq} \vec{U}_{pq} - \dot{m}_{qp} \vec{U}_{qp} \quad (2)$$

The momentum equation is expressed through the previous relation. \vec{R}_{pq} represents the interaction force between the phases, while \vec{U}_{pq} and \vec{U}_{qp} denote the interphase velocities. The tangential stress tensor $\vec{\tau}_q$ is expressed through the following relation.

$$\vec{\tau}_q = \alpha_q \mu_q (\nabla \vec{U} + \nabla \vec{U}^T) + \alpha_q (\lambda_q - \frac{2}{3} \mu_q) \nabla \cdot \vec{U} \vec{I} \quad (3)$$

μ_q represents the dynamic viscosity of the phase, while λ_q is the bulk viscosity of the phase.

$$\vec{R}_{pq} = K_{pq} (\vec{U}_p - \vec{U}_q) \quad (4)$$

K_{pq} is the interphase momentum exchange coefficient, \vec{U}_p and \vec{U}_q are the phase velocities. The energy equation is expressed through the following relation.

$$\frac{\partial}{\partial t} \left(\alpha_q \rho_q \left(e_q + \frac{\vec{U}^2}{2} \right) \right) + \nabla \cdot \left(\alpha_q \rho_q \vec{U} \left(h_q + \frac{\vec{U}^2}{2} \right) \right) = \nabla \cdot \left(\alpha_q k_{eff,q} \nabla T_q + \vec{\tau}_{eff,q} \vec{U} \right) + Q_{pq} + \dot{m}_{pq} h_{pq} - \dot{m}_{qp} h_{qp} + p \frac{\partial \alpha_q}{\partial t} \quad (5)$$

e_q represents the internal energy of the phase, while the term $\frac{\vec{U}^2}{2}$ represents the kinetic energy of the phase, and h_q represents the enthalpy of the phase. The thermal conductivity coefficient is represented by $k_{eff,q}$, and the heat transfer rate between phases is given by Q_{pq} . The interphase enthalpies are h_{pq} and h_{qp} . Additionally, the change in the volume fraction of the phase over time is also considered with term $\frac{\partial \alpha_q}{\partial t}$.

K_{pq} can be expressed in the following form, where α_s is the volumetric fraction of the solid phase, f is a function determined differently depending on the model used and τ_s is particulate relaxation time.

$$K_{pq} = \frac{\alpha_s \rho_s f}{\tau_s} \quad (6)$$

τ_s is expressed in the following form, where d_s is the diameter of solid particles, μ_g is the dynamic viscosity of fluid phase.

$$\tau_s = \frac{\rho_s d_s^2}{18 \mu_g} \quad (7)$$

In this study, parametrized Syamlal-O'Brien model was used to determine K_{pq} . Function f is determined through the next equation, where C_D is drag function, Re_s is relative Reynolds number, α_g is the volumetric fraction of the fluid phase and $v_{r,s}$ is terminal velocity correlation for the solid phase. [16]

$$f = \frac{C_D Re_s \alpha_g}{24 v_{r,s}^2} \quad (8)$$

Drag function C_D has a form derived by [17], which is represented through the following equation.

$$C_D = \left(\frac{0.63}{v_{r,s}} + \frac{4.8}{\sqrt{v_{r,s} Re_s}} \right)^2 \quad (9)$$

The following relation shows the method for calculating Re_s , where Re_{single} is used for single particle. This occurs when the conditions for minimum fluidization are achieved. This model is used to under/over-predict bed expansion in fluid bed reactors. [18]

$$Re_s = Re_{single} \left(\frac{A + 0.06 B Re_{single}}{1 + 0.06 Re_{single}} \right) \quad (10)$$

Re_{single} is the Reynolds number at the terminal settling condition for a single particle and can be expressed as:

$$Re_{single} = \left(\frac{(4.8^2 + 2.52 \sqrt{4Ar/S})^{0.5} - 4.8}{1.26} \right)^2 \quad (11)$$

The Archimedes number, Ar , can be written as a function of the drag coefficient and the Reynolds number:

$$Ar = \frac{3}{4} C_D Re_s^2 \quad (12)$$

$v_{r,s}$, minimum fluidization velocity, can be obtained from next equation:

$$v_{r,s} = 0.5(A - 0.06 Re_s + \sqrt{(0.06 Re_s)^2 + 0.12 Re_s (2B - A) + A^2}) \quad (13)$$

Calculation of A is shown in next relation.

$$A = \alpha_g^{4.14} \quad (14)$$

Calculation of B is shown in next relation.

$$B = \begin{cases} c_1 \alpha_g^{1.28} & \alpha_g \leq 0.85 \\ \alpha_g^{d_1} & \alpha_g > 0.85 \end{cases} \quad (15)$$

Formulation for d_1 :

$$d_1 = 1.28 + \frac{\log_{10} c_1}{\log_{10} 0.85} \quad (16)$$

Once the particle diameter and the expected minimum fluidization velocity are known, the coefficients c_1 and d_1 can be found by iteratively solving previous equations.

The volumetric rate of energy transfer between phases, Q_{pq} , is assumed to be a function of the temperature difference and the interfacial area, A_i :

$$Q_{pq} = h A_i (T_p - T_q) \quad (17)$$

h is the volumetric heat transfer coefficient between phases which depends on three parameters: Nusselt number for p-phase Nu_p , thermal conductivity of q-phase k_q and bubble diameter d_p .

$$h = \frac{k_q Nu_p}{d_p} \quad (18)$$

k- ε Mixture model was used for turbulence modeling in this two-phase flow. The k (turbulence kinetic energy) and ε (turbulence dissipation rate) equations describing this model (and without including buoyancy, dilation, and source terms) are as follows:

$$\frac{\partial}{\partial t} (\rho_m k) + \nabla \cdot (\rho_m \vec{U}_m k) = \nabla \cdot \left(\left(\mu_m + \frac{\mu_{t,m}}{\sigma_k} \right) \nabla k \right) + G_{k,m} - \rho_m \varepsilon + \Pi_{k,m} \quad (19)$$

$$\frac{\partial}{\partial t} (\rho_m \varepsilon) + \nabla \cdot (\rho_m \vec{U}_m \varepsilon) = \nabla \cdot \left(\left(\mu_m + \frac{\mu_{t,m}}{\sigma_\varepsilon} \right) \nabla \varepsilon \right) + \frac{\varepsilon}{k} (C_{1\varepsilon} G_{k,m} - C_{2\varepsilon} \rho_m \varepsilon) + \Pi_{\varepsilon,m} \quad (20)$$

In previous transport equations, velocity, density and dynamic viscosity are used for mixture. The following relations show that, in order to obtain the quantities corresponding to the mixture, it is necessary to know these quantities for each component of the mixture.

$$\rho_m = \sum_{i=1}^N \alpha_i \rho_i \quad (21)$$

$$\mu_m = \sum_{i=1}^N \alpha_i \mu_i \quad (22)$$

$$\vec{U}_m = \frac{\sum_{i=1}^N \alpha_i \rho_i \vec{U}_i}{\sum_{i=1}^N \alpha_i \rho_i} \quad (23)$$

The turbulent viscosity for the mixture, $\mu_{t,m}$, is computed from:

$$\mu_{t,m} = \rho_m C_\mu \frac{k^2}{\varepsilon} \quad (24)$$

Production of turbulence kinetic energy, $G_{k,m}$, is computed from:

$$G_{k,m} = \mu_{t,m} \left(\nabla \vec{U}_m + (\nabla \vec{U}_m)^T \right) : \nabla \vec{U}_m \quad (25)$$

The terms, $\Pi_{k,m}$ and $\Pi_{\varepsilon,m}$ are source terms that can be included to model the turbulent interaction between the dispersed phases and the continuous phase. σ_k , σ_ε , $C_{1\varepsilon}$, $C_{2\varepsilon}$ and C_μ are empiric constants.

The simulation conducted in Fluent® was unsteady. The energy equation was considered, along with the Eulerian Multiphase model and the k- ε Mixture model. Air ($\rho = 1.225 \text{ kg/m}^3$) was selected as the primary phase, while sand ($\rho = 1380 \text{ kg/m}^3$) was the secondary phase. Given that the sand is granular, the particle diameter was set to 0.00096 m. The minimum fluidization velocity was set at 0.4 m/s, and the program calculated the values of $c_1 = 0.8386178$ and $d_1 = 2.362952$. The turbulence model uses standard wall functions. For the burner inlet, a velocity-inlet boundary condition was applied, specifying a velocity of 19.2 m/s and a temperature of 723 K. The outlet, where flue gases are expected to be present, was defined using a pressure-

outlet boundary condition, with atmospheric pressure and a temperature of 300 K. The boundaries of the control volume were marked with a wall boundary condition, assuming an adiabatic case.

The Phase Coupled Simple algorithm was used for Solution Methods, with the convergence criterion for residuals set to 10^{-4} , and a standard initialization was performed. At the initial moment, the sand's volume fraction was set to 0.6 at the location of the inert sand bed. Since the simulation is unsteady, the timestep was set to 0.0001 s to ensure the residuals could converge. The total simulation time was set to 10 s. Boundary condition values were selected to facilitate comparison with experimental results when the combustion process is taken into account.

4. Results and discussion

To begin, the velocity fields of air and sand will be presented. The velocity of air is limited to 19 m/s, while the velocity of sand is limited to 4 m/s, as these are the maximum velocities reached by the respective phases. It is clearly observed that the air in the pipes entering the furnace reaches the highest velocity, but upon contact with the sand, its velocity decreases. The air continues its upward flow and exits through the outlet pipes at an increased velocity due to the narrowing of the cross-section. The sand reaches its maximum velocity upon initial contact with the air, after which it begins to decrease. Due to the influence of the fluidized bed, the sand behaves like a fluid, allowing for more efficient combustion compared to a scenario where only air enters from the burners. This is because both vertical and transverse mixing of the fluidized bed with the fuel occurs, leading to more intense heat transfer.

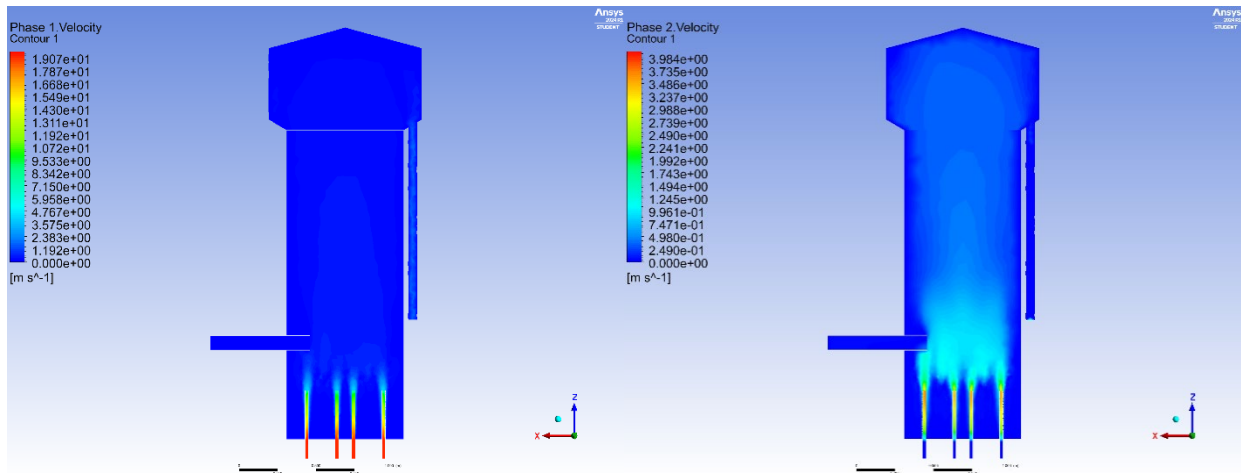


Figure 5. (left) air velocity; (right) sand velocity at time $t = 5$ s

The next figure shows the volume fraction of air at different time intervals, which allows for observation of the development of the fluidized bed and interphase interactions. Initially, air enters the burners while the inert sand layer remains stationary. Upon exiting the burners and entering the furnace, the air contacts the sand, with the air velocity significantly exceeding the minimum fluidization velocity, causing the sand to initiate its upward flow. In the lower corners of the furnace and at the bottom, sand that is not fluidized remains in place, but the majority of the sand moves with the air, forming a fluidized layer that rises. At later time intervals, this layer fills the entire volume of the furnace, allowing for uniform combustion. The velocities used for the air correspond to those in a circulating fluidized bed, where rapid fluidization occurs. However, there is no cyclone present to separate unburned material and sand, instead, the movement of the fluidized bed through the furnace in a single pass is examined to determine its impact on combustion.

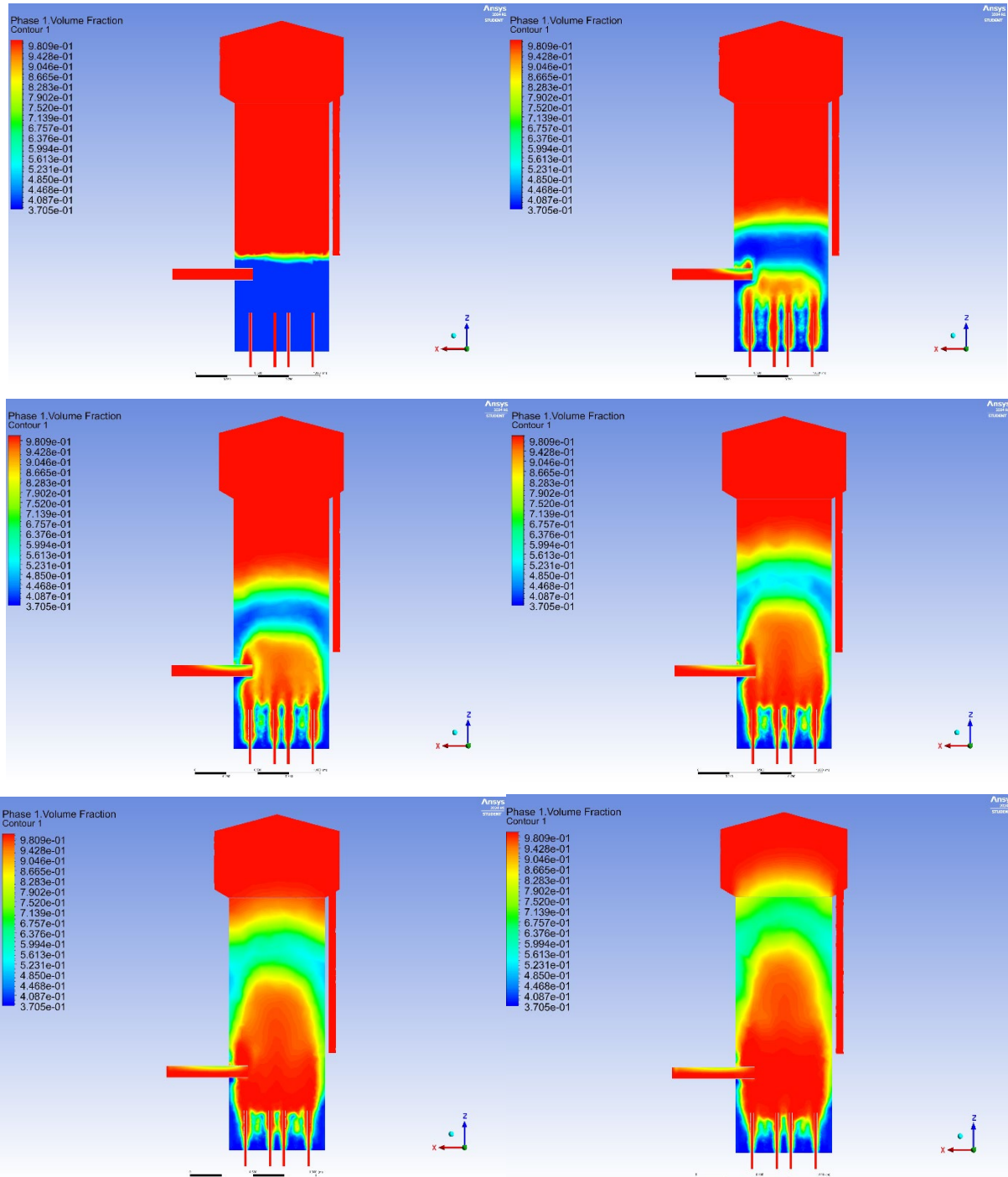


Figure 6. Development of the fluidized bed observed through the volume fraction of air at different time intervals ($t = 0\text{ s}$, $t = 1\text{ s}$, $t = 2\text{ s}$, $t = 3\text{ s}$, $t = 4\text{ s}$, $t = 5\text{ s}$)

It is crucial to observe the temperature distribution within the combustion chamber for the subsequent analysis of the combustion process. Therefore, Figure 7 shows the vertical temperature field, where it can be seen that the temperature is uniformly distributed throughout the entire combustion chamber. This is a result of the mixing of air and sand particles within the fluidized bed, which enhances the efficiency of the combustion process. In Figure 8, three cross-sectional planes are visible at distances of 0.315 m, 0.55 m and 1 m from the origin along the z-axis. On the first plane, the highest temperature is observed in areas where air from the burner enters the combustion chamber. On the second plane, the temperature is the most uniform and highest due to the intense mixing of air and sand at this location, indicating that once fuel is injected, combustion will predominantly occur at this point. On the third plane, the temperature remains uniform, though less so than in the previous case, but still sufficient for combustion to proceed intensively at this location.

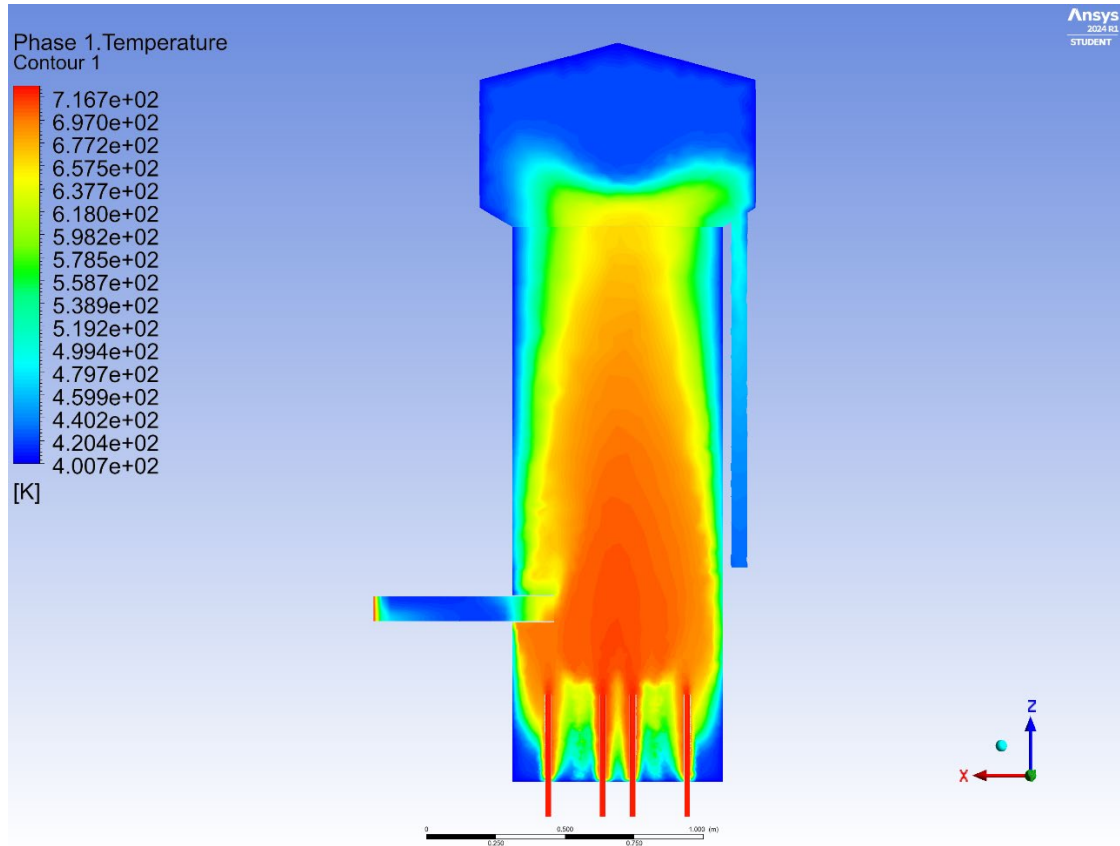


Figure 7. Temperature distribution in the vertical direction of the combustion chamber at $t = 10$ s

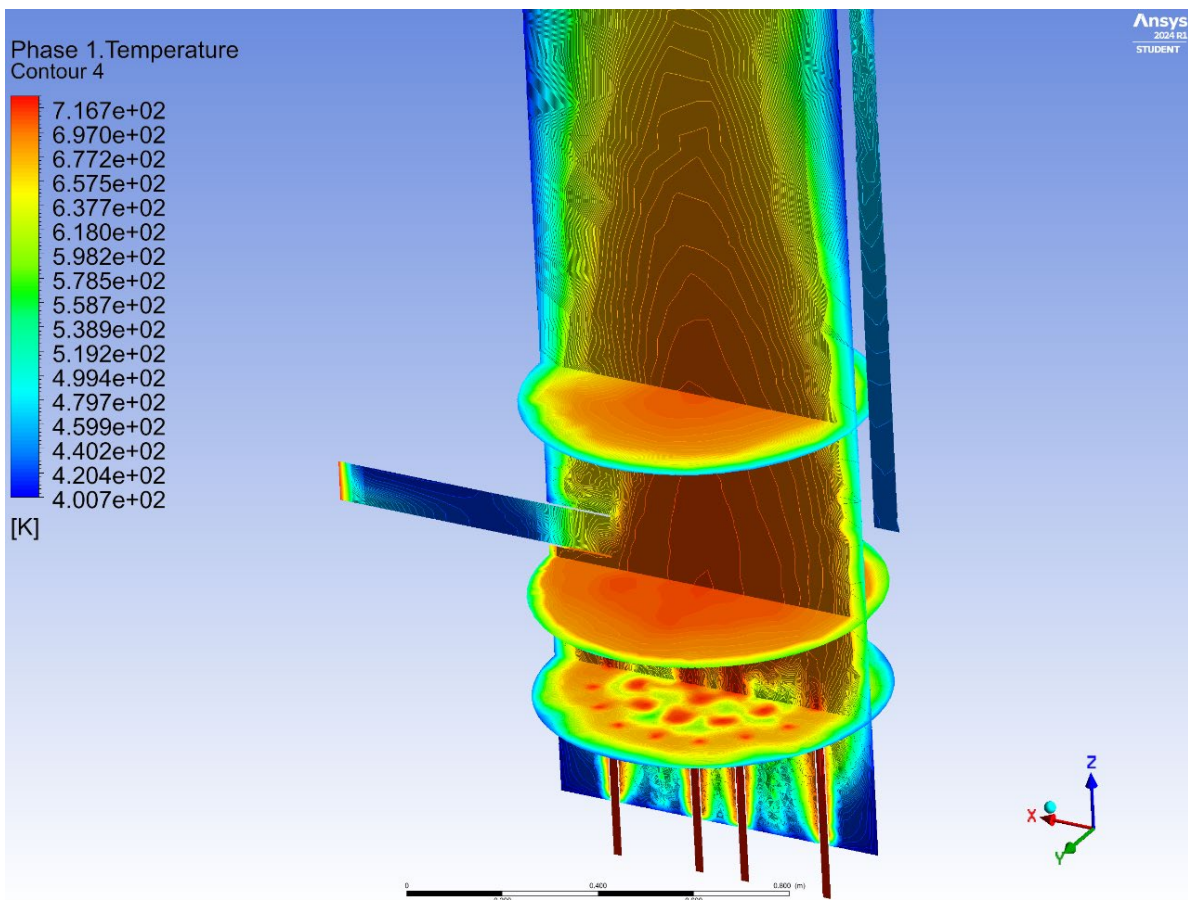


Figure 8. Temperature distribution in three cross-sections of the combustion chamber at $t = 10$ s

5. Conclusion

In conclusion, numerical simulations offer a valuable tool for optimizing experimental efforts by reducing the resources needed for physical testing. When appropriate boundary and initial conditions are applied, and the problem is accurately modeled, the results can closely interpret real-world behavior.

In this study, Fluent® software was utilized to simulate the fluidized bed process, specifically focusing on boiler combustion applications. The 3D computational model, adopted for a real gasifier geometry, effectively captured the turbulent, multiphase flow dynamics within a pilot-scale gasifier, accurately representing the interactions between gas and solid phases, as well as temperature distribution.

The preliminary results showed a strong alignment between the simulated and actual gasifier performance, demonstrating the model's reliability.

Future work will focus on incorporating combustion modeling to simulate chemical reactions and heat generation, followed by validation through comparison with pilot plant data, ultimately leading to a deeper understanding of fluid dynamics and thermochemical processes in fluidized bed systems.

Acknowledgment

This research was funded by the Ministry of Science, Technological Development and Innovation of the Republic of Serbia, Grant no. 451-03-66/2024-03/200017 («Vinča» Institute of Nuclear Sciences, National Institute of the Republic of Serbia, University of Belgrade), Fund for Young Talents of the Republic of Serbia, and Science Fund of the Republic of Serbia - Green Program of Cooperation between Science and Industry - project STABILISE.

References

- [1] Oka, S., Sagorevanje u fluidizovanom sloju, Jugoslovensko društvo termičara, Beograd, (1994)
- [2] Alobaid, F., Almohammed, N., Farid, M.M., May, J., Rößger, P., Richter, A., Epple, B., Progress in CFD Simulations of Fluidized Beds for Chemical and Energy Process Engineering, Progress in Energy and Combustion Science, 91, pp. 1-213, (2022)
- [3] Oka, S., Sagorevanje u fluidizovanom sloju, nova tehnologija za sagorevanje uglja i drugih čvrstih goriva, u knjizi Energija i razvoj, Izdanje Društva „Nikola Tesla“, Beograd, str. 147-156., (1986)
- [4] Ehrlich, Sh., Fluidized Combustion, Is it achieving its promise? Keynote address, 3rd Int. Fluidized Bed Combustion Conference, 16/17 Oct, London, Proc. Vol. 2, KA/1/1-29., (1984)
- [5] Oka, S., Arsić, B., Dakić, D., Razvoj ložišta i kotlova sa sagorevanjem u fluidizovanom sloju, Primenjena nauka, No 1, str. 25-35, (1985)
- [6] Makansi, J., Schwieger, B., Fluidized Bed Boilers, Power, August, pp. s-1, s-16., (1982)
- [7] Wiegand, D., Technical and Economical Status of FBC In West-Germany, Presented at Int. Conf. on Coal Combustion, Copenhagen, 3th November 1986
- [8] Pallarès, D., Johnsson, F., Macroscopic Modelling of Fluid Dynamics in Large Scale Circulating Fluidized Beds, Progress in Energy and Combustion Science, 32, pp. 539-569, (2006)
- [9] Leckner B., Lind F., Combustion of municipal solid waste in fluidized bed or on grate – A comparison, Waste Management, Volume 109, Pages 94-108, ISSN 0956-053X, <https://doi.org/10.1016/j.wasman.2020.04.050>, (2020)
- [10] Mladenović, M., Vučićević, B., Marinković, A., Buha Marković, J., Combustion of waste solids in a fluidized bed to generate sustainable energy, Chemical Industry, <https://doi.org/10.2298/HEMIND230606008M>, (2024)
- [11] Fluent User's Guide, Fluent Inc., (2024)
- [12] Fluent Theory Guide, Fluent Inc., (2024)
- [13] Erić A., Cvetinović D., Milutinović N., Škobalj P., Bakić V., Combined parametric modelling of biomass devolatilisation process, Renewable Energy 193, 13-22, <https://doi.org/10.1016/j.renene.2022.04.129>, (2022)
- [14] Stefanović P.L., Cvetinović D.B., Živković G., Oka S.N., Pavlović P.B., Numerical modeling of disperse material evaporation in axisymmetric thermal plasma reactor, Thermal Science, Vol. 7 (1), pp. 63-100, <https://doi.org/10.2298/TSCI0301063S>, (2003)
- [15] Cvetinović D.B., Stefanović P.L., Bakić V.V., Oka S.N., Review of the Research on the Turbulence in the Laboratory for Thermal Engineering and Energy, Thermal Science, Vol. 21 (suppl. 3), pp. 875-898, <https://doi.org/10.2298/TSCI160221330C>, (2017)
- [16] Syamlal, M., O'Brien, T.J., Computer Simulation of Bubbles in a Fluidized Bed, AIChE Symp. Series, Vol. 85, pp. 22-31., (1989)
- [17] Dalla Valle, J.M., Micromeritics, Pitman, London, (1948)
- [18] Richardson, J.R., Zaki, W.N., Sedimentation and Fluidization: Part I, Trans. Inst. Chem. Eng. 32, 35-53., (1954)

Development of a Mathematical Model of a Drum Steam Boiler by Using the Automatic Control System – Second Step

Aleksandra Janković^a, Milica Ivanović^a

*^aAcademy of Technical Studies Politehnika – Department Požarevac, Požarevac, RS,
ajankovic@politehnika.edu.rs, mivanovic@politehnika.edu.rs*

Abstract: Steam boiler or steam generator is widespread equipment for energy conversion in the industry for obtaining steam and later electricity. Processes in energy states are complex and require the application of automatic control theory, which basically relies on mathematical models of objects and processes given in the state space. This approach requires knowledge of both the static and dynamic properties of the processes taking place in the thermoelectric plant. The general approach to mathematical modeling consists in setting bilas equations as well as an appropriate number of supplementary equations which, together with the previous ones, give a closed system of equations to be solved. In this paper, the second step in the modeling of a steam boiler is presented, and for the specific case, a simulation of the mathematical model was performed on the basis of experimentally collected data.

Keywords: steam boiler, mathematical model, combustion dynamics, automatic control

1. Introduction

The demand for energy, and consequently electricity, is rapidly increasing both globally and within our country, leading to a greater reliance on thermal power plants for overall electricity generation. Advances in modern thermal power plants are evident in enhanced working conditions, optimized steam block operating parameters, improved signaling and safety measures, the emergence of more effective technical designs, and the increasing implementation of computer-controlled machinery in production processes. Significant attention is focused on enhancing the dynamic performance of both individual units and the overall thermal power plant. This improvement translates into more stringent requirements for operating and managing the steam unit, particularly the steam boiler [1]. Consequently, the control units of the thermal power plant are expected to meet specific criteria, enabling them to monitor substantial changes in operating conditions and maintain relevant parameters within narrow tolerances. Furthermore, their economy and reliability are called into question, which comes to the fore when the plant is put into operation, the sudden disconnection of certain units from the operation, a sudden change in load and the event of an emergency mode. Classic control systems in thermal power plants are not designed for such strict requirements. They are designed to act independently of each other, as there are a large number of influences of the relevant physical quantities that need to be regulated. The design of control units for thermal power plants includes knowledge of the processes' static and dynamic properties. Additionally, concerns about their economic efficiency and reliability arise, particularly during the commissioning of the plant, abrupt disconnections of specific units, sudden load changes, or emergency situations. Traditional control systems in thermal power plants do not meet these stringent demands [2]. They typically function independently, responding to various factors that must be controlled. Designing control units for thermal power plants requires a deep understanding of both the static and dynamic characteristics of the processes involved [3].

A steam boiler is a facility designed to generate steam at pressures exceeding atmospheric levels [4]. From an energy perspective, the steam boiler functions as an open, flowing system, facilitating numerous energy exchanges. In thermodynamic terms, it operates as a heat exchanger. However, when considering the boiler from the standpoint of automatic control, it is regarded as a complex entity due to the various processes occurring within the exchanger [5].

These processes are intricate owing to their occurrence in spaces with varying dimensions, and they involve both single-phase and two-phase flows. From a control and regulation perspective, this complexity arises from the interconnections among multiple physical quantities that need to be maintained simultaneously. As a result,

it necessitates the implementation of advanced management concepts, including local, cross, and feedback strategies.

Numerous mathematical models have been developed in the literature to characterize the dynamics of steam boilers. Some of these models focus on monitoring the stability of steam boilers under various initial operating conditions, while also controlling key parameters such as drum level, boiler pressure, and steam pressure [6][7]. Additionally, some models are non-linear, providing insights into the dynamic processes occurring within power plants [8][9]. Furthermore, there are models that track the dynamics of processes in plants [10][11] as well as those specifically designed for steam generators utilized in heat recovery within combined cycle power plants [12][13].

In this paper, a mathematical model was developed that follows the dynamics of drum steam boilers when the combustion process takes place in a layer. The model is formed for each part, which includes the boiler plant, drum, downcomer pipe and grate. Also, balance equations were formed for each element individually. During the formation of the model, additional simplifications were introduced to obtain an adequate mathematical model, which was the goal of the work.

2. Formation of a structural diagram

When forming the structural diagram of the boiler plant, it started by defining the tracts of the primary working media and the position of the basic heating surfaces along their path. However, in addition to the previous one, output (control) quantities are also defined. By defining them, the requirements that are imposed during the operation of the steam boiler are stated, and the basic parameters are the superheated steam θ_p and the pressure of the superheated steam p_p . Figure 2.1 shows a diagram of the boiler plant.

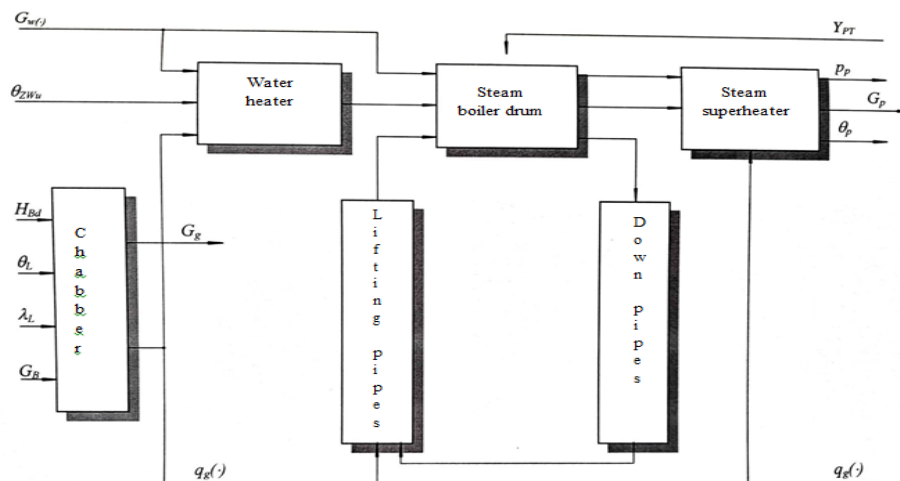


Figure 1. Global structural diagram of a steam boiler (Adopted from [3])

Disturbances that significantly affect the operation of the boiler plant are the lower heating value of the fuel H_B , the temperature of the supplied water θ_w , the temperature of the primary air θ_L i of the cooling water θ_{rw} , the change in the position of the regulating valve of the steam turbine Y_{pT} and excess air λ_L . During the formation of the model, these quantities were taken into account because of the management concept. The second group of disturbances, such as changes in fuel temperature θ_B , changes in specific heats of air c_{pl} , fuel c_B , and cooling water c_{rw} , are classified in the second order of importance when forming a mathematical model.

3. Mathematical model of the boiler

Equations of the mathematical model with the introduction of relative deviations according to the author [14] were formed for the nominal operating mode, while neglecting non-linear terms.

During the formation of the mathematical model, a number of simplifications were introduced in order to solve the problem. Those simplifications are as follows:

1. The dynamics of the water heater is neglected for two reasons: firstly, due to the flow of incompressible fluid, and secondly, due to the small amount of absorbed heat from the gaseous products of combustion. This stems from the fact that modeling the water heater would significantly but unnecessarily increase the performance of the entire model. With this simplification, it was practically adopted that the entrance to the boiler plant is at the point of entry where the feed water enters the drum.
2. The process of complete combustion was considered, which implies that boiling water enters the drum and dry saturated steam leaves it.
3. The primary and secondary steam superheaters are treated as one heating surface. This is due to the unnecessary increase in the order of the system of equations that describe the process.
4. The dynamics of the surface steam cooler is neglected.
5. The speed of movement of the chain grate is adopted for the control effect although there is a regulator of the height of the coal layer. This was done with the aim of avoiding the dynamics of the grid as a classic conveyor because then there is a pure time delay in the control, which in the mathematical sense makes the problem much more difficult and introduces differential equations with a delay.
6. All geometric characteristics of the boiler plant are determined from the drawing and thermal calculation of the boiler.

After defining the simplification of the mathematical model and knowing that the considered boiler consists of several parts, below are the equations for each part separately.

Drum

$$\frac{d(\overline{\Delta\rho_{pczp}})}{dt} + \frac{d(\overline{\Delta V_{dzp}})}{dt} = \frac{x_N G_{pcN}}{\rho_{pczpN} V_{dzpN}} (\overline{\Delta x} + \overline{\Delta G_{pc}}) + \frac{G_{wpN}}{\rho_{pczpN} V_{dzpN}} \overline{\Delta G_{wp}} - \frac{G_{ppuN} \overline{\Delta G_{pp}}}{\rho_{pczpN} V_{dzpN}} \quad (1)$$

$$\begin{aligned} \frac{d(\overline{\Delta V_{dw}})}{dt} + \frac{d(\overline{\Delta\rho_w})}{dt} &= \frac{G_{eN}}{V_{dwN} \rho_{wN}} \overline{\Delta G_e} + \frac{(1-x_N) G_{pcN}}{V_{dwN} \rho_{wN}} \overline{\Delta G_{pc}} - \frac{x_N G_{pcN}}{V_{dwN} \rho_{wN}} \overline{\Delta x} - \\ &- \frac{G_{scN}}{V_{dwN} \rho_{wN}} \overline{\Delta G_{sc}} - \frac{G_{wpN}}{V_{dwN} \rho_{wN}} \overline{\Delta G_{wp}} \end{aligned} \quad (2)$$

$$\begin{aligned} \frac{d(\overline{\Delta V_{dw}})}{dt} + \frac{d(\overline{\Delta\rho_w})}{dt} + \frac{d(\overline{i_w})}{dt} &= \frac{i_{eN} G_{eN}}{V_{dwN} \rho_{wN} i_{wN}} (\overline{\Delta G_e} + \overline{\Delta i_e}) + \frac{G_{pcN} i_{pcN}}{V_{dwN} \rho_{wN} i_{wN}} \overline{\Delta i_{pc}} + \\ &\frac{G_{pcN} i_{pcN}}{V_{dwN} \rho_{wN} i_{wN}} \overline{\Delta G_{pc}} - \frac{x_N G_{pcN} i_{pcN}}{V_{dwN} \rho_{wN} i_{wN}} (\overline{\Delta i_{pc}} + \overline{\Delta G_{pc}} + \overline{\Delta x}) - \\ &\frac{G_{scN} i_{scN}}{V_{dwN} \rho_{wN} i_{wN}} (\overline{\Delta G_{sc}} + \overline{\Delta i_{sc}}) - \frac{G_{wpN} i_{pczpN}}{V_{dwN} \rho_{wN} i_{wN}} (\overline{\Delta G_{wp}} + \overline{\Delta i_{pczp}}) \end{aligned} \quad (3)$$

Downpipe

$$\begin{aligned} \frac{d(\overline{\Delta G_{sc}})}{dt} &= \frac{p_{dN} A_{sc}}{i_{sc} G_{scN}} \overline{\Delta p_d} - \frac{p_{scN} A_{sc}}{i_{sc} G_{scN}} \overline{\Delta p_{sc}} - \frac{4\rho_{sc} G_{scN}}{d_{sc} A_{sc} \rho_{wN}} \overline{\Delta G_{sc}} - \frac{G_{scN}}{A_{sc} i_{sc} \rho_{wN}} \overline{\Delta G_{sc}} + g\rho_{wN} \frac{A_{sc}}{G_{scN}} \overline{\Delta\rho_w} \\ \frac{d(\overline{\Delta\rho_{pc}})}{dt} &= \frac{G_{scN}}{\rho_{pcN} V_{pvc}} \overline{\Delta G_{sc}} - \frac{G_{pcN}}{\rho_{pcN} V_{pc}} \overline{\Delta G_{pc}} \end{aligned} \quad (4)$$

$$\frac{d(\overline{\Delta\rho_{pc}})}{dt} + \frac{d(\overline{\Delta i_{pc}})}{dt} = \frac{G_{scN} i_{scN}}{V_{pc} \rho_{pcN} i_{pcN}} (\overline{\Delta G_{sc}} + \overline{\Delta i_{sc}}) - \frac{G_{pcN} i_{pcN}}{V_{pc} \rho_{pcN} i_{pcN}} (\overline{\Delta G_{pc}} + \overline{\Delta i_{pc}}) + \frac{Q_{pcN}}{V_{pc} \rho_{pcN} i_{pcN}} \overline{\Delta Q_{pc}} \quad (5)$$

$$\frac{d(\overline{\theta_{zpc}})}{dt} = \frac{Q_{gpcN}}{m_{zpc} c_{zpc} \theta_{zpcN}} \overline{\Delta Q_{gpc}} - \frac{Q_{pcN}}{m_{zpc} c_{zpc} \theta_{zpcN}} \overline{\Delta Q_{pc}} \quad (6)$$

$$\frac{d(\overline{\Delta\rho_{pp}})}{dt} = \frac{G_{ppuN}}{V_{pp} \rho_{ppN}} \overline{\Delta G_{ppu}} - \frac{G_{Tvp}}{V_{pp} \rho_{ppN}} \overline{\Delta G_{Tvp}} \quad (7)$$

$$\begin{aligned} \frac{d(\overline{\Delta\rho_{pp}})}{dt} + \frac{d(\overline{\Delta\theta_{pp}})}{dt} &= \frac{G_{ppuN} i_{ppuN}}{V_{pp} \rho_{ppN} i_{ppN}} (\overline{\Delta G_{ppu}} + \overline{\Delta i_{ppu}}) - \frac{G_{TvpN} i_{TvpN}}{V_{pp} \rho_{ppN} i_{ppN}} (\overline{\Delta G_{Tvp}} + \overline{\Delta\theta_{pp}}) + \\ &+ \frac{Q_{ppN}}{V_{pp} \rho_{ppN} i_{ppN}} \overline{\Delta Q_{pp}} + \frac{d(\overline{\Delta\theta_{zpp}})}{dt} = \frac{Q_{gppN}}{m_{zpp} c_{zpp} \theta_{zppN}} \overline{\Delta Q_{gpp}} - \frac{Q_{ppN}}{m_{zpp} c_{zpp} \theta_{zppN}} \overline{\Delta Q_{gpp}} \end{aligned} \quad (8)$$

Stokehole with grate

$$0.6T_{R\check{s}} \frac{d(\overline{\Delta\lambda})}{dt} - 0.4T_{R\check{s}} \frac{d(\overline{\Delta G_{Bsg}})}{dt} = \overline{\Delta G_{Bsg}} - K_{R\check{s}2} \overline{\Delta W_{R\check{s}}} \quad (9)$$

Previously formed equations (1 - 9) represent a linearized mathematical model of a drum boiler with combustion in a layer.

Selection of state quantities, disturbance control and managed quantities

Knowing the processes that take place in a steam boiler, and based on the obtained system of equations and in order to perform a simulation of the operation of the boiler as well as the subsequent analysis of the obtained results, the following selection of sizes is adopted:

Sizes of the balance	Disturbing sizes	Management sizes	Managed sizes
$\overline{\Delta p_d}(t) = x_1(t)$	$\overline{\Delta x}(t) = z_1(t)$	$\overline{\Delta G_e}(t) = u_1(t)$	$x_{i1}(t) = \overline{\Delta p_d}(t)$
$\overline{\Delta h_{dw}}(t) = x_2(t)$	$\overline{\Delta w_{pc}}(t) = z_2(t)$	$\overline{\Delta W_{R\check{s}}}(t) = u_2(t)$	$x_{i2}(t) = \overline{\Delta h_{dw}}(t)$
$\overline{\Delta \theta_w}(t) = x_3(t)$	$\overline{\Delta \theta_{pczp}}(t) = z_3(t)$		$x_{i3}(t) = \overline{\Delta \theta_{pp}}(t)$
$\overline{\Delta G_{sc}}(t) = x_4(t)$	$\overline{\Delta w_{ppu}}(t) = z_4(t)$		
$\overline{\Delta \rho_{pc}}(t) = x_5(t)$	$\overline{\Delta i_e}(t) = z_5(t)$		
$\overline{\Delta i_{pc}}(t) = x_6(t)$	$\overline{\Delta i_{sc}}(t) = z_6(t)$		
$\overline{\Delta \theta_{zpc}}(t) = x_7(t)$	$\overline{\Delta p_{sc}}(t) = z_7(t)$		
$\overline{\Delta \rho_{pp}}(t) = x_8(t)$	$\overline{\Delta \theta_{pc}}(t) = z_8(t)$		
$\overline{\Delta \theta_{pp}}(t) = x_9(t)$	$\overline{\Delta w_{ppi}}(t) = z_9(t)$		
$\overline{\Delta \theta_{zpp}}(t) = x_{10}(t)$			
$\overline{\Delta G_{sg}}(t) = x_{11}(t)$			
$\overline{\Delta Q_g}(t) = x_{12}(t)$			
$\overline{\Delta \lambda}(t) = x_{13}(t)$			

The final forms of the linearized mathematical model of the considered boiler were obtained by the selection of state, disturbance, control and controlled quantities using the equations shown in the paper [15]. The differential vector equation of state reads:

$$E \dot{\underline{x}}(t) = A^* \underline{x}(t) + B^* \underline{u}(t) + F^* \underline{z}(t) \quad (10)$$

and the output equation:

$$\underline{x}_i(t) = C \underline{x}(t) \quad (12)$$

Since the elements of the matrix E are such that $\det E \neq 0$, for the adopted steam drum steam boiler, equation (10) reduces to the standard form of the form:

$$\dot{\underline{x}}(t) = E^{-1} A^* \underline{x}(t) + E^{-1} B^* \underline{u}(t) + E^{-1} F^* \underline{z}(t) \quad (13)$$

Ie:

$$\dot{\underline{x}}(t) = A \underline{x}(t) + B \underline{u}(t) + z(t) \quad (4)$$

Where the $A = E^{-1} A^*$; $B = E^{-1} B^*$; $F = E^{-1} F^*$, and are the matrices of the system. The elements of the matrix are determined on the basis of the operational and structural characteristics of the considered boiler.

4. Results and discussion

Based on the vector equations of state (4) and the output equation (2), a simulation of the operation of the steam boiler was performed. When conducting the simulation, only state variables in transition modes created under the influence of control variables were considered.

The dynamic behavior of the steam boiler was considered with simultaneous changes of the jump type of control variables, and with all zero initial conditions.

On the ordinates of the diagram, the variables of the state in the label were given as $x(j)$, $j = 1, 2, \dots, 13$ which further gives the state sizes x_j . The time in seconds is given on the abscissa, and the simulation time interval is 120 seconds

Bearing in mind the choice of controlled (output) quantities, the changes in state quantities x_1, x_2 , and x_9 represent at the same time the quantities of changes in output quantities, i.e. changes in pressure in the drum of the steam boiler, water level and temperature at the outlet of the steam superheater, so the discussion of the obtained simulation is directed on these three sizes.

The simulation results are shown on the change diagrams which are marked as Figure 2 to Figure 14

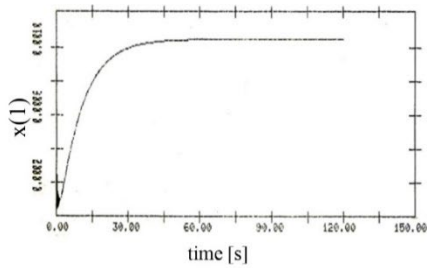


Figure 2. Change of pressure in the drum steam boiler

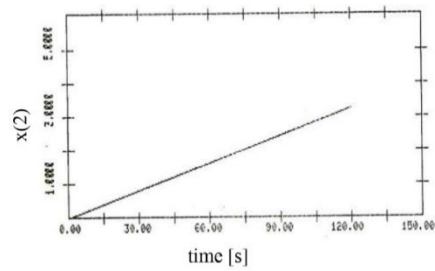


Figure 3. Change in water level at the output from steam superheater

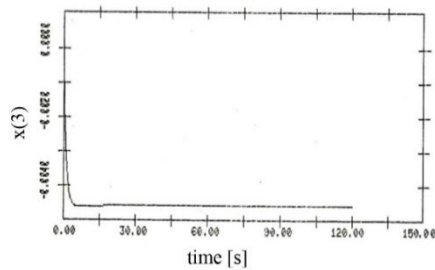


Figure 4. Change in water temperature at the output of the steam superheater

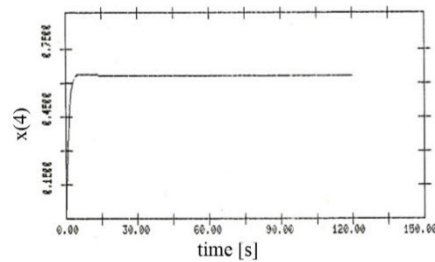


Figure 5. Change in water flow downpipes

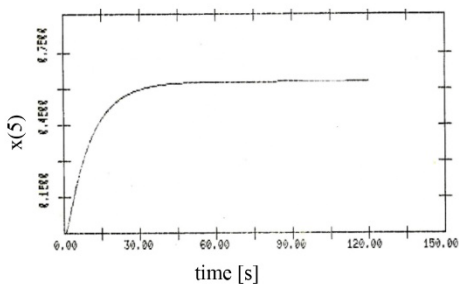


Figure 6. Change in the density of the lift pipe mixture

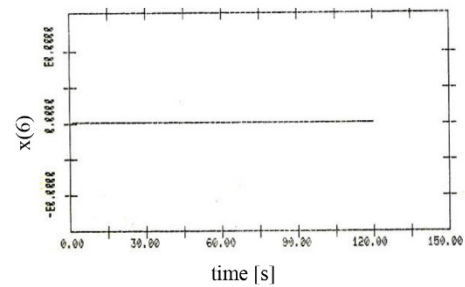


Figure 7. Enthalpy of the lift pipe mixture

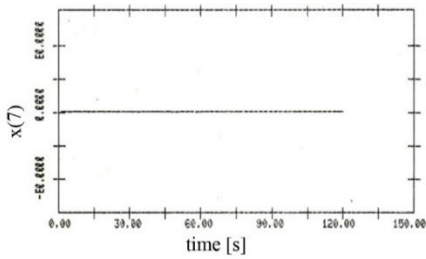


Figure 8. Change in the temperature of the lift pipe wall

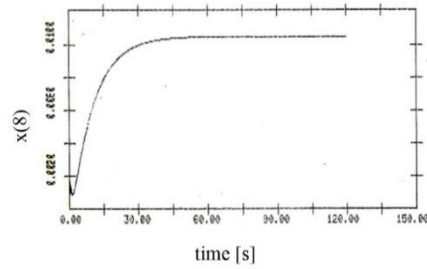


Figure 9. Change in steam density at the output of the steam superheater

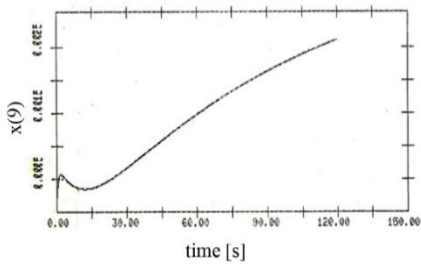


Figure 10. Temperature change at the output of the steam superheater

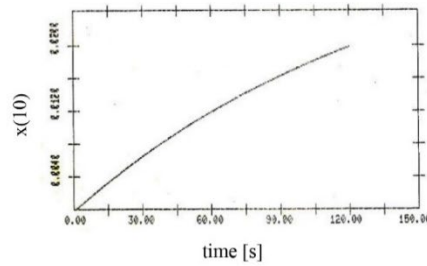


Figure 11. Change in the temperature of the steam superheater tube walls

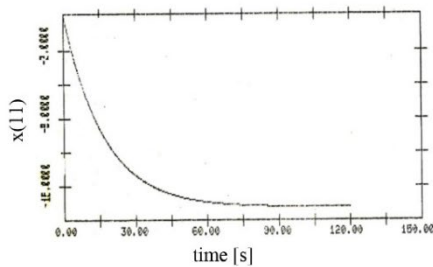


Figure 12. Change in fuel mass flow through the combustion chamber

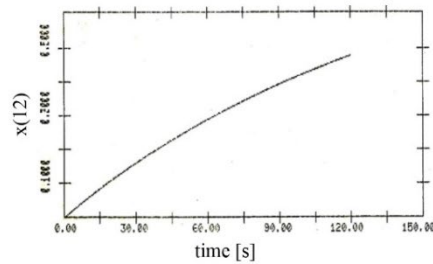


Figure 13. Change in the total amount of heat supplied to the combustion chamber

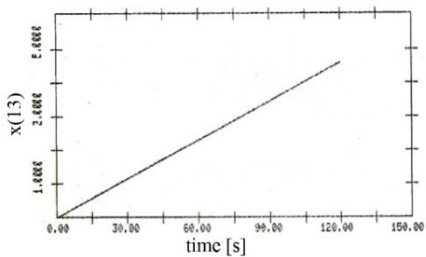


Figure 14. Change of excess air in the combustion chamber

Diagrams 2 and 3 show that with simultaneous changes in water flow and fuel flow (increase), the pressure in the drum will grow up to some new stationary value, while the water level will grow indefinitely, showing the integral nature of the transmission. This result arises because the simulation was performed on a steam boiler as an object of automatic control without the presence of a control system that certainly reacts in such situations.

Diagram 10 shows that with the same changes in the control parameters, the temperature of the steam at the outlet of the steam superheater rises and it stabilizes at the new value.

It should be pointed out that the used simulation time was not enough to cover the entire duration of the transition process, although the tendency towards a new stationary state can easily be concluded. It can be seen that the transient process in the steam superheater takes a very long time, that is, it has a large settling time value. This result stems from the location of the steam superheater, that is, the last exchanger is in the water-steam tract and has a large volume, as well as the fact that it contains a compressible fluid - superheated steam.

The obtained results, shown in the other diagrams, correspond to the results that can be found in the literature. They are qualitatively satisfactory, and a quantitative assessment could only be given after comparison with the experimental determined transition curves on the boiler itself.

5. Conclusion

In this paper, a mathematical model of a drum steam boiler with combustion in a layer is presented. During the implementation of the simulation, the mathematical model was first concretized in concrete numerical values, which required the knowledge of a whole series of working and constructive sub-systems of a particular boiler with a chain grate. A large number of operational and structural parameters of this model were adopted due to the impossibility of their exact determination. The jump responses of all state variables as well as output variables of the steam boiler (pressure in the drum, water level and temperature of superheated steam at the superheater inlet) gave results that correspond to real conditions. In some cases, due to the insufficient duration of the transition process and the large values of the settling time of some physical quantities, the conclusions were not drawn to the end.

Nomenclature

List of symbols

A - flow surface	[m ²]
c - specific heat	[kJ/kgK]
d - pipe diameter	[m]
G - mass flow	[kg/s]
H _B - lower heating value	[kJ/kg]
h - water level	[m]
i - enthalpy	[kJ/kg]
K - heat transfer coefficient	[kW/m ² K]
k - constant	
l - length	[m]
m - mass	[kg]
p - pressure	[kN/m ²]
Q - heat flow	[kW]
T - time constant	[s]
t - time	[s]
V - volume	[m ³]
w - flow rate	[m/s]
ρ - density	[kg/m ³]
ξ - spatial coordinate	[m]
θ - temperature	[K]
b - width	[m]
λ - excess air	

Bottom marks

B - fuel
d - drum
e - economizer
g - gaseous combustion products
gB - gaseous products - fuel
ge - from gas to economizer
gpc - from gases to lifting pipes
i - at the exit
L - air
lož - fireplace
N - nominal mode
pc - lifting pipes
pp - primary steam superheater
sc - down pipes
sg - combustible part
TVP - high pressure turbine
u - at the entrance
w - water
wp - from water to steam
z - pipe wall
zc - the wall of the economizer pipe
zpc - the wall of the riser pipes
zpp - primary superheater tube wall
zr - radiation
rš - grid

References

- [1] D. Debeljković, D. Stoiljković, D. Radosavljević, G. Simonović, Dynamics of objects and processes in automatic control systems Part XII, Faculty of Mechanical Engineering, University of Belgrade, Belgrade, 2014
- [2] D. Debeljković, V. Mulić, A. Sićović, G. Simeunović, Dynamics of steam boilers, Faculty of Mechanical Engineering, University of Belgrade, Belgrade, 2007.
- [3] D. Debeljković, A. Sićović, G. Simeunović, V. Mulić, Dynamics of water heaters, combustion spaces and auxiliary equipment, Faculty of Mechanical Engineering, University of Belgrade, Belgrade, 2007.
- [4] M. Gulić, Lj. Brkić, P. Perunović, Steam boilers, Faculty of Mechanical Engineering, University of Belgrade, Belgrade 1983.
- [5] D. Debeljković, A. Sićović, V. Mulić, G. Simeunović, Dynamics of Processes with Distributed Parameters - Dynamics of Boiler Evaporators, Faculty of Mechanical Engineering, University of Belgrade, Belgrade, 2006.
- [6] Bracco, S., M. Troilo, Trucco, A., A simple dynamic model and stability analysis of a steam boiler drum, Proceedings of the Institution of Mechanical Engineers, Part A: Journal of Power and Energy, 223(7) (2009), pp. 809-820.
- [7] Maican, C., Vinatoru, M., Canureci, G., Iancu, E. (2008, July). Control system simulator for steam boiler parameters, WSEAS TRANSACTIONS on SYSTEMS and CONTROL, 3(11) (2008).
- [8] Åström, K. J., Bell, R. D., Drum-boiler dynamics, *Automatica*, 36(3) (2000), pp. 363-378.
- [9] Halauca, C., & Lazar, C., Dynamic simulation model for a steam drum boiler system, In *2009 European Control Conference (ECC) 2009, Budapest, Hungary, August 23–26, 2009, WeA1.1*, pp. 3480-3485.
- [10] Adam, E. J., Marchetti, J. L., Dynamic simulation of large boilers with natural recirculation, *Comput. Chem. Eng.*, 23(1999), pp. 1031–1040.
- [11] Franke, R., Krüger, C., Rode, M., On-line optimization of drum boiler startup, In *Proceedings of the 3rd International Modelica Conference, Linköping, Sweden, November 3 - 4, 2003*, pp. 287–296.
- [12] Kim, T. S., Lee, D. K., Ro, S. T., Dynamic behaviour analysis of a heat recovery steam generator during startup, *Int. J. Energy Res.*, 24 (2000), pp. 137–149.
- [13] Alobaid, F., Postler, R., Ströhle, J., Epple, B., Hyun-Gee, K., Modelling and investigation start-up procedures of a combined cycle power plant, *Appl. Energy*, 85 (2008), pp. 1173–1189.
- [14] D. Debeljković, Dynamics of heat exchangers, First part, first edition, Faculty of Mechanical Engineering, University of Belgrade, Belgrade, 2002.
- [15] A. Janković, M. Ivanović, Development of a mathematical model of a drum steam boiler by using the automatic control system –first step; *Simterm*, 18 – 2. 10.2022, pp. 506 - 512



X. Energy management

Life Cycle Impact Assessment - A Review of Tools for Sustainable Energy Management

Milena Rajić^a, Zorana Stanković^b, Peđa Milosavljević^c

^a University of Niš, Faculty of Mechanical Engineering, Niš, Serbia, milena.rajic@masfak.ni.ac.rs

^b University of Niš, Faculty of Mechanical Engineering, Niš, Serbia, zorana.stankovic@masfak.ni.ac.rs

^c University of Niš, Faculty of Mechanical Engineering, Niš, Serbia, pedja.milosavljevic@masfak.ni.ac.rs

Abstract: Life Cycle Assessment (LCA) has become an important tool for evaluating the environmental impacts of energy systems, in the context of sustainable energy management. This paper provides a review of LCA software tools, including OpenLCA, SimaPro, GaBi, Umberto, Brightway2, and OpenEco, with a focus on applications in renewable energy systems. The comparison of these tools in terms of their functionalities, data handling capacities, and impact assessment methodologies, provides the results of how suitable they are for different energy systems and industrial applications. Particular attention is given to the interpretation and reporting of LCA results, bearing in mind the challenges associated with uncertainty, sensitivity analysis, and trade-offs in energy systems. The paper also includes a discussion on how LCA tools contribute to environmental protection measures, energy efficiency improvements, and socio-economic considerations in energy policies. The implications for policymakers and industries are also given, with recommendations for improving LCA practices in future energy projects. This review offers practical data for stakeholders in order to optimize energy systems and provide a sustainable and low-carbon future.

Keywords: Life Cycle Assessment, Life Cycle Impact Assessment, Sustainable management, Energy management, Circular economy.

1. Introduction

LCA has become an important and needed tool in the sustainable management of energy systems due to the increasing global emphasis on environmental preservation, decarbonization, and the need for a low-carbon economy. The concept of sustainability in energy management is linked to minimizing environmental impacts through the lifecycle of energy production, distribution, and consumption. LCA is therefore needed, providing a systematic framework to assess the environmental consequences of energy systems, beginning with raw material extraction and ending with waste management [1,2]. This rising trend of LCA application in sustainable energy management can be connected to global problems. One of the most important drivers is the need to meet carbon reduction targets, such as those outlined in the Paris Agreement, which aims to limit global warming to below 2°C compared to pre-industrial levels [3]. The energy sector, which accounts for over 70% of global greenhouse gas emissions, is under significant pressure to decarbonize. LCA has been identified as a methodology to evaluate and assess the environmental footprints of various energy technologies, such as solar, wind, hydropower, and bioenergy, in comparison to conventional fossil-fuel-based systems. Research indicates that renewable energy systems, when assessed through LCA, generally exhibit lower GHG emissions over their lifecycle than fossil fuels, but significant differences exist depending on geographic location, production methods, and supply chains [4-7].

In addition to gas emissions, LCA helps quantify other environmental impacts, including resource consumption, water consumption, air pollution, and land use. For example, LCA studies have demonstrated that while PV energy significantly reduces carbon emissions, it also has relatively high material intensity, including the consumption of rare earth elements [8]. This material demand has implications for resource sustainability, making LCA an important approach to understanding the broader impacts of renewable energy systems. LCA has been used to assess the water consumption associated with energy production, highlighting, for instance, the high water intensity of bioenergy production compared to wind or solar power [9]. Such data just highlights the importance of LCA in environmental impact assessments, guiding policy and investment decisions toward the most sustainable energy options. The growing importance of LCA is also connected with

its ability to evaluate trade-offs and co-benefits between different environmental factors. Energy systems are complex, and improvements in one area may lead to unintended consequences in another. However, LCAs have identified potential impacts on biodiversity, especially concerning bird and bat populations [10]. These findings show how LCA provides a holistic view, considering not only direct emissions but also secondary and tertiary environmental effects. This makes LCA an important tool for policymakers and industries seeking to balance decarbonization goals with broader ecological and social responsibilities.

The integration of LCA into sustainable energy management also aligns with the increasing trend of environmental, social, and governance reporting, where stakeholders, investors, governments, and consumers, demand greater transparency and accountability from energy companies. According to ISO 14040 and 14044 standards, LCA offers a globally recognized framework for measuring environmental impacts, making it a preferred tool for environmental, social, and governance reporting [11]. Companies using LCA to report their environmental performance can provide verifiable data on their sustainability claims. By integrating LCA data, organizations can systematically identify inefficiencies, reduce energy consumption, and lower greenhouse gas emissions, supporting ISO 50001's goal of improving energy performance by an average of 10% over a three-year certification period [12]. This data-driven approach can improve decision-making and foster continuous improvement in line with ISO 50001's energy efficiency targets. However, for LCA to serve as a decision-making tool, the methodologies, tools, and reporting systems must be transparent, and adaptable to the specific needs of energy systems. The complexity of energy systems, the variety of technologies, and the diverse environmental impacts necessitate that LCA methodologies are both flexible and scientifically sound. Various LCIA methodologies, such as ReCiPe, Eco-indicator 99, and ILCD, offer different approaches to impact categorization and normalization, which can lead to varied results depending on the method chosen [13,14]. This variability makes it important to standardize LCA methodologies in the context of energy systems to ensure consistency and comparability across studies.

In recent years especially, the availability of LCA software tools has provided the adoption of LCA in energy management at a higher level. OpenLCA, SimaPro, and GaBi are among the most used software platforms, offering detailed databases and impact assessment methods for environmental analysis [15,16]. OpenLCA, in particular, has gained prominence due to its open-source availability, making it accessible to a broader range of users. Studies have shown that OpenLCA provides capabilities for conducting detailed lifecycle inventories and impact assessments, especially in the context of renewable energy projects [17]. The accuracy and reliability of LCA outcomes are dependent on the quality of data and assumptions used in the analysis. Energy systems often involve complex supply chains and operational conditions, and inaccuracies in lifecycle inventories can lead to unreliable results, potentially undermining the effectiveness of LCA as a decision-making tool. LCA reporting must be clear, transparent, and adaptable to different stakeholder needs. The interpretation of LCA results is often a challenging task due to the complexity of impact categories, the interrelationships between environmental factors, and the inherent uncertainty in lifecycle data. A study by Laurent et al. [18] highlights the difficulties in making LCA results understandable to non-experts, such as policymakers, who may not have the technical expertise to interpret detailed environmental data. This underscores the need for developing standardized reporting formats that simplify LCA findings without compromising scientific rigor. Clear reporting helps ensure that LCA findings can be effectively integrated into energy policy frameworks, guiding the transition to more sustainable energy systems.

This paper aims to conduct a critical review of available LCA tools, with a focus on OpenLCA, in the context of energy management and environmental protection. Then, the paper has the aim to highlight the aspects of LCIA methodologies, interpretation, and reporting in energy and environmental contexts. LCIA represents a phase in LCA where environmental impacts are evaluated across various categories, such as global warming potential, resource consumption, and water usage. This study will examine the applicability and limitations of these methodologies when applied to energy systems. For instance, while ReCiPe provides a detailed analysis of environmental categories, it can sometimes underrepresent the socio-economic implications of energy systems, which is increasingly relevant in policy contexts.

2. Life Cycle Assessment methodologies

LCA represents a structured framework, composed of four key phases: (1) goal and scope definition, (2) life cycle inventory (LCI) analysis, (3) life cycle impact assessment (LCIA), and (4) life cycle interpretation (Fig.1). Each phase plays a crucial role in ensuring the accuracy and reliability of the environmental assessment

[19,20]. The ISO has formalized this framework in the ISO 14040 and ISO 14044 standards, which provide guidelines for conducting LCAs in a consistent and transparent manner [11]. Goal and scope definition, as the first phase represents the basis of any LCA. It involves clearly defining the purpose of the study, the system boundaries, and the functional unit. The functional unit represents the core element as it quantifies the function of the product or system under assessment, ensuring that comparisons between different systems are meaningful. In an LCA of energy systems, the functional unit might generate 1 MWh of electricity, allowing a fair comparison of the environmental impacts of different energy technologies such as coal, wind, and solar [21]. Defining system boundaries is equally important because it determines what processes and life cycle stages will be included in the assessment. This can range from the beginning to the end of the lifecycle analysis, which covers the entire cycle from raw material extraction to disposal. The scope definition should also outline the environmental impacts that will be assessed, such as global warming potential, water consumption, resource consumption, or human toxicity. Research has shown that unclear or inconsistent goal and scope definitions can lead to different LCA results, even when assessing similar systems, highlighting the importance of precision in this phase [19].

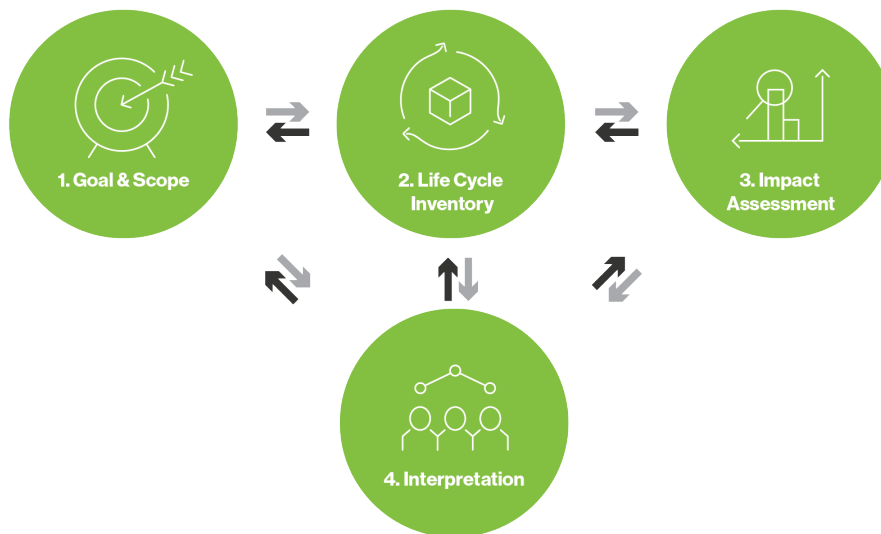


Figure 1. The four key steps of LCA [22]

Inventory analysis is the second phase of LCA and involves the collection and quantification of data on all inputs and outputs associated with the system being studied. This includes raw material inputs, energy use, emissions to air, water, and soil, and waste generation across all life cycle stages, from raw material extraction to end-of-life disposal. The accuracy of the LCI phase is heavily dependent on the quality of the data used, which can be a significant challenge. Data can come from a variety of sources, including industrial databases such as Ecoinvent, Agri-footprint, or ELCD, as well as site-specific measurements or academic literature [23]. The use of generic data from databases, while convenient, may not fully capture the specificities of a system or geographic region, leading to uncertainty in the results. The carbon footprint of renewable energy technologies can vary significantly depending on location-specific factors such as solar insolation for PV systems or wind patterns for wind turbines [24]. The complexity of modern supply chains also makes inventory analysis a difficult task. Many energy systems rely on materials sourced from multiple countries, each with different environmental regulations and practices. This makes data collection and management an important aspect of the inventory phase. The LCIA phase translates the data from the inventory analysis into potential environmental impacts. This is done using a set of predefined impact categories, such as global warming potential, eutrophication, acidification, and ozone depletion. These impact categories are selected based on the goals and scope defined in the first phase and are calculated using established LCIA methodologies, such as ReCiPe, Eco-indicator 99, ILCD, and TRACI [25]. For instance, ReCiPe represents often used method that includes environmental impacts into a single score, making it easier to interpret complex results [26]. However, each LCIA method has its strengths and limitations. ReCiPe focuses on environmental impacts and may not adequately capture the socio-economic aspects of sustainability, which are increasingly important in energy systems [27]. The choice of impact assessment method can influence the outcomes of the LCA, as different methods may prioritize different environmental indicators. The study found that using ILCD versus ReCiPe to assess the ecological impact of wind energy led to different conclusions regarding its material use and overall

sustainability [28]. As such, the LCIA phase requires detailed consideration of which methodology best aligns with the objectives of the study and the specific characteristics of the system being assessed. The final phase, life cycle interpretation, includes evaluating the results from the previous phases to draw meaningful conclusions and provide recommendations. The interpretation phase is important for identifying the most significant environmental impacts and determining areas for improvement within the system being assessed. Interpretation also includes uncertainty analysis, sensitivity analysis, and scenario analysis to evaluate the robustness of the results. The uncertainty analysis can quantify how variations in input data (such as energy consumption or emissions) affect the final results, which is crucial in complex energy systems where data may be uncertain or incomplete [29]. Sensitivity analysis, on the other hand, helps identify which parameters have the most influence on the LCA results. In an LCA of bioenergy systems, sensitivity analysis might reveal that the type of feedstock used (e.g., corn, switchgrass, or algae) has an impact on the overall greenhouse gas emissions [30]. Scenario analysis allows for the comparison of different alternatives, such as the use of different energy sources or production technologies and is used in LCAs to evaluate the potential environmental benefits of future technological improvements or policy changes. The interpretation phase is also important in communicating LCA results to stakeholders, including policymakers, industry leaders, and the public. Effective interpretation requires not only technical expertise but also an understanding of how to present complex data in a clear and actionable way. Especially in the energy sector, where LCA results are used to inform policy decisions related to decarbonization and renewable energy deployment [18]. Misinterpretation of LCA results can lead to poor decision-making, such as underestimating the environmental impacts of certain technologies or overestimating the benefits of others.

3. LCA methodologies application in energy sectors and industries

It is important to emphasize that LCA is not a novel approach, it emerged in the late 1960s and early 1970s and developed as a tool to assess the resource use and waste generation of industrial processes. The first application of LCA to energy systems occurred in the context of evaluating different power generation technologies and their environmental impacts, particularly in response to the energy crises of the 1970s. During this period, energy efficiency became a focus of both government policies and corporate strategies, leading to the adoption of LCA methodologies to understand the full lifecycle environmental impacts of energy production [31]. In the early stages of its development, LCA methodologies were primarily focused on evaluating the resource and energy inputs of conventional energy systems, such as coal and oil-based power plants. These initial assessments were relatively simple, focusing on direct emissions and fuel consumption, and did not consider the broader environmental impacts, such as land use or biodiversity loss. The focus was mainly on improving energy efficiency, which was seen as a critical strategy to reduce dependency on fossil fuels. For instance, early LCAs on coal-fired power plants primarily assessed fuel consumption and CO₂ emissions, providing insights into how efficiency improvements in plant design lower emissions could and reduce resource use [32]. However, these early assessments were limited in scope, as they did not fully account for the environmental burdens associated with upstream processes, such as mining and transportation, or downstream impacts, such as waste disposal and decommissioning. As environmental awareness grew during the 1980s and 1990s, particularly following the publication of the Brundtland Report in 1987, which introduced the concept of sustainable development, LCA methodologies began to expand in scope. Researchers recognized that energy systems needed to be assessed not only in terms of their direct energy use but also in terms of their full environmental impacts, including resource depletion, pollution, and ecosystem degradation. This led to the development of more comprehensive LCA frameworks that included impact categories such as global warming potential, acidification, and eutrophication. During this period, the first standardized LCA methodologies were introduced, with the publication of the ISO 14040 and ISO 14044 standards in the late 1990s [33]. These standards provided a consistent framework for conducting LCAs, allowing for better comparability between studies and the inclusion of a broader range of environmental impacts. The application of LCA to renewable energy systems gained momentum in the 1990s as renewable technologies such as wind, solar, and hydropower began to scale up. As these technologies were viewed as more sustainable alternatives to fossil fuels, researchers sought to assess their environmental benefits using LCA. Early LCAs on wind energy, for example, focused on the energy payback time, and how long a wind turbine needed to operate to produce the same amount of energy required for its manufacture and installation [34]. These studies showed that wind energy had a lower environmental impact compared to coal and natural gas, with shorter energy payback times and lower greenhouse gas emissions. However, as renewable energy technologies grew in

complexity and scale, the need for more sophisticated LCA methodologies became apparent. Issues such as land use, material scarcity (e.g., rare earth metals for wind turbines), and end-of-life disposal started to gain attention, leading to more detailed LCAs that considered these additional factors [35]. The 2000s marked a shift in the application of LCA to energy systems, as the focus expanded from energy efficiency to decarbonization and climate change mitigation. The growing recognition of climate change as a global challenge prompted a surge in LCAs that specifically focused on the carbon footprint of energy systems. Studies increasingly compare the global warming potential of various energy technologies, with an emphasis on renewable energy sources like solar, wind, and bioenergy. LCAs of PV systems demonstrated that while solar power produces very low emissions during operation, the manufacturing process for PV panels, especially the extraction and processing of silicon, contributed to their overall environmental impact [36]. This highlighted the need for improvements not only in energy generation technologies but also in the production processes that support them. Bioenergy also became a focus of LCA in the 2000s, particularly in the context of biofuels. The introduction of biofuels as an alternative to fossil fuels led to a wave of LCA studies assessing their environmental benefits and drawbacks. Initial assessments were optimistic, showing that biofuels, particularly ethanol and biodiesel, could significantly reduce greenhouse gas emissions compared to gasoline and diesel [37]. However, subsequent studies revealed a complex picture, showing that the full lifecycle impacts of biofuels, particularly in terms of land use change, water consumption, and biodiversity loss, were not always as favorable as initially thought. LCAs of bioenergy systems, for example, revealed that large-scale biofuel production could lead to deforestation, soil degradation, and increased food prices, raising concerns about the sustainability of biofuels [38]. These findings showed a reevaluation of bioenergy policies and led to more detailed LCA methodologies that could better capture the trade-offs associated with biofuel production. In recent years, LCA methodologies have continued to evolve in response to the growing complexity of energy systems and the increasing emphasis on sustainability. The rise of integrated energy systems, which combine multiple renewable technologies with energy storage and grid management solutions, has prompted the development of more dynamic and flexible LCA approaches. Modern LCAs of integrated energy systems assess not only the environmental impacts of individual technologies but also the synergies and trade-offs between them. The LCAs of hybrid renewable systems, such as wind-solar installations with battery storage, evaluate how these systems can reduce greenhouse gas emissions and improve energy reliability while minimizing resource use and land occupation [17]. But it should be mentioned that recent findings in LCA methodologies have placed greater emphasis on incorporating socio-economic and technological factors into the assessment of energy systems. The development of dynamic LCA models, which can simulate changes in energy systems over time, has allowed researchers to assess how technological advancements, policy interventions, and market trends may influence the environmental performance of energy systems in the future. Dynamic LCAs of energy systems, for example, can model how improvements in battery storage technology or advancements in carbon capture and storage could reduce the overall environmental impacts of renewable energy systems [24]. The overview of the application of LCA methodologies in various energy sectors and industries is given in Table 1, including solar energy, wind energy, bioenergy, hydropower, nuclear energy, oil and gas, and energy storage systems.

Table 1. LCA methodologies application in energy sectors and industries

Energy sector/ Industry	LCA methodology	Description	Findings	References
Solar Energy	ReCiPe, ILCD	LCA for solar energy often focuses on the production and end-of-life disposal of photovoltaic panels. Studies show low operational emissions but higher impacts during manufacturing.	Solar power has low lifecycle emissions but high impacts during panel manufacturing and disposal.	[24, 36]
Wind Energy	ReCiPe, Eco- indicator 99	LCAs on wind energy reveal that operational emissions are minimal, with material use (e.g., rare earth metals) and land use being significant factors.	Wind energy has low emissions during operation, but material use and land occupation are critical environmental concerns.	[28, 34]
Bioenergy	ReCiPe, CML	Bioenergy LCAs assess the lifecycle from feedstock cultivation to energy production,	Bioenergy's sustainability is highly dependent on feedstock and land use;	[37, 38]

		showing significant variability in emissions depending on the feedstock type and land use.	certain biofuels may have negative impacts on biodiversity.	
Hydropower	ILCD, Eco-indicator	Hydropower LCAs focus on land use, ecosystem disruption, and sedimentation, with minimal operational emissions but large-scale environmental impacts during dam construction.	Hydropower is generally considered a low-emission energy source, but it causes significant ecological disruption and land use.	[39, 40]
Nuclear Energy	ReCiPe, ILCD	Nuclear energy LCAs primarily focus on uranium mining, plant construction, and waste management. Operational emissions are low, but long-term waste disposal presents challenges.	Nuclear power has a low carbon footprint but faces issues with long-term waste disposal and the environmental impacts of uranium mining.	[41,42]
Oil and Gas	CML, TRACI	Oil and gas LCAs often assess upstream emissions during extraction and refining, with a focus on greenhouse gases, acidification, and water consumption.	Oil and gas are high in lifecycle emissions, with significant greenhouse gas output during extraction and refining.	[8,43]
Energy Storage Systems	ReCiPe, ILCD	Energy storage systems, particularly batteries, are assessed using LCA for their entire lifecycle, with high environmental impacts noted during material extraction and disposal.	Batteries used in energy storage systems have high environmental impacts during raw material extraction and end-of-life disposal.	[24,44]

4. Review of LCA software tools

The most widely used LCA tools, OpenLCA, SimaPro, GaBi, Umberto, Brightway2, and OpenEco, offer a range of functionalities that facilitate the collection, modeling, and interpretation of lifecycle data. These tools enable the evaluation of the environmental impacts of products and processes across their full lifecycle, from raw material extraction to end-of-life disposal. Each software has distinct strengths and limitations, particularly in the context of sustainable energy management, where the complexity and scale of systems can vary significantly. OpenLCA is an open-source LCA software that has gained attention due to its accessibility and flexibility [16]. One of its major advantages is its open-source nature, allowing users to freely access and customize the software according to specific project needs. OpenLCA supports a range of lifecycle databases, including Ecoinvent, Agribalyse, and the European Life Cycle Database. Its modular structure also allows for the integration of new methods and impact categories, which is useful for assessing renewable energy technologies, such as wind and solar power, where specific environmental impacts, like rare earth material usage, need to be tracked. OpenLCA's ability to handle large datasets and complex supply chains makes it ideal for detailed studies of renewable energy systems. In PV system assessments, OpenLCA can model the entire lifecycle, from silicon extraction to panel disposal, and calculate the global warming potential and energy payback time with high precision [36]. On the other hand, while it offers customization options, its user interface can be challenging for those without a strong technical background, requiring more knowledge to navigate the tool. Additionally, its reliance on external databases means that the quality of results is dependent on the accuracy and completeness of the input data. This can be a concern in regions where specific lifecycle data for renewable technologies are limited, potentially affecting the robustness of the assessments.

SimaPro, developed by PRé Sustainability, is another LCA tool that is often considered the industry standard for lifecycle assessments. SimaPro represents proprietary software, meaning users need to purchase a license, which can be costly for smaller organizations or academic institutions. However, SimaPro's strength lies in its functionality and ease of use. It offers an intuitive user interface, making it accessible to users with varying levels of expertise. SimaPro supports many impact assessment methods, including ReCiPe, CML, and TRACI, which are used for analyzing energy systems. Its ability to handle multi-scenario comparisons for studies that assess multiple energy sources, such as wind, solar, and nuclear power, allows it to evaluate trade-offs between different environmental impacts [26]. SimaPro is designed for large-scale industrial applications, where

detailed product lifecycle data and environmental performance tracking are required. In the wind energy sector, SimaPro has been used to model the environmental impacts of turbine manufacturing, installation, operation, and decommissioning. The software's comprehensive database and scenario modeling capabilities allow for a detailed comparison of different turbine designs, materials, and geographic locations, providing insights into energy efficiency and material optimization [34]. One limitation of SimaPro, is its reliance on proprietary databases, which may limit access to the latest lifecycle data for certain emerging energy technologies. Also, the cost of licensing can be a barrier for smaller entities who may seek more affordable or open-source alternatives.

GaBi, developed by Thinkstep (part of Sphera), is LCA software used extensively in both academic and industrial applications. GaBi is known for its strong focus on industrial applications, particularly in sectors such as automotive, electronics, and energy. GaBi's strength lies in its extensive database, which includes regional-specific lifecycle inventories, for assessments in global supply chains. For energy systems it is used because they rely on international supply chains, such as solar PV and wind turbines, where material sourcing and transportation have the overall environmental impact [24]. GaBi supports a range of impact assessment methods, including ILCD and ReCiPe, to allow users to model the environmental impacts of different energy technologies with high precision. One of GaBi's advantages is its industrial focus with a focus on companies seeking to integrate LCA into product development and sustainability strategies. GaBi has been used in the oil and gas sector to assess the environmental impacts of upstream operations, such as extraction, refining, and transportation. The software's ability to handle complex supply chains shows its good results in identifying opportunities for reducing greenhouse gas emissions and improving resource efficiency in these energy-intensive industries. But, GaBi is a proprietary tool, requiring users to purchase a license, which can be a significant investment for smaller companies and GaBi's user interface may require a higher level of expertise compared to other tools.

Umberto is a proprietary LCA tool developed by Ifu Hamburg, designed with a focus on industrial applications. It is used for modeling material and energy flows within complex industrial systems, used by companies seeking to optimize their production processes and reduce environmental impacts. Umberto's advantage lies in its process modeling. It also allows for the integration of economic and environmental data, for analyzing the financial costs and environmental benefits of process improvements [45]. In the energy sector, Umberto has been applied to assess energy efficiency in manufacturing systems, evaluate the environmental impacts of renewable energy technologies, and model the integration of energy storage solutions in industrial networks. Umberto can model the lifecycle of wind turbine manufacturing, from raw material extraction to the decommissioning phase, allowing users to assess not only environmental impacts such as greenhouse gas emissions but also economic trade-offs related to material use and energy consumption [46]. A limitation of Umberto is that it may not offer the same level of flexibility for purely academic LCA studies that require more customization in impact assessment categories.

Brightway2 is an open-source LCA software designed for advanced users who need a high level of customization and control over their LCA models. Unlike other tools that provide graphical user interfaces, Brightway2 is a Python-based framework that requires coding knowledge to operate. This makes it highly flexible, allowing users to build and customize their own LCA models, integrate new impact assessment methods, and even develop their own databases. Brightway2 is used for academic research and advanced LCA applications that require new methodological approaches or large-scale data manipulation [47]. It can handle large, complex datasets and perform computationally intensive tasks, such as Monte Carlo simulations for uncertainty analysis and sensitivity testing, important in energy systems where the variability in data, such as renewable energy production or material inputs, can significantly affect LCA results. Brightway2 has been used to model the environmental impacts of hybrid renewable energy systems, including wind-solar-battery configurations, allowing the analysis of how changes in energy production patterns influence overall lifecycle emissions [48]. Brightway2's steep learning curve and reliance on coding make it less accessible to non-technical users, limiting its application in industry settings where ease of use is a priority.

OpenEco represents an open-source LCA tool developed as part of collaborative efforts to promote open-access tools, OpenEco is designed for energy systems assessments and integrates environmental databases such as Ecoinvent and the ELCD, allowing to have lifecycle analyses with pre-configured templates and impact categories customized to renewable energy systems, such as solar and wind power [49]. It is used often for smaller-scale LCA projects or in order to conduct rapid assessments of their environmental impacts. In energy systems, OpenEco has been applied to assess the lifecycle impacts of PV installations, focusing on greenhouse

gas emissions, material intensity, and land use. The simplified approach offered by OpenEco allows the identification of hotspots in energy systems and to development of strategies to mitigate environmental impacts, and it can be used for initial sustainability assessments [50]. Its limitations in handling more complex datasets and its relatively simplified methodology compared to other LCA tools like SimaPro and GaBi make it less suitable for detailed industrial applications or research requiring high levels of precision.

Table 2. Comparative table of LCA tools

LCA tool	License	Access	Focus	User interface	Data libraries	Integration with energy systems	Impact assessment methods	Ref
OpenLCA	Open Source	Free	General LCA, customizable for various sectors	Moderate, requires technical expertise	Ecoinvent, Agribalyse, ELCD	Highly suitable for energy systems, including renewables	ReCiPe, ILCD, CML	[23,36]
SimaPro	Proprietary	Paid	Comprehensive LCA, industrial and academic applications	User-friendly, easy to navigate	Ecoinvent, Agri-footprint, Industry-specific databases	Suitable for detailed industrial and energy systems comparisons	ReCiPe, CML, TRACI	[26,34]
GaBi	Proprietary	Paid	Industry-focused LCA, particularly in energy-intensive sectors	Highly User-friendly, suitable for industrial use	Ecoinvent, GaBi proprietary databases	Optimized for industrial energy systems, especially for large-scale operations	ReCiPe, ILCD, CML	[19,24,28]
Umberto	Proprietary	Paid	Material and energy flow modeling in industrial systems	Graphical, drag-and-drop interface	Ecoinvent, Industry-specific databases	Effective for industrial energy systems and process optimization	ReCiPe, ILCD, CML	[45,46]
Brightway 2	Open Source	Free (requires Python knowledge)	Highly customizable LCA modeling, academic research	No GUI, Python-based coding	Custom databases via Python integration	Advanced modelling for energy systems with complex supply chains	Custom methods, full flexibility in assessment	[47,48]
OpenEco	Open Source	Free	Simplified LCA for rapid sustainability assessments	User-friendly, simplified templates	Ecoinvent, ELCD	Simplified assessments for renewable energy technology	ReCiPe, ILCD	[49,50]

In order to have a clear overview of the analyzed LCA tools a comparative table (Table 2) is given. The table shows features such as license type, accessibility, main focus, user interface, data libraries, integration with energy systems, impact assessment methods, and other criteria. It can be useful in selecting the appropriate tool based on project requirements, complexity, and user expertise.

The main focus in this paper analysis is the following comparative table (Table 3), analyzing their use in renewable energy and low-carbon economy projects. In this analysis is presented each tool's strengths, limitations, and main use cases in renewable energy assessments and modeling transitions to low-carbon economies. This comparison provides insights into which tool best fits different project needs, whether for small-scale renewable energy assessments or complex decarbonization analysis.

Table 3. Comparative table of LCA tools for renewable energy and low carbon economy

LCA tool	Use of renewable energy	Low carbon economy uses	Strengths in renewable energy	Strengths in the low carbon economy	Limitations	Ref
OpenLCA	Used for assessing renewable energy systems like wind, solar, and bioenergy. Highly adaptable for decarbonization projects, providing detailed lifecycle inventories for renewable energy technologies and allowing users to model system-wide impacts of energy transitions.	Highly effective for modeling decarbonization pathways in energy systems. OpenLCA's modular design allows users to assess carbon reductions across various scenarios, including renewable energy adoption and improvements in energy efficiency. Used in academic and policy studies for national and regional energy transitions.	Open-source, customizable, and flexible. Supports extensive renewable energy datasets. Used in academic research for evaluating renewable energy adoption and decarbonization pathways.	OpenLCA flexibility and modular structure allow for detailed decarbonization pathway modeling. Frequently used in policy studies to assess energy transition scenarios and carbon reduction impacts.	Requires technical expertise and familiarity with databases like Ecoinvent. Limited for users looking for rapid assessments without significant customization.	[23,36]
SimaPro	Frequently used for renewable energy comparisons, such as evaluating the environmental impact of solar vs. wind power. Also used in policy scenarios for energy transitions and industrial-scale LCAs for energy efficiency improvements.	Frequently used to assess low-carbon technologies and their impacts on reducing greenhouse gas emissions. SimaPro allows multi-scenario comparisons, making it an ideal tool for modelling transitions to low-carbon economies through energy technology improvements.	Comprehensive, with large datasets that support multi-scenario comparisons. Ideal for industry and policy applications where different renewable energy systems need to be compared.	Strong in multi-scenario comparisons, making it an ideal tool for assessing the transition to low-carbon economies. Frequently used by industries and policymakers to model low-carbon technology adoption.	Proprietary, high cost, and less flexible for users who need fully customizable solutions. Typically requires a larger investment to access data for industry-wide analyses.	[26,34]

GaBi	<p>Strong focus on renewable energy in large-scale industrial applications. Used to assess the impacts of energy-intensive processes, such as the production of solar panels and wind turbines, with detailed regional data for supply chains.</p>	<p>Primarily focused on industrial energy systems and the low-carbon economy at a large scale. Its comprehensive databases and advanced scenario modelling make it well-suited for assessing carbon reduction strategies in manufacturing and energy production, particularly in energy-intensive industries.</p>	<p>Extensive regional and industry-specific data. Focuses on renewable energy technologies within large-scale industrial supply chains, making it highly applicable for companies involved in energy production.</p>	<p>Focuses on large-scale, industrial low-carbon strategies. GaBi excels in integrating regional data for detailed lifecycle assessments of industrial energy systems transitioning to a low-carbon economy.</p>	<p>Proprietary and focused heavily on industrial use, making it less accessible for smaller projects or academic studies. High cost limits its use for non-commercial applications.</p>	[19,24,28]
Umberto	<p>Primarily used for industrial applications but can be adapted to model energy efficiency in renewable energy processes. Particularly suited for assessing material flows in renewable energy systems, including energy storage and integration with grid infrastructure.</p>	<p>Mainly used for modelling process efficiency improvements in industrial systems. Umberto is capable of assessing material flows and energy savings in low-carbon production systems, though less commonly applied in macro-level energy transition scenarios.</p>	<p>Excels in process modelling, including energy flows and storage. Can be used to optimize renewable energy systems at an industrial level, especially for integrating renewable energy with existing processes.</p>	<p>Capable of modelling material and energy flows in low-carbon production systems. Best used for process optimization within industries looking to reduce their carbon footprint.</p>	<p>Proprietary and not as adaptable for large-scale energy system decarbonization. Primarily used for industrial applications with limited use in macro-level energy transitions.</p>	[45,46]
Brightway 2	<p>Highly flexible for complex renewable energy systems, including hybrid energy models (e.g., wind-solar-battery systems). Provides extensive customization for researchers focusing on</p>	<p>Ideal for advanced low-carbon economy studies due to its customization. Researchers can model specific decarbonization strategies, such as the integration of renewables with carbon capture</p>	<p>Fully customizable for complex, hybrid renewable energy systems. Ideal for academic research on long-term renewable energy impacts and decarbonization pathways in the</p>	<p>Highly flexible for advanced decarbonization strategies. Ideal for academic and policy studies that require complex, long-term low-carbon economy modelling, particularly in combination</p>	<p>Requires Python coding expertise, making it less accessible for users without a technical background. The steep learning curve, but highly flexible for complex research.</p>	[47,48]

	long-term decarbonization studies and scenario modelling in renewable energy development.	and storage (CCS) or hydrogen fuel cells and assess their long-term impacts on global emissions.	low-carbon economy.	with renewables and CCS technologies.	
OpenEco	Optimized for rapid assessments of renewable energy systems. Often used for small-scale solar and wind energy LCAs with predefined templates, but lacks the capacity for detailed, large-scale modeling of complex energy systems.	Best suited for initial assessments in small-scale low-carbon economy projects. OpenEco can quickly model renewable energy adoption in communities or businesses but lacks the complexity needed for comprehensive national or industry-wide low-carbon transition analyses.	User-friendly and accessible for quick renewable energy assessments. Best suited for small-scale projects or early-stage renewable energy modeling in businesses or communities.	Quickly models small-scale transitions to low-carbon energy solutions. Best used for initial assessments and community-based low-carbon projects, but lacks the depth needed for broader policy or industry-scale applications.	Limited capacity for handling large datasets and complex energy systems. Simplified templates restrict detailed analysis of low-carbon and renewable energy transitions. [49,50]

5. Discussion

Each analyzed tool provides different features and functionalities, suitable for different applications, from small-scale renewable energy assessments to large-scale industrial decarbonization facilities. One of the most significant challenges in interpreting LCA results is managing uncertainty and variability in the data. Especially for renewable energy systems, where regional variations, supply chain complexities, and operational conditions can significantly influence the outcomes. In solar energy systems, the carbon footprint of PV panels can vary depending on the geographic location of the manufacturing site and the energy mix used during production [8,36]. Sensitivity analysis helps identify the parameters that most influence the results, such as the efficiency of solar panels or the energy intensity of the production process. However, conducting these analyses requires tools like OpenLCA and Brightway2, which offer flexibility for scenario modeling and uncertainty quantification [47,48]. It is important to highlight that LCA is used for assessing the environmental impacts of energy systems and identifying the path towards decarbonization. Tools like SimaPro and GaBi are often used for evaluating the lifecycle emissions of industrial-scale energy projects, helping to quantify the benefits of transitioning from fossil fuels to renewable energy sources [19,24,26,34]. These tools provide detailed insights into the environmental impacts of renewable energy technologies, including their effects on air, water, and soil quality. Wind energy, despite its low operational emissions, can have significant land use impacts, which are often highlighted in LCA studies using GaBi or SimaPro [26]. These are important for policymakers who need to balance the environmental benefits of decarbonization with the potential ecological trade-offs. Energy efficiency improvements are important to reducing the environmental impact of industrial processes and energy systems. LCA tools like OpenLCA and Umberto enable detailed assessments of energy efficiency measures, particularly in sectors such as civil engineering and transportation. It was shown that the use of energy-efficient building materials and transportation technologies can be evaluated in terms of their lifecycle energy use and emissions reductions [7]. Identifying the stages of the lifecycle where energy efficiency gains can be made, LCA can show where to put investments in technology and infrastructure that offer the greatest environmental benefits.

Beyond environmental impacts, LCA is used in understanding the socio-economic effects of energy systems, particularly about local communities and energy policies. The adoption of renewable energy technologies can have significant socio-economic benefits, including job creation, energy access, and improved public health outcomes due to reduced air pollution [24]. LCA tools like Brightway2, which allow for complex modeling of socio-economic variables, are ideal for assessing the broader impacts of energy transitions on communities, particularly in the context of low-carbon policies. ISO standards, ISO 14040 and ISO 14044, provide guidelines for conducting and reporting LCA studies. Tools like SimaPro and GaBi, which integrate ISO-compliant reporting formats, help ensure that LCA findings are communicated clearly and are readily usable by stakeholders in energy systems [23,28].

6. Conclusion

Successful examples of LCA reporting in renewable energy projects include studies on wind energy, where the full lifecycle impacts of turbine manufacturing, installation, and operation have been documented. These case studies, often using tools like GaBi or SimaPro, highlight the environmental benefits of wind energy in terms of reduced greenhouse gas emissions, while also addressing concerns related to land use and biodiversity impacts. Such case studies provide results and best practices for future LCA reporting in energy systems. The findings from LCA studies have significant implications for both energy policy and industrial practices. The results of LCIA can inform decisions on how to prioritize investments in renewable energy, energy efficiency, and pollution control measures. But also LCA findings can guide energy policies by identifying the most effective strategies for reducing carbon emissions and promoting sustainable energy transitions. LCA results from tools like OpenLCA or SimaPro can be used to justify investments in renewable energy technologies, energy efficiency measures, or carbon capture and storage. For industries, LCA offers a roadmap for improving energy efficiency, reducing pollution, and integrating renewable energy into production processes. Tools like Umberto, which focus on material and energy flow modeling, provide insights into how industries can optimize their processes to reduce their environmental footprint/ As energy systems become more complex and decarbonization efforts are even more analyzed, LCA tools should evolve to meet these needs. Future developments in LCA software, such as the integration of AI, will improve the ability of users to process large datasets and conduct more sophisticated analyses.

Acknowledgments

This research was financially supported by the Ministry of Science, Technological Development, and Innovation of the Republic of Serbia (Contract No. 451-451-03-65/2024-03). This research was supported by the COST actions CA20133 - Cross-Border Transfer and Development of Sustainable Resource Recovery Strategies Towards Zero Waste and the COST actions CA22124 - EU Circular Economy Network for All: Consumer Protection through reducing, reusing, repairing.

References

- [1] Akhtar, M. S., Khan, H., Liu, J. J., Na, J., Green hydrogen and sustainable development—A social LCA perspective highlighting social hotspots and geopolitical implications of the future hydrogen economy, *Journal of Cleaner Production*, 395 (2023), 136438.
- [2] Barbhuiya, S., Das, B. B., Life Cycle Assessment of construction materials: Methodologies, applications and future directions for sustainable decision-making, *Case Studies in Construction Materials* (2023), e02326.
- [3] Rogelj, J., Den Elzen, M., Höhne, N., Fransen, T., Fekete, H., Winkler, H., Schaeffer R., Sha F., Riahi K., Meinshausen, M., Paris Agreement climate proposals need a boost to keep warming well below 2 C, *Nature*, 534 (2016), 7609, pp. 631-639.
- [4] Rajić, M. N., Maksimović, R. M., Milosavljević, P., Energy management model for sustainable development in hotels within WB6, *Sustainability*, 14 (2022), 24, 16787.
- [5] Rajić, M. N., Maksimović, R. M., Milosavljević, P., Pavlović, D., Energy management system application for sustainable development in wood industry enterprises, *Sustainability*, 12 (2019), 1, 76.
- [6] Baumann, H., Tillman, A. M., *The hitch hiker's guide to LCA (Vol. 1)*, 2004.
- [7] Klöpffer, W., Grahl, B. *Life cycle assessment (LCA): a guide to best practice*. John Wiley & Sons, 2014.
- [8] Hsu, D. D., O'Donoghue, P., Fthenakis, V., Heath, G. A., Kim, H. C., Sawyer, P., Choi, J. K., Turney, D. E., Life cycle greenhouse gas emissions of crystalline silicon photovoltaic electricity generation: systematic review and harmonization, *Journal of Industrial Ecology*, 16 (2012), S122-S135.

- [9] Gerbens-Leenes, P. W., Hoekstra, A. Y., Van der Meer, T. H., The water footprint of energy from biomass: A quantitative assessment and consequences of an increasing share of bio-energy in energy supply, *Ecological economics*, 68 (2009), 4, pp. 1052-1060.
- [10] Saidur, R., Rahim, N. A., Islam, M. R., Solangi, K. H., Environmental impact of wind energy, *Renewable and sustainable energy reviews*, 15 (2011), 5, pp. 2423-2430.
- [11] ISO, Environmental management – Life cycle assessment – Principles and framework (ISO 14040:2006), International Organization for Standardization, 2006.
- [12] ISO, Energy management systems - Requirements with guidance for use (ISO 50001:2018), International Organization for Standardization, 2018.
- [13] Rybaczewska-Błażejowska, M., Jezierski, D., Comparison of ReCiPe 2016, ILCD 2011, CML-IA baseline and IMPACT 2002+ LCIA methods: a case study based on the electricity consumption mix in Europe, *The International Journal of Life Cycle Assessment*, (2024), pp. 1-19.
- [14] Dekker, E., Zijp, M. C., van de Kamp, M. E., Temme, E. H., van Zelm, R., A taste of the new ReCiPe for life cycle assessment: Consequences of the updated impact assessment method on food product LCAs, *The International Journal of Life Cycle Assessment*, 25 (2020), pp. 2315-2324.
- [15] Silva, D., Nunes, A. O., da Silva Moris, A., Moro, C., Piekarski, T. O. R., How important is the LCA software tool you choose Comparative results from GaBi, openLCA, SimaPro and Umberto, In *Proceedings of the VII Conferencia Internacional de Análisis de Ciclo de Vida en Latinoamérica*, Medellin, Colombia, June 2017, pp. 10-15.
- [16] Kalverkamp, M., Karbe, N., Comparability of life cycle assessments: modelling and analyzing LCA using different databases, In *Cascade Use in Technologies 2018: Internationale Konferenz zur Kaskadennutzung und Kreislaufwirtschaft–Oldenburg*, Springer Berlin Heidelberg, 2018, pp. 51-63.
- [17] Shamoushaki, M., Koh, S. L., Comparative life cycle assessment of integrated renewable energy-based power systems, *Science of The Total Environment*, 946 (2024), 174239.
- [18] Laurent, A., Olsen, S. I., Hauschild, M. Z., Limitations of carbon footprint as indicator of environmental sustainability, *Environmental science & technology*, 46 (2012), 7, pp. 4100-4108.
- [19] Rebitzer, G., Ekvall, T., Frischknecht, R., Hunkeler, D., Norris, G., Rydberg, T., Schmidt, W.P., Suh, S., Weidema, B.P., Pennington, D. W., Life cycle assessment: Part 1: Framework, goal and scope definition, inventory analysis, and applications, *Environment international*, 30 (2004), 5, pp. 701-720.
- [20] Curran, M. A., Overview of goal and scope definition in life cycle assessment (pp. 1-62), Springer, Netherlands, 2017
- [21] Finnveden, G., Hauschild, M. Z., Ekvall, T., Guinée, J., Heijungs, R., Hellweg, S., Koehler, A., Pennington, D., Suh, S., Recent developments in life cycle assessment. *Journal of environmental management*, 91 (2009), 1, pp. 1-21.
- [22] RIT Sustainability Institute, What is life cycle assessment (LCA)? RIT Sustainability Institute, Retrieved from <https://www.rit.edu/sustainabilityinstitute/blog/what-life-cycle-assessment-lca>
- [23] Frischknecht, R., Jungbluth, N., Althaus, H. J., Doka, G., Heck, T., Hellweg, S., Hischier, R., Nemecek, T., Rebitzer, G., Spielmann, M., Wernet, G., Overview and Methodology ecoinvent report No. 1. Swiss Centre for Life Cycle Inventories, 2007, Dübendorf.
- [24] Pehl, M., Arvesen, A., Humpenöder, F., Popp, A., Hertwich, E. G., Luderer, G., Understanding future emissions from low-carbon power systems by integration of life-cycle assessment and integrated energy modelling, *Nature Energy*, 2 (2017), 12, pp. 939-945.
- [25] Hauschild, M. Z., Huijbregts, M. A., *Introducing life cycle impact assessment* (pp. 1-16). Springer, Netherlands, 2015
- [26] Goedkoop, M., Heijungs, R., Huijbregts, M., De Schryver, A., Struijs, J., Van Zelm, R., ReCiPe 2008. A life cycle impact assessment method which comprises harmonized category indicators at the midpoint and the endpoint level, 1 (2009), pp. 1-126.
- [27] Suh, S., Yang, Y., On the uncanny capabilities of consequential LCA, *The International Journal of Life Cycle Assessment*, 19 (2014), pp. 1179-1184.
- [28] Frischknecht, R., Birgisdottir, H., Chae, C. U., Lützkendorf, T., Passer, A., Alsema, E., Balouktsi, M., Berg, B., Dowdell, D., García Martínez, A. and Habert, G., Comparison of the environmental assessment of an identical office building with national methods. In *IOP Conference Series: Earth and Environmental Science*, 2019, August, Vol. 323, No. 1, p. 012037, IOP Publishing.
- [29] Heijungs, R., Huijbregts, M. A., A review of approaches to treat uncertainty in LCA, *Environmental Science & Technology*, 38 (2004), 3, pp. 481-490.
- [30] Cherubini, F., Strømman, A. H., Life cycle assessment of bioenergy systems: state of the art and future challenges, *Bioresource technology*, 102 (2011), 2, pp. 437-451.
- [31] Guinée, J. B., Heijungs, R., Huppes, G., Zamagni, A., Masoni, P., Buonamici, R., Ekvall, T., Rydberg, T., Life cycle assessment: past, present, and future, *Environ. Sci. Technol.*, 45 (2011), pp. 90–96.
- [32] Hendrickson, C. T., Lave, L. B., Matthews, H. S., *Environmental life cycle assessment of goods and services: an input-output approach*. Routledge, 2010
- [33] Finkbeiner, M., Inaba, A., Tan, R., Christiansen, K., Klüppel, H. J., The new international standards for life cycle assessment: ISO 14040 and ISO 14044, *The international journal of life cycle assessment*, 11 (2006), pp. 80-85.

- [34] Lenzen, M., Munksgaard, J., Energy and CO₂ life-cycle analyses of wind turbines—review and applications, *Renewable energy*, 26 (2002), 3, pp. 339-362.
- [35] Vestas Wind Systems A/S, Life cycle assessment of offshore and onshore sited wind power plants based on Vestas V90-3.0 MW turbines, 2005
- [36] Fthenakis, V. M., Kim, H. C., Alsema, E., Emissions from photovoltaic life cycles, *Environmental science & technology*, 42 (2008), 6, pp. 2168-2174.
- [37] Cherubini, F., Bird, N. D., Cowie, A., Jungmeier, G., Schlamadinger, B., Woess-Gallasch, S., Energy-and greenhouse gas-based LCA of biofuel and bioenergy systems: Key issues, ranges and recommendations, *Resources, conservation and recycling*, 53 2009, 8, pp. 434-447.
- [38] Searchinger, T. D., Biofuels and the need for additional carbon, *Environmental Research Letters*, 5 (2010), 2) 024007.
- [39] Nautiyal, H., Goel, V., Sustainability assessment of hydropower projects, *Journal of Cleaner Production*, 265 (2020), 121661.
- [40] Yuguda, T. K., Li, Y., Xiong, W., Zhang, W., Life cycle assessment of options for retrofitting an existing dam to generate hydro-electricity, *The International Journal of Life Cycle Assessment*, 25 (2020), pp. 57-72.
- [41] Pomponi, F., Hart, J., The greenhouse gas emissions of nuclear energy—Life cycle assessment of a European pressurised reactor, *Applied Energy*, 290 (2021), 116743.
- [42] Nian, V., Chou, S. K., Su, B., Baully, J., Life cycle analysis on carbon emissions from power generation—The nuclear energy example, *Applied energy*, 118 (2014), pp. 68-82.
- [43] Bahmannia, G., Life cycle assessment (LCA) in oil and gas industries as an effective sustainability development measure: case study, Sarkhoon gas treating plant. In *World Petroleum Congress* (pp. WPC-19), June 2008, WPC.
- [44] David, B. R., Spencer, S., Miller, J., Almahmoud, S., Jouhara, H., Comparative environmental life cycle assessment of conventional energy storage system and innovative thermal energy storage system, *International Journal of Thermofluids*, 12 (2021), 100116.
- [45] Beccali, M., Cellura, M., Iudicello, M., Mistretta, M., Life cycle assessment of Italian citrus-based products. Sensitivity analysis and improvement scenarios, *Journal of Environmental Management*, 91 (2010), 7, pp. 1415-1428.
- [46] Haque, N., The life cycle assessment of various energy technologies. In *Future Energy* (2020), pp. 633-647, Elsevier.
- [47] Wu, S. R., Wang, L., Higher transparency: A desideratum in environmental life cycle assessment research, *Journal of Cleaner Production*, 374 (2022), 134074.
- [48] Zhang, Z., Douziech, M., Perez-Lopez, P., Wang, Q., Yang, Q., Identify Parameters Hindering Renewable Hydrogen Production in France: Life Cycle Sensitivity and Uncertainty Analysis, In *E3S Web of Conferences* (EDP Sciences), 2022, Vol. 350, p. 01021.
- [49] GreenDelta, OpenEco: Open-source LCA software for energy systems, (2017). Retrieved from www.green-delta.com
- [50] Russell, W. G., Abdul-Ali, S., Friend, G., & Lipsky, D., Sustainable enterprise metrics and measurement systems, In *The Sustainable Enterprise Fieldbook*, 2017, pp. 162-202, Routledge.

Thermal Comfort Models for Future Tourism using Heart Rate Variability

Miloš D. Milovančević^a

^aFaculty of Mechanical Engineering, Niš, RS, milos.milovancevic@masfak.ni.ac.rs

Abstract: Current thermal comfort technologies for future tourism, known for their high energy usage, often fall short by creating uniformly neutral conditions that lack efficiency. The key body areas crucial for tourist thermal comfort are the wrists, feet, and head. Thus, there's a pressing need for technologies that specifically target these areas to optimize thermal comfort. Changes in the thermal environment are observed to influence the heart rate variability (HRV) of individuals, indicating fluctuations in their physiological responses to thermal conditions. The primary objective of this study was to identify which HRV indicators significantly affect individual thermal comfort levels. Accurately assessing thermal comfort is essential for energy-efficient environments, yet predicting tourists' thermal comfort proves challenging due to the multitude of influencing factors.

Keywords: Future tourism; Thermal comfort; HRV; Regression; Neuro fuzzy JEL classification: Z31, Z38.

1. Introduction

Thermal comfort, a subjective state reflecting satisfaction with the surrounding thermal conditions, is traditionally catered to by technologies aiming to establish neutral thermal environments for all occupants [1, 2]. This approach, however, lacks efficiency due to the individual differences among occupants, questioning the rationale behind providing uniform thermal conditions, which also leads to higher energy consumption [3]. It is crucial to recognize that thermal comfort is primarily influenced by the temperature of the head, wrists, and feet, rendering the conditioning of other body parts unnecessary for achieving desired thermal comfort levels [4, 5].

The concept of a personal comfort model introduces a tailored approach to thermal comfort, predicting individual responses rather than relying on average population responses, which is essential for the design and control of thermal environments [6]. Current heating, ventilation, and air conditioning (HVAC) systems use an automatic control strategy to set environmental conditions based on design principles or occupant preferences [7]. To understand human thermal comfort across various settings, continuous electrocardiogram (ECG) monitoring in environments with controlled temperature, humidity, and airspeed is utilized [8]. Among the key parameters in the classic human thermal comfort model, metabolic rate stands out for its significance and the general lack of precision in its assessment in both research and practical applications [9]. For subjective thermal comfort assessment, discrete Likert scales are preferred to minimize intra-individual variances [10]. The Pennes bioheat equation has been employed to examine heat conduction in human tissue under standard thermal comfort conditions [11], highlighting the substantial impact of metabolic rate changes on thermal sensation and comfort [12]. Research indicates no notable difference in thermal sensation and comfort between older and younger individuals [13], while another study explored the use of an infrared thermal camera network to gauge skin temperature and predict occupants' thermal preferences from various distances and angles [14]. The design of side interfaces in buildings, affecting air velocity, plays a significant role in thermal comfort, suggesting that enhancing natural ventilation could improve comfort levels [15]. Physiological factors such as age, gender, and body mass index (BMI) also contribute to an individual's thermal comfort in indoor spaces [16]. Air temperature, followed by relative humidity and air velocity, are pivotal in determining the acceptable range of metabolic rate fluctuations within the thermal comfort zone [17]. Current thermal comfort theories emphasize the importance of metabolic rate and clothing insulation in influencing thermal sensation [18].

Given the subjective nature of thermal comfort, aligning comfort measures with physiological signal fluctuations, such as heart rate variability (HRV), offers a more efficient strategy [19]. Changes in the thermal environment are known to affect HRV, signifying fluctuations in physiological responses to thermal conditions

[20, 21]. The study's primary goal is to identify the HRV indices most influential on personal thermal comfort, employing a neuro-fuzzy logic system to address the high nonlinearity between input and output data [22].

2. Methodology

HRV indices, as outlined by the Task Force of the European Society of Cardiology and The North American Society of Pacing and Electrophysiology and later revised by the e-Cardiology ESC Working Group and the European Rhythm Association, play a critical role in this study [23, 24, 25, 26]. The process begins with extracting inter-beat intervals from the ECG signal peaks of each participant. These intervals are then analyzed over a 5-minute moving window to compute HRV samples, which are combined to create a comprehensive dataset. New HRV features are generated from this dataset, and a regression analysis is conducted for each HRV index to assess its correlation with thermal comfort factors. The effectiveness of these indices in predicting thermal comfort is evaluated based on the accuracy of the regression models. Thermal comfort is measured in terms of comfort sensation, thermal sensation, and skin sweat sensation, rated by participants on a 0-10 visual analog scale.

The HRV indices used in this study include:

- MEAN_RR: Mean of all RR intervals (input 1)
- MEDIAN_RR: Median of all RR intervals (input 2)
- SDRR: Standard deviation of all RR intervals (input 3)
- RMSSD: Square root of the mean sum of squares of differences between adjacent RR intervals (input 4)
- SDSD: Standard deviation of differences between adjacent RR intervals (input 5)
- SDRR/RMSSD: Ratio of SDRR to RMSSD (input 6)
- HR: Heart rate in beats per minute (input 7)
- pNN25: Percentage of adjacent RR intervals with more than 25 ms difference (input 8)
- pNN50: Percentage of adjacent RR intervals with more than 50 ms difference (input 9)
- SD1: Short-term HRV Poincaré plot descriptor (input 10)
- SD2: Long-term HRV Poincaré plot descriptor (input 11)
- KURT: Kurtosis of all RR intervals (input 12)
- SKEW: Skewness of all RR intervals (input 13)
- MEAN_REL_RR: Mean of all relative RR intervals (input 14) [27]
- MEDIAN_REL_RR: Median of all relative RR intervals (input 15) [27]
- SDRR_REL_RR: Standard deviation of all relative RR intervals (input 16) [27]
- RMSSD_REL_RR: Square root of the mean sum of squares of differences between adjacent relative RR intervals (input 17) [27]
- SDSD_REL_RR: Standard deviation of differences between adjacent relative RR intervals (input 18) [27]
- SDRR_RMSSD_REL: Ratio of SDRR_REL to RMSSD_REL (input 19)
- KURT_REL_RR: Kurtosis of all relative RR intervals (input 20) [27]
- SKEW_REL_RR: Skewness of all relative RR intervals (input 21) [27]
- VLF: Very low frequency band of the HRV power spectrum (input 22) [28]
- LF: Low frequency band of the HRV power spectrum (input 23) [28]
- HF: High frequency band of the HRV power spectrum (input 24) [28]
- TP: Total power of the HRV spectrum (input 25) [28]
- LF/HF: Ratio of LF to HF (input 26) [28]
- HF/LF: Ratio of HF to LF (input 27) [28]
- Sample entropy of the RR signal (input 28) [29]
- Higuchi Fractal Dimension (input 29) [30]

The outputs from this study include thermal sensation, comfort sensation, and skin sweat sensation, crucial factors in assessing thermal comfort [22, 23].

3. ANFIS methodology

EAs depicted in fig. 1, the Adaptive Neuro-Fuzzy Inference System (ANFIS) architecture is structured into five distinct layers, with the core being the fuzzy inference mechanism. At Layer 1, input variables, denoted as x , are processed through membership functions to be transformed into fuzzy values. In this particular study, the bell-shaped membership function, defined by equation (1), is selected for its superior performance in nonlinear data regression tasks.

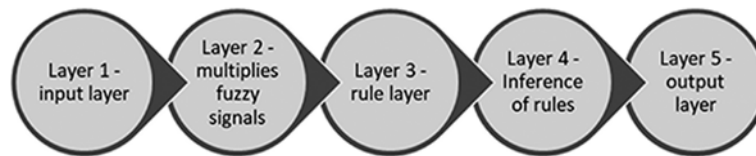


Figure 1: ANFIS layers; Source: [10]

Bell-shaped membership function is defined as follows:

$$\mu(x) = \text{bell}(x; a_i, b_i, c_i) = \frac{1}{1 + \left[\frac{(x - c_i)^2}{a_i} \right]^{b_i}} \quad (1)$$

where $\{a_i, b_i, c_i\}$ is the parameters set and x is input.

Proceeding to Layer 2, the output from the initial layer, which consists of fuzzy values, is subjected to a product operation to determine the firing strength of each rule. Layer 3, often referred to as the rule layer, normalizes these firing strengths, ensuring they are proportionally adjusted across all rules. Layer 4 is responsible for rule inference, where it processes the normalized firing strengths to generate crisp values through defuzzification. Finally, Layer 5 aggregates these crisp values, culminating in a singular output value that represents the system's response to the given inputs.

4. Results

Regression models for the thermal comfort estimation are modeled based on neuro fuzzy logic. There are three thermal comfort outputs: thermal sensation, comfort sensation and skin sweat sensation. Tables 2,3 shows ANFIS regression models of the thermal comfort outputs respectively based on single inputs. There are two root mean square (RMSE) values, one for training and one for testing of the ANFIS model. One can see that the regression model with HR (heart rate) has the smallest training RMSE therefore the highest influence on the each thermal comfort output. fig. 3-5 shows ANFIS predicted relationships between HR and given outputs of the thermal comfort.

Table 1. Thermal Sensation regression models:

MEAN_RR -->	training RMSE=1.8203, testing RMSE=1.8824
MEDIAN_RR -->	training RMSE=1.8159, testing RMSE=1.8835
SDRR -->	training RMSE=2.0252, testing RMSE=2.0497
RMSSD -->	training RMSE=2.0316, testing RMSE=2.0654
SDSD -->	training RMSE=2.0316, testing RMSE=2.0654
SDRR_RMSSD -->	training RMSE=2.0139, testing RMSE=2.0538
HR -->	training RMSE=1.7751, testing RMSE=1.8496
PNN25 -->	training RMSE=2.0427, testing RMSE=2.0428
PNN50 -->	training RMSE=2.0959, testing RMSE=2.1072
SD1 -->	training RMSE=2.0316, testing RMSE=2.0654
SD2 -->	training RMSE=2.0145, testing RMSE=2.0300
KURT -->	training RMSE=2.0279, testing RMSE=2.0531
SKEW -->	training RMSE=2.0188, testing RMSE=2.0518

MEAN_REL_RR --> training RMSE=2.0572, testing RMSE=2.1019
MEDIAN_REL_RR --> training RMSE=1.9891, testing RMSE=2.0216
SDRR_REL_RR --> training RMSE=2.0215, testing RMSE=2.0516
RMSSD_REL_RR --> training RMSE=2.0196, testing RMSE=2.0506
SDSD_REL_RR --> training RMSE=2.0196, testing RMSE=2.0506
SDRR_RMSSD_REL --> training RMSE=2.0484, testing RMSE=2.0777
KURT_REL_RR --> training RMSE=2.0279, testing RMSE=2.0531
SKEW_REL_RR --> training RMSE=2.0188, testing RMSE=2.0518
VLF --> training RMSE=2.0554, testing RMSE=2.0672
LF --> training RMSE=2.0347, testing RMSE=2.0526
HF --> training RMSE=2.0274, testing RMSE=2.0490
TP --> training RMSE=2.0225, testing RMSE=2.0347
LF/HF --> training RMSE=2.0718, testing RMSE=2.1016
HF/LF --> training RMSE=2.0610, testing RMSE=2.0966
Sampan --> training RMSE=2.0063, testing RMSE=2.0479
Higuci --> training RMSE=2.0809, testing RMSE=2.1053

The regression models dedicated to predicting comfort sensation, a critical component of thermal comfort, are developed within an Adaptive Neuro-Fuzzy Inference System (ANFIS) framework. These models are specifically tailored to understand and quantify the influence of various physiological and environmental inputs on the perceived comfort sensation.

For each input variable, a separate ANFIS regression model is constructed, aiming to elucidate the complex interactions between the input and the comfort sensation outcome. The performance of these models is quantitatively evaluated using the Root Mean Square Error (RMSE) metric, which is calculated for both the model's training and testing phases. This dual-phase evaluation provides insights into the model's ability to generalize beyond the training data to unseen inputs.

Notably, the models that incorporate Heart Rate (HR) as a predictive variable consistently exhibit lower RMSE values during the training phase. This trend suggests that HR is a particularly potent predictor of comfort sensation, likely due to its direct correlation with the body's physiological stress and comfort levels.

Table 2. Comfort sensation regression models:

MEAN_RR --> training RMSE=2.5815, testing RMSE=2.6167
MEDIAN_RR --> training RMSE=2.5778, testing RMSE=2.6203
SDRR --> training RMSE=2.7549, testing RMSE=2.7644
RMSSD --> training RMSE=2.7313, testing RMSE=2.7548
SDSD --> training RMSE=2.7313, testing RMSE=2.7548
SDRR_RMSSD --> training RMSE=2.6912, testing RMSE=2.7305
HR --> training RMSE=2.5512, testing RMSE=2.5946
PNN25 --> training RMSE=2.7440, testing RMSE=2.7200
PNN50 --> training RMSE=2.7871, testing RMSE=2.7838
SD1 --> training RMSE=2.7313, testing RMSE=2.7548
SD2 --> training RMSE=2.7609, testing RMSE=2.7596
KURT --> training RMSE=2.7452, testing RMSE=2.7642
SKEW --> training RMSE=2.7493, testing RMSE=2.7626
MEAN_REL_RR --> training RMSE=2.7638, testing RMSE=2.7891
MEDIAN_REL_RR --> training RMSE=2.7633, testing RMSE=2.7655
SDRR_REL_RR --> training RMSE=2.7105, testing RMSE=2.7351
RMSSD_REL_RR --> training RMSE=2.7036, testing RMSE=2.7298
SDSD_REL_RR --> training RMSE=2.7036, testing RMSE=2.7298

SDRR_RMSSD_REL --> training RMSE=2.6784, testing RMSE=2.7103
KURT_REL_RR --> training RMSE=2.7452, testing RMSE=2.7642
SKEW_REL_RR --> training RMSE=2.7493, testing RMSE=2.7626
VLF --> training RMSE=2.7981, testing RMSE=2.7891
LF --> training RMSE=2.7495, testing RMSE=2.7551
HF --> training RMSE=2.7411, testing RMSE=2.7507
TP --> training RMSE=2.7544, testing RMSE=2.7552
LF/HF --> training RMSE=2.7569, testing RMSE=2.7767
HF/LF --> training RMSE=2.7459, testing RMSE=2.7708
Sampan --> training RMSE=2.7211, testing RMSE=2.7399
Higuci --> training RMSE=2.7795, testing RMSE=2.7842

Table 3. Skin sweat sensation regression models:

MEAN_RR --> training RMSE=2.7382, testing RMSE=2.7635
MEDIAN_RR --> training RMSE=2.7493, testing RMSE=2.7789
SDRR --> training RMSE=3.0138, testing RMSE=2.9876
RMSSD --> training RMSE=3.0306, testing RMSE=3.0181
SDSD --> training RMSE=3.0306, testing RMSE=3.0181
SDRR_RMSSD --> training RMSE=2.9708, testing RMSE=2.9597
HR --> training RMSE=2.6275, testing RMSE=2.6628
PNN25 --> training RMSE=2.8857, testing RMSE=2.8250
PNN50 --> training RMSE=2.9722, testing RMSE=2.9099
SD1 --> training RMSE=3.0306, testing RMSE=3.0181
SD2 --> training RMSE=2.9827, testing RMSE=2.9497
KURT --> training RMSE=2.9822, testing RMSE=2.9635
SKEW --> training RMSE=2.9807, testing RMSE=2.9665
MEAN_REL_RR --> training RMSE=3.0366, testing RMSE=3.0291
MEDIAN_REL_RR --> training RMSE=3.0285, testing RMSE=3.0101
SDRR_REL_RR --> training RMSE=3.0308, testing RMSE=3.0188
RMSSD_REL_RR --> training RMSE=3.0262, testing RMSE=3.0165
SDSD_REL_RR --> training RMSE=3.0262, testing RMSE=3.0165
SDRR_RMSSD_REL --> training RMSE=2.9981, testing RMSE=2.9735
KURT_REL_RR --> training RMSE=2.9822, testing RMSE=2.9635
SKEW_REL_RR --> training RMSE=2.9807, testing RMSE=2.9665
VLF --> training RMSE=3.0217, testing RMSE=2.9837
LF --> training RMSE=3.0299, testing RMSE=3.0114
HF --> training RMSE=3.0317, testing RMSE=3.0124
TP --> training RMSE=3.0128, testing RMSE=2.9926
LF/HF --> training RMSE=3.0671, testing RMSE=3.0394
HF/LF --> training RMSE=3.0460, testing RMSE=3.0326
Sampan --> training RMSE=2.9747, testing RMSE=2.9670
Higuci --> training RMSE=3.0852, testing RMSE=3.0473

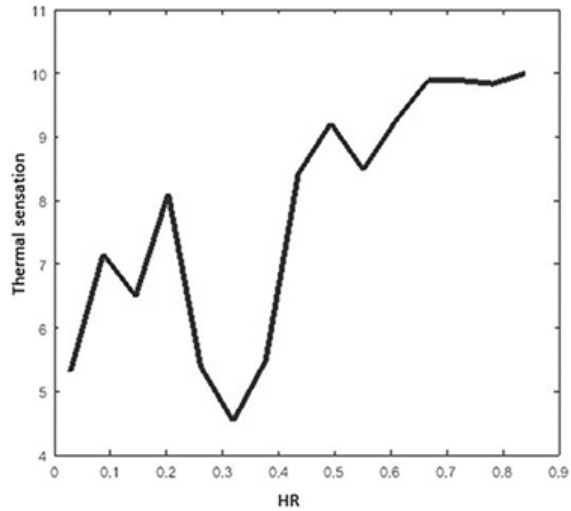


Figure 2: ANFIS predicted relationship between HR and thermal sensation
Source: Authors' own work

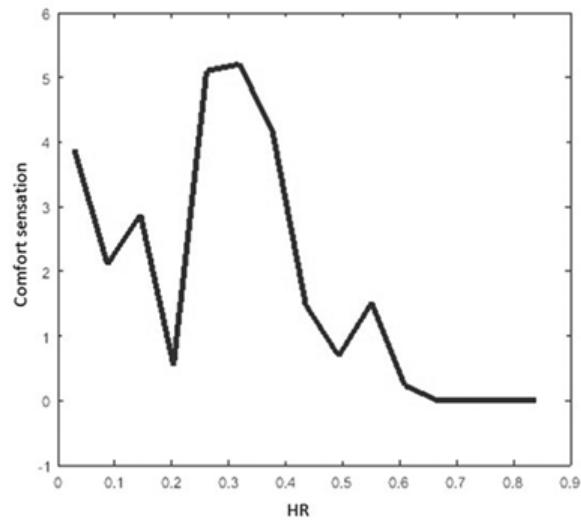


Figure 3: ANFIS predicted relationship between HR and comfort sensation
Source: Authors' own work

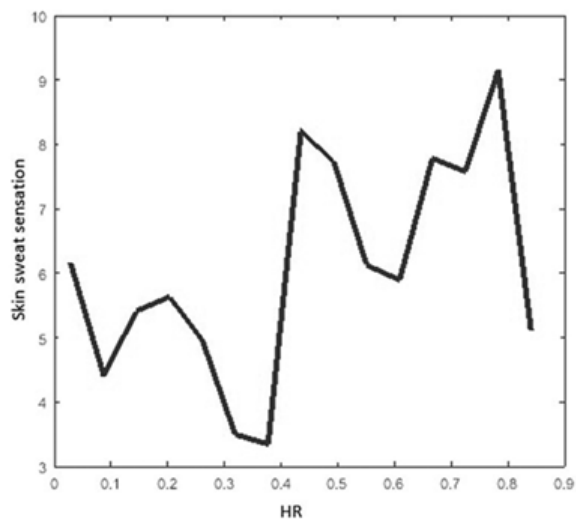


Figure 4: ANFIS predicted relationship between HR and skin sweat sensation
Source: Authors' own work

5. Conclusion

The prevailing approaches to achieving thermal comfort within architectural spaces predominantly revolve around the comprehensive conditioning of entire rooms, either by cooling or heating. This method, while widespread, exhibits significant inefficiencies in energy consumption due to its lack of personalization; it does not account for the individual thermal comfort requirements of each occupant within a space. The nuanced nature of human thermal comfort, inherently subjective and psychophysiological, is influenced by a myriad of factors that vary from one individual to another. Notably, alterations in the thermal environment have been observed to induce variations in the heart rate variability (HRV) of individuals, suggesting a direct link between one's physiological state and their thermal surroundings.

Acknowledging the complex interplay between the thermal environment and physiological responses, this research endeavors to pinpoint specific HRV indices that hold the most substantial influence over individual thermal comfort perceptions. The premise of this study rests on the understanding that thermal comfort transcends mere physical parameters; it is a psychophysiological sensation shaped by diverse and unpredictable elements, rendering broad-brush predictive models inadequate for capturing the intricacies of personal thermal comfort experiences.

To navigate the complexities of this subject, the study adopts neuro-fuzzy logic as its analytical framework. This choice is motivated by the technique's proficiency in managing nonlinear data pairings, a common characteristic of the variables involved in thermal comfort studies. Neuro-fuzzy logic, with its ability to blend the interpretability of fuzzy logic with the learning capabilities of neural networks, provides a robust tool for dissecting the nuanced relationships between HRV indices and thermal comfort.

Through a meticulous analysis, the research unveils that among the various physiological indicators, the heart rate, measured in beats per minute, emerges as the predominant factor affecting an individual's thermal comfort. This finding underscores the critical role of cardiovascular responses in the subjective experience of thermal comfort and highlights the potential for personalized thermal comfort solutions that prioritize energy efficiency and individual well-being.

References

- [1] Nkurikiyeyezu, K. (2019). An efficient thermal comfort delivery in workplaces. 2019 IEEE International Conference on Pervasive Computing and Communications Workshops (PerCom Workshops), 427–428. <https://doi.org/10.1109/PERCOMW.2019.8730680>
- [2] Nkurikiyeyezu, K., Yokokubo, A., & Lopez, G. Affect-aware thermal comfort provision in intelligent buildings.
- [3] Nkurikiyeyezu, K., Yokokubo, A., & Lopez, G. (2019). Importance of individual differences in physiological-based stress recognition models.
- [4] Lopez, G., Kawahara, Y., Suzuki, Y., Takahashi, M., Takahashi, H., & Wada, M. (2016). Effect of direct neck cooling on psychological and physiological state in summer heat environment. *Mechanical Engineering Journal*, 3(1), 15-00537.
- [5] Nkurikiyeyezu, K., Yokokubo, A., & Lopez, G. (2019). Importance of individual differences in physiological-based stress recognition models. 2019 15th International Conference on Intelligent Environments (IE). Rabat: IEEE.
- [6] Liu, S., Schiavon, S., Das, H. P., Jin, M., & Spanos, C. J. (2019). Personal thermal comfort models with wearable sensors. *Building and Environment*, 106281.
- [7] Li, W., Zhang, J., & Zhao, T. (2019). Indoor thermal environment optimal control for thermal comfort and energy saving based on online monitoring of thermal sensation. *Energy and Buildings*, 197, 57-67.
- [8] Zhu, H., Wang, H., Liu, Z., Li, D., Kou, G., & Li, C. (2018). Experimental study on the human thermal comfort based on the heart rate variability (HRV) analysis under different environments. *Science of the Total Environment*, 616, 1124-1133.
- [9] Luo, M., Wang, Z., Ke, K., Cao, B., Zhai, Y., & Zhou, X. (2018). Human metabolic rate and thermal comfort in buildings: the problem and challenge. *Building and Environment*, 131, 44-52.
- [10] Wang, J., Wang, Z., de Dear, R., Luo, M., Ghahramani, A., & Lin, B. (2018). The uncertainty of subjective thermal comfort measurement. *Energy and Buildings*, 181, 38-49.
- [11] Marn, J., Chung, M., & Iljaž, J. (2019). Relationship between metabolic rate and blood perfusion under Fanger thermal comfort conditions. *Journal of thermal biology*, 80, 94-105.
- [12] Ji, W., Luo, M., Cao, B., Zhu, Y., Geng, Y., & Lin, B. (2018). A new method to study human metabolic rate changes and thermal comfort in physical exercise by CO₂ measurement in an airtight chamber. *Energy and Buildings*, 177, 402-412.
- [13] Soebarto, V., Zhang, H., & Schiavon, S. (2019). A thermal comfort environmental chamber study of older and younger people. *Building and Environment*, 155, 1-14.

- [14] Li, D., Menassa, C. C., & Kamat, V. R. (2019). Robust non-intrusive interpretation of occupant thermal comfort in built environments with low-cost networked thermal cameras. *Applied Energy*, 251, 113336.
- [15] Huang, X., Ma, X., & Zhang, Q. (2019). Effect of building interface form on thermal comfort in gymnasiums in hot and humid climates. *Frontiers of Architectural Research*, 8(1), 32-43.
- [16] Thapa, S. (2019). Insights into the thermal comfort of different naturally ventilated buildings of Darjeeling, India—effect of gender, age and BMI. *Energy and Buildings*, 193, 267-288.
- [17] Yang, C., Yin, T., & Fu, M. (2016). Study on the allowable fluctuation ranges of human metabolic rate and thermal environment parameters under the condition of thermal comfort. *Building and Environment*, 103, 155-164.
- [18] Choi, J. H., Loftness, V., & Lee, D. W. (2012). Investigation of the possibility of the use of heart rate as a human factor for thermal sensation models. *Building and Environment*, 50, 165-175.
- [19] Lopez, G., Tokuda, T., Oshima, M., Nkurikiyeyezu, K., Isoyama, N., & Itao, K. (2018). Development and Evaluation of a Low-Energy Consumption Wearable Wrist Warming Device. *International Journal of Automation Technology*, 12(6), 911-920.
- [20] Nkurikiyeyezu, K. N., Suzuki, Y., & Lopez, G. F. (2018). Heart rate variability as a predictive biomarker of thermal comfort. *Journal of Ambient Intelligence and Humanized Computing*, 9(5), 1465-1477.
- [21] Schnell, I., Potchter, O., Epstein, Y., Yaakov, Y., Hermesh, H., Brenner, S., & Tirosh, E. (2013). The effects of exposure to environmental factors on heart rate variability: An ecological perspective. *Environmental pollution*, 183, 7-13.
- [22] Jang, J.-S.R, ANFIS: Adaptive-Network-based Fuzzy Inference Systems, IEEE Trans. On Systems, Man, and Cybernetics (1993), Vol.23, 665-685.
- [23] <https://www.kaggle.com/qiriro/comfort/version/4>
- [24] Nkurikiyeyezu, K., Yokokubo, A., & Lopez, G. (2019). Affect-aware thermal comfort provision in intelligent buildings. 8th International Conference on Affective Computing & Intelligent Interaction (ACII 2019). Cambridge, United Kingdom: IEEE.
- [25] Camm, A. J., Malik, M., Bigger, J. T., Breithardt, G., Cerutti, S., Cohen, R. J., ... & Lombardi, F. (1996). Heart rate variability: standards of measurement, physiological interpretation and clinical use. Task Force of the European Society of Cardiology and the North American Society of Pacing and Electrophysiology.
- [26] Sassi, R., Cerutti, S., Lombardi, F., Malik, M., Huikuri, H. V., Peng, C. K., ... & Lip, G. Y. (2015). Advances in heart rate variability signal analysis: joint position statement by the e-Cardiology ESC Working Group and the European Heart Rhythm Association co-endorsed by the Asia Pacific Heart Rhythm Society. *Ep Europace*, 17(9), 1341-1353.
- [27] Vollmer, M. (2015, September). A robust, simple and reliable measure of heart rate variability using relative RR intervals. In *2015 Computing in Cardiology Conference (CinC)* (pp. 609-612). IEEE.
- [28] Malik, M., Bigger, J. T., Camm, A. J., Kleiger, R. E., Malliani, A., Moss, A. J., & Schwartz, P. J. (1996). Heart rate variability: Standards of measurement, physiological interpretation, and clinical use. *European heart journal*, 17(3), 354-381.
- [29] Gomes, R. L., Vanderlei, L. C. M., Garner, D. M., Vanderlei, F. M., & Valenti, V. E. (2017). Higuchi fractal analysis of heart rate variability is sensitive during recovery from exercise in physically active men. *MedicalExpress*, 4(3).
- [30] Sassi, R., Cerutti, S., Lombardi, F., Malik, M., Huikuri, H. V., Peng, C. K., ... & Lip, G. Y. (2015). Advances in heart rate variability signal analysis: joint position statement by the e-Cardiology ESC Working Group and the European Heart Rhythm Association co-endorsed by the Asia Pacific Heart Rhythm Society. *Ep Europace*, 17(9), 1341-1353.

Is There a Circular Economy Business Model That can be Easily Implemented?

Ana Kitić^a, Miloš Milovančević^a

^aFaculty of Mechanical Engineering, Niš, RS, ana.kitic@masfak.ni.ac.rs

Abstract: Strategic management, operations management, and technology management are just a few of the areas where the circular economy concept is gaining more and more attention. It requires that businesses create their business models around a new idea of sustainable development that reduces resource consumption and protects the environment. This includes the value network, interactions with supply chain partners, and value offerings to customers. Existing research, however, falls short of fully describing how businesses design their business models in accordance with the concepts of the circular economy. This paper presents an overview of the current business models of the circular economy.

Keywords: circular economy, business model, value, environment, strategic management

1. Introduction

The most developed economies in the world and, more recently, some of the biggest businesses worldwide, are adopting this model more frequently. The three guiding principles of this concept, 3R (reducing, reusing, and recycling), speak to its core. The circular economy concept has both economic and environmental implications as its end result. cost-saving measures include resuming the manufacture of used materials and lowering trash production, which has a positive influence on the environment.

In the process of implementing the circular economy, certain business models or circular business models are available to states. Business models by definition are instruments that understand how a company operates, and can be used for various analysis, comparisons and performance evaluations [1].

In order to apply the circular economy, managers had to apply certain managerial practices, and at the same time include: value creation, value transfer and capture value. There are three factors that are important when applying the circular economy, the first factor is the role of policy makers or international institutions, the second factor is to support the creation, transfer and capture of value in the circular economy, it is important to understand the importance of Industry 4.0 which could be supports the implementation of the circular economy and the third factor is that the implementation of the circular economy requires constant monitoring of the achieved goals of the circular economy. [2]

When we discuss the main challenges to the practical application of the circular economy, we primarily refer to the scarcity of accurate data and information, the absence of cutting-edge technologies, the lack of strong or even nonexistent economic incentives, the poor application of laws, the management and management of the development strategy, the lack of public awareness of the benefits and promises of the circular economy, and the absence of a comprehensive circular system for evaluating the effects of the circular economy. [3] As for the design of circular business models, the existing literature has identified several business activities related to the circular economy and some guidelines on how to adapt the existing business model to this "newly composed" business model. While existing business model frameworks can be used to apply circular economy principles, hardly any study has identified how circular economy principles can be applied to each component of a business model framework. Therefore, there is a need for a comprehensive conceptual framework for a circular business model that would support practitioners in the transition of their jobs to a circular economy. [4]

Value creation, value transfer, and value capture are the three basic conceptual categories that appear in the literature. If we take into account these dimensions of the circular economy, the question arises whether it is possible to define all the actions that a nation or company needs to take in order to introduce a circular economy?

2. Business model canvas vs Circular Business model canvas

2.1 Business model canvas

A business model simply explains how an organization creates value, delivers it to customers, and captures value for itself (Osterwalder and Pigneur, 2010). A business model is one of the critical topics that deals with creating a business model and transitioning from an existing model to a new one (De Reuver, Bouwman and Haaker, 2013; Murray and Scuotto, 2016). One of the practical and strategic questions is the transition to a new business model, which means that existing value propositions for clients need to be replaced with new ones, how to acquire new resources and capabilities, and whether to start or terminate partnerships (De Reuver, Bouwman and Haaker, 2013). Certain authors have utilized the business model canvas to develop strategies for business growth. The business model canvas and SWOT analysis were employed. By using these two tools, weaknesses and threats were leveraged to create an appropriate strategy (Mustaniroh, Prabaningtias and Citraresmi, 2020). Based on this study, it is clear that a business model does not have to be standalone; it can also be used to create better strategies for strengthening a company's position.

2.1.2 The Framework of the Business Model Canvas

A popular framework for organizing business models is the Business Model Canvas (BMC), which was developed by Osterwalder and Pigneur is presented in the following figure. The BMC consists of nine building blocks that focus on different aspects of how value is created, delivered, and captured.

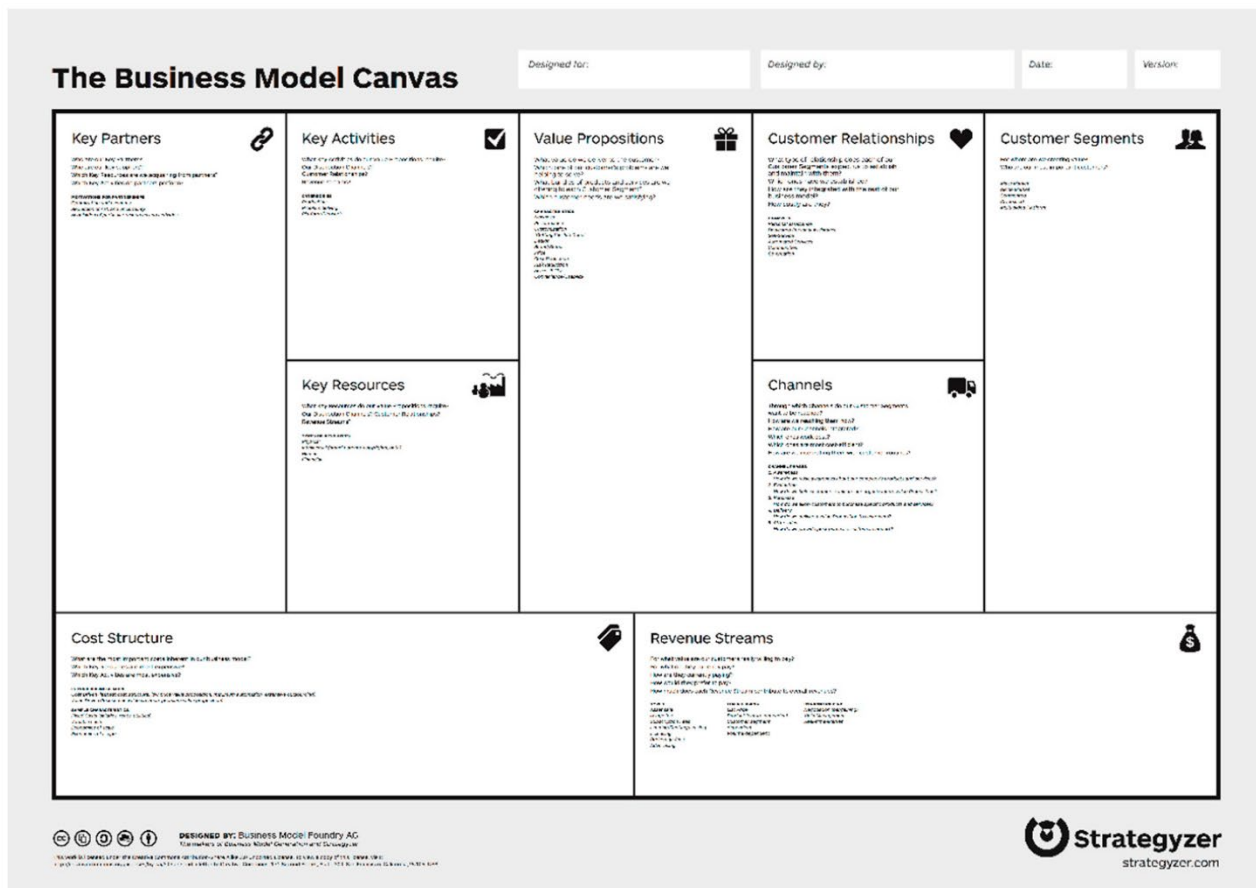


Figure 1 A framework of the Business Model Canvas(Osterwalder and Pigneur, 2010)

- Customer Segments: For whom is the organization creating value? What products and services are the organization offering to each customer segment?
- Value Proposition: What value is the organization delivering to its customers? Which customer pain-points are the organization addressing?
- Channels: Which channels are the organization using to reach the desired customer segments? How are those channels integrated? Which ones are the most cost-effective?

- **Customer Relationships:** What type of relationship does the organization maintain with each customer segment? What are the expectations of the customers? How does the organization establish those relationships?
- **Revenue Streams:** How does the organization make money? Who are the customers willing to pay and for what benefit? How do they prefer to pay? How are they currently paying? How does each stream add up to the total revenue, i.e., asset sale, subscription fees, leasing, licensing, advertising, etc.?
- **Key Activities:** What are the key activities the organization's value proposition require?
- **Key Resources:** What key resources does the organization's value proposition require?
- **Key Partners:** The organization's key partners and suppliers. Which key resources do the organization acquires from them? Which key activities does the organization's partners perform?
- **Cost Structure:** What are the most important cost drivers in the organization's business model? Which key resources and activities are most expensive?

This structure of the BMC allows organizations to develop innovative business models by redesigning the contents of any one of its nine blocks to uncover new business opportunities and turn customers' needs into profitable activities. (Giourka *et al.*, 2019)

2.2 The Framework of the Circular Business Model Canvas

The circular business model canvas builds on and adapts the traditional business model canvas developed by (Osterwalder and Pigneur, 2010), incorporating principles of the circular economy. It consists of 11 components, one of which includes three sub-components. These building blocks help design business models aligned with circular economy principles and include:

1. **Value propositions:** Circular products that enable product-life extension, product-service systems, virtualized services, and collaborative consumption. This component also includes incentives for customers to return used products.
2. **Customer segments:** Directly linked to the value propositions, focusing on aligning offerings with specific customer needs and preferences.
3. **Channels:** Can be virtual, enabling the sale and delivery of virtualized value propositions, or using virtual channels for non-virtual products and customer communication.
4. **Customer relationships:** Emphasizes production based on customer demand, social marketing strategies, and collaboration with community partners, especially when implementing advanced recycling systems (Recycling 2.0).
5. **Revenue streams:** Based on circular products or services, with payments tied to availability, usage, or performance. Additional revenue may come from the value of resources recovered from material loops.
6. **Key resources:** Focuses on sourcing better-performing materials, virtualizing resources, regenerating natural capital, and using resources from customers or third parties to maintain closed material loops.
7. **Key activities:** Aims to boost performance through efficient practices, technological upgrades, product redesign for better recyclability, and eco-friendliness. It may also involve advocacy and lobbying.
8. **Key partnerships:** Collaborating with value and supply chain partners who support circular economy initiatives.
9. **Cost structure:** Reflects financial implications of the circular model, including customer incentives. It requires special evaluation criteria and accounting methods.
10. **Take-back system:** Designing systems for managing product returns, including associated channels and customer interactions.
11. **Adoption factors:** Successful transition to a circular business model depends on organizational capabilities and external support factors.
12. These components ensure that the circular business model integrates sustainability throughout the value chain. (Lewandowski, 2016)

Partners <ul style="list-style-type: none"> Cooperative networks Types of collaboration 	Activities <ul style="list-style-type: none"> Optimising performance Product Design Lobbying Remanufacturing, recycling Technology exchange Key Resources <ul style="list-style-type: none"> Better-performing materials Regeneration and restoring of natural capital Virtualization of materials Retrieved Resources (products, components, materials) 	Value Proposition <ul style="list-style-type: none"> PSS Circular Product Virtual service Incentives for customers in Take-Back System 	Customer Relations <ul style="list-style-type: none"> Produce on order Customer vote (design) Social-marketing strategies and relationships with community partners in Recycling 2.0 Channels <ul style="list-style-type: none"> Virtualization Take-Back System <ul style="list-style-type: none"> Take-back management Channels Customer relations 	Customer Segments <ul style="list-style-type: none"> Customer types
Cost Structure <ul style="list-style-type: none"> Evaluation criteria Value of incentives for customers Guidelines to account the costs of material flow 		Revenue Streams <ul style="list-style-type: none"> Input-based Availability-based Usage-based Performance-based Value of retrieved resources 		
Adoption Factors <ul style="list-style-type: none"> Organizational capabilities PEST factors 				

Figure 2 A framework of the circular business model canvas (Lewandowski, 2016)

3. Value creation bases

The concept of the "power of the inner circle" emphasizes prolonging the lifespan of products, ideally with the original owner or user. This involves ensuring products remain functional through straightforward maintenance, repairs, and updates. Effective product design and supportive business models are crucial to maximizing this opportunity. The inner circles of reuse and maintenance offer significant potential for profitability, as they yield greater savings in materials, labor, energy, and capital, while also reducing environmental impacts such as greenhouse gas emissions and resource consumption. (MacArthur, 2013)

The "power of circling longer" focuses on extending the number of consecutive cycles a product can go through and maximizing the duration of each cycle. For durable goods like cars, manufacturers can achieve this by ensuring long initial use through high-quality production, easy repairs, upgrades, or service programs that keep the product in excellent condition. Once the product's first life ends, it can continue serving subsequent users, benefiting from the same support systems. Eventually, the product can be repurposed for spare parts or its components can be reused to create new products. This approach aligns with the principle of cascaded use, which involves maximizing value extraction from products and materials. For consumables, different strategies may be more suitable. For instance, while soft drink cans or bottles have short lifespans with users, resource optimization can still be achieved by selecting the right packaging materials and implementing efficient return systems. Glass bottles, for example, can be reused about 27 times before recycling, while aluminum cans are typically recycled after a single use. However, due to material losses during each recycling loop, even at a 50% recycling rate, the original aluminum is lost after 17 cycles. Increasing the recycling rate to 90% extends this to 35 cycles. Despite practical considerations such as convenience, glass offers superior resource conservation in comparison. (MacArthur, 2013)

For energy-consuming products, the environmental benefits of repairing versus replacing must be weighed against the improved energy efficiency of newer models. For example, white goods like refrigerators, freezers, washing machines, and dishwashers with an energy efficiency rating of B or better should generally be repaired rather than replaced, as this yields better environmental performance. However, products with a C rating or lower should be replaced with more efficient models. For mobile air-conditioning units and tumble dryers, a C rating or better is sufficient to justify repairs over replacement. (MacArthur, 2013)

The "power of cascaded use" is another principle companies can leverage in circular business models. This involves diversifying the reuse of products and materials across different industries. Textiles illustrate this well: clothing can first be reused as second-hand apparel, then repurposed as upholstery in the furniture industry, and eventually used as insulation material in construction. Each step reduces the need for virgin materials, cutting raw material costs for businesses. (MacArthur, 2013)

Lastly, the "power of pure circles" emphasizes the importance of uncontaminated material streams to preserve material quality over multiple cycles. Using cleaner, purer materials aligns with established ecodesign principles and remains crucial for maintaining the sustainability of circular systems. (MacArthur, 2013; Guldmann, 2016; Widmer, 2016)

3.1 Five distinct types of circular business models

Drawing from an analysis of over 120 circular economy case studies across industries such as high-tech, textiles, automotive, and consumer goods, has identified five key types of circular business models. These models are: circular supplies, resource recovery, product life extension, sharing platforms, and product-as-a-service. Each represents a distinct approach to embedding circular economy principles into business operations. (Lacy, 2014)

On the following image, we can see how the circular business model connects with these four value bases. The left side outlines these value bases, while the top row lists the five generic business models, starting with "circular supplies." The colored sections highlight shared principles between the value bases proposed by the (MacArthur, 2013 and the business model archetypes identified by Lacy, 2014.

Table 1 Interlinkages between five business models and four principles of value creation. (Guldmann, 2016)

	Circular supplies	Resource recover	Product life extension	Sharing platforms	Product as a service
Inner circle					
Circling longer					
Cascaded use					
Pure circles					

Lacy, 2014 outlines five distinct circular business models, each aligned with core principles of circular value creation:

1. **Circular Supplies:** This model focuses on replacing scarce resources with renewable, recyclable, or biodegradable materials while minimizing waste and inefficiencies. It is particularly relevant for industries with a significant environmental footprint and is closely linked to the principles of *circling longer* and *pure circles*.
2. **Resource Recovery:** Emphasizing the capture of embedded value from end-of-life products, this model leverages innovative recycling and upcycling processes, such as industrial symbiosis and Cradle-to-Cradle certified systems. It aligns with the principles of *pure circles*, *circling longer*, and *cascaded use*.
3. **Product Life Extension:** This model extends the lifecycle of products through repair, upgrades, remanufacturing, and resale. It is particularly suitable for capital-intensive industries and consumer markets where new product iterations offer marginal performance improvements. The value creation is grounded in the principles of the *inner circle* and *circling longer*.
4. **Sharing Platforms:** By facilitating the shared use of underutilized products or assets, this model promotes increased productivity and efficiency. It is commonly adopted by companies that do not manufacture the shared products themselves but can also be relevant for manufacturers. This model supports the principles of the *inner circle* and *circling longer*.
5. **Product as a Service:** Offering products through leasing or pay-per-use arrangements, this model ensures product durability and upgradability. It transforms traditionally perceived risks, such as product longevity and reusability, into revenue-generating opportunities. This approach aligns with the principles of the *inner circle* and *circling longer*.

These models provide a structured framework for integrating circular economy principles into business operations, highlighting opportunities for sustainable value creation. (Lacy, 2014)

4. Conclusion

The Circular Economy (CE) has proven successful in engaging the business community with sustainable development initiatives. The concept is compelling because it recognizes the inherent value of natural resources. Rather than using these resources just once, as is common in the traditional linear economic model, CE encourages their repeated use, adding value through multiple cycles. This approach not only makes sound business sense but also offers a clear environmental advantage. By maximizing the utility of resources, companies reduce the need for virgin materials, thereby minimizing waste and emissions associated with production processes. This cyclical use of resources aligns economic activities with sustainability goals, making it a rational and strategic choice for businesses. (Korhonen, Honkasalo and Seppälä, 2017)

While the circular economy presents exciting opportunities, it is not without its challenges. One of the main barriers to implementing a circular business model is the need for collaboration and systemic change across the value chain. Transitioning to a circular economy requires cooperation among multiple stakeholders, including manufacturers, suppliers, distributors, consumers, and policymakers. This level of collaboration can be complex and challenging, as it involves rethinking traditional business relationships, supply chains, and regulatory frameworks.

Another challenge lies in the economic viability of circular business models. Implementing circular practices often requires upfront investments in infrastructure, technology, and new business processes. These costs can be a deterrent for companies, particularly small and medium-sized enterprises (SMEs) with limited financial resources. Overcoming this barrier requires financial incentives, supportive policies, and access to funding mechanisms that encourage and reward circular practices.

Furthermore, consumer behavior and attitudes play a significant role in the success of the circular economy. While there is a growing awareness and demand for sustainable products and services, consumer preferences and behaviors are still largely influenced by convenience, affordability, and short-term value. Shifting consumer perceptions and behaviors towards a circular mindset requires education, awareness campaigns, and clear communication about the environmental and economic benefits of the circular economy.

References

- [1] Giourka, P. et al. (2019) 'The smart city business model canvas—A smart city business modeling framework and practical tool', *Energies*, 12(24)
- [2] Guldman, E. (2016) Best Practice Examples of Circular Business Models. Available at: www.mst.dk/english.
- [3] Korhonen, J., Honkasalo, A. and Seppälä, J. (2017) Circular Economy: The Concept and its Limitations. Available at: www.elsevier.com/locate/ecocon.
- [4] Lacy, P., K.J., M.R., R.J., H.T., C.M. and B.P. (2014) 'Circular Advantage: Innovative Business Models and Technologies to Create Value in a World without Limits to Growth/Accenture'
- [5] Lewandowski, M. (2016) 'Designing the business models for circular economy-towards the conceptual framework', *Sustainability (Switzerland)*. MDPI
- [6] MacArthur, F.E. (2013) *Towards the circular economy Vol. 1: an economic and business rationale for an accelerated transition*.
- [7] Murray, A. and Scuotto, V. (2016) 'The Business Model Canvas', *Symphonya. Emerging Issues in Management*, pp. 94–109.
- [8] Mustaniroh, S.A., Prabaningtias, N. and Citraresmi, A.D.P. (2020) 'Analysis of Business Development Strategies with Business Model Canvas Approach', in *IOP Conference Series: Earth and Environmental Science*. Institute of Physics Publishing.
- [9] Osterwalder, A. and Pigneur, Y. (2010) *Business model generation: a handbook for visionaries, game changers, and challengers*.
- [10] De Reuver, M., Bouwman, H. and Haaker, T. (2013) 'Business model roadmapping: A practical approach to come from an existing to a desired business model', in *International Journal of Innovation Management*. World Scientific.
- [11] Widmer, T. (2016) 'Assessing the strengths and limitations of Business Model Frameworks for Product Service Systems in the Circular Economy: Why Canvas and co. are not enough'.



Notes



The 21st International Conference on
Thermal Science and Engineering of Serbia

SimTerm2024

Niš, Serbia, October 22-25

